N84-13067
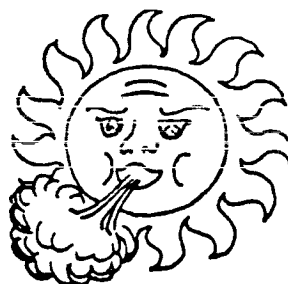
NASA Conference Publication 2280

Solar
Wind
Five

Proceedings of a conference held in
Woodstock, Vermont
November 1-5, 1982

25

NASA

25th Anniversary
1958-1983

Solar Wind Five

Edited by
Marcia Neugebauer
Jet Propulsion Laboratory
Pasadena, California

The fifth solar wind conference was held at the Woodstock Inn, Woodstock, Vermont, November 1-5, 1982. It followed the successful pattern set by earlier solar wind conferences in Pasadena, California, in 1964, in Asilomar, California, in 1971 and 1974, and in Berghausen, Federal Republic of Germany, in 1978.

Solar Wind Five was the first solar wind conference to be held as an AGU Chapman Conference. These topical conferences are a memorial to Sidney Chapman, who was one of the pioneers of solar wind research. Chapman not only attended the first solar wind conference, but also wrote the foreward to the Proceedings of that meeting. This time we have no volunteer to summarize the entire meeting and put it into perspective. We have instead obtained brief summaries of some of the sessions, usually written by the session chairman.

Detailed plans for Solar Wind Five began to take place at an organizational meeting in Baltimore in June, 1981. A rather informal organizing committee consisting of A. Barnes, J. Belcher, D. Bohlin, L. Burlaga, R. Carovillano, M. Dobrowolny, L. Fisk, J. Gosling, J. Hollweg, A. Lazarus, M. Neugebauer, K. Ogilvie, R. Rosner, C. Russell, G. Siscoe, R. Schwenn and E. Smith gave advice, both at that meeting and through the mail. Most of the real work of organizing the technical aspects of the conference, rounding up papers for the Proceedings, and getting the papers refereed was done by the Program Chairmen. These people worked hard, and much of the success of the conference was due to their efforts. They are:

Solar corona: J. Hollweg and G. Withbroe
MHD waves and turbulence: A. Barnes and K. Denskat
Acceleration of the solar wind: T. Holzer and J. Belcher
Stellar coronae and winds: R. Rosner and E. Leer
Long-term variations: J. Feynman and G. Siscoe
Energetic particles: L. Fisk
Plasma distribution functions and waves: W. Feldman, M. Dobrowolny, and E. Marsch
Spatial dependences: E. Smith, V. Pizzo, and R. Schwenn
Minor ions: K. Ogilvie
Dynamics: J. Gosling and L. Burlaga

The logistics of the Conference were very ably handled by Anne Greenglass and her staff at the American Geophysical Union and Anne Bowes of MIT.

V. Pizzo of the High Altitude Observatory has volunteered to organize Solar Wind Six a few years hence.

Alan Lazarus
Marcia Neugebauer
May 27, 1983

TABLE OF CONTENTS

SESSION 3. SOLAR WIND ACCELERATION

Organizers: T. Holzer, J. Belcher
Chairman: R. MacQueen

SESSION 6. PLASMA DISTRIBUTION FUNCTIONS AND WAVES

Organizers: W. Feldman, M. Dobrowolny, E. Marsch
Chairman: H. Rosenbauer

SESSION 9. MINOR IONS

Organizer: K. Ogilvie
Chairman: D. Bohlin

SESSION 10. DYNAMICS

Organizers: J. Gosling, L. Burlaga
Chairman: J. Gosling

SESSION 1.

SOLAR CORONA

Page intentionally left blank

SUMMARY OF THE SESSION ON THE SOLAR CORONA

Joseph V. Hollweg

SW5 began characteristically with a look at the source of the problem: the solar corona. Several methods of heating the corona to the desired million degrees values were explored, among them Alfven "waves," surface waves and direct dissipation of magnetic fields. A successful quantitative analysis still eludes us, particularly in attempting to heat the corona above coronal holes where the magnetic field configuraration lacks the complicated closed loop structure found above more active regions. Observations of the Sun in EUV and x-ray reveal a fascinating picture of magnetic structures and emission which exist from very small scales (e.g. x-ray bright points) to large sunspots and active regions. Moreover, mass motions and transients are also evident over this wide range of length scales. These features were dramatically displayed in recent full-disk observations and movies in, for example, x-rays and scattered white light. The variations in these phenomena over the 11 year solar cycle are considerable, although, interestingly, the emergence of new magnetic flux, mass motions, etc. are omnipresent in one form or another. Finally, UV spectroscopic methods are beginning to identify the initial acceleration of the solar wind in small ($\sim$ tens of km/s) outflow velocities in the corona.

Page intentionally left blank

CORONAL HEATING BY WAVES

Joseph V. Hollweg

Space Science Center, Dept. of Physics, Univ. of New Hampshire, Durham, NH 03824

Abstract. We show that Alfven waves or Alfvenic surface waves can carry enough energy into the corona to provide the coronal energy requirements. Coronal loop resonances are an appealing means by which large energy fluxes can enter active region loops. The wave dissipation mechanism still needs to be elucidated, but a Kolmogoroff turbulent cascade is fully consistent with the heating requirements in coronal holes and active region loops.

Introduction

The solar chromosphere and corona are heated mechanically. The energy requirements of the chromosphere and corona are roughly comparable but one usually speaks of 'the coronal heating problem', presumably because of the spectacularly high temperatures there; it is probably a mistake to conceptually separate the chromospheric and coronal heating problems, but space constraints require us to do so here. Spicules present the dual problems of heating and accelerating the chromospheric gas. Locally, in a spicule, the energy requirements are comparable to the chromospheric and coronal heating requirements; again, it is probably a mistake to separate the spicule problem from the overall energy balance of the solar atmosphere.

In this review we discuss theories which invoke waves to heat the corona. If we are willing to interpret the word 'waves' broadly enough, there are good reasons for invoking waves. First, any mechanical process requires that the convection zone do work, followed by the mechanical transfer of energy upwards into the corona. The solar atmosphere must move if work is to be done, and it is a fact of life that virtually all motions in the solar atmosphere obey hyperbolic equations which yield wave or wave-like solutions. For example, the linearized versions of the twisting motions invoked by Parker in the next paper obey the Alfvenic wave equation. Second, the corona is observed to contain ubiquitous non-thermal motions of the order of 10-30 km s^{-1} (rms) (e.g. Bonnet, 1978; Cheng et al., 1979; Doschek and Feldman, 1977; Feldman et al., 1975). These motions are unresolved in space and time. For the reasons given above, it is likely that these motions can be thought of as waves. We will argue below that the observed motions may contain sufficient energy to heat the corona, and a wave theory of coronal heating seems possible. Third, the solar wind may serve as a prototype. Alfven waves (e.g. Belcher and Davis, 1971) and/or surface waves (Hollweg, 1982a) appear copiously in the solar wind beyond 0.3AU and there is some radio evidence for the presence of significant wave fluxes in the acceleration region of the wind (Hollweg et al., 1982a). Successful Alfven-wave-driven solar wind models have been constructed (e.g. Hollweg, 1978a). And the behavior of heavy ions in the solar wind suggests the operation of wave-particle interactions (see Isenberg's review in this volume). The solar wind may be telling us that the sun radiates energetically significant wave fluxes, and that waves can heat (and accelerate) at least part of the solar atmosphere.

In short, it seems that it should be possible to construct a successful wave theory for coronal heating. And in view of the first point in the previous paragraph, it is possible that virtually every theory can at some level

be thought of as a wave theory. Nonetheless, a successful wave theory has not yet emerged. In the following we will summarize some current thinking on the subject. We will point out where wave theories succeed and where they fail. And we will suggest some possible routes to be followed in the future.

Some other recent reviews are Hollweg (1981a), Kuperus et al. (1981), Priest (1982a), and Wentzel (1978a, 1981).

Energies Required and Available

We begin with a brief definition of the problem in terms of the energies required to heat the corona. It is useful to split the corona into three types of regions: i. coronal holes, out of which high-speed solar wind streams flow (e.g. Hundhausen, 1977; Zirker, 1977); ii. quiet corona, consisting of large-scale closed field regions, such as the helmet streamers; iii. active region loops, consisting of small-scale coronal regions of enhanced pressure with a loop-like morphology, presumably tracing out closed magnetic field lines (e.g. Rosner et al., 1978; Webb, 1981; Withbroe, 1981). Convenient summaries of the energy requirements of these regions have been given by Withbroe (1976, 1981).

Coronal holes and quiet corona lose energy via radiation and heat conduction back down into the chromosphere. In addition, coronal holes lose energy by heat conduction out into the solar wind; this latter energy loss could be very large if the high-speed streams are driven thermally, as discussed by Olbert in this volume. Holes and quiet corona require an energy flux density of a few times 10^5 erg cm^{-2} s^{-1} entering from below. And if the high-speed streams are thermally driven, the holes may require as much as 10^6 erg cm^{-2} s^{-1}. The volumetric heating rate can be estimated by dividing the energy flux density by the distance over which the heating occurs. If we take 3×10^5 erg cm^{-2} s^{-1} for the flux density, then the heating rate lies between 10^{-4} and 10^{-5} erg cm^{-3} s^{-1} for heating distances in the range $(0.05 - 0.5) r_s$.

The active region loops lose energy via radiation and via heat conduction along the magnetic field lines back down into the chromosphere. In this case a useful rule-of-thumb can be obtained by paraphrasing Rosner et al. (1978) and Withbroe (1981). Let E_H be the volumetric heating rate of the loop plasma. The radiation loss out of the (optically thin) plasma is $n_e^2 \Phi$ erg cm^{-3} s^{-1}, where n_e is electron concentration and Φ is a function of T_e (electron temperature) only. If we neglect flows, the energy equation is

$$\nabla \cdot \underset{\sim}{q} = E_H - n_e^2 \Phi \tag{1}$$

where $\underset{\sim}{q}$ is heat conduction. Assuming that $\underset{\sim}{q}$ is classical electron heat conduction along the magnetic field, we can rewrite (1) in the form

$$-\frac{1}{2} q_e^2 = K_o \int E_H T_e^{5/2} dT_e - \frac{K_o}{\kappa^2} \int p_e^2 \Phi T_e^{\frac{1}{2}} dT_e \tag{2}$$

where it has been assumed that the loop's cross-sectional area is constant (κ is Boltzmann's constant, p is pressure, and $K_o T_e^{5/2}$ is the heat conductivity). We now take E_H, Φ and p_e to be constants. The loop is assumed to have a maximum temperature T_{max} where $q_e = 0$, and it is assumed that $q_e \to 0$ as $T_e \to 0$; the latter constraint requires

$$E_H = \frac{7}{3} \frac{p_e^2 \Phi}{\kappa^2 T_{max}^2} \tag{3}$$

and we obtain

$$q_e^2 = \frac{4}{3} \frac{K_o P_e^2 \Phi}{\kappa^2} T_e^{3/2} \left[1 - (\frac{T_e}{T_{max}})^2 \right] \tag{4}$$

The quantity Φ can be eliminated in favor of the loop length as follows: From the usual expression for q_e we have

$$ds = \frac{K_o T_e^{5/2} \, dT_e}{|q_e|} \tag{5}$$

where s is distance along the loop. Inserting (4) into (5) and integrating from $T_e = 0$ to $T_e = T_{max}$ gives

$$P_e L \sim (\frac{3K_o}{\Phi})^{\frac{1}{2}} \kappa \left(T_{max} \right)^{11/4} \tag{6}$$

where L is twice the distance from $T_e = 0$ to T_{max}. Inserting (6) into (3) gives finally

$$E_H L \sim \frac{7K_o}{L} T_{max}^{7/2} \tag{7}$$

Since Φ does not appear in (7), it is probable that errors associated with restricting Φ to be a constant will not be very significant. Equation (7) gives the required energy flux density if all the energy comes up along the loop from one of its footpoints; half that value is required if equal fluxes come up both footpoints. For a short (long) loop we take $L = 6 \times 10^9$ (6×10^{10}) cm and $T_{max} = 2 \times 10^6$ (2.5×10^6) K, and with $K_o = 8.4 \times 10^{-7}$ (c.g.s.) we obtain $E_H L \sim 1.1 \times 10^7$ (2.4×10^6) erg cm^{-1} s^{-1}; the corresponding volumetric heating rates are 1.8×10^{-3} (4×10^{-5}) erg cm^{-3} s^{-1}. It is interesting to note that both the energy flux density and the volumetric heating rate are smaller on longer loops; it is the task of theory to explain this.

Can the observed nonthermal velocities in the corona supply the required energy flux densities? It is easy to show that slow (sound) waves cannot do the job, and we will henceforth ignore them. For the fast or Alfven modes, we calculate the energy flux density to be $2\rho_o \, \delta v_{rms}^2 \, v_A$ where v_A is the Alfven speed and ρ_o is the coronal density (the factor '2' allows for 2 polarization states). For coronal holes we take $\rho_o = 3.3 \times 10^{-16}$ gm cm^{-3}, B = 8 Gauss, $\delta v_{rms} = 30$ km s^{-1}, and the energy flux density is 7.4×10^{-5} erg cm^{-2} s^{-1}. For active region loops we take $\rho_o = 5.2 \times 10^{-15}$ gm cm^{-3} (for a mean molecular weight of $\frac{1}{2}$, this density yields a total pressure of 2 dyne cm^{-2} if $T = 2.3 \times 10^6$ K), B = 100 Gauss, $\delta v_{rms} = 30$ km s^{-1}, and we obtain 3.7×10^7 erg cm^{-2} s^{-1} for the energy flux density. These energy fluxes are adequate to supply the required energies, if the 30 km s^{-1} nonthermal motions are fast or Alfven waves.

Can the nonthermal velocities supply the required volumetric heating rates? Write

$$E_H = 2\omega_i (2\rho_o \delta v_{rms}^2) \tag{8}$$

where ω_i is the imaginary part of the wave (angular) frequency (the second factor '2' again allows for 2 polarization states). Coronal holes require $E_H \lesssim 10^{-4}$ erg cm^{-3} s^{-1}, and (8) implies $\omega_i/\omega \lesssim 0.4$ if the wave period is 300s (the

latter figure is a guess). Active region loops require $E_H \lesssim 2 \times 10^{-3}$ erg cm^{-3} s^{-1}, and (8) implies $\omega_i/\omega \lesssim 0.17$ if the period is 100s (the reason for this choice of period will be given below). Our estimates of ω_i/ω are not larger than 1, and it can be meaningful to talk about propagating, but damped, waves.

Finally, we must ask whether the convection zone can do enough work on the system. We will assume that the work is done on the intense photospheric magnetic flux tubes (for a review see Spruit, 1981a). If the energy propagates as an Alfven wave, the convective motions can supply an energy flux density to the corona of

$$2\rho_c \; \delta v_{c,rms}^2 \; v_{Ac} \; (B_{cor}/B_c) \tag{9}$$

Here the subscript 'c' refers to the top of the convection zone, the factor '2' allows for two polarizations, and the factor (B_{cor}/B_c) represents the area expansion of the flux tube. Taking $\rho_c = 3 \times 10^{-7}$ gm cm^{-3} and $\delta v_{c,rms} = 1$ km s^{-1}, we obtain energy flux densities of 2.5×10^7 erg cm^{-2} s^{-1} in a coronal hole ($B_{cor} = 8$ Gauss) and 3×10^8 erg cm^{-2} s^{-1} in an active region loop ($B_{cor} = 100$ Gauss). These values exceed the requirements by more than an order-of-magnitude. As we shall see, this is fortunate, since most of the wave energy is reflected before reaching the corona. (Strictly speaking, equation 9 ignores the details of the wave generation process at the top of the convection zone. A detailed analysis of the coupling between convection and the photospheric flux tubes is really needed, but not available.)

Reflection and Transmission

Fast waves

The coronal pressure is small compared to the magnetic pressure. The fast mode dispersion relation is then approximately $\omega^2 = k^2 v_A^2$, where k is the wavenumber. Upon splitting k into horizontal (h) and vertical (v) components, we obtain

$$k_v^2 = \frac{\omega^2}{v_A^2} - k_h^2 \tag{10}$$

Taking the $\omega - k_h$ structure for the known solar motions in the photosphere and chromosphere, Hollweg (1978b) found that the sun yields $k_v^2 < 0$ in the corona. Fast waves can be expected to be evanescent in the corona, i.e. they suffer total internal reflection somewhere below the corona. Fast waves can not be expected to supply the required energies to the corona. Moreover, the situation is worst in the active regions, which have the greatest energy requirements; the reason is that the active regions are observed to be highly structured (implying large k_h) and to have strong magnetic fields (implying large v_A). Leroy and Schwartz (1982) and Schwartz and Leroy (1982) concur with this conclusion. (See also Osterbrock, 1961.)

However, we note that interesting results have been obtained by Habbal et al. (1979). They postulate the presence of coronal fast waves with a period of 3s. They use ray-tracing techniques to follow the propagation of the wave energy, and emphasize the tendency of the fast waves to refract into regions with smaller v_A; some waves can even be trapped inside a dense loop, in analogy with the trapping of light in an optical fiber. They consider the Landau/transit-time damping of the waves (e.g. Barnes, 1966). An interesting feature of the damping is that it increases with $\beta_p = 8\pi p_p/B^2$, if β_p is small

8

(the subscript 'p' refers to the protons). In the isothermal model of Habbal et al., β_p is largest where v_A is smallest. Thus the waves refract toward regions of larger damping. This means that the fast waves can heat some coronal regions more strongly than others. The effect is enhanced by a 'positive feedback', whereby local heating increases β_p along a given field line (since heat conduction spreads the heat along $\underset{\sim}{B}$), which in turn increases the heating, and so on. A 'catastrophic' situation can occur in which once fast waves begin heating the plasma, they dump all their energy in a small flux tube. Habbal et al. suggest that such a scenario can account for the highly structured nature of the corona in a natural way. But it has to be shown that the waves exist, and that equation (10) can be overcome.

Alfven waves

Unlike fast waves, these waves never totally internally reflect, and we consider them in some detail. Hollweg (1981b) has considered the propagation of small-amplitude (linearized) axisymmetric twists on a background potential magnetic field which has an axisymmetric untwisted fleur-de-lis structure. If the axis of symmetry is vertical, the twisting motions do not couple to gravity or to the radiation field, and they are non-compressive. If the motions vary as $\exp(i\omega t)$, they obey

$$-\omega^2 r^2 \chi = \frac{B_o}{4\pi\rho_o} \frac{\partial}{\partial s} \left[r^2 B_o \frac{\partial \chi}{\partial s} \right] \tag{11}$$

$$-\omega^2 y = r^2 B_o \frac{\partial}{\partial s} \left[\frac{B_o}{4\pi\rho_o r^2} \frac{\partial y}{\partial s} \right] \tag{12}$$

$$i\omega y = r^2 B_{os} \frac{\partial \chi}{\partial s} \tag{13}$$

where $\chi \equiv \delta v_\theta / r$, $y \equiv r \, \delta B_\theta$, the subscript 'o' refers to the background, the prefix 'δ' refers to the wave, θ is the angle about the axis of symmetry, s is distance along any field line, and r(s) is the distance from the axis to the field line. For field lines near the axis we expect $r^2 B_o \sim$ constant, and (11) becomes

$$\left(v_A^2 \frac{\partial^2}{\partial s^2} + \omega^2 \right) \frac{\delta v_\theta}{r} = 0 \tag{14}$$

Equation (14) is the Alfvenic wave equation; we deal with it in what follows. If $v_A \sim e^{s/2h}$, then (14) has the solution

$$\frac{\delta v_\theta}{r} = \left[a H_o^{(1)}(\xi) + b H_o^{(2)}(\xi) \right] e^{i\omega t} \tag{15}$$

where $\xi = 2h\omega / v_A(s)$, and a and b are complex constants. From (13)

$$\delta B_\theta = \frac{-ir\ B_{os}}{v_A}\ [aH_1^{(1)}(\xi) + bH_1^{(2)}(\xi)]\ e^{i\omega t} \tag{16}$$

The time-averaged Poynting flux, $\langle \underset{\sim}{S}\rangle$, is along the magnetic field:

$$\langle \underset{\sim}{S}\rangle = -\frac{\underset{\sim}{B}_o}{4\pi}\ \langle \delta v_\theta\ \delta B_\theta\rangle \tag{17}$$

From (15) and (16) we obtain

$$\langle S_s\rangle = \frac{B_o^2 r^2}{8\pi^2 h\omega}\ (|a|^2 - |b|^2) \tag{18}$$

From the form of (18), we interpret the $H^{(1)}$ part of (15) as the upward-going wave, and the $H^{(2)}$ part of (15) as the downward-going wave (Hollweg, 1972). Now the exponential behavior of v_A used in (15) – (18) roughly represents the probable behavior in the chromosphere and transition region of a flux tube, but v_A is much more nearly constant in the coronal part of a flux tube (Figs. 3 and 10 of Hollweg, 1981b). If the corona extends to infinity, as in a coronal hole, it is possible to obtain some useful analytical results by considering a two-layer model, in which

$$v_A = v_{A,cor} = \text{constant, } s > 0 \tag{19a}$$

$$v_A = v_{A,cor}\ e^{s/2h}\ , s < 0 \tag{19b}$$

Here $s > 0$ represents the corona, and $s<0$ represents the chromosphere and transition region. Equations (15) – (18) apply in $s < 0$, while the usual harmonic solutions apply in $s > 0$. At $s = 0$ we apply the matching conditions that δv_θ and δB_θ be continuous (this ensures continuity of $\langle S_s\rangle$). The matching conditions give

$$\frac{b}{a} = -\frac{H_o^{(1)} - i\ H_1^{(1)}}{H_o^{(2)} - i\ H_1^{(2)}} \tag{20}$$

where the argument of the Hankel functions is $2h\omega/v_{A,cor} \equiv \alpha$. From (20) we can calculate the reflection coefficient, R, i.e. the ratio of downward-going energy flux to upward-going:

$$R = |b|^2/|a|^2 \tag{21}$$

In the limit of small α, we obtain

$$R \underset{\sim}{\sim} 1-2\pi\alpha \tag{22}$$

(Equations 19-22 have been given by Leer et al. (1982). They are a special case of Hollweg (1972).) Since equations (20) – (22) are obtained from the matching conditions at $s = 0$ it seems natural to think of the reflection as

10

occurring at the discontinuity in scale height there (Hollweg, 1972). However, Wentzel (1978b), following Tolstoy (1973), and Leroy (1980) have argued that R is really the accumulated reflection off of the entire chromosphere and transition region. The latter interpretation is probably correct, but we are then perplexed as to why R can be calculated solely from the matching conditions at s = 0.

For a flux tube entering a coronal hole we might have h = 250 km, and $v_{A,cor}$ = 1200 km s^{-1}. If the wave period is 300s, the energy transmission coefficient is 1-R = 0.055. In the previous section we estimated that the convective work can supply 2.5 x 10^7 erg cm^{-2} s^{-1}. Multiplying by 1-R gives 1.4 x 10^6 erg cm^{-2} s^{-1} available to the corona. This is enough to supply the energy requirements.

The situation is different on an active region loop. We imagine the loop to be stretched out so that (possibly important) complications arising from the curvature are ignored (e.g. Wentzel, 1978b). But we must now at the very least consider a 3-layer model, since there is a chromosphere and transition region at each end of the loop (an 18-layer model was considered by Hollweg, 1981b). We take

$$v_A = v_{A,cor} \exp(s/2h), \quad s < 0 \tag{23a}$$

$$v_A = v_{A,cor}, \quad 0 < s < L \tag{23b}$$

$$v_A = v_{A,cor} \exp[-(s-L)/2h'], \quad s > L \tag{23c}$$

We imagine there to be a source at the far end of the loop, in s > L. We impose the boundary condition that there be only an outgoing (from the source) wave in the region s < 0. The other two regions have both upward-and downward-going solutions. Applying matching conditions at s = 0 and s = L allows us to calculate the ratio of downward-going energy flux to upward-going flux in the region s > L. Again calling this ratio R, we obtain

$$R = \left| N/D \right|^2 \tag{24}$$

where

$$N = \left[H_1^{(1)}(\beta) H_0^{(2)}(\alpha) + H_0^{(1)}(\beta) H_1^{(2)}(\alpha) \right] \cos kL$$
$$+ \left[H_1^{(1)}(\beta) H_1^{(2)}(\alpha) - H_0^{(1)}(\beta) H_0^{(2)}(\alpha) \right] \sin kL \tag{25}$$

and

$$D = \left[H_1^{(2)}(\beta) H_0^{(2)}(\alpha) + H_0^{(2)}(\beta) H_1^{(2)}(\alpha) \right] \cos kL$$
$$+ \left[H_1^{(2)}(\beta) H_1^{(2)}(\alpha) - H_0^{(2)}(\beta) H_0^{(2)}(\alpha) \right] \sin kL \tag{26}$$

We have defined $\alpha = 2h\omega/v_{A,cor}$, $\beta = 2h'\omega/v_{A,cor}$, and $k = \omega/v_{A,cor}$.

Expressions (24) - (26) have not yet been analyzed in detail. But they take a simpler form if $\alpha = \beta$, and if $\alpha, \beta \ll 1$. Then

$$N \approx Y_1^2 \sin kL + 2 Y_o Y_1 \cos kL \tag{27}$$

and

$$D \approx N + 2iY_1 \cos kL \tag{28}$$

It is interesting to note that N can be exactly zero at certain resonant frequencies which are approxmately given by

$$\omega_{res} \approx m\pi v_{A,cor}/L \tag{29}$$

where $m = 1, 2, 3\ldots$ (For example, the resonant period is 40s if $m = 1$, $v_{A,cor}$ = 3000 km s^{-1}, and $L = 6 \times 10^4$ km.) At these frequencies the reflections vanish, and a large energy flux can pass through the corona and out the other end of the loop. In the vicinity of one of the resonances it is possible to use (24), (27) and (28) to obtain the following expression for the energy transmission coefficient:

$$1-R = \frac{1}{1 + (Y_1 L/2v_{A,cor})^2 (\omega-\omega_{res})^2} \tag{30}$$

Denoting the full-width-at-half-maximum by $\Delta\omega$, we find

$$\frac{\omega_{res}}{\Delta\omega} \equiv Q \approx \frac{L}{4\pi h} \tag{31}$$

(Q denotes the quality). If $L = 6 \times 10^4$ km and $h = 150$ km, then $Q = 32$; the resonance is moderately high quality.

We have already estimated that the convection zone work can supply 3×10^8 erg cm^{-2} s^{-1}. If this power is in a band width B_ω, then the energy flux density passing through the corona in one resonant peak is

$$F_{res} = (3 \times 10^8) \frac{\Delta\omega}{B_\omega} \frac{\pi}{2} \tag{32}$$

where the factor $(\pi/2)$ comes from integrating the area under (30). From Fig. 3 of Ionson (1982), we estimate $B_\omega \approx 3 \times 10^{-2}$ s^{-1}. Then from (29) and (31)-(32) we find

$$F_{res} = 6.2 \times 10^{11} mh\ v_{A,cor}/L^2 \tag{33}$$

Note that longer loops receive less power, as (qualitatively) observed. If we take $h = 150$ km, $v_{A_{cor}} = 3000$ km s^{-1}, $L = 6 \times 10^4$ km and $m = 1$, then $F_{res} = 7.8 \times 10^7$ erg cm^{-2} s^{-1}. This is more than enough energy to supply the loop, but this energy goes right through the loop, since we have put no damping into the calculation. The calculation with damping still needs to be done, but work in progress shows that adequate energies can reach and stay in the loop, since damping tends to broaden the resonance peak, compensating for its reduction in height.

Equations (25)-(33) are new, but some of these ideas have been considered previously. Ionson (1978) was the first to show that standing waves can be excited on active region loops. The first paper to show that resonances can eliminate the reflections and allow Alfven wave energy to enter the corona was by Hollweg (1981b). The same point was made independently by Zugzda and Locans (1982), but their Alfven wave equation differs from (11) and (12) above. Ionson (1982) has discussed the resonances using RLC circuits as an analogy. This approach omits some physics, however. For example, in the absence of dissipation Ionson gets $Q = \infty$, and he uses $Q = 10^3 - 10^4$ in his paper; by contrast, we find $Q = 30$ or so, even in the absence of dissipation.

An interesting point made by Ionson (1982) is that there appear to be two classes of loops (active region loops and 'large scale structures'). There may also be two peaks in the photospheric power spectrum. Ionson suggests that a narrow-band resonance is a natural means by which the details of the power spectrum could be mapped into the corona, and thus a double-peaked spectrum can give rise to two classes of loops.

Alfvenic Surface Waves

The corona is highly structured. In the limit that the structuring takes the form of discontinuities, it is possible to find new wave modes supported by the surfaces. These surface waves have recently been of considerable interest. See Edwin and Roberts (1982), Gordon and Hollweg (1983), Hollweg (1982a), Ionson (1978), Roberts (1981a, b), Wentzel (1979).

Consider a cold, stationary background plasma which varies only in the χ - direction. The background magnetic field vector varies in χ, but its magnitude is constant. The system supports small-amplitude fluctuations obeying

$$\epsilon \delta v_\chi = \frac{\partial}{\partial \chi} \left[\frac{\epsilon}{q^2} \frac{\partial \delta v_\chi}{\partial \chi} \right] \tag{34}$$

where $q^2 \equiv k^2 - \omega^2/v_A^2$ and $\epsilon \equiv 4\pi\rho_0 \omega^2 - (\underset{\sim}{k} \cdot \underset{\sim}{B}_0)^2$; the fluctuations vary as $\exp[ik_y y + ik_z z - i\omega t]$. Now assume that everything is uniform except at a discontinuity at $\chi = 0$. If $q^2 > 0$ everywhere, it is possible to find solutions which evanesce away from the discontinuity as $\exp[\pm qx]$. The dispersion relation for these surface waves follows by requiring that δv_x and $(\epsilon/q^2)\partial\delta v_x/\partial\chi$ be continuous at $\chi = 0$.

For example, suppose $\underset{\sim}{B}_0$ is constant and in the z-direction. Suppose also that k_y is large, so that $q^2 \cong k_y^2$. The dispersion relation turns out to be

$$\frac{\omega^2}{k_z^2} = \frac{B_0^2}{4\pi\rho_{av}} \tag{35}$$

where ρ_{av} is the average of the densities on the two sides of the discontinuity. Equation (35) is similar to the dispersion relation for Alfven waves. These surface waves generally turn out to be rather similar to Alfven waves.

In particular, they propagate energy along $\underset{\sim}{B}_o$.   Much of what was said about Alfven waves in the previous section applies to surface waves as well. They may be suitable candidates for coronal heating, although many details, such as their ability to propagate energy through the chromosphere and transition region, remain to be worked out.

It is interesting to note that surface waves may be present in the solar wind (Hollweg, 1982a).

Wiggles of Thin Flux Tubes.
_____

Spruit (1981a, b) has considered transversal oscillations of thin vertical magnetic flux tubes imbedded in a field-free gas. If the tube is in pressure and temperature equilbrium with its surroundings, then the (small) horizontal displacements of the tube obey:

$$(2\beta_t + 1) \frac{\partial^2 \xi}{\partial t^2} = -g \frac{\partial \xi}{\partial z} + 2 \frac{p}{\rho} \frac{\partial^2 \xi}{\partial z^2} \tag{36}$$

where g is the gravitational acceleration, and β_t = constant is the ratio of gas to magnetic pressures inside the flux tube. If the atmosphere is isothermal, we can take $\xi \sim \exp[ikz - i\omega t]$ and (36) yields:

$$k = \frac{g\rho}{4p} [-i \pm (\frac{\omega^2}{\omega_c^2} - 1)^{\frac{1}{2}}] \tag{37}$$

where

$$\omega_c^2 = \frac{g^2 \rho}{8p(2\beta_t + 1)} \tag{38}$$

The waves have a low-frequency cutoff. If the temperature is 10^4K, if the molecular weight is 1.3, and if β_t = 1, we find from (38) that periods longer than 900s are evanescent; this is not a severe restriction.

These waves carry energy along the magnetic field. If $\omega \gg \omega_c$, the phase and group velocities are comparable to the sound speed. They could carry energy into the low chromosphere. However, the tubes cease to be thin above the low chromosphere, and a more detailed analysis is necessary. They could couple some energy into the fast and Alfven modes, which could carry the energy to greater heights.

Dissipation

The general conclusion of the previous section is that Alfven or Alfvenic surface waves, and to some extent transversal tube waves, can in principle supply the corona with its energy requirements. This is the first requirement of a coronal heating theory. The second requirement is that the waves deposit energy as heat. Wave theories of coronal heating have so far failed in this regard, but we will summarize some of the possibilities.

One point to note at the outset is that the observed coronal motions, if interpreted as magnetic waves, are quite linear. In a coronal hole we might have $v_A \sim 1200$ km s^{-1} (if B = 8 Gauss and $\rho = 3.3$ x 10^{-16} gm cm^{-3}), while in an active region loop we might have $v_A \sim 4000$ km s^{-1} (if B = 100 Gauss and ρ =

5.2×10^{-15} gm cm^{-3}). In all cases $\delta v_{rms}/v_A \ll 1$, in contrast to the solar wind.

Viscous Heating.

Coronal viscosity is mainly due to the protons. Following Braginskii (1965), the proton collision time in an electron-proton plasma is

$$\tau_p = 0.75 T_p^{3/2} n_p^{-1} \text{ s} \qquad (39)$$

for a Coulomb logarithm of 22. In the corona $\omega_{cp}\tau_p \gg 1$ (ω_{cp} is the proton cyclotron frequency) and the protons are well-tied to the field lines. Of the five viscosity coefficients given by Braginskii, $\eta_o \sim 10^{-16} T_p^{5/2}$ (cgs) is by far the largest; shear viscosity is smaller by $(\omega_{cp}\tau_p)^{-2}$ (roughly). If only η_o is considered, the viscous heating rate is

$$Q_p = \eta_o \left[\frac{1}{3} (\nabla \cdot \underset{\sim}{v})^2 - 2 \frac{\partial v_z}{\partial z} \nabla \cdot \underset{\sim}{v} + 3 \left(\frac{\partial v_z}{\partial z} \right)^2 \right] \qquad (40)$$

where z is along the magnetic field. For purely parallel motion $Q_p = (4/3)\, \eta_o (\nabla \cdot \underset{\sim}{v})^2$ while for purely transverse motions $Q_p = \eta_o (\nabla \cdot \underset{\sim}{v})^2 /3$. As a rule-of-thumb we will take $Q_p = \eta_o (\nabla \cdot \underset{\sim}{v})^2$.

In an active region loop we observe $Q_p \lesssim 2 \times 10^{-3}$ erg cm^{-3}s^{-1}. Using the equation of continuity, this requires $\delta\rho_{rms}/\rho_o \lesssim 0.8$ if $T_p = 2.3 \times 10^6$ K and if the wave period is 100s. In a coronal hole we observe $Q_p \lesssim 10^{-4}$ erg cm^{-3}s^{-1}. This requires $\delta\rho_{rms}/\rho_o \lesssim 0.9$ if $T_p = 1.5 \times 10^6$ K and if the wave period is 300s. Such large density fluctuations may occur occasionally in small regions in the corona, but they are not compatible with the requirements of heating the entire corona by any of the waves discussed so far.

Heat Conduction

Coronal heat conduction is due mainly to the electrons. They too are tied to the field lines and the heat conduction is along the magnetic field. The plasma heating rate due to heat conduction damping of waves is

$$Q_e = \kappa_{\parallel, e} \left(\frac{\partial \delta T_e}{\partial z} \right)^2 T_{oe}^{-1} \qquad (41)$$

where the heat conductivity is $\kappa_{\parallel, e} = 8.4 \times 10^{-7} T_e^{5/2}$ (cgs) for a Coulomb logarithm of 22.

Low-frequency waves induce nearly adiabatic temperature fluctuations, i.e. $|\delta T_e| \sim (\gamma - 1) T_{eo} |\nabla \cdot \underset{\sim}{\delta v}|/\omega$, where $\gamma = 5/3$ is the ratio of specific heats. We then find (taking $T_e = T_p$)

$$\frac{Q_e}{Q_p} = 8.4 \times 10^9 (\gamma-1)^2 T_e k_z^2 /\omega^2 \qquad (42)$$

If $T_e = 2 \times 10^6$K, we find that viscous heating dominates heat conduction if $\omega/k_z > 860$ km s^{-1}. Coronal Alfven speeds generally exceed this value, and we deduce that heat conduction will be even less effective than viscosity in damping the waves.

For completeness we should mention that heat conduction smooths out the temperature fluctuations in high-frequency waves. This reduces the

effectiveness of heat-conduction damping even further. See Gordon and Hollweg (1983).

Shocks.

We have already mentioned that Alfven, fast, or Alfvenic surface waves are to a good approximation linear in the corona. Shocks probably do not form in the corona. However, Hollweg et al. (1982b) have suggested the possibility that shocks can form in the chromosphere, on their way to the corona. Hollweg et al. considered Alfven waves, which steepen into a train of shocks which are nearly switch-on shocks (see, for example, Boyd and Sanderson, 1969). These shocks enter the corona, and can carry substantial energy fluxes. Hollweg et al. suggested that some of the impulsive events observed in the transition region (see the article by Dere in this volume) could in fact be the shocks.

The volumetric heating rate due to a periodic train of weak switch-on shocks with period τ is

$$Q_{sos} = \frac{B_o^2}{32\pi\tau} \left(\frac{\Delta v_t}{v_{Ao}} \right)^4 \tag{43}$$

if the coronal pressure is small compared to the magnetic pressure (Hollweg, 1982b); Δv_t is the jump in the velocity component transverse to the shock normal. Since $Q \sim B_o^{-2}$, this mechanism yields negligibly small heating rates in active regions. However, it could conceivably work in coronal holes or quiet corona if B_o and τ are small enough, and if Δv_t is large enough. For example, if $B_o = 5$ Gauss, $\rho = 3.3 \times 10^{-16}$ gm cm^{-3}, $\Delta v_t = 200$ km s^{-1}, and $\tau = 100$s, we obtain $Q_{sos} = 10^{-5}$ erg cm^{-3} s^{-1}. The corona can be heated over an extended distance by this mechanism.

Switch-on shocks are probably a worst case. A best case for shocks is a train of fast shocks propagating across the magnetic field. If the shocks are weak and if the coronal pressure is small compared to the magnetic pressure, the volumetric heating rate is

$$Q_{fs} = \frac{B_o^2}{16\pi\tau} \left(\frac{\Delta v}{v_{Ao}} \right)^3 \tag{44}$$

where Δv is the velocity jump across the shock. In an active region loop we might have $B_o = 100$ Gauss and $v_{Ao} = 3000$ km s^{-1}. If we take $\Delta v = 200$ km s^{-1} and $\tau = 100$s we find $Q_{fs} = 6 \times 10^{-4}$ erg cm^{-3} s^{-1}. This is comparable to the heating requirements of some moderate length loops. In a coronal hole we might have $B_o = 5$ Gauss and $v_{Ao} = 800$ km s^{-1}, and we find $Q_{fs} = 7.8 \times 10^{-5}$ erg cm^{-3} s^{-1}. The heating of the coronal hole is substantial in this case.

Thus fast shocks propagating across $\underset{\sim}{B}_o$ can yield substantial heating. The same is presumably true for fast shocks propagating at some not-too-small angle to $\underset{\sim}{B}_o$. But where would such shocks come from? One guess is that they could form in the chromosphere in the manner investigated by Hollweg et al. (1982b) for switch-on- shocks. In fact, the study of Hollweg et al. is probably unrealistically restricted, since there is no reason to expect that the sun will yield shock normals which are nearly aligned along the magnetic field; in view of the strong cross-field structuring observed on the sun, the opposite is probably the case, and further studies must be done. In any event, we will ultimately have to rely on observations to tell us whether shocks with the required frequency and amplitude do in fact form in the chromosphere and enter the corona.

16

Phase Mixing and Turbulence.

Consider two neighboring magnetic field lines along which energy is propagating in the form of an Alfven wave. If the phase velocities are different on the two field lines, then the motions on those field lines will not always maintain the same phase relationship. The motions will move in and out of phase, and (in the latter case) extremely large cross-field velocity gradients can develop. Heyvaerts and Priest (1982) (see also Priest, 1982b) have pointed out that this phase mixing is ripe for viscous dissipation. They consider the special case where $B_{\sim o}$ is in the z- direction, $\delta v_{\sim}$ is in the y-direction, and $v_A = v_A(\chi)$. Unfortunately, since the motions in this case are shears, the viscous damping will be weak, because $\omega_{cp} \tau_p >> 1$; this limitation of the efficacy of viscosity was not considered by Heyvaerts and Priest.

Heyvaerts and Priest consider also the possibility that large velocity shears between neighboring field lines can result in Kelvin-Helmholz instabilities. (They consider in particular the situation on coronal active region loops, where the resonances discussed in section IIIB lead to nearly-standing waves on the loops. A similar idea was mentioned earlier by Hollweg (1981b) with regard to Alfven waves in the chromosphere. Since the solar atmosphere is not homogeneous, and since there is no reason to expect phase coherence between motions on different field lines, phase mixing may be a ubiquitous and important effect.) Priest (1982b) estimates the Kelvin-Helmholz growth rate to be $\omega_i \sim k_\perp |\delta v_{\sim}|$, where $k_\perp$ is the transverse wave number associated with the velocity shears. But it must be kept in mind that the driving velocity shears in this problem are time-dependent. For the analysis (which assumes that the driving shears are steady) to hold, it is necessary that $\omega_i >> \omega$. If we take $\omega = 2\pi/(100s)$, and $|\delta v_{\sim}| = 40$ km s^{-1} (corresponding to $\delta v_{rms} \sim 30$ km s^{-1}), we require $\lambda_\perp = 2\pi/k_\perp << 4000$ km. This is not a strong constraint (the active region loops are only a few thousand km in diameter), and Kelvin-Helmholz instabilities may occur. The instabilities may initiate a turbulent cascade to higher wavenumbers where viscosity (or some other process) can convert the energy into heat.

Heyvaerts and Priest (1982) and Priest (1982b) consider also the possibility that the phase relationship between Alfven waves on neighboring field lines is such as to produce large magnetic shears. Tearing-mode instabilities are then possible. (This idea was also discussed earlier by Hollweg, 1981b.) Priest (1982b) estimates the tearing growth time to be

$$\tau_{tmi} \sim |\delta v_{\sim}|^{-4/7} \eta^{-3/7} k_\perp^{-10/7} \qquad (45)$$

where $\eta \sim 2 \times 10^{13} T_e^{-3/2}$ (cgs) is the magnetic diffusivity; in computing η we have taken the perpendicular electrical conductivity (Braginskii, 1965) and a Coulomb logarithm of 22. (Note that η is so small in the corona that classical electrical resistivity fails miserably as a dissipation mechanism.) For the analysis (which assumes that the magnetic shears are steady) to be valid, it is necessary that $\omega\tau_{tmi} << 1$. If the wave period is 100s, this requires $\lambda_\perp << 10$ km, where we have taken $T_e = 2.3 \times 10^6$ K, and $|\delta v_{\sim}| = 40$ km s^{-1}. It is not known whether the coronal waves are structured on these scales. But tearing instabilities, if they occur, can initiate a turbulent cascade to higher wavenumbers.

Suppose a turbulent cascade is initiated. How effective will it be? Unfortunately, most turbulence theory has been developed for incompressible fluids with isotropic turbulence. Neither condition can be expected to apply in the corona. However, as Montgomery (this volume) says, "it's the only game

in town", so we'll play anyway. For fully-developed Kolmogoroff turbulence one expects

$$E(k) \simeq C_o \, \varepsilon^{2/3} \, k^{-5/3} \tag{46}$$

where k is wavenumber, $C_o \sim 1.5$ is a universal (?) constant, $\int E(k)dk = <\delta v^2>$, and ε (dimensions = velocity^2 time^{-1}) is the rate at which $<\delta v^2>$ cascades to high wavenumbers. Integrating (46) from k_o to ∞ gives

$$\frac{\varepsilon}{2<\delta v^2>} = \frac{k_o <\delta v^2>^{1/2}}{2(1.5 \, C_o)^{3/2}} \tag{47}$$

where it has been assumed that all the energy is in $k > k_o$. Now we can regard $\varepsilon/(2<\delta v^2>)$ as a measure of the damping rate, ω_i, since the cascade pumps energy to arbitrarily high wavenumbers where it is absorbed and converted into heat. Equation (47) then yields (c.f. Section II)

$$E_H = \frac{2^{3/2} k_o \rho_o \, \delta v_{rms}^3}{(1.5 \, C_o)^{3/2}} \tag{48}$$

(we have again allowed for 2 polarization states). The problem is that we are not sure what to put in for k_o. If we take $k_o = 2\pi/\lambda_i$ with $\lambda_i = 3000$ km (a reasonable guess for an active region loop), $\rho_o = 5.2 \times 10^{-15}$ gm cm^{-3}, and $\delta v_{rms} = 30$ km s^{-1}, we find $E_H = 2.5 \times 10^{-3}$ erg cm^{-3} s^{-1}. Comparison with Section II shows that this is adequate to heat the active region loops. In a coronal hole we might have λ_i to be the mean distance between the photospheric magnetic flux tubes $\sim 10^4$ km, and with $\rho_o = 3.3 \times 10^{-16}$ gm cm^{-3} we obtain $E_H = 4.7 \times 10^{-5}$ erg cm^{-3} s^{-1}. Again, we obtain an adequate heating rate. We tentatively conclude that a turbulent cascade can provide the required heating. But a theory for turbulence which is applicable to the corona must be developed. We suggest that this subject be vigorously pursued in the future. (The author thanks Dr. C. Smith for advice on this paragraph.)

Surface Waves

Ionson (1978) has considered the propagation of surface waves on non-discontinuous 'surfaces'. He considers the problem discussed previously, which has (35) as its dispersion relation in the case of a truly discontinuous surface. He finds, however, that ω is now complex, with

$$\frac{\omega_i}{|\omega_r|} = -\pi \left(\frac{\rho_{o1}}{\rho_{o2}} + \frac{\rho_{o2}}{\rho_{o1}} + 2\right)^{-1} \frac{|k_y| a \Delta v_A (4\pi\rho_{av})^{1/2}}{B_o} \tag{49}$$

where 'a' is the thickness of the 'surface' and Δv_A is the difference between the Alfven speeds on the two sides. Ionson interpreted ω_i as a damping rate, but Lee (1980) pointed out that it is not correct to think of damping of a normal mode, because there are no normal modes in this problem (unless a = 0). Instead, the appearance of ω_i represents a readjustment of the system's energy distribution. (Lee suggests[1] that the situation is analogous to leakage of particles out of a potential well, as in radioactive decay. ω_i represents the leakage out of the well, but there is no net loss of particles.) The energy flows into the surface. Steep gradients develop in the surface, and viscous dissipation will eventually occur in a thin layer. It seems likely that the dissipation in the thin layer will adjust itself to absorb the energy flow

18

into the surface, as suggested by Ionson (1978). The problem with dissipation still needs detailed study, but it may represent a promising mechanism for converting wave energy into heat in many thin layers in the corona. (See also Lee et al., 1983).

Summary

The corona is observed to move with velocities of 30 km s^{-1} or so, rms. Since most coronal motions obey hyperbolic equations, it is reasonable to think of the motions as being waves.

If the motions are Alfven or Alfvenic surface waves, they can carry the required energies into the corona. Some large fraction of the energy is presumably reflected in the chromosphere and transition region, but theory indicates that sufficient energy can be transmitted into the corona. Loop resonances may play a special role in allowing energy to enter the active region corona.

The problem is with the dissipation. Viscosity is the most promising dissipation mechanism, but special conditions have to be fulfilled. The wave energy must ultimately appear at sufficiently short spatial scales so that viscosity becomes effective. Fast shocks may be suitable, since the shock thickness automatically adjusts itself to yield the required entropy jump across the shock. A turbulent cascade seems even more promising, but an anisotropic compressive turbulence theory still needs to be formulated. Surface waves may be yet another route by which the wave energy finds itself at small enough spatial scales for viscous heating to be effective. But the detailed analyses of these processes still need to be done.

Another area where more work is needed is the following: We have conceptually separated the coronal heating from the chromospheric heating. And we have regarded the chromosphere and transition region as being fixed entities which carry (and reflect) the waves. But the coupling between the chromosphere, corona, and transition region may be an integral part of the entire atmosphere's energy balance. And the coupling may be strong and dynamic. For example, Hollweg (1981b) and Hollweg et al. (1982b) have argued that the chromosphere and transition region may themselves be set into vigorous motion as the waves propagate from the photosphere into the corona. (A possible connection with the spicules has been noted by Hollweg et al. (1982b) and by Hollweg (1982c).) It is not yet clear how this dynamic coupling affects the ideas presented in this review.

Finally, we have been implicitly regarding the waves as non-impulsive. Yet the observations discussed by Dere in this volume suggest the opposite: the transition region moves violently and impulsively. What are the implications of these observations for coronal heating? We have already mentioned that the impulses could be shocks, but the issue is far from being resolved. These observations demand further study.

References

Barnes, A., Collisionless damping of hydromagnetic waves, Phys. Fluids, 9, 1483, 1966.
Belcher, J.W., and L. Davis Jr., Large-amplitude Alfven waves in the

interplanetary medium, 2, J. Geophys. Res., 76, 3534, 1971.

Bonnet, R.M., High resolution UV solar spectroscopy, Space Sci. Rev., 21, 379, 1978.

Boyd, T.J.M., and J.J. Sanderson, Plasma Dynamics, Barnes and Noble, New York, 1969.

Braginskii, S.I., Transport processes in a plasma, Rev. Plasma Phys., 1, 205, 1965.

Cheng, C.-C., G.A. Doschek, and U. Feldman, The dynamical properties of the solar corona from intensities and line widths of EUV forbidden lines of Si VIII, Fe XI, and Fe XII, Astrophys. J., 227, 1037, 1979.

Doschek, G.A., and U. Feldman, The coronal temperature and nonthermal motions in a coronal hole compared with other solar regions, Astrophys. J., 212, L143, 1977.

Edwin, P.M., and B. Roberts, Wave propagation in a magnetically structured atmosphere, 3, the slab in a magnetic environment, Solar Phys., 76, 239, 1982.

Feldman, U., G.A. Doschek, and R. Tousey, The intensities and profiles of XUV transition zone lines in a quiet sun region compared to a polar coronal hole, Astrophys. J., 202, L147, 1975.

Gordon, B., and J.V. Hollweg, Collisional damping of surface waves in the solar corona, Astrophys. J., 266, in press, 1983.

Habbal, S.R., E. Leer, and T.E. Holzer, Heating of coronal loops by fast mode MHD waves, Solar Phys., 64, 287, 1979.

Heyvaerts, J., and E.R. Priest, Coronal heating by phase-mixed shear Alfven waves, Astron. and Astrophys., in press, 1982.

Hollweg, J.V., Supergranulation-driven Alfven waves in the solar chromosphere and related phenomena, Cosmic Electrodyn., 2, 423, 1972.

Hollweg, J.V., Some physical processes in the solar wind, Rev. Geophys. Space Phys., 16, 689, 1978a.

Hollweg, J.V., Fast wave evanescence in the solar corona, Geophys. Res. Lett., 5, 731, 1978b.

Hollweg, J.V., Mechanisms of energy supply, in Solar Active Regions, ed. by F.Q.Orrall, Colorado Associated University Press, 277, 1981a.

Hollweg, J.V., Alfven waves in the solar atmosphere, 2, open and closed magnetic flux tubes, Solar Phys., 70, 25, 1981b.

Hollweg, J.V., Surface waves on solar wind tangential discontinuities, J. Geophys. Res., 87, 8065, 1982a.

Hollweg, J.V., Heating of the corona and solar wind by switch-on shocks, Astrophys. J., 254, 806, 1982b.

Hollweg, J.V., On the origin of solar spicules, Astrophys. J., 257, 345, 1982c.

Hollweg, J.V., M.K. Bird, H. Volland, P. Edenhofer, C.T. Stelzried and B.L. Seidel, Possible evidence for coronal Alfven waves, J. Geophys. Res., 87, 1, 1982a.

Hollweg, J.V., S. Jackson, and D. Galloway, Alfven waves in the solar atmosphere, 3. nonlinear waves on open flux tubes, Solar Phys., 75, 35, 1982b.

Hundhausen, J.R., An interplanetary view of coronal holes, in Coronal Holes and High-Speed Wind Streams, ed. by J. Zirker, Colorado Associated University Press, 225, 1977.

Ionson, J., Resonant absorption of Alfvenic surface waves and the heating of solar coronal loops, Astrophys. J., 226, 650, 1978.

Ionson, J., Resonant electrodynamic heating of stellar coronal loops: an LRC circuit analog, Astrophys. J., 254, 318, 1982.

Kuperus, M., J.A. Ionson, and D.S. Spicer, On the theory of coronal heating mechanisms, Ann. Rev. Astron. Astrophys., 19, 7, 1981.

Lee, M.A., Comments on the dissipation of hydromagnetic surface waves, Astrophys. J., 240, 693, 1980.

Lee, M.A., I. Rae, and B. Roberts, On the dissipation and propagation of hydromagnetic surface waves, Astrophys. J., submitted, 1983.

Leer, E., T.E. Holzer, and T. Fla, Acceleration of the solar wind, preprint, 1982.

Leroy, B., Propagation of waves in an atmosphere in the presence of a magnetic field, 2, the reflection of Alfven waves, Astron. Astrophys., 91, 136, 1980.

Leroy, B., and S.J. Schwartz, Propagation of waves in an atmosphere in the presence of a magnetic field, 5, the theory of magneto-acoustic-gravity oscillations, Astron. Astrophys., 112, 84, 1982.

Osterbrock, D.E., The heating of the solar chromosphere, plages, and corona by magneto-hydrodynamic waves, Astrophys. J., 134, 347, 1961.

Priest, E.R., Solar Magnetohydrodynamics, Reidel, Dordrecht, Holland, 1982a.

Priest, E.R., The magnetohydrodynamcs of solar activity, Plasma Phys., in press, 1982b.

Roberts, B., Wave propagation in a magnetically structured atmosphere, 1, surface waves at a magnetic interface, Solar Phys., 69, 27, 1981a.

Roberts, B., Wave propagation in a magnetically structured atmosphere, 2, waves in a magnetic slab, Solar Phys., 69, 39, 1981b.

Rosner, R., W.H. Tucker, and G.S. Vaiana, Dynamics of the quiescent solar corona, Astrophys. J., 220, 643, 1978.

Schwartz, S.J., and B. Leroy, Propagation of waves in an atmosphere in the presence of a magnetic field, 6, Application of magneto-acoustic-gravity mode theory to the solar atmosphere, Astron. Astrophys., 112, 93, 1982.

Spruit, H.C., Magnetic flux tubes, in The Sun as a Star, ed. by S. Jordan, NASA-SP-450, 1981a.

Spruit, H.C., Motion of magnetic flux tubes in the solar convection zone and chromosphere, Astron. Astrophys., 98, 155, 1981b.

Tolstoy, I., Wave propagation, McGraw-Hill, New York, 1973.

Webb, D.F., Active region structures in the transition region and corona, in Solar Active Regions, ed. by F..Q. Orrall, Colorado Associated University Press, 165, 1981.

Wentzel, D.G., Heating of the solar corona: a new outlook, Rev. Geophys. Space Phys., 16, 757, 1978a.

Wentzel, D.G., Wave reflection and wave disorder in the solar transition zone and corona, Solar Phys., 58, 307, 1978b.

Wentzel, D.G., Hydromagnetic surface waves, Astrophys. J., 227, 319, 1979.

Wentzel, D.G., Coronal heating, in The Sun as a Star, ed. by S. Jordan, NASA-SP-450, 1981.

Withbroe, G., in Energy Balance and Hydro-dynamics of the Solar Chromosphere and Corona, ed. by R.M. Bonnet and Ph. Delache, IAU Colloq. 36, 1976.

Withbroe, G.L., Physics of static loop structures and scaling laws, in Solar Active Regions, ed. by F.Q. Orrall, 199, 1981.

Zirker, J.B., Coronal holes-an overview, in Coronal Holes and High-Speed Wind Streams, ed. by J. Zirker, Colorado Associated University Press, 1, 1977.

Zugzda, Y.D., and V. Locans, Tunnelling and interference of Alfven waves, Solar Phys., 76, 77, 1982.

Page intentionally left blank

DIRECT CORONAL HEATING FROM DISSIPATION OF MAGNETIC FIELD

E. N. Parker
Department of Physics
University of Chicago
Chicago, Illinois 60637

ABSTRACT

It was pointed out some time ago by Rosner, Tucker, and Vaiana that the visible corona of the sun appears to be heated by direct dissipation of magnetic fields. The magnetic fields in the visible corona are tied at both ends to the photosphere where the active convection continually rotates and shuffles the footpoints in a random pattern. We have shown that the twisting and wrapping of flux tubes about each other produce magnetic neutral sheets in a state of dynamical nonequilibrium such that the current sheets become increasingly concentrated with the passage of time. Dissipation of the high current densities takes place regardless of the high electrical conductivity of the fluid. We suggest that the work done by the convection on the feet of the lines of force at the surface of the sun goes directly (within a matter of 10-20 hours) into heat in the corona. The rate of doing work seems adequate to supply the necessary 10^7ergs/cm^{2}sec for the active corona.

The preceding paper, by Hollweg, on coronal heating by waves provides a sufficient introduction to coronal heating for the purposes of the present paper. Here we are interested in the heat supply to the active corona, composed of x-ray loops and filaments emitting a total energy of the order of 10^7ergs/cm^{2}sec.

The convective motions in the photosphere supply a variety of magnetic strains and fluid motions (MHD waves) to the solar corona, forming the basis for the many ideas presently in vogue for coronal heating. Indeed, it would be surprising if there was not some contribution from each of several classes of waves. The problem is to establish the principal contribution, and that brings us to the physics of the dissipation. The familiar viscous and resistive effects yield characteristic dissipation times of l^2/ν and l^2/η in field structures with a scale l . Neither is adequate to provide significant dissipation of waves with scales of km or more. For instance, magnetic structures with a scale of 10^3km decay in periods of 10^4 years. Evidently something more effective than passive diffusion of magnetic structures and wave motions must be operating universally in the corona. Something very much more effective!

Now it has been known for a couple of decades that the corona of the sun is particularly hot and dense in regions of strong magnetic field. The UV and x-ray observations in recent years have established just how close this relation really is. Rosner, Tucker, and Vaiana (1978), summarizing the observations and the implications of the theoretical models of coronal loops, conclude that, for various reasons, all sources can be ignored except direct conversion of "static" magnetic energy into thermal energy. They suggest that the visible corona is entirely a magnetic creation, supported, confined, and heated directly by the magnetic field. And that brings us firmly up against the problem of the dissipation of magnetic fields in the highly conducting gases of the solar corona.

How can magnetic energy be converted directly and rapidly into heat?

In view of the high electrical conductivity ($\sigma = 10^{16}-10^{17}$/sec) of the coronal gas and the relatively weak fields ($\lesssim 10^2$ gauss), the only known means for converting magnetic energy directly into heat is through concentration of the magnetic strain $\nabla \times \mathbf{B}$ (i.e. the electric current $\mathbf{j} = (c/4\pi) \nabla \times \mathbf{B}$) into thin sheets. One can estimate that the current sheet must have a thickness of 1 km or less if the resistive tearing mode is effective, or if sufficient plasma turbulence can be generated by an electron conduction velocity comparable to the ion thermal velocity, or 1 m or less if it is necessary to drive the electron conduction velocity as high as the electron thermal velocity to achieve the necessary dissipation. So consider why electric currents (i.e. the magnetic strains) might concentrate into exceedingly thin sheets.

The usual state of affairs in the magnetic regions of the solar corona involves re-entrant fields arching up from the photosphere into the corona over dimensions of 10^3-10^5 km, with typical field strengths of 10^2 gauss. The fields are rooted in the dense convecting gas of the photosphere which shuffles the footpoints of the lines of force and causes the lines to wrap and wind about their neighbors, as sketched in **Figure 1**. The basic physics of the situation is contained in the topology of the winding pattern of lines of force, which is more easily treated in the straightened configuration sketched in Figure 2. The principal field may be taken to be uniform with strength $\mathbf{B_0}$ extending in the z-direction from the anchor plane $z = -L$ to the anchor plane $z = +L$. The surfaces $z = \pm L$ represent the photosphere where the fluid shuffles about in complex patterns, wrapping the lines of force around each other as sketched in Fig. 2. So long as the scale l of the shuffling is sufficiently small compared to the length L of the lines, the field direction deviates but little from the z-direction and the change in the field from the original uniform $\mathbf{B_0}$ is small. One can write

$$\mathbf{B} = \mathbf{e_z} B_0 + \epsilon \, \mathbf{b} \, (x, y, z) \qquad (1)$$

where $\epsilon \ll 1$.

To treat the simplest case, consider static equilibrium of the magnetic field $\mathbf{B}$ in an incompressible medium of uniform density ρ , so that the total pressure in the fluid can be written $P - \rho g z$, and the equation for equilibrium reduces to

$$4\pi \nabla P = (\nabla \times \mathbf{B}) \times \mathbf{B}. \qquad (2)$$

Write $P = p_0 + \epsilon p$. It is then a simple matter to show that equilibrium far removed ($\gg l$) from the boundaries $z = \pm L$ is possible only for $\partial \mathbf{b}/\partial z = 0$ (Parker, 1972, 1979, pp. 359-391; Yu, 1973; Rosner and Knobloch, 1982). That is to say, the winding pattern of the lines of force must be invariant along the uniform field $\mathbf{B_0}$ in the z-direction. If this condition is not satisfied, one finds that the resulting dynamical nonequilibrium takes the form of localized neutral point reconnection at various locations throughout the field where the topology of the winding pattern changes. In other words, the nonequilibrium involves the formation of current sheets whose thickness declines with the passage of time until dissipation, of one form or another, becomes important. The transverse components of $\mathbf{b}$ that cause the nonequilibrium are then "eaten" away by the dissipation at a rate v cm/sec,
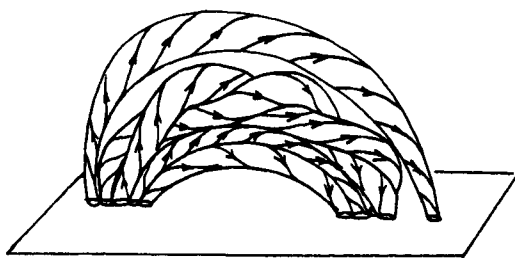
Fig. 1: A sketch of the field above a bipolar magnetic region, illustrating the wrapping of the lines about their neighbors.
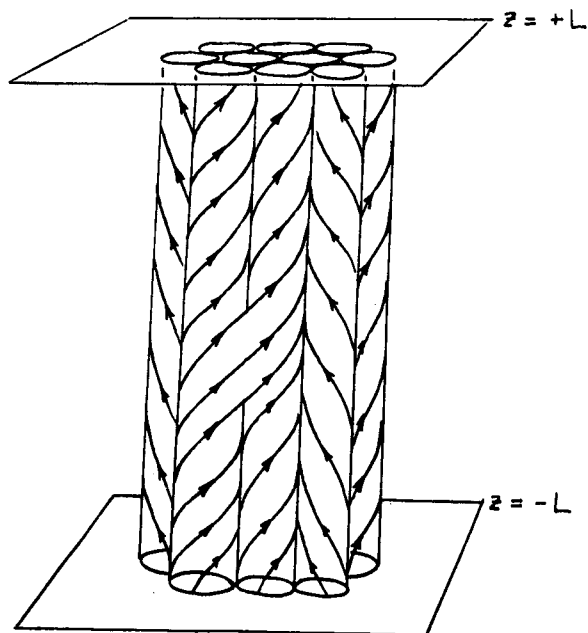
Fig. 2: A straightened field in which the lines of force wrap in irregular patterns about their neighbors.

where

$$V_A / N_M^{1/2} \lesssim u \lesssim V_A / \ln N_M \qquad (3)$$

in order of magnitude (Parker, 1957, 1979, pp. 392-439; Petschek, 1964) where V_A is the characteristic Alfven speed computed in the transverse field $\mathbf{b}$, and N_M is the effective magnetic Reynolds number lV_A / η. The resistive diffusion coefficient η may or may not be enhanced by plasma turbulence, and a local resistive tearing mode may become operative depending upon local conditions.

One recognizes that the random shuffling of the footpoints of the coronal fields must introduce transverse components $\mathbf{b}$ whose topology varies along the field, causing that part of $\mathbf{b}$ to be dissipated directly into heat through the familiar neutral point reconnection.

It can also be shown that any tube of flux that is displaced and misaligned relative to its neighbors is dissipated through unlimited decrease of the transverse dimension (Parker, 1981a,b).

But what about the transverse field that is invariant along $\mathbf{B}_z$, i.e. $\partial \mathbf{B} / \partial z = 0$? Such fields are composed of twisted flux tubes that extend uniformly from $z = -L$ to $z = +L$. The equilibrium conditions are well known. With $\nabla \cdot \mathbf{B} = 0$ one writes

$$B_x = + \partial A / \partial y, \quad B_y = -\partial A / \partial x. \qquad (4)$$

Substituting into (2) yields the conditions

$$P = P(A), \quad B_z = B_z(A)$$

so that

$$P + B_z^2 / 8\pi = F(A) \qquad (5)$$

where F is an arbitrary function of its argument. The vector potential is then required to satisfy the field equation

$$\nabla^2 A + 4\pi F'(A) = 0. \qquad (6)$$

The fluid pressure is uniform along each line of force so that P is controlled at the boundaries $z = \pm L$. There are generally infinitely many solutions to (6) for any reasonable choice of the arbitrary pressure function $F(A)$, and there are infinitely many reasonable choices for $F(A)$, so solutions to (6) cover many field configurations. It is a curious fact, however, that all such solutions possess special symmetries that are generally not honored in nature. In fact, there is generally no equilibrium among more than two close-packed twisted flux tubes, and then only if they are of opposite twist. Three or more close packed twisted tubes produce neutral point reconnection (called coalescence of islands in laboratory plasmas) which reduces the transverse field A toward two opposite twisted tubes across the entire xy-plane (Parker, 1983a, c), which we will explain in a moment.

Altogether it follows that the transverse field introduced by the shuffling and rotation of the footpoints is dissipated directly, through neutral point reconnection, into heat, whatever the topology of $\mathbf{B}$, invariant or otherwise. That is to say, the formation of thin current sheets is a natural consequence of

26

the dynamical nonequilibrium of the field.

It follows that the heat input to the corona is equal to the average rate at which the convection in the photosphere does work on the footpoints of the magnetic field. Unfortunately the rate at which the convection does work on the field is not easy to estimate, but it is generally believed to be as large as the 10^7ergs/cm^{2}sec required for active coronal regions (Sturrock and Uchida, 1981; Parker, 1983b). Remembering that the field is composed of isolated intense flux tubes of some 1600 gauss at the photosphere, consider an active region where the mean field is 10^2 gauss, so that approximately one sixteenth of the area of the photosphere is occupied by flux tubes of 1600 gauss. If the transverse component in the mean field is, say, 20 gauss, then the transverse field in the concentrated flux tube is of the order of 80 gauss. The transverse Maxwell stress is then $B_z B_\perp /4\pi \cong 10^4$dynes/cm^2 in the concentrated tube at the photosphere. If such a stress acts against fluid velocities of the order of 200m/sec, the rate at which work is done on the field is 2×10^8ergs/cm^{2}sec. This occurs over one sixteenth of the area, so the mean rate at which work is done is approximately 10^7ergs/cm^{2}sec.

It would seem, therefore, that the visible corona can be understood as a direct consequence of the shuffling and rotation of the solar magnetic field in the photospheric convection, through the general dynamical nonequilibrium of the resulting distorted magnetic field. We presume that this is generally the case in all stars where a magnetic field extends into a tenuous atmosphere from a dense convecting surface below. The dynamical nonequilibrium (i.e. the neutral point reconnection) goes sufficiently rapidly in the tenuous atmosphere, where V_A is large, that the work done on the field by the convection is converted directly into heat. The x-ray corona, then, is the magnetic offspring of surface convection.

But now let us go back to the assertion that close-packed twisted flux tubes generally have no static equilibrium, in spite of the variety of solutions to (6). The problem with the solutions to (6) is most readily demonstrated by considering a solution to (6). To treat the simplest case, suppose that

$$4\pi F(A) = c + k^2 A^2 ,$$

where c and k are constants. Then (6) becomes

$$\nabla^2 A + 2k^2 A = 0 . \tag{7}$$

The solution

$$A = C \sin kx \sin ky \tag{8}$$

represents close packed flux tubes of opposite twist arranged in a checkerboard pattern. The projection of the lines of force on the xy-plane is given by $A(x,y) = \underline{constant}$, sketched in Figure 3. Note that each twisted tube would be circular in cross-section were it not squashed into a square cross-section by the pressure of its four neighbors, all with opposite twist to the tube in question. Each tube presses hardest against its neighbors at the middle of each face, of course. The pressure $F(A)$ is constant along each line of force, so the pressure around the boundary of each cell is uniform. Hence, the deformation into a square cross-section is carried out, not by the uniform pressure $F(A)$, but by the pressure of the transverse field (B_x, B_y).

27
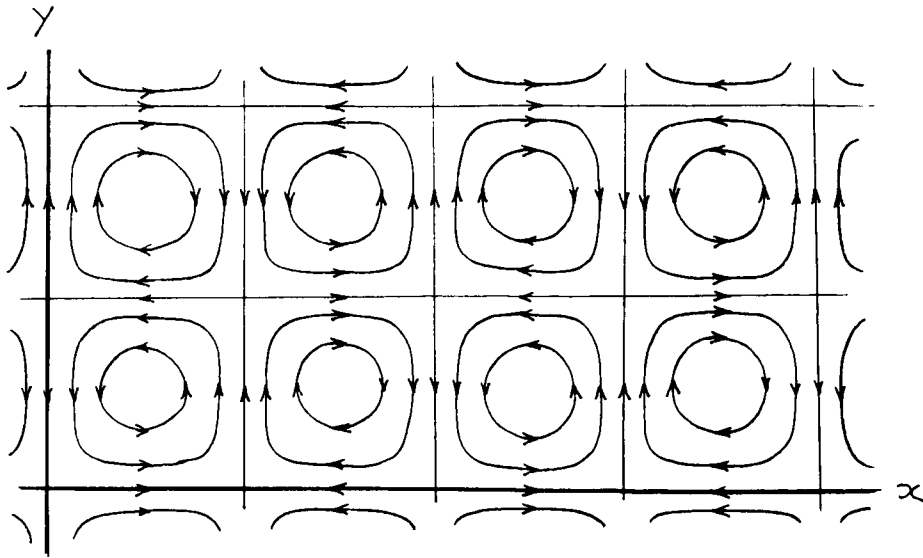
Fig. 3: The projection of the regular field (8) onto the xy-plane showing the regular checkerboard pattern of opposite twisting.
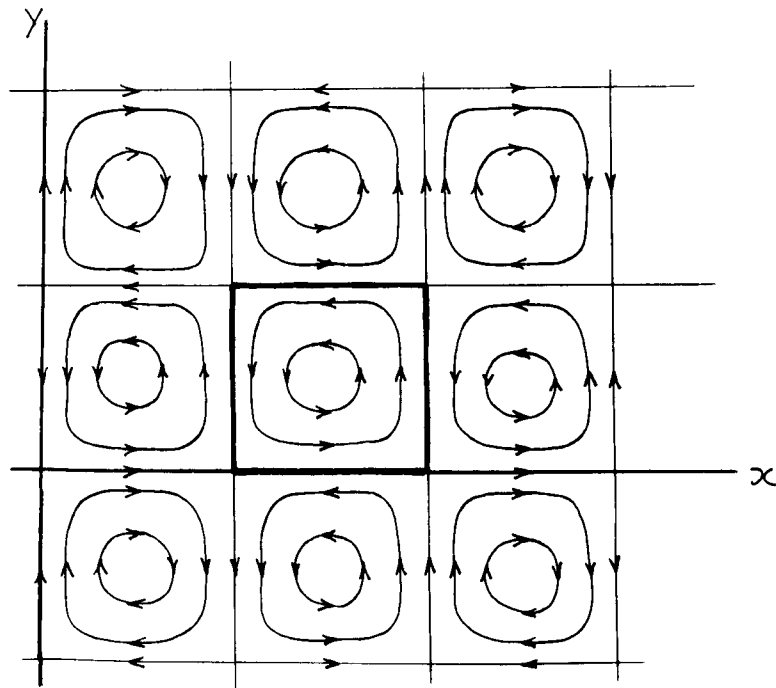
Fig. 4: The same projection as shown in Fig. 3 with one cell reversed so that it is surrounded by current sheets (heavy lines).

Now consider what would happen if a flux tube were replaced by a tube of opposite twist, as sketched in Figure 4. It would then be surrounded by four neighbors with the same twist as itself, with the result that the transverse field (B_x, B_y) changes sign abruptly across each common boundary. Nothing else but the sign of (B_x, B_y) is changed, of course, so that the equilibrium condition (6) is satisfied everywhere except perhaps at the boundaries. Needless to say, the reversed tube is squashed into a square cross-section by the extra pressure exerted by its neighbors on each of its four faces. But that pressure is not transferred across the boundary by the transverse field because the transverse field passes through zero as it changes sign across the boundary. Hence, the extra pressure can only devolve upon the fluid, causing the fluid pressure to be larger near the middle of each face. The higher pressure near the middle of each face squeezes the fluid out from between the opposite fields on either side of the boundary, expelling the fluid along the boundary into the region around the vertices. It is just the familiar neutral point reconnection scenario, of course, leading to coalescence of the transverse fields of neighboring tubes, as sketched in Figure 5.

The general principle is that no tubes with the same sense of twist can be in equilibrium where they are pressed together over a common boundary of finite length. The equilibrium solutions to (6) surround each cell with cells of opposite twist, permitting contact of cells with the same twist only at point vertices. The fact is that in nature the twisted tubes are formed to sizes and strengths that generally do not pack together with the necessary delicate balance at their vertices. They tend to mash together to form common boundaries instead of common points, as sketched in Figure 6. And even if we imagine the unlikely situation that all tubes have the same size and strength, all neatly assembled in an alternate checkerboard pattern as sketched in Figure 3, we should be aware that they would soon slip into the lower energy state of hexagonal close packing, in which all vertices involve three, rather than four, cells. Whenever three cells are packed together, at least two have the same sense of twisting, providing neutral point reconnection on at least one of the three common boundaries.

To express the problem in different terms, consider the common vertex of three close-packed flux tubes. At least two of the tubes must have the same sense of twist, with the result that they undergo neutral point reconnection on their common boundary. The reconnection can be avoided, of course, if a fourth flux tube with opposite twist is pressed in between the two with the same twist. The difficulty is that the fourth tube must be pressed in between with just enough force that it extends to the common vertex. If it fails to press in all the way to the vertex, the two tubes with the same twist still have a common boundary, with its nonequilibrium neutral point reconnection. On the other hand, if it presses a little too far, then it finds itself with a common boundary with the third of the original three flux tubes, which has the same sense of twist as the fourth, and again there is nonequilibrium. The vertices shown in Fig. 6 illustrate this problem, where the four-way junctions of cells are in fact made up of two three-way junctions or vertices because the pressures in the four participating flux tubes generally do not balance perfectly to meet only at a point vertex. The fourfold (or sixfold, etc.) vertex necessary for equilibrium is something that is achieved only in mathematical constructions, never in physical constructions by chaotic nature.
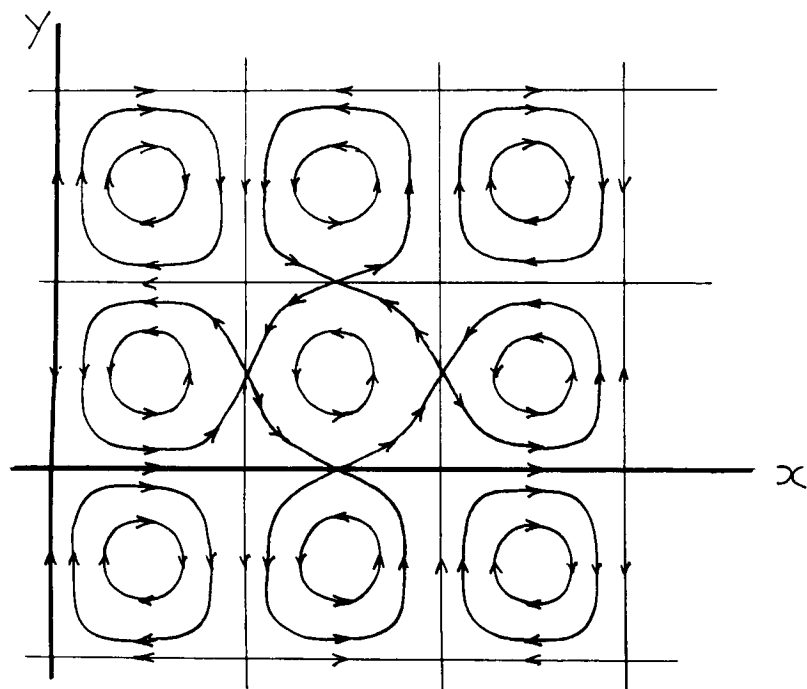
Fig. 5: A sketch of the magnetic lines of force following neutral point reconnection across the neutral sheets shown in Fig. 4.
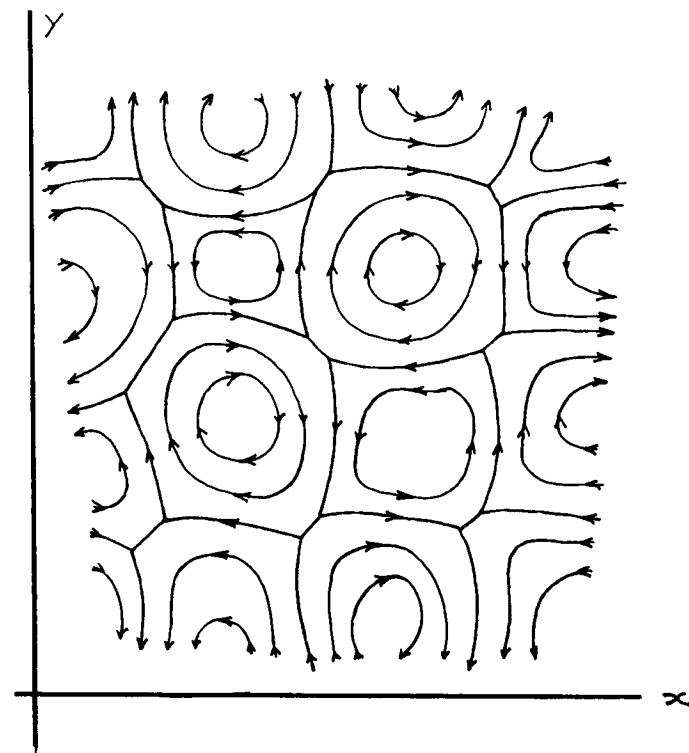
Fig. 6: A sketch of the magnetic lines of force of twisted flux tubes of various sizes and strengths packed closely together, illustrating the common boundaries of tubes with the same sense of twist.

The general absence of equilibrium for any close-packed collection of twisted flux tubes of various strengths and sizes can be demonstrated in more formal ways (Parker, 1983c,d,e). The present qualitative description is designed to illustrate how the neutral point reconnection comes about. The basic fact is that any close-packed wrapping of fields leads directly to neutral point reconnection until the field is reduced to no more than two invariant tubes of opposite twist. We suggest that this general dynamical nonequilibrium of magnetic fields is the basic source of heating in the active stellar corona. The net result is that the work done by the fluid in shuffling the footpoints goes more or less directly into heat in the fluid above.

References

Parker, E.N., Sweet's mechanism for merging magnetic fields in conducting fluids, J. Geophys. Res.,62, 509–520, 1957.

Parker, E.N., Topological dissipation and the small-scale fields in turbulent gases, Astrophys. J., 174, 499–510, 1972.

Parker, E.N., Cosmical Magnetic Fields, Clarendon Press, Oxford, 1979.

Parker, E.N., The dissipation of inhomogeneous magnetic fields and the problem of coronae. I. Dislocation and flattening of flux tubes, Astrophys. J., 244, 631–643, 1981a.

Parker, E.N., The dissipation of inhomogeneous magnetic fields and the problem of coronae. II. The dynamics of dislocated flux, Astrophys. J., 244, 644–652, 1981b.

Parker, E.N., Magnetic neutral sheets in evolving fields. I. General theory, Astrophys. J., 264, 635–641, 1983a.

Parker, E.N., Magnetic neutral sheets in evolving fields. II. Formation of the solar corona, Astrophys. J., 264, 642–647, 1983b

Parker, E.N., The rapid dissipation of magnetic fields in highly conducting fluids, Geophys. Astrophys. Fluid Dynamics,22, 195–218, 1983c.

Parker, E.N., Absence of equilibrium among close-packed twisted flux tubes, Geophys. Astrophys. Fluid Dynamics (in press) 1983d.

Parker, E.N., The hydrodynamics of magnetic nonequilibrium, Geophys. Astrophys. Fluid Dynamics (in press) 1983e.

Petschek, H.E., Magnetic field annihilation, AAS–NASA symposium on the physics of solar flares, U.S. Government Printing Office, Washington, DC, ed. by W.N. Hess, pp. 425–439, 1964.

Rosner, R. and E. Knobloch, On perturbations of magnetic field configurations, Astrophys. J., 252, 349–357, 1982.

Rosner, R., W.H. Tucker, and G.S. Vaiana, Dynamics of the quiescent solar corona, Astrophys. J., 220, 643–665, 1978.

Sturrock, P.A. and Y. Uchida, Coronal heating by stochastic magnetic pumping, Astrophys. J., 246, 331–336, 1981.

Yu, G., Hydrostatic equilibrium of hydromagnetic fields, Astrophys. J., 181, 1003–1008, 1973.

Page intentionally left blank

HRTS OBSERVATIONS OF THE FINE STRUCTURE AND DYNAMICS
OF THE SOLAR CHROMOSPHERE AND TRANSITION ZONE

Kenneth P. Dere
E. O. Hulburt Center for Space Research
Naval Research Laboratory
Washington, D.C. 20375

ABSTRACT

Arc-second UV observations of the Sun by the NRL High Resolution Telescope and Spectrograph (HRTS) have led to the discovery of dynamic fine structures such as 400 km s^{-1} coronal jets and chromospheric jets (spicules) and have provided new information about the structure and dynamics of the transition zone. These observations are reviewed and their relevance to the origin of the solar wind is discussed.

Introduction

Recent results derived from UV observations of the solar chromosphere and transition zone made by the NRL High Resolution Telescope and Spectrograph (HRTS) are presented here. These observations have an inherent interest since they are made with the highest spatial resolution yet obtained in the UV and show the first UV observations of solar fine structure. They are also of specific interest to this conference since the solar wind and many of its disturbances presumably originate somewhere near the solar surface. The HRTS instrument consists of a Cassegrain telescope which focuses a solar image with 1 arc-sec. resolution onto the slit jaw of the spectrograph which produces stigmatic photographic spectra of the 1000 arc-sec. long slit in the 1175-1710 Å wavelength range. To date, there have been four rocket flights of the HRTS instrument (referred to as HRTS 1-4) and it is scheduled to be flown on Spacelab 2.

The Chromosphere

Figure 1 shows some of the general properties of the quiet Sun in the HRTS spectra. On the left is a spectroheliogram obtained in Hα by Sacramento Peak Observatory essentially simultaneously with the HRTS spectra obtained during the third flight. The Hα image consists of dark absorption features, the dark mottles, which outline the supergranulation cells. Also indicated is the position of the HRTS slit and the corresponding stigmatic spectra in lines of C I (10^4 K), Si II (2×10^4 K) and C IV (10^5 K). All three ions show intense emission where the slit crosses the supergranular cell boundaries although the C IV emission appears in some cases to be shifted towards the limb. This is consistent with limb brightening curves which show C IV to be produced 4 arc-sec. above the photosphere. An absolute wavelength scale can be determined from the narrow Si I lines in the vicinity with a accuracy of about 2 km s^{-1}.

Examples of small scale structures observed in the HRTS spectra are shown in Figure 2. Here, a short segment of HRTS 1 C IV and C I spectra near the limb are displayed. At the top of the C IV spectra is a coronal jet with line
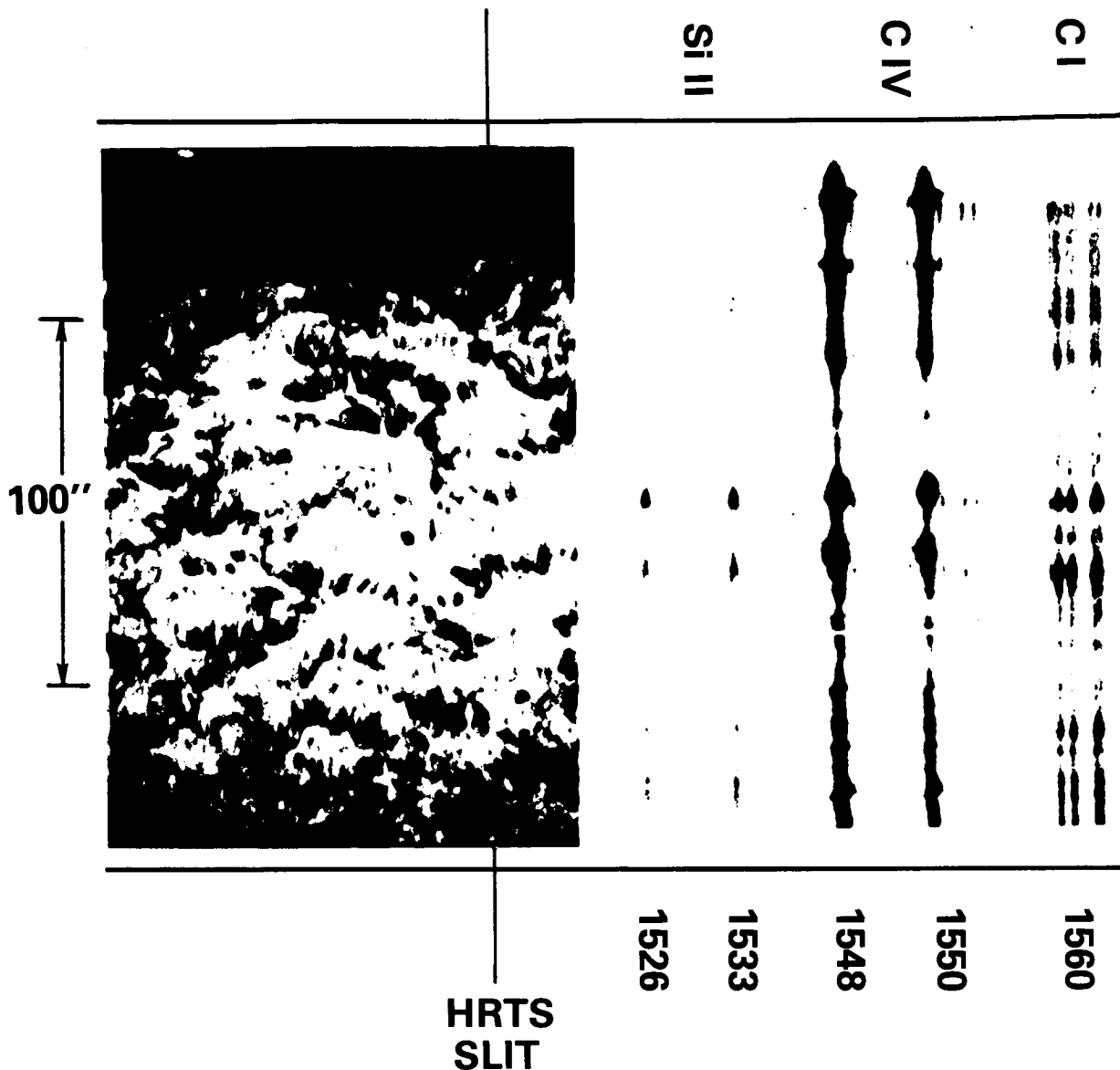
Figure 1. HRTS spectra of Si II, C IV, C I and an Hα spectro-
heliogram at the limb of the solar south pole.

of sight velocities of 200 km s^{-1} and projected radial velocities of 400 km s^{-1}.
Shifts to the left are blueshifts and are caused by plasma moving toward the
observer or away from the Sun. Near the bottom of that figure is a "turbulent"
event characterized by wide, symmetric C IV profiles which are produced by random
nonthermal velocities on the order of 150 km s^{-1}. In the C I spectra, at least
six chromospheric jets are seen as emission features in the line wings which are
caused by plasma moving at 10-20 km s^{-1}. It is interesting to note that the
coronal jet and turbulent event seen in C IV have no noticeable cospatial signa-
ture in the C I profiles and the chromospheric jets seen in C I both occur where
the C IV intensity is quite low. This is true for the particular events seen in
Figure 2 and in general.
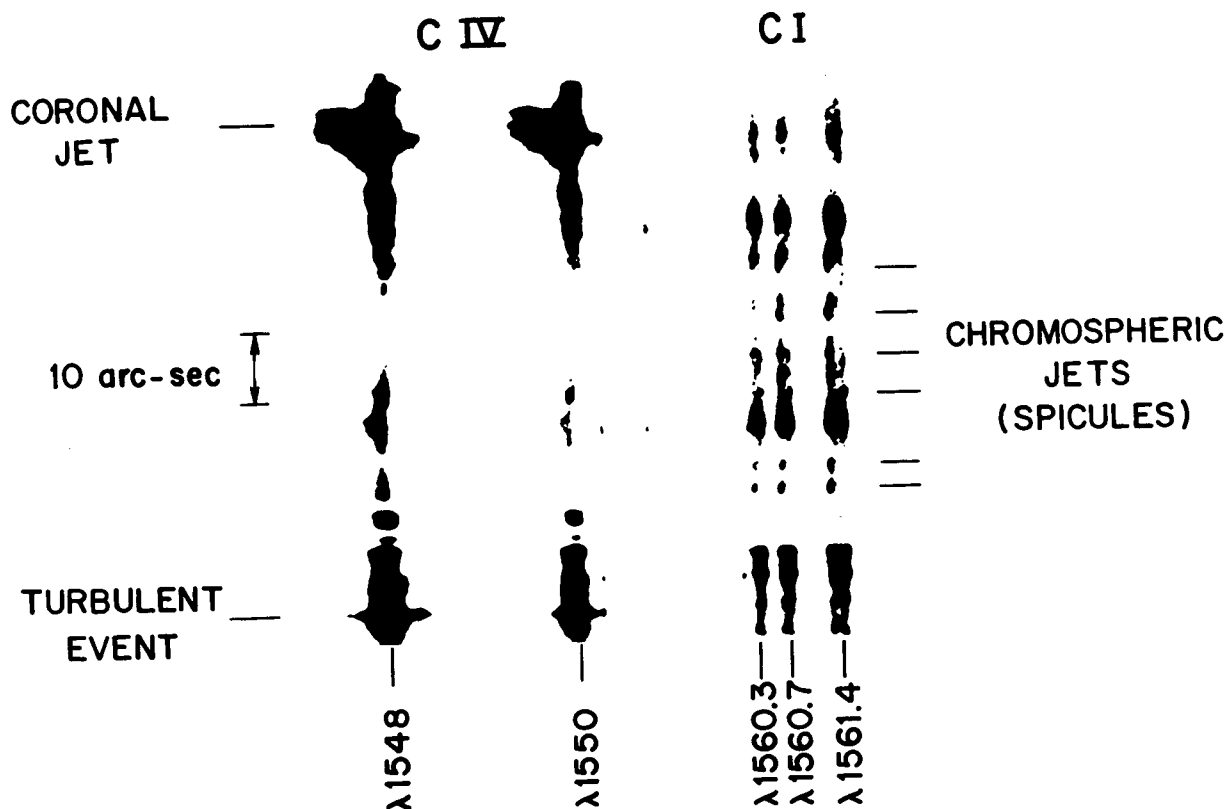
Figure 2. Examples of fine structures observed in HRTS spectra: coronal jets, turbulent events and chromospheric jets (spicules).

Spicules, which play a important role in the convective transport in the solar atmosphere, have been seen in visible light above the solar limb for over a hundred years. They are slender jets of gas which are observed to rise and often fall at a velocity of 25 km s^{-1}. However, there has never been an identification of spicules with any known phenomenon on the disk although it is often assumed that they are the dark Hα mottles. We now believe there is sufficient evidence to identify the chromospheric jets seen in Figure 2 as spicules on the disk (Dere, Bartoe and Brueckner, 1983).

Typically the chromospheric jets (spicules) have a size of 1-2 arc-sec. projected along the slit and twice as many blue shifted (rising) events are seen as the weaker redshifted (falling) events. It is possible that with greater sensitivity we would see equal numbers of the two. The chromospheric jets can be seen in other lines of C I such as the allowed multiplet at 1657 Å and the intercombination lines near 1613 Å as well as in lines of other chromospheric ions such as Si I, Si II and S I. However, they are not seen in lines of somewhat hotter ions such as C II or Si III and as we have previously noted, C IV is often extremely weak at the sites of chromospheric jets. Clearly they are exclusively a chromospheric phenomenon. Spicule profiles of the C I 1560 Å lines are shown in Figure 3 as well as nearby nonspicular profiles for comparison. The spicular emission peak is shifted to the blue by .05 to .1 Å
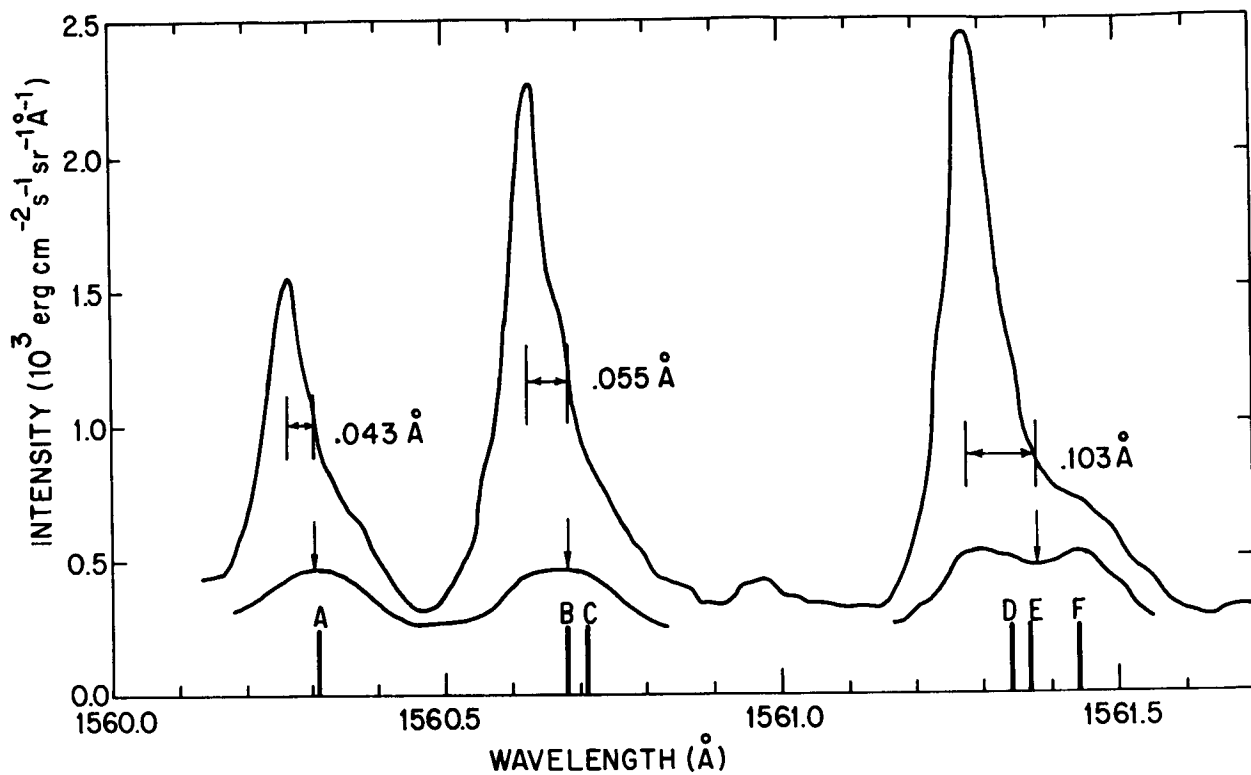
Figure 3. The profiles of the C I lines near 1560 Å in a spicule. The arrows indicate the observed average wavelength of the three lines (blends) made up of the five C I lines labelled A through F.

corresponding to line of sight velocities of 10 to 20 km s^{-1} and shows no self reversal as do more typical nonspicular profiles. From the intensity and lack of self absorption in these profiles a temperature of 1.6×10^4 K and density of 10^{11} cm^{-3} are derived. These are comparable to what is found from visible light observations.

Many observers have come to believe that the dark Hα mottles observed on the disk should be identified with the spicules seen at the limb although a study of Hα mottle profiles (Grossmann Doerth and v. Uexkull, 1971) shows that the velocities in the mottles are significantly lower than those in spicules. This same study did find region of 20 km s^{-1} flows but only in "quite unconspicuous, little gray features" which were not considered important. Our own observations confirm the low velocities in the supergranular cell boundaries where the mottles are found. The chromospheric jets (spicules), while not as bright as the network emission, are nevertheless quite conspicuous in the ultraviolet spectra. The chromospheric jets are generally unrelated to the dark Hα mottles.

In conclusion, we confirm many of the known physical properties of spicules derived from ground-based observations as is to be expected. The surprising new result is that spicules occur in the supergranulation cell interiors and not at the boundaries where the strongest magnetic fields tend to be clustered.

The two strong C IV lines near 1550 Å are our primary diagnostics for the transition zone. Both lines are formed around 10^5 K and are optically thin on the disk. The regions viewed by the HRTS 3 slit include the limb above a polar coronal hole which extended up to a latitude of 50°, mostly quiet Sun and a filament near Sun center. We quantify the information in the profiles by taking moments of the wavelength weighted by the specific intensity. In this way we derive the integrated line intensity, the net Doppler velocity and the line width. These three quantities are shown in Figure 4 for HRTS 3 data along the entire slit. Some of the more intense regions, such as the limb, are over-
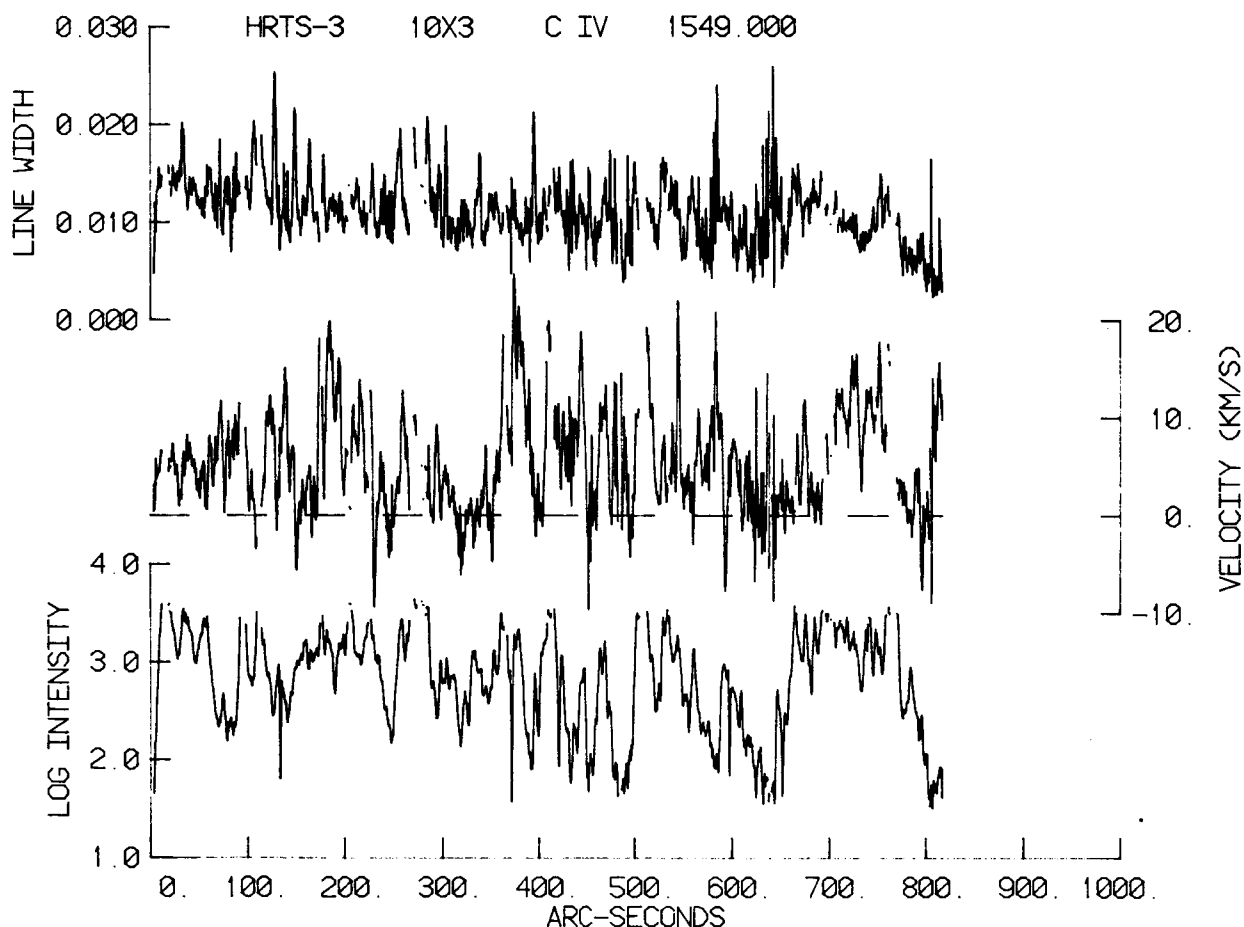
Figure 4. Intensity (erg cm^{-2} s^{-1} sr^{-1}), velocity (km s^{-1}) and line width (Å^2) for C IV λ1548 and λ1550 as a function of position along the slit.

exposed and are not plotted. The limb defined by the continuum is near an indicated height of 17 arc-sec. Again, the regions of high C IV intensity generally pick out the chromospheric network although there is no strong point for point correlation with C I intensities which also pick out the network. In fact, from their respective autocorrelation coefficients for line intensity, the C IV transition zone structures have a typical size of 1.5 arc-sec compared

to 8 arc-sec for the C I chromospheric structures. Preliminary two-dimensional images in C I and C IV show this large scale relationship (the network) between the two but show little similarity in the small scale features.

The line of sight velocities displayed in Figure 4 are predominately away from the observer and from this one can conclude that the transition zone consists of material generally falling toward the solar surface. The velocity data, as summarized in Figure 5, do show some regions of upflows but the average Doppler shift is 0.028 Å which corresponds to a downflow a 5.4 km s^{-1}
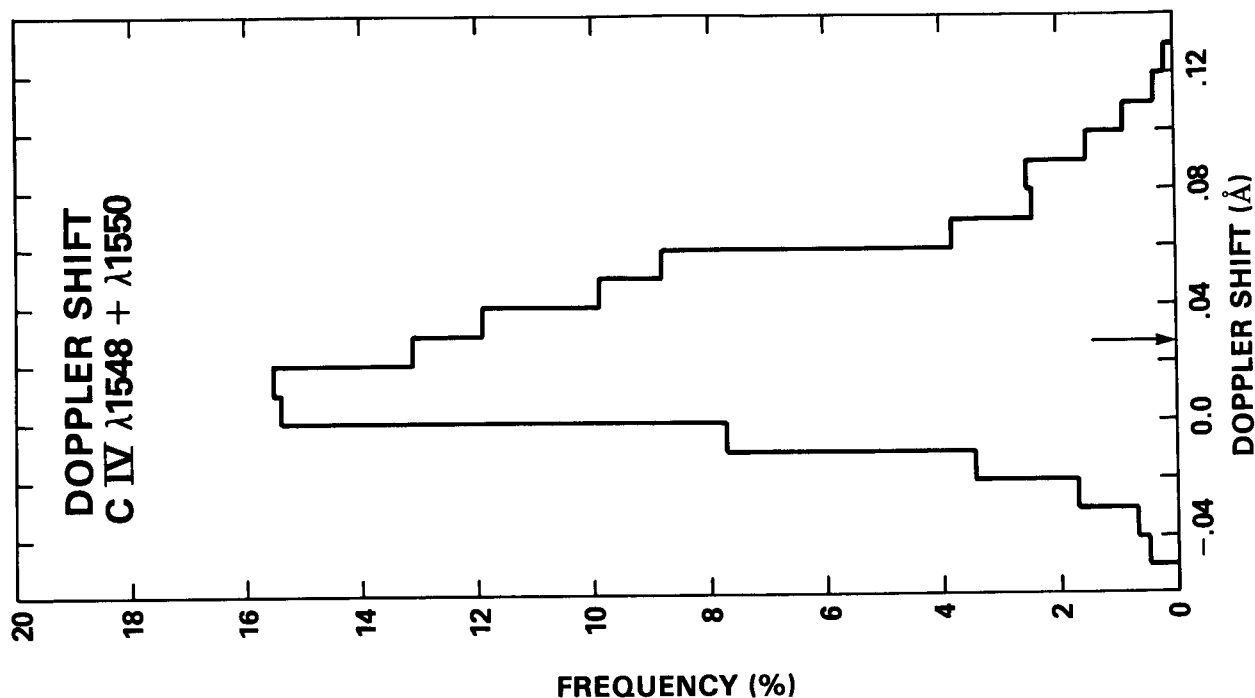
Figure 5. Relative frequency of occurrence of the C IV Doppler shifts.

at disk center. We emphasize that our velocity scale is relative to the narrow chromospheric Si I lines and should be accurate to 0.01 Å or 2 km s^{-1}. Above the limb redshifts are also seen. An examination of these C IV line profiles shows that their peak is near the rest wavelength and the derived redshift is due to the greater strength of the red wing as compared with the blue. As we noted, a polar hole extended up to a latitude of about 50° during the HRTS 3 flight. This latitude corresponds to a relative position of 240 arc-sec on Figure 4. There is no sign of major large scale outflows in the transition zone of this polar coronal hole. Using a wavelength scale referenced to chromospheric lines, Doschek, Feldman and Bohlin (1976) also find little evidence for outflows in coronal holes. Rottman and Orrall (1982) show a relative blueshift between coronal holes and other solar regions but in the light of the above results, it is not clear that this can be interpreted as an absolute blueshift in coronal holes.

Previous studies of the transition zone at lower resolution (Lites et al. 1976 and Gebbie et al. 1981) have found that regions of downflow are correlated with regions of high intensity. However our own data show no real correlation between these two quantities as presented in Figure 6. In a large
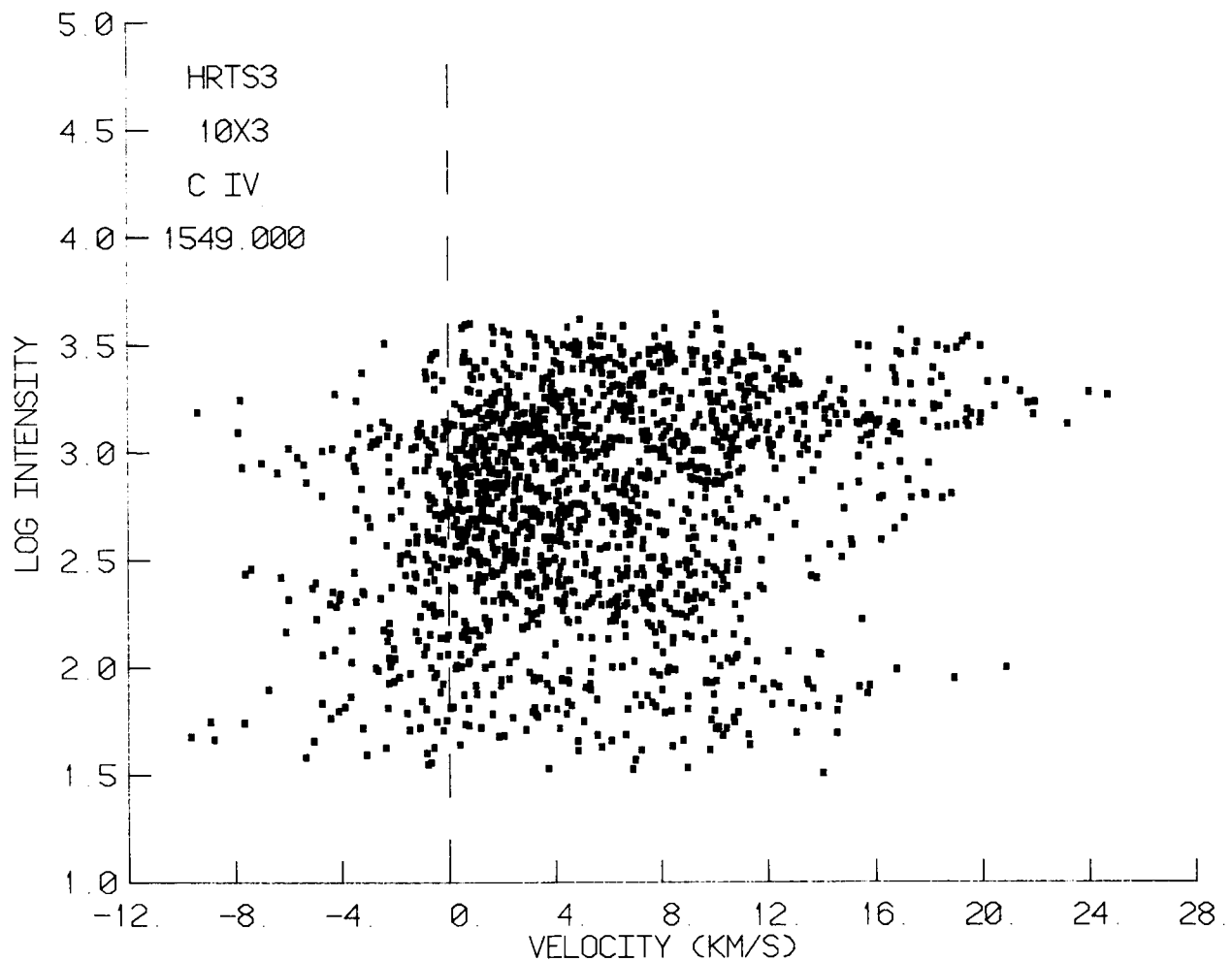
Figure 6. A scattergram of C IV intensity versus C IV velocity near Sun center.

scale sense, there are certainly some bright regions which show strong down-flows but this relationship breaks down in general and when these regions are examined in detail. An autocorrelation analysis also shows that the size of the bright C IV regions is around 1.5 arc-sec. and the 3 arc-sec. size of the flowing structures is significantly larger.

The line width data shown in Figure 4 reveal a number of wide profile events along the slit which consist of both the jets and the turbulent events, examples of which were displayed in Figure 2. Brueckner and Bartoe (1983) provide a detailed anlysis of the jets and turbulent events. Even the more typical profiles have a line width which requires turbulent or nonthermal

velocities on the order of 21 km s^{-1} together with thermal broadening to explain the observed width. The rise in the line width toward the limb is due to the integration over an increasingly larger number of flow fields.

Turbulent velocities in the turbulent events range from 50 km s^{-1} to 250 km s^{-1}. Most of these events occur only once but some of the larger ones are observed to reoccur at the same position in our 4 minute observing time. Size scales are often at the instrumental resolution (1 arc-sec.). They are seen in lines spanning the temperature range 2 x 10^4 to 2 x 10^5 K although apparently similar events have also been observed in coronal (2 x 10^6 K) lines in the Skylab data.

A time history of one of the more spectacular jets is shown in Figure 7.
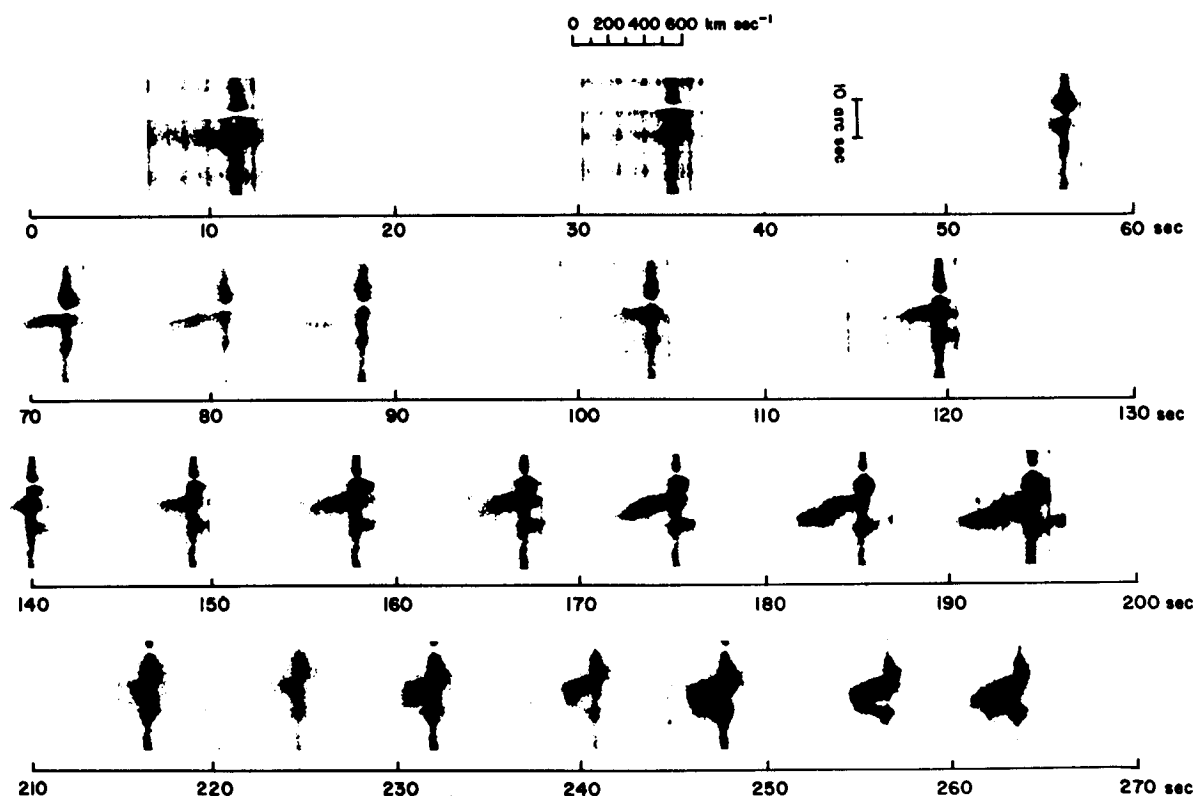
Figure 7. A time sequence of coronal jets observed in C IV.

This particular jet, seen as the strongly blue shifted emission in C IV λ1548, appears four times at the same location during a four minute rocket flight. The maximum velocities which reach 400 km s^{-1} are consistent with an acceleration of 5 km s^{-2} that persists throughout the observed lifetime. The jets contain material over a wide range of temperatures (2 x 10^4 - 2 x 10^5 K). One interpretation is that of a magnetic loop being expelled outward through the solar atmosphere. The Hα slit jaw pictures do not show any feature that might correspond to the jets.

The time sequence of C IV spectra in Figure 8 shows numerous examples of a less spectacular but more prevalent sort of jet. These have maximum velocities of from 80 to 150 km s^{-1} and often have both blueshifted and redshifted components. Their size is generally near the instrumental resolution.
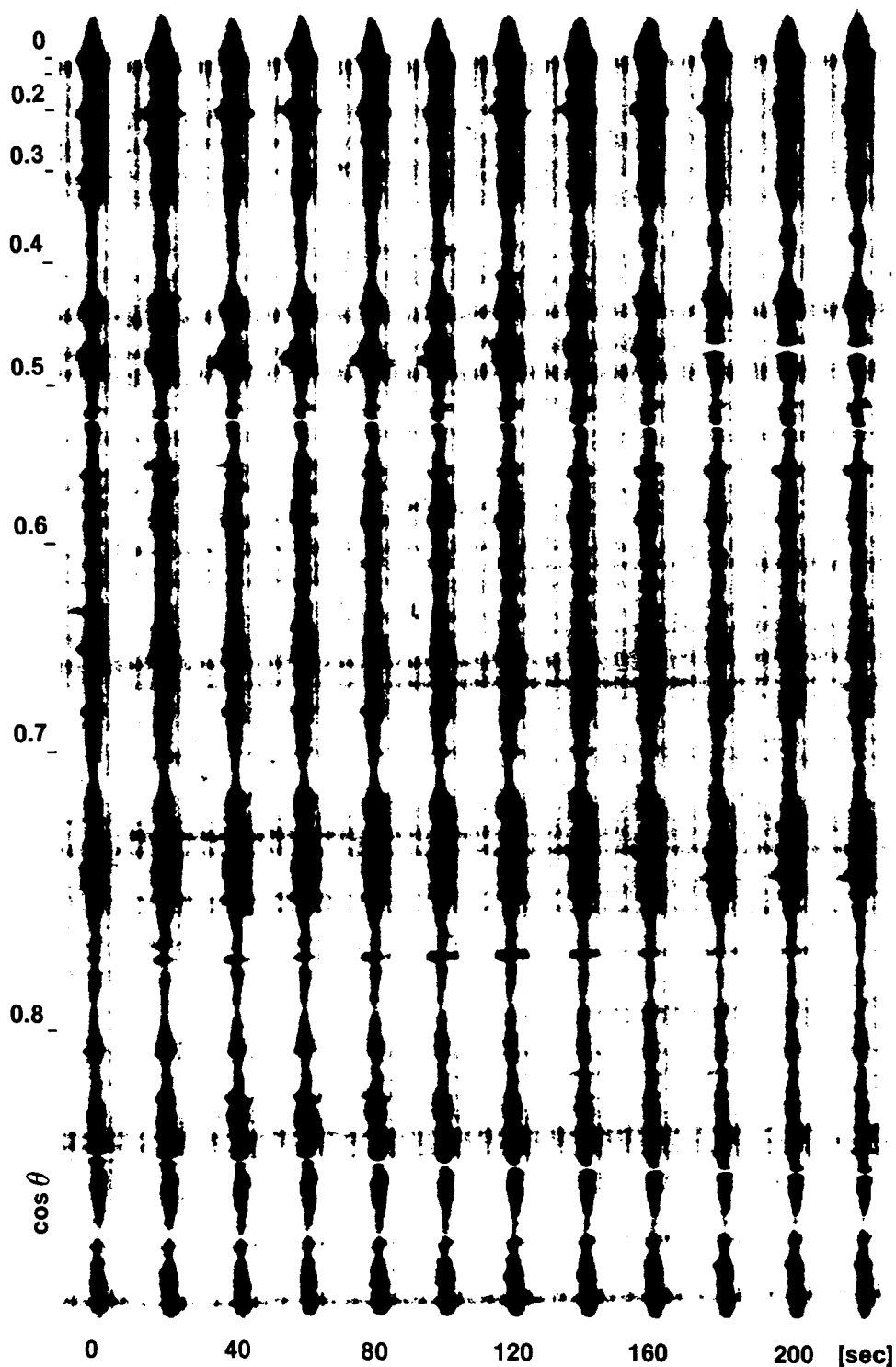
Figure 8. A time sequence of C IV spectra showing numerous 100 km s^{-1} jets.

Origin Of The Solar Wind

The solar wind has an associated mass flux of 2×10^{12} g s^{-1} which must be present at chromospheric and transition zone levels and should be observable with suitable instrumentation. In the chromosphere the only significant vertical flows that we observe are in the spicules; about 2/3 are outflows and 1/3 downflows (since the downflows are less intense, it is possible that there are equal numbers of each). Roughly only one in 10 spicules produces a measurable blueshift in the transition zone. From a density of 10^{10} cm^{-3}, a velocity of 25 km s^{-1} and a fill factor of 2%, the average outward mass loss in spicules observed at transition zone temperatures is 2×10^{13} g s^{-1}, an order of magnitude above solar wind requirements. The downward mass flow in the transition zone for a pressure $n_e T_e = 10^{15}$ cm^{-3} K and a velocity of 5 km s^{-1} is 5×10^{14} g s^{-1}. This latter figure assumes a fill factor of unity which rests on the interpretation of the transition zone as an extremely thin (20 km) layer. Since most high resolution spectroheliograms of the upper chromosphere and corona show the ubiquitous presence of filamentary structures, it is likely that the transition zone has a similar consistency. In that case, fill factors of 0.1 can be derived and the downward transition zone mass flow is reduced to 5×10^{13} g s^{-1} still an order of magnitude above the solar wind value.

The are two ways to consider these order of magnitude mass flow estimates. First, the origin of the solar wind can be explained with only small changes in these very rough numbers, so that the transition zone downflows return the spicular mass not needed to sustain the solar wind. The second approach is to say that the spicule upflows and transition region downflows constitute a closed circulation system with no mass flux available for the solar wind. It is perhaps even more likely that the spicules themselves produce no net mass transport. In this case we must look elsewhere. The HRTS data suggest the jets as likely candidates (Brueckner, Bartoe and VanHoosier, 1977).

An upper limit on the mass in one of the numerous 100 km s^{-1} jets is about 3×10^8 g. The birthrate for these jets is 170 s^{-1} on the solar surface and the consequent mass loss is about 5×10^{10} g s^{-1} which is much less than that in the solar wind. The mass content in the large 400 km s^{-1} jet seen in Figure 8 is estimated to be 2×10^{11} g. During three rocket flights, a total of six large jets have been observed. In the third flight which had the greatest spatial coverage, only one of the large jets was observed and a rate of 4 jets per second on the entire solar surface was derived. Observations of jet-like structures in C IV spectroheliograms above the limb indicate that on the entire solar surface, jets occur at the rate of 5 s^{-1}. Thus the mass loss due to the large 400 km s^{-1} jets is 10^{12} g s^{-1}, which is quite close to the mass loss of the solar wind. The kinetic energy released in these jets is 3×10^{28} erg s^{-1} which is higher than the total energy flux in the solar wind at the Sun. Thus, there is sufficient mass and energy in these high speed jets to supply the solar wind. Such a non-steady source would imply highly variable solar wind parameters, especially near the Sun.

References

Brueckner, G. E., A High Resolution View of the Solar Chromosphere and Corona, Highlights of Astronomy, 5, 557 1980.

Brueckner, G. E. and J.-D. F. Bartoe, Observations of High Energy Jets in the Corona and the Acceleration of the Solar Wind, Ap. J., in press, 1983.

Brueckner, G. E., J.-D. F. Bartoe and M. E. VanHoosier, High Spatial Resolution Observations of the Solar EUV Spectrum, Proc. of the OSO-8 Workshop, 1977.

Dere, K. P., J.-D. F. Bartoe and G. E. Brueckner, Chromospheric Jets: Possible EUV Observations of Spicules, Ap. J. (Letters), in press, 1983.

Doschek, G.A., U. Feldman and J. D. Bohlin, Doppler Wavelength Shifts of Transition Zone Lines Measured in Skylab Solar Spectra, Ap. J. (Letters), 205, L177, 1976.

Gebbie, K. B. et al., Steady Flows in the Solar Transition Region Observed with SMM, Ap. J. (Letters), 251, L115, 1981.

Grossmann-Doerth, U. and M. v. Uexkull, Spectral Investigations of Chromospheric Fine Structure, Solar Phys., 20, 31, 1971.

Lites, B. W., E. C. Bruner, E. G., Chipman, G. A. Shine, G. J. Rottman, O. R. White, and R. G. Athay, Preliminary Results from the Orbiting Solar Observatory 8: Persistent Velocity Fields in the Chromosphere and Transition Region, Ap. J. (Letters), 210, L11, 1976.

Rottman, G. J. and F. Q. Orrall, Observational Evidence for Solar Wind Acceleration at the Base of Coronal Holes, This conference, 1982.

Page intentionally left blank

X-RAY OBSERVATIONS OF THE SOLAR CORONA

L. Golub
Smithsonian Astrophysical Observatory

X-ray observations of the Solar corona during the past two decades have shown the fundamental importance of closed loop structures in determining x-ray emission properties. We summarize the major observational facts relating inner coronal structure and brightness to the emergence and subsequent diffusion of surface magnetic fields, including the formation of coronal holes and their relation to high-speed Solar wind streams. The small size scale end of the emerging magnetic flux spectrum, known as x-ray bright points, dominates the magnetic flux emergence process and may be related to the existence of polar plumes. Flares in bright points are known to be linked to macrospicule events in the XUV and Hα. We will also show a movie of the x-ray corona as seen from Skylab, covering eight Solar rotations at time resolution down to 90 seconds.

Page intentionally left blank

SPECTROSCOPIC MEASUREMENTS OF SOLAR WIND GENERATION

John L. Kohl, George L. Withbroe, Carlos A. Zapata
Harvard-Smithsonian Center for Astrophysics, Cambridge, MA 02138

and

Giancarlo Noci
Istituto di Astronomia, Universita di Padova, Padova, Italy

ABSTRACT

Spectroscopically observable quantities are described which are sensitive to the primary plasma parameters of the solar wind's source region. The method is discussed in which those observable quantities are used as constraints in the construction of empirical models of various coronal structures. Simulated observations are used to examine the fractional contributions to observed spectral intensities from coronal structures of interest which co-exist with other coronal structures along simulated lines-of-sight. The sensitivity of spectroscopic observables to the physical parameters within each of those structures is discussed.

I. INTRODUCTION

High resolution spectroscopic measurements of UV, EUV and XUV radiation from the extended solar corona can provide highly constrained empirical models of the coronal plasma structures that produce solar wind. New spectroscopic diagnostic techniques are being developed to specify electron temperatures and densities, ion velocity distributions and densities, outflow velocities of coronal particles into the solar wind, chemical abundances and vector magnetic fields.

Although spectroscopic measurements are somewhat less straightforward to interpret than *in situ* measurements, their use in astrophysics and in controlled thermonuclear research is well established as a powerful means of determining the properties of plasmas that may not be amenable to *in situ* techniques. The usual approach for interpreting spectroscopic data is to develop a model of the plasma of interest that is constrained by the values of observable quantities. Ideally, each observable is sensitive to and governed by a specific plasma parameter (e.g. a spectral line profile that is primarily controlled by the velocity distribution of the corresponding particle species). Empirical models that are used to specify plasma parameters and their spatial variations are relatively unconstrained by theory, take into account the basic physics of spectral line formation, and treat the line-of-sight contributions in a self consistent manner. Such models do not depend upon, nor specify, the physical processes that may be operating within the plasma such as the energy and momentum transport and deposition mechanisms. The model is an empirical description of the observed plasma and specifies throughout the plasma structure, the local values of the basic plasma parameters (e.g. particle velocities and densities). To establish a high level of confidence in a model it is necessary to determine a large number of partially redundant observational constraints

which are sensitive to all of the primary plasma parameters and to require the model to reproduce all of the measured spectroscopic quantities.

Once the derived plasma parameters are specified in this way, they can be introduced into more sophisticated models which contain a theoretical description of probable physical processes that may be responsible for maintaining the properties of the plasma of interest. These models inevitably lead to an improved understanding of the physics of the observed plasma because the empirical constraints result in the rejection of candidate physical processes whose presence would be inconsistent with the observations. With an increasing number of empirical constraints, the range of possible physical models is narrowed and a meaningful understanding of the nature of the plasma of interest can be established.

In the case of the solar wind acceleration regions of the solar corona, empirically derived knowledge of plasma conditions has been extremely limited, and, hence, energy and momentum deposition processes as well as the principal mechanisms for energy and momentum transport (other than radiation and thermal conduction) have not been identified. Spectroscopic measurements of open and closed magnetic structures of the extended corona and detailed modeling can help to establish the identity and magnitude of transport and deposition processes operating in representative coronal structures, thus improving the understanding of the physics of solar wind acceleration and determining the role of different types of coronal structures in the production of the solar wind. Observations of a broad range of ionic species in different structures may help to explain abundance enhancements that have been observed in solar wind streams at 1 AU (Hirshberg, 1975). Improved knowledge of the physical conditions in the solar wind acceleration region may also lead to a better understanding of interactions between magnetic fields and low density flowing plasmas, both for steady-state flow and coronal transients.

The spectroscopic techniques that we are developing to study the physics of the source regions of the solar wind have been described elsewhere (Kohl and Withbroe, 1982; Withbroe et al., 1982a) and will be only briefly identified here. The primary purpose of this paper is to discuss the approach that is being used to interpret the observations; in particular, the analysis of the line-of-sight contributions to the emergent coronal intensities and the sensitivity of specific observables to the plasma parameters of representative coronal structures. The final section includes a brief summary of our initial ultraviolet spectroscopic measurements of the extended corona from sounding rockets and our plans for more extensive measurements.

II. SPECTROSCOPIC DIAGNOSTICS

The spectroscopic diagnostics that we are developing for the solar wind acceleration region of the extended corona (radii > 1.3 $R_\odot$ from sun center) make use of information contained in measurements of the intensities and profiles of spectral features in the UV, EUV and XUV wavelength ranges. Because the particle densities in the extended corona are low, the thermalization and ionization equilibrium times are long and, hence, the various particle species such as electrons, protons and other ions have velocity distributions that are not characterized by the same temperature and have ionization distributions that are frozen-in at various heights. Several physical processes that have

48

been suggested as possibilities for energy and momentum transport (e.g. Alfvén and MHD fast mode waves) affect in characteristic ways the particle velocity distributions as a function of height. A knowledge of the velocity distributions of particles of unlike mass would help to distinguish thermal velocity components from nonthermal velocities due to energy and momentum transport processes (e.g. the transverse velocities of propagating waves). If the large number of plasma parameters required to describe the solar wind acceleration region are to be studied spectroscopically, it is necessary to measure a diversity of spectral features that are sensitive to the velocity distributions and densities of each of the major and some minor constituents of the solar wind plasma, and also to measure spectral quantities that are sensitive to a broad range of outflow velocities. In order to understand the role of the coronal magnetic fields, it would be extremely advantageous to determine coronal values of that quantity.

A meaningful representation of a coronal plasma must include, among others, descriptions of the behavior of the two major constituents, the protons and the electrons. The electron density has traditionally been determined from observations of electron scattered visible light and this continues to be the best method. A measurement of electron density together with the plasma neutrality condition and an estimate of the chemical abundance and ionization balance of helium permit a straightforward determination of proton density in a model.

Random Velocity Diagnostics from H I Lyman-α

Measurements of the line profiles of resonantly scattered and electron scattered H I Lyman-α radiation in the corona are very sensitive to the velocity distributions of the protons and the electrons, respectively. The resonantly scattered component depends upon the scattering of chromospheric Lyman-α photons by neutral hydrogen atoms in the corona. Even though the ratio of neutral hydrogen to free protons is about 10^{-7} at coronal temperatures and densities (Gabriel, 1971), the large coronal proton abundance coupled with the high intensity of the chromospheric Lyman-α radiation gives rise to a coronal resonantly scattered component of Lyman-α that is strong enough to be measured out to large distances above the solar surface. The formation of the resonantly scattered Lyman-α line has been described by Gabriel (1971), Beckers and Chipman (1974) and Withbroe et al. (1982a). Because the tenuous coronal plasma is optically thin to ultraviolet radiation, an observed Lyman-α profile is a direct measurement of the run of H I velocities along the line-of-sight. This velocity distribution includes the thermal motions, nonthermal motions such as the transverse velocities of propagating waves and the components of the outflow velocities along the line-of-sight. Since the thermal velocities of hydrogen at coronal temperatures are relatively large (160 km s^{-1} for a thermal temperature of 1.5×10^6 K), thermal motions are expected to be a major contributor to coronal H I velocity distributions.

The profile of the resonantly scattered component of H I Lyman-α is also a measure of the velocity distribution of protons in regions where the coronal expansion time is much longer than the characteristic time for charge exchange between hydrogen atoms and protons. For $r < 8$ $R_\odot$ in quiet coronal regions and $r < 3$ $R_\odot$ in low density coronal holes, the proton and hydrogen velocities are expected to be nearly identical and, hence, the profile of the resonantly

scattered H I Lyman-α line can be used in models to constrain both the H I and proton velocity distributions (Withbroe et al., 1982a).

The electron scattered component of the coronal H I Lyman-α line is much weaker (by about 3 orders of magnitude) than the resonantly scattered component and has a FWHM ≈50 Å compared to the ≈1 Å width of the resonantly scattered profile. It is produced in the corona by Thomson scattering of chromospheric H I Lyman-α radiation. The formation of electron scattered Lyman-α has been discussed by Withbroe et al. (1982a). Calculated profiles provided in Figure 4 of that reference show that the shape of the profiles are very sensitive to the velocity distribution of coronal electrons. The line profile of the electron scattered radiation is a stronger function of the scattering geometry than is the resonantly scattered profile.

Random Velocities and Densities from Other Lines

Profiles of the spectral lines of ions such as C IV, N V, O VI, Ne VIII, Mg X, Si XII, Fe XII and He II which should be observable in the corona out to $r = 3$ to $5 R_\odot$, can yield information on the velocity distributions of those particles (Kohl and Withbroe, 1982). For most of the UV, EUV and XUV lines, the emergent intensity is a combination of collisionally excited and resonantly scattered components. For ions that are more massive than H I, the thermal component of the velocity distribution in the corona is not expected to be as large as for hydrogen. Hence, the profiles of those systems are expected to be sensitive to nonthermal velocities and, in the case of the more massive species, to be dominated by them. The ability to distinguish between thermal and nonthermal velocities is probably the key to discovering the identities of energy and momentum transport processes that are expected to impart characteristic velocities to the coronal ions.

It is highly desirable to determine the relative intensities of the collisionally excited and resonantly scattered components of a spectral line because the former component is sensitive to the density of the corresponding ion and the latter to outflow velocity. In the case of Li-like resonance lines (Kohl and Withbroe, 1982), the respective contributions from each mechanism can be determined from the ratio of the intensities of the 2s $^1S_{1/2}$ - 2p $^2P_{3/2}$ and 2s $^1S_{1/2}$ - 2p $^2P_{1/2}$ fine structure lines (e.g. O VI λ1032 and λ1037). For the case where the resonantly scattered components of the lines are being pumped by radiation from identical ions in deeper layers of the solar atmosphere, the resonantly scattered components will have a 4:1 ratio while the collisionally excited components of the lines will have a 2:1 ratio.

Outflow Velocity Diagnostics

The intensity of the resonantly scattered component depends upon the number of particles along the line-of-sight that are capable of scattering radiation in the spectral line and upon the intensity of the incoming radiation. The intensity of scattered photons is a function of the net outflow velocity of coronal scatterers. This can be understood by considering a static atmosphere where the central wavelength of the coronal scattering profile is identical to that of the incoming radiation and the case of an outflowing plasma where the incoming radiation is red-shifted off the center of the scattering profile. In

the former case there will be a maximum amount of resonant scattering and in the latter, the amount of resonant scattering will decrease with increasing velocity. Notice that spectral lines of unlike widths are sensitive to different ranges of outflow velocity. This intensity dependence, termed Doppler-dimming (Hyder and Lites, 1970; Beckers and Chipman, 1974), provides the sensitivity of observable quantities that is needed to constrain the values of outflow velocities in a model of an observed coronal structure. In Figure 1, we see that the H I Lyman-α line is sensitive to flow velocities greater than 100 km s^{-1} while the O VI λ1032 line is sensitive to velocities in the 30-100 km s^{-1} range and the other lines are sensitive to somewhat larger velocities.
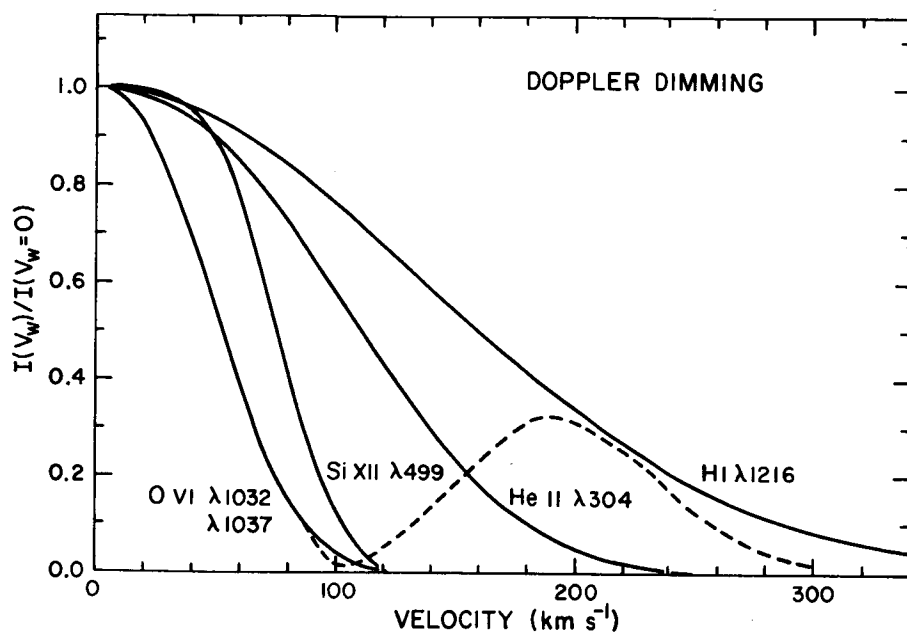
Figure 1. Doppler dimming calculated as a function of flow velocity for the resonantly scattered components of several spectral lines. The solid O VI curve applies to both the λ1031.766 and λ1037.587 lines. For velocities greater than 120 km s^{-1}, the resonantly scattered intensity of λ1031.766 Å approaches zero, but the λ1037.587 Å intensity begins to increase due to pumping by the chromospheric C II line at 1037.018 Å as indicated by the dashed curve.

The Doppler-dimming of the O VI line at 1037.587 Å is particularly interesting because the resonantly scattered component of this line can be pumped either by O VI λ1037 radiation from deeper atmospheric layers or by the C II line at 1037.018 Å (Noci, Kohl and Withbroe, 1983). Pumping by the latter line occurs when the outflow velocity is large enough that the incoming C II profile is red shifted in the coronal ion rest frame by an amount that is large enough to make the incoming C II radiation profile and the O VI λ1037 scattering profile overlap. The dashed line in Figure 1 shows the effect of the C II line on the velocity dependence of the O VI λ1037 line. Because of this effect, the ratio of the intensities of the coronal O VI λ1032 and λ1037 lines as a function of radial height in the corona provides a very useful diagnostic of coronal outflow velocities that is illustrated in Figure 2. At low heights where velocities are small, the coronal O VI lines are formed by both resonant scattering from incoming O VI radiation and collisional excitation and the ratio is between 2 and 4. As the velocity increases with height, the resonant scattering of incoming O VI radiation is Doppler-dimmed in both the λ1032 and λ1037 lines and C II pumping of the λ1037 line begins to decrease the λ1032/λ1037 ratio. At ρ = 1.5 the λ1037 resonantly scattered intensity from O VI and C II pumping are about equal. At even greater heights, the resonant scattering component of the λ1037 line due to C II begins to dominate and the ratio becomes very small. At larger heights where the velo-
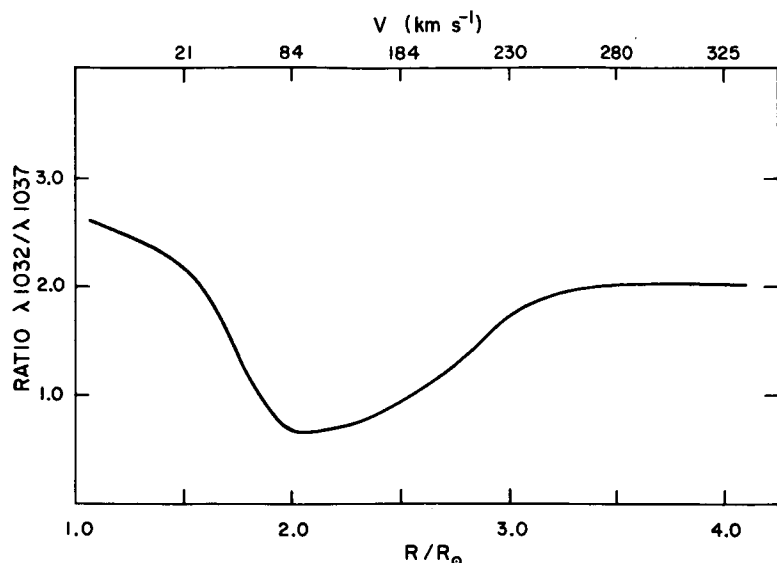
Figure 2. Calculated ratio of the intensities of the O VI λ1032 and λ1037 lines as a function of height for the indicated coronal hole velocities of Munro and Jackson (1977).

city is large enough to shift the C II line beyond the O VI λ1037 line, only the collisional components remain and the ratio again becomes 2.

Magnetic Field Diagnostics

Of all the physical quantities that describe the extended coronal plasma, the magnetic field may be the most significant, but also it is one of the most difficult to measure. The magnetic field appears to influence strongly the structure of the corona and its outward extension into the heliosphere. The strength and configuration of the magnetic field in the low corona ($r \lesssim 1.5$ R$_\odot$ where the magnetic pressure generally exceeds the gas pressure) appears to control the location, size and shape of coronal holes and streamers. At greater heights the coronal magnetic field is swept into interplanetary space. The spatial variations of coronal densities, and most likely other plasma parameters such as temperatures, also appear to be strongly influenced by coronal magnetic fields which can channel energy carried by waves and/or electron thermal conduction. In addition, solar flares and coronal transients probably have magnetic origins. A possibility to use the Hanle effect (Hanle, 1924; Mitchell and Zemansky, 1934) for magnetic field diagnostics in astrophysics was originally suggested by Hyder (1965). Quantitative approaches have been described more recently. In particular, Bommier and Sahal-Bréchot (1982) have computed the effect of a magnetic field on the linear polarization of resonantly scattered H I Lyman-α. Coronal Lyman-α, which has been observed out to 3.5 R$_\odot$ using coronagraphic techniques (Kohl et al., 1980), is polarized in the absence of a magnetic field. The Hanle effect is the modification of this linear polarization, due to the presence of the magnetic field. Bommier and Sahal-Bréchot provide analytical formulae which describe the Hanle effect for H I Lyman-α. In principle, those formulae could be used in models to specify the degree of polarization and the polarization direction of H I Lyman-α for a given coronal magnetic field configuration. Although the H I Lyman-α line is only sensitive to fields greater than about 6 gauss, other members of the H I Lyman series are sensitive to smaller fields.

III. SENSITIVITY OF OBSERVABLES AND LINE-OF-SIGHT EFFECTS

For the purpose of discussing the line-of-sight contributions to the spectroscopic observables and for demonstrating the sensitivity of those observables to the basic physical quantities which describe a coronal structure, we use a model which specifies the temperatures, densities and outflow velocities of the electrons and protons as a function of height in several coronal structures that can be located at selected positions along the line-of-sight of a simulated observation (see Figure 3). With this model the contributions to the spectral

Figure 3. The geometry of simulated observations of a coronal hole surrounded by quiet coronal regions and of a coronal streamer .

line intensity profile of H I Lyman-α are calculated for volume elements along the line-of-sight. All outflow velocities are taken to be directed radially outward. Neutral hydrogen atoms are assumed to behave identically to the protons and the ionization balance of hydrogen is taken from Gabriel (1971). Only observations of H I Lyman-α are considered here, although the line-of-sight effects for observations of ions would be similar.

For models of coronal holes, we use Allen's (1963) electron density gradient for a polar region at solar minimum. For each of the two coronal holes that are discussed, we adopt an absolute scale which is chosen to be an integral multiple of Allen's absolute scale. The resulting densities are roughly based on the empirical values of Munro (1983) for coronal holes of a similar size. The outflow velocities are taken to have the radial dependence given by Munro and Jackson (1977) with an absolute scale that is a specified multiple of their values. The electron temperature is taken to have a $r^{-2/7}$ dependence and the absolute scale is normally taken from Withbroe et al. (1982a, Figure 11). Their values of electron temperature (e.g. 1.5×10^6 K at r = 1.76 $R_\odot$) were estimated from ratios of the H I Lyman-α and white light intensities. The ratios depend upon the ionization balance of hydrogen which is primarily a function of electron temperature. The proton and hydrogen random velocity distributions are assumed to be Maxwellian and to be characterized by the H I temperatures given by Withbroe et al. (1982a, Figure 11) who based their values upon measurements of H I Lyman-α profiles. In some cases, we specify an incremental change in the temperature.

For models of quiet coronal regions, the electron densities are Allen's values for an equatorial region at solar minimum; the outflow velocities are calculated assuming conservation of mass flux in spherical symmetry with 100 km s^{-1} at 4.5 $R_\odot$; the electron temperature is normally taken from Withbroe et al. (1982b, Figure 7) and the proton and hydrogen random velocity distributions are from the same source. The streamer model is similar to that of the quiet corona except the electron densities are taken to be 5 times Allen's (1963) equatorial values for solar minimum.

Basic Geometry of Simulations

The geometry of the simulated observations is shown in Figure 3 where the plane of the figure lies at a position angle of 90° (i.e. the apparent equatorial plane). The height of observation ρ is the radial height in solar radii where the line-of-sight intersects the "plane of the disk" (i.e. the plane which is

perpendicular to the line-of-sight and passes through sun center). Angles θ are measured from the line-of-sight to radial lines passing through specified locations in coronal structures. Observations of several coronal structures were simulated for the present study but most of the following discussion refers to the line-of-sight and coronal structures shown in the upper half of Figure 3. The structure of interest there is the coronal hole with radial boundaries between it and two quiet coronal regions. The θ angle of the axis of symmetry is 90° and the boundaries are at ±30° from the center line. This is a typical polar coronal hole for the declining phase of the cycle and is similar to one we observed during our July 20, 1982 rocket flight (Kohl et al., 1982). Broader holes are commonly found nearer to solar minimum (e.g. the 1973 polar coronal hole that was described by Munro and Jackson (1977) had boundaries at ±70° from its center line). Smaller coronal hole-like structures also exist, especially in polar regions near the time of solar maximum. We observed a region on February 16, 1980 that had boundaries of about ±15° from its center line. A similar structure is considered in Figure 4 and in the related discussion. The geometry of a simulated streamer observation is shown in the lower half of Figure 3. The streamer has cylindrical geometry with the axis of symmetry at angle θ. Radial lines passing through the boundaries of the streamer at r = 1.5 R$_\odot$ would subtend an angle of 18°. The streamer is surrounded by quiet corona.
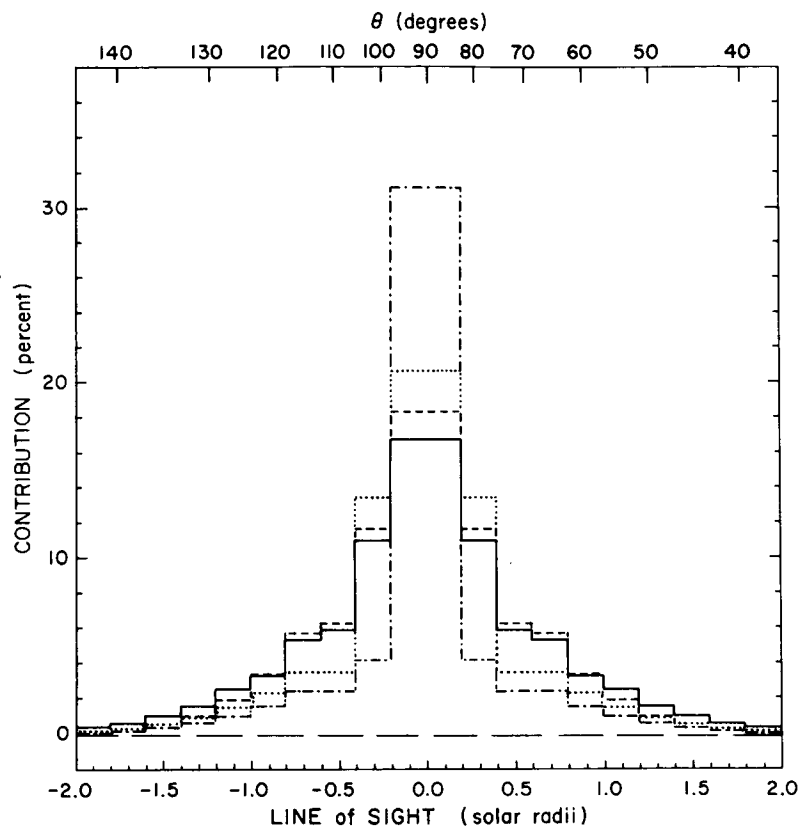
Figure 4. Contributions to observed intensities of H I Lyman-α for volume elements of 0.2 R$_\odot$ lengths which are located along the line-of-sight. Curves are plotted for simulated observations of a spherically symmetric corona (dash), a 60° coronal hole (solid line), a 30° coronal hole (dots) and a streamer at θ = 90° (dot-dash).

Fractional Contributions of Structures Along Line-of-Sight

If a spectroscopic observable is suitable for constraining the local values of a physical quantity in a model, then the contribution to that observable from the coronal structure of interest should be significant compared to the contributions from other regions. This is particularly important for the observations of line profiles, but as we shall see in Figure 6, is not quite as important for the line intensity. Figure 4 provides the fractional contribution to the intensity of H I Lyman-α from volume elements which have lengths of 0.2 R$_\odot$ along the line-of-sight. The lines-of-sight for the observations of Figure 4 intersect the plane of the disk at ρ = 1.5. The contributions are plotted against the

distance of the volume element from the plane of the disk in solar radii. The angles θ to the centers of the individual volume elements are also provided.

The solid line histogram in Figure 4 refers to the corona illustrated in the upper part of Figure 3. The 60° wide coronal hole has a center line at θ = 90°. Its plasma parameters are the values for a coronal hole that were discussed earlier. The radial variations of the outflow velocity are taken to be identical (i.e. multiplier of one) to those of Munro and Jackson (1977) and the multiplier for density is 2 (i.e. densities twice as high as those in Allen's model for polar minimum). The hole is surrounded by a quiet coronal region with the parameters described earlier. The maximum contribution from a volume element is about 17% in this case and the fractional contribution from the coronal hole is 82% with the remaining 18% being contributed by the surrounding quiet corona. For a spherically symmetric corona with the same plasma parameters as the coronal hole, the fractional contribution would be 87% from the same region of space occupied by the coronal hole (i.e. 60° < θ < 120°). The fractional contribution from a smaller coronal hole with boundaries at θ = 75° and 105°, and the same outflow velocities but with a density multiplier of 4 (twice the value for the previous example) is 69%. In each of these instances the structures of interest provide the dominant contribution and so for similar coronal holes or larger ones, the Lyman-α intensity and line profile at ρ = 1.5 should be controlled by the parameters of the coronal hole and not by any surrounding quiet regions. Figure 4 also provides the contributions for a small streamer that is identical to the one shown in Figure 3 except that the center line is at θ = 90°. The total contribution from the streamer is 64% with the surrounding quiet corona providing the remaining 36%. Although it is not shown in Figure 4, we also calculated, for ρ = 1.5, the total streamer contributions for the cases where the streamer was centered at θ = 60° and 30°. The fractional contributions to the streamer in those cases are 40% and 18%, respectively. Those reduced contributions are due to the smaller densities at the observed radial heights in the streamer. This example illustrates the desirability of observing structures of interest that are located near the plane of the disk.

Sensitivity to Outflow Velocity

Recall from the discussion of spectroscopic diagnostics, that the resonantly scattered intensity is affected by the outflow velocity. For an observation of the corona depicted in the upper half of Figure 3, the fractional contribution from the coronal hole is plotted in Figure 5 for several absolute scales of outflow velocity. The coronal hole density multiplier is 2. The outflow velocities versus height for a multiplier of one times the Munro and Jackson (1977) values are indicated in the figure. In the case of zero outflow in the coronal hole, the fractional contribution from the hole decreases with increasing ρ because the adopted density gradient is larger in the hole than in the surrounding quiet corona. Because Doppler-dimming reduces the intensity of H I Lyman-α, the total contribution from the coronal hole decreases with increasing outflow velocity. Due to the small velocities encountered by observations at ρ = 1.5, the hole contribution at that height is >80% for every curve of Figure 5. For the Munro-Jackson velocity scale, the contribution reaches 36% at ρ = 2.5 and 25% (not shown) at ρ = 3.0. Of course, broader holes, such as the 1973 polar hole modelled by Munro and Jackson (1977), would tend to contribute larger fractional amounts to the observed intensity.
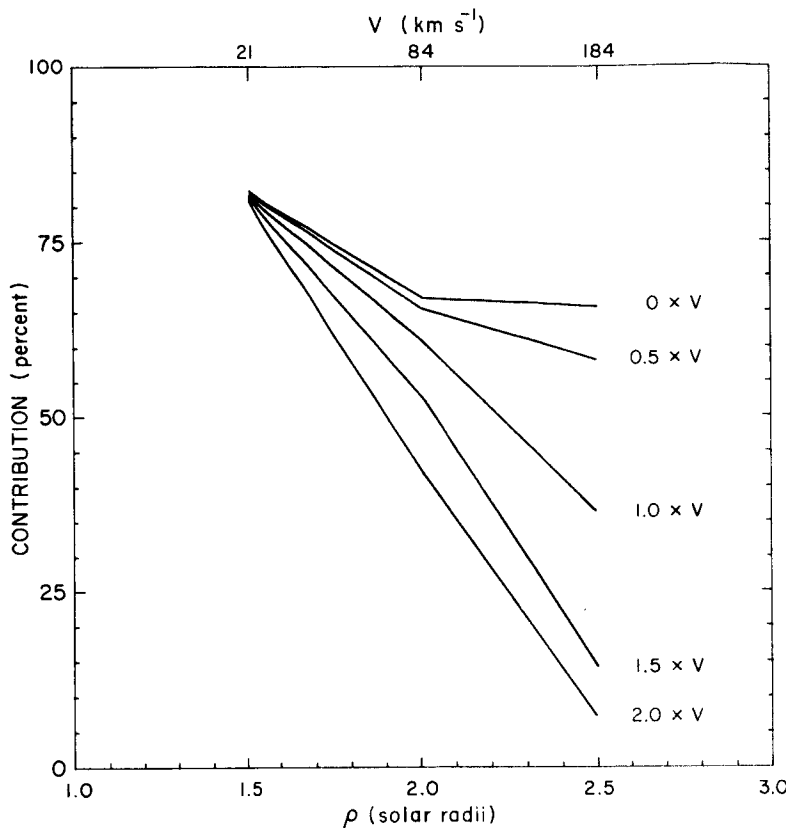
Figure 5. Total fractional contributions from
           the coronal hole for observations
of a simulated 60° coronal hole surrounded by
quiet coronal regions. Curves are plotted for
outflow velocities in the hole that are 0.0,
0.5, 1.0, 1.5 and 2.0 times the outflow veloci-
ties of Munro and Jackson (1977).

observed Lyman-α line intensity versus ρ for the same 60°-wide coronal hole and surrounding region that were discussed in reference to Figure 5. Figure 6 illustrates the sensitivity of the observed H I Lyman-α intensity to the outflow velocity in the hole for the case where it is surrounded by a more dense coronal structure. For $\rho = 2.5$ the observed intensity for zero outflow is about 1.8 times the value for the Munro and Jackson velocity scale and about 2.4 times the intensity for 1.5 times those velocities. Notice that the observed intensity is sensitive to outflow even in the case where the fractional contribution from the coronal hole is fairly small (see Figure 5). Also note that the observed intensity for $\rho = 1.5$ is fairly insensitive to the range of outflow velocities that are expected at the contributing heights of that observation. This can also be seen from Figure 1. Therefore, the observed intensity at a given height relative to the intensity at $\rho = 1.5$ is an observable quantity which is particularly sensitive to outflow velocity.

The situation is similar for observations of other lines although in the case of the O VI $\lambda 1032$ and $\lambda 1037$ lines, the sensitivity to small velocities makes an observation at 1.3 $R_\odot$ highly desirable for ensuring an observable intensity that is insensitive to expected outflow velocities. In the case of those lines, there is the added advantage of observing their line ratio as described earlier.

Sensitivity to Hydrogen Random Velocities

The primary purpose of Figure 7 is to demonstrate the sensitivity of observed Lyman-α profiles to the hydrogen random velocity distribution in a coronal structure of interest that co-exists with other structures along the line-of-sight. For this purpose we again consider the 60° coronal hole and surrounding quiet corona shown in Figure 3. Representative portions of line profiles are plotted in Figure 7 for simulated observations at $\rho = 2.0$. The profiles have a
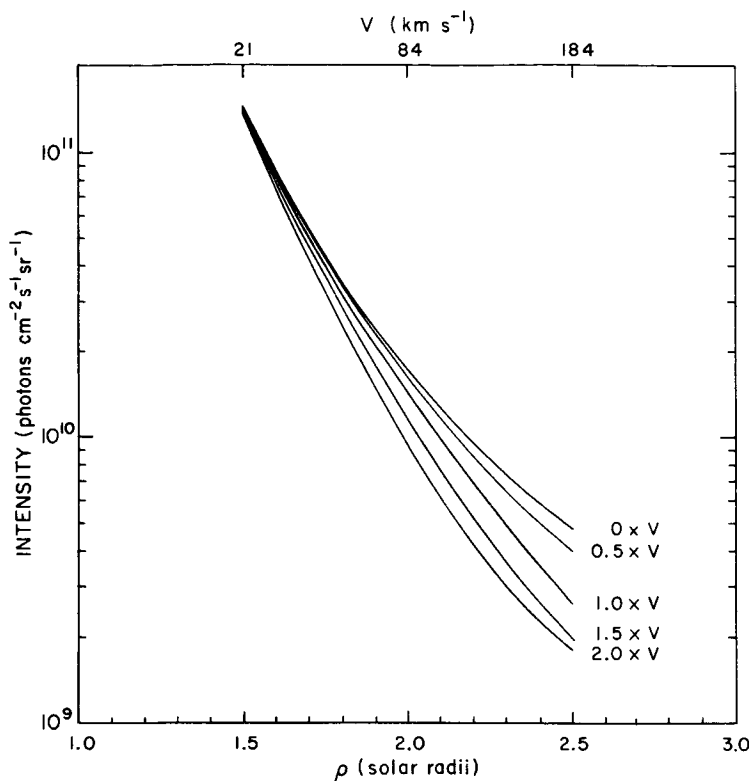
Figure 6. H I Lyman-α line intensities for simulated observations of a 60° coronal hole surrounded by quiet coronal regions. Curves are plotted for the outflow velocities of Figure 5.

relative intensity scale normalized to the intensities at line center. The primary observations to be considered here are line profiles for several different absolute scales of outflow velocity in the coronal hole (multipliers of 0, 1 and 2 times the Munro and Jackson scale). Those simulated profiles are compared in Figure 7 to other observations where the value of certain parameters in the coronal hole or in the quiet corona are changed from their normally adopted values. For the primary observations (represented by the solid curves), the increase in line width with increasing outflow velocity is due to the components of that velocity along the line-of-sight. Even for a velocity multiplier of two (corresponding to 168 km s^{-1} at 2 R$_\odot$) the fractional increase in width at e^{-1}I$_0$, due to this effect, is only 2%. Although this effect should be included in the models, the profiles are relatively insensitive to outflow velocities.

For the purpose of discussing the sensitivity of the observed profiles to the random velocity of hydrogen atoms and protons, it is convenient to parameterize the random coronal velocity by defining an effective hydrogen temperature which specifies a Doppler width for the adopted hydrogen velocity distribution. For coronal holes, the value of this parameter is taken to be 1.4 ×10^6 K at 2.0 R$_\odot$ (Withbroe et al., 1982a). A value of 2.1 × 10^6 K (Withbroe et al., 1982b) is adopted for that height in the quiet coronal region. The only difference in the model between the group of solid profile segments in Figure 7 and the group of dashed curves is that, for the latter curves, the effective temperature in the hole was increased by 2 × 10^5 K at all heights. By comparing the dashed curve for zero outflow velocity to the corresponding solid curve, it is immediately obvious that the observed profiles are very sensitive to small differences in the random velocity distribution of hydrogen within the coronal hole. Similar comparisons for the profiles corresponding to the two non-zero outflow velocities indicate that the observed profiles are only slightly less sensitive in those cases. The reason for the slight decrease in sensitivity with increasing velocity is primarily because Doppler-dimming decreases the contribution from the coronal hole (see Figure 5). The smaller separations among the dashed curves compared to those among the solid curves is due to the domination of the random velocities over the outflow velocities in the hotter coronal hole models. The dotted profile in Figure 7 is for the case where the effective hydrogen temperature is increased in the quiet region by 2 × 10^5 K while the
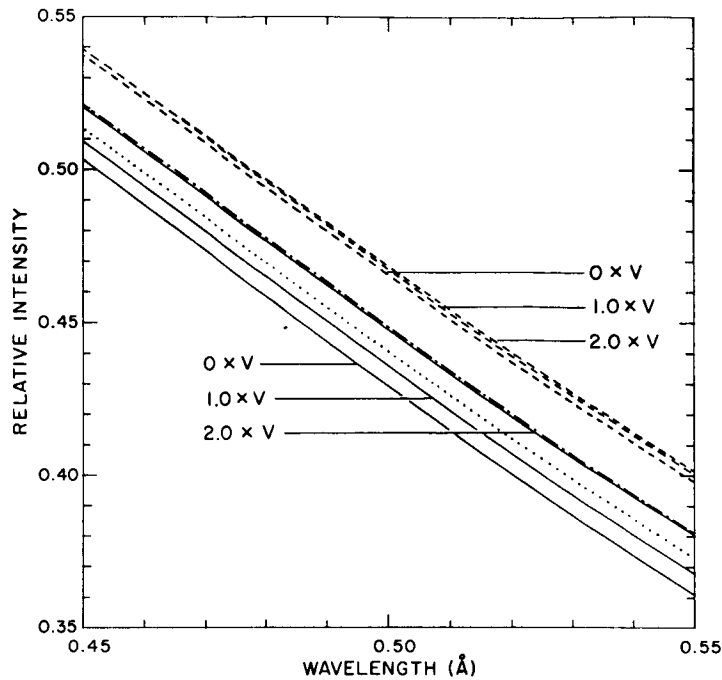
Figure 7. Segments of H I Lyman-α profiles for simulated observations of structures described in the text.

coronal hole has a velocity scale multiplier of one and has the other normally adopted parameters. This profile is only slightly wider than the corresponding profile (middle solid curve) for the usual effective temperature in the quiet region. This illustrates that the observed profiles are not overly sensitive to the effective temperature of the surrounding quiet corona.

A pure Gaussian profile (dot-dash curve) corresponding to the adopted random velocity distribution in the coronal hole at $r = 2.0$ $R_\odot$ is also plotted. It is clear from a comparison to this profile that the line-of-sight effects, including the physics of the resonant scattering process, do not produce extremely large departures in the profile shapes from the simple profile that would be emitted by a hydrogen gas with the velocity distribution of the coronal hole at the height of observation.

IV. SUMMARY

Spectroscopic observables, including the line profiles and intensities of resonantly scattered and collisionally excited radiation from atoms and ions and the electron scattered profile of H I Lyman-α, are sensitive to all of the primary plasma parameters of the outflowing solar wind plasma in the extended solar corona. Individual observables have been identified that tend to be controlled, primarily, by particular plasma parameters. Therefore, in many respects, a measurement of a particular spectroscopic quantity can be considered to be a direct determination of the corresponding plasma parameter. However, the more rigorous approach, that has been emphasized in this paper, is to treat the observable quantities as constraints on an empirical model of the observed coronal structure and to recognize that individual observables are primarily controlling the value of particular parameters in the model. High confidence in the model as an empirical description of the observed plasma can be realized if the number of measured quantities is sufficient to constrain all of the primary parameters of the modeled plasma. The advantage of the model is that, in simultaneously predicting all of the observable quantities, it takes the relationships among the various physical variables of the plasma into account.

Because the UV, EUV and XUV spectral lines used for coronal diagnostics are optically thin in the corona, an actual observation samples every structure along the line-of-sight. Our study has shown that the contributions from coronal structures lying in the plane of the solar disk ($\theta = 90°$) are enhanced over those of neighboring structures along the line-of-sight. Therefore, it is preferable for the coronal structure of interest to be located in this plane at the time of its observation. Measurements of polar coronal holes are particularly advantageous in this respect. Even in the case of a fairly narrow (60°) coronal hole with outflow velocities as large as those in the Munro-Jackson model, the maximum contribution to the observed intensity out to $\rho = 2.2$ was found to be from the coronal hole (see Figure 5) rather than the surrounding quiet corona. Also, for this example, the observed intensity is highly sensitive to outflow velocity out to beyond $\rho = 2.5$ and the line profile at $\rho = 2.0$ is very sensitive to the hydrogen velocity distribution in the hole. Broader coronal holes such as the 1973 polar hole that was discussed by Munro and Jackson (1977), would dominate observations out to higher heights. Narrower coronal hole-like structures of higher density and smaller outflow velocity, such as the one reported by Withbroe et al. (1982a), also provide the dominant contribution out to beyond $\rho = 2.5$.

Line-of-sight contributions tend to be of more concern for observations of coronal holes than for other coronal structures because they have the smallest densities and the highest outflow velocities. For observations of other coronal structures, the fractional contributions tend to be at least as large as the contributions from the coronal holes considered here and other structures tend to be observable at larger heights. The simulated observations that were considered in this paper have shown that spectroscopic observables are sensitive to the physical parameters of coronal holes and other structures even in representative cases where the structures of interest are surrounded by other regions along the line-of-sight. The examples used here were for relatively small coronal holes and streamers. Larger structures would provide an even larger fraction of the observed intensities.

To demonstrate the feasibility of making EUV spectroscopic observations of the extended corona and to obtain a sample of scientific data, we have observed the intensity and spectral line profile of H I Lyman-α from $\rho = 1.5$ to 3.5 during three sounding rocket flights. Results for observations of a coronal hole on April 13, 1979 were reported by Kohl et al. (1980) and observations of a quiet coronal region from the same rocket flight were discussed by Withbroe et al. (1982b). A coronal hole-like structure near the south solar pole was observed on February 16, 1980 and reported by Withbroe et al. (1982a). Observation of the polarization and brightness of the white-light corona were made during each flight by a coronagraph of the High Altitude Observatory. During a rocket flight on July 20, 1982, we observed a coronal hole (near the north solar pole) and a nearby streamer. Measurements were made of both the H I Lyman-α profile and the intensities of O VI λ1032 and λ1037. Although the analysis of those measurements is still in progress, it appears that the data will provide an empirical model of the observed coronal hole that will specify, for the first time, a value for the outflow velocities as well as the random velocities of hydrogen and the electron densities (the latter from white-light data).

Our next EUV spectroscopic measurements of the source region of the solar wind are planned for 1986 on board the Spartan 2 mission which is expected to provide 27 hours for measurements of resonantly scattered H I Lyman-α intensities

and profiles, O VI λ1032 and λ1037 intensities, and the intensities and line profiles of the electron scattered component of H I Lyman-α.

References

Allen, C.W., Astrophysical Quantities, 2nd ed. (University of London: Athlone Press, 1963).

Beckers, J.M., and E. Chipman, The Profile and Polarization of the Coronal Lyman-α Line, Solar Phys., 34, 151, 1974.

Bommier, V., and S. Sahal-Bréchot, The Hanle Effect of the Coronal Lα Line of Hydrogen: Theoretical Investigation, Solar Phys., 78, 157, 1982.

Gabriel, A.H., Measurements on the Lyman Alpha Corona, Solar Phys., 21, 392, 1971.

Gabriel, A.H., W.R.S. Garton, L. Goldberg, T.J.L. Jones, C. Jordan, F.J. Morgan, R.W. Nicholls, W.H. Parkinson, H.J.B. Paxton, E.M. Reeves, D.B. Shenton, R.J. Speer, and R. Wilson, Rocket Observations of the Ultraviolet Solar Spectrum During the Total Eclipse of 1970 March 7, Astrophys. J., 169, 595, 1971.

Hanle, W., Über magnetische Beeinflussung der Polarisation der Resonanzfluoreszenz, Z. f. Phys., 30, 93, 1924.

Hirshberg, J., Composition of the Solar Wind: Present and Past, Rev. Geophys. Space Phys., 13, 1059, 1975.

Hyder, C.L., The Polarization of Emission Lines in Astronomy II. Prominence Emission-Line Polarization and Prominence Magnetic Fields, Astrophys. J., 141, 1374, 1965.

Hyder, C.L., and B.W. Lites, Hα Doppler Brightening and Lyman-α Doppler Dimming in Moving Hα Prominences, Solar Phys., 14, 147, 1970.

Kohl, J.L., H. Weiser, G.L. Withbroe, R.H. Munro, and G. Noci, New Observations of the Extended Ultraviolet Corona, Bull. Am. Astron. Soc., 14, 976, 1982.

Kohl, J.L., H. Weiser, G.L. Withbroe, R.W. Noyes, W.H. Parkinson, E.M. Reeves, R.M. MacQueen, and R.H. Munro, Measurements of Coronal Kinetic Temperatures from 1.5 to 3 Solar Radii, Astrophys. J., 241, L117, 1980.

Kohl, J.L., and G.L. Withbroe, EUV Spectroscopic Plasma Diagnostics for the Solar Wind Acceleration Region, Astrophys. J., 256, 263, 1982.

Mitchell, A.C.G., and M.W. Zemansky, Resonance Radiation and Excited Atoms, (Cambridge University Press, 1934).

Munro, R.H., Corona Over a Solar Cycle (Holes, Plumes, Transients, Field Strengths), Proc. of Solar Wind 5, 1983.

Munro, R.H., and B. Jackson, Physical Properties of a Polar Coronal Hole from 2 to 5 R$_\odot$, Astrophys. J., 213, 874, 1977.

Noci, G., J.L. Kohl, and G.L. Withbroe, Velocity Sensitivity of Coronal O VI Lines, to be published, 1983.

Withbroe, G.L., J.L. Kohl, H. Weiser, and R.H. Munro, Probing the Solar Wind Acceleration Region Using Spectroscopic Techniques, Space Sci. Rev., 33, 17, 1982a.

Withbroe, G.L., J.L. Kohl, H. Weiser, G. Noci, and R.H. Munro, Analysis of Coronal H I Lyman Alpha Measurements from a Rocket on 13 April 1979, Astrophys. J., 254, 361, 1982b.

IMPULSE RESPONSE OF THE CORONA[*]

S. T. Suess[1] and J. V. Hollweg[2]

ABSTRACT

Considering the corona to be a stratified, compressible gas in the presence of a gravitational field, it is possible to examine the propagation of an impulse through the corona and to thereby study characteristic modes of oscillation that could be excited by an arbitrary impulse. Some recent papers (Rae and Roberts, 1982; Hollweg, 1982) have considered the impulse response of the solar atmosphere. Here, we extend these ideas to the solar corona and solar wind using the analytical techniques developed in the above studies together with numerical techniques recently developed for studying transonic flow in the corona (Suess, 1982). It is shown that the impulse response consists of a propagating wave front, followed by a 'wake' which oscillates at the local natural frequency — having a period of less than one hour to a few hours. These oscillations are gravitationally modified acoustic waves. This work is motivated by two observations. First, that there are impulsive events in the lower corona in the form of coronal transients and, on a smaller scale, spicules and 'coronal bullets'. Second, a variety of observations indicate the dominant period of fluctuation in the corona and solar wind is a few hours, and some coronal transients exhibit a density profile that may be a manifestation of the wake discussed above. The value of relating the theory to observations lies in the result that the observational characteristics of the wake depend most sensitively on the temperature and flow speed.

Hollweg, J. V., On the origin of solar spicules, Astrophys. J., 257, 345, 1982.

Rae, I. C., and Hollweg, J. V., Pulse propagation in a magnetic flux tube, Astrophys. J., 256, 761, 1982.

Suess, S. T., Unsteady, thermally conductive coronal flow, Astrophys. J., 259, 880, 1982.

Page intentionally left blank

CORONAL TRANSIENTS IN FE XIV 5303Å:
FIRST TWO-DIMENSIONAL PHOTOELECTRIC GROUND-BASED OBSERVATIONS

Richard C. Altrock and Howard L. DeMastus
Air Force Geophysics Laboratory
Sacramento Peak Observatory
Sunspot, New Mexico 88349

ABSTRACT

An observational program has been undertaken at Sacramento Peak Observatory to photoelectrically detect coronal transients. Continuous observations are made in the Fe XIV 5303Å green line, utilizing the 40-cm coronagraph and the Photoelectric Coronal Photometer. Scans at three heights above the limb are combined to form a low-resolution picture of the green-line corona every 20 – 30 minutes. Difference pictures, relative to an initial scan, can be generated to search for sudden changes in the corona. The first few days of operation of this program have yielded three low-lying events (<1.55 solar radii) following minor chromospheric activity (a surge and eruptive prominences), which propagated up through the corona with velocities on the order of 100 km/s.

Introduction

Photoelectric observations of the corona have been made daily at Sacramento Peak Observatory (SPO) since 1975. The 40-cm-aperture coronagraph is used to form an occulted image of the corona, which passes through a narrow-band filter that spectrally chops at 100 kHz between the corona in the green line of Fe XIV 5303Å and an off-band wavelength. This technique allows the sky background contribution to be electronically subtracted. The output is sensed by a photomultiplier, digitized, and recorded. The entrance aperture of 1.1 arcmin is scanned around the limb at radius vectors of 1.15, 1.35 and 1.55 solar radii (R_o). Data points are recorded every three degrees in latitude. For further information on the instrument and the data, refer to Fisher (1973, 1974, 1978), Fisher and Musman (1975), Musman and Altrock (1978) and Altrock (1980, 1982).

The Coronal Transient Patrol

Since 1976, sporadic observations by Altrock (unpublished) and Fisher (1977) have shown that transient processes can be observed with the SPO coronal photometer. However, no systematic approach has been taken, due partially to slow data rates in the original instrument. Recent comprehensive improvements in computer control of this system have allowed much faster data acquisition rates, making systematic observations more attractive. On 15 Sep 1982 a program was started to patrol for green-line transients approximately one week each month. Every 20 to 30 minutes (depending on the time required for recentering, rezeroing, etc.) a set of scans is taken at the above three heights. From these scans, a "picture" of the corona can be generated, as in Figure 1a.

If an error in centering the image occurs prior to making a circular scan in the corona, the resultant intensity $I(\theta)$, where θ is the azimuth angle of the scan, contains additive errors $\Delta I(\theta)$ that may be expressed analytically. The only assumption required is that $I \alpha R^{-a}$, where a is some positive constant and R is the radius vector. In addition to the radius errors, the analytic

(a)   (b)
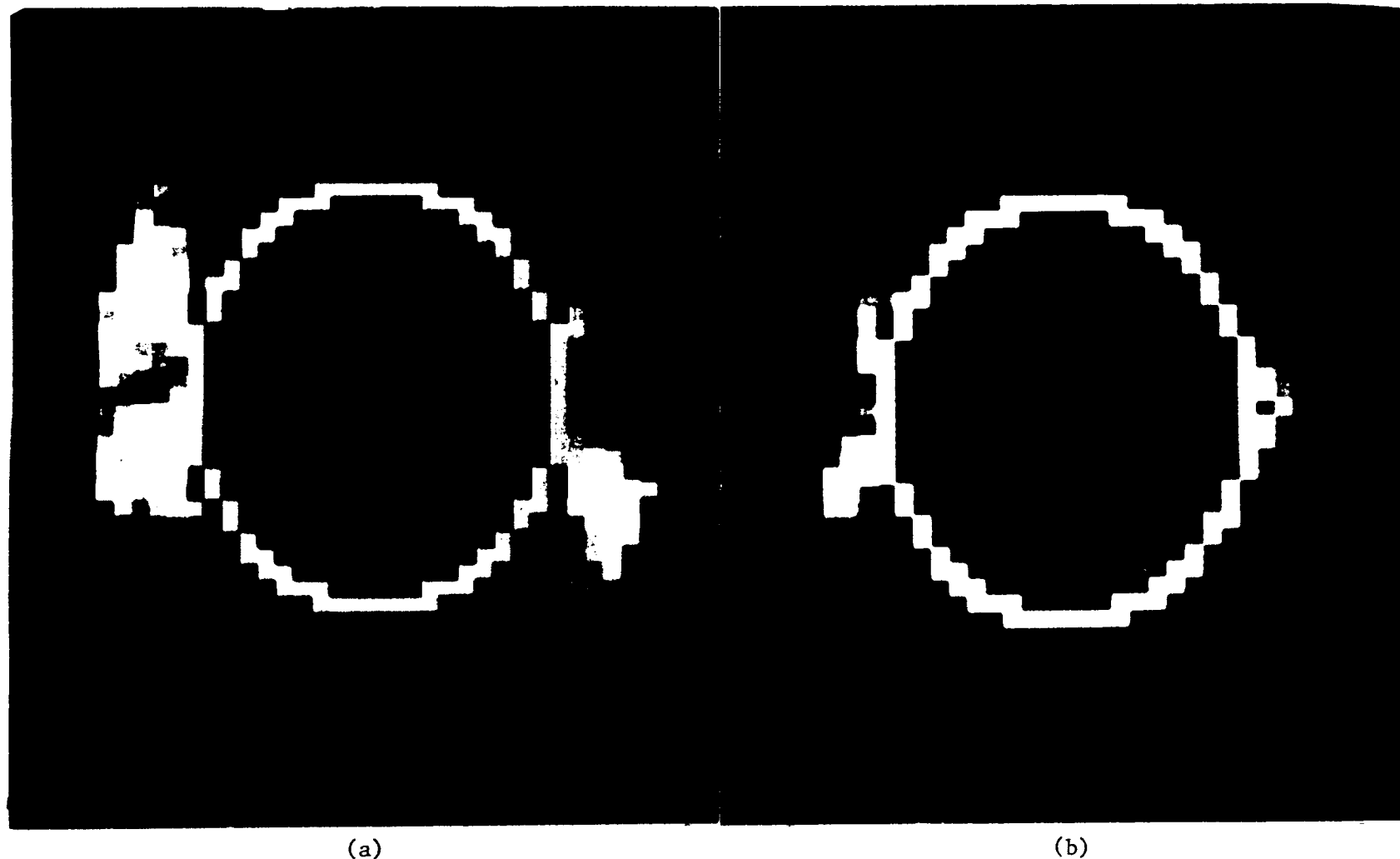
Figure 1. (a) A grey-scale picture of the solar green-line corona from 1.15 to 1.55 R_0 taken from 14:49 to 15:10 UT on 19 Oct 1982. The bright inner circle represents the solar disk. Intensities have been scaled to yield a constant average intensity with height. Solar north is at the top and east is on the left. Note the two active regions on the east limb and one on the west limb. (b) A difference picture of the solar green-line corona, with the scan of (a) subtracted from one made from 22:02 to 22:25 on the same day. The transient discussed in the text is on the left, just below the equator (azimuth angle 105°). Two other transients are visible near azimuth angles 80° and 270°. The intensity scale is not the same as in (a).

expression can easily be modified to include changes in atmospheric and instrumental transmission from scan i to scan j. The resultant expression is

$$\Delta I_{i,j}(\theta)/I_i(\theta) = A_j + B_j \cos(\theta - \theta'_j),$$

where A_j, B_j, and θ'_j are constants to be determined by a least-squares fit to $\Delta I_{i,j}(\theta_k)$, $k = 1,\ldots,120$. Thus, each scan I_j during the day can be adjusted relative to a standard scan I_i, usually one near the beginning of the day. Figure 2 shows the result of applying this technique to all the scans on a given day.

The Transients of 19 Oct 1982

After applying the correction for image drifts and changes in instrument and sky transmission, difference pictures can be generated relative to the standard scan. Figure 1b shows such a picture for 19 Oct 1982. There was obviously at least one major change in the corona during that day, seen in the lower left hand corner of the image. In order to determine if this change could be considered a transient, as opposed to a gradual evolution or an effect of solar rotation, we first examined the SPO Hα patrol for that day.

At 17:48 UT a small bright surge on the disk occurred just inside the limb near an azimuth angle of 105° east of north. It propagated across the limb to a maximum projected height of 55 Mm (1.08 R_0) with a projected radial velocity of 70 ± 10 km/s early in the event (through 18:00). In the green-line data, strong increases in intensity near azimuth angle 105° were seen at 1.15 and 1.35 R_0 at 18:10 ± :24 and 18:16 ± :24, respectively (precursor activity, which will be discussed below, was seen prior to). If we consider this main coronal intensity increase to be due to the mospheric disturbance, the propagation velocities to 1.15 and 1.35 R_0 are > 40 km/s and > 80 km/s, respectively. The inferred propagation velocity from 1.15 to 1.35 R_0 is > 40 km/s. These coronal velocities are highly uncertain due to the long scan times and the difficulty of determining precisely when a "disturbance" starts at a given height.

Discussion

As the Hα surge rose above the east limb, it appeared to follow a loop-like trajectory, curving off to the south in the plane of the sky. The final configuration of the coronal event (Figure 1b) shows a nearly identical shape. Although it may not be apparent in this figure, there is evidence in the data for closure of the loop on the south side, with brightening at 1.15 R_0 at 100° ± 5 and 120° ± 5 and at 1.35 R_0 at 110° ± 5. In addition, there is marginal evidence for darkening in the center of the loop.

The vertical development of the main brightening appears to be consistent with a density perturbation (pressure pulse) travelling up with the surge. The surge velocity of 70 ± 10 km/s is consistent with velocities inferred from brightenings in the green-line corona (> 40 km/s). Preliminary data from the Mauna Loa Solar Observatory K-Coronameter (Fisher, 1982a) indicate enhancements up to 1.72 R_0, and perhaps higher, by 18:51, consistent with propagation velocities of 130 km/s (from the surface) to 70 < V(1.72 R_0) < 310 km/s (from 1.35 R_0).

The precursor activity referred to above was a brightening at R/R_0 = 1.35 prior to 17:30 at a location directly above the site at which the surge occurred
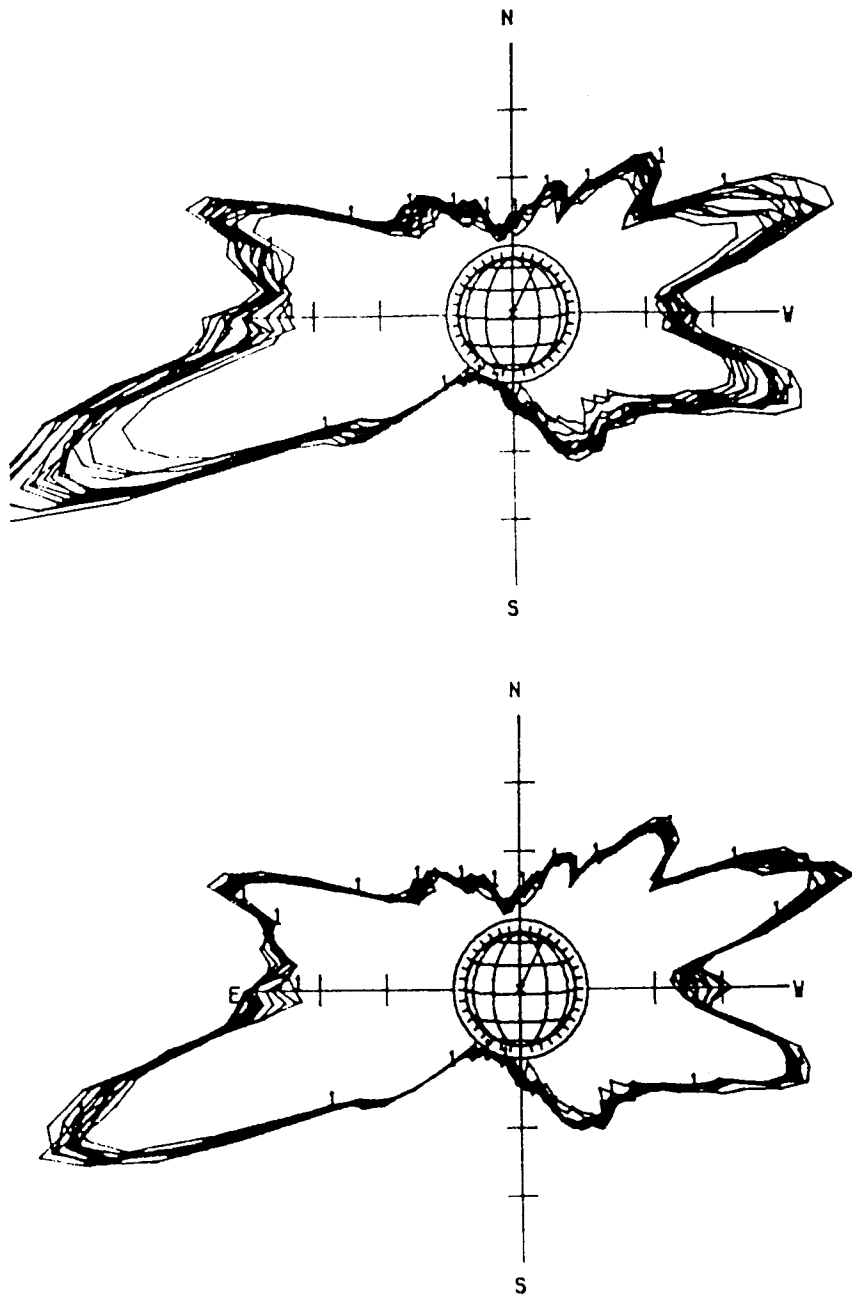
Figure 2. Top: a polar plot of all scans at 1.15 R_o taken on 18 Oct 1982. Bottom: the same scans after correction for image drifts and changes in sky and instrument transmission.

later. Similar observations by other investigators of precursors or forerunners prior to mass-ejection events appear to fit in the class of internal-energy events described by Fisher(1982b). Now, as we have seen, the main coronal intensity increase can be attributed to the mechanical effects of the rising surge. What then is the cause of the precursor brightening, which had no visible preceding Hα activity? One possibility is a density increase or heating in the corona due to magnetic activity prior to the surge. If such a physical connection does exist between the precursor and the surge, we may be seeing evidence for the first time of coronal magnetic-field activity as the cause of surges.

The qualitative model would then be: (i) Coronal magnetic-field activity causes a density increase or heating in the corona, which is reflected in green-line brightening; (ii) This same coronal magnetic-field activity creates an instability in the chromosphere that results in the expulsion of matter ("melon-seed" model?) into the corona (the surge); (iii) As the surge rises through the corona, the pressure pulse connected with it compresses the coronal material, causing the second, main brightening.

Finally, we note in passing that the two other brightenings of that day (cf. Figure 1b) on the west and northeast limbs also have associated Hα activity (eruptive prominences) and therefore also qualify as coronal transients. The coronal manifestations of these events at $1.15\ R_0$ appear to have propagation velocities of < 140 km/s.

References

Altrock, R.C., Anomalous satellite drag and the green-line corona, Solar-Terrestrial Prediction Proc., 4, (ed. R.R. Donnelly), NOAA, Boulder, CO, E1-E4, 1980.

Altrock, R.C., An anomalous twenty-seven-day periodic variation in satellite drag and possible solar-induced causes, Workshop on Satellite Drag Proc., (ed. J.C. Joselyn), NOAA, Boulder, CO, 162-177, 1982.

Fisher, R.R., A photoelectric photometer for the Fe XIV solar corona, Rep. AFCRL-TR-73-0696, Air Force Geophysics Lab., Hanscom AFB, MA, 1973.

Fisher, R.R., The Fe XIV brightness measurements: 30 June 1973, Solar Phys., 36, 343-344, 1974.

Fisher, R.R., Photoelectric observations of Fe XIV coronal depletion: 20 April 1976, Solar Phys., 55, 135-141, 1977.

Fisher, R.R., Lambda 5303 Fe XIV density models of the inner solar corona, Solar Phys., 57, 119-128, 1978.

Fisher, R.R., Private communication, 1982a.

Fisher, R.R., Coronal transient events, Trans. AGU, 63, 1086, 1982b.

Fisher, R.R., and S.A. Musman, Detection of coronal holes from lambda 5303 Fe XIV observations, Astrophys. J., 195, 801-803, 1975.

Musman, S.A., and R.C. Altrock, Recurrent geomagnetic disturbances and coronal holes as observed in Fe XIV lambda 5303A, J. Geophys. Res., 83, 4817-4822, 1978.

Page intentionally left blank
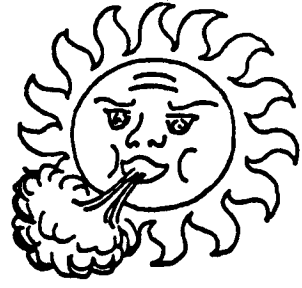
SESSION 2.

MHD WAVES AND TURBULENCE

SUMMARY OF THE SESSION ON MHD WAVES AND TURBULENCE

A. Barnes

The papers of this session reflect a shift of emphasis in the interpretation of interplanetary fluctuations. Up until about the time of Solar Wind 4, the language of hydromagnetic wave theory had been the primary mode of description. However, the wave approach runs into observational problems, suggesting that the language of turbulence theory might be more appropriate. The paper of Mathaeus and Goldstein represents some first attempts in this direction. They applied tests of statistical stationarity to sets of magnetic data, confirming that "weak stationarity" is a justified assumption. They presented the first measurements of the MHD helicity. The magnetic helicity is mixed, indicating an equal mixture of right and left polarizations. Cross-helicity normally indicates propagation outward (antisunward) for all but the lowest wave numbers, although one counter-example containing substantial inward propagation was given.

Denskat reviewed the observations of interplanetary MHD waves over the range 0.3-5 AU. The slope of the power spectra at ~ 0.3 AU is flatter than at ~ 1 AU. The relative intensity of fluctuations in field magnitude to fluctuations in field direction increases with increasing heliocentric distance.

Ovenden and Schwartz reported calculations that indicate the possibility of decay of an Alfven wave (allowing for finite Larmor radius) into a soliton, and suggested that a complex of such solitons might be an important component of interplanetary turbulence.

Bavassano reported an observational study testing the stochastic model of interplanetary Alfvenic fluctuations. The model is qualitatively successful, but has quantitative limitations.

Hollweg presented a theory of surface waves on tangential discontinuities. These waves have many properties in common with Alfven waves, and it was suggested that the observed Alfvenic fluctuations may, at least in part, be due to surface waves.

Montgomery presented a comprehensive review of the present state of hydromagnetic turbulence theory. The theory has had a reasonable development only for the case of incompressible isotropic turbulence, and therefore may not be completely applicable to the solar wind. Nevertheless, the concepts and language may be useful, if only in a qualitative way.

Page intentionally left blank

MAGNETOHYDRODYNAMIC TURBULENCE IN THE SOLAR WIND

by

William H. Matthaeus and Melvyn L. Goldstein

Laboratory for Extraterrestrial Physics
Code 692, NASA/Goddard Space Flight Center,
Greenbelt, MD 20771

Abstract

Recent work in describing the solar wind as an MHD turbulent fluid has shown that the magnetic fluctuations are adequately described as time stationary and to some extent as spatially homogeneous. Spectra of the three rugged invariants of incompressible MHD are the principal quantities used to characterize the velocity and magnetic field fluctuations. Unresolved issues concerning the existence of actively developing turbulence are discussed.

INTRODUCTION

To describe a fluid system as turbulent is to say that the dynamical fluid variables exhibit complex and essentially non-reproducible behavior as a function of time. This is generally due to the presence of nonlinearities in the fluid equations which strongly couple a large number of degrees of freedom. Turbulent systems are usually very far from equilibrium states for which detailed analytically tractable theories might exist.

By all appearances, the solar wind plasma flow and the interplanetary magnetic field carried along with it are such a turbulent system. In the zero momentum frame, the magnetic and velocity field fluctuations are energetically comparable to the mean magnetic field over length scales of order 1 AU and display the type of complicated behavior expected of turbulence.

The prospect that plasma turbulence techniques may be applied and developed in the context of solar wind studies is attractive. Although the interplanetary medium cannot be controlled in the ways a laboratory plasma might be, it does persist in time in what might be thought to be a statistically steady state. More importantly, interplanetary exploration has provided us with a vast data base of magnetic field and plasma properties along spacecraft trajectories. The availability of these data, reduced to a form compatible with the language of turbulence theory, now provides the opportunity to evaulate existing theories and may provide guidelines for the development of new approaches. In this paper, we summarize some of our recent work [Matthaeus and Goldstein, 1982a,b] which begins to address the questions: to what extent does the interplanetary medium resemble a turbulent MHD medium and what can one learn about the validity of turbulence theory from experimental space physics.

The theoretician studying turbulence properties of the interplanetary medium must deal primarily with appropriately defined ensemble averaged properties of the interplanetary fields [Batchelor, 1970]. The connection between statistical theories of turbulence and experimental reality can be made only when it is possible to show that the theoretician's abstract notion

of an ensemble has a plausible correspondence to some experimentally implement-
ed averaging procedure. The connection usually sought is that time averages
of the products of the turbulent fields at fixed points in space are equiva-
lent, in practice, to ensemble averaging. When this is so, the fluctuations
are 'ergodic'. If time averages are also insensitive to the origin in time,
the fluctuations are statistically stationary. As a first step in deciding
whether it is even appropriate to describe interplanetary fluctuations using
turbulence theory, we establish that the interplanetary magnetic field often
behaves as a stationary and ergodic random function of time.

TIME STATIONARITY

Consider a component of the magnetic field, $B(t)$, at a fixed point in
space. Frequency spectra and two-time correlation functions indicate that
$B(t)$ consists of a continuum of frequency components superposed on coherent
signals with periods of the solar rotation period and its first few harmonics.
The signals commensurate with the solar rotation are indicative of sector
structure, stream structure and other nearly periodic phenomena relating to
the origin of the solar wind and its possible continued forcing by high speed
streams.

Stationarity of the average field, $\langle B(t) \rangle = a$, and second order moments
such as the correlation function $R(\tau) = \langle B(t)B(t+\tau) \rangle$ is just the property that
the ensemble average denoted by the brackets $\langle ... \rangle$ does not depend on t. To
determine the extent to which this property is reflected in the data, we
consider sequences of time averages of the field covariances of duration T.
According to the ergodic theorem [Panchev, 1971] for stationary random
processes, the mean values of these averages converge to the ensemble means in
a calculable fashion. We have shown [Matthaeus and Goldstein, 1982b] that the
expected variance of the time averages of $B(t)$, say $[B(t)]_T$, is, for large T

$$\Delta^2[B]_T = \langle ([B]_T - a)^2 \rangle = 2\sigma^2 T/T_c + 4\sigma_o^2 \sin^2(\omega_o T/2)/(\omega_o T)^2 \qquad (1)$$

when coherent power at frequency ω_o is properly taken into account. In (1),
σ^2 is the incoherent power, σ_o^2 the coherent power and T_c is the correlation
time of $B(t)$. The right hand side depends only on bulk statistical properties
of B. However, the left hand side can also be estimated from a large dataset
by carrying out many time averages of duration T and averaging the results.
Comparing the asymptotic ensemble prediction in (1) with the averages from the
data provides a test of the stationarity hypothesis.

The longest dataset we have analyzed in this manner utilized the (X, Y, Z)
= (radial, tangential, normal) components of the interplanetary magnetic field
taken from a 621 day IMP dataset in the National Data Center. The results
show that the ergodic theorem is an excellent predictor of the behavior of the
averages. The apparent convergence of the variance of estimates of $\langle B \rangle$
indicates that both first and second order moments are stationary since the
mathematics leading to (1) requires that the two-time correlation $R(\tau)$ be
independent of t. For this result to be useful, we also need to be able to
obtain good estimates of second order moments from the same finite amount of
data. This requirement is equivalent to using time averaging to obtain
convergence of certain fourth-order moments of $B(t)$ (namely, the variance of
estimates of the variance of B, each of which is a time average). This has
also been established for the IMP dataset.

The stationarity test has also been applied to a number of other magnetic
field datasets using ISEE and Voyager data at heliocentric distances of 1 - 10

AU. The length of the data records ranged from about 10 to 100 days. The degree of convergence of large T time averages to predictions such as (1) was used as a figure of merit. These analyses indicate that 'good' convergence is obtained for datasets containing many (> 10) correlation times, provided that significant organized structures such as isolated shocks and sector crossings are not undersampled. For example, a dataset spanning two or three sectors cannot be expected to give statistical estimates which are as well behaved as those obtained from a smaller subset of the data which includes no sector crossing.

These results suggest that the interplanetary magnetic field can be meaningfully viewed as a 'weakly' stationary random function. Strict stationarity requires that all moments, not just means and second order correlation functions, be independent of time.

It should be noted that the stationarity test described above is far from a mathematically rigorous procedure. One difficulty is that estimates of the left hand side of (1) utilize an average over a finite number of realizations of duration T rather than an average over the entire ensemble. It was also necessary to estimate the values of the ensemble parameters a, σ_o^2, σ^2 and T_c from the same finite span of data. The values of T used were restricted to be less than one-fifth the total data record to minimize the effects of those approximations. We believe that this type of restriction is essential to prevent spurious results, though we have been unable to show this analytically.

SPATIAL HOMOGENEITY

Spatial homogeneity is another possible symmetry of turbulent fluctuations [Batchelor, 1970] and is particularly important if wavenumber spectral analysis is to be performed. Much of the existing turbulence theory deals with this case. Moreover, the dynamical processes which characterize homogeneous turbulence may play an important role in turbulence which is, at the largest scales, inhomogeneous. This statement is most easily justified in the very large Reynolds number case, in which turbulent fluctuations are found at all spatial scales ranging from energy containing scales down to a dissipation scale. If the length scales in this range are well separated from the lengths characterizing the scale of the entire system, homogeneity is a reasonable expectation.

In the most general case, time stationarity and spatial homogeneity are separate issues. However, the solar wind is a super-Alfvenic flow which allows the approximate identification,

$$\langle B(\underline{x},t)B(\underline{x+r},t)\rangle = \langle B(\underline{x},t)B(\underline{x},t+\tau)\rangle \tag{2}$$

where $\underline{r} = -v_{sw}\underline{R}$, v_{sw} is mean solar wind speed and $\underline{R}$ is the radial unit vector in heliocentric coordinates. This 'frozen-in flow' property is valid for phenomena occuring on a MHD time scale. If the time-stationary property holds at all points in space, (2) implies that $B(\underline{x},t)$ is also spatially homogeneous. Equation (2) cannot be valid for spatial separations $\underline{r}$ which approach the scale over which the bulk heliospheric quantities vary, which can be plausibly taken to be the local heliocentric radial coordinate, R. In view of the results of the previous section, we have concluded that interplanetary MHD fluctuations at frequency ω correspond to spatially homogeneous structures provided that their scale v_{sw}/ω is much less than R. It seems reasonable from a theoretical point of view to assume that interplanetary fluctuations are both stationary and locally homogeneous with macroscopic parameters varying

slowly, over scales of order R. This limited connection between stationarity and homogeneity can only be useful when the correlation length $L_c << R$, in order that the spatial dependence of the fluctuations can be well sampled without encountering effects due to the scale size of the heliosphere.

RUGGED INVARIANTS OF MHD IN THE SOLAR WIND

Theoretical descriptions of fully developed MHD turbulence often dissuss the behavior of the 'rugged' invariants of the MHD equations. We have developed techniques for determining the rugged invariants of three dimensional MHD and their reduced wavenumber spectra from single spacecraft data [Matthaeus and Goldstein, 1982a]. The three known rugged invariants are the energy density, $E = <B^2 + v^2>$, the cross helicity, $H_c = <\underline{v} \cdot \underline{B}>$, and the magnetic helicity, $H_m = <\underline{A} \cdot \underline{B}>$. The energy density is the sum of magnetic and kinetic energy densities, with the magnetic field $\underline{B}$ written in Alfven speed units. The magnetic helicity is the mean projection of the magnetic vector potential, $\underline{A}$, on the magnetic field $\underline{B}$. In the above definitions, $\underline{B}$ is taken to be the fluctuating field and $\underline{A}$ is assumed to be in the Coulomb gauge. These three quantities are invariants of ideal MHD and they are "rugged" because their invariance obtains for finite dimensional Galerkin-type representations of MHD, as well as the usual continuum model. In all cases tested so far [see for example, Fyfe and Montgomery, 1976] rugged invariants have been shown to be the isolating constants of motion necessary to describe the unphysical, but theoretically suggestive finite dimensional statistical mechanics models of turbulent ideal MHD and Navier Stokes flows. In physically realistic turbulence, which always admits dissipation at the smallest spatial scales, rugged invariants are no longer constants of the motion. However their values are not changed by the action of nonlinearities in the equations of motion. Since nonlinear couplings alone induce transfer of excitations from one length scale to another, the set of rugged invariants imposes direct restrictions on how turbulent energy transfer occurs. For this reason much of turbulence theory is couched in the vocabulary of rugged invariants and their wavenumber spectra.

Here we shall not reproduce detailed analyses of data, but merely summarize the type of spectra which have most frequently been seen.

The energy spectra analyzed between 1 and 10 A.U. show power law wavenumber dependences of k^{-a} with a = -1.55 to - 1.7. The power law region extends from scales near the correlation length, which is usually between 10^{12} and 10^{13} cm, down to scales at least as small as our usual cutoff, about 10^8 cm. We have not yet analyzed data at high enough frequencies to resolve any sort of dissipation range where the spectrum is expected to steepen considerably. The power law is usually very near the Kolmogorov exponent of -5/3. The appearance of this type of power law dependence is strongly suggestive that a turbulent inertial range is being observed, even though the solar wind is probably quite anisotropic [Belcher and Davis, 1971] and the Kolmogorov spectral prediction presumes isotropy. Others have sometimes reported different power law dependences [Sari and Ness, 1969; Denskat, these proceedings], particularly for observations inside of 1 AU where homogeneity is less likely a good approximation. It is also possible that at these smaller heliocentric distances the turbulence may not yet have had time to become fully developed.

Typical solar wind magnetic helicity spectra alternate in sign throughout the power law range and usually at lower wavenumbers as well. Because the magnetic helicity spectrum is a measure of the topological handedness of the

fluctuations near a given wavenumber, the observed spectra indicate that the inertial range consists of both left and right handed magnetic structures. The net magnetic helicity for a "normal" solar wind period is that which is due to the largest scales sampled and the lengths characterizing the helicity scale are larger than the correlation length which is an estimate of the energy containing scale. This is similar to what one might expect in a steady state inverse cascade [Frisch et al., 1975] or freely decaying selective decay situation [Matthaeus and Montgomery, 1980]: MHD turbulence is thought to transfer magnetic helicity preferentially to the largest allowed scales. Near interplanetary shocks [Russell, these proceedings] and the terrestrial [Hoppe et al., 1981] and Jovian [Smith et al., 1983] bow shocks the presence of circularly polarized waves is signaled by a distinct bias in the helicity spectra.

The cross helicity spectrum is a measure of the correlation between the velocity and magnetic fluctuations as a function of wavenumber. Similar quantities have been previously used [for example, see Coleman, 1967 and Belcher and Davis, 1971] to detect "Alfvenic fluctuations". In highly Alfvenic periods, the inertial range cross helicity is generally single-signed and attains a large fraction of its largest allowed values. However, it is not unusual to see the opposite sign of cross helicity at scales at or larger than the correlation length. In a wave interpretation, these wavenumber intervals correspond to inward-propagation, while the inertial range has a cross helicity indicating outward propagation. In at least one other interval, the cross helicity has been seen to be of mixed sign throughout the inertial range but with a fixed sign corresponding to outward propagation at the largest scales sampled.

DISCUSSION

We have attempted the beginnings of a systematic description of inter-planetary fluctuations in a vocabulary appropriate to MHD turbulence theory despite serious questions which can be raised regarding the applicability of the model [see the review by D. Montgomery in these proceedings]. Even within the context of this model, there appear to be three distinct dynamical scenarios which might describe the observations.

The first of these is that, for one reason of another, the nonlinear couplings between the fluctuations are short circuited so that small amplitude wave theory encompasses the important physics. In this view geometrical considerations are sufficient to determine the radial dependence of the fluctuations, which influence the large scale dynamics only through perturba-tive wave-pressure effects and slow laminar dissipation. This perspective has often been motivated [Dobrowolny et. al, 1980a] by the occurrence of periods of highly Alfvenic fluctuations such as those reported by Belcher and Davis [1971]. It has been suggested that the linearization of incomressible MHD which obtains for exactly correlated velocity and magnetic fields allows large amplitude fluctuations to propagate outward without wave-wave interactions [Dobrowolny et al., 1980b]. One would then need to understand why the solar wind is generated with waves propagating in the outward direction only, and plausible scenarios for this have been proposed. However, there are a number of difficulties with this model, which because it lacks spectral transfer, is not turbulent at all. However, this lack of turbulence would be consistent with the view that nonlinear interactions occur in the solar corona only below the critical point. Thus only outward propagating waves, with their remnant turbulence frozen in, actually escape into the interplanetary medium. This

picture is not ruled out by any of our analyses, except perhaps the observation that there are times when the cross helicity spectrum suggests the presence of both inward and outward directed fluctuations in the inertial range.

In the previous section we have noted that even highly Alfvenic periods sometimes show admixtures of fluctations correlated in the sense opposite to that of outward propagation. In terms of rugged invariants, some wavelengths have the opposite sign of cross helicity. These modes reintroduce nonlinearities in the dynamics and at this time we do not know if their levels are high enough to reinstate turbulent cascade processes. Recently, however, we have reported [Matthaeus, Goldstein and Montgomery, 1982] preliminary two dimensional MHD results which suggest that levels of cross helicity even higher than those typically seen in Alfvenic periods are inadequate to prevent the development of a power law inertial range. In fact, the simulations show that the resulting nonlinear processes "almost always" act to enhance the initial alignment of magnetic and velocity fields. Even if coronal dynamics preferentially generate fluctuations correlated in the outward propagating sense, it is likely that turbulence proceeds.

A second perspective is that fluctuations are initially produced near the sun and subsequently participate in turbulent decay processes superposed on the overall heliospheric expansion, but do not couple in any direct way to the mean solar wind fields. In this case interplanetary turbulence can be studied somewhat independently of other solar wind processes.

A third possiblity, which we suggest may be the most realistic, is that the initially decaying turbulence is "stirred" or forced by interactions of the local fluctuations with mean field gradients and organized structures such as high speed streams and magnetic clouds. This has been previously considered, for example by Coleman [1968]. Turbulence of this type is an intrinsic part of the overall heliospheric dynamical system and quantities such as ohmic heating rates and the radial dependence of the mean magnetic field cannot be adequately accounted for without incorporating the turbulence at some level. By way of analogy, hydrodynamicists have traditionally recognized that high Reynolds number shear flows can be properly understood only when turbulence effects are included [see e.g., Tritton, 1977]. While even the existence of an effective coupling mechanism to pump turbulence at the expense of energy loss in the mean fields must be viewed as conjectural at this time, interaction regions at the leading edge of high speed streams are one class of candidates for the location where this occurs. Other possible "stirring" mechanisms include solar transients and magnetic clouds. In interaction regions, strong gradients in flow speed may stretch field lines, producing dynamo action as well as giving rise to Kelvin-Helmhotz instabilites. The typically large variance of the fluctuations in interaction regions relative to average conditions also draws our attention to them as localized sources of turbulence.

Any assessment of the role of turbulence processes in the solar wind must include a determination of the time scales over which the turbulence occurs. This is well beyond our reach at this time since we cannot measure or predict forcing, dissipation or energy transfer rates without introducing unmotivated assumptions. However, a nonlinear time can be constructed by forming the ratio of the scale size of the energy containing structures to their characteristic speed. In hydrodynamics this 'eddy turnover time' is an estimate of the lifetime of the system and the rate of relaxation of the excitations through cascade to smaller scales and subsequent dissipation. Using a scale of 10^{11} cm and a fluctuation speed of 30 km/sec gives an estimate of the MHD eddy

turnover time of 3×10^4 sec, appropriate to nominal conditions at 1 AU. Comparing this with the transit time of 350 km/sec solar wind over an A.U. indicates that ten eddy turnover times are incurred for each AU of outward solar wind convection. This suggests that turbulence processes can be observed by 1 AU and that fully developed turbulence should be observed in transit to 10 AU.

The fact that observed spectra of rugged invariants are qualitatively reproducible does not allow us to unambiguously conclude that turbulence is active in the solar wind. It is possible to argue that the observed power law spectra are due to noninteracting Alfven waves. The presence of MHD structures over a wide range of spatial scales, while often associated with turbulence, is not a sensitive enough indicator to distinguish actively evolving turbulence from noninteracting waves. Continual spectral transfer from large to small scales is an essentially turbulent feature, but it is one which analysis techniques developed so far have been unable to evaluate.

Every aspect of our understanding of solar wind turbulence is primitive enough at this stage that it is fair to say that theory and observation will both have to evolve considerably before the subject is judged as complete. Problems associated with widely varying spatial scales need to be addressed. Inclusion of turbulence modelling in the large scale heliospheric expansion equations [Hundhausen, 1972; Holzer, 1979] may contribute to the resolution of heating and radial dependence problems. Systematic radial dependences of large scale fluctuations such as the apparent coalescence of stream structure [Burlaga, these proceedings] may be related to inverse cascade or selective decay processes. At the very smallest scales the dissipation mechanism and dissipation spectra are not well understood. We anticipate that the resolution of some of these issues will play a role in our future understanding of the solar wind plasma and perhaps turbulent plasmas in general.

References

Batchelor, G. K., _Theory of Homogeneous Turbulence,_ Cambridge Univ. Press, 1970.

Belcher, J. W. and L. Davis, Large amplitude Alfven waves in the interplanetary medium, 2, _J. Geophys. Res.,_ 76, 3534, 1971.

Coleman, P. J., Wave-like phenomena in the interplanetary medium, _Pl. Sp. Sci.,_ 15, 953, 1967.

Coleman, P. J., Turbulence, viscosity and dissipation in the solar wind plasma, _Astrophys. J.,_ 153, 371, 1968.

Dobrowolny, M., A. Mangeney and P. Veltri, Properties of magnetohydrodynamic turbulence in the solar wind, _Astron. Astrophys.,_ 83, 26, 1980a.

Dobrowolny, M., A. Mangeney and P. Veltri, Fully developed anisotropic hydromagnetic turbulence in interplanetary space, _Phys. Rev. Letters,_ 45, 144, 1980b.

Frisch, U., A. Pouquet, J. Léorat and A. Mazure, Possibility of an inverse cascade of magnetic helicity in magnetohydrodynamic turbulence, _J. Fluid Mech.,_ 68, 769, 1975.

Fyfe, D., and D. Montgomery, High beta turbulence in two dimensional magnetohydrodynamics, _J. Plasma Phys.,_ 16, 181, 1976.

Grappin, R., U. Frisch, J. Léorat and A. Pouquet, Alfvenic fluctuations as asymptotic states of MHD turbulence, _Astron. Astrophys.,_ 105, 6, 1982.

Holzer, T. E., The solar wind and related astrophysical phenomena, in Solar System Plasma Physics, ed. C. F. Kennel, L. J. Lanzerotti and E. N. Parker, vol. 1, North-Holland, 1979.

Hoppe, M. M., C. T. Russell, L. A. Frank, T. A. Eastman, and E. W. Greenstadt, Upstream hydromagnetic waves and their association with backstreaming ion populations: ISEE 1 and 2 observations, J. Geophys. Res., 86, 4471, 1981.

Hundhausen, A. J., Coronal Expansion and Solar Wind, Springer-Verlag, 1972.

Matthaeus, W. H., and D. C. Montgomery, Selective decay hypothesis at high mechanical and magnetic Reynolds numbers, Ann. N. Y. Acad. Sci., 357, 203, 1980.

Matthaeus, W. H., and M. L. Goldstein, Stationarity of magnetohydrodynamic fluctuations in the solar wind, J. Geophys. Res., 87, 10347, 1982a.

Matthaeus, W. H., and M. L. Goldstein, Measurement of the rugged invariants of magnetohydrodynamic turbulence in the solar wind, J. Geophys. Res., 87, 6011, 1982b.

Matthaeus, W. H., M. L. Goldstein and D. C. Montgomery, Dynamic alignment of velocity and magnetic fields in magnetohydrodynamic turbulence, EOS, 63, 1069, 1982.

Panchev, S., Random Functions and Turbulence, Pergammon Press, 1971.

Sari, J. W. and N. F. Ness, Power spectra of the interplanetary magnetic field, Solar Phys., 8, 155, 1969.

Smith, C. W., M. L. Goldstein, and W. H. Matthaeus, Turbulence analysis of the Jovian upstream wave phenomenon, J. Geophys. Res., in press, 1983.

Tritton, D. J., Physical Fluid Dynamics, Van Nostrand Reinhold, 1977.

OBSERVATIONS OF HYDROMAGNETIC TURBULENCE
IN THE SOLAR WIND

K. U. Denskat
Institut für Geophysik und Meteorologie
Technische Universität Braunschweig
Mendelssohnstraße 3
D-3300 Braunschweig
F. R. Germany

F. M. Neubauer
Institut für Geophysik und Meteorologie
der Universität zu Köln
Albertus-Magnus-Platz
D-5000 Köln 41
F. R. Germany

ABSTRACT

MHD turbulence is studied by analysing magnetic field and plasma observations from Helios-1 and -2 at minimum solar activity. The steady conditions in the plasma flows and the magnetic field sector structure in 1975/1976 facilitate an investigation of the radial evolution of the turbulence from 0.29 to 1AU. In high speed streams the fluctuations in the solar wind velocity $\underline{v}$ and the magnetic field $\underline{b}$ are highly correlated (the correlation coefficient almost being one), which indicates that the turbulence is mainly Alfvénic in high speed plasma. While some general fluctuation properties remain essentially unchanged from 0.29 to 1AU, power spectral analysis reveals a different frequency composition of the Alfvénic turbulence at different heliocentric distances. At 0.3AU much more 'high' frequency fluctuations (up to 1.2×10^{-2}Hz) contribute to the total power in the magnetic field and velocity fluctuations than at 1AU. The contributions of field magnitude fluctuations are found to be distance and frequency dependent. Magnetic field spectra with an extended frequency range up to 470Hz show certain frequency bands, where the steepness of the spectra is independent of the heliocentric distance.

INTRODUCTION

Since Solar Wind 4 in 1978 some progress has been made in the analysis of observations of the radial evolution of MHD-turbulence in the solar wind. Magnetic field and plasma data from 0.29 to 1AU are provided by the Helios-spacecraft, data outside 1AU are provided by the Voyager-spacecraft. This paper mainly treats the Helios observations from 0.29 to 1AU. A comprehensive review of theory and observations of hydromagnetic waves and turbulence in the solar wind, which does not yet include Helios and Voyager observations, is available from Barnes [1979].

To study the radial evolution of MHD-turbulence in the interplanetary plasma, we use proton plasma data from the Max-Planck-Institut at Katlenburg-Lindau and magnetic field data from the Technical University of Braunschweig. In this paper we mainly analyse fluctuations in high speed plasma streams, which are usually named Alfvénic fluctuations [Belcher and Davis, 1971] or Alfvénic turbulence. The time periods studied are the primary missions of Helios-1 and Helios-2 (December 74 to April 75 and January 76 to May 76).

Alfvénic turbulence and the stream structure of the solar wind

To study the occurrence of Alfvénic turbulence we compute the correlation be-
tween b and v for heliocentric distances from 0.29 to 1AU, which is a necessary
condition for Alfvén waves. For the calculations we choose the 'mean field' (MF)
coordinate system defined such that the z-axis is taken along the average direc-
tion of the vector magnetic field, the x-axis is perpendicular to z and lies in
the xz_{SE}-plane and y completes the right-handed orthogonal set. Considering a cor-
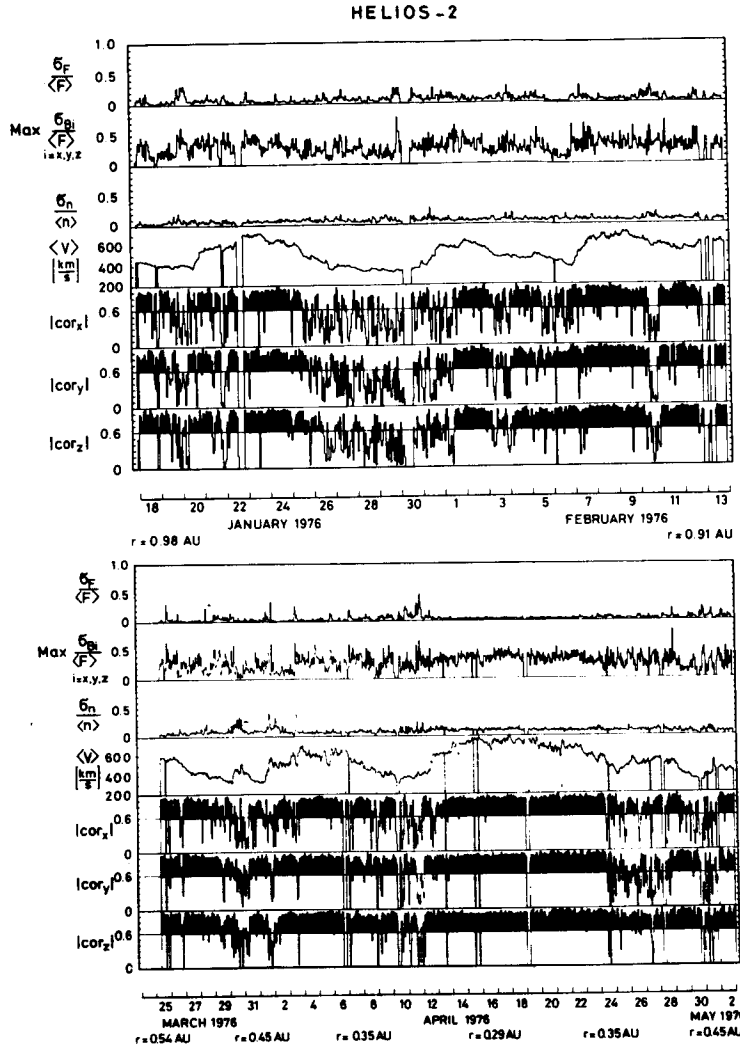
Figure 1. General properties of the Helios-2 fluctuations in relation to the speed
profile between 0.98 and 0.91AU and between 0.29 and 0.54AU. The panels denote
(from the top) normalized fluctuations in field magnitude, field components (given
by the maximum value of the three components), proton density, average bulk speed,
and the absolute values of the correlation coefficients between b and v (MF-coordi-
nates). σ_F, σ_{Bi}, and σ_n are the one hours rms-values of F, Bi, and n, respectively.

82

relation to exist for correlation coefficients larger than |0.6| for the three components leads to a more than 75% occurrence of Alfvénic turbulence during one solar rotation at aphelion (figure 1a) and perihelion (figure 1b), respectively. The occurrence of Alfvénic turbulence is essentially restricted to high speed plasma streams. Within high speed streams the purest examples of Alfvénic turbulence (characterized by a high correlation between $\underline{v}$ and $\underline{b}$ and a low level of proton density and magnetic field magnitude fluctuations) occur in the centers and trailing edges. These results were already found by Belcher and Davis [1971] for fluctuations near 1AU and are now also found to hold for fluctuations at 0.3AU. At the leading edges of high speed streams there occurs a stronger amount of compressional fluctuation activity, which indicates a local generation mechanism.

Figure 1 shows that the correlation between $\underline{b}$ and $\underline{v}$ in high speed streams is often larger than |0.9|. The choice of |0.6| as a limit for correlated fluctuations was chosen due to results from earlier investigations [Burlaga and Turner, 1976; Denskat and Burlaga, 1977], where lower correlations have been found. These differences are presumably due to an increased accuracy of the plasma experiment on board of Helios. The highly correlated $\underline{v}$-$\underline{b}$ fluctuations indicate the almost pure Alfvénic character of the turbulence. However, there always is an additional compressive component present, which needs to be explained. These compressive fluctuations could be static structures convected by the solar wind or magnetoacoustic waves or both.

Together with the direction of the interplanetary magnetic field the sign of the $\underline{b}$-$\underline{v}$-correlation gives the propagation direction of the fluctuations. For the primary missions of Helios-1 and -2 all of the Alfvénic fluctuations in high speed plasma are found to propagate in the anti-solar direction. This clearly points to a generation of Alfvénic turbulence inside the Alfvén radius (10 to 20 solar radii).

Radial evolution of fluctuation amplitudes

The investigation of radial dependences of plasma and field parameters at solar activity minimum is facilitated by the magnetic field sector boundaries remaining stable over several solar rotations [Behannon et al., 1981] and the high speed streams occuring at the same solar longitudes at subsequent solar rotations [Marsch et al., 1982].

To study the radial evolution of the fluctuation amplitudes, we calculated for one hour intervals the rms or standard deviations σ_F and $\sigma_{\underline{B}}$, where σ_F is the rms deviation of field magnitude fluctuations, and $\sigma_{\underline{B}}$ is the rms deviation of vector magnetic field fluctuations with contributions from both magnitude and directional fluctuations. The rms deviation $\sigma_{\underline{B}}$ is computed from the individual rms deviations according to

$$\sigma_{\underline{B}} = \sqrt{\sigma_{Bx}^2 + \sigma_{By}^2 + \sigma_{Bz}^2} \ .$$

Figure 2 shows $\sigma_{\underline{B}}/<F>$ and $\sigma_F/<F>$ for perihelion and aphelion time periods. Apparently there are no significant differences in the class of directional fluctuations. Since in the case of Helios-1 Musmann et al. [1977] found for the field magnitude F a distance dependence $F \sim r^{-1.6}$, these results are consistent with an $r^{-1.5}$ law for wave amplitudes predicted for Alfvén waves propagating outward without attenuation in a spherically symmetric solar wind [Whang, 1973; Belcher and Burchstedt, 1974]. However, these results are also consistent with satu-
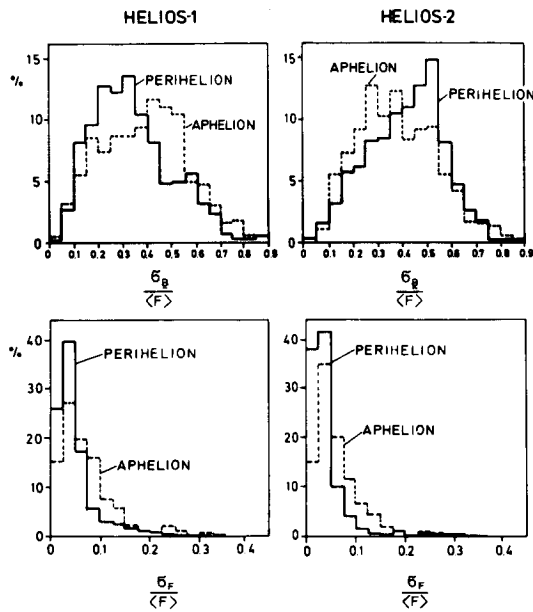
Figure 2. Distribution of normalized standard deviation of vector magnetic field fluctuations σ_B and magnetic field magnitude fluctuations σ_F normalized by the average field magnitude for one hour time intervals. The time periods for the calculations cover one solar rotation for the first aphelion and perihelion time periods of both spacecraft corresponding to distance intervals from 0.91 to 0.98AU and from 0.29 (0.31) to 0.54AU.

rated wave amplitudes, since $\sigma_B/<F>$ never exceeds a value of 0.9. Burlaga et al. [1982] studied the evolution of fluctuation amplitudes with magnetic field data from Voyagers 1 and 2 at heliocentric distances from 1 to 5AU. They found a slight decrease in $\sigma_B/<F>$ with increasing heliocentric distance. However, the variability was quite large and no distinction between unattenuated and saturated waves was possible.

The distributions $\sigma_F/<F>$ in figure 2, which show that the field magnitude fluctuations are quite smaller in amplitude than the directional fluctuations, are broader for the aphelion periods than for the perihelion periods. This relative increase of $\sigma_F/<F>$ with increasing heliocentric distance may point to a local generation of compressive fluctuations. Coleman et al. [1969] found the same results in Mariner 4 data between 1 and 1.5AU. However, Burlaga et al. [1982] found $\sigma_F/<F>$ to remain almost constant from 1 to 5AU. There are two possible explanations for this discrepency. Firstly, $\sigma_F/<F>$ may only increase with heliocentric distance out to ~ 1.5AU and remain approximately constant further out, where the constancy possibly is maintained by an equilibrium between generation and damping of compressive fluctuations. Secondly, the Helios-results shown were observed at minimum solar activity and may therefore be unique for these conditions.

Period range of the Alfvénic turbulence

To determine the period range of the Alfvénic turbulence we computed cross-spectra between $\underline{B}$ and $\underline{V}$. Figure 3 shows for one component auto power spectra, coherence and phase computed from data in high speed plasma near the first perihelion passage of Helios-2. These results are representative for spectra in high speed streams near perihelion. Coherence and phase between B_x and V_x show an almost perfect anticorrelation over a broad frequency range. At frequencies below 2.4×10^{-5} Hz the coherence is low, and therefore the fluctuations are not Alfvénic. These
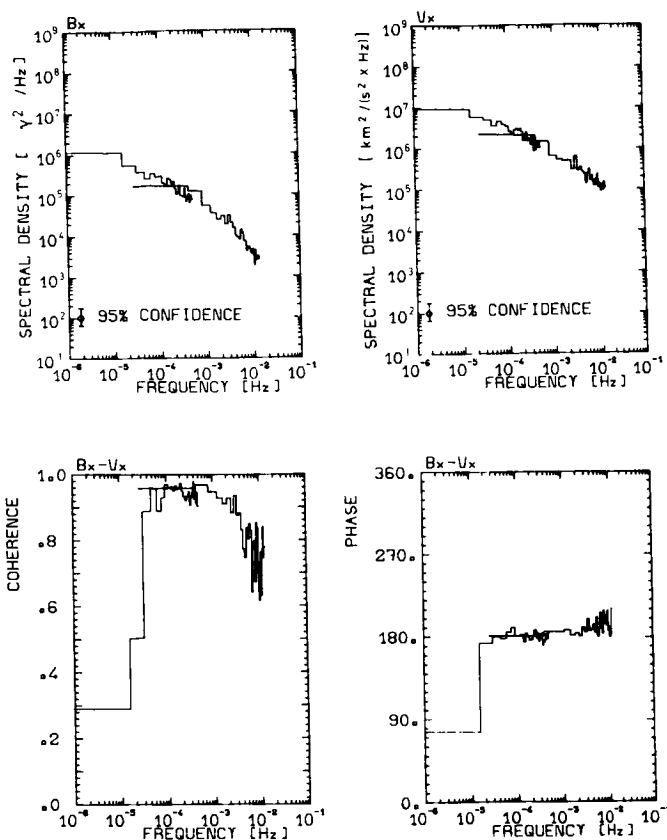
Figure 3. Power spectra B_x and V_x and coherence and phase between B_x and V_x for fluctuations in high speed plasma between 0.29 and 0.34 AU at the first perihelion passage of Helios-2. At low frequencies (10^{-6}Hz to 5×10^{-4}Hz) the spectra were computed from 1000s averages, in the higher frequency part (2.4×10^{-5}Hz to 1.2×10^{-2}Hz) from 40.5s averages.

fluctuations are apparently generated by larger-scale dynamical processes. The somewhat lower coherence above 3×10^{-3}Hz can at least in part be explained by the different kind of data which are correlated. The magnetic field data are averages over 40.5 sec, while the plasma experiment provides one data set each 40.5 sec, which is not necessarily the average value. A second reason may be a higher amount of compressive fluctuations at the higher frequencies. However, the coherence is still high up to 1.2×10^{-2}Hz and we consider the frequency range from 2.4×10^{-5}Hz to 1.2×10^{-2}Hz to contain Alfvénic turbulence. 1.2×10^{-2}Hz is certainly not the high frequency limit for Alfvénic turbulence, since from physical reasons we expect this limit at the proton gyrofrequency.

The coherences between $\underline{B}$ and $\underline{V}$ were computed for all data in high speed streams during the primary missions of the Helios spacecraft. At all heliocentric distances the results are quite similar, and we find no systematic variation. This may be surprising with respect to the low frequency limit, since the maximum Doppler shift at perihelion is 4 to 5 and at aphelion 8 to 9. However, one must consider that the resolution of the procedure in determining this lower frequency limit is quite poor (details may be found in Denskat and Neubauer [1982]).

For the primary missions of Helios-1 and -2 we computed power spectra of the interplanetary magnetic field in the frequency range containing Alfvénic turbulence (2.4×10^{-5}Hz to 1.2×10^{-2}Hz). Due to a larger number of data gaps from Helios-1, more spectra could be computed from the Helios-2 data. Only these were used for further analysis. Figure 4 shows examples of magnetic field power spectra at different distances from the sun. These spectra are quite representative for the locality where the data have been taken (both spectra were computed from data in high speed plasma streams). The power spectral density increases as the sun is aproached, in addition the slope of the power spectral density as a function of frequency changes significantly. The spectra are considerably flatter at 0.29AU than at 0.97AU with clear differences between the spectra for the field components and the field magnitude. For the components the major flattening at 0.29AU occurs below, say 2×10^{-3}Hz. Assuming a power law dependence for the spectral density P with $P \sim f^{-\alpha}$ the avarage best fit exponent α (determined by a least square method) varies between 1.59 and 1.69 at 0.97AU and between 0.87 and 1.15 at 0.29AU. The uncertainties are estimated with ± 0.12. Since at 0.29AU the power law fit $P \sim f^{-\alpha}$ does not seem to be the best possibility of representing the frequency dependence of the spectral densities, we made an additional exponential fit with $P \sim e^{-\beta f}$. However, for most of the distance range the power law fit was superior.

HELIOS-2
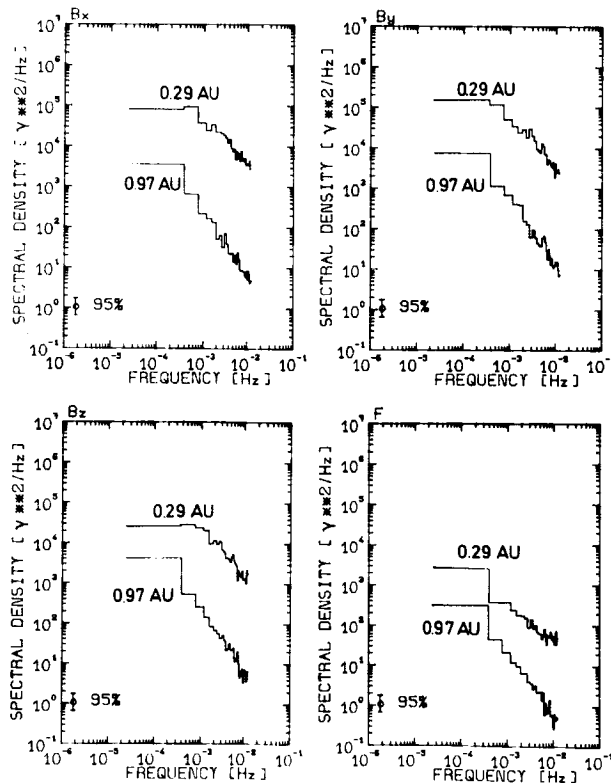
Figure 4. Magnetic field power spectra (vector components in MF-coordinates and magnitude) at different heliocentric distances from data in high speed plasma streams.
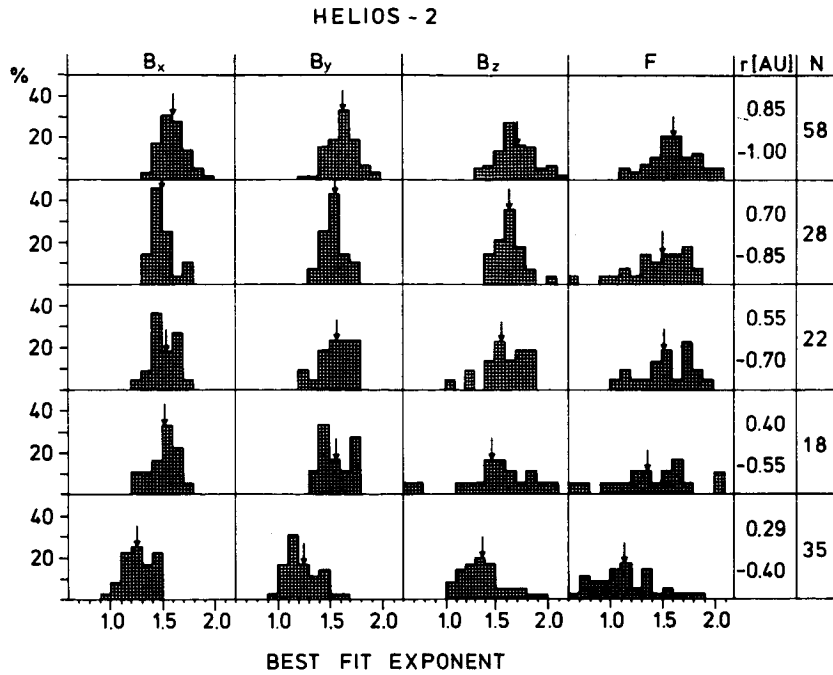
Figure 5. Distributions of best fit exponents α of magnetic field power spectra P (assumption P ~ f⁻ᵅ) for 5 heliocentric distance ranges. N gives the number of spectra computed in each distance interval, arrows mark the mean values of the distributions.

HELIOS-2
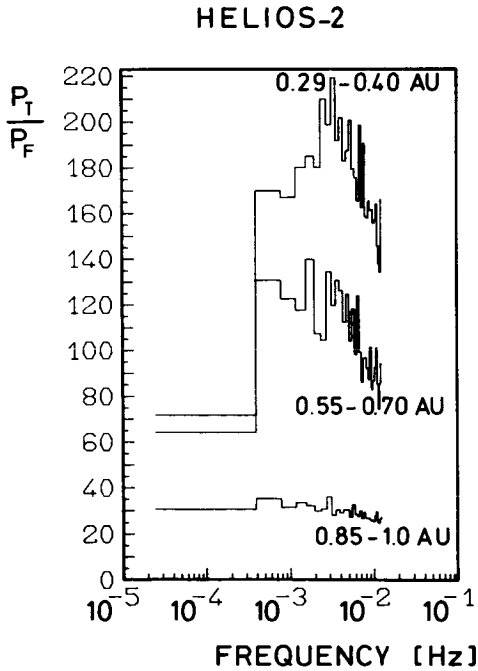
Figure 6. Average ratio P_T/P_F (P_T is the trace of the power spectral matrix; P_F is the power of the fluctuations in F) for three distance ranges as a function of frequency. The number of spectra averaged may be taken from figure 5.

Figures 5 and 6 give general information about the radial dependences of the steepness of the magnetic field spectra and about the different contribution of field magnitude fluctuations to the total power at different heliocentric distances for the Helios-2 primary mission. In figure 5 the spectral exponents generally show a large variability, but a systematic change only inside 0.4AU. This means that the very flat spectra at frequencies below 2×10^{-3}Hz occur only inside 0.4AU. Further out the spectra become increasingly steeper in this frequency range leading to spectra with a constant steepness from 2.4×10^{-5}Hz to 1.2×10^{-2}Hz.

We have no final explanation for these observations yet. There are several possibilities to explain this radial evolution of power spectral densities of magnetic field fluctuations. The reason may be a frequency dependent damping (at high frequencies) or a frequency dependent generation of magnetic field fluctuations (at low frequencies). Also possible is an inverse energy cascade in wave number space leading to this evolution of the spectra.

Figure 6 shows that the radial evolution of field magnitude fluctuations is quite different from the evolution of fluctuations in the field components. The ratio P_T/P_F varies with heliocentric distance and with frequency. At 1AU we find a non-frequency dependent behaviour of P_T/P_F, but inside 0.70AU this ratio is clearly frequency dependent. Obviously, the compressive magnetic field fluctuations become increasingly more powerful relative to the directional fluctuations with increasing heliocentric distance. In addition, this radial evolution is frequency dependent.

Parker [1982] studied spectral properties of the magnetic component of hydromagnetic fluctuations near 4 and 5AU from Pioneer-10 and -11 data. In a frequency range similar to our study he found magnetic field power spectra with smaller amplitudes than the ones found from the Helios-data at 1AU, but with very similar slopes. Apparently, the magnetic field power spectra of hydromagnetic fluctuations do not evolve further outside 1AU apart from a general amplitude decrease with increasing heliocentric distance.

Some years ago Coleman [1968] tried to explain the extremely structureless power spectra of magnetic field fluctuations in high speed plasma with the presence of an energy cascade in wave number space. In this context it is interesting to analyse magnetic field fluctuations in a frequency range extended well above the proton gyrofrequency. With the search coil magnetometer on board of Helios we are able to study magnetic field fluctuations with frequencies up to 2.2 kHz.

Figure 7 gives two examples of magnetic field spectra in high speed plasma streams from 2.4×10^{-5}Hz up to 470 Hz at 0.30AU and up to 100 Hz at 0.98AU. The power spectral densities in the frequency range of Alfvénic turbulence show the behaviour presented before. In the higher frequency range up to 2 Hz the power spectral density decreases with increasing heliocentric distance, but the steepness of the spectra remains unchanged. This is a typical feature of directional magnetic field fluctuations in this frequency range at all heliocentric distances analysed. Above 2 Hz there is a drop in spectral density together with a major change in spectral slope at the higher frequencies, where P is proportional to about f^{-3} as found by Beinroth and Neubauer [1981].
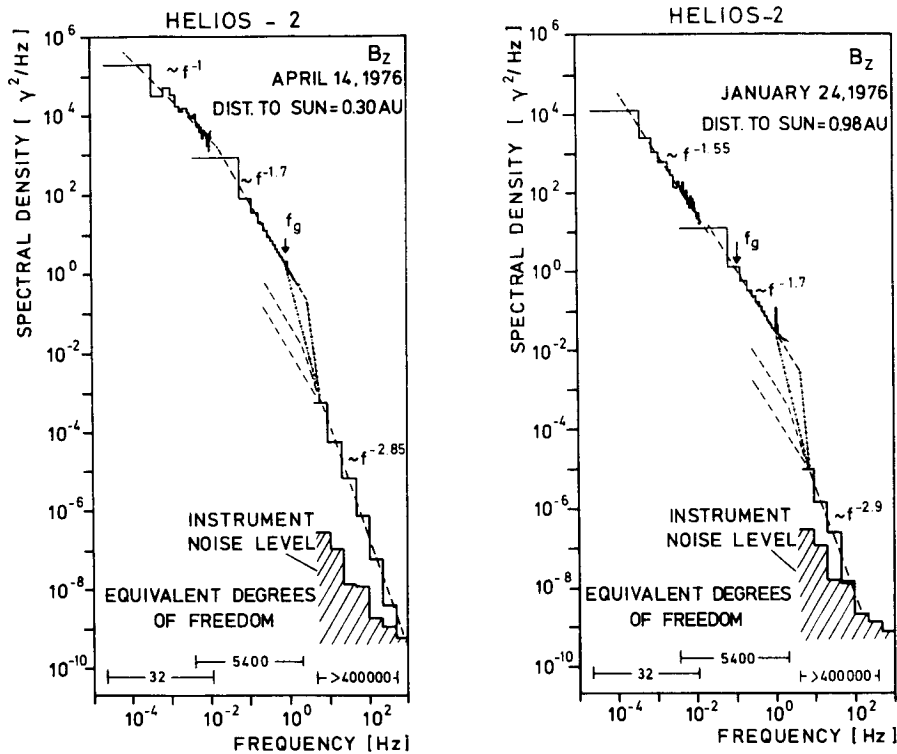
Figure 7. Power spectra of B_z at 0.30 and 0.98AU. Up to 2 Hz spectra are computed from fluxgate-magnetometer-data. The spectra above 4.7 Hz were measured with the search-coil-magnetometer. The spectral enhancement at 1 Hz is due to the spin of the spacecraft, which could not be removed totally from the data.

To interpret the radial evolution of magnetic field power spectra in this wide frequency range, one must consider the different wave modes possible at particular frequencies. The linear theory of wave propagation in a hot collisionless magnetoplasma described by the Vlasov-Maxwell set of equations (e.g. Montgomery and Tidman, 1964) yields an infinite number of wave modes most of which are strongly damped. At low frequencies below the dominant ion cyclotron frequency there are three important wave modes: the Alfvén wave and the fast and slow magnetoacoustic waves (e.g. Barnes, 1979). As the frequency approaches the He^{++} and the proton cyclotron frequencies the Alfvén waves are severly damped by ion cyclotron damping. Hence we expect an appreciable drop in power spectral density which is somewhat stretched out in frequency due to the Doppler-shift. The remaining power spectral densities at high frequencies than represent the continuation of the magnetoacoustic wave mode at the low frequencies usually called 'whistler' mode above the proton gyrofrequency. We therefore attribute the drop in spectral density between ≤ 2 Hz and 4.7 Hz to the damping of the Alfvén portion of the spectrum, which close to the ion gyro frequencies are generally refered to as ion cyclotron waves. Possible variations of the total spectral densities across the gap are indicated by dotted lines. The possible contributions of the magnetoacoustic component is indicated by dashed lines.

Conclusion

The Helios-observations between 0.29 and 1AU show that the occurrence of Alfvénic turbulence is essentially restricted to the high speed plasma streams independent of heliocentric distance. The fluctuation amplitudes of Alfvénic turbulence normalized by the average magnetic field magnitude show no systematic heliocentric distance dependence indicating that the fluctuation amplitudes may be in a saturated state. This is different for normalized field magnitude fluctuations, which become larger with increasing heliocentric distance.

The period range of Alfvénic turbulence is found to be between at least 81s (lower limit owing to the resolution of the plasma experiment) and approximately 12 hours (in the spacecraft frame).

Power spectra of the interplanetary magnetic field show a clear distance dependence. Up to 0.4AU the spectral slope is extremely flat at low frequencies up to $\sim 2 \times 10^{-3}$) and becomes increasingly steeper with increasing frequency. Further out in the solar wind the spectral slope up to 1.2×10^{-2}Hz is well represented by a power law with $P \sim f^{-1.6}$ on average. The reason for this behaviour may be frequency dependent damping (at the high frequencies) or frequency dependent generation (at the low frequencies) of the magnetic fluctuations. Another possibility is an inverse energy cascade in wave number space. Magnetic field power spectra extended up to 470 Hz show an increasing steepness of the spectra with increasing frequency. Spectra from 2×10^{-3}Hz up to the proton gyrofrequency are well represented by a power law $P \sim f^{-1.7}$ independent of heliocentric distance and the spectra above the proton gyrofrequency are well represented by a power law $P \sim f^{-3}$ independent of distance as well.

References

Barnes, A., Hydromagnetic waves and turbulence in the solar wind, Solar and Solar Wind Plasma Physics, Vol. 1, ed. by E.N. Parker, C.F. Kennel, and L.J. Lanzerotti, North-Holland Publ. Comp., 1979.

Behannon, K.W., F.M. Neubauer, and H. Barnstorf, Fine-scale characteristics of interplanetary sector boundaries, J. Geophys. Res., 86, 3273, 1981.

Beinroth, H.J., and F.M. Neubauer, Properties of whistler-mode waves between 0.3AU and 1.0AU from Helios observations, J. Geophys. Res., 86, 7755, 1981.

Belcher, J.W., and L. Davis, Jr., Large-amplitude Alfvén waves in the interplanetary medium, 2, J. Geophys. Res., 76, 3534, 1971.

Belcher, J.W., and R. Burchsted, Energy densities of the Alfvén waves in the interplanetary medium, J. Geophys. Res., 79, 4765, 1974.

Burlaga, L.F., and J.B. Turner, Microscale "Alfvén waves" in the solar wind at 1AU, J. Geophys. Res., 81, 73, 1976.

Burlaga, L.F., R.P. Lepping, K.W. Behannon, L.W. Klein, and F.M. Neubauer, Large-scale variations of the interplanetary magnetic field: Voyager 1 and 2 observations between 1-5AU, J. Geophys. Res., 87, 4345, 1982.

Coleman, P.J., Jr., Turbulence, viscosity, and dissipation in the solar wind plasma, Astrophys. J., 153, 371, 1968.

Coleman, P.J., Jr., E.J. Smith, L. Davis, Jr., and D.E. Jones, The radial dependence of the interplanetary magnetic field: 1.0 - 1.5AU, J. Geophys. Res., 74, 2826, 1969.

Denskat, K.U., and L.F. Burlaga, Multispacecraft observations of microscale fluctuations in the solar wind, J. Geophys. Res., 82, 2693, 1977.

Denskat, K.U., and F.M. Neubauer, Statistical properties of low-frequency magnetic field fluctuations in the solar wind from 0.29 to 1.0AU during solar minimum conditions: HELIOS 1 and HELIOS 2, J. Geophys. Res., 87, 2215, 1982.

Marsch, E., K.H. Mühlhäuser, R. Schwenn, H. Rosenbauer, W. Pilipp, and F.M. Neubauer, Solar wind protons: Three-dimensional velocity distributions and derived plasma parameters measured between 0.3 and 1AU, J. Geophys. Res., 87, 52, 1982.

Montgomery, D.C., and D.A. Tidman, Plasma kinetic theory, McGraw-Hill, New York, 1964.

Musmann, G., F.M. Neubauer, and E. Lammers, Radial variation of the interplanetary magnetic field between 0.3AU and 1.0AU, observations by the Helios 1 spacecraft, J. Geophys., 42, 591, 1977.

Parker, G.D., Spectral properties of hydromagnetic fluctuations near 4 and 5AU, Planet. Space Sci., 30, 57, 1982.

Whang, Y.C., Alfvén waves in spiral interplanetary field, J. Geophys. Res., 78, 7221, 1973.

Page intentionally left blank

ALFVEN SOLITONS IN THE SOLAR WIND

Chris Ovenden and Steven J. Schwartz[*]

Department of Applied Mathematics
Queen Mary College
Mile End Road
London E1 4NS
UK

ABSTRACT

We present here a nonlinear Alfven soliton solution of the MHD equations. This solution may represent the final state of modulationally unstable Alfven waves. We also briefly describe a model of the expected turbulent spectrum due to a collection of such solitons.

1. Introduction

The Alfvenic nature of the large amplitude turbulence in the solar wind has been known for some time (Belcher and Davis 1971). The relationship between this turbulence and traditional linear MHD waves or special large amplitude solutions (Barnes and Hollweg 1974; Abraham-Shrauner and Feldman 1977) remains unclear. Equally unclear are the consequences this turbulence may have for solar wind particle populations, although ion drift speeds proportional to the Alfven speed and high perpendicular temperatures suggest some wave-particle connections (Schwartz et al. 1981).

Efforts to describe solar wind turbulence usually begin with a perturbation expansion, leading either to the "decay cascade" (Chin and Wentzel 1972; Cohen and Dewar 1974; Schwartz 1977) if the system is described purely in terms of its linear modes, or to the modulational instability (Derby 1978; Goldstein 1978) of a single large amplitude Alfven wave. We discuss here a third alternative which leads to a nonlinear soliton solution. This solution may represent the state to which a modulationally unstable Alfven wave relaxes. Using an ensemble average of collections of these solitons, we find a turbulence power spectrum $\epsilon(k) \propto k^{-2}$ at high frequencies which flattens toward the low frequency end. Details of the calculations can be found in Ovenden et al. (1983). Further work on alternative turbulence models and particle-soliton interactions is currently in progress.

2. The Soliton Solution

We begin with the one fluid description of a plasma: continuity and momentum equations and the generalized Ohm's law coupled with Maxwell's equations (eg. Boyd and Sanderson 1969 3.40, 3.54 and 3.61-3.63). Assuming quasi-neutrality, an isothermal equation of state, and neglecting the displacement current, resistivity and the $\partial j/\partial t$

term in the generalized Ohm's law, it is easy to eliminate the electric field and transverse fluid velocity. For simplicity we consider only parallel-propagation so that $\partial/\partial x = 0 = \partial/\partial y$ where the z direction corresponds to that of the background magnetic field B_0. Ultimately, the resulting equations can be written

$$\frac{\partial^2 B_\pm}{\partial t^2} - \frac{\partial}{\partial z}\left[\frac{v_A^2}{n}\frac{\partial}{\partial z}B_\pm \right] + \frac{\partial}{\partial z}\left[v\frac{\partial B_\pm}{\partial t} + \frac{d}{dt}(vB_\pm) \right]$$

$$\pm \frac{i}{\Omega_i}v_A^2\frac{\partial}{\partial z}\left[\frac{d}{dt}\left[\frac{1}{n}\frac{\partial B_\pm}{\partial z} \right] \right] = 0 \qquad (1.1)$$

and

$$\left[\frac{\partial^2}{\partial t^2} - c_s^2\frac{\partial^2}{\partial z^2} \right]n = \frac{v_A^2}{2}\frac{\partial^2}{\partial z^2}(|B_\pm|^2) + \frac{\partial^2}{\partial z^2}(nv^2) \qquad (1.2)$$

where $B_\pm = B_x \pm iB_y$, v is the z-component of the fluid velocity, n is the density, $v_A = B_0/\sqrt{(4\pi\rho)}$ is the Alfven speed, Ω_i the proton gyrofrequency, c_s the isothermal sound speed, and $d/dt = \partial/\partial t + v\partial/\partial z$. Both $B_\pm$ and n have been normalized to their background values (B_0 and n_0 respectively). The harmonic solutions to (1.1) and (1.2) with $|B_\pm|$ independent of z are just the Alfven-Ion cyclotron modes investigated by Abraham-Shrauner and Feldman (1977).

We are interested in modes with small but nonzero fluctuations δn and v in the density and velocity respectively. To this end, we linearize (1.1) and (1.2) with respect to these quantities. Furthermore, we insert an Alfven wave with slowly varying amplitude, viz.,

$$B_\pm = b(z,t) e^{i(k_A z - \omega_{0\pm} t)} \qquad (1.3)$$

where $\omega_{0\pm} = \omega_A (1 \mp \omega_A/2\Omega_i)$ and assuming $\omega_A \ll \Omega_i$ with $\omega_A = k_A v_A$. At this point, the modulational instability calculation proceeds by perturbing the b = constant solution with fluctuations δb, δn, v all varying harmonically in space and time. Such a calculation yields instabilities with e-folding lengths $\approx 10^{-2}$ AU.

Here, following Zakharov (1972) we search instead for soliton solutions of (1.1)-(1.2) with a wave amplitude in (1.3) given by

$$b(z,t) = b_0 \text{ sech }[\kappa(z-Vt)] e^{i\delta\omega t} \qquad , \qquad (1.4)$$

keeping terms to third order in $|b|$ and assuming b varies slowly

compared to the original Alfven wave. This process yields self-consistent constants V, κ, and $\delta\omega$ given by

$$V \approx v_A \left[1 - \frac{\omega_A}{\Omega_i} \right] \tag{1.5a}$$

$$\kappa = \frac{k_A b_0}{2} \left[\frac{\Omega_i / \omega_A}{1-\beta} \right]^{1/2} \tag{1.5b}$$

and

$$\delta\omega = - \frac{\omega_A |b_0|^2}{8(1 - \beta)} \tag{1.5c}$$

for values of the ratio of sound to Alfven speed squared (β) $<< 1$ and for the ω_{0+} (left hand polarized) wave. The density (in non-dimensional units) and velocity variations are given by

$$\delta n = \frac{|b(z,t)|^2}{2(1-\beta)} \tag{1.6}$$

and

$$v = V \, \delta n \tag{1.7}$$

Physically, the increased density (1.6) leads to a lower local Alfven speed causing the associated build up in wave energy in this region. The energy transport is achieved by forcing this material to move at the wave group velocity (1.5a), thereby resulting in the unchanged soliton envelope. It is not yet clear whether the solution (1.4)-(1.9) represents a true soliton, in the sense that two such solutions would pass through one another without interacting.

2. Turbulence Spectrum

To build a picture of a turbulent spectrum out of solitons, we follow the work of Kingsep et al. (1973) and Yu and Spatschek (1976) who consider an ensemble of systems with a common energy density W (normalized to $B_0^2 / 8\pi$) and length L. The various realizations correspond to different numbers, N, of non-overlapping, assumed identical, solitons into which this energy is divided. The value of N lies in the interval

$$1 \leqslant N \leqslant \kappa L$$

Ensemble averaging over these realizations, which we take with equal probablities, yields an energy spectrum

$$\langle |b_k|^2 \rangle \propto \frac{1}{(\sigma k)^2} \left[\sigma k \tanh (\sigma k) - \log \cosh (\sigma k) \right] \tag{2.1}$$

where

$$\sigma = \frac{\pi}{k_A} \left[\frac{\omega_A (1-\beta)}{\Omega_i 8\pi W} \right]^{1/2}$$

As can be seen in the plot of (2.1) shown in Fig. 1 (or directly from the explicit form of (2.1)), this spectrum is flat at low frequencies and falls off steeply as k^{-2} at high frequencies. Although this is qualitatively similar to solar wind observations (eg. Bavassano et al. 1982; Denskat and Neubauer 1982), it is not yet clear whether quantitative agreement can be improved within the soliton description by, eg., an alternative ensemble average, collections of unequal solitons, etc.
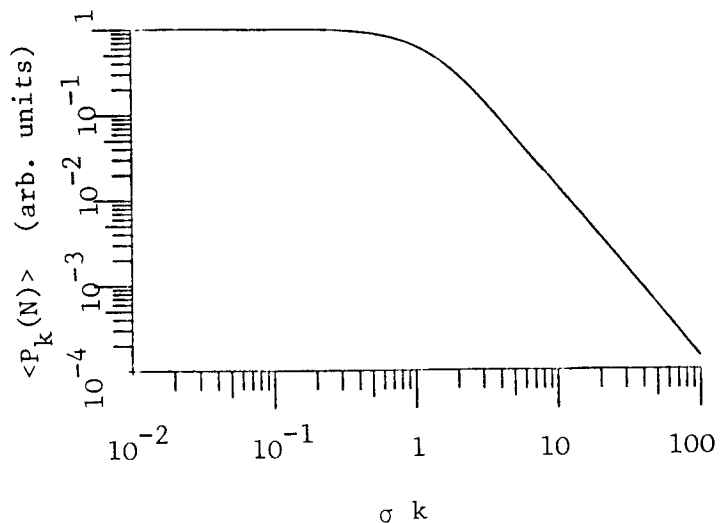
Fig. 1. Ensemble averaged power spectrum of various collections of solitons describing the same total turbulent energy.

3. Summary

We have found a nonlinear Alfven soliton solution which we envisage as the final state of a modulationally unstable Alfven wave. Dividing turbulent energy in a given region into such solitons and averaging over the different possible arrangements yields a turbulent spectrum which is flat at low k and falls as k^{-2} at large k. Remaining questions concern other possible descriptions of solar wind turbulence within this context and the consequences of particle–soliton interactions for solar wind ion distributions.

References

Abraham–Shrauner, B. and W.C. Feldman: Nonlinear Alfven waves in high–speed solar wind streams, J. Geophys. Res. 82, 618, 1977.

Barnes, A. and J.V. Hollweg: Large–amplitude hydromagnetic waves, J. Geophys. Res. 79, 2302, 1974.

Bavassano, B., M. Dobrowolny, F. Mariani and N.F. Ness: Radial evolution of power spectra of interplanetary Alfven turbulence, J. Geophys. Res. 87, 3617, 1982.

Belcher, J.W. and L. Davis Jr.: Large-amplitude Alfven waves in the interplanetary medium, 2, J. Geophys. Res. 76, 3534, 1971.

Boyd, T.J. and J.J. Sanderson: Plasma dynamics, Thomas Nelson & Sons Ltd., London, 1969.

Chin, Y. and D.G. Wentzel: Nonlinear dissipation of Alfven waves, Astrophys. Sp. Sci. 16, 465, 1972.

Cohen, R.H. and R.L. Dewar: On the backscatter instability of solar wind Alfven waves, J. Geophys. Res. 79, 4174, 1974.

Denskat, K. and F.M. Neubauer: Statistical properties of low frequency magnetic field fluctuations in the solar wind from 0.29 to 1.0 AU during solar minimum conditions: HELIOS I and II, J. Geophys. Res. 87, 2215, 1982.

Derby, N.F. Jr.: Modulational instability of finite-amplitude, circularly polarized Alfven waves, Astrophys. J. 224, 1013, 1978.

Goldstein, M.L.: An instability of finite amplitude circularly polarized Alfven waves, Astrophys. J. 219, 700, 1978.

Kingsep, A.S., C.I. Rudakov and R.N. Sudan: Spectra of strong Langmuir turbulence, Phys. Rev. Lett. 31, 1482, 1973.

Ovenden, C.R., H. Shah and S.J. Schwartz: Alfven solitons in the solar wind, J. Geophys. Res., in press, 1983.

Schwartz, S.J.: Cosmic ray generated anisotropic magnetohydrodynamic turbulence, Mon. Not. R. Astr. Soc. 178, 399, 1977.

Schwartz, S.J., W.C. Feldman and S.P. Gary: The source of proton anisotropy in the high speed solar wind, J. Geophys. Res. 86, 541, 1981.

Yu, M.Y. and K.M. Spatschek: Anomalous damping of ion-acoustic waves in the presence of strong Langmuir turbulence, Phys. Pl. 19, 705, 1976,

Zakharov, V.E.: Collapse of Langmuir waves, Sov. Phys. J.E.T.P. 35, 908, 1972.

Page intentionally left blank

INTERPLANETARY ALFVENIC FLUCTUATIONS: A STATISTICAL STUDY OF THE DIRECTIONAL VARIATIONS OF THE MAGNETIC FIELD

B.Bavassano[1] and F.Mariani[1,2]

1) Istituto di Fisica dello Spazio Interplanetario, CNR, Frascati, Italy
2) Istituto di Fisica "G. Marconi", Università di Roma, Roma, Italy

ABSTRACT

Magnetic field data from HELIOS 1 and 2 are used to test a stochastic model for Alfvénic fluctuations recently proposed by A. Barnes. A reasonable matching between observations and predictions is found. A rough estimate of the correlation length of the observed fluctuations is inferred.

Introduction

In a recent paper Barnes (1981) proposes a simple stochastic model for interplanetary Alfvénic turbulence based on the random wandering of a vector of constant length. Let us locate this vector with the usual spherical coordinates θ, ϕ and assume it initially along the polar axis ($\theta=0$). As time advances the tip of the vector walks over a sphere, moving at each step of an angle ϵ along a great circle in a random direction. In other words if the position of the vector after N steps is (θ, ϕ), at the (N+1)th step the vector will lie at an angle ϵ away along a great circle, whose tangent at (θ, ϕ) makes a random angle ψ with the unit vector in the θ direction. A field direction confinement can be simulated with reflecting boundaries. This model, with certain qualifications, reproduces the well known observational feature of the Alfvénic fluctuations of a well defined direction of minimum variance aligned with the mean magnetic field. The model predicts also the statistical distributions of the field directions in terms of a density of probability $W(\mu,t)$ and an integrated probability $P(\mu,t)$, being $\mu=\cos\theta$. $W(\mu,t)d\mu$ gives the probability that after a time t the angle θ that the vector makes with its initial position has its cosine between μ and $\mu+d\mu$. $P(\mu,t)$, integral of W between -1 and μ, gives the probability that, at the time t, $\cos\theta$ lies between -1 and μ. Figures 4 and 5 of Barnes (1981) show the evolution with time of these functions.

An observational test of the temporal evolution of the fluctuating field direction as predicted by the model has been performed by using interplanetary magnetic field data (6 s averages) of HELIOS 1 and 2 (Rome/GSFC experiment). We have selected four periods of 2-4 days in the trailing edge of high velocity streams characterized by the presence of fluctuations whose Alfvénic character had been already established by previous analyses (Bavassano et al., 1982a and b). Table 1 of the latter reference gives a list of the periods considered. Three of them refer to HELIOS 2 observations of the same stream during three successive solar rotations. The fourth period refers to an observation of the same stream by HELIOS 1 almost contemporary to the second of the HELIOS 2 stream encounters. To obtain a statistical description of the temporal evolu-

tion of the direction of the measured fluctuating field we have divided the selected periods in intervals of 20 minutes, for each interval we have determined how the magnetic field vector evolves (starting from its initial position at the beginning of the interval) as time advances, and finally for each of the four stream encounters we have grouped the results from the various intervals to have statistical distributions for the parameters characterizing, following the Barnes model, the field evolution with time. The parameters considered are ϵ, the angle between consecutive vectors (6 s averages), ψ, the direction of the field variation as defined in the model, and θ, the angle that the magnetic vector has with its initial position at the beginning of the interval. We would note that our results do not change significantly if intervals longer than 20 minutes are taken for the statistics. Finally, all intervals including discontinuities as identified through automatic selection criteria (Mariani et al., 1983) and visual inspection of the data have been rejected.

Experimental Results

In Figure 1 we show the histograms of the angles ϵ and ψ at the four heliocentric distances considered. The 20 minutes intervals contributing to the statistics are (in order of decreasing R) 111, 110, 104 and 235 respectively. The histograms of ϵ show that most of the values fall between 0° and 15°. A dependence on heliocentric distance is clearly apparent, the average value of ϵ being 6.1° at 0.87 AU and becoming 11.0° at 0.29 AU. These histograms should be compared with the fixed step length assumption in the model. The histograms of ψ do not show on the contrary any dependence on the heliocentric distance. In Figure 1 we give only the curve for 0.87 AU, representative within 1% for all distances. To a good approximation ψ has a uniform distribution, in agreement with the assumption of the model that the direction of each step is random.
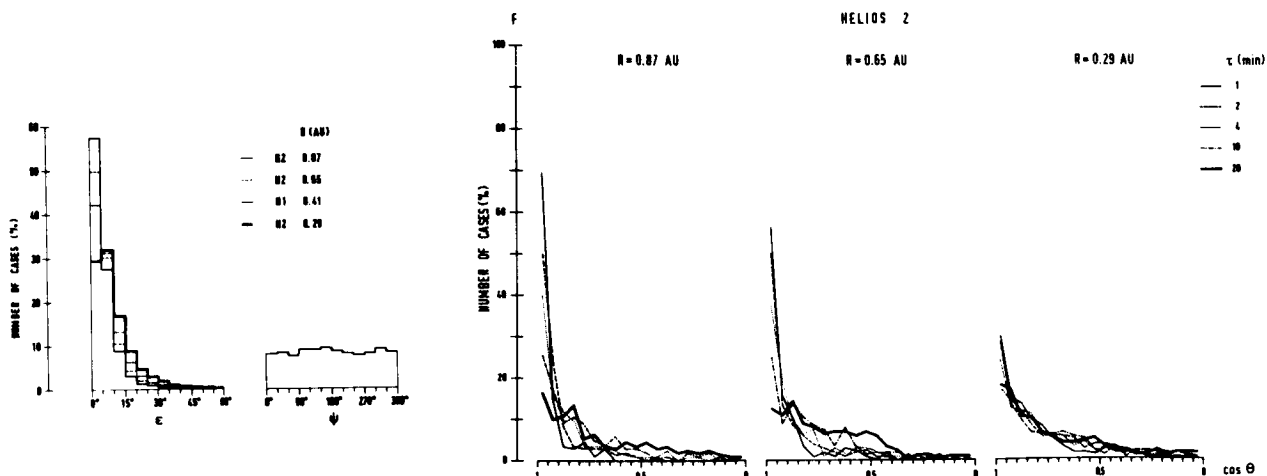
Figure 1. Frequency distributions of ϵ and ψ.

Figure 2. Frequency distributions of cosθ.

Let us consider now the evolution with time of the magnetic field

direction in terms of the angle θ between the current vector and its initial position at the beginning of the 20 minutes interval. In Figure 2 we show the frequency distributions of cosθ for different delay times τ (time elapsed from the beginning of each interval). These histograms correspond to the curves of the function W of the model of Barnes (see his Figures 4 and 5), taking care that W is a probability density. The features of the temporal evolution of cosθ are perhaps more clearly seen in Figure 3 in terms of the integrated frequency distributions, giving the number of cases for which cosθ is between - 1 and a given value. These curves should be compared with those of the function P given by Barnes in his Figures 4 and 5. One is easily convinced that the experimental curves look like those of the model. When the delay time τ is small (e.g., τ=1 min) most of the values of cosθ are close to 1. For increasing τ the distributions spread out in a quite regular way. The final state is not very different at the various distances but it is reached more rapidly near the Sun. This is clearly seen in Figure 3 where at 0.29 AU the curve for τ=10 min is almost coincident with that for τ=20 min (i.e., final state is already reached after about 10 minutes), whereas at 0.87 AU they differ noticeably (i.e., after 10 minutes some evolution is still necessary before reaching final situation). This different time scale can be related to the radial gradient of the angle ε (see Figure 1), the evolution being more rapid near the Sun where the angle between consecutive vectors is larger. Another experimental evidence is that our curves do not reach a uniform distribution, as those of the model, and this holds also if τ increases up to 1 hour.
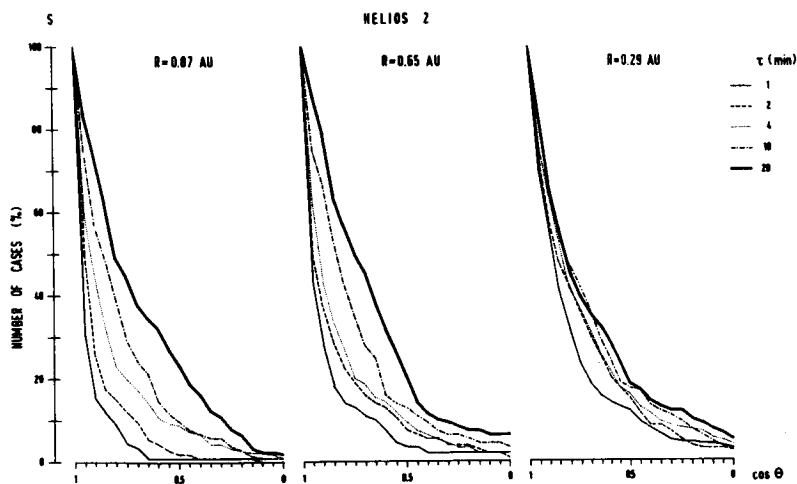
Figure 3. Integrated frequency distributions of cosθ.

The evolution of the frequency distributions of cosθ has been also seen in terms of variation of their moments. Figures 4 and 5 show the variation with the delay time τ of the average value of cosθ, <cosθ>, and of its standard deviation, σ(cosθ), respectively. The changes in the histograms of cosθ shown in Figure 2 are here seen as a regular decrease of <cosθ> and a corresponding increase of σ(cosθ). Again it is clearly apparent that the variation is more rapid near the Sun (heavy line). These trends almost completely

disappear after 10-15 minutes, with <cosθ> remaining around 0.7 and σ(cosθ) around 0.3 for delay times up to 1 hour. In other words most of the variation of <cosθ> and σ(cosθ) takes place in the first minutes (∿ 10 near the Sun and ∿15 near the Earth), after that only a very slight dependence from τ is found. We would notice that the observations made at 0.65 AU by HELIOS 2 and at 0.41 AU by HELIOS 1 are almost contemporary and at the same heliographic latitude. This allows us to exclude that the observed trends are due to slow temporal variations or heliographic latitude dependence.

Figure 4. <cosθ> vs. τ.

Figure 5. σ(cosθ) vs. τ.
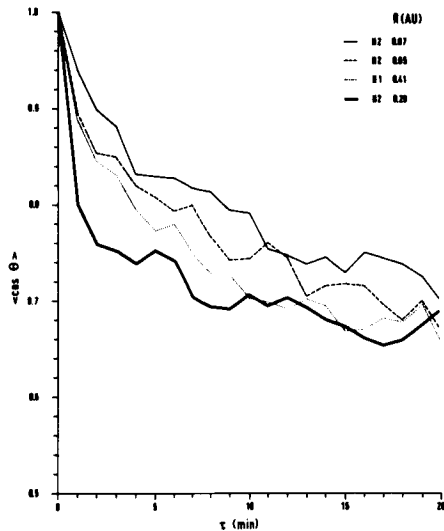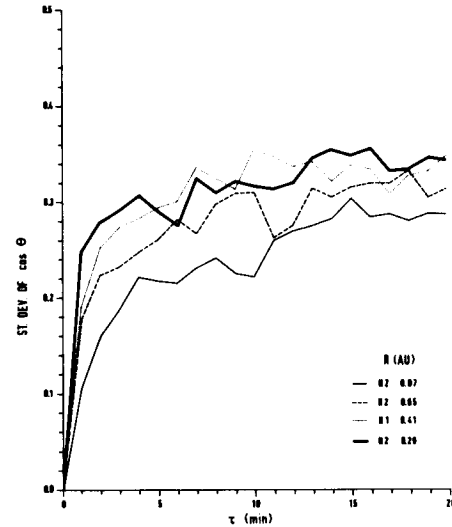
Concluding Remarks

As regards the observational test of the Barnes model we can summarize the results as follows: a) the direction of the variation of the magnetic field, as given by the angle ψ, has a uniform distribution, in agreement with the assumption of the model that the direction of each step is random; b) the angle ε between consecutive vectors (6 s averages) is of the order of 5°-10° and increases near the Sun (in the model this angle is taken as a constant); c) the frequency distribution of cosθ spreads out when τ increases but does not reach a uniform distribution (as in the model). In conclusion the model of Barnes, although essentially local, can be considered in reasonable agreement with the experimental results. On the other hand, as already indicated by the author himself, the model can be considerably improved, for example by using a variable step length and by simulating the confinement of the field around the spiral direction. In this way a better matching with the observations could be obtained.

The time scale of the variation of cosθ can give some information about the correlation time of the fluctuations. Barnes (1981) shows that, in terms of population statistics, the autocorrelation function of the temporal series of random fluctuating vectors is just given by the average value of cosθ. His computations show also that, with a reflecting boundary, the average value

102

of cosθ initially decreases as time advances but <u>beyond the correlation time</u> tends towards a constant value. Figure 4 shows that the decrease of <cosθ> lasts 10-15 minutes, the evolution being faster near the Sun, after that this trend almost completely disappears. We can then infer that the correlation time of the observed fluctuations is of the order of 10 minutes near the Sun and 15 minutes near the Earth. With the knowledge of the average solar wind speed in the different periods this gives a correlation length of $\sim$65 R_E near the Sun and $\sim$90 R_E near the Earth. Our estimate for the correlation length at 0.87 AU agrees with previous determinations near the Earth's orbit (Chang and Nishida, 1973; Fisk and Sari, 1973; Sari and Valley, 1976; Crooker et al., 1982). The decrease of the correlation length approaching the Sun should be essentially related to the greater angular variability of the magnetic field near the Sun.

REFERENCES

Barnes, A., Interplanetary Alfvénic fluctuations: a stochastic model, <u>J. Geophys. Res.</u>, <u>86</u>, 7498, 1981.

Bavassano, B., M. Dobrowolny, G. Fanfoni, F. Mariani, and N. F. Ness, Statistical properties of MHD fluctuations associated with high speed streams from HELIOS 2 observations, <u>Solar Phys.</u>, <u>78</u>, 373, 1982a.

Bavassano, B., M. Dobrowolny, F. Mariani, and N. F. Ness, Radial evolution of power spectra of interplanetary Alfvénic turbulence, <u>J. Geophys. Res.</u>, <u>87</u>, 3617, 1982b.

Chang, S. C., and A. Nishida, Spatial structure of transverse oscillations in the interplanetary magnetic field, <u>Astrophys. Space Sci.</u>, <u>23</u>, 301, 1973.

Crooker, N. U., G. L. Siscoe, C. T. Russell, and E. J. Smith, Factors controlling degree of correlation between ISEE 1 and ISEE 3 interplanetary magnetic field measurements, <u>J. Geophys. Res.</u>, <u>87</u>, 2224, 1982.

Fisk, L. A., and J. W. Sari, Correlation length for interplanetary magnetic field fluctuations, <u>J. Geophys. Res.</u>, <u>78</u>, 6729, 1973.

Mariani, F., B. Bavassano, and U. Villante, A statistical study of MHD discontinuities in the inner solar system: HELIOS 1 and 2, <u>Solar Phys.</u>, in press, 1983.

Sari, J. W., and G. C. Valley, Interplanetary magnetic field power spectra: mean field radial or perpendicular to radial, <u>J. Geophys. Res.</u>, <u>81</u>, 5489, 1976.

Page intentionally left blank

SURFACE WAVES ON SOLAR WIND TD's

Joseph V. Hollweg (Physics Department and Space Science Center, University of New Hampshire, Durham, NH 03824

The most successful interpretation of the solar wind microscale fluctuations has been in terms of Alfven waves. However, this inter-pretation does not fit all data perfectly, and some authors have questioned the presence of Alfven waves. We would like to point out that the difficulties may be resolved if the data are interpreted in terms of Alfvenic surface waves.

Page intentionally left blank

THEORY OF HYDROMAGNETIC TURBULENCE

David Montgomery

The College of William and Mary

Williamsburg, Virginia 23185   U. S. A.

Abstract

The present state of MHD turbulence theory as a possible solar wind research tool is surveyed. The theory is statistical, and does not make statements about individual events. It is unreasonable to expect ever to be able to "explain" individual events with turbulence theory. The ensembles considered typically have individual realizations which differ qualitatively, unlike equilibrium statistical mechanics. Most of the theory deals with highly symmetric situations; most of these symmetries have yet to be tested in the solar wind. The applicability of MHD itself to solar wind parameters is highly questionable; yet it has no competitors, as a potentially comprehensive dynamical description. The purposes of solar wind research require sharper articulation. If they are to understand radial turbulent plasma flows from spheres, laboratory experiments and numerical solution of equations of motion may be a cheap alternative to spacecraft. If "real life" information is demanded, multiple spacecraft with variable separation may be necessary to go further. The principal emphasis in the theory so far has been on spectral behavior for spatial covariances in wave number space. There is no respectable theory of these for highly anisotropic situations. A rather slow development of theory acts as a brake on justifiable measurement, at this point.

I. INTRODUCTION

One question solar wind research may ultimately have to answer for itself is whether it will resemble geography or dynamic meteorology more closely. Geography must concern itself with events which are specific and in a very real sense accidental. Its use of analytical mathematics is limited and may sometimes be simply decorative. Dynamic meteorology proceeds from the assumption that a largely complete mathematical description can be found and should be pursued, even if the complexity of the differential equations and the incompleteness of the boundary data guarantee that the program will be a long time coming to completion (see, e.g., Pedlosky, 1979).

Much of what happens in any individual rainstorm is extraordinarily striking, but it cannot usefully be considered in the light of a detailed mathematical theory. It will never happen in quite the same way again. Austere discipline is required to focus on those aspects of the weather which are at least statistically reproducible, and therefore susceptible to a mathematical theory.

Space physics has frequently taken the "event" as its unit of concern. Such-and-such a set of fluctuating field signals were seen on such-and-such a detector on such-and-such a day. Plausible hypotheses about what might have been responsible for the signals are produced, and are buttressed by such mathematics as lies ready to hand. The kind of boundary and initial data that would be necessary to extract sharp conclusions from the mathematics are invariably lacking, and the machinery for extracting the conclusions often also does not exist. A rather subjective opinion is usually necessary at the end as to whether or not the "event" has been satisfactorily "explained". This paradigm is by now deeply ingrained, and is an unconscious ingredient in the evaluation of many of the papers, say, which one finds in Journal of Geophysical Research.

The subject is at a natural stage to begin to ask what the possibilities are for making it into a mathematically tighter and more intellectually crisp area of endeavor. It is equally natural to inquire into the range of available models which have been pursued in comparable and more highly developed continuous-media situations such as meteorology, say, or ocenography.

The purpose of the following material is a consideration of the adequacy of the available solar-wind mathematical description to the task of

providing a comprehensive dynamical description. If precedents from nearby subjects are any guide, there would seem to be only one serious contender as a model for what such a mathematical description might look like. That is classical Navier-Stokes hydrodynamics, which is the basis for such theories as there are for the dynamics of the earth's atmospheres and oceans. Some exposure to hydrodynamic theory will be assumed--sufficient, at least, to take for granted the unquestioned role hydrodynamics plays as theoretical research tool in those subjects. The following pages are a survey of the present status of magnetohydrodynamic (hereafter: MHD) turbulence theory and its adequacy as an off-the-shelf research tool for describing solar wind measurements. The conclusions are not all rosy, and the analysis of the available mathematical descriptions and techniques leads to the belief that they should only be applied to solar wind data with extreme caution, and perhaps with a sense of humor.

In order of ascending complexity, the possible dynamical descriptions for the solar-wind plasma are: (1) one-fluid magnetohydrodynamics (MHD); (2) multi-species, charged-fluid hydrodynamics with assumed closures for the pressure tensors (equations of state); (3) the Vlasov description in terms of particle distribution functions; (4) Vlasov equations modified by adding Fokker-Planck collision terms on the right hand sides. Specialized models, such as the Chew-Goldberger-Low approximation, which rather arbitrarily drops heat flow along magnetic field lines, can be accommodated in various niches in the above list.

If the expected dynamics of the system were linear and non-turbulent, at least the first three models could be taken seriously as contenders. The controlled fusion (CTR) community has done so, gambling on the hope that laboratory experimentalists will be able to produce confined plasmas whose dynamics remain linear and at most weakly turbulent. But by anyone's definitions, the solar wind's behavior is unmistakably turbulent and nonlinear. The fluctuating magnetic fields, flow velocities, and electric fields are as large as anything that can be defined as averages in the local zero-momentum frame. The time history of any component of the fields behaves for all practical purposes like a random variable. This is the definition of "strong turbulence", if one is needed.

Because it is the only one of the four descriptions that is close to being manageable, even numerically, MHD assumes the role of the only serious

contender for a "strong turbulence" mathematical description. It is far simpler, mathematically, than any of the others, and yet the number of strong turbulence problems that we can handle with it will be seen to be extremely limited, even assuming its correctness.

The following material is intended as a brief look at nonlinear MHD turbulence theory, as it may be considered as a potential solar-wind research tool. Section II deals with the applicability of MHD itself to a plasma with solar-wind densities and temperatures, stressing the roles of incompressibility, collisionality, and the proper analytical form for the essential dissipative terms. Section III summarizes the status of incompressible MHD turbulence theory as it has been developed so far, emphasizing the high degrees of symmetry required if even the crudest theories are to have extractible consequences. Section IV suggests some tentative implications of Sections II and III for solar-wind research.

Anticipating the conclusions, one of them is that there is presently available at best only an outline of a theoretical framework in which kinds of solar wind data that have been collected could be sensibly interpreted. If we are serious about wanting to go beyond a largely descriptive understanding of the solar wind, a far higher fraction of our effort will have to go into understanding the basic plasma physics of the medium. The analytical and numerical tools now in hand are not adequate to the demands being placed on them by the sophisticated collection of vast quantities of data, whose quality is far higher than any framework available for making use of it.

II. THE APPLICABILITY OF MHD

The one-fluid MHD equations, in the simplest form in which they might be considered realistic, is

$$\nabla \cdot \underset{\sim}{v} = 0 \tag{1}$$

$$\rho(\frac{\partial \underset{\sim}{v}}{\partial t} + \underset{\sim}{v} \cdot \nabla \underset{\sim}{v}) = -\nabla p + \frac{\underset{\sim}{B} \cdot \nabla \underset{\sim}{B}}{4\pi} + \rho \nu \nabla^2 \underset{\sim}{v} \tag{2}$$

$$\frac{\partial \underset{\sim}{B}}{\partial t} + \underset{\sim}{v} \cdot \nabla \underset{\sim}{B} = \underset{\sim}{B} \cdot \nabla \underset{\sim}{v} + \eta \nabla^2 B, \tag{3}$$

with a fluid velocity $\underset{\sim}{v}$, and a magnetic field $\underset{\sim}{B}$, a mass density ρ, a kinematic viscosity ν, and a magnetic diffusivity η. The solenoidal condition $\nabla \cdot \underset{\sim}{B} = 0$, imposed initially, is preserved by Eq. (3). p is the total pressure, magnetic plus mechanical, and is obtained from the Poisson equation which results when the divergence of Eq. (2) is taken and use is made of Eq. (1).

Eqs. (1)-(3) are the simplest closed-form mathematical description known for the mechanical motions of a fluid which is both energetic enough and electrically-conducting enough to modify the magnetic field imbedded in it. Yet the simplicity of Eqs. (1)-(3) is misleading. We are far from being able to give analytical solutions except in highly simplified special cases, or in the linear limit. For reasons which are by now well known (although we will review them later), they make demands on computing capability which we cannot always expect to meet, even numerically.

Some of the assumptions which go into the derivation of Eq. (1)-(3) are widely known, such as the neglect of the displacement current relative to the conduction current, or the assumption that electrostatic forces are capable of keeping the electron and ion charge densities approximately equal. Three assumptions need to be singled out for mention in connection with the solar wind. They are not obviously fulfilled by solar wind parameters, and the serious failure of any one of them can leave us with a mathematical description which is even far less tractable than Eqs. (1)-(3). They are: (1) incompressibility ($\nabla \cdot \underset{\sim}{v} = 0$); (2) scalar dissipation coefficients ν and η; and (3) collision-dominated inequalities required in the derivation of Eqs. (1)-(3).

(1) Incompressibility ($\nabla \cdot \underline{v} = 0$)

Incompressibility is an undisputed feature of normal fluid mechanics that is difficult to justify rigorously. It is usually done (Landau and Lifshitz, 1959; Batchelor, 1967) by using estimates for the dominant force terms in the equation of motion and their effect, through the compressibility, on the density ρ of a moving fluid element. The change in density $\Delta\rho$ for a fluid element which experiences a change in pressure Δp may be taken to be:

$$\Delta\rho = \frac{\Delta p}{dP/d\rho} = \frac{\Delta p}{c_s^2} \tag{4}$$

If the medium obeys an equation of state $p = p(\rho)$. The sound speed is $c_s^2 \equiv dP/d\rho$. Δp may be estimated by using either the $\rho\underline{v}\cdot\nabla\underline{v}$ term in Eq. (2) or the $\underline{B}\cdot\nabla\underline{B}/4\pi$ term. (These are expected to dominate the $\rho\partial\underline{v}/\partial t$ term and the viscous term $\rho\nu\nabla^2\underline{v}$ in cases which have significant amounts of turbulence.) For ∇, we will use L^{-1}, where L is a characteristic length over which the fields vary. Δp may be estimated from the convective term, first, as of order $\sim\rho v^2$. In this case, the fractional variation in density is small for a typical fluid element if

$$\frac{\Delta\rho}{\rho} \sim \frac{\rho v^2}{\rho c_s^2} = v^2/c_s^2 \ll 1 \tag{5}$$

as in ordinary hydrodynamics. Then we may estimate Δp from the magnetic force term as $\Delta p \sim B^2/4\pi$, and instead of (5), we get

$$\frac{\Delta\rho}{\rho} \sim \frac{B^2}{4\pi\rho c_s^2} \ll 1 \tag{6}$$

or that the magnetic pressure shall be small compared to the mechanical pressure ($\beta \gg 1$, in conventional plasma physics jargon). If there is a strong mean field B_0 present which is large compared to the fluctuating B, $\Delta p \sim B_0 B/4\pi$, and (6) is replaced by

$$\frac{\Delta\rho}{\rho} \sim \frac{B^2}{4\pi\rho c_s^2} \frac{B}{B_0} \ll 1 \tag{7}$$

or that (again in conventional plasma terms) $B/B_0 \ll \beta$.

Though the fulfilment of conditions (5) and (7) might give some confidence in (say) the applicability of incompressible MHD for a tokamak plasma, no one of the three inequalities (5)-(7) can be said to characterize the solar wind. Yet the solar wind, except for occasional shock transitions, often shows surprisingly little density variation. From the point of view of considerations presently known, this tendency toward incompressibility is still slightly mysterious.

(2) Dissipation Coefficients

Derivations from first principles lead to far more elaborate dissipative terms than those which appear in Eqs. (1)-(3). Only those who have actually dragged themselves through a Chapman-Enskog calculation of magnetized-plasma transport coefficients can probably appreciate the fragility of the enterprise, but a widely-accepted derivation due to Braginskii (1965) [see also: Book, 1980] yields a considerably more involved term for the viscous dissipation than that given in Eq. (2). Reverting to component notation, $\rho \nu \nabla^2 v_i$ should be replaced by the ion viscosity term $-\sum_{j=1}^{3} \partial P_{ji}/\partial x_j$, where, in a coordinate system with the z-axis along the magnetic field $\underset{\sim}{B}$,

$$P_{xx} = -\frac{\eta_0}{2}(W_{xx} + W_{yy}) - \frac{\eta_1}{2}(W_{xx} - W_{yy}) - \eta_3 W_{xy}$$

$$P_{yy} = -\frac{\eta_0}{2}(W_{xx} + W_{yy}) + \frac{\eta_1}{2}(W_{xx} - W_{yy}) + \eta_3 W_{xy}$$

$$P_{xy} = P_{yx} = -\eta_1 W_{xy} + \frac{\eta_3}{2}(W_{xx} - W_{yy})$$

$$P_{xz} = P_{zx} = -\eta_2 W_{xz} - \eta_4 W_{yz}$$

$$P_{yz} = P_{zy} = -\eta_2 W_{yz} + \eta_4 W_{xz}$$

$$P_{zz} = -\eta_0 W_{zz}. \tag{8}$$

The coefficients in Eq. (8) are

$$\eta_0 = 0.96 \; nk_B T_i \tau_i$$

$$\eta_1 = \frac{3}{10} \frac{nk_B T_i}{\omega_{ci}^2 \tau_i} = \frac{1}{4} \eta_2$$

$$\eta_3 = \frac{1}{2} \frac{nk_B T_i}{\omega_{ci}} = \frac{1}{2} \eta_4 \qquad (9)$$

$3k_B T_i/2$ is an ion thermal energy, and $\omega_{ci} = eB/m_i c$ is the proton gyrofrequency. τ_i is an ion collision time and is given by

$$\tau_i = \frac{3\sqrt{m_i} \; (k_B T_i)^{3/2}}{4\sqrt{\pi} \; n\lambda e^4} \qquad (10)$$

where m_i is the ion (proton) mass, n is the proton number density, e is the proton charge, and λ is the Coulomb logarithm, typically 10 to 20. The rate of strain tensor W_{jk} is

$$W_{jk} = \frac{\partial v_j}{\partial x_k} + \frac{\partial v_k}{\partial x_j} - \frac{2}{3} \delta_{jk} \; \nabla \cdot \underline{v} \qquad (11)$$

The viscosity coefficients η_0, η_1, η_2, η_3, η_4 differ mainly by the numbers of powers of $\omega_{ci}\tau_i$ they contain in the denominators. The largest term for solar-wind plasmas is η_0. A formal estimate of the η_0-containing terms at 1AU, using measured values for the length scales and typical fluctuating velocities, leads to the conclusion that the η_0 terms are by orders of magnitude the largest terms in the equation of motion! There is nothing else in the equations of motion that they could be equated to unless the coefficients multiplying the η_0 were themselves small. These coefficients turn out to be linear combinations of $\nabla \cdot \underline{v}$ and $\nabla_\perp \cdot \underline{v}_\perp$ (here, the subscript "⊥" applied to a vector means the components perpendicular to $\underline{B}$). Only if $\nabla \cdot \underline{v} \approx 0$ <u>and</u> $\nabla_\perp \cdot \underline{v}_\perp \approx 0$ does it appear that the viscous terms can do anything but completely overpower every other term in the equation. This may be a more convincing argument for incompressibility than any that can be given in the conventional way, as in the previous subsection. It does, however, leave an additional constraint, incompressibility in the plane perpendicular to $\underline{B}$, which is not built into

Eqs. (1)-(3). The constraint $\nabla_\perp \cdot \underline{v}_\perp = 0$ does come up in the Strauss (1976; Montgomery, 1982) equations of "reduced" MHD, which are appropriate to the case of strong externally-imposed dc magnetic field ($\beta \ll 1$), but its content without the presence of such an externally-imposed $\underline{B}$-field is far from clear.

Finally, and perhaps most annoyingly, even if the divergences of $\underline{v}$ and $\underline{v}_\perp$ are small, that does not mean that the terms containing η_0 are negligible. The jungle of terms involved in Eqs. (8) and (9) does not lead, by any known asymptotic expansion, to a simple diffusion-like viscous term such as the last term of Eq. (2), at the time of this writing. It is possible that we will remain in the unpleasant position of settling for the relatively tractible $\rho\nu\nabla^2\underline{v}$ term as a crude model of short-wavelength dissipation, knowing full well that it is not an accurate representation.

(3) Collisionality

Such expressions as Eqs. (8) and (9) are the output of lengthy, tedious Chapman-Enskog calculations which begin with a transport (e.g., Braginskii, 1965) equation with a Fokker-Planck collision term, and iterate about a local Maxwell distribution. The expansion parameter, assumed small, is the ratio of the mean collision time (τ_i for ions, τ_e for electrons) to the time scale T over which the macroscopic field variables vary, or equivalently, the ratio of mean free paths to macroscopic length scales. In the solar wind, these ratios, rather than being $\ll 1$, are $\gg 1$ if standard estimates are used for mean free paths and collision times. From one perspective, it is astonishing that MHD has any relevance to solar wind phenomena. It has been suggested, not unconvincingly, that the Fokker-Planck collision terms which are used to compute expressions such as Eqs. (8) and (9), are improper because of the observed high level of turbulence in the solar-wind magnetic field. Free-flight straight-line trajectories are used in evaluating collision integrals and are cut off at a Debye length, and these may be less than appropriate for a particle following a tangled field line. But these are no more than suggestions at this point, and what their implied modification of Eqs. (8) and (9) might be has not been suggested.

In summary, there are three respects at least in which the validity of incompressible MHD with scalar dissipation coefficients might legitimately

be doubted for solar-wind parameters. Yet is is the only contender among mathematical descriptions which have so far proved tractable enough to lead to any comprehensive theory of turbulent situations. Even then, we shall see in the following section that further severe restrictions are necessary in order to have concrete results emerge.

III. MAGNETOHYDRODYNAMIC TURBULENCE

If the previously-enumerated reservations about the validity of
the MHD description are passed over, it may be noticed that a certain amount
of relatively clean theory of MHD turbulence has emerged in the last two decades.
The theory relies on certain idealizations that render it less than wholly
applicable to real-life solar wind conditions. Applicable or not, it constitutes
the only presently-existing framework in which statements about the solar wind
can be made which are more than impressionistic or anecdotal. Virtually all
of it is for the uniform-density (ρ = const.) case, and the incompressibility
restriction is important. No significant body of strong turbulence theory
exists for compressible fluids, even for ordinary neutral gases, and it would
be unreasonable to expect MHD to yield where the simpler compressible system
has not.

Use of the term "strong turbulence" in the preceding paragraph is
intended to differentiate it from "weak turbulence" theory, which is a perspec-
tive which has shaped most thinking about nonlinear disordered processes in
plasmas since about 1962. In weak turbulence theory (e.g., Montgomery, 1977),
the emphasis is on systems whose dynamics may be considered to be the interac-
tion of oscillatory normal modes, whose oscillation period is short compared
to the characteristic time of transfer of excitations from one normal mode to
another. Our reasons for discounting the value of weak turbulence theory in
discussing the solar wind will become apparent when we write Eqs. (1)-(3) in
appropriate dimensionless units.

We first observe that there are at least three physically distinct
time scales represented in the dynamics described by Eqs. (1)-(3). If we call
a typical rms flow speed U_o (in a coordinate system moving with the local mean
velocity of the solar wind), a typical rms magnetic field strength B_o, a
typical suitably defined mean magnetic field $\langle \underset{\sim}{B} \rangle$, and a typical length scale
over which the fields vary $1/k$, then these three time scales may be defined
as follows. There are: (1) the "eddy turnover time" $(kU_o)^{-1}$ associated with
the fluid motions [in the solar wind, often $B_o \sim U_o$]; (2) the "Alfvén transit
time" $(k|\langle B \rangle|/\sqrt{4\pi\rho})^{-1}$; and (3) two dissipative time scales $(k^2\nu)^{-1}$ and $(k^2\eta)^{-1}$
which may be the same or different, depending upon the magnetic Prandtl number

ν/η. The situation becomes more complex when we realize that there is not one length scale $\sim 1/k$, but a whole spectrum of scales, present at any instant, and the U_o and B_o may be defined locally in the wavenumber k as well. In the short wavelength range (large k), the dissipative effects may be dominant, while at large scales (small k) they may be negligible. There is no sharp dividing line where one passes from one regime to another.

Weak turbulence theory assigns orders of magnitude to its time scales of its excitations once and for all, and makes no provision for these to change. Its limitations are apparent in any situation in which there are fluxes of excitations in k space which move from one regime to another.

The point is that it is unacceptable to neglect any of the terms in Eqs. (1)-(3). It is important to resist the temptation to try to treat a limited range of k in dynamical isolation from the rest, making approximations there that do not apply elsewhere in k, because of some inequalities which obtain locally. Eqs. (1)-(3) are a package, no part of which can be ignored without peril. It might be argued, as in Sec. II, that more terms are needed in Eqs. (1)-(3) to do justice to the dynamics of the solar wind; if so, then the effect is to complicate an already almost prohibitively difficult problem. It cannot be argued that terms can be dropped because they may be "small" in certain ranges of k.

For the solar wind, U_o and the Alfvén speed $C_A = B_o/\sqrt{4\pi\rho}$ are comparable in the zero-momentum frame. The coefficients ν and η are uncertain for reasons already given, and may not even be well-defined. If the Spitzer formula for the conductivity σ is adopted, $\eta = c^2/4\pi\sigma$. If we use the Braginskii η_1 to estimate the viscosity, then $\nu = \eta_1/\rho$. We get, in cgs units,

$$\sigma \sim 2.5 \times 10^{15} \text{ sec}^{-1}$$

$$\nu \sim \eta_1/\rho \sim 3 \times 10^4 \text{ cm}^2/\text{sec},$$

at a number density of $n \sim 10$ cm^{-3} and a temperature of $10^5 \,^\circ$K. Both U_o and C_A are typically 2 or 2.5×10^6 cm/sec, and the most typical length scales have been measured to be $L \sim 10^{11}$ cm [e.g., Matthaeus and Goldstein, 1982].

We rewrite all velocities in units of $U_o = B_o/\sqrt{4\pi\rho}$, all lengths in units of L, all times in units of L/U_o, and all magnetic fields in units of B_o. The dimensionless version of Eqs. (1)-(3) becomes

$$\nabla \cdot \underset{\sim}{v} = 0, \tag{12}$$

$$\frac{\partial \underset{\sim}{v}}{\partial t} + \underset{\sim}{v} \cdot \nabla \underset{\sim}{v} = -\nabla p + \underset{\sim}{B} \cdot \nabla \underset{\sim}{B} + \frac{1}{R} \nabla^2 \underset{\sim}{v}, \tag{13}$$

and

$$\frac{\partial \underset{\sim}{B}}{\partial t} + \underset{\sim}{v} \cdot \nabla \underset{\sim}{B} = \underset{\sim}{B} \cdot \nabla \underset{\sim}{v} + \frac{1}{S} \nabla^2 \underset{\sim}{B}. \tag{14}$$

The dimensionless numbers R and S are the Reynolds number and magnetic Reynolds number, respectively: $R \equiv U_0 L/\nu$ and $S \equiv C_A L/\eta = U_0 L/\eta$ (since $U_0 \sim B_0/\sqrt{4\pi\rho}$, here). For the numbers cited, $R \sim 10^{12}$ and $S \sim 10^{13}$. These large values put us far into the regime of high Reynolds number turbulence, which is the domain of applicability of such theory as we have (e.g., Batchelor, 1970; Panchev, 1971).

The picture of high-Reynolds number fluid turbulence which has served as a model for the recent development of magnetofluid turbulence theory is due to Richardson, G. I. Taylor, and Kolmogoroff, and is elegantly summarized and developed in the classic monograph by Batchelor (1970). It does not make reference to specific solutions of the dynamical equations, which are regarded as irreproducible random variables. Instead, statements are made about ensemble averages, indicated by angular brackets < >, which are hoped to be relatively smooth and reproducible. Thus B_i, a measured component of the magnetic field, might be divided up into a "mean" plus a "fluctuation" δB_i:

or
$$B_i = <B_i> + \delta B_i,$$
$$v_i = <v_i> + \delta v_i \tag{15}$$

for the velocity field, and so on.

What the brackets < > mean experimentally is a tricky question. Ideally, they should represent ensemble averages over a very large number of experiments prepared in the same way, based on measurements made after a fixed, elapsed time. Even in the laboratory this is difficult, and in the solar wind it is out of the question. What must be done is to conjecture something like an ergodic hypothesis, which makes it possible to equate phase space averages (or ensemble averages) and time averages. Because there is in the solar wind an inevitable relative velocity between the solar wind plasma and the measuring instruments, these time averages are really averages over a space-time trajectory,

in the zero-momentum frame. By the time the various symmetries necessary to interpret the data have been invoked, one has assumed a certain fraction of the consequences that one would, ideally, have liked for the experiment to demonstrate. A shaky consistency is often the most conclusive imaginable outcome.

Very nearly all the results so far on MHD turbulence concern the case of <u>homogeneous turbulence</u>, for which the statistical properties of the fields $B_i(\underset{\sim}{x}, t)$, $v_i(\underset{\sim}{x}, t)$ are independent of $\underset{\sim}{x}$. One conventionally works in the zero-momentum frame, $<v_i> = 0$. If the direction of the magnetic field is not externally constrained in some way by boundary conditions, then $<B_i> = 0$. The quantities of theoretical interest then are mostly derivable from the <u>covariances</u>

$$R_{ij}^{v}(\underset{\sim}{r}, t) \equiv <v_i(\underset{\sim}{x}, t)\ v_j(\underset{\sim}{x} + \underset{\sim}{r}, t)> \qquad (16)$$

$$R_{ij}^{B}(\underset{\sim}{r}, t) \equiv <B_i(\underset{\sim}{x}, t)\ B_j(\underset{\sim}{x} + \underset{\sim}{r}, t)> \qquad (17)$$

$$R_{ij}^{Bv}(\underset{\sim}{r}, t) \equiv <v_i(\underset{\sim}{x}, t)\ B_j(\underset{\sim}{x} + \underset{\sim}{r}, t)> \qquad (18)$$

which, by the assumption of spatial homogeneity, are independent of $\underset{\sim}{x}$.

Virtually all serious theoretical attempts in both fluid and magneto-fluid turbulence so far have centered around such quantities as these covariances. Attempts to calculate R_{ij}^{v}, R_{ij}^{B}, R_{ij}^{Bv} from a closed, deterministic dynamical description have displayed great ingenuity and some results, but nothing that is of obvious use for explanation of solar wind phenomena, so far.

Analytical approaches to data have been concerned with the <u>rotationally</u> <u>isotropic</u> case. In this case, the tensor description of Eqs. (16)-(18) contracts drastically. The $R_{ij}^{B}(\underset{\sim}{x}, t)$, for example, may be Fourier-decomposed as

where
$$R_{ij}^{B}(\underset{\sim}{x}, t) = \int dk\ S_{ij}^{B}(\underset{\sim}{k}, t)e^{i\underset{\sim}{k}\cdot\underset{\sim}{r}}$$

$$S_{ij}^{B}(\underset{\sim}{k}, t) = E_B(k, t)(\frac{k_i k_j - k^2\delta_{ij}}{k^2}) \qquad (19)$$

with a single scalar variable $E_B(k, t)$ determining the evolution of the covariance. $E_B(k, t)$ is the energy spectrum, and is related to the rms fluctuating

field variable $\delta \underset{\sim}{B}$ by

$$\frac{<(\delta \underset{\sim}{B})^2>}{8\pi} = \int_0^\infty E_B(k, t)dk. \qquad (20)$$

Eq. (19) does imply rotational isotropy, and the presence of a finite mean $<B_i>$ will not in general permit this. Analytical impediments to a deductive theory are best illustrated by illustrating the dynamics in a Fourier decomposition of $\underset{\sim}{v}$ and $\underset{\sim}{B}$ over a large cubical box, assuming periodic boundary conditions:

$$\underset{\sim}{v}(\underset{\sim}{x}, t) = \Sigma_{\underset{\sim}{k}} \; \underset{\sim}{v}(\underset{\sim}{k}, t)e^{i\underset{\sim}{k}\cdot\underset{\sim}{x}}$$

$$\underset{\sim}{B}(\underset{\sim}{x}, t) = \Sigma_{\underset{\sim}{k}} \; \underset{\sim}{B}(\underset{\sim}{k}, t)e^{i\underset{\sim}{k}\cdot\underset{\sim}{x}} \qquad (21)$$

If we make up a large column vector whose i^{th} element X_i can be the real or imaginary part of any component of any one of the expansion coefficients $\underset{\sim}{B}(\underset{\sim}{k}, t)$ or $\underset{\sim}{v}(\underset{\sim}{k}, t)$, the Fourier decomposed structure of Eqs. (12)-(14) can be written symbolically as [see, e.g., Orszag 1977, or Kraichnan and Montgomery, 1980]:

$$\frac{dX_i}{dt} = \underset{jk}{\Sigma} \; C_{ijk} \, X_j X_k - \nu_i X_i \qquad (22)$$

where the coupling coefficients C_{ijk} are known, and of a kinematical nature. The dissipation coefficients ν_i come from the viscous and resistive (linear) terms, and generally increase quadratically with increasing wavenumber magnitude.

The essential problem with any analytical approach to Eq. (22) is that the nonlinear (quadratic) terms are much larger, throughout most of $\underset{\sim}{k}$-space, than the linear dissipative ones. No linearization can be justified. The inequality is measured by the Reynolds numbers R and S, so that, particularly for the solar wind, the nonlinearity may be expected to be strong.

Attempts at ensemble avaraging moments of the X_i lead to an acute closure problem exemplified by (e.g., Orszag, 1977):

$$\frac{d}{dt} <X_i^2/2> + \nu_i <X_i^2>$$

$$= \underset{jk}{\Sigma} \; C_{ijk} <X_j X_k X_i> \qquad (23)$$

with a corresponding equation for the time derivative of each nth moment in terms of the (n + 1)st.

The situation is reminiscent of the BBGKY hierachy derived from the Liouville equation, with the difference that no small parameters suggest themselves as bases for perturbation expansions. Great ingenuity has been brought to bear, particularly by R. H. Kraichnan (1959, 1964, 1975), on the problem of closure approximations for the moment hierarchy derived from Eqs. (22). The calculations are lengthy, require (Kraichnan, 1964) extensive numerical analysis, and so far have been limited to the isotropic case. Their generalization to anisotropic cases poses formidable problems, and has not been done.

Eq. (23) expresses the growth or decay of the energy in a particular Fourier mode as a sum of a large number of contributions from interacting triads of modes whose wave numbers sum to zero. Physical intuition is of limited utility in assessing the cumulative effect of the large number of these terms which contribute to each mode: the expansion in Fourier series (or other orthogonal functions) leave behind any simple resolution into forces and responses, "frozen-in field lines", or any of the other readily visualizable but often non-quantitative conceptualizations in terms of which MHD has often been discussed. The C_{ijk}, or modal interaction coefficients, are smoothly-varying functions of wavenumber where they are non-zero.

The statistical mechanics of the system (22) with all the dissipation coefficients ν_i set $\equiv 0$ is tractable. In the cases investigated (Navier-Stokes and MHD in two and three dimensions), truncation at a large but finite number of expansion coefficients and equations has led to systems which seem to be _ergodic_. Time averages of phase functions are predictable as ensemble averages (canonical or microcanonical) based on the constancy of those invariants which are still invariant after the truncation. These conclusions have been repeatedly verified numerically [Seyler, et al, 1975; Fyfe et al, 1977a,b; Kells and Orszag, 1978], and they need only to be alluded to here.

The difficulty is that the dissipative terms, if non-zero ($\nu_i \neq 0$), modify the dynamics qualitatively. Even though they may be relatively small over a good part of the wavenumber space, they in effect "pull the plug" at the high end of wavenumber space. Because they originate from terms like $\nu\nabla^2\underset{\sim}{v}$ and $\eta\nabla^2\underset{\sim}{B}$, they become arbitrarily large, when Fourier-represented, at the large

122

values of k. The effect of the (conservative) nonlinear terms is basically to scramble, in virtually a stochastic way, excitations from one value of $\underset{\sim}{k}$ to another. Those excitations that find themselves at large values of $|\underset{\sim}{k}|$ get gobbled up by dissipation. The flow in $\underset{\sim}{k}$ space tends to be toward those regions which are deficient, relative to the predictions of the non-dissipative equilibrium ensembles. The nonlinear scrambling terms continually try to replenish the excitations which are being drained away at high $\underset{\sim}{k}$. Raising the Reynolds numbers R and S in Eqs. (13)-(14) only increases the "dissipation wave number", at which the dissipation sets in, but does not make it go away. The prevailing opinion is that the integrated dissipation rate for Eqs. (13), (14) remains finite even as $R \to \infty$ and $S \to \infty$. This gives transfer from one part of the wave-number spectrum to another a central role in the dynamics that it does not have in linear, or nearly linear, systems.

Very large numbers of Fourier modes are required to resolve all the dynamically important spatial scales, as R, S become large. This provides severe limits on numerical attempts to solve Eqs. (13) and (14). A pessimistic rule of thumb is that one grid point (or finite element, or Fourier coefficient) per dimension per unit Reynolds number is required. Thus, a three-dimensional $(64)^3$ simulation (which will not quite fit in core on a CRAY-1) would be required to resolve turbulence with a Reynolds number of 64. This requirement can be relaxed somewhat, but not by an order of magnitude---a Reynolds number 1000 run could probably not ever be resolved on a $(64)^3$ grid, if the Reynolds number were to be based on the mean length scale in the flow. When one begins to talk about Reynolds numbers many orders of magnitude larger, the real limitations of foreseeable computers, in dealing with turbulence, become apparent.

Dimensional analysis, applied to isotropic, homogeneous situations, have led to predictions of power laws in wave number space for the energy spectra $E_B(k)$, $E_V(k)$ in different situations. The predictions differ from fluids to magnetofluids, and from two to three dimensions. They are virtually the only simple, testable analytic predictions that four decades of turbulence theory have been able to come up with. There are ingenious closures of the hierarchy of which Eq. (23) is the first member, but they are not simple, and so far they all assume higher degrees of symmetry than the solar wind has been shown to possess. These dimensional analysis arguments can be grouped under the rubric of "cascade theory".

High Reynolds number turbulence theories and computations have been formalized around two general classes of situations: "forced" and "decay" situations. These are at best loose approximations to actual physical cases, but they are as close to a universal or situation-independent problem as can be isolated. Because the magnetofluid equations are dissipative, a turbulent field will eventually decay away, and one can seek features of the decay which may be insensitive to initial spectra. Steady-state situations require a source of excitations, or "forcing", that is balanced against the dissipation rate, averaged over time. The nature of the forcing, often regarded as band-limited in wavenumber space, is usually not restricted very specifically, and is often modelled by a random function. The search in turbulence theory, as elsewhere in physics, is for soluble situations from which a universal, repro-ducible, and transferable core of general behavior can be extracted.

Cascades and Inverse Cascades

Power laws and cascade processes are expected for forced situations, not for decaying ones, unless there is reason to believe that the lifetime of the long-wavelength components is sufficiently great that the short wavelength components cannot distinguish them from a maintained "source". Under circum-stances that have been discussed at great length in the published literature, the following table (Table 1) shows what has been done so far in the way of conjecturing and establishing inertial subrange exponents for fluids and magneto-fluids.

There is insufficient scope within this article to review in detail the evidence and arguments for and against inertial-subrange power laws which have been accumulated. There is little doubt that the question of exponents has come to occupy more of the territory than it deserves, to some extent because there are concrete theoretical predictions. The exponents derive not from any dynamical arguments but from conjectured similarity variables. Deriv-ing them from dynamics has been the most pursued of all subjects in turbulence theory, but no wholly satisfactory resolution has been achieved. Even if it were achieved, relatively little light would be shed on the dynamics of the solar wind.

Table 1

Situation	NAVIER-STOKES, 3D	NAVIER-STOKES, 2D	MHD, 3D	MHD, 2D
Cascaded Quantity	ENERGY	ENERGY & ENSTROPHY	ENERGY & MAGNETIC HELICITY	ENERGY & MAGNETIC POTENTIAL
Direction of Cascade in k space	ENERGY UP	ENSTROPHY UP, ENERGY DOWN	ENERGY UP, HELICITY DOWN	ENERGY UP, MAGN. POT. DOWN
Predicted Power Law, Energy Spectrum	$k^{-5/3}$ KOLMOGOROFF-OBUKHOV (1941)	k^{-3}, $k^{-5/3}$ KRAICHNAN (1967), BATCHELOR, LEITH	$k^{-5/3}$ or $k^{-3/2}$, k^{-1} FRISCH et al (1975)*	$k^{-5/3}$, $k^{-1/3}$ FYFE et al (1977b)
Experimental Verification Attempted	GRANT, STEWART, & MOLLIET (1962)	NO	MATTHAEUS & GOLDSTEIN (1982)	NO
Computational Verification Attempted	NO	FYFE et al, (1977) [insufficient spatial resolution]	NO*	FYFE et al (1977) [insufficient spatial resolution]

* See also Meneguzzi et al (1981).

Table 1. Cascades, Inverse Cascades, and Power Law Predictions. Original references are cited in bibliography.

The strongest single limitation which the present cascade and inverse cascade theory may have when applied to the solar wind concerns the assumption of isotropy, which underlies all of the predictions listed in Table 1, and all of the dimensional analysis arguments formulated in the Kolmogoroff style since 1941. We are virtually certain that the solar wind is not isotropic, and the weaker assumption of axisymmetry may be regarded as open to serious legitimate doubt. It is naive to regard the removal of the isotropic restrictions on cascade power-law predictions as only a technical point which is sure to be overcome soon; its status is at present very dark, and no resolution is in sight.

Selective Decays

An even more tentative class of generalizations, not without implications for the solar wind, are those processes called selective decays, in which all the fields decay as in the initial value problem, but some of the global, non-dissipative invariants may decay less rapidly than others. Qualitatively, there are two possible reasons for this. First, the dissipation is effective only at the shorter wavelengths, and quantities transferred to long wavelengths may simply stay out of reach of the dissipation. Second, dissipation integrands for some variables may be peaked at higher wavenumbers than for others and to be more effective at dissipation for this reason. Arguments and computations for these possible "selective decay" processes have been presented by Montgomery, Turner and Vahala (1978), by Matthaeus and Montgomery (1980), and by Riyopoulos, Bondeson, and Montgomery (1982).

Each such selective decay process, if valid, would imply a temporally decreasing magnitude of the ratio of two of the ideal invariants: energy to magnetic helicity for 3D MHD, for example (Taylor 1974 made use of such an assumption in predicting asymptotic states of decaying toroidal Z pinches). A variational problem arises by minimizing this ratio, which often has for its solution a relatively simple Euler equation which predicts a quiescent state. Needless to say, this is an attractive possibility. If the tendency of highly disordered turbulent motions is to decay to some universal non-trivial quiescent state, regardless of the path of the decay, then this is indeed a wonderfully simple ingredient to add to the few pieces of general information we have about turbulence.

For example, if for 3D MHD, the energy-to-helicity ratio were to decay toward its minimum value, this is simply a force-free state, a solution of $\nabla \times \underline{B} = \lambda\underline{B}$, where λ is a Lagrange multiplier, and $\underline{v} = 0$ everywhere. For 2D MHD, the decay of energy to mean square magnetic potential again leads to a quiescent state with a mean magnetic field derivable from a vector potential $\underline{B} = \nabla \times \underline{A} = \nabla \times A\hat{e}_z$, where

$$(\nabla_\perp^2 + \lambda^2)A = 0.$$

Some numerical evidence has been presented for both of these kinds of selective decays. The results are encouraging but should be held with extreme caution; the conclusions are difficult to document and expensive, and very few runs have been carried out [Matthaeus and Montgomery 1980; Riyopoulos et al 1982].

A second class of decay hypothesis, not entirely consistent with the first, concerns the ratio of the <u>cross-helicity</u> (another ideal invariant) to the energy. The ratio

$$R_{H_c} \equiv \left| \frac{2\int \underline{v}\cdot\underline{B} \; d\underline{x}}{\int (\underline{v}^2 + \underline{B}^2) d\underline{x}} \right| ,$$

a constant in the absence of dissipation, has been shown under some circumstances to increase monotonically (Grappin et al, 1982; Matthaeus, Goldstein, and Montgomery 1982) with time in the presence of dissipation. This increase points to an equipartitioned state, certainly not quiescent, with $\underline{v} = \pm\underline{B}$. From the point of view of solar wind observations, this is an attractive possibility, because many observations, from Belcher and Davis (1971) on, have shown solar wind velocity fields and magnetic fields to be closely aligned or anti-aligned. These are sometimes referred to as "Alfvénic fluctuations".

The paradox of MHD turbulence's tending apparently both to states in which R_{H_c} is maximal and helicity to energy is also maximal is an example of the wide-open character of research into MHD turbulence. There is compelling evidence for both conjectures, but both cannot be simultaneously true. If either is true, it may well determine the asymptotic state toward which solar wind turbulence is trying to decay.

IV. SUMMARY

MHD turbulence theory provides the most nearly adequate framework in which to discuss the physics of solar wind turbulence. The collected data, however, are far superior both to the available justification of the MHD description and to its systematic development for turbulent fields which lack high degrees of symmetry such as rotational isotropy. Understanding the physics of the solar wind at the present time is probably more limited by the unanswered questions in turbulence theory than by any scarcity of measurements. Expanded experimental programs to probe solar wind turbulence, such as that advocated by the 1980 Plasma Turbulence Explorer Panel (Montgomery et al, 1980) would require a considerably broader attack than has so far been mounted on the basic plasma physics of the turbulent medium.

REFERENCES

Batchelor, G. K., _An Introduction to Fluid Mechanics_, Cambridge Univ. Press, Cambridge (U.K.), 1967 [Chapt. 1].

Batchelor, G. K., _Theory of Homogeneous Turbulence_, Cambridge Univ. Press, New York, 1970.

Belcher, J. W., and L. Davis, Large-amplitude Alfvén Waves in the Interplanetary Medium, J. Geophys. Res. _76_, 3534, 1971.

Book, D. L., _NRL Plasma Formulary_, Office of (U.S.) Naval Research, Washington, D.C., 1980.

Braginskii, S. I., "Transport Processes in a Plasma", translated in _Reviews of Plasma Physics_, Vol. I, ed. by M. A. Leontovich; Consultants' Bureau, New York, 1965, pp. 205-309.

Frisch, U., A. Pouquet, J. Léorat, and A. Mazure, Possibility of an Inverse Cascade of Magnetic Helicity in Magnetohydrodynamic Turbulence, J. Fluid Mech. _68_, 769, 1975.

Fyfe, D., G. Joyce, and D. Montgomery, Magnetic Dynamo Action in Two-Dimensional Turbulent Magnetohydrodynamics, J. Plasma Phys. _17_, 317, 1977a.

Fyfe, D., D. Montgomery, and G. Joyce, Dissipative Forced Turbulence in Two-Dimensional Magnetohydrodynamics, J. Plasma Phys. _17_, 369, 1977b.

Grant, H. L., R. W. Stewart, and A. Moilliet, Turbulence Spectra from a Tidal Channel, J. Fluid Mech. _12_, 241, 1962.

Grappin, R., U. Frisch, A. Pouquet, and J. Leorat, Alfvénic Fluctuations as Asymptotic States of MHD Turbulence, Astronomy and Astrophysics _105_, 6, 1982.

Kells, L. C. and S. A. Orszag, Randomness of Low-Order Models of Two-Dimensional Inviscid Dynamics, Phys. Fluids _21_, 162 1978.

Kolmogoroff, A. N., The Local Structure of Turbulence in Incompressible Viscous Fluid for Very Large Reynolds Numbers, C. R. Acad. Sci. URSS _30_, 201, 1941.

Kraichnan, R. H., Remarks on Turbulence Theory, Adv. in Math. _16_, 305 (1975).

Kraichnan, R. H., Inertial Ranges in Two-Dimensional Turbulence, Phys. Fluids, _8_, 1385, 1967.

Kraichnan, R. H., The Structure of Isotropic Turbulence at Very High Reynolds Number, J. Fluid Mech. _5_, 497 (1959).

Kraichnan, R. H., Decay of Isotropic Turbulence in the Direct-Interaction Approximation, Phys. Fluids _7_, 1030 (1964).

Kraichnan, R. H., and D. C. Montgomery, Two-Dimensional Turbulence, Rep. Prog. Phys. _43_, 547 (1980).

Landau, L. D., and Lifshitz, E. M., Fluid Mechanics, Pergamon Press, London, 1959. [Chapt. 1].

Matthaeus, W. H., and M. L. Goldstein, Rugged Invariants of MHD Turbulence, J. Geophys. Res. 87, 6011, 1982.

Matthaeus, W. H., M. L. Goldstein, and D. Montgomery, Dynamic Alignment of Velocity and Magnetic Fields in Magnetohydrodynamic Turbulence, EOS (Trans. of the AGU) 63, 5532-10, 1982.

Matthaeus, W. H., and D. Montgomery, Selective Decay Hypothesis at High Mechanical and Magnetic Reynolds Numbers, Ann. N.Y. Acad. Sci. 357, 203, 1980.

Meneguzzi, M., U. Frisch, and A. Pouquet, Helical and Non-helical Turbulent Dynamos, Phys. Rev. Lett. 47, 1060, 1981.

Montgomery, D., Implications of Navier-Stokes Turbulence Theory for Plasma Turbulence, Proc. Indian Acad. Sci. 86A, 87, 1977.

Montgomery, D., Major Disruptions, Inverse Cascades, and the Strauss Equations; to appear in Physica Scripta, 1982.

Montgomery, D., Chairman, Report of the NASA Plasma Turbulence Explorer Study Group, 715-78, NASA Jet Propulsion Laboratory, Pasadena, CA, 1980.

Montgomery, D., L. Turner, and G. Vahala, Three Dimensional Magnetohydrodynamic Turbulence in Cylindrical Geometry, Phys. Fluids 21, 757 (1978).

Orszag, S. A., "Lectures on the Statistical Theory of Turbulence", in Fluid Dynamics: 1973 Les Houches Summer School of Theoretical Physics, ed. by R. Balian and J. -L. Peube, pp. 235 ff. Gordon and Breach, New York, 1977.

Panchev. S., Random Functions and Turbulence, Pergamon Press, New York, 1971.

Pedlosky, J., Geophysical Fluid Dynamics, Springer-Verlag, New York, 1979.

Riyopoulos, S., A. Bondeson, and D. Montgomery, Relaxation Toward States of Minimum Energy in a Compact Torus, Phys. Fluids 25, 107, 1982.

Seyler, C. E., Jr., Y. Salu, D. Montgomery, and G. Knorr, Two-Dimensional Turbulence in Inviscid Fluids or Guiding Center Plasmas, Phys. Fluids 18, 803, 1975.

Strauss, H. R., Nonlinear Three-Dimensional Magnetohydrodynamics of Noncircular Tokamaks, Phys. Fluids 19, 134, 1976.

Taylor, J. B., Relaxation of Toroidal Plasma and Generation of Reverse Magnetic Fields, Phys. Rev. Lett. 33, 1139, 1974.
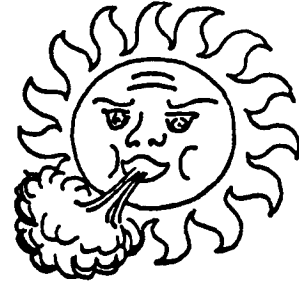
SESSION 3.

SOLAR WIND ACCELERATION

Page intentionally left blank

SUMMARY OF THE SESSION ON SOLAR WIND ACCELERATION

R. MacQueen

Neugebauer set the stage for the following theoretical papers by summarizing the 1 AU observed properties of three classifications of solar wind flows – transient, sector boundary and coronal hole. She included in the former category a synthesis of previous work on helium-enriched events, alpha-particle flux enhancements, low proton and low electron temperature events, high ionization signatures, helium plus enhanced occurrences and magnetic clouds.

Leer considered thermally-driven wind theory and stressed the relative roles of energy and mass flux in determining the flow kinetic energy. He noted that the effects of addition of energy or momentum into the corona would affect the wind properties differently, depending upon the spatial region of input. Finally he suggested that Alfven wave input into highly divergent geometries might result in energy deposition into the region center, due to wave refraction.

Olbert discussed the dynamical implications of non-local heat transport owing to the presence in the corona and solar wind of a large suprathermal tail in the electron velocity distribution function. He concluded that such heat transport provides the possibility of producing high-speed solar wind streams in the absence of energy addition to the solar wind above the coronal base. (Ed. note. Scudder's closely related paper is included in this chapter although the papaper was given in another session.)

Seuss summarized two dimensional, numerical magnetohydrodynamic modeling of the near solar wind flow, particularly (a) the case of the flow field interaction with a dipole magnetic field, and (b) the case with a highly divergent field representative of conditions in coronal holes.

Wolfson considered the suggestion of R. N. Thomas that an intrinsic stellar mass flux is the major factor determining the properties of stellar winds, and found that this suggestion is not consistent with the principles of steady gas dynamics.

Habbal, Tsinganos, and Rosner presented a theoretical model of an isothermal stellar wind in which either momentum addition or rapid divergence of flow tubes would lead to multiple transonic solutions, all but one of which exhibit a shock transition near the base of the wind.

Akasofu conjected that small bipolar regions, associated with x-ray bright points, may dynmically evolve to provide acceleration of material into the solar wind.

Rottman and Orrall surveyed UV rocket measurements of the outflow of material in the transition region and low corona. From four rocket flights sampling a variety of hole conditions they showed that coronal-hole associated outflow ranged from 5-10 km/sec to 10-15 km/sec in the transition region and low corona, respectively.

Gold briefly presented multi spacecraft observations in support of his suggestion that, in the late 1960's, two time scales existed for development of flows from stationary objects on the sun – 2 days and longer.

Page intentionally left blank

OBSERVATIONAL CONSTRAINTS ON SOLAR WIND ACCELERATION MECHANISMS

Marcia Neugebauer
Jet Propulsion Laboratory
California Institute of Technology
Pasadena, CA 91109

ABSTRACT

A complete theoretical understanding of the acceleration of the solar wind must account for at least three types of solar wind flow: high-speed streams associated with coronal holes, low-speed boundary layer flows associated with sector boundaries, and both high- and low-speed flows associated with impulsive ejections from the Sun. The properties of each type of flow are summarized.

Types of Flow

Three types of solar wind flow are considered for the purpose of placing observational constraints on theories of solar wind acceleration. These are: the fast, hot flow from coronal holes, the slow, dense, cool flow near sector boundaries, and transient flows. This trichotomy is simply a convenient system for describing extremes of solar wind behavior, and should not imply that three and only three distinct theories of solar wind acceleration are required. A single steady state theory could perhaps explain both the hole and the boundary flows, but such a theory would have to include an explanation of the sharp latitude and longitude boundaries of high-speed streams from coronal holes (Rosenbauer et al., 1977; Schwenn et al., 1978). It is also possible that there are solar wind flows which are not included in this three-way classification. For example, Burlaga et al. (1978) and Levine (1978) have presented evidence for the existence of flows from magnetically open regions of the corona which are neither holes nor streamers. Even if such flows are important contributors to the solar wind, however, they are not included in this survey because their properties have not been determined.

The first transient flows to be identified were the driver gases behind interplanetary shocks. Their properties are discussed in the paper by Zwickl et al. in these Proceedings. Observations of coronal transients and mass ejections have led to a realization that there are transient inputs to the solar wind which are not associated with either flares or shocks. Approximately 70% are associated with eruptive prominences (Munro et al., 1979), many of which are not sufficiently energetic to yield an interplanetary shock.

Table 1 compares the properties of the several types of impulsively ejected plasma which I believe are really different manifestations of one class of plasma flow. The numbers in this table were either compiled from the referenced work or computed from King's (1977, 1979) Interplanetary Medium Data Tape (IMDT) using the authors' lists of event times. The composition and the thermal and magnetic properties of the differently named events are all quite similar. Transient flows occur in both the low-speed and the high-speed solar wind. Their plasma density is highly variable, both from event to event and within a single event. Most of the material added to the solar wind in transient events is the hot coronal material originating in a large region of space above a flare

135

Table 1. Properties of different manifestations of transient flows

Type:	He Enrichment	Anom low T_p	Low T_e	High Ionization	He$^+$	He Abund. Enhancements	Magnetic Clouds
Reference:	Hirshberg et al, 1972	Gosling et al, 1973	Montgomery et al, 1974	Bame et al, 1979 Fenimore, 1980	Schwenn et al, 1980 Zwickl et al, 1982	Borrini et al, 1982	Klein & Burlaga, 1982
Definition:	$\frac{n_\alpha}{n_p} \geq .15$	post shock $T_p <2\times10^5 \times (\frac{v}{350}-1)$	$T_e <6\times10^4$	$T_{Fe} > 2.3 \times 10^6$	recognizable peak at M/Q = 4	$\frac{n_\alpha v_\alpha}{n_p v_p} \geq .10$	duration ∿ 1 day B > 10 γ large ΔB_z
Speed, km/s range average	358-655 546	411-612 532	345-616 478		360-500	281-674 434	318-665 417
n_p, cm^{-3} range average		2.6-9.9 6	2.5-20 7		6.5-50	1.8-51 10	2.5-27 12
T_p, 10^4K		7	3	low in 43%	1.5-3	6	7
T_e, 10^4K			5	low in 43%			
n_α/n_p	.21(pk)	.18(pk)		43% > .09	.025-.094	>.10	
Ionization temp.				$T_{Fe} = 2.3-17\times10^6$	mixture	"Anom. high"	
Q_e, erg/cm^{2}s			∿1×10^{-3}				
B, γ	11	6.8	7.3			8.5	10.6(pk = 12)
$\frac{B^2}{8\pi} + n_p k T_p$						local max	local max
$\beta = \frac{8\pi n k T_p}{B^2}$		0.3	0.3			0.2	0.2 - 0.5
Shock assoc.	75%	100%(def'n)	83%	27%	75%	44%	31%
Duration		≤36 h	10 - >40 hr		1-6 hr	∿ 1 day	∿ 1 day
No. events	12	12	13	14	4	73	45

site or an erupting prominence. A small fraction of the ejected mass is the much cooler prominence material itself, which can evidently pass through the corona without reaching ionization equilibrium with the surrounding gas. In this way both unusually high and unusually low ionization states, and sometimes mixtures of the two, can be associated with transient flows. The combination of high ionization state and low kinetic temperature suggests that the gas has been cooled by greater than average expansion and/or that heat conduction has been inhibited, perhaps by disconnection of the magnetic field from the Sun. The electron heat flux is less than usual, with both superthermal and energetic electrons streaming along the field nearly symmetrically towards and away from the Sun (Palmer et al., 1978; Bame et al., 1981). The picture which has emerged is that the magnetic topology is closed, either with the field closing on itself in a bubble configuration or with both ends of the field lines remaining attached to the Sun.

Correlations of solar wind observations with x-ray and EUV observations obtained by Skylab in 1973-4 indicated that coronal holes are the source of long-lived, high-speed solar wind streams (Krieger et al., 1973,1974; Nolte et al., 1976). Feldman et al. (1976; 1978) and Bame et al. (1977) have summarized the properties of those high-speed streams observed between 1971 and 1974 which

attained speeds > 650 km/s. These streams were broad, extending over solar longitudes ranging up to 159°; the average FWHM was 89 ±34°. At 1 AU, the plasma in these streams is less dense, much hotter, and has less helium than the plasma from impulsive ejections. The hour-to-hour variability of plasma parameters within these streams is also much less than in low-speed flows (Bame et al., 1977).

Comparison of coronal observations with solar wind data shows that the plasma in which long-lived sector boundaries are embedded probably originates in helmet streamers which separate the flows from neighboring coronal holes (Hansen et al., 1974). The coronal temperatures of boundary flows estimated by Feldman et al. (1981) from heavy ion charge states are consistent with streamer temperatures.

It has long been known that sector boundaries preferentially occur in low speed, low temperature, high density plasma (Wilcox and Ness, 1965; Ness et al., 1971). To this body of knowledge, Borrini et al. (1981) have added the observations that the helium abundance, the differential flow between alphas and protons, and the alpha to proton temperature ratio all reach local minima near sector boundaries.

The electron temperature, electron heat flux, break-point energy between the thermal and the nonthermal electron distributions, and the electron strahl strength all exhibit local minima at sector boundaries (Pilipp et al., 1981; Feldman et al., 1981). Helios data also show that the electron temperature at sector boundaries decreases adiabatically with distance from the Sun, unlike the electrons in high speed streams, which cool significantly more slowly. From these data, Pilipp et al. concluded that the field lines within the sector boundary have become disconnected from the Sun. On the other hand, the visual form of coronal streamers suggests an open magnetic topology. The postulated reconnection may occur only within the small scale, often complex structure of the sector boundary. Further evidence for reconnection associated with sector boundaries is presented below.

Figure 1 summarizes my categorization of different solar wind flows. It could be misleading to average solar-wind properties as a function of solar-wind speed (although I am one of many people who have done this in the past), because two or more different acceleration processes contribute to the sample at any speed.
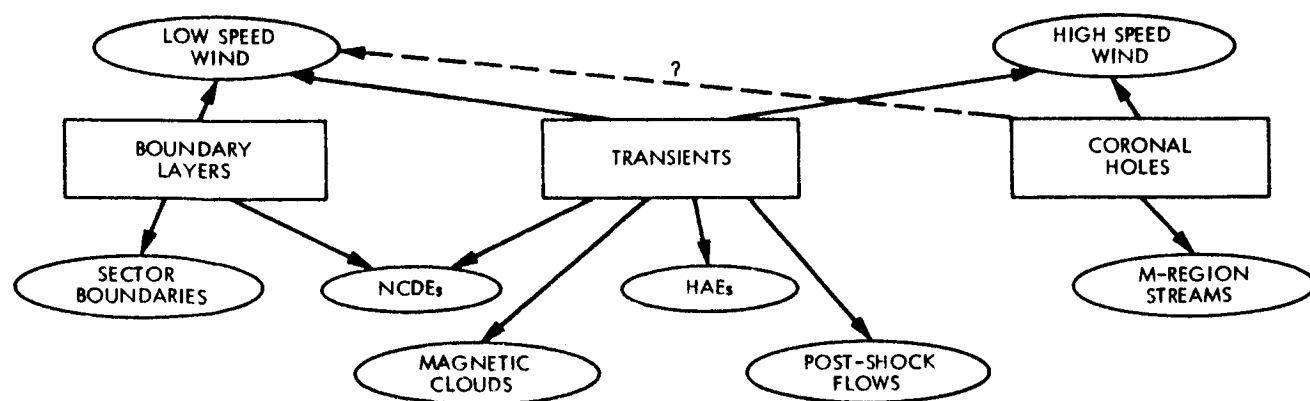
Figure 1. Suggested relation between various types of solar wind flow.

137

Figures 2 and 3 illustrate the similarities and the differences between the properties of the three different types of flow.

Transient flows are represented by a superposed epoch analysis centered on the onsets of the helium abundance enhancement events listed by Borrini et al. (1982). Many of the plots in Figures 2 and 3 nearly reproduce those given by Borrini et al., with some minor differences arising from my use of the IMDT rather than the Los Alamos data alone. Figures 2 and 3 contain several solar wind parameters which were not calculated by Borrini et al.

Boundary flows are represented in Figures 2 and 3 by a superposed epoch analysis around 45 sector boundary crossings observed between December, 1972, and September, 1975, during the period of low solar activity and recurrent streams from coronal holes. This time limitation was made in an effort to avoid inclusion of reversals of field direction associated with transient flows. For this reason, I have included fewer sector boundaries than were used in the study of Borrini et al. (1981). It is usually the case that, by the time it has reached 1 AU, the fast plasma from a coronal hole has overtaken the slower plasma from its leading sector boundary. There were 9 sector boundaries included in my sample for which the arrival of the leading edge of the high-speed stream was at least a day later than the passage of the sector boundary, a separate superposed epoch analysis was performed on these sector boundaries, and are labelled "no stream" in Figures 2 and 3.

Average properties of the high-speed streams from coronal holes are represented by horizontal lines on the right-hand side of the sector-boundary plots. The averages were computed by combining start and stop times of the high speed streams listed by Feldman et al. (1976) with the hourly average solar wind parameters from the IMDT. Feldman et al. corrected the data taken at 1 AU for the evolution of the high speed streams between 20 solar radii and 1 AU, but where there is overlap, my results agree with theirs within 20%.

Figure 2a shows superposed epoch plots of solar wind speed for ±3 days around an HAE or a sector boundary. There is no obvious trend in the plot for HAE's; by 1 AU the transient plasma travels at the same speed as the ambient plasma. On the right side, one can see the low speed associated with sector boundaries as well as the increasing speed associated with the encroaching leading edge of the following coronal hole flow. The relative noisiness of the curve for HAEs compared to the "all" sector boundary curve arises from the combined effect of data gaps and the large range of speeds included in the sample.

Proton density is plotted in Figure 2b. The only trend associated with the transient events is the modest (30 %) increase several hours before the zero epoch time, probably indicating pile up of plasma ahead of the expanding transiently ejected plasma. Again, the event to event variance is large.

There is a definite density enhancement at sector boundaries. Comparison of the two curves on the right side of Figure 2b shows that a large part of the signal is, however, caused by the compression at the leading edge of the following high speed stream. The "no stream" data show two density peaks, one at the sector boundary and a larger one on the leading edge of the stream.
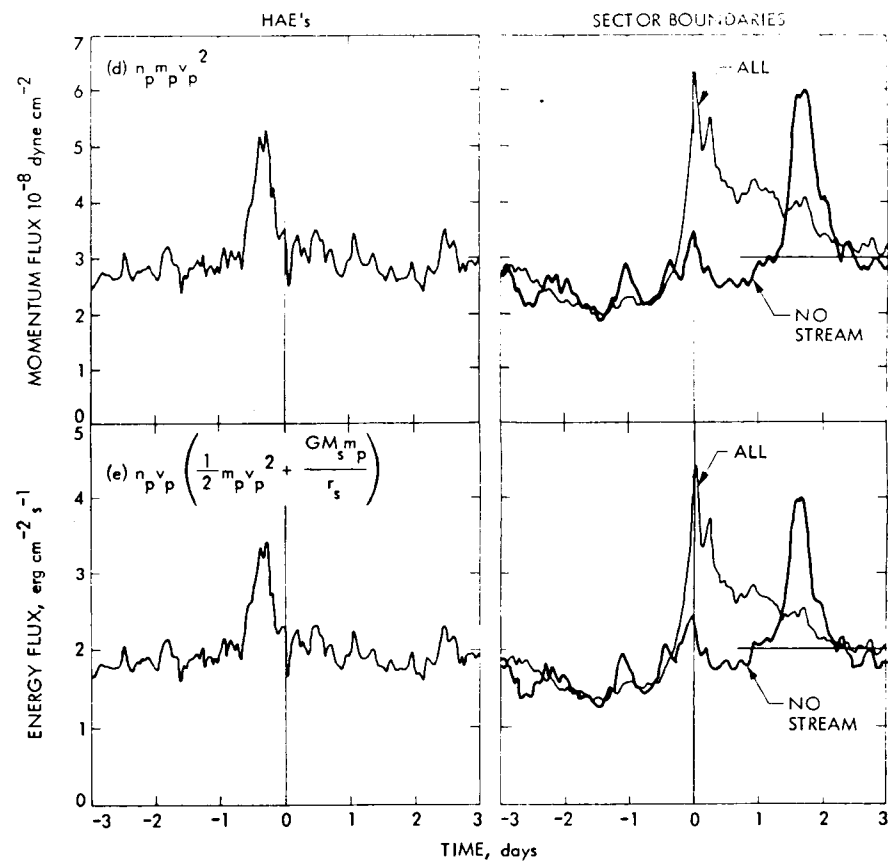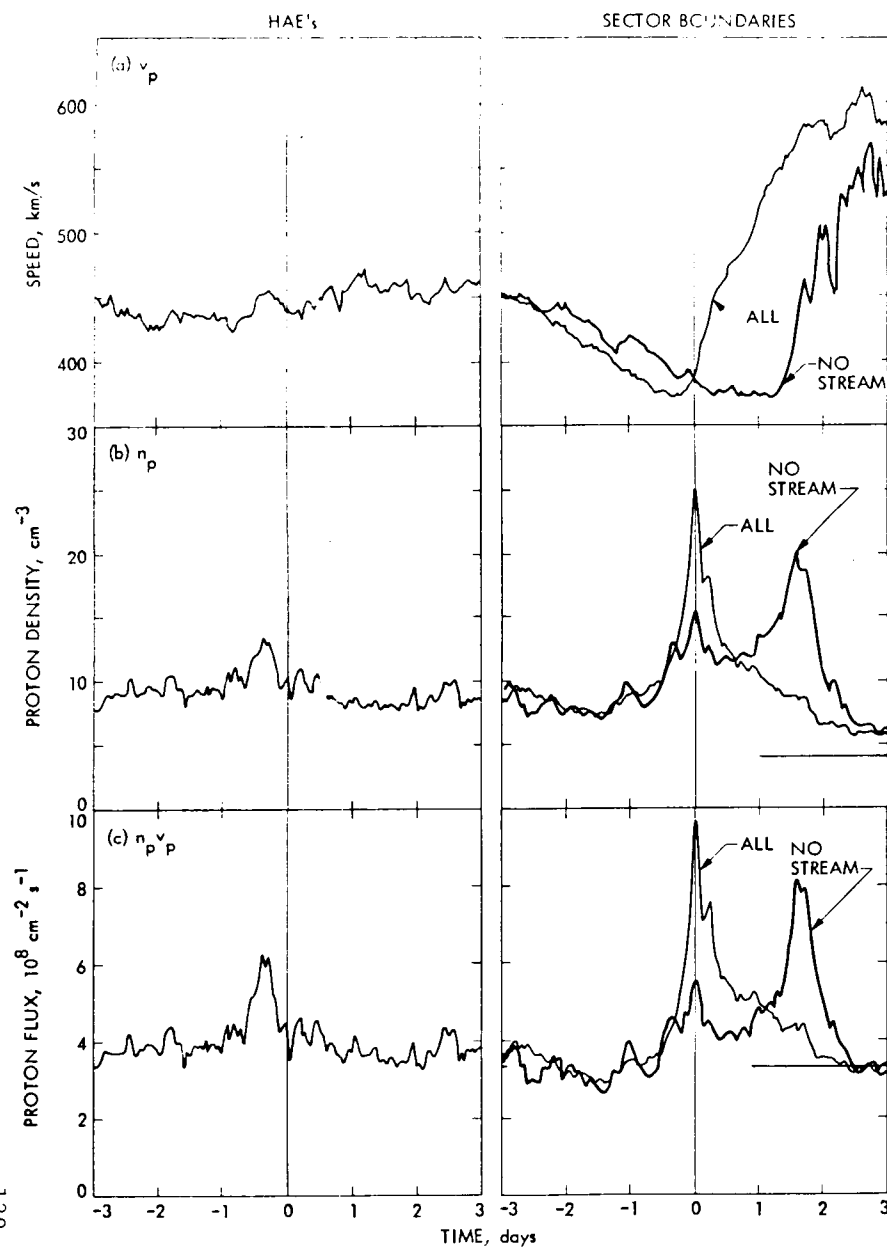
Figure 2. Superposed epoch plots of the dynamical properties for helium abundance enhancements and sector boundaries. For sector boundaries, the "no stream" plots are subsets of the "all" plots for which the sector boundary crossing preceeded the leading edge of a high speed stream by at least one day. The horizontal lines represent average values for high speed streams.
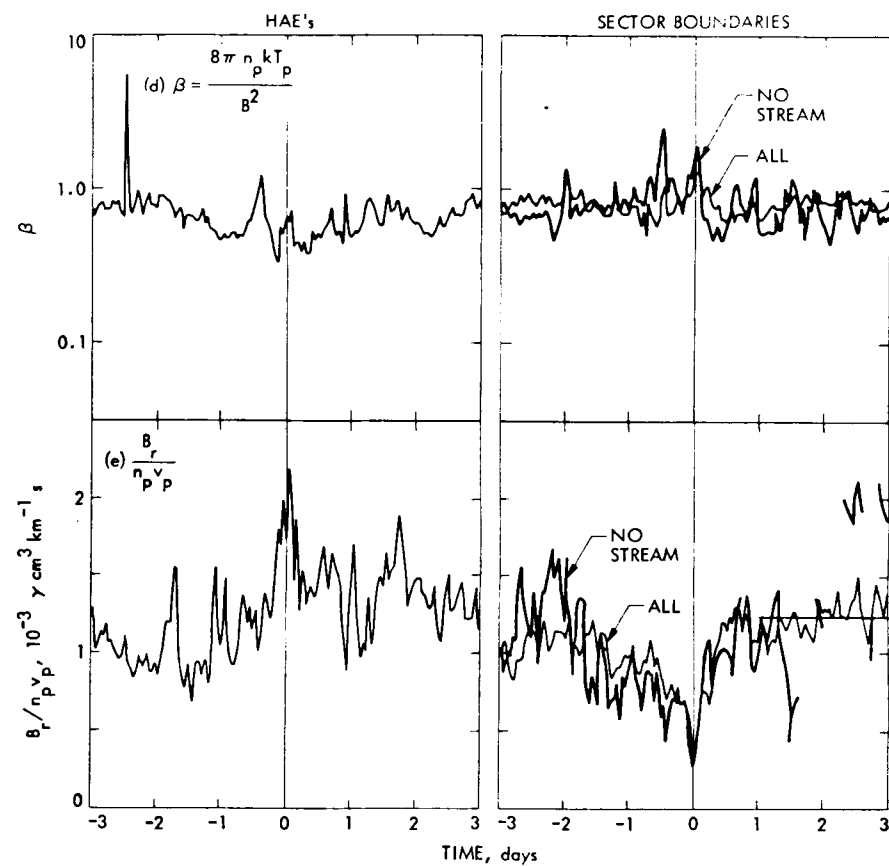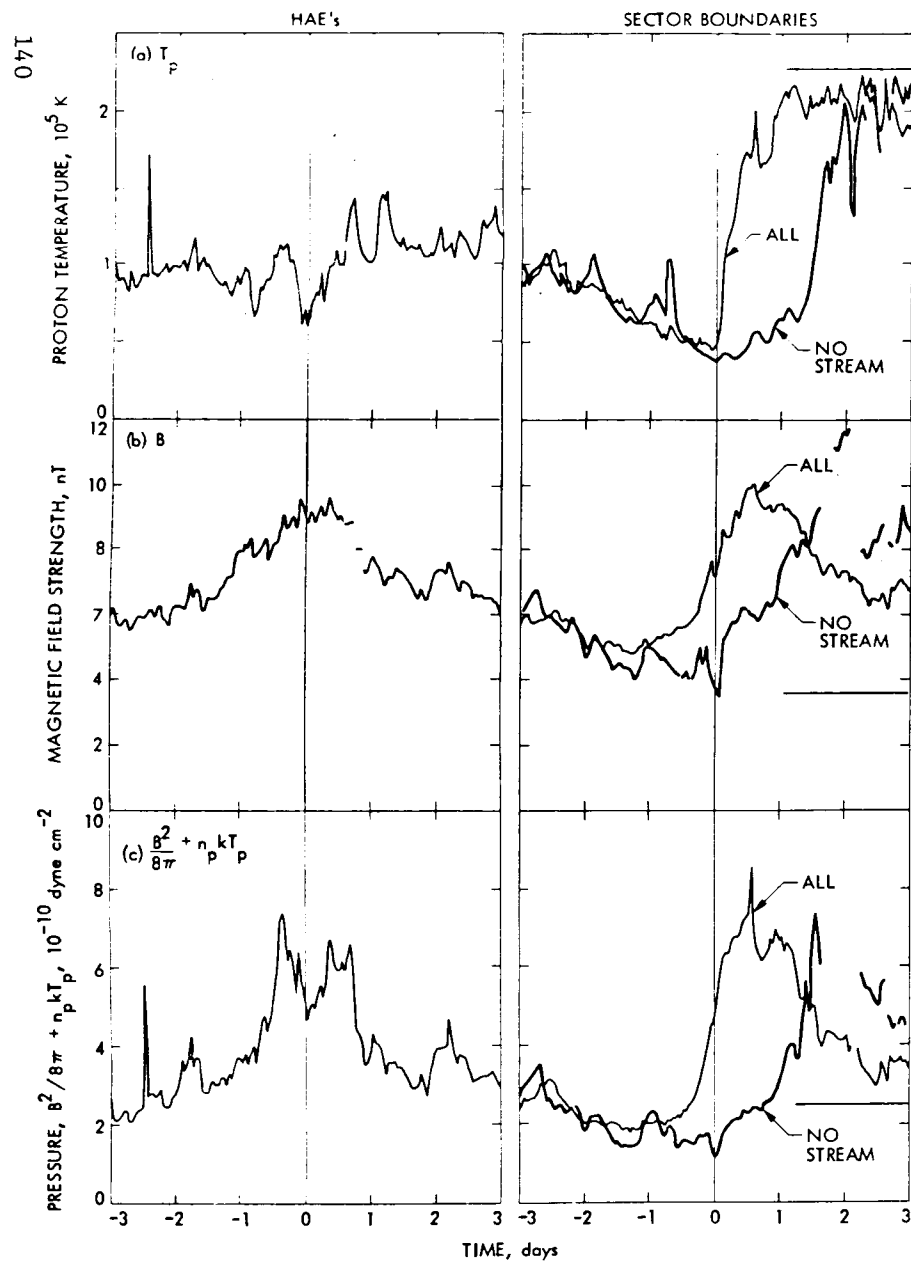
Figure 3. Superposed epoch plots of the thermal and magnetic properties for helium abundance enhancements and sector boundaries. For sector boundaries, the "no stream" plots are subsets of the "all" plots for which the sector boundary crossing preceeded the leading edge of a high speed stream by at least one day. The horizontal lines represent average values for high speed streams.

Figure 2c shows the product of density and speed, or the proton flux. The flux is roughly the same, $(4 \pm 1) \times 10^8$ cm^{-2} s^{-1}, for all three types of flow, and consistently less than in stream interaction regions.

The proton momentum flux ($n_p m_p v_p^2$) is plotted in Figure 2d. The values for the three different types of flow are remarkably similar, in agreement with studies by Steinitz and Eyni (1980) and Steinitz et al. (1982). The difference between my value of 3 dyne cm^{-2} (based primarily on IMP data) and the Steinitz et al. value of 2 dyne cm^{-2} (based on Mariner 2, Vela 3, and Helios data) may be largely explained by systematic differences between instruments. Density is the least accurately determined parameter; it could be in error by 30%, perhaps more. See Neugebauer (1982) for a discussion of the accuracy of solar wind measurements.

Figure 2e displays the variation of energy flux, $n_p v_p (m_p v_p^2/2 + m_p M_s G/r_s)$, where the second term accounts for the work done against solar gravity. The energy flux is close to 2 erg cm^{-2}s^{-1} for each of the three types of flow. The invariance of this parameter was not tested by Steinitz and coworkers.

Figure 3, in the same format as Figure 2, shows the distribution of internal energy in the plasma. Proton temperature (Figure 3a) reaches a minimum of about 5 x 10^4 K in both transient and boundary flows, as opposed to a very hot 2.3 x 10^5 K in coronal hole flows.

In Figure 3b, it can be seen that the magnetic field reaches a broad local maximum in transient flows and a narrow local minimum at sector boundaries. The field in coronal hole flow is similarly low.

The sum of the proton and magnetic pressures is plotted in Figure 3c, illustrating the local pressure maximum in transient flows mentioned earlier. Although the local minimum at sector boundaries is probably not statistically significant, it is possible that the plasma is locally falling into the sector boundary.

Figure 3d shows $\beta = 8\pi n_p k T_p / B^2$, which is lowest in the transient flows and highest at sector boundaries.

Finally, we consider the ratio $B_r/n_p v_p$, where B_r is the radial component of the interplanetary magnetic field. This ratio should be independent of distance from the Sun and unaffected by stream interactions if the field is frozen into the plasma and develops no kinks large enough to cause a local reversal of the sign of B_r. Figure 4 shows hourly averages of selected solar wind parameters for the solar rotation starting February 10, 1974. From top to bottom are plotted the solar wind speed, the logarithm of the proton flux, the logarithm of $B_r/n_p v_p$, and the longitude angle of the interplanetary magnetic field direction. The amplitude of the variation of $B_r/n_p v_p$ is about an order of magnitude greater than the amplitude of the variation of $n_p v_p$. Particularly noteworthy are the broad minimum in $B_r/n_p v_p$ around the sector boundary crossing on day 51 and the maximum near the HAE on day 53. The origin of the many small dips in $B_r/n_p v_p$ is still under investigation.
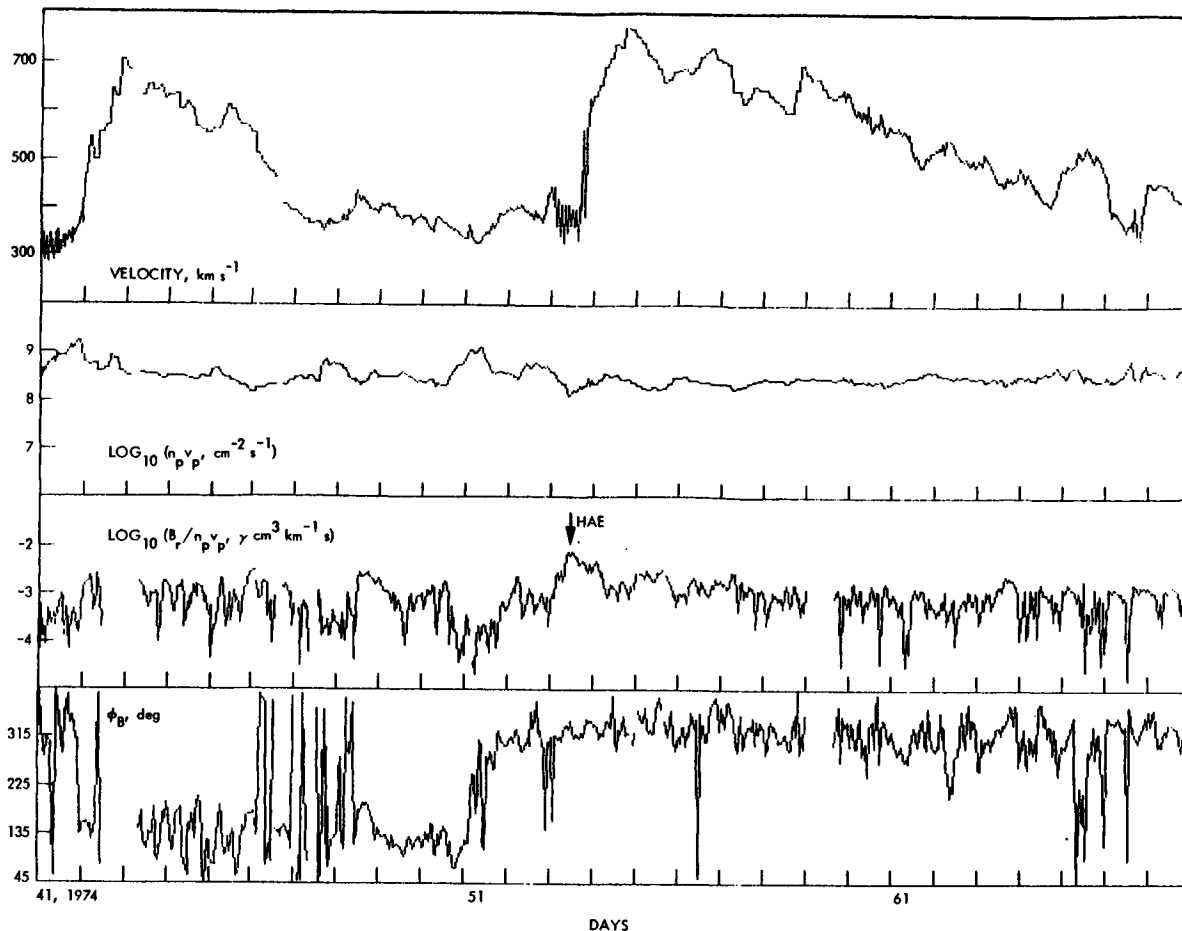
Figure 4. Hourly averaged data over one solar rotation to show the relation of variations in the parameter $B_r/n_p v_p$ to other solar wind features.

Superposed epoch plots of $B_r/n_p v_p$ for HAEs and sector boundaries are shown in Figure 3e. The similarity of the "all" and the "no stream" curves near the sector boundary is testimony to the invariance of this parameter through stream interactions. On the average, $B_r/n_p v_p$ peaks at about 2 (units of $10^{-3} \gamma cm^3 km^{-1} s$) in HAEs, 1.2 in coronal hole flows, and reaches a minimum near 0.2 at sector boundaries. It is tempting to interpret the local minimum in $B_r/n_p v_p$ near sector boundaries as evidence for field line reconnection, in keeping with suggestions by Bavassano et al. (1976) and Pilipp et al. (1981).

Table 2 presents a numerical summary of the differences between the three types of flow. For those parameters plotted in Figures 2 and 3, the zero epoch values have been tabulated. Theories of solar wind acceleration must explain why fast, hot flows come from coronal holes while slow, cool boundary flows come from coronal streamers. There are probably some relevant clues in the ratios T_p/T_e, β, $n_a v_a/n_p v_p$, and $B_r/n_p v_p$ and in the ionization states of heavy ions.

After 20 years of solar wind observations, the number of question marks in Table 2 is remarkable. Different measurements of heavy ion ionization temperatures in high speed flow from coronal holes yield conflicting results (see Section 6 of paper by Bame, this Volume). Studies of anisotropies and

double streaming in high speed streams have not differentiated between transient and coronal hole flows; I have assigned these properties to flows from coronal holes, perhaps incorrectly.

TABLE 2. Comparison of solar wind parameters in three types of flow

	HOLE	BOUNDARY	TRANSIENT
v, km/s	700	380	440
n, #/cm^3	4	15	10
nv, 10^8/cm^{2}s	3	5	5
nmv^2, dyne/cm^2	3	3	3
$nm(mv^2/2 + mMG/r)$, erg/cm^{2}s	2	2	2
T_p, 10^5 K	2.3	0.7	0.6
T_e, 10^5 K	1.0	1.3	0.5
$n_\alpha v_\alpha/n_p v_p$	.05	.02	.10
Ionization temperatures			
T_O, 10^6 K	?	2.1	up to 3.4
T_{Fe}, 10^6 K	?	1.6	up to 17
Q_e, 10^{-3} erg/cm^2/s	3	<3	1
B, γ	6	3	9
Field topology	Open	?	Closed
$\beta = 8\pi k T_p/B^2$	1	2	0.3
B_r/nv, 10^{-3} γ cm^{3}s/km	1	0.3	2
Internal state	Double streams	No double streams	?
	$T_{p\perp} > T_{p\|}$	$T_{p\perp} < T_{p\|}$	?
	$v_\alpha > v_p$	$v_\alpha \simeq v_p$	$v_\alpha \simeq v_p$
	$T_\alpha/T_p > 4$	$T_\alpha/T_p < 4$	?
	Strong strahl	Weak strahl	?

References

Bame, S. J., J. R. Asbridge, W. C. Feldman, and J. T. Gosling, Evidence for a structure-free state at high solar wind speeds, _J. Geophys. Res._, 82, 1487, 1977.

Bame, S. J., J. R. Asbridge, W. C. Feldman, E. E. Fenimore, and J. T. Gosling, Solar-wind heavy ions from flare-heated coronal plasma, _Solar Phys._, 62, 179, 1979.

Bame, S. J., J. R. Asbridge, W. C. Feldman, J. T. Gosling, and R. D. Zwickl, Bi-directional streaming of solar wind electrons 80 eV: ISEE evidence for a closed-field structure within the driver gas of an interplanetary shock, _Geophys. Res. Lett._, 8, 173, 1981.

Bavassano, B., M. Dobrowolny, and F. Mariani, Evidence of magnetic field line merging in the solar wind, _J. Geophys. Res._, 81, 1, 1976.

Borrini, G., J. T. Gosling, S. J. Bame, and W. C. Feldman, Helium abundance enhancements in the solar wind, _J. Geophys. Res._, 87, 7370, 1982.

Borrini, G., J. T. Gosling, S. J. Bame, W. C. Feldman, and J. M. Wilcox, Solar wind helium and hydrogen structure near the heliospheric current sheet: a signal of coronal streamers at 1 AU, _J. Geophys. Res._, 86, 4565, 1981.

Burlaga, L. F., K. W. Behannon, S. F. Hansen, G. W. Pneuman, and W. C. Feldman, Sources of magnetic fields in recurrent interplanetary streams, _J. Geophys. Res._, 83, 4177, 1978.

Feldman, W. C., J. R. Asbridge, S. J. Bame, and J. T. Gosling, High-speed solar wind flow parameters at 1 AU, _J. Geophys. Res._, 81, 5054, 1976.

Feldman, W. C., J. R. Asbridge, S. J. Bame, J. T. Gosling, and D. S. Lemons, Characteristic electron variations across simple high-speed solar wind streams, _J. Geophys. Res._, 83, 5285, 1978.

Feldman, W. C., J. R. Asbridge, S. J. Bame, E. E. Fenimore, and J. T. Gosling, The solar origins of solar wind interstream flows: near-equatorial coronal streamers, _J. Geophys. Res._, 86, 5408, 1981.

Fenimore, E. E., Solar wind flows associated with hot heavy ions, _Astrophys. J._, 235, 245, 1980.

Gosling, J. T., V. Pizzo, and S. J. Bame, Anomalously low proton temperatures in the solar wind following interplanetary shock waves -- evidence for magnetic bottles?, _J. Geophys. Res._, 78, 2001, 1973.

Hansen, S. F., C. Sawyer, and R. T. Hansen, K corona and magnetic sector boundaries, _Geophys. Res. Lett._, 1, 13, 1974.

Hirshberg, J., S. J. Bame, and D. E. Robbins, Solar flares and solar wind helium enrichments: July 1965 - July 1967, _Solar Phys._, 23, 467, 1972.

King, J. H., _Interplanetary Medium Data Book_, Rep. NSSDC 7704, NASA Goddard Space Flight Center, Greenbelt, MD, 1979.

King, J. H., _Interplanetary Medium Data Book, Supplement 1_, Rep. NSSDC 7904, NASA Goddard Space Flight Center, Greenbelt, MD, 1979.

Klein, L. W., and L. F. Burlaga, Interplanetary clouds at 1 AU, _J. Geophys. Res._, 87, 613, 1982.

Krieger, A. S., A. F. Timothy and E. C. Roelof, A coronal hole and its identification as the source of a high velocity solar wind stream, _Solar Phys._, 29, 505, 1973.

Krieger, A. S., A. F. Timothy, G. S. Vaiana, A. J. Lazarus, and J. D. Sullivan, X-ray observations of coronal holes and their relation to high velocity solar wind streams, _Solar Wind Three_, C.T. Russell, ed., p. 132, University of California, Los Angeles, 1974.

Levine, R. H., The relation of open magnetic structures to solar wind flow, J. Geophys. Res., 83, 4193, 1978.

Montgomery, M. D., J. R. Asbridge, S. J. Bame, and W. C. Feldman, Solar wind electron temperature depressions following some interplanetary shock waves: evidence for magnetic merging?, J. Geophys. Res., 79, 3103, 1974.

Munro, R. H., J. T. Gosling, E. Hildner, R. M. MacQueen, A. I. Poland, and C. L. Ross, The association of coronal mass ejection transients with other forms of solar activity, Solar Phys., 61, 201, 1979.

Ness, N. F., A. J. Hundhausen, and S. J. Bame, Observations of the interplanetary medium: Vela 3 and Imp 3, 1965-1967, J. Geophys. Res., 76, 6643, 1971.

Neugebauer, M., Measurements of the properties of solar wind parameters relevant to studies of its coronal origin, Space Sci. Rev., 33, 127, 1982.

Nolte, J. T., A. S. Krieger, A. F. Timothy, R. E. Gold, E. C. Roelof, G. Vaiana, A. J. Lazarus, J. D. Sullivan, and P. S. McIntosh, Coronal Holes as sources of solar wind, Solar Phys., 46, 303, 1976.

Palmer, I. D., F. R. Allum, and S. Singer, Bidirectional anisotropies in solar cosmic ray events: evidence for magnetic bottles, J. Geophys. Res., 83, 75, 1978.

Pilipp, W. G., R. Schwenn, E. Marsch, K.-H. Muhlhauser, and H. Rosenbauer, Electron characteristics in the solar wind as deduced from Helios observations, Solar Wind Four, H. Rosenbauer, ed., Max-Planck-Institut fur Aeronomie Report MPAE-W-100-81-31, p. 241, Katlenburg-Lindau, 1981.

Rosenbauer, H., R. Schwenn, E. Marsch, B. Meyer, H. Miggenrieder, M. D. Montgomery, K. H. Muhlhauser, W. Pilipp, W. Voges, and S. M. Zink, A survey on initial results of the Helios plasma experiment, J. Geophys. Res., 42, 561, 1977.

Schwenn, R., M. D. Montgomery, H. Rosenbauer, H. Miggenrieder, K. H. Muhlhauser, S. J. Bame, W. C. Feldman, and R. T. Hansen, Direct observations of the latitudinal extent of a high speed stream in the solar wind, J. Geophys. Res., 83, 1011, 1978.

Schwenn, R., H. Rosenbauer, and K. H. Muhlhauser, Singly ionized helium in the driver gas of an interplanetary shock wave, Geophys. Res. Lett., 7, 201, 1980.

Steinitz, R., and M. Eyni, Global properties of the solar wind. 1. The invariance of the momentum flux density, Astrophys. J., 241, 417, 1980.

Steinitz, R., Y. Klemens, and M. Eyni, Momentum flux density of the solar wind: invariance and the solar cycle, preprint, 1982.

Wilcox, J. M., and N. F. Ness, Quasi-stationary corotating structure in the interplanetary medium, J. Geophys. Res., 70, 5793, 1965.

Zwickl, R. D., J. R. Asbridge, S. J. Bame, W. C. Feldman, and J. T. Gosling, He^{+} and other unusual ions in the solar wind: a systematic search covering 1972-1980, J. Geophys. Res., 87, 7379, 1982.

Page intentionally left blank

THEORY OF SOLAR WIND ACCELERATION[*]

Egil Leer[†]

High Altitude Observatory, The National Center for Atmospheric Research[‡]

Abstract. We discuss the outflow of fully ionized hydrogen gas from magnetically open regions of the solar corona. The effects of changes in the coronal temperature and of energy addition to the flow beyond the coronal base on the proton flux and flow speed at 1AU are considered.

For a reasonable value of the base pressure we find an increase in the proton flux and a decrease in flow speed when the coronal temperature is increased. The asymptotic flow speed is smaller than the speed measured in high speed solar wind streams at 1AU.

The energy flux in the wind can be increased by adding energy beyond the coronal base. When the density and temperature at the base are held fixed and energy is added to the subsonic region of the flow the flux increases and the flow speed at 1AU generally decreases. Energy addition to the supersonic region does not change the proton flux, but the energy per particle and the flow speed at 1AU increase.

As one particular mechanism for energy addition we consider Alfven waves propagating outward from the coronal base. For small wave amplitudes, almost all the wave energy flux is added to the supersonic region of the flow. The increase in energy flux is much larger than the increase in proton flux, so the energy per particle and the flow speed at 1AU increase. The protron flux increases steadily with increasing wave amplitude, whereas the flow speed reaches a maximum when the wave velocity amplitude in the subsonic region is comparable to the thermal speed. For larger wave amplitudes the flow is driven primarily by waves, and the asymptotic flow speed decreases with increasing amplitude. We find that Alfven waves with a velocity amplitude of $20 kms^{-1}$ at the coronal base can drive high speed solar wind streams with a protron flux of 3.10^8 cm^{-2}s^{-1} and a flow speed of $600-800 kms^{-1}$ at 1AU if the coronal temperature is around $1.2.10^6 K$. For higher temperatures the proton flux is too large, and the flow speed at 1AU is too small compared to values observed in high speed streams. These results are not very sensitive to changes in flow tube geometry.

Page intentionally left blank

ROLE OF THERMAL CONDUCTION IN THE ACCELERATION OF THE SOLAR WIND

Stanislaw Olbert
Center for Space Research and Department of Physics
Massachusetts Institute of Technology
Cambridge, Massachusetts 02139

ABSTRACT

The thermal and suprathermal processes involving solar wind electrons are discussed from a theoretical point of view. A model for the electron distribution function, f_e, based on the solutions of the Boltzmann equation in Krook's approximation is outlined: the angular and energy dependences of f_e for various distances from the sun between the coronal base and the earth are presented with the express purpose of obtaining the radial profile of the heat flux generated by the suprathermals. The calculations take into account the effects of the morphology of the interplanetary magnetic field, the electrostatic polarization potential and coulomb scattering, but assume that, as far as the suprathermals are concerned, the effects of wave-particle interactions are negligible. This surmised knowledge of the heat flux allows us to solve the basic fluid-dynamical equations for the solar wind plasma as a whole along any given magnetic field line. The results, although containing a variety of idealizing assumptions, are in surprisingly good agreement with observations. In particular, the predicted density and temperature profiles for positive ions exhibit the characteristics of recent measurements, both in the corona (above the coronal holes) and between 0.3 and 1 A.U. (the Helios region). It is concluded that the suprathermal electrons play an important role in the formation and the dynamics of the solar wind.

1. Introduction

The discovery of Coronal Holes confirmed a belief of long standing that the stream structure of the solar wind in the steady state is closely related to the morphology of the magnetic field lines in the corona. The open field lines in the regions above the Coronal Holes serve as a nozzle for the coronal plasma to flow into the far regions of the Heliosphere. The high-velocity streams observed by various spacecraft can be thought of as originating in the central portion of a Coronal Hole above the coronal base (say, between 1.03 $r_\odot$ and 1.50 $r_\odot$). Enough information is now available to surmise empirical radial profiles of the macroscopic parameters of such high-velocity streams. Figures 1, 2, and 3 show, respectively, typical radial dependences of the interplanetary magnetic field, the plasma density and the electron and proton temperatures. Several features of these profiles merit special emphasis: 1) the radial component of the magnetic field, $\vec{B}$, between 1.03 $r_\odot$ and 2 $r_\odot$ decreases much more rapidly than the $(1/r^2)$ field of the spherical model; 2) the density above Coronal Holes is substantially lower than the average and exhibits a much steeper gradient; 3) the temperature of the core electrons can be approximated roughly by an empirical polytropic relation: $T_c \propto n^\beta$ where $\beta \simeq .185$ and n is the density; 4) the proton

temperature displays a strong correlation with the wind velocity (in particular, the high-velocity streams are characterized by high temperature protons). This last point deserves further elaboration: Helios data show that the proton temperature, T_p, in a high-velocity stream grows rapidly as one approaches the Sun and reaches about one million degrees at 0.3 A.U. This type of radial dependence of T_p precludes any possibility of a polytropic relation between T_p and n.

The above sketched features of the solar wind beg for a physical explanation. As a first step in this direction, we have initiated a "feasibility" study of a model that emphasizes the role of the suprathermal electrons in the heat conduction along any given field line. We have attempted to adhere to first principles and the empirical facts as much as possible, and purposely ignored the possible importance of any other ad hoc driving mechanism. In other words, we have attempted to answer the following question: Do the suprathermal electrons generate enough heat flux to drive a high-velocity solar wind? The following is the preliminary report of our findings to date.

2. Basic Equations for the Field-aligned Solar Wind Flow

We confine our discussion to a steady field-aligned flow along a radial tube of force emanating from the central portion of a given Coronal Hole and concern ourselves only with the inner region of the solar cavity (from 1.03 $r_\odot$ to 1 A.U.). This allows us to ignore the effects of the rotation of the Sun and the curvature of the field lines. Furthermore, we assume that the r-dependence of B is known on empirical grounds. Finally, except for the appearance of a new term for the heat flux, we take the basic MHD equations as valid. Using standard notation, (B for the magnitude of the magnetic field, V for the wind speed, ρ for the mass density, P for the thermal pressure of electrons and positive ions combined, and $\vec{q}$ for the heat flux vector) we have for the plasma as a whole:

$$\rho V = \alpha B \tag{1}$$

$$\rho V \frac{dV}{dr} = -\frac{dP}{dr} - \rho G \frac{M_\odot}{r^2} \tag{2}$$

$$\frac{3}{2} \rho^{5/3} V \frac{d}{dr} \left(\frac{P}{\rho^{5/3}} \right) = - \text{div } \vec{q} \tag{3}$$

where α is a streamline constant. Eq. (1) follows from conservation of mass (div($\rho\vec{V}$)=0) and magnetic flux (div $\vec{B}$=0). Equations (2) and (3) express

conservation of momentum and energy, respectively. Note that, since $\vec{q}$ is field aligned, one can replace div $\vec{q}$ by $\vec{B} \cdot \nabla$ ($\vec{q} \cdot \vec{B}/B^2$) or, for our geometry,

$$\text{div } \vec{q} = \frac{dW}{dr} \rho V \qquad (4)$$

where

$$W = \frac{q}{\alpha B} = \frac{q}{\rho V} \qquad (5)$$

If the function W is assumed to be a known function of the radial distance, r, or alternatively, of any of the dependent dynamical variables ρ, V, P, equations (1), (2) and (3) represent a closed system of equations for three unknowns: ρ, V and P. Two of these unknowns can be eliminated immediately. First, Equations, (2) and (3) yield the integral:

$$\frac{1}{2} V^2 + \frac{5P}{2\rho} - \frac{GM_\odot}{r} + W = \frac{1}{2} U^2 \qquad (6)$$

where U is a streamline constant representing the asymptotic value of the wind speed. Equation (6) allows us to eliminate P in terms of remaining variables. Secondly, Equation (1) allows the elimination of, say, V in favor of ρ. We obtain after some algebra, the following first-order differential equation for ρ:

$$\frac{r}{\rho} \frac{d\rho}{dr} = \frac{H(\rho, r)}{L(\rho, r)} \qquad (7)$$

where

$$H = \frac{3r dB}{B \ dr} \left(\frac{\alpha B}{\rho}\right)^2 + \frac{3 GM_\odot}{r} \qquad (8)$$

$$L = 4\left(\frac{\alpha B}{\rho}\right)^2 + 2W + 2\rho \frac{dW}{d\rho} - \frac{2GM_\odot}{r} - U^2 \qquad (9)$$

In Section 4, we shall explain the procedures which we used to construct an explicit form of W as a function of ρ. For the present, we need only the result. Figure 4 shows the (dimensionless) quantity W/U^2 plotted versus electron density n_e; it has been computed under the assumption that $\alpha^2 = 2.4 \times 10^{-23}$ g/cm^3, $U^e = 700$ km/sec and that B of Figure 1 may be approximated by the empirical formula:

$$B = 2.2 \; (\frac{r_s}{r})^2 \sqrt{1+47 \; (\frac{r_s}{r})^6} \quad \text{(gauss)} \tag{10}$$

where $r_s \equiv 1.03 \; r_\odot$.

For the purpose of numerical integration of Equation (7), we found it convenient to represent W in Figure 4 by an analytical formula:

$$\ln(\frac{W}{W_0}) = 0.0514 \; \ln(\frac{\rho}{\rho_0}) + 2.87 \; erf(0.2 \; \ln \frac{\rho}{\rho_0}) \tag{11}$$

where $\rho_0 \simeq 10^{-22}$ g/cm^3 and $W_0 \simeq 10^4$ (km/sec)^2

3. Numerical Calculations of (ρ, V, P) profiles

Detailed analytical study near the critical point of Equation (7) (i.e., the radial distance r_c at which H=L=0) has shown that Equation (7) allows a two-branch solution through r_c: one for the accretion and one for the outflow. The topology of the solution in the neighborhood of the critical point is analogous to that of the polytropic Parker model. Figure 5 shows the density profile corresponding to the outflow with U=700 km/sec. A comparison of Figure 2 data referring to the high-velocity streams (lower segments of the n_e curves) reveals an excellent agreement with the curve of Figure 5. Once the density profile is obtained, it is a simple matter to compute the remaining profiles for V and P. Figure 6 shows the wind-speed profile based on Equations (1) and (10) and Figure 7 shows the quantity:

$$T_{eff} = \frac{P}{2kn_e} \tag{12}$$

Since $P \simeq k(n_e T_c + n_p T_p + n_\alpha T_\alpha)$ (n_α and T_α indicate the number density and the temperature of the α-particles, respectively) - T_{eff} may be interpreted as the "effective" temperature of a high-velocity stream. A comparison of the T_{eff} -curve with the combined data for T_c, T_p and $T_\alpha \simeq 4T_p$ in the explored region of the heliosphere (r > 0.3 A.U.) shows a surprisingly good agreement both in slope and the levels of the ion temperatures. The agreement is improved further when a (relatively minor) correction for the presence of the Alfvén-wave pressure is made in the expression for P. Of course, the unexpected result of our calculations lies in the unexplored region (2 $r_\odot$ < r < 0.3 A.U.): T_{eff} exhibits a rise with a maximum of 2.5×10^6 °K at 9 $r_\odot$. Since the core-electron temperature in our model decreases monotonically with r (see next section) and thus at 9 $r_\odot$ is substantially lower than 2.5×10^6 °K, one is forced to conclude that the model requires surprisingly high proton and α-particle temperatures in the outer

152

regions of the corona. We must stress that if one accepts the form of the heat flux used in the calculations, this conclusion is forced upon us by nothing else but the basic laws of conservation of mass, momentum and energy. Since our form of the heat flux predicts correct density profiles of the high-velocity streams, we find the conclusion inescapable.

4. Heat Flux Calculations

We now outline briefly the method and the steps that we have taken to arrive at the result shown in Figure 4. Space limitation does not allow us to go into detail but only to mention that one can develop a variety of cogent arguments demonstrating that the conventional theory for heat conduction in collision dominated plasma (e.g., Spitzer's theory) is not applicable to any portion of the solar corona. The traditional Fourier law ($q_{\shortparallel}$ =-$K\nabla_{\shortparallel}T$) breaks down right at the base of the corona where $T \simeq 10^6$ °K and $n_e \simeq 10^8$ cm^{-3}. This is so in spite of the fact that the coulomb mean free path (mfp) of thermal electrons, $\bar{\lambda}_c$, at the base is still very small compared to the solar radius ($\bar{\lambda}_c \simeq 10^{-3}$ $r_\odot$). The main reasons for it are: a) the mfp grows rapidly with the electron energy (a suprathermal electron of 7kT has a mfp 50 times larger than $\bar{\lambda}_c$); b) the steep density gradient above Coronal Holes leads to a short scale height H (H $\simeq$ 0.1 $r_\odot$); c) small H leads to a rapid development of skewness in the distribution function of suprathermals; and d) the forward skewness of suprathermals is fostered by the paucity of collisions and the open line morphology of the rapidly decreasing magnetic field. For these reasons, any perturbation method relying on the smallness of the Knudsen number ($\bar{\lambda}_c$/H) will lead to erroneous results concerning the physical characteristics of the heat flux. The reader is invited to read more on this in the paper presented by J. Scudder during these proceedings.

There seems to emerge from these types of considerations a clear cut possibility: the suprathermals may carry enough heat to drive the solar wind. To check this in a quantitative manner we saw no way out but to rely on the first principles of the plasma kinetic theory, i.e., to evaluate first the electron distribution function, f_e, at various points along some given tube of force and then by direct numerical integration compute the heat flux at these points. Since the solution of the Boltzmann equation for f_e in its more rigorous form (say, in the Fokker-Planck approximation) is prohibitively difficult, we have opted for the Krook's approximation which, although not as accurate as the Fokker-Planck approximation, is on physical grounds far superior to any perturbation method (such as that of Chapman and Enskog).

First, let us list the simplifications that can be made in the general Boltzmann equation. We are interested in the distribution function, f_e, of transthermal and suprathermal electrons. For these electrons, the proper plasma frame and the inertial heliocentric frame of reference practically coincide. The gravitational effects are negligible. Moreover, f_e is gyrotropic, i.e., in the steady state, f_e is a function of only three variables: radial distance r, the speed v and pitch angle θ. With these stipulations, f_e (r,v,θ) obeys the following equation:

$$v \cos\theta \frac{\partial f_e}{\partial r} - \frac{eE_{\shortparallel}}{m_e} \cos\theta \frac{\partial f_e}{\partial v}$$

$$+ \left(\frac{eE_{\shortparallel}}{m_e} + \frac{v^2}{2B} \frac{\partial B}{\partial r}\right) \frac{\sin\theta}{v} \frac{\partial f_e}{\partial\theta} = -\frac{f_e - f_M}{\tau} \tag{13}$$

where $E_{\shortparallel}$ is the component of the electric field parallel to $\vec{B}$ and is related to "interplanetary polarization potential", ϕ, by $E_{\shortparallel} = -d\phi/dr$; τ is the mean coulomb collision time for momentum transfer and is given by

$$\frac{1}{\tau(r,v)} = \xi \frac{4\pi e^4 n_e \ln\Lambda}{m_e^2 v^3} \tag{14}$$

In our case the numerical factor $\ln\Lambda \simeq 25$ and ξ is of order of unity. For the "source function" f_M, which coincides approximately with that of the distribution of the core electrons, we adopt a maxwellian form

$$f_M(r,v) \simeq \frac{n_e}{\pi^{3/2} w_c^3} e^{-v^2/w_c^2} \tag{15}$$

where w_c is the thermal speed related to the temperature, T_c, of the core electrons by $m_e w_c^2 = 2kT_c$. Note that the number density, n_e, and w_c are functions of r. Other forms for f_M, compatible with observations of thermal and subthermal electrons, may be chosen to improve the description of the electron transport. The reader will find more on this in the aforementioned report by J. Scudder. Since the brunt of the dynamical processes shaping the evolution of the solar wind takes place in the coronal region, we are primarily concerned about the adequacy of Equation (15) in that region. Since in the limit of τ being very small f_e should approach a maxwellian form, Equation (15) ought to represent a reasonable first step in an iteration process to which Equation (13) could be subjected. Note that in the limit of a very large τ (collisionless plasma) Equation (13) has a well known general solution

$$f_e = \psi(E,\mu) \tag{16}$$

where ψ is any appropriately chosen function of the two constants of motion:

$$E = \frac{1}{2} m_e v^2 - e\phi; \quad \mu = \frac{m_e v^2 \sin^2\theta}{2B} \qquad (17)$$

Not much is known about f_e for finite τ's. But it turns out that Equation (13) can be integrated formally for any given form of f_M and τ by methods of characteristics. If one confines oneself to the particle trajectories in the forward direction ($0 \leq \theta \leq 90°$) one finds:

$$f_e(r,v,\theta) = f_M(r,v) - \int_{r_o}^{r} \frac{df_M(r',v')}{dr'} e^{-p(r,r';v,\theta)} dr' \qquad (18)$$

where

$$v' = \sqrt{v^2 + \frac{2e}{m_e}(\phi(r') - \phi(r))} \qquad (19)$$

and

$$p(r,r';v,\theta) = \int_{r'}^{r} \frac{dr''}{\tau(r'',v'')v''\cos\theta''} \qquad (20)$$

In Equation (20) v'' is given by Equation (19) upon replacing r' by r''

and

$$\cos\theta'' = \sqrt{1 - \sin^2\theta \frac{B(r'')v^2}{B(r)v''^2}} \qquad (21)$$

Note that, for a fixed r, v and θ, Equation (21) imposes a lower limit r_m on r' given implicitly by the equation:

$$\frac{v_m^2}{B(r_m)} = \sin^2\theta \frac{v^2}{B(r)} \qquad (22)$$

where v_m is given by Equation (19) upon replacing r' by r_m; r_m is the point where $\theta'' = 90°$, i.e., the mirror point of the trajectory. This implies that care must be taken while evaluating Equation (18) that the inequality chain:

$$r_o \leq r_m \leq r' \leq r'' \leq r \qquad (23)$$

155

be not broken; r_0 identifies the boundary of the onset of the outward heat flow. The precise value of r_0 cannot be ascertained, but it ought to fall somewhere between 1.03 $r_\odot$ and 1.30 $r_\odot$; fortunately, f_e for $r > 2$ $r_\odot$ is not sensitive to r_0. The explicit numerical evaluation of Equation (18) requires the knowledge of n_e, T_c, ϕ and B as functions of r. We made the following choices:

$$n_e(r) = n_1 \exp[13.25 - 5.50 \ln \frac{r}{r_s} + 3.50 \sqrt{(\ln \frac{r}{r_s} - 0.82)^2 + .79}] \qquad (24)$$

$$T_c(r) = T_1 (\frac{n_e}{n_1})^\beta \qquad (25)$$

$$\phi(r) = \omega k T_c; (\omega = 1 + \frac{1}{\beta}) \qquad (26)$$

B is assumed to be given by Equation (10)

and $\qquad\qquad \beta = 0.185, \; T_1 = 8 \times 10^4 \; °K, \; n_1 = 2 \; cm^3.$

In constructing formulas (24) and (25) we were guided by the observational data referring to the high-velocity streams. Equation (24) reproduces well the Coronal Hole and the high speed profiles of Figure 2. Equation (25) agrees with the dashed curve in Figure 3 and the empirical findings of Sittler and Scudder; its validity in the solar corona must remain at the present moment an open question although the numerical values it offers in the inner corona are not in contradiction with the observational estimates. Equation (26) is primarily based on theoretical considerations involving the generalized Ohm's law; for our purposes, it is in a sufficiently good agreement with the findings of other authors; but again, its validity in the inner corona must remain an open question.

The entire subject matter of finding self-consistent functional relations between n_e, T_c and ϕ from the first principles is still unresolved. It is a subject of current investigations by Dr. Scudder and myself.

"Armed" with the empirical formulas (24) through (26), we are in a position to evaluate f_e as a function of v and θ, for various values of r. Since the computer costs involving this project have proven to be very high, we had to confine ourselves to only six values of r (r/r_s = 1, 2, 4.7, 16, 63 and 208). Figures 8, 9, 10 and 11 show the forward portions of the contours of constant f_e plotted in the velocity space for r/r_s=2,4.7,16 and

156

and 63. Note that the coordinates are $v_\shortparallel$ and $v_\perp$ measured in terms of the local thermal speed, i.e., the horizontal coordinate is $v \cos\theta/w_c$ and the vertical coordinate is $v \sin\theta/w_c$. The ratio of the values of f_e of two neighboring contours is $\sqrt{10}$; the outermost (lowest value) contour corresponds to $f_e = 8\times10^{-31}$ $(sec/cm^2)^3$. As one proceeds outward from the Sun one witnesses a gradual evolution of a highly skewed, forward "strahl", very much like the strahl observed onboard Helios spacecraft. There are various other features in the distribution that are of potential value from the plasma-theoretical point of view; e.g., the development of a col in the transthermal region of the velocity space. Such cols are sources of various plasma waves which in turn affect the thermal electrons. Clearly, the results shown here open up a new area of future investigations.

We have not computed the backward portions of the distribution function $(90° < \theta < 180°)$ for the simple reason that we believe that f_e cannot develop any significant backward "strahl" and, for the purposes of the heat flux calculations, may be approximated by a maxwellian form for all speeds.

The knowledge of f_e allows us to compute the heat flux q at various values of r. We have

$$q(r) = \pi m_e \int\int v^5 \cos\theta \, f_e(r,v,\theta) \sin\theta \, d\theta \, dv \qquad (27)$$

Because of the complexity of f_e as a function of v and θ, the double integration required to obtain q is enormously expensive and we had to confine ourselves to the six r-values quoted above. Thus, the entire effort leaves us with only six numbers which must serve us as "beacons" for the construction of the curve shown in Figure 4. Needless to say, we had to take some liberties to perform the necessary interpolation leading to the results shown in Figure 4.

Finally, we should like to comment why we have chosen to represent the function $W=q/(\alpha B)$ as a function of density rather than as a function of distance. Firstly, purely on practical grounds, it is more economical to evaluate f_e when one replaces the integration variable r' in Equation (18) by $n_e(r')$ or $T_e(r')$ via Equation (24) or (25). Secondly, the dependence of W on r is primarily predicated by its dependence on n_e. Thus, on physical grounds, it is more instructive to know W as a function of n_e rather than as a function of the arclength along a specific field line. This does not mean to imply that W may be looked upon as a unique function n_e for all field lines. On the contrary, our calculations show that q is quite sensitive to the behavior of the magnetic field. Since the possibility for relating B to n_e by some theoretical "law" is quite remote, we must treat B and n_e as separate entities and thus regard W as a function of n_e and B.

5. Summary

Our preliminary calculations show that the heat flux generated by the suprathermal electrons plays an important role in the dynamics of the solar

wind. In fact, there is a possibility that it might account entirely for the salient features of steady, pure high-velocity streams. Of course, more work is required to resolve the issue, but we believe that the initial results presented here invite such work as worthwhile.

FIGURE CAPTIONS

Figure 1: Typical radial profile of the interplanetary magnetic field, $\vec{B}$. Except for the shaded area near the Sun, the curves are based on Parker's spiral model and are in agreement with observations averaged over fluctuations.

Figure 2: Typical radial profiles of the electron number density, n_e, in the solar wind. The curves were constructed from a variety of observational sources. The two lower segments labeled "density above polar Coronal Hole" and "fast streams" are characteristic of the central portion of a high-velocity stream.

Figure 3: Typical radial profiles of proton and electron temperatures in the solar wind. The solid curves represent the scalar proton temperature, $T_p=(1/3)(2T_\perp + T_\parallel)$, for three adjacent intervals of the wind speed, I, II and III. The dashed curve refers to the core electron temperature, T_c; the dot-dashed curve, labeled T_H, represents $7T_c$ and is meant to indicate the domain of the suprathermals. Except for the tentative markings near the Sun, the plots are a "smoothed out" version of the Helios and Voyager data.

Figure 4: The heat conduction W, measured in terms U^2 and plotted versus electron number density, n_e; W is related to the heat flux q by: $W = q/(\rho V) = q/(\alpha B)$. See text for the definition of symbols and the theoretical considerations leading to this plot. (The arrow labeled C.P. indicates the position of the critical point).

Figure 5: Calculated radial profile of the electron number density, n_e. The curve represents the "critical" solution of Equation (7) (see text) and should be compared with the lower segments of the data of Figure 2.

Figure 6: Calculated radial profile of the wind speed, V. The curve is computed from $V = \alpha B/\rho$ using the result shown in Figure 5. The point labeled C.P. indicates the position of the critical point.

158

Figure 7: Calculated radial profile of the "effective temperature" of a high-velocity stream (see text for the definition of T_{eff} and P).

Figure 8: Contours of constant electron distribution function, f_e, plotted in the velocity space for $r = 2r_s$. The horizontal (vertical) coordinate represents the parallel (perpendicular) component of the electron velocity measured in terms of the local thermal speed, w_c. The ratio of two neighboring contours is $\sqrt{10}$; the outermost (lowest) contour represents $f_e = 8\times10^{-31}$ $(sec/cm^2)^3$. The figure implies gyrotropy and shows only the forward portion of f_e $(0° \leq \theta \leq 90°)$; $r_s = 1.03$ $r_\odot$.

Figures 9, 10 and 11: Same as Figure 8 but referring, respectively, to $r/r_s = 4.7$, 16 and 63.

Fig. 1

Fig. 2

Fig. 3

Fig. 4

160

Density Profile

[High Velocity Stream]

coronal base

1 A.U.

$r/(1.03r_\odot)$

Fig. 5

High Wind Velocity Profile

coronal base

1 AU

$r/(1.03r_\odot)$

Fig. 6

Effective Temperature Profile

[High Velocity Stream]

$$T_{eff}^{calc.} = \frac{P}{ikn_e}$$

coronal base

1 AU

$r/(1.03r_\odot)$

Fig. 7

$\bar{u} = 2\bar{u}_c$

$\frac{u_\perp}{u_c}$

$\frac{v_\parallel}{u_c}$

Fig. 8

Fig. 9 — $\kappa = 4.7 \kappa_s$

Fig. 10 — $\kappa = 16 \kappa_s$

Fig. 11 — $\kappa = 63 \kappa_s$
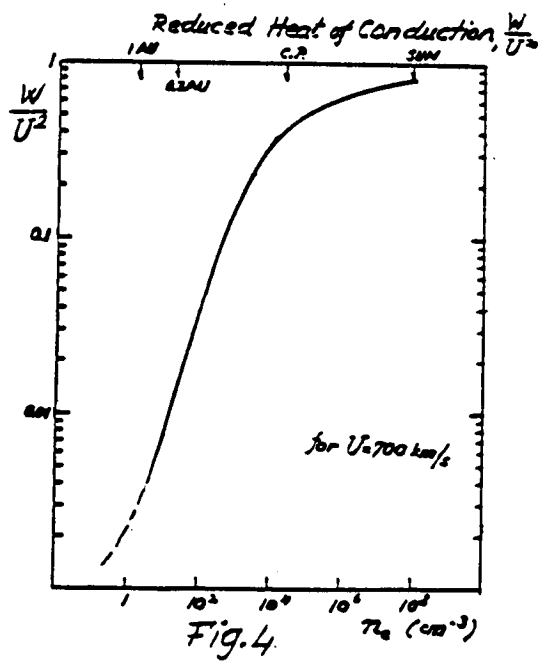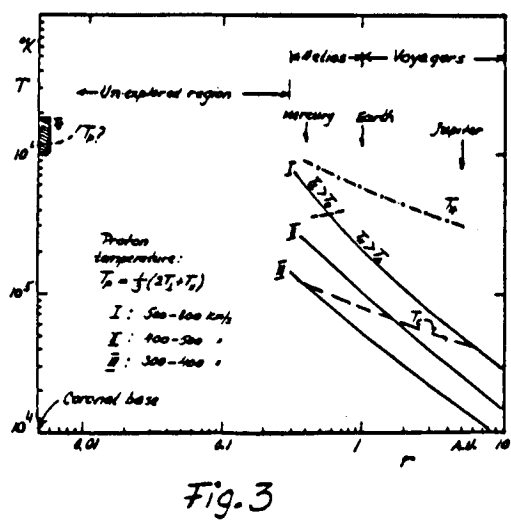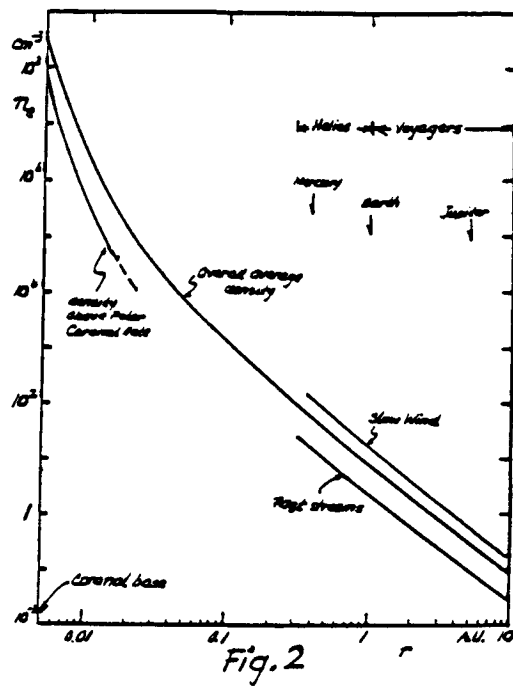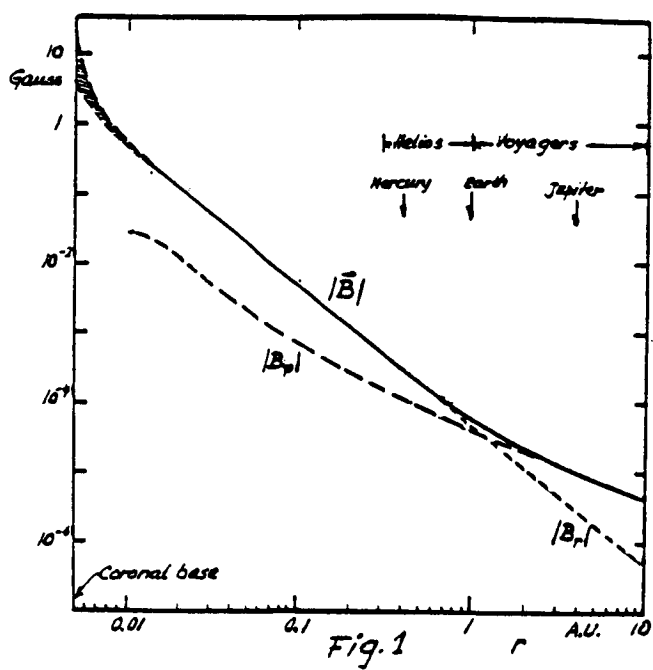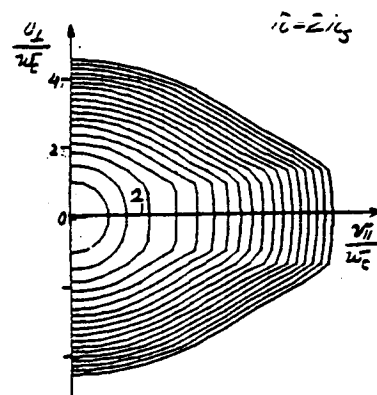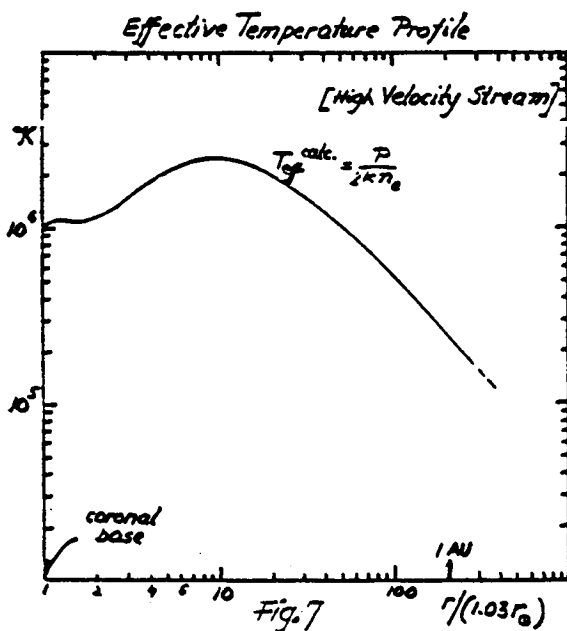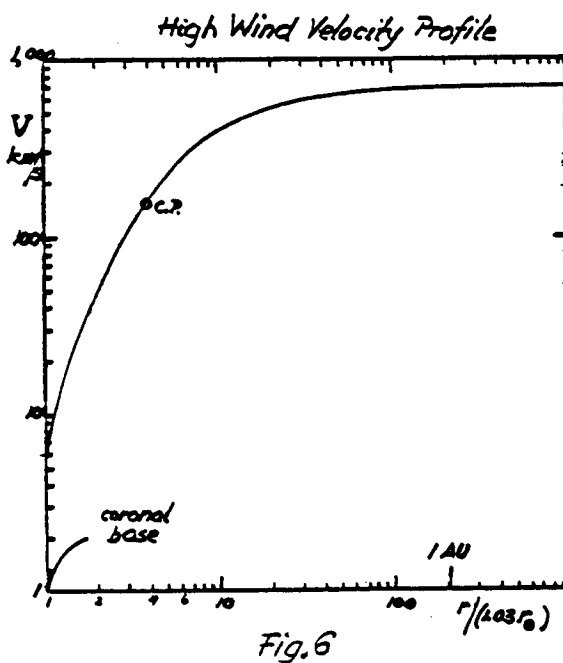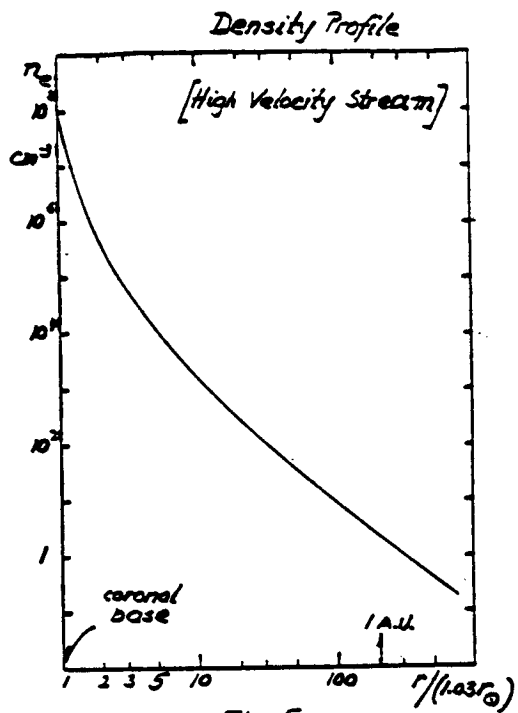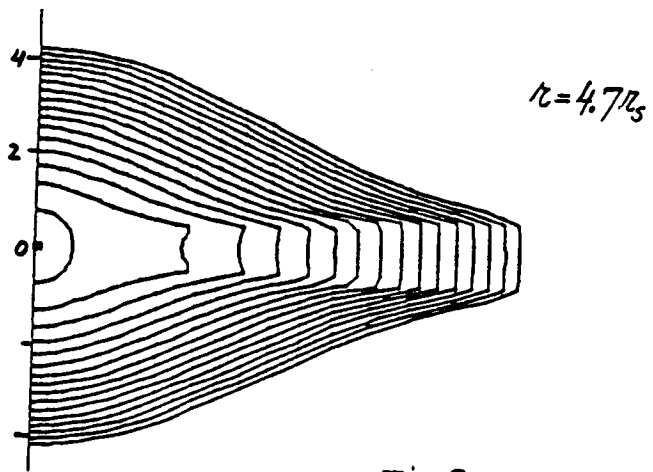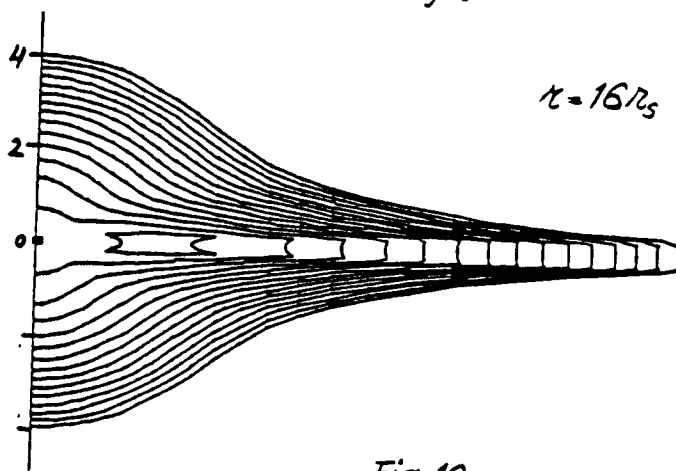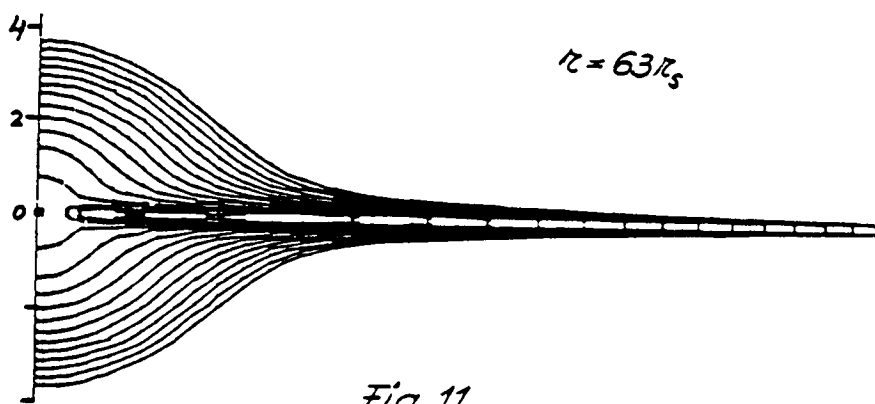
THE COLLAPSE OF THE LOCAL, SPITZER-HÄRM FORMULATION AND A GLOBAL-LOCAL GENERALIZATION FOR HEAT FLOW IN AN INHOMOGENEOUS, FULLY IONIZED PLASMA

Jack D. Scudder
NASA/Goddard Space Flight Center
Laboratory for Extraterrestrial Physics
Greenbelt, MD 20771

Stanislaw Olbert
Department of Physics and
Center for Space Research
Massachusetts Institute of Technology
Cambridge, MA 02139

ABSTRACT

This paper addresses the breakdown of the classical (CBES) field aligned transport relations for electrons in an inhomogeneous, fully ionized plasma as a mathematical issue of radius of convergence, defines for the first time the finite Knudsen number conditions when CBES results are accurate, and presents a global-local (GL) way to describe the results of Coulomb physics moderated conduction that is more nearly appropriate for astrophysical plasmas. This paper shows the relationship to and points of departure of the present work from the CBES approach. It also presents an analytical, more tractable, and economical way of evaluating the global aspects of the collisional physics than has been done numerically in the previous paper. The CBES heat law in current use is then shown to be an especially restrictive special case of the new, more general GL result. A preliminary evaluation of the dimensionless heat function discussed in the previous paper (Olbert, (1983)), but using analytic formulas, as presented below, shows that the dimensionless heat function profiles versus density of the type necessary for a conduction supported high speed solar wind appear possible.

Introduction

It has long been recognized that the Chapman (1916)-Chapman and Cowling (1939)-Braginskii (1965)-Enskog (1917)-Spitzer-Härm (1953)-Spitzer (1962) (CBES) transport results become unreliable when the Knudsen number, K, (a kinetic free path over macroscopic scale length) is not small. A serious outstanding issue in this regard is how small must K be in order that these transport formulas are accurate. This difficulty plagues the theoretical investigation of conduction supported, fully ionized stellar winds. The usual interpretation of this breakdown is that relevant physics has been omitted. Wave particle effects are often suggested to be important in these locales. However, this conclusion is not inescapable. Subtle prejudices have, until now, led to the insistence that the physics of these regions must remain local, even if wave particle effects must be invoked to do this. These assumptions are largely shaped by our everyday experience and are fortified by attendant mathematical convenience. The physics of Coulomb moderated transport is not amenable to this ad hoc approach as we have previously shown (Scudder and Olbert 1979a,b, SO I, II, Olbert (1983)).

Since electrons carry almost all the heat flux in a plasma the kinetic discussion that follows is oriented toward electron transport signatures. Because

the bulk flows of astrophysics are usually smaller than characteristic electron thermal speeds certain dimensionless ratios are tailored for this electron situation. Unless specifically stated otherwise we will refer to electron kinetic properties for the remainder with the major exception of the plasma conservation equations where certain results pertain to the fluid as a whole. Because astrophysical plasmas are strongly "magnetized" we confine our attention to field aligned transport signatures.

1. The CBES Postulates

The CBES transport description for electrons proceeds under the interlocking postulates

1) that the microscopic electron velocity distribution in the proper frame, $f_e(\underline{w})$, that solves the kinetic equation is separable into a sum of two terms:

$$f_e \overset{CBES}{=} f_e^o + \delta f_e(K) \qquad (1)$$

such that all finite free path effects are solely contained in the Knudsen number, K, functional dependence of δf;

2) that the velocity dependence of $f_e^{(o)}$ is only through proper frame speed $w \equiv |\underline{w}|$;

3) that f_e^o is a local Maxwellian distribution:

$$f_e^o(\underline{x}) \overset{CBES}{=} n_e(\underline{x}) \left(\frac{m_e}{\pi\, 2kT_e(\underline{x})} \right)^{3/2} \exp\left(- \frac{m_e w^2}{2kT_e(\underline{x})} \right) \qquad (2)$$

(where k is Boltzman's constant, n, T, and m are the local density, temperature and mass, respectively);

4) that δf_e is a perturbation of $f_e^{(o)}$ such that

$$\frac{\delta f_e(\underline{w})}{f_e^o(\underline{w})} = O(K), \qquad (3)$$

for a sufficiently broad range of speeds to control the transport signature sought; and

5) that the perturbation ordering parameter is the Knudsen number, K, which is assumed infinitesimal and defined as the ratio of a kinetic scale, λ, to a macroscopic scale, L_M. The macroscopic length L_M, defined by

$$L_M^{-1} = \left| \frac{d}{ds} \ell n\, M \right|, \qquad (4)$$

is the shortest scale length along the arc length s of the magnetic field among the macroscopic variables, M: density, n, temperature, T, magnetic field

strength, B, or bulk speed, U. In the astrophysical context L_M is usually set by the density profile; we assume this in the remainder. The kinetic scale, λ, is strongly speed dependent in a plasma. It is usually chosen as that spatial length within which substantial isotropization and approach to a Maxwellian takes place. Those two physical time/length scales are commensurate (cf. Spitzer, 1962, p. 133) for particles with speeds $w_{T,e}$ equal that

of the root mean square speed $\sqrt{\dfrac{3kT_e}{m_e}}$. Spitzer (1962) defines the related

characteristic time, t_c, (eqtn 5-26) for this process for electrons to yield a Spitzer kinetic scale free path of the root mean square (rms) electron,

$$\lambda_{rms} \equiv w_{T,e} \, t_c \, (w_{T,e})$$
$$= \frac{(3kT_e)^2}{8(0.714) \, \pi n e^4 \, \ell n \, \Lambda} \, , \tag{5}$$

where $\ell n \, \Lambda$ is the Coulomb logarithm. Braginskii (1965) defines "the electron... collision time" with a formula (cf. 2.5e) that differs from Spitzer's by 3%. According to this practice "the Knudsen number" defined by

$$K \equiv \frac{\lambda_{rms}(w_{T,e})}{L_n} \tag{6}$$

appears as the dimensionless parameter for the plasma style Chapman-Enskog expansion.

The CBES approach attempts a perturbation expansion for δf_e of the form

$$\delta f_e^{CBES} = \mathcal{F}(L_n/L_{Te}, \, L_n/L_U, \, L_n/L_B, \, n, \, T_e, \, U, \, \underline{w}) \, K + 0 \, (K^2), \tag{7}$$

and the approximation is usually truncated with the first term in (7). Note that the structure of $\mathcal{F}$ depends only on the velocity space w, on local macroscopic variables and ratios L_n/L_M of the scale length of the density to those of other macroscopic variables evaluated at the point $\underline{x}$. Consequently $\mathcal{F}$ is independent of K.

The CBES truncation (7) of δf_e translates immediately into a similar truncation of a Maclaurin series for $Q_{\shortparallel}$ since

$$Q_{\shortparallel} \equiv \int\!\!\int\!\!\int \, (f_e^{(o)} + \delta f_e) \, 1/2 \, m_e \, w^5 \, \cos\theta \sin\theta \, d\theta \, d\phi \, dw. \tag{8a}$$

By postulate (2) $f_e^{(o)}$ is even in velocity space so that (8a) reduces to

$$Q_{\shortparallel} = 0 + \int\!\!\int\!\!\int \, (\delta f_e) \, 1/2 \, m_e \, w^5 \, \cos\theta \sin\theta \, d\theta \, d\phi \, dw. \tag{8b}$$

Using equation (7) we obtain

$$Q_{\shortparallel} \approx K \int\!\!\int\!\!\int \mathcal{F}^{CBES} \, 1/2 \, m_e \, w^5 \, \cos\theta \sin\theta \, d\theta \, d\phi \, dw. \tag{8c}$$

The remaining CBES postulates allow a reduction of (8c) to functional dependence on lower order moments; this permits a heat law for the fully ionized plasma, parallel to Fourier's law, that permits closure, viz:

$$Q_\parallel^{CBES} \propto 0 + \mathcal{X}_0 T_e^{5/2} \frac{dT_e}{ds} \tag{9a}$$

which is easily rewritten as the <u>infinitesimal</u> heat flux

$$Q_\parallel^{CBES} \simeq [\frac{\mathcal{X}_0 T_e^{7/2}}{\lambda_{rms}} \frac{L_n}{L_{Te}}] K, \tag{9b}$$

where for a proton-electron plasma (Spitzer (1962))

$$\mathcal{X}_0 = (0.419)(0.225) 20 (\frac{2}{\pi})^{3/2} \frac{k^{7/2}}{m_e^{1/2} e^4 \ell n \Lambda}. \tag{10}$$

Notice that the flow of heat in the CBES approach (8c) arises out of the non-zero <u>perturbative</u> correction to adiabatic ($Q_\parallel = 0$) behavior.

If the assumptions made to derive (9) are violated this marks the failure of a mathematical artifice: a simple, straightforward Maclaurin series perturbation scheme. It is, for example, well known that the Chapman-Enskog scheme does not provide access (even in principle) to the broadest class of solutions to the Boltzmann equation (Grad (1958)). Coulomb moderated transport effects are unavoidably present, but inaccessible within the CBES mathematical machinery. Extensions of the CBES approximation after the form of Burnett and others are analogous to attempts to enhance the radius of convergence of the Maclaurin series for the velocity distribution function, f(w), and, therefore $Q_\parallel$ beyond those in equation (9) by retaining additional terms in the power series. These procedures are cumbersome. This is made clear by looking at a mathematical model of the perturbation issues at hand.

2. Model Perturbation Issues and their Resolution

Consider a system whose physical behavior is exactly described by the following function

$$g(K) = \tanh(K). \qquad K > 0 \tag{11}$$

[In the heat transport problem the exact $g(K) \alpha Q_\parallel(K)$ is an unknown solution of an integro-partial differential equation]. If a description of the physical system were desired for the $K \ll 1$ regime a one term Maclaurin series expansion for $\tanh(K)$ would yield nearly indistinguishable results for $g(K)$, viz

$$g(K) \sim g^{(1)}(K) \equiv K \qquad K \ll 1 \tag{12}$$

(In our model problem $g^{(1)}(K)$ is proportional to $Q_\parallel^{CBES}$.) If equation (11) (the solution of the integro-differential equation) is the complete and accurate description of the physical system even for large K, the fact that $g^{(1)}(K)$ is inaccurate as K gets large implies nothing about the completeness of the physics embodied in equation (11).

166

To parallel the multi-term expansion of $f(\underline{w})$, and, therefore $Q_{\shortparallel}$, in the higher moment methods, consider additional truncated Taylor expansions $g^{(n)}(K)$ for $g(K)$

$$
\begin{aligned}
g_{(1)}^{(1)}(K) &= K, \\
g_{(2)}^{(2)}(K) &= K - K^3/3, \\
g_{(3)}^{(3)}(K) &= K - K^3/3 + 2K^5/15, \\
g_{(4)}^{(4)}(K) &= K - K^3/3 + 2K^5/15 - 17K^7/315.
\end{aligned}
\tag{13}
$$

Any finite truncation $g^{(n)}$ of g chosen in (13) is a polynomial in K which must diverge for large K in contradiction to the boundedness of $g(K)$ as $K \to \infty$. In any case the Maclaurin series for $g(K)$ of course diverges for $K > \pi/2$. This result is known because the full Maclaurin series of $g(K)$ is in hand. Clearly $g^{(\infty)}$ is a desperate way to approximate g — even for $K < \pi/2$. In constructing perturbation solutions that approximate $Q_{\shortparallel}$ the full expansion analogous to (13) is not available. The finite radius of applicability of the CBES expression for $Q_{\shortparallel}$ needs to be defined as we do below for the first time. It is quite common in non-linear, physical problems that boundedness of certain quantities such as total energy or the magnitude of the heat flow regardless of the size of K available impacts the forms of perturbation that are allowed and drive the physicist to seek

more tractable approximations such as $g^{(p)}$ provides for g regardless of K described below. As such, this feature of this model is realistic.

The inapplicability of $Q_{\shortparallel}^{CBES}$ in the finite Knudsen number regime is essentially a failure of the above type: namely of a straightforward, local, one term, Maclaurin series expansion in K. (Recall that elementary discussions of heat flow e.g., Reif (1965) give intuitive derivations based on the energy flux imbalance across a mean free path element of the medium centered on the observer.)

Different kinds of perturbation expansions (c.f., e.g., Baker (1975)) are possible that attempt to bridge asymptotic regimes in a way that truncated Taylor series cannot. An example of this for the model problem is to use a Padé approximant (which is by no means unique!) for $g(K)$ given by

$$
g^P(K) = \frac{K + cK^2 + dK^3}{1 + aK + bK^2 + dK^3}, \quad K > 0,
\tag{14}
$$

with a, b, c, and d, chosen to optimize the approximation for intermediate K such as by matching the Maclaurin series of (14) to that of g as far as the free constants allow. Notice that for small K, i.e., $K \ll 1/a$

$$
g^P(K) \sim K \qquad K \ll 1
$$

but that for $K \gg (1/d)^{1/2}$

$$
\lim_{K \to \infty} g^P(K) = \lim_{K \to \infty} g(K) = 1
$$

Also note that $g^P(K)$ is not a polynomial in K. In a practical sense (14) represents a physically viable, if approximate, re-summed form of the infinite

Maclaurin series for g(K) which is well behaved in either the small or large K regime as well as for $K > \pi/2$, the radius of convergence of the Maclaurin series for g. Obviously, the exact solution (11) is preferable to (14), if available. In most realistic physical problems the exact solution is not available in closed form. This implies that physical arguments as for example the boundedness of the heat flux even for large K can guide the ansatz.

This paper reports on an initial attempt to provide the analogue of equation (14) for Coulomb physics controlled heat flow $Q_{\shortparallel}(K)$ for finite K, whose leading order Maclaurin series reduces for $K <<< 1$ to $Q_{\shortparallel}^{CBES}$.

3. Established Kinetic Facts vs. CBES Postulates

At the Solar Wind 4 Meeting in 1978 at Burghausen, we reported on the properties of velocity distributions shaped by the Coulomb cross section without making gradient expansions (cf. SO I, II; a portion of the previous paper in this monograph reports on extensions of that work). We have demonstrated that non-local aspects of the steady state distributions of material along the tubes of force play a vital role in shaping the speed dependence in the trans, $(E > kT_c)$, and extra-thermal, $(E > 7kT_c)$, electrons; the latter group, by observations, controls the magnitude of the net skew of $f_e^{obs}(\underline{w})$ and, therefore, the magnitude of the heat flux (eqtn 8a,b).

In the presence of general finite gradients, Maclaurin series perturbation expansions for $f_e^{obs}(\underline{w})$ about a local Maxwellian are doomed because the strong speed dependence of the Coulomb cross section allows a global communication for electrons $E > 7kT_c$ along the magnetic tube of force (cf. SO I). The information that f_e (corona) $>>$ f_e (observer) manifests itself in the over populated, skewed, tails of the local distribution which observationally exceed a local Maxwellian population by several orders of magnitude above 100 eV at 1 AU. cf. SO II Figure 1. These are Knudsen number effects of the system's distribution of material in the even part of $f_e^{(o)}$. The speed dependence of $f_e^{(o)}$ has been observationally and theoretically shown to be non-Maxwellian as a result of Knudsen number effects. This violates CBES postulate 1 and 3. In this important trans and extrathermal regime $\delta f/f_{Maxwellian}$ is not even the same order of K local, which at 1 AU for example is $\sim 1/2$, much less infinitesimal as assumed by CBES.

4) Conservation Laws vs. CBES Implications

Provided $Q_{\shortparallel}$ is not zero, conservation laws for the plasma as a whole neglecting viscosity and ohmic entropy production (cf. eg., Rossi and Olbert, 1970) in steady, field aligned flow imply that

$$(3PV)/(2Q_{\shortparallel}) \frac{d}{ds} \ell n (P/\rho^{5/3}) = - \frac{d}{ds} \ell n W. \tag{15}$$

In the above P is the total gas pressure of electron and ions, $P \equiv P_e + \Sigma P_i$, ρ is the total mass density, V the magnitude of the field aligned flow velocity, $Q_{\shortparallel}$ the

parallel heat flux, and W is the dimensionless heat function defined by

$$W = Q_{\shortparallel}/(\rho\, VU_{\infty}^2) = Q_{\shortparallel}/(\alpha\, BU_{\infty}^2)\,,\qquad(16)$$

where U_{∞} is the asymptotic flow speed and α is the flux tube stream constant defined by the ratio of mass to magnetic flux:

$$\rho\,\underline{V} \equiv \alpha\,\underline{B}\,.\qquad(17)$$

As discussed by Olbert (1981) using current notation (and others) in steady state there exists an energy streamline constant defined by

$$U \equiv \frac{1}{2}\,V^2 + \frac{5}{2}\frac{P}{\rho} + \psi + \frac{Q_{\shortparallel}}{\rho V}\,,$$

where ψ is the gravitational potential. Dividing this expression by the square of the asymptotic radial wind speed U_{∞}^2 and using (17) yields an equivalent streamline constant where the dimensionless heat function is involved:

$$(U/U_{\infty}^2) \equiv \frac{1}{2}\,(V/U_{\infty})^2 + \frac{5}{2}\frac{P}{\rho\, U_{\infty}^2} + \frac{\psi}{U_{\infty}^2} + W\,.$$

At 1 AU the leading term is the largest and dominant term. At the base of the corona the last term is the dominant term. The viability of the coronal expansion via conduction reduces to showing that

$$\frac{1}{2}\left(\frac{V(1\ AU)}{U_{\infty}}\right)^2 \underset{\sim}{<} W\ (1.03\ R_{\odot})$$

In this sense the size of the dimensionless heat function W is crucial to the energetic feasibility of a conduction supported solar wind expansion (cf. discussion below).

Equation (15) may be rewritten without further approximations as

$$(PV/Q_{\shortparallel}) = (2\ L_D)/(3\ L_W)\qquad(18)$$

where the spatial scale for departures from adiabatic expansion, the "diabatic" scale, is implied by

$$L_D^{-1} = \left|-\frac{d}{ds}\ \ell n\ (\rho^{5/3}/P)\right|\qquad(19)$$

and the spatial scale for heat divergence, L_W is implied by

$$L_W^{-1} = \left|-\frac{d}{ds}\ \ell n\ W\right|\qquad(20)$$

In the CBES perturbation scheme, gradients of all macroscopic variables, M, are assumed to be weak in the sense that

$$\lambda_{rms}/L_M = O(K) \qquad (21)$$

is sufficiently small to ensure the validity of all the postulates. For a given experimental regime of K the practical question arises if it is small enough to assure quantitative precision of the CBES formulas. We proceed now to delineate what implied conditions on other macroscopic variables are <u>sufficient</u> to guarantee the validity of the CBES results.

Since D and W are combinations of macroscopic variables, CBES ordering (21) implies that the associated inverse scales, L_D^{-1} and L_W^{-1} are also $O(K)$ in the sense of (21). Within the CBES framework the general conservation of energy, (18), can only be consistently satisfied if the enthalpy and parallel heat flux are of the same order:

$$PV^{CBES}/ Q_{\shortparallel}^{CBES} = O(1). \qquad (22a)$$

This constitutes a restriction on the physical problems for which CBES is internally consistent since (22a) together with (9b) imply that the enthalpy flux must be proportional to K for small K:

$$PV^{CBES} = K \delta \qquad (22b)$$

Except for the consequences of the CBES <u>postulates</u> (21) there is no general ab initio argument that all physical systems will satisfy conservation of energy in such a way that the enthalpy flux is comparable to or less than the CBES heat flux <u>in the Knudsen</u> regime (K <<< 1) where $Q_{\shortparallel}^{CBES}$ calculation is rigorous. By explicitly determining δ and, therefore, the limits on V^{CBES} in the CBES regime, we argue that $V_{solar\ wind} > V^{CBES}$ throughout the entire solar wind expansion.

It is worth noting that CBES transport is usually discussed (cf. for example Cohen et al. (1950)) for plasmas at rest so that the speed, V, vanishes identically. Correspondingly (22) is satisfied in the CBES approach as a result of a postulate (V $\equiv$ 0) which is generally not true in astrophysical contexts. For the remainder we proceed on the assumption that V does not vanish throughout the system.

The CBES heat flux may be rewritten as

$$Q_{\shortparallel} = P_e\ w_o K, \qquad (23)$$

where

$$w_o = 3.3\ (L_n/L_{Te})\ w_{T,e}. \qquad (24)$$

It then follows that the CBES regime refers for a flowing medium to physical systems such that the inverse diabatic scale, L_D^{-1}, is second order small in the formal expansion parameter, K, (Rossi and Olbert, 1970, p. 436), since equations (18, 21-24) imply

$$\text{CBES}$$
$$\lambda_{rms}/L_D \; \underset{\sim}{\sim} \; G \, K^2, \tag{25a}$$

where

$$G = 1.1 \, (2P_e/P) \, (\tau_{p,n}/\tau_{e,T_e}) \, (L_n/L_W). \tag{25b}$$

In the above the rms electron transit time of its temperature scale, τ_{e,T_e} is given by

$$\tau_{e,T_e} = + \, L_{T_e}/w_{T,e},$$

and the fluid transit time of the electron density scale height, $\tau_{p,n}$, is given by

$$\tau_{p,n} = L_n/V.$$

For naturally occurring systems L_{T_e} is usually larger than L_n; however $w_{T,e}$ is usually larger than V and the ratio of the two times is more nearly commensurate than either the ratio of scales or speeds separately. On this basis G is not an enormous number being clearly $\underset{\sim}{\sim} 1$ for CBES ordering. Using the solar corona as a prototype for evaluating G we obtain $G \underset{\sim}{<} 1/6$ beyond the sonic point, where we have used the relationship that $d\ell n T_e/d\ell n \, n_e \underset{\sim}{\sim} 1/6$ (Sittler and Scudder (1980)) and that $d\ell n \, W/d\ell n \, n_e \underset{\sim}{\sim} 1/50$ (Olbert (1983)). These considerations reinforce the important conclusion that indeed

$$\text{CBES}$$
$$\lambda_{rms}/L_D \; \underset{\sim}{<} \; K^2, \tag{26}$$

which is a more restrictive, but, nevertheless, consistent ordering of scales with the initial CBES ordering (21).

Apart from trivial constants, the inverse scale length, $L_{f^o}^{-1}$, associated with the change of the electron velocity distribution function at zero proper frame velocity is the same as that of the diabatic expansion (26). Therefore, (26) may be restated in microscopic language to establish contact with SO I, II: the CBES description is internally consistent with conservation of energy for systems (such as thermodynamic equilibrium (!)) with L_{f^o} that is much larger than any of the driving gradient scales of the macroscopic variables, L_M. Rewriting in symbols equation (26) the inverse scales of f^o must be one order weaker than those of the macroscopic variables.

$$L_{f^o}^{-1} \underset{\sim}{\sim} (L_M^{-1}) \, K.$$

This is precisely what is <u>not</u> realized in astrophysical plasmas and leads, via the Coulomb cross section "window", to global lowest order signatures in the distribution functions and correspondingly in the transport SO I, II.

5. Enforcing CBES Postulate (3) in an Inhomogeneous Plasma

In order that the lowest order $f_e^{(o)}$ be Maxwellian in an inhomogeneous, fully ionized plasma (CBES postulate 3), it is no longer sufficient to only require that the rms free path, λ_{rms}, be small compared to the scale height. When K is finite in a fully ionized plasma then the rms free path of the thermal and suprathermal electrons are no longer infinitesimal, being related to the rms free path by the formula

$$\lambda(u) = u^4 \lambda_{rms}, \qquad (26a)$$

where $u = w/w_{Te}$. By contrast collisions between neutral molecules have a free path with essentially no speed dependence for speeds above $\sqrt{3kT/m}$, Meyer (1899).

If, as is usual (cf. Parker (1964)), one assumes K << 1 is sufficient for CBES heat transport results to ensue then (26a) implies that there always exists a finite u_Q so that the following ordering of scales is possible:

$$\lambda_{rms} <<< L_n < \lambda(u_Q). \qquad (26b)$$

Unlike the situation for collisions between neutrals, equation (26a) implies that no matter what the size of the Knudsen number (so long as it is finite), there always exists a speed domain $(u > u_Q)$ of the velocity space for which the (shortest) macroscopic scale length L_n is shorter than the free path of members of the velocity distribution which have speeds in this domain. This domain need not be the sole province of the cosmic rays!

Having established (26b) it is important to assess the potential impact it may have on the kinetic determination of transport in the system. If K be so small that u_Q is a relativistic cosmic ray and the mean energy of the gas is ultra non-relativistic, the practical impact of (26b) on the CBES regime is not severe. However, u_Q needs to be well above the dominant proper frame speeds where the perturbations to $f_e^{(o)}$ kinetically determine the heat flux (equation 8), the highest moment in the Onsager relations. The precise size of u_Q so as to assure that non-local effects are collisionally destroyed and do not dominate the transport becomes the prerequisite for allowing postulate 3 of CBES to be reasonable: find u_Q such that

$$\lambda_{rms} < \lambda(u_Q) << L_n. \qquad (26c)$$

Based on the theoretical properties of the Coulomb cross section SO II argued that significant non-local suprathermal particles will be present above the dimensionless speed u = 2.16. The observed solar wind electron velocity distribution function was shown to develop strongly overpopulated skewed suprathermal tails (the halo) above this speed. As an empirical fact the in situ heat flux is determined by the skew of the electron distribution near but above this transition. We suggest that

$$u_Q \gtrsim 3.5 \qquad (26d)$$

is appropriate for the inequality in (26c). Using this result in (26c) and noting (26a), we can restate the sufficient local condition that $f^{(o)}$ be locally

Maxwellian, in an inhomogenous, fully ionized plasma without postulating special spatial distributions of the plasma in the adjoining volume, viz

$$150 \, K^{CBES} \ll 1. \tag{27}$$

Notice that this result is considerably more restrictive than the usually stated (and implied sufficient) condition in the astrophysical context for CBES validity: $K \ll 1$. Equation (27) defines the regime for finite K that is consistent with use of CBES results.

From the internal energy equation, (25), in the consistent Knudsen number regime K^{CBES} is algebraically equal to

$$K^{CBES} \equiv \frac{3}{2} (L_W/L_D) \, (P/P_e) \, (V/w_o); \tag{28}$$

however, as the prerequisite for fulfilling CBES postulate (3) equation (27) must be satisfied. This yields the compatibility condition

$$M_S^A <<< \eta, \tag{29}$$

where the adiabatic Mach number is defined as

$$M_S^A = V/(5/3 \, P/\rho)^{1/2} \tag{29b}$$

and

$$\eta = 0.73 \, (2P_e/P)^{1/2} \, (L_D/L_W) \tag{29c}$$

which follows from (28) using (27):

$$K^{CBES} <<< 6.6 \times 10^{-3} \tag{30}$$

Equations (29) and (30) are not physical constraints but are corollaries of the mathematical postulates made for the CBES approach which render the (electron) transport problem to be "local".

Unless a fully ionized plasma is prepared in a contrived way (as described below) the contradiction of either (29, 30) implies that CBES is no longer appropriate for electron signatures. Depending on the observational technique(s) one or the other of these constraints may be more accessible for a distant observer of astrophysical phenomena.

For specially prepared equilibria (as discussed by CBES) such as an isothermal flux tube that has slight temperature and density variation but still "superadiabatic" in the sense of (26) and, therefore possessing very low contrast in $f^{(o)}$ between its extremities (a very difficult idealization to achieve in an astrophysical setting) condition 30 can be relaxed by several orders of magnitude to

$$K_{isothermal}(s) \ll 1,$$

provided this condition is met everywhere along the magnetic tube of force

connected to the point of interest. This is the system to which CBES refers. The relaxation of (30) results from a very special preparation of the inhomogeneous system. For this circumstance individual trans and extrathermal particles still have a global range over arc lengths large compared to λ_{rms}; however, the probability function f^o refers to the pattern of phase space occupation and it is not modified in lowest order in the presence of finite $K \ll 1$ provided the system is prepared in this special way. Alternatively, in the presence of an absolutely uniform T_e and a macroscopic density gradient the individual trans and extrathermal electrons give up sufficient energy to the polarization electric field that the lowest order pattern for $f^{(0)}$ can still be self-similar along B even in the presence of strong density gradients.

We submit that these special systems are so contrived that they are unlikely prototypes of plasmas in the astrophysical or other contexts and that conditions (29, 30) are more generally applicable. Gravity destroys the weak density gradient regimes; T_e can not be artificially assumed constant throughout a given astrophysical flux tube and the lowest order $f(\underline{w})$ becomes global in character.

For the solar wind it is clear by direct observation that at 1 AU that $M_S^A \gg 1$, that $K \sim 1/2$, that both the inequalities (29 and 30) are strongly violated, and that the observed $f_e(\underline{w})$ is not deformed as predicted by CBES theory (Montgomery, 1972). What is forcefully driven home by (30) is that the CBES description of thermal conduction, for example, is invalid at the very base of the coronal expansion. Given observed coronal velocities in the range of 10's km/s

and an implied base sonic Mach number at 10^{6o} K of approximately .08 and the determination in the previous paper that $L_n \ll L_w$ in approximately the ratio of 1:50 implies (if $P_e = P_i$) that

$$\eta_o = 5 \times 10^{-3}$$

and that

$$M_S^A \bigg|_{1.03 r_o} \sim .08 > \eta_o$$

and that the CBES determination of supply of conduction flux to the expansion is in error <u>from the base of the corona</u>. This conclusion should be contrasted with Parker's (1964, eqtn 76) original argument that CBES should be appropriate for the initial portion of expansion possibly as far as 1 AU on the basis of an argument like

$$\text{"CBES Flux"} = \chi_o T_e^{5/2} \frac{dT_e}{dr} \lll \frac{3}{2} NkT_e \left(\frac{3kT_e}{m_e}\right)^{1/2} = \text{"Saturation Flux"}$$

which is equivalent (using (6, 9b, 10, 24) to

$$K^{Parker} \ll .45 \left(\frac{L_T}{L_N}\right) \sim 2.5 \tag{32}$$

which we now recognize as an overly generous upper bound for K when contrasted with (27).

Use of the CBES heat transport description within the conservation equations for a flowing medium with $M_s^A > \ll 1$ (eqtn 29) is clearly inconsistent with the entire set of postulates necessary to derive equation (9). The failure of such a kinetically inconsistent model to predict the observed solar wind properties implies nothing about the importance of conduction in driving winds. This point is especially crucial since the properties of the conduction flux near the supersonic transition are extremely critical for the determination of the essentially asymptotic wind properties that are accessible to spacecraft observations.

6. The Global-Local Formulation of the Transport Problems

In the present restricted monograph we only outline the philosophy and present the results of the procedure used to obtain the heat flux form quoted below.

The philosophy of this approach is that, like in eqtns 11-13, a simple Maclaurin series of either 1 or n terms about a Maxwellian is hopeless because such a procedure neglects the global distribution of phase density along the tube of force. The tails of $f(\underline{w})$ and their skew cannot be accurately predicted by a one term Maclaurin perturbation expansion of f about a local Maxwellian. It is the boundary conditions at the origin and at infinity in the mathematical example and at the sun and infinity in the physical example, as well as the strong speed dependence of the Coulomb cross section that force a more useful approximation scheme. Both from considerations of the conservation equations and from integral formulations for the local form of $f(\underline{w})$ (SO I, II and Olbert (1983)) global

correction must be incorporated in the lowest order ansatz for $f^{(o)}(\underline{w}, x)$ before attempting to determine the skew and, therefore, the net heat flux $\overline{(8b)}$. In mathematical language this represents an attempt to renormalize the perturbation expansion of CBES.

In the face of significant non-local corrections to local gaussian behavior

we have adopted a lowest order functional ansatz for $f^o(\underline{w}, x)$ that while still only speed dependent contains an additional shape parameter, κ, beyond the shape factor in a gaussian identified with the temperature. This is a significant departure from CBES postulate (3). This ansatz is called the kappa distribution:

$$f_\kappa^{(o)}(\underline{w},x) = f_\kappa(\kappa(x),w_c^2(x), n(x), \underline{w}^2) = \frac{A_\kappa n}{(\sqrt{\pi}w_c^3)} (1 + w^2/(\kappa w_c^2))^{-(\kappa+1)} \quad (33)$$

originated by Olbert et al. (1967) and Olbert (1969). This lowest order distribution contains extrathermal tails which can support the global Coulomb physics, but asymptotes to a gaussian/Maxwellian distribution as $\kappa \to \infty$. In every respect the kappa function represents a mathematical "extension" of the Maxwellian function. The physical meaning of n is the usual number density, w_c is the speed of the most probably occurring member of the speed distribution, w is the proper frame speed, and $\kappa(x)$ controls the local strength of the extrathermal tails: small κ implies strong tails, κ going toward infinity implies increasingly weaker tails. $A_\kappa(\kappa(\underline{x}))$ is a normalization constant which ranges between 0.75 to 1. Paralleling in concept the Padé approximant (14) for g by choosing a, b, c and d appropriately, $\kappa(x)$ must be determined. This is done self-consistently within the perturbation scheme described below.

Clearly, as in any perturbation theory, the better the ansatz, the better the approximation becomes. In our choice of ansatz we have been influenced by economy of free variables, the energy dependence of the observed $f(\underline{w})$, the global aspects of the Coulomb physics (as outlined in SO I, II and previous paper) and that a member of the functional ansatz should be a gaussian.

We have used a speed dependent Krook collision term as in SO I and II and have successfully imposed conservation of electrons through a mandated $\kappa(s)$. The imposition of this collisional invariant constraint is well known; the equation of constraint relates κ to other state variables (cf. (34) below). In the presence of a speed dependent Krook collision operator this equation of constraint relates the variation of the non-thermal tail index, $d\kappa$, to the variation of the normalization of phase density $d \ln (n_e/w_c^{-3})$ along the tube of force. This equation has the form

$$ d\kappa(s) = - \ell(\kappa(s),\kappa_o(s_o)) \, d \ln (n_e(s)/w_c^3(s)). \tag{34a} $$

For reasonable interplanetary profiles κ is smaller near the sun than at 1 AU. This implies that the isotropic part of $f(\underline{w})$ near the sun has more of a non-thermal tail than at 1 AU.

Equation (34a) may be recast to show its non-local character

$$ \nu(s)/\nu(s_o) = \exp \left[-\int_{\kappa_o(s_o)}^{\kappa(s)} \frac{d\kappa'}{\ell(\kappa',\kappa_o)} \right], \tag{34b} $$

where $\nu(s) \equiv t_c^{-1}(s)$ is proportional to n_e/w_c^3. Notice that equation (34b) (implicitly) prescribes $\kappa(s)$ as a function of the contrast of collision frequency which equals the contrast in the phase space density (at zero proper frame energy) between s and some reference point, s_o, where $\kappa=\kappa_o$ is known. Mathematically we have succeeded in instilling sufficient information in (renormalizing) the lowest order $f^{(o)}$ so that the global, velocity dependent, Coulomb moderated mobility of the electrons does not violate charge neutrality. This lowest order failure of the CBES, Maclaurin series approach to obtaining extrathermal tails on $f(w)$ is now removed.

It is crucial to appreciate that it is the skewness of the increasingly non-local trans and extra-thermals which determine the heat flux (8) for astrophysical plasmas. The "resummation" of non-local effects embedded in our ansatz (33) as constrained by (34b) heavily impacts the dominant speed, w^*, where subsequently obtained skews of f make the principal contribution to $Q_\parallel$ (8). This effect is exacerbated by the high power of w involved in determining Q and the fact that the perturbation δf_e about $f_e^{(o)}$ itself has significant speed dependence.

We then obtain a gradient expansion about the local, isotropic $f_\kappa^{(o)}$ to obtain the skew correction term that represents the flow of heat. The analogue of (9a) has the global-local (GL) structure (if there exists no current in the proper frame which determines the proper frame parallel electric field):

$$Q_\parallel{}^{GL}(s) = -CTS(\kappa(s), \kappa_0(s_0)) \frac{d}{ds} \ln T_c - CSS(\kappa(s), \kappa_0(s_0)) \frac{d}{ds} \ln (n/T_c{}^{3/2}) \quad (35)$$

$$CTS \gtrsim CSS > 0; \quad kT_c = \frac{1}{2} mw_c{}^2,$$

where CTS and CSS are <u>global</u> functions of system parameters, which sense, through equation 34b, the <u>collision frequency contrast</u> of the physical system connected to the observer, while the gradients sense <u>local</u> changes in the state variables. The functional dependence of the global-local form of $Q_\parallel{}^{GL}$ (35) should be contrasted with the completely local form of CBES in equation 9.

7. The CBES Limit of Global-Local

We recall that a condition via equations (25, 26) for internal consistency of the CBES regime in the presence of flows ($K \to 0$) is that

$$\lambda \frac{d}{ds} \ln(n/T^{3/2}) = O(K^2).$$

This implies that the second term of (35) is quadratic while the first is linear in the expansion parameter K. [As an aside CTS $\sim$ CSS]. The imposition of near adiabaticity implies large collision frequencies, $\nu = O(1/K)$, which implies progress toward Maxwell-Boltzmann distribution. Therefore, from the equation of constraint (34) since $\ell(\kappa, \kappa_0)$ is bounded and $O(1)$

$$\kappa - \kappa(s_0) = O(K^2),$$

which implies that the CBES regime is characterized by a constant

$$\kappa \sim \kappa_0 + O(K^2) \to \infty,$$

which by construction of our ansatz is functionally possible.

Since $\lim\limits_{K \to \infty} T_c = T_e$

we may now form the CBES limit of $Q_\parallel{}^{GL}$ (eqtn 11) as

$$\lim_{\substack{\to CBES \\ (K \to 0)}} Q_\parallel{}^{GL} = -\lim_{\substack{K \to \infty \\ \kappa_0 \to \infty}} [CTS(\kappa, \kappa_0) \frac{d}{ds} \ln T_c + O(K^2)] = Q_\parallel{}^{CBES} + O(K^2),$$

where the quadratic terms throughout the CBES approach have already been neglected. We reemphasize here the extremely narrow classes of astrophysical problems (delimited by equation (29, 30)) for which CBES results are quantitative.

8. The Global-Local Evaluation of the W Function for High Speed Wind Conditions

As a final result we illustrate in Figure 1 the dimensionless heat function $W(\rho)$ defined by (16) and central to the previous paper by Olbert (1983), but here evaluated with $Q_{\parallel}^{GL}$ from equation (35). We have used the same coronal hole density and magnetic profiles as used in Olbert (1983) for the high speed solar wind ($U_\infty = 700$ km/s) and a composite electron temperature profile that has a coronal hole value at $1.03\ r_0$ ($8 \times 10^{5\,\circ}$K), has the correct $d\ell n T/d\ell n n$ characteristics near 1 AU (Sittler and Scudder (1980)), and an electron temperature characteristic of the high speed solar wind at 1 AU of $8 \times 10^{4\,\circ}$K. We emphasize that these results are preliminary as discussed below, since all aspects of the calculation are not fully self-consistent, such as picking a density and temperature profile that are actually compatible with the postulate of steady state. In that respect the results of Figure 1 represent a feasibility study for investigating qualitative regimes of $W(\rho)$ that are possible without doing the quadruple numerical integrals as have been painstakingly done in the previous paper. This matter of complete self-consistency is an issue in both these papers and is currently under investigation.

We note the properties of W^{GL} that the previous paper (Olbert (1983)) reports as essential for a conduction supported high speed wind: 1) the initial plateau at large densities; 2) the plateau magnitude (this implies sufficient random energy available to be converted to directed energy for 700 km/s wind) and 3) the sharp decrease near the critical point. The second plateau at lower densities has little effect on the dynamics of the solar wind expansion. Figure 2 illustrates the relative contributions of the two terms of equation (35) to the final $Q_{\parallel}^{GL}$: note that different density regimes reflect different relative importance of the two terms and neither term is negligible and that the second term of (35) (neglected by CBES) determines a larger share of the heat than the conventional grad T term at the base of the coronal expansion.

Figure 1 represents a realization of $W(\rho)$ using the hybrid-global-local approach instead of the quadruple numerical integrals required in the integral formulation of the previous paper. In the preceding paper (Olbert (1983)) all gradations of global Coulomb effects are accounted for in the presence of a leading term Ohm's law electric field. In this paper the electric field has been set by the zero current condition, particles are conserved and there is a hybrid global-local approach to the tail/skew problem. Both approaches attempt, with different levels of precision, to assess the importance of the strong velocity dependence of the Coulomb cross section which invalidates the CBES approach.

The $W(\rho)$ function is very sensitive to the profiles of n and T_e. For a given density and magnetic tube geometry the electron temperature profile is not free to be prescribed, but is determined by the energy equation (15). In future this internal self-consistency will be addressed. For the present these results represent significant progress toward affirming the existence of stellar winds with large asymptotic velocities supported by Coulomb mediated heat conduction, with the solar wind as a prime example.

GLOBAL-LOCAL CHAPMAN-ENSKOG
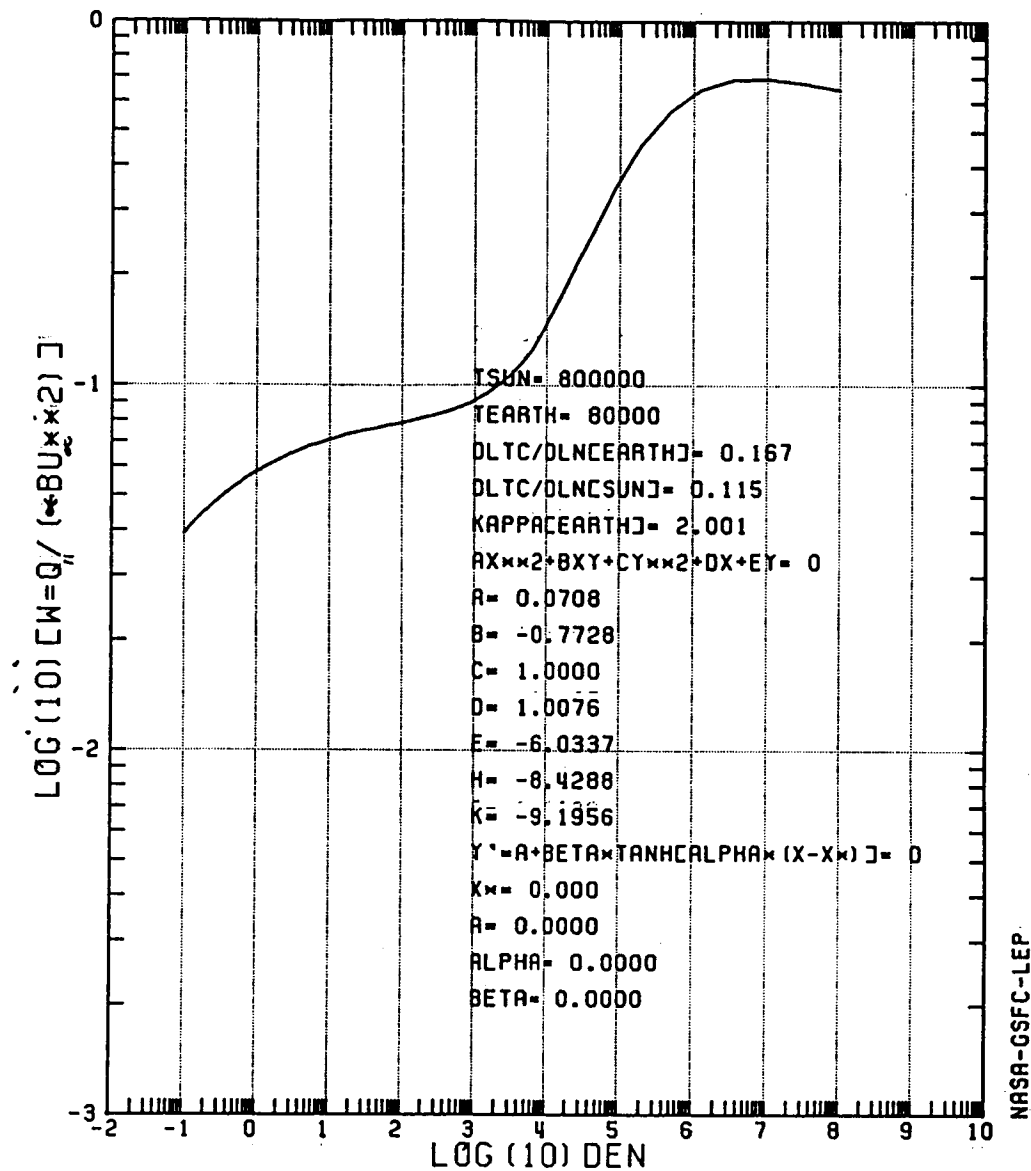
Fig. 1   Profile of the dimensionless heat function $W = Q_{||}/(\alpha BU^2)$ for coronal hole magnetic field and density profile used by Olbert[∞] (1983), but evaluating $Q_{||}$ via the global local approach outlined in text. Abscissa is electron density.
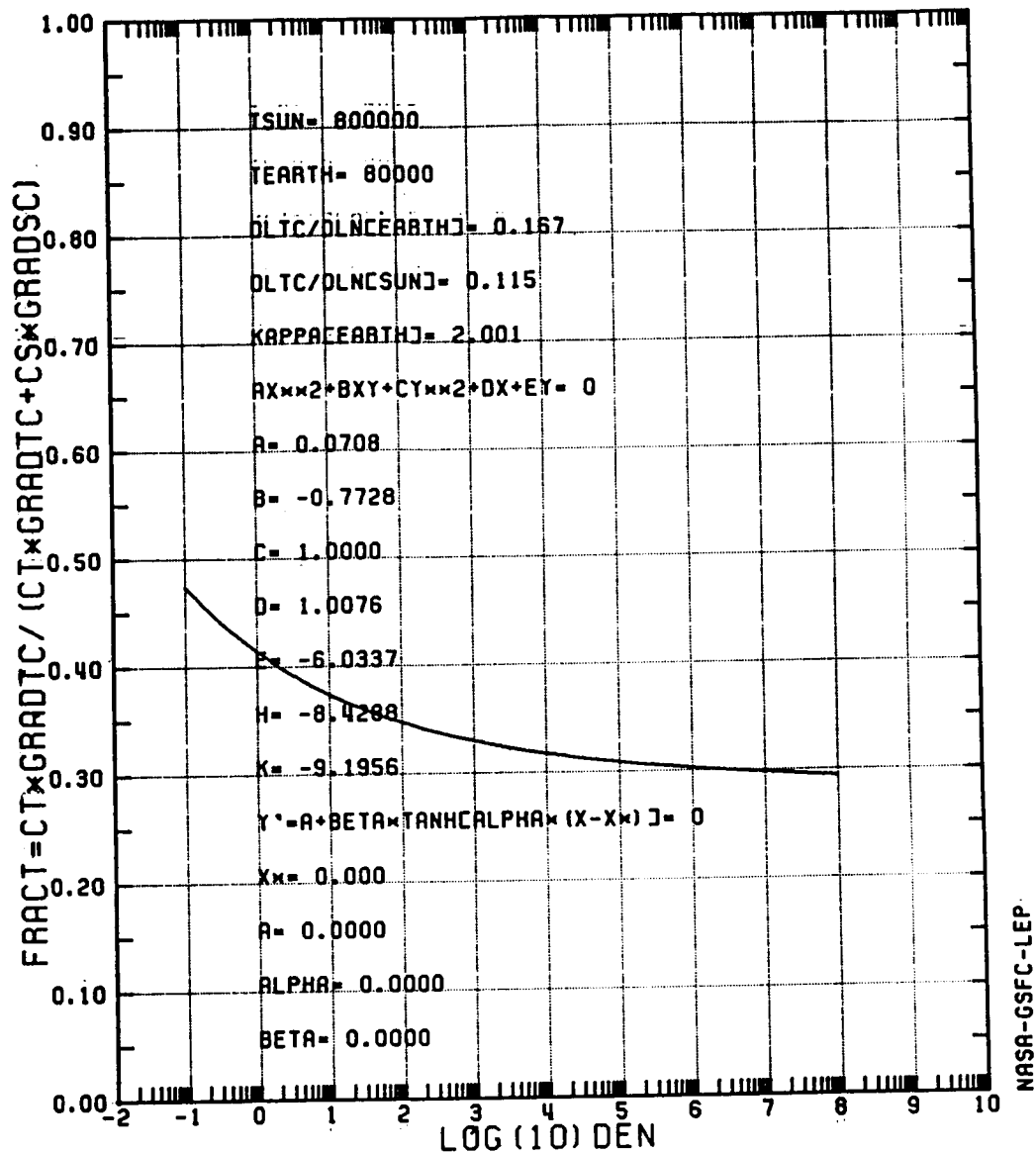
Fig. 2   The fraction of the suggested heat flux determined by the first term of the full heat expression of equation 35 for the heat flow profile of Figure 1. Note that there exists varying domains of relative importance with the second term of (35), not included in the CBES expression of equation (9), playing the dominant role near base of coronal expansion.

References

Baker, G. A., Jr., Essentials of Padé Approximants, Academic Press, New York, 1975.

Braginskii, S. I., Transport processes in a plasma, Reviews of Plasma Physics, 1, 205, 1965.

Chapman, S., On the law of distribution of molecular velocities and on the theory of viscosity and thermal conduction in a non-uniform, simple monatomic gas, Phil. Trans. R. Society A, 216, 279, 1916.

Chapman, S. and T. G. Cowling, The Mathematical Theory of Non-Uniform Gases, Cambridge University Press, Cambridge, 1939.

Cohen, R. S., L. Spitzer, Jr., and D. McR. Routly, The electrical conductivity of an ionized gas, Phys. Rev., 80, 230, 1950.

Enskog, D., Inaugural Dissertation, Uppsala, 1917.

Grad, H., Handbuch Physik, XII, S. Flugge, ed., 205, 1958.

Meyer, O. E., Kinetic Theory of Gases, English Trans. R. E. Baynes, Longman, Green and Co., London, 1899.

Montgomery, M. D., Cosmic Plasmas, K. Schindler, ed., 61, Plenum Press, New York, 1972.

Olbert, S., A. Egidi, G. Moreno, L. G. Pai, Transactions of American Geophysical Union, 48, 177, 1967 (abstract).

Olbert, S., Physics of Magnetospheres, R. C. Carovillano, J. F. McClay, H. R. Radoski, eds., 641, D. Reidel, Dordrecht, Holland, 1969.

Olbert, S., Inferences about solar wind dynamics from observed distributions of electrons and ions, Proc. International School and Workshop on Plasma Astrophysics, in ESA SP-161, 1981.

Olbert, S., "The Role of Thermal Conduction in Solar Wind Acceleration" this monograph, preceding article, 1983.

Parker, E. N., Dynamical properties of stellar coronas and stellar winds. II. Integration of the heat flow equation, Ap. J., 139, 93, 1964.

Reif, F. Fundamentals of Statistical and Thermal Physics, McGraw-Hill Book Co., New York, 1965.

Rossi, B. and S. Olbert, Introduction to the Physics of Space, McGraw-Hill Book Co., New York, 1970.

Scudder, J. D. and S. Olbert, A theory of local and global processes which affect solar wind electrons, 1. The origin of typical 1 AU velocity distribution functions, J. Geophysical Res. 84, A6, 2755, 1979a.

Scudder, J. D. and S. Olbert, A theory of local and global processes which affect solar wind electrons, 2. Experimental support, J. Geophysical Res. 84, A11, 6603, 1979b.

Sittler, E. C., Jr., and J. D. Scudder, An empirical polytrope law for solar wind thermal electrons between 0.45 and 4.76 AU: Voyager 2 and Mariner 10, J. Geophys. Res., 85, 5131, 1980.

Spitzer, L., Jr., Physics of Fully Ionized Gases, J. Wiley Interscience, New York, 1962.

Spitzer, L., Jr., and R. Härm, Transport phenomena in a completely ionized gas, Phys. Rev., 89, 977, 1953.

Page intentionally left blank

MAGNETOHYDRODYNAMIC MODELING
OF CORONAL STRUCTURE AND EXPANSION

S. T. Suess+
Space Environment Laboratory
NOAA / ERL
325 Broadway
Boulder, Colorado 80303

ABSTRACT

The presence of a magnetic field in the corona adds structure to the solar wind and almost certainly plays an important role in the energetics of the flow. Here I will discuss analytical and numerical modeling of gas-magnetic field interactions as used to compute steady, global flow. After a brief and incomplete review, I will describe the approach used in, and results from a recent global model (Steinolfson, Suess and Wu, 1982). I will then outline my own ideas on the most effective ways to improve the physical content and numerical efficiency of these models. Throughout, I will limit myself to discussing solutions of the MHD equations only in order to find steady-state flows, even though this will often entail solving time-dependent equations.

INTRODUCTION

One of the more difficult problems in coronal dynamics is to self-consistently compute the large-scale interactions between the plasma and the magnetic field in order to find the flow geometry. The theoretical models that have been published generally either incorporate very important approximations in order to make the analysis tractable, or use "brute force" numerical solutions. As an example of an essentially analytic approach to MHD modeling, I describe the results from a quasi-radial flow approximation (Suess, Richter, Winge and Nerney, 1977; Suess, 1979; Winge and Coleman, 1974; Nerney and Suess, 1975; Suess, 1972). This approximation invoked flow that was nearly radial, deriving conditions for this requirement as a result from the analysis. Single-fluid, polytropic flow with no dissipation was assumed, and the flow was taken to be axisymmetric. The geometrical approximation means that the analysis cannot be applied near a magnetic cusp. The model was applied to the northern polar coronal hole of 1973 because observations provided a density distribution throughout the hole and showed that the hole was essentially axisymmetric (Munro and Jackson, 1977). The observed density was matched throughout the entire volume, and the observed geometry of the boundary was matched to a streamline, minimizing the impact of the polytrope assumption. The results are shown in Figures 1 and 2. Important deductions include an "effective" temperature of $1-2 \times 10^6$ deg., a field strength of 0.5 to 1.0 gauss, and a flow speed of a few up to 150 km/s at 2 solar radii. By 5 solar radii, the flow speed varies from less than 50 to over 300 km/s while the magnetic field is approximately uniform across the hole.

+Also, Department of Astro-Geophysics, University of Colorado, Boulder, Colorado 80309.
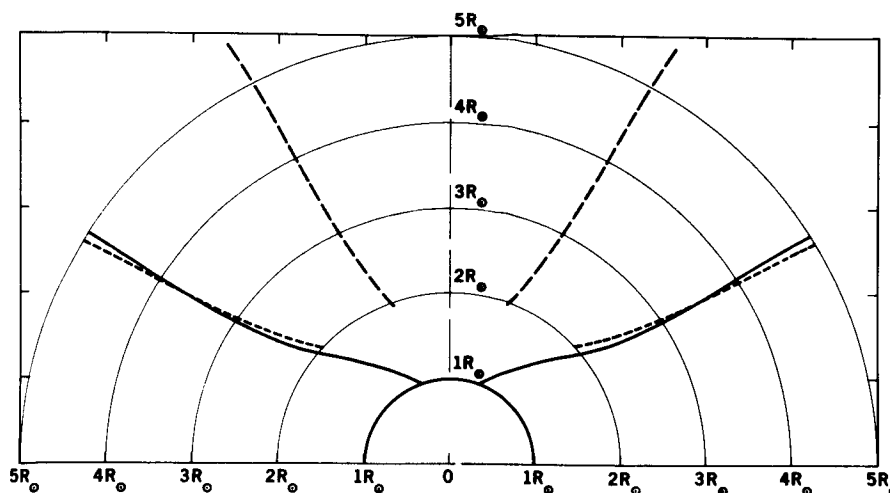
Figure 1. The observed boundary of the northern polar coronal hole (solid curve, from Munro and Jackson, 1977) and streamlines beginning at 2 solar radii and polar angles of 20 and 50 degrees. The streamlines have been computed using a quasi-radial approximation to the MHD equations of motion together with latitude dependent boundary conditions (from Suess, et al., 1977).
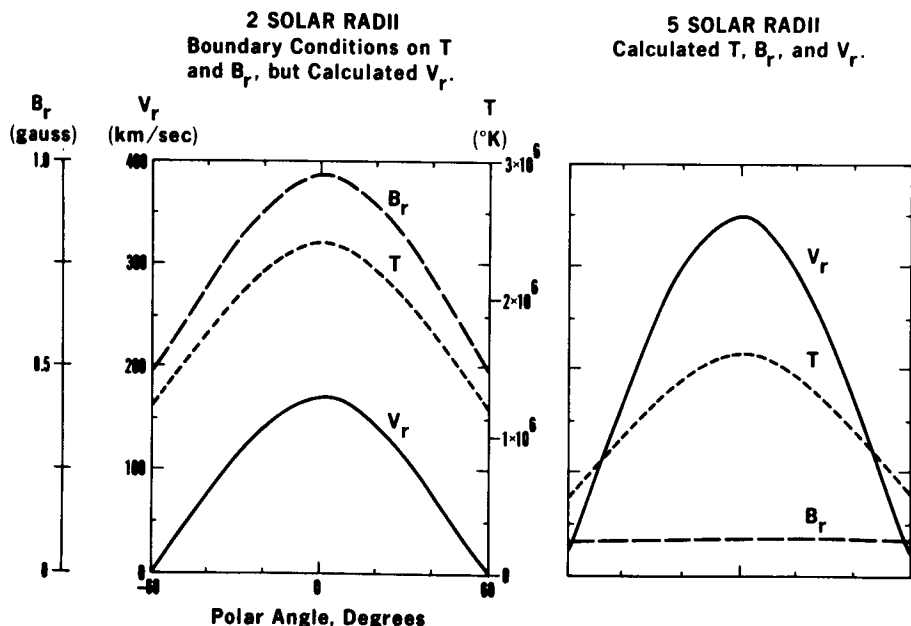
Figure 2. Latitudinal variations of the radial magnetic field, temperature and radial velocity at 2 and 5 solar radii. The radial magnetic field, temperature and observed density variation at 2 solar radii are the boundary conditions for this, and the streamline results in Figure 1 (Suess, et al., 1977).

Significant energy deposition is implied between 2 and 5 solar radii. However, because this analysis cannot treat global flows that include regions of closed magnetic fields, it cannot be carried much beyond this particular example. The only obvious extensions would be to relax the polytrope assumption to permit thermal dissipation, and to include momentum and energy source terms.

In a corona with both closed, magnetostatic regions, and open, coronal-hole-like regions, the problem of the global gas-magnetic field interactions is both totally nonlinear and geometrically complex, almost requiring numerical solution. Probably the most pioneering work was that by Pneuman and Kopp (1971), who constructed a solution for an axisymmetric, isothermal streamer configuration on a two-dimensional grid. Their solution was found through a procedure which iterated on the current distribution, and they assumed isothermal flow.

The ultimate fieldline geometry computed by Pneuman and Kopp is shown in Figure 3. Originally, there were questions regarding their assumption about the nature of the cusp. However, these were laid to rest using a numerical solution of the time-dependent equations of motion (Endler, 1971; Weber, 1978). If the situation is treated as an initial-boundary value problem, then it is guaranteed that the final state is a true equilibrium configuration. In this approach, one starts with an initial state consisting of an essentially arbitrary choice for the fluid and magnetic field variables. The numerical solution of the time-dependent equations, starting with this non-equilibrium state, then gradually approaches a stationary coronal configuration. In applying this approach, it was not only shown that the cusp geometry assumed by Pneuman and Kopp was a valid equilibrium configuration, but also that the solution was stable.

These results demonstrated that treatment of steady, global coronal flow as an initial-boundary value problem is: (i) feasible, (ii) efficient, and (iii) probably the most powerful approach to the general problem. I would now like to describe results from an application of this approach to polytropic rather than isothermal flow, for a survey of the effect of varying magnetic field strength (Steinolfson, et. al, 1982).

THE PROBLEM AND THE EQUATIONS

The assumptions are that the corona can be described by polytropic, axisymmetric, single fluid flow. The initial state consists of a hydrodynamic solution to the steady radial equations of motion for a polytropic gas, superimposed on a dipole magnetic field. No explicit dissipation is included. This is a generalization over previous work by relaxing the assumption of isothermal flow. With these assumptions, the time-dependent equations of motion, in MKS units, are:

$$\frac{\partial \rho}{\partial t} + \frac{\partial}{\partial r}(\rho u) + \frac{\partial}{\partial \theta}\left(\frac{\rho v}{r}\right) = -\frac{2\rho u}{r} - \frac{\rho v}{r}\cot\theta,$$

(1a)

$$\frac{\partial u}{\partial t} + u\frac{\partial u}{\partial r} + \frac{B_\theta}{\mu\rho}\frac{\partial B_\theta}{\partial r} + \frac{1}{\rho}\frac{\partial p}{\partial r} + \frac{v}{r}\frac{\partial u}{\partial \theta} - \frac{B_\theta}{\mu\rho r}\frac{\partial B_r}{\partial \theta}$$

$$= -\frac{GM_s}{r^2} + \frac{v^2}{r} - \frac{B_\theta^2}{\mu\rho r}, \qquad (1b)$$

$$\frac{\partial v}{\partial t} + u\frac{\partial v}{\partial r} - \frac{B_r}{\mu\rho}\frac{\partial B_\theta}{\partial r} + \frac{v}{r}\frac{\partial v}{\partial \theta} + \frac{B_r}{\mu r\rho}\frac{\partial B_r}{\partial \theta} + \frac{1}{r\rho}\frac{\partial p}{\partial \theta}$$

$$= \frac{B_r B_\theta}{\mu r\rho} - \frac{uv}{r}, \qquad (1c)$$

$$\frac{\partial B_r}{\partial t} - \frac{\partial}{\partial \theta}\left(\frac{uB_\theta - vB_r}{r}\right) = \frac{1}{r}(uB_\theta - vB_r)\cot\theta, \quad (1d)$$

$$\frac{\partial B_\theta}{\partial t} + \frac{\partial}{\partial r}(uB_\theta - vB_r) = -\frac{1}{r}(uB_\theta - vB_r), \quad (1e)$$

$$\frac{\partial p}{\partial t} + \gamma p\frac{\partial u}{\partial r} + u\frac{\partial p}{\partial r} + \frac{\gamma p}{r}\frac{\partial v}{\partial \theta} + \frac{v}{r}\frac{\partial p}{\partial \theta}$$

$$= -\frac{\gamma p}{r}(2u + v\cot\theta), \qquad (1f)$$

where the dependent variables are the density, ρ, radial velocity, v_r, meridional velocity, v_θ, pressure, p, radial magnetic field, B_r and meridional magnetic field, B_θ. The independent variables are the radius, r, and the colatitude, Θ. The constants are the polytropic index, γ, magnetic permeability, μ, universal graviational constant, G, and the solar mass, M_s.

These equations are solved between 1.0 and 5.0 solar radii, and from the pole to the equator - the solution is symmetric about the equator. The grid spacing is 0.1 solar radii in the radial direction, 2.5 degrees in the meridional direction, the numerical solution uses a modified Lax-Wendroff differencing scheme, and the time step is chosen to be the maximum allowable from the usual stability criterion for dissipationless schemes; i.e.,

$$\Delta t = \min(\Delta t_r, \Delta t_\theta) \qquad (2)$$

where

$$\Delta t_r = r/\lambda_r$$

and

$$\Delta t_\theta = r\Theta/\lambda_\theta$$

and $(\lambda_r, \lambda_\theta)$ are the maximum eigenvalues (the sum of the fluid velocity and the characteristic velocity) in the radial and meridional directions. A smoothing term is used to reduce numerical oscillations, and it was necessary to watch for nonzero values of div.$\underline{B}$ which otherwise often exist in numerical solutions of multi-dimensional time-dependent MHD problems (Brackbill and Barnes, 1980). At the inner boundary, two of the six radial characteristic directions are negative, and consequently, information from the region of interest propagates upstream to the boundary. In this case, four dependent variables at the lower boundary can be specified arbitrarily, and two must be calculated from some form of compatibility relations (Steinolfson and Nakaga-

- —— Exact Solution, Isothermal Corona
- ---- Zero Potential Solution, R_w=2.492 $R_\odot$
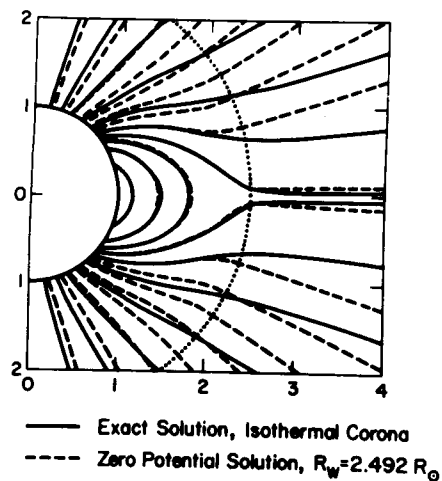
Figure 3. The coronal expansion
calculation by Pneuman & Kopp
(1971), compared to a potential
field model (Newkirk, 1972).
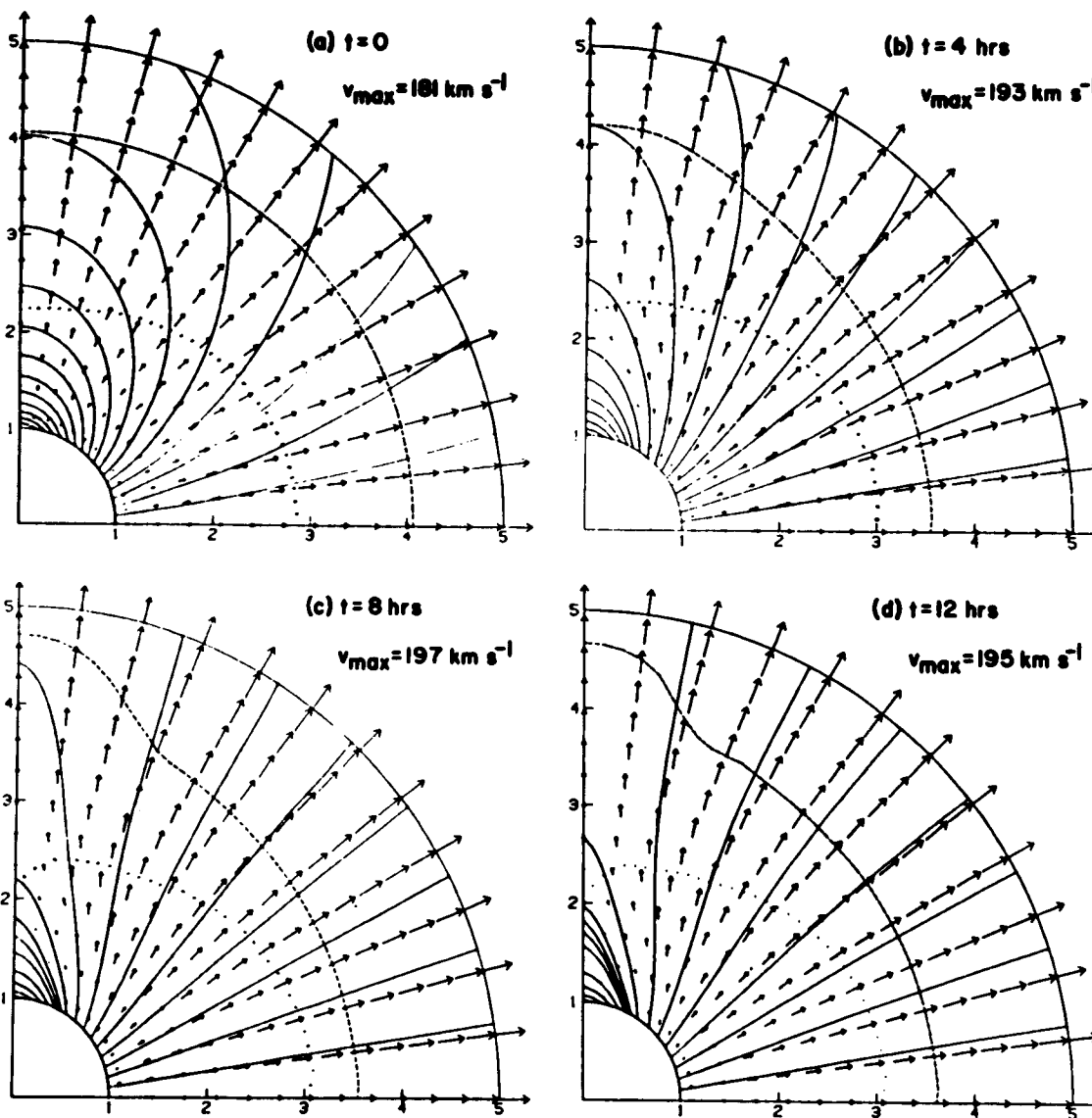
Figure 4. The evolution of the
coronal magnetic field and velo-
city for beta = 0.5. The sonic
curve is the dashed line, the
Alfven curve is the dotted line,
and the equator is the vertical
axis. The velocity vectors
point in the direction of the
flow at their base, and their
length is proportional to the
velocity magnitude (Steinolf-
son, et al., 1982).

(a) t = 0 v_{max} = 181 km s^{-1}

(b) t = 4 hrs v_{max} = 193 km s^{-1}

(c) t = 8 hrs v_{max} = 197 km s^{-1}

(d) t = 12 hrs v_{max} = 195 km s^{-1}

wa, 1976). Strictly speaking, the compatibility relations are equations that can be derived from the equations of motion which must be satisfied by the dependent variables in each of the characteristic directions. Steinolfson and Nakagawa have shown that first-order or second-order (linear) extrapolation often works as well as using the more complex compatibility relations. Steinolfson, et. al used linear extrapolation to obtain the pressure and meridional magnetic field at the inner boundary. The radial magnetic field was held at its initial value so that the total magnetic flux through the solar surface remains constant. The radial velocity was also held constant with the exception that it could decrease to zero at the surface inside the closed field region. The meridional velocity was calculated so that the total velocity and magnetic field were parallel at the surface. The surface density was selected so that p/ρ^γ was constant.

In the initial state of spherically symmetric flow and a dipole potential field, the boundary values at 1 solar radius, and the system constants are:

$$T_o = 1.8 \times 10^6 \text{ degrees}$$

$$n_o = 2.25 \times 10^8 \text{ cm}^{-3}$$

$$\gamma = 1.05$$

$$\beta = \frac{2n_o k T_o}{B_o^2/8\pi} \tag{3}$$

$B_o = |\underset{\sim}{B}|$ at 1 solar radius, at the equator.

Using this definition of the plasma beta, results are summarized below for values of beta from 0.1 to 100. Values for the reference magnetic field of 0.83 G and 2.35 G at the equator yield values for the plasma beta of 4 and 0.5, respectively.

RESULTS: RELAXATION TO A STEADY STATE

Beginning with the previously stated initial configuration of a dipole potential field superimposed on a spherically symmetric flow, the relaxation then procedes in time until the solution is approximately steady - meaning the solution did not change appreciably over a period of 2 hours. The intermediate states themselves have little physical meaning. However, the relaxation time to a steady state does have physical meaning - it is typical of the time the corona would take, given the assumptions of the model, to return to equilibrium after a large-amplitude perturbation. Figure 4 shows the evolution of the coronal magnetic field (solid lines) and velocity (vectors) for beta = 0.5. The initial state is in panel (a), and subseqent states at 4, 8 and 12 hours are shown in panels (b), (c) and (d) respectively. There is little change after 12 hours. It is easy to see the field lines evolving from a closed dipole field to a coronal streamer with the closed field lines lying

188

beneath and adjacent to open field lines. The dashed line is the sonic curve and the dotted line is the Alfven curve. The sonic curve is displaced inwards in the final state, except for a small region around the equator, due to the general increase in the velocity. In the closed region, the pressure and density are increased over their initial values, and the velocity is approximately zero. Figure 5 shows cuts through the final configuration, at the pole and the equator. The high density and pressure in the closed region are evident, as is the zero velocity. Enhanced flow in the center of the open region is due essentially to the effects described by Kopp and Holzer (1976). However, the overall results are not exactly equivalent because they held the energy per gram, or flow speed infinitely far from the sun fixed, whereas here the boundary condition on temperature and velocity was held fixed on the sun. The Kopp and Holzer study dealt with the effects of changing "spreading factor" (overall flux tube divergence), whereas here a change in divergence occurs naturally along different streamlines.

Some of the effects of differing divergence can be simulated by changing the magnetic field strength. This was done by changing beta in steps from 100.0 to 0.1. Again, the results cannot be directly compared with those of Kopp and Holzer because the energy per gram at infinity is not a constant. The results from changing field strength are summarized in Figures 6 and 7. Figure 6, showing the maximum pressure and density in the closed region after scaling by the initial flow values, indicates the physical relevance of the beta parameter. The curves remain near a value of unity until beta < 1.0. Then, they rise steeply for values of beta less than ca. 0.5. At the same time, there is a corresponding general increase in the height of the streamer. However, the width of the base of the streamer has only a weak dependence on beta.

Figure 7 shows the latitudinal variation of the pressure, density and temperature at five solar radii, for a range of beta on either side of unity. Again, these variables are scaled by their initial values. The velocity is shown in Figure 8. For values of beta >= 1, the only substantial effect is that the velocity is slightly depressed and the density is enhanced in the streamer. As beta is reduced below unity, a more rapid change begins to appear over the open region. Simultaneously, the velocity in the hole begins to increase rapidly, and the density and temperature begin to decrease. This is, in general terms, the same phenomenon observed by Kopp and Holzer (1976) and Steinolfson and Tandberg-Hanssen (1977), and is due to the divergence along a streamline being more than the underlying radius-squared divergence - which is commonly called a spreading factor of more than unity.

Note that the maximum velocity at 5 solar radii is not at the center of the hole, but instead near the edge at a polar angle of 60 degrees at 5 solar radii. This reflects a combination of the boundary condition on velocity being spherically symmetric, together with the overall spreading factor between 1 and 5 solar radii being dominated by potential field-like effects near the sun. The spreading factor is largest near the edge of the hole, although it is also larger than unity near the center of the hole. As beta decreases below unity, the increasing spreading factor causes the sonic critical point to begin moving rapidly inward (from 3.5 to 2.9 solar radii for beta decreasing from 0.5 to 0.1). As in earlier studies, the consequence is a rapid increase in local flow speed (but not the terminal flow speed), with the
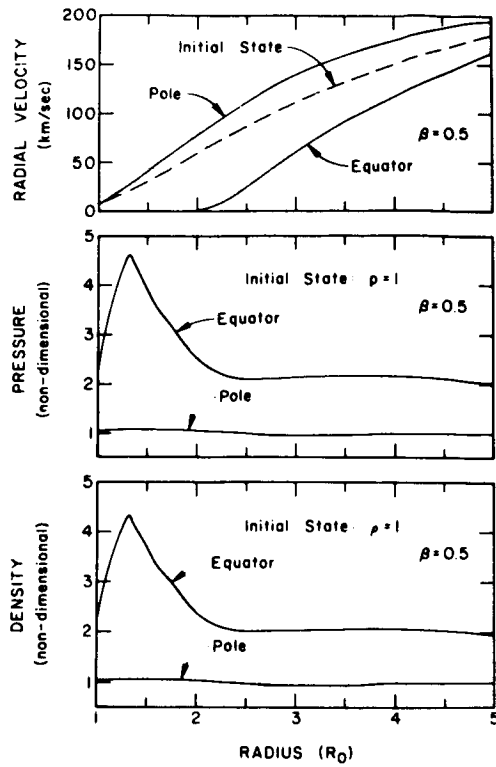
Figure 5. Radial distribution of the density, pressure and radial velocity initially (dashed line) and in the coronal streamer for beta = 0.5, at the pole and equator (Steinolfson, et al., 1982).
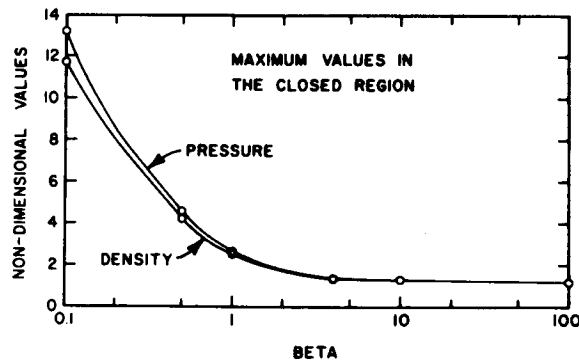
Figure 6. The dependence of the maximum pressure and density in the magnetically closed region on the reference beta (Steinolfson, et al., 1982).

largest increase occurring where the spreading factor is largest.

The result of this simulation and survey of magnetic field stength effects has been to produce a self-consistent streamer-coronal hole configuration. The streamer, in which the closed field region extends slightly more than 1 solar radius above the surface and whose width is somewhat less than the height, is quite similar to a typical streamer in its general features. The coronal hole is geometricaly similar to, for example, the polar coronal hole observed during the Skylab period , and the density at the center of the hole is less than at the edges. However, there is good reason to believe the velocity should also increase towards the center of the hole (Suess, et. al, 1977). That it doesn't is due to the choice of boundary conditions and the lack of extended energy and momentum addition other than what is implicit in the polytrope formulation. The simulation shown in Figures 1 and 2 gave a detailed fit to the polar coronal hole data reported by Munro and Jackson (1977). There, it was shown that a large variation in density and temperature was required at the inner boundary - 2 solar radii - in order to fit the observations. In order to fit those data using the model of Steinolfson, et al., it would be necessary to invoke a corresponding variation at 1 solar radius, or to deposit energy into the flow between 1 and 2 solar radii. The conclusion then must be that to simulate at least one specific coronal hole, energy and momentum must be deposited in the flow between 1 and 2 solar radii because there is little evidence for the alternative possibility of significantly higher temperatures and densities beneath the hole, at the transition region level.

Before leaving this topic, there are two additional important specific results worth noting (R. S. Steinolfson, pers. comm.). First, there has been a question of whether the final configuration shown in Figure 4 is unique. To address this first question, Steinolfson began with an initial state that was radically different that that shown in Figure 4. It had the same spherically symmetric flow field, but now with a strictly radial magnetic field whose strength at the surface varied in the same way as the radial component of a dipole field. This exercise requires that field lines can "reconnect" as they are advected inward through the outer boundary in order to form the closed field region of the streamer. This is possible here not because ohmic diffusion is specifically included, but because there is sufficient numerical diffusion to allow a similar process to occur. The simulation produced exactly the same final configuration as was found when starting with a dipole potential field, so that the conclusion is: the present example has a unique solution. The second question has to do with the suggestion that standing shock waves may exist for certain ranges of spreading factor and initial conditions (Holzer, 1977; Habbal and Tsinganos, 1983). The study of Steinolfson, et al. cannot completely answer the question of whether these shocks ever actually occur in flows where the transverse pressure balance in the presence of a magnetic field is explicitly computed, because a beta of 0.1 is not sufficiently small to produce the extreme spreading factors invoked in some of those studies. However, these computations for beta between 100 and 0.1 are probably sufficient to cover most cases of relevance to the sun. Since no standing shocks were observed, it is suggested that the phenomenon may not be of importance in the solar atmosphere.

PROSPECT FOR FUTURE MODELING

The most interesting direction that can be taken in the development of numerical models of the steady corona would be to include a more detailed description of the energetics of the flow. The polytropic description is limited by many well known deficiencies. An obvious step would be to treat thermal conduction explicitly, and later to expand the calculation to deal with non-collisional forms of the conductive energy transfer. Other similar, but less important generalizations would be to include radiative losses and ohmic diffusion. For detailed models of specific observations, until the actual processes are discovered, it may also be necessary to include an empirical description of energy and momentum deposition. As stated earlier, the model described by Steinolfson, et al. used a modified Lax-Wendroff differencing scheme, which incorporates explicit time-differencing. Because of the Courant condition for stability on the maximum time-step, such models are effectively unuseable for calculations including thermal or ohmic diffusion because the maximum allowable time step decreases linearly with the largest characteristic speed. Literally thousands of time-steps would be required with thermal diffusion in order to do the analogous problem to the relaxation described earlier.

The alternative is to use implicit time-differencing which, although algebraically complex, is not limited by the Courant condition or round-off errors proportional to $(\Delta t/\Delta x)^2$ - as is the case with the Dufort-Frankel method (Richtmeyer & Morton, 1967). In fact, it is probable that these schemes would result in a considerable improvement in computational efficiency - even for the problem treated by Steinolfson, et al. The reason for this is that, because no particular physical interest exists for the intermediate steps between the arbitrary initial state and the final steady-state, time steps too large to resolve specific intermediate dynamic fluctuations can be used and still arrive at the desired final state. This is because the steady-state solution, if one exists, is found totally independent of the step size. The one qualification is that if multiple steady-state solutions exist, then there is the possibility that the solution that is actually realized will depend on the step size because a sufficiently large dynamic fluctuation can cause the asymptotic approach to a final solution to jump to an alternative branch.

To the best of my knowledge, no implicit scheme has been applied to the problem described by Steinolfson, et al. As a substitute, I will summarize the results from a prototype calculation on one-dimensional, transonic, thermally conductive flow (Suess,1982), and outline how the analysis is extended to multi-dimensional magnetohydrodynamic flow. First, for the one-dimensional problem, the equations are:

$$\frac{\partial \rho}{\partial t} + \frac{1}{r^2}\frac{\partial}{\partial r}\left(r^2 \rho v_r\right) = 0, \tag{4a}$$

$$\rho\left(\frac{\partial v_r}{\partial t} + v_r\frac{\partial v_r}{\partial r}\right) = -\frac{\partial p}{\partial r} - \rho\frac{GM}{r^2}, \tag{4b}$$

192
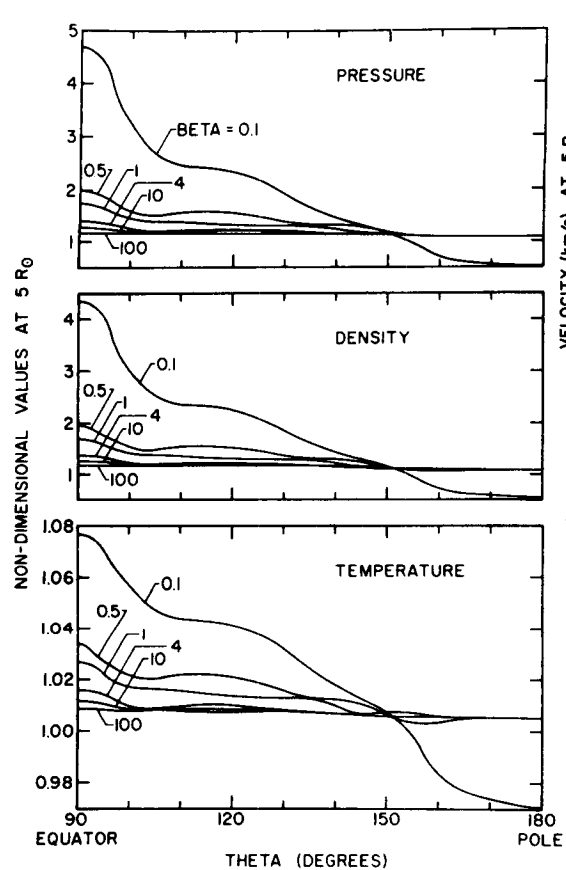
Figure 7. The meridional distribution of the thermodynamic variables at 5 solar radii, as a function of the reference beta. The variables are referenced to their initial values at 5 solar radii, before the relaxation (Steinolfson, et al.·, 1982).
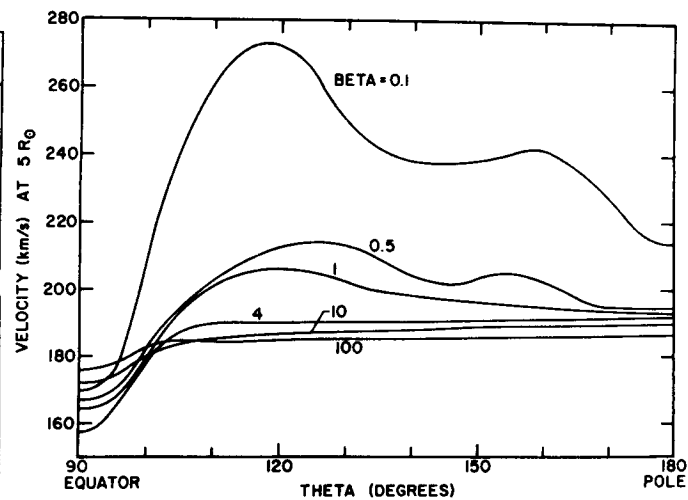
Figure 8. The meridional distribution of the radial velocity at 5 solar radii, as function of the reference beta (Steinolfson, et al., 1982).
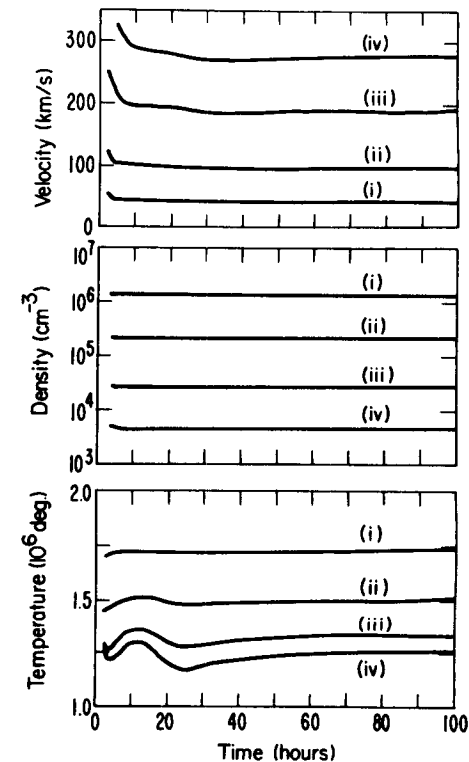
Figure 9. Relaxation from an initial state of isothermal flow to a final, thermally conductive, steady state. The curves begin at the third time step. In the plots for density, temperature and velocity, the curves labelled (i)-(v) are at 1.01, 1.51, 2.51, 5.12 and 10.24 solar radii, respectively.

$$\frac{\partial e}{\partial t} + \frac{1}{r^2}\frac{\partial}{\partial r}\left[r^2 v_r(e+p)\right] + \frac{1}{r^2}\frac{\partial}{\partial r}(r^2 q) + \rho v_r \frac{GM}{r^2} = 0, \tag{4c}$$

where ρ is the density, v_r is the radial velocity, p is the pressure, e is the total (kinetic plus internal) energy per unit volume, and M is the mass of the Sun.

$$p = 2nkT = 2\rho\left(\frac{k}{m_p + m_e}\right)T \equiv 2\rho RT,$$

$$R \approx 8.317 \times 10^7 \quad \text{(cgs)}.$$

$$q = -\kappa T^{5/2}\frac{\partial T}{\partial r},$$

$$\kappa = \frac{1.99 \times 10^{-5}}{\ln \Lambda} \quad \text{(cgs)},$$

$$\Lambda \approx 1.246 \times 10^4 (T^3/n)^{1/2}.$$

The details of the calculation are described by Suess (1982). The solution uses three-level implicit time-differencing that is unconditionally stable for any time-step. Solutions are found on a variable temporal and spatial grid using a near-conservation form of the equations and occasionally with a small amount of artificial dissipation inserted in such a way as to preserve the formal accuracy of the differencing scheme. The spatial grid is not split, and the solution is fully implicit – treating all equations simultaneously. The algorithm uses a Taylor series expansion and Jacobian matrices to deal with nonlinear coefficients so that there is no iteration of any kind between time levels. Finally, although three levels in time are used, the algorithm requires only two levels to be stored – thereby minimizing memory requirements. The algorithm is applied here to a one-dimensional problem, but I will illustrate, in general terms, application to multi-dimensional problems after the example. The example is a demonstration of the efficiency of such algorithms on a classical problem. The initial state is isothermal solar wind flow with a temperature and density at 1 solar radius of 2×10^6 degrees and 10^{+7} cm^{-3} respectively, resulting in a flow speed at 1 AU of ca. 400 km/s. Figure 9 shows the relaxation at several different radii, beginning with the third time-step. The time step is allowed to grow if the solution is changing sufficiently slowly. The relaxation procedes rapidly at first, with some large oscillations and overshoot, settling down to a steady state inside 30 solar radii after 75-100 hours. The final time step was 22.2 hours and 19 steps were required for a total elapsed time of 108 hours.

The relaxation provides the correct, known solution and the relaxation time is essentially the advection time. This example is approximately equal

in computational efficiency to solving the steady-state equations in the standard way. As soon as an additional process such as radiative loss is introduced, the relaxation becomes the most efficient technique.

To indicate the procedure for multi-dimensional flow, I begin with the form of the time-differenced equations in the one-dimensional case:

$$L \left[\frac{\partial}{\partial r}, \frac{\partial^2}{\partial r^2} \right] \Delta U^n = F \tag{5}$$

where spatial differences have not yet been introduced, L is a matrix operator, ΔU^n is the vector of variables in conservation form - being the unknown at the next time step, and F is a matrix of known quantities at the present and previous time steps. Solution involves a matrix inversion or solution of a system of equations in order to find ΔU^n. In multiple dimensions, an approximate factorization can be made to give a corresponding equation of the form (for two dimensions):

$$L_1 \left[\frac{\partial}{\partial r}, \frac{\partial^2}{\partial r^2} \right] L_2 \left[\frac{\partial}{\partial \Theta}, \frac{\partial^2}{\partial \Theta^2} \right] \Delta U^n = F + \text{cross terms.} \tag{6}$$

which is solved in two steps:

$$L_1 \left[\frac{\partial}{\partial r}, \frac{\partial^2}{\partial r^2} \right] \Delta U^{n*} = F + \text{cross terms.}$$

$$L_2 \left[\frac{\partial}{\partial \Theta}, \frac{\partial^2}{\partial \Theta^2} \right] \Delta U^n = \Delta U^{n*}$$

That is, intermediate solutions are found by sweeping in one direction through the grid, at each time step, and the final solution for that time step is the produced by sweeping in the other direction through the grid. This is possible because the equation has been "factored" into operators depending on spatial gradients in only one direction. In the presence of magnetic fields, the factorization is not complete — some cross terms involving only the magnetic field remain. These cross terms are treated explicitly.

This factored implicit algorithm has been applied to a variety of ordinary hydrodynamic problems (Beam and Warming, 1976), with great success. It has been found generally to have superior stability limits and great flexibility. There is every reason to believe that it would work equally as well for determining steady-state structure in the corona.

CONCLUSION

I have described the approach to global modeling of the corona as an initial-boundary value problem in which the configuration is allowed to relax

in time from some initial state into a steady state. It is established that the technique is powerful, flexible and stable. The results include a survey of changing magnetic field strength effects and address questions about the uniqueness of the steady state and the possibility of standing shock waves. Application of advanced numerical methods now holds promise for being able to extend the present results by addressing the all-important problem of energy transfer in the corona, even in the presence of magnetic fields.

REFERENCES

Beam, R. M., and Warming, R. F., An implicit finite difference algorithm for hyperbolic systems in conservation law form, J. Comput. Phys., 22, 87, 1976.

Brackbill, J. U., and Barnes, D. C., The effect of nonzero div.B on the numerical solution of the magnetohydrodynamic equations, J. Comput. Phys., 35, 426, 1980.

Endler, F., Ph.D. thesis, University of Gottingen, Germany, 1971.

Habbal, S., and Tsinganos, K., Multiple transonic solutions with a new class of shock transitions in steady isothermal solar and stellar winds, J. Geophys. Res., 88, 1965, 1983.

Holzer, T. E., Effects of rapidly diverging flow, heat addition, and momentum addition in the solar wind and stellar winds, J. Geophys. Res., 82, 22, 1977.

Kopp, R. A., and Holzer, T. E., Dynamics of coronal hole regions, Sol. Phys., 49, 43, 1976.

Munro, R. H., and Jackson, B. V., Physical properties of a polar coronal hole from 2 to 5 solar radii, Astrophys. J., 213, 874, 1977.

Nerney, S. F., and Suess, S. T., Restricted three-dimensional stellar wind modelling. I. Polytropic case, Astrophys. J., 196, 837, 1975.

Newkirk, G., Coronal magnetic fields and the solar wind, in Solar Wind, Proceedings of the Solar Wind Conference, Asilomar, Calif. (Sonett, Coleman & Wilcox, eds.), NASA Publication SP-308, p.11, 1972.

Pneuman, G. W., and Kopp, R. A., Gas-magnetic field interactions in the solar corona, Sol. Phys., 18, 258, 1971.

Richtmeyer, R. D., and Morton, K. W., Difference Methods for Initial Value Problems, Interscience, New York, 1967.

Steinolfson, R. S., and Nakagawa, Y., Dynamical reponse of the solar corona. II. Numerical simulations near the Sun, Astrophys. J., 207, 300, 1976.

Steinolfson, R. S., Suess, S. T., and Wu, S. T., The steady global corona, Astrophys. J., 255, 730, 1982.

Steinolfson, R. S., and Tandberg-Hanssen, E., Thermally conductive flows in coronal holes, Sol. Phys., 55, 99, 1977.

Suess, S. T., Three dimensional solar wind, J. Geophys. Res., 77, 567, 1972.

Suess, S. T., Models of coronal hole flows, Space Sci. Rev., 23, 159, 1979.

Suess, S. T., Unsteady, thermally conductive coronal flow,
Astrophys. J., 259, 880, 1982.

Suess, S. T., Richter, A. K., Winge, C. R., and Nerney, S. F.,
Solar polar coronal hole - a mathematical simulation,
Astrophys. J., 217, 296, 1977.

Weber, W. J., Ph.D. thesis, University of Utrecht, Holland, 1978.

Winge, C. R., and Coleman, P. J., First order latitude effects
in the solar wind, Planet. and Space Sci., 22, 439, 1974.

OBSERVATIONAL EVIDENCE FOR SOLAR WIND

ACCELERATION AT THE BASE OF CORONAL HOLES

G.J. Rottman[1] and F.Q. Orrall[2]

ABSTRACT

A new EUV spectrometer with a CODACON microchannel plate detector has been developed to measure Doppler shifts of coronal and transition region lines. The results of three sounding rocket flights of this instrument indicate that EUV resonance emission lines are systemaically shifted toward shorter wavelength within coronal holes. This "blue-shift" signature, first identified within compact low latitude holes, has now also been observed in a well developed polar coronal hole. The maximum measured shift within these coronal holes corresponds to a velocity relative to the remaining solar disc of 12 km s^{-1} in λ625 Mg X (T~$10^{6.15}$K) and 7 km s^{-1} in λ629 OV (T~$10^{5.4}$K). The existing data indicate that these blue-shifts are a common (and possibly universal) signature of coronal holes. These data provide important information on the acceleration of coronal plasma in open magnetic field regions, although the interpretation of observed Doppler shifts to derive a systematic mass flux is to some extent model dependent. A straightforward hypothesis is that the blueshift signature is a direct manifestation of the high speed solar wind deep within the transition region and inner corona.

[1]Laboratory for Atmospheric and Space Physics, University of Colorado, Boulder, Colorado.

[2]Institute for Astronomy, University of Hawaii, Honolulu, Hawaii.

Introduction

During the past decade it has become well established that most of the solar wind and most of the "open" solar magnetic field lines of interplanetary space emanate from a few evolving regions on the solar disk whose total area varies from perhaps 5 to 20% of the solar surface. In the inner corona above such regions the density is low, and the intensities of emission lines characteristic of these higher temperatures are much reduced relative to the quiet corona. Low density, open magnetic regions had long been known to exist in high heliographic latitudes, especially near the minimum of the sunspot cycle, but the understanding that these coronal holes also commonly occur at low latitudes and that they are the source of the high speed solar wind streams was not established until the mid 1970s. The fact that the high speed solar wind originates within coronal holes has placed severe demands on theories of solar wind acceleration, but it has also focused and clarified the problem. Certainly an important constraint on theory would be measurements of flow velocity and mass flux as a function of height in the inner corona.

In 1973 during the Skylab mission Cushman and Rense flew an EUV rocket experiment and found a region on the solar disk where the coronal emission line $\lambda303$ Si XI was very faint and also shifted to shorter wavelength with respect to the rest of the solar disk. They suggested that the region was a coronal hole, and interpreted the blueshift (which corresponded to 13 km s^{-1}) as evidence for plasma outflow from it. It subsequently turned out that this region did not fall within one of the coronal holes catalogued by the Skylab experimenters based on the ATM soft X-ray and He II solar images. This observation is considered in more detail below.

More recently a new stable high resolution EUV spectrometer has been developed at the Laboratory for Atmospheric and Space Physics (LASP) at the University of Colorado to study motions in the inner corona. This rocket-borne normal incidence Rowland mount spectrometer forms a spectrum on a multi-element linear array detector consisting of a micro-channel plate using the CODACON readout scheme developed by G. Lawrence of LASP. The 1024 channels of this array are aligned along the dispersion direction with 28 mÅ per channel in second order. As presently configured, the instrument is optimized for efficiency and resolution near 600Å and covers the region $\lambda605-\lambda635$ in second order with the first order spectrum superposed on it.

We have flown this experiment three times. On each flight the solar pointing system (SPARCS) was programmed to scan back and forth along a chord on the Sun's disk throughout the flight. The scan line was chosen to cross a coronal hole as defined by $\lambda10830$ He I spectroheliograms from Kitt Peak. Each scan took about 30 sec and 9 or 10 scans were completed on each flight. The effective spatial resolution was reduced to 1 x 1 arcmin by motion of the slit along the scan line during the 0.4 second readout time of the detector. On each flight, where the scan crossed the coronal hole, emission lines formed in the corona and transition region were shifted to shorter wavelengths relative to the rest of the disk. No significant shift was seen in the chromospheric lines of Si II.

In this paper we summarize the results of these three recent LASP rocket flights and some pertinent results by other investigators. We discuss the

200

implication that these measurements have for solar wind flow at the base of coronal holes down to the transition region.

Observations

The target for the first flight (June 5, 1979) of the LASP experiment was a rather small low latitude hole near Sun center just south of an active region (McMath 16046). The relative Doppler displacement of the transition region line λ629 OV (T~$10^{5.4}$K) (Rottman, Orrall and Klimchuk, 1981) is shown in Figure 1.
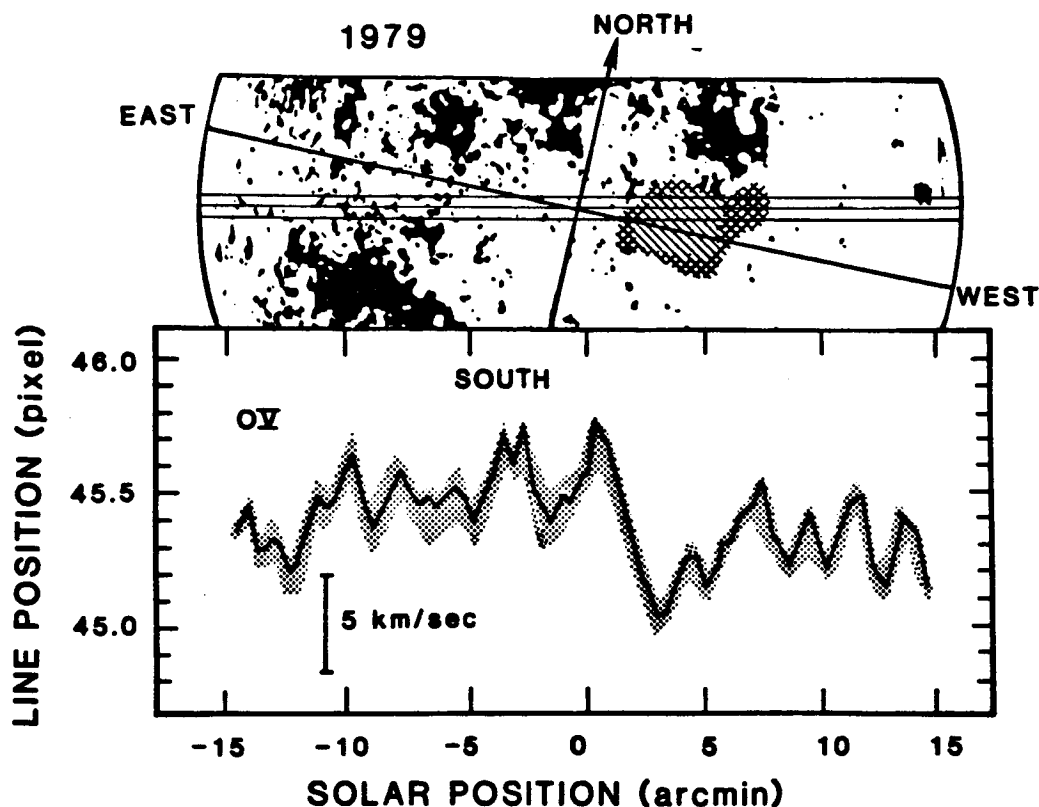
Figure 1. Mean line position of OV λ629 as measured along a solar diameter during the rocket flight of June 5, 1979. The shaded band represents ±1 standard deviation of the mean. In the top panel the dark markings indicate regions bright in the K-line (Ca II) and the crosshatched region is the coronal hole observed in λ10830 He I.

The shading represents one standard deviation of the mean of 9 scans across the solar disk. The top panel of the figure is a schematic representation of active regions bright in Ca II emission (dark areas) and the coronal hole from the λ10830 He I spectroheliogram (cross hatched). There is a clear relative blue-shift where the scan crosses the hole. On this first flight, internally scattered Lyman-alpha radiation made measurements of the coronal lines such as λ625 Mg X uncertain within the hole where coronal emission is very weak.

On the second flight (July 15, 1980) the scan line crossed a very compact
low latitude hole near Sun-center very closely associated with active region HL
16974 (Rottman, Orrall and Klimchuk, 1982). Figure 2 presents line position
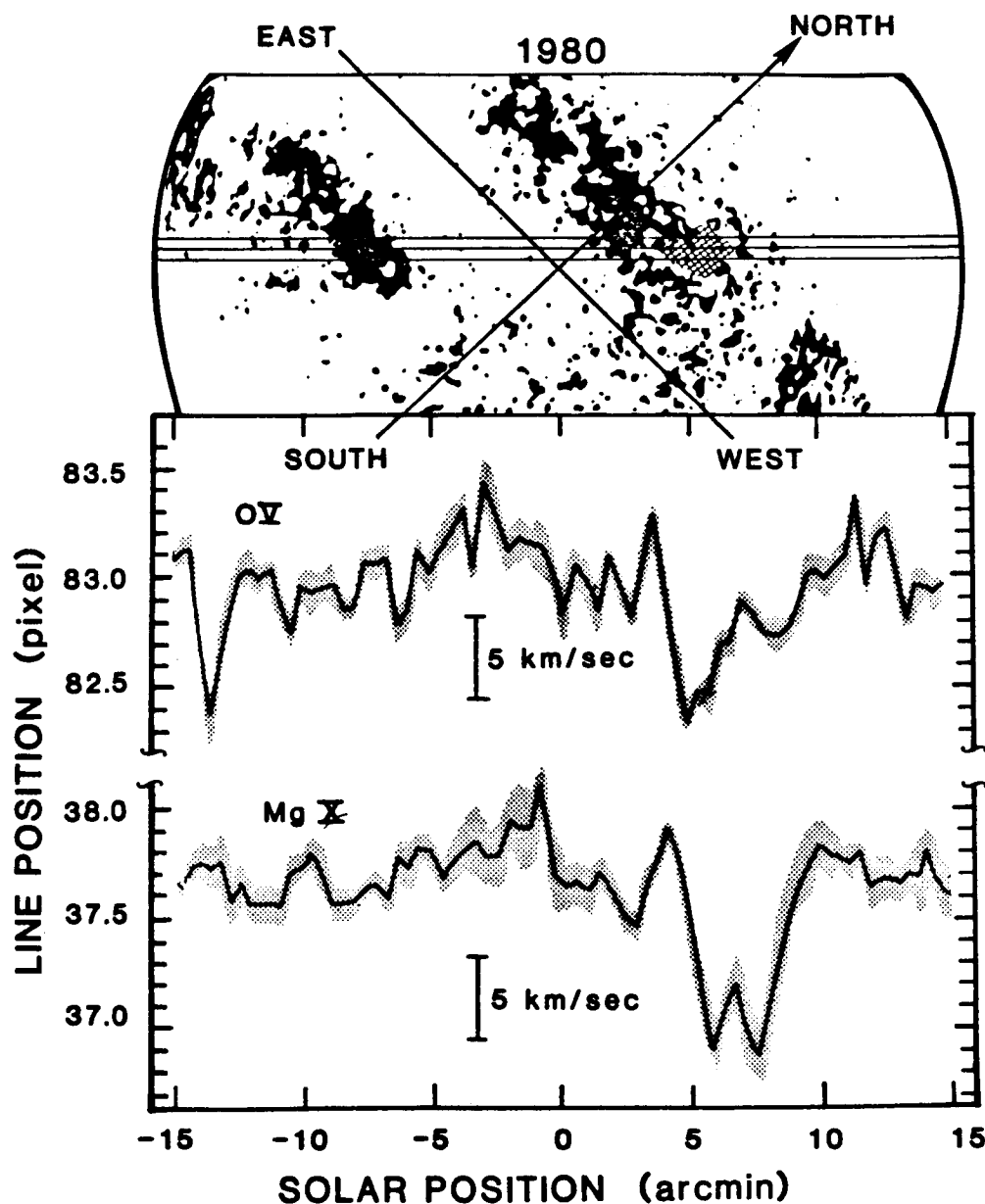
Figure 2. Mean line positions of the OV λ 629 and MgX λ 625 measured along a
chord of the solar disk during the rocket flight of July 15, 1980. The format
of the figure is similar to Figure 1.

data for the λ629 OV line and also the coronal line λ625 Mg X. Here the signa-
ture is clear in both lines and is larger in the coronal line than in the tran-
sition region line. The shape of this "blueshift" signature is different in the

two lines, an effect that may be due in part to the inclusion of closed magnetic field regions within the hole or from surrounding plages. This contamination probably also reduces the observed blueshift. There is another striking feature, also an apparent outflow seen here only in OV. This is a real feature and is associated with a prominence or filament that crosses the scan line. Such filament-associated outflows were occasionally seen by the OSO-8 observers (Lites et al. 1976 and Lites 1980).

These first two flights occurred on either side of sunspot maximum of solar cycle 21, a time when polar holes were not prominent. At the time of the third flight on November 12, 1981 the polar holes were becoming stronger and the north polar hole had a well developed low latitude extension. The scan line was chosen to cross this north polar hole and also a compact low latitude hole near Sun-center which is surrounded on three sides by plage emission from active region HL 18031. Intensity and line position data for the coronal line (Mg X) and the transition region line (OV) are shown in Figure 3 (Orrall, Rottman and Klimchuk, 1983). There is again a blueshift associated with a filament, this time visible in Mg X and not in OV. The partial reversal of the blueshift within the polar hole may be the result of the intrusion of non-hole emission into the scan line, which passed quite close to the hole boundary near that point. The area of the low latitude extension of the hole is comparable to the smaller low latitude holes of the Skylab era. The polar portion (above 60° latitude) has only 1/3 to 1/2 the area of the great polar holes observed in the declining phase of solar cycle 20.

Our experience on three rocket flights is that wherever the scan of the spectrometer crosses a coronal hole as defined in λ10830 He I we see a clear blueshift in both the transition region and corona. We have not seen this signature where there is not enhanced λ10830 emission indicating a coronal hole. (The occasional blueshifts seen above filaments are a distinct and different phenomenon.) Thus our data support the conjecture that relative blueshifts in EUV coronal and transition region lines are a common and perhaps universal signature of coronal holes.

We are aware of two other sets of pertinent data that bear on this question. One is that of Cushman and Rense (1976) mentioned earlier. In Figure 4 we have replotted their data in a format similar to our own. The top panel is a λ284 Fe XV intensity contour map obtained with the GSFC spectrometer on OSO-7 (published in Solar Geophysical Data 1973) and rotated to the time of the rocket observation. Only the faintest contours on the disk are plotted. The horizontal line represents the slit of Cushman and Rense's stigmatic spectrograph, and it is clear that their blueshifted region coincides with the faint contour. It seems likely that this open magnetic region would have appeared as a hole on a λ10830 spectroheliogram had one been available. Skylab coronal hole No. 4 appeared nearby within this same open magnetic region on the next rotation (see Rottman, Orrall and Klimchuk, 1982).

Another similar outflow was observed by Brueckner, Bartoe and Van Hoosier (1977) on the first flight of the NRL High Resolution Telescope and Spectrograph (HRTS) on July 21, 1975. The slit of their stigmatic spectrograph crossed one small region which showed a systematic outflow of about 12 km s^{-1} in the forbidden coronal line λ1349 Fe XII. They describe the region as a "magnetic weak region" and do not suggest that it was a coronal hole. There is no low
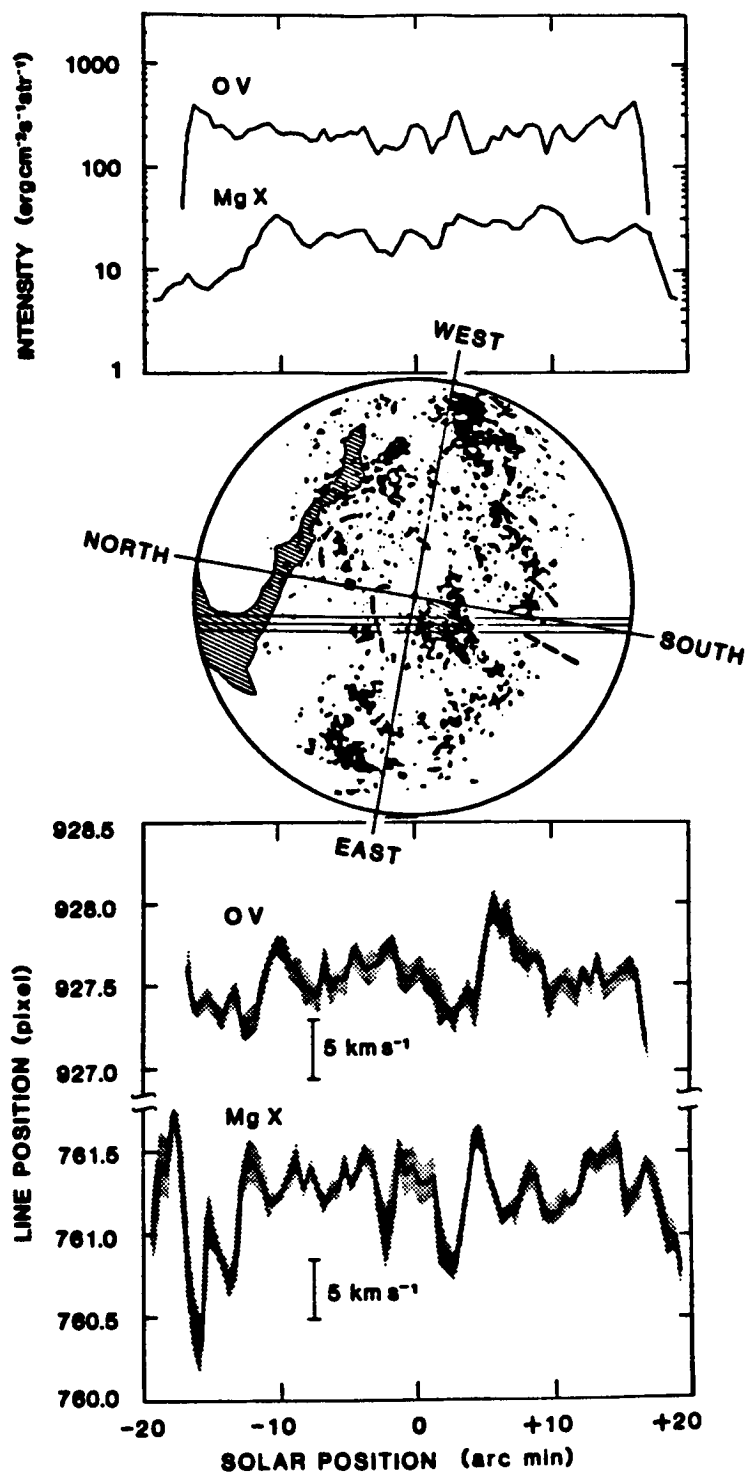
Figure 3. The mean line positions of OV λ629 and MgX λ625 measured along the North/South chord of the solar disk during the rocket flight of November 23, 1981. The format of the figure is similar to Figure 1 with the addition of the top panel giving the absolute total intensities of the two lines.
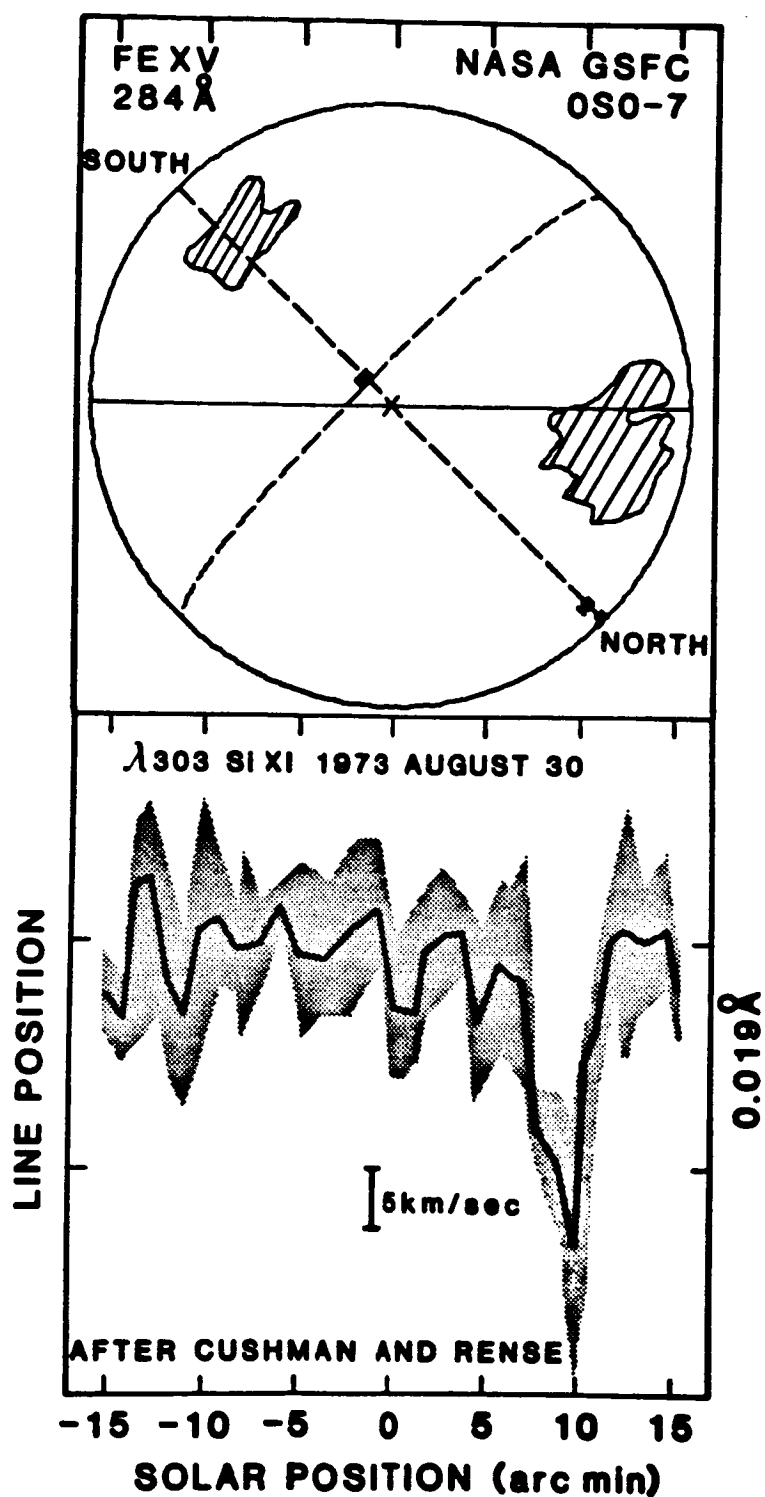
Figure 4. The relative displacement of the Si XI λ303 line along a diameter of the solar disk as measured by Cushman and Rense on August 30, 1973. The top panel shows low density contours of the corresponding Fe XV λ284 spectroheliogram from OSO 7.

205

latitude λ10830 coronal hole near this longitude on this rotation listed in the compilation of Sheeley, Harvey and Feldman (1976), but during 1975 holes less than 13° in extent were not listed. We have examined a Kitt Peak λ10830 spectroheliogram for the day of the HRTS-I flight provided to us by J.W. Harvey. The outflow region lay about 4 arcmin to the southeast of a large active region (McM 13766) and within 1.5 arcmin of a small short-lived active region (McM 13779). At the region of observed outflow, the slit crossed a small region 1 to 2 $arcmin^2$ in area where the He I network elements were absent or weakened. This is a primary indicator of coronal holes (Harvey and Sheeley 1977), although the quality of the spectroheliogram for that day was relatively poor. It is certainly possible that this outflow region was a compact hole similar to the small holes that we have observed. This is consistent with the weakness of the λ1349 Fe XII emission in the region of outflow. This observation is of special interest because the shifts of the coronal line were measured with respect to lines of CI which are formed in the low chromosphere.

Discussion

Basic parameters of the observed outflows within compact low latitude holes discussed above are summarized in Table I. The implied velocities are the

TABLE I

OBSERVATIONS OF LOW LATITUDE HOLES

Date	Position B	Position L	Associated Active Region	Area arcmin^2	Area % of Solar Surface	Lifetime (Rotations)	Apparent Velocity (km s^{-1}) Transition Region	Apparent Velocity (km s^{-1}) Corona
11/23/81	−5°	157°	HL 10831	2	0.06	3	4	7
07/15/80	+21°	239°	HL 16974	3	0.09	≥ 4	7	12
06/05/79	+2°	205°	McM 16046	11	0.33	≥ 7	5	−
07/21/75	−10°	185°	McM 13779	−	−	−	−	12
08/30/73	+30°	210°	McM 12508	−	−	−	−	13

maximum measured blueshifts uncorrected for projection. All of the outflows were quite close to active regions. The close association of low latitude coronal holes and active regions was noted by Bohlin and Sheeley (1978). They also found evidence on λ284 Fe XV Skylab spectroheliograms for very small coronal holes within active regions, similar to the small holes that we observed in

1980 and 1981 which are almost engulfed by their adjacent active regions. Examination of rocket X-ray spectroheliograms and λ10830 data (Kahler, et al. 1983) indicate that weak low-latitude holes as determined by λ10830 data do not correspond to obvious and deep X-ray holes.

The most straightforward and least contrived explanation for these negative wavelength shifts associated with coronal holes is that they are a direct manifestation of systematic mass flow from the base of coronal holes, and moreover that the apparent velocities (multiplied by the local density) are a rather direct measure of the mass flux into interplanetary space. The observed velocities are consistent with this hypothesis and with the equation of continuity for the interplanetary mass flux to within the uncertainties in coronal density and the effective fraction of the solar surface that contributes to the solar wind (Rottman, Orrall and Klimchuk, 1982).

The wavelength shifts measured so far are relative and are not absolute with respect to the rest frame of the photosphere. Pneuman and Kopp (1978) have suggested that coronal lines might be systematically redshifted relative to the photosphere due to the downflow of condensing spicular material returning to the photosphere. If so, then the apparent blueshifts in holes might be due to a difference in downflow speeds. We have recently incorporated a platinum hollow cathode lamp in our spectrometer as an absolute wavelength standard that should be capable of testing this possibility. But existing observations at least suggest that any such systematic shift in coronal wavelengths is too small to account for the blueshift signature in holes. We discussed above the HRTS measurements of Brueckner, Bartoe and Van Hoosier (1977) which show no large systematic displacement of the coronal line λ 1349 Fe XII relative to CI lines formed in the low chromosphere, over most of the quiet solar surface covered by their slit. In another experiment Behring, Cohen, Feldman and Doschek (1976) found an upper limit of 4 km s^{-1} for any systematic displacement of coronal lines relative to lines of the low transition region from spectra of the entire solar disc between 160 and 770 angstroms.

Finally we stress that even with absolute wavelength measurements, the relationship between the actual mass flux and the observed Doppler shift is to some extent model-dependent in the presence of unresolved structures and flows, and in particular will depend on the density structure of the transition region and inner corona.

Summary and Future Observations

As discussed above, all of the existing observations suggest that apparent or relative coronal outflows are a common signature of coronal holes. A similar signature of smaller amplitude is also observed in lines formed in the transition region. The observed magnitudes of these outflows are consistent with the conjecture that they are a direct manifestation of the high speed solar wind flow from coronal holes to within present uncertainties in coronal density and geometry. Evidently EUV observations of coronal emission lines made with high spectroscopic resolution and stability can supply information about the acceleration and heating of coronal plasma in open magnetic regions deep in the inner corona that can be obtained in no other way. Few such observations have been made below 1200 Å, where most of the abundant coronal ionic species have their

resonance lines. In a continuing program of EUV spectroscopy we hope to address a number of problems of coronal dynamics. In what follows we outline some studies that are direct extensions of current work that will contribute to understanding the inner corona as the source of the solar wind.

High priority should be given to making absolute measurements of Doppler displacements of coronal lines. During the 1981 November 23 flight of the spectrometer we obtained comparison spectra from an on-board hollow cathode platinum lamp. Since the motion of the rocket with respect to the Sun's center of mass is accurately known, absolute wavelengths can be inferred. We are not yet confident that we have anticipated all important sources of systematic error in these measurements, especially those that arise from the changing thermal environment of the spectrometer within the sounding rocket. But absolute measurements are certainly attainable and an improved system has been incorporated in the payload for the next flight. Such measurements are needed to infer the mass flux and to test the conjecture of Pneuman and Kopp (1978) mentioned earlier.

Coronal emission lines are broadened primarily by the combined effects of thermal, wave and turbulent motions, and probably also by the ordered motion of unresolved structures. Line width measurements are therefore an important diagnostic. Numerous line width observations have been made in EUV lines formed in the underlying transition region, and in visible coronal forbidden lines observed well above the Sun's limb at eclipse or with the ground based coronographs. But very few line widths have been measured in EUV coronal lines directly against the Sun's disk, which arise at the very base of the corona. We are making center-to-limb measurements of line widths that may make it possible to separate the vertical and horizontal components of the small scale non-thermal velocity field, and to compare these motions in open and closed magnetic regions. The on-board standard lamp provides an inflight determination of the spectrograph instrumental profile.

It is feasible within the limited duration of a sounding rocket flight to obtain spectra over a small raster. This would make it possible for example to map the outflow within a hole and thus infer the geometry of flow. It is also feasible to obtain time series of spectra from a limited region of the disk to search for direct evidence of waves in both open and closed magnetic regions. The ability to carry out either of these experiments on a sounding rocket will be enhanced by the use of a two dimensional array detector. One such detector for the EUV has been developed at LASP also using the CODACON readout scheme and is presently being flight tested.

It is clear that longer periods of observation are needed to explore the origin of the solar wind in the inner corona than can be provided by sounding rockets. One opportunity for obtaining such observations would be the planned Solar Corona Diagnostic Mission (formerly called the Solar Corona Explorer). With an extended observing period it will be readily feasible to map systematic coronal velocity fields over the entire disk on a synoptic basis. Such observations will supply essential data for modeling coronal holes as the source of the solar wind. They will establish how solar wind outflow evolves with the evolution of a coronal hole or more broadly with the evolution of an open magnetic region.

Finally, the observations of coronal outflow described here strongly complement the indirect method of inferring outflow velocities at greater heights (1.5 to 8 solar radii) from observations of Doppler-dimmed resonantly scattered EUV emission lines made above the Sun's limb (Kohl and Withbroe 1982, Kohl 1983).

Acknowledgements

REFERENCES

Behring, W.E., L. Cohen, U. Feldman, and G.A. Doschek, The solar spectrum: wavelengths and identification from 160 to 770 Å Astrophys. J., 203, 521, 1976.

Bohlin, J.D. and N.R. Sheeley, Jr., Extreme ultraviolet observations of coronal holes, Solar Physics, 56, 125, 1978.

Breuckner, Bartoe and Van Hoosier, High spatial resolution observations of the solar EUV spectrum, Proceedings of the November 7-10 OSO-8 Workshop, University of Colorado, p. 380, 1977.

Cushman, G.W. and W.A. Rense, Evidence of outward flow of plasma in a coronal hole, Astrophys J. (Letters) 207, L61. (as corrected ibid. 211, L57, 1977), 1976.

Harvey, J.W. and N.R. Sheeley, A comparison of HeII 304 Å and HeI 10830 Å spectroheliograms, Solar Physics, 54, 343, 1977.

Kahler, S.W., J.M. Davis, and J.W. Harvey, Comparison of coronal holes observed in soft X-ray and HeI 10830 Å spectroheliograms, Solar Physics (in press), 1983

Kohl, J.L. and G.L. Withbroe, EUV Spectroscopic plasma diagnostics for the solar wind acceleration region, Astrophys J. 256, 263, 1982.

Kohl, J.L. (These Proceedings), 1983.

Lites, B.W., E.C. Bruner, Jr., E.G. Chipman, and G.J. Rottman, Preliminary results from the Orbiting Solar Observatory 8: persistent velocity fields in the chromosphere and transition region, Astrophys J. (Letters) 210, L116, 1976.

Lites, B.W. Steady flows in the chromosphere and transition zone above active regions as observed by OSO-8, Solar Physics. 68, 327, 1980.

Orrall, F.Q., G.J. Rottman, and J.A. Klimchuk, Outflow from the Sun's polar corona, Astrophys. J. (Letters), 266, (in press), 1983.

Pneuman, G.W. and R.A. Kopp, Downflow in the supergranulation network and its implications for transition region models, Solar Physics, 57, 49, 1978.

Rottman, G.J., F.Q. Orrall, and J.A. Klimchuk, Measurement of systematic outflow from the solar transition region underlying a coronal hole, Astrophys J. (Letters) 247, L135, 1981.

Rottman, G.J., F.Q. Orrall, and J.A. Klimchuk, Measurements of outflow from the base of solar coronal holes, Astrophys J. 260, 326, 1982.

Sheeley, N.R. Jr., J.W. Harvey, and W.C. Feldman, Coronal holes, solar wind streams, and recurrent geomagnetic disturbances: 1973-1976, Solar Physics, 49, 271, 1976.

INTRINSIC MASS FLUX AND THE ORIGIN OF STELLAR WINDS

Richard Wolfson
Department of Physics
Middlebury College
Middlebury, VT 05753

ABSTRACT

The conventional view that winds from stars like the Sun result from the existence of a hot corona and a low-pressure interstellar medium has recently been challenged by R.N. Thomas and colleagues. They suggest that the rates of mass loss from these and other stars are determined by conditions imposed on the flow at or below photospheric levels and that the warm chromosphere and hot corona of a solar-like star are simply consequences of this imposed photospheric flow and dissipation in the resultant stellar wind. We have examined this suggestion through the application of gas dynamic theories including dissipation. Extensive analytic and numerical calculations for both polytropic and thermally conductive flows, with viscosity included, indicate that the specification of an arbitrary intrinsic mass flux is not consistent with steady, radial, spherically symmetric flow in the absence of energy addition. We conclude that there is at present no theoretical support for the suggestion of Thomas and colleagues, and that if any such support is to be found, it will require, at the very least, a more extensive theoretical gas dynamic analysis, including explicit time dependence, spatial inhomogeneities, and/or nonclassical momentum and energy transport.

Page intentionally left blank

MULTIPLE TRANSONIC SOLUTIONS AND A NEW CLASS OF SHOCK TRANSITIONS IN SOLAR AND STELLAR WINDS

Shadia R. Habbal, Kanaris Tsinganos and Robert Rosner
Harvard-Smithsonian Center for Astrophysics
60 Garden Street, Cambridge, MA 02138

ABSTRACT

The steady isothermal solar wind equations are shown to admit, under certain circumstances, multiple transonic solutions when, for example, momentum deposition gives rise to multiple critical points in the flow. These multiple solutions consist of a continuous solution and solutions which involve shock transitions between critical solutions. The ambiguity arising from the multiplicity of the solutions can be resolved by following the time evolution of a wind profile with one critical point. Results of the numerical integration of the time-dependent equations with momentum addition show that each of these multiple solutions is physically accessible and depends on the rate of change of momentum deposition. These results suggest that standing shocks are likely to be present in the inner solar wind flow.

1. Introduction

The importance of multiple critical points arising in the solar wind flow as a result of momentum addition, heat addition, and/or area divergence was first pointed out by Holzer [1977]. Leer and Holzer [1980] noted that if the wind velocity becomes supersonic at an inner critical point, shifting from one further downstream, the requirement for extended energy addition originating from the coronal base to the supersonic flow could be relaxed (e.g. waves need not propagate far out in the corona to be dissipated and add energy to the supersonic flow). In this paper we point out additional interesting properties of the transonic wind solutions to the isothermal solar wind equation of motion when multiple critical points arise in the flow. We show that, if as a result of momentum addition or rapid area divergence the wind velocity becomes supersonic at an inner critical point, leaving other critical points further downstream, the steady solar wind equation of motion can admit multiple transonic solutions, one of which is continuous, while the others involve a shock transition. We also show that the transonic wind solution with initially one critical point can evolve in time to either one of these multiple solutions depending on the rate of change of momentum deposition to the flow.

2. Mathematical Description

To study the time evolution of an isothermal, one-fluid proton-electron solar wind with momentum addition we write the time-dependent mass and momentum conservation equations for a locally radial flow in the form,

$$\frac{\partial n}{\partial t} + \frac{1}{A}\frac{d}{dr}(nAv) = 0 \tag{1}$$

and

$$\frac{\partial}{\partial t}(nv) + \frac{1}{A}\frac{d}{dr}(nAv^2) = -\frac{1}{m}\frac{dP}{dr} - \frac{GM}{r^2} + nD \tag{2}$$

213

where A is the cross-sectional area of a flow-tube, n is the electron (or proton) density, m is the proton mass, and p = 2nkT is the fluid pressure. The phenomenological term D has the dimensions of force per unit mass, and nmD represents the volume rate of momentum addition [see Holzer [1977]]. To discuss the solutions of the time-dependent equations in connection with those of the steady state equations we combine the above two equations in the form,

$$(\frac{1}{c^2} \frac{\partial v}{\partial t} - \frac{1}{nv} \frac{\partial n}{\partial t}) + \frac{M^2 - 1}{2M^2} \frac{dM^2}{dr} = \frac{2}{r} - \frac{GM}{r_s c^2 r^2} + \frac{d \ln f}{dr} + \frac{D}{c^2}$$
(3)

where $M = v/c$ is the flow Mach number, and c the constant sound speed. The cross-sectional area of a flow-tube is written as $A(r) = A_s (r/r_s^2) f(r)$, with r_s the coronal base, and f(r) a function parameterizing the divergence from spherical symmetry. The properties of the solution topologies of the steady state limit ($\partial/\partial t = 0$) are discussed in detail in Habbal and Tsinganos [1983]. We merely note here the equivalent effects of rapid area divergence (d ln f/dr) and momentum addition (D/c^2) in producing topological changes in the solutions, and the possibility for steady shock transitions to occur between critical solutions as determined by the condition

$$v_1 v_2 = c^2$$
(4)

3. Results

The changes in the steady transonic wind solution as a result of changes, f(r), in the areal divergence of the flow tube, where [see Kopp and Holzer [1976]]

$$f(r) = \frac{f_{max} e^{(r-r_1)/\sigma} + 1 - (f_{max}-1) e^{(r_s-r_1)/\sigma}}{e^{(r-r_1)/\sigma} + 1}$$
(5)

are shown as thick solid lines in Figure 1 for different values of f_{max}. Two multiple transonic solutions coexist as soon as the velocity becomes supersonic at an inner critical point, Figure 1d. For a further increase in the areal divergence of the flow tube, three solutions are possible and consist of one continuous transonic solution and two transonic solutions involving a steady shock transition between critical solutions, Figure 1e-1f.

The temporal behavior of the wind profile with initially one critical point to a final steady profile with multiple critical points as a result of momentum addition is shown in Figures 2 and 3. In Figure 2, the strength, D_0, is such that the steady state equations allow for multiple solutions to coexist, such as in Figure 1e. The resulting steady state velocity and density solutions are shown in the top panels, Figure 2a-2b, while the time evolution profiles are shown below. To vary the rate of momentum addition, we introduce the parameter τ , where

$$D(r,t) = D_0 (1 - e^{-t/\tau}) e^{-((r-r_p)/\alpha)^2}$$
(6)

214
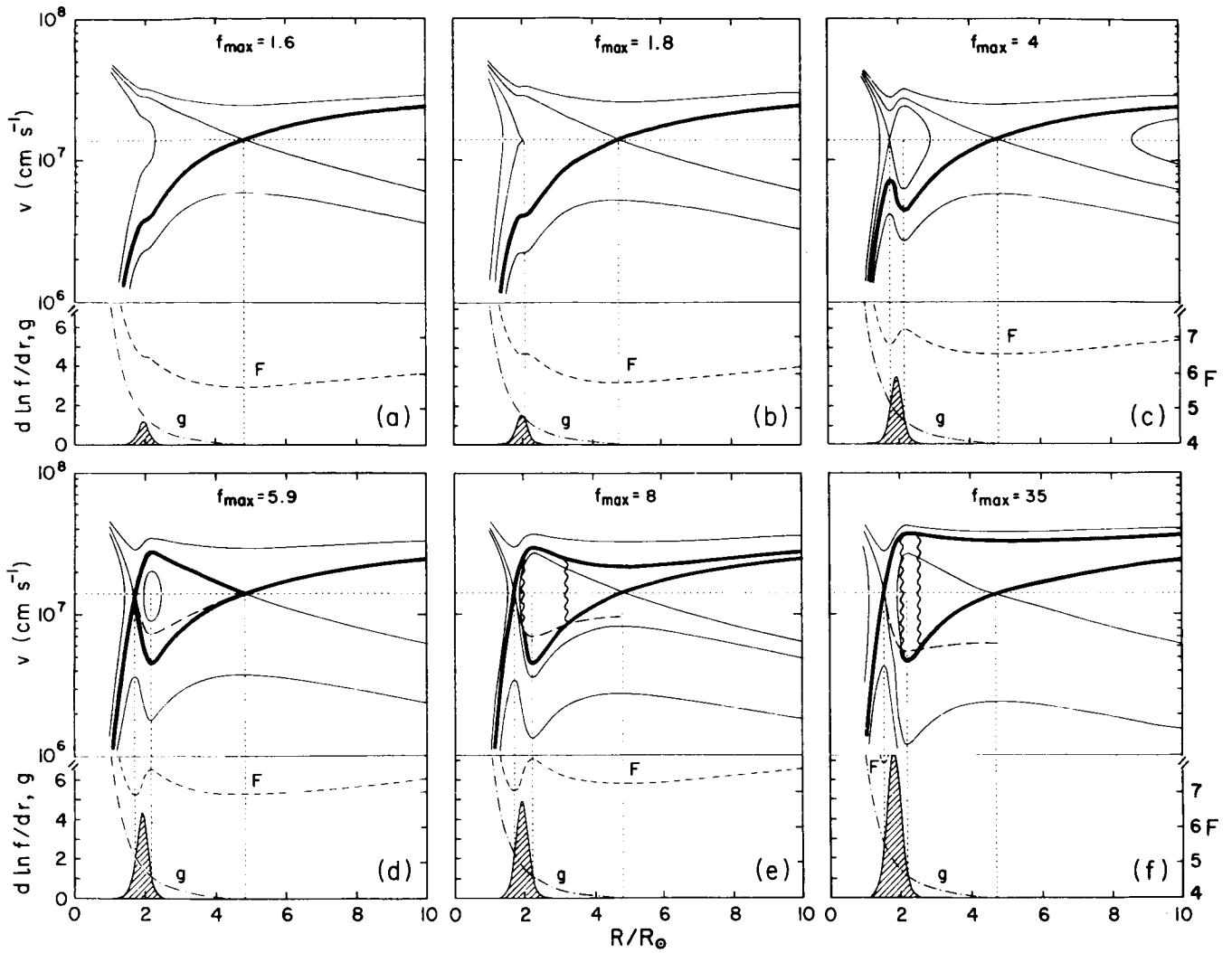
Figure 1. Sequence of solution topologies resulting from an increase in the area divergence of the flow tube, as indicated by f_{max}, for $r_1 = 2\ r_s$ and $\sigma = 0.1\ r_s$ [see (5)]. Additional critical points arise in the flow as the area function, $d\ln f/dr$, intersects the curve $g = GM_s c^2 r^2 - 2/r$. The transonic wind solutions are drawn as thick solid lines, and the shock transitions, when present, are indicated by the wavy lines satisfying the condition (4). The wind is assumed isothermal at $T = 1.2\times10^6$ K with a sonic point at $4.8\ r_s$ for a spherically symmetric flow [from Habbal and Tsinganos [1983]].

The results shown correspond to three different values of τ. The integration time step is 10 s, and the time interval between neighboring curves is 10^4 s. The initial state is the solution to the steady state solar wind equation of motion with no momentum addition for an isothermal wind at $T = 1.2\times10^6$ K, with a sonic point at $4.8\ r_s$. The momentum is then applied in time either slowly (large τ), or rapidly (small τ). For $\tau = 4\times10^4$ s, Figure 2c-2d, the velocity and density profiles evolve to form a standing shock at the inner position predicted by the steady state calculations, while for $\tau = 2 \times 10^4$ s, Figure 2e-2f, the velocity and density profiles evolve with a standing shock further downstream

215
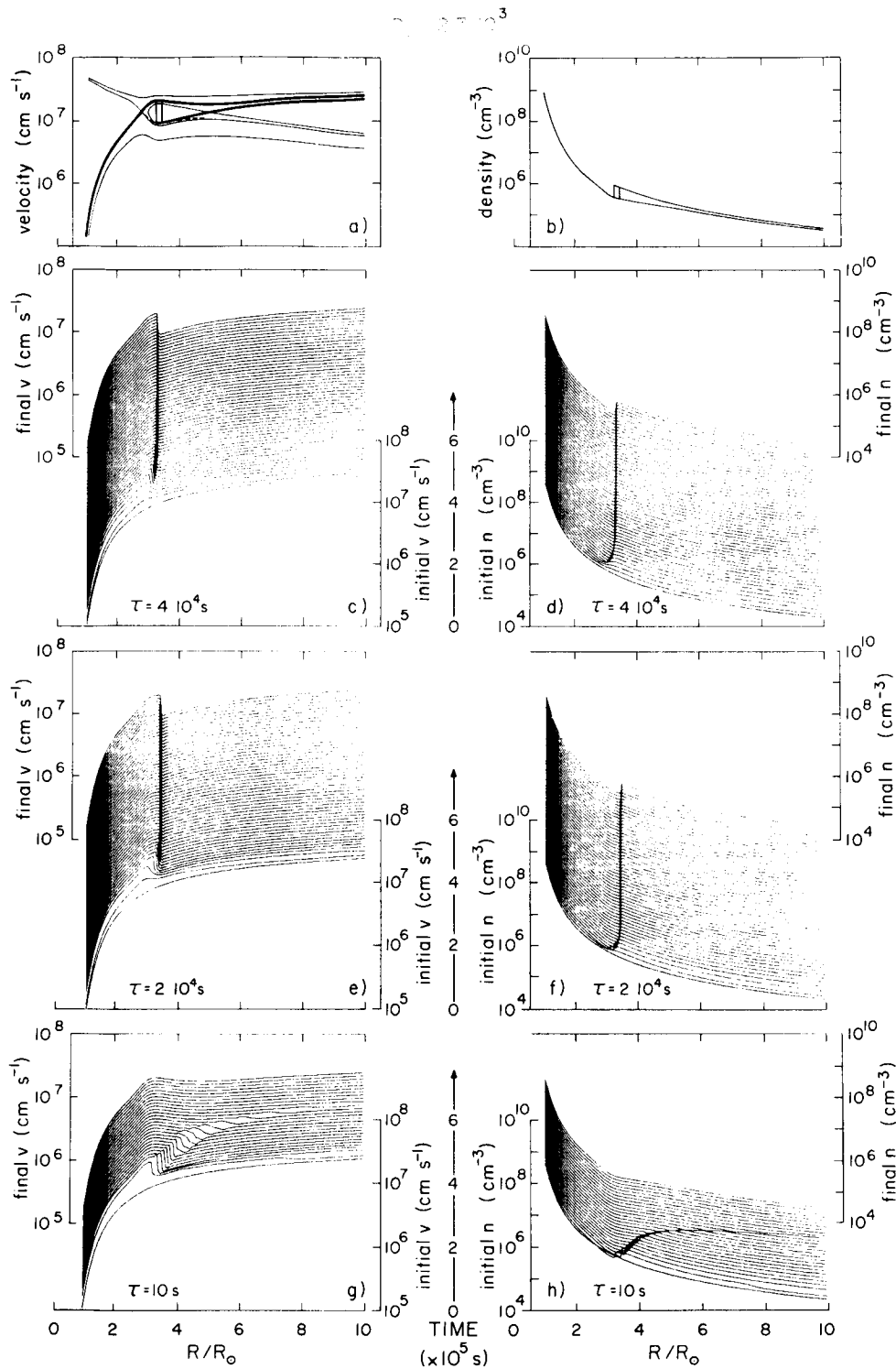
Figure 2. Sequence of time evolution of the velocity and density profiles to a final steady state as a result of momentum addition, with $D_0 = 2.7 \times 10^3$, $\alpha = 0.3$, and $r_p = 3r_s$, for different values of τ [see (6)]. The sequence shows how each of the steady multiple transonic solutions, shown as dark solid lines in (a)-(b), are accessible. In (c)-(d), the wind profile evolves in time to the steady state solution with the standing shock at the inner position for $\tau = 4 \times 10^4$ s. The second standing shock develops for a slightly smaller value of $\tau = 2 \times 10^4$ s, (e)-(f). For $\tau = 10$ s, the velocity and density profiles evolve to continuous ones.

216

than in the previous case. By reducing τ further to $\tau = 10$ s, the velocity and density profiles evolve in such a way that a shock discontinuity develops only temporarily, as soon as the velocity becomes sonic closer to the base, but disperses and propagates outwards. Hence, by changing the rate of momentum deposition, this example illustrates how each of the multiple solutions is physically realizable. For a further increase in D_0 (Figure 3), the condition for the existence of steady shocks is no longer satisfied. The velocity and density profiles evolve to continuous steady solutions for either value of τ , despite the temporary formation of a shock discontinuity.

4. Conclusion

In the present study we have illustrated how the multiplicity of the transonic solutions to the steady isothermal wind equations arises as a result of changes in the areal divergence of the flow tube and/or as a result of momentum addition. By changing the rate of momentum deposition, and by following the corresponding temporal evolution pattern of the wind profile with initially one critical point, we have shown how each one of the multiple solutions is physically realizable and corresponds to different intermediate temporal states of the solar wind. In particular, we have shown how a transonic solution with a standing shock could occur in the wind flow as predicted by Holzer [1977] (albeit without the restriction of an isothermal flow).

The multiplicity of the transonic solutions to the steady isothermal solar wind equations, however, is not unique to this study. Multiple solutions have originally been found by Leer et al. [1982] in their study of Alfvén wave driven stellar winds. They find two continuous transonic solutions characterized by different velocities at the base, for a certain range of wave damping lengths. In our case, the steady multiple transonic solutions exhibit some form of degeneracy since they all have the same velocity at the base, although the continuous solution and those involving a shock transition have different asymptotic flow speeds.

Finally, as an example based on our results, we note that if the rate of change of momentum addition or the temporal change in the area divergence of a flow tube, such as in a coronal hole, occurs over time scales of the order of 10^4 s, and the final value reached is maintained for time scales of the order of 10^5 s, i.e. days, a standing shock can develop within 5 r_s from the coronal base for a solar wind at say 1.2×10^6 K. In a realistic solar wind model the formation of a standing shock in the solar wind could lead to a reduction in the energy flux per particle, since the temperature rise in the shock will result in energy loss by thermal conduction to the base if the shock occurs within 1 or 2 R_s of the inner critical point [E. Leer, private communicaton [1983], see also Holzer and Leer [1980] for a detailed discussion of conductive solar wind models]. For an isothermal wind, however, and an isothermal shock, although the infinite thermal conductivity is implicit, the loss of energy flux to the wind as a result of shock formation is apparent in the lower asymptotic flow speed, yet there is no corresponding increase in particle flux at the base when compared with the particle flux associated with the continuous transonic solution.

$D_0 = 3 \ 10^3$
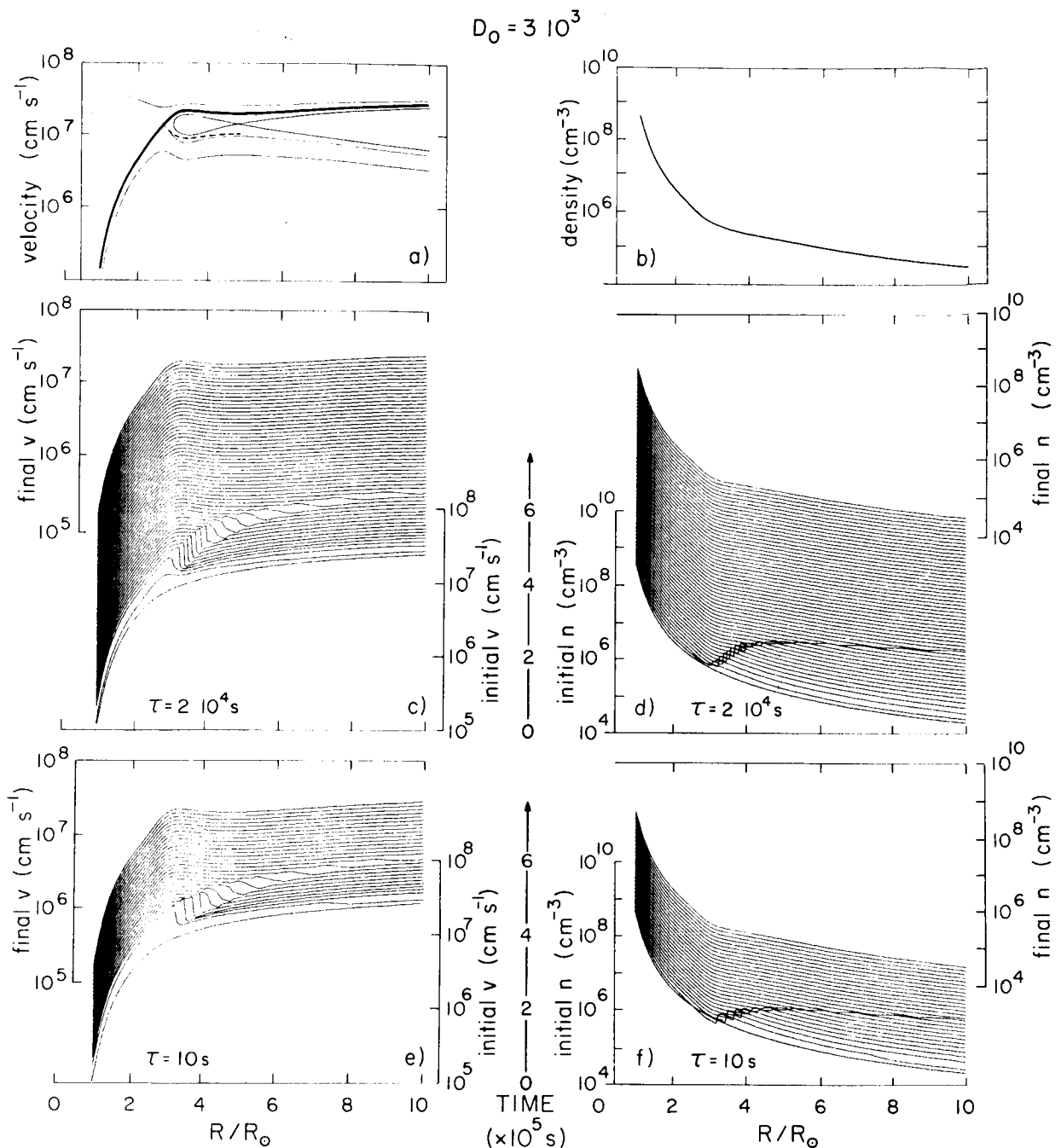
Figure 3. Same as Figure 2 for a strength of momentum addition such that the steady state equations do not admit multiple solutions. The temporal behavior of the wind profile is such that shock discontinuities form temporarily in the flow but disperse and propagate outwards.

References

Habbal, S. R., and K. Tsinganos, Multiple Transonic Solutions and a New Class of Shock Transitions in Steady Isothermal Solar and Stellar Winds, to appear in J. Geophys. Res., 1983.
Holzer, T. E., Effects of Rapidly Diverging Flow, Heat Addition and Momentum

Addition in the Solar Wind and Stellar Winds, J. Geophys. Res., 82, 23, 1977.

Holzer, T. E., and E. Leer, Conductive Solar Wind Models in Rapidly Diverging Flow Geometries, J. Geophys. Res., 85, 4665, 1980.

Kopp, R. A., and T. E. Holzer, Dynamics of Coronal Hole Regions. I. Steady Polytropic Flows with Multiple Critical Points, Solar Physics, 49, 43, 1976.

Leer, E., Holzer, T. E. and T. Flå, Acceleration of the Solar Wind, Space Sci. Rev., 33, 161, 1982.

Leer, E. and T. E. Holzer, Energy Addition in the Solar Wind, J. Geophys. Res., 85, 4681, 1980.

X-RAY BRIGHT POINTS AND SOLAR WIND GENERATION

S.-I. Akasofu
Geophysical Institute
University of Alaska
Fairbanks, Alaska

ABSTRACT

The apparent contradiction between the fact that there is a high correlation between a high speed stream and a coronal hole (Krieger et al., 1973) and the fact that the thermal structure of the coronal hole, based on X-ray, EUV and radio observations, does not support the thermally driven solar wind models (cf. Rosner and Vaiana, 1977) may be solved by considering that a dynamo process around X-ray bright points (XBP) in a coronal hole is partly responsible in accelerating coronal plasma away from the sun. The present theoretical difficulty in explaining solar wind generation may indicate that it is difficult to overcome the solar gravitational force by the thermal expansion process alone.

Let us consider eddy motions around both feet of the magnetic loop structure of XBP, as shown in Figure 1A. Note that the magnetic loop is embedded in a unipolar magnetic field region of the coronal hole. In terms of the standard MHD description, such eddy motions twist the magnetic loop structure (Parker, 1979); note that the direction of the eddy motions should be the same for both eddies. The twisting can also be interpreted in terms of the presence of field-aligned currents $J_{\parallel}$ along the magnetic loop, which are caused by the dynamo process associated with the eddy motions in the photospheric level. As shown in Figure 1B, the horizontal currents $\underline{I}$ tend to flow radially in the eddies and generate $J_{\parallel}$; note that $J_{\parallel} = -\nabla \cdot \underline{I}$.

In this situation, it is quite likely that an electric potential structure appears along the magnetic loop as a result of $J_{\parallel}$. This is because hot coronal electrons cannot carry a large amount of current towards the foot of the magnetic loop without a significant potential drop. The presence of such a potential structure has been demonstrated in a magnetospheric situation which is basically similar to our XBP situation (cf. Kan, 1982). The suggested potential structure can accelerate current-carrying electrons to more than 10 keV around XBP; those electrons may be responsible for X-ray emissions from XBP.

Both the chromospheric and coronal plasmas should participate in the eddy motions or any other motions. As is well-known, coronal structures vary in association with changes of magnetic fields in the photospheric level. Such changes must be accomplished by the Lorentz force $\underline{J}_{\perp} \times \underline{B}_o$. Further, the current $\underline{J}_{\perp}$ across the magnetic field $\underline{B}_o$ must be diverted from $J_{\parallel}$. The resulting circuits are shown in Figure 1B, in which one can easily see that the Lorentz force $\underline{J}_{\perp} \times \underline{B}_o$ drives the chromospheric and coronal plasmas to participate in the same eddy motions in the photospheric level.

Now, such current circuits generate a secondary magnetic field $\underline{b}$, as shown in Figure 1C. The Lorentz force associated wth $\underline{J}_{\perp} \times \underline{b}$ is always directed upwards, regardless of the direction of the eddy motions and of the magnetic field polarity around the XBP including the unipolar field. It is suggested that
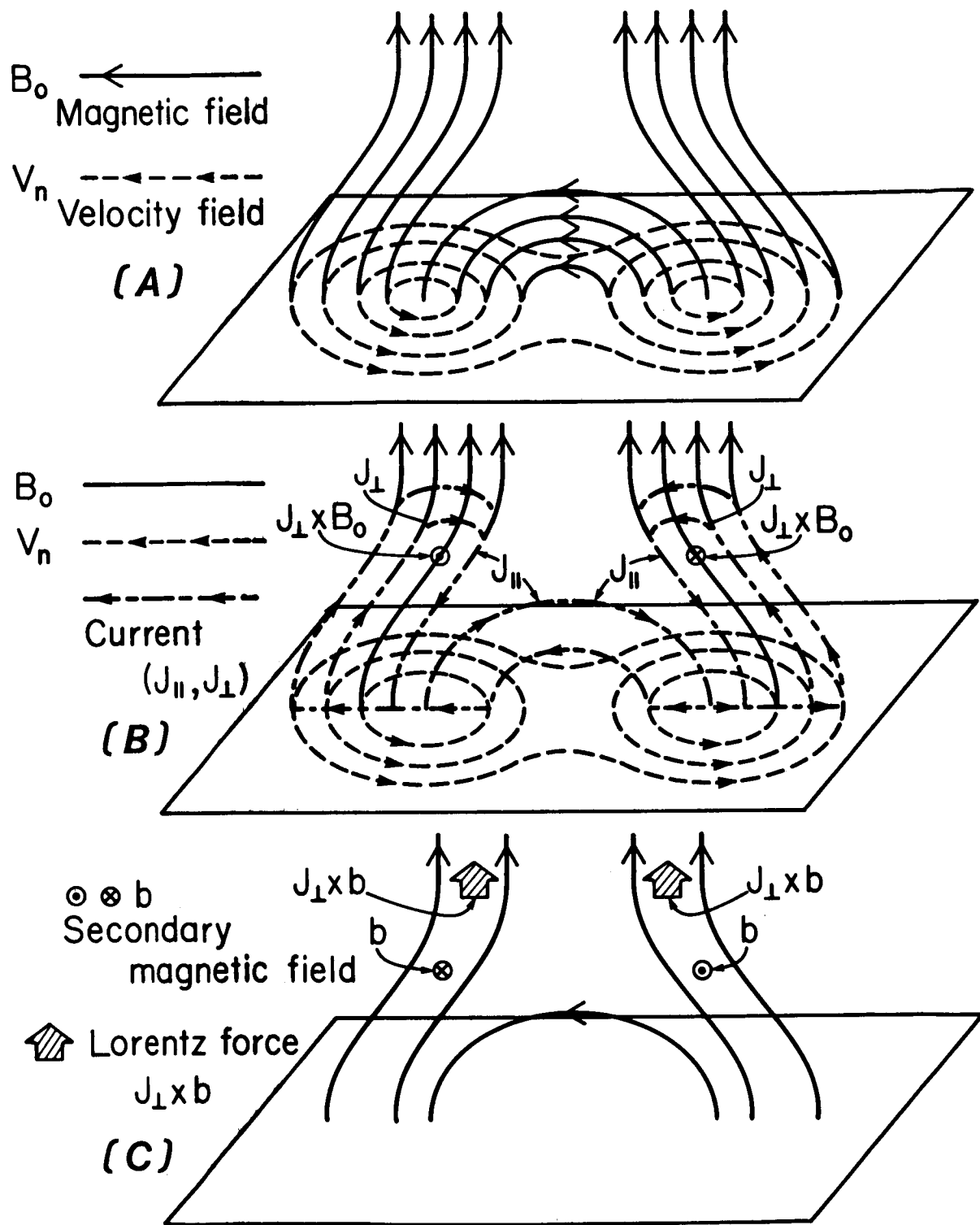
Figure 1. Schematic illustration of effects of the counterclockwise vortex motion around the feet of a bi-polar structure emerging in a unipolar region. In (a), the primary magnetic field configuration ($\underline{B}_o$) and the vortex motion ($\underline{v}_n$) are shown. In (b), the resulting current system ($J_{\parallel}$ and $J_{\perp}$) and the primary Lorentz force $\underline{J}_{\perp} \times \underline{B}$ are indicated. The secondary magnetic field $\underline{b}$ and the associated upward Lorentz force ($\underline{J}_{\perp} \times \underline{b}$) are indicated in (c).

222

it is this upward acceleration which is responsible for the upward flow of the chromospheric and coronal plasmas.

The power associated with this particular dynamo process is 6×10^{24} erg/sec for the eddy (of radius 10^6 m) speed of 100 m/sec, $B_0 = 10$ gauss, the conductivity $\Sigma_p = 10^7$ mho. The observed total energy loss from an XBP is of the order of 1.4×10^{19} watt. A rough estimate indicates that the maximum value of $J_\perp$ will be of the order of 10^{-4} amp/m^2. If b is $0.1 \sim 1.0$ gauss, the resulting Lorentz force $J_\perp \times b$ will be $10^{-10} \sim 10^{-9}$ dyne/cm^3. Thus, assuming the number density of the plasma of the order of 10^8/cm^3, the acceleration due to the Lorentz force will be $10^6 \sim 10^7$ cm/sec^2; such values may be compared with the gravitational acceleration on the photospheric surface ($= 2.4 \times 10^4$ cm/sec^2); for details of these estimates, see Akasofu (1983). It may well be that this is an overestimate, but it is not difficult to infer that the Lorentz force associated with the dynamo process around an XBP can provide a powerful upward acceleration of the chromospheric and coronal plasmas. Indeed, Ahmad and Webb (1978) suggested that XBP could be an important source of the solar wind. Bohlin et al. (1975) also suggested that macrospicules in coronal holes are a source of the solar wind.

References

Ahmad, I.A. and D.F. Webb, S-ray analysis of a polar plasma, Solar Phys., 58, 323, 1978.

Akasofu, S.-I., A comprehensive view of solar-terrestrial relationships in terms of a chain of four dynamo-powered plasma acceleration processes, Planet. Space Sci., 31, 25, 1983.

Bohlin, J. D., S. N. Vogel, J. D. Purcell, and N. R. Sheeley, Jr., A newly observed solar feature: Macrospicules in H$_e$ II 304Å, Ap. J., 197, 133, 1975.

Kan, J. R., Towards a unified theory of discrete auroras, Space Sci. Rev., 31, 71, 1982.

Krieger, A. S., A. F. Timothy, and E. C. Roelof, A coronal hole and its indication as the source of a high velocity solar wind stream, Solar Phys., 29, 505, 1973.

Parker, E. N., Cosmical Magnetic Fields, Oxford Univ. Press., 1979.

Rosner, R. and G. S. Vaiana, Hydrostatic and dynamic models of solar coronal holes, Ap. J., 216, 141, 1977.
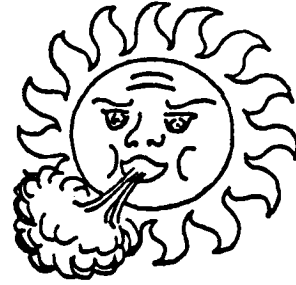
SESSION 4.

STELLAR CORONAE AND WINDS

Page intentionally left blank

SUMMARY OF THE SESSION ON STELLAR CORONAL WINDS

R. Rosner

Observations of winds on stars other than the Sun are restricted to stars of solar temperature, but far lower surface gravity (i.e., "late-type" giants and supergiants) and massive (high surface temperature) stars. In these stars, the mass flux is sufficiently large that available spectral diagnostics suffice to observe the doppler-shifted line emission and absorption due to the expanding outflowing plasma; the question is thus whether the "solar anology" remains applicable under such extreme circumstances. For the late-type (cool) giants and supergiants, Dupree and McGregor argued that the governing physics is likely to be an extreme version of that thought to apply to the Sun: the major goal is to understand the simultaneous presence of large mass fluxes ($\sim 10^{-8}$ $M_\odot$ yr^{-1}), low terminal speed ($\sim v_{esc}$) and low wind temperature. Holzer pointed out that simplified (parametrised) models of Alfven wave damping do not give reasonable results. (The equations are very stiff if the damping length is free). As reviewed by Cassinelli, the winds of hot stars, in contrast, are very non-solar: the wind column densities are sufficiently large that radiation pressure driving due to resonance lines is very likely the dominant term in the momentum equation. The major problems here are to account for the "zeroth-order" spatial structure of the wind (for example, to understand the spatial relation of the observed x-ray emitting plasma and the cool wind), to understand multiple photon scattering (reviewed by Friend), and to understand wind instabilities (which may lead to the hot x-ray emitting plasma by formation of multiple stocks). In summary, it is evident that stellar winds offer a challenging testing ground for developing wind theory, although even the isothermal wind turns out to still hold surprises for us, such as the existence of degenerate solutions discussed by Tsinganos.

Page intentionally left blank

OBSERVATION OF WINDS IN COOL STARS

A. K. Dupree
Harvard-Smithsonian Center for Astrophysics
Cambridge, MA 02138

ABSTRACT

Sufficient observational material - ultraviolet spectroscopic measures, quantitative optical spectroscopy, and X-ray photometry - has accumulated to enable us to discern the presence and character of mass loss in cool stars and to establish meaningful constraints on theoretical models. Two determinants of atmospheric wind structure - temperature and gravity - may suffice in a most superficial way to define the wind and atmospheric structure in a star, however more extensive observations demonstrate the importance of magnetic surface activity and its particular geometrical configuration. Successive observations of an active binary system and a supergiant star have revealed that magnetic activity and perhaps mass loss occur on restricted regions of a stellar surface and that long lived structures are present in a wind.

Introduction

It was in 1935 that Adams and MacCormack detected the Doppler shift of neutral and lowly ionized species towards a cool supergiant star - α Her. The outflow velocity was only a few kilometers per second, substantially less than the escape velocity from the stellar surface, and led Spitzer (1939) to conjecture that the outflowing material became ionized and then returned to the star. Almost twenty years passed before Deutsch (1956) discovered stationary lines in the spectroscopic binary that is a companion to the supergiant star. These ground state lines from species of low ionization, defined the extended nature of the wind from the supergiant (1000 a.u.); and their velocities confirmed that the material was actually escaping from the supergiant star. Since then, optical, infrared, and ultraviolet studies have generally confirmed the existence of mass loss in a great variety of cool stars. However, to date the Sun is still the only dwarf star in which there is direct evidence for mass loss.

Recent spectroscopic measurements with the International Ultraviolet Explorer satellite have enabled us to develop a comprehensive view of the mass loss phenomenon for stars more luminous and cooler than the Sun. Complementary X-ray measurements and ground-based spectroscopy allow the character of a stellar chromosphere and corona to be defined and its role in the presence of a stellar wind to be explored. Placing the Sun in the stellar context - with the extended domain of physical conditions - can confront and enhance our theoretical understanding of the mass loss process.

There are several means to infer the presence of mass outflow and eventual loss in a stellar atmosphere. These include the detection of circumstellar lines of metals and low species of ionization, the measurement of molecular and continuum emission at infrared or radio frequencies from circumstellar material, the observation of asymmetric line profiles, and the direct measure of an outward Doppler shift in the position of a line. It is through optical and ultraviolet spectroscopy that a large number of stars have been surveyed, and from which most recently it has been possible to draw a comprehensive picture of the mass loss process.

Frequently used spectroscopic signatures of mass loss are the asymmetry of an optically thick chromospheric emission line and/or the presence of narrow circumstellar absorption features. Transitions such as the resonance lines of Ca II and Mg II are formed in the chromosphere of a star, and can indicate mass motions in luminous stars. Figure 1 shows three spectra typical of cool stars.
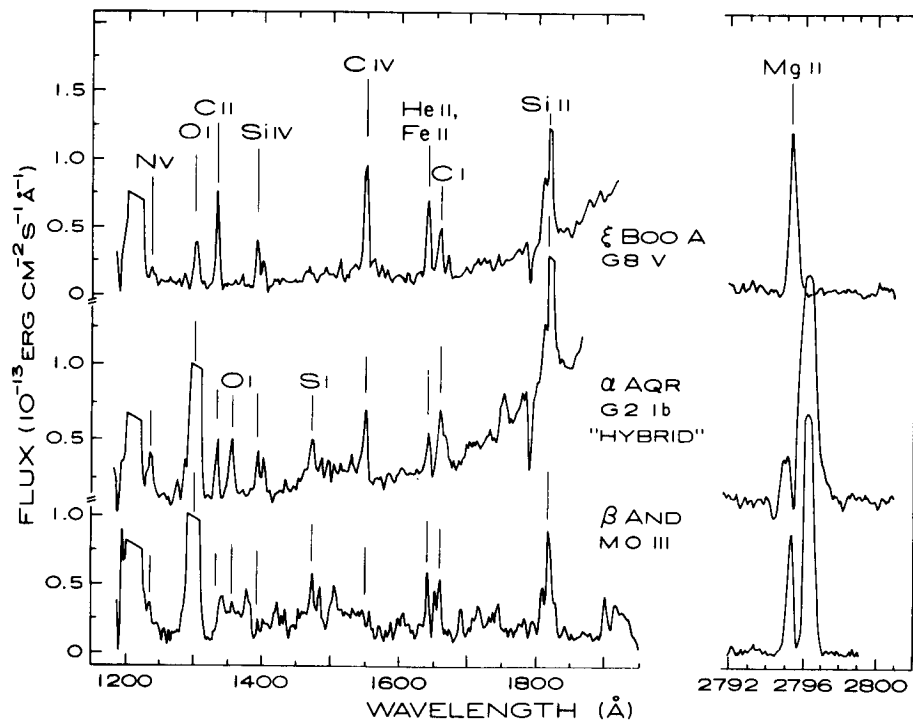
Figure 1. Ultraviolet spectra of cool stars from IUE showing three types of stellar atmospheres: a dwarf similar to the Sun (ξ Boo A); a hybrid supergiant star, α Aqr with both a hot (10^5 K) atmosphere and the asymmetric Mg II profile typical of an expanding atmosphere; a cool luminous supergiant β And showing predominantly species of low excitation and a massive wind. Data from Hartmann, Dupree, and Raymond (1982).

The Mg II emission line is narrow in the dwarf star (ξ Boo A) and at the spectral resolution now available, shows no sign of any absorption or asymmetry. Contrast this with the profiles of the more luminous stars α Aqr and β And where an asymmetry is found in the emission peaks. This asymmetry in the sense, long wavelength peak > short wavelength peak or red > violet - and the accompanying blue-shifted line core (here somewhat distorted by narrow interstellar absorption features) signal the presence of a massive stellar wind. It was the original suggestion of Hummer and Rybicki (1968) that a differentially expanding atmosphere could produce such a profile; this has been confirmed in simultaneous measurements of profiles and direct Doppler shifts in regions of the Sun (Brueckner, Bartoe, and van Hoosier, 1977) and by theoretical calculations for the Sun (see Dupree 1981).

Observations of the Mg II and the Ca II profiles are used to identify stars undergoing mass outflow - which is assumed to eventually lead to mass loss - and to measure the radial velocity of circumstellar absorption features. The highest outflow velocity corresponding to the maximum short wavelength extension of the circumstellar absorption is commonly identified as the terminal velocity of the wind (V_∞) and is taken as a constraint on wind theories. It is believed that such blue-shifted features result from recombination to Mg II and Ca II ions far out in the wind as it cools and flows into the interstellar medium. Corresponding features in both the Mg II and Ca II profiles support this empirical interpretation; and current calculations offer confirmation.

Emission from cool stars at shorter wavelengths in the ultraviolet spectral region can indicate the presence of plasma with temperatures from $10^4 - 2 \times 10^5$ K. The strong C IV and N V emission lines found the dwarf ξ Boo A and the supergiant star α Aqr in Figure 1 testify to the existence of hot (2×10^5 K) gas in the atmospheres of these objects. For the dwarf star, as is the Sun, it is no surprise to find the signature of hot plasma; in the supergiant, the spectra clearly demonstrate that hot gas can coexist with a massive stellar wind. The coolest and most luminous stars of all, exemplified by β And in Figure 1 give no indication of high temperature species, suggesting a cool atmosphere and a massive wind.

The appearance of profile asymmetries in stars of various temperatures and luminosities is summarized in Figure 2. As a star becomes cooler and more luminous, there is a progression of the mass outflow signature from lines in the high chromosphere and wind (Mg II) to the lower levels (Ca II). When sufficient material has accumulated, circumstellar absorption features become detectable. Moreover, the terminal velocity of the wind as inferred from the presence of narrow absorption features decreases too. Hybrid supergiants, such as α Aqr, have a terminal velocity ~ 60 km s^{-1}; the cooler more luminous giants and supergiants exhibit absorption features indicating outflow of ~ 10 km s^{-1} (Reimers 1977).
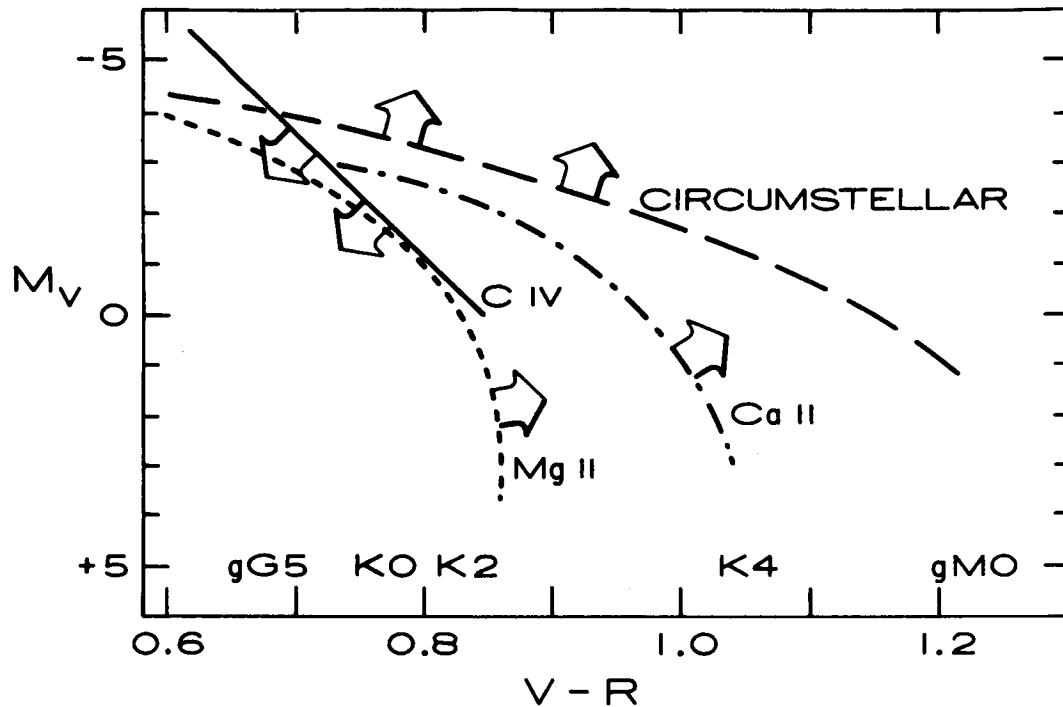
Figure 2. The appearance of various spectral features as a function of color (V-R index) and absolute magnitude (M_v) for the most luminous stars. C IV emission is prominent to the left of the solid line; the ratio of red:blue emission peaks for Mg II and Ca II is greater than 1 to the right of the appropriate broken lines (Stencel 1978; Stencel and Mullan 1980). Circumstellar Ca II features are found above the long broken line (Reimers 1977). For the Sun, the values are M_v = +4.79 and V-R = +0.52.

Atmospheric Conditions

The domain of hot atmospheric plasma can be related to the presence of mass outflow. In Figure 3 is summarized the presence of various spectral features in cool stars. Spectra of dwarf stars (luminosity class V) generally contain detectable C IV emission, whereas most cool luminous stars (spectra type M0-M5, luminosity class I-III) show no indication of C IV. If C IV is undetected in a sufficiently long exposure, upper limits result that are 10^{-1} to 10^{-2} of the surface flux of the quiet Sun (Hartmann, Dupree and Raymond 1982). In the latter case, these luminous stars possess strong winds as can be inferred from Figure 2. Moreover, there is a substantial intermediate region of stars showing both the presence of C IV emission and of low excitation features - the "hybrid" stars (Hartmann, Dupree, and Raymond 1980). X-ray surveys (Vaiana et al. 1981;

232

Helfand and Caillault 1982) from the HEAO-2 ("Einstein") satellite confirm the C IV results in the extremes. X-rays are generally found in dwarf (main-sequence) stars, but there is an absence of detectable X-ray emission in the luminous giant and supergiant stars - except for active binary systems.
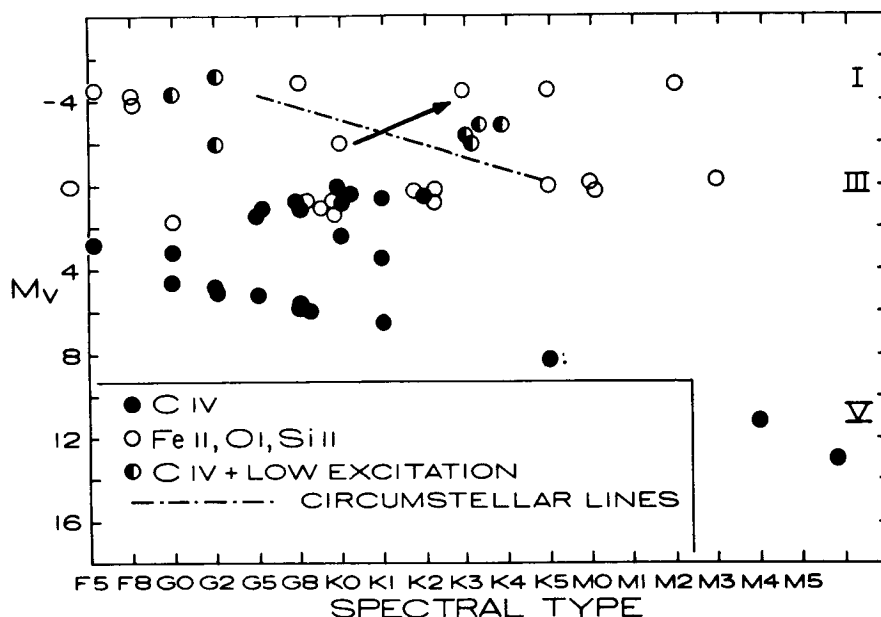
Figure 3. The presence of various spectral features in stars of different spectral types and luminosities. Stars exhibiting low and high (C IV) excitation species are termed "hybrid" - and denoted by the half filled circles (Hartmann, Dupree, and Raymond 1980). The broken line denotes the boundary above which circumstellar lines appear in optical spectra (Reimers 1977). Soft X-rays are generally detected only in stars which show C IV (Vaiana et al. 1981).

More detailed study of the radiative losses from an atmosphere in the luminous lines shows substantial variation in the surface fluxes (see Figure 4). The Mg II lines show a dispersion of 2.5 dex, whereas for the high temperature species, C IV and N V, the difference can amount to more than 4.0 dex. The pattern of enhanced emission with temperature of formation is similar to that found in a solar active region and is exemplified by the emissions in VW Cep and HR4665, two binary systems, and ξ Boo. In the more luminous stars, where signatures of mass outflow are evident, there is a dearth of high temperature material. And for stars which are optically very similar viz: 77 Tau, δ Tau and η Dra, there can be several orders of magnitude difference in their surface fluxes.

233
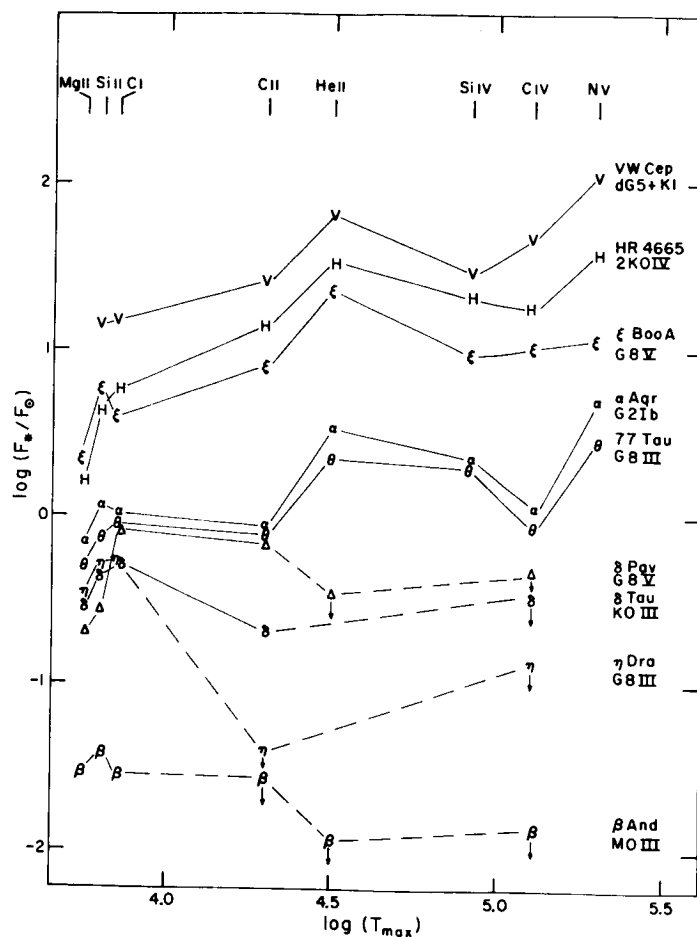
Figure 4. The stellar surface flux (erg cm^{-2} s^{-1}) in various emission lines as compared to solar values. The temperature of formation of these lines can be inferred for collisionally dominated ionization and excitation equilibrium. Stars showing the highest surface fluxes, VW Cep and HR4665, are close binaries having rapid rotation (from Hartmann, Dupree, and Raymond 1982).

It is obvious that a two-dimensional classification of temperature and gravity is insufficient to predict the character of a cool stellar atmosphere.

A comparison of typical stellar and wind parameters is given in Table 1, where we note the vast scale changes in the stellar dimensions and more than eight orders of magnitude in the mass loss rate. Of particular interest is the rapid decay of the terminal velocity as a fraction of the escape velocity from the stellar surface. Reimers (1977) has noted a rough correlation from a survey of many stars that $V_\infty \sim V_{esc}$, but the values diverge a great deal at any given value of T_{eff} and g. Table 1 also illustrates that the radiative losses (here underestimated by only 2 lines) are commensurate with the energy losses in the wind. The total losses in both wind and radiation are also a remarkably constant portion of the total stellar luminosity as measured by σT^4.

234

Table 1: Typical Physical Parameters of Stars and Winds[*]

Stellar Characteristics	Dwarf (Sun)	Giant (KO III)	Supergiant (M2Ia)
Mass ($M_\odot$)	1	4	20
T_{eff} (K)	5600	4100	2800
Radius ($R_\odot$)	1	15	800
Luminosity ($L_\odot$)	1	100	50000
log g (cm s^{-2})	4.4	2.5	0.0
V_{esc} (surface, km s^{-1})	600	300	100
Coronal Temperature (K)	1(6)	1(5)	1(4)
Radiative Losses			
Mg II (erg s^{-1})	6(28)	1(31)	4(32)
C IV (erg s^{-1})	6(27)	1(30)	<4(31)
Wind Parameters			
V_∞ (km s^{-1})	500	100	20
$\dot{M}$ ($M_\odot$ yr^{-1})	1(-14)	1(-8)	1(-6)
Time for 1 R_* (hrs)	0.5	30	8760
Kinetic energy (erg s^{-1})	8(26)	3(31)	1(32)
Grav. pot. energy (erg s^{-1})	2(27)	4(32)	4(33)

[*] The notation 2(6) implies 2×10^6.

Criteria for Wind Theory

Figure 5 gives an overview of the constraints placed by stellar observations on a quantitative theory of stellar winds. Our understanding of the behavior of winds from dwarf stars is based on remote measurements of the Sun and direct sampling of its wind in space. To date there is no spectroscopic evidence for mass loss or circumstellar absorption in any other dwarf star. This is perhaps not surprising since the asymmetries associated with mass outflow are only apparent - if at all - over restricted regions of the Sun. Coronal holes in the solar atmosphere are not detectable in the strong chromospheric lines of Ca II and Mg II. This results from the relatively narrow line formation regions in a dwarf star, coupled with the fact that the outward acceleration associated with eventual mass loss does not occur to a significant extent, if even at all, at low chromospheric levels in the Sun.
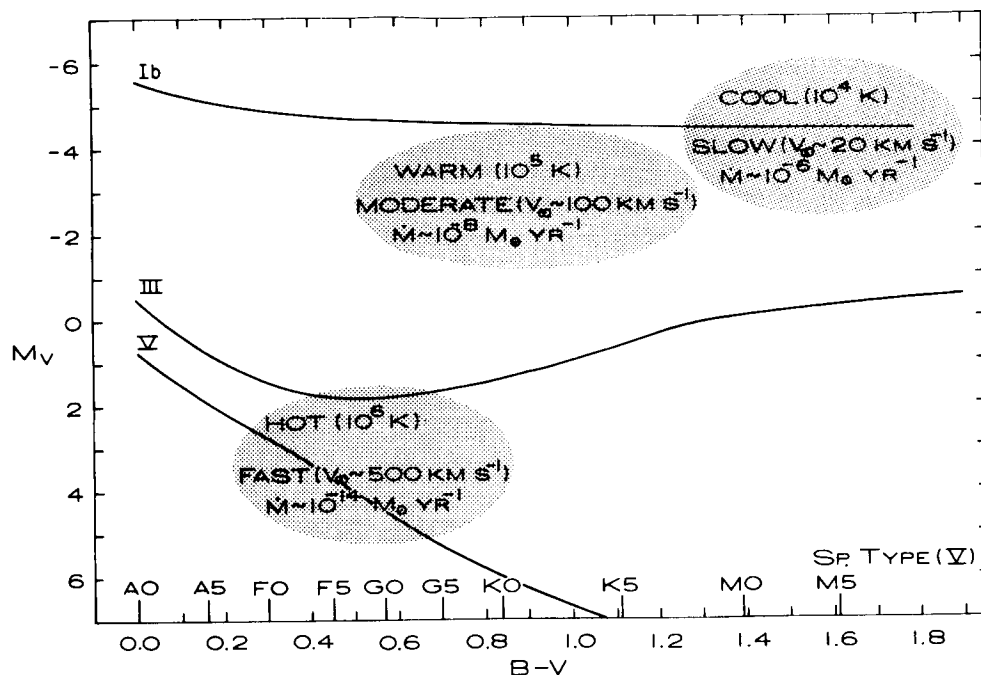
Figure 5. Characteristics of mass loss rates and winds in stars of various luminosities. Luminosity class V indicates dwarf stars; Class III denotes giant stars; the curve for class Ib marks the position of supergiant stars (from Dupree 1981). Details of the physical conditions are in Table 1.

For the cooler, more luminous giant and supergiant stars, the electron temperature in the wind decreases as the effective temperature and/or gravity decrease. This has been inferred from both the presence of ultraviolet emission lines as well as their profiles (Hartmann, Dupree, and Raymond 1981). The terminal velocity of the winds decreases (as deduced from measurement of circumstellar absorption features) concurrently with the decrease in effective temperature and gravity.

Mass loss rates themselves are very uncertain, and have been obtained by a variety of direct radio, infrared, and optical measures combined with modeling of line profiles where available. It appears that mass loss can result from a similar and continuous mechanism for cool stars. For the most luminous stars the acceleration begins in the chromosphere.

Various mass loss mechanisms have been considered. If a purely thermally driven wind is invoked, the high mass loss rates required can only be achieved with a hot atmosphere - for which there is no spectroscopic evidence - and moreover, expansion will not begin in the chromosphere as indicated by the observations. A particularly attractive mechanism relies on Alfven waves to carry the required mechanical flux. Such models developed by Hartmann and MacGregor

236

(1980) are successful in reproducing the general behavior of cool star winds, but require arbitrary assumptions of characteristic damping length in order to produce the observed (slow) terminal velocities. An extended discussion of various mechanisms is given by MacGregor in this volume.

Wind Variability

The previous discussion tacitly assumes that the outer atmospheres of stars are homogeneous and that a stellar wind has constant density, temperature and velocity. The Sun, of course contradicts this assumption. And as observations accumulate, it is apparent that cool stars show substantial variation as well.

Remarkable behavior has been found in λ Andromedae - a binary system whose primary star is a giant or subgiant of spectral class G8 III-IV. This close, but detached system has a 20.5-day orbital period but a stellar rotation period - 54 days - which is not synchronous with the orbital period. λ And is a member of a class of active binary stars, the RS CVn type stars, and displays surface activity in the form of spots, active regions, and flare activity. The chromospheric and coronal emissions are strong (with surface fluxes enhanced by factors of 10 to 100 times the quiet Sun) and variable. Most recently, a clear dichotomy in the atmosphere was discovered (Baliunas and Dupree 1982). When optically darker spots are on the disk, the brightening of chromospheric and coronal emissions occurs in conjunction with line profiles whose shapes indicate downflow of material. When the spots are at a minimum, the line luminosities decrease and the chromospheric line profiles of Ca II and Mg II indicate outflow. The analogy with solar coronal holes is striking, and these observations suggest that mass loss or mass transfer is probably occurring. The profiles have not been modeled in detail to obtain mass loss rates, but an estimate of $10^{-9}-10^{-11}$ $M_\odot$ yr^{-1} is generally consistent with profile shapes, the lack of circumstellar absorption, and as Weiler (1978) et al. noted, the observed lack of X-ray self-absorption.

Supergiant stars, in particular of the "hybrid" type, show variability of the wind opacity. The Mg II line profiles in α Aquarii were found (Dupree and Baliunas 1979) to undergo a substantial decrease in the blue peak of its Mg II emission over a period of $\sim$ 1 year which corresponds to increased Mg II opacity in the high velocity part of the wind. During this time, the Ca II (K) line varied on a timescale of days. The increased opacity appears to result from a long-lived phenomenon since the line profile has exhibited its new form for about two years.

Young stars such as T Tauri stars are believed to be pre-main sequence objects that will eventually be dwarf stars of spectral type F5 to M5. They have extremely active chromospheres and coronae exhibiting higher fluxes than even the active RS CVn binary systems. It is not clear whether the emission is just a naturally highly active atmosphere (Dumont et al. 1973; Imhoff and Giampapa 1980) or results from infall of material that is being accreted in final stages of premain sequence evolution (Ulrich 1976; Ulrich and Knapp 1979). Or perhaps, both phenomena are present. The ultraviolet Mg II profiles (see Figure 6) show

the typical asymmetry and circumstellar features found in evolved stars, and the mass loss rate has been estimated at $\sim 4 \times 10^{-7}$ $M_\odot$ yr^{-1} with terminal velocities on the order of 200 km s^{-1} (Kuhi 1964). This also leads to an energy flux in the stellar wind that is comparable to the radiative losses in the chromosphere and corona (Giampapa et al. 1981).
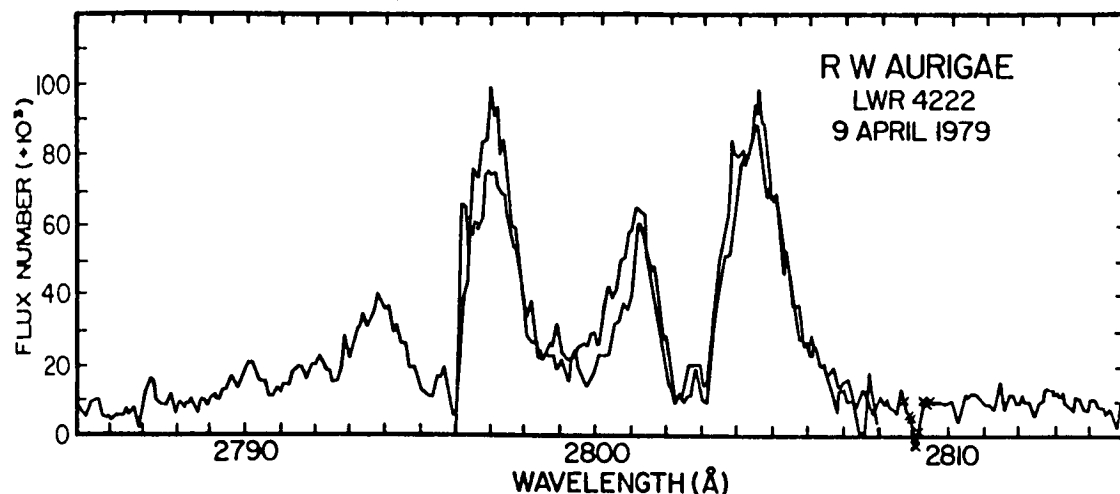
Figure 6. The Mg II lines in the T Tauri star RW Aur as observed with IUE. The line asymmetry coupled with multiple absorption features suggests a strong stellar wind in this pre-main sequence object (from Imhoff and Giampapa 1980).

A particularly active star, RW Aur, showed changes in the emission flux from 10^5 K lines by factors of 2 to 4 during a week's time while the Mg II profiles remained constant to 70 percent (Imhoff and Giampapa 1980). However, high resolution optical observations by Hartmann (1982) have revealed relatively stable blue absorption cores in the Na D lines, accompanied by dramatically variable emission components from night to night. This observation and others suggest (Hartmann 1982) a continuing mass loss process in conjunction with extremely complicated motions (perhaps even infall) in lower atmospheric layers.

The study of variability of such objects and their implications for the theory of stellar winds can now be a major focus of observing programs with the availability of high resolution spectroscopy and photon counting detectors, both in space and on the ground.

References

Adams, W. S., and K. E. MacCormack, Systematic Displacements of Lines in the Spectra of Certain Bright Stars, Astrophys. Journ., 81, 119, 1935.

Baliunas, S. L., and A. K. Dupree, Ultraviolet and Optical Spectrum Studies of Lambda Andromedae: Evidence for Atmospheric Inhomogeneities, Astrophys. Journ., 252, 668, 1982.

Brueckner, G. E., J. D. F. Bartoe, and M. E. van Hoosier, High Spatial Resolution Observations of the Solar EUV Spectrum, in Proceedings of the Nov 7-10 1977 OSO-8 Workshop, (ed. E. Hansen and S. Schaffner), Lab. for Atmospheric and Space Physics, University of Colorado, Boulder, pp. 380-418, 1977.

Deutsch, A. J., The Circumstellar Envelope of Alpha Herculis, Astrophys. Journ., 123, 210, 1956.

Dumont, S., N. Heidmann, L. V. Kuhi, and R. N. Thomas, Chromospheres of T Tauri-type Stars, Astron. Astrophys., 29, 199, 1973.

Dupree, A. K., Mass Loss from Cool Stars, Effects of Mass Loss on Stellar Evolution, (eds. C. Chiosi and R. Stalio), IAU Colloq. No. 59, D. Reidel, pp. 87-110, 1981.

Dupree, A. K., and S. L. Baliunas, Chromospheric Event in α Aquarii, IAU Circ. No. 3435, 1979.

Giampapa, M. S., N. Calvet, C. I. Imhoff, and L. V. Kuhi, IUE Observations of Pre-Main Sequence Stars. I. Mg II and Ca II Resonance Line Fluxes for T Tauri Stars, Astrophys. Journ, 251, 113, 1981.

Hartmann, L., Line Profiles of T Tauri Stars: Clues to the Nature of the Mass Flow, Astrophys. Journ. Suppl., 48, 109, 1982.

Hartmann, L., A. K. Dupree, and J. C. Raymond, Hybrid Atmospheres and Winds in Supergiant Stars, Astrophys. Journ., 236, L143, 1980.

Hartmann, L., A. K. Dupree, and J. C. Raymond, On the Relationship Between Coronae and Mass Loss in Late-Type Stars, Astrophys. Journ., 246, 193, 1981.

Hartmann, L., A. K. Dupree, and J. C. Raymond, Ultraviolet Observations of Chromospheric Activity, Astrophys. Journ., 252, 214, 1982.

Hartmann, L., and K. B. MacGregor, Momentum and Energy Deposition in Late-Type Stellar Atmospheres and Winds, Astrophys. Journ., 242, 260, 1980.

Helfand, D. J., and J. P. Caillault, An Unbiased Survey of Field Star X-Ray Emission, Astrophys. Journ., 253, 760, 1982.

Hummer, D. G., and G. Rybicki, Redshifted Line Profiles from Differentially Expanding Atmospheres, Astrophys. Journ., 153, L107, 1968.

Imhoff, C. L., and M. S. Giampapa, The Ultraviolet Variability of the T Tauri Star RW Aurigae, in The Universe at Ultraviolet Wavelengths, NASA Conf. Pub. 2171, (ed., R. D. Chapman), p. 185, 1980.

Kuhi, L. V., Mass Loss from T Tauri Stars, Astrophys. Journ., 140, 1409, 1964.

Reimers, D., Observational Evidence for Mass-Loss from K-giants, G and K Supergiants, Astron. Astrophys., 57, 395, 1977.

Spitzer, L., Jr., Spectra of M Supergiant Stars, Astrophys. Journ., 90, 494, 1939.

Stencel, R. E., The Ca II V/R Ratio and Mass Loss, Astrophys. Journ., 223, L37, 1978.

Stencel, R. E., and D. J. Mullan, Detection of Mass Loss in Stellar Chromospheres, Astrophys. Journ., 238, 221, 1980.

Ulrich, R. K., An Infall Model for the T Tauri Phenomenon, Astrophys. Journ., 210, 377, 1976.

Ulrich, R. K., and G. F. Knapp, The Gas Flow Near T Tauri Stars, Astrophys. Journ., 230, L99, 1979.

Vaiana, G. S., et al., Results from an Extensive Einstein Stellar Survey, Astrophys. Journ., 245, 163, 1981.

Weiler, E. J. et al., Coordinated Ultraviolet, Optical, and Radio Observations of HR 1099 and UX Arietis, Astrophys. Journ., 225, 919, 1978.

Page intentionally left blank

Theory of Winds in Late-type Evolved
and Pre-Main-Sequence Stars

K. B. Mac Gregor
High Altitude Observatory
National Center for Atmospheric Research[1]

I. Introduction

A variety of recent observational results has confirmed what solar and stellar astro-
nomers have long suspected, namely, that many of the physical processes which are
known to occur in the Sun also occur among late-type stars in general. One such process
is the continuous loss of mass from a star in the form of a wind. There now exists an
abundance of either direct or circumstantial evidence which suggests that most (if not
all) stars in the cool portion of the HR diagram possess winds. In the present brief review,
an attempt is made to assess the current state of our theoretical understanding of mass
loss from two distinctly different classes of late-type stars: the post-main-sequence
giant/supergiant stars and the pre-main-sequence T Tauri stars. Toward this end, the
observationally inferred properties of the winds associated with each of the two stellar
classes under consideration are briefly summarized and then compared against the pred-
ictions of existing theoretical models. Through this analysis it will become apparent that
although considerable progress has been made in attempting to identify the mechanisms
responsible for mass loss from cool stars, many fundamental problems remain to be
solved.

II. Mass Loss From Late-type Giants and Supergiants
a. Wind Properties

The existence of winds from cool giant and supergiant stars is inferred from the
detection of one or more characteristic spectral features whose formation requires that
the stellar atmosphere be extended and in a state of outward expansion. Among the most
frequently used such indicators are: 1) blue-shifted circumstellar absorption lines due to
resonance transitions of neutral or singly-ionized metals; 2) profiles of collision-
dominated chromospheric emission lines (e.g., Ca II H and K, Mg II h and k) in which the
intensity of the blue K_2 (or k_2) peak is lower than that of the red K_2 (or k_2) peak; and 3),
the presence of a 10 μm emission feature and/or infrared excess, attributed to radiating
silicate dust grains contained in an outflowing circumstellar gas shell. Observations of
any or all of these features can in principle be analyzed to determine the mass loss rate $\dot{M}$
of a given star. For giants and supergiants with spectral types K through M the $\dot{M}$ values
so derived are generally in the range $10^{-11} \lesssim \dot{M} \lesssim 10^{-5}$ $M_\odot$ yr^{-1}, with the coolest supergiant
stars exhibiting the highest rates of mass loss. Unfortunately, these results are
extremely model-dependent in that they are sensitive to assumptions made concerning:
1) the velocity, density, and temperature distributions throughout the wind; 2) the ioniza-
tion and chemical equilibrium (or the lack thereof) in the outflowing gas; 3) the geometry
of the flow and the spatial extent of the region in which a particular spectral feature is
formed; and 4), the transfer of radiation in the wind. Consequently, although it can be
safely said that late-type, low-gravity stars lose mass at rates significantly higher than
the rate at which the Sun loses mass due to the solar wind ($\dot{M}_\odot \sim 10^{-14}$ $M_\odot$yr^{-1}),

quantitatively reliable estimates of $\dot{M}$ for individual stars are presently unavailable. Indeed, because of the factors enumerated above, rates of mass loss derived for the same star by different observers can sometimes disagree by more than two orders of magnitude. A more detailed discussion of the methods and assumptions used in extracting mass loss rates from observations is contained in the review by Castor (1981).

In addition to the mass loss rate, two other observationally determined quantities are essential to the task of comparing the various theoretical models for mass loss from late-type evolved stars. These are the terminal velocity V_∞ and the temperature T of the outflow. In the case of the former, since blue-shifted absorption cores result from the scattering of photospheric radiation by atoms or ions in an expanding circumstellar envelope, estimates for V_∞ can be obtained by measuring the shortward displacements of observed lines. For those G, K, and M giants and supergiants whose spectra exhibit such line profiles, analyses of this type yield values for V_∞ in the range $10 \lesssim V_\infty \lesssim 100$ km s^{-1} (Reimers 1975; 1977), and indicate that V_∞ (on the average) decreases with decreasing stellar gravity (i.e., V_∞ is generally lowest for cool M supergiants). Moreover, if the measured wind terminal velocities are compared with surface gravitational escape speeds deduced from evolutionary considerations, it is found that $V_\infty \sim (0.1\text{-}0.5) \, V_{esc}$, where for a star of mass M_* and radius R_*, $V_{esc} = (2GM_*/R_*)^{\frac{1}{2}}$. This property (i.e., that $V_\infty < V_{esc}$) distinguishes the winds of cool giants and supergiants from the outflows associated with main-sequence or evolved stars located in other portions of the HR diagram. For example, the terminal velocities of the winds from luminous O stars follow the approximate relation $V_\infty \approx 3 \, V_{esc}$ (Abbott 1978), where in this case the escape speed V_{esc} includes the effect of the outward radiation force due to electron scattering opacity (see also the review by Cassinelli in this volume).

For stars having effective temperatures $T_{eff} \lesssim 6000$ K, information concerning the temperature of the gas contained within a stellar atmosphere or wind is obtained through observations of spectral lines (either in emission or absorption) and continua formed under physical conditions similar to those found in the outer solar atmosphere. Thus, the presence of chromospheric ($T \sim 10^4$ K) gas is inferred from the detection of lines such as Ca II H ($\lambda3968$) and K ($\lambda3934$), Mg II h ($\lambda2803$) and k ($\lambda2796$), and the $L\alpha(\lambda1216)$ line of H I, while gas at transition region temperatures ($T \sim 10^5$K) is indicated by emission lines due to multiply-ionized species such as Si IV, C III, C IV, and N V. Likewise, evidence for the existence of coronal regions ($T \gtrsim 10^6$ K) in the atmospheres of late-type stars is derived from attempts to observe emission at soft X-ray wavelengths. The results of numerous observational programs intended to survey the thermal properties of cool star atmospheres can be summarized as follows. While chromospheric emission lines are present in the spectra of virtually all late-type stars, transition region emission lines are not exhibited by stars whose location in the HR diagram is above and to the right of a line with approximate coordinates (K2, III), (G5 Ib) (Linksy and Haisch 1979; Simon, Linsky, and Stencel 1982). Moreover, the giant and supergiant stars which occupy this portion of the HR diagram are largely undetected as sources of coronal soft X-ray emission (Vaiana et al. 1981; Ayres et al. 1981). On this basis, we conclude that the expanding atmospheres of the coolest low-gravity stars are characterized by temperature distributions in which (for the most part) $T \lesssim 10^4$ K. The reader is referred to the papers by Castor (1981), Dupree (1981; 1983, this volume), Linsky (1981a), and Cassinelli and Mac Gregor (1983) for additional information concerning the observationally inferred properties of mass loss from cool stars.

b. Mass Loss Mechanisms

In the present section, several of the theories which have been proposed to explain mass loss from cool giant and supergiant stars are described. The applicability of each of

242

the theories is measured by comparing the results of qualitative model calculations for the wind from a hypothetical K5 supergiant ($M_* = 16M_\odot$, $R_* = 400R_\odot$, $T_{eff} = 3500$ K) with the "average" wind properties (e.g., $\dot{M}$, V_∞, T) derived from observations (cf. sec. IIa).

i. Thermally-Driven Winds

It is instructive to consider the possibility that the winds of late-type low-gravity stars are driven by the same mechanism which is responsible in part for the acceleration of the solar wind; namely, the force due to the thermal pressure gradient in the outflowing gas. For an isothermal, single-fluid wind model which is taken to be both spherically-symmetric and inviscid, it can be shown (see, e.g., Parker 1963; Leer, Holzer, and Flå 1982) that the flow velocity V_0 at a reference level r_0 in the stellar atmosphere is approximately

$$V_0 \approx a \ z_s^2 \exp\left(\frac{3}{2} - 2z_s\right) . \tag{1}$$

where for a gas of temperature T and mean mass per particle μ, $a = (kT/\mu)^{1/2}$ is the sound speed, $z_s = r_s/r_0 = (GM_*/2a^2 r_0)$ is the sonic point location (i.e., the distance r at which the wind velocity V becomes equal to a) in units of r_0, and it has been assumed that $V_0 \ll a$. From conservation of mass, it follows that the rate of mass loss is given by $\dot{M} = 4\pi r_0^2 \mu N_0 V_0$ where N_0 is the total number density at r_0. To apply equation (1) to a star with the physical parameters given above, note that the absence of detectable transition region and coronal emission implies $T \lesssim 10^4$ K (cf. sec. IIa). Adopting $T = 10^4$ K, $r_0 = R_*$, and $\mu = 0.667 \ m_H$ (the value appropriate to a plasma composed of H and He with $N_* = N_H$, $N_{He}/N_H = 0.1$), it is found that $z_s \approx 31$ and $V_0 \approx 8 \times 10^{-18}$ cm s^{-1}, indicating that for physically reasonable values of N_0 mass loss at rates $\gtrsim 10^{-11} M_\odot$ yr^{-1} cannot be thermally-driven. This conclusion is not particularly dependent upon the assumed isothermal temperature distribution (cf. Leer, Holzer, and Flå 1982), and can also be reached in the following equivalent way (Weymann 1962; 1978). For a given value of N_0 we ask, what is the value of T such that the initial velocity V_0 calculated from equation (1) yields a particular mass loss rate $\dot{M}$? Assuming $N_0 = 10^{11}$ cm^{-3}, the temperature required to produce a wind having $\dot{M} = 10^{-8} M_\odot$ yr^{-1} from a star with the hypothetical K5 supergiant parameters is $T \approx 70,000$ K. Such a temperature is incompatible with the observed lack of transition region emission lines (e.g., these due to C IV) in the spectra of cool supergiants, since for a gas in collisional ionization equilibrium at $T \approx 70,000$ K, approximately 10% of all C is in the form of C IV (Jordan 1969).

ii. Radiatively-Driven Winds

Numerous authors have suggested that the winds of cool giants and supergiants can be driven by the force arising from the scattering and absorption of radiation from the stellar photosphere by sources of opacity in the outflow. Although this mechanism appears to be responsible for mass loss from luminous early-type stars (see e.g., the review by Cassinelli in this volume), some fundamental problems are encountered in attempting to account for the outflows from late-type stars in terms of a radiation-driven wind model. One such difficulty arises from the fact that the atoms and ions known to be prevalent in the winds of cool stars have strong resonance lines located in the visible and UV portions of the spectrum, while the photospheric continuum radiation field is most intense in the red or near IR (Goldberg 1979). Several efforts have been made to circumvent this spectral mismatch, including the use of molecular opacity (Maciel 1976, 1977) and the force due to the scattering of chromospheric $L\alpha$ radiation by hydrogen atoms in the flow (Wilson 1960; Haisch, Linsky, and Basri 1980). Both of these models are unsatisfactory in that the small values of the respective opacities requires inordinately large stellar luminosities to produce outflows with momentum fluxes $\dot{M} V_\infty$ comparable to those inferred from observations (see the discussion of Mac Gregor 1982). In the remainder of

this section we consider a third proposal, namely, that the condensation of dust grains and their subsequent outward acceleration by radiative forces can cause the entire circumstellar envelope to expand into a wind (Gehrz and Woolf 1971).

To investigate the efficacy of this mechanism, consider a spherically-symmetric wind model in which the collisional coupling of the grains to the background gas is sufficiently strong (see Gilman 1972) to ensure that the optically-thin radiative force per unit volume exerted on the envelope can be written as

$$f_{rad} = \frac{K_d \, \rho_g \, L_*}{4\pi c r^2} \, ,$$ (2)

where L_* is the stellar luminosity, ρ_g is the gas mass density, and

$$K_d = \frac{3 Q_{pr}}{4 r_{gr} \rho_{gr}} \cdot \frac{\rho_d}{\rho_g} \, ,$$ (3)

is the dust opacity. In equation (3), ρ_d is the dust mass density, r_{gr} and ρ_{gr} are, respectively, the radius and density of an individual grain, and Q_{pr} is the radiation pressure efficiency factor. For illustrative purposes, adopt $\rho_d / \rho_g = 10^{-2}$ and consider grains of radius $r_{gr} = 10^{-5}$ cm composed of the common silicate olivine ($Mg_2 \, SiO_4$) for which $\rho_{gr} = 3.2$ g cm^{-3}. For pure ("clean") silicate grains, $Q_{pr} \sim 0.1$ (Gilman 1974) and $K_d \approx 23.4$ cm^2 g^{-1}, while for silicate grains containing impurities (i.e., "dirty" grains) Q_{pr} may be as much as a factor of 10 larger (using the results of Gilman [1974] for graphite) yielding $K_d \approx 234.0$ cm^2 g^{-1}. To simulate the formation of grains in the flow, assume that $K_d = 0$ at a reference level $r_0 (\approx R_*)$ and increases linearly in magnitude to either of the values given above within a distance Δr, remaining constant for $r > r_0 + \Delta r$. Under these conditions, the equation of motion for an isothermal wind can be integrated to obtain the following approximate expressions for the critical point location $z_c (= r_c / r_0)$, initial velocity V_0, and terminal velocity V_∞:

$$z_c = z_s \frac{1 + \Gamma / \Delta z}{1 + \Gamma z_s / \Delta z} \, ,$$ (4)

$$V_0 \approx a \exp\left(- z_s \Delta z / \Gamma \right) \, ,$$ (5)

$$V_\infty \approx V_{esc} (\Gamma - 1)^{\frac{1}{2}} \, ,$$ (6)

In equations (4) through (6), a is the sound speed, V_{esc} is the escape speed at r_0, z_s is the sonic point location, and $\Gamma = (K_d L_* / 4\pi GM_* c)$ is the ratio of the radiative force to the gravitational force acting on the gas. To apply these results, consider a star having the K5 supergiant parameters given above, and assume $r_0 = R_*$, $\Delta z = 0.1$, $N_0 = 10^{11}$ cm^{-3}, T=3000 K (≈ 0.85 Teff). In the case of "clean" silicate grains $\Gamma = 2.43$ and equations (4) through (6) yield $z_c = 1.041$, $\dot{M} \approx 4.5 \times 10^{-9} \, M_\odot$ yr^{-1}, $V_\infty \approx 1.2 \, V_{esc}$ (=148 km s^{-1}), while for "dirty" grains $\Gamma = 24.3$ with $z_c = 1.004$, $\dot{M} \approx 6.5 \times 10^{-8} \, M_\odot$ yr^{-1}, and $V_\infty \approx 4.8 \, V_{esc}$ (=596 km s^{-1}). These qualitative results indicate that values of $\dot{M}$ in accord with observations can be produced by the mechanism, a conclusion which is substantiated by more detailed calculations (Salpeter 1974; Kwok 1975; Goldreich and Scoville 1976; Lucy 1976; Menietti and Fix 1978; Philips 1979). Moreover, the computed values of V_∞ may be reduced through the inclusion of grain destruction through sputtering (cf. Kwok 1975).

At this point, it is important to consider whether or not the schematic picture of grain formation adopted above is consistent with the derived wind models. To investigate this question, we follow the analysis of Draine (1981) who has noted that condensation

244

requires (among other things) the vibrational temperature T_v of small olivine clusters to be less than a saturation value $T_{v,sat}$. given implicitly by the relation

$$T_{v,sat.} = \frac{6.13 \times 10^4 \; K}{\ln\left[\frac{1.16 \times 10^{35} \; cm^{-3}}{N}\left[\frac{T_{v,sat}}{T}\right]^{1/2}\right]} \tag{7}$$

Solution of equation (7) for physical conditions appropriate to the critical point in the "clean" grain model ($N_c \approx 2.8 \times 10^7$ cm^{-3}, T = 3000 K) given above yields $T_{v,sat}$ = 973 K. The actual temperature T_v of silicate grains with radius $r_{gr} = 10^{-5}$ cm at the critical point can be straightforwardly determined from a simple description of the grain energy balance which includes the effects of radiative and collisional heating and cooling (cf. Draine 1981, eq. [22]). For the derived critical point conditions T_v is controlled by radiative processes and has the value $T_v = 2475 K > T_{v,sat}$, indicating that grain formation *cannot* occur in the manner assumed.

Since the grain energy balance is dominated by radiative heating and cooling, condensation is possible (for sufficiently high densities) only at larger distances where the stellar radiation field is dilute. Draine (1981) has shown that the nucleation of small ($r_{gr} \sim 3\text{Å}$), "clean" silicate grains can take place within several stellar radii of the photosphere when Teff ≤ 3500 K, but for grains of this size, $Q_{pr} < 10^{-5}$ (Gilman 1974) making them dynamically unimportant. Hence, because formation of grains with desirable optical properties cannot occur close enough to the stellar surface to ensure production of a wind with a mass loss rate $\gtrsim 10^{-9} \; M_\odot$ yr^{-1}, we conclude that the mechanism is unable (by itself) to account for the winds from the majority of cool, low-gravity stars. The reader is referred to the reviews by Castor (1981), Linsky (1981b), Mac Gregor (1982), and Cassinelli and Mac Gregor (1983) for additional discussion of dust-driven wind models.

iii. Shock Wave-Driven Winds

Observational evidence for mass loss from long period (Mira) variables has led several investigators (Willson 1976; Slutz 1976; Wood 1979; Willson and Hill 1979) to suggest that the outflows associated with these stars may be produced by the pulsations responsible for their brightness variations. The physical mechanism by means of which mass is ejected from the stellar atmosphere can be understood as follows. The periodic oscillations of the surface of the star give rise to compressional disturbances which propagate outward in the form of shock waves. In the lower atmospheric layers where the gas density is high and radiative cooling is efficient, these travelling shocks behave isothermally. Consequently, each parcel of shocked gas tends to return to its pre-shock dynamical state following the passage of discontinuity. However, higher in the atmosphere where the gas density is lower, the shocks become adiabatic and the energy gained by the post-shock gas can be sufficient to produce mass loss.

The discussion given above suggests that an estimate of the mass loss rate due to a shock wave-driven wind can be obtained if the density at the atmospheric level above which the shocks behave adiabatically is known (Willson and Hill 1979; Castor 1981). Assuming that the volume radiative cooling rate of the post-shock gas can be written as $N^2 P_R(T)$ where $P_R(T)$ is the cooling coefficient, the cooling time is of order $t_{cool} \sim kT / N P_R(T)$. Similarly, if the flow time for the post-shock gas is taken to be the time required to travel a distance equal to the local density scale height, then $t_{flow} \sim a / g$ where $g = GM_*/ r^2$ is the gravitational acceleration and it has been assumed that the flow velocity is the sound speed a. The transition from isothermal to adiabatic shock behavior occurs at the level where $t_{cool} \sim t_{flow}$; equating derived expressions for the flow and cooling times yields $N \sim gkT/ aP_R(T)$, from which it follows that the maximal mass loss rate is

$$\dot{M} \lesssim 4\pi \, r^2 \, \mu \, Na \sim 4\pi GM_*\mu kT / P_R(T) \ . \tag{8}$$

According to equation (8), $\dot{M}$ is inversely proportional to the radiative cooling coefficient $P_R(T)$, a quantity which should be determined from a consistent transfer calculation. To obtain an order of magnitude estimate for $\dot{M}$, however, we assume that the emitting post-shock material is characterized by a chromospheric gas temperature (cf. Wood 1979; Willson and Hill 1979; Willson and Pierce 1982) and evaluate $P_R(T)$ from the approximate chromospheric cooling law given by Hartmann, MacGregor, and Avrett (1983). Using this prescription for $T = 10^4$ K, $P_R(T) \approx 2.6 \times 10^{-24}$ erg cm^3 s^{-1} and $\dot{M} \lesssim 1.6 \times 10^{-11}$ $(M_*/M_\odot)M_\odot$yr^{-1}. If the post-shock gas temperature is as low as $T = 5000$ K, then $P_R(T) \approx 2.2 \times 10^{-26}$ erg cm^3 s^{-1} and $\dot{M} \lesssim 1.8 \times 10^{-9}$ $(M_*/M_\odot)M_\odot$yr^{-1}. The extreme sensitivity of these results demonstrates the need for detailed calculations including transfer effects in order to determine whether or not substantial mass loss can be driven by this mechanism; preliminary steps in this direction have been taken by Willson and Pierce (1982). We further note that although the shock wave-driven wind model has been developed primarily to explain mass loss from Mira variables, virtually all M supergiants are semi-regular or irregular variables (see, e.g., Feast 1981). However, it is not known at the present time whether this variability is the result of actual pulsation or is due instead to the motions of large convective elements on the stellar surface (Schwarzschild 1975). Moreover, as Linsky (1981b) has noted, the mechanism is probably unable to account for the winds from stars having lower luminosities and higher surface gravities than the Mira variables (e.g., the G-K supergiants) since there is no observational evidence for the presence of large amplitude shock waves in the atmospheres of these stars.

iv. Alfven Wave-Driven Winds

The effects of an outwardly propagating flux of Alfvén waves on the dynamics of winds from cool giants and supergiants has been considered by Hartmann and MacGregor (1980, 1982a). This investigation was motivated by the fact that direct observations of the solar wind plasma and the interplanetary magnetic field typically reveal the presence of hydromagnetic fluctuations, many of which appear to be Alfvénic in character (see, e.g., the review by Barnes 1979). Numerous authors have suggested that such wave modes may be responsible for providing the additional energy required to produce high-speed streams in the solar wind (Belcher 1971; Alazraki and Couturier 1971; Hollweg 1973, 1978; Belcher and Olbert 1975; Jacques 1977, 1978; Leer, Holzer, and Flå 1982).

To examine the properties of a wind driven by Alfvén waves, consider a steady, spherically-symmetric outflow which emanates from a star having a radially-directed magnetic field B. Assume that the wave amplitude δB is everywhere smaller than B, and that the wavelength of the fluctuation is shorter than any of the scale lengths over which the wind properties vary (i.e., the WKB approximation). The frequency ω of a wave which propagates in the radial direction is then a constant and is given in terms of the wave vector k, wind velocity V, and Alfven speed $A = B(4\pi\rho)^{-\frac{1}{2}}$ by the dispersion relation $\omega = k(V + A)$. For a wave of energy density $\varepsilon = \delta B^2 / 8\pi$ which propagates without attenuation, a Lagrangian treatment of the wave properties (see, e.g., Jacques 1977) indicates that the action density $S = \varepsilon/(\omega - kV)$ is conserved in the sense that $\underline{\nabla} \cdot (\underline{V}_g S) = 0$, where $\underline{V}_g = \underline{V} + \underline{A}$ is the group velocity. From the definition of S and the assumed spherical symmetry of the outflow, it follows that $\varepsilon \propto [M_A(1 + M_A)^2]^{-1}$, where $M_A = V/A \propto \rho^{-\frac{1}{2}}$ is the Alfvénic Mach number. The time-averaged force exerted by the wave on the moving background plasma through which it travels is simply $-\frac{1}{2} d\varepsilon/dr$; since ε decreases with distance from the star, the wave exerts an outward force on the gas. Physically, the local reduction in ε is accompanied by an increase in the streaming energy per unit mass of the wind. This can be seen by straightforwardly calculating the divergence of the wave

energy flux $E_A = \varepsilon\,(\tfrac{3}{2}V + A)$ (cf. Belcher 1971), and recognizing that the non-zero result is equal to the rate at which the wave does work on the flow.

An approximate solution to the equation of motion for a wave-driven wind can be obtained for the limit in which the wave force dominates the thermal pressure gradient force (cf. Leer, Holzer, and Flå 1982). Defining $\beta = \varepsilon_0 / (\tfrac{1}{2}\rho_0\,V_{esc}^2)$ (the subscript "0" denotes evaluation at a reference level r_0), the resulting expressions for the critical point location r_c, initial velocity V_0, and terminal velocity V_∞ are

$$r_c / r_0 \approx \frac{7}{4(1 + \beta/2)} \; .$$ (9)

$$V_0 / V_{esc} \approx \frac{1}{8}\,\beta^2 \left[\frac{7}{4(1 + \beta/2)}\right]^{7/2} \; ,$$ (10)

$$V_\infty / V_{esc} \approx (\beta / M_{A0} - 1)^{1/2} \; .$$ (11)

where equation (11) is applicable for β, $V_0 / V_{esc} \ll 1$. For illustration, adopt the K5 supergiant parameters given earlier in this section and assume $r_0 = R_*$, $N_0 = 10^{11}$ cm^{-3}, $\mu = 0.667 m_H$, $B_0 = 10\,G$, $\delta B_0 = B_0 / \sqrt{10}$ (corresponding to $\beta = 4.7 \times 10^{-2}$, $F_{A0} = 3.36 \times 10^6$ erg cm^{-2} s^{-1}). For this specific (but arbitrary) choice of reference level location and parameters, equations (10) and (11) then yield $\dot{M} = 4\pi\, r_0^2\,\mu\,N_0\,V_0 \approx 3.8 \times 10^{-7}\,M_\odot\,\mathrm{yr}^{-1}$ and $V_\infty \approx 4.1\,V_{esc} = 509$ km s^{-1}. These qualitative results are representative of those obtained from more detailed calculations (cf. Hartmann and Mac Gregor 1980; Holzer, Flå, and Leer 1983): mass loss rates in the range $10^{-9} - 10^{-6}\,M_\odot\,\mathrm{yr}^{-1}$ can be obtained for $F_{A0} \sim 10^5 - 10^6$ erg cm^{-2} s^{-1}, but because the waves increase the streaming energy of the gas in the supersonic portion of the outflow, they give rise to winds having $V_\infty > V_{esc}$, in contradiction to observations.

It was noted by Hartmann and Mac Gregor (1980) that the terminal velocity V_∞ of an Alfven wave-driven wind could be reduced if it was assumed that the waves were dissipated at a rate such that the e-folding length L for the decrease in wave energy density (the damping length) was constant and equal in magnitude to the stellar radius. Such a prescription causes most of the wave energy to be deposited near the base of the flow, resulting in winds with mass loss rates which are nearly the same as those obtained for undamped waves, but which have terminal velocities $V_\infty < V_{esc}$. An important consequence of the required wave dissipation is that the flow is heated at a rate $\Gamma = \varepsilon(V + A)/L$, leading to the production of a region containing gas at chromospheric temperatures which extends several stellar radii above the base of the wind. That such extended chromospheres do in fact exist about late-type giants and supergiants is indicated by a variety of recent observations (Stencel 1982 and reference therein; Newell and Hjellming 1982; Hjellming and Newell 1983; Beckers et al. 1983). Unfortunately, recent more detailed studies indicate that the conditions under which Alfvén wave dissipation can be described in terms of a constant damping length are unlikely to be realized in the winds of cool, low-gravity stars. Holzer, Flå, and Leer (1983) have computed wind models which include a consistent treatment of the frictional wave damping due to ion-neutral collisions in the partially-ionized gas. They find that the wave-induced changes in the background flow properties cause the frictional damping length to vary in size by several orders of magnitude, resulting in (among other things) winds for which $V_\infty > V_{esc}$. These authors have also shown (see also Leer, Holzer, and Flå 1982) that even if L is taken to be constant, winds with $V_\infty \sim (0.1-0.5)V_{esc}$ correspond to an unrealistically narrow range of assumed L values. Hence, it would appear that the model as it presently stands suffers from a fundamental (and not easily correctable) deficiency in that it is unable to produce outflows having terminal velocities which are a small fraction of V_{esc}.

v. Magnetic Reconnection-Driven Winds

A final mass loss mechanism involves physical processes which are thought to occur when magnetic flux (in the form of bipolar magnetic loops) emerges through the surface of the Sun. This model has been applied to the acceleration of the solar wind (Pneuman 1983) and the winds of cool giant and supergiant stars (Mullan 1980, 1981, 1982), and bears a resemblance to the so-called "melon seed" mechanism for the ejection of flare-associated surges (Schlüter 1957; Svestka 1976). It can be described in the following way. Distortion of an ambient magnetic field by the upward motion an emerging flux loop gives rise to restoring forces which cause the footpoints of the loop to be pinched off. Rapid, small-scale reconnection leads to the formation of a self-contained diamagnetic "plasmoid". If the plasma β is small compared to unity and if the strength of the external field decreases with height, then this element experiences an outward magnetic force, similar to the force experienced by a localized current distribution when placed in a non-uniform external magnetic field (Parker 1957). For a geometrically thin plasmoid containing gas of temperature T and density ρ which is assumed to be in pressure equilibrium with the surrounding external field B (i.e., $B^2/8\pi = 2 k \, T\rho/m_p$), the magnitude of this force is (Pneuman 1983)

$$F = -\frac{3M}{2\rho}\frac{d}{dr}\left[\frac{B^2}{8\pi}\right] \, . \tag{12}$$

where M is the total mass of the gas in the plasmoid.

It is of interest to determine the strength B of the external magnetic field required in order that the force given by equation (12) exceed the gravitational force acting on a plasmoid. To do this, we follow Pneuman (1983) and assume that $B \propto r^{-n}$, so that $F = (3nMB^2/8\pi\rho r)$. It then follows that $F > GM_*M/r^2$ at $r = R_*$ when $B > (8\pi GM_* \rho/3nR_*)^{\frac{1}{2}}$. Adopting $n = 2$ and $N = 10^{10}$ cm^{-3} along with the physical parameters of the previously considered K5 supergiant, this criterion yields $B > 2.3\,G$. Although this value is not unreasonable, note that the plasmoid gas temperature required by the condition of pressure equilibrium is $T = (B^2/16\pi Nk) \approx 77,000$ K. In view of the absence of transition region emission lines from the spectra of late-type supergiants (cf. sec. IIa), this temperature is clearly too high if most of the observed mass loss is in the form of such discrete plasmoids.

III. Mass Loss From Pre-Main-Sequence (T Tauri) Stars
a. Physical Properties of T Tauri Stars

The group of objects known as T Tauri stars are thought to be the progenitors of stars like the sun, still in the process of contracting to the main sequence. They are probably among the youngest stellar objects, and have been defined by Herbig (1962) as stars whose spectra contain the Balmer lines of hydrogen (in emission and/or absorption), and emission lines due to Ca II, Fe I, and Fe II. They are variable, often exhibit ultraviolet and/or infrared excesses, and are frequently associated with low-density nebulosities. On the basis of optical and infrared observations of several hundred such objects, Cohen and Kuhi (1979) have concluded that most T Tauri stars have spectral types from mid to late K, and luminosity classes between III and V. Comparison with calculated pre-main-sequence evolutionary tracks suggests that the masses and radii of these stars are typically in the ranges $M_* \sim (0.2-3)M_\odot$ and $R_* \sim (1-5)R_\odot$, respectively. Their average age is $\sim 10^6$ years, a value comparable to the initial free-fall time for the spherical collapse of a $1M_\odot$ protostellar cloud (Larson 1978). The luminosities of T Tauri stars are generally $\lesssim 5L_\odot$, with an average effective temperature $T_{eff} \sim 4000 K$.

b. Wind Properties

The primary evidence for mass loss from T Tauri stars comes from the detection of spectral lines having P Cygni-type profiles. These profiles consist of a blue-shifted absorption feature together with a redward-displaced emission peak, and are interpreted as arising from the scattering of stellar radiation by a spectral line formed in an expanding atmosphere (see, e.g., the review by Cassinelli in this volume for a discussion of line formation in a moving medium). From an analysis of spectra obtained by Herbig (1977) for approximately 75 T Tauri stars, Kuhi (1978) has drawn the following conclusions concerning the frequency of occurrence of different types of $H\alpha$ line profiles. About 5% of the stars observed exhibit the classical type I P Cygni line profiles in which the bottom of the blue-displaced absorption feature is well below the level of the nearby continuum; such profiles constitute unambiguous evidence for the presence of an outflow. Another 10% of the stars studied have single $H\alpha$ emission peaks which are symmetric about the laboratory wavelength of the line. Of the remaining stars, most (~60% of the total) exhibit $H\alpha$ line profiles of the P Cygni type III, in which the blue-shifted absorption does not go below the continuum level and is bounded on the short wavelength edge by a second emission peak of lower intensity than the one situated to the red of the rest wavelength of the line. The displacement of this blue emission feature generally corresponds to velocities in the range 100-200 km s^{-1} toward the observer along the line of sight to the star, with the red emission peak having velocities 50-150 km s^{-1} in the opposite direction (Kuhi 1978).

Despite the fact that there is considerable uncertainty regarding the way in which spectral lines having type III P Cygni profiles are formed, the presence of a blue-shifted absorption dip has led many investigators to adopt them as a signature of mass outflow. For example, Kuhi (1964, 1966) has analyzed the $H\alpha$ line profiles in the spectra of 8 T Tauri stars using a model in which the observed emission arises from material which is ballistically ejected (and subsequently gravitationally decelerated) from the stellar surface. This emitting region is surrounded by a layer of cool, absorbing gas which expands radially with constant velocity in order to produce a shortward-displaced absorption feature. By attempting to fit the observed line profiles, Kuhi derived mass loss rates in the range $2.5\times10^{-8} \lesssim \dot{M} \lesssim 5.8\times10^{-7} M_\odot yr^{-1}$ for the stars in his sample, with an average mass loss rate of $\dot{M} \sim 3\times10^{-8} M_\odot yr^{-1}$. Given the schematic character of the model used to interpret the data, it is difficult to assess the accuracy of Kuhi's mass loss rate estimates. However, De Campli (1981) has noted that a determination of $\dot{M}$ from the analysis of a single feature (e.g., an asymmetric $H\alpha$ emission profile) in the spectrum of a T Tauri star is subject to the same uncertainties enumerated earlier in connection with the inferred mass loss rates of cool giants and supergiants (cf. sec. IIa). Because of this, the values of $\dot{M}$ deduced from observed emission line intensities can differ by as much as three orders of magnitude, with the rate of mass loss from an "average" T Tauri star only constrained to lie somewhere within the range $3\times10^{-9} \lesssim \dot{M} \lesssim 10^{-6} M_\odot yr^{-1}$ (De Campli 1981).

An alternative interpretation of the type III P Cygni profiles seen in the spectra of T Tauri stars has been proposed by Ulrich (1976). He has noted that the collapse of an interstellar gas cloud to form a star is decidedly non-homologous, with the central portions of the cloud contracting rapidly to make a largely hydrostatic core, onto which a tenuous outer envelope slowly accretes (see, e.g., Larson 1969). If both the core and envelope rotate, the infalling gas must pass through an oblique accretion shock located near the surface of the core. Material traversing this discontinuity is compressed and heated, thereby producing the observed Balmer line emission. Moreover, because matter which impacts the far hemisphere of the core moves toward the observer while that striking the near hemisphere moves away, blue-shifted and red-shifted emission features are formed. The blue-shifted absorption dip between the red and blue emission peaks is a

consequence of the fact that for some velocities, radiating post-shock gas is not visible to an outside observer (cf. Ulrich 1976). As it stands, the model utilizes an approximate treatment of the transfer of radiation within the emitting region, and neglects entirely the effects of the outer portions of the infalling envelope and an equatorial accretion disk on the observed radiation (Ulrich 1978). However, there does exist observational evidence which suggests that inflows can occur in association with some T Tauri stars. For example, the higher Balmer series lines in the spectra of those T Tauri stars typified by the star YY Orionis are observed to have *inverse* P Cygni profiles (i.e., containing a redward-displaced absorption component) (Walker 1972). Estimates for the fraction of T Tauri stars which are of the YY Ori type range between 5 and 50% (Kuhi 1978; Appenzeller 1978), although no inverse P Cygni profiles were seen in the spectra of 50 T Tauri stars observed by Herbig (1977), including the star YY Ori itself. This result (and others like it; cf. Kuhi 1978; Hartmann 1982) suggests that the physical conditions which characterize the atmospheres of T Tauri stars are highly variable. To further complicate matters, the envelopes would also appear to be quite inhomogeneous since some T Tauri stars exhibit Balmer line profiles signifying the presence of outflowing gas *and* Na D line profiles indicative of infalling material (Ulrich and Knapp 1979).

Few conclusive results are available regarding the terminal velocities and temperatures of the outflows from T Tauri stars. For those stars which exhibit fairly unambiguous evidence for mass loss (e.g., T Tau itself), measurements of the blueshifts of observed absorption and/or emission features generally yield velocities $V \sim$ several $\times 10^2$ km s^{-1}. If it is assumed that the velocities so derived represent the terminal velocity V_∞ of a wind, then for the stellar masses and radii inferred from the HR diagrams constructed by Cohen and Kuhi (1979; cf. sec. IIIa) $V_\infty \sim V_{esc} = (2GM_*/R_*)^{1/2}$. Evidence for the existence of atmospheric regions in which $T > T_{eff}$ is obtained from the detection of numerous emission lines (cf. sec. IIa) due to species such as H I, He I, Ca II, Mg II, Si IV, C III, C IV, and N V in ultraviolet, visible, and infrared spectra of some well-studied T Tauri stars (see, e.g., Gahm *et al.* 1979; Cram, Giampapa, and Imhoff 1980; Imhoff and Giampapa 1980; Herbig and Soderblom 1980; Ulrich and Wood 1981; Giampapa *et al.* 1981). Such emission lines are indicative of gas at chromospheric ($T \sim 10^4 K$) and transition region ($T \sim 10^5 K$) temperatures, and in the case of T Tauri stars, measured surface fluxes in individual lines are frequently more than 10 to 100 times the corresponding average solar values. Flux enhancements of this magnitude are more characteristic of solar active regions, and may be due in part to the onset of the low chromospheric temperature rise at a much deeper atmospheric level than in the Sun (Herbig 1970; Cram 1979). Furthermore, approximately one-third of the T Tauri stars observed with The Imaging Proportional Counter on the *Einstein* satellite have been detected as soft X-ray sources, with luminosities in the range $L_X \sim 10^{30} - 10^{31}$ erg s^{-1} (Gahm 1980; Feigelson and DeCampli 1981). It has been proposed that this emission arises from coronal ($T \gtrsim 10^6 K$) gas occupying a region near the photosphere whose spatial extent is small in comparison with the dimensions of the extended circumstellar envelope formed by the wind (Gahm 1980; Feigelson and DeCampli 1981; Walter and Kuhi 1981; Kuhi 1982). In this picture, the absence of detectable soft X-ray emission from all T Tauri stars may be the result of X-ray attenuation by the cooler, Hα-emitting wind material. However, Montmerle *et al.* (1983) have used the *Einstein* Observatory to study the ρ Oph dark cloud, a region in which star formation is believed to be occurring. Repeated observations of portions of the cloud on a variety of time scales have revealed the presence of approximately 50 highly-variable soft X-ray sources, most of which are probably pre-main-sequence objects. Hence, the failure of earlier surveys to detect more T Tauri stars as X-ray sources may be a consequence of the fact that the high-temperature emission from these objects is dominated by strong, flare-like events and is discernible only from longer or repeated observations.

We conclude this section by noting that while asymmetric or blue-shifted spectral line profiles provide fairly direct information regarding the dynamical state of T Tauri

star atmospheres, there is additional indirect evidence for mass loss from these stars (see, e.g., Cohen 1982). For example, the proper motions and optical emission of Herbig-Haro objects (nebulous, "semi-stellar" knots frequently associated with T Tauri stars) have been attributed to the interaction between a condensation and the wind from a nearby pre-main-sequence star (Schwartz and Dopita 1980; Herbig and Jones 1981; Dopita, Schwartz, and Evans 1982). Likewise, recent observations of T Tauri stars at radio wavelengths have resulted in several detections of continuum (free-free) emission (Cohen, Bieging, and Schwartz 1982) and high-velocity molecular (CO) gas (Edwards and Snell 1982), both presumably arising from an extended, outflowing circumstellar envelope.

c. Mass Loss Mechanisms

As was done in the case of cool giants and supergiants, the predictions of theoretical models for mass loss from T Tauri stars are now compared against the observationally inferred properties described in the preceding section. For this purpose, we consider the wind from a hypothetical T Tauri star having physical parameters $M_* = 0.75 M_\odot$, $R_* = 4 R_\odot$, and $T_{eff} = 4000$K.

i. Thermally-Driven Winds

In order to ascertain whether or not T Tauri stars can undergo significant thermally-driven mass loss, the isothermal, spherically-symmetric wind model described in section II b is adopted (see also Bisnovatyi-Kogan and Lamzin 1977; Ulrich 1978; DeCampli 1981). We first note that according to the results of that section, mass loss rates in the range $3 \times 10^{-9} \lesssim \dot{M} \lesssim 10^{-8}$ $M_\odot$ yr^{-1} (DeCampli 1981; cf. sec. III b) cannot be obtained if $T \lesssim 3 \times 10^4$ K throughout the wind as the observed Balmer line emission would appear to indicate. However, this difficulty can be alleviated if it is assumed that the subsonic portion of the outflow is characterized by coronal gas temperatures, as suggested by the fact that some T Tauri stars have been detected as soft X-ray sources (cf. sec. III b). Assuming $T = 10^6$K, $\mu = 0.609 m_H$ (the value appropriate to a fully-ionized plasma composed of H and He) and using the T Tauri star parameters given at the beginning of this section, the sonic point location (in units of the stellar radius) is $z_S = (GM_*\mu / 2kT R_*) \approx 1.32$. From equation (1), it then follows that the velocity V_0 at a reference level $r_0 (= R_*)$ in the stellar atmosphere is $V_0 \approx 0.56a$, yielding $\dot{M} = 4\pi R_*^2 \mu N_0 V_0 \approx 1.02 \times 10^{-7} M_\odot$ yr^{-1} for $N_0 = 10^{12}$ cm^{-3}. While this value for $\dot{M}$ falls within the range dictated by observations, the model can be ruled out on the basis of the heating rate required to maintain a coronal region having the stipulated temperature and density. To see this, assume for simplicity that the corona is hydrostatic and isothermal, and occupies a volume $4\pi R_*^2 h$, where $h = (kTR_*^2 / GM_*\mu)$ is the density scale height. For an optically-thin gas in collisional ionization equilibrium, the radiative cooling rate Λ is expressible in the form $\Lambda = N_e N_H P_R(T)$ (units: erg cm^{-3}s^{-1}), from which it follows that the coronal luminosity is $L_c \approx 4\pi R_*^2 h N_e N_H P_R(T)$. Adopting $P_R(T) \approx 10^{-22}$ erg cm^3 s^{-1} (Raymond, Cox, and Smith 1976) for $T = 10^6$K, it is readily seen that $L_c \approx 2.4 \times 10^{36}$ erg s^{-1}, implying a rate of energy addition to the corona far in excess of the stellar luminosity $L_* \approx 1.4 \times 10^{34}$ erg s^{-1}. Moreover, for the assumed coronal temperature a significant fraction of L_c is radiated in the form of soft X-rays, in contradiction to the observational result that the X-ray luminosities of T Tauri stars are generally in the range $L_x \sim 10^{30} - 10^{31}$ erg s^{-1} (cf. sec. III b). Note that this problem cannot be ameliorated by reducing T (and thereby, $\dot{M}$) to soften the spectrum of emitted coronal radiation. Since $P_R(T)$ increases with decreasing T for $10^5 \lesssim T \lesssim 10^6$ K, the power input required to maintain a cooler corona is actually comparable to the value derived above. For example, adopting $T = 350,000$ K with $N_0 = 10^{12}$ cm^{-3}, the preceding analysis yields $z_S \approx 3.77$, $V_0 \approx 0.034a$, and $\dot{M} \approx 3.67 \times 10^{-9} M_\odot$ yr^{-1}. However, the cooling coefficient corresponding to this temperature is $P_R(T) \approx 3.25 \times 10^{-22}$ erg cm^{3}s^{-1}, so that $L_c \approx 2.7 \times 10^{36}$ erg s^{-1}.

ii. Rotationally/Magnetically-Driven Winds

The arguments given in the preceding section indicate that physically unreasonable coronal heating rates are required to produce thermally-driven mass loss from T Tauri stars at rates $3 \times 10^{-9} \lesssim \dot{M} \lesssim 10^{-6} M_\odot$ yr^{-1}. However, if T Tauri stars are both rapidly rotating and strongly magnetized, the apparent necessity of a high coronal gas temperature can be circumvented through the inclusion of centrifugal and magnetic forces. To investigate this possibility, consider a steady, axisymmetric outflow in the equatorial plane of a T Tauri star which rotates rigidly with angular frequency $\Omega = \alpha(GM_*/r_0^3)^{1/2}$, where α is a constant. In the absence of magnetic effects, the initial velocity of an isothermal centrifugally-driven wind is approximately

$$V_0 \approx az_c^2 \exp\{-\tfrac{1}{2} - 2z_S[1 - \frac{\alpha^2}{2}(1 - \frac{1}{z_c^2}) - \frac{1}{z_c}]\} \ , \tag{13}$$

where $a = (kT/\mu)^{1/2}$ is the sound speed,

$$z_c = r_c/r_0 = \tfrac{1}{2}z_S[1 + (1 - 4\alpha^2/z_S)^{1/2}] \tag{14}$$

is the critical point location, $z_S = (GM_*\mu/2kTr_0)$, and α is restricted to the range $0 \leq \alpha \leq (1 - 1/z_S)^{1/2}$ (Weidelt 1973; Mufson and Liszt 1975; Hartmann and MacGregor 1982b). If a magnetic field is included according to the prescription of Weber and Davis (1967), then

$$V_0 \approx az_c^2 \exp\{-\tfrac{1}{2} - 2z_S[1 - \frac{\alpha^2}{2}(z_c^2 - 1) - \frac{1}{z_c}]\} \ , \tag{15}$$

with

$$z_c \approx 3z_S/(1 + 3\alpha^{2/3}z_S) \tag{16}$$

(Hartmann and MacGregor 1982b). The validity of equations (15) and (16) requires that the stellar magnetic field be strong enough to ensure approximate corotation of the gas throughout the region $1 \leq z \leq z_c$ (cf. Hartmann and MacGregor 1982b).

It is important to note that in order to produce a cool ($T \sim 10^4 K$), rotationally and/or magnetically-driven outflow having $\dot{M} \gtrsim 10^{-9} M_\odot$ yr^{-1} from a T Tauri star, values of $\alpha \sim 1$ are needed. For example, using the stellar parameters given earlier in this section and assuming $r_0 = R_*$, $T = 10^4$K, $N_0 = 10^{12}$ cm^{-3}, $B_0 = 10 G$, it follows from equations (15) and (16) that $z_c \approx 1.07$, $V_0 \approx 0.1a$, and $\dot{M} \approx 1.9 \times 10^{-9} M_\odot$ yr^{-1} for $\alpha = 0.90$, while for $\alpha = 0.95$, $z_c \approx 1.03$, $V_0 \approx 0.4a$, and $\dot{M} \approx 7.6 \times 10^{-9} M_\odot$ yr^{-1}. The plausibility of the mechanism is therefore dependent upon whether or not T Tauri stars are rapid rotators. A preliminary indication that the answer to this question might be affirmative is provided by the work of Skumanich (1972). He has found that the rotational velocities of solar-type stars decay in time according to (stellar age)$^{-1/2}$; extrapolation of this relation to pre-main-sequence objects would imply rotational velocities $\gtrsim 100$ km s^{-1} for T Tauri stars. Unfortunately, this expectation is not supported by observational results. In particular, Vogel and Kuhi (1981) have measured rotational velocities for 64 pre-main-sequence stars and find that virtually all T Tauri stars with masses $< 1.5 M_\odot$ have rotation speeds $\lesssim 25$-35 km s^{-1}. Since this implies $\alpha \sim 0.1$-0.2 for a T Tauri star with the adopted physical parameters, it is unlikely that winds with $\dot{M} \gtrsim 10^{-9} M_\odot$ yr^{-1} could be rotationally/magnetically-driven.

iii. Radiatively-Driven Winds

The possibility that mass loss from T Tauri stars is radiatively-driven can be eliminated on the basis of a comparison of the rate of momentum transport by the wind $\dot{M} V_\infty$ with the rate at which momentum can be supplied to the flow by the stellar radiation field L_*/c. If each photon emitted by the star is scattered once in the wind, conservation of momentum indicates that $\dot{M} V_\infty = L_*/c$. For a T Tauri star having $M_* = 0.75 M_\odot$, $R_* = 4 R_\odot$, and $T_{eff} = 4000$ K, $V_{esc} = (2GM_*/R_*)^{1/2} \approx 267$ km s^{-1} and $L_* = 1.4 \times 10^{34}$ erg s$^{-1} = 3.7 L_\odot$. Assuming $V_\infty = V_{esc}$ and $3 \times 10^{-9} \lesssim \dot{M} \lesssim 10^{-6} M_\odot$ yr^{-1} (DeCampli 1981), the resulting range of wind momentum fluxes is $5.1 \times 10^{24} \lesssim \dot{M} V_\infty \lesssim 1.7 \times 10^{27}$ dyne, while $L_*/c = 4.7 \times 10^{23}$ dyne. Since $\dot{M} V_\infty \gg L_*/c$ we conclude that the winds of T Tauri stars cannot be driven by single-scattering radiation pressure alone. It is important to note that this result is a consequence of the low stellar luminosity (L_* is typically $\lesssim 5 L_\odot$ for T Tauri stars), and may be modified if provision is made for the multiple scattering of photons in the flow (Friend and Castor 1983). However, models for the winds of luminous ($L_* \sim 10^5 - 10^6 L_\odot$) early-type stars which include a consistent treatment of this effect are generally characterized by $\dot{M} V_\infty c / L_* \lesssim 10$ (see, e.g., the paper by Friend in this volume), whereas the above analysis suggests that for T Tauri stars $\dot{M} V_\infty c / L_* \gtrsim 10$.

iv. Alfven Wave-Driven Winds

Several authors (DeCampli 1981; Hartmann, Edwards, and Avrett 1982) have suggested that mass loss from T Tauri stars can be driven by the force associated with an outwardly propagating flux of Alfven waves. The applicability of such a mechanism can be examined by using the qualitative wind model described in section II b (iv). For a spherically-symmetric outflow, equation (9) for V_0 together with conservation of mass can be used to derive an approximate expression for the mass loss rate due to a wave-driven wind, (cf. Leer, Holzer, and Flå 1982),

$$\dot{M} \approx 1.825 \times 10^{-13} \left[\frac{r_0}{R_\odot} \right]^{7/2} \left[\frac{M_*}{M_\odot} \right]^{-3/2} \left[\frac{F_{AO}}{10^6 erg \, cm^{-2} s^{-1}} \right]^2 \left[\frac{B_0}{gauss} \right]^{-2} M_\odot yr^{-1} \, , \quad (17)$$

where F_{AO} and B_0 are, respectively, the wave energy flux and magnetic field strength at a reference level $r_0 (= R_*)$. To obtain an estimate of the maximum mass loss rate possible with this mechanism, we first impose the restriction that F_{AO} be less than or equal to the stellar radiative flux $L_*/4\pi R_*^2$. For the hypothetical T Tauri star considered throughout this section, this constraint, implies $F_{AO} \leq 1.45 \times 10^{10}$ erg cm^{-2}s^{-1}. Alternatively, note that for an Alfvénic disturbance with the arbitrarily chosen initial amplitude $\delta B_0 = B_0/\sqrt{10}$, the wave energy flux is simply $F_{AO} \approx (\delta B_0^2/8\pi) \cdot (B_0/\sqrt{4\pi\rho_0}) \approx 1.06 \times 10^9 B_0^3 N_0^{-1/2}$ erg cm^{-2}s^{-1}. Adopting $N_0 = 10^{12}$cm^{-3}, it then follows that the requirement $F_{AO} \leq L_*/4\pi R_*^2$ limits the field strength B_0 to values ≤ 239 gauss. From equation (17), the corresponding limit on the mass loss rate is $\dot{M} \lesssim 1.32 \times 10^{-7} M_\odot$ yr^{-1}. This qualitative result is substantiated by detailed model calculations carried out by DeCampli (1981) and Hartmann, Edwards, and Avrett (1982): namely, mass loss rates in the range $\dot{M} \sim 10^{-9} - 10^{-7} M_\odot$ yr^{-1} can be obtained for wave energy fluxes F_{AO} of a magnitude such that $4\pi R_*^2 F_{AO} \sim 10^{-1} - 10^0 L_*$. Moreover, although wave dissipation and heating may occur throughout the wind (perhaps giving rise to a variety of optical and ultraviolet emission features; cf. Hartmann et al. 1982), the observed terminal velocities appear to be adequately accounted for by models in which the waves propagate without damping (cf. DeCampli 1981). The central (and presently unanswerable) question regarding the applicability of the mechanism to T Tauri star winds is whether or not wave energy fluxes of the required magnitude are physically realizable.

IV. Conclusions

It is apparent from the discussion given in the preceding sections that completely satisfactory theories for mass loss from late-type evolved and pre-main-sequence stars are presently unavailable. It should also be evident that if significant progress is to be made toward the goal of identifying and understanding the physical processes responsible for the winds of cool stars, quantitatively reliable estimates of mass loss rates, terminal velocities, and wind temperatures are necessary. In this regard, it is imperative that the analysis of observational data be carried out using the best available theoretical techniques.

In the case of mass loss from cool giant and supergiant stars, the central problem with which potential driving mechanisms must contend is not just the production of winds having $10^{-11} \lesssim \dot{M} \lesssim 10^{-6} M_\odot$ yr^{-1}. Indeed, for giants and supergiants a substantial portion of the increase in $\dot{M}$ above the solar wind mass loss rate ($\dot{M}_\odot \sim 10^{-14} M_\odot$yr^{-1}) can be attributed to the fact that such stars have larger surface areas; simply scaling the solar wind mass flux density to a star of M supergiant size ($R_* \sim 1000 R_\odot$) yields $\dot{M} \sim \dot{M}_\odot$ $(R_*/R_\odot)^2 \sim 10^{-8} M_\odot$ yr^{-1}. Rather, the most enigmatic property of the observed outflows is that they are generally characterized by expansion velocities which are well below the gravitational escape speed from the stellar surface. The production of a wind having both a large mass loss rate *and* $V_\infty < V_{esc}$ requires that: (i) most of the energy supplied to the wind by the acceleration mechanism be deposited in the subsonic portion of the flow (to ensure a large $\dot{M}$); and (ii), the driving force exceed gravity by only a small amount throughout the supersonic portion of the flow (to ensure $V_\infty < V_{esc}$) (cf. Leer and Holzer 1980; Holzer, Flå, and Leer 1983). Virtually all of the mechanisms which have been proposed to account for mass loss from cool, low-gravity stars lack these properties. This difficulty represents perhaps the most formidable obstacle which must be overcome if observation and theory are to be brought into agreement.

An outstanding problem which must be addressed by any theory of mass loss from T Tauri stars is to account for the apparent efficiency with which the driving mechanism operates (cf. DeCampli 1981). Assuming $V_\infty \sim V_{esc}$, the rate at which kinetic energy is transported by the wind is $\frac{1}{2} \dot{M} \, V_\infty^2 \sim GM_* \dot{M} / R_*$. If the rates of mass loss from T Tauri stars are actually as large as $10^{-8} - 10^{-7} M_\odot$ yr^{-1}, then $\frac{1}{2} \dot{M} V_\infty^2 / L_* \sim 10^{-2} - 10^{-1}$ for the stellar parameters given at the beginning of section III. The corresponding values of this parameter for the sun, an M supergiant ($\dot{M} \sim 10^{-6} M_\odot$yr^{-1}, $V_\infty \sim 10$km s^{-1}, $L_* \sim 10^5 L_\odot$), and an O supergiant ($\dot{M} \sim 10^{-6} M_\odot$yr^{-1}, $V_\infty \sim 1000$ km s^{-1}, $L_* \sim 10^6 L_\odot$) are $\sim 10^{-7}$, 10^{-7}, and 10^{-4}, respectively. Because of their intrinsic inefficiency, the mass loss mechanisms considered in section III require excessive energy input rates in order to drive winds with $\dot{M} \gtrsim 10^{-9} M_\odot$yr^{-1}.

References

o Abbott, D. C., The terminal velocities of stellar winds from early-type stars, Astrophys. J. 225, 893, 1978.

o Alazraki, G., and P. Couturier, Solar wind acceleration caused by the gradient of Alfvén wave pressure, Astron. Astrophys. 13, 380, 1971 .

o Appenzeller, I. The frequency of YY Orionis objects among the T Tauri stars, in Proc. IAU Colloq. No. 42, The Interaction of Variable Stars With Their Environment, edited by R. Kippenhahn, J. Rahe, W. Stroheimer, p. 80, Bamberg Observatory, Bamberg, 1978.

o Ayres, T. R., J. L. Linsky, G. S. Vaiana, L. Golub, and R. Rosner, The cool half of the HR diagram in soft X-rays, Astrophys. J. 250, 293, 1981.

o Barnes, A., Hydromagnetic waves and turbulence in the solar wind, in Solar System Plasma Physics, Vol. I, edited by C. F. Kennel, L. J. Lanzerotti, and E. N. Parker, p. 249, North-Holland, Hingham, Mass., 1979.

o Beckers, J. M., E. K. Hege, H. P. Murphy, and F. Burnette, First results of imaging of supergiant envelopes with the differential speckle interferometer, Bull. Amer. Astron. Soc. 14, 918, 1983.

o Belcher, J. W., Alvénic wave pressures and the solar wind, Astrophys. J. 168, 509, 1971.

o Belcher, J. W., and S. Olbert, Stellar winds driven by Alfvén waves, Astrophys. J. 200, 369, 1975.

o Bisnovatyi-Kogan, G. S., and S. A. Lamzin, Models of the outflowing envelopes of T Tau stars, Sov. Astron. 21, 720, 1977.

o Cassinelli, J. P., and K. B. MacGregor, Stellar chromospheres, coronae, and winds, in Physics of the Sun, edited by P. A. Sturrock, D. M. Mihalas, T. E. Holzer, and R. K. Ulrich, University of Chicago Press, Chicago, in press, 1983.

o Castor, J. I., Origin of winds in cool giants and supergiants in Physical Processes in Red Giants, edited by I. Iben, Jr. and A. Renzini, p. 285, Reidel, Dordrecht, 1981.

o Cohen, M., The case for anisotropic mass loss from T Tauri stars, Pub. Astron. Soc. Pac. 94, 266, 1982.

o Cohen, M., and L. V. Kuhi, Observational studies of pre-main-sequence evolution, Astrophys. J. Suppl. 41, 743, 1979.

o Cohen, M., J. H. Bieging, and P. R. Schwartz, VLA observations of mass loss from T Tauri stars, Astrophys. J. 253, 707, 1982.

o Cram, L. E., Atmospheres of T Tauri stars: the photosphere and low chromosphere, Astrophys. J. 234, 949, 1979.

o Cram, L. E., M. S. Giampapa, and C. L. Imhoff, Emission measures derived from far ultraviolet spectra of T Tauri stars, Astrophys. J. 238, 905, 1980.

o DeCampli, W. M., T Tauri winds, Astrophys. J. 244, 124, 1981.

o Dopita, M. A., R. D. Schwartz, and I. Evans, Herbig-Haro objects 46 and 47: evidence for bipolar ejection from a young star, Astrophys. J. Lett. 263, L73, 1982.

o Draine, B. T., Dust formation processes around red giants and supergiants, in *Physical Processes in Red Giants*, edited by I. Iben, Jr. and A. Renzini, p. 317, Reidel, Dordrecht, 1981.

o Dupree, A. K., Mass loss from cool stars, in *Proc. IAU Colloq. No. 59, Effects of Mass Loss on Stellar Evolution*, edited by C. Chiosi and R. Stalio, p. 87, Reidel, Dordrecht, 1981.

o Edwards, S., and R. L. Snell, A search for high-velocity molecular gas around T Tauri stars, *Astrophys. J., 261*, 151, 1982.

o Feast, M. W., Red variables of spectral class M, in *Physical Processes in Red Giants*, edited by I. Iben, Jr. and A. Renzini, p. 193, Reidel, Dordrecht, 1981.

o Feigelson, E., and W. M. DeCampli, Observations of X-ray emission from T Tauri stars, *Astrophys. J. Lett., 243*, L89, 1981.

o Friend, D. B., and J. I. Castor, Stellar winds driven by multi-line scattering, preprint, 1983.

o Gahm, G. F., X-ray observations of T Tauri stars, *Astrophys. J. Lett., 242*, L163, 1980.

o Gahm, G. F., K. Fredga, R. Liseau, and D. Dravins, The far-UV spectrum of the T Tauri star RU Lupi, *Astron. Astrophys., 73*, L4, 1979.

o Gehrz, R. D., and N. J. Woolf, Mass loss from M stars, *Astrophys. J., 165*, 285, 1971.

o Giampapa, M. S., N. Calvet, C. L. Imhoff, and L. V. Kuhi, IUE observations of pre-main-sequence stars. I. Mg II and Ca II resonance line fluxes for T Tauri stars, *Astrophys. J., 251*, 113, 1981.

o Gilman, R. C., On the coupling of grains to the gas in circumstellar envelopes, *Astrophys. J. 178*, 423, 1972

o Gilman, R. C., Planck mean cross-sections for four grain materials, *Astrophys. J. Suppl., 28*, 397, 1974.

o Goldberg, L., Some problems connected with mass loss in late-type stars, *Quart. J. Royal Astron. Soc., 20*, 361, 1979.

o Goldreich, P., and N. Scoville, OH-IR stars. I. Physical properties of circumstellar envelopes, *Astrophys. J., 205*, 144, 1976.

o Haisch, B. M., J. L. Linsky, and G. S. Basri, Outer atmospheres of cool stars. IV. A discussion of cool stellar wind models, *Astrophys. J., 235*, 519, 1980.

o Hartmann, L., Line profiles of T Tauri stars: clues to the nature of the mass flow, *Astrophys. J. Suppl., 48*, 109, 1982.

o Hartmann, L., and K. B. Mac Gregor, Momentum and energy deposition in late-type stellar atmospheres and winds, *Astrophys. J., 242*, 260, 1980.

256

o Hartmann, L., and K. B. Mac Gregor, Wave-driven winds from cool stars. I. Some effects of magnetic field geometry, Astrophys. J. 257, 264, 1982a.

o Hartmann, L., and K. B. Mac Gregor, Protostellar mass and angular momentum loss, Astrophys. J. 259, 180, 1982b.

o Hartmann, L., S. Edwards, and E. Avrett, Wave-driven winds from cool stars. II. Models for T Tauri stars, Astrophys. J. 261, 279, 1982.

o Hartmann, L., K. B. Mac Gregor, and E. Avrett, Wave-driven winds from cool stars. III. Energy balance, in preparation, 1983.

o Herbig, G. H., The properties and problems of T Tauri stars and related objects, Adv. Astron. Astrophys. 1, 47, 1962.

o Herbig, G. H., Introductory remarks on pre-main-sequence stellar evolution, Mem. Soc. Roy. Sci. Liege (5th Ser.) 19, 13, 1970.

o Herbig, G. H., Radial velocities and spectral types of T Tauri stars, Astrophys. J. 214, 747, 1977.

o Herbig, G. H., and D. R. Soderblom, Observations and interpretation of the near-infrared line spectra of T Tauri stars, Astrophys. J. 242, 628, 1980.

o Herbig, G. H., and B. F. Jones, Large proper motions of the Herbig-Haro objects HH1 and HH2, Astron. J. 86, 1232, 1981.

o Hjellming, R. M., and R. T. Newell, Radio observations of the inner and outer regions of red supergiant winds, Bull. Amer. Astron. Soc. 14, 918, 1983.

o Hollweg, J. V., Alfvén waves in a two-fluid model of the solar wind, Astrophys. J. 181, 547, 1973.

o Hollweg, J. V., Some physical processes in the solar wind, Rev. Geophys. Space Phys. 16, 689, 1978.

o Holzer, T. E., T. Flå, and E. Leer, Alfvén waves in stellar winds, preprint, 1983.

o Imhoff, C. L., and M. S. Giampapa, The ultraviolet spectrum of the T Tauri star RW Aurigae, Astrophys. J. Lett. 239, L115, 1980.

o Jacques, S. A., Momentum and energy transport by waves in the solar atmosphere and solar wind, Astrophys. J. 215, 942, 1977.

o Jacques, S. A., Solar wind models with Alfvén waves, Astrophys. J. 226, 632, 1978.

o Jordan, C., The ionization equilibrium of elements between carbon and nickel, Mon. Not. Roy. Astron. Soc. 142, 501, 1969.

o Kuhi, L. V., Mass loss from T Tauri stars, Astrophys. J. 140, 1409, 1964.

o Kuhi, L. V., Mass loss from T Tauri stars. II., Astrophs. J. 143, 991, 1966.

o Kuhi, L. V., Spectral characteristics of T Tauri stars, in Protostars and Planets, edited by T. Gehrels, p. 708, University of Arizona Press, Tucson, 1978.

o Kuhi, L. V., Evolution of stellar activity during the pre-main-sequence phase, in Second Cambridge Workshop on Cool Stars, Stellar Systems, and the Sun, Vol. II, edited by M. S. Giampapa and L. Golub, p. 141, Smithsonian Astrophysical Observatory Special Report No. 392, 1982.

o Kwok, S., Radiation pressure on grains as a mechanism for mass loss in red giants, Astrophys. J. 198, 583, 1975.

o Larson, R. B., Numerical calculations of the dynamics of a collapsing protostar, Mon. Not. Roy. Astron. Soc. 145, 271, 1969.

o Larson, R. B., The stellar state: formation of solar-type stars, in Protostars and Planets, edited by T. Gehrels, p. 43, University of Arizona Press, Tucson, 1978.

o Leer, E., and T. E. Holzer, Energy addition in the solar wind, J. Geophys. Res. 85, 4681, 1980.

o Leer, E., T. E. Holzer, and T. Flå, Acceleration of the solar wind, Space Sci. Rev. 33, 161, 1982.

o Linsky, J. L., Outer atmospheres of late-type stars, in Physical Processes in Red Giants, edited by I. Iben, Jr. and A. Renzini, p. 247, Reidel, Dordrecht, 1981a.

o Linsky, J. L., Winds in late-type stars: mechanisms of mass outflow, in Proc. IAU Collq. No. 59, Effects of Mass Loss on Stellar Evolution, edited by C. Chiosi and R. Stalio, p. 187, Reidel, Dordrecht, 1981b.

o Linsky, J. L., and B. M. Haisch, Outer atmospheres of cool stars. I. The sharp division into solar-type and non-solar-type stars, Astrophys. J. Lett. 229, L27, 1979.

o Lucy, L. B., Mass loss by cool carbon stars, Astrophys. J. 205, 482, 1976.

o Mac Gregor, K. B., Momentum and energy balance in late-type stellar winds, in Second Cambridge Workshop on Cool Stars, Stellar Systems and the Sun, Vol. I., edited by M. S. Giampapa and L. Golub, p. 83, Smithsonian Astrophysical Observatory Special Report No. 392, 1982.

o Maciel, W. J., Mass loss from Mira variables by the action of radiation pressure on molecules, Astron. Astrophys. 48, 27, 1976.

o Maciel, W. J., Mass loss from Mira variables. II. The supersonic flow, Astron. Astrophys. 57, 273, 1977.

o Menietti, J. D., and J. D. Fix, Models of mass flows from cool, luminous stars, Astrophys. J. 224, 961, 1978.

o Montmerle, T., L. Koch-Miramond, E. Falgarone, and J. E. Grindlay, Einstein observations of the Rho Ophiuchi dark cloud: an X-ray X-mas tree, preprint, 1983.

o Mufson, S. L., and H. S. Liszt, Mass loss from the infrared star CIT 6, Astrophys. J. 202, 183, 1975.

o Mullan, D. J., Non-thermal stellar winds in cool stars, in Cool Stars, Stellar Systems, and the Sun, edited by A. K. Dupree, p. 189, Smithsonian Astrophysical Observatory Special Report No. 389, 1980.

o Mullan, D. J., Mass loss from warm giants: magnetic effects, in Physical Processes in Red Giants, edited by I. Iben, Jr. and A. Renzini, p. 355, Reidel, Dordrecht, 1981.

o Mullan, D. J., Onset of rapid mass loss in cool giant stars: magnetic field effects, Astron. Astrophys. 108, 279, 1982.

o Newell, R. T., and R. M. Hjellming, Radio emission from the extended chromosphere of alpha Orionis, Astrophys. J. Lett. 263, L85., 1982.

o Parker, E. N., The gross dynamics of a hydromagnetic gas cloud, Astrophys. J. Suppl. 3, 51, 1957.

o Parker, E. N., Interplanetary Dynamical Processes, Interscience, New York 1963.

o Philips, J. P., Supersonic mass flow in Mira variables, Astron. Astrophys. 71, 115, 1979.

o Pneuman, G. W., Ejection of magnetic fields from the sun: acceleration of a solar wind containing diamagnetic plasmoids, Astrophys. J. 265, 468, 1983.

o Raymond, J. C., D. P. Cox, and B. W. Smith, Radiative cooling of a low-density plasma, Astrophys. J. 204, 290, 1976.

o Reimers, D., Circumstellar absorption lines and mass loss from red giants, Mem. Roy. Soc. Sci. Liege, 8, 369, 1975.

o Reimers, D., Observational evidence for mass loss from K giants, G and K supergiants, Astron. Astrophys. 57, 395, 1977.

o Salpeter, E. E., Formation and flow of dust grains in cool stellar atmospheres, Astrophys. J. 193, 585, 1974.

o Schlüter, A., Solar radio emission and the acceleration of magnetic-storm particles, in IAU Symp. No. 4: Radio Astronomy, edited by H. C. Van de Hulst, p. 356, Cambridge University Press, Cambridge, 1957.

o Schwarzschild, M., On the scale of photospheric convection in red giants and supergiants, Astrophys. J. 195, 137, 1975.

o Schwartz, R. D., and M. A. Dopita, Dynamical consequences of a stellar wind in Herbig-Haro objects, _Astrophys. J._, _236_, 543, 1980.

o Simon, T., J. L. Linsky, and R. E. Stencel, On the reality of a boundary in the HR diagram between late-type stars with and without high temperature outer atmospheres, _Astrophys. J._, _257_, 225, 1982.

o Skumanich, A., Time scales for Ca II emission decay, rotational braking, and lithium depletion, _Astrophys. J._, _171_, 565, 1972.

o Slutz, S., On the acceleration of shock waves in the atmosphere of cool Mira variable giants, _Astrophys. J._, _210_, 750, 1976.

o Stencel, R. E., Evidence for extended chromospheres surrounding red giant stars, in _Second Cambridge Workshop on Cool Stars, Stellar Systems, and the Sun_, Vol. I., edited by M. S. Giampapa and L. Golub, p. 137, Smithsonian Astrophysical Observatory Special Report No. 392, 1982.

o Svestka, Z., _Solar Flares_, Reidel, Dordrecht, 1976.

o Ulrich, R. K., An infall model for the T Tauri phenomenon, _Astrophys. J._, _210_, 377, 1976.

o Ulrich, R. K., The status of T Tauri models, in _Protostars and Planets_, edited by T. Gehrels, p. 718, University of Arizona Press, Tucson, 1978.

o Ulrich, R. K., and G. R. Knapp, The gas flow near T Tauri stars, _Astrophys. J. Lett._, _230_, L99, 1979.

o Ulrich, R. K., and B. C. Wood, Observations and analysis of the helium I recombination lines λ 5876 and λ 10830 in eight T Tauri stars, _Astrophys. J._, _244_, 147, 1981.

o Vaiana, G. S. et al., Results from an extensive _Einstein_ stellar survey, _Astrophys. J._, _245_, 163, 1981.

o Vogel, S. N., and L. V. Kuhi, Rotational velocities of pre-main-sequence stars, _Astrophys. J._, _245_, 960, 1981.

o Walker, M. F., Studies of extremely young clusters. VI. Spectroscopic observations of the ultraviolet-excess stars in the Orion nebula cluster and NGC 2264, _Astrophys. J._, _175_, 89, 1972.

o Walter, F. M., and L. V. Kuhi, The smothered coronae of T Tauri stars, _Astrophys. J._, _250_, 254, 1981.

o Weber, E. J., and L. Davis, Jr. The angular momentum of the solar wind, _Astrophys. J._, _148_, 217, 1967.

o Weidelt, R. D., Mass loss from rotating stars, _Astron. Astrophys._, _27_, 389, 1973.

o Weymann, R., Comments on mass ejection mechanisms in red giants, Astrophys. J. 136, 476, 1962.

o Weymann, R., Theoretical aspects of mass loss from late-type stars, in Proc. IAU Colloq. No. 42, The Interaction of Variable Stars With Their Environment, edited by R. Kippenhahn, J. Rahe, and W. Stroheimer, p. 577, Bamberg Observatory, Bamberg, 1978.

o Willson, L. A., Shock wave interpretation of emission lines in long-period variable stars. I. The velocity of the shock, Astrophys. J. 205, 172, 1976.

o Willson, L. A., and S. J. Hill, Shock wave interpretation of emission lines in long-period variable stars. II. Periodicity and mass loss, Astrophys. J. 228, 854, 1979.

o Willson, L. A., and J. N. Pierce, Shock waves, atmospheric structure, and mass loss in Miras, in Second Cambridge Workshop on Cool Stars, Stellar Systems, and the Sun, Vol. I., edited by M. S. Giampapa and L. Golub, p. 147, Smithsonian Astrophysical Observatory Special Report 392, 1982.

o Wilson, O. C., A suggested mechanism for the ejection of matter from M-type stars, Astrophys. J. 131, 75, 1960.

o Wood, P. R., Pulsation and mass loss in Mira variables, Astrophys. J. 227, 220, 1979.

THE WINDS AND CORONAE OF EARLY-TYPE STARS

J. P. Cassinelli
Astronomy Department
University of Wisconsin
Madison, WI 53706

ABSTRACT

The properties of the winds of hot stars as derived from radio, ultraviolet and X-ray observations is presented. Special focus is given to observations that test line driven wind theory. In this theory the wind properties are determined by the stellar effective temperature and surface gravity, but not parameters that specify the mechanical or wave fluxes from the star. Alternate explanations of the X-ray emission from the early-type stars are discussed. Evidence is given for the presence of coronal zones at the base of the stellar winds.

Conclusive evidence for winds from early-type stars was provided in the early days of ultraviolet astronomy by observations of OB supergiants by Morton (1967). Figure 1 shows a tracing of one of the early spectra of the supergiant ζ Ori(O9.5Ia). The lines of C IV and Si IV show profile with emission longward of line center and absorption extending far shortward of line center. Such profiles are called "P Cygni" profiles after the star P Cyg which shows prominent lines with this shape in the visible part of the spectrum. The lines observed in the ultraviolet have shown that luminous hot stars have fast massive winds. The velocities are typically in the range 1000 to 3000 km/sec or approximately 3 times the escape speed (Abbott 1978). The mass loss rates are greater than 10^{-6} solar masses per year. The wind temperature, T_W, appears to be comparable to the stellar effective temperature (30 to $50 \times 10^3 K$) as estimated from the low ion stages such as Si^{+3} that are observed to have P Cygni lines. These properties are very different from those associated with the solar wind ($v \sim 300$-700 km/sec, $\dot{M} \sim 10^{-14}$ $M_\odot/yr$, $T_p \sim 10^6 K$).
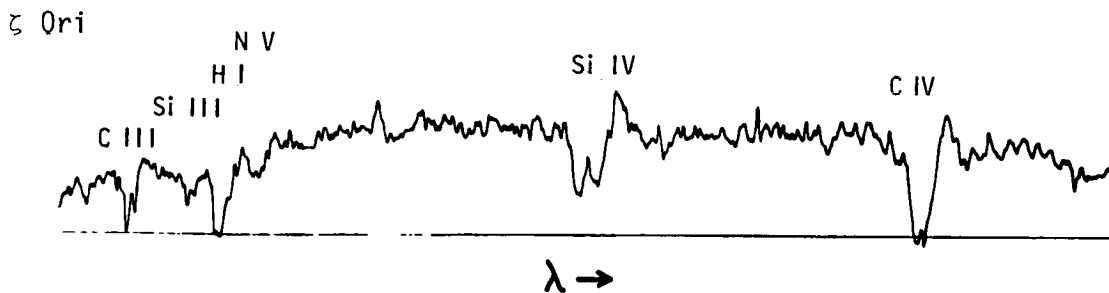
ζ Ori

Fig. 1 - Shows Morton's (1967) early observation of the ultraviolet spectrum of ζ Ori O9.5Ia. Wavelengths increase to the right from 1140 to 1630 Å. Shown are the P Cygni profiles of C IV and Si IV and shortward displaced absorption lines of C III, N V, and Si III.

Three topics will be discussed in this review: 1) The basic methods that have been developed to derive the properties of winds; 2) The physical mechanisms for driving the fast massive winds; and 3) A summary of current research problems.

Stellar Wind Properties Derived from Observations

The most important diagnostic of the structure of the winds are the P Cygni profiles. The formation of a P Cygni profile for a strong resonance line that has a rest wavelength, λ_0, is illustrated in figure 2. Let us assume the velocity $v(r)$ increases monotonically in the outward direction and reaches a terminal speed v_∞. In such a flow any parcel of gas sees light emitted from any other parcel or light from the star as redshifted. A photon emitted radially from the star at a wavelength slightly shortward of line center ($\lambda < \lambda_0$) may, in traversing the wind, become scattered in a "resonance shell" at a radius where the wind has the speed $v(r) = c(\lambda_0-\lambda)/\lambda_0$. If the line opacity is very large, the intercepted photon may be scattered many times in the resonant shell. The radiation transfer is well described by the Sobolev escape probability theory (Sobolev 1960, Castor 1970, Mihalas 1978). After the many scatterings, the photon may escape in a direction, θ, relative to the radial direction. The wavelength as seen by a distant observer will be redshifted to λ' from its original wavelength λ by an amount determined by the angle θ: $\lambda'=\lambda+(1-v/c \cos\theta)$. Thus the photon labelled 2' that was scattered from the back side of the envelope is seen at a wavelength larger than λ_0, and photon 1', last scattered from the front side will be seen shortward of λ_0. If we assume that the ion which is doing the scattering is very abundant in the wind, all of the photospheric photons shortward of line center from λ_0 to $\lambda_0(1-v_\infty/c)$, will be scattered out of the direct line of sight to the observer and will be redistributed over the band $\lambda_0(1 \pm v_\infty/c)$. The net effect is a depletion of photons shortward of line center and an excess longward of line center, thus forming a P Cygni profile. We can see from this that it is very easy to determine the terminal velocity from the star of the lines showing a sharp shortward edge. Weak lines are also useful because from their shapes it is possible to derive information about the spatial distribution of the ion in the wind. If we assume the ion/proton abundance varies as r^β, the resulting P Cygni lines have the shapes shown in figure 3 for various values of β. For example, for $\beta = 2$ the ions are concentrated far from the star and the line shows a sharp displaced absorption near $\Delta\lambda=\lambda v_\infty/c$. The dashed lines in Figure 3 show saturated profiles; for these strong lines the information about the spatial distribution of the ion is lost.

A useful way to derive the rate of mass loss by stellar winds is to measure the long wavelength continua of hot stars. At infrared and radio wavelengths the dominant opacity is free-free absorption. This increases as λ^2, so if one observes the star at sufficiently long wavelength the radius at which optical depth equals unity can occur in the wind itself. This "effective photosphere" can grow larger as one looks at even longer wavelengths. This increasing area of the photosphere as a function of λ gives rise to an infrared and radio excess illustrated figure 4. At radio wavelengths the monochromatic photosphere may be
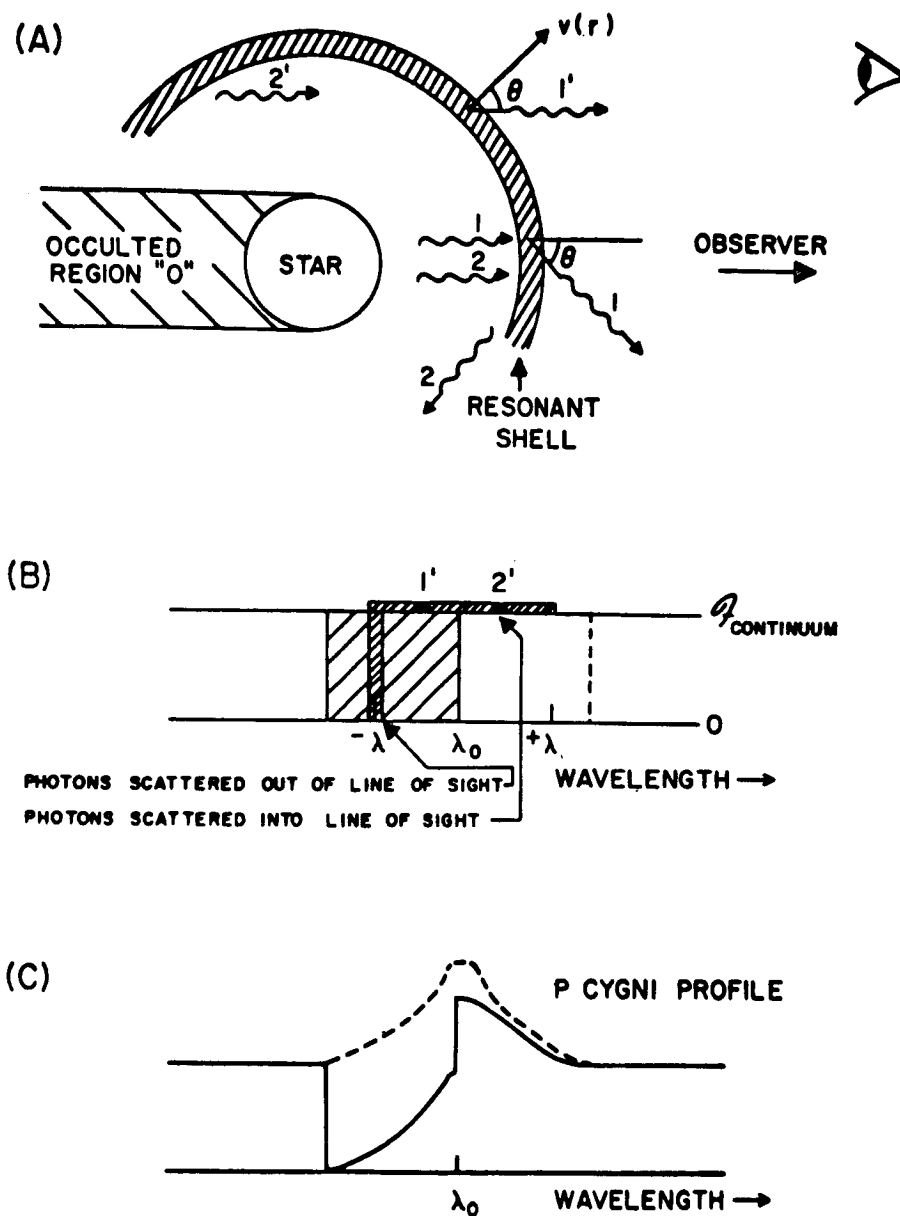
Fig. 2 - Illustrates the formation of a P Cygni profile of a resonance line. Panel A shows the scattering of two photons 1 and 2 <u>out of</u> the line of sight. In a spherically symmetric system, two other photons 1' and 2' will be scattered <u>into</u> the line of sight. As shown in Panel B these will be redshifted because of the expansion of the resonant shell.   So scattered photons are redistributed over a region -λ to +λ. This produces the P Cygni profile shown in Panel C.   The dashed line shows the distribution of re-emitted photons. The region labelled O corresponds to photons not seen by the observer because of the occultation by the star.

FLUX

$\beta = -2$ $\beta = 0$ $\beta = 2$

$\lambda \rightarrow$
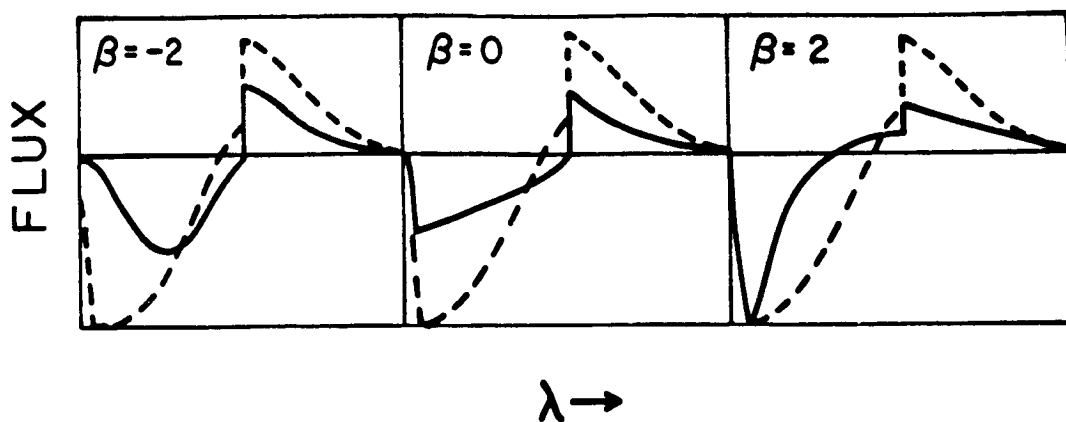
Fig. 3 - The dependence of P Cygni profiles on the ionization abundance of a line producing ion in the wind. The ion abundance is assumed to vary with radius as $g_i \propto r^\beta$. The results for three different values of β are shown. A) If an ion decreases in abundance with radius the absorption is at maximum depth for small velocity displacement. C) If an ion increases in abundance with r, the line may show little emission but a strong displaced absorption. The dashed lines show the results for a saturated line. Note these are all identical independent of β. (Adopted from Olson 1978).
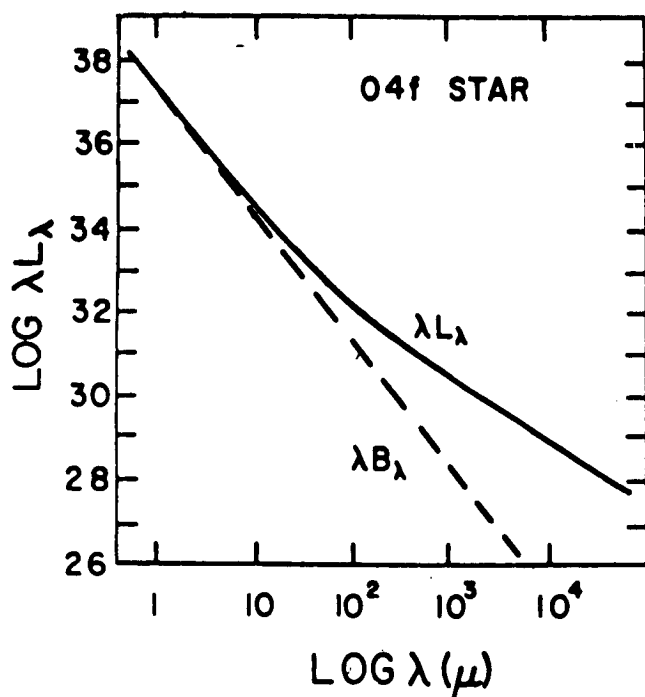
Fig. 4 - The effects of a massive wind on the free-free flux from an O4 star. In absence of the wind, the flux from the O4 star would resemble the Planck distribution B_λ. The flux in the radio region (6 cm) yields a good measure of the mass loss rate. The infrared 1 to 100 μ is sensitive to the density structure near the base of the wind. The data for the O4f star is from Cassinelli and Hartmann (1977).

at tens of stellar radii where the flow has reached terminal speed, and therefore ρ is decreasing as r^{-2}. Thus the optical depth to the photosphere ($\tau_\lambda \simeq 1$) is determined only by the mass loss rate $\dot{M}$, and we find for the energy distribution $\lambda L_\lambda = \text{const } \lambda^{-5/3}(\dot{M}/v_\infty)^{4/3}$ (Cassinelli and Hartmann 1977). Infrared and radio observations have become one of the most important methods for deriving basic properties of stellar winds (Barlow and Cohen 1977; Abbott et al. 1980, 1981; Leitherer et al. 1982). With the Very Large Array (VLA) radio telescope in New Mexico it is even possible to marginally resolve the radio monochromatic photosphere. Resolved observations of the massive wind of P Cyg are discussed by White and Becker (1982) and they derive interesting results about the temperature and geometry of the flow.

The results for the mass loss rates in the HR diagram are shown in Figure 1 in MacGregor's paper present earlier. For the stars at the luminous hot end of the HR diagram, the mass loss rates are $>10^{-6}$ $M_\odot$/yr and can even approach 10^{-4} $M_\odot$/yr for Wolf Rayet and O3 f$^+$ and O4 f$^+$ stars.

Wind Dynamics

What can drive such fast massive winds? Lucy and Solomon (1970), and Castor, Abbott, and Klein (1976) argued that a Parker coronal wind mechanism could not be responsible. This is because speeds of 2000 km/sec would require a coronal temperature of 6×10^7K. This is incompatible with the low ionization stages such as C^{+3} and Si^{+3} which indicate cool wind temperature.

The early-type stars are very luminous, and it is reasonable to think that radiation pressure gradients play an important role in the mass loss. Line driven wind theory has become well developed over the past dozen years by Lucy and Solomon (1970), Castor, Abbott, and Klein (1975) (referred to as CAK), and Abbott (1980, 1982). The dominant question since 1970 has been Can the radiation alone from quiescent luminous stars be the cause of the fast massive winds? By "quiescent star" I mean a star with no source for mechanical energy deposition such as acoustic or magneto-acoustic waves. Early-type stars have negligible convection zones, but there may be other sources of mechanical energy associated with their fast rotation or possible magnetic fields or stellar pulsations. The question asks, however, whether the radiation field alone, in isolation from all these other effects, can drive the winds. It is a straightforward but difficult question.

The basic idea for line driven winds is as follows. Radiative acceleration of the gas is proportional to the product of the wind opacity, κ, and the flux F_λ. Opacity is very large at the wavelengths of the resonance lines, but the flux tends to be negligible at line wavelengths because of the line absorption deeper in the atmosphere. However if a parcel of gas is moving outward, the opacity is doppler shifted, and the parcel can be pushed by the large radiation flux that is present on the shortward side of the line. The flux and hence the outward acceleration varies as r^{-2} and thus the radiation effectively leads to a decrease in the gravitational field. In the presence of the radiation field the Parker momentum equation becomes;

$$\frac{1}{v}\frac{dv}{dr} = \frac{\frac{2a^2}{r} - \frac{GM}{r^2}(1-\Gamma)}{v^2 - a^2} \qquad (1)$$

where a is the sound speed and Γ is the ratio of the outward acceleration due to radiation to the inward acceleration of gravity. Note, firstly that because of the presence of Γ in Eq. 1, the effective gravity is greatly reduced and transonic flow can occur at relatively low sound speeds as appears to be required by the presence of low ion stages.

For there to be an outward increase of v in the subsonic region (where the denominator is negative), it is necessary that Γ be less than unity. However beyond the sonic point Γ is allowed to be greater than unity and this can lead to a very large velocity gradient. This is sometimes known as the "after burner" effect.

Lucy and Solomon (1970) showed that C IV $\lambda 1550$ alone could drive a mass loss rate of $\dot{M} > 10^{-9}$ $M_{\odot}/yr$ to speeds $v_{\infty} > 1000$ km/sec. Thus the line formation process discussed in section 1 is directly associated with the acceleration of the flow.

To get the observed large mass loss rates of $\dot{M} > 10^{-6}$ $M_{\odot}$ yr^{-1}, it is presumably necessary to account for thousands of lines. CAK developed a convenient way to do this. The total acceleration is a sum over all lines of the products of line opacity, κ_{ρ}, and the flux in the line. The flux, in turn, depends on the line radiation transfer through the wind, and this can be treated using escape probability methods. Consider the resonance shell refered to in Figure 2. The flux at λ in the line is the stellar flux F_{λ}, times a penetration probability, $(1-e^{-\tau})/\tau$.

The optical depth, τ, through the shell is $\tau = \kappa_{\ell} \rho \Delta r \simeq \kappa_{\ell} \rho$ $v_D(dv/dr)^{-1}$, which can be normalized to the optical depth for unit opacity as $\tau' = \kappa_{\ell} t$. The acceleration on a strong line (i.e., $\tau \gg 1$) becomes;

$$\kappa_{\ell} F_{\lambda} = F_{\lambda}^{*}(\rho v_D)^{-1} dv/dr$$

From which we see that the opacity cancels out and the acceleration is proportional to dv/dr (or to 1/t). If we ignore weak lines, the total acceleration is proportional to the number of strong lines, N, times dv/dr. Using extensive line lists CAK and Abbott (1982) find that N can be fitted as $N = N_o t^{\gamma}$. Therefore the total line acceleration is proportional to $(dv/dr)^{\alpha}$ with $\alpha = \gamma-1$. The problem of line driven winds is complicated by two problems. 1) A very extensive line list is required. Abbott (1980) found that 20 chemical elements have potentially optically thick lines and must be included in the driving force. 2) the acceleration from line opacity varies as $(dv/dr)^{\alpha}$ with $0 < \alpha < 1$. The wind momentum equation for dv/dr is therefore non-linear and so is quite unlike the solar wind equation of Parker. It is interesting that Abbott (1982) finds that for stars with a wide range in effective temperatures $5000 < T_{eff} <$ 50,000K, the acceleration is $K(dv/dr)^{0.56}$ with approximately same force constant K and index α. This results in part because as T_{eff} changes the ions doing the driving changes, but they tend to have their strongest lines at wavelengths in the general region of the maximum of the Planck function.

268

The main predictions of the line driven theory are (Abbott 1982)

$$v_\infty = (\frac{\alpha}{1-\alpha})^{.5} \times v_{esc} = 1.5 \, v_{esc},$$

which is to be compared with the empirical result $v = 3 \, v_{esc}$, and

$$\dot{M} = const \, (L/L_\theta)^{1.98},$$

versus the empirical result $\dot{M} \propto (L/L_\theta)^{1.77}$.

The difference from 1.5 to 3 v_{esc} for v_∞ can be explained if multiple scattering is accounted for, as shown by Friend and Castor (1983). Thus we see that the line driven wind theory does an amazingly good job in explaining the observations of early-type stars. One must conclude that the dominant mechanism in the acceleration of the winds of early-type stars has been identified.

The only stellar parameters accounted for so far are T_{eff}, and g. No mention has been made of wave energy and momentum or magnetic field phenomena that we associate with the solar wind. It sounds too good to be true. Maybe it is. There are several major problems that may not be explainable using the CAK theory and these problems are at the focus of current research. - 1) Wolf-Rayet stars present a serious problem because they appear to have an extremely large mass loss rate. If we equate the photon momentum per second from the star L/c to the momentum flow rate by the wind $\dot{M} v_\infty$, we derive an estimate of the maximum mass loss rate that can be driven by radiation; $\dot{M}_{Max} = L/v_\infty c$. Wolf-Rayet stars exceed this limit by a factor of 10 to 30 (Barlow 1982; Cassinelli 1982; and Abbott 1982). Several explanations are being considered. Firstly, within the context of line driven wind theory, it has been argued that the limit can be exceeded by a factor of 3 to 10 if multiple scattering is accounted for. The photons from the stars are not destroyed in being scattered in the wind but merely have been sent off in different directions, allowing further scattering and momentum deposition to occur. The problem can also be alleviated somewhat, if Wolf-Rayet stars are hotter and therefore have a higher luminosity than assumed in the deriving $\dot{M} > 10 \, L/v_\infty c$. Panagia and Felli (1982) argue that the effective temperature may be 50% higher then usually assumed.

An alternate solution is that the winds of Wolf-Rayet stars are not driven by radiation pressure but by magnetic acceleration mechanisms (Cassinelli 1982). If the fields on Wolf-Rayet stars are $>10^4$ gauss the winds could be driven by Alfven waves as suggested for the solar wind by Belcher (1971), Jacques (1978) and for red supergiants by Hartmann and MacGregor (1980). As early-type stars are rapid rotators it is also plausible that Wolf-Rayet winds could be driven by the "fast magnetic rotator mechanism" of Belcher and MacGregor (1976) as applied to pre-main-sequence stars by Hartmann and MacGregor (1982).

2) A second major current topic of research concerns observational evidence for heating of the winds. Ionization stages higher than could be expected from the CAK line driven wind theory are seen in the UV spectra of O and B stars. Figure 5 shows the broad P Cygni lines in ζ Pup O4f and wind displaced lines in the main-sequence star τ Sco at the resonance lines of N V $\lambda1239$ and O VI $\lambda1032$. Lamers and Morton (1976) suggested that these indicate that the winds are heated to temperatures high enough to collisionally produce O VI ($\sim 2\times10^5$K). Cassinelli, Castor, and Lamers (1978) commented on several problems with this "warm wind" explanation. For example, to account for O VI over the entire wind of ζ Pup a mechanical luminosity of $\sim$10% the radiative luminosity would be required to balance the very efficient cooling that occurs at T = 2×10^5K.
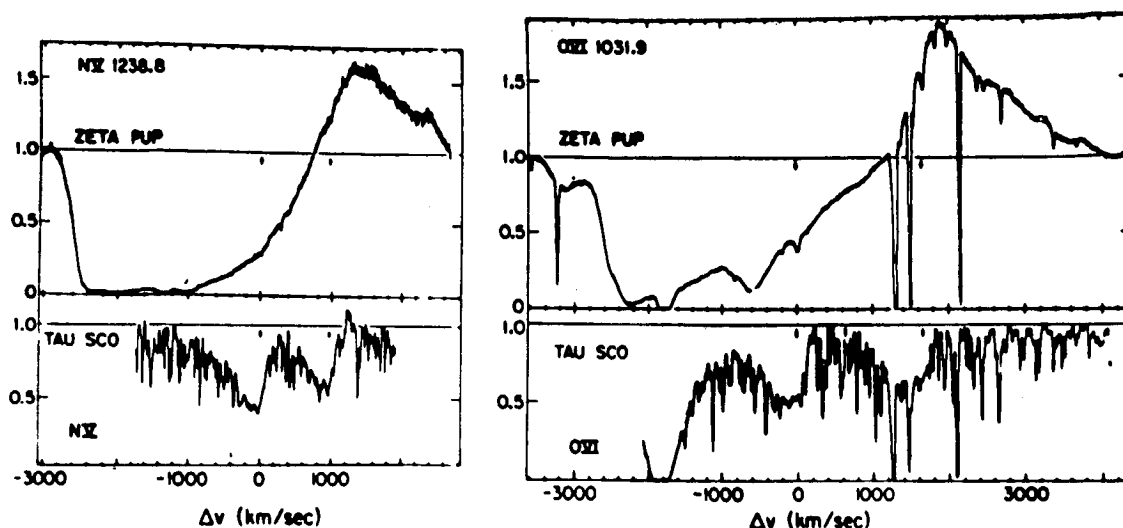
Fig. 5 - The spectra of ζ Pup O4f and τ Sco B0V in the region of the resonance doublets of O VI and N V. The horizontal axes give the velocity (km s^{-1}) in the frame of the star. The arrows indicate the laboratory wavelength of the lines. In the O VI spectral region, the strong line at -1900 km s^{-1} is Ly β. The sharp lines in the spectrum of ζ Pup are interstellar lines. Adapted from Lamers (1975).

Cassinelli and Olson (1979) suggested that the high ion stages could be produced as a result of X-rays emitted from a coronal region at the base of the wind. The Auger effect leads to the removal of two electrons upon K shell ionization of carbon, nitrogen or oxygen. Thus since O^{+3} is the dominant ion stage in the cool wind of an O star, K shell ionization can lead to a trace amounts of O^{+5} and thereby explain the observed O VI line. This model predicted that Of and OB supergiants would be X-ray sources with luminosities of $\sim 10^{32}$ ergs/sec. The first observations made with the Einstein satellite (1979) confirmed that essentially all O stars are X-ray sources (Harnden et al. 1979, Seward et al. 1979). The X-ray luminosities for various stars on the HR diagram are shown in Figure 6. The region over which the Auger enhanced lines of the O VI, N V, C IV, and Si IV are seen are also shown. For the early-type stars the X-ray luminosity is proportional the total luminosity of the star. ($L_x/L \simeq 10^{-7}$, Long and White, 1980; Vaiana et al., 1980; Cassinelli et al., 1981; and Seward and Chlebowski, 1982).

270
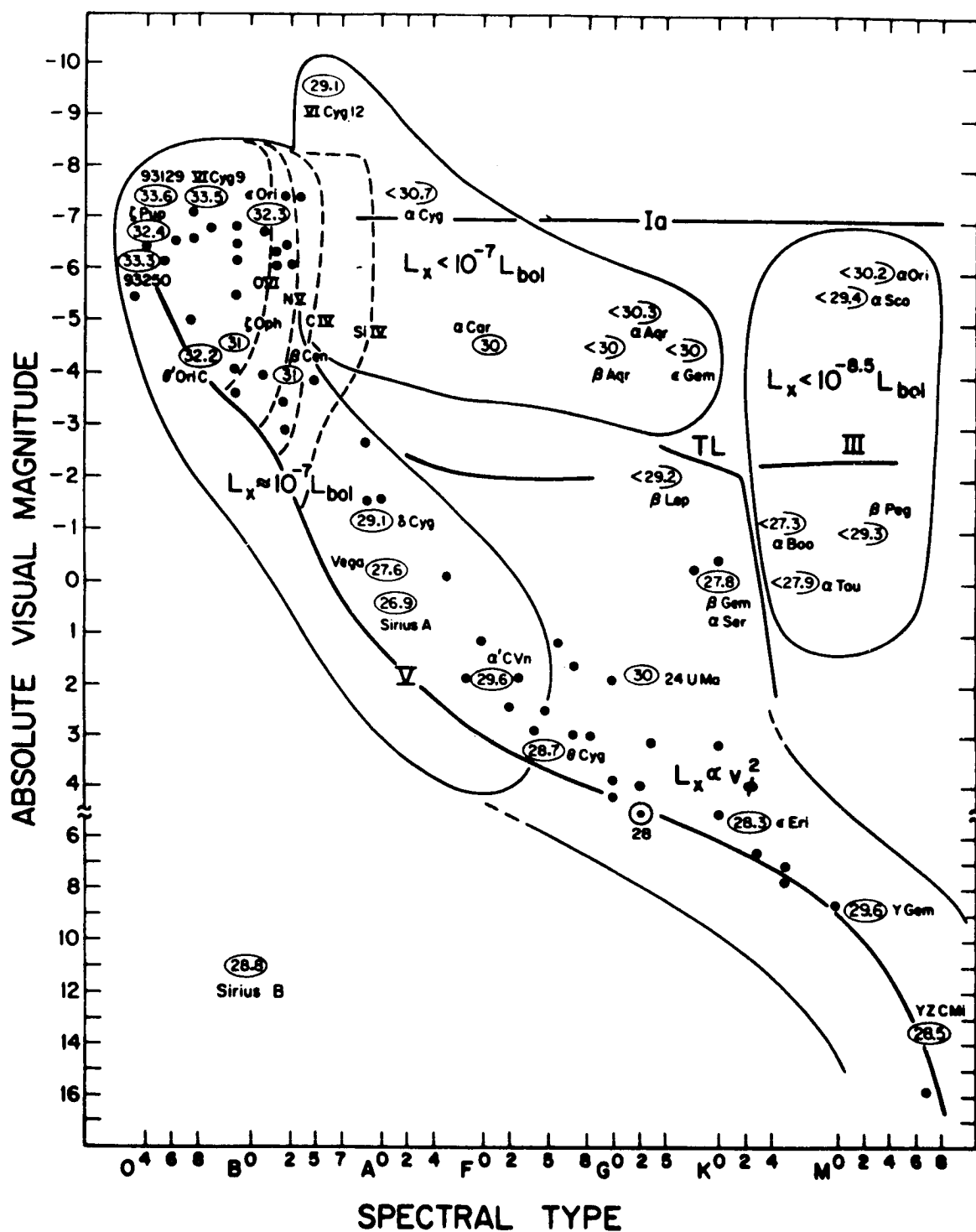
Fig. 6 - X-ray emission in the HR diagram. The solid dots indicate stars detected as X-rays sources by the Einstein satellite. For several stars the logarithm of the X-ray luminosity is shown in the ovals. Upper limits are also shown for a few supergiants and late-type giants. The extent of the presence of broad lines of the "superionization" ions in the UV spectra at O VI, N V, C IV, and Si IV are indicated by the dashed lines for the early-type stars. For early-type stars L_x is proportional to the stellar luminosity, as indicated, while for late-type stars the X-ray luminosity is proportional to rotation speed squared as might be expected from coronal emission that depends on a dynamo mechanism. This figure is from the review by Cassinelli and MacGregor (1983).

Does the detection of X-rays mean that the base corona plus cool wind picture is correct? If so, it implies that there is mechanical heating occurring at the base of the wind; and there is a flux of mechanical energy emergent from the stellar interior; and the mass loss is not fully explained by line driven wind theory. Figure 7a shows the X-ray energy distribution predicted from the slab corona plus cool wind model of Cassinelli and Olson (1979) compared with the observations of ε Ori B0.5Ia made from the Einstein satellite using the solid state spectrometer (SSS), (Cassinelli and Swank 1983). The empirical model predicted that there should be a sharp decrease in the flux at 0.6 keV because of attenation in the cool wind by the K shell edge opacity of oxygen. The observations show clearly that the edge is not there. The X-rays must be formed further out in the wind. The need for a base corona is no longer evident.

A recent explanation for the X-ray energy distribution gives fresh support for the radiatively initiated wind idea. Lucy and White (1981) and Lucy (1982b) have proposed that the X-rays arise in shocks embedded in the wind. Shocks should form, they argue, because line driven winds are unstable. Consider two neighboring gas elements at the same height in the atmosphere. If one is given a slight outward velocity increment relative to the other, it will have its line opacity doppler displaced into a frequency band with more flux (i.e. less blocking by the line opacity deeper in the atmosphere). Therefore the velocity increment will grow. This and the related instabilities of line driven winds has been analyzed by Nelson and Hearn (1978), MacGregor, Hartmann, and Raymond (1979), Carlberg (1980), and Kahn (1981). Lucy and White (1980) proposed that the instabilities grow to form blobs that are radiatively driven through the ambient gas and have X-rays formed in a bow shock at the front face of the blob. The X-rays are still formed relatively close to the base of the wind in this model and still predict a significant edge at 0.6 keV as is seen in Figure 7b. Lucy (1982b) has proposed a different limiting form for the flow instability. He suggests a periodic shock model, in which the shock is accelerated by radiation in the wavelength band corresponding to the increment in velocity that occurs from one shock to the next. (See Fig. 8).

The predictions of Lucy (1982b) are analyzed for ε Ori by Cassinelli and Swank (1983) (Figure 7c). To explain the X-rays some very strong shocks are needed with shock velocities >500 km/sec to provide $T \simeq 3 \times 10^6$K. One strong shock is needed every 21 hours. The wind flushing time, however, is only ~3 hours and large variations in the X-ray flux might be expected. The X-rays of ε Ori are not variable, however, (Cassinelli et al. 1983). Therefore the strong shock is not spherically symmetric about the star but must be broken into at least 25 or so "shreds" distributed through the flow. Lucy (1982a) offers further empirical support for his periodic shock model by arguing that the observed P Cygni profiles with their broad dark absorption imply the flow velocity is a non-monotonic function of radius.
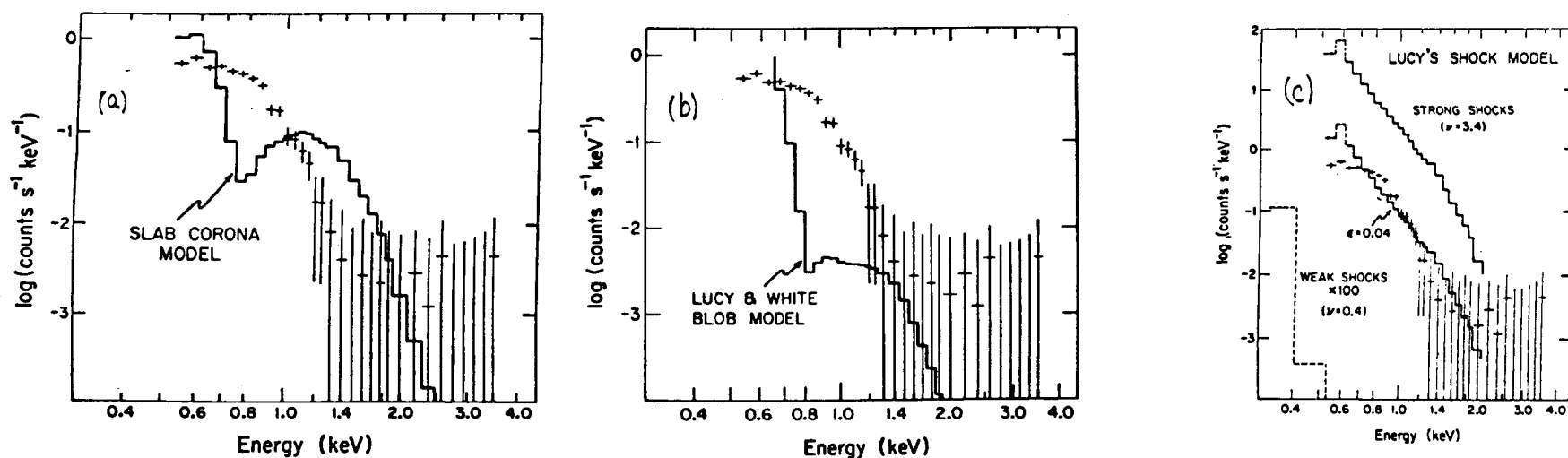
Fig. 7 - Shows the Solid State Spectrometer (SSS) spectrum of ε Ori (B0Ia)
compared with predictions of 3 models. A) The heavy line shows the SSS spectrum
predicted by a model in which the X-rays originate at the base of the wind in a
thin slab corona. The absorption edge clearly seen at 0.6 keV is caused by K
shell ionization of oxygen in the cool wind. The lack of this absorption in the
observed spectrum suggests that much of the soft X-ray emission comes from
sources well above most of the wind opacity. B) Shows the spectrum predicted
from the radiatively driven blob model of Lucy and White(1980) for ζ Pup in which
X-rays are expected to be formed near the base of the wind. C) Snows the
spectrum of ε Ori predicted by Lucy's (1982b) periodic shock model. The shocks
are parameterized by the quantity, ν,. Results for 2 values of ν are shown. The
preferred value in the theory is ν = 0.4, but is seen to yield a spectrum that is
far below (even after multiplying by 100) the observed distribution. The model
with ν = 3.4 gives rise to a spectrum that is sufficiently hard but predicts
more X-rays than are needed to fit the observation. If a fraction, ε = 0.04 of
the X-rays are assumed to come from these strong shocks a reasonably good fit is
achieved as is shown.

With the modification of radiation driven wind theory to include radiatively driven instabilities, it does appear that the answer to our original question is: Yes, a quiescient luminous star can push off a fast massive wind, and can explain the presence of "coronal" phenomena such as X-ray and anomalously high ionization lines. The debate is going on, nonetheless. Cassinelli and Swank (1983) point out that there is evidence for gas at $\sim 15\times10^6$K in OB supergiants and O main-sequence stars. The stars show X-ray lines of Si XIII and S XV at ~ 2 keV. These may be difficult to explain with radiation driven wind models, but are easily explainable if the stars have magnetic loops analogous to magnetic structures in the solar corona. The Wolf-Rayet problem discussed earlier is also not yet resolved in that it is not yet clear whether an alternate wind driving mechanism is required. It is surprising, nevertheless, that so straightforward a model as the radiation driven wind model has withstood so many tests. Solar wind physicists are certainly encouraged to use their expertise to develop other diagnostics of the structure of the fast massive winds of early-type stars.
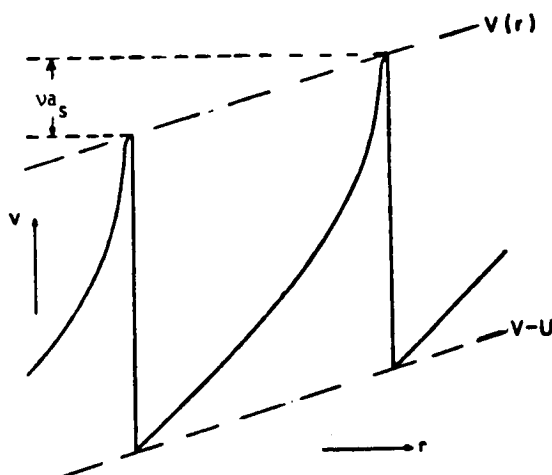
Fig. 8 - The phenemenological description of the hypersonic motions adopted by Lucy (1982b). The functions V(r) and U(r) denote the shock's velocity in the star's frame and their propagation speed, respectively, at radial distance r. The quantity ν is the basic parameter of the model and is defined such that νa_s is the velocity interval within which matter in a shock's wake is irradiated by unattenuated photospheric continuum. (adopted from Lucy 1982b).

References

Abbott, D.C., The terminal velocities of stellar winds from early-type stars, Astrophys.J., 225, 893, 1978.

Abbott, D.C., The theory of radiatively driven stellar winds. I. A physical interpretation, Astrophys.J., 242, 1183, 1980.

Abbott, D.C., The theory of radiatively driven stellar wind. II. The line acceleration, Astrophys.J., 259, 282, 1982a.

Abbott, D.C., The theory of radiation driven stellar winds and the WR phenomenon, in IAU Symposium No. 99, Wolf-Rayet Stars: Observations, Physics, Evolution, edited by C.W.H. deLoore and A.J. Willis, p. 185, Reidel, Dordrecht, 1982b.

Abbott, D.C., J.H. Bieging, E. Churchwell, and J.P. Cassinelli, VLA radio continuum measurements of mass loss from early-type stars, Astrophys.J., 238, 196, 1980.

Abbott, D.C., J.H. Bieging, and E. Churchwell, Mass loss from very luminous OB stars and the Cygnus superbubble, Astrophys.J., 250, 645, 1981.

Barlow, M.J., Observations of mass loss from OB and WR stars, in IAU Symposium No. 99, Wolf Rayet Stars: Observations, Physics, Evolution, edited by C.W.H. deLoore and A.J. Willis, p. 149, Reidel, Dordrecht, 1982.

Barlow, M.J., and M. Cohen, Infrared photometry and mass loss rates for OBA supergiants and Of stars, Astrophys.J., 213, 737, 1977.

Belcher, J.W., Alfvenic wave pressures and the solar wind, Astrophys.J., 168, 509, 1971.

Belcher, J.W., and K.B. MacGregor, Magnetic acceleration of winds from solar-type stars, Astrophys.J., 210, 498, 1976.

Carlberg, R.G., The instability of radiation driven stellar winds, Astrophys.J., 241, 1131, 1980.

Cassinelli, J.P., Theories for the winds from WR stars, in IAU Symposium No. 99, Wolf Rayet Stars: Observations, Physics, Evolution, edited by C.W.H. deLoore and A.J. Willis, p. 173, Reidel, Dordrecht, 1982.

Cassinelli, J.P., J.I. Castor, and H.J.G.L.M. Lamers, Expanding envelopes of early-type stars: current status, Publ.Astron. Soc.Pac., 90, 496, 1978.

Cassinelli, J.P., and L. Hartmann, The effects of winds and coronae of hot stars on the infrared and radio continua, Astrophys.J., 212, 488, 1977.

Cassinelli, J.P. and K.B. MacGregor, Stellar chromospheres, coronae, and winds, in Physics of the Sun, edited by P.A. Sturrock, D.M. Mihalas, T.E Holzer, and R.K. Ulrich, University of Chicago Press, Chicago, in press, 1983.

Cassinelli, J.P., L. Hartmann, W.T. Sanders, A.J. Dupree, and R.V. Myers, The simultaneous X-ray and ultraviolet observations of ε Orionis and κ Orionis, Astrophys.J., 268, 205, 1983.

Cassinelli, J.P. and G.L. Olson, The effects of coronal regions on the X-ray flux and ionization conditions in the winds of OB supergiants and Of stars, Astrophys.J., 229, 304, 1979.

Cassinelli, J.P. and J.H. Swank, X-ray spectra of Orion and OB supergiants, Astrophys.J., 271,   , 1983.

Cassinelli, J.P., W.L. Waldron, W.T. Sanders, F.R. Harnden, R. Rosner, and G.S. Vaiana, X-ray emission from Of stars and OB supergiants, Astrophys.J., 250, 677, 1981.

Castor, J.I., Spectral line formation in Wolf-Rayet envelopes, Mon.Not.Roy.Astr.Soc., 149, 111, 1970.

Castor, J.I., D.C. Abbott, and R.I. Klein, Radiation-driven winds in Of stars, Astrophys.J., 195, 157, 1975.

Castor, J.I., D.C. Abbott, and R.I. Klein, Radiation driven stellar winds, in Physique des Mouvements dans les Atmospheres Stellaires, edited by R. Cayrel, M. Steinberg, p. 363, Cent.Nat.Rech.Sci., Paris, 1976.

Friend D.B., and J.I. Castor, Stellar winds driven by multi-line scattering, preprint 1983 (see also D. Friend, this volume).

Harnden, F.R., G. Branduardi, M. Elvis, P. Gorenstein, J. Grindlay, J.P. Pye, R. Rosner, K. Topka, and G.S. Vaiana, Discovery of an X-ray star association in VI Cygni (Cyg OB2), Astrophys.J.Lett.,234, L51, 1979.

Hartmann, L., and K.B. MacGregor, Momentum and energy deposition in late-type stellar atmospheres and winds, Astrophys.J., 242, 260, 1980.

Hartmann, L., and K.B. MacGregor, Protostellar mass and angular momentum loss, Astrophys.J., 259, 180, 1982.

Jacques, S.A., Solar wind models with Alfven waves, Astrophys.J., 226, 632, 1978.

Kahn, F.D., On the stability of stellar winds from early-type stars, Mon.Not.Roy.Astr.Soc., 196, 641, 1981.

Lamers, H.J.G.L.M., and D.C. Morton, Mass ejection from the O4f star Zeta Puppis, Astrophys.J.Suppl., 32, 715, 1976.

Leitherer, C., H.Hefele, O. Stahl, and R. Wolf, Spectroscopy and infrared photometry of Cyg OB2 stars: Velocity law and mass loss rates, Astron.Astrophys., 108, 102, 1982.

Long, K.S., and R.L. White, A survey of soft X-ray emission from hot stars, Astrophys.J.Lett., 239, L65, 1980.

Lucy, L.B., The formation of resonance lines in locally nonmonotonic winds, Astrophys.J., 255, 278, 1982a.

Lucy, L.B., X-ray emission from the winds of hot stars. II., Astrophys. J., 255, 286, 1982b.

Lucy, L.B., and P.M. Solomon, Mass loss by hot stars, Astrophys.J., 159, 879, 1970.

Lucy, L.B., and R.L. White, X-ray emission from the winds of hot stars, Astrophys.J., 241, 300, 1980.

MacGregor, K.B., L. Hartmann, and J.C. Raymond, Radiative amplification of sound waves in the winds of O and B stars, Astrophys.J., 231, 514, 1979.

Mihalas, D., Stellar Atmospheres, Freeman, San Francisco, pp. 511-566, 1978.

Morton, D.C. The far ultraviolet spectra of six stars in Orion, Astrophys. J., 147, 1017, 1967.

Nelson, G., and A.G. Hearn, A line driven Rayleigh-Taylor-Type instability in hot stars, Astr.Ap., 65, 223, 1978.

Olson, G.L., An analysis of ultraviolet resonance lines and the possible existence of coronae in O stars, Astrophys.J., 226, 124, 1978.

Panagia, N., and M. Felli, in IAU Symposium No. 99, Wolf-Rayet Stars: Observations, Physics, Evolution, edited by C.W.H. deLoore and A.J. Willis, p. 149, Reidel, Dordrecht, 1982.

Seward, F.D., and T. Chlebowski, X-ray emission from the Carina nebula and the associated early stars, Astrophys.J., 256, 530, 1982.

Seward, F.D., W.R. Forman, R. Gracconi, R.E. Griffiths, F.R. Harnden, Jr., C. Jones, and J.P. Pye, X-rays from Eta Carina and the surrounding nebula, Astrophys.J.Lett., 234, L55, 1979.

Sobolev, V.V., Moving Envelopes of Stars, Harvard University Press, Cambridge, 1960.

Vaiana, G.S. et al., Results from an extensive Einstein stellar survey, Astrophys.J., 245, 163, 1981.

White, R.L., and R. Becker, The resolution of P Cygni's stellar wind, *Astrophys.J.*, *262*, 657, 1982.

ALFVEN WAVES IN STELLAR WINDS[*]

Thomas E. Holzer

High Altitude Observatory
The National Center for Atmospheric Research[†]
Boulder, CO 80307

ABSTRACT

We examine the propagation and damping of Alfvén waves in stellar winds and the effects of these waves on the wind mass-loss rate, asymptotic flow speed, and radial temperature profile. A simple, analytic description of a wind with waves which are undamped in the region of subsonic flow is developed for a broad range of stellar conditions, and numerical models with wave damping are applied to the massive winds from cool, low-gravity stars. We find no basis for the widely held belief that Alfvén-wave driven winds from these cool, low-gravity stars can exhibit both a very large mass-loss rate and a very small asymptotic flow speed. This difficulty for the Alfvén-wave mechanism is common to other mechanisms for driving these massive winds and points to the need for a careful evaluation of the observational inferences of asymptotic flow speeds. We also find that the radial temperature profile produced by invoking a constant damping length for the waves is significantly different from that produced by a self-consistent description of frictional wave damping for a wave frequency which is presumably consistent with the chosen constant damping length. An interesting sidelight of the present study is the discovery of the existence of two (rather than just one) transsonic solutions to the stellar wind equation of motion for a given set of boundary condition.

STELLAR WINDS DRIVEN BY MULTI-LINE SCATTERING

David B. Friend
Advanced Study Program/High Altitude Observatory
National Center for Atmospheric Research*
Boulder, Colorado 80307

ABSTRACT

This paper presents a model of a radiation-driven stellar wind with over-lapping spectral lines. It is based on the Castor, Abbott, and Klein (CAK) theory. The presence of overlapping lines allows a photon to be scattered many times in different lines. I assume a random separation between strong lines, which makes it possible to find the angular distribution of the wavelength-averaged intensity of radiation from the star. The properties of the wind at any point depend on this intensity, which in turn depends on the structure of the wind. A self-consistent wind model is found. The mass loss rate does __not__ saturate as line overlap becomes more pronounced, but continues to increase. The terminal velocity is much larger than in the CAK model, while the velocity law is shallower. This model might help explain the massive winds from Wolf-Rayet stars.

Introduction

Previous models for radiation-driven stellar winds [e.g., Castor, Abbott, and Klein, 1975; hereafter CAK] have not considered the fact that if the spectral lines that drive the wind are packed densely enough, a photon can scatter in more than one line. Multiple scatterings of photons in overlapping lines may explain some aspects of the winds from early-type stars. "Overlap" in this context means that the lines are separated by less than twice the wind velocity Doppler shift:

$$\frac{\Delta\lambda}{\lambda} = \frac{2v}{c} , \tag{1}$$

where v is the velocity of the wind. How overlap causes multiple scatterings, and how we include this effect in the radiation force, is discussed in the next section.

Another shortcoming of the earliest stellar wind models is that they do not include the correct angle integration of the core radiation in the calculation of the radiation force, but instead assume radial streaming. This angle integration is important for the multi-scattering process because, as we shall see, line overlap affects the wind __through__ the angular distribution of radiation.

The combination of the angle integration and overlapping lines may be able to explain the observed terminal velocities of early-type stellar winds. The CAK theory predicts that the terminal velocity is proportional to the escape velocity:

$$v_\infty = \left(\frac{\alpha}{1-\alpha}\right)^{1/2} v_{esc} , \tag{2}$$

where α is essentially independent of spectral type, and has a value between 0.5 and 0.7 [Abbott, 1982a]. Thus, the CAK model would predict $v_\infty =$ (1.0-1.5)v_{esc}. This relation may be correct for late B and early A stars [Abbott, 1982a], but is incorrect for O stars, which have a constant of proportionality of about 3 [Abbott, 1978; Garmany et al., 1981]. In section IV of this paper we will see that a self-consistent multi-scattering model does indeed predict that the terminal velocity is higher than in CAK, and increases with increasing line overlap.

The quantity $\varepsilon = \dot{M}v_\infty c/L$, which is the ratio of the momentum carried to infinity by the wind to the radiative momentum of the star, can be thought of as an efficiency of ejecting matter in the wind. ($\dot{M}$ is the mass loss rate and L is the stellar luminosity.) In the "single scattering limit," in which a photon can give its momentum to the wind only once, ε cannot exceed unity. ε is observed to be greater than one in some Of stars [Ferrari-Toniolo, Persi, and Grasdalen, 1981] and much greater than one in Wolf-Rayet stars [Barlow, Smith and Willis, 1981; Abbott, 1982b]. It is often claimed that this is evidence that these winds are not radiatively driven. We will see that the multi-scattering model presented here has ε values substantially larger than unity, and it appears that ε could be arbitrarily large if there are enough lines.

Method

If we consider only monotonically increasing velocity laws, a photon is continually redshifted, in the reference frame of the expanding gas, as it travels outward through the wind. After scattering in a line, if there is no other line with a rest wavelength within the wind-velocity Doppler shift of the first line (as described by Eq. (1)), the photon can escape from the atmosphere. If the lines overlap, as is the case for the UV resonance lines in OB star atmospheres [Panagia and Macchetto, 1982], the photon can now scatter in another line. It will continue scattering in lines with longer wavelengths until it escapes from the atmosphere or collides with the photosphere. Figure 1 illustrates the process schematically.

This is a formidable problem to treat accurately. One feasible, but costly, approach is to do a Monte-Carlo simulation of the multiple scattering process using a complete tabulation of scattering lines. A more approximate but much less costly method is to make a statistical assumption. The real wavelength distribution of lines is markedly clumpy, since lines are often present as fairly closely spaced multiplets. When the richness of the spectrum increases, however, the chance groupings of lines of different elements and ions may become more prominent than the multiplet structure. This is the regime in which a statistical treatment may succeed.

The statistical model that is advanced is this: lines have random wavelengths and strengths such that different strengths form independent processes. This assumption enables us to use the crucial simplification that the intensity of the radiation field depends only on the wavelengths and strengths of lines that have already scattered photons, and hence the presence or absence of a line at a given location, and its strength if there is one, are statistically independent of the intensity. The radiative transfer problem is then tractable, and we may solve for the angle-dependent intensity of radiation (averaged over a suitable wavelength range). For the details of this calculation, see Friend and Castor [1983].

282
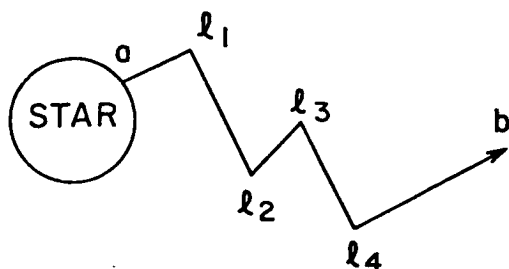
(a)   (b)
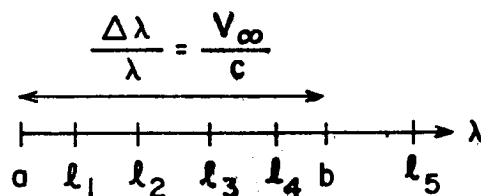
Figure 1. (a) Diagram of the path of a photon from the stellar surface (point a) to its escape from the atmosphere (point b). It is scattered by four lines in the process. (b) Wavelengths of spectral lines ℓ_1 through ℓ_5 are shown, along with the wavelength of the photon at points a and b and the wind terminal velocity Doppler shift $\Delta\lambda/\lambda = v_\infty/c$, in the reference frame of the expanding wind. Lines ℓ_1 through ℓ_4 "overlap" and each scatters the photon, while line ℓ_5 is at too long a wavelength.

The solution gives the blocking factor, B, which is the fraction of the outward flux that is reflected back into the photosphere, and the correction factor to the line force in the CAK model of radially-streaming radiation, which we call F_a.

The radiation force in our model is obtained by multiplying the force multiplier function M(t) of CAK by the correction factor F_a. Recall that in CAK M(t) is approximated by $kt^{-\alpha}$, where t is the optical depth parameter [see CAK equation (5)]. We will add an additional complication here, which takes into account the variation of ionization state with density. Abbott [1982a] showed that the dependence of the radiation force on density is approximately given by $(\rho/W)^{0.1}$ (see his eq. (12)), where W is the dilution factor. Since ρ is proportional to $\dot{M}/vr^2$ and W is approximately $(1/4)(R_*/r)^2$, we write the new force multiplier as

$$M(t) = A \left(\frac{\dot{M}}{R_*^2 v}\right)^{0.1} \left(\frac{v_{th}}{t}\right)^\alpha F_a \ . \tag{3}$$

The v_{th}^α term is included since the CAK force constant k is actually proportional to it (see CAK, eq. (15)). For ease of comparison with CAK, we will use $\alpha = 0.7$ as they did. The constant A is a measure of the number of strong lines.

Solution of Equation of Motion

The equation of motion for the wind, from CAK, is

$$v\frac{dv}{dr} = -\frac{GM}{r^2} + \frac{\sigma_e L}{4\pi c r^2}[1+M(t)] - \frac{1}{\rho}\frac{dP_g}{dr} \quad . \qquad (4)$$

(σ_e is the electron scattering opacity.) The gas pressure P_g will be written as ρa^2, where a is the isothermal sound speed (assumed constant). Using Eq. (3) for $M(t)$, substituting ρa^2 for P_g, and using the continuity equation $\dot{M} = 4\pi\rho v r^2$ to eliminate ρ, yields

$$\left(v - \frac{a^2}{v}\right)\frac{dv}{dr} = \frac{-GM(1-\Gamma)}{r^2} + \frac{2a^2}{r} + \frac{\Gamma GMA}{r^2}\left(\frac{\dot{M}}{R_*^2 v}\right)^{0.1} F_a\left(\frac{4\pi}{\sigma_e \dot{M}}r^2 v\frac{dv}{dr}\right)^\alpha \qquad (5)$$

for the equation of motion. Γ is the ratio of the luminosity to the Eddington luminosity:

$$\Gamma = \frac{L}{L_{EDD}} = \frac{\sigma_e L}{4\pi GMc} \quad . \qquad (6)$$

The topology of solutions is exactly the same as in CAK, and the only acceptable wind solution passes through a unique critical point. The critical point conditions give us the velocity and velocity gradient at the critical point, and the mass loss rate, given the critical radius.

   We must find a wind model whose velocity law and mass loss rate are consistent with the angle-dependent radiation force. We may begin by specifying the factor F_a as a function of radius, and then solving the wind equation of motion and critical point conditions to get the wind structure. We must make an intitial guess for the location of the critical point, and then adjust the critical radius until the electron scattering optical depth is unity at the specified photospheric radius. The wind parameters thus found can then be used to calculate the radiation field and $F_a(r)$. The process is repeated until convergence is obtained. About 10 to 20 iterations were required for $F_a(r)$ to converge.

Results

   The procedure described in the previous section was performed for stellar data representing an O5f star and five values of the radiation force constant A (see section II). The stellar parameters chosen were the ones used in section IV of CAK: $L = 9.66 \times 10^5 \, L_\odot$, $M = 60 \, M_\odot$, and $R_* = 13.8 \, R_\odot$. Figure 2 shows $F_a(r)$ for three different values of log A (in cgs units). For small r there is not much variation in F_a for different A, but at large radii the force is much larger for larger A. The radiation force is smaller than in CAK at small r ($r < 2R_*$) and larger than in CAK for large r. This has the effect of making the velocity law more gradual and the terminal velocity larger.

284
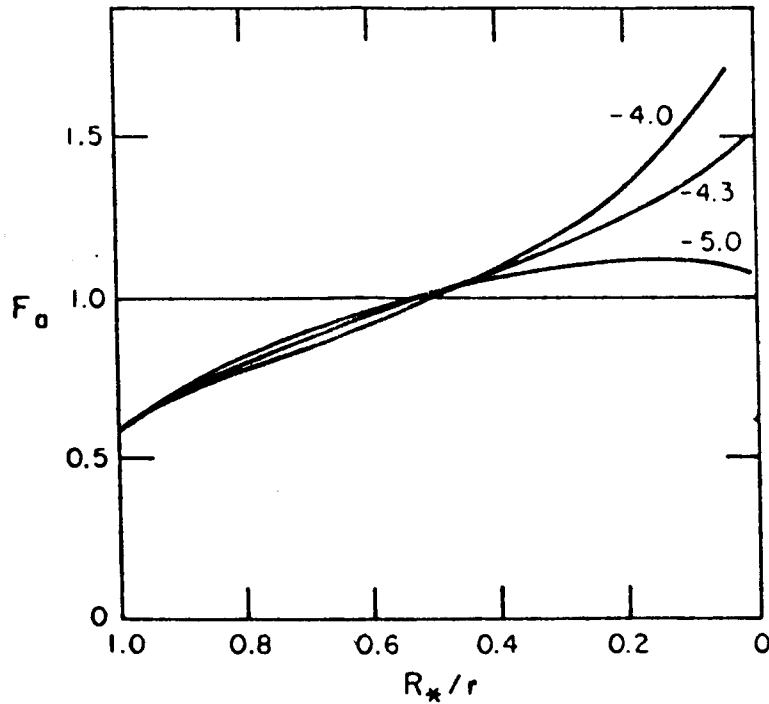
Figure 2. Correction factor F_a as a function of radius (plotted as $R*/r$). The three curves are labelled with the value of log A (in cgs units).

The increase of F_a at large radii with increasing A is due to a broadening of the angular distribution of radiation. Increasing the overlap (larger A) means increasing the number of scatterings, which broadens the angular distribution. (The intensity at large angles goes up as more photons are scattered.) This makes the optical depth parameter t smaller (for large r). The radiation force then increases since it is proportional to $t^{-\alpha}$.

Figure 3 shows velocity laws for the three cases of Fig. 2. For all A values, and especially for the intermediate one, v(r) is close to the relation

$$v(r) = v_\infty(1-R_*/r) \quad , \tag{7}$$

which is closer to what observations indicate is the actual velocity law in early-type stars [Lamers and Morton, 1976; Barlow and Cohen, 1977; Van Blerkom, 1978].

Table 1 gives the mass loss rate and terminal velocity, the blocking factor B, and the radius, velocity and F_a function at the critical point, for the five different values of A. The CAK results for the same star are also shown. The terminal velocity is much higher than in CAK, even for the smallest value of A. This means that simply including the angle integration in the radiation force increases the terminal velocity to a value more consistent with observations.
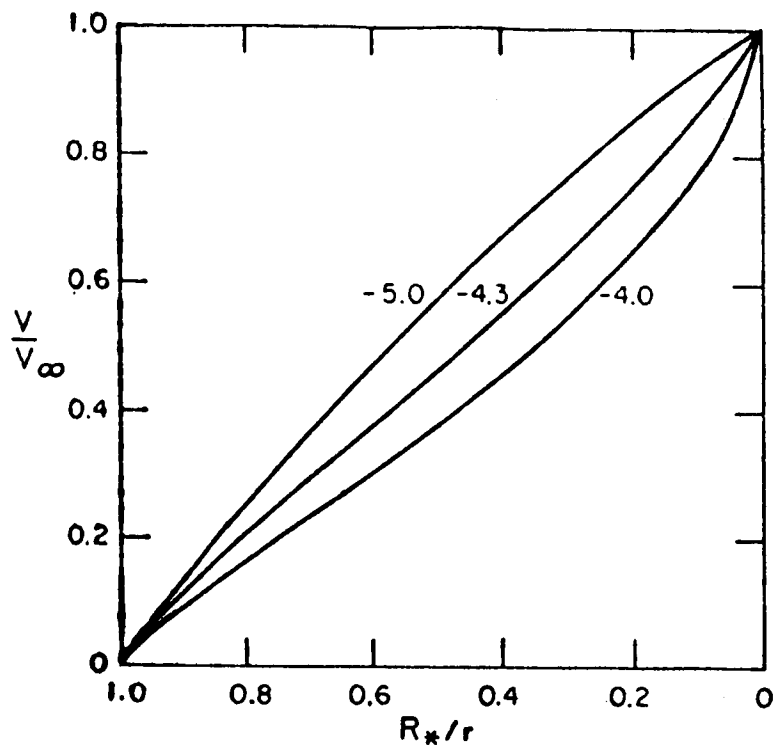
Figure 3. Velocity laws for the three cases shown in Fig. 2.

Table 1. Results of Model

log A	-5.0	-4.6	-4.3	-4.1	-4.0	CAK
$\dot{M}$ (10^{-6} $M_\odot$ yr^{-1})	0.59	2.7	8.6	18	28	6.6
v_∞ (km s^{-1})	3350	3500	3900	4300	4600	1515
B	0.03	0.12	0.32	0.49	0.62	-
$10B/3(1-B)$	0.103	0.455	1.57	3.20	5.44	-
$\dot{M}v_\infty c/L$	0.101	0.483	1.71	3.95	6.58	0.511
r_c/R_*	1.05	1.05	1.06	1.06	1.07	1.50
v_c (km s^{-1})	250	255	274	288	307	950
$F_a(r_c)$	0.65	0.65	0.66	0.66	0.67	-

The mass loss rate for the log A = -4.3 case (which corresponds most closely to CAK) is only slightly higher than the CAK value, so line overlap does not have a significant effect. The variation of $\dot{M}$ with A is due to the increase in the number of lines. What is unexpected is that $\dot{M}$ does not saturate as line line overlap becomes more pronounced. This is probably due to the assumption of random line spacing, as clustering of lines tends to reduce the force [see Olson, 1982]. Another result of Table 1 is that the blocking factor correlates well with the "wind efficiency" $\varepsilon = \dot{M} v_\infty c/L$ (see Table 1):

$$\frac{B}{1-B} \approx 0.3 \, \varepsilon \, . \tag{8}$$

For blocking factors approaching one, ε can become very large, so winds with multiple scatterings are much more efficient in ejecting matter than single-scattering winds. This may be especially relevant for Wolf-Rayet stars.

References

o Abbott, D. C., The terminal velocities of stellar winds from early-type stars, Astrophys. J., 225, 893, 1978.

o Abbott, D. C., The theory of radiatively driven stellar winds. II. The line acceleration, Astrophys. J., 259, 282, 1982a.

o Abbott, D. C., the theory of radiation driven stellar winds and the Wolf-Rayet phenomenon, in Wolf-Rayet Stars: Observations, Physics, and Evolution, edited by C. de Loore and A. Willis, p. 185, Reidel, Dordrecht, 1982b.

o Barlow, M. J., and M. Cohen, Infrared photometry and mass loss rates for OBA supergiants and Of stars, Astrophys. J., 213, 737, 1977.

o Barlow, M. J., L. J. Smith, and A. J. Willis, Mass-loss rates for 21 Wolf-Rayet stars, Monthly Notices Royal Astron. Soc., 196, 101, 1981.

o Castor, J. I., D. C. Abbott, and R. I. Klein, Radiation-driven winds in Of stars, Astrophys. J., 195, 157, 1975, (CAK).

o Ferrari-Toniolo, M., P. Persi, and G. L. Grasdalen, Infrared excess and mass-loss rate of the extreme Of star HD108, Publ. Astron. Soc. Pac., 93, 633, 1981.

o Friend, D. B., and J. I. Castor, Stellar winds driven by multiline scattering, Astrophys. J., 272, (in press), 1983.

o Garmany, C. D., G. L. Olson, P. S. Conti, and M. E. van Steenberg, Mass loss rates from O-stars in OB associations, Astrophys. J., 250, 660, 1981.

o Lamers, H. J. G. L. M., and D. C. Morton, Mass ejection from the O4f star Zeta Puppis, Astrophys. J. Suppl., 32, 715, 1976.

o Olson, G. L., An escape probability treatment of doublet resonance lines in expanding stellar winds, Astrophys. J., 255, 267, 1982.

o Panagia, N., and F. Macchetto, Wind acceleration in early-type stars: the momentum problem and the terminal velocity, Astron. Astrophys., 106, 266, 1982.

o Van Blerkom, D., Mass loss from P Cygni: the evidence of the Balmer lines, Astrophys. J., 221, 186, 1978.

Page intentionally left blank

FORMATION OF STANDING SHOCKS IN STELLAR WINDS
AND RELATED ASTROPHYSICAL FLOWS.

K. Tsinganos, S.R. Habbal, R. Rosner
Harvard-Smithsonian Center for Astrophysics
Cambridge, MA, 02138.

ABSTRACT

Stellar winds and other analogous astrophysical flows can be described, to lowest order, by the familiar one-dimensional hydrodynamic equations which, being nonlinear, admit in some instances discontinuous as well as continuous transonic solutions for identical inner boundary conditions. We elaborate on the physics underlying the formation of the discontinuous transonic solutions; discuss the *characteristics* of the time-dependent differential equations of motion to show how a perturbation changes profile in time and, under well-defined conditions, develops into a stationary shock discontinuity; and show how the formation of standing shocks in wind-type astrophysical flows depends on the fulfillment of appropriate *necessary* conditions, which are determined by the conservation of mass, momentum and energy across the discontinuity, and certain *sufficient* conditions, which are determined by the flow's "history".

1. Introduction

The present paper continues the study of the solution topologies of the time-dependent isothermal wind equations presented by Habbal, Rosner & Tsinganos (1983; Paper I) in these Proceedings; these two studies are motivated by the desire to understand how the simplest hydrodynamic equations describing spherically symmetric solar-wind type astrophysical flows (Parker 1963) respond to perturbations which disturb the radial symmetry of the outflow (Kopp & Holzer 1976; Munro & Jackson 1977) or, equivalently (cf. Habbal & Tsinganos 1983), perturb the outflow by means of a localized non-thermal momentum deposition in the thermal gas (Holzer 1977). In this paper, we consider the consequences of a localized phenomenological momentum perturbation term of the form (Paper I)

$$D_{[D_o, R_p, \sigma, \tau]}(R, t) = D_o \left[1 - e^{-t/\tau} \right] e^{-(R-R_p)^2/\sigma^2} \quad \text{dyn/gm} , \tag{1}$$

where the free parameters D_o, R_p, σ, and τ characterize the amplitude, location, spatial and temporal width, respectively, of the function $D(R,t)$. The detailed dependence of the steady solutions of the governing hydrostatic equations on the parameters D_o, R_p, and σ for $\tau = 0$ can be found in Habbal & Tsinganos (1983). The specific purpose of this note is to further elaborate on the physics underlying the response of the governing hydrodynamic equations to perturbations of the form (1) above (discussed in Paper I), and, in particular, to discuss qualitatively the conditions leading to the formation of shocks in the flow. We shall show that in certain limiting cases much of the relatively complex behavior can be understood on the basis of the straightforward theory of characteristics.

2. Nature of the Equations of Motion

In the following we discuss briefly the nature of the equations of motion and how they allow the development of shocks in the flow. First, it is convenient to write the continuity and momentum balance equations in the following form

$$A \frac{\partial \rho}{\partial t} + Av \frac{\partial \rho}{\partial R} + A\rho \frac{\partial v}{\partial R} = -\rho \frac{\partial A}{\partial t} - \rho \frac{\partial A}{\partial R} , \tag{2a}$$

$$c^2 \frac{\partial \rho}{\partial R} + \rho \frac{\partial v}{\partial t} + \rho v \frac{\partial v}{\partial R} = \rho D - \rho \frac{GM}{R^2} , \tag{2b}$$

289

where $c = [dp/d\rho]^{1/2}$ is the isothermal sound speed and $A(R,t)$ and $D(R,t)$ are the *given* functions of the flow tube's cross section and non-thermal momentum deposition, respectively.

Eqs. (2) form a system of two quasilinear partial differential equations of the first order for the functions ρ and v of the two independent variables R and t, for which solutions in closed form are not known. However, the *qualitative* behavior of their solutions and the associated physical effects can be simply understood by exploiting the hyperbolic nature of these equations; the formal theory of hyperbolic partial differential equations shows then that there exist two characteristic directions at every point of the (R,t)-plane which define the *characteristics* of Eqs. (2) (Courant & Friedrichs 1948),

$$\frac{dR}{dt} = v \pm c \ .$$

(3)

The *physical significance* of these characteristics can be understood as follows. Expressing the velocity in terms of the potential $\Phi(R,t)$,

$$\frac{\partial\Phi(R,t)}{\partial R} \equiv v \ , \quad -\frac{\partial\Phi(R,t)}{\partial t} = \frac{v^2}{2} + \int\frac{c^2\,d\rho}{\rho} - \frac{GM}{R} - \int D(\hat{R})\,d\hat{R} \ ,$$

(4)

we obtain a single differential equation for $\Phi(R,t)$,

$$\frac{\partial^2\Phi}{\partial t^2} + 2v\frac{\partial^2\Phi}{\partial R\partial t} + (v^2 - c^2)\frac{\partial^2\Phi}{\partial R^2} = v\left[c^2\frac{\partial\ln A}{\partial R} + D - \frac{GM}{R^2}\right] + c^2\frac{\partial\ln A}{\partial t} + \frac{\partial}{\partial t}\int_{R_0}^{R} D(\hat{R},t)d\hat{R} \ .$$

(5)

Consider then a *small* perturbation $\delta\Phi(R,t)$ superimposed on some solution $\Phi_0(R,t)$ of Eq. (5). Following Landau & Lifshitz (1975), we substitute $\Phi = \Phi_0 + \delta\Phi$ in (5) and obtain to lowest order the following equation for $\delta\Phi$,

$$\frac{\partial^2\delta\Phi}{\partial t^2} + 2v_0\frac{\partial^2\delta\Phi}{\partial R\partial t} + (v_0^2 - c^2)\frac{\partial^2\delta\Phi}{\partial R^2} = 0 \ ,$$

(6)

where $v_0 = \partial\Phi_0/\partial R$ is the "background" flow field (see below). We write $\delta\Phi = Be^{i\Psi}$, where B is a slowly varying function of R and t and the "eikonal" Ψ is almost linear in R and t; the "group velocity" of the disturbance is then $dR/dt = d\omega/dk$, where $k = \partial\Psi/\partial R$ and $\omega = \partial\Psi/\partial t$. We obtain from (6) for this "group velocity" of the perturbation,

$$\frac{dR}{dt} = v_0(R,t) \pm c \ ,$$

(7)

a relation which coincides with the slope (3) of the characteristic directions on the plane R-t. From the physical point of view Eq. (7) gives the velocity of propagation of sound waves in the moving gas relative to some fixed coordinate system; and since a disturbance of finite amplitude and duration can be regarded as a superposition of a sequence of small amplitude and duration perturbations, Eq. (7) describes the propagation of finite perturbations in the atmosphere as well (Courant & Friedrichs 1948, Landau & Lifshitz 1975). It is evident then that the characteristics represent the paths of all possible disturbances in the $(R-t)$-plane. The inevitable result of having a non-uniform velocity field, $dv_0/dR \neq 0$, is that the profile of some initial perturbation changes as it propagates in the atmosphere. For example, if $dv_0/dR < 0$ somewhere in the flow, an outward-propagating wave finds its leading segment travelling slower than its trailing edge; the result is that its amplitude profile "steepens". The perturbation then may "break," i.e., it may steepen enough so that the total density and velocity are no longer single-valued; in that case the characteristics intersect (Landau & Lifshitz 1975), and a shock has been formed in the flow. Whether this indeed leads to an equilibrium solution with a discontinuity depends on two facts: first, on the existence of such equilibrium solutions involving shocks for the given set of spatial parameters in the steady state equations (Habbal & Tsinganos 1983); and second, on the temporal history of the flow, as discussed below.

290

# 3. Evolution of the Perturbation and Shock Formation

We would now like to see whether the above discussion of characteristics can shed any light on an understanding of the behavior of a perturbed isothermal wind flow. We begin with a steady and isothermal (single critical point, or Parker) wind flow at t=0, and apply a perturbation of the type given in Eq. (1). As shown in Paper I, which of the (maximally three in the present, simplest case) distinct steady solutions the perturbed flow finally approaches depends upon the time scale parameter τ of the perturbation; whereas the character of these possible alternative steady states is determined by the remaining parameters of the perturbation [D_o, R_o, and σ], which fix the spatial form and strength of the perturbation (Habbal & Tsinganos 1983). How is one of these steady states selected by virtue of the time scale of the perturbation?

The first point to note is that the flow is characterized by three distinct time scales: the advection time scale τ_a=R/v, the downstream signal propagation time scale τ_+ = R/(v+c) [corresponding to propagation along the C^+ characteristics], and the upstream signal propagation time scale τ_- = R/(v-c) [corresponding to propagation along the C^- characteristics]; the crucial element is that although τ_a and τ_+ are comparable in the region of interest (i.e., of order of 3×10^5 sec near the sonic point), τ_- may be very large; the question is then how τ compares with these three flow time scales.

Consider then the evolution of the solutions sketched in Figs. (a)-(d) [see also Fig. 2 of Paper I], which qualitatively reproduce the essential features of the time-dependent solutions. In each case, we have sketched the velocity profiles of the initial Parker-type flow field, v_{in}(R,t=0), the final equilibrium flow field v_{eq}(R,t$\rightarrow\infty$) consistent with some given set of the spatial parameters [D_o, R_p, σ] characterizing D(R) and, finally, an intermediate velocity field v(R,δt) which results after, say, a time δt of the order 10^4 secs of momentum deposition. The question we would like to address then is: given the initial state v_{in}(R,t=0) and the parameters [D_o, R_p, σ, τ] of our momentum deposition, what is the final state towards which the intermediate state v(R,δt) evolves? That is, which of the three possible states — the continuous transonic solution, or any one of the allowed (if any) discontinuous transonic solutions — the system chooses to relax to after a sufficiently long evolution?

In the first case (Fig. a), no difficulty arises: in this case, the asymptotic value of D is sufficiently small that the steady perturbed solution (corresponding to t $\rightarrow\infty$) is unique and continuous, and always passes through the outer critical point; the eventual evolution of the intermediate solution is hence unambiguous. This is, however, not the case for the three other examples given, for which the asymptotic value of D is sufficiently large to result asymptotically in three distinct steady transonic solutions. In the first of the latter cases (Fig. b), τ is large (=40,000 secs) when compared to τ_+ and τ_a everywhere, and when compared to τ_- almost everywhere. Hence the flow profile evolves slowly, and the propagation of disturbances along characteristics may be viewed as occurring on a background flow field which is relatively steady almost everywhere; the exceptional location is near the sonic point(s), where the C^- characteristic becomes vertical (as can be seen from the sketch of the C^- characteristics in Fig. f, derived from the numerical solutions given in Paper I). Thus, the flow is near equilibrium essentially during the entire course of its history; but which sequence of equilibria is followed? The key point is that this sequence of equilibria (corresponding to a gradually increasing amplitude for D_o, cf. Habbal & Tsinganos 1983) is characterized by always having an outer sonic point downstream from the (eventual) inner critical point, and hence always has a region of subsonic flow between these two "x-type" critical points. Hence, once the flow becomes supersonic near the (eventual) inner critical point, the C^- characteristics are "trapped" between the two critical points, and the downstream-facing C^- characteristics emanating just downstream from the inner critical point must intersect the upstream-facing C^- characteristics emanating from the subsonic region just upstream from the outer critical point; a shock results (Fig. f), and the subsequent sequence of quasi-steady solutions corresponds to the discontinuous solution branch of the steady equations (for this choice of τ, that corresponding to the upstream shock). Note that from the characteristics one may readily obtain the time scale for, viz., formation of shocks by locating their first intersection.

The opposite extreme is obtained for very small τ ($\cong$10 secs; Fig. d); in this case the time scale for the perturbation is far shorter than any signal propagation time scale in the flow. Hence, the flow is never near any equilibrium solution during the time of significant change in the perturbing momentum deposition term; for 0 < t < τ, the flow's evolution is essentially entirely determined by

291
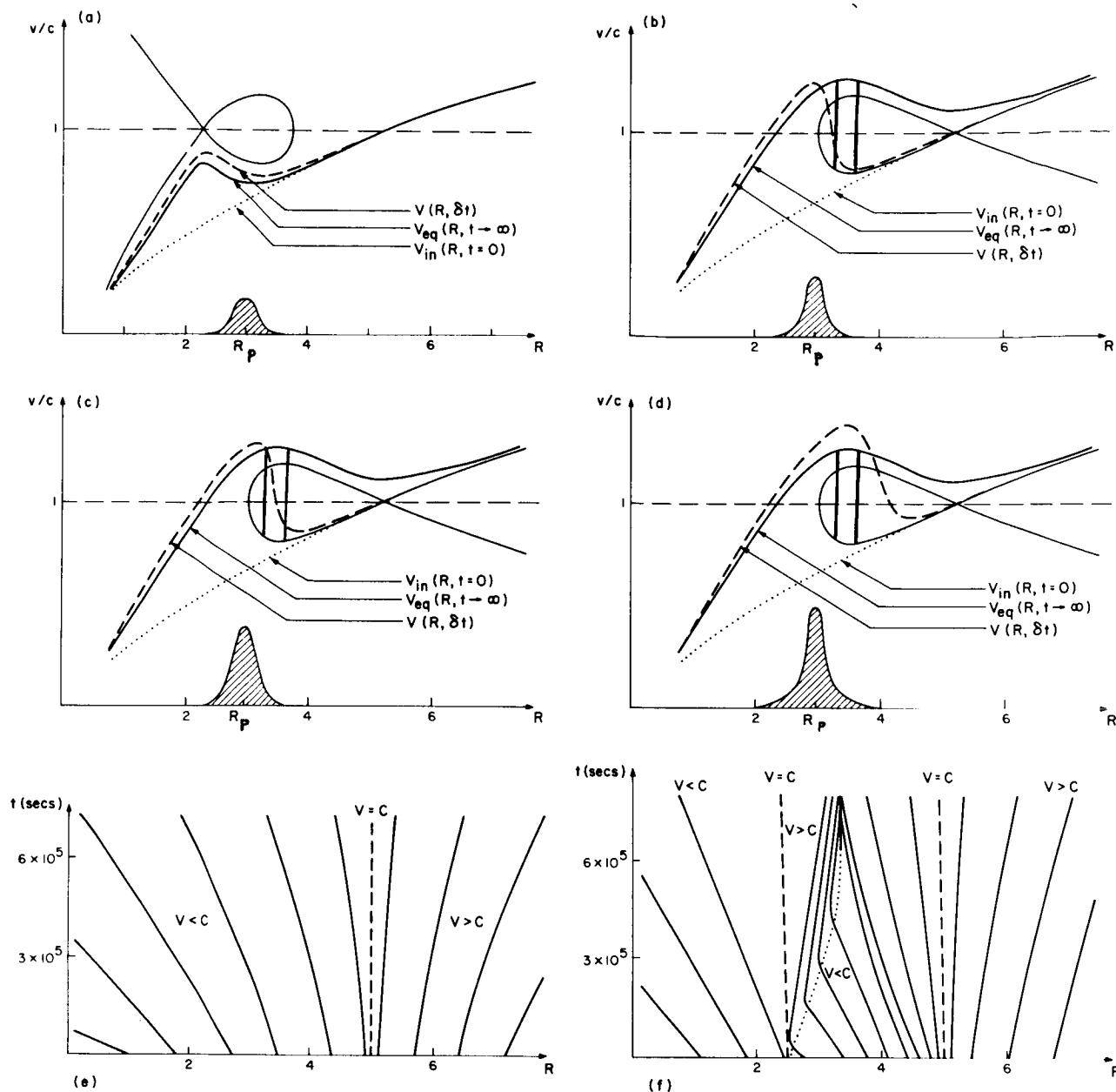
Figures (a)-(d) are sketches (taken from the solutions obtained in Paper I) of the solution topologies for the velocity field of the wind equations (2) with a localized momentum deposition function similar to the gaussian given by expression (1), for different values of the parameters D_α, R_p, σ and τ and at three representative times: t=0, t=δt>0 and t$\rightarrow\infty$. The dotted solution is the initial velocity v_{in}(R,t=0), the dashed solution is the intermediate velocity v(R,δt) and the solid velocity curves, v_{eq} (R,t$\rightarrow\infty$), represent the solution topologies of the steady state equations (2). All figures (a)-(d) have the same values of the parameters R_p and σ while figures (b)-(d) correspond to the same set of the spatial parameters [D_α, R_p, σ] with τ decreasing from (b) to (d). The two vertical solid lines in figures (b)-(d) indicate the location of the steady state shocks.

Figures (e)-(f) are sketches of the C$^-$ characteristics. In Fig. (e) are plotted the fan-like characteristics of the initial flow v_{in}(R,t=0); and in Fig. (f) the intersecting characteristics of the evolving flow field (Fig. b). The effect of this momentum addition with a large value of τ is to "turn" downstream the characteristics just downstream of the inner critical point such that they intersect the upstream facing characteristics just upstream of the outer critical point.

292

the local acceleration due to the imposed perturbation. Thus, by the time the perturbation has reached its final amplitude and form, the flow has been locally accelerated (by the external force) to virtually its final (steady) spatial form throughout the region of application of the perturbation. Note that the discontinuity which temporarily forms is advected downstream from the position of the second shock because the C^- characteristics immediately downstream from this position face downstream; the continuous transonic solution is obtained.

Finally, in the intermediate case sketched in Fig. (c), the intermediate solution $v(R,\delta t)$ finds itself close to the equilibrium solution which involves the second (downstream) shock. Subsequent propagation along the C^- characteristics leads to the steepening of the velocity profile and the intersection of the characteristics at a location between the two equilibrium shocks; the intersection is convected downstream until it finds an equilibrium at the position of the second shock, and the system relaxes to the equilibrium solution which involves this second shock.

In all these cases the discontinuity forms because of the dispersive properties of the non-uniform background flow which lead to the gradual intersection of the C^- characteristics. The value of the time constant of the perturbation τ determines how soon and where in the flow, in relation to the position of the equilibrium shocks, this intersection occurs. In other words, τ determines how rapidly the fan-like C^- characteristics of the unperturbed flow (Fig. e) will be "turned" so as to "face" one another, i.e., converge, and inevitably intersect before the changes in the background flow are convected downstream past the positions of the equilibrium shocks (Fig. f). Notice that propagation along the C^+ characteristics does not lead to any interesting effects since the changes are advected away relatively fast due to the smaller value of τ_+.

4. Summary

We have shown that the formation of standing shocks in wind-type astrophysical flows with some effective, localized, non-thermal momentum deposition depending on the spatial parameters D_0, R_p and σ - which determine its amplitude, location and width, respectively - and the temporal parameter τ - which determines its temporal width - requires both *necessary* and *sufficient* conditions. The *necessary* conditions are simply the Rankine-Hugoniot relations for the conservation of mass, momentum and energy - but not entropy - across the shock discontinuity, which in turn depend on the set of the spatial parameters $[D_0, R_p, \sigma]$. The *sufficient* conditions are determined by the detailed temporal evolution of the non-thermal momentum addition and, in particular, on the intersection of the C^- characteristics of the flow upstream of the position of the equilibrium shocks, which in turn depends on the fourth parameter τ. It is expected that such standing shocks might be formed in astrophysical flows such as the solar and stellar winds, or flows in astrophysical jets, when these necessary and sufficient conditions are satisfied.

5. References

Courant, R. and K.O. Friedrichs, Supersonic Flow and Shock Waves, Interscience, New York, 1948.

Habbal, S.R., R. Rosner and K. Tsinganos, Multiple Transonic Solutions and a New Class of Shock Transitions in Solar and Stellar Winds, these Proceedings, 1983, (Paper I).

Habbal, S.R. and K. Tsinganos, Multiple Transonic Solutions and a New Class of Shock Transitions in Steady Isothermal Solar and Stellar Winds, J. Geophys. Res., in press, 1983.

Holzer, T.E., Effects of Rapidly Diverging Flow, Heat Addition and Momentum Addition in the Solar Wind and Stellar Winds, J. Geophys. Res. 82, 23, 1977.

Kopp, R.A. and T. Holzer, Dynamics of Coronal Hole Regions. I. Steady Polytropic Flows with Multiple Critical Points, Solar Phys. 49, 43, 1976.

Landau, L.D. and E.M. Lifshitz, Fluid Mechanics, Pergamon Press, 1975.

Munro, R.H. and B.V. Jackson, Geometry and Density of a Polar Coronal Hole, Ap.J. 213, 874, 1977.

Parker, E.N., Interplanetary Dynamical Processes, Interscience, New York, 1963.

STELLAR WIND MODELS AND FLOW-TUBE GEOMETRY

D. Summers
Department of Mathematics and Statistics
Memorial University of Newfoundland
St. John's, Newfoundland, Canada
A1B 3X7

ABSTRACT

We examine the influence of flow-tube geometry on a fluid-dynamic model of a solar wind type flow (i.e. a thermal wind). We find that as the divergence of the flow-tube increases the expansion speed of the wind increases throughout the flow, over a given parameter range. Further, corresponding to a specified flow-tube geometry the terminal velocity of the wind may be far in excess of the value corresponding to purely spherically symmetric flow.

In this paper we shall investigate the influence of flow-tube geometry on a thermal stellar wind by means of a flow-tube model originally proposed by Parker (1963). The model describes steady, polytropic gas flow along a radially oriented flow-tube whose cross-sectional area is proportional to r^s, where r denotes radial distance and s is a divergence parameter. The equation for the wind speed u is

$$\frac{\xi^2}{\psi}\frac{d\psi}{d\xi}\left[\psi - \frac{\alpha}{2}\left(\frac{\psi_0}{\psi}\right)^{(\alpha-1)/2}\xi^{-s(\alpha-1)}\right] = \alpha s\left(\frac{\psi_0}{\psi}\right)^{(\alpha-1)/2}\xi^{1-s(\alpha-1)} - \beta, \quad (1)$$

where

$$\psi = \frac{mu^2}{2kT_0}, \qquad \xi = \frac{r}{r_0}, \qquad \beta = \frac{mGM}{kT_0 r_0}, \qquad \psi_0 = \frac{mu_0^2}{2kT_0},$$

and m is the mean particle mass, u_0 and T_0 are the values of the speed and temperature evaluated at the coronal base radius r_0, and α is the polytropic index. From equation (1) may be derived the Bernoulli integrals,

$$\psi + \frac{\alpha}{\alpha-1}\left(\frac{\psi_0}{\psi}\right)^{(\alpha-1)/2}\xi^{-s(\alpha-1)} - \frac{\beta}{\xi} = \psi_0 + \frac{\alpha}{\alpha-1} - \beta, \qquad \alpha \neq 1 \qquad (2)$$

$$\psi + \log\left[\left(\frac{\psi_0}{\psi}\right)^{\frac{1}{2}}\xi^{-s}\right] - \frac{\beta}{\xi} = \psi_0 - \beta, \qquad \alpha \neq 1 \qquad (3)$$

If $1 \leq \alpha < (2s+1)/(2s-1)$ then equation (1) has a critical (sonic) point of the saddle-type which is given by

$$\psi_c = \left[\frac{\alpha}{2} \left(\frac{2s}{\beta} \right)^{s(\alpha-1)} \psi_0^{(\alpha-1)/2} \right]^{2/[2s+1-\alpha(2s-1)]} , \qquad \xi_c = \beta/(2s\psi_c) . \qquad (4)$$

When we require that this critical point lie on the solutions (2) and (3) we obtain the fundamental 'eigenvalue' equations for ψ_0,

$$\psi_0 + \frac{\alpha}{\alpha-1} - \beta = \left[\frac{2s+1-\alpha(2s-1)}{\alpha-1} \right] \left[\frac{\alpha}{2} \left(\frac{2s}{\beta} \right)^{s(\alpha-1)} \psi_0^{(\alpha-1)/2} \right]^{2/[2s+1-\alpha(2s-1)]} ,$$

$$1 < \alpha < (2s+1)/(2s-1) ; \qquad (5)$$

$$\psi_0 - \beta = \tfrac{1}{2} - s + \log \left(\frac{s}{\beta} \right)^s (2\psi_0)^{\tfrac{1}{2}} , \qquad\qquad \alpha = 1 . \qquad (6)$$

The zero subscript is used in equations (5) and (6), and will hereafter be used in this paper, to denote the base speed of the transonic solution.

If $1 < \alpha < (2s+1)/(2s-1)$, then from (2) the wind speed u approaches a terminal value u_∞ given by

$$\psi_\infty = \frac{m u_\infty^2}{2kT_0} = \psi_0 + \frac{\alpha}{\alpha-1} - \beta . \qquad (7)$$

Equations (5) and (6) may be regarded as equations determining the wind speed u_0 at the coronal base, for given values of α, β, and s. Equation (7) then gives the terminal wind speed u_∞ in terms of u_0. In particular, it is clear that u_0 and u_∞ are functions of the divergence parameter s. Expected physical requirements (see Summers, 1982) on the wind lead to the conditions $\alpha s < \beta < \alpha/(\alpha-1)$ for $1 < \alpha < (2s+1)/(2s-1)$, and $s \leq \beta$ for $\alpha = 1$. In order to illustrate the influence of the parameter s on the values of u_0 and u_∞, we have taken solar parameters (i.e. $r_0 = R_\odot$, $M = M_\odot$, and $m = \tfrac{1}{2} *$(proton mass)), and we have calculated u_0 and u_∞ both for $s = 2$, corresponding to purely spherically symmetric flow, and for $s = s* = \beta/\alpha$, corresponding to the limiting situation when the critical (sonic) point occurs at the coronal base $r = r_0$. The results, which are shown in Table 1, are given for various values of α and T_0.

Table 1

Variation of the wind speeds u_0 and u_∞ (each measured in km s^{-1}) with the divergence parameter s, for given polytropic indices α, and given base temperatures T_0.

	$T_0 = 2 \times 10^6 K$			$T_0 = 1.5 \times 10^6 K$		$T_0 = 10^6 K$
α	1.01	1.1	1.2	1.01	1.1	1.01
$[u_0]_{s=2}$	20.2	9.26	0.045	4.14	0.29	0.12
$[u_\infty]_{s=2}$	2508	588	122	2150	404	1719
$s*$	5.72	5.25	4.81	7.62	7	11.43
$[u_0]_{s=s*}$	183	191	199	158	165	129
$[u_\infty]_{s=s*}$	2514	618	234	2155	437	1723

Increases in u_∞ over its corresponding spherically symmetric value range from insignificant (0.23%, for $\alpha = 1.01$, $T_0 = 2 \times 10^6 °K$) to highly significant (91.8%, for $\alpha = 1.2$, $T_0 = 2 \times 10^6 °K$). Thus, contrary to the statements of some authors (e.g. Adams and Sturrock, 1975), we find that the terminal wind speed is not only dependent on s, but possibly significantly so. The basic results of this paper are published elsewhere (Summers, 1982), though with a slightly different emphasis.

Our conclusions are as follows:

(i)   In general, u_0 and u_∞ are functions of the divergence parameter s of the flow-tube.

(ii)   As s increases from s = 2 to s = s* (corresponding to the critical point occurring at the coronal base) the wind speed increases throughout the flow.

(iii)   Though in the present paper we have set s > 2 throughout the flow in order to simulate a flow with 'faster-than-r^2 divergence', if we had set s > 2 near the coronal base and s = 2 downstream of the sonic point then such a change in s would <u>not</u> have affected the above calculated values of u_∞.

(iv)   Explicitly, u_0 and u_∞ are determined by the flow-tube geometry *in the subsonic region*.

(v)   In models of thermal stellar winds the flow-tube geometry may significantly influence the value of the terminal wind speed (see also Kopp and Holzer, 1976).

References

Adams, W.M., and Sturrock, P.A., A model of coronal holes, Astrophys J., 202, 259, 1975.

Kopp, R.A., and Holzer, T.E., Solar Phys., 49, 43, 1976.

Parker, E.N., Interplanetary Dynamical Processes, Interscience, New York-London, 1963.

Summers, D., Flow tube dynamics and coronal holes, Solar Phys., in press, 1982.

Page intentionally left blank
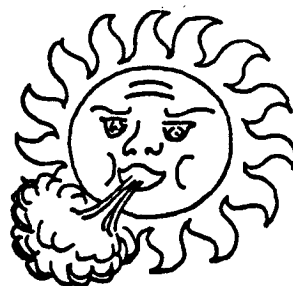
SESSION 5.

LONG-TERM VARIATIONS

Page intentionally left blank

SUMMARY OF THE SESSION ON LONG-TERM VARIATIONS

J. A. Eddy

In four separate papers and by different techniques, Crooker, Rickett, Slavin, and Gold each endeavored to bring order and clarification to the complex issue of solar-cycle variations in the solar wind. Strong differences of opinion still characterize the basic questions of whether and by how much such parameters as velocity, density, temperature, composition or field strength obey the classical, 11-year drum beat of solar surface activity. On the issue of secular, longer-term variations, Feynman presented mixed evidence in solar and geophysical records for the oft-cited "Gleissberg cycle" of about 80 years, and Mendillo told of his collaboration with colleagues in China on ancient observations of the aurora from the Orient. Eddy summarized fallacies in recent, historical papers that purport to challenge the reality of the Maunder Minimum and secular solar change.

Page intentionally left blank

SOLAR CYCLE VARIATIONS OF THE SOLAR WIND

N. U. Crooker
Department of Atmospheric Sciences
University of California, Los Angeles, CA   90024

ABSTRACT

Throughout the course of the past one and a half solar cycles, solar wind parameters measured near the ecliptic plane at 1 AU varied in the following way: Speed and proton temperature have maxima during the declining phase and minima at solar minimum and are approximately anti-correlated with number density and electron temperature, while magnetic field magnitude and relative abundance of helium roughly follow the sunspot cycle. These variations are described in terms of the solar cycle variations of coronal holes, streamers, and transients. The solar wind signatures of the three features are discussed in turn, with special emphasis on the signature of transients, which is still in the process of being defined. It is proposed that magnetic clouds be identified with helium abundance enhancements and that they form the head of a transient surrounded by streamer-like plasma, with an optional shock front. It is stressed that relative values of a parameter through a solar cycle should be compared beginning with the declining phase, especially in the case of magnetic field magnitude.

INTRODUCTION

Not long ago very little was understood about solar cycle variations of the solar wind. The observed variations near Earth's orbit had been disappointingly small through the maximum of sunspot cycle 20. It was only when first papers appeared on the occurrence of the large, stable high-speed streams during the declining phase of cycle 20 (Krieger et al., 1973; Bame et al., 1976; Gosling et al., 1976) that it became clear that the solar wind could change appreciably over the long term. Since then our understanding of changing coronal and solar wind structure through the solar cycle has grown rapidly (Hundhausen, 1979). As suggested by Borrini et al. (1983) for helium abundance, the large scale patterns of change in other solar wind parameters over the solar cycle may be relatively well-understood as reflections of the solar cycle variations of three major coronal features: the large stable equatorial excursions of polar coronal holes which peak in the declining phase (e.g., Hundhausen, 1977), the equatorial streamer belt at solar minimum (e.g., Gosling et al., 1981), and coronal transients at solar maximum (e.g., Hildner et al., 1976). The solar wind signature of each feature and how these signatures fit into the pattern of solar cycle variations in the ecliptic plane at 1 AU are discussed below.

CORONAL HOLE SIGNATURES

Of the three signatures under consideration, the high speed stream signature of flow from coronal holes has been studied the most extensively and is the most well-established. For example, an entire monograph has been written on the subject of coronal holes and transients (Zirker, 1977).

The occurrence of high-speed streams during the declining phase of solar cycle 20 is illustrated in the 27-day Bartels format in Figure 1, which is a black-and-white reproduction of a colored figure from Feldman et al. (1979). Although the colored version conveys information more readily, and the interested reader

is urged to refer to it, the major features discussed below are apparent in the black-and-white version. Each shaded square represents a daily average of a solar wind plasma parameter. The averages range from their lowest values in black (unfortunately indistinguishable here from missing values) through shades of gray to their highest values in white. In each block, representing a different parameter, the daily squares are arranged in 27-day columns. Time increases from bottom to top in each column and from left to right across the figure.

Figure 1. Daily averages of solar wind proton bulk speed, density, and temperature and electron temperature arranged in sequential strips of 27-day Carrington rotations, with values increasing from dark to light shades, after Feldman et al. (1979). (See their colored version and code table for quantitative information.)

304

In the top block the two bright patches extending from the end of 1973 through 1975 are formed by two velocity peaks which recurred with every 27-day rotation of the sun. These two streams emanated from two large, stable, offset, polar coronal holes, one in each hemisphere (e.g., Hundhausen, 1977). The remaining blocks show how other plasma parameters vary in the stream structure. In the high-speed region, the proton temperature is high, while the density and electron temperature are low. In general the solar wind speed and proton temperature vary in the same way and are anticorrelated with the density and electron temperature. This is most obvious in the high-speed stream structure, but it is also the trend in the remaining portions of the diagram. The second and fourth blocks have the overall appearance of negatives of the first and third blocks.

Figure 2, also adapted from Feldman et al. (1979), is a plot of half-year averages of the parameters in Figure 1, with sunspot number plotted at the top for reference. It is clear that the characteristics of the high-speed flow from the stable coronal holes dominate the solar cycle variations of these parameters during the latter part of the declining phase of the sunspot cycle; the speed and proton temperature reach their highest values, and the density and electron temperature are depressed.

STREAMER SIGNATURES

The tendency for speed and proton temperature to be anticorrelated with density and electron temperature, as noted in Figure 1, also is apparent in Figure 2. Soon after sunspot minimum, in contrast to the declining phase, speed and proton temperature are low, and density and electron temperature are high. These are characteristics of the flow between the high-speed streams in Figure 1, and they come to dominate the solar cycle variations of the parameters as the stream signatures decline.

Recently the low-speed flow between streams has been identified as the signature of coronal streamers (Borrini et al., 1981; Feldman et al., 1981; Gosling et al., 1981). Throughout most of the solar cycle the heliospheric current sheet encircles the sun and separates magnetic fields of opposite polarity, which are carried outward by solar wind flow from polar coronal holes (e.g., Schulz, 1973; Svalgaard et al., 1975; Hundhausen, 1977; Smith et al., 1978; Hundhausen et al., 1981). The current sheet is embedded in a coronal streamer belt. Its projection onto a sphere at 1 AU is shown schematically in Figure 3, from Gosling
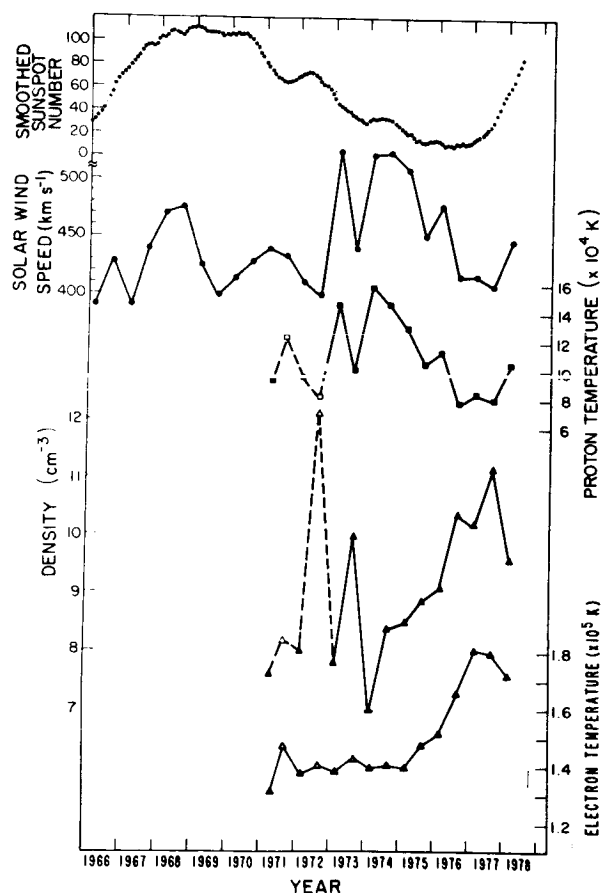

Fig. 2. Variations over the past solar cycle of monthly averages of the smoothed sunspot number and 6-monthly averages of proton bulk speed, temperature, and density and electron temperature, after Feldman et al. (1979).
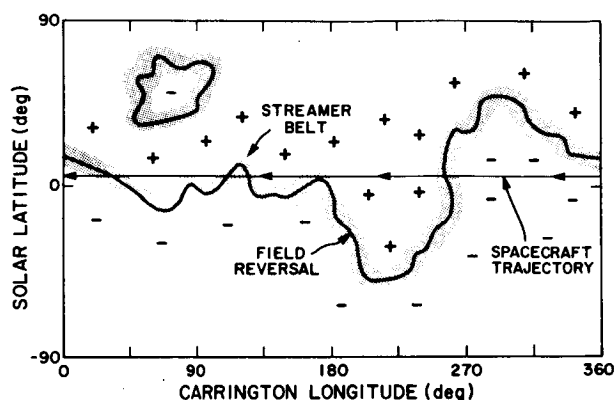
Figure 3. Schematic diagram of the inter-
section of the equatorial streamer belt
and embedded heliospheric current sheet
with the 1 AU sphere, from Gosling et al.
(1981).

et al. (1981). The line labeled spacecraft
trajectory shows the position of a near-
Earth spacecraft as the sun completes one
full rotation. During the declining phase
of the solar cycle, the streamer belt makes
large excursions from the solar equatorial
plane, as on the right side of the figure,
and an Earth-orbiting spacecraft would spend
little time within it. On the other hand,
during solar minimum, the streamer belt is
confined to lower latitudes, as on the left
side of the figure, and an Earth-orbiting
spacecraft would skim and intersect it often.

The plasma signature of the streamer
material surrounding the current sheet is
shown in Figure 4, from Gosling et al.(1981),
adapted from Borrini et al. (1981). The
plots are the result of a superposed epoch
analysis centered on the times of current
sheet crossings. In order to obtain a clear
signature, only crossings well-separated
from stream interaction regions were used.
The figure shows that the streamer signature
has low proton temperature and flow speed
and high density, which are the same extrema
reached just after solar minimum in the so-
lar cycle variations of these parameters in
Figure 2. Figure 4 also shows that the re-
lative abundance of helium (A(He)) is low in
the streamer. The solar cycle variation of
A(He) will be discussed in the next sections.
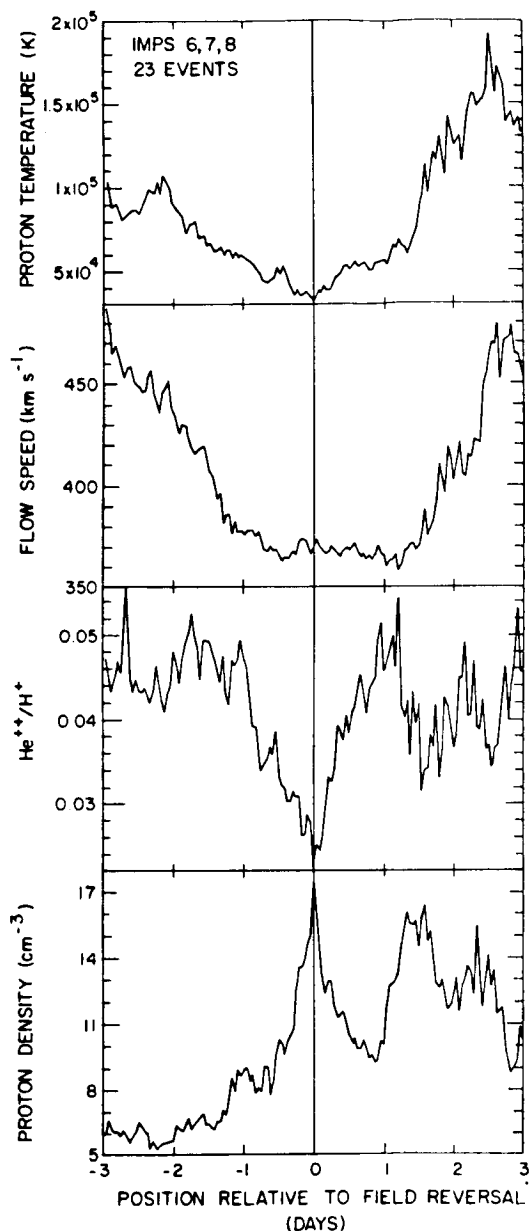
Figure 4. Superposed epoch
plots of solar wind proton tem-
perature, flow speed, helium
abundance, and proton density
centered on 23 well-defined cur-
rent sheet crossings more than
one day removed from speed rises
associated with high speed
streams, from Gosling et al.
(1981), after Borrini et al.(1981).

306

In contrast to the relatively well-defined solar wind signatures of coronal holes and streamers, the signature of coronal transients is still in the process of being defined. A simple synthesis of proposed transient features is given here.

Transients have been associated with shock waves (e.g., Borrini et al., 1982a), helium abundance enhancements (e.g., Borrini et al., 1982b), non-compressive density enhancements (Gosling et al., 1977), and magnetic bottles, bubbles, and clouds (e.g., Klein and Burlaga, 1982). Figure 5 shows two examples of these transient associated signatures. Both are the results of superposed epoch analyses. The shaded regions in Figure 5a give the signature of a magnetic cloud (Klein and Burlaga, 1982). A cloud is characterized by an increase in magnetic field strength and a large excursion in the north-south field angle θ, consistent with the configuration of a magnetic loop. The plasma speed in the cloud is relatively steady, there is a small density peak at the leading edge, and the temperature is somewhat depressed. Figure 5b gives the plasma and field strength signatures accompanying an enhancement in A(He) (Borrini et al., 1982b). Similar to the characteristics of a magnetic cloud, the enhancement lasts for about one day, is preceded by a density peak, and is a region of high magnetic field strength and depressed temperature. The high degree of similarity in the signatures suggests that helium enhancements may be identified with magnetic clouds.
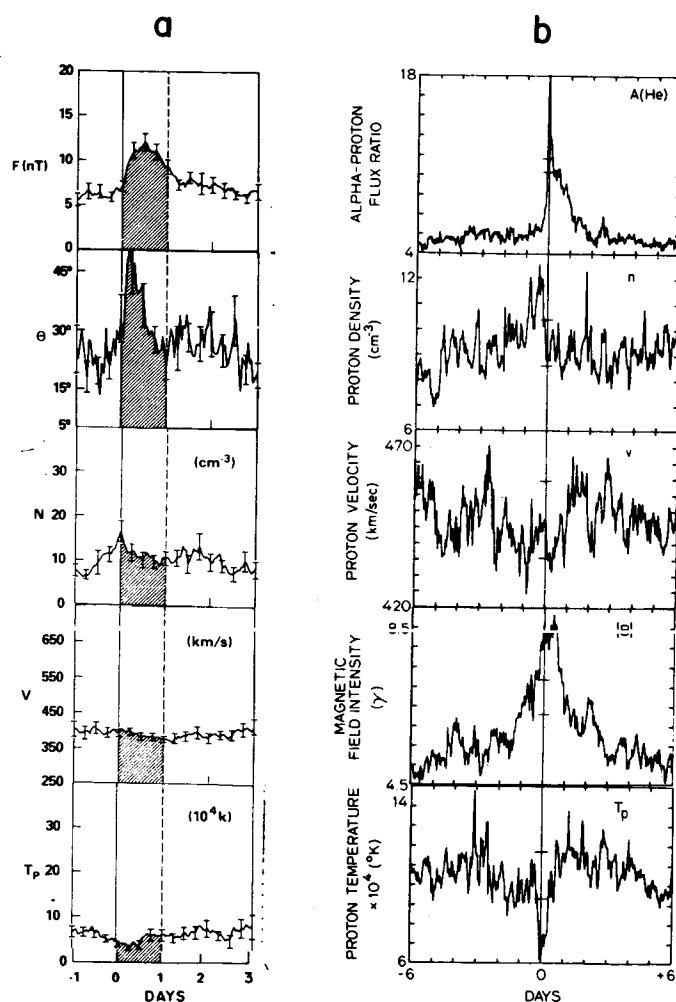
Figure 5. Superposed epoch plots of selected solar wind parameters for a.) magnetic clouds, after Klein and Burlaga (1982) and b.) helium abundance enhancements, after Borrini et al. (1982b). The parameters are magnetic field magnitude F and |B|, magnitude of the magnetic field angle θ of elevation out of the ecliptic plane, proton density N and n, bulk speed V and v, temperature T_p, and helium abundance A(He).

A schematic drawing of a coronal transient is shown in Figure 6. It is patterned after Hundhausen's (1972) diagram of the flare-associated, shock-wave disturbance which traditionally has been considered as the source of nonrecurrent geomagnetic activity at sunspot maximum. It incorporates the identification of a helium enhancement with a magnetic cloud, as discussed above. The cloud has a shape similar to the magnetic bubbles near 1 AU modeled by Newkirk

Coronal Transient

Fig. 6. Schematic diagram of a cross-section of a coronal transient in the ecliptic plane. The helium abundance enhancement is identified with a magnetic cloud, and the formation of a shock front depends upon the speed of the transient relative to the ambient solar wind.

et al. (1981). Its dimension in the radial direction is about 0.25 AU, consistent with observations (Klein and Burlaga, 1982).

The streamer-like plasma surrounding the transient is drawn as an extended version of the transient configuration observed in the white-light coronographs from Skylab (e.g., Gosling et al., 1974). It may give the signature of a noncompressive density enhancement (NCDE) with elevated helium content because of its closed magnetic bottle configuration, in contrast with streamers, which have low helium content and occur on open field lines. Gosling et al. (1981) noted that streamer signatures are identical to NCDE signatures except that NCDEs occur both with high and low A(He), whereas streamers always have low A(He). They suggested that NCDEs with high A(He) may be associated with transients, consistent with the interpretation presented here. The density peak which occurs at the leading edge of the magnetic cloud and the A(He) enhancement signature in Figure 5 also is consistent with this interpretation. Outside the streamer-like plasma the magnetic field lines are open. Thus, if a shock is present, the "sheath" region between the shock and the bubble would contain first a layer with normal A(He) followed by a layer with increased A(He). The highest A(He) would then occur within the cloud. Of course, caution must be used in interpreting literally such a simple schematic diagram. Observations of transient signatures in the solar wind show a wide range of variability (e.g., Zwickl et al., in these Proceedings).
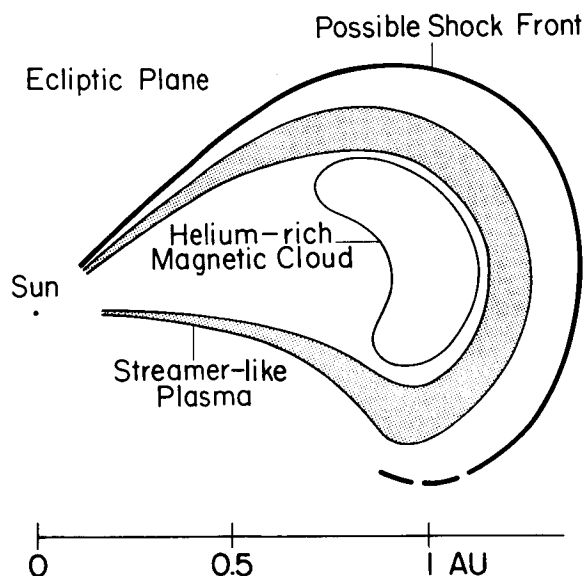
The shock front in Figure 6 is optional, depending upon the relative speed of the transient material. This option is consistent with the finding that only about half of the observed helium enhancements occur with shocks (Borrini et al., 1982b). It also has been found that only about half of the observed shocks are followed by helium enhancements (Borrini et al., 1982a). Assuming that all shocks are signatures of coronal transients and that all transients have helium enhancements, these authors suggest that the observations of shocks without helium enhancements were made by spacecraft intersecting the flanks of the shock wave and missing the central gases in the transient. If the highest concentrations of helium are confined by the closed magnetic field configuration of a magnetic cloud, as pictured in Figure 6, then this suggestion seems highly plausible.

The identification of the helium enhancement with a magnetic cloud helps to explain the result of Borrini et al. (1982a) that shocks observed with helium enhancements produce much more pronounced geomagnetic storms than do shocks without

helium enhancements. The magnetic field just inside a cloud passing over a space-craft has either a large northward or southward component which then rotates by nearly 180° (Klein and Burlaga, 1982; Smith, 1983). In either case a period of strong southward field occurs, and such periods are correlated with geomagnetic storms (e.g., Russell et al., 1974).

If it is assumed that magnetic clouds form the heart of transients and pro-duce geomagnetic storms and that shocks produce sudden commencements, then vary-ing the characteristics of coronal transient passage can account for the observed combinations in which these ground-based signatures occur: Central passage of transients with and without shocks will produce storms with sudden and gradual commencements, respectively, and peripheral passage of transients with shocks will produce sudden commencements or impulses without subsequent storms.

The solar cycle variation of coronal transients is inferred to be in phase with the sunspot cycle, following the solar cycle variation of geomagnetic sudden commencements, although direct measurements of the transient occurrence cycle is still incomplete (e.g., Hundhausen, in these Proceedings). Clearly the solar wind signature of coronal transients is the most complicated of the three which have been discussed, and it may be too soon to draw conclusions about their effect on solar cycle variations. Nevertheless, the somewhat irregular and intermediate averages of solar wind speed, and, by inference, density and temperatures, which occurred during sunspot maximum (see Figure 2) are consistent with the sporadic flow of intermediate-speed, shock-associated transients in a background of lower speed flow.
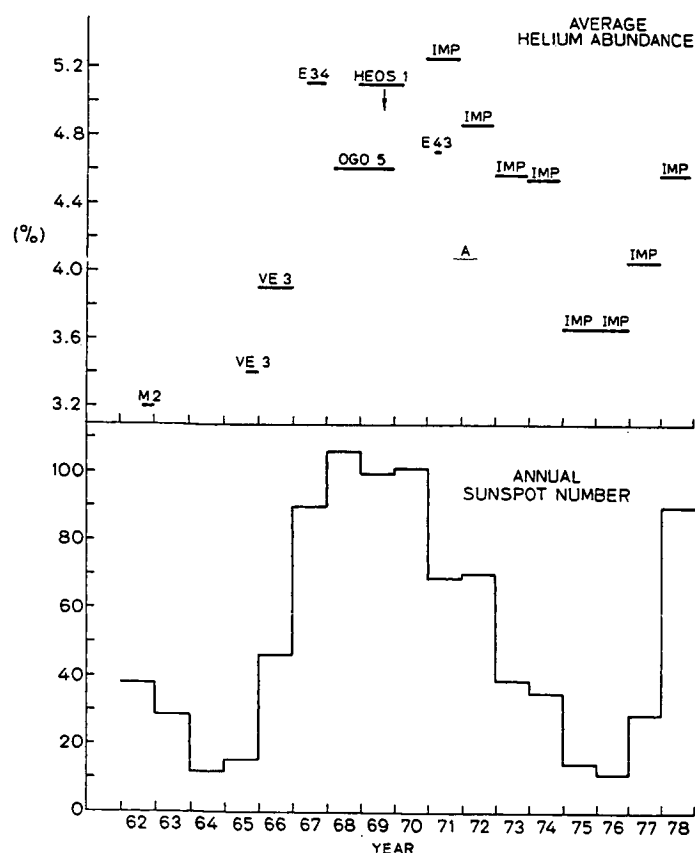
HELIUM ABUNDANCE AND MAGNETIC FIELD MAGNITUDE

Unlike the solar cycles of the plasma parameters in Figure 2, the solar cycles of A(He) and magnetic field magnitude roughly follow the sunspot cycle. Figure 7 from Bor-rini et al. (1983) shows the solar cycle variation of A(He), along with the sunspot cycle for refer-ence. The figure is an extension of a previous analysis by Ogilvie and Hirshberg (1974). At sunspot maximum the averages are high, as observed in coronal transient sig-natures; at minimum they are low, as in streamer signatures.

This consistency does not im-ply that transient and streamer sig-natures fill most of interplanetary space in the ecliptic plane during these respective phases, as high speed stream signatures do during the declining phase. Rather the

Figure 7. Variation of relative helium abundance in the solar wind over the past solar cycle, compared with sunspot cycle, from Borrini et al. (1983).

309
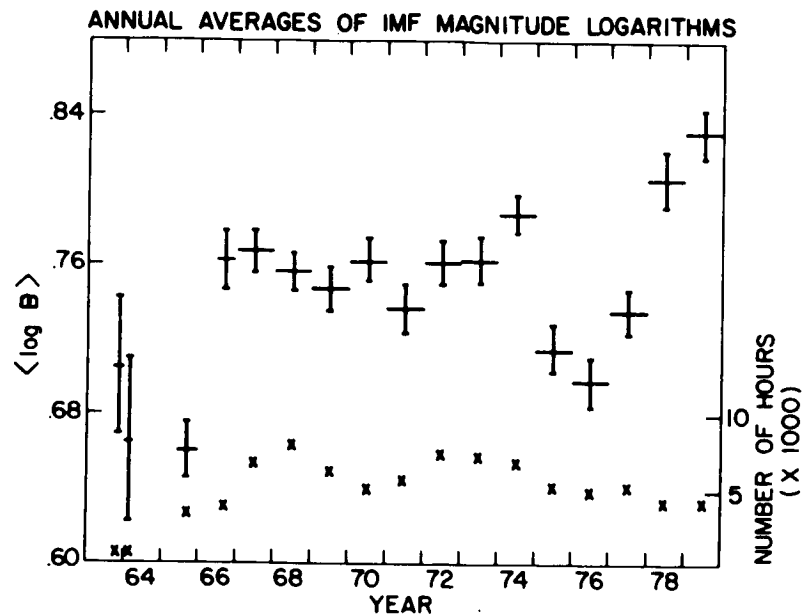
Figure 8. Variation of interplanetary magnetic field (IMF) magnitude logarithms over the past solar cycle, from King (1981). The number of hours in each yearly average are given at the bottom of the plot. Vertical bars show standard errors, and horizontal bars show portion of year for which data are available.

relatively low occurrence rate of streamers and streams and increased occurrence rate of transients during maximum result in relatively high values of A(He) at that time. The reversed relative occurrence rates of streamers and transients result in low values of A(He) at solar minimum.

During the declining phase of the past solar cycle, A(He) in the high speed streams was observed to be almost constant at an intermediate level (e.g., Gosling et al., 1981). The intermediate averages of A(He) during the declining phase in Figure 7 are consistent with this observation.

The variation of average interplanetary magnetic field magnitude over the past solar cycle is shown in Figure 8, from King (1981). There are clear minima at the two solar minima, consistent with the near proximity of the heliospheric current sheet at that time. Although Borrini et al. (1981) state that no pattern was apparent in the superposed epoch analysis of field strength in the streamer belt surrounding the current sheet, in analogy with the current sheet embedded in Earth's plasma sheet, one might expect generally depressed field strength there.

During solar maximum, the frequent occurrence of coronal transients should give rise to high averages of field magnitude, as it does for helium, since the field magnitude is elevated in magnetic clouds. This appears to be the case for the present solar cycle, indicated by the 1978 and 1979 averages in Figure 8 and as presented by Slavin and Smith (in these Proceedings). However, the cycle 20 maximum has only intermediate field magnitude averages. This lack of a maximum may be simply a problem of comparing relative values. As has been argued on the basis of geomagnetic records (e.g., Ol', 1971; Feynman, 1982), each individual sunspot cycle should begin with the declining phase, and relative values of a parameter should be compared from there. If the beginning of the present cycle

is set back to include the declining phase of cycle 20, then the magnetic field values there are intermediate between those of the following minimum and maximum phases, in phase with the sunspot cycle.

SUMMARY

Figure 9 is a summary plot from Borrini et al. (1983), upon which this topical review is a generalization. Helium abundance is used as a key to organizing the signatures of the three coronal structures which influence different phases of the solar cycle. Low values of helium correspond to the characteristics of streamers at solar minimum, intermediate values to characteristics of high speed streams during the declining phase, and high values to characteristics of coronal transients at solar maximum.

A summary of solar cycle variations in simple tabular form is given in Table 1. From descending to minimum phase of the sunspot cycle, the signatures of the coronal features characteristic of each phase produce the indicated relative values of solar wind parameters. Briefly stated, the velocity and proton temperature vary together, with maxima in the declining phase, and are anticorrelated with the density and electron temperature, while the helium abundance and magnetic field strength follow the pattern of the sunspot cycle. Of course these patterns are approximate and vary in detail, with some time lag between the solar wind cycle and the sunspot cycle. Nevertheless, it is somewhat remarkable to find that the solar wind parameters follow such a simple, first-order pattern.
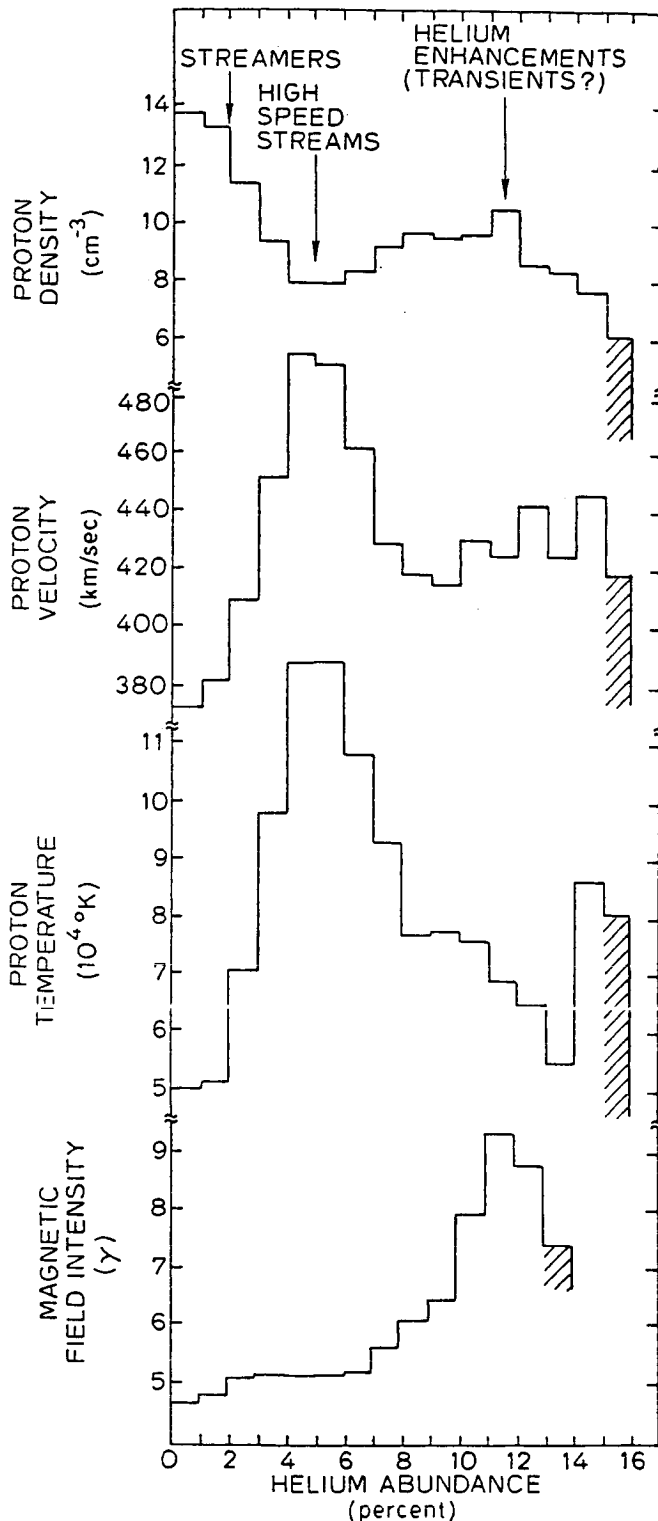
Figure 9. Solar wind parameters plotted against relative helium abundance, after Borrini et al. (1983). The shaded end bars include all case of helium abundance higher than 16%.

Table 1. ... of Solar Wind Parameters

SUNSPOT CYCLE PHASE	descending	minimum	maximum
CORONAL FEATURES	stable holes	streamer belt	transients
SOLAR WIND			
V, T_p	high	low	medium
n, T_e	low	high	medium
$A(He)$, $|B|$	medium	low	high

REFERENCES

Bame, S. J., J. R. Asbridge, W. C. Feldman, and J. T. Gosling, Solar cycle evolution of high-speed solar wind streams, Astrophys. J., 207, 977-980, 1976.

Borrini, G., J. T. Gosling, S. J. Bame, W. C. Feldman, and J. M. Wilcox, Solar wind helium and hydrogen structure near the heliospheric current sheet: A signal of coronal streamers at 1 AU, J. Geophys. Res., 86, 4565-4573, 1981.

Borrini, G., J. T. Gosling, S. J. Bame, and W. C. Feldman, An analysis of shock wave disturbances observed at 1 AU from 1971 through 1978, J. Geophys. Res., 87, 4365-4373, 1982a.

Borrini, G., J. T. Gosling, S. J. Bame, and W. C. Feldman, Helium abundance enhancements in the solar wind, J. Geophys. Res., 87, 7370-7378, 1982b.

Borrini, G., J. T. Gosling, S. J. Bame, and W. C. Feldman, Helium abundance variations in the solar wind, Solar Phys., in press, 1983.

Feldman, W. C., J. R. Asbridge, S. J. Bame, and J. T. Gosling, Long-term solar wind electron variations between 1971 and 1978, J. Geophys. Res., 84, 7371-7377, 1979.

Feldman, W. C., J. R. Asbridge, S. J. Bame, E. E. Fenimore, and J. T. Gosling, The solar origins of solar wind interstream flows: Near-equatorial coronal streamers, J. Geophys. Res., 86, 5408-5416, 1981.

Feynman, J., Geomagnetic and solar wind cycles, 1900-1975, J. Geophys. Res., 87, 6153-6162, 1982.

Gosling, J. T., E. Hildner, R. M. MacQueen, R. H. Munro, A. I. Poland, and C. L. Ross, Mass ejections from the sun: A view from Skylab, J. Geophys. Res., 79, 4581-4587, 1974.

Gosling, J. T., J. R. Asbridge, S. J. Bame, and W. C. Feldman, Solar wind speed variations: 1962-1974, J. Geophys. Res., 81, 5061-5070, 1976.

Gosling, J. T., E. Hildner, J. R. Asbridge, S. J. Bame, and W. C. Feldman, Noncompressive density enhancements, J. Geophys. Res., 82, 5005-5010, 1977.

Gosling, J. T., G. Borrini, J. R. Asbridge, S. J. Bame, W. C. Feldman, and R. T. Hansen, Coronal streamers in the solar wind at 1 AU, J. Geophys. Res., 86, 5438-5448, 1981.

Hildner, E., J. T. Gosling, R. M. MacQueen, R. H. Munro, A. I. Poland, and C. L. Ross, Frequency of coronal transients and solar activity, Solar Phys., 48, 127-135, 1976.

Hundhausen, A. J., Coronal Expansion and Solar Wind, p. 192, Springer-Verlag, New York, 1972.

Hundhausen, A. J., An interplanetary view of coronal holes, in Coronal Holes and

High Speed Wind Streams, edited by J. B. Zirker, Colorado Associated University Press, Boulder, pp. 225-329, 1977.

Hundhausen, A. J., Solar activity and the solar wind, Rev. Geophys. Space Phys., 17, 2034-2048, 1979.

Hundhausen, A. J., R. T. Hansen, and S. F. Hansen, Coronal evolution during the sunspot cycle: Coronal holes observed with the Mauna Loa K-coronameters, J. Geophys. Res., 86, 2079-2094, 1981.

King, J. H., On the enhancement of the IMF magnitude during 1978-1979, J. Geophys. Res., 86, 4828-4830, 1981.

Klein, L. W., and L. F. Burlaga, Interplanetary magnetic clouds at 1 AU, J. Geophys. Res., 87, 613-624, 1982.

Krieger, A. S., A. F. Timothy, and E. C. Roelof, A coronal hole and its identification as the source of a high velocity solar wind stream, Solar Phys., 29, 505-525, 1973.

Newkirk, G., Jr., A. J. Hundhausen, and V. Pizzo, Solar cycle modulation of galactic cosmic rays: Speculation on the role of coronal transients, J. Geophys. Res., 86, 5387-5396, 1981.

Ogilvie, K. W., and J. Hirshberg, The solar cycle variation of the solar wind helium abundance, J. Geophys. Res., 79, 4595-4602, 1974.

Ol', A. I., Physics of the 11-year variation of magnetic disturbances, Geomag. Aeron., 11, 549-551, 1971.

Russell, C. T., R. L. McPherron, and R. K. Burton, On the cause of geomagnetic storms, J. Geophys. Res., 79, 1105-1109, 1974.

Schulz, M., Interplanetary sector structure and the heliomagnetic equator, Astrophys. Space Sci., 24, 371-383, 1973.

Smith, E. J., B. T. Tsurutani, and R. L. Rosenberg, Observations of the interplanetary sector structure up to heliographic latitudes of 16°: Pioneer 11, J. Geophys. Res., 83, 717-724, 1978.

Smith, E. J., Observations of interplanetary shocks: Recent progress, Space Sci. Rev., in press, 1983.

Svalgaard, L., J. M. Wilcox, P. H. Scherrer, and R. Howard, The sun's magnetic sector structure, Solar Phys., 45, 83-91, 1975.

Zirker, J. B., editor, Coronal Holes and High Speed Wind Streams, Colorado Associated University Press, Boulder, 1977.

Page intentionally left blank

SOLAR CYCLE EVOLUTION OF THE SOLAR WIND IN THREE DIMENSIONS

B. J. Rickett and Wm. A. Coles
Department of Electrical Engineering and Computer Sciences
University of California, San Diego
La Jolla, Ca 92093

ABSTRACT

Measurements of the solar wind speed both in and out of the ecliptic are presented for 1971-82. The speed estimates, which were made with the interplanetary scintillation system at UC San Diego, have been compared to in situ spacecraft measurements for ecliptic radio sources. Good agreement is found for large, slowly evolving structures, and thus such structures can be studied up to 60 degrees north and south heliographic latitude. Annual average wind speeds are presented versus latitude for an entire solar cycle. Fast wind streams from the poles persisted through declining and low solar activity, but were closed off during four years of high activity. This evolution follows that of the polar coronal holes, as displayed by comparing averaged speed and coronal density over latitude and longitude. The most recent data (1982) show the reestablishment of large tilted polar holes and associated fast streams. Coronal magnetic field data show that the neutral sheet is confined to low latitudes at solar minimum and extends to high latitudes at solar maximum; thus the slow solar wind comes from the same latitude range as that of the neutral sheet.

We have investigated the three-dimensional structure of the solar wind during the last eleven years using the technique of interplanetary scintillation (IPS). Three radio antennas at 74 MHz are used to measure the velocity of the scintillation pattern, which is caused when waves from a small-diameter radio source travel through inhomogeneities in the solar wind plasma and are detected at the earth (Armstrong and Coles 1972). Figure 1 illustrates the geometry, showing as a heavy line the region on the line of sight to the source which contributes most of the scintillation. The velocity of the pattern is an average of the velocities weighted by the level of "micro-turbulence" (on scales of 50-300km). In this paper we present results on the simple assumption that the IPS velocity estimates the solar wind velocity at the point P where the line of sight passes closest to the sun. The unique aspect of the IPS method is that the point P is not confined to the ecliptic and reaches 60 degrees north and south latitudes. Results from 1972-79 were described by Coles et al, 1980.

The "point interpretation" of IPS data has been checked by comparison of velocities from an ecliptic radio source with estimates of the solar wind velocity at the point P made by spirally mapping in situ measurements from earth-orbiting spacecraft. There is generally good agreement, as is shown in Figure 1 of Coles et al. (1978) for 1973. Similar agreement to within 50 km/s was also found during 1974 and 1975 (Harmon, 1975); these were periods when the solar wind was dominated by stable recurrent fast streams. We are in the process of extending the comparison through solar maximum when there are more transient variations; here we find a somewhat worse agreement. In particular, the IPS data underestimate the speed during brief increases due to either narrow streams or transient disturbances. Nevertheless, it is clear that a reliable first-order
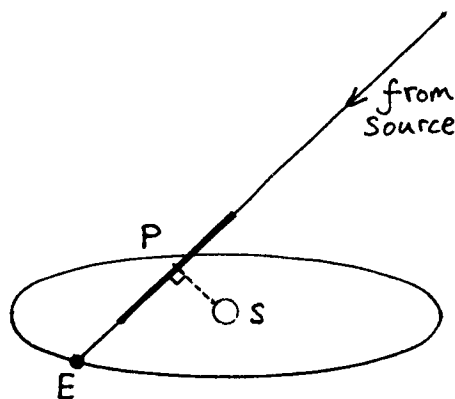
Figure 1. Geometry of IPS
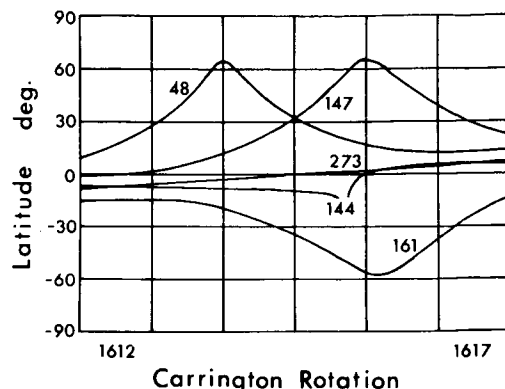observation.

Carrington Rotation

Figure 2. The latitude-longitude
tracks of the point P during six
rotations in 1974.

description of the large-scale slowly varying wind structure in three dimensions
is available from our observations, covering 1972 to 1982.

Each observation provides a wind speed estimate characteristic of the point
P whose heliographic coordinates vary as the earth moves round the sun and the
sun rotates.   For a given radio source the latitude changes systematically
through the calendar year.   The distribution of good scintillators in the sky
gives our best latitude coverage in the north and south during March to August
each year, as shown in Figure 2 for 1974.   Here the latitude and longitude of
point P mapped to the sun at 400km/s are displayed for six Carrington
rotations.   In order to study the shape of solar wind structures we have mapped
each observation from P to the sun along a spiral assuming constant radial
velocity equal to the observed value.   Thus each observation gives an estimate
of the wind speed at a point on the effective source surface beyond which the
plasma flow is radial.   See Sime and Rickett (1978) for a discussion of the
limitations of such mapping.   Since for a single rotation the coverage in
latitude and longitude is rather sparse, we average the data for periods of six
or twelve months.

The general picture that has emerged from our observations is that the
polar regions of the sun are the source of long-lived fast streams through much
of the solar cycle.   This is seen in plots of the average wind speed against
solar latitude both to the north and south (see Figure 1 of Coles et al. 1980).
In Figure 3 we show such plots for the years from 1972 to 1982.   These show the
fast polar streams as elevated average speeds at high latitudes and a U-shaped
dip to lower speeds in the ecliptic.   Throughout declining solar activity (1972-
75) the fast polar streams were a persistent feature, but were sometimes tilted
from the poles and intercepted the ecliptic; this is seen as a wider U-shape and
elevated speeds in the ecliptic.   At solar minimum (1976) the fast polar streams
were centered on the rotation axis and were wide, extending down to latitudes of
30 deg N and S. Through solar maximum (1978-81) they disappeared and only with
current decline of solar activity (1982) have they started to reappear.

It is clear that this pattern of evolution matches that of the polar
coronal holes, which persist through most of the cycle but close off during
solar maximum while the dipolar fields reverse.   We can examine the structure of
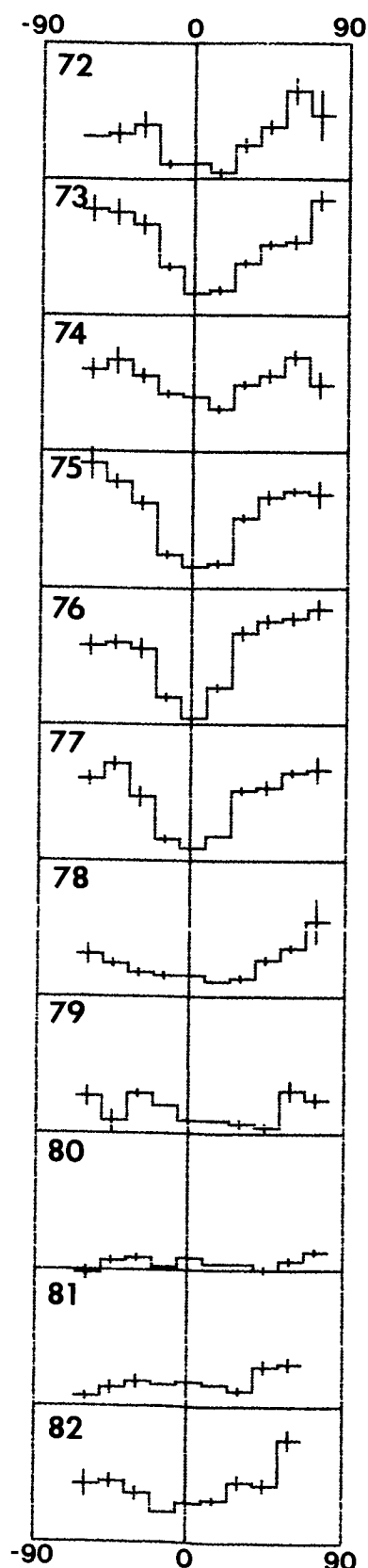
316

Figure 3. Annual averages of solar wind speed versus latitude in 15 degrees bins. The horizontal lines are at 300 km/s and 600 km/s. Vertical bars are $\pm 2\sigma$ in the mean.

the polar streams in more detail by studying the velocities averaged over several rotations into a longitude and latitude map. Figure 4 shows averages over seven Carrington rotations centered on the March to August interval for each of the even years from 1972 to 1982. The average wind speed in 15x15 degree bins is displayed in the left hand panel by five shades of grey (250-349km/s as light shading, up to over 650 km/s as black, with white indicating no data). The middle panel shows the coronal electron density in similar format estimated from the HAO white light coronameter (Mark II data supplied by D. Sime 1972-78 and Mark III data supplied by R. Fisher 1980-82 (they come from $1.5R_0$ and $1.7R_0$ from solar center, respectively). Regions of low density are white ($<1.510^{-8}$ pB) and represent the large coronal holes; particularly clear are those over the poles which correspond to the regions of fast solar wind (polar streams). For 1976-80 the right hand panels show the coronal magnetic field for a single rotation at the center of each seven rotation average. These data are the magnitude of the radial magnetic field at a source surface assumed to be at $2.2R_0$, derived from a potential field model fitted to the line-of-sight surface field measured at the Stanford solar observatory and supplied by J. Wilcox. Darker shading corresponds to stronger radial fields; the light band marks the neutral sheet separating positive and negative fields.

The polar streams can be seen as generally faster wind speeds at the top and bottom of each map. In 1974, however, they were centered about 30 degrees from the poles and so were seen as two fast streams per rotation by ecliptic spacecraft. Note also how the band of slow wind corresponds well with the band of high density, which separated coronal magnetic fields of opposite polarities. The data for 1973 are similar in form though the streams were at different longitudes and in 1973 the
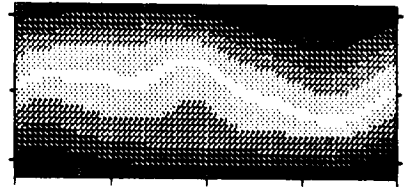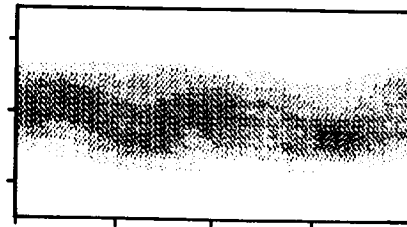
317

1972
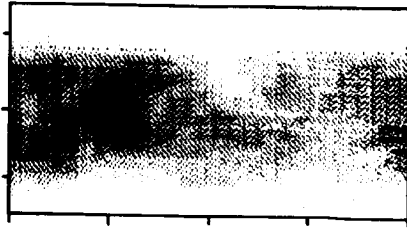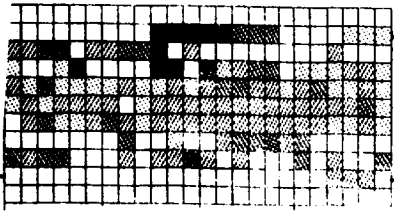
1974
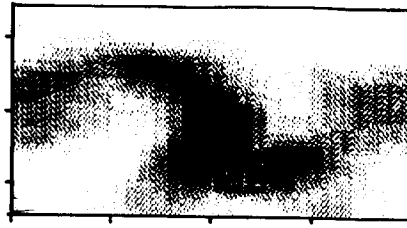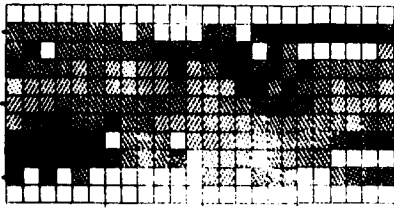
1976

1978

1980

1982

318
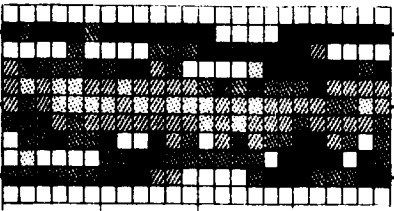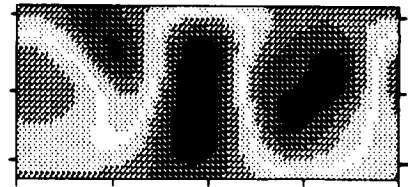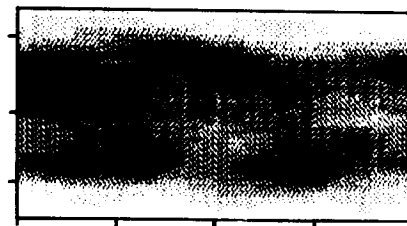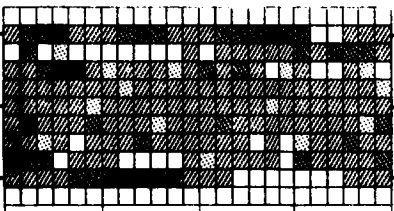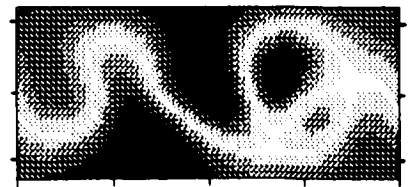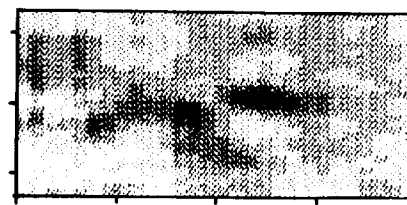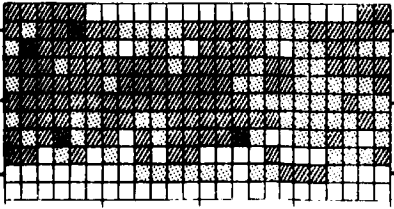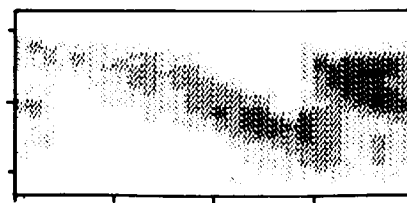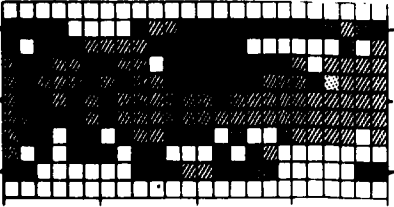
Figure 4. Left panels show solar wind speed as synoptic maps. Ticks on the vertical scale are at 60 degree intervals of latitude, on the horizontal scale are at 90 degree intervals of longitude. IPS data are averaged over six rotations. Fast is dark, slow is light, no data is blank. Middle panels show coronal electron density; dense is dark, holes are white. Right panels show coronal radial magnetic field magnitude; strong fields are dark, neutral sheet is white. Details are in the text.

southern stream was much wider than the northern one. The map for 1975 showed almost no change from 1974. In 1976 (solar minimum) the data show a narrow straight band of slow speeds along the solar equator, corresponding to wide fast streams which were well centered on the poles. For 1976 the small undulations in the current sheet match those in the locus of maximum density and would correspond to four magnetic sectors at the equator.

The first sunspots of the new cycle were seen at the end of 1977, and at the same time our IPS observations showed the north polar stream started to contract. The 1978 maps show that north and south polar streams had both contracted; slow wind extended to at least 60 degrees and also dense corona and
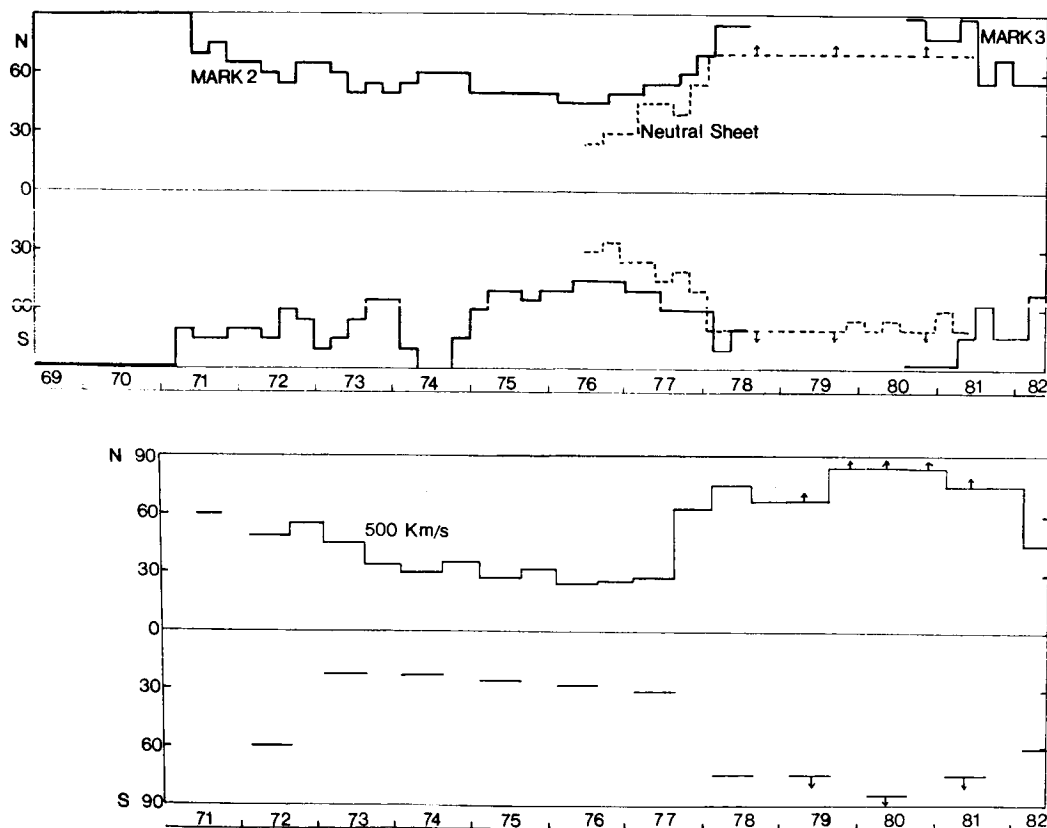
Figure 5. Upper panel shows six-month average boundary in latitude of the polar coronal holes from Mark II and III coronagraph data. Also shown are the extreme latitudes of the neutral sheet in an average magnetic field map over the same intervals. Lower panel shows the 500 km/s contour of six-month average speed, denoting the boundaries of the fast polar streams. Data from the south were only available once per year.

319

the neutral sheet extended to similar latitudes. Such (solar maximum) conditions persisted from 1978 to 1981, as typified by the 1980 maps. These show low velocities and high density at all latitudes and a complex neutral sheet with extensions to all latitudes. However the details of the neutral sheet are not easily traced in the density or velocity plots. The velocity map also shows a large region of slow wind (average speed less than 350 km/s at longitudes 250-330). This covered north and south latitudes and must have persisted over many rotations. There is no obvious corresponding feature in density but the neutral sheet shows an unusual tube structure separated from the main band of the sheet. It seems that the average wind speed from this complex magnetic topology is slower than from the rest of the sun.

The speed map for 1982 shows clear-cut regions of the fast polar streams and indeed, faster average speeds at all latitudes. The polar streams are again tilted away from the axis by more than 30 degrees at a longitude close to that of 1974. The density data also reveal a substantial change from 1980-81, showing large north and south polar coronal holes with equatorial extensions at the same longitudes as the polar streams. Spacecraft observations near the earth will presumably show two streams per rotation in this period.

Figure 5 summarizes the results for a solar cycle by displaying the 500 km/s contour of six-month average speed in latitude versus year. This represents the typical boundary of the polar streams and should be compared with the density contour chosen to represent the typical boundary of the polar holes, which is shown together with the highest latitude reached by the neutral sheet determined from the Stanford solar fields.

In summary, we note that in contrast to the equatorial solar wind the polar wind shows a very clear variation with solar cycle; it is slow when solar activity is high, and fast as activity declines or is low. The polar conditions are seen in the ecliptic when the fast polar stream becomes tilted from the axis, as tends to happen in the declining phase. The solar maximum observations show no large coronal holes and uniformly low velocities all over the sun. This clearly contradicts the view that all of the solar wind originates from large coronal holes (e.g., Hundhausen, 1977, page 295). The source of the wind must include open field regions which are not part of large coronal holes. At solar maximum we identified a persistent slow speed stream originating above a closed tube in the neutral sheet. Our conclusions affirm the close relation between the large coronal hole structures and high-speed solar wind, and inversely, between dense closed-field regions and slow speed solar wind.

References

Armstrong, J.W., and W. A. Coles, Analysis of three station interplanetary scintillation, J. Geophys. Res., 77, 4602, 1972.

Coles, W. A., J. K. Harmon, A. J. Lazarus, and J. D. Sullivan, Comparison of 74 MHz interplanetary scintillation and IMP7 observations of the solar wind during 1973, J. Geophys. Res., 83, 3337, 1978.

Coles, W. A., B. J. Rickett, V. H. Rumsey, D. G. Turley, S. Ananthakrishnan, J. W. Armstrong, J. K. Harmon, S. L. Scott, and D. G. Sime, Solar cycle changes in the polar solar wind, Nature, 286, 239, 1980.

Harmon, J. K., Scintillation studies of the density microstructure in the solar wind plasma, Ph.D. thesis, University of California, San Diego, 1975.

Hundhausen, A. J., An interplanetary view of coronal holes, Coronal Holes and High Speed Wind Streams, 225-329, J. Zirker (ed.), Colorado Assoc. University Press, 1977.

Sime, D. G., and B. J. Rickett, The latitude and longitude structure of the solar wind speed from IPS observations, J. Geophys. Res. 83, 5757, 1978.

SOLAR CYCLE VARIATIONS IN THE INTERPLANETARY MAGNETIC FIELD

J.A. Slavin and E.J. Smith
Jet Propulsion Laboratory
California Institute of Technology
Pasadena, CA 91109

Abstract

ISEE 3 interplanetary magnetic field measurements have been used to extend the NSSDC hourly averaged IMF composite data set through mid-1982. Most of sunspot cycle 20 (start:1964) and the first half of cycle 21 (start:1976) are now covered. The average magnitude of the field was relatively constant over cycle 20 with ~5-10% decreases in 1969 and 1971, when the sun's polar regions changed polarity, and a 20% decrease in 1975-6 around solar minimum. Since the start of the new cycle, the total field strength has risen with the mean for the first third of 1982 being about 40% greater than the cycle 20 average. As during the previous cycle, a ~10% drop in IMF magnitude accompanied the 1980 reversal of the solar magnetic field. While the interplanetary magnetic field is clearly stronger during the present solar cycle, another 5-7 years of observations will be needed to determine if cycle 21 exhibits the same modest variations as the last cycle. Accordingly, it appears at this time that intercycle changes in IMF magnitude may be much larger than the intracycle variations. The magnitude of the interplanetary field is not highly correlated with solar wind speed, the sunspot cycle, or magnetograph measures of the total solar magnetic flux. However, the B_z component was well correlated with smoothed sunspot number over both cycles. The solar cycle variation in B_z and the cycle to cycle changes in IMF intensity may be of considerable importance to the study of long term cycles in geomagnetic activity.

Introduction

Routine measurements of the interplanetary magnetic field (IMF) from earth and sun orbiting spacecraft have been carried out since the early 1960's. Given the strong periodic variations in the strength and polarity of the solar magnetic field on a time scale of 11 years, it is not surprising that a number of studies have searched for similar changes in the IMF. The identification and successful modeling of such variations could provide important insights into the configuration of the inner heliosphere and the low altitude sites from which the solar wind emanates.

While the reversal in the dominant polarity of the IMF near solar maximum has been observed for both cycles 20 and 21 (Fairfield, 1974, Hedgecock, 1975, Smith et al., 1982), no clear variation in the strength of the IMF was detected prior to the 1975-6 solar minimum (Hedgecock, 1975; Mariani et al., 1975, King, 1976). At that time a 10-20% drop in the interplanetary field intensity occurred (King, 1979). Following this interval of low field strength, the magnitude of the IMF was seen to rise with the approach of cycle 21 maximum (King, 1981).

In this study we have used the ISEE 3 vector helium magnetometer observations to extend the IMF database through day 126 of 1982. Our analyses of this 1966-1982 set of measurements have confirmed the findings of the earlier studies through 1979 and determined that the IMF has remained strong following cycle maximum in 1979-80. These results are examined in comparison with recent studies of the solar magnetic field.

IMF Observations

For the years 1966-1977, our investigation has used the same National Space Science Data Center hourly averaged interplanetary composite data set as most of the previous studies (King, 1976; 1981). While a large number of different earth orbiting satellites have contributed to the observations, IMP 8 was the only source of IMF measurements between 1975 and the launch of ISEE 3 in 1978. ISEE 3 is particularly well suited to this purpose because of its unique orbit about the forward earth-sun Lagrange point which keeps it always in the solar wind. For these reasons we have used ISEE 3 observations for 1978-1982 to update the NSSDC data set and enhance its temporal coverage.

Following Burlaga and King (1979), the log-normal nature of the IMF field strength has been noted and yearly averages of the logarithm of the hourly average total field computed as displayed in Figure 1. Autocorrelations were performed for each year and used to compute the standard errors (Bell and Glazer, 1957). Between 1966 and 1974 only weak variations are present with statistically significant small decreases of $\sim 5\%$ in 1969, 1971 (King, 1979) and a maximum in 1974. The total field shows a $\sim 20\%$ decrease that is nearly symmetric about solar minimum, June-1976. By 1978 the IMF intensity has again reached its previous 1974 maximum of just over 6 nT. Since that time, the total field strength has continued to climb, with the exception of a $\sim 10\%$ dip near solar maximum, to almost 8 nT during the first third of 1982. This increase corresponds to a 40% enhancement over the cycle 20 average and a 55% climb from solar minimum.

The field strength distributions themselves have also been examined to determine the nature of the cycle 21 maximum increase. As shown in Figure 2 the log-normal distribution of IMF intensity about solar minimum, defined here as Bartels Rotations 1920-1965, is very similar to the solar maximum distribution, Bartels Rotations 1988-2022, save for a larger mean value. Accordingly, it does not appear that the increase is associated with any particular phenomenon, such as interplanetary shocks or magnetic bubbles, producing a skewed distribution at cycle maximum. The shape and width of the log B distributions are comparable at solar maximum and minimum.

The idealized interplanetary magnetic field model of Parker (1963) gives the total field strength, B, at a distance from the sun, R, where the radial field stength is B_x as

$$B = (B_x^2 + B_y^2)^{1/2} = B_x(1 + \Omega^2 R^2/V^2)^{1/2} \quad (1)$$

Changing solar wind velocity influences the field in two ways: (1) by affecting the source field strength, and hence B_x, and (2) by varying the magnitude of B_y and the tightness of the spiral. King (1981) investigated the latter of
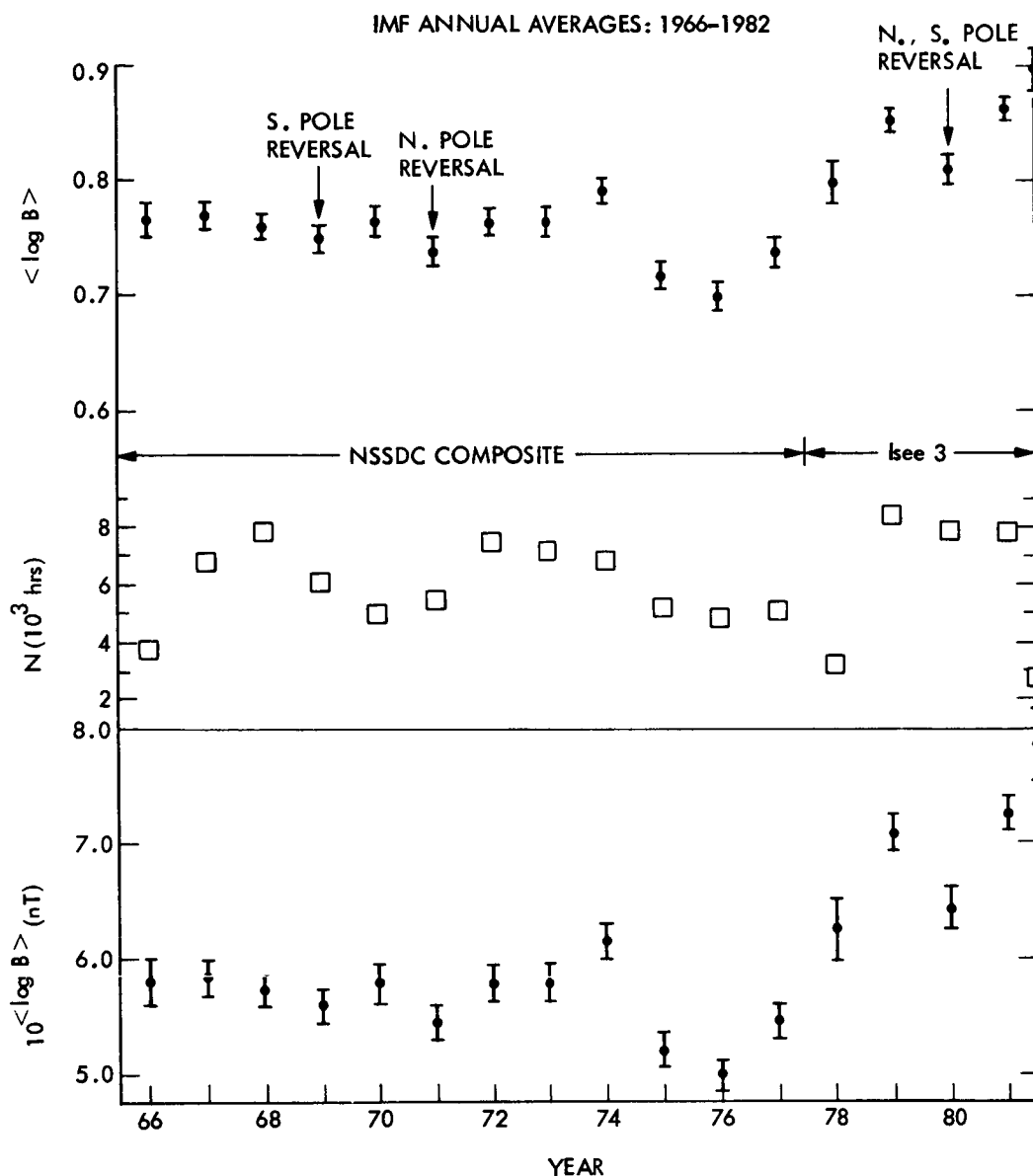
Figure 1. Yearly averages of the logarithm of the total interplanetary magnetic field strength, the number of hourly averages per year, and the inverse log of the annual averages are all plotted as a function of time. The intervals of solar polarity reversal are indicated.

these two effects by comparing annual averages of the solar wind speed and IMF strength. The yearly average solar wind velocities for 1966-79 all fell between about 400 and 460 km/s except for the high speed years 1973-5 which spanned 480-520 km/s. For a constant radial source field, the Parker model, equation (1), would predict a ~10% drop in field strength during the high speed years. However, as shown in Figure 1 the total field magnitude stayed constant from 1972 to 1973, increased from 1973 to 1974, and fell only in 1974-5 as the solar wind speed decreased. The more typical 10-20 km/sec changes in the annual mean solar wind velocities produce only ~1-2% changes in the field strength by varying B_y magnitude. We therefore conclude, in agreement with King (1981), that the long term changes in the interplanetary magnetic field are largely due to variations in the solar source fields.
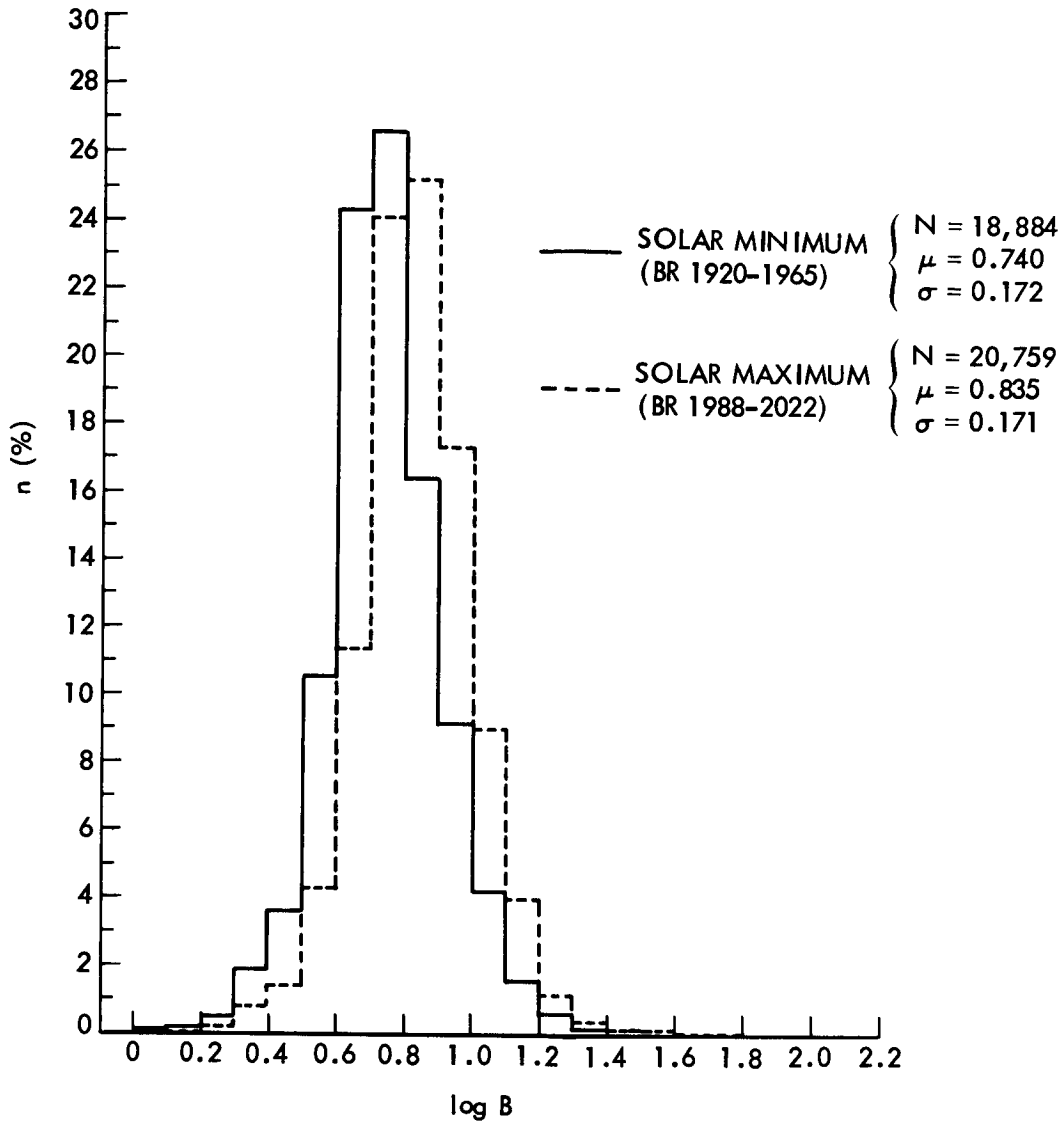
Figure 2. Histograms of log B during solar maximum and minimum are plotted as dashed and solid lines, respectively.

Solar Observations

Having examined the long term variations in the strength of the IMF, we investigated how the interplanetary field relates to the sunspot cycle and other ground based measures of the low altitude solar magnetic field. Figure 3 displays annual averages of the three GSE IMF components, the magnitude of the ecliptic component, the ratio of the field normal to the ecliptic to that in the ecliptic, the smoothed sunspot number (Solar Geophysical Data, 1982), and the years of solar polarity reversal (Howard, 1974, Howard and LaBonte, 1981, R. Howard, private communication, 1983). Overall the components of the interplanetary field are well correlated with the total field, albeit the correlation is weakest for B_z. All three components exhibit the same long term changes as the total field, but with the effects of changing solar wind conditions also evident in B_x and B_y. In particular, only during the the high speed years mentioned earlier was the ratio of $\langle |B_x| \rangle$ to $\langle |B_y| \rangle$ greater than unity in the annual averages.
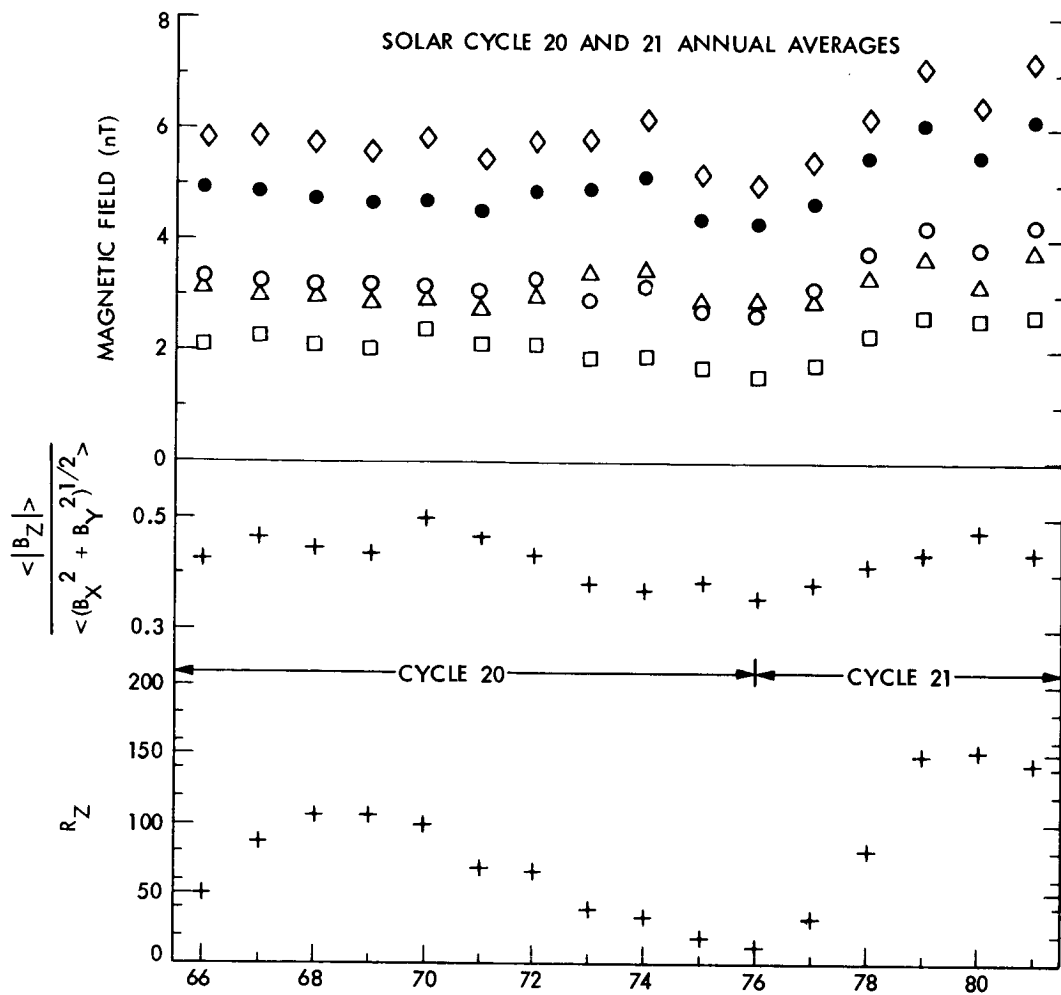
Figure 3. Annual averages of $|B_x|$, triangles, $|B_y|$, open circles, $|B_z|$, squares, $(B_x^2+B_y^2)^{1/2}$, solid circles, the inverse log of the total field magnitude, diamonds, the relative magnitude of the component normal to the ecliptic, and the average sunspot number are all plotted as a function of time.

Cycle 21 maximum in sunspot number, December-1979, was about 50% higher than cycle 20 and possessed a more crested shape. Among the IMF quantities, the relative strength of the out-of-ecliptic component, $\langle|B_z|\rangle/\langle(B_x^2+B_y^2)^{1/2}\rangle$, best reproduces the period of the sunspot curve with two peaks and one trough clearly visible. This parameter can be considered to be a measure of the ratio of the strength of the "ac" type waves/bubbles/turbulence that produce B_z to the steadier spiralled "dc" field in the ecliptic. However, the correlation is far from perfect with the low 1968 and 1969 values the most salient discrepancies. In addition, the cycle 21 maximum in the relative strength of B_z does not appear to have been any greater than during the weaker preceeding cycle. It is not yet known how this result compares with the variation in the number of shocks, bubbles, and streams observed from cycle 20 to 21.

The magnitude of the IMF and its components, with the exception of B_z, show little correlation with sunspot number until the start of cycle 21. As reported by Siscoe et al. (1978), $|B_z|$ increased in phase with sunspot number

327
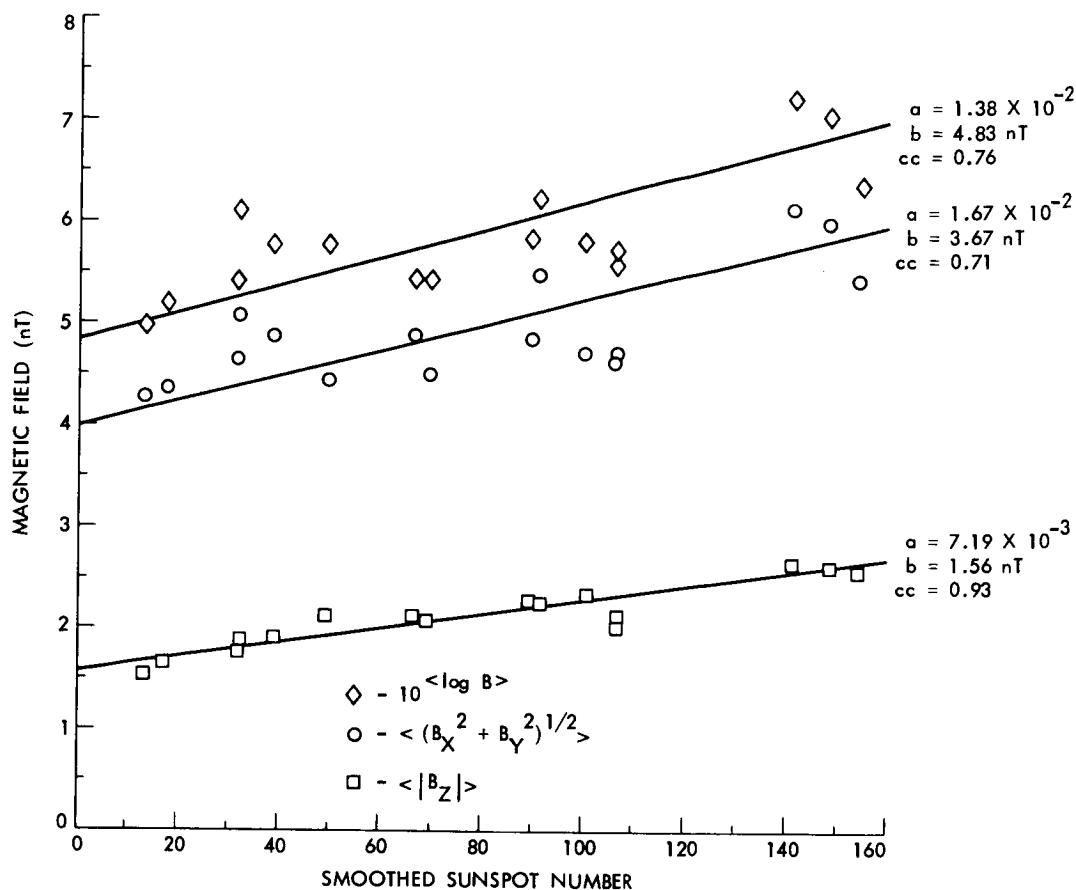
Figure 4. Annual averages of the total field strength and its components in and out of the ecliptic are correlated with smoothed sunspot number over the interval 1966-1982. Correlation coefficients, least square slopes, a, and intercepts, b, are also displayed.

during cycle 20. That behavior is reproduced, including a dip in strength near maximum, by the cycle 21 observations shown in Figure 3. This finding and the solar cycle to solar cycle variations in IMF strength may provide the ultimate explanation of the 11 and 22 years cycles in some components of geomagnetic activity (e.g Chernosky, 1966). Furthermore, the results may aid the studies of long term geomagnetic activity which often must infer interplanetary conditions from historic records of sunspot numbers. Figure 4 correlates IMF field intensity with annual average sunspot number over the years 1966-82 and confirms the close relationship between $<|B_z|>$ and $<R_z>$. The correlation between R_z, the component of the IMF in the ecliptic, and the total field is largely due to the stronger IMF fields and higher sunspot numbers during cycle 21 as opposed to any good agreement in the shapes of the curves over the two individual cycles.

In Figure 5 the annual averages of the IMF components parallel and perpendicular to the ecliptic have been compared to the Mt. Wilson magnetograph measurements of "total solar flux" compiled by Howard and LaBonte (1981). To within the limits of the instrument's aperture, daily measurements of the flux have been rectified and summed. The flux measurements refer to large scale magnetic fields. For example, a flux of 6 x 10^{22} Mx in Figure 5 would be produced by a uniform field of only 1 Gauss. Most of the magnetic flux is concentrated at lower latitudes with 69% being

found between $\pm 28.1°$. In examining 13 years of observations, they determined ratios of sunspot maximum to minimum total flux of 2:1 for cycle 20 and 3:1 for cycle 21. Using Kitt Peak magnetograms and He images, Harvey et al. (1982) have found that the enhanced solar fields near cycle 21's maximum are due to low latitude coronal holes similar in size to those existing at solar minimum, but possessing 3 times the magnetic field strength.
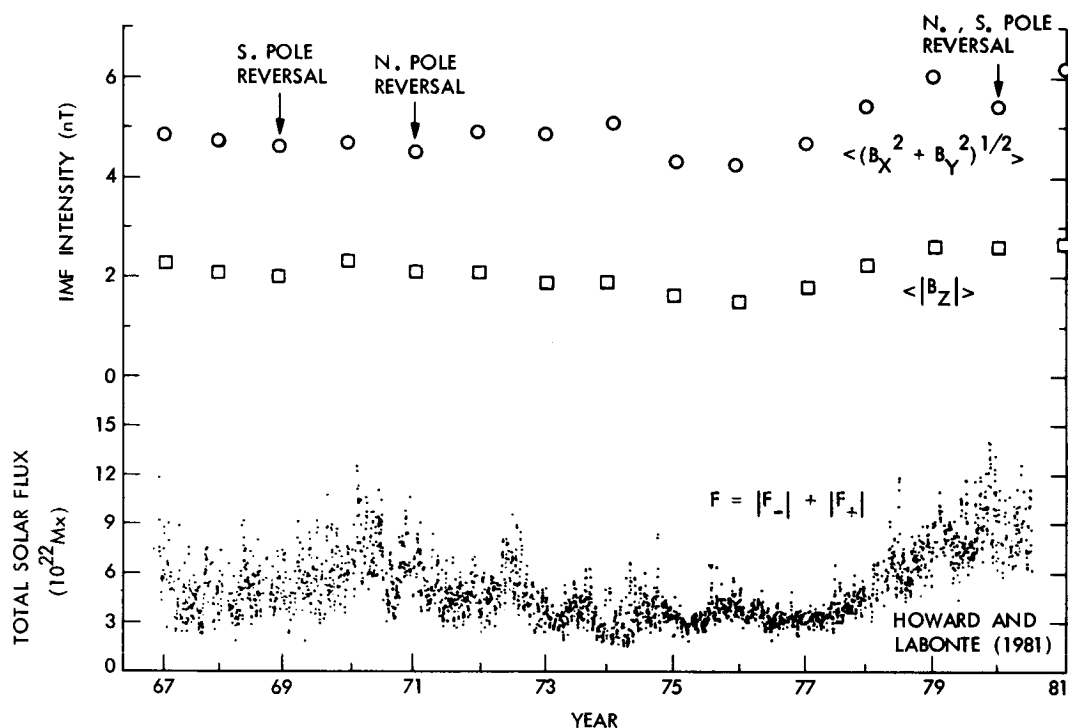
Figure 5. Yearly averages of the IMF components in and out of the ecliptic are compared with the daily total solar magnetic flux measurements of Howard and LaBonte (1981).

In general, the correlation between the magnitude of the IMF and full disk solar flux appears no better than for sunspot number. The factor of 2 total flux increase during cycle 20 maximum appears to have gone almost unnoticed by the IMF at earth orbit while the factor of 3 increase for the current cycle produced only a 55% change in the 1 AU field. Conversely, the enhanced interplanetary fields accompanying the high speed solar wind streams of cycle 20's declining phase, 1972-4, do not correspond to any overall increase in the total photospheric flux which continued its march toward minimum. For enhanced IMF to have been observed during the 1972-4 interval without any increase in the solar field strength, it is neccessary that a greater than normal fraction of photospheric field lines have been "open" (i.e. not connect back to the sun as with, for example, sunspot pairs). Such a geometry is certainly consistent with the presence of large equatorward-dipping coronal holes. Similarly, the strong solar fields around cycle 21 maximum could not have produced so modest a rise in the IMF strength if the same fraction of the low altitude field lines were carried to 1 AU as during the decline of cycle 20. The lack of strong stream activity in 1978-80 supports the presence of a more closed solar field configuration.

For these reasons there must be very siginficant variations in the low altitude field geometry as well as the field strength during the solar cycle. In agreement with previous studies (Levine, 1977; Harvey and Sheeley, 1979), it appears that we do not yet possess sufficient knowledge of the sun's magnetic field geometry to be able to generally predict low latitude heliospheric magnetic field strength from coronal hole and magnetograph observations.

Concluding Remarks

Over the last 16 years the interplanetary magnetic field has undergone a number of changes which appear related to the sun's magnetic cycle. The reversals in the dominant polarity of the IMF and the solar field have not been examined here, but are known to be well correlated (Smith et al., 1982). Minima in the intensity of the total interplanetary field and its radial component occur around solar minimum and, to a lesser extent, during the intervals of polarity reversal. The solar minimum decrease in the IMF can be directly ascribed to the weak source fields on the sun in Figure 5. However, the smaller decreases about the time of the polarity reversal in 1969, 1971, and 1980 are more difficult to interpret. These dips in the IMF do not correspond to any decreases in the magnetograph determinations of the solar field. For this reason it does not seem reasonable to attribute them to a decrease in solar dynamo action in association with the polarity reversal. In our opinion, a more likely hypothesis is that the intermingling of positive and negative oriented field lines during the reversal (e.g. Howard and LaBonte, 1981) produces enhanced reconnection which closes off a larger than usual fraction of the solar field lines and decreases the number being carried out to 1 AU by the solar wind.

It is not yet apparent whether the growth in IMF intensity over the years 1976-82 is associated with a solar minimum to maximum change or a cycle 20 to cycle 21 variation. However, the weak changes in interplanetary field magnitude during cycle 20 and the continued strength of the field after cycle 21 maximum suggest that the current solar cycle may simply have a stronger magnetic field than cycle 20. In this case the change in field strength from 1976-1982 is associated not with the 11 year sunspot cycle, but perhaps one of the longer 80-100 year cycles whose existence has been inferred from historic records (e.g. Feynman and Silverman, 1980). Finally, alternate solar cycles of stronger and weaker IMF could be the cause of the 22 year cycles in some measures of geomagnetic activity (Chernosky, 1966).

References

Bell, B., and H. Glazer, Geomagnetism and the emission-line corona: 1950-1953, Smithson. Contrib. Astrophys., 2, 51, 1957
Burlaga, L.F., and J.H. King, Intense interplanetary magnetic fields

observed by geocentric spacecraft during 1963-1975, J. Geophys. Res., 84, 6633, 1979

Chernosky, E.J., Double sunspot cycle variation in terrestrial magnetic activity, 1884-1963, J. Geophys. Res., 71, 965, 1966.

Fairfield, D.H., and N.F. Ness, Interplanetary sector structure: 1970 - 1972, J. Geophys. Res., 79, 5089, 1974.

Feynman, J., and S.M. Silverman, Auroral changes during the eighteenth and nineteenth centuries and their implications for the solar wind and the long term variation of sunspot activity, J. Geophys. Res., 85, 2991, 1980.

Harvey, J.W., and N.R. Sheeley, Jr., Coronal holes and solar magnetic fields, Space Sci. Rev., 23, 139, 1979.

Harvey, K.L., N.R. Sheeley, Jr., and J.W. Harvey, Magnetic measurements of coronal holes during 1975-1980, Solar Phys., 79, 149, 1982.

Hedgecock, P.C., The heliographic latitude dependence and sector structure of the interplanetary magnetic field 1969-1974: Results from the Heos satellites, Solar Phys., 44, 205, 1975.

Howard, R., Studies of solar magnetic fields, I. The average field strengths, Solar Phys., 38, 238, 1974.

Howard, R., and B.J. LaBonte, Surface magnetic fields during the solar activity cycle, Solar Phys., 74, 131, 1981.

King, J.H., A survey of long-term interplanetary magnetic field variations, J. Geophys. Res., 81, 653, 1976.

King, J.H., Solar cycle variations in IMF intensity, J. Geophys. Res., 84, 5938, 1979.

King, J.H., On the enhancement of the IMF magnitude during 1978-1979, J. Geophys. Res., 86, 4828, 1981

Levine, R.H., Large scale solar magnetic fields and coronal holes, Coronal Holes and High Speed Streams, ed. J.B. Zirker, pp. 103-145, Colorado Univ. Press, 1977.

Mariani, F., L. Diodato, and G. Moreno, Search for long term variations of the interplanetary magnetic field, Solar Phys., 45, 241, 1975.

Parker, E.N., Interplanetary Dynamical Processes, Interscience, New York, 1963

Siscoe, G.L., N.U. Crooker, and L. Christopher, A solar cycle variation of the interplanetary magnetic field, Solar Phys., 56, 449, 1978

Smith, E.J., B.T. Thomas, B.T. Tsurutani, and J.A. Slavin, Reversal of the interplanetary sector structure: Observations and modeling (abstract), EOS Trans. Amer. Geophys. Union, 63, 425, 1982.

Page intentionally left blank

SOLAR WIND VARIATIONS IN THE 60-100 YEAR PERIOD RANGE: A REVIEW

J. Feynman

Department of Physics

Boston College, Chestnut Hill, MA 02167

ABSTRACT

The evidence for and against the reality of a solar wind variation in the period range of 60-100 year is re-examined. Six data sets are reviewed: sunspot numbers, geomagnetic variations, two auroral data sets and two ^{14}C data sets. These data are proxies for several different aspects of the solar wind and the presence or absence of 60-100 year cyclic behavior in a particular data set does not necessarily imply the presence or absence of this variation in other sets. We conclude that two different analyses of proxy data for a particular characteristic of the heliospheric solar wind yielded conflicting results. This conflict can be resolved only by future research. We also definitely confirm that proxy data for the solar wind in the ecliptic at 1 A.U. undergo a periodic variation with a period of approximately 87 years. The average amplitude and phase of this variation as seen in eleven cycles of proxy data are presented.

INTRODUCTION

The existence of a solar variation with a period in the range of 60 to 100 years has been the subject of controversy for many years. Data on the amplitudes of the sunspot cycle, auroral frequencies, ^{14}C, the weather, tree rings and the thickness of varves in Australian rocks (Williams, 1981) have been cited for or against the existence of a periodic variation in this time range. The suspected variation has been called, among other things, the Gleissberg variation, the Long Cycle, the 87 year cycle and the secular variation.

In this paper we take a much more restricted view of the proposed phenomenon. We note that many of the data sets used in the past refer to aspects of the solar wind rather than the sun itself and so we here confine our study to a review of data concerning variations of the solar wind with characteristic times in the 60-100 year range. Because the solar wind has been observed in situ for less than 2 eleven year solar cycles, we will have to rely on a data base that gives indirect information on the solar wind, that is, proxy data will be used. We will further restrict our study to proxy data for which the relationship between the observed quantities and the solar wind is understood at least in principle. For this reason no data involving solar weather relationships will be examined. In section 1 of this paper the 6 data sets used will be introduced briefly. We then discuss each set, its relation to other sets and the evidence it gives as to the reality of a long period variation in the solar wind. The results of the review are brought together in section 2 where it is concluded that there is conflicting evidence concerning a possible heliospheric-wide solar wind periodicity in the period range of interest but there is extremely good evidence for a long cycle of about 87 years in the solar wind in the vicinity of the earth. The amplitude and phase of the variation are displayed.

SECTION 1 - THE DATA

The six data sets to be used and the time periods they cover are shown schematically in figure 1. The sunspot number record starting in about 1700 provides proxy data for certain aspects of the sources of the solar wind since the beginning of the 18th century. The next three data sets, aa, Swedish auroras and medieval auroras, are proxy data for the solar wind in the vicinity of the earth since that wind drives the aurora and geomagnetic activity. The aa denotes the geomagnetic indices scaled by Mayaud (1973) from existing observatory records for the period since 1868. The Swedish auroral data set was constructed by Rubenson (1882) from reports from observers throughout Sweden and covers the period from 1721 to 1876. The data set denoted as "medieval aurora" are taken from the review by Siscoe (1980) who gives the number of auroras reported per decade in Europe and/or the Orient from 450 A.D to 1450 A.D. The bottom two data sets of ^{14}C are proxy data for the solar wind throughout the heliosphere since the ^{14}C abundance in the earth's atmosphere is indirectly determined by the cosmic ray intensity, which is in turn modulated by the heliospheric solar wind. The differences between the two ^{14}C data sets will be described when they are discussed in detail below.

In the remainder of this section the data sets in fig. 1 are reviewed, their reliability assessed and some comments made on intercalibration with other data sets. Each set is then examined separately to see what evidence it gives concerning the existence of a periodic solar wind variation in the 60-100 year period range. Each data set will be assigned to one of three categories,

> 1 - shows periodicity in the 60-100 year period range
> 2 - does not show periodicity
> 3 - is compatible with a periodicity but too short to be considered a member of category 1

There were no data sets that would belong to the 4th logical category, i.e. not compatible with a 60-100 year periodicity but too short to be considered a member of category 2. Before proceeding it is important to emphasize that since the data sets are proxy for three different aspects of the solar wind; the sources, the solar wind in the vicinity of the earth and the solar wind throughout the heliosphere, a periodicity in any one of these quantities does not necessarily imply a periodicity in the other two. The data sets will be discussed in the order shown in figure 1 except that the medieval auroras will be reviewed last.

Sunspot Numbers

The sunspot number is defined somewhat arbitrarily as the number of individual spots plus 10 times the number of spot groups (c.f. Gibson, 1973). Considering this definition it would be rather remarkable if the daily sunspot number had a very high correlation with any other physical quantity. The reliability of data on sunspots has been reviewed by Eddy (1976) during the course of his work establishing the reality of the Maunder minimum. Eddy concluded that sunpsot data have been very reliable for more than the last hundred years but that the reliability of the data declines for earlier periods. However, since perhaps the beginning of the 18th century the

approximate amplitude and time of the eleven year solar cycle variation of the yearly averaged sunspot number is quite well established. Recently a great deal of work has been done on deducing sunspot numbers during the 17th century Maunder minimum, but the relative amplitudes of the sunspot cycles described for that period can not be determined because of the rarity of spots and of systematic observations. For this reason the 17th century sunspot data will be omitted from this study.

The relationship between the sunspot number and the parameters of the solar wind is not close and in general neither daily nor yearly average sunspot numbers can be used to predict velocities or magnetic fields of the solar wind near the earth (c.f. Gosling et al. 1977). However, the sunspot number does yield some information on the sources of the solar wind since the number of sudden commencements of geomagnetic storms arriving at earth each year is correlated to annual sunspot number with a correlation coefficient of 0.85, as shown by Mayaud (1975) using 100 years of data. Sudden commencements (i.e. sudden world wide increases in the horizontal intensity of the geomagnetic field observed at low and midlatitude magnetic observatories) are usually caused by solar wind shocks due to sudden ejections of high velocity solar wind, and so the number of sudden solar ejections is proportional to the sunspot number. In this sense the sunspot number gives information on the sources of one type of solar wind disturbance.

Fig. 2 (adapted from Eddy, 1976) gives the annual mean sunspot number from 1610 to 1975. The Maunder minimum is shown on the top panel. The second and third panels show the data used in this review; i. e. the data that give evidence concerning a 60-100 year variation in solar wind sources. The envelope of the 11 year sunspot cycle shows three relative minimums, circa 1755, circa 1810, and a broad minimum from 1880 to 1930. If we adopt a criterion that to be counted as a minimum cycle, the sunspot number can not exceed 70, then two minimum periods remain, one at the beginning of the 19th century and the other at the end of the 19th or the beginning of the 20th century. These minimums are weak evidence in favor of a 60-100 year period in solar wind sources since they are compatible with such a period. From this view the appearance of the minimum to be expected in the early 18th century would have been obscured by the general rise caused by the ending of the Maunder minimum. On the basis of this admittedly weak argument this data set is put in category 3; that is, it is compatible with a 60-100 year variation in properties of the sources of the solar wind but too short to be used as evidence for any such periodic behavior.

aa Indices

The second data set to be considered is the 100 years of aa indices produced by Mayaud in 1973 from the original magnetograms from Greenwich Observatory and the antipodal Australian stations. In contrast to the more familiar indices such as ΣKp or C_9, aa is a real physical quantity. The data set consists of half daily values of the range of geomagnetic disturbances measured in nanoteslas. It covers the period from 1868 to the present but can be considered a modern data set because, within the last 10 years, the actual traces of the magnetometer pens were used to produce it. This is in contrast to the case of, for example, sunspot data in which we have only the record of what the observer reports as having been seen and no hard copy record of the observations themselves that could be re-examined using modern methods.

60-100 YEAR VARIATION DATA SETS

YEAR (A.D.)

Annual Mean Sunspot Number, A.D. 1610-1975

SUNSPOT NUMBER

YEAR
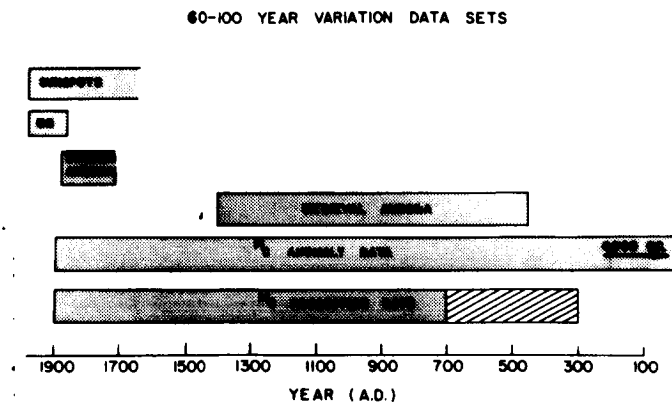
Fig. 1. Schematic of data sets discussed and the time period each covers. These data are proxies for three different aspects of the solar wind, as discussed in the text

Fig. 2. The annual mean sunspot number, from Eddy,(1976). The low amplitude cycles near the beginning of the 19th and 20th centuries are weak evidence for a Long Cycle variation in one aspect of the sources of the solar wind.

GEOMAGNETIC ACTIVITY

aa

YEAR

ALL SWEDEN
(1868-1876)
r = 0.97

NUMBER OF AURORAS

LEAST SQUARES FIT

Fig. 3. The aa index of geomagnetic activity. These data are a proxy for the solar wind at 1 A.U. in the ecliptic plane (after Mayaud, 1973).
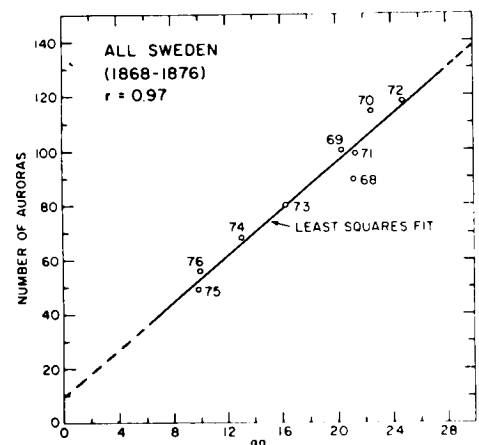
Fig. 4. A comparison of the aa index and the number of auroras reported each year in Sweden for the period when both data sets exist. (From Silverman and Feynman, 1980).

If we consider the magnetosphere as a solar wind detector and magnetic and/or auroral activity as read-out parameters, the aa indices, shown in fig. 3, form a data set that refers to the solar wind at 1 A.U. and in the ecliptic plane. The relationship between the sunspot data and the aa index has been the subject of several studies in the last few years (c.f. Legrand and Simon 1981, Feynman, 1982). In examining the relationship it should be kept in mind that both sunspot number and aa are accurate and reliable for the period since 1868 and the differences in their long term behavior must be caused by their being measures of two different phenomena. It is clear in figures 2 and 3 that geomagnetic activity remains strong during the declining phase of the 11 year sunspot cycle. In fact the level of aa during the declining sunspot number phase is so strongly related to the maximum sunspot number in the next cycle, about 6 years later, that aa has successfully been used to predict the value of the annual average sunspot number at the next maximum (Ohl 1976, Sargent, 1978). This strong relationship verifies that both the sunspot number and aa are reliable and have a physical meaning.

Evidence for a long period variation in the solar wind at earth is seen in figure 3 in the general rise of aa at sunspot minimum between 1900 and 1954 (Feynman and Crooker, 1978, Feynman 1982). This rise is not present in the sunspot number at minimum but is present in the ^{14}C data (Stuiver and Quay, 1980). The annual average aa is related to some combination of average solar wind velocity and southward interplanetary magnetic field (c.f. Crooker et al. 1977) and the extrapolations of the empirical relations derived from in situ solar wind data imply a very low annual average velocity or southward interplanetary field near the turn of the century, minimizing about 1901 (Svalgaard, 1977, Feynman and Crooker 1978, Gringaus, 1981). A further analysis of aa was interpreted as showing a systematic intensification of variations associated with the 11 year cycle from 1900 to 1960 which was ascribed to a Gleissber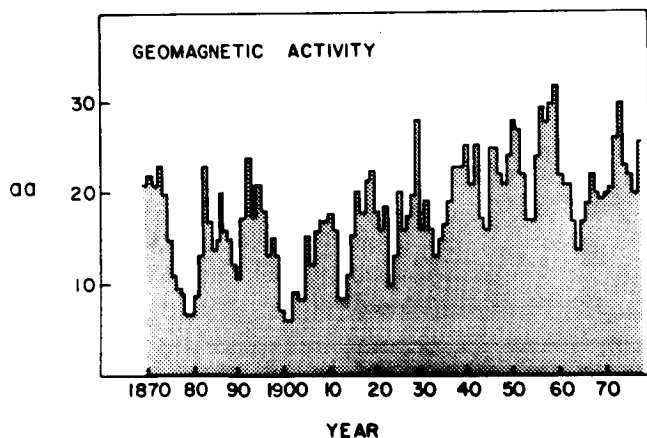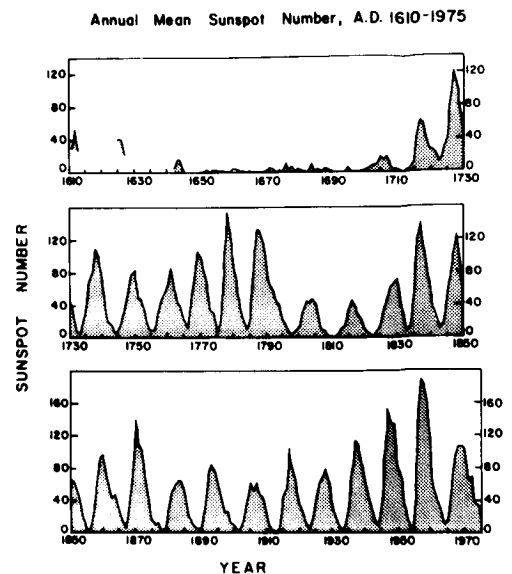g variation (Feynman, 1982). These studies of the aa index indicate the solar wind variations are consistent with a Long Cycle variation minimizing about 1900. This phase is of course consistent with the broad minimum seen in sunspot number cycle amplitude, but in the aa data the time of minimum can be more firmly determined. The aa data, then, are also placed in category 3.

Swedish Auroras

Swedish auroral observations from 1720 to 1882 were catalogued by the Director of the Central Meteorolgical Institute of Sweden, Robert Rubenson (1882). The data were collected from a variety of sources in all parts of Sweden. Rubenson's catalogue includes the geographical positions at which the observations were made. The yearly numbers of auroras seen in all Sweden and in the regions north and south of 61° 30" are available and have been restudied for their relavance to the long cycle variation (Silverman and Feynman, 1980, Feynman and Silverman 1980).

The Swedish auroral observations and the aa both refer to the solar wind in the vicinity of the earth but they are measurements of somewhat different phenomena. Both annual averages are available for the 9 years from 1868 to 1876 and the relationship between them shown in figure 4 (Silverman and Feynman, 1980) is remarkably close. Although the overlap of the two sets is

small, they are so closely proportional to one another that the figure gives confidence in the accuracy of the Swedish auroral observations, as well as reaffirming the well known relation between the range of geomagnetic disturbances and the latitude at which auroras are seen.

The number of auroras reported for Sweden south of 61° 30" is shown in Fig. 5. There is an impressive minimum in the 2nd decade of the 19th century. There are six years from 1809 to 1814 during which fewer than three auroras were reported each year. The number of auroras did not recover until sometime after 1825. The existence of a world-wide minimum in solar-terrestrial relationships at this time is confirmed by observations made in the United States (Feynman and Silverman, 1980). This solar wind minimum of 1809-1814 took place about 90 years before the solar wind minimum of 1901 implied by the aa data. Merging these two data sets would result in a solar wind proxy data set going through two minimums, with a period of something like 90 years. Considering either the Swedish auroral data set or the merged aurora-aa set, these data are placed in category 3.

Carbon 14 Data Sets

The next two data sets to be discussed are derived from ^{14}C in tree rings (Lin et al. 1975; Stuiver and Quay, 1981). ^{14}C is indirectly produced by galactic cosmic rays which, in turn, are modulated by the interplanetary medium. Interaction with the solar wind throughout the heliosphere modifies the cosmic ray flux which arrives at the earth's atmosphere. Changes in the cosmic ray flux cause changes in neutron production rate. The production of ^{14}C depends on interactions of the neutrons with atmospheric nitrogen. The ^{14}C then mixes into the atmosphere and is incorporated into living organisms. When life processes stop, the ^{14}C in the organism is no longer exchanged with the atmospheric ^{14}C.

Although ^{14}C production rate is dependent on the heliospheric solar wind in a very complex way, studies of ^{14}C have been made for many years and methods of analysis are well advanced and sophisticated. The major changes in ^{14}C levels during the last few milleniums are caused by known changes in the earth's main field (Creer, 1981) but these can be accounted for. There is also a small residual variation of a few percent from the long-term trend. This residual is due to heliospheric cosmic ray modulation. The data set labeled ^{14}C anomoly data in fig. 1 consists of these residual variations and covers 8,000 years. The solar-terrestrial minimum around 1810 and major solar terrestrial events such as the Maunder and Sporer minimiums are clearly seen in the ^{14}C residual record (Stuiver and Quay, 1980). Lin et al., (1975) calculated the autocovariance function using this data set and their results are shown in fig. 6. There appears to be a 350 year variation but since that is out of the period range of interest here it will not be discussed further. There is also a general rise in the autocovariance at periods between 20 and 150 years. Superposed on this general rise is added power at about 80 years. Lin et al. (1975) interpret this in terms of a periodic variation in the range from 60 to 100 years. This data set then will be assigned to category 1 since it shows a periodicity.

Recently another analysis of ^{14}C data has been carried out by Stuiver and co-workers. Stuiver and Quay (1980) increased the temporal precision of the ^{14}C data by constructing counters which could measure the ^{14}C activity in tree rings with a precision of 1.5 to 2 parts per million. Then, instead of using

338
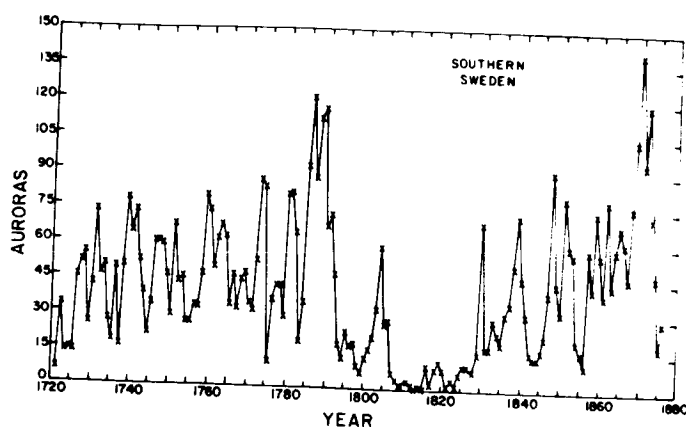
Fig. 5. The number of auroras reported each year in the region of Sweden south of 61° 31". Evidence for a solar-terrestrial minimum is seen is the small number of auroras reported between 1809 and 1825.
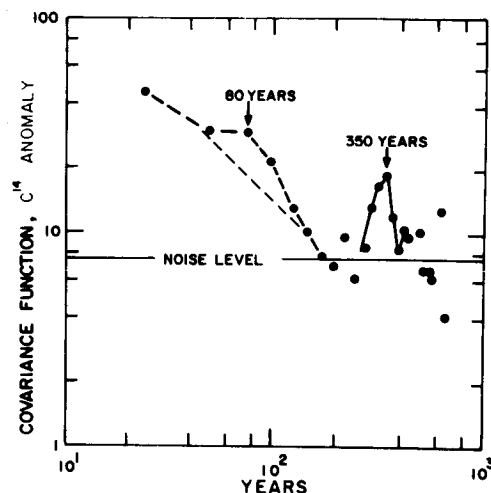
Fig.6. Autocovariance function for ^{14}C anomoly data (adapted from Lin et. al. 1975) showing increased covariance in the 60-100 year period range. ^{14}C data is proxy for the solar wind in the heliosphere.
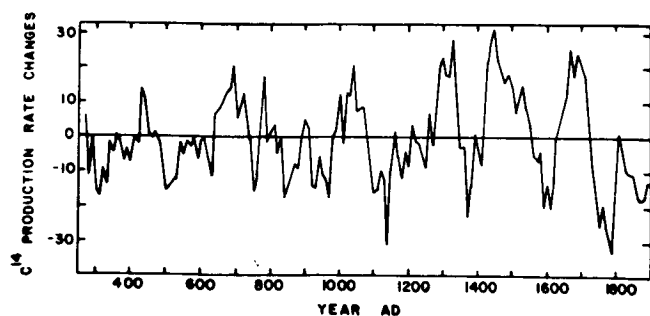
Fig. 7. The ^{14}C production data set from Stuiver and Quay, 1980 . As discussed in the text, this data set is derived using a model in which ^{14}C a 60 year residence time in the atmosphere.

AURORAS PER CENTURY
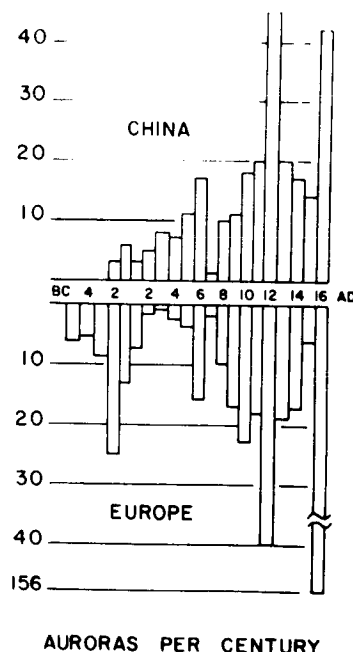
Fig. 8. A comparison of the number of auroras reported per century in Chinese and European records. (from Siscoe, 1980).

the ^{14}C anomoly data directly, they calculated the production rate of ^{14}C using a complex model in which the ^{14}C was stored in the earth's atmosphere before it interacted with the biosphere. The residence time of the ^{14}C in the atmosphere was an adjustable parameter. The ^{14}C production rates from 300 AD to 1900 AD were calculated using a 20 year and a 60 year atmospheric residence time and the results for the 60 year residence time is shown in fig. 7 (Stuiver and Quay, 1980). Maximums in about 1450, 1650 and 1810 correspond to the Sporer, Maunder and 19th century solar-terrestrial minimums. Stuiver and Quay compared the behavior of the ^{14}C production rates to the aa series and the sunspot numbers for the last 100 years and concluded that the ^{14}C production behaves more like the aa index than like the sunspot numbers. They found that the correlation coefficient between the ^{14}C production rate and the annual average aa was 0.67, which is quite high considering the aa is related to the solar wind at earth whereas ^{14}C probes the entire heliosphere.

Stuiver (1980) has carried out a power spectral analysis of the post 700 A.D. ^{14}C production rates shown in fig. 7. He does not find any increase of power in the 60 to 100 year frequency range so that this ^{14}C production data set must be placed in category 2, i.e. it does not shown any periodic behavior in the period range of interest here. Both the ^{14}C anomaly data and the ^{14}C production data will be discussed further in section 2.

Medieval Auroras.

The final data set to be discussed is derived from reports of auroras seen in Europe and the Orient from 450 A.D. to 1450 A.D. and will be referred to as medieval auroras. This data set was reviewed by Siscoe (1980) who, following Keimatsu (1976), investigated the accuracy of auroral report data by comparing the number of auroras per century reported from China and Europe separately as shown in fig. 8. Not only are the envelopes of the two frequency distributions almost the same but the actual number of reports from both areas are remarkably close. These results give confidence in the accuracy of the data. Siscoe (1980) also presented the thirty year running averages of the number of auroras seen per decade in the combined European-Oriental data set as shown in fig. 9. These data, like the Swedish auroras and aa are proxy for the solar wind at 1 A.U. in the ecliptic plane. The minimums circa 600-700 A.D., 1050 A. D., and 1350 A. D., are reflected in the ^{14}C data as is the maximimum from 1100 to 1200 (Stuiver & Quay, 1980).

As Siscoe points out and as has often been suggested before, (see review by Siscoe, 1980), this data set appears to show a periodic variation with a mean period of about 87 years. In order to test the validity of this observation in a more objective way the data will be analysed here by a modified superposed epoch method. The zero times of the epochs are chosen to make the average interval length 87 years. Since the data consist of the number of auroras per decade, it is not possible to use intervals of exactly 87 years each. Instead each interval consists of 9 decades of data but the zero time is adjusted so that the last decade of a few intervals is also used as the first decade of the next interval. A second modification must be made to the usual superposed epoch method because of the large amplitude of variations with characteristic times longer than 100 years, i.e. The Maunder and Sporer type minimums and the 12th century medieval maximum. If a standard superposed epoch analysis were carried out the results would be dominated by these events. To

340

prevent this, the number of auroras observed in each interval was normalized to one, and the fractional number of auroras in each bin calculated. The resulting data were arranged to perform the superposed epoch analysis shown in the upper panel of fig. 10. Each point represents the ratio of the number of auroras reported for a decade to the total number of auroras reported for the 90 year interval. The average of all the values is 0.11, shown by a bar in the figure. The data appear to be very systematically distributed about the average. For example almost all the points in the 3rd and 4th bins are above the average whereas almost all the points in the 2nd to last and last bins are below average. In order to test the validity of the method the analysis was repeated for several other choices of cycle length and the results for a 70 year cycle are shown in the lower panel of fig. 10. These results are typical of those for the other cycle periods tested. Here, although there is perhaps a hint of some systematic behavior within each of the bins, the distributions of points about the average of 0.14 does not appear to deviate significantly from chance.

The top panel of fig. 10 then is interpreted as demonstrating 1000 years of an 87 year period in the frequency of auroras at midlatitudes. This implies a variation of the solar wind at 1 A. U. in the ecliptic with a period of about 87 years. The uncertainty in the period is about a year or two. The period can not be determined more precisely by the superposed epoch method because a change of a year or two in the interval length will not make a statistically significant difference in the data distributions.

The amplitude and phase of the variation can also be determined reasonably accurately. The points in fig. 11 give the averages of the data in each bin of the upper panel of fig. 10. The first and last points in the figure are the same and are the bin 9 average. The dashed line is a simple sine function that was chosen to approximately fit the data. The phase of the curve was also chosen to give the best fit. The horizontal line is the average of the entire data set as in fig. 10. The minimum phase is about two decades before the first bin so the statistical minimum corresponds to about 435 A. D. (before the fall of Rome). On the average in a cycle, 2 1/2 times as many auroras will be seen at midlatitudes for cycle maximum as for cycle minimum. Due to uncertainties in period length and phase we can not meaningfully extrapolate to the 19th and 20th centuries.

The medieval auroral data set is assigned to category 1.

TABLE 1

data set	proxy for solar wind at	number of cycles	category
sunspot number	sources	2	3
aa indices	earth	1	3
Swedish auroras	earth	1	3
^{14}C anomoly	heliosphere	~100	1
^{14}C production	heliosphere	~16	2
medieval auroras	earth	11	1

EUROPEAN AND ORIENTAL AURORAL REPORTS
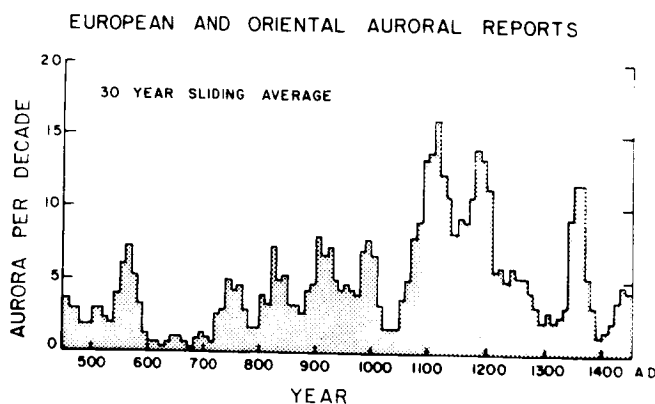
Fig. 9. A thirty year running average of the number of auroras reported per decade in the combined European-Chinese data set (from Siscoe, 1980).

Fig. 10. Modified superposed epoch analysis of the data in fig. 9. The top panel shows the data using an average interval length of 87 years. The lower panel shows the results of using a 70 year interval length.
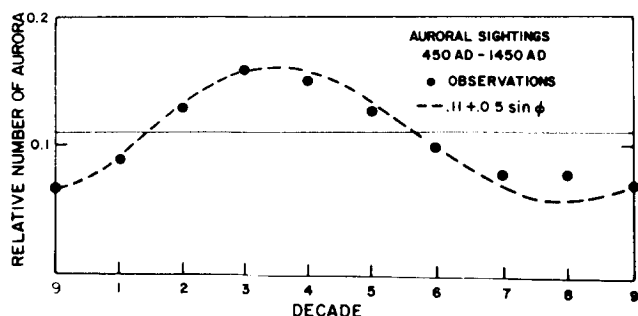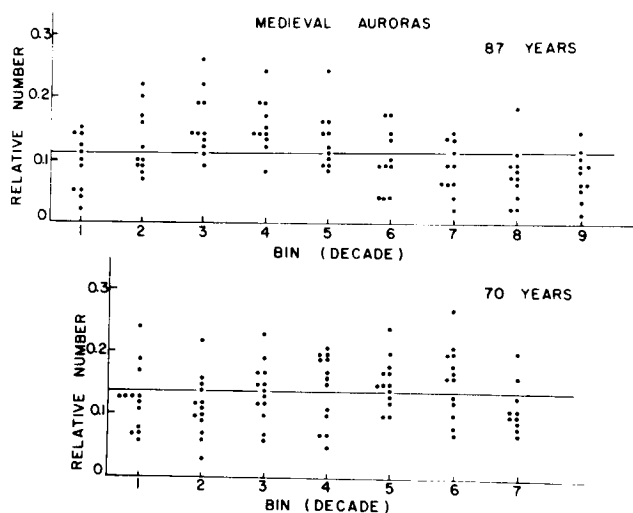
Fig. 11. The bin averages of the data in the top panel of figure 10. The sine curve is an approximate fit to the observations giving the amplitude and phase of the 87 year periodic variation. This figure demonstrates that there is a real variation in the solar wind at earth with a period and phase approximately as shown.

342

SECTION 2. THE CONCLUSIONS

The results of this review are gathered together in table 1. Since the data sets refer to three different aspects of the solar wind, a long period variation of one of these aspects does not require or imply a long period variation in either of the other aspects. Disagreements exist among the results only when two analyses of proxy data for the same aspect of the wind result in conflicting results. From table 1:

1). We have insufficient evidence to tell whether or not the annual sunspot number, and therefore the annual number of shocks in the solar wind, changes with the Long Cycle, but what data we have are compatable with such a change.

2). All of the proxy data for the solar wind at earth either show a definite long period variation or are compatible with such a variation. This finding is discussed further below.

3). A single type of proxy data for the solar wind in the heliosphere has been analyzed by two seperate groups and the results are conflicting, one being interpreted as showing a Long Cycle and the other as ruling a Long Cycle out.

The resolution between the two analyses of the ^{14}C data is not at all clear at this time. There are several possibilities. For example, the increase in the autocovariance function at about 80 years may not be statistically significant, or, conversely, it may be that the variation is very weak and 100 cycles of data are needed in order to be apparant in a power spectral analysis. It may also be possible that the long period variation was suppressed when the ^{14}C production data were derived from the ^{14}C residual anomoly data. The data set for which Stuiver (1980) ran the power spectral analysis used a 60 year atmospheric residence time in calculating the production rate from the residual anomolies. This may have significantly lowered the intensity of an already weak variation. Stuiver and Quay (1980) show both the production data with a 20 year residence time and with a 60 year residence time for the period around 1811-1813 when we know that solar terrestrial phenomena in general were weak. Although both data sets show a variation of the expected sign for that time, the signal is relatively suppressed for the 60 year residence time data set. However, all that can be said now is that two analyses of ^{14}C data disagree. Until that disagreement is resolved we can not come to any conclusion concerning the existence of a long period variation in the properties of the heliospheric solar wind that modulate atmospheric ^{14}C.

The situation is quite different for proxies of the solar wind at earth. Here there is no conflict of results. Swedish auroras and geomagnetic activity are easily consistent with a long period, and they agree with each other in phase, i. e. the minimums are about 87 years apart. The medieval auroras form a long enough data set so that the cycle is clearly seen in a modified superposed epoch analysis and the average amplitude during the 1,000 years from 450 A. D. to 1450 A. D. was such that more than twice the number of auroras were seen at maximums as at minimums.

Even if the controversy concerning the heliospheric solar wind were to be settled against the long cycle appearing in that data, it would not constitute any contradiction with the data on the solar wind at earth. It might imply that the solar wind had an 87 year cycle in some local property. As one example, the neutral sheet might rock relative to the ecliptic plane. However, the hypothesis of a local change is not required by the observations at this time.

It is concluded that we have definitely observed a long period variation in the solar wind at earth for at least 1,000 years and probably 1,500.

The existence of a Long Cycle expressed in auroral frequency would not necessarily be obvious to individual observers. Fig. 9 shows that the slower changes, such as those associated with the medieval maximum can be much larger than those of the 87 year type. Furthermore, the minimums and maximums are separated by forty years and few people are likely to keep records that long. Even when auroras are the subject of much interest and speculation, changes on that time scale are likely to be discounted. For example, space sciences graduate students of the 1970's may well have taken their professor's descriptions of the magnificent auroras of 1935-1959 with a grain of salt.

ACKNOWLEDGMENTS

REFERENCES

Creer, K. M. Long period geomagnetic secular variations since 12,000 yr. B.P. Nature, 292, 208, 1981.

Crooker, N. U., J. Feynman, J. Gosling, On the high correlation between long-term averages of solar wind speed and geomagnetic activity., J. Geophys. Res. 82, 1933, 1977.

Eddy, John A., The Maunder minimum, Science, 192, 1189, 1976.

Feynman, J., Geomagnetic and solar wind cycles, 1900-1975, J. Geophys. Res., 87, 6153, 1982.

Feynman, J. and N. U. Crooker, The solar wind at the turn of the century, Nature, 275, 626, 1978.

Feynman, J., and S. M. Silverman, Auroral changes during the 18th and 19th centuries and their implications for the solar wind and long term variation of sunspot activity, J. Geophys. Res., 85, 2991, 1980.

Gibson, E. G., The quiet sun, NASA, SP303, U.S. Gov't Printing Office, Wash. D. C., 1973.

Gosling, J. T., J. R. Asbridge, S. J. Bame, An unusual aspect of solar wind speed variations during solar cycle 20, J. Geophys. Res., 82, 3311, 1977.

Gringaus, K. I. Average characteristics of the solar wind and its variation during the solar cycle, Solar Wind Four, H. Rosenbauer, Ed. Max-Planck-Institut fur Aeronomie, Katenburg-Lendau, West Germany, 84, 1981.

Keimatsu, M. A., A chronology of aurorae and sunspots observed in China, Korea and Japan, Ann. Sci, 13, 1, 1976.

Legrand, J. P. and P. A. Simon, Ten cycles of solar and geomagnetic activity, Solar Physics, 70, 173, 1981.

Lin, Y. C., C. Y. Fan, P. E. Damon and E. L. Wallick, Long term modulation of cosmic-ray intensity and solar activity cycle, Conference papers, 14th International Cosmic-Ray Conference, Munich, Germany, 1975.

Mayaud, P. N. A hundred year series of geomagnetic data 1868-1967, Indices aa, Storm sudden commencements, IAGA Bulletin #33, 1973.

Mayaud, P. N., Analysis of storm sudden commencements for the years 1868-1967, J. Geophys. Res. 80, 111, 1975.

Ohl, A. I. A preliminary forecast of some parameters of cycle No. 21. of the solar activity, Solnechmaya Dannyye, 9, 73, 1976.

Rubenson, R. Catalogue des Aurores Boreales observees en Suede, Kongl Svenska: Vetenskape-Akademeins Handlingar 18, 1, 216, 1882.

Sargent, H. H., A prediction for the next sunspot cycle, Conference Record of Vehicular Technology Society, 28th IEEE Vehicular Technology Conference, Denver, Co., 490, 1978.

Silverman, S. M., and J. Feynman, The changing aurora of the past three centuries, p. 407, in Exploration of the Polar Upper Atmosphere, C. S. Deehr and J. A. Holtet, eds. D. Reidel Pub. Co., 1980.

Siscoe, G. L., Evidence in the auroral record for secular solar variability, Rev. of Geophys. and Space Phys., 18, 647, 1980.

Stuiver, M., Solar variability and climate change during the current millennium, Nature, 286, 868, 1980.

Stuiver, M., and P. D. Quay, Changes in Atmospheric carbon 14 attributed to a variable sun, Science, 207, 11, 1980.

Stuiver, M., and P. D. Quay, A 1,600 year long record of solar change derived from atmospheric ^{14}C levels, Solar Physics, 74, 479, 1981.

Svalgaard, L. Geomagnetic activity: dependence on solar wind parameters, in Coronal Holes and High Speed Wind Streams, Jack B. Zirker, Ed., 1977.

Williams, G. E., Sunspot periods in the late Precambian glacial climate and solar-planetary relations, Nature, 291, 624, 1981.

Page intentionally left blank

THE MAUNDER MINIMUM AND THE CONTINUANCE OF THE SUNSPOT CYCLE

John A. Eddy
High Altitude Observatory, NCAR
Box 3000, Boulder, Colorado 80307

A number of recent reports, particularly from studies of naked-eye sunspot records from China, have challenged the reality of the Maunder Minimum and solar secular changes in general. We examine this evidence in the fuller light of other observations and modern radiocarbon analyses to reaffirm the case for real, major changes in the level of solar activity. The question of the continuance of the 11-year solar cycle is also reviewed, based on analyses of historical sunspot numbers and auroral reports. There is probable evidence for the existence of an 11-year cycle in isolated epochs in medieval time, and tantalizing suggestions of strong solar cycle of like period in the Precambrian Era, almost a billion years ago. At present, however, it seems impossible to establish whether the sunspot cycle operated, clocklike, maintaining its present phase, before about AD 1700, and possibly not before AD 1800.

Page intentionally left blank

PERIODICITIES IN THE OCCURRENCE OF AURORA
AS INDICATORS OF SOLAR VARIABILITY

Dai Nian-zu and Chen Mei-dong
Institute of the History of Natural Science
Chinese Academy of Science
Beijing, PRC

Zhang Zhen-jin   and   Michael Mendillo
Physics Department   Astronomy Department
Central China Teacher's College   Boston University
Wuhan, Hubei, PRC   Boston, MA   02215   USA

ABSTRACT

A compilation of records of the aurora observed in China from the Time of the Legends (2000 - 3000 B.C.) to the mid-18th century has been used to infer the frequencies and strengths of solar activity prior to modern times. A merging of this analysis with auroral and solar activity patterns during the last 200 years provides basically continuous information about solar activity during the last 2000 years. The results show periodicities in solar activity that contain average components with a long period ($\sim$412 years), three middle periods ($\sim$38 years, $\sim$77 years, and $\sim$130 years), and the well known short period ($\sim$11 years).

Introduction

The use of historical auroral records to infer secular and quasi-periodic variations of the sun has received considerable attention in the last decade (Eddy, 1976; Feynman and Silverman, 1980; Siscoe, 1980). In China, beginning in 1974, a comprehensive study was initiated to document the rich, but often misinterpreted, observations of auroral displays contained in ancient records from China, Korea and Japan. Some earlier attempts to describe aurorae in Japan (Matsushita, 1956) have been made, and a chronology for aurorae in the Orient was prepared by Keimatsu (1965, 1976) and used to infer that the geomagnetic dipole axis might have been inclined towards China in the 11-12th centuries A.D. (Keimatsu et al., 1968).

In preparing a chronology of auroral displays for ancient times, it is possible to confuse passages from ancient texts that deal with meteor showers, comets, meteorological phenomena, lightning, novae and even Earthquakes with entries that truly pertain to the aurora. The chronology prepared by Keimatsu (1965) appears to include a very large number of such non-auroral events. The methods required to document a reliable database of auroral records in the Orient during ancient times have been described by Dai and Chen (1980a). The preparation of a new chronology for such events (Dai and Chen, 1980b) and its use to infer solar variability (Dai and Chen, 1980c) over extended time intervals have now been completed. In this brief paper we wish to summarize a set of preliminary results that deal with the occurrence frequencies and intensities of aurora during the period 212 B.C. to 1968 A.D., and their implications for solar variability.

Analysis

Dai and Chen (1980a, b) examined ancient records of the aurora in the East and established a chronology of 929 occurrences of aurorae from the Time of the Legends (2000-3000 B.C.) to 1747 A.D. These included 585 observations recorded in China, 294 in Korea and 50 in Japan. With this chronology added to the observations between 40°-50° latitude contained in the compilation prepared by Link (1962, 1964) from Western records, Dai and Chen (1980c) prepared a combined distribution plot of the number of nights in Oriental and Occidental historical times (from 222 B.C. to 1747 A.D.) when the aurora occurred. The resultant occurrence frequency diagram for 1300 separate auroral observations from middle to lower latitudes provided basically continuous information about solar activity during the last 2000 years. Dai and Chen (1980c) established a set of selection criteria to designate a series of "upper extremal years (UEY's)" and "lower extremal years (LEY's)" from these data, following a basic assumption that the period between two successive UEY's could not be shorter than 5 years, nor longer than 18 years. Once the UEY's were determined, additional analyses were performed to characterize the strengths of these years of peak auroral activity. To do this, the past 2000 years were divided into four major auroral epochs (prior to 400 A.D., 400-1050, 1050-1750 and 1750-1968) during which the historical records of aurora were essentially consistent and comparable. Within each epoch, specific criteria were established that used occurrence rates, observing latitudes, morphology types and luminosities to assign one of seven designations for the strength of each UEY. The strength criteria established for each of the first three epochs were related to the mean sunspot numbers used to specify the UEY strengths in the modern epoch in order to arrive at a uniform and consistent scale to guage overall solar variability by the auroral UEY strength patterns. The results of this analysis appear in Figure 1.

Discussion

The results used to arrive at Figure 1 showed that during the 1967-year period from 217 B.C. to 1750 A.D., that is, during the three ancient auroral epochs defined above, there were 173 upper extremal years (UEY's) of auroral activity that can be used to define 172 separate solar activity cycles. The durations of those cycles fell between 6 and 18 years, with a mean period of 11.4 years. Statistical analyses of the 172 cycles showed that 84% had periods of 7-14 years, 55% between 10-13 years, and only a few percent with 6 or 18 year periods. The mean period of 11.4 years may therefore be taken to describe the Short Period of solar activity.

The time series of UEY strength levels given in Figure 1 show that five "First Strong Years" (designated as F-years) occurred in 103 B.C., 305 A.D., 707, 1128 and 1957. These yield separations of 408, 402, 421, 428 and 401 years, respectively. The mean value of 412 years may be taken as an estimate of the Long Period of solar activity.

In arranging the Long Periods beneath each other in Figure 2, several similarities emerge between the segments:

1)   After each F-year, there is a neighboring "Second Strong Year" (S-year). The intervals between them are 88, 95, 55, 77 and 70 years, respectively, with an average spacing of 77 years.

2) Prior to an F-year, there is a "Third Strong Year" (T-year). The spacings between the T-years and F-years are 139, 127, 113, 151 and 120 years, respectively, with an average of 130 years.

3) In examining the overall pattern in Figure 1, there are 57 peaks between 217 B.C. and 1957 A.D., corresponding to an average of one peak every 38 years. Within each of the 412 year Long Period segments in Figure 1, there are 8, 11, 9, 11 and 12 peaks, respectively, again showing that about every fourth Short Period cycle (∿11 years) becomes a local peak.

The Strength of Solar Activity
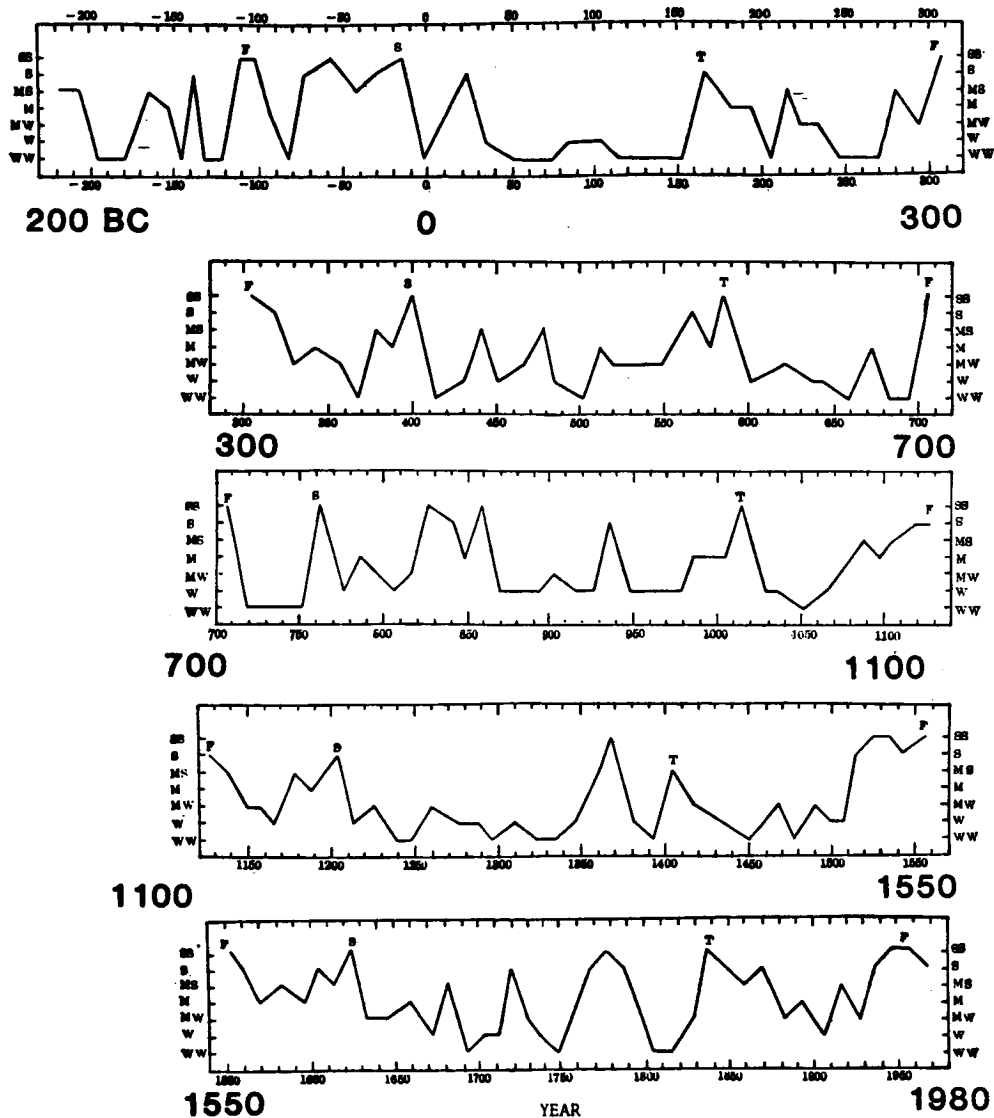
Figure 1. The strength of solar activity from 217 B.C. to 1968 A.D. determined from an analysis of chronologies of auroral occurrence patterns observed in the Orient (Dai and Chen, 1980a, b) and in Europe (Link, 1962, 1964). The strength designations from very strong (SS), to moderate (M), to very weak (WW) are intended to portray sunspot number values over the 2000 year period according to the following key: SS (>145), S (111-145), MS (96-110), M (81-95), MW (71-80), W (60-70), WW (<60).

Efforts to use historical auroral observations to search for the existence of periodicities in solar activity have thus yielded average components with a Long Period (∿412 years), three Middle Periods (∿38 years, ∿77 years and ∿130 years), and the well-known Short Period (∿11 years). Such signatures of solar-terrestrial activity patterns may well be a major source for learning about solar activity itself, as discussed in detail by Eddy (1976), Siscoe (1980), Feynman and Silverman (1980) and Feynman (1982).

References

Dai Nian-zu and Chen Mei-dong, Some views on ancient records of aurora in China, Korea and Japan, and a chronology of historical aurora data in China, Korea and Japan (in Chinese), J. Hist. Sci. Tech., 6, 56, 1980 (a).

Dai Nian-zu and Chen Mei-dong, Historical aurora data in China, Korea and Japan, from the Time of Legends to 1747 A.D. (in Chinese), J. Hist. Sci. Tech., 6, 87, 1980 (b).

Dai Nian-zu and Chen Mei-dong, Aurora and solar activities in ancient times (in Chinese), J. Hist. Sci. Tech., 6, 69, 1980 (c).

Eddy, J.A., The Maunder minimum, Science, 192, 1189, 1976.

Feynman, J., Geomagnetic and solar wind cycles, 1900-1975, J. Geophys. Res., 87, 6153, 1982.

Feynman, J., and S.M. Silverman, Auroral changes during the eigtheenth and nineteenth centuries and their implications for the solar wind and the long-term variation of sunspot activity, J. Geophys. Res., 85, 2991, 1980.

Keimatsu, M., Documentary catalogue of northern lights observed in China, Korea and Japan, College of Liberal Arts, Kanazawa University, Japan, 1965.

Keimatsu, M., A chronology of aurorae and sunspots observed in China, Korea and Japan, Ann. Sci., 13, 1, 1976.

Keimatsu, M.A., N. Fukushima and T. Nagata, Archaeoaurora and geomagnetic secular variation in historic time, J. Geomag. Geoelec., 20, 45, 1968.

Matsushita, S., Ancient aurorae seen in Japan, J. Geophys. Res., 61, 297, 1956.

Link, F., Observations et catalogue des aurores boreales apparues en Occident de 626 a 1600, Geofys. Sb., X, 297, 1962.

Link, F., Observations et catalogue des aurores boreales apparues en Occident de 1601 a 1700, Geofys. Sb., XII, 501, 1964.

Siscoe, George L., Evidence in the auroral record for secular solar variability, Rev. Geophys. Space Sci., 18, 647, 1980.
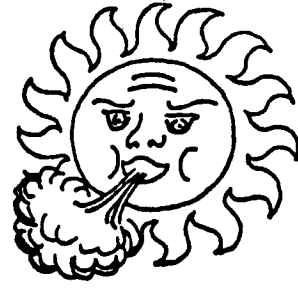
SESSION 6.

PLASMA DISTRIBUTION
FUNCTIONS AND WAVES

Page intentionally left blank

RADIAL EVOLUTION OF ION DISTRIBUTION FUNCTIONS

Eckart Marsch
Max-Planck-Institut für Aeronomie
D-3411 Katlenburg-Lindau, FRG

ABSTRACT

A survey of solar wind ion velocity distributions and derived parameters (temperature, ion differential speed, heat flux, adiabatic invariants) is presented with emphasis on the heliocentric distance range between 0.3 and 1 AU traversed by the Helios solar probe. We discuss the radial evolution of non-thermal features (e.g., $T_{p\perp} > T_{p\parallel}$, $\Delta v_{\alpha p} \cong V_A$), which are observed to be most pronounced at perihelion. Within the framework of quasilinear plasma theory, wave-particle interactions that may shape the ion distributions are considered. Some results of a self-consistent model calculation are presented accounting for ion acceleration and heating by resonant momentum and energy exchange with ion-cyclotron and magnetosonic waves propagating away from the sun along the interplanetary magnetic field. Another tentative explanation for the occurrence of large perpendicular proton temperatures is offered in terms of heating by Landau damping of lower hybrid waves.

1. Introduction

The purpose of this paper is to review some experimental and theoretical work that has recently been done on the problem of the radial evolution of solar wind ion velocity distributions. We shall concentrate on Helios observations which complement previous in situ measurements at 1 AU and at larger heliocentric distances with very detailed ion measurements in the inner heliosphere between 0.3 and 1 AU. For this radial distance range average gradients of fluid parameters are now available that put further contraints on theoretical modeling of the solar wind expansion. Our results may also help to better understand the evolution of ion internal energy and non-thermal characteristics of the distributions. To date, the most detailed reviews on this subject have been published by Feldman et al. (1974) on observations of interpenetrating solar wind streams and non-thermal distributions, by Hollweg (1974) on waves and instabilities, and by Feldman et al. (1979a, b), and Schwartz (1980) on kinetic processes and microinstabilities, respectively, that affect and shape ion distribution functions. Associated plasma waves have been reviewed by Gurnett (1981) and Scarf et al. (1981). This brief paper does not aim at a complete treatment of all relevant issues but is biased towards the author's preferences. We apologize at the outset for inevitable omissions of references. An exhaustive discussion of all topics is beyond the scope of this contribution.

2. Survey of Helios observations in the inner heliosphere

The results in this section represent a selection out of a more comprehensive data set obtained by the Helios solar probes during the phase about solar activity minimum from late 1974 until the first month of 1976. A complete dis-

cussion of the present topics can be found in a series of papers by Rosenbauer et al. (1977) and Marsch et al. (1981, 1982a, b, 1983) where a full description of the data evaluation and analysis procedure is given as well as an outline of the Helios plasma instruments and measurement techniques. The magnetic field data used in this paper have been obtained by the TU Braunschweig magnetometer experiment (Neubauer et al. 1977).

The Figure 1 illustrates the variety of shapes and range of functional forms of observed proton velocity distributions encountered under various plasma conditions between 1 AU (top row) and 0.3 AU (bottom row). The three colums pertain to low (v_p < 400 km/s), intermediate speed wind (400 - 600 km/s) and fast solar wind streams (v_p > 600 km/s). The isodensity contour plots represent cuts through the distribution in a plane defined by the magnetic field vector (dashed line, axis of gyrotropy) and bulk flow direction (VX-axis). Spacing of contours corresponds to 80, 60, 40, 20 % of the maximum phase space density which defines the origin of velocity space. The "core" part of the distributions may be defined by this continuous contour line system. Broken contours are spaced logarithmically at 0.1, 0.03, 0.01, 0.003, and 0.001 times the maximum. The last contour line roughly delineates the instrument one-count level.

Apparently, solar wind proton distributions come in various shapes and as a rule deviate considerably from a Maxwellian. Most of the non-thermal features shown here have previously been observed at 1 AU by many spacecraft. Field-aligned bulges constituting a total temperature anisotropy $T_{p\parallel} > T_{p\perp}$ and a heat flux appear to be ubiquitous (see also Hundhausen et al. 1967, Feldman et al. 1973a) with the exception at magnetic sector boundaries (distributions A and G in Figure 1) where fairly isotropic distributions usually occur. Frequently, the heat flux tail attains the shape of a second resolved peak giving rise to a double humped ion distribution (see also Feldman et al. 1973b, 1974, Goodrich and Lazarus 1976, and Belcher et al. 1981). Double streams are temporarily also observed in the alpha particle distributions (Feldman et al. 1973b, Asbridge et al. 1974, and Marsch et al. 1982b). A statistical analysis of the speed difference between two resolved proton peaks revealed a close correlation of this drift with the Alfvén speed (Asbridge et al. 1974, 1976 and Marsch et al. 1982a, b). This observation suggests a local regulation of the differential speed by wave-particle interactions.

Inspection of the right column shows that in the core part of fast solar wind velocity distributions the temperature is larger perpendicular than parallel to the magnetic field. This finding may indicate the effects of transverse wave heating (Feldman et al. 1973a, and Bame et al. 1975) and of cyclotron resonance (Marsch et al. 1982a). Further evidence for local interplanetary ion heating in the Helios data is discussed below. In fast solar wind the protons show $T_{p\perp} > T_{p\parallel}$ in the core whereas for alphas one finds $T_{\alpha\perp} \lesssim T_{\alpha\parallel}$ in the central part of the distributions (Marsch et al. 1982a). This result suggests that the processes shaping ion distributions affect the various ion species in a very different manner. We also recall that in the body of high speed streams alphas move faster than protons by about the local Alfvén speed (Asbridge et al. 1976, Marsch et al. 1982b). In summary, Helios observations yield an entire "zoo" of distribution functions exhibiting various non-thermal features that become most pronounced at perihelion (0.3 AU). The association of these diversely shaped distributions with macroscopic stream structures has been investigated by Feldman et al. (1974) and in the paper by Marsch et al. (1982a), that also contains a more
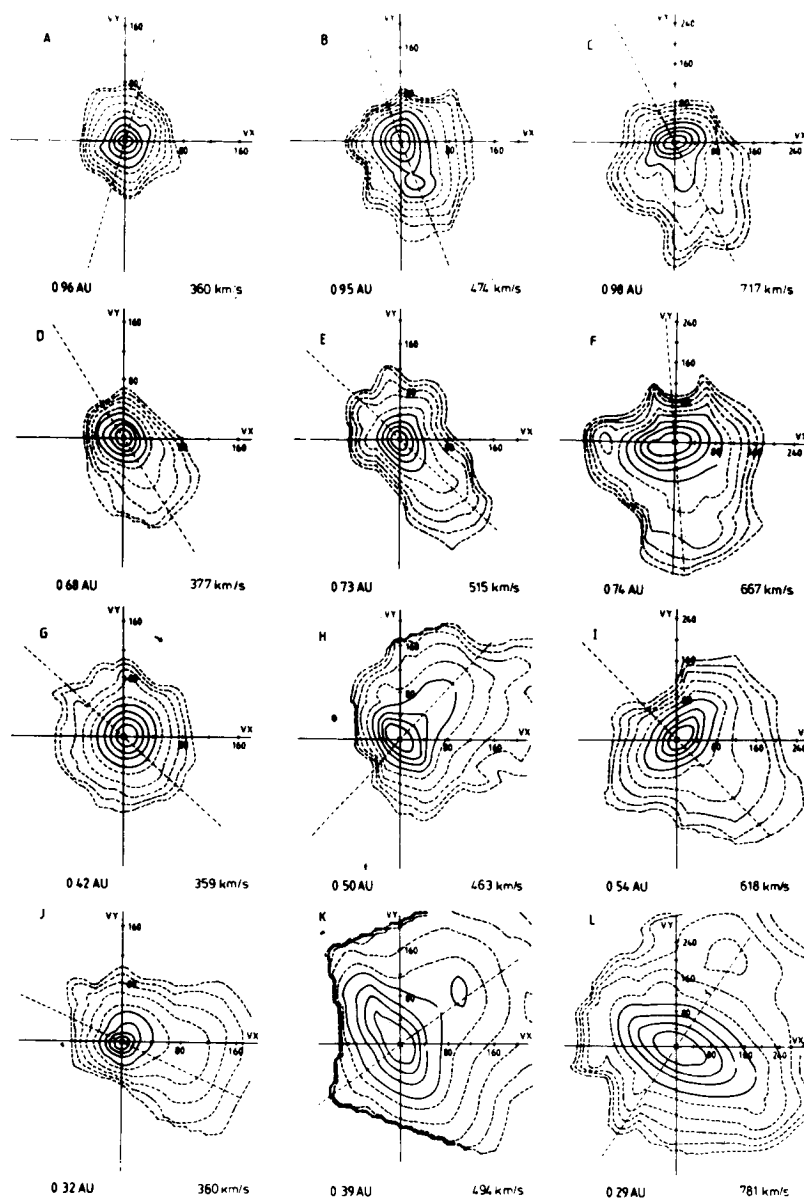
Figure 1 Helios 2 proton velocity distributions as measured for various solar
wind speeds (increasing from the left to the right-hand side) and
various radial distances (decreases from above to below). The cuts
through the three-dimensional distributions are provided in a plane
defined by the bulk velocity vector (VX-axis) and the magnetic field
vector (dashed line). Contour lines correspond to fractions 0.8, 0.6,
0.4, 0.2 of the maximum phase space density (continuous lines) and
logarithmically spaced to fractions 0.1, 0.032, 0.01, 0.0032, 0.001
(dashed lines), respectively. The origin of velocity space is defined
by the velocity of the maximum phase space density and scales are
given in km/s.

detailed discussion of double humped ion distributions and tables of relevant ion parameters. Here, we don't have space enough to discuss all these features. Therefore, in the remainder of this section we shall concentrate on the heliocentric radial temperature profiles, the so-called adiabatic invariants, and the proton heat flux density.

Before embarking on the discussion of actual data we briefly recapitulate the energy equations which are obtained for each ionic species within the framework of fluid models (Chew et al. 1956)

$$\frac{D^j}{Dt} T_{j\shortparallel} + 2T_{j\shortparallel} \; \underline{b}\cdot(\nabla_{\shortparallel}\underline{V}_j) = \frac{\partial T_{j\shortparallel}}{\partial t}\Big|_{w,c} - \frac{1}{n_j m_j} (\nabla_{\shortparallel}q_{j\shortparallel} - (q_{j\shortparallel}-2q_{j\perp}) \; \nabla_{\shortparallel} \ln B) \quad (1a)$$

$$\frac{D^j}{Dt} T_{j\perp} + T_{j\perp}(\underline{\nabla}\cdot\underline{V}_j - \underline{b}\cdot(\nabla_{\shortparallel}\underline{V}_j)) = \frac{\partial T_{j\perp}}{\partial t}\Big|_{w,c} - \frac{1}{n_j m_j} (\nabla_{\shortparallel}q_{j\perp} - 2q_{j\perp} \; \nabla_{\shortparallel} \ln B) \quad (1b)$$

Here the Boltzmann constant is $k_B = 1$, $\frac{D^j}{Dt} = \frac{\partial}{\partial t} + \underline{V}_j\cdot\underline{\nabla}$ is the species' convective derivative, and $\nabla_{\shortparallel} = \underline{b}\cdot\underline{\nabla}$ with the magnetic field unit vector $\underline{b} = \underline{B}/|\underline{B}|$. The two components of the heat flux tensor are $q_{j\shortparallel,\perp}$ defined by third order moments. If the random velocity in the species rest frame with velocity $\underline{V}_j$ is denoted by $\underline{w}$, one has $q_{j\shortparallel} = < w_{\shortparallel}^3 > n_j m_j$ and $q_{j\perp} = < w_{\shortparallel}w_{\perp}^2/2 > n_j m_j$ where brackets indicate averages over the normalized distribution function. The field aligned heat flux vector is given by $\underline{Q}_j = \underline{b} (q_{j\shortparallel} + 2q_{j\perp})/2$. The right hand sides of equation (1a, b) comprise the heat sources due to the divergence of the heat flux tensor and also contain heating or cooling rates related to Coulomb collisions or wave-particle interactions (index c, w). Without these dissipative terms one can combine the two equations with the result $\frac{D^j}{Dt} (T_{j\shortparallel} T_{j\perp}^2 / n_j^2) = 0$. By exploiting the frozen-in-field condition and the continuity equation we can also write the double-adiabatic equations of state in the usual form

$$T_{j\perp} / B = \text{const} \quad (2a)$$

$$T_{j\shortparallel} (B/n_j)^2 = \text{const} \quad (2b)$$

The validity of these equations can be tested by analyzing radial profiles of ion temperatures and densities, and the gradient of the independently measured magnetic field strength along individual stream lines. The practical difficulties encountered in an experimental test of (2a, b) and the assumptions to be made in that analysis are extensively addressed in the paper by Marsch et al. (1983). Our following discussion is based on heliocentric gradients of ion plasma parameters that have been obtained by sorting the data according to the wind speed and by averaging over radial distance bins of 0.1 AU width.

The perpendicular proton temperature $T_{p\perp}$ is shown versus radial distance from the sun in Figure 2 in a double logarithmic plot for various wind velocity

classes indicated at the curves, respectively. Within a velocity class, the temperature increases with decreasing solar distance. At a fixed radial distance, $T_{p\perp}$ increases with increasing wind speed (Burlaga and Ogilvie, 1973). Note the very high temperatures of almost 10^6 °K at perihelion. Steepest gradients are observed in fast streams. Least squares-fits yield power laws $T_{p\perp} \sim r^{-a}$ with an index "a" ranging between 0.8 and 1.2. These average radial profiles are flatter than expected for an adiabatic expansion that implies $T_{p\perp} \sim r^{-2}$ for simple spherical geometry.

This result becomes more apparent by plotting the proton magnetic moment. As can be seen in Figure 3, $T_{p\perp}/B$ increases with increasing heliocentric distance demonstrating that the magnetic moment is not conserved and that adiabatic invariance is violated. Similar curves are obtained for alphas, however in fast streams ($v_\alpha > 600$ km/s) the curves are almost horizontal. For protons least-squares fits yield $\mu_p \sim r^{-a}$ with $0.6 \leq a \leq 0.9$. This trend would be even more pronounced if the magnetic moment were solely based on the "core" distribution. We interpret Figure 3 as evidence that proton distributions are transversely heated in the interplanetary medium between 0.3 and 1 AU (see also Bame et al. 1975). A more complete discussion of heliocentric temperature profiles and adiabatic invariants of solar wind ions can be found in Marsch et al. (1982a, b, 1983). It should be mentioned that a recent analysis of Voyager plasma data at large heliocentric distances of several AU also provided evidence for a non-adiabatic evolution of the proton temperature and the occurence of interplanetary heating (Gazis and Lazarus, 1982).

In Figure 4 the second adiabatic invariant of the alphas is shown versus radial distance in the same format as before. Apparently, on the average $T_{\alpha\parallel}(B/n_\alpha)^2$ decreases during the solar wind radial expansion. Despite large scatter in the data caused by large absolute uncertainties in the measured n_α and by spatial inhomogeneities and temporal variations the radial trend in Figure 4 is believed to be statistically significant. This finding may be interpreted as evidence for a non-adiabatic evolution of $T_{\alpha\parallel}$, the alpha-particle parallel temperature. $T_{\alpha\parallel}$ seems to decline more rapidly than expected for adiabatic cooling. This result could well be related to the radial evolution of the ion differential velocity which is observed to trace the Alfvén velocity (that roughly scales like $\sim r^{-1}$) and which thus decreases during the radial expansion.

In equation (1a, b) the terms giving rise to a non-adiabatic behaviour of ion temperatures are the divergence of the heat flux tensor and Coulomb or anomalous (wave-particle interactions) collisional transfer rates for $T_{j\parallel,\perp}$. For Coulomb collisions analytic expressions for "temperature exchange" between the ions can be found in the classical article by Braginskii (1965) on collision dominated transport. Observations in slow, cold solar wind indicate the possibility of an effective coupling between the various kinetic degrees of freedom for protons and alphas by Coulomb collisions (Feldman et al. 1974b, Neugebauer 1976, Neugebauer and Feldman 1979, Grünwaldt and Rosenbauer 1978, Neugebauer 1981, Marsch et al. 1981, 1982b). High speed wind data on the other hand indicate, though, that Coulomb collisions are much less important in hot, fast solar wind streams. Without invoking wave-particle interactions under these conditions there only remain the heat flux terms as a possible source of ion thermal energy.

The Figure 5 displays the proton heat flux density $Q_p = (q_{p\parallel} + 2q_{p\perp})/2$ versus radial solar distance in a semi-logarithmic plot for various solar wind velocities. Note that the variations in Q_p extend over two orders of mag-
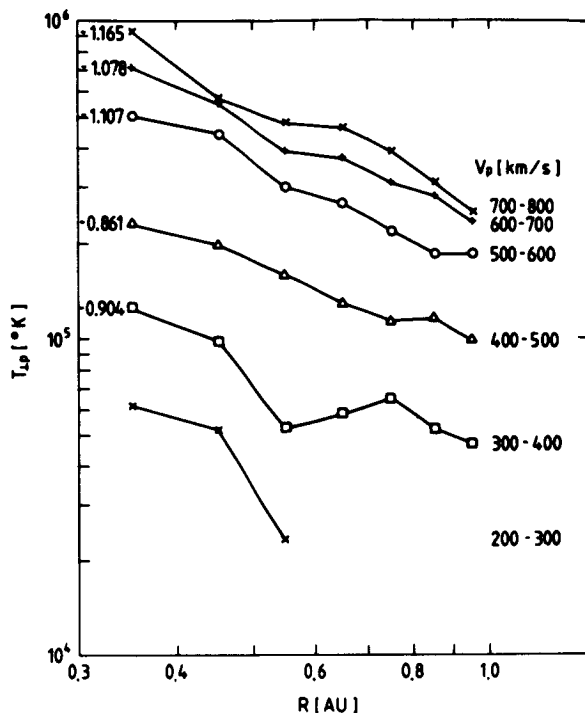
Figure 2 Average dependence of proton temperature $T_{p\perp}$ on solar radial distance for various solar wind speeds in a double logarithmic plot. Least squares fits result in a simple power law $T_{p\perp} \sim R^a$ with the index a given at the respective curves.

Figure 3 Proton magnetic moment $T_{p\perp}/B$ versus heliocentric distance for various solar wind velocities ranging from 300-400 km/s (bottom curve) up to 700-800 km/s (top curve). Points have been linearly connected to guide the eye. Error bars indicate the standard deviation of the mean within the respective bins.

Figure 4 Second adiabatic invariant $T_{\alpha\parallel}(B/n_\alpha)^2$ of alphas versus heliocentric radial distance for various solar wind velocity ranges indicated by the same symbols as in Figure 3.
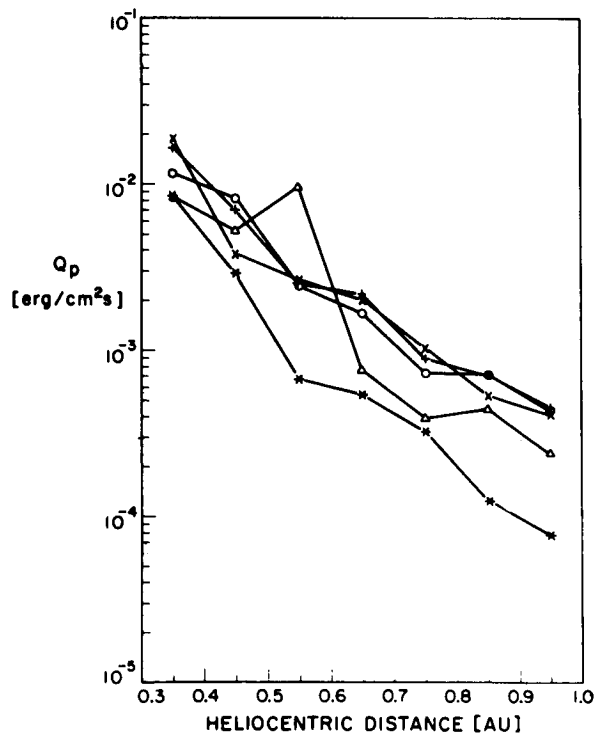
Figure 5 Heat flux density Q_p for protons versus heliocentric radial distance for various solar wind speeds indicated by the same symbols as in Figure 3. The vertical scale for Q_p is logarithmic extending over four orders of magnitude

nitude. Between 0.3 and 1 AU Q_p ranges from several 10^{-4} to about 10^{-2} ergs/cm²s. Least squares fit yield $Q_p \sim r^{-a}$ with $3.8 \leq a \leq 4.7$ and $Q_p \sim 3-4 \; 10^{-4}$ ergs/cm²s at 1 AU for intermediate and high speed solar wind. Alpha particle heat flux densities turn out to be almost an order of magnitude smaller (Marsch et al. 1983) which means that $q_{\alpha",\perp}$ can be entirely ignored in equation (1a, b). For protons one finds that $q_{p\perp}$ is much smaller than $q_{p"}$ (implying $Q_p \sim q_{p"}$). Thus in equation (1b) the terms with $q_{p\perp}$ can also be neglected. In view of these results, one needs wave-particle interactions in order to account for the radial course of the proton magnetic moment in Figure 3. This conclusion seems to be compelling if one considers the temperature anisotropy in the high speed proton distributions of Figure 1. An anisotropic local heat source $\partial T_{p\perp}/\partial t \big|_w$ in terms of wave heating should be invoked to explain this detail in proton distributions and to further explain the differences in the shapes of the alpha and proton distribution functions (Marsch et al. 1982a,b).

Concerning the parallel temperature $T_{p"}$ one can roughly estimate the strength of the interplanetary heat source represented by $- \nabla \cdot (q_{j"}b)$. By integrating this quantity over the radial heat flux profiles given by the least squares fits in Figure 5, Marsch et al. (1983) found that the temperature increase resulting from a degradation of the heat flux cannot account for the non-adiabatic radial evolution of the proton temperatures. For the alphas the result of Figure 4 even suggests the need for an interplanetary heat "sink" or effective redistribution of thermal energy in order to explain the stronger than adiabatic cooling of $T_{\alpha"}$ between 0.3 and 1 AU.

We conclude with a presentation of Helios 2 data that pertain to the phase of the solar cycle inclining to solar maximum. In contrast to the typical solar minimum pla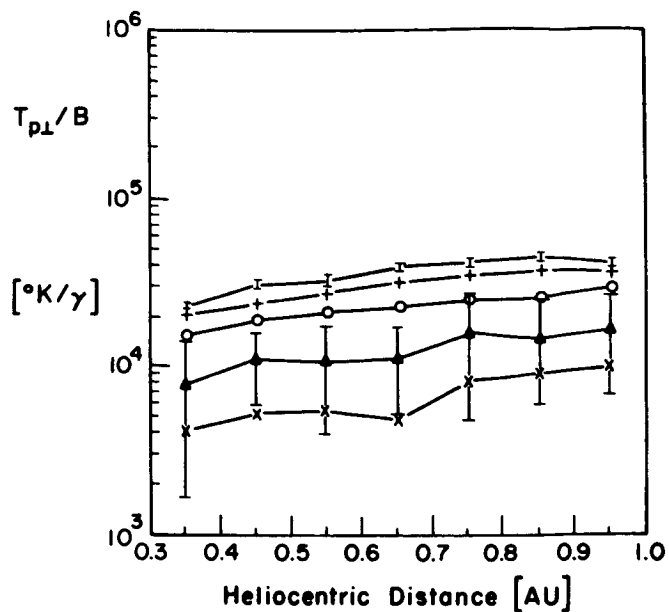sma conditions, during a few hours on day 117 in May 1978 in the perihelion at 0.3 slow solar wind was observed associated with pronounced ion differential speeds ($\Delta V_{\alpha p} \sim 100$ km/s) and temperature anisotropies ($T_{p\perp} > T_{p"}$) and with unusually intense Alfvénic type wave activity (Marsch et al. 1981). Figure 6 shows from top to bottom proton speed, ion differential speed (Alfvén speed is indicated by points), the dot product of $\Delta V_{\alpha p}$ and $\underline{B}$, and the proton and alpha temperature anisotropies $T_{j"}/T_{j\perp}$. The core temperature ratio is marked by points. Note the low wind velocity. It stays low at about 400 km/s despite large Alfvénic-type velocity fluctuations. Simultaneously, the alphas move faster than the protons by more than 100 km/s. They move at about the local Alfvén speed along the interplanetary magnetic field (panel three). In the core part of the proton distribution one finds $T_{p\perp} > T_{p"}$ whereas for the alphas the reversed situation occurs. Despite large scatter in the data due to worse counting statistics, on the average $T_{\alpha\perp} \leq T_{\alpha"}$ is observed. These contrary features have earlier been found to be characteristic of distributions in fast recurrent streams as discussed in Figure 1. In our opinion, this result is a key observation towards understanding the mechanism of solar wind heating and acceleration. Obviously, these ion distributions exhibited properties that have been considered typical of high speed wind originating from coronal holes during solar activity minimum. However, the unusual plasma investigated here was embedded in "normal", low speed wind. The ambient plasma showed the typical signatures of slow wind as discussed in the beginning of this section.
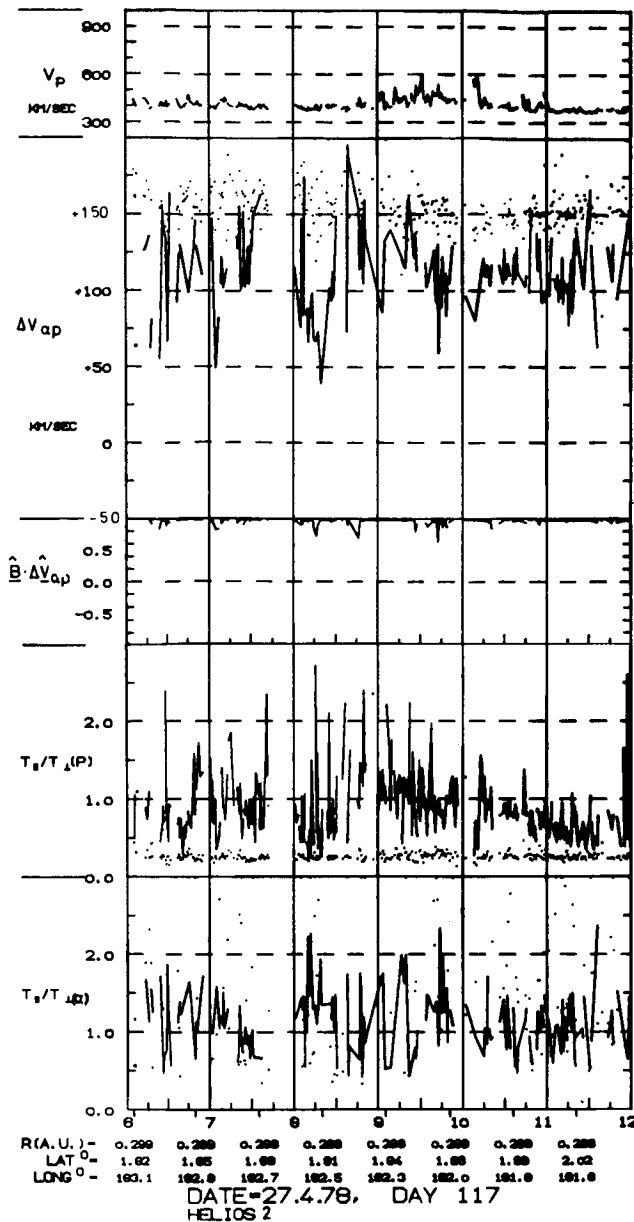
Figure 6

Six hours of Helios 2 ion data from day 117 in 1978, measured at 0.29 AU. Reading from above, the proton bulk speed, the ion differential speed (and indicated by points in the same panel, the local Alfvén speed), the cosine of the spatial angle between $\Delta v_{\alpha p}$ and the magnetic field $\underline{B}$, and finally, in the lowest panels, the proton and helium ion total temperature anisotropies are shown (the core anisotropy is marked by points).

3. Theoretical models and discussion

Certainly, the radial evolution of the detailed solar wind ion distributions cannot be explained within the framework of magnetohydrodynamic fluid theories but rather requires a kinetic treatment. Such an approach to the problem has yet not been tried. However, a vast amount of literature exists concerned with analysing the stability of distributions observed in the interplanetary medium. A comprehensive review on microinstabilities is given by Schwartz (1980) and on various kinetic aspects by Feldman (1979 a, b). A theoretical discussion of wave-particle interactions with emphasis on MHD-waves is also included in Barnes' (1979) review on wave turbulence in the solar wind.

362

In instability calculations particle distributions are shown to relax "locally" to a state that corresponds to less free energy than the original state. Reordering of internal ion energy is accompanied by excitation of various wave modes where growth time and dispersion characteristics sensitively depend on the shape of the actual distribution. As demonstrated in Figure 1, the main free energy sources for local wave excitation are represented by temperature aniso-tropies, heat fluxes and double streams, and also by the differential proton alpha-particle motion that was discussed in some detail before. Instability cal-culations have been performed for given this free energy in non-thermal ion distributions. However, no attempt has yet been made to explain, e.g. double ion streams in the first place by dynamic processes in the corona or during the initial phase of solar wind expansion. Feldman et al. (1974) proposed conceptual models in terms of double ion streams originating from time variations in the corona or from the interpenetration of fast into slow ambient plasma. However, these ideas are highly speculative and at present very little is understood con-cerning the origin of non-thermal features of ion distributions.

Goodrich (1981) investigated the kinetic effects of Alfvén wave pressure on the ion distributions. By solving the relevant diffusion equation he could show that the kinetic nature of Alfvén wave-particle interaction is reflected in distortions of the distribution function that give rise to well known fluid results like bulk acceleration. However, these model calculations are far from accounting for the detailed shape of the observed distributions. Modeling the radial evolution of ion distributions in terms of convected Bi-Maxwellians re-presents an intermediate step between a fluid and fully kinetic treatment. Namely, by calculating the temperatures and speeds relative to the solar wind frame one readily knows the structure of the distribution functions that are entirely specified in terms of their moments. Such model assumptions have almost universally been adopted for plasma instability calculations.

Along these lines Marsch et al. (1982c) have developed a self consistent fluid-type model in order to explain the ion temperature anisotropies and differ-ential speeds by means of wave heating and acceleration of solar wind ions by cyclotron resonance with ion-cyclotron and magnetosonic waves propagating away from the sun along the interplanetary magnetic field. Local temperature and momentum transfer terms based on the quasilinear expressions for wave-particle interactions in weak electromagnetic turbulence (see also Dusenbery and Hollweg, 1981, and McKenzie and Marsch, 1982) have been employed in the fluid equations. It was shown by Marsch et al. (1982c) that the magnetosonic waves are capable of accelerating the minor ions to differential speeds of the order of the local Alfvén speed. Furthermore, it was demonstrated that interaction with ion-cyclo-tron waves can lead to an equalization of ion thermal velocities and the observed anisotropy of proton temperatures in close qualitative accord with the obser-vations.

However, the required wave intensity exceeds the values observed (at 0.3 AU) by at least one order of magnitude, which is a serious problem all theories are faced with that rely on resonant wave-particle interactions at about the ion gyro-frequencies (Schwartz et al., 1981). This problem might be circumvented by invoking a cascade process from the low frequency Alfvén waves to the resonant frequency regime (Isenberg and Hollweg, 1982) in order to replenish the intensity at higher frequencies. Still, the physics of tapping the energy reservoir of Alfvén waves by a cascade remains rather obscured. In addition, the assumption of rigid model

distributions in the quasilinear expressions represents another problem since the plasma may in reality not conform to these model constraints simply by changing the shape of the distribution function. This effect can be crucial in case the interactions take place in the tails of the distribution. Using real distribution functions measured on Helios, Dum et al. (1980) showed that for the ion acoustic mode and whistlers the growth and damping characteristics depend rather meticulously on the detailed shape of the particle distributions. At present a fully kinetic treatment of the problem is still lacking, although it appears to be needed for an explanation of the radial evolution of ion distribution functions.

Finally, we briefly mention an alternative explanation of the large perpendicular ion temperatures in terms of Landau damping of lower hybrid waves. Marsch and Chang (1983) have demonstrated that the broad band low frequency electrostatic noise frequently observed in the disturbed solar wind at interplanetary shocks (Coroniti et al., 1982; Kennel et al., 1982) and in high speed solar wind streams (Beinroth and Neubauer, 1981, and Gurnett et al., 1979) may generally have a lower hybrid component. These modes accompanied by "hybrid-like" whistler waves can be excited by resonant halo electrons in the heat flux tail of the electron distribution (Rosenbauer et al., 1977; Feldman et al., 1981). Model calculations based on convected Bi-Maxwellian electron distributions (Marsch and Chang, 1983) have shown that electromagnetic lower hybrid waves at several $\omega_{LH} = \sqrt{|\Omega_e \Omega_i|}$ since these can energize solar wind ions transverse to the magnetic field, waves propagate almost perpendicularly. By means of Landau damping of lower hybrid waves the proton distributions could thus attain large perpendicular temperatures in the core. Furthermore, the effective coupling between protons and suprathermal electrons, being simultaneously in Landau resonance with the waves, should be of major importance for understanding solar wind transport and the regulation of the electron heat flux.

4. Conclusions

In this paper we have discussed some selected aspects of the radial evolution of ion velocity distributions that exhibited collisional and collision-less behaviour. In slow, cold, and dense solar wind there is evidence for a collisional redistribution of internal ion energy (see also review by Neugebauer, 1981). In contrast, high speed ion distributions indicate significant influence of waves that render the solar wind expansion non-adiabatic. Various processes shaping ion distributions by means of microinstabilities and models that attempt to describe the radial evolution of internal ion energy have been proposed in the literature. Two basic lines, that a theoretical description of the solar wind expansion in principle could follow, are sketched in Figure 7. The standard fluid approach has widely been used in many theoretical papers at this conference (see also the "SW4" review by Cuperman, 1981). However, very little work has been done in terms of kinetic equations (Griffel and Davis, 1969, and Eviatar and Schulz, 1970) that are solely appropiate to describe the radial evolution of detailed ion distributions and internal energy and to take dissipation properly into account. At present, observational knowledge is far ahead of a coherent theoretical understanding of solar wind microprocesses and transport. Therefore, a kinetic description of solar wind ions that incorporates collisions and wave-particle interactions is urgently required.

VLASOV EQUATION FOR EACH SPECIES IN A
MULTI-COMPONENT PLASMA

FULL OR REDUCED
DISTRIBUTION FUNCTIONS

MOMENTS

| KINETIC EQUATIONS |
| MICRO + MACRO SCALES |

| FLUID EQUATIONS |
| MACRO-SCALES |

$+$

HYBRID EQUATIONS
IN TERMS OF MOMENTS
OF MODEL DISTRIBUTIONS
"DRIFTING BI-MAXWELLIANS"

$+$

COULOMB COLLISIONS
$+$
WAVE PARTICLE INTERACTIONS
IN TERMS OF "QUASILINEAR
DIFFUSION OPERATORS"
$+$
CHOICE OF PROPER FRAME, PHASESPACE,
AND GLOBAL BOUNDARY CONDITIONS

EVOLUTION OF

— DETAILED PARTICLE DISTRIBUTION
FUNCTIONS

— FLUCTUATING FIELD SPECTRA AND
PLASMA MICROINSTABILITIES

COLLISIONS
$+$
MHD-WAVE TERMS

$+$

ADDITIONAL ENERGY
AND MOMENTUM

STANDARD SINGLE
OR MULTI-FLUID
DESCRIPTION OF THE
SOLAR WIND

Figure 7 Schematic sketch of two possible basic approaches to a theoretical description of the solar wind expansion.

References

Asbridge, J. R., S. J. Bame, and W. C. Feldman: Abundance differences in solar wind double streams. Solar Phys. 37, 451, 1974.

Asbridge, J. R., S. J. Bame, W. C. Feldman, and M. D. Montgomery: Helium and Hydrogen Velocity Differences in the Solar Wind. J. Geophys. Res. 81, 2719, 1976.

Bame, S. J., J. R. Asbridge, W. C. Feldman, S. P. Gary, and M. D. Montgomery: Evidence for local ion heating in solar wind high speed streams. Geophys. Res. Lett. 9, 373, 1975.

Barnes, A.: Hydromagnetic waves and turbulence in the solar wind. In "Solar System Plasma Physics", Twentieth Anniversary Review, edited by C. F. Kennel, L. J. Lanzerotti, and E. N. Parker, North-Holland, Amsterdam, 1979.

Beinroth, H. J., and F. M. Neubauer: Properties of whistler-mode waves between 0.3 and 1 AU from Helios observations. J. Geophys. Res. 86, 7755, 1981.

Belcher, J. W., H. S. Bridge, A. J. Lazarus, and J. D. Sullivan: Preliminary results from the Voyager Solar Wind Experiment. In "Solar Wind 4", H. Rosenbauer, ed., MPAE-W-100-81-31, Report of the Max-Planck-Institut für Aeronomie, F. R. Germany, 1981.

Burlaga, L. F., and K. W. Ogilvie: Solar wind temperature and speed. J. Geophys. Res. 78, 2028, 1973.

Braginskii, S. I.: Transport Processes in Plasma. In "Reviews of Plasma Physics", Vol. 1, M. A. Leontovich editor, Consultants Bureau, New York, 1965.

Chew, G. F., M. L. Goldberger, and F. E. Low: The Boltzmann Equation and the One-Fluid Hydromagnetic Equations in the Absence of Particle Collisions. Proc. Roy. Soc., A236, 112, 1956.

Coroniti, F. V., C. F. Kennel, F. L. Scarf, and E. J. Smith: Whistler mode turbulence in the disturbed solar wind. J. Geophys. Res. 87, 6029, 1982.

Cuperman, S.: Solar wind models. In "Solar Wind 4", editor H. Rosenbauer, MPAE-W-100-81-31, Report of the Max-Planck-Institut für Aeronomie, F. R. Germany, 1981.

Dum, C. T., E. Marsch, W. G. Pilipp: Determination of wave growth from measured distribution functions and transport theory. J. Plasma Physics 23, 91, 1980.

Dusenbery, P. B., and J. V. Hollweg: Ion Cyclotron Heating and Acceleration of Solar Wind Minor Ions. J. Geophys. Res. 86, 153, 1981.

Eviatar, A., and M. Schulz: Ion-temperature anisotropies and the structure of the solar wind. Planet. Space Sci. 18, 321, 1970.

Feldman, W. C., J. R. Asbridge, S. J. Bame, and M. D. Montgomery: On the origin of solar wind proton thermal anisotropy. J. Geophys. Res. 28, 6451, 1973a.

Feldman, W. C., J. R. Asbridge, S. J. Bame, and M. D. Montgomery: Double Ion Streams in the Solar Wind. J. Geophys. Res. 78, 2017, 1973b.

Feldman, W. C., J. R. Asbridge, S. J. Bame, and M. D. Montgomery: Interpenetrating Solar Wind Streams. Rev. Geophys. Space Phys. 4, 715, 1974a.

Feldman, W. C., J. R. Asbridge, and S. J. Bame, Solar wind He^{2+} to H^{+} temperature ratio, J. Geophys. Res. 79, 2319, 1974b.

Feldman, W. C.: Solar wind plasma processes and transport. Rev. Geophys. Space Phys. 7, 1743, 1979a.

Feldman, W. C.: Kinetic processes in the solar wind. In "Solar System Plasma Physics", Twentieth Anniversary Review, edited by C. F. Kennel, L. J. Lanzerotti, E. N. Parker, North-Holland, Amsterdam, 1979b.

Feldman, W. C.: Electron characteristics in high speed solar wind. In "Solar Wind 4", H. Rosenbauer, editor, MPAE-W-100-81-31, Report of the Max-Planck-Institut für Aeronomie, F. R. Germany, 1981.

Gazis, P. R., and A. J. Lazarus: Voyager Observations of Solar Wind Temperature 1-10 AU. Geophys. Res. Lett., 9, 431, 1982.

Goodrich, C. C., and A. J. Lazarus: Suprathermal Protons in the Interplanetary Solar Wind. J. Geophys. Res. 81, 2750, 1976.

Goodrich, C. C.: The kinetic effects of Alfvén wave pressure in the solar wind. In "Solar Wind 4", H. Rosenbauer, editor, MPAE-W-100-81-31, Report of the Max-Planck-Institut für Aeronomie, F. R. Germany, 1981.

Griffel, D. H., and L. Davis: The anisotropy of the solar wind. Planet. Space Sci. 17, 1009, 1969.

Grünwaldt, H., and H. Rosenbauer: Study of Helium and Hydrogen velocity differences as derived from HEOS-2 S210 solar wind measurements. Proceedings of Second European Solar Meeting, Centre National de la Recherche Scientifique, Toulouse, France, 1978.

Gurnett, D. A., E. Marsch, W. Pilipp, R. Schwenn, and H. Rosenbauer: Ion-acoustic waves and related plasma observations in the solar wind. J. Geophys. Res. 84, 2029, 1979.

Gurnett, D. A.: Plasma waves in the solar wind: A review of observations. In "Solar Wind 4", H. Rosenbauer, editor, MPAE-W-100-81-31, Report of the Max-Planck-Institut für Aeronomie, F. R. Germany, 1981.

Hollweg, J. V.: Waves and Instabilities in the solar wind. Rev. Geophys. Space Phys. 13, 263, 1974.

Hundhausen, A. J., S. J. Bame, and N. F. Ness: Solar wind thermal anisotropies: Vela 3 and Imp 3. J. Geophys. Res. 72, 5265, 1967.

Isenberg, P. A., and J. Hollweg: On the preferential acceleration and heating of solar wind heavy ions. Submitted to J. Geophys. Res., 1982.

Kennel, C. F., F. L. Scarf, and F. V. Coroniti: Non-local plasma turbulence associated with interplanetary shocks. J. Geophys. Res. 87, 17, 1982.

Marsch, E., K. H. Mühlhäuser, H. Rosenbauer, R. Schwenn, and K. U. Denskat: Pronounced proton core temperature anisotropy, ion differential speed, and simultaneous Alfvén wave activity in slow solar wind at 0.3 AU. J. Geophys. Res. 86, 9199, 1981.

Marsch, E., K. H. Mühlhäuser, R. Schwenn, H. Rosenbauer, W. Pilipp, F. M. Neubauer: Solar Wind Protons: Three-Dimensional Velocity Distributions and Derived Plasma Parameters Measured Between 0.3 and 1 AU. J. Geophys. Res. 87, 52, 1982a.

Marsch, E., K. H. Mühlhäuser, H. Rosenbauer, R. Schwenn, F. M. Neubauer: Solar Wind Helium Ions: Observations of the Helios Solar Probes Between 0.3 and 1 AU. J. Geophys. Res. 87, 35, 1982b.

Marsch, E., C. K. Goertz, K. Richter: Wave Heating and Acceleration of Solar Wind Ions by Cyclotron Resonance. J. Geophys. Res. 87, 5030, 1982c.

Marsch, E., and T. Chang: Lower hybrid waves in the solar wind. Geophys. Res. Lett. 9, 1155, 1982 .

Marsch, E., K. H. Mühlhäuser, H. Rosenbauer, R. Schwenn: On the Equation of State of solar wind ions derived from Helios measurements. In press, J. Geophys. Res., 1983.

Marsch, E., and T. Chang: Electromagnetic lower hybrid waves in the solar wind. Submitted to J. Geophys. Res., 1983.

McKenzie, J. F., and E. Marsch: Resonant wave acceleration of minor ions in the solar wind. Astrophys. Space Sci. 81, 295, 1982.

Neubauer, F. M., G. Musmann, and G. Dehmel: Fast Magnetic Fluctuations in the Solar Wind: Helios 1. J. Geophys. Res. 82, 3201, 1977.

Neugebauer, M.: The role of Coulomb collisions in limiting differential flow and temperature differences in the solar wind. J. Geophys. Res. 81, 78, 1976.

Neugebauer, M., and W. C. Feldman: Relation between superheating and superacceleration of Helium in the solar wind. Solar Phys. 63, 201, 1979.

Neugebauer, M.: Observations of Solar Wind Helium. Fundamentals of Cosmic Physics 7, 131, 1981.

Rosenbauer, H., R. Schwenn, E. Marsch, B. Meyer, H. Miggenrider, M. D. Montgomery, K. H. Mühlhäuser, W. Pilipp, W. Voges, and S. M. Zink: A Survey of Initial Results of the Helios Plasma Experiment. J. Geophys. 42, 561, 1977.

Scarf, F. L., D. A. Gurnett, and W. S. Kurth: The first year of Voyager plasma wave observations in the solar wind. In "Solar Wind 4", H. Rosenbauer, editor, MPAE-W-100-81-31, Report of the Max-Planck-Institut für Aeronomie, Katlenburg-Lindau, F. R. Germany, 1981.

Schwartz, S. J.: Plasma Instabilities in the Solar Wind: A Theoretical Review. Rev. Geophys. Space Phys. 18, 313, 1980.

Schwartz, S. J., W. C. Feldman, and S. P. Gary: The source of proton anisotropy in the high-speed solar wind. J. Geophys. Res. 86, 541, 1981.

Page intentionally left blank

ELECTROSTATIC WAVES AND ANOMALOUS TRANSPORT IN THE SOLAR WIND

C.T. Dum

Max-Planck-Institut für Physik und Astrophysik
Institut für extraterrestrische Physik
D-8046 Garching, F.R.G.

ABSTRACT

In situ measurements of fluctuation spectra and particle distribution functions have now been carried out throughout interplanetary space. The link between these observations is established by theories of wave-particle interaction. Linear instability analysis for the actual non-Maxwellian particle distribution functions and an examination of the velocity dependence of microscopic diffusion coefficients form the basis of such an investigation. It is described in more detail for the short wavelength, ion acoustic like turbulence which is found by linear instability analysis to correspond to the observed electrostatic fluctuations. Of the transport processes associated with these fluctuations, electron heat conduction and electron-ion energy transfer are of particular importance for macroscopic solar wind expansion. These effects are studied with the aid of an anomalous transport theory. This theory (Dum, 1978 a, b) is based on the dominance of elastic scattering of electrons by fluctuations, similar to (enhanced) electron-ion collisions. It has a much wider range of applicability than classical transport theory, which assumes dominance of Coulomb collisions for elastic and inelastic scattering. Nevertheless, a substantial fraction of the heat flux is often carried by strongly anisotropic electrons of elevated energy (Strahl) which should be handled by a nonlocal transport theory, describing the modification of exospheric (collisionless) expansion by residual scattering and the enhancement of the ambipolar electric field by anomalous momentum transfer.

Solar Wind Models and Breakdown of Classical Transport Theory

The solar wind like most plasmas we encounter is both turbulent and nearly collisionless. Macroscopic studies may point to the importance and direction for modifications of classical transport theory but, due to the interdependence of many parameters and the uncertainty of coronal boundary conditions, generally allow no unique conclusions on the underlying microscopic physics (Hundhausen, 1972, p.81). The rationale and some principal results from microscopic studies that make direct use of the detailed in situ measurements available now for the interplanetary solar wind are outlined in the following.

The need for a modification of classical transport theory as applied to solar wind expansion was recognized at an early stage of theoretical development. (For a review see Hundhausen, 1972.) According to one-fluid theory of radial expansion

$$r^{-2} \frac{d}{dr} r^2 \rho u \left[\frac{u^2}{2} + \frac{5}{2} \frac{p}{\rho} - \frac{GM_o}{r}\right] = -r^{-2} \frac{d}{dr} r^2 q \tag{1}$$

where ρ is the mass density, p the pressure, u the speed and the last term in the bracket is the gravitational potential, the heat flux q provides the major internal source term to which external sources due to hydrodynamic waves propagating beyond the corona may be added. The heat flux predicted by classical transport theory, however, was much too large to fit observations at 1 AU. Various ad hoc

reductions have been introduced to allow for a more efficient conversion of thermal energy into kinetic energy of expansion. Heat flux is dominated by electrons. Two fluid models, however, brought even more problems. Not only were electron temperatures too high, but ion temperatures were an order of magnitude too low to fit observations at 1 AU. Again, the way out appeared to be an ad hoc increase in the electron-ion energy transfer rate. Both modifications have been carried out in a number of different ways. The introduction of "fudge factors" in the classical transport relations may be interpreted in terms of an increase in the effective collision frequency, typically by a factor of 10-100 over the frequency of Coulomb collisions, which arises presumably by scattering from enhanced fluctuations. Anomalous transport with even larger increases in the effective collision frequency is of course by now a well established fact for many space and laboratory plasmas. It was also recognized very early that solar wind expansion may in turn provide the free energy source for enhanced fluctuations. In fact, the various two fluid models themselves imply the onset of microinstabilities already at heliocentric distances ranging from 3-11 solar radii, using the skewed electron distribution function corresponding to classical heat flux (Forslund, 1970; Singer and Roxburgh, 1977).

Fluid models also imply total breakdown of classical collision dominated transport at about the same heliocentric distances even without account of instabilities, especially for rapidly diverging non-radial flow geometries (Durney and Pneuman, 1975). Clearly, heat flux must remain limited as the plasma becomes nearly collisionless,

$$\hat{q}_e \equiv q_e / (nmv_e)^3 = - \varkappa_T \lambda_{ei} \nabla_{\shortparallel} \ln T_e < \alpha_q , \qquad (2)$$

where n is the electron density, $v_e = (T_e/m)^{1/2}$ the electron thermal velocity, $\lambda_{ei} = v_e \tau_{ei} \propto (T_e^2/n)$ the mean free path for collisions of thermal electrons with ions, $L_T = (\nabla_{\shortparallel} \ln T_e)^{-1}$ the temperature gradient scale along the magnetic field and $\varkappa_T$ a dimensionless heat conductivity which depends on the ion charge Z as electron-electron collisions with collision time $\tau_{ee} = Z\tau_{ei}$ try to restore a Maxwellian distribution. For protons, Z=1, $\varkappa_T = 3.16$ in the normalization of Braginskii (1967) for τ_{ei}. The classical (first) relation holds for $(\lambda_{ei}/L_T) \ll 1$ and $\alpha_q = O(1)$ corresponds to free streaming. Variations of $\hat{q}_e$ and λ_{ei}/L_T between 0.1 and 1 are typical for the interplanetary solar wind. The shape of the electron distribution is strongly non-Maxwellian in this case, consisting of a nearly isotropic core and a hotter low density halo which may be considered collisionless and may be strongly anisotropic (e.g. Feldman et al., 1975, 1979; Ogilvie and Scudder, 1978; Pilipp et al., 1981).

The normalized heat flux $\hat{q}_e$ depends only on the shape of the electron distribution, or more precisely the isotropic part f_0 and the l=1 anisotropy f_1/f_0

$$\hat{q}_e = \int_0^\infty dx \frac{8\pi}{3} f_0 \frac{f_1}{f_0} x^2 \qquad (3)$$

where $x = mv^2/2T_e$, $f_1(x) = (3/2) \int_{-1}^{+1} d\cos\theta \, f(x,\theta)\cos\theta$. The replacement $x^2 \rightarrow x$ in (3) gives $\langle v_{\shortparallel}/v_e \rangle$. For the electron rest frame to be used here, $\langle v_{\shortparallel}/v_e \rangle = 0$ thus implies $f_1 < 0$ at lower energies.

Classical transport theory assumes the dominance of Coulomb collisions, leading to a nearly Maxwellian, $f_0 = f_M = (2\pi)^{-3/2} e^{-x}$, and weakly anisotropic distribution, with f_1/f_M proportional to λ_{ei}/L_T or the parameter $(B_T/Z) = (8/3)(2/\pi)^{1/2} \lambda_{ei}/L_T$ of Spitzer and Härm (1953). As the collision frequency for large speeds de-

creases as v^{-3} these assumptions must break down at some speed v_c. This is signaled by an ever increasing anisotropy (see Fig. 1).
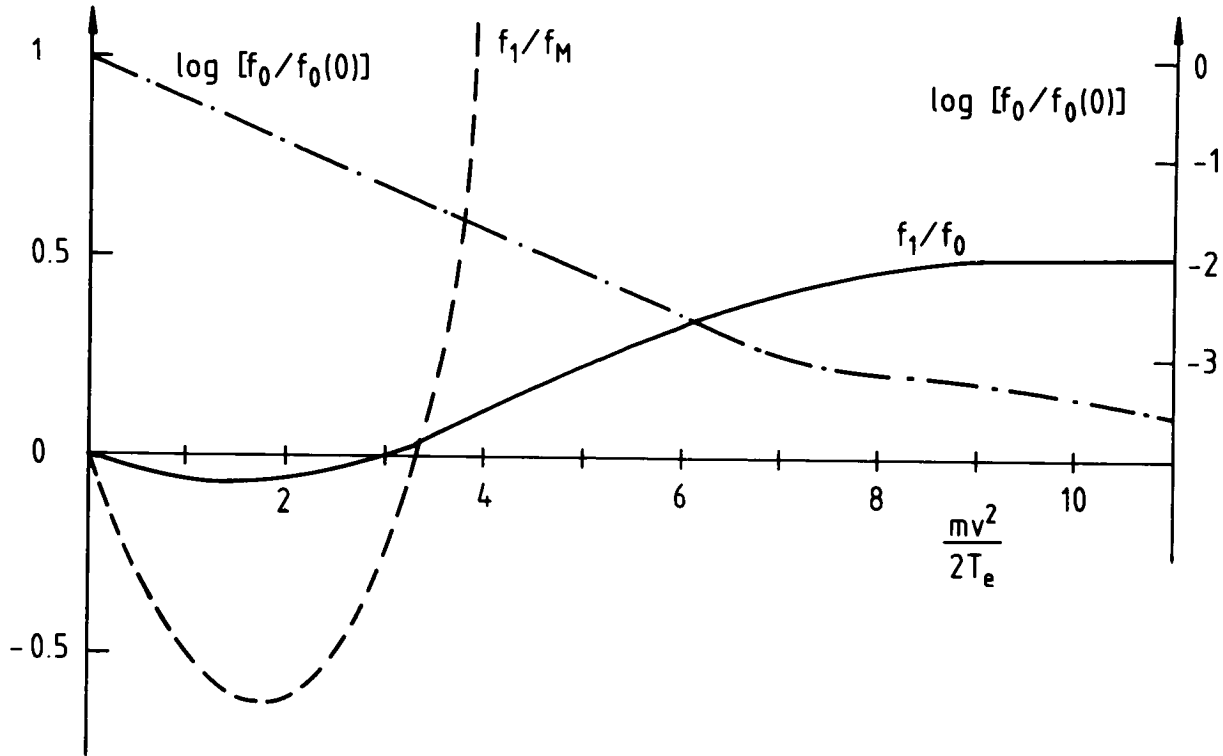

Figure 1. Heat flux limitation for weakly collisional electrons. Shown are (schematically): (a) the isotropic part (-.-.-) f_0 of the distribution $f(\underline{v})$ exhibiting core and halo, (b) the 1 = 1 component (-) $f_1(v)$, which determines the return current of low energy electrons ($f_1 \lesssim 0$) and the heat flux, due mostly to strongly anisotropic high energy electrons. Also shown is $f_1/f_M \propto \lambda_{ee}/L_T$ (---, f_M Maxwellian) predicted by classical transport theory e.g. for $\lambda_{ee}/L_T = 0.32$ ($\lambda_{ee} = \lambda_{ei}$ mean free path for thermal electrons, L_T temperature gradient scale), demonstrating total breakdown of this local theory.

A generous condition for the applicability of the classical transport relation in (2) may be found from the requirement that 90% of the predicted heat flux (3) should arise from the population $v < v_c$. This gives $x_c = 9$ for the Spitzer-Härm distribution. Assuming that the validity of the theory can be streched to $|f_1/f_M| < 1$ gives then the remarkable small values, $\lambda_{ei}/L_T < 10^{-2}$, $\hat{q}_e < 0.03$. Because breakdown is rapid (f_1/f_M) = $O(x^3)$, even more generous criteria give similar results, see Gray and Kilkenny (1980). For the commonly assumed limit of validity, $\lambda_{ei}/L_T = 1$ we obtain $x_c = 1/2$ for $|f_1/f_M| < 1$, corresponding to a population $x < x_c$ which carries a negligible portion of the heat flux.

In contrast to the predictions of classical transport theory, $|f_1/f_0| < 3$ by definition of the 1 = 0,1 components for any $f(\underline{v})$. For other physical situations, e.g. neutron transport and laser heated plasmas where one has the same problem of scale lengths comparable to the mean free path, ad hoc microscopic flux limits $|f_1/f_0| < \alpha_f$ have long been introduced in order to salvage diffusive transport theory. The usual limitation, $\alpha_f \leq 1$ simply comes from the requirement $f = f_0 + f_1 \cos\theta > 0$ and ignores the fact that $\lambda_{ei}/L_T = 0$ (1) also implies significant terms

$1 \geq 2$ in a Legendre expansion of $f(v, \cos\theta)$. The level at which f_1/f_0 saturates is not a universal constant but determined by the nearly scatter free motion of energetic electrons in the global electric and magnetic fields. Collisionless expansion from some exospheric base with magnetic field B_0 suggests an approximate distribution $f(v, \theta) = f(v)$, $\theta < \theta_m$, where $\cos\theta_m = (1-B/B_0)^{1/2}$ is the asymptote resulting from conservation of magnetic moment, $mv_\perp^2/2B = const$. This model yields $f_1/f_0 = (3/2)(1+\cos\theta_m)$, independent of energy for $x > x_c$. Observed high energy electron distributions are similarly restricted in pitch angle (Strahl) with a half width that varies but may become as small as 10° in the interior of a magnetic sector. Near isotropy in the vicinity of sector boundaries, however, suggests strongly enhanced scattering (Pilipp et al., 1981).

Instabilities and Anomalous Transport

Breakdown of classical transport theory relatively close to the solar corona results in observable strongly non-Maxwellian distribution functions at greater distances. Exospheric theory, or more correctly a theory that accounts for the rapid increase in Coulomb mean free path with speed, $\lambda_{ei}(v) \propto v^4$ (Scudder and Olbert, 1979) can in principle account for this non-local transport. However, model distribution functions related to these theories or actual observations not only allow for essentially the same heat flux instabilities as the weakly non-Maxwellian electron distribution for classical heat flux (Schulz and Eviatar, 1972; Gary et al., 1975), but open up a wealth of new free energy sources such as anisotropies and ion beams (see e.g. a recent review by Schwartz, 1980). To be sure, instability depends on the assumed range of plasma parameters, but as is well known small scale turbulence of varying nature and intensity has now been observed throughout the interplanetary solar wind (e.g. Gurnett, 1981).

Associated anomalous transport in the solar wind as for many other plasmas is most frequently discussed by determining plasma parameters corresponding to marginal stability, or more generally by estimating anomalous relaxation rates for these parameters. Such a simplified description is suitable for inclusion in global solar wind models (Hollweg, 1978). A simple model for heat flux that includes rates for core electron deceleration by the global electric and magnetic fields against acceleration to the proton frame by Coulomb collisions and the phase speed of waves by wave-electron interactions, for example, on comparison with observations indicates the importance of all three effects in regulating heat flux (Feldman et al., 1979).

If phenomenological models indicate the potential importance of anomalous transport then evidently the need for deriving new transport relations from a first principle theory is even greater. This difficult task not only involves the calculation of particle distribution functions from a kinetic equation with given collision terms, as in classical transport theory, but also another kinetic equation for the evolution of the wave spectrum. Diffusion coefficients with a velocity dependence that usually is quite different from that of corresponding terms for Coulomb collisions, and wave growth rates for the self-consistent highly non-Maxwellian distribution function are basic new elements in these equations. The important questions if and how the detailed microscopic description can be reduced systematically to a fluid type dynamical description that is at least tractable for numerical codes have been examined previously and were answered in the affirmative for the interaction of electrons with ion acoustic like fluctuations (Dum, 1978a,b). The key role anomalous transport connected with these fluctuations undoubtely can play e.g. in collisionless shocks and laser heated plasmas (e.g. Gray and Kilkenny, 1980) motivated this research. Because very similar electrostatic fluctuation spectra are frequently observed in the solar wind (Gurnett, 1981) their origin and

their effect on electron heat flux, electron-ion energy exchange and the global electric field should be studied, also with the aim of finding extensions of anomalous transport theory. Such a program in no way prejudices the role electromagnetic instabilities can possibly play for these transport processes and certainly not the role of e.g. anisotropy driven electromagnetic instabilities in shaping solar wind ion distributions.

To see the effect on electrons, ion acoustic like fluctuations may be considered an extension of the stable fluctuation spectrum responsible for electron-ion collisions with wave number range $1 < k\lambda_{De} < \Lambda = \lambda_{De}/b_o \gg 1$ to the range $\lambda_{De}/\rho_e < k\lambda_{De} < 1$ and phase velocities $\omega/k > v_i$ (λ_{De} Debye length, ρ_e electron gyroradius, b_o minimum impact parameter, v_i ion thermal velocity). For most electrons $v > \omega/k$, thus scattering is predominantly elastic with diffusion coefficient $D^t = \nu v^2/2$ and frequency (Dum, 1978a)

$$\nu(v) = \nu_{ei} + \nu_{ew} = 3 \, \omega_e (v_e/v)^3 \left[Z \frac{\ln\Lambda}{\Lambda} + \frac{\pi}{3} \frac{W}{nT_e} \left\langle \frac{1}{k\lambda_{De}} \right\rangle \right], \tag{4}$$

where ω_e is the electron plasma frequency, and the average in the second term is over the wave spectrum with energy density $W = \langle \delta E^2/8\pi \rangle$. Wave activity in the interplanetary solar wind (Gurnett, 1981) with $W/nT_e = 10^{-7} - 10^{-5}$ (peak) completely dominates elastic scattering, as $\Lambda = 1.24.10^4 (T_e^3/n)^{1/2} = 10^{11} - 10^{12} (T_e \, ^\circ K, n \, cm^{-3})$. Inelastic scattering with diffusion coefficient $D^l = \nu_{ei} v^2 + \nu_{ew} \langle (\omega/k)^2 \rangle$ although comparatively slow, still dominates electron-electron scattering, at least for thermal electrons, and tends to flatten the electron distribution. Because of the v^{-3} dependence of D^l, this process is most rapid for low energy electrons, taking a time that may be estimated from (Dum, 1978a, Fig. 1)

$$\int_o^{T_o} dt \, \pi \, \omega_e \frac{W(t)}{nT_{eo}} \left\langle \frac{1}{k\lambda_{Deo}} \left(\frac{\omega}{k v_{eo}} \right)^2 \right\rangle \gtrsim \frac{1}{5} \tag{5}$$

for an initially Maxwellian distribution with temperature T_{eo}.

An anomalous transport theory that includes classical transport may be constructed under the assumption that elastic scattering is sufficiently frequent to maintain a nearly isotropic electron distribution function against the perturbing forces such as gradients, the electric field etc. (Dum, 1978b). The anisotropic part $\tilde{f}$ of the distribution function becomes a functional of the isotropic part f_o, with $|\tilde{f}/f_o| \ll 1$. In contrast to classical transport theory, f_o is generally non-Maxwellian and is to be determined from a kinetic equation which includes the much slower inelastic scattering and nonlocal propagation effects in time or distance. If local relaxation by ion acoustic like fluctuation dominates, then f_o takes the shape $f_o \propto \exp -(v/v_o)^5$. The structure of the transport relations depends strongly on the shape of f_o. For example, in addition to a heat flux proportional to the temperature gradient, there is for non-Maxwellian f_o also a heat flux, usually in the opposite direction, that is proportional to the density gradient. The effective collision frequency, in contrast to the Coulomb collision frequency, is not simply a number that depends on a few plasma parameters but is proportional to the fluctuation level and thus is a dynamic quantity connected with wave growth. Also (4) was written for simplicity assuming an isotropic wave spectrum. Actual spectra are usually strongly anisotropic and the collision frequency depends thus on the pitch angle (Dum, 1978b).

The anomalous transport theory provides the framework for estimating the effects

of the observed short wavelength turbulence in the interplanetary solar wind. Taking e.g. $W/nT_e = 10^{-7}$, $k\lambda_{De} = 1/2$, $n = 17$ cm^{-3} gives $\tau_{ew} \equiv (\pi/8)^{1/2}$ $3/v_{ew}(v_e) = 25$ sec from (4) and $\tau_0 \approx 100$ τ_{ew} from (5). The time τ_0 for flattening may be still longer as the average fluctuation level required by (5) is reduced from the peak values by the fact that wave activity occurs in form of many bursts that individually may be as short as a fraction of a second (Gurnett, 1981). The observed shape of f_0 (Fig. 1) also indicates that the effect of the turbulence on f_0 is nonlocal, except perhaps at very low energies where f_0 cannot be measured due to contamination with photoelectrons and distortions by the spacecraft potential. Effective collision times during wave activity are much shorter than the Coulomb collision time $\tau_{ee} = \tau_{ei}$ $(Z=1) = 1.3 \times 10^5$ sec for $T_e = 3.6 \times 10^5$ $^\circ$K (parameters correspond to Fig. 3-5 of Dum et al., 1980). Coulomb collisions may still play a role in regions of velocity space where the resonance condition $\omega - \underline{k} \cdot \underline{v} = 0$ is satisfied only for a small part of the wave spectrum and obviously during periods of no wave activity.

An estimate for the applicability of the anomalous transport theory may be obtained in a similar manner as described above for classical transport. The anomalous theory obviously has a much wider range of applicability because it does not demand that f_0 is Maxwellian and the effective mean free path $\lambda_{ew} = v_e/\tau_{ew}$ for scattering from waves is generally much shorter than for Coulomb collisions ($\lambda_{ee} = 2$ AU for the example given above). Still, the theory assumes dominance of elastic scattering and for the v^{-3} dependence in (4) also must break down at some speed, v_c, which, however, is larger than in the case of scattering solely by Coulomb collisions.

The detailed measurements of distribution functions available for the solar wind are of particular value for an investigation of the physical mechanism of heat flux limitation. In order to test the anomalous transport theory, the ratios of effective mean free path to the gradient scales of temperature and density as well as the ratio of interplanetary electric field to effective runaway field were determined from fits of measured and predicted distributions for $v < v_c$, because these values are not known sufficiently well. They come out to be quite reasonable, however, also in relation to the prevailing fluctuation levels. For the highest measured fluctuation levels among the cases studied so far, using Helios measurements (Dum et al., to be published), the $l = 1$ component of the distribution function predicted by anomalous transport theory for measured f_0 can be fitted with observations in a large velocity range $v < v_c$, thus describes almost the entire heat flux. For more quiet conditions and large heat fluxes, a substantial fraction of the heat flux is carried by energetic electrons $v > v_c$, which are strongly anisotropic. Enhancement of the ambipolar electric field by anomalous momentum transfer to bulk electrons still affects these electrons, however.

An instability analysis for waves in the solar wind which directly uses the measured distribution functions rather than model distributions has been described previously (Dum et al., 1980a, 1981). We now find that most of the observed electrostatic short wavelength fluctuation may definitely be identified as ion acoustic waves. Wave growth and wave characteristics such as ω, $\underline{k}$, depend very strongly on the actual detailed distribution functions. This is also demonstrated by the fact that we found both weak electron (heat flux) and more recently also ion (beam) driven modes, whereas previous calculations with model distribution functions never established instability when parameters in these models were not simply assumed but determined from fits to actual measurements (Lemons et al., 1979). The instabilities we find are very weak, highly variable and limited to relatively narrow ranges

)f phase velocity and angles of the wave vector, all consistent with observations (Dum et al., 1980b). The short duration of individual wave bursts can be under- stood if we close the loop by estimating the time in which e.g. minute changes in the electron distribution by isotropization change the sign of the growth rate $\gamma_k = \gamma_{ke} + \gamma_{ki}$, cf. also Lemons et al. (1979). Relaxation oscillation around mar- ginal stability $\gamma_k \approx 0$ are to be expected if these relaxation effects are combined with the perturbing forces that provide the free energy for wave growth. They are a common feature of other turbulent collisionless plasmas (Dum, 1981) and imply an exchange of energy between electrons and ions, with energy extracted from the electrons for $\gamma_{ke} > 0$, i.e. electron (heat flux) driven modes. Rates for energy and momentum transfer may be computed from a given wave spectrum once the dielec- tric properties are known from the stability analysis with the actual distribution functions (e.g. Dum, 1978a, 1981). The rate of momentum transfer (mostly to core electrons) is

$$\underline{R}_e = \int d\underline{k} \ W(\underline{k}) \ 2 \ \text{Im} \ \epsilon_e(\underline{k}, \ \omega_{\underline{k}}) \ \underline{k} \tag{6}$$

where $\text{Im}\epsilon_e$ is the electron contribution to the imaginary part of the dielectric constant. In the energy transfer rate K_e, $\underline{k}$ is replaced by $\omega_{\underline{k}}$. Using the parameters given before, $T_e/T_i = 7.5$, and wave information from Fig. 4 of Dum et al. (1980a) gives an acceleration rate $du/dt = R_e/nm \approx 32 \ km/sec^2$ as compared to $\omega/k \approx 64 \ km/sec$ and u = 392 km/sec. The cooling time is $-(3/2)nT_e/K_e \approx 3900$ sec as compared to 1.34 10^8 sec for energy exchange by Coulomb collisions. It is emphasized again that integral effects over many individual wave bursts must be considered, but these numbers certainly indicate the potential importance of scattering by ion acoustic turbulence.

In conclusion, we have tried to demonstrate that the recent in situ measure- ments of fluctuations and particle distribution functions offer an excellent oppor- tunity for a test of theories of wave particle interaction and for finding neces- sary extensions.

References

Braginskii, S.I., Transport processes in a plasma, Rev. Plasma Physics Vol. I, 205, M.A. Leontovich, ed., Consultants Bureau, New York, 1967.

Dum, C.T., Anomalous heating by ion sound turbulence, Phys. Fluids, 21, 945, 1978a.

Dum, C.T., Anomalous electron transport equations for ion sound and related turbu- lent spectra, Phys. Fluids, 21, 956, 1978b.

Dum, C.T., E. Marsch, and W. Pilipp, Determination of wave growth from measured distribution functions and transport theory, J. Plasma Phys., 23, 91, 1980a.

Dum, C.T., E. Marsch, K.H. Mühlhauser, W. Pilipp, D.A. Gurnett, H. Rosenbauer, and R. Schwenn, Free energy source for ion sound turbulence in the solar wind, Eos 61, 1097, 1980b and to be published.

Dum, C.T., E. Marsch, W. Pilipp, and D.A. Gurnett, Ion Sound Turbulence in the Solar Wind, Solar Wind Four, H. Rosenbauer, ed., Max-Planck-Institut f. Aero- namic Report MPAE-W-100-81-31, p. 241, Katlenburg-Lindau, 1981.

Dum, C.T., Anomalous resistivity and plasma dynamics, Physics of auroral arc forma- tion, S.I. Akasofu and J. Kan, ed., AGU, Geophys. Monograph series, 25, 408, 1981.

Durney, B.R., and G.W. Pneuman, Solar-interplanetary modeling: 3-D solar wind solutions in prescribed non-radial magnetic field geometries, Solar Physics, 40, 461, 1975.

Feldman, W.C., I.R. Asbridge, S.J. Bame, M.D. Montgomery, and S.P. Gary, Solar

Wind Electrons, J. Geophys. Res., 80, 4181, 1975.

Feldman, W.C., J.R. Asbridge, S.J. Bame, J.T. Gosling, and D. Lemons, A Possible Closure Relation for Heat Transport in the Solar Wind, J. Geophys. Res., 84, 6621, 1979.

Forslund, D.W., Instabilities associated with heat conduction in the solar wind and their consequences, J. Geophys. Res., 75, 17, 1970.

Gary, S.P., W.C. Feldman, D.W. Forslund, and M.D. Montgomery, Heat flux instabilities in the solar wind, J. Geophys. Res., 80, 4197, 1975.

Gray, D.R., and J.D. Kilkenny, The measurement of ion acoustic turbulence and reduced thermal conductivity caused by a large temperature gradient in a laser heated plasma, Plasma Physics, 22, 81, 1980.

Gurnett, D.A., Plasma Waves in the Solar Wind: A review of Observations, Solar Wind Four, p. 286, 1981.

Hollweg, J.V., Some physical processes in the solar wind, Rev. Geophys. Space Phys., 16, 689, 1978.

Hundhausen, A.J., Coronal Expansion and Solar Wind, p. 74-82, Springer-Verlag, New York, 1972.

Lemons, D.S., J.R. Asbridge, S.J. Bame, W.C. Feldman, S.P. Gary, and J.T. Gosling, The source of electrostatic fluctuations in the solar wind, J. Geophys. Res., 84, 2135, 1979.

Ogilvie, K.W., and J.D. Scudder, The Radial Gradients and Collisional Properties of Solar Wind Electrons, J. Geophys. Res., 83, 3776, 1978.

Pilipp, W.G., R. Schwenn, E. Marsch, K.H. Mühlhäuser and H. Rosenbauer, Electron Characteristics in the solar wind as deduced from Helios observations, Solar Wind Four, p. 241, 1981; also Solar Wind Five and to be published.

Schwartz, S.J., Plasma instabilities in the solar wind: A theoretical review, Rev. Geophys. Space Phys., 18, 313, 1980.

Scudder, J.D., and S. Olbert, A theory of local and global processes which affect solar wind electrons, I, The origin of typical 1 AU velocity distribution functions - steady state theory, J. Geophys. Res., 84, 2755, 1979.

Schulz, M., and A. Eviatar, Electron temperature asymmetry and the structure of the solar wind, Cosmic Electrodyn.,2, 402, 1972.

Singer, C., and I.W. Roxburgh, The onset of microinstability and its consequences in the solar wind, J. Geophys. Res., 82, 2677, 1977.

Spitzer, L., and R. Härm, Transport theory in a completely ionized gas, Phys. Rev., 89, 977, 1953.

MEASUREMENT OF MACROSCOPIC PLASMA PARAMETERS WITH A RADIO EXPERIMENT : INTERPRETATION OF THE QUASI-THERMAL NOISE SPECTRUM OBSERVED IN THE SOLAR WIND.

P. Couturier, S. Hoang, N. Meyer-Vernet and J.L. Steinberg
Département de Recherche Spatiale, Observatoire de Paris-Meudon
92190 Meudon, France

ABSTRACT

The ISEE-3 SBH radio receiver has provided the first systematic observations of the quasi-thermal (plasma waves) noise in the solar wind plasma. The theoretical interpretation of that noise involves the particle distribution function so that electric noise measurements with long antennas provide a fast and independent method of measuring plasma parameters: densities and temperatures of a two-component (core and halo) electron distribution function have been obtained in that way. The polarization of that noise is frequency dependent and sensitive to the drift velocity of the electron population. Below the plasma frequency, there is evidence of a weak noise spectrum with spectral index -1 which is not yet accounted for by the theory. The theoretical treatment of the noise associated with the low energy (thermal) proton population shows that the moving electrical antenna radiates in the surrounding plasma by Cerenkov emission which becomes predominant at the low frequencies, below about 0.1 f_p.

Introduction

Using the SBH radio experiment on ISEE-3 (Knoll et al, 1978), we have observed systematically the noise spectrum associated with the quasi-thermal fluctuations of the solar wind plasma (Hoang et al., 1980; see also Grigorieva and Slysh, 1970). From the theoretical interpretation of the measured spectra (Andronov, 1966; Meyer-Vernet, 1979), using a bi-maxwellian model, we were able to deduce the density and temperature of the two electron components (Couturier et al., 1981, paper A) The results are in excellent agreement with the parameters measured at the same time on the same spacecraft by the Los Alamos plasma analyzer. Sentman (1982) investigated the electron quasi-thermal noise in a magnetized plasma to account for the noise spectrum observed near plasma resonances in planetary magnetospheres.

The purpose of the present paper is to introduce the physics involved in the plasma and antenna description in order to make clear some fundamental points to solar wind physicists who may not be familiar with the subject developed at length in the quoted literature.

The antenna as a thermometer and densitometer.

Let us first consider a passive receiving antenna in vacuum, in equilibrium with blackbody radiation at temperature T_1. The spectral component e_ω of the voltage measured at the terminals of that antenna is related to the fluctuations of the electromagnetic field inducing that voltage; Nyquist's theorem provides a relation between the output voltage, the antenna radiation resistance in vacuum R_{a0} and its temperature:

$$e_\omega{}^2 = 4 \, K \, T_1 \, R_{a0} \qquad (1)$$

For a thin short dipole antenna of half-length ℓ, R_{a0} is given by:

$$R_{a0} = \frac{(\mu_o/\varepsilon_o)^{\frac{1}{2}} \omega^2 \ell^2}{6 \pi c^2} \qquad (2)$$

Let us now consider the same antenna in equilibrium with blackbody radiation at temperature T_1, but immersed in a lossless dielectric. Equation(1) remains valid if we replace R_{a0} by the radiation resistance R_a which takes into account the dielectric permittivity ε_r which affects the phase velocity of the radiation; namely, if the antenna remains short: $R_a = R_{a0}\varepsilon_r^{\frac{1}{2}}$. The plasma surrounding the antenna may be considered as a pure dielectric when $\omega \gg \omega_p$ where $\varepsilon_r = 1-(\omega_p/\omega)^2$, ω_p is the plasma frequency and we assume there is no static magnetic field. This cold plasma approximation breaks down near the plasma frequency and is of no use for $\omega < \omega_p$ since no transverse mode can propagate and couple the antenna to the blackbody.

Finally, let us consider an antenna immersed in the solar wind, a hot collisionless electron plasma if we neglect the ions in a first approximation. Now, longitudinal modes do propagate and contribute predominantly to the voltage measured at the antenna terminals. In fact, there is a detailed energy balance which allows a separate calculation of the transverse and longitudinal modes contributions with appropriate Nyquist's formulas. When $\omega > \omega_p$, the transverse modes couple the antenna to radio-sources; since the solar wind is optically thin for this mode, it contributes an output voltage given by: $e_T^2 = 4KT_{eff}R_T$ where T_{eff} is an effective temperature deduced from the integration of the electromagnetic flux incident on the antenna taking into account its directivity pattern. R_T is the transverse mode radiation resistance which is the classical radiation resistance R_a previously mentioned.

The longitudinal modes couple the antenna to the natural electrostatic oscillations of the plasma. Landau damping provides the thermalisation process between electric field fluctuations associated with longitudinal plasma waves and the electrons. The electrons with velocity larger than the plasma wave velocity are slowed down and transfer energy to the plasma waves; electrons which are slower than the plasma waves are accelerated and damp the waves. At thermal equilibrium, electric field fluctuations and the electron temperature are related by the fluctuation-dissipation theorem (Sitenko, 1967). Thus, the output voltage associated with these fluctuations is again given by: $e_L^2 = 4KT_LR_L$, where R_L is the radiation resistance of the antenna for the longitudinal modes.

The method used to evaluate that radiation resistance will be given later; we now present some analytical results (paper A) which describe the resonance peak of the radiation resistance near the plasma frequency for a dipole antenna of half length $\ell \gg \ell_D = v_T/(2^{\frac{1}{2}}\omega_p)$ the Debye length, $v_T = (2KT/m)^{\frac{1}{2}}$ is the electron thermal velocity.

For low frequencies $\omega < \omega_p$, R_L can be analytically approximated by:

$$R_L = \frac{(\pi \mu_o)^{\frac{1}{2}} c \, \ell_D}{4 \varepsilon_o^{\frac{1}{2}} v_T \ell} = \frac{(\pi \mu_o)^{\frac{1}{2}} c}{4 (2 \varepsilon_o)^{\frac{1}{2}} \omega_p \ell} \qquad (3)$$

For high frequencies, $\omega \gg \omega_p$, R_L decreases with frequency as ω^{-3}:

$$R_L = \frac{\mu_o^{\frac{1}{2}} \omega_p^2 c}{2 \epsilon_o^{\frac{1}{2}} \omega^3 \ell} \qquad (4)$$

The resonance peak appears just above the plasma frequency; for $\omega \approx \omega_p$, the radiation resistance increases rapidly (cut-off) and reaches a maximum value for:

$$(1 - \frac{\omega_p^2}{\omega^2})^{\frac{1}{2}} \frac{\ell}{\ell_D} \sim 3.5 \qquad (5)$$

which corresponds to the antenna in tune with the plasma waves. The constant 3.5 is valid for cylindrical antennas, it would be slightly different for spherical antennas. So, there is a well defined resonance peak only if $\ell/\ell_D > 1$. The peak value is roughly equal to the low frequency asymptotic value (3) multiplied by $(\ell/\ell_D)^2$. In the resonant frequency range the transverse mode contribution can be neglected.

These expressions show that we can deduce the plasma frequency from the cut-off frequency of the spectrum and the electron temperature from the peak noise voltage and the width of the resonance peak.

Basic equations for a multicomponent plasma

Using the preceding model results in a good fit to the observations for the resonance peak position but the predicted values of the noise peak are too low. The noise peak is produced by plasma waves with frequency close to ω_p and phase velocity much larger than v_T. The discrepancy between the theoretical predictions based on a one-component model and the observations must therefore be solved by using a multicomponent model with cold core and hot halo electrons. We shall later discuss the limitations imposed by the quasi-thermal assumption on the distribution functions. Now we summarize the results (paper A) derived from a plasma model made of two maxwellian isotropic electron populations.

For a multicomponent plasma Nyquist's theorem is not valid, there is no longer any linear relationship between the output voltage at the antenna terminals and the antenna resistance; these quantities must be evaluated separately. The particle distribution functions set the plasma dielectric properties and are used to evaluate the dispersion tensor $\Lambda_{ij}(\vec{k}, \omega)$ and the dielectric permittivity tensor $\epsilon_{ij}(\vec{k}, \omega)$. The antenna geometry sets the current distribution $\vec{J}(\vec{r})$. The antenna output voltage is related to the fluctuating electric field:

$$V(t) = \int d^3r \frac{\tilde{E}(\vec{r},t) \cdot \vec{J}(\vec{r})}{I_o} \qquad (6)$$

I_o is the current flowing at the center of the antenna. The plasma fluctuations give a spectral distribution of the electric field fluctuations $[\tilde{E}_i \tilde{E}_j]_{\vec{k},\omega}$; this tensor is deduced from the fluctuation-dissipation theorem (Sitenko, 1967):

$$[\tilde{E}_i \tilde{E}_j] = \frac{2K}{\epsilon_o \omega} \frac{k_i k_j}{k^2} \sum_q \frac{T_q (\text{Im } \epsilon_L)_q}{[\epsilon_L]^2} \qquad (7)$$

q is an index for the different components of the plasma, ε_L is the longitudinal part of the dielectric permittivity tensor, $(Im \ \varepsilon_L)_q$ is the contribution of the q-component to its imaginary part.

Calculating the autocorrelation of the output voltage (6) and using Parseval' theorem ,we obtain:

$$V^2_\omega = \frac{2}{8 \ \pi^3 \ I_o^{\ 2}} \ \int d^3k \ J_i(\vec{k}) \ [E_i E_j]_{k,\omega} \ J_j(\vec{k}) \tag{8}$$

We emphasize that <u>this output voltage at the antenna terminals is not the input voltage at the receiver</u>.The transfer function from the antenna terminals to the receiver involves the antenna impedance and the receiver input impedance (paper A). For ISEE-3, this transfer gain varies with frequency by one order of magnitude due to the variations of the Debye length. The antenna impedance is given by:

$$Z_a = \frac{1}{I_o^{\ 2}} \int d^3r \ \vec{E}(\vec{r}).\vec{J}(\vec{r}) \tag{9}$$

Plasma dielectric properties relate the current distribution to the electric field so that, by Fourier transform, we obtain:

$$Z_a = \frac{1}{8 \ \pi^3 \varepsilon_o \omega \ I_o^{\ 2}} \int d^3k \ J_i(\vec{k}) \ \Lambda_{ij}^{-1}(\vec{k},\omega) \ J_j(\vec{k}) \tag{10}$$

For a multicomponent plasma, there is no longer a linear relation between the longitudinal resistance deduced from (10) and the output voltage given in (8). Figure 1 shows the difference between the calculated spectrum of a one-component plasma with electron density N_c and temperature T_c and the calculated spectrum of a two-component plasma with a cold (N_c,T_c) and a hot (N_h,T_h) electron population. These spectra have been calculated for the receiver input voltage. As shown by Fejer and Kan (1969) and in paper A, the hot population plays a dominant role close to the resonance peak. As compared to the single cold population case, the peak voltage is multiplied by T_h/T_c, the asymptotic low frequency value by a factor $1+(N_h T_c^2)/(N_c T_h^2)$ and the high frequency decreasing part of the spectrum by a total pressure factor $(N_h T_h+N_c T_c)/N_c T_c$.

Observations and discussion

Figure 1 shows spectra obtained on October 6, 1979 before and after a shock (figure 1 is a corrected version of paper A figure 11). The parameters of the two maxwellian populations used to determine the calculated radio spectrum are given in table 1; figure 2 represents the corresponding electron distribution functions (thin line) and the distribution function deduced from the Los Alamos plasma analyzer measurements made at the same time (thick line). The difference between the two curves is essentially due to our use of a two maxwellian model to interpret the radio spectrum while the Los Alamos distribution shows evidence of a hot population with a high energy tail somewhat like a lorentzian (Feldman et al, 1982). Apart from this tail, the shapes of the two distribution functions are essentially the same; note also, from the parameters of table 1, that we have not

used the same normalization factor for the two distribution functions; the plasma density given by the radio experiment differs slightly from that given by the plasma analyzer, this difference is less than the roughly $\mp 30\%$ uncertainty in estimating plasma densities from measurements of solar wind electron velocity distributions. We have repeated this fitting exercise many times, and in every case, we obtained the same agreement. We are quite sure that a purposedly designed radio experiment tracking the plasma resonance "line" in frequency with a multichannel receiver would be a fast and efficient means to acquire macroscopic plasma parameters with a high time resolution.

TABLE 1. Summary of plasma parameters

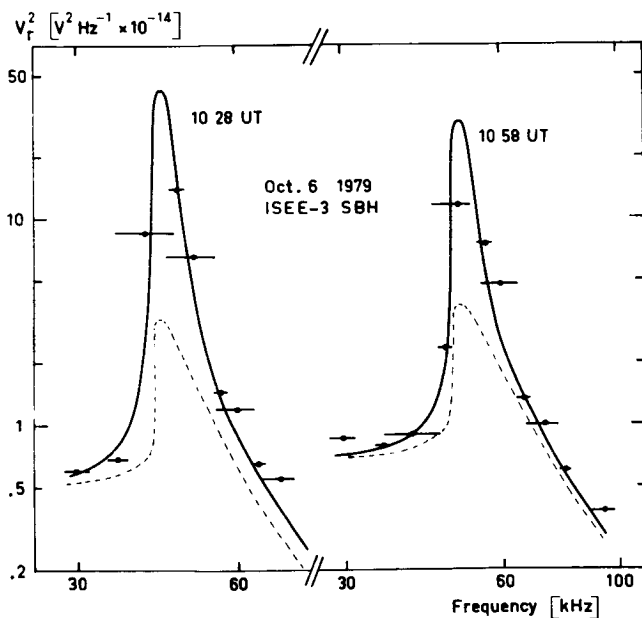| Parameters	N_h/N_c	T_c	T_h	N_c (SBH)	N_c (LANL)
Oct.6, 1979, 10:28 UT	0.016	0.92 10^5 °K	16 10^5 °K	22 cm^{-3}	18 cm^{-3}
Oct.6, 1979, 10:58 UT	0.011	1.50 10^5 °K	16 10^5 °K	29 cm^{-3}	31 cm^{-3}

Figure 1. Thermal noise spectra at the receiver input terminals as measured (closed circles) and computed. The dotted curves were computed with a single (cold) electron population; the solid curves with two populations. In both cases, the plasma parameters are those of table 1 obtained from the distribution functions plotted on figure 2. The horizontal bars show the bandwidth of the receiving channels.
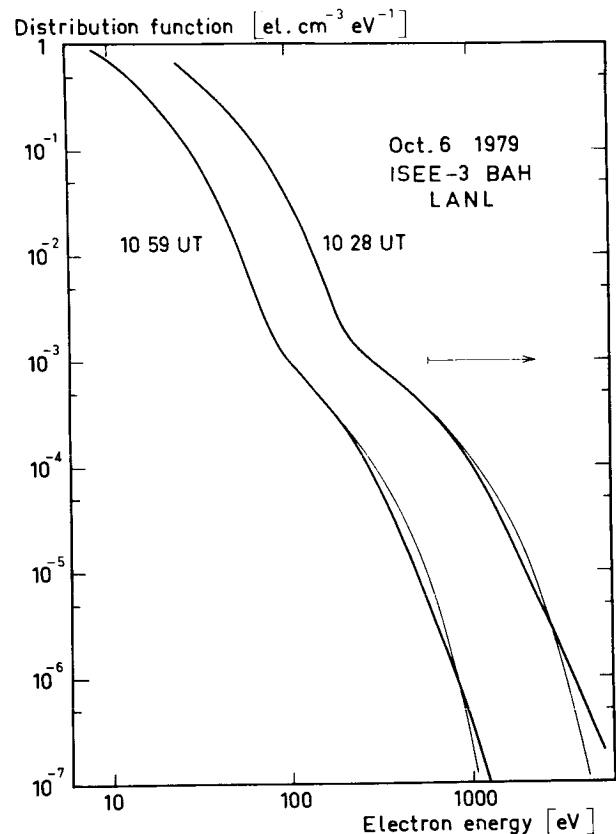

Figure 2. Electron distribution functions on October 6, 1979. The thick line is the function measured with the Los Alamos plasma analyzer. The thin line is the two-maxwellian function used to compute the noise

spectra shown on figure 1. The 10 28 UT curves are displaced to the right, for clarity, by the length of the horizontal arrow.

However, some constraints are imposed for such a method to be efficient. We need an antenna length larger than the Debye length. We need electromagnetic cleanliness of the spacecraft to achieve a low instrumental noise level ($4 \, 10^{-16} \, V^2Hz^{-1}$ has been achieved on ISEE-3). The method cannot be used effectively in the presence of intense radio waves. It is model-dependent and does not describe distribution functions which would differ widely from a multi-maxwellian. Finally, the "quasi-thermal" equilibrium between the plasma and the antenna and the use of the fluctuation-dissipation theorem imply (Sitenko, 1967) that the relaxation time of the observed distribution function towards a mono-maxwellian distribution function (exact thermal equilibrium) is long compared to the time needed to acquire a complete spectrum. The noise spectrum arising from an unstable distribution function cannot be interpreted assuming quasi-thermal equilibrium.

The effect of the antenna velocity relative to the solar wind

Further developments of the theoretical interpretation have been motivated by the ISEE-3 observations. For $\omega \lesssim \omega_p$ the observed noise spectrum is not flat as predicted by our models. An electric noise component with a spectral index -1 has been identified, a spin modulation of the plasma noise is observed on the spinning antennas and the anisotropy is clearly correlated with the solar wind velocity (Hoang et al, 1982). These observations led us to take into account the thermal ion distribution function and the velocity of the antenna relative to the solar wind plasma. Longitudinal electron and ion plasma waves are Doppler-shifted in the antenna frame ; this effect is particularly important for low frequency waves ($\omega \lesssim \omega_p$) which are the slowest. The ion contribution to the noise calculated in that case yields a bump in the low frequency part of the spectrum but it is far from being sufficient to explain the observed f^{-1} noise spectrum. The anisotropy introduced by the Doppler shift of the waves results in a spin modulated noise (Couturier et al., 1983) which is frequency-dependent ; the direction of the minimum electric field changes by 90° in the plasma resonance peak region in agreement with the observations.

A property of this model was predicted earlier by Andronov (1966) : for typical solar wind parameters, the ISEE-3 antenna resistance may become negative below 0.1 f_p when the dipole antenna is parallel to the solar wind velocity. In such a case, we get an unstable situation similar to the beam-plasma instability; Cerenkov effect due to the antenna velocity explains this behaviour. When such a process is predominant, the low frequency electric field measurements are quantitatively and qualitatively affected since the antenna gain has nothing in common with the gain evaluated in vacuum. We cannot encounter such a situation on ISEE-3 because our lowest receiver frequency is 30 kHz.

In conclusion, we wish to emphasize the fact that passive electric field measurements with antennas long as compared to the Debye length have been demonstrated to be useful tools for plasma diagnosis.

REFERENCES

o Andronov, A.A., Antenna impedance and noise in space plasma (in Russian),Kosm. Issled., 4, 558, 1966.

o Couturier, P., S. Hoang, N.Meyer-Vernet and J.L. Steinberg, Quasi thermal noise in a stable plasma at rest : theory and observations from ISEE-3,J.Geophys.Res. 86, 11 127, 1981. (paper A)

o Couturier, P., S. Hoang, N. Meyer-Vernet, C. Perche and J.L. Steinberg, Quasi thermal noise in a stable flowing plasma : theory and observations from ISEE-3. In preparation for submission to J. Geophys. Res. in 1983.

o Fejer, J.A. and J.R. Kan, Noise spectrum received by an antenna in a plasma, Radio Sci., 4, 721, 1969.

o Feldman, W.C., R.C. Anderson, J.R. Asbridge, S.J. Bame, J.T. Gosling and R.D. Zwickl, Plasma electron signature of magnetic connection to the Earth bow shock: ISEE-3, J. Geophys. Res., 87, 632, 1982.

o Grigorieva, V.P. and V.I. Slysh, Long wave cosmic radio radiation in circumlunar space (in Russian), Kosm. Issled., 8, 284, 1970.

o Hoang, S., J.L. Steinberg, G. Epstein, P. Tilloles, J. Fainberg and R.G. Stone, The low frequency continuum as observed in the solar wind from ISEE-3 : thermal electrostatic noise, J. Geophys. Res., 85, 3419, 1980.

o Hoang, S., J.L. Steinberg, P. Couturier and W.C. Feldman, An electric noise component with density f^{-1} identified on ISEE-3, J. Geophys. Res., 87, 9025, 1982.

o Knoll, R., G. Epstein, S. Hoang, G. Huntzinger, J.L. Steinberg, J. Fainberg, F. Grena, S.R. Mosier and R.G. Stone, The 3-dimensional radio mapping experiment (SBH) on ISEE-3, IEEE Trans. Geosci. Electron., GE-16, 199, 1978.

o Meyer-Vernet, N., On natural noises detected by antennas in plasmas, J. Geophys. Res., 84, 1979.

o Sentman, D.D., Thermal fluctuations and the diffuse electrostatic emissions, J. Geophys. Res., 87, 1455, 1982.

o Sitenko, A.G., Electromagnetic Fluctuations in Plasma, Academic, New York, 1967.

Page intentionally left blank

MULTIPLE SPACECRAFT OBSERVATIONS OF INTERPLANETARY SHOCKS: CHARACTERISTICS OF THE UPSTREAM ULF TURBULENCE

C.T. Russell
Institute of Geophysics and Planetary Physics
University of California
Los Angeles, California   90024

E.J. Smith and B.T. Tsurutani
Jet Propulsion Laboratory
Pasadena, California   91109

J.T. Gosling and S.J. Bame
Los Alamos National Laboratory
Los Alamos, New Mexico   87545

ABSTRACT

All interplanetary shocks observed by ISEE-3 and either ISEE-1 or ISEE-2 or both in 1978 and 1979 are examined for evidence of upstream waves. In order to characterize the properties of these shocks it is necessary to determine accurate shock normals. We invert an overdetermined set of equations to obtain shock normals, velocities and error estimates for all these shocks. Tests of the method indicate it is quite reliable. Using these normals we then calculate the Mach number and angle between the interplanetary magnetic field and the shock normal for each shock. These parameters allow us to separate the upstream waves into two classes: whistler-mode precursors which occur at low Mach numbers and upstream turbulence whose amplitude at Mach numbers greater than 1.5 is controlled by the angle of the field to the shock normal. The former waves are right-hand circularly polarized and quite monochromatic. The latter waves are more linearly polarized and have a broadband featureless spectrum.

Introduction

Upstream from the earth's bow shock there is a wide variety of wave phenomena, both at ULF and VLF frequencies (cf. Russell and Hoppe, 1983 and references therein). Similar wave phenomena are observed upstream from the bow shocks of Mercury, Venus and Jupiter (Hoppe and Russell, 1981). Interplanetary shocks differ from planetary bow shocks in that they have much larger radii of curvature and in general are weaker than planetary bow shocks. Thus it is of interest to compare the properties of waves upstream from interplanetary shocks with those upstream from planetary bow shocks. One such comparison has been made by Kennel et al. (1982) who showed that ion-acoustic-like waves occurred at VLF frequencies in front of interplanetary shocks, in a manner similar to the occurrence in front of the terrestrial bow shock. This observation suggests that there are upstream particle phenomena associated with interplanetary shocks. In fact, energetic particles are observed in front of some of these shocks (Gosling et al., 1983). Thus, we might expect to observe ULF wave phenomena there also.

We expect differences in the nature of these waves from those observed upstream of planetary bow shocks because of the different geometry of planetary bow shocks and their lower Mach numbers. For example, because the radius of curvature of the interplanetary shock is much greater than that of a planetary shock, the

time of connection of a field line to the shock is generally much greater for the interplanetary shock. Depending on how far upstream the shock associated energetic particles propagate, these waves may grow over a large region in front of the shock. In planetary bow shocks, in general, the waves grow in a very limited region defined by the field lines tangent to the nose of the bow shock, behind which any waves generated are convected downstream toward the bow shock by the solar wind.

Understanding these waves is important to further our knowledge of cosmic ray acceleration. One of the mysteries of cosmic rays is that they seem to be accelerated very efficiently. It is often suggested that cosmic ray acceleration is associated with interstellar shock waves produced by supernova explosions (e.g., Axford, 1981). Long after the explosion when the shock has expanded to large distances and is weak, the interstellar shock may resemble typical interplanetary shocks. It is important to note that cosmic rays are thought to be accelerated in a multi-step process with repeated scattering centers being necessary. The ULF waves, seen upstream of planetary bow shocks, are excellent candidates for these scattering centers if they indeed occur in front of interplanetary shocks. To date few studies of upstream turbulence have been undertaken. Morfill and Scholer (1977) examined power spectra of the interplanetary magnetic field in the period range 100 to 1000 seconds upstream and downstream of four interplanetary shocks. They found that the ULF power increased across these shocks but since the field strength increased a similar amount there was little change in the diffusion coefficient. They did not attempt to determine shock normal directions nor to relate wave properties to shock parameters. Russell and Hoppe (1983) in a preliminary study of these same shocks have shown that upstream wave turbulence is correlated with the angle between the upstream magnetic field and the shock normal. Most recently Tsurutani et al. (1983) have used minimum variance analysis to characterize the properties of waves seen upstream of interplanetary shocks.

In this paper, we examine the properties of the upstream turbulence and relate these properties to the parameters of the interplanetary shocks. To accomplish this we will use plasma and magnetic field data from the ISEE-1, -2 and -3 spacecraft. The plasma instrumentation has been described by Bame et al. (1978 a, b). The ISEE-1 magnetometer has been described by Russell (1978) and the ISEE-3 magnetometer by Frandsen et al. (1978). A difficult aspect of studying interplanetary shocks and the most critical, is determining their normals. Thus, before examining the properties of the waves we discuss the procedure we have used to obtain the best fit normals for these shocks.

<center>Shock Normal Determination</center>

Eighteen interplanetary shocks in the ISEE-1 and -2 records from 1978-1979 were selected for this study. Most of these were selected because of the simultaneous availability of ISEE-3 data. IMP-8 or Prognoz 7 measurements were also available for some of these shocks. Five of the shocks were observed by four spacecraft. Under such conditions it is possible to determine the average shock orientation from the time delays and separation vectors between the spacecraft. This has been done for these five shocks and the analysis reported elsewhere (Russell et al., 1983a, b).

As a result of these analyses we have developed the following technique for determining the shock normal, $\underline{N}$, using an over-determined set of equations.

First, the separation vectors and separation times are used:

$$
\begin{pmatrix} \underline{\Delta x}_{10} \\ \underline{\Delta x}_{20} \\ \vdots \end{pmatrix} \cdot \begin{pmatrix} Nx \\ Ny \\ Nz \end{pmatrix} = V \begin{pmatrix} \Delta t_{10} \\ \Delta t_{20} \\ \vdots \end{pmatrix}
$$

where $\underline{\Delta x}_{i0}$ and Δt_{i0} are the separation vectors and time lags between satellite 'i' and satellite '0'. Then the change in vector magnetic field $\underline{\Delta B}_1$ is incorporated:

$$
\begin{pmatrix} \underline{\Delta B}_0 \\ \underline{\Delta B}_1 \\ \vdots \end{pmatrix} \cdot \begin{pmatrix} Nx \\ Ny \\ Nz \end{pmatrix} = 0
$$

Velocity coplanarity is also used when 3-D plasma data are available on both sides of the shock.

$$
\begin{pmatrix} (\underline{B}_u \times \underline{\Delta V})_0 \\ (\underline{B}_u \times \underline{\Delta V})_1 \\ \vdots \end{pmatrix} \cdot \begin{pmatrix} Nx \\ Ny \\ Nz \end{pmatrix} = 0
$$

and

$$
\begin{pmatrix} (\underline{B}_d \times \underline{\Delta V})_0 \\ (\underline{B}_d \times \underline{\Delta V})_1 \\ \vdots \end{pmatrix} \cdot \begin{pmatrix} Nx \\ Ny \\ Nz \end{pmatrix} = 0
$$

where $\underline{B}_u$ and $\underline{B}_d$ are the upstream and downstream fields and $\underline{\Delta V}$ is the change in the velocity across the shock. Magnetic coplanarity can also be used whenever the upstream and downstream fields are separated by a sufficiently large angle.

$$
\begin{pmatrix} (\underline{B}_u \times \underline{B}_d)_0 \\ (\underline{B}_u \times \underline{B}_d)_1 \\ \vdots \end{pmatrix} \cdot \begin{pmatrix} Nx \\ Ny \\ Nz \end{pmatrix} = 0
$$

The number of constraints available for our shock normal determinations is quite variable. Furthermore, the quality of the data itself varies. If a shock is encountered in a quiet solar wind background, then "good" upstream and downstream

values can be measured. However under disturbed solar wind conditions, the measured "upstream" and "downstream" values may, in fact, not correspond to the appropriate instantaneous values. Thus, it is highly desirable to have an independent check of the accuracy of the obtained solutions. We can do this two ways in our inversion process. First, we can calculate the eigenvalues and eigenvectors of the 3 x 3 real symmetric matrix which is inverted in our solution. These correspond to three directions in space which are determined to an accuracy which is measured by the size of the associated eigenvalues. In analogy to finding the error in determining a minimum variance direction we let the minimum eigenvalue be a measure of the background noise level of the inversion method. Then the error in the minimum eigenvector direction, $\delta\phi$, in the plane perpendicular to the maximum eigenvector is given by:

$$\delta\phi = \sin^{-1} (\lambda_3/\lambda_2)^{1/2}$$

If the normal $\underline{N}$ makes an angle α to the direction of the maximum eigenvector then the error in the direction of $\underline{N}$ due to the error in the eigenvector directions along the eigenvector associated with the maximum eigenvalue λ_1 is:

$$\delta\beta_1 = \cos^{-1} (\cos^2\alpha + (1 - \lambda_3/\lambda_2)^{1/2} \sin^2\alpha)$$

The error in the plane orthogonal to the intermediate eigenvector is similar but smaller.

$$\delta\phi_2 = \cos^{-1} (\cos^2\gamma + (1 - \lambda_3/\lambda_1)^{1/2} \sin^2\gamma)$$

where γ is the angle between the normal and the eigenvector associated with the intermediate eigenvalue. As a final error estimate, $\delta\phi$, we have summed these two errors and list them in Table 1 together with the normals, shock speed and constraints used in the solutions.

As a second method of evaluating our normals we have compared the orientation of the vector constraints that we have used to determine the direction of the normal. The constraints, except for the separation vector constraints, should all be perpendicular to the normal. We have calculated the average deviation of the "normal" constraints from being strictly orthogonal and list those as $\delta\theta$ in Table 1. We note that although this estimate has a very straight-forward physical basis it is not a perfect measure because all constraints could be exactly perpendicular to the normal and not constrain the orientation of the normal at all if the constraints were mutually parallel.

Table 1 contains the best fit normals and the associated shock velocity measured in the observer's frame, together with our two error estimates, the first, $\delta\beta$, being an error estimate for the orientation of the normal and the second, $\delta\theta$, being the average angular deviation of the constraints from 90°. Finally, the constraints used in the determinations are given. The numbers refer to the spacecraft: 1-ISEE-1; 2-ISEE-2; 3-ISEE-3; 7-Prognoz 7 and 8-IMP-8. The letter 'T' designates a separation vector and time delay constraint. The symbol 'ΔB' signifies a vector field jump constraint; BUV signifies the cross product of the upstream field direction and the change in plasma flow velocity across the shock; BDV signifies the cross product of the downstream field and the change in plasma flow velocity across the shock. Finally, UCD signifies the cross product between upstream and downstream magnetic fields.

Table 1. Best Fit Normals

Day	N(GSE)	V km/s	$\delta\beta$	$\delta\theta$	Constraints
78 230	(-.747, -.433, .505)	422	2.4°	1.3°	T_{21}, T_{23}, T_{28}, ΔB_1, ΔB_3, ΔB_8, UV_1, DV_1, UV_3, DV_3
78 254	(-.895, -.134, .425)	436	8.6°	6.5°	T_{23}, T_{28}, ΔB_1, ΔB_3, ΔB_8, UV_1, DV_1, UV_3, DV_3
78 263	(-.943, -.278, -.182)	334	0.3°	10.1°	T_{21}, T_{23}, ΔB_1, ΔB_3, UV_1, DV_1, UV_3, DV_3
78 268	(-.768, -.633, -.092)	811	5.3°	-----	T_{23}, ΔB_3, UCD_3
78 271	(-.934, -.332, .135)	672	1.3°	3.1°	T_{21}, T_{23}, ΔB_1, ΔB_3, UV_1, DV_1, UV_3, DV_3
78 290	(-.860, -.374, .347)	395	0.3°	0.9°	T_{21}, T_{23}, ΔB_1, ΔB_3, UV_1, DV_1, UV_3, DV_3
78 302	(-.893, .054, .447)	424	4.1°	1.0°	T_{23}, T_{28}, ΔB_1, ΔB_3, ΔB_8, UV_1, DV_1, UV_3, DV_3
78 312	(-.882, -.193, .492)	447	3.8°	4.4°	T_{23}, ΔB_2, ΔB_3, UCD_2, UCD_3, UV_3, DV_3
78 316	(-.963, .095, -.253)	606	9.5°	6.6°	T_{13}, ΔB_1, ΔB_3, UCD_1, UV_1, DV_1
78 359	(-.802, -.488, .344)	432	3.3°	6.0°	T_{21}, T_{23}, T_{27}, ΔB_1, ΔB_3, UV_1, DV_1, UV_3, DV_3
79 243	(-.625, .288, -.725)	402	6.4°	9.6°	T_{21}, T_{23}, T_{28}, ΔB_1, ΔB_3, ΔB_8, UV_1, DV_1, UV_3, DV_3
79 315	(-.897, .368, .244)	466	11.1°	7.7°	T_{13}, ΔB_1, ΔB_3, UCD_1, UCD_3, UV_1, DV_1, UV_3, DV_3
79 322	(-.816, .568, -.103)	504	2.9°	4.4°	T_{21}, T_{23}, ΔB_1, ΔB_3, UV_1, DV_1, UV_3, DV_3
79 324	(-.445, -.688, .573)	282	14.1°	1.0°	T_{23}, ΔB_1, ΔB_3, UCD_1, UCD_3, UV_1, DV_1
79 333	(-.773, -.286, .567)	286	3.3°	3.1°	T_{21}, T_{23}, ΔB_1, ΔB_3, UV_1, DV_1, UV_3, DV_3
79 334	(-.978, -.047, -.201)	404	2.2°	3.0°	T_{21}, T_{23}, ΔB_1, ΔB_3, UV_1, DV_1, UV_3, DV_3

Legend

Spacecraft: 1, 2, 3, 7, 8 refer to ISEE 1, 2, 3, Prognoz 7 and IMP 8, respectively.

Constraints: T - Time delay and separation vector

ΔB - Change in magnetic field across shock

UCD - Vector cross product of upstream and downstream magnetic field

UV - Vector cross product of upstream magnetic field and velocity change

DV - Vector cross product of downstream magnetic field and velocity change

It is interesting to note which constraints were statistically the most accurate. The median deviation of the field jump from its expected orthogonality was only 2°, and 90% of the jumps were within 23° of being perpendicular to our fitted normal. The plasma jump constraints, BUV and BDV, were almost as good. The median errors were 7° and 6°, respectively, with 90% of the deviations less than 25° for both constraints. The UCD or magnetic coplanarity constraint did not do as well as the others. Its median error was 21° with 90% of the errors being 46° or less. The problem with this technique lies in the need to calculate a cross product of nearly parallel vectors in a noisy environment. It should be used only when the magnetic field is relatively quiet and the shock moderately strong, with a reasonably large angle between the upstream and downstream field directions. Otherwise it should not be used or else given little weight in the overall solution.

We emphasize that the shock normal we obtain is an average shock normal and that the instantaneous shock normal may and probably does differ from the average value. However, this "real" deviation will not alter the relative ranking of the various constraints. The change in field across the shock was most often in the expected direction and the two field-velocity jump constraints were only slightly worse. We note that if there were large deviations of the instantaneous shock normal from its average value we would not expect the median deviation of the field jump constraint from its expected 90° value to be as low as 2°.

Testing the Normals

Before proceeding to use these determined shock normals we will use the redundancy inherent in these data to test the normal. First we can check our estimate of shock speed using the continuity equation (cf. Abraham-Shrauner and Yun, 1976).

$$V_{sh} = (\rho_2 \underline{V}_2 - \rho_1 \underline{V}_1) \cdot \underline{N} / (\rho_2 - \rho_1)$$

where ρ_1 and ρ_2 are the upstream and downstream solar wind densities, $\underline{V}_1$ and $\underline{V}_2$ the corresponding solar wind velocities and $\underline{N}$ is our best fit shock normal. This computation has been performed for ISEE-1 and -3 for each of our shocks whenever there was a complete plasma scan both upstream and downstream of the shock. Table 2 shows the comparison of these speeds with the best fit speed. Only the shock of 9/25/78 has significantly different speeds. Reference to Table 1 shows that this is the shock with the least number of constraints used in the best fit normal determination. Five constraints appear to be the minimum necessary to be assured of a moderately accurate normal.

Another test we can perform is to compare the Mach number of the shock calculated from the best fit shock speed and the magnetosonic velocity corresponding to the observed plasma conditions with the Mach number necessary to give the observed field jump. We list both these Mach numbers for the two spacecraft in Table 2. The last two columns give the angle between the upstream field and the best fit shock normal for the two spacecraft.

The Mach numbers necessary to give the observed field jumps according to the Rankine-Hugoniot equations, RH1 and RH3, are always greater than 1, by definition. However, because of the imprecision of our measurements of the shock velocity, the solar wind velocity and the plasma density, the magnetosonic velocity that we

Table 2. Shock Parameters

Date	Day	Shock Velocity Best Fit	Cont. 1	Cont. 3	Magnetic Mach Numbers BF1	BF3	RH1	RH3	θ_{Bn} 1	3
8/18/78	230	422km/s	454km/s	431km/s	1.4	1.6	1.6	1.5	73°	78°
9/11/78	254	436	410	409	0.9	1.2	1.3	1.2	32	36
9/20/78	263	334	313	338	1.4	1.6	1.2	1.1	75	76
9/25/78	268	811	453	-	4.9	-	3.0	2.0	60	57
9/28/78	271	672	713	717	0.9	0.9	1.5	1.5	57	55
10/17/78	290	395	419	408	1.0	1.7	1.4	1.4	63	76
10/29/78	302	424	432	421	0.7	1.3	1.4	1.4	69	61
11/8/78	312	447	-	532	-	1.5	1.7	1.6	43	41
11/12/78	316	606	570	-	2.4	-	2.4	2.2	42	40
12/25/78	359	432	414	427	2.2	2.3	1.6	1.7	80	87
8/31/79	243	402	372	392	1.5	1.1	1.4	1.3	40	75
11/11/79	315	466	436	451	2.8	2.4	2.7	1.3	57	67
11/18/79	322	504	474	531	1.7	1.4	1.5	1.7	76	82
11/20/79	324	282	290	-	1.3	-	1.3	1.3	48	39
11/29/79	333	286	290	274	2.0	2.3	2.7	2.0	66	62
11/30/79	334	404	465	417	2.6	2.8	2.5	2.5	89	87

calculate is sometimes greater than the shock speed relative to the upstream plasma. Most often the difference between the two techniques is rather small. However, on 9/25/78 the difference is large. This is also the shock for which we found large differences with shock speed calculation and which had the fewest constraints. Because of these uncertainties, we will not use this shock in the analysis which follows. Further, to characterize the Mach number of the shocks we will use the "Rankine-Hugoniot" Mach numbers. The only exception to this will be the shock of 11/11/79 for which the Rankine-Hugoniot value from the ISEE-3 data differs significantly from the other three values. For this shock we will use the best fit value of 2.7.

Precursor Waves

Visual inspection of the interplanetary shock data reveals two upstream wave types. Furthest upstream from the shocks there is often irregular turbulence, whose frequency spectrum is featureless. Closer to the shock, but not observed as often, a nearly monochromatic wave, which we call a precursor wave, grows in amplitude and terminates at the shock. It does not extend downstream, in contrast to the irregular turbulence which is usually seen both upstream and downstream. It is important to distinguish these two wave types because they have very diff-
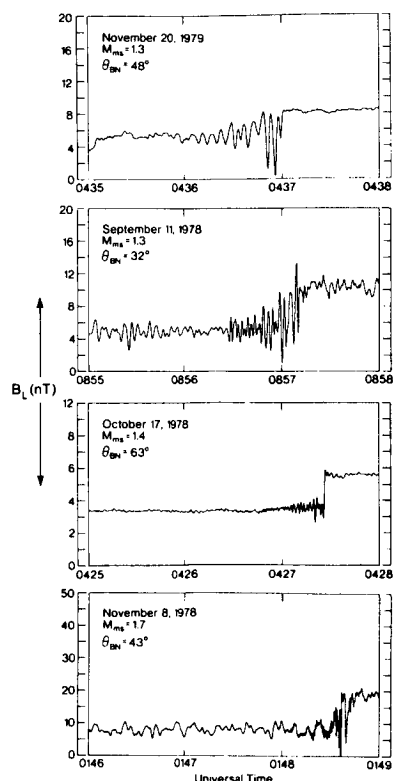
Figure 1. Whistler precursors for four interplanetary shocks as observed by ISEE-2. The component of the magnetic field shown is along the projection of the interplanetary magnetic field on the shock plane and contains the jump in the magnetic field across the shock.
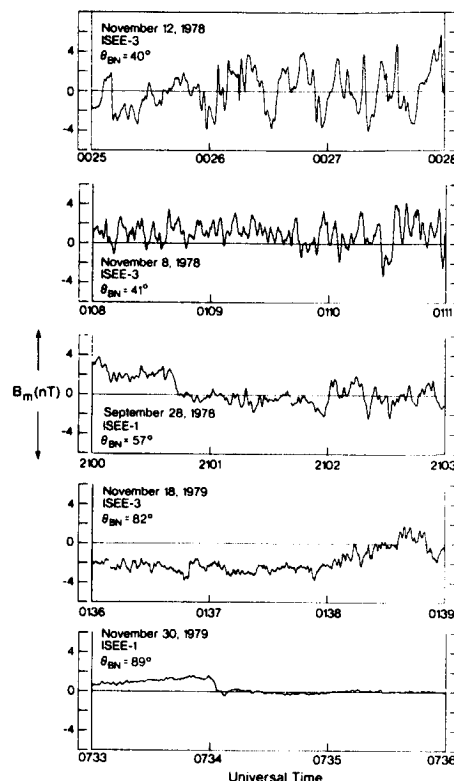
Figure 3. Turbulence seen upstream of five interplanetary shocks. The component shown is perpendicular to the upstream magnetic field and the shock normal.

erent properties. Figure 1 shows examples of the precursor waves for four shocks in the direction perpendicular to the projection of the upstream field on the shock plane. We have identified nine examples of such waves in our shock dataset. These events and their properties are listed in Table 3.

Power spectra were calculated over the duration of the precursor wave in shock normal coordinates (L, M, N) in which N is in the direction of the best fit normal and L is in the shock plane along the direction of the upstream magnetic field. A well defined spectral peak was found for each precursor. The frequency of this peak was calculated by multiplying the frequency by the power of each estimate of the power contributing to the peak, summing, and dividing by the power in the peak. These frequencies are listed in Table 3. The direction of the wave normal, the angle between the wave normal and the magnetic field direction, θ_{Bk}, the percent polarization and the eccentricity were calculated according to the method of Means (1972) and are also listed in this Table. For the ISEE-3 shock

Table 3. Precursor Wave Properties

Event	Day	Spacecraft	Mach. No.	θ_{Bn}	Frequency	Wave Normal	θ_{Bk}	%P	ϵ
1	11/20/79	2	1.3	48	0.21 HZ	(−.543, .064, −.838)	16.3°	99.6%	.95
2	11/20/79	3	1.3	39	0.17	(−.548, −.004, −.837)	4.0	98.7	.92
3	9/11/78	2	1.3	32	0.34	(−.577, −.009, .817)	1.1	96.3	.92
4	10/17/78	2	1.4	63	0.51	(.767, .085, .641)	12.5	98.9	.98
5	10/29/78	3	1.4	61	0.81	(−.770, .280, .574)	17.1	−	−
6	8/18/78	3	1.5	78	2.26	(.877, .159, −.454)	16.9	96.3	−.66
7	9/28/78	3	1.5	55	2.53	(−.112, .121, .985)	44.6	90.1	.88
8	11/8/78	3	1.6	41	0.67	(.670, .358, −.650)	17.9	95.1	.71
					1.13	(.437, .190, −.879)	19.0	96.0	.85
9	11/8/78	2	1.7	43	1.25	(.355, .279, −.892)	27.6	98.5	.86
a	10/29/78	2	1.4	69	0.08	(−.987, −.107, .122)	9.9	90.7	.85
b	10/17/78	3	1.4	76	0.37	(.059, .708, .704)	52.9	73.7	−.62

on October 29, 1978 we used minimum variance analysis to get the wave normal because the data contained too many gaps for our usual wave analysis techniques to work. A glance at the wave normals reveals that the M components are small. Thus these waves are principally propagating in the plane defined by the shock normal and the upstream magnetic field. The waves generally propagate at a small angle to the magnetic field. The wave normal on September 28, 1978 made the largest angle to the field, almost 45°. This was also the briefest precursor, lasting only a few seconds. The percent polarization for all these waves is large, greater than 90% for every event and usually over 95%. The polarization for the precursors is very nearly circular and right-handed in every case but one, the August 18, 1978 event on ISEE-3. We believe that this apparent left-hand polarization is not real but that the wave is actually right-handed and oscillating at 3.74 Hz. The 3 Hz Nyquist frequency of ISEE-3 then aliases the signal to 2.26 Hz and reverses the polarity. The wave spectrum for ISEE-3 November 12, 1978 reveals two peaks both of which have precursor-like properties, i.e., small θ_{Bk}, large percent polarization and right-handed nearly circular polarization. It is not obvious why two waves are present for this case. We note that since these are forward propagating shocks, not reverse shocks like planetary bow shocks, we do not expect
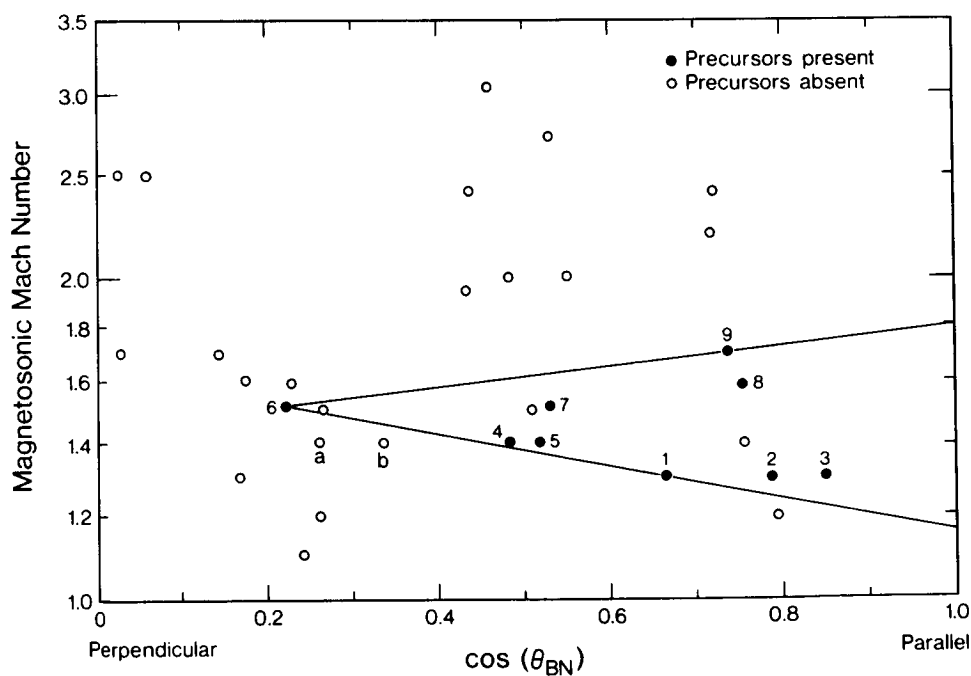

Figure 2. The location of the interplanetary shocks examined in the Mach number - cos θ_{Bn} plane. Solid circles are used to denote those shocks which had whistler precursors. The wedge encloses the region in which precursors were observed.

Doppler shifted polarization reversals. Hence the right-handed polarization identifies these as whistler mode waves.

A glance at Table 3 also reveals that these precursors are present only for shocks with M<1.7. Figure 2 shows the location of these events in the Mach number - cos(θ_{Bn}) plane. A wedge with its vertex at M = 1.5 and cos θ_{Bn} = .22 and its feet at M = 1.16 and 1.8 on the cos θ_{Bn} = 1.0 axis contains all the events. However, there are three shocks within this wedge without precursors. The first near point 6 is from ISEE-2 on November 18, 1979. No precursor waves were seen at ISEE-3 either on this day but none would be expected to be observed because the shock at ISEE-3 was stronger, M = 1.7, and more perpendicular. Perhaps the reason for no precursors at ISEE-2 is that we have incorrectly calculated the Mach number for the ISEE-2 shock. However, there is a simpler explanation. Table 3 reveals that the frequency of the wave at point 6, (ISEE-3 on 8/18/78), is observed to be at least 2.26 Hz and is probably 3.74 Hz. This is well above the ISEE-2 Nyquist frequency on November 18, 1979 of 2.0 Hz. Since the ISEE-2 magnetometer is strongly filtered above the Nyquist frequency before the signal is sampled, no aliased signal is telemetered by the spacecraft.

A second exception occurs near point 7. The exceptional point is from ISEE-1 on September 28, 1978 and point 7 is from ISEE-3 on this same day. Table 3 indicates that the (brief) precursor wave seen at ISEE-3 oscillated at 2.53 Hz. This again was well above the 2 Hz Nyquist frequency of ISEE-1 on September 28, 1978. The final exception is near point 2. This point corresponds to ISEE-2 observations on August 31, 1979. The nearby observations, points 1, 2 and 3, have frequencies well below the Nyquist frequency of ISEE-2. We note that ISEE-3 did not observe precursor waves but we would not have expected to observe them because the shock was very nearly perpendicular at ISEE-3 (θ_{Bn} = 80°). The only unusual condition in the solar wind on this day was that the upstream electron and ion temperatures were about equal. However, it is not obvious to us how this condition would affect the precursor waves.

It is obvious from Table 3 and our discussion above that the cause of the top leg of the wedge through points 6 and 9 is the disappearance of the precursor waves as they become undetectable above the passband of our instruments. We have no means of determining from these data how high in Mach number or frequency these waves extend.

The reason for the lower leg is not as obvious. The point below point 2 that has no precursors is, in fact, very unshock-like in the magnetic field. There is merely a very slow rise in field strength and rotation lasting 35 seconds. Perhaps this represents one cycle of a very long wavelength whistler wave. Points a and b do show some upstream wave activity. Point a corresponds to the ISEE-2 shock on October 29, 1978. The waves at ISEE-2 have properties very similar to the precursors discussed above. They propagate nearly along the magnetic field and they are highly polarized. However, they occur at a frequency an order of magnitude less than were observed on ISEE-3 for this same event. On the other hand, the waves corresponding to point b at ISEE-3 on October 17, 1978 are similar in frequency to those seen at ISEE-2 for this same event (point 4). However, these waves are propagating at a large angle to the field, are less well polarized, are elliptical rather than circular and are left-handed. Moreover they are weak and do not grow as the shock approaches. The frequency also is suspiciously close to the spin frequency of the spacecraft. The other three low Mach number cases at

M = 1.3, 1.2 and 1.1 correspond to ISEE-3 on August 31, 1979, ISEE-2 on September 20, 1978 and ISEE-3 on September 20, 1978. The first two cases are well defined sharp shocks with no precursors but have many data gaps upstream including one right at the shock crossing. The absence of precursor waves at the lowest Mach numbers appears to be a real phenomenon. Its explanation is not obvious.

Upstream Turbulence

In addition to the precursor waves which exist in the shock ramp and for a short distance upstream, irregular waves with rather featureless spectra are seen upstream of some interplanetary shocks. Figure 3 shows samples of these waves for a variety of angles between the upstream magnetic field and the shock normal. Figure 4 shows power spectra for these waves. The magnetic component shown is the M component, i.e., the direction in the plane of the shock perpendicular to the upstream field. As discussed in the previous section the precursor waves which we are able to observe are a low Mach number phenomenon. At higher Mach numbers the precursor waves occur at higher frequencies eventually rising above our pass band. To avoid mixing the two wave types we will use the simple expedient of studying the upstream turbulence only at Mach numbers above 1.5.

Table 4 shows the properties of the upstream turbulence for the one minute just prior to shock passage for all the interplanetary shocks in our study which had Mach numbers greater than 1.5 and were not contaminated with ions backstreaming from the terrestrial bow shock. We have also eliminated any intervals for which we did not have a full minute of upstream measurements and those for which an obvious tangential discontinuity occurred during the analysis interval. The frequency interval 0.03 to 0.3 Hz was chosen for analysis. There is little power in these waves above 0.3 Hz and 30 seconds is as low a period one could safely analyze utilizing a minute's worth of data. We have used the analysis of Born and Wolf (Rankin and Kurtz, 1970) as it is more appropriate for the study of linearly polarized signals such as these waves tend to be.

As for the precursors, the wave normals in L, M, N, coordinates show that the waves are mainly propagating in a plane defined by the magnetic field and the shock normal. Further, the waves are propagating nearly parallel to the magnetic field. For the two exceptions to this rule, ISEE-3 on December 25, 1978 and ISEE-2 on November 30, 1979, it may be argued that since the shocks are very nearly perpendicular and the waves very small that the direction of propagation is not well determined. The percent polarization is much less than for the precursors ranging from 26 to 73%. The waves are polarized about equally left and right-handed and are at times very nearly linearly polarized. The maximum eccentricity observed was 0.76. The waves are almost entirely transverse fluctuations, as shown by the last column of Table 4 which gives the ratio of compressional power to transverse power. Except for two nearly perpendicular shocks which have almost no transverse power upstream, this ratio is less than 10%. This is consistent with the observed direction of propagation of the waves which is nearly parallel to the field and in contrast to waves upstream of the bow shock.

The amplitudes of these waves are strongly correlated with θ_{Bn}, the angle between the upstream magnetic field and the shock normal. Figure 5 shows the logarithm of the amplitude of the waves as a function of the $\cos \theta_{Bn}$. The straight line is the best fit straight line omitting the two low points on November 29, 1979. It has a correlation coefficient of 0.935. If we include the two low
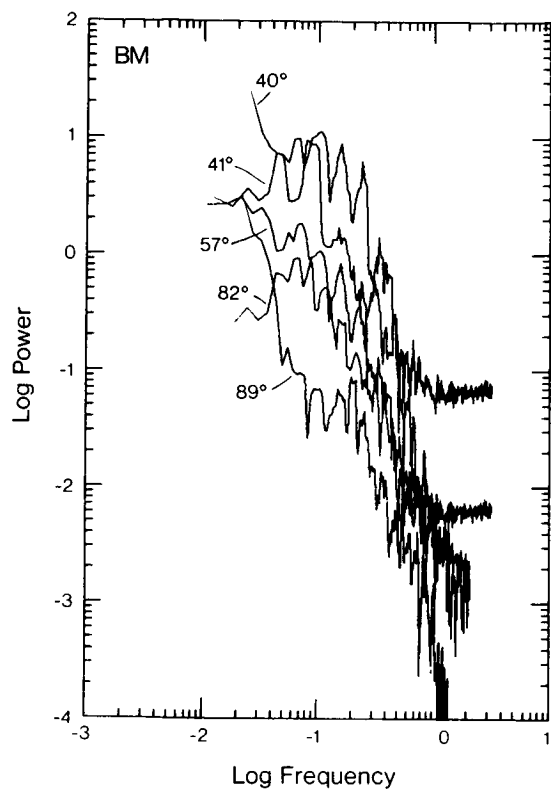
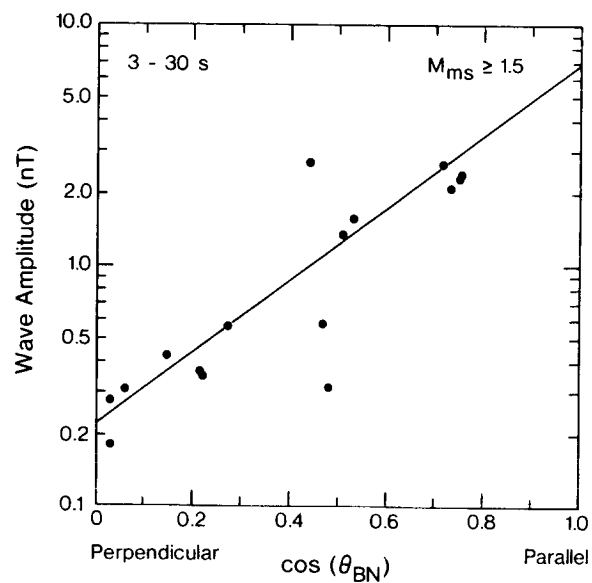Figure 4.   Power spectra of the waves shown in Figure 3.

Figure 5.   The logarithm of the wave amplitude of upstream turbulence as a function of the cosine of the angle between the interplanetary field and the shock normal. The amplitude is the square root of the trace of the spectral matrix integrated over the frequency band from 0.03 to 0.3 Hz.

Table 4. Properties of Upstream Turbulence

Day	Spacecraft	Mach No.	θ_{Bn}	Amplitude	Wave Normal	θ_{Bk}	%P	ε	% Comp.
8/10/78	3	1.5	78°	0.36nT	(.953, -.021, -.185)	4.0^{o}	51.7%	-0.12	.009
8/18/78	2	1.6	73	0.37	(.974, .032, -.226)	4.0	66.3	-0.76	.034
9/28/78	1	1.5	57	1.37	(.872, -.059, .487)	3.4	29.3	0.56	.034
11/8/78	3	1.6	41	2.33	(.638, .150, -.756)	9.1	60.4	0.70	.039
11/8/78	2	1.7	43	2.12	(.670, .079, -.738)	3.7	25.9	0.36	.069
11/12/78	3	2.2	40	2.71	(-.519, -.084, -.850)	13.7	56.5	-0.26	.031
12/25/78	3	1.6	87	0.28	(-.629, -.081, -.773)	52.6	61.4	0.21	.239
11/11/79	3	2.4	67	2.70	(-.843, -.151, -.517)	10.6	58.5	-0.56	.029
11/11/79	2	2.7	57	1.57	(-.690, -.181, -.701)	16.8	73.0	0.68	.051
11/18/79	3	1.7	82	0.44	(.935, -.010, -.355)	14.3	68.2	0.01	.013
11/18/79	2	1.5	76	0.56	(.937, .300, .181)	18.3	48.4	0.15	.071
11/29/79	3	2.0	62	0.31	(-.943, -.212, -.257)	18.3	33.0	-0.21	.061
11/29/79	2	2.7	66	0.58	(-.838, .027, -.546)	6.3	32.6	-0.01	.025
11/30/79	3	2.5	87	0.31	(-.788, .364, -.497)	35.3	72.6	-0.02	.071
11/30/79	2	2.5	89	0.18	(-.864, .500, .066)	58.6	72.4	0.39	.230

November 29 points the correlation drops to 0.838. However, on November 29 the upstream magnetic field strength is only 2.5 nT, less than half its usual magnitude. Since we expect that these waves grow through resonance with the upstream ions we expect that the ion gyro frequency orders these waves. Then the spectral power of the waves would occur on this day at a much lower frequency and our one minute analysis interval is not long enough to determine the proper wave power. It seems clear that the wave amplitudes are controlled by θ_{Bn}. We note that we have used here a one minute average of the upstream field just upstream of the shock to define θ_{Bn}. In actuality, the waves observed were generated at an earlier time when the IMF may have had a different direction. Furthermore, the presence of discontinuities in the solar wind can add power to the wave analysis even though they have no association with the shock.

Discussions and Conclusions

The results of our investigations of waves upstream from interplanetary shocks indicate that, while their successful study is difficult, they can be profitably examined if data from both magnetometers and plasma instruments are available. The most important step in this process is determining an accurate normal. The mixed mode technique for a single spacecraft appears to be quite accurate in general. When an accurate normal is available, the shock speed can be determined quite accurately from the continuity equation. However, to guarantee an accurate normal determination one should use data from multiple spacecraft and over-determine the solution. This allows calculation of probable error and the time delay between spacecraft gives the velocity, independent of the plasma measurements.

In sorting out the plethora of phenomena associated with interplanetary shocks, it is important to realize that there are two different wave types in the upstream region with quite different wave properties. The precursor waves are an integral part of the shock structure at low Mach numbers at moderate and small angles of the IMF to the shock normal. These waves are right-handed and are obviously propagating in the direction of the shock motion, that is with the solar wind flow. Thus, while they are Doppler shifted, their polarization is not reversed. Hence, they must also be right-handed, i.e., whistler mode waves, in the plasma frame also. The whistler precursors are highly polarized and are very nearly circularly polarized.

At the lowest Mach numbers and for nearly perpendicular shocks, there seem to be few waves upstream of the shock. However, above a Mach number of 1.5 there are broadband irregular waves with low to moderate percent polarization, propagating generally at small angles to the field with almost linear polarization. The amplitude of these waves is strongly correlated with the direction of the IMF relative to the shock normal. These waves seem to be those predicted by Lee (1983).

Much analysis is yet to be done with both the precursor waves and the upstream turbulence. For example, we have not investigated what controls the wavelength or direction of propagation and hence the apparent frequency of the precursor waves. Nor have we examined their amplitude and duration. Similarly, we must examine the full spectrum of the upstream turbulence, not just the arbitrary 3-30 second band, and the size of the region of occurrence of these waves upstream of interplanetary shocks.

References

Abraham-Shauner, B. and S.H. Yun, Interplanetary shocks seen by Ames plasma probe on Pioneer 6 and 7, J. Geophys. Res., 81, 2097-2102, 1976.

Axford, W.I., Acceleration of cosmic rays by shock waves, in Proceedings of an International School and Workshop on Plasma Astrophysics held at Varenna, Como, Italy, from 27 August to 7 September 1981 (ESA SP-161), pp. 425-449, ESTEC, Noordwijk, Holland, 1981.

Bame, S.J., J.R. Asbridge, H.E. Felthauser, J.P. Gore, G. Paschmann, P. Hemmerich, K. Lehmann and H. Rosenbauer, ISEE-1 and ISEE-2 fast plasma experiment and the ISEE-1 solar wind experiment, IEEE Trans. Geoscience Electronics, GE-16, 216, 1978a.

Bame, S.J., J.R. Asbridge, H.E. Felthauser, J.P. Gore, H.L. Hawk and J. Chavez, ISEE-C solar wind plasma experiment, IEEE Trans. Geosci. Electronics, GE-16, 160-162, 1978b.

Frandsen, A.M.A., B.V. Connor, J. Van Amersfoort and E.J. Smith, The ISEE-C vector helium magnetometer, IEEE Trans. Geoscience Electronics, GE-16, 195-198, 1978.

Gosling, J.T., S.J. Bame, W.C. Feldman, G. Paschmann, N. Sckopke and C.T. Russell, Suprathermal ions upstream from interplanetary shocks, J. Geophys. Res., 88, in press, 1983.

Hoppe, M.M. and C.T. Russell, On the nature of ULF waves upstream of planetary bow shocks, in Advances in Space Research, 1, 327-332, 1981.

Kennel, C.F., F.L. Scarf, F.V. Coroniti and E.J. Smith, Nonlocal plasma turbulence associated with interplanetary shocks, J. Geophys. Res., 87, 17-34, 1982.

Lee, M.A., Coupled hydromagnetic wave excitation and ion acceleration at interplanetary travelling shocks, J. Geophys. Res., submitted, 1983.

Means, J.D., Use of the three-dimensional covariance matrix in analyzing the polarization properties of plane waves, J. Geophys. Res., 77, 5551, 1972.

Morfill, G. and M. Scholer, Solar cosmic ray diffusion coefficient behind interplanetary shock waves, in Contributed Papers to the Study of Travelling Interplanetary Phenomena/1977, (edited by M.A. Shea, D.F. Smart and S.T. Wu), pp. 231-241, 1977.

Rankin, D. and R. Kurtz, Statistical study of micropulsation polarizations, J. Geophys. Res., 75, 5444-5458, 1970.

Russell, C.T., The ISEE-1 and -2 fluxgate magnetometers, IEEE Trans. Geoscience Electronics, GE-16, 239-242, 1978.

Russell, C.T. and M.M. Hoppe, Upstream waves and particles, Space Sci. Rev., in press, 1983.

Russell, C.T., M.M. Mellott, E.J. Smith and J.H. King, Multiple spacecraft observations of interplanetary shocks: Four spacecraft determination of shock normals, J. Geophys. Res., submitted, 1983a.

Russell, C.T., J.T. Gosling, R. Zwickl and E.J. Smith, Multiple spacecraft observations of interplanetary shocks: ISEE 3-D plasma measurements, J. Geophys. Res., submitted, 1983b.

Tsurutani, B.T., E.J. Smith and D.E. Jones, Waves observed upstream of interplanetary shocks, J. Geophys. Res., submitted, 1983.

LOW ENERGY (E $\lesssim$ 30 KEV) SUPRATHERMAL IONS UPSTREAM FROM INTERPLANETARY SHOCKS

J. T. Gosling, S. J. Bame and W. C. Feldman (ESS-8, MS D438, Los Alamos National Laboratory, Los Alamos, NM 87545) G. Paschmann and N. Sckopke (Max-Planck-Institut fur Physik und Astrophysik, Institut fur extraterrestrische Physik, 8046 Garching, West Germany)

Suprathermal ions at energies below $\sim$ 30 keV have been observed for the first time upstream from several interplanetary (IP) shocks with the Los Alamos/Garching fast plasma experiments on ISEE 1 and 2. Although in one event these ions were observed at least several hours before shock passage, more typically the countrate rises above the instrument threshold of $\sim$ 3.7 x 10^2 (cm^2 s sr kev)$^{-1}$ at 28.6 keV approximately 5 minutes before shock passage. Velocity distribution functions for these ions are always roughly isotropic in the shock frame of reference, and thus these ions appear to be the interplanetary counterpart of the "diffuse" ions observed immediately upstream from the earth's bow shock. Other types of ion velocity distributions common to the earth's foreshock-field-aligned beams, kidney bean shaped distributions, and torus-like distributions-which appear to be essential ingredients of the ion acceleration process near the bow shock have not yet been observed upstream from IP shocks despite occasional favorable observing geometries. Nor is there a clear correspondence between the interplanetary upstream ions and compressive waves with periods near 30 S as at the bow shock. These differences may be a result of the relatively low Mach number of IP shocks, the relatively long field line connection times for IP shocks, or differences in details of the ion acceleration process.

ELECTRON HEATING AT INTERPLANETARY SHOCKS

W. C. Feldman, J. R. Asbridge, S. J. Bame,
J. T. Gosling, and R. D. Zwickl
Los Alamos National Laboratory
Los Alamos, NM 87545

ABSTRACT

Data for 41 forward interplanetary shocks measured between August 1978 and December 1979 show that the ratio of downstream to upstream electron temperatures, $T_e(d/u)$ is variable in the range between 1.0 (isothermal) and 3.0. On average, $\langle T_e(d/u)\rangle = 1.5$ with a standard deviation, $\sigma_e = 0.5$. This ratio is less than both the average ratio of proton temperatures across the same shocks ($\langle T_p(d/u)\rangle = 3.3$ with $\sigma_p = 2.5$) and the average ratio of electron temperatures across the earth's bow shock. Individual samples of $T_e(d/u)$ and $T_p(d/u)$ appear to be weakly correlated with the number density ratio. However the amounts of electron and proton heating are well correlated with each other as well as with the bulk velocity difference across each shock. The stronger shocks appear to heat the protons relatively more efficiently than they heat the electrons.

Introduction

Although extensive research has been devoted to the various characteristics of interplanetary shocks, not much work has been devoted to their effects on solar wind electrons. Early work based on data measured using the Vela 4 plasma analyzers indicated a low efficiency for heating the ambient plasma electrons (Hundhausen et al., 1970; Hundhausen, 1970a). This result was interpreted to be a consequence of the high solar wind thermal conductivity. Any heating would then be quickly distributed over a large volume of plasma thereby increasing the thermal energy per electron only slightly (Hundhausen and Montomgery, 1971).

Most studies of solar wind electrons have been made using measurements from satellites in near earth orbit. The earth's bow shock is known to preheat the magnetically connected upstream solar wind by variable amounts having an average magnitude (Feldman et al., 1973) of the order of that caused by interplanetary shocks (Hundhausen, 1970a; Hundhausen et al., 1970). Since it is difficult to isolate data measured from these orbits which are completely unperturbed by the bow shock, the early Vela 4 shock results have not been followed by more extensive and deeper studies. This difficulty has been overcome by the launch of ISEE-3 which was stationed for approximately 4 years about 10^6 km upstream of the earth. This orbit was sufficiently far upstream that ISEE-3 was usually not connected magnetically to the earth's bow shock (Feldman et al., 1982).

This paper reports the results of a study of electron heating at interplanetary shocks using data measured with the Los Alamos electron plasma analyzer aboard ISEE 3. Analysis procedures are described briefly in Section 2 and the results and conclusions are given in Sections 3 and 4 respectively.

In the following presentation, a standard notation is adopted. The symbols N, V, and T will denote the proton density, bulk velocity and numerically-integrated total temperature. Subscripts e and p on the temperature refer to electrons and protons respectively. Parenthetical use of the combinations (d/u) and (d-u) denote the ratio of downstream to upstream parameters and the difference between downstream and upstream parameters respectively.

2) Data and Analysis Procedures

Details of the Los Alamos ISEE-3 plasma analyzers along with their operation modes have been published elsewhere (Bame et al., 1979a). Ion and electron plasma data measured between August 1978 and December 1979 were used in the present study. Fluid parameters were calculated by integrating numerically over that portion of the ion count-rate distribution dominated by protons and over the electron velocity distribution between about 10 eV and 1 keV.

A list of possible shocks passing ISEE 3 between 18 August 1978 and 1 January 1980 was prepared using the ion data in conjunction with magnetic field data (for a description of the magnetometer see Frandsen et al., 1979). Forward shocks were identified by abrupt increases in bulk velocity, number density, proton temperature and magnetic field strength. The 41 events on the list which had the unambiguous signature of a forward shock and no data gap at shock passage, comprised the base for the present study. Number densities, bulk velocities and total proton temperatures determined using the ion data, as well as total electron temperatures determined from the electron data, were averaged over an approximately 5 min interval upstream and downstream of each shock and tabulated. The results of an analysis of these parameters is given next.

3) Experimental Results

a) Statistics

The statistics of particle heating at these 41 shocks are collected in Table 1. Inspection shows that this set of shocks is on the average weaker than the earth's bow shock. Whereas $\langle N(d/u) \rangle = 1.9$ and $\langle V(d-u) \rangle = 76$ km s^{-1} for this set, they are ~3 and ~100 km s^{-1} respectively for the earth's bow shock (see e.g. Hundhausen, 1970b; Montgomery et al., 1970; Scudder et al., 1973 Bame et al., 1979b). Electron heating at these interplanetary shocks is also weaker than at the bow shock. On average $\langle T_e(d/u) \rangle = 1.5$ with a standard deviation of 0.5 as compared to $\langle T_e(d/u) \rangle = 3$ for the earth's bow shock (Hundhausen, 1970b ; Scudder et al., 1973; Bame et al., 1979b). The electron heating at these shocks is also less than the proton heating averaged over the same shocks. This fact is demonstrated by comparing the rows in Table 1 giving the statistics for $T_e(d/u)$ and $T_e(d-u)$, with those giving $T_p(d/u)$ and $T_p(d-u)$ respectively. This result is also similar to that obtained at the earth's bow shock (Montgomery et al., 1970).

b) Parameter Correlations

The associations of electron and proton heating with each other as well as with the density and velocity changes at interplanetary shocks can best be displayed by scatter plots of pairs of parameters. Since the ratio of number

Table 1

Statistics of Particle Heating at 41 Interplanetary Shocks Observed Between August 1978 and December 1979

Parameter	Units	Average	Standard Deviation	Low 5%	High 5%
$N(d/u)$	---	1.9	0.6	1.2	3.1
$V(d-u)$	km s^{-1}	76	53	17	225
$T_e(d/u)$	---	1.5	0.5	1.0	2.5
$T_e(d-u)$	10^5K	0.8	0.9	0.0	2.7
$T_p(d/u)$	---	3.3	2.5	1.3	10.0
$T_p(d-u)$	10^5K	1.6	2.2	0.1	9.2

The entries in the last two columns give the second lowest and second highest parameter values from the full set of 41 shocks.

density measured just downstream to that just upstream, $N(d/u)$, is a measure of the shock strength, we explore first how well it orders the data. If particle heating at interplanetary shocks obeys a polytrope law then $\ln[T(d/u)]$ = $(\gamma - 1)\ln[N(d/u)]$ where γ is the ratio of specific heats. Such a law is used sometimes as a guide for interpreting theoretical simulations of collisionless shocks (see e.g. Forslund et al., 1982) and has been found useful for organizing data showing electron heating across high speed stream interaction zones at 1AU (Feldman et al., 1978). The averages listed in Table 1 would then provide estimates of γ for electron and proton heating separately, $(\gamma_e - 1)$ = 0.6 and $(\gamma_p - 1)$ = 1.9.

Plots of the ratio of upstream to downstream electron and proton temperatures, $T_e(d/u)$ and $T_p(d/u)$, respectively, against the ratio of proton number density, $N(d/u)$, are given in Figure 1. The solid lines represent polytrope laws having γ = 5/3, 2 and 3 representing adiabatic heating in 3, 2, and 1 dimensions, respectively. Inspection of the plots shows only weak positive correlations between either temperature ratio and the number density ratio. It also shows that a polytrope law does not describe adequately the parametric dependences of particle heating at interplanetary shocks. This conclusion is reinforced by examining the slopes, m, y intercepts, b, and correlation coefficients, r, of the linear regressions between $\ln[T_e(d/u)]$ and $\ln[N(d/u)]$ and between $\ln[T_p(d/u)]$ and $\ln[N(d/u)]$ listed in Table 2. Not only are both correlation coefficients low, r ~ 0.5, but the y intercepts are nonzero and the slopes differ substantially from those estimated from the averages given in Table 1.

Table 2

Correlations Between Pairs of Fluid Parameters at 41 Interplanetary Shocks Observed Between August 1978 and December 1979

$$Y = mX + b$$

Y Parameter	Units	X Parameter	Units	m	b	r
$\ln T_e(d/u)$	---	$\ln N(d/u)$	---	0.27	0.16	0.51
$\ln T_p(d/u)$	---	$\ln N(d/u)$	---	1.23	0.22	0.53
T_e (d/u)	---	T_p (d/u)	---	0.14	1.03	0.75
T_e (d-u)	10^5K	T_p (d-u)	10^5K	0.29	0.31	0.72
V(d-u)	km s^{-1}	N(d/u)	---	74.6	-69.0	0.82
T_e(d-u)	10^5K	V(d-u)	km s^{-1}	0.015	-0.36	0.89
T_p(d-u)	10^5K	V(d-u)	km s^{-1}	0.035	-1.06	0.83
$\ln T_e(d/u)$	---	$\ln$ V(d-u)	km s^{-1}	0.31	-0.94	0.76
$\ln T_p(d/u)$	---	$\ln$ V(d-u)	km s^{-1}	0.70	-1.87	0.73
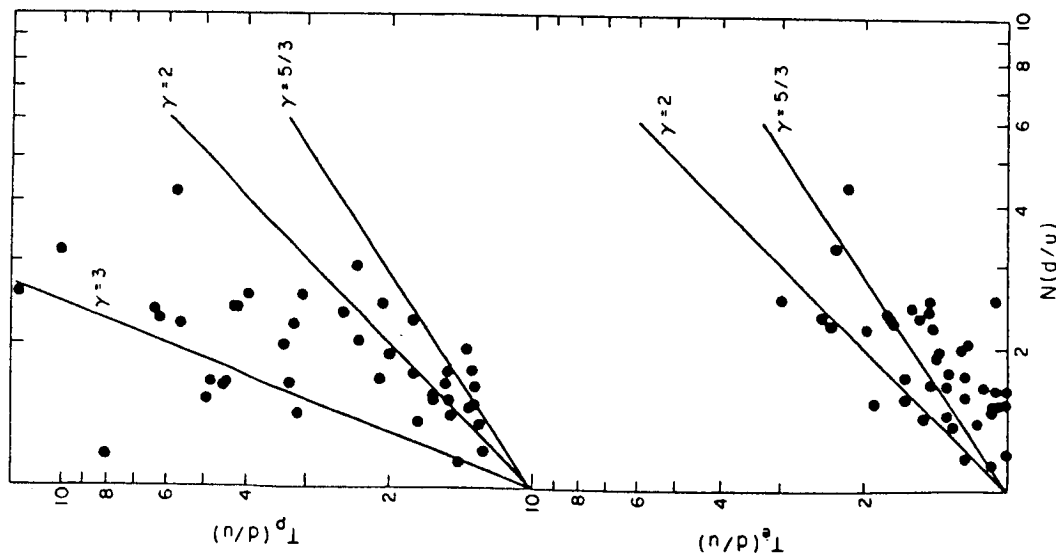
Figure 1. Scatter plots of the ratio of downstream to upstream proton temperatures (above) and electron temperatures (below) against the ratio of downstream to upstream proton number density for 41 forward interplanetary shocks observed at ISEE 3 between August 1978 and December 1979. The solid lines represent polytrope laws with ratios of specific heats, $\gamma = 3$, 2 and 5/3.

Electron and proton heating are more strongly correlated with each other as well as with the difference in bulk velocity across the shocks, V(d-u), than they are with the density jump across the shocks. Scatter plots showing the correlation between electron and proton heating are shown in Figures 2 and 3. Both temperature ratio and temperature difference correlations are roughly equal, r = 0.75 and 0.72 respectively. Although these correlations are significantly better than those between $\ln T$ and $\ln N$, the data in Figures 2 and 3 show substantial scatter. Comparison of the data with the solid lines, which represent equal fractional heating in figure 2 and equal amounts of heating in figure 3, shows that interplanetary shocks heat the protons more than they heat the electons. This condition holds true also for the earth's bow shock (Montgomery et al., 1970).

Electron and proton heating at interplanetary shocks are best correlated with the difference in bulk velocity across the shocks. This velocity difference is also a measure of shock strength as defined by the ratio of downstream to upstream densities, N(d/u). This fact is evident by the good correlation between V(d-u) and N(d/u) shown in Figure 4. The parameters of the linear regression are given in the fifth row of Table 2 showing r = 0.82.

Scatter plots showing the correlations between T_e(d-u) and V(d-u) as well as between T_p(d-u) and V(d-u) are shown in Figures 5 and 6. The parameters of the respective linear regressions are given in rows 6 and 7 of Table 2. Although not shown here, plots of T_e(d/u) against V(d-u) and of T_p(d/u) against V(d-u) show similar correlations. An important property of these correlations is that the shocks having the larger velocity differences are relatively more effective in heating protons than they are in heating electrons. This effect can be seen by comparing Figures 5 and 6 and is quantified in the last 2 rows of Table 2. Specifically the slope for the correlation between $\ln T_p$(d/u) and $\ln V$(d-u) is larger than that for the correlation between $\ln T_e$(d/u) and $\ln V$(d-u).

4) Summary and Conclusions

Detailed comparisons between the foregoing results and the many theories of particle heating at collisionless shocks is not possible since these theories depend importantly on parameters which were not included in the present study. Specifically they depend on the upstream β (ratio of particle pressure to magnetic field pressure), the shock-normal-magnetic field angle, the Mach number, and the conductivity of both the upstream-ambient, and downstream-shocked plasmas. However electron heating at a large set of interplanetary shocks is reported here for the first time. Comparison of the measured heating with the $\gamma = 2$ line in Figure 1 indicates that if such heating is confined to two dimensions as many theories predict (see e.g. Tidman and Krall, 1971; Lemons and Gary, 1978; Forslund et al., 1982), then heat conduction must be an important electron cooling mechanism. This conclusion is consistent with that reached previously (Hundhausen and Montgomery, 1971). Finally, the relatively larger efficiency for heating protons at the stronger interplanetary shocks is consistent with theories of ion reflection (Forslund and Shonk, 1970; Auer et al., 1971; Leroy et al., 1982) although to date, no evidence for such reflection has been found (Gosling et al., 1983). This lack of evidence may indicate that few if any of the interplanetary shocks observed at ISEE-3 were supercritical.
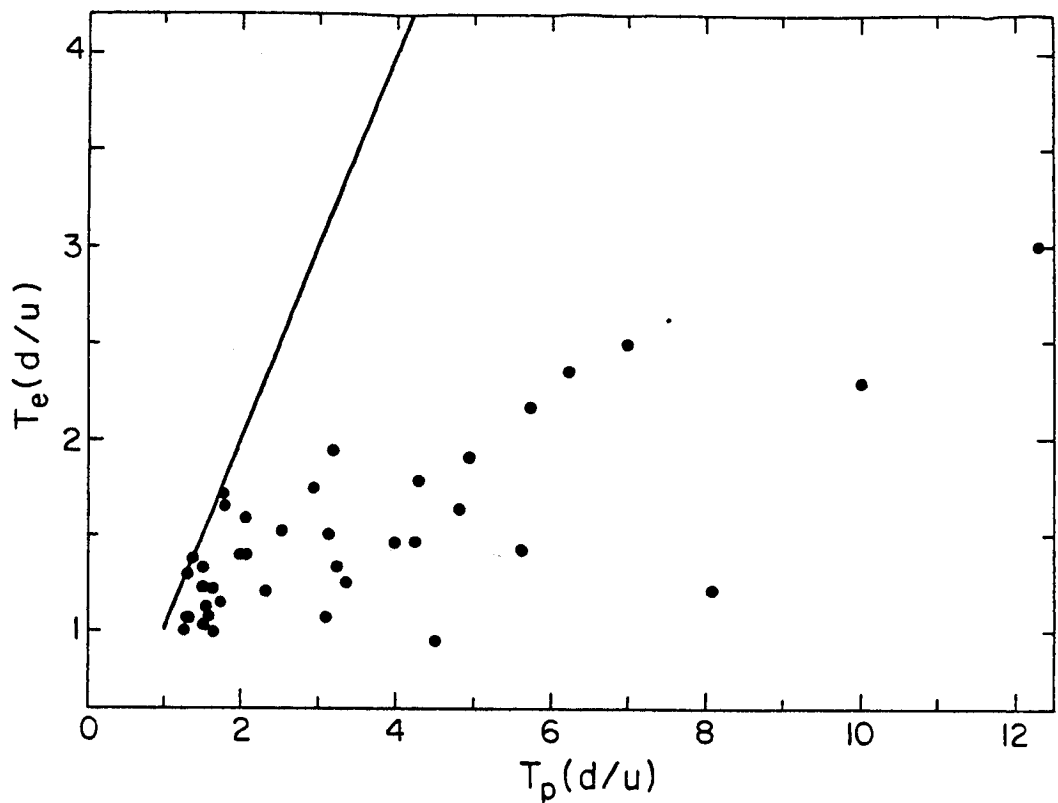
Figure 2. A scatter plot showing the correlation between the ratios of downstream to upstream electron and proton temperatures at 41 forward interplanetary shocks observed at ISEE 3 between August 1978 and December 1979. The solid line represents equal ratios of downstream to upstream electron and proton temperatures.
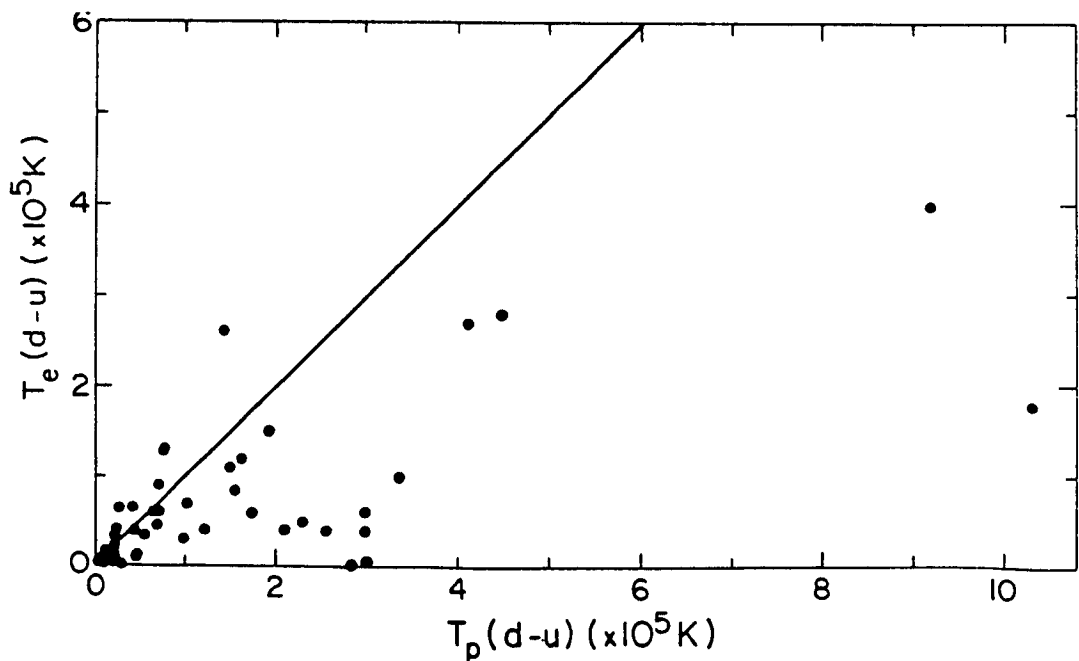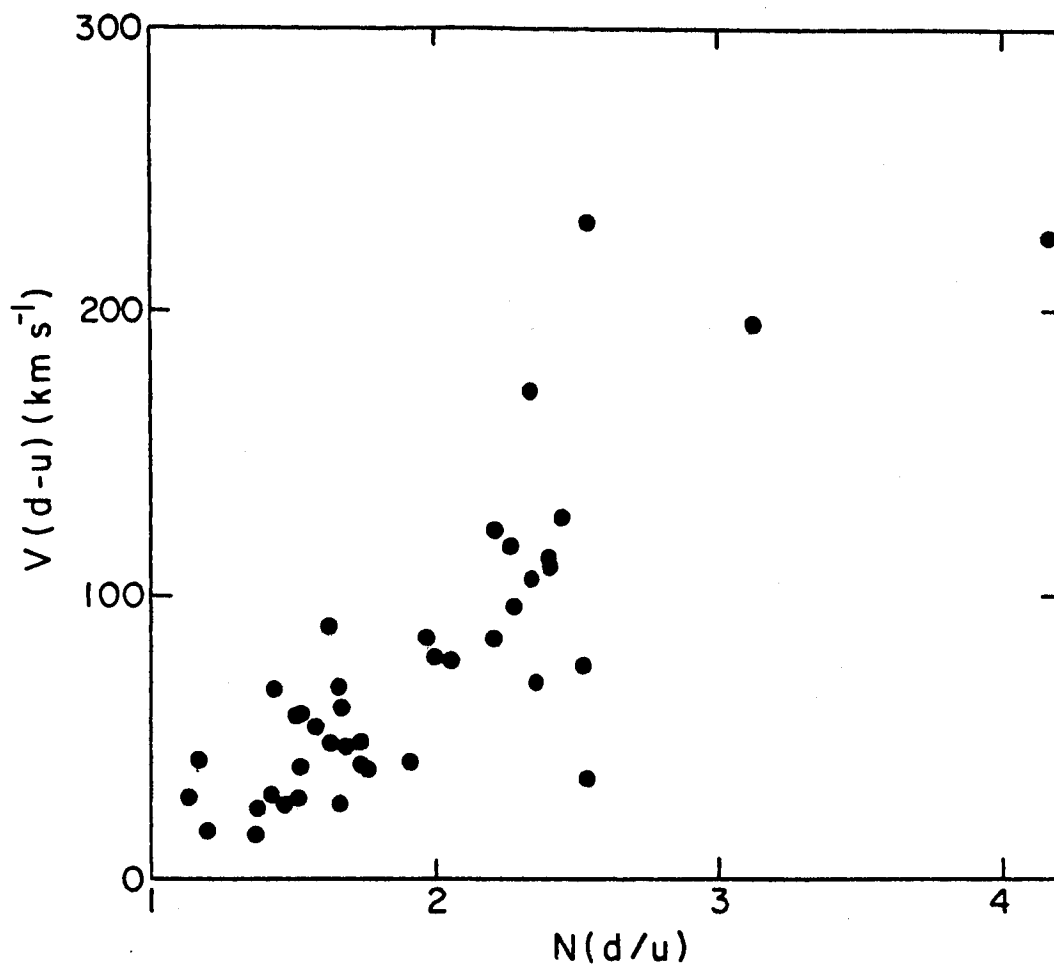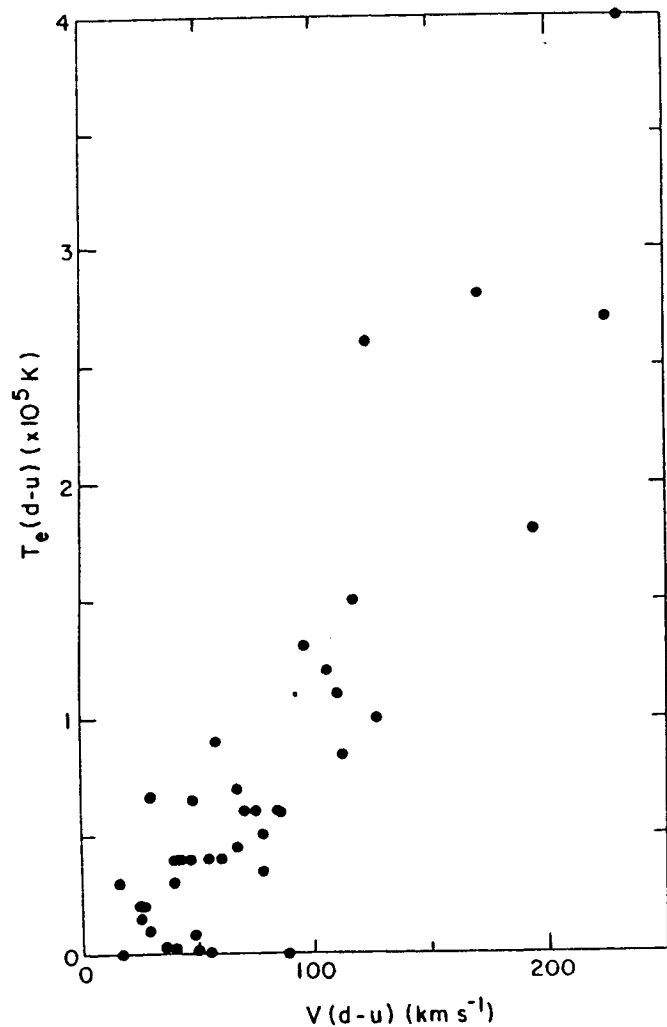

Figure 3. A scatter plot showing the correlation between the amounts of electron and proton heating at 41 forward interplanetary shocks observed at ISEE 3 between August 1978 and December 1979. The solid line represents equal electron and proton heating.

Figure 4. A scatter plot showing the correlation between the velocity differences and ratios of downstream to upstream proton densities at 41 forward interplanetary shocks observed at ISEE 3 between August 1978 and December 1979.
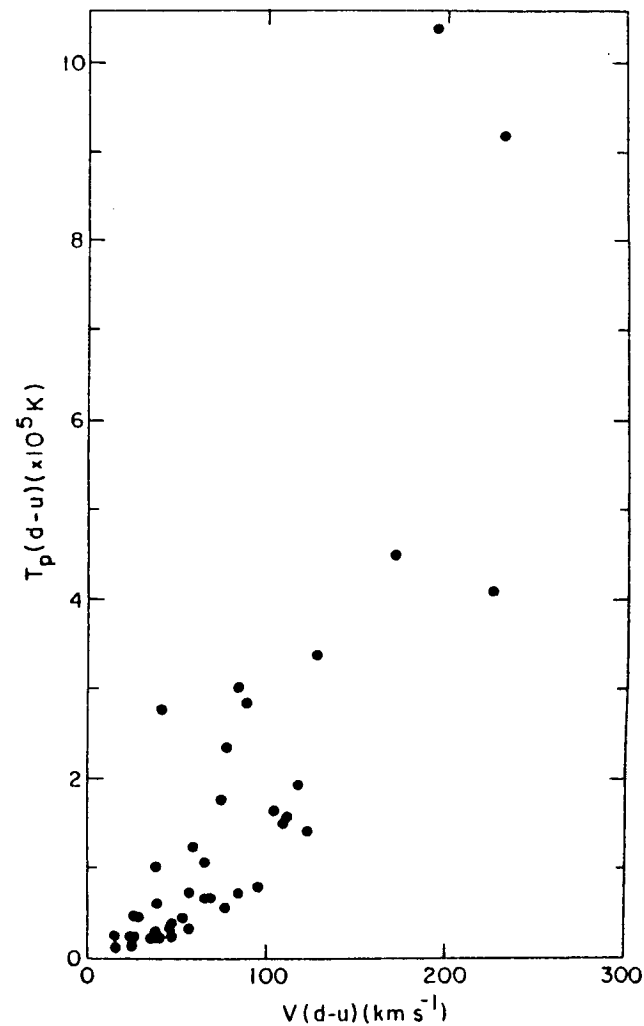
Acknowledgments

Figure 5. A scatter plot showing the correlation between the amount of electron heating and velocity difference at 41 forward interplanetary shocks observed at ISEE 3 between August 1978 and December 1979.

Figure 6. A scatter plot showing the correlation between the amount of proton heating and velocity difference at 41 forward interplanetary shocks observed at ISEE 3 between August 1978 and December 1979.

References

Auer, P. L., R. W. Kilb, and W. F. Crevier, Thermalization in the earth's bow shock, J. Geophys. Res., 76, 2927, 1971.

Bame, S. J., J. R. Asbridge, H. E. Felthauser, J. P. Glore, H. L. Hawk, and J. Chavez, ISEE-C Solar wind plasma experiment, IEEE Trans. Geosci. Electron., GE-16, 160, 1979a.

Bame, S. J., J. R. Asbridge, J. T. Gosling, M. Halbig, G. Paschmann, N. Sckopke, and H. Rosenbauer, High temporal resolution observations of electron heating at the bow shock, Space Sci. Rev., 23, 75, 1979b.

Feldman, W. C., J. R. Asbridge, S. J. Bame, and M. D. Montgomery, Solar wind heat transport in the vicinity of the earth's bow shock, J. Geophys. Res., 78, 3697, 1973.

Feldman, W. C., J. R. Asbridge, S. J. Bame, J. T. Gosling, and D. S. Lemons, Electron heating within interaction zones of simple high-speed solar wind streams, J. Geophys. Res., 83, 5297, 1978

Feldman, W. C., R. C. Anderson, J. R. Asbridge, S. J. Bame, J. T. Gosling and R. D. Zwickl, Plasma electron signature of magnetic connection to the earth's bow shock: ISEE3, J. Geophys. Res., 87, 632, 1982.

Forslund, D. W., and C. R. Shonk, Formation and structure of electrostatic collisionless shocks, Phys. Rev. Letters, 25, 1699, 1970

Forslund, D. W., K. Quest, J. U. Brackbill, and K. Lee, Collisionless dissipation in quasi-perpendicular shocks, submitted to Geophys. Res. Lett., 1982

Frandsen, A. M. A., B. V. Connor, J. Van Amersfoort, and E. J. Smith, ISEE-C vector helium magnetometer, IEEE Trans. Geosci. Electron., GE-16, 195, 1979.

Gosling, J. T., S. J. Bame, W. C. Feldman, G. Paschmann, N. Sckopke, and C. T. Russell, Suprathermal ions upstream from interplanetary shocks, submitted to J. Geophys. Res., 1983

Hundhausen, A. J., Shock Waves in the Solar Wind, in "Particles and Fields in the Magentosphere," B. M. McCormac, ed., D. Reidel, Dordrecht-Holland, p. 79, 1970a.

Hundhausen, A. J., Plasma measurements across the bow shock and in the magnetosheath, in "Intercorrelated Satellite Observations Related to Solar Events,: V. Manno and D. E. Page, eds., D. Reidel, Dordrecht-Holland, p. 155, 1970b.

Hundhausen, A. J., S. J. Bame, and M. D. Montgomery, An observation of the February 26, 1969 interplanetary shock wave, in "Intercorrelated Satellite Observations Related to Solar Events,: V. Manno and D. E. Page, eds., D. Reidel, Dordrecht-Holland, p. 567, 1970.

Hundhausen, A. J., and M. D. Montgomery, Heat conduction and nonsteady phenomena in the solar wind, J. Geophys. Res., 76, 2236, 1971.

Lemons, D. S., and S. P. Gary, Current-driven instabilities in a laminar perpendicular shock, J. Geophys. Res., 83, 1625, 1978.

Leroy, M. M., D. Winske, C. C. Goodrich, C. S. Wu, and K. Papadopoulos, The structure of perpendicular bow shocks, J. Geophys. Res., 87, 5081, 1982.

Montgomery, M. D., J. R. Asbridge, and S. J. Bame, Vela 4 plasma observations near the earth's bow shock, J. Geophys. Res., 75, 1217, 1970

Scudder, J. D., D. L. Lind, and K. W. Ogilvie, Electron observations in the solar wind and magnetosheath, J. Geophys. Res., 78, 6535, 1973

Tidman, D. A., and N. A. Krall, "Shock Waves in Collisionless Plasmas," Wiley-Interscience, New York, 1971.

VARIATIONS OF ELECTRON VELOCITY DISTRIBUTION FUNCTIONS

W.G. Pilipp
Max-Planck-Institut für Physik und Astrophysik
Institut für extraterrestrische Physik
8046 Garching, West Germany

ABSTRACT

The variation of the distribution functions of solar wind electrons with the sector structure of the interplanetary magnetic field (IMF) as well as with the stream structures of the solar wind and with distance from the sun is discussed. The Helios observations indicate that electron properties are more strongly correlated with the sector structure of the IMF than with the plasma stream structures. The distribution functions are largely isotropic and relatively cool at sector boundaries being usually embedded in the slow solar wind where the electron temperatures often show a sharp minimum. Outside of sector boundaries but still close to them in the slow solar wind, the electron spectra are relatively hot and moderately anisotropic, and the electron temperatures often show maxima shortly before and after the sector boundaries. Within the interior of magnetic sectors where high speed streams usually occur, the electron spectra are again cool but show an extreme anisotropy and skewing along the magnetic field for particle energies well above 50 eV. This narrow non-thermal feature has been termed "Strahl". Here the pitch angle distributions (i.e. the phase space density as a function of the pitch angle relative to the magnetic field direction for constant particle energies as seen in a frame of reference moving with the peak of the electron distribution functions) show a sharp peak around the pitch angle of zero degrees corresponding to electrons moving along the magnetic field away from the sun. The angular width of this peak decreases with increasing particle energy being less than 10 degrees for energies of few 100 eV and above. Due to the Strahl the electron temperature $T_{e\parallel}$ parallel to the magnetic field is larger than the electron temperature $T_{e\perp}$ perpendicular to the magnetic field typically by a factor 1.5. In addition the electrons cool down with increasing distance from the sun where the radial decrease of the electron temperatures is significantly steeper around sector boundaries than in the high speed streams within the interior of magnetic sectors.

The most likely interpretation of these variations is that within the interior of magnetic sectors the magnetic field lines are 'open' being connected to the sun and extending outward to distances far beyond the position of the space craft where the more energetic electrons escape along the magnetic field to large distances with their high particle velocity without major scattering. In contrast around sector boundaries the electrons seem to be trapped in closed magnetic field loops disconnected from the sun where they are isotropized by some unknown microscopic scattering mechanisms occurring mainly at the sector boundaries and where they cool down much faster during the solar wind expansion due to the reduced thermal conduction with the corona.

This hypothesis is also supported by the variation of the pitch angle distribution which is observed when the space craft moves from the interior of a magnetic sector towards a sector boundary. As the space craft approaches the sector boundary, the angular width of the Strahl broadens and, at the same time, the more or less isotropic phase space density at larger pitch angles corresponding to electrons moving towards the sun increases. In addition within the interior of magnetic sec-

tors the phase space density $F(v_{\shortparallel}, v_{\perp} = 0)$ of the Strahl electrons (above 100 eV) is larger than the phase space density $F(-v_{\shortparallel}, v_{\perp} = 0)$ of the electrons returning to the sun by a factor 10 to 100 near the orbit of earth and by a factor 100 to 1000 near 0.3 AU. Approaching a sector boundary $F(v_{\shortparallel}, v_{\perp} = 0)$ decreases and $F(-v_{\shortparallel}, v_{\perp} = 0)$ increases where both phase space densities become about equal right at the sector boundary.

ENERGETIC ELECTRONS AND PLASMA WAVES ASSOCIATED WITH SOLAR TYPE III RADIO BURSTS

R. P. Lin (Space Sci. Lab., Univ. of Calif., Berkeley), D. A. Gurnett (Dept. of Physics and Astron., Univ. of Iowa), and F. L. Scarf (TRW Defense and Space Systems, Redondo Beach, Calif.)

We present detailed in situ observations from the ISEE-3 spacecraft of energetic electrons, plasma waves, and radio emission for type III solar radio bursts. Since the faster electrons arrive before the slower ones, the reduced one-dimensional distribution function f(v) of the electrons shows a bump on tail which is unstable to the growth of Langmuir waves. The wave growth computed from f(v) agrees with the observed onset of the waves, and there is qualitative agreement between variations in the plasma wave levels and in the development of regions of positive slope in f(v). The evolution of f(v), however, usually predicts far higher plasma wave levels than those observed. The maximum levels observed are about equal to the threshold for nonlinear wave processes, such as oscillating two-stream instability and soliton collapse. Also, the lack of obvious pla-teauing of the distribution suggests that the observed waves have been removed from resonance with the beam electrons. The Langmuir waves are observed to be highly impulsive in nature. Occasionally, low frequency ($\sim$ 50 - 300 Hz) turbulence is enhanced simultaneous with the plasma waves, while ion acoustic turbulence is often suppressed. The onset of the in situ radio emission, identified by its lack of directivity as that pro-duced near 1 AU, almost always precedes the plasma wave onset by $\sim$ 20 minutes. This delay raises serious questions about the hypothesis of the generation of type III radio emission from the plasma waves.
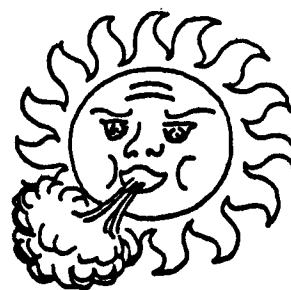
SESSION 7.

ENERGETIC PARTICLES

COSMIC RAY STUDIES IN THE OUTER HELIOSPHERE

Frank B. McDonald, NASA/Goddard Space Flight Center, Code 660
Greenbelt, MD 20771

The data from the cosmic ray experiments on Pioneer 10 (now at
∿ 28 AU), Voyagers 1 and 2 (11-13 AU) combined with those from ISEE-3
and Helios 1 in the inner solar system have provided new insight into
both the physical processes involved in producing the long term solar
modulation of galactic cosmic rays and the interplanetary magnetic field
configuration in the distant heliosphere. At both 1 AU and 25 AU the
integral cosmic ray intensity with energies > 200 MeV decreased by a
factor of ∿ 2 while 150 MeV galactic cosmic ray protons were reduced
by some 600%. The fact that the percentage change was the same at both
1 and 25 AU was completely unexpected. Essentially all of the reduction
occurred in 3 major episodes extending over 4-9 solar rotations in the
1978-1980 period. The existence of these discrete steps provides a
means of estimating the size of the heliosphere using the data from the
recovery phase which started in early 1981. Preliminary analysis places
the heliospheric radius in the 100-120 AU range. There is a quasi -26
day periodicity within two of the episodes, suggesting the formation of
an apparent co-rotating structure in the outer heliosphere. Flare gener-
ated shock waves appear to play a role in the formation of this "merged-
interaction region". At ∿ 10 AU this magnetic feature plays a dominant
role in channeling solar cosmic ray events and in further energizing
solar energetic particles.

FLARE TRIGGERED PARTICLE INCREASES BEYOND 1 AU

G. Gloeckler
University of Maryland, Dept. of Physics and Astronomy, College Park,
MD 20742

During the last decade it has become abundantly clear that particles
are accelerated to MeV energies in interplanetary space - most common
examples being co-rotating particle increase and various enhancement
associated with passages of interplanetary shocks. Combining Voyager and
ISEE observations of energetic (0.5 to 20 MeV/nucleon) particles we find
evidence for yet another, apparently common, interplanetary acceleration
mechanism. The seed population in this mechanism are ions preaccelerated
to $\lesssim$MeV at the sun. Propagating shocks and/or CIR's in regions extending
to several AU and beyond are then effective in further accelerating these
solar flare ions to energies up to tens of MeV. Our conclusions are based
on simultaneous observations made at 1 AU and at distances up to $\sim$6 AU of
energetic particle increases with time-intensity profiles and of duration
comparable to typical flare particle events. In these events, contrary
to ordinary flare particle events, the fluxes of $\sim$10's of MeV ions at
large heliographic distance are comparable to or larger than at 1 AU.

PARTICLE DRIFTS, THE INTERPLANETARY MAGNETIC FIELD
AND COSMIC-RAY MODULATION

J. R. Jokipii
University of Arizona
Tucson, Arizona

Particle gradient and curvature drifts in the large-scale inter-
planetary magnetic field, under plausible extrapolation of the field
to higher latitudes, can have profound effects on the modulation of
galactic cosmic rays by the sun. Recent numerical modelling efforts
at Arizona have explored the effects of drifts within the context of
the full Fokker-Planck transport equation. These models will be
summarized and their implications for our understanding of modulation
will be discussed. Our most-recent, fully three-dimensional simula-
tions appear to be consistent with a variety of observations,
including 22-year solar magnetic cycle effects which must be intro-
duced ad-hoc in other models. The models suggest the possibility
that a major part of the 11-year sunspot cycle variation of galactic
cosmic rays may be caused by variations in the large-scale structure
of the interplanetary magnetic field. Possible implications of
drifts for shock-wave acceleration and the origin of the anomalous
component of cosmic rays will also be discussed.

THE MODULATION AND ACCELERATION OF ENERGETIC PARTICLES IN THE SOLAR WIND

L. A. FISK
Department of Physics, University of New Hampshire, Durham, NH 03824

Two topics of current interest on the modulation and acceleration of energetic particles in the solar wind are discussed: (i) A time-dependent numerical model is presented of the solar-cycle variation in the cosmic ray flux, in which the modulation is produced by disturbances which are convected outward with the solar wind. The model can account for the observed solar-cycle variation, spatial gradients and the hysterisis effect. (ii) A numerical model is presented of the acceleration of the anomalous component at the termination shock of the solar wind near the equatorial plane of the Sun. The model can account for the observed spectra of the anomalous component, and makes an interesting prediction of the shock location.

Temporal Variations of the Anomalous Oxygen Component

A. C. Cummings

California Institute of Technology, Pasadena, CA 91125

W. R. Webber

University of New Hampshire, Durham, NH 03824

We have used data from the cosmic ray experiment (CRS) on Voyagers 1 and 2 to examine anomalous oxygen in the time period from launch in 1977 to the end of 1981. We find several time periods where large periodic (typically 26 day) temporal variations of the oxygen intensity between ~5 - 15 MeV/nuc are present. Variations in intensity by up to a factor of 10 are observed during these periods. We find that several characteristics of these variations indicate that they are not higher energy extensions of the low energy particle (~1 MeV/nuc) increases found in many corotating interaction regions (CIR's). Many of these periodic temporal variations are correlated with similar, but much smaller, recurrent variations in the >75 MeV proton rate. We have compared Voyager 1 and Voyager 2 counting rates to estimate the local radial gradient for both the protons and the oxygen. The proton gradients during periods of both maximum and minimum fluxes are consistent with the overall positive radial gradients reported by others from Pioneer and near-Earth observations, supporting the view that these variations are due to local modulation of a source outside the radial range of our measurements. In contrast, the oxygen gradients during periods of maximum proton flux differ in sign from those during minimum proton fluxes, suggesting that the origin of the oxygen variations is different from that of the protons.

INTRODUCTION

The anomalous component of cosmic rays has now been studied for about a decade. As described in the accompanying paper the anomalous particle populations exhibit long term variations due to solar modulation effects. Indeed, almost all of the existing studies of anomalous oxygen have been made using rather long time averages, typically on the order of months. The four CRS telescopes on each of the two Voyager spacecraft, with their large collecting power, have allowed us to look at the anomalous oxygen rates with finer time resolution for the first time. We have examined the period from launch in late 1977 to the end of 1981 and we find several time periods where large recurrent temporal variations are present, with an ~26 day periodicity. Variations in intensity by a factor of up to 10 are observed. We have investigated the origin of these variations by comparing the oxygen rates to rates of other particle types and by intercomparing the rates of the two Voyagers.

OBSERVATIONS

An example of the oxygen counting rate variations during 1980 is shown in the lower panel of Figure 1. The high energy proton rate is plotted in the upper panel and four major correlated peaks in the two rates are indicated by the dashed lines. The amplitude of the proton variations is ~10 - 15% , whereas the variation in the oxygen rate is much larger with a peak to valley ratio of perhaps 10 to 1 for the largest peaks. The average spacing between the four large proton peaks in the figure is ~26 days.

The first report of ~26 day intensity variations in anomalous oxygen was by *Webber et al.* [1979] based on a subset of this data for the period just after launch in 1977. In that observation variations in amplitude by a factor of two were found. *Von Rosenvinge and Paizis* [1981] reported 27-day variations of a factor of two in anomalous oxygen using near-Earth data during 1976. We also note that 27-day intensity variations of up to a factor of two for the anomalous helium component have been previously re-
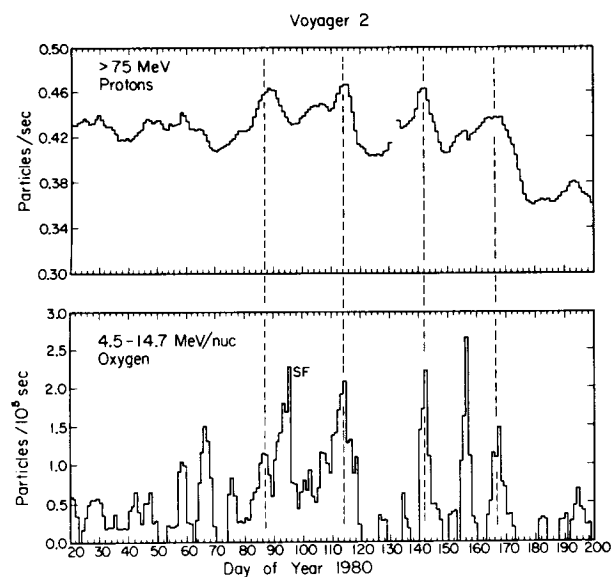
Fig. 1. Voyager 2 3-day moving average counting rates versus time of high energy protons and anomalous oxygen in 1980. The dashed lines relate the largest peaks in the proton rate to peaks in the oxygen rate. The peak labeled SF is probably due to a solar flare.
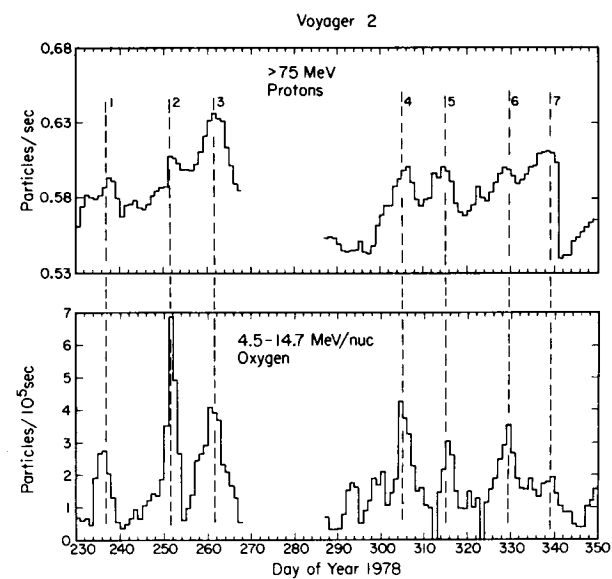
Fig. 2. Voyager 2 3-day moving average counting rates versus time of high energy protons and anomalous oxygen in 1978. The seven dashed lines mark correlated peaks in the two rates. The data from day 269 to day 286 have been removed because of a large solar flare.

ported by several groups [*Garcia-Munoz et. al*, 1977; *Bastian et. al*, 1979; *Von Rosenvinge and Paizis*, 1981]. Our analysis of the anomalous helium data is only preliminary but we are finding that the amplitude of the helium intensity variations are a factor of two or less throughout the period while the oxygen variations are much larger.

In Figure 2 the oxygen and proton counting rates are shown for a 120 day period in 1978. Here again, oxygen intensity variations of up to a factor of 10 are observed. Seven correlated increases are marked by the dashed lines. The odd numbered lines are on ∼ 26 day increments. The even numbered lines are also essentially on 26 day increments and occur ∼ 10 days in advance of an odd numbered line. This timing is suggestive of increases associated with CIR's and indeed this period has been studied for CIR increases at lower energies, ∼ 1 MeV/nuc, by other Voyager investigators [*Hamilton et al.*, 1979].

COMPARISON WITH CIR-TYPE INCREASES

We have investigated the possibility that the oxygen variations are the result of CIR acceleration. Plots of the rate of oxygen, the rate of > 0.5 MeV protons, which are a sensitive indicator of CIR acceleration, and plots of the solar wind speed and magnetic field magnitude are shown in Figure 3 for the period 1978, days 230-270. Two CIR's are indicated by the dashed line pairs labeled 1 and 3 which mark associated forward/reverse shock pairs. *Hamil-*
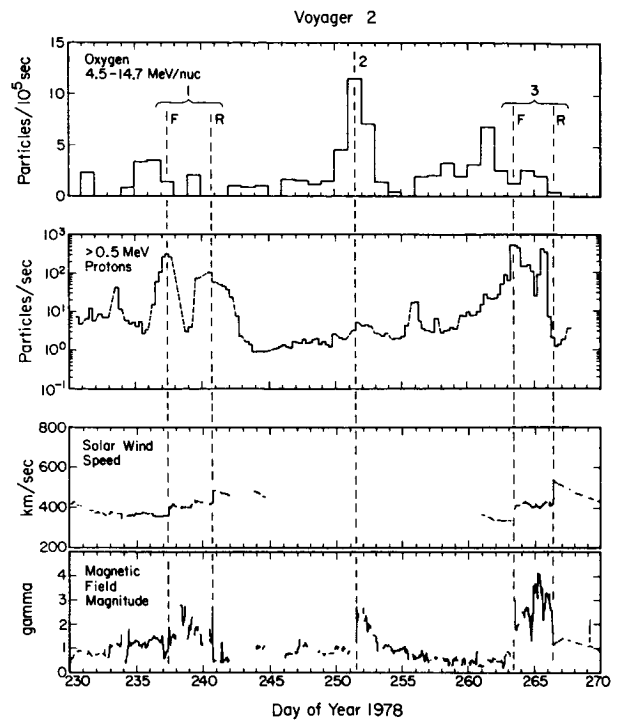

Fig. 3. Four plots from Voyager 2: (upper panel) daily averaged counting rate versus time for anomalous oxygen; (second panel) 6-hour averaged counting rate versus time for low energy protons; (third panel) hourly averaged solar wind speed from the MIT plasma experiment; (lower panel) hourly averaged magnetic field magnitude from the GSFC magnetometer experiment. Two CIR's are indicated by the dashed line pairs labeled 1 and 3, respectively. The forward and reverse shocks are labeled F and R, respectively. The number labels associated with the dashed lines correspond to those on Figure 2.

ton et al. [1979] found that at ∼ 1 MeV/nuc most of the enhanced carbon and oxygen intensity was concentrated near the reverse shocks and that the C/O ratio at this time was ∼ 0.68. We find, on the other hand, that most of the higher energy oxygen precedes the forward shock. In addition, the oxygen increase near day 251, labeled with the dashed line number 2, is not associated with an identified CIR. Furthermore, we find very little carbon in our energy interval. For the sum of the seven peaks in the 1978 120 day period shown in Figure 2 the C/O ratio is less than 0.05. Finally, the energy spectrum of the increases is not what one would expect from a normal CIR event. The oxygen energy spectra in and between the seven 1978 peaks on Voyager 2 are shown in Figure 4. The shape of the two spectra are similar with both having a plateau near 6 MeV/nuc. The dashed line represents an upper limit to the spectrum of oxygen from a CIR estimated by scaling from our measured CIR helium spectrum on day 265, one of the largest such increases during this period. Indeed, this estimated oxygen CIR spectrum is derived for a reverse shock whereas most of our oxygen particles are at or near the forward shocks. By directly comparing the measured rates of helium and oxygen at comparable energies and by assuming a CIR He to O ratio of 150 to 1, we estimate that at the forward shocks the contribution from CIR-type acceleration to the anomalous oxygen increases is at the 1% level.

COMPARISON WITH HIGH-ENERGY PROTONS AND DETERMINATION OF RADIAL GRADIENTS

Another possibility for the origin of the oxygen variations is that they result from the same process responsible for the variations in the high energy proton rate, examples of which were shown in Figures 1 and 2. The proton variations are probably indicative of short term solar modulation effects. While the percentage variation of the oxygen rate is much larger than that of the proton rate, typically 50 times as large, it is possible that short term modulation effects may be playing a significant role for the oxygen as well. We have investigated this possibility from several viewpoints, including comparing the long and short term correlations of the oxygen and proton rates and comparing the radial gradients of the two particle populations. Here we shall consider the radial gradient data and some of its implications. The large scale radial gradients for the anomalous oxygen and the > 75 MeV protons have been previously reported by others for the 1 - 20 AU range by comparing the intensities at the Pioneer spacecraft to those near Earth. By using the separation of the two Voyager spacecraft we can determine the local radial gradients during the time intervals of the variations and compare these to the large scale gradients.

The relative positions of the two spacecraft projected into the solar equatorial plane are shown in Figure 5. The 1978 and 1980 periods we have studied are indicated by bars along the trajectory. In the 1978 period the spacecraft are ~4 AU from the Sun and ~0.3 AU apart. In 1980 they have moved out to an average radial position of ~7.2 AU and have moved apart ~ 1.25 AU. They are well aligned in both longitude (see Figure 5) and latitude (within 1 degree in 1978 and within ~0.3 degree in 1980). Note that during the 1978 and 1980 time intervals Voyager 1 is always farther from the Sun than Voyager 2. Thus for positive radial gradients Voyager 1 will measure a higher intensity than Voyager 2.

The comparison of the Voyager 1 and 2 proton rates for the 1978 period is shown in Figure 6. The correlation of features in the two plots is generally good. We have taken the ratio of the Voyager 1 to Voyager 2 intensities for the correlated maxima and minima of the vari-
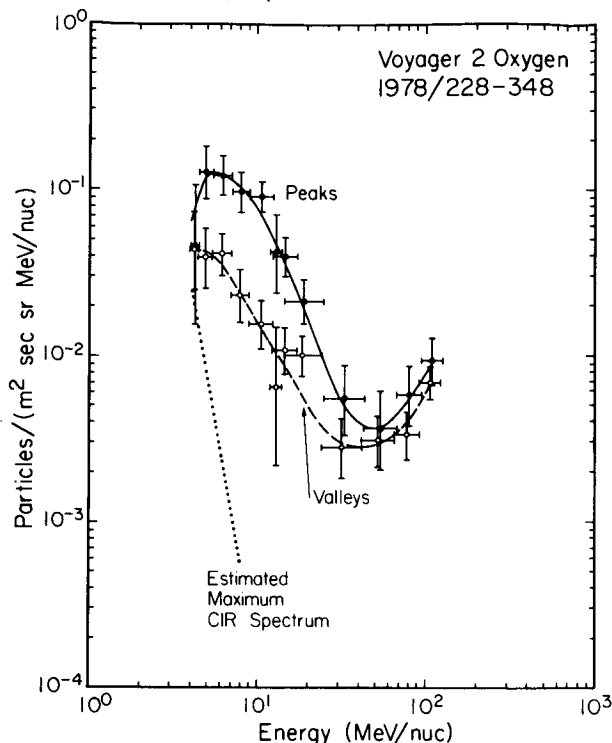

Fig. 4. Energy spectra of oxygen for selected time intervals in the period 1978 days 228-348. The upper points are for intervals in the peaks of the time variations. The lower points are for intervals between the peaks. The dotted line represents an estimated maximum CIR spectrum of oxygen.
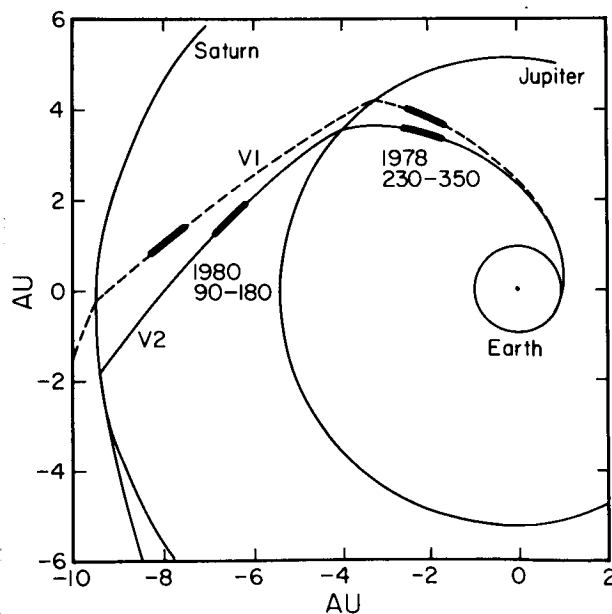

Fig. 5. Trajectory plot of the two Voyager spacecraft. The heavy bars mark the trajectory during the 1978 and 1980 periods of study.
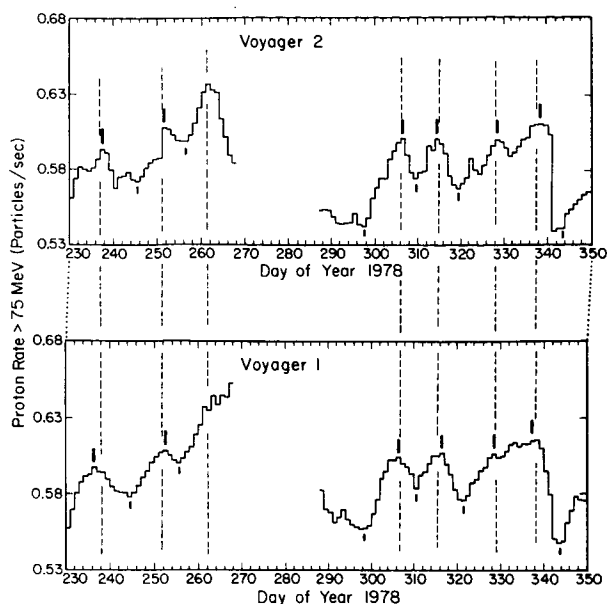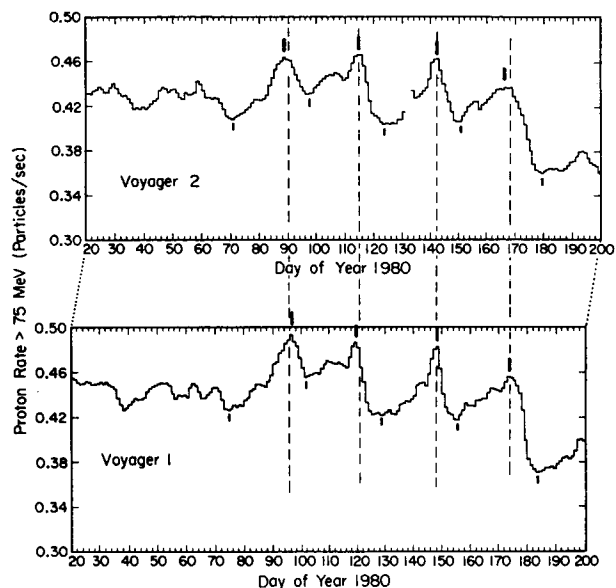
Fig. 6. Three-day moving average counting rate versus time of Voyager 1 and 2 high energy protons in 1978. The two plots are shifted relative to each other by 1 day to approximately account for the corotation delay between the two spacecraft. The dashed lines mark corresponding peaks in the two plots. The long vertical bars mark the actual peak 3-day intervals chosen in calculating the Voyager 1 to Voyager 2 counting rate ratios. The short vertical bars mark the corresponding times between the peaks. The rates were normalized in December 1977 when the two spacecraft were the same distance from the Sun.

Fig. 7. Three-day moving average counting rate versus time for Voyager 1 and 2 high energy protons in 1980. The two plots are shifted relative to each other by 6 days to approximately account for the corotation delay between the two spacecraft. The dashed lines, vertical bars, and normalization are as described in the caption for Figure 6.

ations at the times indicated by the long and short vertical bars. The corresponding plot for the 1980 period is shown in Figure 7. The corotation delay is ~6 days for this time interval and, after making the time shift, the features in the two panels line up well. The intensity ratios corresponding to the data in Figures 6 and 7 are shown in Figure 8 as a function of average radial distance from the Sun as the points near 4 AU for 1978 and near 7.2 AU for 1980. The lower panel of Figure 8 shows the ratio for the peak times and the upper panel shows the ratios for the times between the peaks. The remaining points near 6.4 AU are for a 1979 period when variations were also observed. The dashed lines on both panels show the computed intensity ratio for a given local radial gradient. It is apparent that the data from both panels are consistent with a local radial gradient of ~3 - 5%/AU which is consistent with the large scale gradients found for these particles from the Pioneer and near-Earth observations [McKibben et. al, 1982]. This data therefore supports the notion that the variations in intensity of the protons are due to a local modulation effect, most likely produced by a corotating magnetic field structure.

The Voyager 1 and 2 anomalous oxygen rate comparisons for the 1978 period are shown in Figure 9. The dashed lines indicate times of maximum proton fluxes from Figure 6. We could not duplicate the analysis procedure we used for the protons because of poorer statistics. Therefore we have summed over the time intervals shown by the horizontal bars to get a single ratio for the periods between the maxima of the proton fluxes. We have also summed over the seven 3-day periods associated with the proton flux maxima in order to calculate a single average ratio for the "peak" times. These values are shown in the first column of Table 1. The V1 to V2 ratio for the times between the peaks is within 1σ of the expected ratio of 1.05 for the large scale positive radial gradient of ~15%/AU which has been reported for anomalous oxygen from Pioneer and near-Earth data [Webber et al., 1981]. The ratio for the sum of the seven peaks is ~1.8σ less than 1.05. For comparison the second column of Table 1 shows

the average V1 to V2 ratios for the high energy protons in 1978 as computed from the weighted average of the points shown in Figure 8. Ratios for both the peak and between-peak fluxes are consistent with the expected ratio for a radial gradient of 3 - 5%/AU.

In Figure 10 we show the anomalous oxygen rate comparisons for 1980. Here the situation is more difficult than in 1978. The correlation of features in the Voyager 1 and 2 plots is less clear. We have made a relative shift of 6 days in the two plots just as we did for the protons, and the times of the four major proton peaks are shown by dashed lines and used as a guide in identifying the correlated peaks. The 3-day periods indicated by the vertical bars were summed to get an average ratio for the peak periods. The times indicated by horizontal bars were summed to calculate a between-peak period ratio. This division of time periods is less obvious in 1980 than in 1978. For example, there appear to be additional peak fluxes in oxygen between the times associated with proton flux maxima, particularly near day 157 in Voyager 2 and near day 108 in Voyager 1. In fact there may well be a second sequence of peaks offset from the primary sequence by ~ 10 days. A 5-day data gap from day 130-135 on Voyager 2 possibly obscures one of the peaks in the secondary sequence. The V1 to V2 ratios of the anomalous oxygen intensity are shown for the two time periods in the third column of Table 1. Here again the ratio for the times between the proton peaks is within 1σ of the expected ratio of 1.2. However, the ratio for the sum of oxygen fluxes during periods associated with proton flux maxima is ~ 3.7σ less than expected for a gradient of +15%/AU. The average proton intensity ratios, shown in the fourth column of Table 1, are again consistent with a 3 - 5%/AU radial gradient.
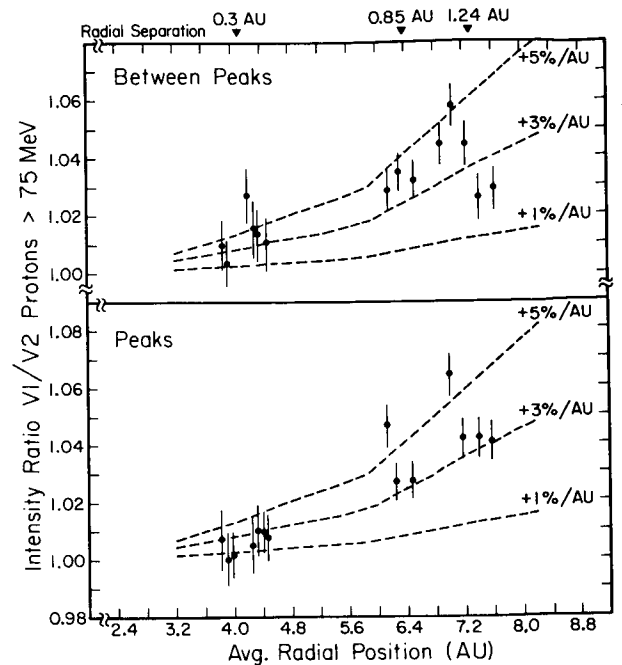

Fig. 8. Voyager 1 to Voyager 2 high energy proton counting rate ratio versus average radial distance from the Sun for selected 3-day periods. The points near 4 AU and 7.2 AU correspond to the indicated days shown in Figure 7 and 8, respectively. The three points near 6.4 AU correspond to similar periods in 1979. The dashed lines represent the expected ratio for a given local radial gradient. The approximate radial separations of the two spacecraft are indicated at the top of the upper panel.

DISCUSSION

As we have noted, the > 75 MeV proton variations appear to be small (~ 10 - 15%) perturbations on a rate which is well correlated over the separation distance of the two spacecraft. The local gradient derived for both the maxima and minima of the variations are consistent with the large scale gradients reported for separation distances of up to 20 AU. The oxygen variations, on the other hand, do not fit a similar picture. Particularly in 1980 (see Figure 10) when the spacecraft are ~ 1.25 AU apart, the features in the two rates are not well correlated; the peaks in Voyager 2 appear to be sharper and more well defined than in Voyager 1, the perturbations on the rate are not small, and the apparent local radial gradients for the peaks do not agree with the overall large scale gradients that have been reported. The oxygen intensity variations appear to be more filamentary in nature than those of the protons, suggesting perhaps that the oxygen nuclei are more sensitive to the detailed configuration of the magnetic field than are the protons. These differences suggest that the origin of the short term oxygen variations is different from that of the protons. (See *Hovestadt et. al* [1979] for an indication of differences in the origin of long term variations of oxygen and protons.)
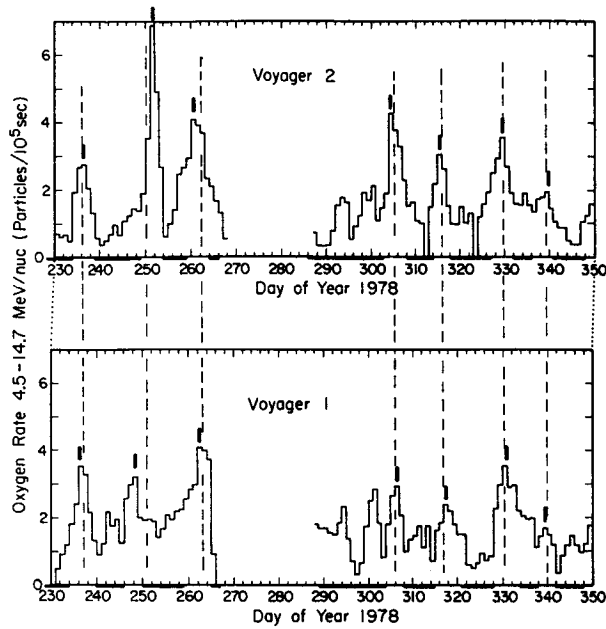
432

Fig. 9. Three-day moving average counting rate versus time for Voyager 1 and 2 anomalous oxygen in 1978. The two plots are shifted relative to each other by 1 day to approximately account for the corotation delay between the two spacecraft. The dashed lines mark the approximate position of correlated peaks in the Voyager 2 high energy proton rate. The heavy vertical bars mark the actual peak 3-day intervals chosen in calculating the Voyager 1 to Voyager 2 counting rate ratio. The horizontal bars mark the corresponding times chosen between the periods associated with proton flux maxima.
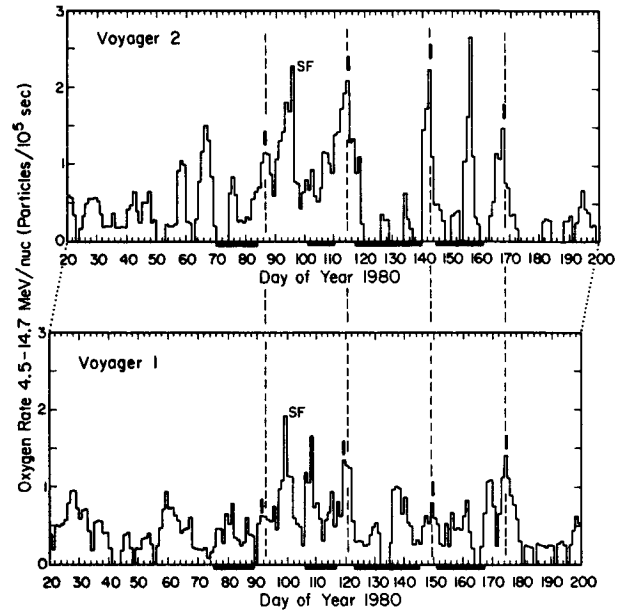
Fig. 10. Three-day moving average counting rate versus time for Voyager 1 and 2 anomalous oxygen in 1980. The two plots are shifted relative to each other by 6 days to approximately account for the corotation delay between the two spacecraft. The dashed lines mark the location of the largest peaks in the Voyager 2 high energy proton counting rate plot. The peak labeled SF in both panels is probably due to a solar flare. The vertical and horizontal bars are as described in the caption for Figure 9.

	TABLE 1. Ratios of V1 to V2 Intensity			
	1978		1980	
	Anomalous oxygen	>75 MeV protons	Anomalous oxygen	>75 MeV protons
Periods of minimum proton flux	1.23 ± .18	1.013 ± .004	1.04 ± .25	1.041 ± .003
Periods of maximum proton flux	0.82 ± .13	1.006 ± .003	0.58 ± .17	1.047 ± .004
Expected for 15%/AU	1.05	---	1.20	---
Expected for 3 - 5%/AU	---	1.009 - 1.015	---	1.038 - 1.065
Average radial position	~ 4 AU		~ 7.2 AU	
Average radial separation	~ 0.3 AU		~ 1.25 AU	

In conclusion we have reported the observation of large recurrent temporal variations in the anomalous oxygen component. Several characteristics of these increases indicate that they are not high energy extensions of CIR events. We cannot, at this time, determine whether they are due to a peculiar short term modulation or transport mechanism or whether the particles are being accelerated locally in the interplanetary medium. In the future we will study the behavior of other particles, in particular the anomalous helium component. In addition, it may be possible to use near-Earth data, particularly in 1978, to determine the large scale radial gradient associated with oxygen increases in the region from 1 to 4 AU.

REFERENCES

Bastian, T. S., R. B. McKibben, and J. A. Simpson, Recurrent modulation of galactic cosmic rays and the anomalous helium, *Proc. 16th Int. Cosmic Ray Conf., Kyoto, 12*, 324, 1979.

Garcia-Munoz, M., G. M. Mason, and J. A. Simpson, The appearance of super fluxes of quiet time cosmic rays, *Proc. 15th Int. Cosmic Ray Conf., Plovdiv, 3*, 209, 1977.

Hamilton, D. C., G. Gloeckler, T. P. Armstrong, W. I. Axford, C. O. Bostrom, C. Y. Fan, S. M. Krimigis, and L. J. Lanzerotti, Recurrent energetic particle events associated with forward/reverse shock pairs near 4 AU in 1978, *Proc. 16th Int. Cosmic Ray Conf., Kyoto, 5*, 363, 1979.

Hovestadt, D., B. Klecker, G. Gloeckler, F. M. Ipavich, C. Y. Fan, and L. A. Fisk, Temporal variations of the anomalous oxygen (1974-1979) and disappearance in 1978, *Proc. 16th Int. Cosmic Ray Conf., Kyoto, 3*, 255, 1979.

McKibben, R. B., K. R. Pyle, and J. A. Simpson, The galactic cosmic-ray radial intensity gradient and large-scale modulation in the heliosphere, *Ap. J. (Lett.), 254*, L23, 1982.

Von Rosenvinge, T. T. and C. Paizis, Amplitudes of solar modulation of low energy cosmic rays, *Proc. 17th Int. Cosmic Ray Conf., Paris, 10*, 69, 1981.

Webber, W. R., E. C. Stone, and R. E. Vogt, The elemental composition of quiet time low energy cosmic rays measured on the Voyager spacecraft, *Proc. 16th Int. Cosmic Ray Conf., Kyoto, 5*, 357, 1979.

Webber, W. R., F. B. McDonald, T. T. Von Rosenvinge, and R. A. Mewaldt, A study of temporal and radial dependencies of the anomalous helium and oxygen nuclei, *Proc. 17th Int. Cosmic Ray Conf., Paris, 10*, 92, 1981.

Voyager Measurements of the Energy Spectrum, Charge Composition, and Long Term Temporal Variations of the Anomalous Components in 1977-1982

W. R. Webber

University of New Hampshire, Durham, NH 03824

A. C. Cummings

California Institute of Technology, Pasadena, CA 91125

We have used the large collecting area and wide energy range of the cosmic ray experiment (CRS) on Voyagers 1 and 2 to examine the energy spectra, charge composition, and long term temporal variations of the anomalous components in 1977-1982. Individual energy spectra are obtained for 17 separate quiet time periods during the time interval. The composite spectra of anomalous He, N, O, and Ne are obtained to a new level of precision. This includes the spectral shape and the relative abundance. Essentially, the spectral shape of N, O, and Ne appear to be similar. The ratios of anomalous N and Ne to O are found to be different from both the solar cosmic ray and galactic cosmic ray source composition. Some evidence is found for the enhancement of Ar as well. In the case of elements such as C, Mg, S, and Fe it is difficult to separate a possible lower intensity anomalous component from a quasi-steady interplanetary component that appears to be present at the lowest energies. The long term temporal variations of the anomalous He and O components have also been studied from 1977-82, a period from minimum to maximum in the modulation cycle. The tracking between these anomalous component intensities and the integral intensity of >75 MeV protons is striking; however, the intensity decrease of the anomalous components is much greater. Whereas the >75 MeV intensity decreases by a factor ~2 from 1977 to 1982, the 11.5 - 30 MeV/nuc anomalous He decreases by a factor ~20 and anomalous O between 4.5 - 14.7 MeV/nuc decreases by a factor ~50! Anomalous O is still observed at the lowest intensity levels, however.

INTRODUCTION

The origin of the anomalous components of low energy cosmic rays, of which He and O are the most obvious examples, presents many intriguing questions. One would like to know where and how these particles are accelerated, what their accelerated spectrum looks like, and indeed what their charge state is. Studies of the effects of solar modulation on these components, their radial gradients, and the relative composition of the various anomalous species should in principle provide answers to some of these questions. Previous studies of these components [e.g., *Bastian et al.*, 1979; *Klecker et al.*, 1977; *Webber et al.*, 1981] have usually been constrained by combinations of limited statistics and/or limited energy range and therefore cannot examine all of these questions completely. The Voyager 1 and 2 data, upon which this paper is based, overcomes several of these limitations, utilizing data from eight low energy telescopes (LET) with a total collecting area ~3.5 cm^2 sr, and four double ended high energy telescopes (HET) with a total collecting area ~4 cm^2 sr. The energy range covered, from ~4 - 124 MeV/nuc for oxygen nuclei, enables the transition from a quasi-steady interplanetary component at the lowest energies to the anomalous components and then to the galactic cosmic ray components at the highest energies to be observed. Individual energy spectra for the various charges are obtained for 17 separate quiet time periods during 1977-82. These quiet time intervals are restricted so that there is negligible contamination of the data for $Z \geq 2$ nuclei above ~4 MeV/nuc by corotating streams or solar energetic particles. Overall, these quiet time intervals contain about 65% of the total active time of the two spacecraft over the entire time period.
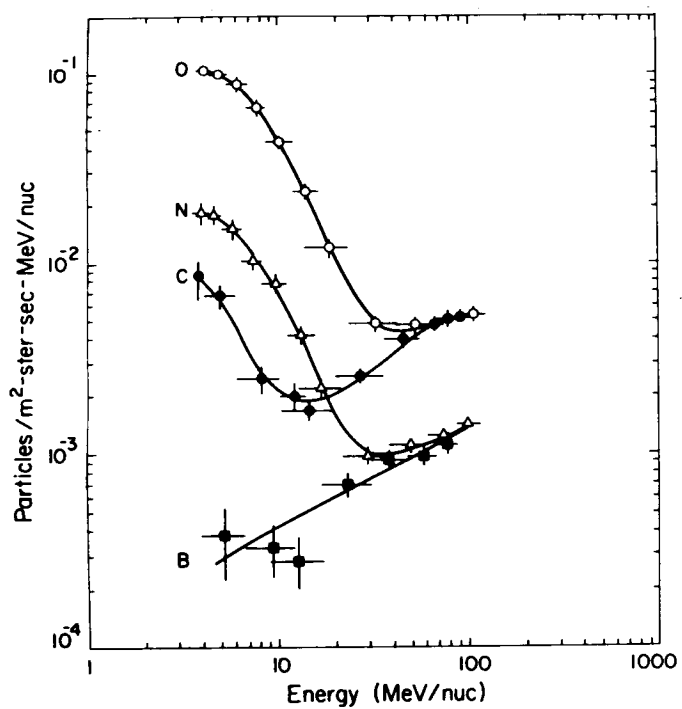
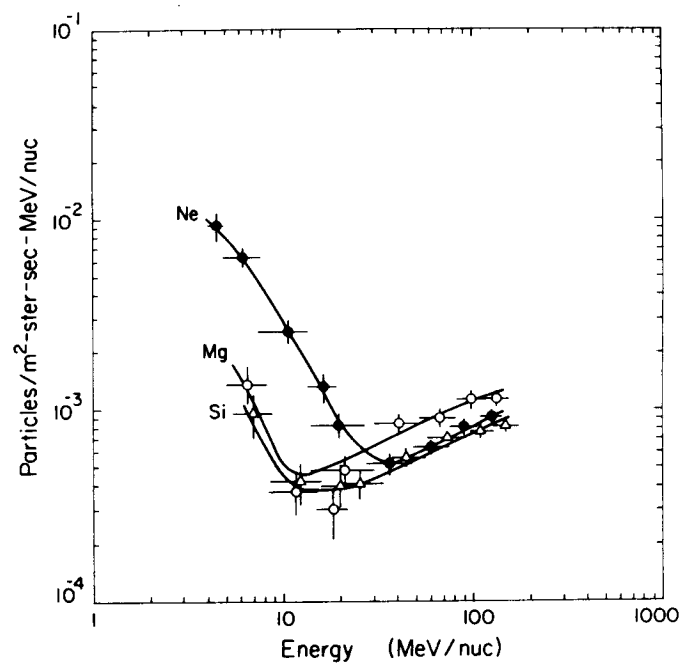Fig. 1. Composite V1 and V2 spectra for B, C, N, and O nuclei.

Fig. 2. Composite V1 and V2 spectra for Ne, Mg, and Si nuclei.

OBSERVATIONS - SPECTRA AND COMPOSITION

Composite spectra for the entire time period, constructed using both V1 and V2 data, are shown in Figures 1, 2, and 3. In Figure 1 the overall details of the anomalous oxygen spectrum are shown clearly, from the initial rise above the galactic component at ~ 50 MeV/nuc to the maximum intensity at ~ 5 MeV/nuc. The anomalous nitrogen spectrum is remarkably similar. The carbon spectrum falls off like a modulated galactic component down to ~ 10 MeV/nuc, below which it begins to increase. It never seems possible to be completely free of this low energy turn-up for carbon and it is not clear whether this is also an anomalous component, but at a much lower intensity, or a quasi-stationary interplanetary component, possibly originating on the Sun and probably accelerated separately from the anomalous components. The boron spectrum falls off like a modulated galactic component down to ~ 4 MeV/nuc with no evidence of a turn-up.

In Figure 2 the behavior of the anomalous neon component is shown clearly for the first time and looks very similar to that for N and O. The Mg and Si spectra look very similar to the C spectrum, exhibiting a fall off consistent with galactic modulation down to ~ 10 MeV/nuc with a turn-up at lower energies. The origin of this turn-up is probably similar to that for C. The S and Fe spectra in Figure 3 show a similar behavior although the turn-up below 10 MeV/nuc is not as well defined. The Ar spectrum shows evidence of a turn-up at lower energies and is well fit by the Ne spectrum divided by ~ 20. We believe that this is the first suggestion that Ar is enhanced as might be expected because of its high ionization potential.
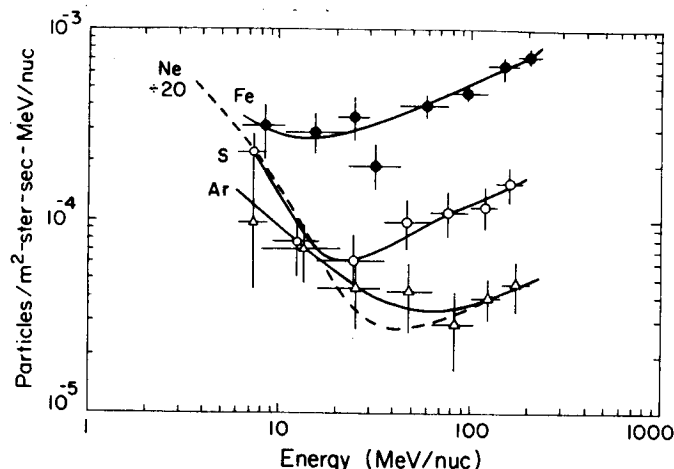

Fig. 3. Composite V1 and V2 spectra for S, Ar, and Ne nuclei.
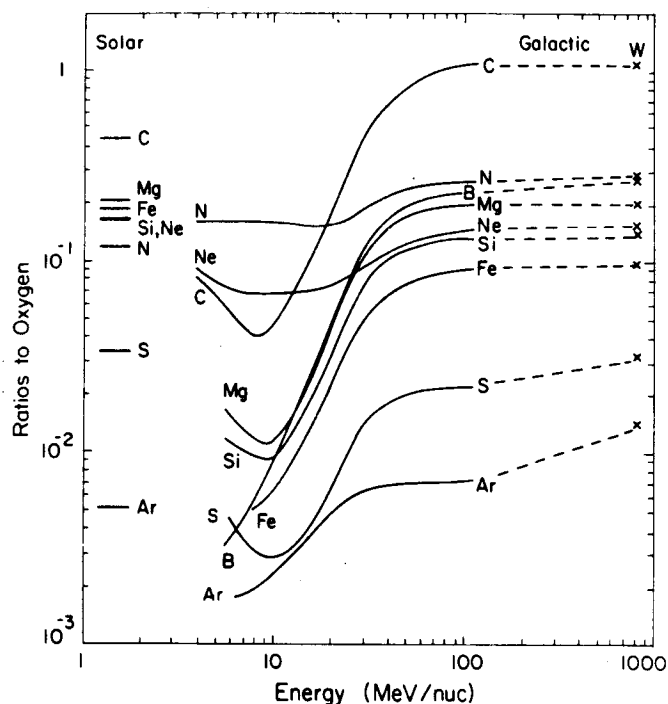
Fig. 4. Abundance of various charges relative to O derived from smooth curves drawn through the data in Figures 1, 2, and 3.

The abundance of the various charges as a function of energy is shown, relative to O, in Figure 4. The values on this Figure are obtained from smooth curves drawn through the data in Figures 1-3. Figure 4 illustrates a progression from a galactic composition above ~ 50 MeV/nuc, down to an intermediate energy range where the anomalous components are dominant, and to the energy range below a few MeV/nuc, where the abundance ratios should approach values more representative of the quiet time interplanetary components which may have a "solar" composition. This new data provides accurate determinations of the various galactic abundance ratios at ~ 100 MeV/nuc. These low energy ratios are in excellent agreement with ratios measured at higher energies [*Engelmann et al.*, 1981] and will be the sub-

ject of future study. At the lowest energies the turn-up in the C, Mg, and Si ratios toward the solar value is possibly indicative of a quiet time interplanetary component of solar composition as noted earlier.

At intermediate energies the behavior of the N and Ne ratios is almost identical to that of O indicating that all 3 anomalous components have essentially the same spectrum. However, the abundance ratios of these anomalous components change from the higher energy galactic value to a value that is also not equal to the solar value. The average observed values N/O = 0.16 and Ne/O = 0.07 for these anomalous components could be the result of a different composition of the source of these particles from that of the galactic or solar cosmic rays, or to preferential effects in acceleration and subsequent modulation, although this must be tempered by the fact that the resultant spectra are nearly identical. The Ar ratio is not well defined at low energies, but it appears that the anomalous Ar/O value must be less than the solar value of 0.005 as well.

OBSERVATIONS - TIME VARIATIONS

We next turn our attention to the long term temporal variations observed during the time period 1977-82. The striking and large short term variations are discussed in an accompanying paper. For the temporal variations we shall use the most abundant components - anomalous He and O as well as C as a reference. The variations of these components in 3 energy ranges are shown for the 17 quiet time intervals in Figure 5. It is seen that the amount of solar modulation is large and progressively increases as one goes to lower energies. C + O nuclei between 60 - 104 MeV/nuc represent the modulation of the galactic component - both C and O show identical variations in this energy range. The total intensity decrease of these components is a factor ~8. Helium in the energy range 11.5 - 30 MeV/nuc represents the peak of the anomalous He component. The overall decrease here is a factor of nearly 20. Oxygen in the energy range 4.5 - 14.7 MeV/nuc represents the peak of the anomalous O component. The overall decrease here is a factor ~50! The variations of all 3 components ap-
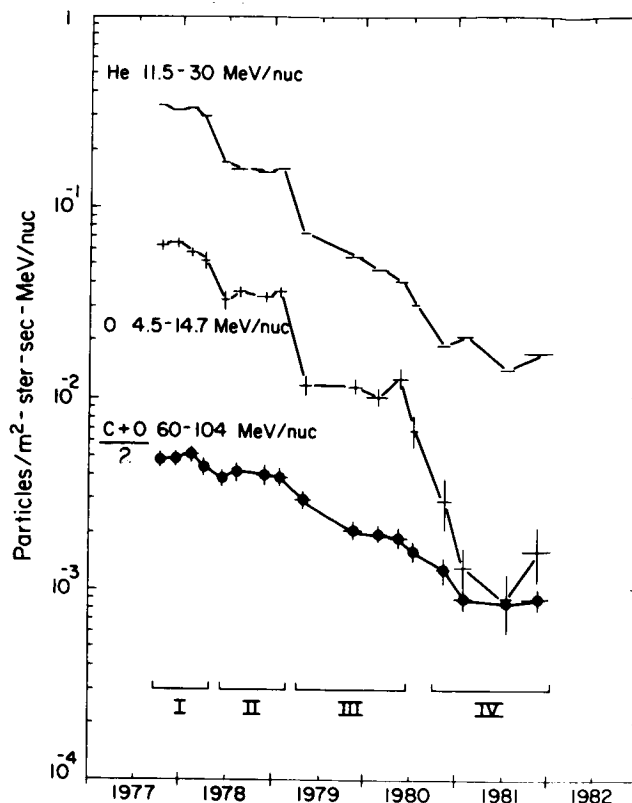
438

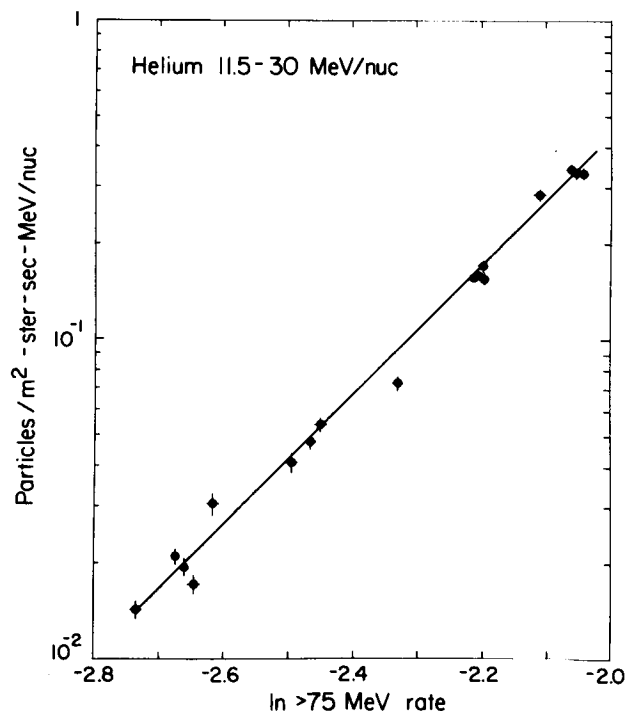Fig. 5. Temporal variations of He, C, and O nuclei during the 1977-82 time period.

Fig. 6. Regression curve of 11.5 - 30 MeV/nuc He intensity and integral rate >75 MeV/nuc during the 1977-82 time period.

pear to track well despite a factor of 10 difference in energy and possibly different origins. The changes of these components also track closely the changes in the higher energy integral rate corresponding mainly to protons > 75 MeV as indicated in Figure 6. [See also *Hovestadt et al.*, 1979, and *Webber et al.*, 1979, for earlier studies.]

It is to be noted that the intensity drops in several steps and for each step the intensity remains roughly constant for several months to a year or longer. For a detailed analysis of spectral changes we have, therefore, grouped the data into 4 separate time intervals as indicated in Figure 5. The He and O spectra observed for these 4 intervals are shown in Figures 7 and 8. Only spectral points are shown in these figures that are uncontaminated by lower energy particles of solar or interplanetary origin. It is clear that there are large and dramatic changes in the spectra of the anomalous components, although a clear signature of anomalous O remains present even at the lowest intensities.

We have tried to analyze the intensity variations of all the components in a systematic manner by constructing plots of β ln (J_1/J_2) vs ρ (rigidity). (J_1 and J_2 are the intensities at two different times, β is the velocity.) The quantity β ln (J_1/J_2) is related to the modulation parameter of the steady state modulation theories. Even though there is considerable uncertainty about the applicability of these theories, plotting the relative modulation of the various components in this way should help to illustrate possible fundamental differences in modulation of the various charges. This data is shown in Figure 9. Consider first the C and O modulation. Carbon is assumed to be a normal $A/Z = 2$ component undergoing modulation. This also applies to oxygen above ~50 MeV/nuc where the spectra of C and O are the same. The rigidity equivalent to this energy is shown by a dashed line in Figure 9. Above this energy the modulation of these two charges should be identical and this is essentially what the data shows. Below this energy the spectra of C and O are different and the relative modulation of O clearly becomes progressively larger than for C. This might be accounted for purely by the difference in spectra of the two components coupled with the effects of energy loss, or by this fact plus the additional assumption that anomalous O has a different A/Q than C (e.g., O is singly charged as in the model of *Fisk, Kovlovsky, and Ramaty* [1974]).

Comparing now the modulation of two anomalous components He and O we see that, at the same rigidity, the modulation of He is always larger than O. This is true even though the He spectrum is flatter than O; thus it is not easy to account for this difference purely in terms of differences in spectral shapes which should act to produce a larger O modulation in conventional theories because of the larger
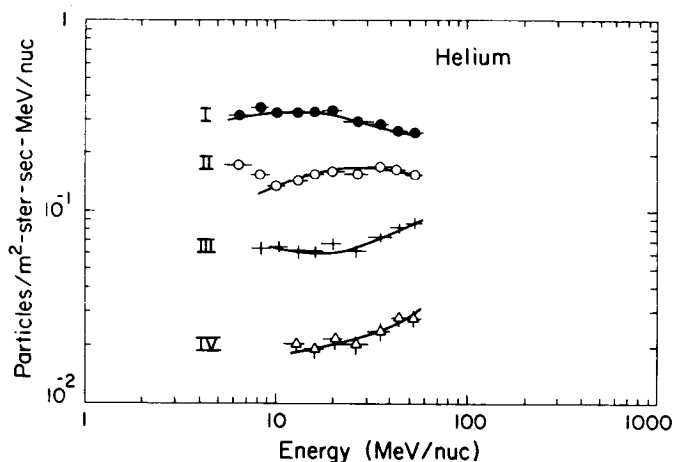

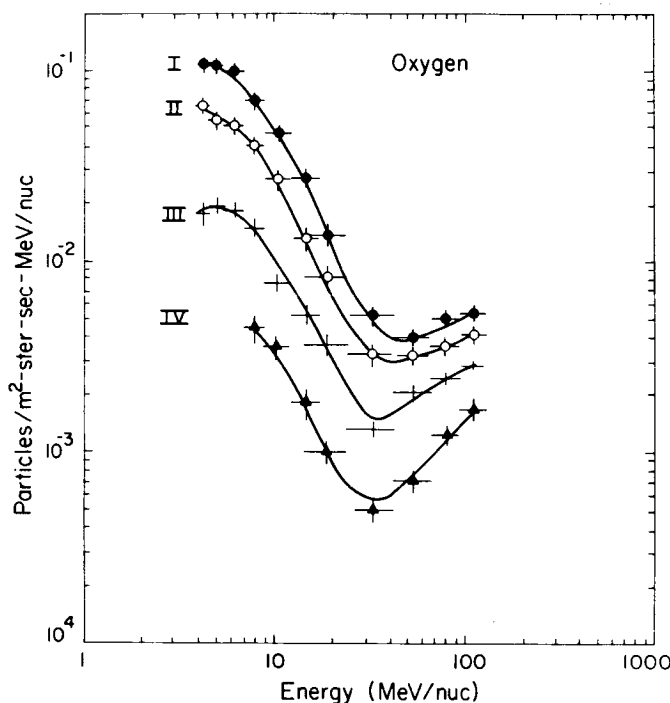Fig. 7. Helium spectra measured during four time periods.

Fig. 8. Oxygen spectra measured during four time periods.

Compton-Getting coefficient associated with the spectrum.

We are continuing to study the implications of this modulation. We are hopeful that having accurate modulation data from 3 charges in overlapping energy ranges and with different spectra should enable one to uniquely determine the A/Z of the charges involved, with a minimum of necessary assumptions regarding the modulation itself.
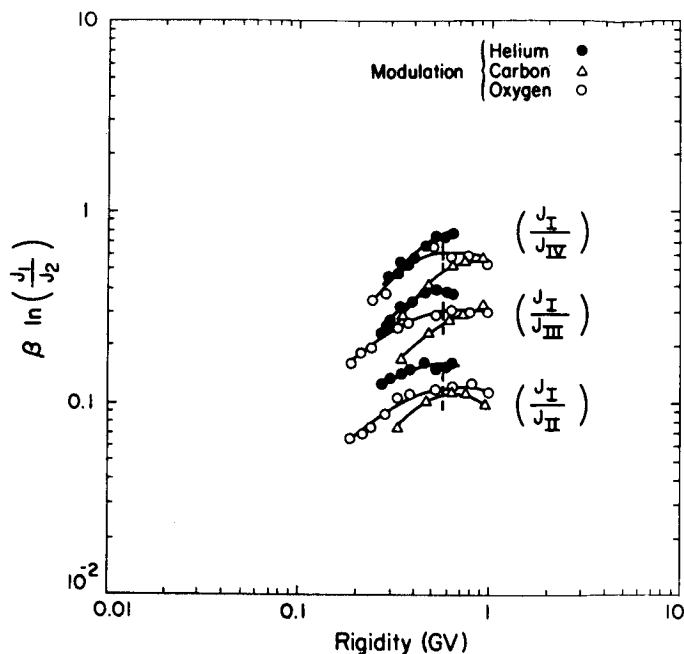
Fig. 9. Modulation parameters observed for He, C, and O nuclei intensity changes in 1977-82.

REFERENCES

Bastian, T. S., R. B. McKibben, K. R. Pyle, and J. A. Simpson, Variations in the intensity of galactic cosmic rays and the anomalous helium as a function of solar latitude, *Proc. 16th Int. Cosmic Ray Conf., Kyoto, 12,* 318, 1979.

Engelmann, J. J., P. Goret, E. Juliusson, L. Koch-Miramond, P. Masse, N. Petrou, Y. Rio, A. Soutoul, B. Byrnak, H. Jakobsen, N. Lund, B. Peters, I. L. Rasmussen, M. Rotenberg, and N. Westergaard, The elemental composition of cosmic rays from Be to Zn as measured by the French Danish Instrument on HEAO-3, *Proc. 17th Int. Cosmic Ray Conf., Paris, 9,* 97, 1981.

Fisk, L. A., B. Kovlovsky, and R. Ramaty, An interpretation of the observed oxygen and nitrogen enhancements in low energy cosmic rays, *Ap. J. Lett., 190,* L35, 1974.

Hovestadt, D., B. Klecker, G. Gloeckler, F. M. Ipavich, C. Y. Fan, and L. A. Fisk, Temporal variations of the anomalous oxygen (1974-1979) and disappearance in 1978, *Proc. 16th Int. Cosmic Ray Conf., Kyoto, 3,* 255, 1979.

Klecker, B., D. Hovestadt, G. Gloeckler, and C. Y. Fan, Composition and energy spectra of cosmic rays between 0.6 and 24 MeV per nucleon during quiet times : transition from a solar to the anomalous component, *Ap. J., 212,* 290, 1977.

Webber, W. R., E. C. Stone, and R. E. Vogt, The elemental composition of quiet time low energy cosmic rays measured on the Voyager spacecraft, *Proc. 16th Int. Cosmic Ray Conf., Kyoto, 5,* 357, 1979.

Webber, W. R., F. B. McDonald, T. T. Von Rosenvinge, and R. A. Mewaldt, A study of temporal and radial dependencies of the anomalous helium and oxygen nuclei, *Proc. 17th Int. Cosmic Ray Conf., Paris, 10,* 92, 1981.

THE EFFECT OF THE SOLAR FIELD REVERSAL ON THE
MODULATION OF GALACTIC COSMIC RAYS

B. T. Thomas   and   B. E. Goldstein

Jet Propulsion Laboratory
California Institute of Technology
Pasadena, CA, 91109

ABSTRACT

There is now a growing awareness that solar cycle related changes in the large-scale structure of the interplanetary magnetic field (IMF) may play an important role in the modulation of galactic cosmic rays. To date, attention has been focussed on two aspects of the magnetic field structure: (1) large scale compression regions produced by fast solar wind streams and solar flares, both of which are known to vary in intensity and number over the solar cycle, and (2) the variable warp of the heliospheric current sheet. In this paper we suggest that another feature of the solar cycle is worthy of consideration: the field reversal itself. If the sun reverses its polarity by simply overturning the heliospheric current sheet (northern fields migrating southward and vice-versa) then there may well be an effect on cosmic ray intensity. However, such a simple picture of solar reversal seems improbable. Observations of the solar corona suggest the existence of not one but several current sheets in the heliosphere at solar maximum. This would be consistent with an interpretation of the field reversal in which the sun 'sheds' its old field and develops new field structures of the opposite polarity (like a dog shedding its winter coat). If this is the case then the effect on cosmic ray intensities can be considerable. We present the results of a simple calculation to demonstrate that the variation in cosmic ray intensities that will result can be as large as is actually observed over the solar cycle.

INTRODUCTION

For a number of years modulation theory has been frustrated in its efforts to account for the solar cycle variation in cosmic ray intensities by a lack of variation in such fundamental solar wind parameters as the interplanetary field strength, the solar wind velocity and the micro-scale turbulence of the magnetic field. Attention has recently turned to the effect of large-scale magnetic structures such as corotating interaction regions (Smith and Wolfe, 1976) and flare induced shock waves (Sonett et al., 1968). These are known to vary in both intensity and number over the solar cycle and recent studies have indicated that they can be expected to produce significant changes in cosmic ray intensity (Gall and Thomas, 1981, Thomas and Gall, 1982, 1983). There has also been interest in the effect of the variable warp of the heliospheric current sheet (Svalgaard and Wilcox, 1974), which has also been shown to be capable of modulating cosmic rays (Kota, 1979; Jokipii and Thomas, 1981).

There is now an indication in the Pioneer and Voyager data obtained in the outer heliosphere that the large solar flares occurring near solar maximum can produce almost circular belts of compressed field (Smith et al., 1983). These result in long-lived Forbush decreases of cosmic ray intensity (Van Allen 1979,

Lockwood et al., 1980). It has been suggested that the large decrease in cosmic ray intensity near solar maximum may be due to a cascade of these long-lived intensity reductions (McDonald et al., 1981). The problem with this interpretation is that flare shocks do not produce such long-lived decreases in intensity at other times in the solar cycle. Furthermore, if the intensity is to be held at low levels for the long periods required it is necessary to suppress the latitudinal drift of cosmic ray particles. Otherwise particles reaching low latitudes can have gained access to the inner heliosphere from high latitudes where the compression effect of these flares is presumably much reduced. Whilst these may not be regarded as strong objections, it is certainly not clear at this time that solar flares are capable of producing the entire modulation effect. It is our suggestion that the apparent cascade effect of these shocks may be due to Forbush decreases (with standard recovery profiles) superimposed on a general downward trend in cosmic ray intensity produced by a different mechanism.

One obvious feature of solar maximum is that the magnetic field reverses polarity. Two-hemisphere models of the solar field interpret this as an increase in inclination of the heliospheric current sheet as solar maximum approaches at which time the current sheet becomes vertical and overturns (Saito, 1975; Kaburaki and Yoshii, 1979). Such a process will undoubtedly have an effect on cosmic ray intensities (Saito et al., 1977; Swinson et al., 1981). The major effect will be simply that a highly inclined current sheet will propagate into the outer heliosphere with very large latitudinal warps and is a simple extension of the analysis reported by Jokipii and Thomas (1981). It seems improbable, however, that the field reversal process is as simple as implied by the two-hemisphere models. The solar corona near solar maximum is extemely complex and suggests the existence of not one but several heliospheric current sheets. If this is the case then the simple picture of northern hemisphere flux migrating southward and vice-versa is implausible.

The model we present is based on the hypothesis that the solar field reverses by shedding the poloidal field of the previous solar cycle and developing a new field of the opposite polarity. This will imply the existence of closed field lines, for the periods near solar maximum, which will greatly impede cosmic ray access to the inner heliosphere.

A MODEL FOR SOLAR REVERSAL

Figure 1 is a schematic representation of a possible mechanism by which the solar magnetic fields may reverse. The three diagrams represent a time sequence. The top diagram shows the interplanetary field (solid lines) as it may appear above the solar corona at a time well before solar maximum. The circle does not represent the sun, but the source surface of the interplanetary magnetic field, located at 2 or 3 solar radii. Thus, all field lines are open at this time. The middle diagram illustrates the situation near solar maximum with isolated regions of opposite polarity now existing in the two hemispheres separated from the background field by additional current sheets. The dashed lines represent new field lines, associated with the developing current systems, which are drawn into the interplanetary medium by the outflowing solar wind. The hypothesis is that as the new regions of opposite polarity grow they push the old flux towards lower latitudes where it is ultimately shed from the sun. Evidence for the existence of these localised regions of anomalous polarity at

Figure 2. A meridian plane projection of a simple model for the heliospheric field, shortly after solar maximum, containing the essential features of the lower panel in Figure 1.
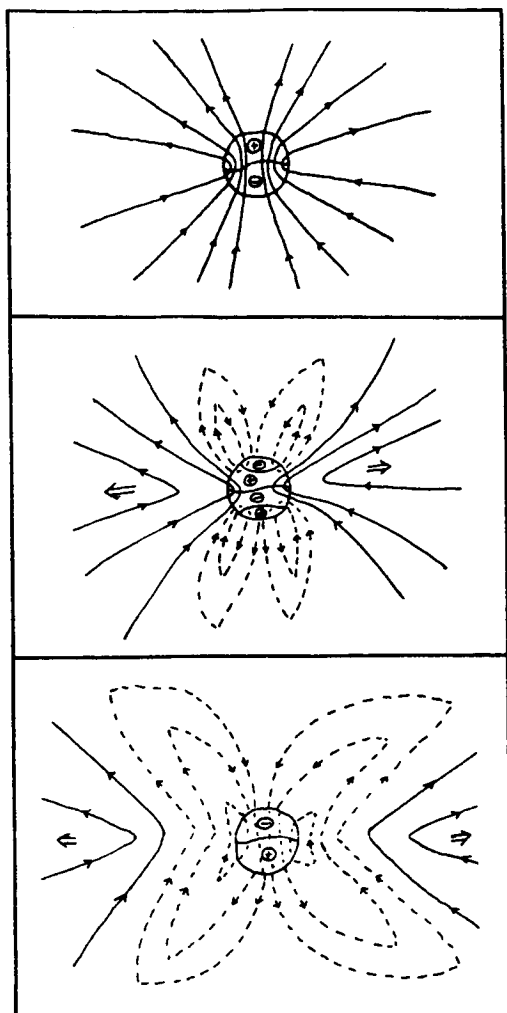
Figure 1. A schematic representation of a model for the solar field reversal. The upper panel shows meridian plane projections of field lines above the solar corona prior to solar maximum (the circle represents the IMF source surface, not the sun). The middle panel shows the field geometry during the reversal period with new current systems and current sheets on the sun producing new magnetic flux (dashed lines). The lower panel shows the situation shortly after the reversal is completed with the new flux having completely displaced the old. The radial distances in these diagrams have been greatly foreshortened.
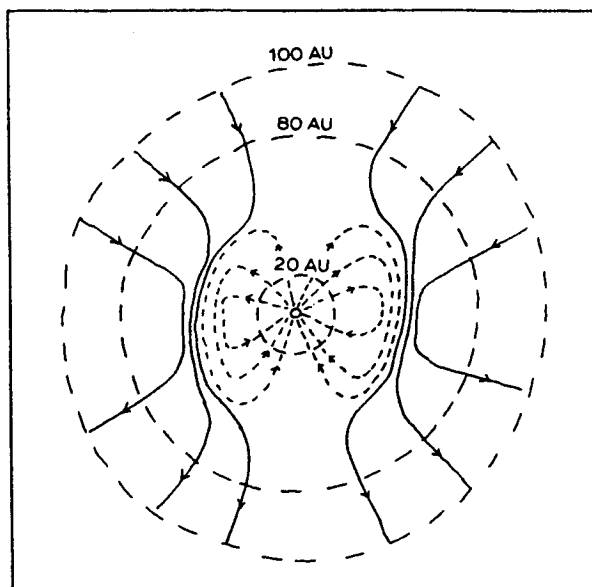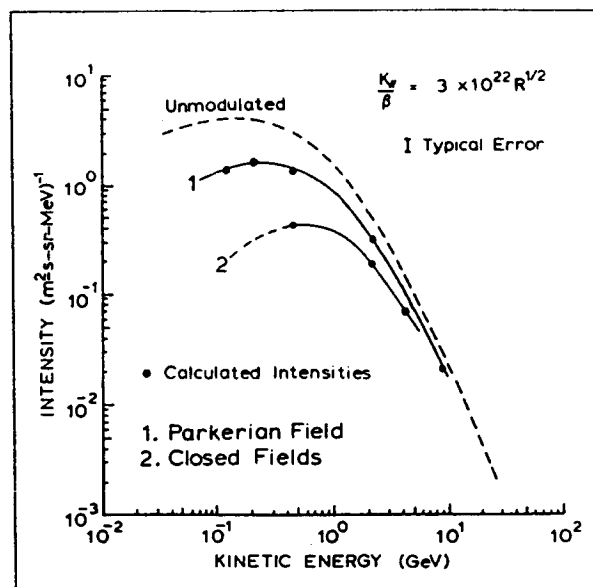

Figure 3. Results of a numerical calculation of cosmic ray intensities at 1 AU in a simple spiral (Parkerian) field and in the closed field geometry of Figure 2. The diffusion coefficient is quoted for 1 AU (R is rigidity in GV).

solar maximum has been reported (Hoeksema et al., 1982). The lower panel illustrates the situation shortly after solar maximum when the new polarity regions have spread completely over both hemispheres, establishing the new solar cycle, with the old field lines now completely shed from the sun. This model for the reversal of the IMF polarity is not inconsistent with dynamo models for the 22 year solar cycle (e.g. Babcock, 1961; Stix 1976). If the bulk of the IMF reversal takes place on a time scale of order one year then the new flux will not have had time to convect to the heliospheric boundary and the field lines in the inner heliosphere at this time will therefore be closed.

This model may be over simplified, there may be more than one region of anomalous polarity which develops in each hemisphere and the flux shedding process, if it occurs, will probably be spasmodic and patchy (i.e. coronal transients or localised bubbles). However, topologically there are only two possible interpretations for the solar reversal process. Either field lines migrate over the solar surface or, alternatively, new flux emerges and displaces the old. Reconnection processes may be expected to play a role in the reversal but if isolated regions of opposite flux do develop on the sun it will not be possible for the field lines in these regions to reconnect with the old field from the opposite hemisphere.

A SIMPLE NUMERICAL MODEL

The magnetic field geometry near solar maximum resulting from the process outlined in the previous section would be quite complex. In this section we outline a greatly simplified model for the field geometry shortly after solar maximum, for which solutions for the cosmic ray intensity at 1 AU can be determined by numerical integration techiques. The objective is to determine if the existence of a closed field line configuration in the inner heliosphere is capable of providing cosmic ray modulation of the required magnitude.

Figure 2 displays the model schematically. The diagram shows only the meridian plane components of the field. Over most of the diagram the azimuthal component is dominant and the field geometry is close to an Archimedian spiral, with a flat current sheet in the equatorial plane. For computational simplicity the outer boundary of the heliosphere is taken to be spherical and is located at 100 AU. Inside 20 AU the field is a pure Archimedian spiral given by the equations:

$$B_r = A \frac{B_0}{r^2} \tag{1a}$$

$$B_\phi = A B_0 \frac{\Omega \sin \theta}{r V_w} \tag{1b}$$

$$B_\theta = 0 \tag{1c}$$

where V_w is the solar wind velocity, Ω the solar rotation frequency and B_0 is chosen to give a 5 nT field at 1 AU. $A = \pm 1$, chosen to give outward fields in the northern hemisphere and inward in the southern hemisphere. This region represents the new field after the reversal process is completed.

444

Outside 80 AU the field equations are identical, but A is chosen to give inward field in the northern hemisphere and outward in the southern hemisphere. This region represents field from the previous solar cycle which has now been completely shed from the sun but which has not yet convected to the model boundary.

Between 20 and 80 AU is the transition region representing the period during which the field reversal occurred. This corresponds to a reversal period of approximately eight months. A simple method of closing the internal and external field regions is given by the divergence free expressions:

$$B_r = A B_o \frac{(r - r_o)}{r^2 \Delta r} \tag{2a}$$

$$B_\phi = A B_o \frac{\Omega \sin \theta \, (r-r_o)}{r V_w \Delta r} \tag{2b}$$

$$B_\theta = A B_o \frac{(\cos\theta - 1)}{r \Delta r \sin\theta} \tag{2c}$$

where r_o is the interface between old and new flux located at 50 AU and Δr is the half-width of the transition region, 30 AU. This model actually corresponds to a field on the sun in which the radial component dies away linearly and builds up again in the opposite direction. Although not a representation of the true situation it contains the essential features: separate regions of old and new flux, closed fields in the inner heliosphere and a field geometry which is almost Parkerian (except very near the interface). The magnitude of the north-south component as this structure convects past 1 AU would be approximately 1/10th nT. The effect of the radial component of the field diminishing over the reversal period may be unrealistic but will have the consequence of providing easier access of cosmic rays to the inner heliosphere and so will weaken the overall modulation rather than exaggerate it.

In the numerical calculation of the cosmic ray intensity at 1 AU, which is described in the next section, we have compared the results obtained in this model with those obtained in the simple spiral field which will exist well away from solar maximum. It is clear that particles will have easier access to the inner heliosphere in the simple spiral field configuration. Particles move in the heliosphere under a combination of diffusive propagation along the field lines and particle drifts. In spiral fields both the field lines and the drift patterns extend to the heliospheric boundary. In a closed field topology exactly the opposite is true. Not only are the field lines closed but, since particle drifts are divergence free, the drift patterns are also closed. Therefore the particles obtain no help from either process and can gain access to the inner heliosphere only by scattering perpendicularly to the field, across the interface between one field region and the other.

NUMERICAL METHOD AND RESULTS

The method used involves full numerical integration of the equation of motion (3) for individual cosmic ray protons.

$$\frac{d\vec{P}}{dt} = e(\vec{E} + \frac{\vec{v} \times \vec{B}}{c})$$

<div align="right">(3)</div>

where P, v and e are the particle momentum, velocity and charge; B the magnetic field and E the convection electric field. The effect of scattering by magnetic field irregularities is represented by introducing small random angular perturbations in such a way that the desired diffusion coefficient is obtained. The diffusion coefficient is allowed to increase in the outer heliosphere such that the mean free path and particle gyroradius have a fixed ratio. Perpendicular scattering is also implicit in this method with the particle scattering typically one gyroradius perpendicular to the field in each parallel mean free path. This leads, in these calculations, to a perpendicular diffusion coefficient approximately 10% of the parallel coefficient. The trajectory of a given particle is obtained by integrating backward in time, starting at 1 AU until the particle reaches the model boundary at 100 AU. A power law in total energy is assumed for the cosmic ray phase space density at the boundary. By direct application of Liouville's theorem each particle gives an independent estimate of the phase space density at 1 AU (at a given particle energy) and by averaging over a large number of individual estimates we obtain a representative value for the omnidirectional intensity at 1 AU. This method has certain advantages over a more traditional numerical solution of the transport equation. Firstly, adiabatic focussing and gradient and curvature drifts are automatic consequences of full trajectory integration and we therefore avoid the unphysically large velocities that can result from first order approximations. Secondly, current sheets and other discontinuities are also dealt with automatically without the need for continuity conditions. The primary advantage is that it can deal with three-dimensional field configurations, although that is of little advantage here, as our model has azimuthal symmetry. The method has been compared with traditional solutions of the transport equations in simple spiral fields and complete agreement is obtained. Further details of this method are given in Thomas and Gall (1983).

Figure 3 displays the cosmic ray intensities obtained as a function of particle energy for simple Parkerian fields and for the closed field line model outlined above. The same diffusion coefficients were used for both calculations. The calculated intensities are subject to errors due to the finite number of individual estimates of the phase space density. A typical error bar is displayed. The difference in the two curves is indeed comparable to the observed variation in cosmic ray intensity over the solar cycle.

<div align="center">DISCUSSION AND CONCLUSION</div>

The mechanism by which the sun reverses polarity is crucial for understanding the solar cycle modulation of galactic cosmic rays. One possible mechanism we suggest is that the sun may completely shed the magnetic flux from the previous cycle and develop a new magnetic field of the opposite polarity. If this is the case then a closed field line topology will exist in the heliosphere for the periods near solar maximum. We have quantitatively investigated the effect of an extremely simple closed field model, representing the heliospheric field shortly after solar maximum, and find the effect on cosmic ray intensities to be comparable to that observed.

We have performed our analysis at just one particular time in the solar cycle shortly after the field reversal has been completed. It is clear, however, that the effect will begin substantially earlier (when the reversal process begins and new flux loops begin to appear in the inner heliosphere) and will not disappear until all of the old flux has been shed and has convected to the heliopause. Thus, the intensity reduction can be expected to persist for several years. It will also display the familiar hysteresis effect.

Our primary objective in this paper is to give a general indication of the effect that closed field configurations may have on cosmic ray intensities in the heliosphere, using reasonable estimates for the particle diffusion coefficient and overall size scale of the interplanetary magnetic field. In reality the field configuration at this time may be very complicated, but if regions of closed field do exist then there may be large effects on cosmic ray intensities which cannot be ignored.

REFERENCES

Babcock, H. W., The topology of the sun's field and the 22-year cycle, Astophys. J., 133,572,1961.

Gall, R., and B. T. Thomas, A theoretical interpretation of Forbush decreases, Proc. Int. Conf. Cosmic Rays 17th, 4,1,1981.

Hoeksema, J. T., J. M. Wilcox, and P. H. Sherrer, The three-dimensional structure of the heliospheric current sheet 1978-1981, (abstract), EOS Trans. Amer. Geophys. Union, 63,45,1982.

Jokipii, J. R., and B. T. Thomas, Effects of drift on the transport of cosmic rays, V, Modulation by a wavy interplanetary current sheet, Astrophys. J., 243,1115,1981.

Kaburaki, O., and Y. Yoshii, On the three-dimensional structure of the solar magnetic field in interplanetary space, Solar Physics, 64, 187,1979.

Kota, J., Drift – The essential process in losing energy, Int. Conf. Cosmic Rays 16th, 1979.

Lockwood, J. A., W. R. Webber, F. B. McDonald, T. T. Von Rosenvinge, J. H. Trainor, Study of the effects of Forbush decreases and the 11-year variation of cosmic rays out to approximately 16 AU, Int. Conf. Cosmic Rays 16th, 5,330,1980.

McDonald, F. B., J. H. Trainor, and W. R. Webber, Pioneer and Voyager observations of Forbush decreases between 6 and 24 AU, Int. Conf. Cosmic Rays 17th, 10,147,1982.

Saito, T., Two-hemisphere model of the three-dimensional magnetic structure of the interplanetary space, Sci. Rep. Tohoku Univ. Ser. 5,23,37,1975.

Saito, T., S. Watanabe, T. Kanno, Y. Ishida, and K. Owada, Interpretation of long-term variation of cosmic ray intensity in terms of the two-hemisphere model, Sci. Rep. Tohoku Univ. Ser., 5,24,29,1977.

Sonett, C. P., D. S. Colburn, L. Davis, Jr., E. J. Smith, and P. J. Coleman, Jr., Evidence for a collision free shock in interplanetary space, Phys. Rev. Lett., 13,N507,1968.

Smith, E. J., and J. H. Wolfe, Observations of interaction regions and corotating shocks between 1 and 5 AU: Pioneers 10 and 11, Geophys. Res. Lett., 3,137,1976.

Smith, E. J., B. T. Thomas, and A. Barnes, Solar wind interaction regions observed near 10 AU by Pioneer 11 and their origin, submitted to J. Geophys. Res., 1983.

Stix, M, Dynamo theory and the solar cycle, Basic Mechanisms of Solar Activity, V. Bumba and J. Kleczek (eds.), IAU Symp., 71,367,1976.

Svalgaard, L., and J. M. Wilcox, The spiral interplanetary magnetic field: A polarity and sunspot variation, Science, 186,51,1974.

Swinson, D. B., T. Saito, and S. Mori, Enhanced cosmic ray anisotropies and the extended solar magnetic field, J. Geophys. Res., 86, 8845,1981.

Van Allen, J. A., Propagation of a Forbush decrease in cosmic ray intensity to 15.9 AU, Geophys. Res. Lett., 6,566,1979.

Thomas, B. T., and R. Gall, The effect of corotating interaction regions on the propagation of relativistic cosmic rays in the heliosphere, J. Geophys. Res., 87,4542,1982.

Thomas, B. T., and R. Gall, Solar flare induced Forbush decreases: A theoretical description, submitted to J. Geophys. Res., 1983.
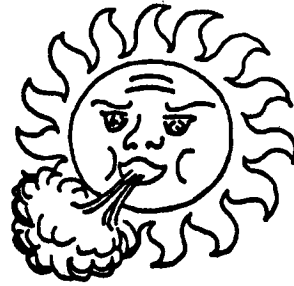
SESSION 8.

SPATIAL DEPENDENCES

SPATIAL DEPENDENCES-THEORETICAL OVERVIEW

G. L. Siscoe
Department of Atmospheric Sciences
University of California, Los Angeles, CA 90024

Viewed as a problem in continuum mechanics, five factors determine the large scale structure and behavior of the solar wind. (1) The pattern of inhomogeneities in the solar corona is imaged by radial projection throughout the solar system. (2) The image at one radial distance is displaced relative to the image at a different distance because of the rotation of the source surface and the finite speed of projection. The image at any distance corotates with the sun with some lagged azimuthal displacement with respect to the source pattern. (3) The image changes in time because of temporal changes in the source pattern. (4) The image is distorted by in-transit dynamical processes. (5) The image may acquire noise, that is features not present in the original pattern, such as corotating shock waves and turbulence which results from instabilities that develop in transit. Significant theoretical progress has been made in most of these areas in the last four years. The source pattern has become better defined and its spiralled projection calculated. Theoretical treatments of in-transit distortion are now three-dimensional and include dynamic effects of the magnetic field. Naturally occurring solar wind conditions that can produce the Kelvin-Helmholtz instability have been identified. This work will be reviewed and some areas for future emphasis suggested.

Interplanetary Scintillation Observations of the Solar Wind
Close to the Sun and Out of the Ecliptic.

D. G. Sime
High Altitude Observatory,
National Center for Atmospheric Research[*]
P. O. Box 3000,
Boulder, Colorado 80307

ABSTRACT

A brief review is given of recent developments in the observation of the solar wind by the method of interplanetary scintillation. The emphasis is on observations of the velocity structure, the electron density and the effect of propagating disturbances in the interplanetary medium as detected principally by intensity and phase scintillation and by spectral broadening.

Introduction

Interplanetary Scintillation (IPS) observations provide our only present method of making routine, although indirect, measurements of the solar wind out of the ecliptic and close to the sun. Although new developments in coronal diagnostics (Withbroe et al, 1982) will permit inference of the flow properties very close to the sun and, for the interval during which International Solar Polar Mission spacecraft will be out of the ecliptic, *in situ* measurements of the solar wind in that region will be available, we will depend on IPS for our continuing knowledge of these regions of interplanetary space. It is thus appropriate to review the contribution made by IPS over the last few years.

Given essentially a solar cycle's worth of observations of the global solar wind velocity, and with the increasing availability of observations close to the sun, the subject has developed to the point where it can provide information of interest to the solar and interplanetary physics community at large. In particular, IPS observations exist now of relevance to three major fields of current interest in interplanetary physics: namely heliospheric structure, the heating and acceleration of the solar wind, and the morphology of transient disturbances in the interplanetary medium following coronal transients.

For brevity, this presentation will be limited in scope and cover only those topics which deal primarily with intensity and phase scintillation and radio source spectral broadening. This choice is based on the ease of discussion of these methods in this context and the fact that it allows presentation of topics related to the fields mentioned above.

Consequently, this is not an exhaustive review and a number of important areas will be omitted entirely. The reader is referred to other articles, beginning with the original work of Hewish and colleagues (Hewish et al., 1964) for more comprehensive treatment of the methods, and the underlying physics, and also for more penetrating discussion of the results. Bird (1982) has given a thorough review of coronal radio sounding measurements made using spacecraft as sources, including a discussion of the detection of Faraday

---

rotation observations; a subject which will be almost entirely neglected here. Woo and Armstrong (1983) have similarly covered the subject of single and multiple station observations of spacecraft telemetry link scintillations. Further, more extensive expositions of the techniques used and applicable theory are also given in Coles et al. (1974), Woo (1975), Coles (1978) and Armstrong and Woo (1981).

Methods and Measurables

It is valuable to begin by outlining briefly the quantities measured in scintillation measurements and the physical bases of the phenomenon, and to indicate the means by which inference of solar wind properties can be made.

The basic process arises from the interaction of a plane wave traversing the interplanetary medium with irregularities in the refractive index, due to an inhomogeneous electron density. The perturbed wave fronts propagate to earth where their amplitudes and phases, or simply intensities, are recorded. Estimates of various field statistics can be made, and from the spatial and temporal distribution of these estimates, inferences of the properties of the scattering medium are drawn.

In perhaps the simplest case, intensity scintillations, the time series of intensity fluctuations is recorded and from this the root mean square fluctuation, or a temporal spectrum, of the flux is estimated. This spectrum is related to the irregularity spectrum. The rms fluctuation, when normalized by the non-varying flux of the source is called the scintillation index. Since the temporal fluctuations in the signal are viewed as being caused by the mapping of the spatial distribution of irregularities in the medium by the moving solar wind into a temporal distribution, appropriate sampling of these variations at several sites enables one to estimate a projected velocity vector for the solar wind. This multi-station technique, the assumptions implicit in it, and various tests of consistency for it have been discussed thoroughly by Coles et al.(1974), Coles and Maagoe, (1972), Coles,(1978), and Coles and Kaufman (1978). The related field of phase scintillations, in which phase fluctuations are recorded, and the practical realization of such observations is discussed by Woo (1977).

It is important to recall in interpreting IPS data that the scattering which leads to the scintillation arises along an extended portion of the line of sight (see figure 1), so the received signal results from the convolution of effects arising at various points in space. An early working assumption was that the electron density irregularities, which are the cause of the scintillation are proportional to the local ambient density ($\Delta n \propto n$) so that the overall radial density fall off would
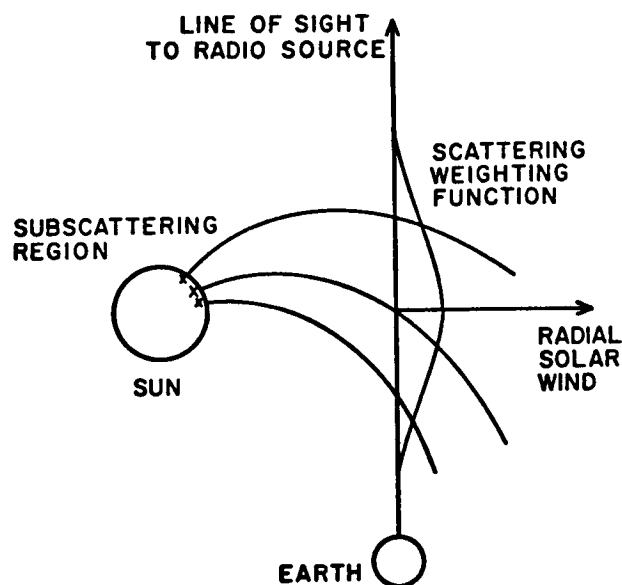

Figure 1: The geometry of an IPS observation showing the line of sight, the scattering weighting function along the line of sight and the point on the sun which is taken as the source of the observation.

maximize the scattering at the point at which the line of sight passes closest to the sun. This assumption has been tested in comparison with *in situ* data, and it does appear, with minor modifications, to be an adequate one. Allusion is thus made to observations at a position in space, the reference being to the point of closest approach to the sun of the particular line of sight. Any references to the heliographic position of the observation usually are to the point on the sun reached by a projection with constant radial velocity from that point of closest approach back towards the sun. As discussed later, it should be recognized that the test of this assumption involved observations which were dominated by large scale, long lived solar wind features and therefore does not necessarily indicate that there is a high degree of certainty in the position of small short lived features.

The efficiency of the scattering which causes the scintillation depends on the radio frequency of the observations in such a sense that the scintillation is measurable only at higher frequencies as the line of sight approaches the sun (Hewish and Symonds, 1969). Thus observations of velocities within the interplanetary medium ($\sim 0.3 \leq R \leq 1.0 AU$) are generally made at meter wavelengths, while the observations closer to the sun involve centimeter wavelengths. Consequently, observations near the sun benefit from the availability of spacecraft in near occultation by the sun, while observations closer to the orbit of the earth utilize natural sources.

The observation of the scintillation effect relies on two physical conditions; the existence of density irregularities and their motion across the line of sight. Interpretation of the observations thus requires the recording of two (at least) data sets, or an assumption concerning one or other of the properties.

The inference of solar wind properties is thus indirect, involves line of sight integration and may not refer to an exactly known location. However, with careful application of the methods and assumptions, much can actually be achieved.

Solar Wind Velocity Measurements

Inference of the solar wind velocity from multiple station intensity scintillation data is the easiest of the observations to understand and interpret; it relies on the adequate detection of a projected intensity pattern as it moves across the ground. For essentially a solar cycle, synoptic 74 MHz IPS measurements of the solar wind velocity have been made by the group at San Diego (Armstrong and Coles, 1972). As a result of this prolonged effort, a large data set has been accumulated which has allowed many of the uncertainties and assumptions involved in the method to be tested (e.g., Coles and Kaufman 1978). This has included the demonstration of a favorable comparison of both velocity and density structure of large scale features as observed by IPS with the results of *in-situ* measurements (Ananthakrishnan et al. 1980).

From these synoptic measurements, made predominantly in the range 0.3 to ~1.0 AU from the sun, the global configuration of the solar wind has been reconstructed, providing resolution of the unclear picture provided by earlier spot observations. This overall structure was expressed by Coles and Rickett (1976) as an average velocity gradient with latitude showing clearly the tendency, in yearly average measurements, to higher velocity at higher heliographic latitudes. Although this result was not confirmed by inferences from comet tail measurements (Brandt et al.,1975),it did verify the earlier indications of such an effect by Dennison and Hewish (1967). It was pointed out by Hundhausen (1978) that, of course, the process of averaging over longitude masked the true gradients which existed in the medium, and that a more appropriate estimate of the actual gradients was

that found from *in situ* observations which did not average (e.g., Rhodes and Smith, 1976a,b).

The identification of the polar regions as areas of high speed flow was further refined and the existence of regions of much higher than average gradients demonstrated with the assembly of averaged distributions of IPS velocity as functions of latitude and longitude (Sime and Rickett, 1978). These showed the restriction of high speed flow to regions which mapped into coronal holes, and demonstrated directly the extension of polar high speed flows into equatorial regions whenever the polar coronal holes were so extended. These maps showed also that the configuration of the solar wind matched that of the corona in being consistent with the geometry of a tilted dipole with flow from the open regions (Hundhausen, 1977), and that the appropriate geometry in which to describe the solar wind was based on the magnetic properties of the sun rather than the rotational axis (Zhao and Hundhausen, 1981).

Further, the evolution of this magnetic configuration as witnessed in the corona (Hundhausen et al., 1981) allowed Sime (1979) to demonstrate that even if individual comet tail observations were highly reliable, the poor sampling across the solar cycle of that data set would probably prevent the cometary observations from showing this large scale gradient. The need exists now for point by point comparison of simultaneous IPS and comet tail observation.

Now that the data exist for a solar cycle, the evolution of this average velocity distribution with latitude can be followed along with the coronal evolution. Coles et al. (1980) have shown the elements of this development, as depicted in figure 2. The overall shape of the velocity vs latitude curves, with a minimum yearly average velocity near the equator and significantly higher velocities above about 30 degs. latitude, is preserved throughout the interval shown. The high values are the result of the prevalence of high speed streams at these latitudes. However, the effect is markedly diminished in 1978 and almost absent in 1979 as the poleward retraction of the coronal holes begins and restricts the high speed regions of the solar wind. This effect was suggested by Hewish and Symonds (1969) at the previous solar maximum, when they failed to repeat the observations of such high speed from a year earlier by Dennison and Hewish (1967). The evolution of the complete cycle of data is discussed elsewhere in these proceedings by Rickett and colleagues.

Figure 2: The average solar wind speed as a function of latitude for the interval 1972 to 1979. Taken from Coles et al. (1980).

These data also allow the construction of the overall, or global, average solar wind velocity. This quantity is plotted in fig. 3 along with the yearly average equatorial IPS velocity estimate. The global value shows an overall variation of 20-25% over the course of the last cycle, again showing the influence of the high speed polar flow at times other than near the maximum.
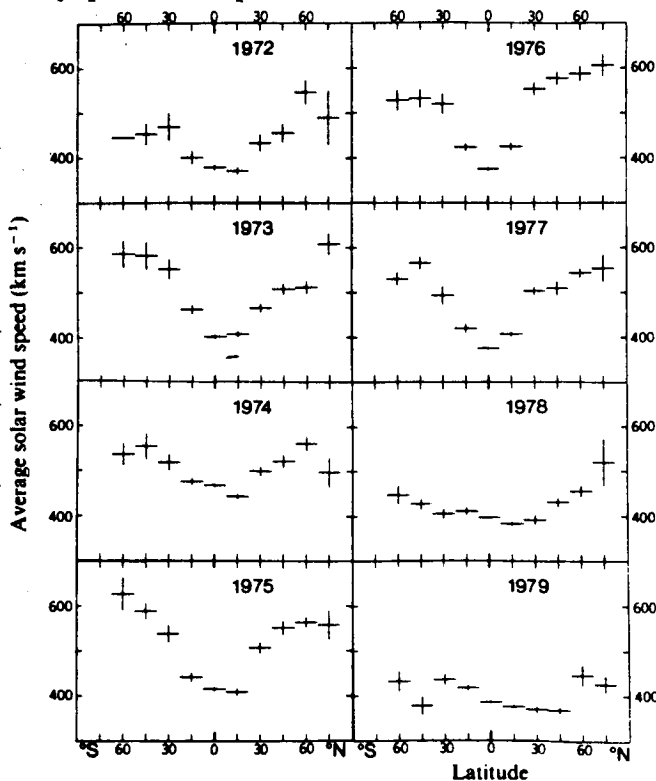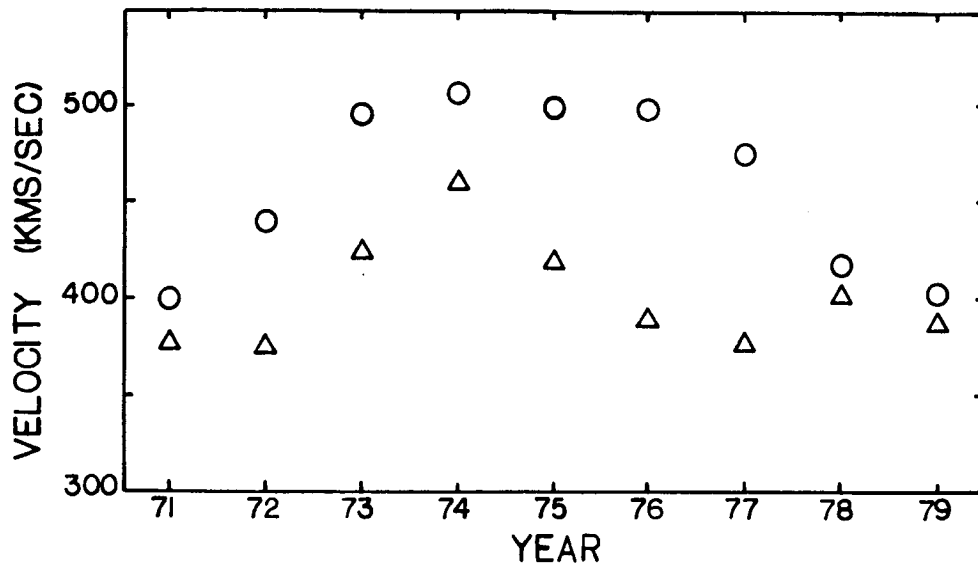
Figure 3: The average solar wind speed for the interval 1971 to 1979 showing both the equatorial average speed (triangles) and the global speed (circles).

Near the maximum, the equatorial and global averages are quite similar, and as the cycle progresses towards minimum, we see an increase in both values, reflecting both the increase in influence of the coronal holes and the rearrangement of the corona to bring the holes close to the equator. Although the global average velocity remains high until 1978, the equatorial value is reduced, beginning in 1975, as the near equatorial extensions of the polar holes retract. That is, as the interplanetary current sheet straightened out,(Zhao and Hundhausen, 1983) the high speed contribution to the equatorial wind was removed and the difference between the equatorial and global values increased; the in ecliptic measurements no longer sampling solar wind far from the current sheet. The IPS equatorial value agrees well with the *in situ* observations over this interval (Feldman et al., 1978; Schwenn, 1983), although there is a slight ($\leqslant$ 50 kms/sec) downward bias on the IPS results. Thus a view of the solar wind based entirely on the in ecliptic data would be somewhat misleading since the solar cycle variation in speed is not as marked as the global estimate indicates, and there is even some indication that the variation seen in the ecliptic during this cycle may be somewhat anomalous (Gosling et al., 1977). Understanding of the evolution of the heliosphere therefore cannot rest on in-ecliptic measurements alone.

The extended heating of the corona to produce the solar wind remains as one of the most fundamental problems in solar physics (Leer et al., 1982). With the acceptance of the importance of coronal holes (Zirker, 1977) and magnetic topology in the acceleration process (Holzer and Leer, 1980) and the apparent exclusion of acoustic waves as important contributors to the energy flux,(e.g., Athay and White, 1978) interest in this question has been renewed. IPS observations can provide information on the acceleration region since the rapid motion of natural sources in elongation near the sun enables a profile of velocity and other attributes with height to be detected readily. The paucity of these observations in part reflects the lack of equipment for doing multi-station observations on natural sources and partly due to the lack of sources. Recently, two interesting approaches have been developed to accommodate this problem.

457

Scott (1978) and others (Coles et al., 1978a) have developed a technique to identify a breakpoint in the spectrum of intensity fluctuations recorded at a single station, and from a characterization of the behavior of that feature, to establish the radial profile of velocity. From such observations, Scott and colleagues have shown a general increase of velocity to interplanetary values at about 20-30 R_o with an increase of about 10 kms/sec/R_o below this. Accompanying the general increase in the bulk flow velocity, there is a decrease in the random component of the velocity estimated from the same data.

Armstrong and Woo (1981) on the other hand, have used spacecraft telemetry scintillations to probe the inner reaches of the solar wind. They have applied the analysis of Ekers and Little (1971) to their two-station observations and estimated both a random and bulk velocity component of the flow within 30 R_o. Their figure 4, reproduced here, summarizes most of the available observations, including those of Scott mentioned above, showing in general, an approximately linear increase of velocity with distance from the sun from values of 100 kms/sec at 5 R_o to ~ 500 kms/sec at 20-30 R_o. There is a slight decrease in the random component estimate over this interval --or rather, a significant decrease in the random *fraction* of the velocity (see their figure 5). Although there are exceptions to the trend (Coles et al., 1978a) the general consistency of these data is rather surprising since they arise from single radial scans taken at significantly different times and in differing coronal conditions.

As mentioned below, Armstrong and Woo also show that the density spectrum steepens with increasing distance from the sun over this same range. The simultaneous evolution of the observed density spectrum and the velocity is presumedly an important diagnostic, but one which has not yet been fully utilized. The time is ripe for a circumspect interpretation of these data.
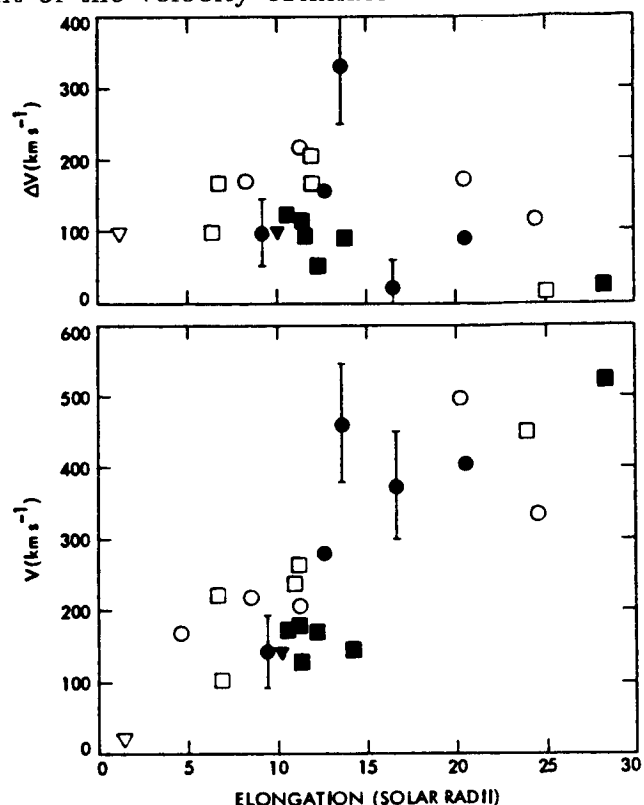

Figure 4: A summary of solar wind speed measurements near the sun, from Armstrong and Woo, 1981. Panel a shows mean solar wind speed and panel b shows the rms solar wind speed versus elongation. Open triangle: James (1964) radar backscatter measurement. Open boxes: Ekers and Little (1971). Open circle: Coles et al.,(1978a), Scott (1978). Filled symbols: Armstrong and Woo, 1981 (triangle = 1976 data; circles = 1977 data; boxes = 1978 data)

It is likely that future work with recently available antennas (Bourgois, this proceedings) and with the VLA will permit a more conclusive picture of the acceleration region to be established, especially in conjunction with the progress in resonance line coronagraph diagnostics, Withbroe et al., (1982).

458

Density Fluctuations

Since the scintillation phenomenon results from the fluctuation in the interplanetary electron density, IPS permits the measurement of only the fluctuations themselves, and not the average or background density. In general, only those fluctuations with scale sizes in a restricted range can be measured by any one technique, all others either averaging to zero or contributing to the effective background. Consequently, any conclusions about the actual background density relies on rather indirect inferences.

The study of the spectrum of electron density irregularities in the interplanetary medium has been the subject of considerable activity over the last decade. Early spacecraft measurements of scales greater than 10^{-5} kms showed a power law dependence on wavenumber with an index of about -3 for the three dimensional spectrum. These measurements were later extended to wave number regimes of about 10^{-4} to 10^{-1} kms^{-1} both by *in situ* measurements and by IPS observations (Unti et al., 1973; Harmon 1975). In each case, a fairly solid estimate for a power law index of close to the Kolmogorov value of -11/3 was established. Observations covering many years and many positions in the interplanetary medium (at $R \gtrsim 0.3 AU$), failed to show any significant variability of the spectrum with solar cycle, radial distance or latitude, at least to the extent that it was tested by inference from the IPS spectrum or from the constancy of the scintillation index. Woo and Armstrong (1979) have now extended the identification of the spectrum in to distances of as low as $2R_o$, and by using measurements of phase scintillations, have sampled the wave number range 10^{-2} to 10^{-4}. Again, the single power law description is best, but at distances of $< 20R_o$, there is considerable evolution of the spectrum, with the index varying from ~11/3 at $20R_o$ to ~3 at ~$5R_o$. This is confirmed by Harmon and Coles (1983) from their observations of planetary radar signals, and appears to be the only systematic variation of spectral properties.

A continuing problem has been the identification of the regions which actually produce the scintillations, and in particular, what exactly does the IPS velocity represent. Early attempts (see, e.g, Coles et al., 1978b) led to a reasonable "consistency" with the notion that the density fluctuations were proportional to the background density. However, models based on this, although they allow calculation of velocity series which are in fairly good agreement with observation, failed to predict scintillation indices which were in good agreement with the data. This is important since it is the index which is most directly related to Δn.

A more recent analysis by Ananthakrishnan et al. (1980), has tied down better the region most responsible for the scintillation signal. They produced a model scintillation signal for a source in the ecliptic using *in situ* spacecraft plasma measurements mapped to the appropriate position along the line of sight. This model yielded a velocity and scintillation index series which could be compared with that actually recorded on the source in question. The initial model, based on $\Delta n \propto n$, was then perturbed to improve the agreement with observation, and yielded the result that for this fit, the position of the Δn peak is at the position of highest positive velocity gradient. Thus the proportionality of Δn and n is not consistent with these observations. It is not yet clear what physical process leads to this increase in levels of "microturbulence", but it should be remembered that the tests were made for in-ecliptic solar wind at a time during which it was dominated by large scale, slowly evolving structures, and it remains to be tested for other conditions.

Even before the identification of coronal mass ejection events, it was apparent that interplanetary disturbances plausibly associated with impulsive solar activity travelled out to the orbit of the earth. *In situ* measurements soon established the shock nature of the events directly and were frequent enough to allow the general properties of these events to be established (Hundhausen, 1972). Statistical assemblies of these single point observations (spacecraft plasma and field measurements(e.g., Taylor, 1969) and sudden commencement occurrence (Hirshberg, 1968; Chao and Lepping, 1974)) showed that the extent of these events at 1 AU in the ecliptic was quite large, typically a circle of radius several tenths of an AU. Theoretical calculations(De Young and Hundhausen, 1971), however, showed that the size at 1 AU was not a powerful discriminator of the conditions near the site of the source of the disturbance.

With the awareness of the existence of coronal transients (MacQueen, 1980) we have the more general problem now of establishing the signature of any interplanetary manifestation of these events. Following the *in situ* identification of a disturbance following one of the transients observed from SKYLAB (Gosling et al.,1975), significant progress has been made in the identification of plasma disturbances within 1AU which are plausibly associated with coronal transients (Sheeley et al., 1983). The recent suggestion of a magnetic signature for the events (Klein and Burlaga, 1982) was followed by the association of one such event with an observed transient (Burlaga et al., 1982). However, we are still far from having established the uniqueness of such identifications and understanding the physics involved.

IPS provides an opportunity of detecting propagating interplanetary disturbances in three dimensions, and can therefore improve our knowledge of the existence, extent and dynamics of propagating disturbances following coronal ejections. However, uncertainty as to the signature of these events and limits on what the IPS technique is sensitive to ,limit progress. For example, if neither a change in the local density fluctuation level, nor in the bulk velocity occurs, then intensity or phase scintillations will not detect the event. Faraday rotation observations, however, could detect changes in the magnetic field (Bird, 1982).

Nonetheless, the potential has been explored, since the multiple lines of sight available for low frequency scintillating sources allow simultaneous detection in all three dimensions and can provide limits on the interplanetary morphology of these events, at least to the same order as is available from other techniques. Further, the repeated observation of a single disturbance at succeeding locations can give an indication of the evolution of the event. It must, however, be stressed that the IPS detection of these features is subject to the same difficulties as all other methods; even if the disturbance is identified, the association with a solar event must be made. This is a difficult step and involves projections across large fractions of an astronomical unit. Two particular points of note with respect to identification by IPS are the relatively coarse time resolution along a particular line of sight (up to ~24 hours) and the uncertainty (up to ~ 1/2 AU) in the distance from the earth at which the disturbance crosses the line of sight. However, by combining information from several observations, one can often diminish the effects of these uncertainties.

The remarkable disturbances in the interplanetary medium following the flares of early August 1972 provided an early opportunity for a demonstration of the IPS detection of such events (Armstrong et al. 1973). Rickett (1975) combined spacecraft and scintillation data to identify three major propagating events following the flares, which could be distinguished from neighbouring recurrent high speed solar wind. The picture that

emerged was of enhancements , both in velocity and in density fluctuation, that were very broad by the time they reached the vicinity of the earth, extending tens of degrees in both latitude and longitude from the flare normal. The comparison of the velocity observed in the disturbed region and the time of flight from the sun, under the assumption that the time of the flare was the start time for the disturbance, indicated very little deceleration for the event, leading Rickett to conclude that the disturbance was driven rather than being a blast wave. This event was also analysed by Kakinuma and Watanabe (1976) who improved the resolution of the data by combining these observation with data from Toyokawa and Cambridge.

By identifying less spectacular, but none the less significant velocity and density fluctuation enhancements, in the IPS measurements Sime (1976) attempted to identify all interplanetary disturbances in 1973 and 1974. Since the data were somewhat noisy, Sime followed the example of Hundhausen (1972) in taking the occurrence of coincident type II and type IV radio bursts to indicate the presence of a propagating disturbance. A fairly high proportion of the events examined led to a detection (33 out of 42), many involving multiple lines of sight so that limits could be put on extent, shape and thickness of the disturbances. Further, by use of repeated observations, an indication of the evolution of many events was built up, showing, in general sense, an initially quite narrow front which gradually broadened as it approached 1AU. Typical broadening is indicated in figure 5, where, for the event of 19, May 1973, the positions of the IPS observation of the disturbance are indicated for the first 2 days after the flare. The front is seen near the flare normal on the first day, and not at wider separations. However, on the second day identification is made at positions less than 1AU from the sun but at much larger angles from the flare normal than on the previous day.
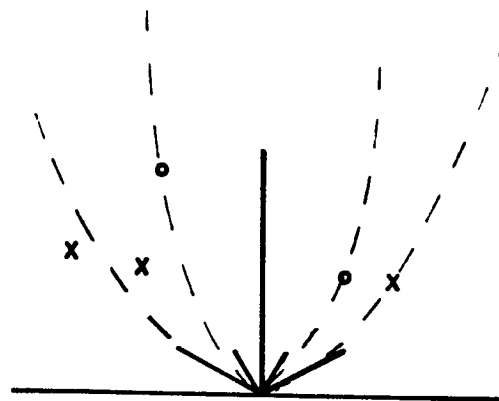

Figure 5: Observations of the interplanetary disturbance following the flare of 19 May 1973 shown relative to the flare site. Identifications are represented on a polar plot with the axes drawn to represent a scale of 1AU. Dots show identifications made between 16 and 20 hours after the flare and crosses show those made between 40 and 54 hours after the flare. A consistent envelope for the front is indicated.

Near the orbit of the earth, the shape of the fronts was quite well described by a spherical shell with radius some fraction of an AU. However, although a generally consistent picture prevailed, variation from event to event in the ambient solar wind, the observing conditions, and presumably in the events themselves prevented an average profile from being built up. As with the results of Rickett, these observations were entirely consistent with the development of the shape of the disturbance as calculated by De Young and Hundhausen (1971), i.e., with the broadening of the disturbance as its radial momentum is lost to the ambient medium until it becomes comparable to the non-radial component. One consequence of this is that the shape of the disturbed front at 1AU is not strongly controlled by the extent or shape of the region over which the ejection from the sun occurred. However, the development of its shape as it travels from the sun does depend on the initial angular extent of the ejection from the corona (De Young and Hundhausen, 1971). IPS, therefore, by providing an outline of that development, should be able to help solve another outstanding problem in coronal physics, the morphology of coronal transients, by inference from their manifestations in the interplanetary medium.

Other investigators have concentrated more on the dynamics of disturbances. Watanabe (1978) has discussed the velocity evolution of the disturbances associated with solar events in March and April 1976. From their velocity measurements, and assuming isotropic expansion of the disturbance, they conclude that the fronts are not well explained by either purely driven or by purely blast waves, but rather a combination of the two mechanisms seems to be required. This may indicate that the disturbances are driven only in the earlier stages of the event.

Other efforts have utilised single line of sight measurements to infer some property of the disturbance. Since they involve essentially a measurement at a single region in space, they do not offer much more than a single *in situ* measurement, except, of course, that they are not restricted to the ecliptic, or to regions $\gtrsim 50$ R_o from the sun. Many depend on the assumption of radial propagation, and some, especially some Faraday rotation observations, may be confused by coronal evolution which would not be classified as transient.

An example of the value of such single line of sight observations has been given by Cane et al.(1982) who utilised observations of Woo and Armstrong (1981) showing the passage of an interplanetary disturbance across their line of sight at about 13 R_o. Although a presumed initiation time for the event at the sun allowed the derivation of a time of flight for the event out to 13 R_o, the subsequent crossing of another line of sight, at 73R_o, permitted a propagation velocity in interplanetary space for the disturbance to be established. Cane et al. (1982) then used this velocity to scale a model density for the interplanetary medium from which they could deduce the shock velocity implied by Type II radio bursts observed on board the ISEE-3 spacecraft. Their final composite velocity profile, comprising data from scintillation, time of flight and radio burst observations spans the range of $\sim 10R_o$ to 1AU. It shows an initially accelerating out to about 30 R_o which is followed by a decreasing velocity proportional to about $r^{-0.8}$. This kind of measurement is especially important since it bridges the gap between interplanetary and solar events, and, in principle, should allow better associations with coronal phenomena to be developed.

One final set of data of particular promise is the 81.5 MHz intensity scintillations reported by Gapper et al., (1982). In these, daily scintillation index data are recorded for some 900 sources covering the entire sky from about -15° to 70° declination. By measuring significant departures from the predicted or mean scintillation indices, these workers can map out regions of the sky which are responsible for enhanced (or indeed depleted) scintillation levels, and which ,by inference, consist of enhanced, or depleted density levels. Large regions of the sky, several hours R.A. by tens of degrees in declination appears to be so affected, both by corotating events and in occasional transient disturbances. Gapper et al. used these maps to distinguish corotating and noncorotating regions of enhanced scintillation, however, since only index data is recorded, propagation velocities for these disturbed regions have to be derived from the fitting of model geometries to the data. Good consistency for the method has been shown, however, in comparison with *in situ* density and velocity measurements. Similar 'all-sky' increases in scintillation indices at large elongations have been reported by Erskine et al. (1978) in coincidence with proton density increases near the earth. In this case, however, the scintillation signal is interpreted as arising near the earth and does not show the expected signature of structures rotating towards the earth. Jackson (1981) has examined the 73.8 MHz data from UCSD for the same effects, but finds no general east-west asymmetry in the days of widespread scintillation enhancement that he observes and concludes that the effects are near earth phenomena rather than interplanetary and, consistently, finds no obvious solar or coronal counterpart. These latter two data sets perhaps involve stronger events intrinsically since they are in general taken from the anti-sun hemisphere, and are

detected (in Jackson's (1981) case) as increased SNR or radical changes in the inferred scale sizes (Coles and Kaufman, 1978) of the scintillation pattern.

Thus, the overall picture which emerges from these attempts to characterize propagating interplanetary disturbances is one of an initially accelerated front with restricted angular width. Once the front is some fraction of an AU from the sun, the acceleration ceases and the event coasts outwards with decreasing radial velocity and increasing angular width. Eventually, once the front is close to 1AU, it covers several tens of degrees in latitude and longitude, and may be fairly well described as lying on a sphere of radius almost 1AU.

Summary

IPS observations exist in a form and to an extent to be of value in a number of current questions in coronal and interplanetary physics. For brevity, this article has emphasized only three topics.

A global view of the solar wind velocity has been derived and its evolution throughout the last solar cycle followed. The large scale relationship to coronal structure has been established. Further, a reasonably consistent, but not yet fully interpreted, view of the flow at heights of $\lesssim 30 \, R_o$ has been developed, and further work in this area holds promise for the understanding of coronal heating and acceleration.

Although the working hypothesis that Δn is proportional to n is still useful, a comparison of scintillation observations with *in situ* spacecraft velocity and density data reveals that the variations to which intensity scintillations are most sensitive peak where the positive velocity gradient is highest. This result, established with ecliptic solar wind dominated by corotating structures remains to be verified for transient increases, but should be kept in mind when positional information is sought from IPS observations.

The potential for sensing the morphology of propagating disturbances associated with solar eruptive phenomena has been demonstrated. The simple approach of testing shape and velocity for these events to establish whether they are driven or not has yielded mixed results indicating both blast and driven waves. However, a large extent at 1AU, in both latitude and longitude is indicated quite clearly. The possibility of detecting frontal passages with observations at $< 50 \, R_o$ and the prospect of full sky snapshots of transiently disturbed regions is exciting and should lead to a better understanding of the processes of importance.

463

References

Ananthakrishnan, S., W. A. Coles and J. J. Kaufman, Microturbulence in solar wind streams, *J. Geophys. Res.*, *85*, 6025, 1980.

Armstrong, J. W., and W. A. Coles, Analysis of three station interplanetary scintillations, *J. Geophys. Res.*, *77*, 4602, 1972.

Armstrong, J. W., W. A. Coles, J. K. Harmon, S. Maagoe, B. J. Rickett and D. G. Sime, Radio scintillation measurements of the solar wind following the flares of August 1972, *World Data Center A, Report UAG-28*, 1973

Armstrong, J. W., and R. Woo, Solar wind motion within 30 R_o; Spacecraft radio scintillation observations, *Astron. Astrophys.*, *103*, 415, 1981.

Athay, R. G., and O. R. White, Chromospheric and coronal heating by sound waves, *Astrophys. J.*, *226*, 1135, 1978.

Bird, M. K., Coronal investigations with occulted spacecraft signals, *Sp. Sci. Rev.*, *33*, 99, 1982.

Brandt, J. C., R. C. Harrington, and R. G. Roosen, Interplanetary gas XX: Does the radial solar wind speed increase with latitude?, *Astrophys. J.*, *196*, 877, 1975.

Burlaga, L. F., L. Klein, N. R. Sheeley, Jr., D. J. Michels, R. A. Howard, M. J. Koomen, R. Schwenn and H. Rosenbauer, A magnetic cloud and a coronal mass ejection, *Geophys. Res. Lett.*, *9*, 1317, 1982.

Cane, H. V., R. G. Stone, and R. Woo, Velocity of the shock generated by a large East limb flare on August, 18, 1979, *Geophys. Res. Let.*, *9*, 897, 1982.

Chao, J. K. and R. P. Lepping, A correlative study of ssc's (sic), interplanetary shocks, and solar activity, *J. Geophys. Res.*, *79*, 1799, 1974.

Coles, W. A., Interplanetary scintillations, *Space Sci. Rev.*, *21*, 411, 1978.

Coles, W. A., and S. Maagoe, Solar wind velocity from IPS observations, *J. Geophys. Res.*, *77*, 5622, 1972.

Coles, W. A. and B. J. Rickett, IPS observations of the solar wind speed out of the ecliptic, *J. Geophys. Res.*, *81*, 4797, 1976.

Coles, W. A. and J. J. Kaufman, Solar wind velocity estimation from multistation IPS, *Radio Sci.*, *13*, 591, 1978.

Coles, W. A., B. J. Rickett and V. H. Rumsey, Interplanetary scintillations, in *Solar Wind Three*, ed. C. T. Russell, U. C. L. A., 1974.

Coles, W. A., B. J. Rickett, and S. L. Scott, Scintillation observations near the sun, in *A Close-Up of the Sun*, 1978a.

464

Coles, W. A., J. K. Harmon, A. J. Lazarus, and J. D. Sullivan, Comparison of 74 MHz interplanetary scintillation and Imp-7 observations of the solar wind during 1973, *J. Geophys. Res., 83*, 3337, 1978b.

Coles, W. A., B. J. Rickett, V. H. Rumsey, J. J. Kaufman, D. G. Turley, S. Ananthakrishnan, J. W. Armstrong, J. K. Harmon, S. L. Scott and D. G. Sime, Solar cycle changes in the polar solar wind, *Nature, 286*, 239, 1980.

Dennison, M. D., and A. Hewish The solar wind outside the plane of the ecliptic, *Nature, 213*, 343, 1967.

De Young, D. S., and A. J. Hundhausen, Two-dimensional simulation of flare-associated disturbances in the solar wind, *J. Geophys. Res., 76*, 2245, 1971.

Ekers , R. D., and L. T. Little, The motion of the solar wind close to the sun, *Astron. Astrophys., 10*, 310, 1971.

Erskine, F. T., W. M. Cronyn, S. D. Shawhan, E. C. Roelof and B. L. Gotwols, Interplanetary scintillation at large elongation angles: Response to solar wind density structure, *J. Geophys. Res., 83*, 4153, 1978.

Feldman, W. C., J. R. Asbridge, S. J. Bame and J. T. Gosling, Long-term variations of selected solar wind properties: Imp 6, 7, and 8 results, *J. Geophys. Res., 83*, 2177, 1978.

Gapper G. R., A. Hewish, A. Purvis, and P. Duffet-Smith, Observing interplanetary disturbances from the ground, *Nature, 296*, 633, 1982.

Gosling, J. T., E. Hildner, R. M. MacQueen, R. H. Munro, A. I. Poland, and C. L. Ross, Direct observations of a flare related coronal and solar wind disturbance, *Solar Physics, 40*, 439, 1975.

Gosling, J. T., J. R. Asbridge and S. J. Bame, An unusual aspect of solar wind speed variations during solar cycle 20, *J. Geophys. Res., 82*, 3311, 1977.

Harmon, J. K., Scintillation studies of density microstructure in the solar wind plasma, Ph.D. Thesis, Univ.of Calif., San Diego, La Jolla, 1975.

Harmon, J. K. and W. A. Coles, Spectral broadening of planetary radar signals by the solar wind, *Astrophys. J.*, in press, 1983.

Hewish, A., P. F. Scott and D. Wills, Interplanetary scintillation of small diameter radiosources, *Nature, 203*, 1214, 1964.

Hewish, A., and M. D. Symonds, Radio investigation of the solar plasma, *Plan. Sp. Sci., 17*, 313, 1969.

Hirshberg, J., The transport of flare plasma from the sun to the earth, *Planet. Space. Sci., 16*, 309, 1968.

Holzer, T. E., and E. Leer, Conductive solar wind models in rapidly diverging flow geometries, *J.Geophys. Res.*, *85*, 4665, 1980.

Hundhausen, A. J., Interplanetary shock waves and the structure of solar wind disturbances, in *Solar Wind*, eds. C. P. Sonnet, P.J.Coleman Jr., and J. M. Wilcox, NASA, SP-308, 1972.

Hundhausen, A. J., An interplanetary view of coronal holes, in *Coronal Holes and High Speed Wind Streams*, ed. J. Zirker, Colorado Assoc. Univ. Press, 1977.

Hundhausen, A. J., Solar wind spatial structure: The meaning of latitude gradients in observations averaged over solar longitude, *J. Geophys. Res.*, *83*, 4186, 1978.

Hundhausen, A. J., R. T. Hansen and S. F. Hansen, Coronal evolution during the sunspot cycle: Coronal holes observed with the Mauna Loa K-coronameters, *J. Geophys. Res.*, *86*, 2079, 1981.

Jackson, B. V., All sky days and their solar cycle dependence, preprint, 1981.

James, J. C., Radar Echoes from the sun, *Trans. IEEE. Ant. Prop. AP-12*, 876, 1964.

Kakinuma, T., and T. Watanabe, Interplanetary scintillation of radio sources during August 1972, *Sp. Sci. Rev.*, *19*, 611, 1976.

Klein, L. W., and L. F. Burlaga, Magnetic clouds at 1 AU, *J. Geophys. Res.*, *87*, 613, 1982.

Leer, E., T. E. Holzer and T. Fla, Acceleration of the solar wind, *Sp. Sci. Rev.*, *33*, 161,1982.

MacQueen, R. M., Coronal transients: A summary, *Phil. Trans. R. Soc. Lond. A*, *297*, 605, 1980.

Rhodes, E. J. and E. J. Smith, Evidence of a large scale gradient in the solar wind velocity, *J. Geophys. Res.*, *81*, 2123, 1976a.

Rhodes, E. J. and E. J. Smith, Further evidence of a latitude gradient in the solar wind velocity, *J. Geophys. Res.*, *81*, 5833, 1976b.

Rickett, B. J., Disturbances in the solar wind from IPS measurements in August 1972. *Solar Phys.*, *43*, 237, 1975.

Schwenn, R., The 'average' solar wind in the inner heliosphere: structures and slow variations, This Proceedings.

Scott, S. L., Density spectrum and velocity of the solar wind inferred from scintillation observations, Ph.D. Thesis, Univ.of Calif., San Diego, La Jolla, 1978.

Sheeley, Jr., N. R., R. A. Howard, M. J. Koomen, D. J. Michels, R. Schwenn, K.-H. Muehlhauser and H. Rosenbauer, Association between coronal mass ejections and interplanetary shocks, this proceedings, 1983.

Sime, D. G., Structure of the solar wind inferred from interplanetary scintillations, Ph.D. Thesis, Univ.of Calif., San Diego, La Jolla, 1976.

Sime, D. G. and B. J. Rickett, The latitude and longitude structure of the solar wind speed from IPS observations, *J. Geophys. Res.*, *83*, 5757, 1978.

Sime, D. G., Indirect measurements of the solar wind speed out of the ecliptic, *EOS*, *60*, 93, 1979.

Taylor, H. E., Sudden commenscment associated discontinuities in the interplanetary magnetic field observed by IMP 3, *Solar Physics*, *6*, 320, 1969.

Unti, T., M. Neugebauer and B. E. Goldstein, Direct measurements of solar wind fluctuations between 0.0048 and 13.3 Hz, *Astrophys. J.*, *180*, 591, 1973.

Watanabe, T., IPS observations of flare-generated interplanetary shock waves during the second STIP interval (March 15 - May 15, 1976), *Proc. Res. Inst. Atmos., Nagoya Univ.*, *25*, 19, 1978.

Withbroe, G. L., J. L. Kohl, H. Weiser and R. H. Munro, Probing the solar wind acceleration region using spectroscopic techniques, *Sp. Sci. Rev.*, *33*, 17, 1982.

Woo, R., Multifrequency techniques for studying interplanetary scintillations, *Astrophys. J.*, *201*, 238, 1975.

Woo, R., Measuring solar wind velocity with spacecraft phase scintillations, *Nature*, *266*, 574, 1977.

Woo, R., and J. W. Armstrong, Spacecraft radio scattering observations of the power spectrum of electron density fluctuations in the solar wind, *J. Geophys. Res.*,*84*, 7288, 1979.

Woo, R., and J. W. Armstrong, Measurements of a solar flare-generated shock wave at $13.1R_O$, *Nature*, *292*, 608, 1981.

Woo, R., and J. W. Armstrong, *Sp. Sci. Rev.*, in press, 1983.

Zhao, X-P., and A. J. Hundhausen, Organization of solar wind plasma properties in a tilted, heliomagnetic coordinate system, *J. Geophys. Res.*, *86*, 5423, 1981.

Zhao, X-P., and A. J. Hundhausen, Spatial structure of solar wind in 1976, *J. Geophys. Res.*, *88*, 451, 1983.

Zirker, J., Coronal holes and high speed wind streams, Colorado Assoc. Univ. Press., 1977.

RADIO EVIDENCE FOR INTERPLANETARY STREAMERS
IN THE RANGE 10-170 SOLAR RADII

J. Fainberg, J.-L. Bougeret (*) and R.G. Stone
Laboratory for Extraterrestrial Physics,
NASA/Goddard Space Flight Center,
Greenbelt MD 20771, U.S.A.

(*) NAS/NRC Postdoctoral Research Associate on leave from the
Laboratory Associated with CNRS # 264, Observatoire de Paris, France.

ABSTRACT

Type III radio storms are observed by the radio experiment on board ISEE-3 out to 0.5-0.8 AU from the Sun, at a rate of 2 to 3 storms per solar rotation near solar maximum. They correlate with the type I and type III radio storms observed at higher frequencies, originating closer to the Sun. They are associated with an almost continuous injection of suprathermal electrons into the interplanetary medium. Some of the properties of the regions where the particles propagate are discussed, using the radio emission as a tracer.

Storms of type III solar radio bursts are frequently observed by the radio instrument on board ISEE-3. This experiment (Knoll et al., 1978) monitors the solar radio phenomena in the interplanetary medium over the height range from about 0.05 AU (10 solar radii) to 1 AU. The interplanetary type III radio storms (hereafter IP storms) consist of many thousands of type III radio bursts emitted per day. They last from 1 to 12 days. About 100 IP storms have been observed during the first four years of observation of ISEE-3, and up to 3 storms were observed per solar rotation near solar maximum. The IP storms are related to other solar radio emissions at all levels of the corona.

Figure 1 shows the intensity profiles at several frequencies during a typical interval. Each point is a 30 minute average. An IP storm is clearly seen from May 31 to June 6, as well as the formation of another storm near June 10. In this case we see a progressive delay in the peak of the storm, probably due to directivity effects.

Figure 2 shows 16.5 months of data from ISEE-3 along with ground based solar data which describe solar activity originating at much lower coronal levels. It is clear that radio emissions from individual storms can be followed through all ranges of elevations, from tens of solar radii, at ISEE-3 frequencies, down to well below 2 solar radii (heliocentric). The IP storms represent the interplanetary extension of solar active regions.

The ISEE-3 radio instrument has the capability of accurately determining the arrival direction (solar elongation) of the storm radio sources in the ecliptic plane. Figure 3 shows the solar elongation measured at a variety of frequencies during a typical IP storm. For each frequency we can see the East to West motion of the storm region as it crosses the line-of-sight to the Sun. The different
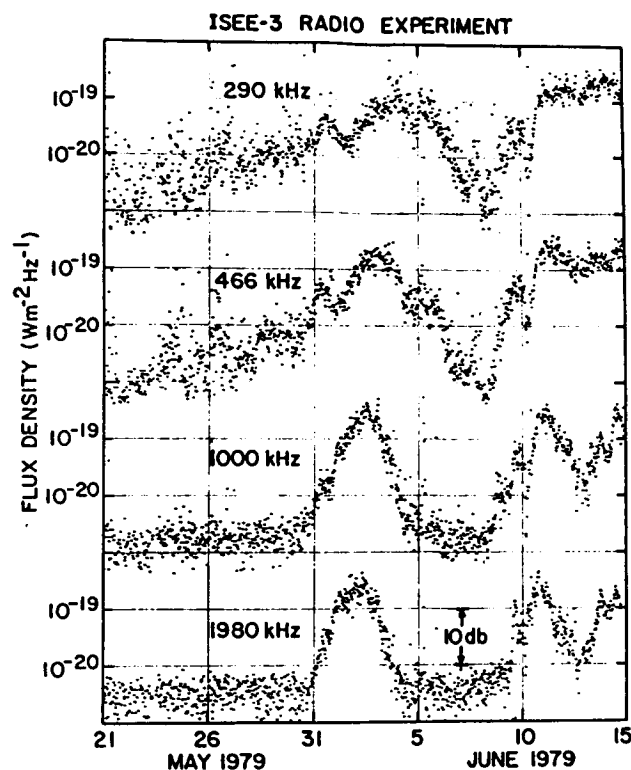
ISEE-3 RADIO EXPERIMENT

Figure 1 - Typical IP storm. Each point is a 30 minute average and may hence represent many individual storm bursts. The flux increase that precedes the storm at the lower frequencies is attributed to earth's radiation (TKR).
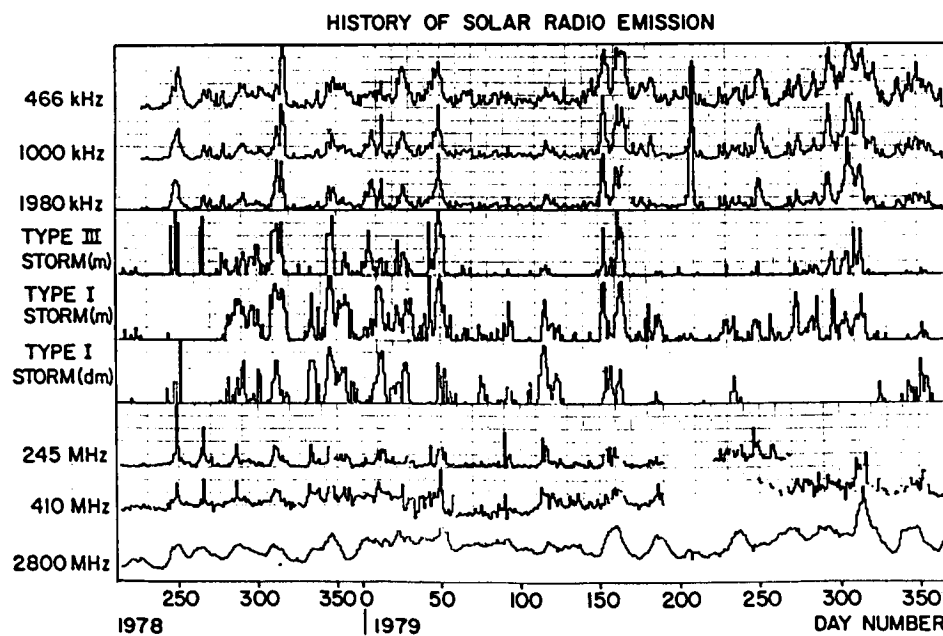
HISTORY OF SOLAR RADIO EMISSION

Figure 2 - Time history of a few ground-observed radio fluxes, of a few indices describing the radio storm activity in the lower corona and of a few ISEE-3 radio fluxes. Each point is a daily average (after Bougeret et al., 1982a).

470

slopes are due to a foreshortening effect. The sources which are closer to the observer (at lower frequencies) cross the line-of-sight with a higher angular velocity than the distant ones (at higher frequencies). This geometrical effect allows us to locate the distance from the spacecraft to the emission region with very few assumptions. In other words, we are able to determine the emission levels directly from the measurement of the slopes of the solar elongation profiles. In addition, we observe that the time of central meridian crossing is later at lower frequencies. This progressive delay is a direct measurement of the time it takes the solar wind to progress between levels we determined from the slope analysis. These results are summarized for one IP storm in Figure 4. Each point results from one frequency of observation. We can see that the data are consistent with an average solar wind speed of about 250 km s^{-1} from 25 to 125 solar radii. Since we are using all data within one or two days around central meridian passage, the earth moves only by a few degrees and we are viewing the same solar wind portion as it moves outward.

In situ observations show that within a few days of the arrival of this storm at 1 AU the velocity ranges from 300 to 400 km s^{-1}. This apparent discrepancy may be due to several reasons. (i) The storm analysis yields a solar wind speed of 250 km s^{-1} in the range 25 to 125 solar radii only; the solar wind may have accelerated between 125 and 215 solar radii. For instance fitting to the 4 last points in Figure 4 implies a higher velocity than is measured otherwise. (ii) This technique averages the solar wind speed over the radio source region and tracks structures that may extend out of the ecliptic plane, thus contributing to speeds different from those observed at 1 AU.

The fluctuations of the observations around the model shown in Figure 4 may suggest a kink or irregularity in the overall magnetic field. This particular storm is one for which these undulations are the most conspicuous. However, we cannot exclude that this is due to large scale refraction and scattering of radio waves (Steinberg, 1972) and at this point we prefer to consider only the average behavior shown by the curve in Figure 4 as significant.

Figure 5 shows the emission frequency versus the heliocentric distance. A slope of -1 on this frequency scale corresponds to -2 in electron density. The heavy black line are levels deduced from the first radio storm observed by RAE-1 (Fainberg and Stone, 1970a,b; 1971). These results were derived by a completely separate technique –from an analysis of the centre-to-limb variation of drift rates. The levels studied by RAE-1 were from 12 to 40 solar radii. The ISEE-3 data from 4 storms are superimposed and show excellent agreement. We also show a four year average of in-situ plasma density measurement from HELIOS (Bougeret, King, and Schwenn, 1983). We see that the radiation in the storm regions is very likely the harmonic of the plasma frequency –a result discussed often in the past. In addition the fall-off is generally faster than R^{-2}. Each storm on this log-log plot is roughly a straight line and can be described by two parameters: a coefficient and an exponent (slope of the emission level scale). Figure 6 shows the results of 16 storms, with each storm described by a value of k (the log of the coefficient) and a value of the exponent alpha. There seems to be a relation between the value of k and alpha. The higher the enhancement the more rapid the fall-off. The implication of these results is that by about 60-100 solar radii the enhanced density regions merge with the average solar wind densities. It is likely that these structures will not be visible at 1 AU.

We have seen that the IP storms are associated with density enhancements in

ISEE-3 RADIO EXPERIMENT

Figure 3 - Time variation of the solar elongation at six frequencies for the storm shown in Figure 1. The source angle is corrected for the Galactic background contribution (after Bougeret et al., 1982b).
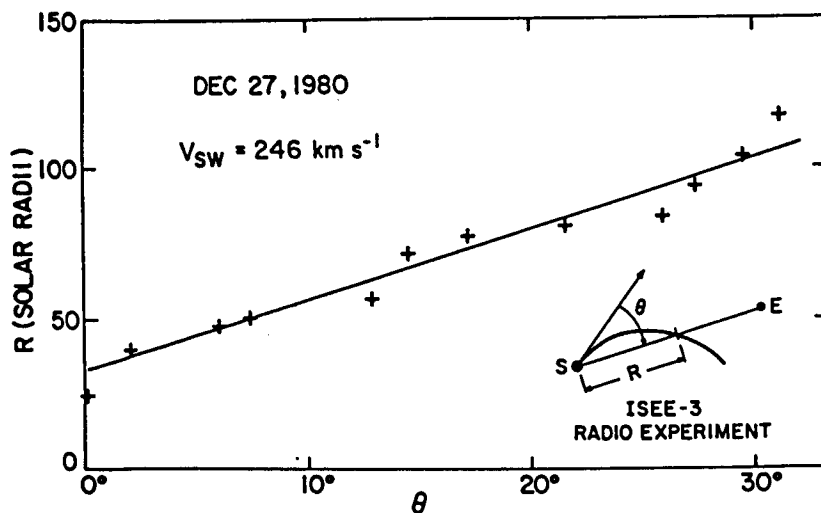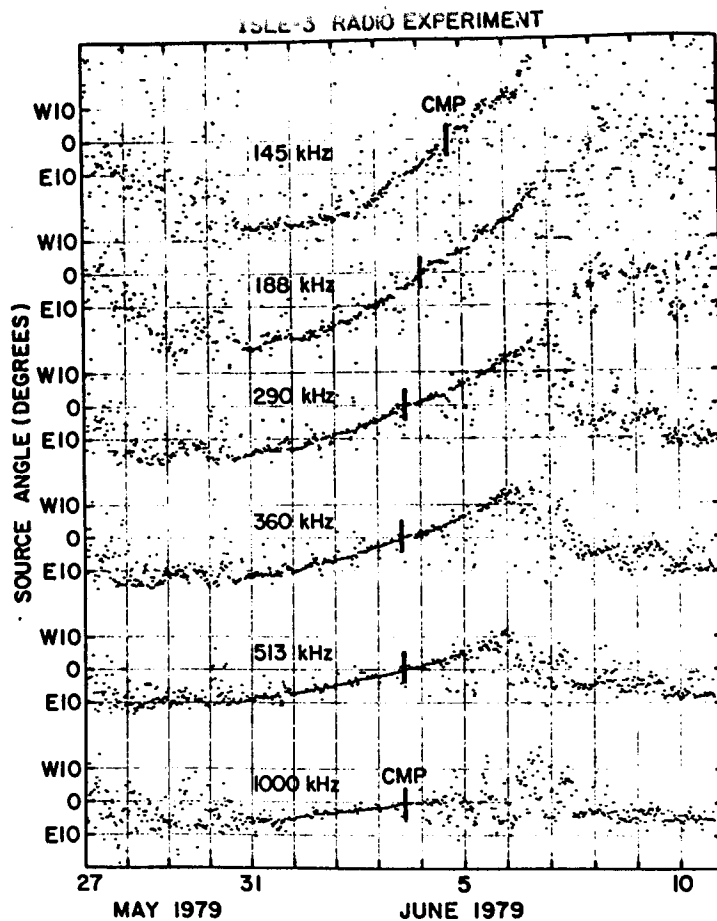

Figure 4 - Outward movement of the IP storm region in a fixed Sun-Earth coordinate system.

Figure 5 - Emission levels of 4 IP storms observed by ISEE-3. The RAE model is also shown (heavy line), as well as observations of type III and type I storms at higher frequencies and in-situ measurements by HELIOS 1 and 2 (after Bougeret et al., 1982b).
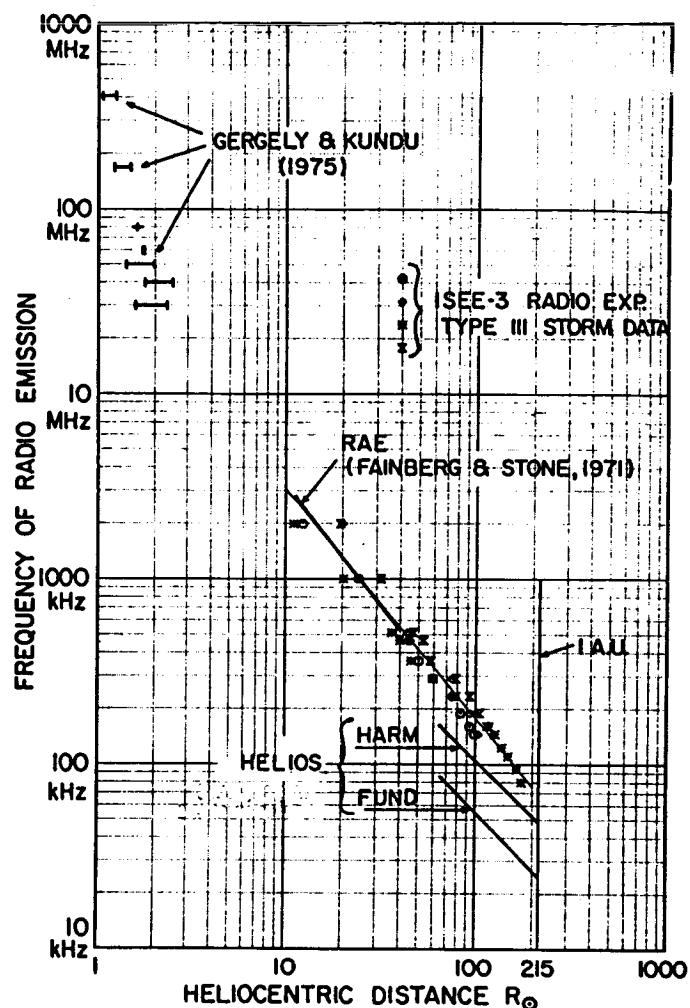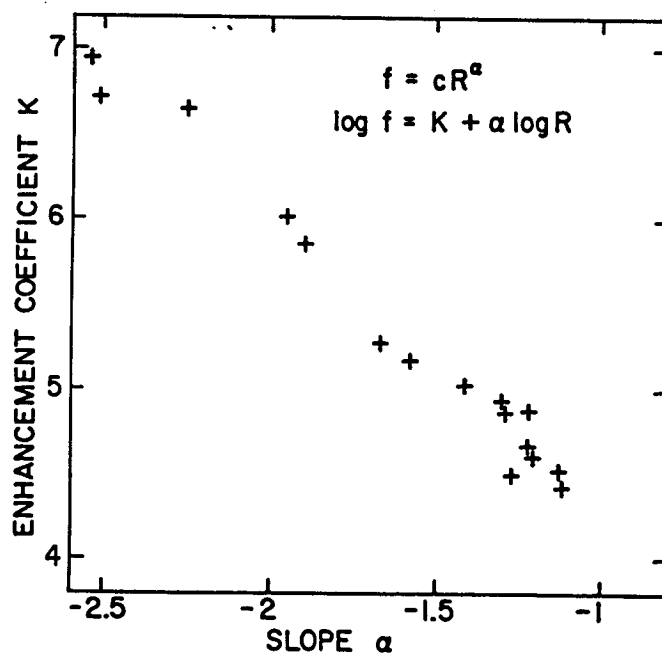

Figure 6 - Diagram of log k vs. alpha for 16 IP storms. The frequency scale of each IP storm was fitted to :
log f = log k + (alpha) log R .
A slope of -1 in this frequency scale corresponds to -2 in density.

473

the interplanetary medium. We have also shown (Figure 2) that they correlate with solar active regions and especially with the type I and type III storm activity in the lower corona (Bougeret et al., 1982a). Type III bursts are produced by packets of energetic electrons which propagate along open field lines. There is some direct evidence that they are associated with white light streamers (Kundu et al., 1983). Hence we suggest that the IP storms trace the extension of streamers into the interplanetary medium.

Our findings can be summarized as follows. The IP storm radiation occurs in regions of enhanced density at levels of 10-170 solar radii (0.05-0.8 AU). These regions are most likely the extension of streamers into the interplanetary medium. The density in these enhancements falls off faster than R^{-2}. Regions of higher density fall off faster, so that there is apparently a merging to the average solar wind density by about 60-100 solar radii. We have also measured the velocity of the solar wind in these regions, and our technique actually follows the same region of solar wind plasma during its transit outward. Finally, in cooperation with R.P. Lin (University of California experiment on-board ISEE-3), we find that these IP storms are usually associated with fluxes of low energy electrons observed at 1 AU.

References

Bougeret, J.L., Fainberg, J. and Stone, R.G., Interplanetary Radio Storms: 1 - Extension of Solar Active Regions through the Interplanetary Medium, Technical Memorandum 84940, NASA/GSFC, (submitted to Astron.Astrophys.), 1982a.

Bougeret, J.L., Fainberg, J. and Stone, R.G., Interplanetary Radio Storms: 2 - Emission Levels and Solar Wind Speed in the Range 0.05-0.8 AU, Technical Memorandum 84946, NASA/GSFC, (submitted to Astron.Astrophys.), 1982b.

Bougeret, J.L., King, J.H., and Schwenn, R., Solar Radio Burst and In Situ Determination of Interplanetary Electron Density, in preparation, 1983.

Fainberg, J. and Stone, R.G., Type III Solar Radio Burst Storms Observed at Low Frequencies: 1 - Storm Morphology, Solar Phys. 15, 222, 1970a.

Fainberg, J. and Stone, R.G., Type III Solar Radio Burst Storms Observed at Low Frequencies: 2 - Average Exciter Speed, Solar Phys. 15, 433, 1970b.

Fainberg, J. and Stone, R.G., Type III Solar Radio Burst Storms Observed at Low Frequencies: 3 - Streamer Density, Inhomogeneities, and Solar Wind Speed, Solar Phys. 17, 392, 1971.

Gergely, T.E. and Kundu, M.R., Decameter Storm Radiation, II, Solar Phys. 41, 163, 1975.

Knoll, R., Epstein, G., Hoang, S., Huntzinger, G., Steinberg, J.L., Fainberg, J., Grena, F., Mosier, S.R. and Stone, R.G., The 3-Dimensional Radio Mapping Experiment (SBH) on ISEE-C, IEEE GE-16, 199, 1978.

Kundu, M.R., Gergely, T.E., Turner, P.J., and Howard, R.A., Direct Evidence of Type III electron streams prpoagating in coronal streamers, Astrophys. J. Letters, in press, 1983.

Steinberg, J.L., Coronal Scattering of Radiobursts at Hectometer and Kilometer Wavelengths, Astron. Astrophys. 18, 382, 1972.

Stone, R.G. and Fainberg J., Solar Radio Bursts at Kilometer Wavelengths, High Energy Phenomena on the Sun, eds. R. Ramaty and R.G. Stone, NASA SP-342, 519, 1973.

SOLAR WIND DISTURBANCES IN THE OUTER HELIOSPHERE
CAUSED BY SUCCESSIVE SOLAR FLARES FROM THE SAME ACTIVE REGION

S.-I. Akasofu
Geophysical Institute
University of Alaska
Fairbanks, Alaska 99701

and

K. Hakamada
Department of Engineering
Chubu Institute of Technology
1200 Matsumoto-cho
Kasugai-shi
Aichi-ken 487
Japan

ABSTRACT

Solar wind disturbances caused by successive flares from the same active region are traced to about 20 au, using the modeling method developed by Hakamada and Akasofu (1982). It is shown that the flare-generated shock waves coalesce with the co-rotating interaction region of the interplanetary magnetic field, resulting in a large-scale magnetic field structure in the outer heliosphere. Such a structure may have considerable effects on the propagation of galactic cosmic rays.

Introduction

During the last decade, a considerable progress has been made in understanding the solar wind flow and the propagation of solar wind disturbances in the heliosphere (Shea et. al., 1977; Dryer and Steinolfson, 1976; Dryer and Tandberg-Hanssen, 1980). A somewhat different approach from the standard hydrodynamic and MHD methods was considered by Hakamada and Akasofu (1982) who devised a method analogous to an aerodynamic technique in simulating some aspects of the disturbed solar wind with a fair accuracy. They construct first a steady state pattern for the so-called 'two-sector' or 'two-stream' situation. For this purpose, they assume that the distribution of the solar wind speed on the source surface (a spherical surface of radius of 2.5 R_o) has the minimum speed (V=300 km/sec) along the heliomagnetic equator which is assumed to be inclined by 20° with respect to the heliographic equator; the speed is assumed to increase toward higher latitudes in both the northern and southern hemispheres. The resulting magnetic field configuration in the equatorial plane is the well-known co-rotating structure which consists of two 'spiral arms' (the corotating interaction region), as faster winds interact with slower winds.

Propagating Flare Disturbances

(a)   Two successive flares from the same region

Effects of solar flares are introduced in this co-rotating structure by adding a high speed flow from a circular area, centered around a solar flare, on

the source surface. In the circular area, the flow speed is assumed to have a Gaussian distribution of the 'half-width' σ; the flow speed V_F at the center of the circular area is assumed to vary in time as $V_F = V_{Fmax} \cdot t \cdot e^{-(t/\tau)}$; thus, a flare is characterized by six parameters, the latitude (θ), longitude (ϕ) and the onset time (T_F) of a flare, the maximum flow V_{Fmax} (km/sec) at the center of the circular area of its size parameterized by $\sigma(^\circ)$, and the time variation of V_{Fmax} by τ(hr). For the method of introducing effects of a solar flare, see also Hakamada and Akasofu (1982). The first flare is located at the magnetic equator ($\theta = 0^\circ$) and the longitude $\phi = 0^\circ$, namely on the crossing point of the positive x-axis through the source surface. This particular flare is parameterized by the maximum wind speed V_{Fmax} = 800 km/sec, τ = 12 hrs and $\sigma = 60^\circ$.

The second flare is introduced 48 hours (2 days) after the first flare. It is assumed that the same active region is responsible for both flares, which have rotated by $\phi = 28.3^\circ$ from the time of the first flare. The second flare is characterized by a faster flow V_{Fmax} = 1000 km/sec, the same growth-decay curve (τ = 12 hrs) and a narrower extent ($\sigma = 20^\circ$) than the first one.

Figure 1a shows the disturbance patterns (< 5 au) in the ecliptic plane at T=0, 1.5, 3.5 and 7.0 days after the onset of the first flare. In this particular example, the shock wave associated with the second flare caught up with the first shock wave on about the 6th day. Note that the spiral structure continued to rotate, while a part of the inner part of the spiral structure was destroyed by the first shock. On the 8th day both shocks reached one of the spiral arms. Behind the shocks, a new spiral arm begins to reform rapidly.

Figure 1b shows the disturbance pattern within a radial distance < 25 au, T = 12, 24, 36 and 48 days after the onset of the first flare. On the 24th day, both shocks reached the second co-rotating structure. Meanwhile, the new spiral arm is clearly established behind both shocks. As the shocks propagate further, the inner spiral structure reforms rapidly and expands outward. On the 48th day, both shocks reach the third co-rotating structure, forming a complex magnetic field structure in the outer heliosphere.

Note that from the 12th day to the 48th day, the co-rotating structure has rotated ~ 1 1/3 times. If there is no solar flare disturbance, two spiral arms pass by regularly at any fixed point in the figure every 27 days, causing two distinct increases of the solar wind speed and the magnetic field magnitude. However, the shock waves caused by the solar flares disturb considerably such a regular pattern. In fact, on the 48th day, two co-rotating structures and the two shocks pile up at a radial distance of about 17 au and it is no longer possible to identify individual co-rotating structures and the shocks.

(b) Six successive flares from the same active region

In this particular example, we assume an extremely active region which produces six successive flares in a period of 10 days. The six flares are parameterized as follows:

Flare 1   T = 0, $\phi = 0^\circ$, $\theta = 0^\circ$
           V_{Fmax} = 800 km/sec, τ = 12 hrs, $\sigma = 60^\circ$

Flare 2   T = 2.0 days, $\phi = 28.3^\circ$, $\theta = 0^\circ$
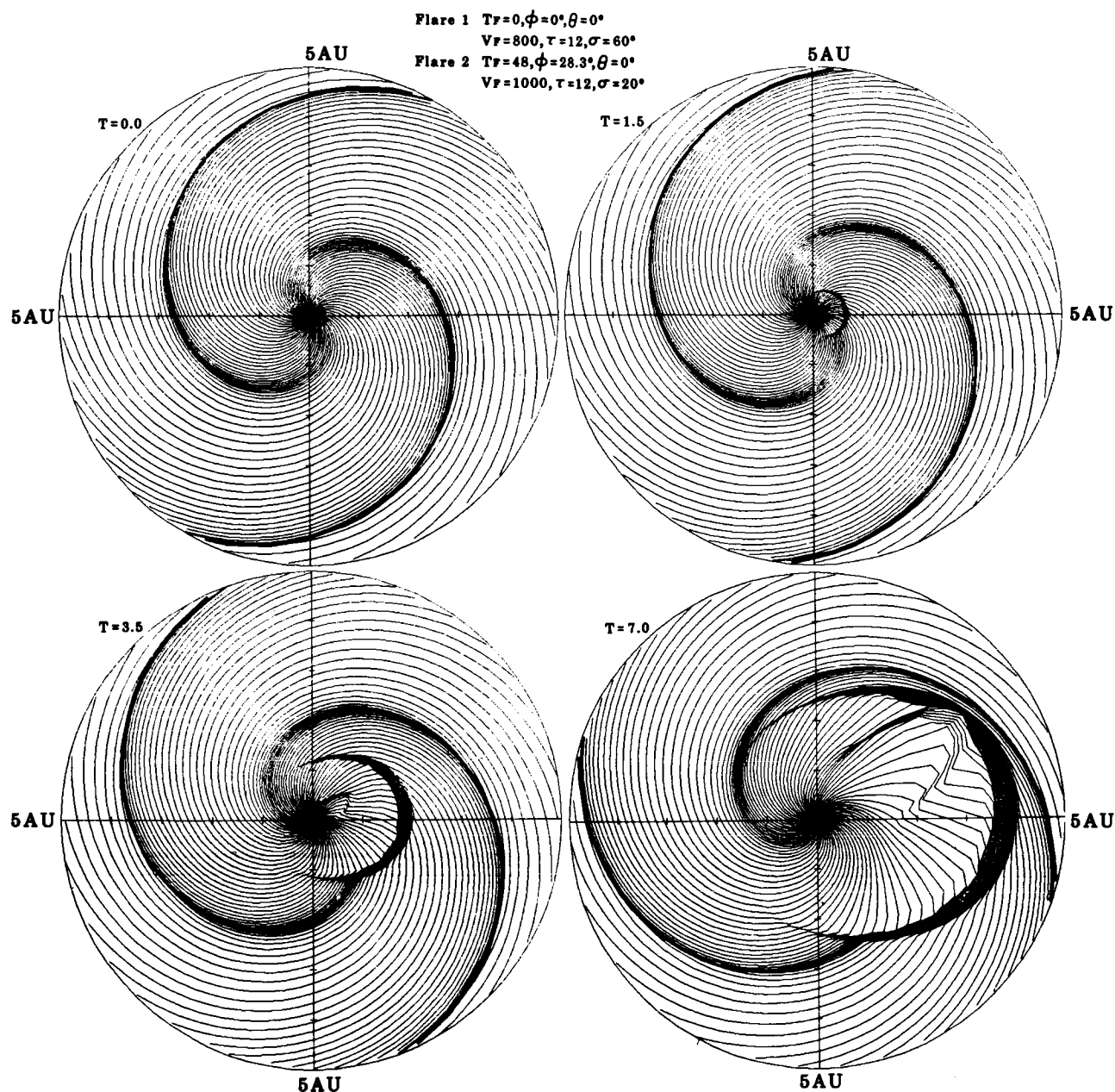 V_{Fmax} = 1000 km/sec, τ = 12 hrs, $\sigma = 20^\circ$

Figure 1a. Solar wind disturbances caused by two successive flares in the ecliptic plane, separated by 48 hours, from the same active region. The figure shows the propagating structure at T=0 (onset), 1.5, 3.5 and 7.0 days after the onset of the first flare. The outer limit of each circular area is at 5 au.
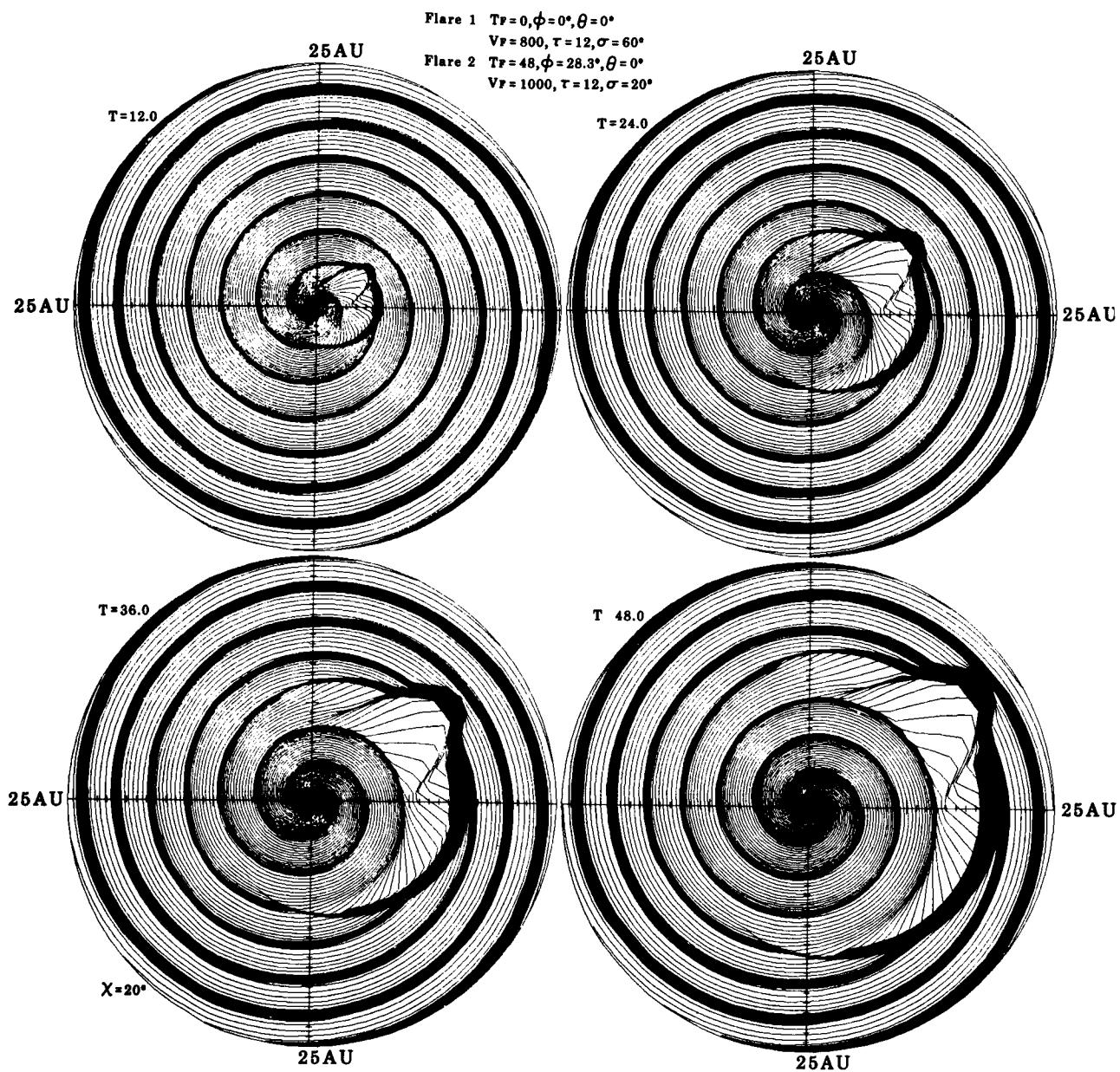
Flare 1 $T_F = 0, \phi = 0°, \theta = 0°$
 $V_F = 800, \tau = 12, \sigma = 60°$
Flare 2 $T_F = 48, \phi = 28.3°, \theta = 0°$
 $V_F = 1000, \tau = 12, \sigma = 20°$

Figure 1b. Continuation of Figure 1a, showing the propagating structure at T = 12, 24, 36 and 48 days. The outer limit of each circular area is at 25 au.

478

Flare 3   T = 4 days, φ = 56.7°, θ = 0°

           V_{Fmax} = 800 km/sec, τ = 12 hrs, σ = 60°

Figure 2 shows the propagating disturbance pattern at T=7, 10, 17, 15, 19 and 25 days after the onset of the first flare. One can see that all the shock waves coalesce with the spiral patterns, forming an extensive magnetic field structure. It is quite likely that such a structure will have considerable effects on the propagation of galactic cosmic rays in the outer heliosphere.

References

Dryer, M. and R. S. Steinolfson, MHD solution of interplanetary disturbances generated by simulated velocity perturbations, J. Geophys. Res., 81, 5413, 1976.

Dryer, M. and E. Tandberg-Hanssen (ed), Solar and Interplanetary Dynamics, IAO Symposium No. 91, D. Reidel Pub. Co., 1980.

Hakamada, K. and S.-I. Akasofu, Simulation of three-dimensional solar wind disturbances and resulting geomagnetic storms, Space Sci. Rev. 31, 3, 1982.

Shea, M. A., D. F. Smart and S. T. Wu (ed), Study of Traveling Interplanetary Phenomena, 1977, D. Reidel Pub. Co., Dordrecht-Holland, 1977.
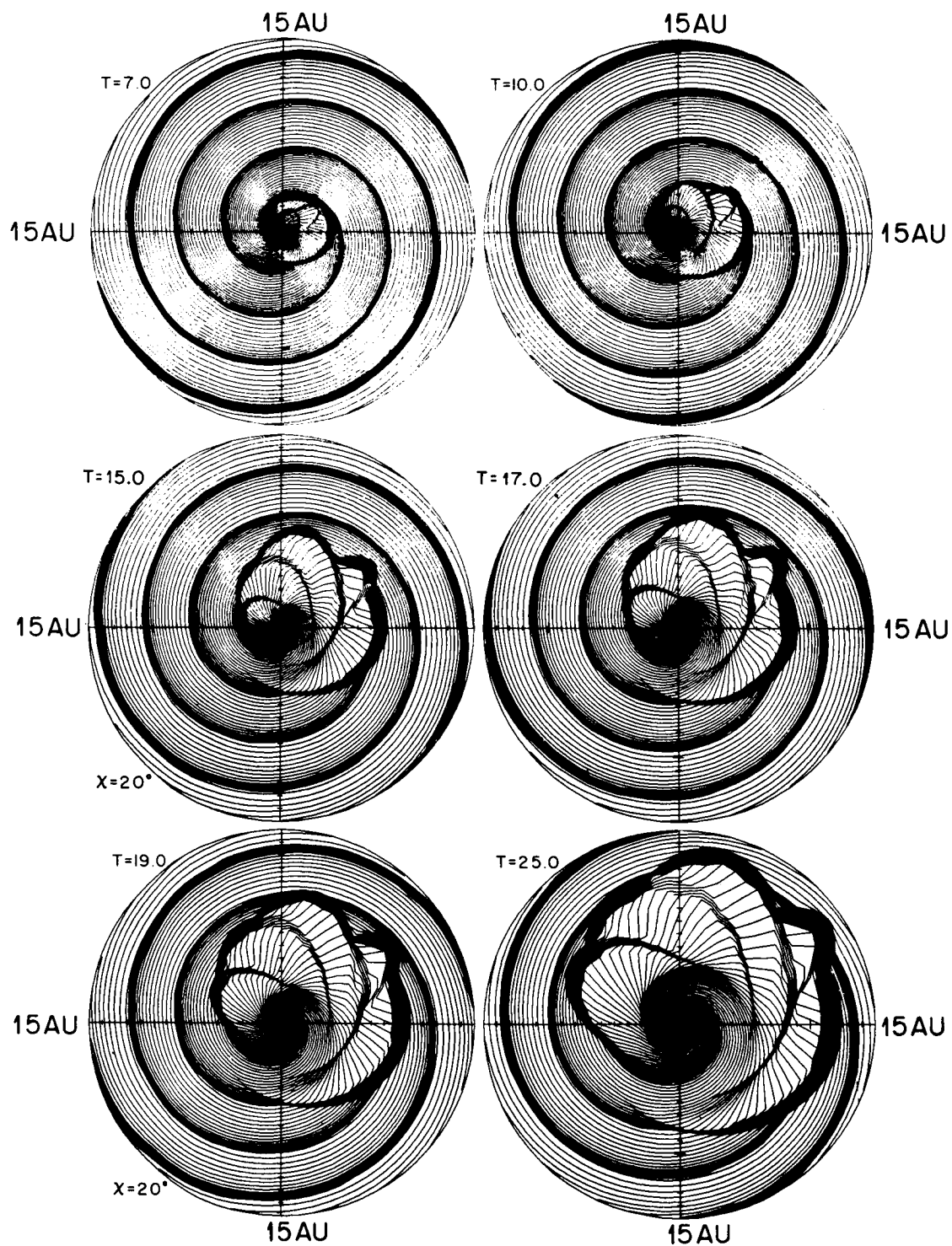
Figure 2. Solar wind disturbances caused by six successive flares during a period of 10 days. The figure shows the propagating structure at T = 7.0, 10.0, 17.0, 15.0, 19.0 and 25.0 days after the onset of the first flare. The outer limit of each circular area is at 15 au.

Comments on "Solar wind disturbances in the outer heliosphere,
caused by successive solar flares from the same active region",

by Akasofu and Hakamada

V. J. Pizzo[*]
HAO/NCAR
P.O. Box 3000
Boulder, CO 80307

In this paper, a kinematic̀ modeling technique (Hakamada and Akasofu, 1982) is used to simulate the interaction of transient flows with a two-sector corotating flow to large heliocentric distances. The input transients, which are characterized by several parameters, have peak speeds in the range of 800-1000 km/s. Hence the corotating flows constitute an inhomogenous slower-speed background, into which the transients continually penetrate. Thus, by 10 AU in the authors' last example (which involves six separate flares), the interaction of the transients with the corotating flows as well as with each other produces a very complicated jumble of magnetic fields. It is further asserted that such contorted magnetic topologies should have important consequences for galactic cosmic ray transport.

With this last point, I have no particular quibble, other than to mention that the basic concept has been around for nearly two decades. Parker (1963), for example, broached the general idea in his book, though he did not offer very specific estimates as to where substantial magnetic complexes would form or what their dimensions might be. Only recently, in fact, have enough detailed data appeared to permit some assessment of the validity of the idea (e.g., see McDonald *et al.*, 1982; Burlaga *et al.*, 1982; and Burlaga *et al.*, 1983).

So the questions to ask are: How faithfully does this modeling technique, with all its obvious practical advantages, simulate the flow interactions? To what extent is it quantitatively accurate? Are there any regions where it fails even in a qualitative sense?

In considering these questions, it must be recognized from the outset that accuracy of the sort usually associated with a full MHD model is not required for the authors' stated purposes. On the other hand, for a model to rank as an effective tool, it must still successfully predict the gross features of the flow: e.g., the heliocentric distance where the major structures interact, the spatial scale of the resultant interaction region, the rate at which CIRs expand, the approximate magnitude of the field enhancements, etc.

It is my contention that the model of Hakamada and Akasofu (1982) meets even these relaxed criteria only in a limited parameter range and only over a fairly restricted span of heliocentric distances. Further, I will argue that the particular examples presented by the authors are in general violation of these limitations and their results are thus compromised.

To begin, let us be clear as to the physical content of their model. The Hakamada and Akasofu (1982) formulation is first and foremost a purely kinematic description, i.e. the evolution is entirely determined by the input velocity variations; the material in no way exerts either a gas pressure or magnetic field force. What is especially poignant is the way the authors handle those regions where fast material overtakes slow. It is inevitable that at some point the fluid elements must begin to overlap, corresponding to a shock in the dynamic case. Here the authors invoke a parameterized curve-fitting method to keep the usual R-t diagram from becoming double-valued (see Sec. 1.3 and 2.3 in Hakamada and Akasofu, 1982). The parameters are chosen such that the resultant V-t or V-R curves resemble some particular observed streams or dynamic model calculations. However, the predictive value of any model is measured by its ability to cope with a wide variety of input flows (such as are encountered in the real solar wind) under a single parameterization. That is, in practical applications one is forced into picking one parameterization that will be in effect throughout the simulation and will have to accurately describe the evolution of all flow states therein. In general, it will not be possible to tinker meaningfully with the parameters after the fact, since if the model is being used in the predictive mode, there is obviously nothing to calibrate it against.

A single parameterization of the type used by the authors may well allow them to mimic a few well-chosen streams, as they have demonstrated. And, indeed, were all solar wind streams more or less alike, such an approach might be viable. However, it hardly needs any emphasis that solar wind flows differ markedly in speeds, field strengths, densities--in fact, over the entire gamut of flow parameters. And all the interesting large-scale interaction phenomena--the rate at which CIR's expand, the rate at which shocks form and decay, the lateral expansion of a directed blast wave, etc.--all depend sensitively upon the local properties of the ambient medium and the input shock strength, i.e. they are inherently dynamic in nature. It is of paramount importance to recognize that the authors' parameterization of shock propagation, for example, is based solely upon kinematic considerations. The speed jump is first computed from kinematics and the ad-hoc parameterization, then density and field are chosen to satisfy flux conservation. Thus, while the Rankine-Hugoniot relations are in some sense satisfied, the thermodynamic and magnetic properties of the medium play no role in the determination of the shock speed. In view of these considerations, then, it is difficult to see how any single parameterization can suffice for the range of flow states studied by the authors. At least, they have not demonstrated such a capability.

That being said, we must now ask how all this specifically impacts the authors' results. The answer will be split into three parts : the model's treatment of the corotating structure alone; its treatment of isolated impulsive flows into an ambient medium; and, its treatment of the interaction between transient and corotating flows.

First, with regard to purely corotating flows, recent observational and theoretical efforts (Burlaga, 1983; Pizzo, this conference) seem to concur that by about 10 AU all the fast material in high-speed streams has been pretty well consumed in the interaction and that the subsequent evolution is governed by large-scale pressure-wave dynamics. In this regime, a kinematic approach is totally irrelevant. The authors are able to maintain an identifiable stream structure to large heliocentric distances only through careful manipulation of input conditions at the inner boundary: their input structure is longitudinally very broad, with the gentlest of velocity gradients. Thus their CIRs do not even form until about 7 AU and are still reasonably compact at 20 AU (see Fig. 1.5 in Hakamada and Akasofu, 1982). In consequence of all the observational experience gained through Pioneer and Voyager, the authors' background flow therefore appears highly unrealistic, to say the least.

482

Next, in the case of an isolated, impulsive transient penetrating into a uniform ambient flow, there are two major shortcomings in this model. First, since all features of the shock propagation in the model are solely contingent upon the input velocity structure, there is no distinction, really, between strongly driven shocks and simple blast waves, which are known to have quite different evolutionary properties (e.g. Hundhausen and Gentry, 1969) . Again, the parameterization in the model could be adjusted for one class, but then it would be inappropriate for the other. Second, an important feature of multi-dimensional shock propagation is that the forward shock expands near the sun to cover a much broader angular span than does the input disturbance, while the reverse shock remains fairly localized within the driver gas (e.g. D'Uston et al., 1981). The lateral expansion of the forward shock front is a purely dynamic phenomenon and has great significance for the field structure. In the kinematic model, of course, the shock is confined to the input angular cone and there is simply no way to reproduce the important spreading effects.

Finally, when transients and corotating streams are allowed to interact, it has long been known that the density (and presumably magnetic) structure of the ambient corotating flow plays at least as large a role in the interaction as does the velocity structure (Heinemann and Siscoe, 1974; Hirschberg et al., 1974). Shock speeds and transit times are thus going to be very poorly modeled in the authors' formulation, particularly when the disturbances are traced over many AU and across many intervening structures.

In light of all these considerations, it is hard to see how the authors' model can possibly provide a quantitatively adequate representation of the flow systems presented in this paper. Their corotating background flow is quantitatively unrealistic inside about 10 AU and is not even qualitatively appropriate beyond that point. And, owing to the serious deficiencies in their treatment of the very complex transient-corotating interaction as outlined above, it is evident that their quantitative estimates for the important physical properties of the flow (the location, dimensions, and amplitude of the resultant magnetic structures) at large heliocentric distances must be regarded with critical suspicion. It is to be stressed that what is at issue here is not a dry technical debate over some trifling 10-20% discrepancies among alternative methods of calculation. Rather, I contend that the kinematic model, as in the grossly over-extended application witnessed in the authors' treatise, is susceptible to such large quantitative error that the accompanying Figures are best viewed as little more than computer-generated schematics.

Bibliography

Burlaga, L. F., Corotating pressure waves without streams in the solar wind, submitted to J. Geophys. Res., 1983.

Burlaga, L. F., F. B McDonald, R. Schwenn, and A. Lazarus, Interplanetary flow systems associated with cosmic ray modulation in 1977-1980, (abstract) APS Bulletin, 27, 571, 1982.

Burlaga, L. F., R. Schwenn, and H. Rosenbauer, Dynamical evolution of interplanetary magnetic fields and flows between 0.3 AU and 8.5 AU: Entrainment, submitted to Geophys. Res. Lett., 1983.

D'Uston, C., M. Dryer, S. M. Han, and S. T. Wu, Spatial structure of flare-associated perturbations in the solar wind simulated by a two-dimensional numerical MHD model, J. Geophys. Res., 86, 525, 1981.

Hakamada, K. and S. -I. Akasofu, Simulation of three-dimensional solar wind disturbances and resulting geomagnetic storms, Space Sci. Rev., 31, 3, 1982.

Heinemann, M. A. and G. L. Siscoe, Shapes of strong shock fronts in an inhomogeneous solar wind, *J. Geophys. Res.*, *79*, 1349, 1974.

Hirshberg, J., Y. Nakagawa, and R. E. Wellck, Propagation of sudden disturbances through a nonhomogeneous solar wind, *J. Geophys. Res.*, *79*, 3726, 1974.

Hundhausen, A. J. and R. A. Gentry, Numerical simulation of flare-generated disturbances in the solar wind, *J. Geophys. Res.*, *74*, 2908, 1969.

McDonald, F. B., L. F. Burlaga, J. H. Trainor, M. A. I. Van Hollebeke, and T. von Rosenvinge, Observation of the long term cosmic ray modulation between 1 and 25 AU, (abstract) *APS Bulletin*, *27*, 571, 1982.

Parker, E. N., *Interplanetary Dynamical Processes*, Interscience Publ., New York, Ch. X-XII, 1963.

REPLY

S.-I. Akasofu
Geophysical Institute
University of Alaska
Fairbanks, Alaska 99701

Pizzo should display first his results graphically on a global scale. We are certain that he would find his results are basically similar to ours. We are aware of neither the basic IMF spiral pattern nor flare-induced patterns published by him.

Hakamada and Akasofu (1981, 1982) were one of the first to consider explicity a particular type of the basic solar wind speed distribution (on the source surface) which was used by Pizzo (1982) without acknowledgement. Figures 1 and 2 in Hakamada and Akasofu (1981) or Figure 1.2 in Hakamada and Akasofu (1982) are basically the same as Figure 10 in Pizzo (1982).

Our method has a limited purpose, and we treated the stream-stream interaction (including the forward and reverse shocks) by a method analogous to one of the standard aerodynamic methods. The usefulness of our method can also be demonstrated in the example shown in Figures A and B in which effects of the six successive flares are introduced into the four-spiral (quadruple) situation, instead of the two-spiral situation. All the flare parameters are the same as those in Akasofu and Hakamada (1983), except that V_F is reduced to half. The basic features of the velocity profile are similar to those observed by space probes (Burlaga et al., 1983).

References

Akasofu, S.-I. and K. Hakamada, Solar wind disturbances in the outer heliosphere, caused by successive solar flares from the same active region, this volume, 1983.

Buralga, L.F., R. Schwenn and H. Rosenbauer, Dynamical evolution of interplanetary magnetic fields and flows between 0.3 au and 8.5 au, Entertainment, this volume, 1983.

Hakamada, K. and S.-I. Akasofu, Simulation of three-dimensional solar wind disturbances and resulting geomagnetic storms, Space Sci. Rev., 31, 3, 1982.

Hakamada, K. and S.-I. Akasofu, A cause of solar wind variations observed at 1 a.u., J. Geophys. Res., 86, 1290, 1981.

Pizzo, V. J., A three-dimensional model of corotating streams in the solar wind, 3. Magnetohydrodynamic streams, J. Geophys. Res., 87, 4374, 1982.
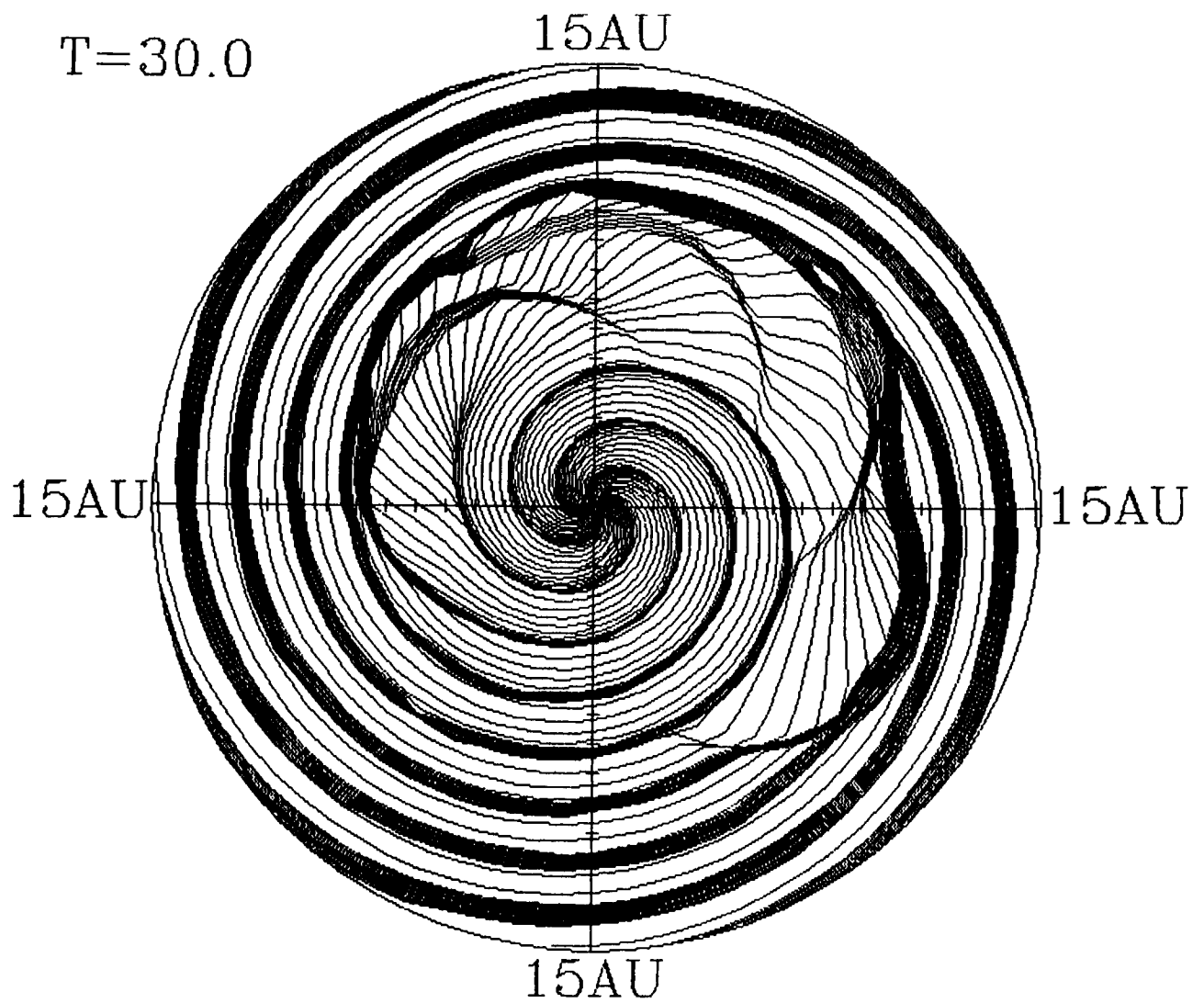
Figure A.   The disturbed IMF pattern by the six successive solar flares 30
days after the onset of the first flares. The flare parameters
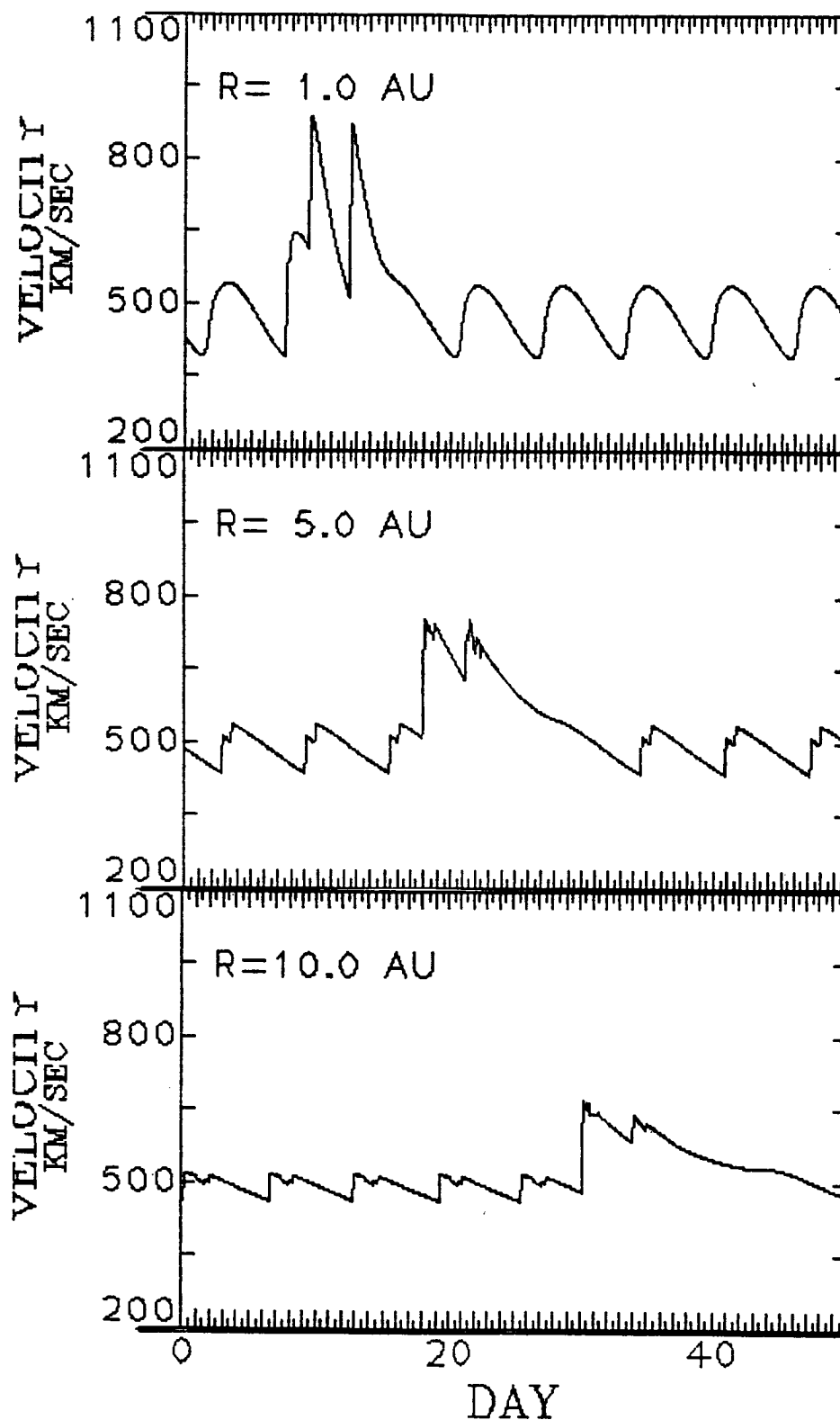are the same as those in our paper, except that V_F is reduced to
half.

Figure B.   The velocity profile of the disturbed solar wind at 1 au, 5 au
and 10 au along the longitude line of 135° in the ecliptic
plane.

THE "AVERAGE" SOLAR WIND IN THE INNER HELIOSPHERE: STRUCTURES AND SLOW VARIATIONS.

Rainer Schwenn
Max-Planck-Institut für Aeronomie
Postfach 20
D-3411 Katlenburg-Lindau, FRG

Abstract

Measurements from the HELIOS solar probes have indicated that apart from solar activity related disturbances there exist two states of the solar wind which might result from basic differences in the acceleration process: the "fast" solar wind ($v > 600$ kms^{-1}) emanating from magnetically open regions in the solar corona and the "slow" solar wind ($v < 400$ kms^{-1}) correlated with the more active regions and its mainly closed magnetic structures. In a comprehensive study using all HELIOS data taken between 1974 and 1982 we analyzed the "average" behavior of the basic plasma parameters as functions of the solar wind speed. We found that some quantities (e.g. momentum flux, total energy flux) are remarkably independent of the speed, others (e.g. particle density, enthalpy flux, angular momentum flux, α-particle to proton ratio) are not. The long term variations of the solar wind parameters along the solar cycle were also determined and numerical estimates given. These modulations appear to be distinct though only minor. In agreement with earlier studies we conclude that the major modulations are in the number and size of high speed streams and in the number of interplanetary shock waves caused by coronal transients. The latter ones usually cause huge deviations from the averages of all parameters. It is demonstrated that, apart from those solar activity related cases, even the "normal" acceleration mechanisms of the solar wind may occasionally become dramatically changed in such a way that large areas of the corona emit low density low speed plasma with a critical point beyond 0.3 AU. The occurrence of such strange excursions may put new constraints on any theory of solar wind expansion.

I. Introduction

Asking for the average solar wind might appear as silly as asking for the taste of an average drink. What is the average between wine and beer? Obviously mere mixing – and averaging means mixing – does not lead to a meaningful result. Better taste and judge separately and then compare, if you wish. After a while you will have developed a set of criteria for differentiating. Then you may eventually come from analysis to synthesis: You really can appreciate what you are drinking. So much for the drinks.

The trouble with the solar wind is more difficult: We do not know the significant criteria to begin with. For a long time the theorists have thought in terms of a "quiet" wind and believed to find it represented in the "slow" wind (for references, see Hundhausen, 1972). This is easily understood since the experimentally determined numbers for the slow wind fitted the available theoretical models much better, and they still do. It wasn't until Feldman et al. (1976) suggested that if there is a "quiet" wind at all it is more likely to be found in the "fast" wind, i.e. in the high speed streams occurring predominantly a few years before

sunspot minimum. During the Skylab era in 1973/74 we learned that these high speed streams emerge from coronal holes (Hundhausen, 1977 and references therein). The unique association between these two phenomena has since then been well established and was found to be valid even in detail (Burlaga et al., 1978). Not only do the Skylab X-ray pictures of coronal holes show surprisingly sharp edges (Bohlin, 1977, and references therein), it was also found that the high speed streams are surrounded by comparatively thin boundary layers separating them from the adjacent slow solar wind. This became especially clear when HELIOS 1 approached the sun for the first time in early 1975 (perihelion at 0.31 AU): there the interaction region between stationary corotating high speed streams and the slow plasma ahead can be as "thin" as $2°$ in solar longitude (Schwenn el al., 1976). A similar number was found for the latitudinal boundaries of high speed streams (Montgomery, 1976, Schwenn et al., 1978). It must now be regarded as normal that two spacecraft moving close to the heliocentric equator but separated in heliocentric latitude by not more than $10°$ observe completely different stream structures in most cases. They can even move on different sides of the interplanetary current sheet, i.e. in opposite magnetic sectors. This was demonstrated in early 1976 when the two HELIOS probes at a latitudinal separation of $12°$ were travelling in opposite magnetic sectors for about a quarter of a solar rotation (Schwenn et al., 1977, Burlaga et al., 1981).

Based on all these results one is tempted to assume almost rectangular flow speed profiles close to the sun (Gosling et al., 1978) which resemble very closely those of the underlying coronal holes. Slow solar wind and high speed streams might be essentially different phenomena and might result from different acceleration mechanisms in the corona (as suggested by Rosenbauer et al., 1977, Schwenn et al., 1981a, b).

There have been attempts to explain the strange "switching" between the two states in terms of multiple critical points which may occur when the divergence of open magnetic field lines, e.g. in coronal holes, exceeds certain limits (Kopp and Holzer, 1976, Holzer, 1977). Unfortunately, there is still no conclusive answer to such basic questions, as what accelerates the fast solar wind to its high speed, what causes the sharp boundaries, and where the slow solar wind really comes from.

From the foregoing remarks it seems reasonable that one criterion for sorting the solar wind into different categories should be the bulk speed. In the second part of this paper I will apply this criterion to all the HELIOS solar wind data taken between 1974 and 1982 and discuss the "average" parameters as functions of the bulk speed. The effects of undesired "mixing" caused by solar activity related disturbances will be considered. In the third part I will show if and how the basic "average" solar wind parameters change during the solar cycle. At the end of the discussion I will mention a few exceptional excursions which obviously do not fit into any of these categories.

II. Long term averages

1. The method

For this comprehensive analysis we took all data from the plasma experiment on both HELIOS solar probes (Schwenn et al., 1975). HELIOS 1 had been launched

on Dec. 10, 1974 into a highly elliptic heliocentric orbit with a perihelion distance of 0.3 AU. HELIOS 2 followed on January 15, 1976 and approaches the sun as close as 0.29 AU. The orbital period is 190 days for HELIOS 1 and 186 days for for HELIOS 2. For further details see Porsche (1977). The plasma data were evaluated by a one-dimensional method briefly described by Rosenbauer et al. (1977). The proton densities were normalized to 1 AU assuming a r^{-2} dependence. All data were used on the basis of individual spectra and no averages were performed beforehand. (Just for comparison we calculated 1 hr averages and used those as inputs for the final analysis. Although the results did not change significantly we feel that this latter method is not appropriate: During many hours there were just single data points, the unavoidable scatter of which gained too much weight by this kind of averaging). The HELIOS 1 data set covered the time period from Dec. 12, 1974 to Feb. 28, 1982 resulting in 1,602,231 total spectra. The HELIOS 2 data cover the time span from Jan. 17, 1976 to Mar. 8, 1980 including 913,142 total spectra. We grouped the data in seven speed classes ($<$ 300; 300 - 400; 400 - 500; 500 - 600; 600 - 700; 700 - 800; $>$ 800 kms^{-1}) and calculated the relevant average parameters within these classes. The bottom panel in Figure 1 shows how the data are distributed over the classes. Within each speed class we sorted the data into radial bins of 0.02 AU width according to the radial distance at which they had been measured. By this technique we were also able to determine radial trends.

2. Average proton parameters

Figure 1 tells us how the proton density n_p, the flux density $n_p v_p$ and the momentum flux density $n_p m_p v_p^2$ depend on the bulk speed. We notice some systematic smooth trends for all these quantities as functions of v_p. Only the group $v_p >$ 800 kms^{-1} shows marked deviations. A closer inspection of the data contributing to this particular group reveals that most of them are due to fast plasma accelerated by shocks associated with increasing solar activity from 1977 on. In order to find the impact of such transient phenomena on our data set we did a similar analysis with a subset of data (445,571 from HELIOS 1 and 238,923 from HELIOS 2) taken before 1977. Data associated with major shocks occurring even before that date were also excluded. The result in Figure 2 shows that the trends are now more distinct. It turns out that the particle flux $n_p v_p$ and even more dramatically the normalized density decreases steadily with increasing speed. On the other hand, the momentum flux is remarkably equal for all speed classes.

The average quantities might be affected by stream-stream interactions as well. We did not study this here since the influence can be expected to be only minor inside 1 AU (Goldstein and Jokipii, 1977). The width of these interactions regions is small compared to the streams themselves (see, e.g., Figure 1 in Rosenbauer et al., 1977) and gets even smaller at decreasing distances from the sun.

3. Average energy flux

In Figures 3 and 4 we find similar histograms for the energy flux density. The kinetic energy flux $n_p v_p$ (1/2 $m_p v_p^2$) shows a marked increase with speed, which is due to its dependence on v_p^3. On the other hand, the gravitational energy flux $n_p v_p$ (G $m_p M_\odot/R_\odot$) which stands for the work required to overcome
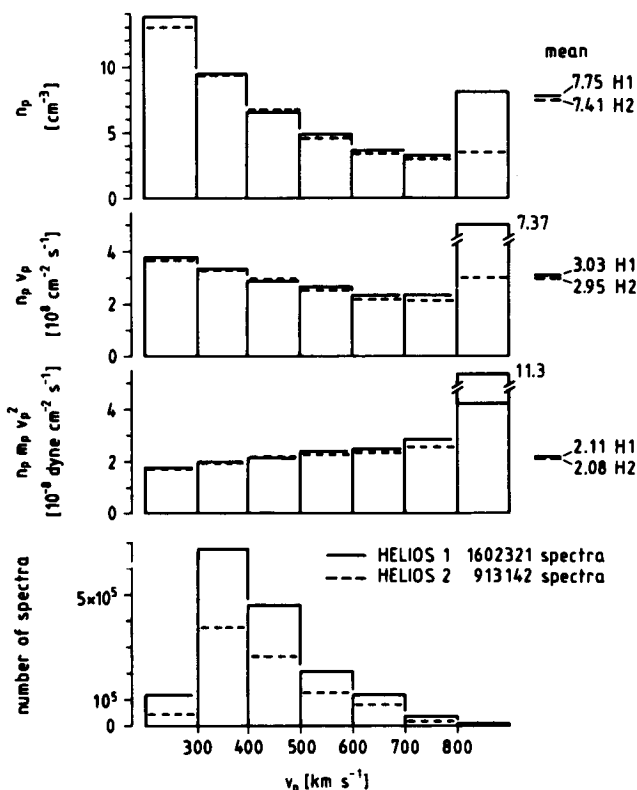
Figure 1   Average values of the solar wind proton density n_p, the proton flux density $n_p v_p$, and the proton momentum flux density $n_p m_p v_p^2$, as functions of the flow speed. The bottom panel shows the number of points in each speed class. All data from both HELIOS solar probes taken between Dec. 12, 1974 and Feb. 28, 1980 are included.
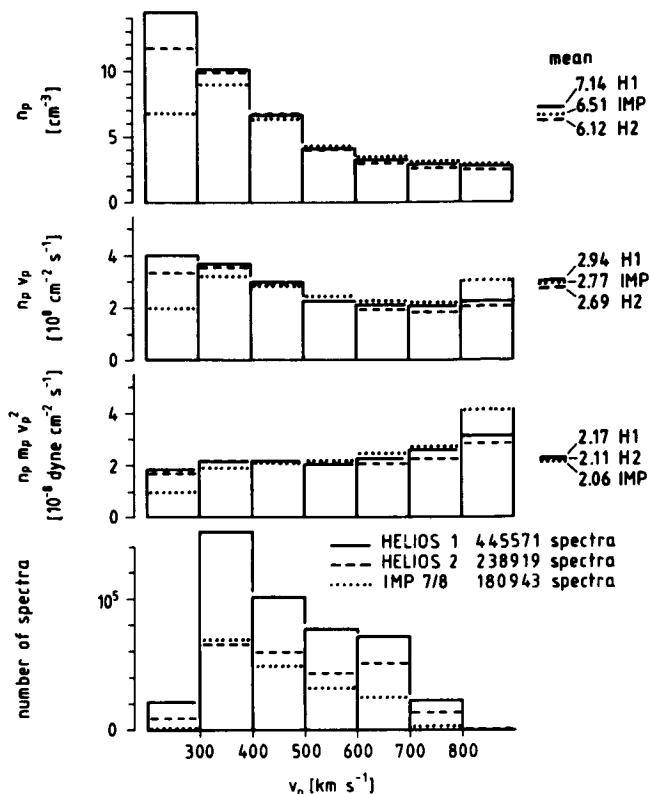
Figure 2   Same as Figure 1, but the data from 1977 on and some other shock disturbed data before 1977 were excluded. The IMP7/8 data were kindly provided by the Los Alamos group.

solar gravity goes only linearly with v_p and is therefore proportional to the particle flux $n_p v_p$. The enthalpy flux $n_p v_p$ $(5/2 \ kT_p)$ does not add more than $\sim$ 3 % to the total energy flux, nor does any other energy flux such as proton and electron heat fluxes and the Alfvén wave energy flux (Denskat, 1982). Adding up all these components we find the flux density of the total energy, i.e. that energy the sun is losing by releasing the solar wind plasma, to be remarkably independent of v_p. This is even more evident from Figure 4 which is again based on HELIOS data before 1977 only.

We checked these results with plasma data obtained at 1 AU from the earth-orbiting IMP7/8 satellites (kindly supplied to us by the Los Alamos group direc-
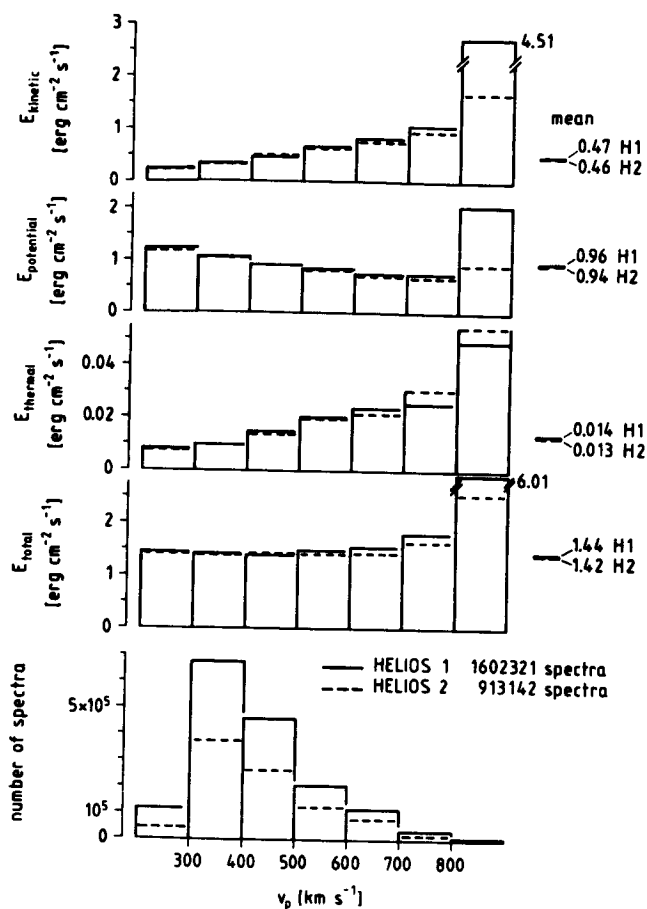
Figure 3 The average solar wind energy flux density, derived from the same data as in Figure 1.
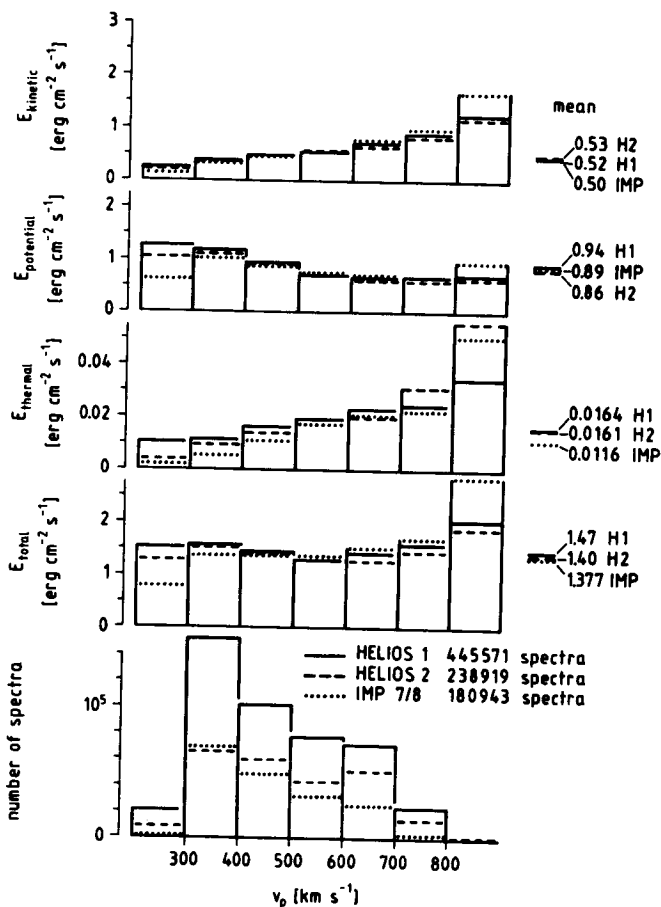
Figure 4 The average solar wind energy flux density, derived from the same data as in Figure 2.

ted by Dr. Sam Bame. Intercalibration between the IMP and HELIOS spacecraft was performed using the data of the first few days after the launches of HELIOS 1 and HELIOS 2, respectively. This led to a correction factor for the IMP proton densities of 0.70). These data, taken between Dec. 12, 1974 and Dec. 31, 1976, show exactly the same trends (see Figures 2 and 4).

We tried to find out the cause for the slightly different trends of the averages in the $v_p > 800$ kms^{-1} class. It turned out that, e.g., in case of HELIOS 2 there were 1077 points in this class (before 1977), 1067 of which stem from one single high speed streams in April 1976 observed at 0.3 AU (see Marsch et al., 1982a, b). In Figure 16 of the paper by Marsch et al. (1982a) we find a time plot of these particular data. We see that in this period v_p is only some 700 kms^{-1} on the average. Values of up to 900 kms^{-1} are reached occasionally in the form of rather sharp peaks, due to strong Alfvénic turbulence. Depending on the instantaneous orientation of the magnetic field the proton speed can reach extreme values while the density remains constant. Because of our procedure these

extrema were grouped in a separate class. This grouping causes the large values of all average quantities involving any power of v_p. By first calculating, e.g., 1 hr averages of these parameters and then sorting those according to the speed classes, we found that now both the momentum flux and the total energy flux are constant within $\pm$ 10 % of the average flux regardless of the proton bulk speed. Similar arguments also hold for HELIOS 1 and IMP where the total number of points in the class $v_p > 800$ kms^{-1} is even less (466 and 13, respectively).

4. Average radial gradient of the proton temperature

The radial gradients of the proton temperature T_p are displayed in Figures 5 (all data) and 6 (data before 1977). For this purpose we fitted the radial dependence of T_p within each speed class by an $r^{-\gamma}$ law. We find that for slow speeds γ
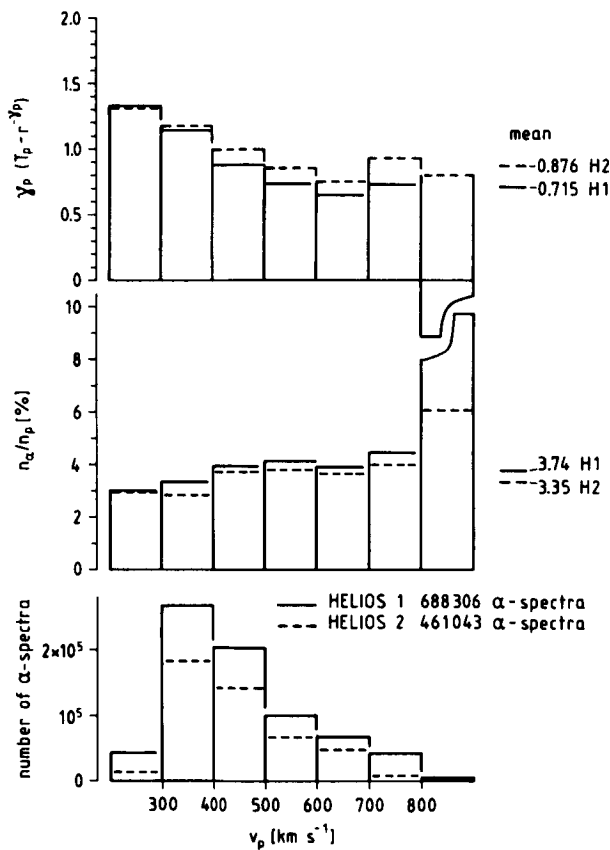
Figure 5   The average proton temperature radial gradient index γ_p (assuming a $r^{-\gamma}$ dependence) and the average α-particle abundance n_α/n_p, derived from the same data as in Figure 1. For n_α/n_p only those data were used, where HELIOS was outside 0.5 AU.
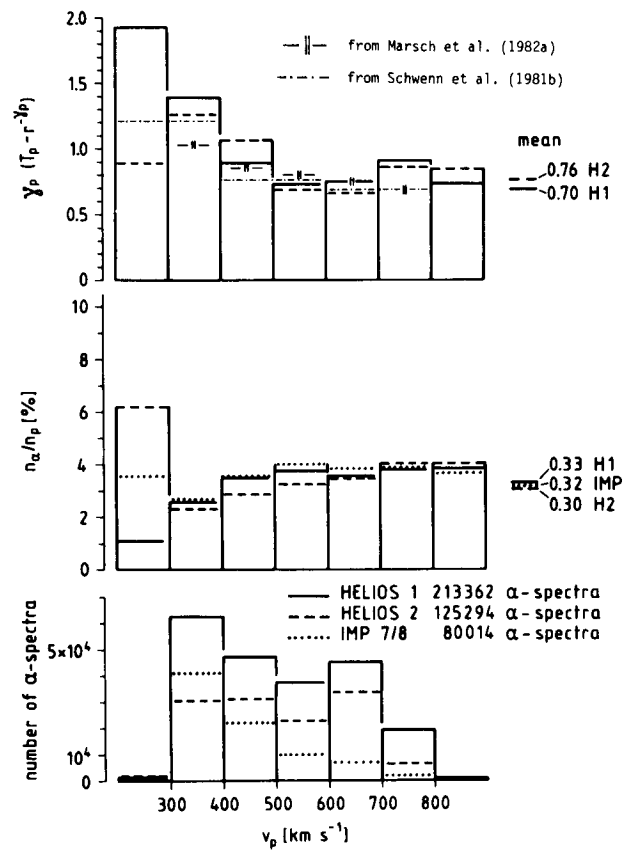
Figure 6   Same as Figure 5, but with the same limited data set as in Figure 2.

494

is close to the adiabatic value of $\gamma = 4/3$. For higher speeds γ is significantly lower. The numbers are in good agreement with those determined by Schwenn et al. (1981b) from radial line-ups between HELIOS 1 and HELIOS 2 and those for $T_{\parallel}$, calculated by Marsch et al. (1982a) from evaluations of the 3D-velocity distribution (one must be aware that T_p as used for this analysis results from a projection of the velocity distribution onto the radial direction and a succeeding 1D evaluation. $T_{\parallel}$ is the second moment of the distribution function parallel to the local magnetic field. Thus T_p can be expected to be equal to $T_{\parallel}$ only if the magnetic field is radial).

5. Average α-particle abundance

The second panels in Figures 5 and 6 show the α-particle abundance (relative to protons) n_α/n_p. For this part of the analysis we used data only from periods in which the HELIOS probes were outside 0.5 AU in order to avoid possible confusion with fast streaming proton components often found inside 0.5 AU (Marsch et al., 1982b). There can be no doubt about a slight but definite dependence on v_p, especially in the undisturbed data taken before 1977 (Fig. 6). The large scatter of n_α/n_p in the speed class $v < 300$ kms^{-1} is certainly a small-sample effect. The fast solar wind contains $\sim 3,6$ % α-particles, the slow plasma only $\sim 2,5$ % (Note that the n_α/n_p ratio tends to be too large, since spectra with too few α-particles had to be excluded from this analysis. Such α-particles depletions occur mainly in the slow solar wind. That means that the real α-abundance difference between slow and fast solar wind could be even more pronounced). Our data are also consistent with a result reported by Borrini et al. (1981). They had found significant depletions in n_α/n_p around magnetic sector boundaries which are normally imbedded in slow solar wind.

This abundance difference might be regarded as indicator of a qualitative difference in the coronal sources of both types of solar wind flow.

6. Average angular momentum flux

Now we regard the angular momentum flux $n_p m_p r v_{pr} v_{p\varphi}$ transported by the solar wind. In an extensive study recently published by Pizzo et al. (1982) it was found (among other important results) that it is the slow solar wind only that takes away positive angular momentum (in the sense of corotation) from the sun. The fast wind carries nearly no angular momentum at 0.3 AU. (Because of stream-stream interactions the momentum flux obtained from averaging all data between 0.3 and 1 AU reaches even a negative value, see Table 2.) The measurements indicate clearly, that this basic difference between slow and fast flow is of solar origin. This appears to be a very important observation since it might mean that the slow plasma is released at a significantly larger Alfvén radius than the fast plasma. This is another additional hint that there are possibly differences in the acceleration mechanisms for slow and fast solar wind (Kopp and Holzer, 1976).

7. Other radial gradients

In a further step we investigated the radial dependence of the solar wind parameters. For simplicity we assumed linear functions with r (except for the tem-

perature which has been discussed already) and performed least square fits. The averages within the radial bins were weighted according to the number of data points included. In Table 1 the average changes between 0.3 AU and 1 AU (in per cent) determined by this procedure are listed.

	HELIOS 1		HELIOS 2	
	all	before 77	all	before 77
v_p	11.0	17.4	4.4	5.7
n_p	-18.1	-22.6	-10.1	- 6.3
$n_p v_p$	- 2.8	- 5.6	10.0	3.3
$n_p m_p v_p^2$	12.7	12.6	10.6	12.4
E_{Kin}	28.7	30.9	17.6	18.8
E_{pot}	- 2.8	- 5.6	10.0	3.3
E_{total}	4.9	5.0	5.5	7.5

Table 1 Radial variations of average solar wind parameters between 0.3 AU and 1 AU, in per cent. The proton density n_p has been normalized to 1 AU assuming a r^{-2} dependence.

The table shows that it is the particle flux $n_p v_p$ that appears to be about constant. This indicates that on the average there is no significant meridional flow out of or into the plane of the ecliptic, to which our measurements are restricted. Owing to a general increase of the flow speed during the radial expansion (mainly in the slow plasma, Schwenn et al., 1981b), the average proton density n_p drops by a few per cent faster than according to a r^{-2} law. The increase in the bulk speed leads to even stronger increases in the flux densities of proton momentum and kinetic energy. The total energy flux in the protons grows by about 5 % between 0.3 and 1 AU. There are only two main energy sources that may supply this energy. Protons could gain
1. the α-particle kinetic energy which at least in high speed streams drops from ≈ 23 % to ≈ 17 % of the proton kinetic energy, due to the decreasing differential speed (Marsch et al., 1982b), and
2. the Alfvén wave energy flux which at times of Alfvénic turbulence drops from 5 % to 2 % of the total energy flux (Denskat, 1982).
However, the mechanism of this energy transfer, probably through some wave particle interactions, still awaits explanation.

8. Average solar wind around sunspot minimum

In Table 2 the average values of the basic parameters for the time between Dec. 12, 1974 and Dec. 31, 1976 are summarized, this time with only two subgroups

for "slow" ($v_p < 400$ kms^{-1}) and "fast" ($v_p > 600$ kms^{-1}) solar wind. Our numbers agree reasonably well with those given by other authors (e.g., Hundhausen, 1972, Feldman et al., 1977, Schwenn, 1981). However, detailed comparisons would require extensive discussions of the differences in the evaluations (instrument techniques, calibrations, data evaluation, selection criteria, status of the solar cycle etc.) and would go beyond the scope of this paper.

		$v_p < 400$ kms^{-1}	$v_p > 600$ kms^{-1}	all data
v_p	kms^{-1}	348	667	481
n_p	cm^{-3}	10.7	3.0	6.8
$n_p v_p$	cm^{-2}s^{-1}	3.66×10^8	1.99×10^8	2.86×10^8
$n_p m_p v_p^2$	dyne cm^{-2}	2.12×10^{-8}	2.26×10^{-8}	2.15×10^{-8}
E_{kin}		0.37	0.76	0.52
$E_{grav.}$	erg cm^{-2}s^{-1}	1.17	0.65	0.91
$E_{Enth.}$		0.011	0.023	0.016
E_{total}		1.55	1.43	1.45
n_α / n_p	%	2.5	3.6	3.2
$n_p m_p r v_{pr} v_{p\varphi}$	dyne cm sterad^{-1}	1×10^{30}	-0.7×10^{30}	0.4×10^{30}
γ	from $T_p \sim r^{-\gamma}$	1.2	0.7	–

Table 2 Average solar wind parameters for the time between Dec. 12, 1974 and Dec. 31, 1976. The proton density n_p has been normalized to 1 AU assuming a r^{-2} dependence.

9. Summary on long term averages

The most important results and conclusions of this first part of the analysis can be summarized as follows:
1. The parameters most sensitive to the bulk speed are the proton density and the angular momentum flux, as well as the particle flux, the α-particle abundance, the proton temperature and its radial gradient.
2. At times of low solar activity the momentum flux and the total energy flux are remarkably insensitive to the bulk speed.
3. The differences in angular momentum flux as well as the α-particle content indicate different release heights in the corona for fast and slow solar wind.

4. The particle flux density does not change between 0.3 AU and 1 AU, i.e. on the average the solar wind flow in the ecliptic is purely radial.
5. The net gain of proton kinetic energy between 0.3 AU and 1 AU requires some energy transfer still to be explained.
6. The relative insignificance of the Alfvén wave energy flux as well as the lack of speed dependence of the fluxes of total energy and momentum might conceal some clues to understanding the solar wind acceleration mechanisms.

III. Slow variations during the solar cycle

1. Solar wind stream structure

The possible modulation of the solar wind during the solar activity cycle has always been a subject of great interest, which is reflected in a number of papers at this conference (see also Hundhausen, 1979 and references therein).

One quantity that is apparently directly related with the solar activity cycle is the occurrence rate of interplanetary disturbances, such as shock waves. I will not discuss this correlation any further except for the impact these disturbances might have on the long term averages.

Bame et al. (1976) pointed out that a significant modulation is also evident in the number, size and amplitude of high speed streams. Figure 7 reproduces the original figure published by Bame et al. (1976), with a few points added. These points have been determined from HELIOS data using the same criteria as were used in the original work. The most prominent feature in Figure 7 is the appearance of large stable high speed streams in the last third of the past sunspot cycle about two years before activity minimum. This caused a simultaneous peak in the average solar wind bulk speed ($\sim$ 550 kms^{-1}) compared to minimum values of $\sim$ 430 kms^{-1} (Feldman et al., 1978). Extrapolating this data set, which already covers more than 11 years, we would expect the next appearance of stable high speed streams not later than by the end of 1983. There is a fair chance that HELIOS 1 might survive until then.

2. Modulation of proton parameters

It has been found that the modulation of the average solar wind, if there is one at all, is only minor compared to intercalibration uncertainties between several instruments on several spacecraft usually required for such a long term study. This is especially true for all those solar wind parameters involving particle densities.

The HELIOS data offer a unique opportunity for a quite comprehensive analysis. This data set is rather "complete" throughout the whole time span of seven years and three months, up to now. It covers for the first time all significant parts of a solar activity cycle: end of the declining phase, activity minimum, activity increase and maximum, beginning of the declining phase. Furthermore, there was no degradation or change in the instruments' performance. This was checked by extensive inflight tests and by cross calibrations between the two completely independent but simultaneously measuring instruments. The wave experi-
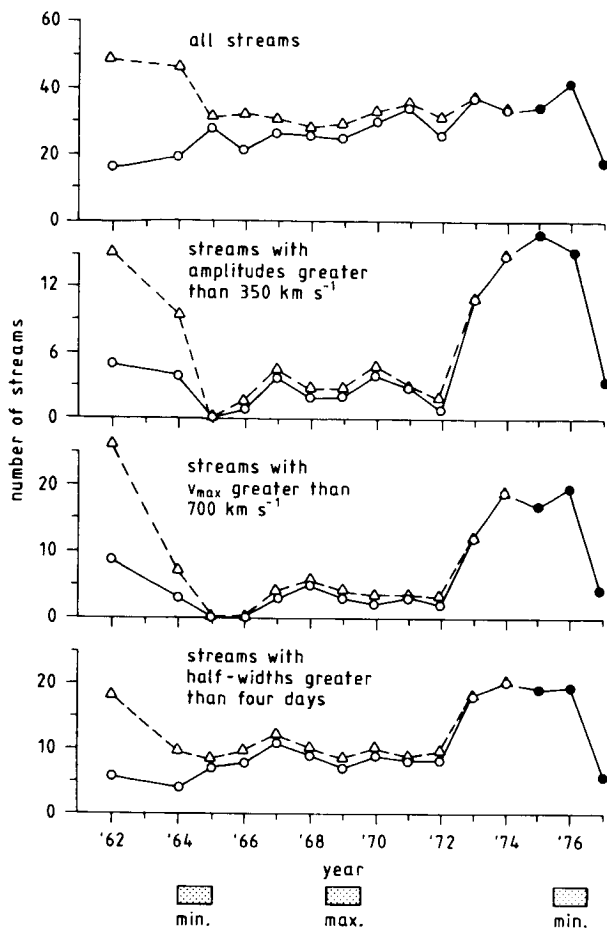
Figure 7 Yearly numbers of all solar wind streams with amplitudes greater than 150 kms⁻¹, with amplitudes greater than 350 kms⁻¹, with maximum speeds greater than 700 kms⁻¹, and with half-widths greater than 4 days (from top to bottom). The solid dots denote the numbers observed directly; the triangles denote extrapolated estimates for complete data coverage. From Bame et al. (1976).

The solid dots were determined from HELIOS data using the same criteria as in the original work.

ments on board the HELIOS probes measured the electron plasma frequency $f_e = (n_e e^2 / \pi m_e)^{1/2}$ in several cases of strong plasma oscillations (Gurnett and Anderson, 1977, Kellogg, private communication, 1976) and confirmed our absolute density calibration within only 20 % uncertainty.

The data points shown in the next few figures are in each figure averages of the relevant parameters through one complete solar rotation. Again we used as input data the individual spectra. No single data point has been omitted. The number of individual points for each rotation average is shown in the bottom panels of Figure 8. The proton densities have been normalized to 1 AU, as before.

In Figure 8 we see the behavior of the proton bulk speed, density, particle and total energy flux densities. The shaded lines are supposed to show what we think are long term trends:

1. There is a definite decrease in v_p from $\sim$ 550 in early 1975 to $\sim$ 370 kms⁻¹ in 1980 with a slight indication of an increase in 1981/82.

2. n_p is modulated by $\pm$ 10 % of the average value with a maximum in 1977 and a minimum at the end of 1979.

3. The particle flux shows a similar modulation with an amplitude of $\sim$ $\pm$ 15 % of average.

4. The total energy flux shows a similar modulation; the maximum is not so well pronounced, but the minimum in early 1980 is by 20 % lower. The increase from 1980 to 1982 is rather steep.
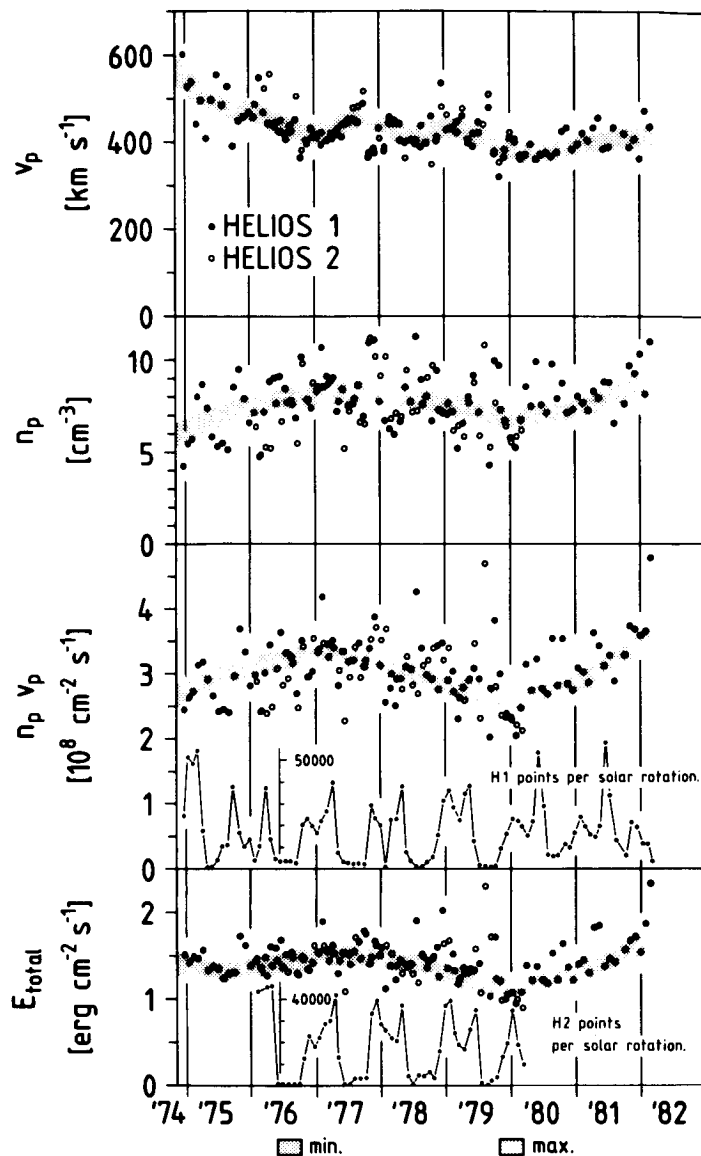
Figure 8 The variation of proton flow speed v_p, density n_p, flux density $n_p v_p$ and total energy flux density from 1974 to 1982, based on all HELIOS data. Each point represents an average value during one complete solar rotation. The number of points per rotation is indicated in the two lower panels.

5. For the fluxes of particles and total energy one might be inclined to see an overall upward trend superimposed on a sinusoidal modulation.

6. The increasing number of solar transients from 1977 on which caused so many shockwaves (up to some 20 per solar rotation) did not at all influence the averages. Even the scatter of the solar rotation averages remained about equal throughout the solar cycle.

In an additional approach we sorted these data with respect to the heliocentric latitude at which they were measured. The result was not surprising. It reflects in all details the fact that a few years before sunspot minimum the high speed streams were faster and broader if they were associated with the south polar coronal hole. Hansen et al. (1976) had reported that the equatorial extension of the south polar hole had been significantly broader than its northern counterpart during 1973/74. This explains why Coles and Rickett (1976) found, based on interplanetary scintillation measurements of the solar wind speed at high lati-

tudes, the yearly average speed to be remarkably higher at southern latitudes in those years. Our in situ measurements confirm that there was more high speed solar wind found at southern latitudes with all its typical features as mentioned above. This asymmetry weakened with rising solar activity and eventually disappeared altogether.

4. Modulation of α-particle abundance

The variation of the n_α/n_p ratio is presented in Figure 9. These data are again taken for $r > 0.5$ AU only. There is a clear trend evident in the data, with a definite minimum of ~ 2.8 % around sunspot minimum in 1976. The big scatter in later years was caused by more and more transients associated with rising solar activity. The average flux of α-particles is obviously much more variable and sensitive to solar activity than that of the protons.

In Figure 10 we split up the data into three speed classes (slow, medium, fast), for two of which the results are shown here. We find, that n_α/n_p is lower in slow solar wind (see also Figure 5 and 6). We also see that the modulation along the sunspot cycle works mainly in the slow solar wind.

Generally, the recent HELIOS data confirm very well the trends published by Feldman et al. (1978). There appears to be a significant variation of n_α/n_p from the average value between 3 % at sunspot minimum and ~ 4.5 % 3 years after sunspot maximum.
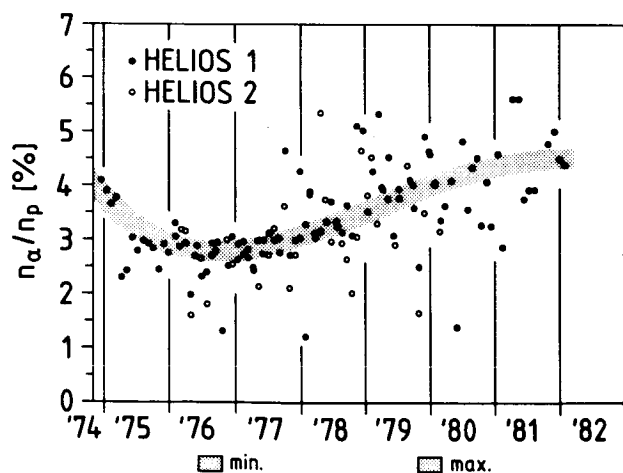

Figure 9 The variation of the α-particle abundance n_α/n_p from 1974 to 1982, based on all HELIOS data taken outside 0.5 AU.
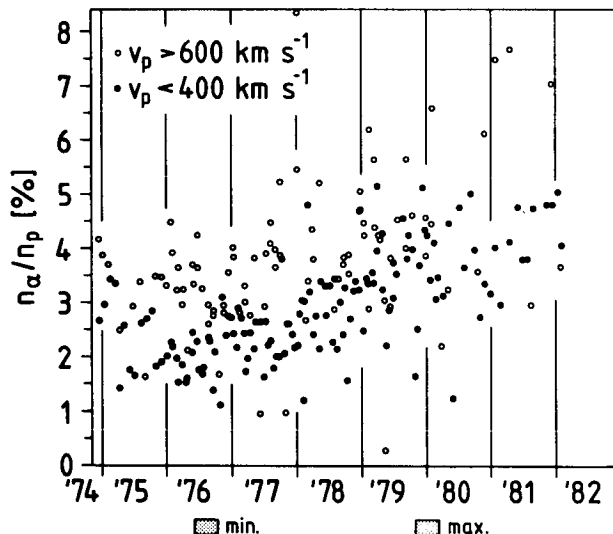
Figure 10 Same as in Figure 9, but only the data for $v_p < 400$ kms^{-1} and $v_p > 600$ kms^{-1} were selected and averaged separately.

501

IV. Exceptional excursions from the average

No rule without exceptions, no average without variances. There are enormous variances on all time scales in the solar wind (see, e.g., Hundhausen, 1972). The reason for finally abandoning the concept of a "quiet" solar wind is the simple fact that there never is a quiet solar wind. Especially the slow solar wind which can be traced back to the more active regions on the sun permanently shows fluctuations of all basic parameters. This holds as well for the times of low activity, when solar flares and other transients and their associated interplanetary disturbances are less frequent.

Occasionally there are unusual events observed in the solar wind which differ from all other phenomena in any respect chosen by which to compare them and which seemingly have no correspondence with any known solar event. Here I will present two examples of only one particular kind of those unusual events: The subalfvénic solar wind. In Figure 11 we see HELIOS 2 data taken from Nov. 9 to Nov. 16 in 1979 at 0.3 AU. The flow speed was generally low, around 300 kms^{-1}. On Nov. 13 the speed dropped further, below 200 kms^{-1}, and finally the peak of the proton velocity distribution went below our lowest E/q-channel (at 0.158 kV, i.e. 171 kms^{-1} for protons) for several hours. That was certainly the slowest solar wind ever reported. Because of the rather low plasma density ($\sim$ 20 cm^{-3}) and the high magnetic
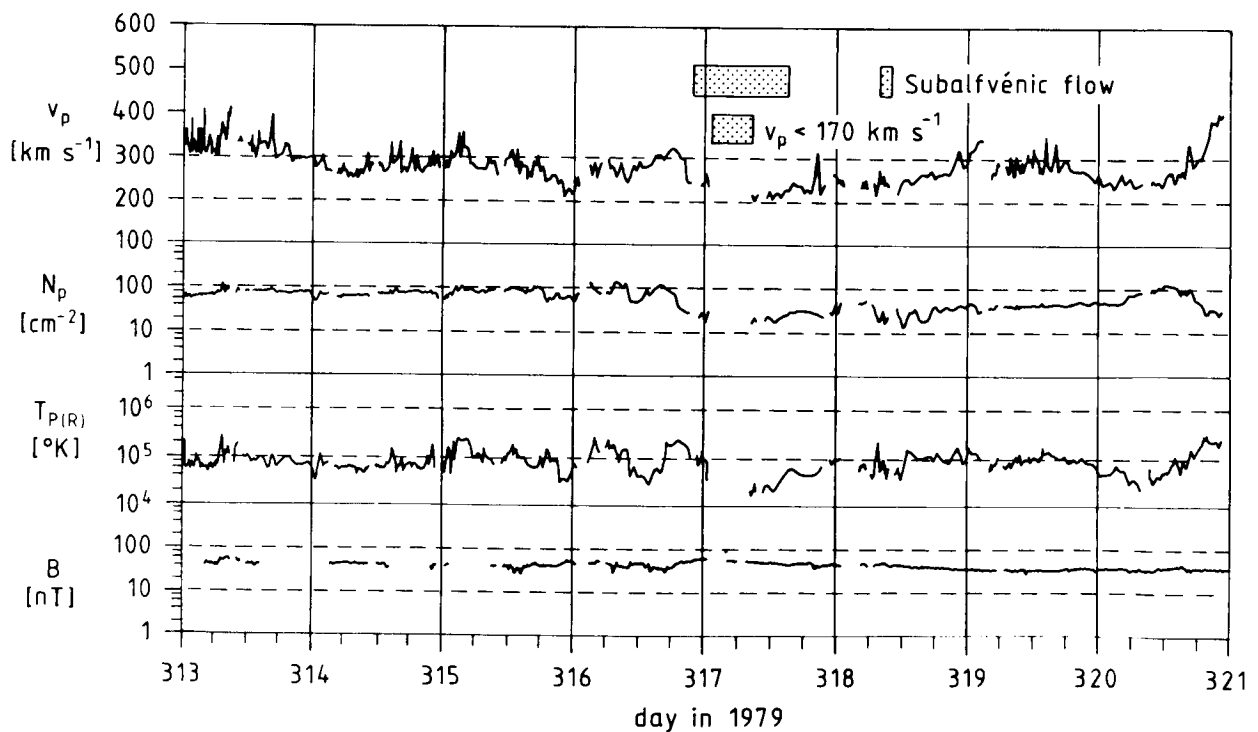

Figure 11 The subalfvénic solar wind flow on Nov. 13, 1979 as seen from HELIOS 2 at 0.3 AU. The magnetic field data were kindly provided by K.U. Denskat and F.M. Neubauer (TU Braunschweig).

field during that time the local Alfvén speed went as high as 300 kms⁻¹ (the local proton sound speed was ~ 15 kms⁻¹), i.e. nearly twice as much as the local plasma speed. In other words, the critical point for this particular plasma flow must have been outside 0.3 AU, if there was one at all. In very few cases have sub-alfvénic flows been observed recently in the piston gas driving strong flare-related interplanetary shocks (Richter, private communication, 1982). In this case, however, there was no shock involved within at least 4 days preceding the event nor was there any unusual coronal feature observed.

This event resembles somewhat another event observed by Gosling et al. (1982) at 1 AU on Nov. 22, 1979. Note that this is only 13 days after the HELIOS 2 event. Regarding the position of HELIOS 2 (100° east of the earth sun-line) and assuming a propagation time between 0.3 and 1 AU of a few days for this very slow solar wind we find it conclusive that both events were caused by the same solar source corotating stationarily. There are some differences in the details; HELIOS 2 found a very slow plasma speed at nearly normal densities, while IMP found a density depletion at normal speed. However, the main result is that in this case a sizeable part of the corona (some 10° of heliocentric longitude due to the event's duration at HELIOS 2, and 5.5° in latitude due to the separation between HELIOS 2 and IMP) could emit continuously for some 10 days very slow solar wind which remained sub-alfvénic until 0.3 AU and even 1 AU.

An even more dramatic event of a similar type was observed by HELIOS 1 on June 6 to 8, 1980 at a solar distance of 0.37 AU (Figure 12). Here the flow speed and the magnetic field remained about constant at 300 kms⁻¹ and 35 nT, respective-
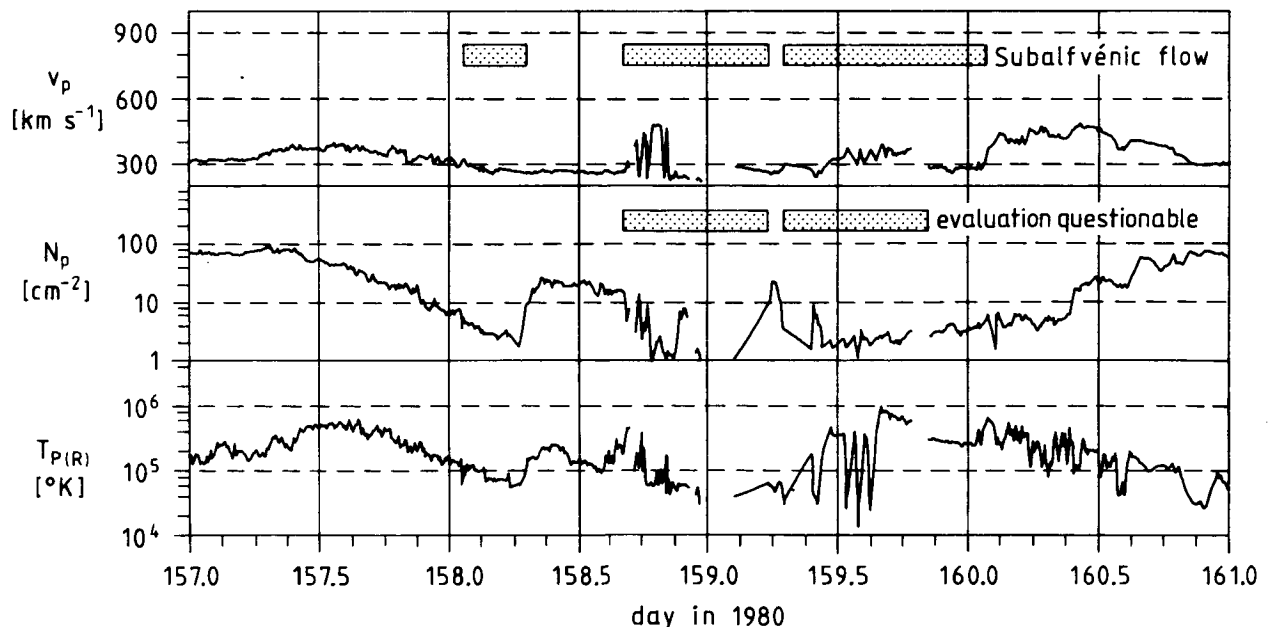

Figure 12   The subalfvénic solar wind flow on June 6 to 8, 1980, as seen by HELIOS 1 at 0.37 AU. During the intervals indicated in the Figure the data evaluation was questionable because of the extremely low particle densities, resulting in some abnormal values.

ly, but the density dropped to extremely low values. The density decreased steadily over an entire day from the normal value of $\sim$ 100 cm^{-3} to less that 1 cm^{-3}. The density was so low and the shape of the distribution function became so anomalous (very flat, up to 3 additional peaks at extreme speeds etc.) that a reasonable evaluation was no longer possible (We indicated the range of questionable data in Figure 12). Altogether, owing to this abnormal density "hole" in the solar wind the flow speed was subalfvénic for about two days, i.e. over about 20° in solar longitude, with only a few hours of interruption. Again, there was no disturbance in the interplanetary medium for several days ahead of the density drop, nor was there any associable solar feature seen.

In summary we have to conclude that the "normal" acceleration mechanisms of the solar wind eventually may become dramatically changed in such a way that large areas of the corona emit low density low speed solar wind with a critical point beyond 0.3 AU. The possibility of such strange though rare excursions from the average which are not related with any known solar phenomenon may put new constraints on any theory of solar wind expansion.

V. Concluding remarks

The properties of the "average" solar wind as described in this study were derived from some 2.5 million individual data points measured during a time span of more than seven years. We were well aware that averaging of data sets may produce problems resulting from unknown underlying mechanisms, as outlined in the introduction. It appears now that, after all, the choice of the solar wind flow speed as a basic parameter for sorting the data in different categories was a good one.

Our study increased the evidence for qualitative differences between high speed and low speed solar wind. In particular, the differences in angular momentum flux as well as the α-particle content indicate different release heights in the corona for fast and slow solar wind, confirming our earlier suggestion of differences in the acceleration process (Rosenbauer et al., 1977). However, other basic parameters such as the fluxes of momentum and total energy are surprisingly insensitive to the bulk speed, particularly if disturbed data (resulting from "mixing" by solar activity related transients) are excluded. In current theoretical models of solar wind acceleration these parameters are normally very sensitive to any variation in the boundary conditions (see, e.g., the paper by Leer, at this conference). Therefore the obvious lack of speed dependence in the actually observed parameters appears to be of particular significance.

The long term variations of the "average" solar wind were also determined. We confirm the result from earlier work (Bame et al., 1976) concerning the definite modulation of the number and size of high speed streams during the solar cycle. This leads to a distinct modulation of the average flow speed as already reported by Feldman et al. (1978). Our study also yields numerical estimates of quantities involving the particle densities, which have always been a problem in the past. We find that the modulations in the years from 1974 to 1982 (which include transitions through solar activity minimum as well as maximum) are also distinct though only minor. The proton flux, e.g., did not vary by more than $\pm$ 15 %. The increasing number of interplanetary shocks and other disturbances due to increasing solar

activity since 1977 did not at all influence the solar rotation averages nor did they cause any enhanced scatter. This means that even huge deviations from the average often caused by interplanetary shock waves are compensated on a rather short term basis, i.e. within one solar rotation. Furthermore, we find it noteworthy that at times of maximum solar activity both the particle flux and the total energy deposited in the solar wind go through a minimum. There is also a definite modulation of the average α-particle content (confirming and extending the work by Feldman et al., 1978), which is most pronounced in the low speed wind. However, one should keep in mind that all these results may be valid only for a rather limited region of the heliosphere, since they were achieved from spacecraft moving only close to the ecliptic plane.

Finally I want to stress again the significance of certain deviations from the average. Of course there are the wellknown though not at all well understood interplanetary disturbances following solar transients such as flares and eruptive prominences. Apart from those even the "normal" acceleration mechanisms of the solar wind may eventually become dramatically changed as was demonstrated here. The existence of such strange though rare excursions from the average has certainly to be taken into account in any theory of solar wind expansion.

References

Bame, S.J., J.R. Asbridge, W.C. Feldman, and J.T. Gosling, Solar Cycle Evolution of High Speed Solar Wind Streams, Astrophys. J. 207, 977, 1976.

Bohlin, D., An observational definition of coronal holes, in Coronal Holes and High Speed Wind Streams, edited by J. Zirker, p. 27, Colorado Associated University Press, Boulder, 1977.

Borrini, G., J.T. Gosling, S.J. Bame, W.C. Feldman, and J.M. Wilcox, Solar wind helium and hydrogen structure near the heliospheric current sheet: a signal of coronal streamers at 1 AU, J. Geophys. Res., 86, 4565, 1981.

Burlaga, L.F., N. Ness, F. Mariani, B. Bavassano, U. Villante, H. Rosenbauer, R. Schwenn, and J. Harvey, Magnetic fields and flows between 1 and 0.3 AU during the primary mission of Helios 1, J. Geophys. Res., 83, 5167, 1978.

Burlaga, L.F., A.J. Hundhausen, and Xue-Pu Zhao, The coronal and interplanetary current sheet in early 1976, J. Geophys. Res., 86, 8893, 1981.

Coles, W.A., and B.J. Ricket, JPS observations of the solar wind speed out of the ecliptic, J. Geophys. Res., 81, 4797, 1976.

Denskat, K.U., Untersuchung von Alfvénischen Fluktuationen im Sonnenwind zwischen 0,29 AE und 1,0 AE, Dissertation at the Technische Universität, Braunschweig, 1982.

Feldman, W.C., J.R. Asbridge, S.J. Bame, and J.T. Gosling, High-speed solar wind flow parameters at 1 AU, J. Geophys. Res., 81, 5054, 1976.

Feldman, W.C., J.R. Asbridge, S.J. Bame, and J.T. Gosling, Plasma and magnetic fields from the sun, in The Solar Output and Its Variation, edited by O.R. White, p. 351, Colorado Associated University Press, Boulder, 1977.

Feldman, W.C., J.R. Asbridge, S.J. Bame, and J.T. Gosling, Long-term variations of selected solar wind properties: Imp 6, 7, and 8 results, J. Geophys. Res., 83, 2177, 1978.

Goldstein, Bruce E., and J.R. Jokipii, Effects of Stream-Associated Fluctuations Upon the Radial Variation of Average Solar Wind Parameters, J. Geophs. Res., 82, 1977.

Gosling, J.T., J.R. Asbridge, S.J. Bame, and W.C. Feldman, Solar wind stream interfaces, J. Geophys. Res., 83, 1401, 1978.

Gosling, J.T., J.R. Asbridge, S.J. Bame, W.C. Feldman, R.D. Zwickl, G. Paschmann, N. Sckopke, and C.T. Russell, A sub-alfvénic solar wind: interplanetary and megnetosheath observations, J. Geophys. Res., 87, 239, 1982.

Gurnett, D.A., and R.R. Anderson, Plasma wave electric fields in the solar wind: Initial results from Helios 1, J. Geophys. Res., 82, 632, 1977.

Hansen, R.T., S.F. Hansen, and C. Sawyer, Long lived coronal structures and recurrent geomagnetic patterns in 1974, Planet. Space Sci., 24, 381, 1976.

Holzer, T.E., Effects of rapidly diverging flow, heat addition, and momentum addition in the solar wind and stellar winds, J. Geophys. Res., 82, 23, 1977.

Hundhausen, A.J., Coronal Expansion and Solar Wind, Springer-Verlag, Berlin-Heidelberg-New York, 1972.

Hundhausen, A.J., An interplanetary view of the coronal holes, in Coronal Holes and High Speed Wind Streams, edited by J. Zirker, p. 225, Colorado Associated University Press, Boulder, 1977.

Hundhausen, A.J., Solar Activity and the Solar Wind, Rev. Geophys. Space Phys., 17, 2034, 1979.

Kopp, R.A., and T.E. Holzer, Dynamic of coronal hole regions. I. Steady polytropic flows with multiple critical points, Solar Phys., 49, 43, 1976.

Marsch, E., K.-H. Mühlhäuser, R. Schwenn, H. Rosenbauer, W. Pilipp, and F.M. Neubauer, Solar Wind Protons: Three-Dimensional Velocity Distributions and Derived Plasma Parameters Measured Between 0.3 and 1 AU. J. Geophys. Res., 87, 52, 1982a.

Marsch, E., K.H.-Mühlhäuser, H. Rosenbauer, R. Schwenn, and F.M. Neubauer, Solar Wind Helium Ions: Observations of the Helios Solar Probes Between 0.3 and 1 AU, J. Geophys. Res., 87, 35, 1982b.

Montgomery, M.D., Solar wind observations throughout the heliosphere. In: Physics of Solar Planetary Environments, Ed. D.J. Williams, AGU Publ., p. 319, 1976.

Pizzo, V., R. Schwenn, E. Marsch, H. Rosenbauer, K.-H. Mühlhäuser, and F.M. Neubauer, Determination of the solar wind angular momentum flux from the Helios data - an observational test of the Weber and Davis theory, submitted to Astrophys. J., 1982.

Porsche, H., General Aspects of the Mission Helios 1 and 2, J. Geophys., 42, 551, 1977.

Rosenbauer, H., R. Schwenn, E. Marsch, B. Meyer, H. Miggenrieder, M.D. Montgomery, K.-H. Mühlhäuser, W. Pilipp, W. Voges, and S.M. Zink, A survey of initial results of the Helios plasma experiment, J. Geophys. 42, 561, 1977.

Schwenn, R., H. Rosenbauer, H. Miggenrieder: Das Plasmaexperiment auf Helios (E1), Raumfahrtforschung 19, 226, 1975.

Schwenn, R., H. Rosenbauer, H. Miggenrieder, and B. Meyer, Preliminary results of the Helios plasma experiment. In: Space Research XVI, Ed. M.J. Rycroft, Akademieverlag, p. 671, 1976.

Schwenn, R., H. Rosenbauer, and K.-H. Mühlhäuser, The Solar Wind during STIP II Intervall: Stream Structures, Boundaries, Shocks and other Features as Observed by the Plasma Instruments on Helios-1 and Helios-2, Proceedings of COSPAR Symposium B, M.A. Shea, D.F. Smart, S.T. Wu (Ed.), AFGL-TR-77-0309 Special reports, No 209, 351, 1977.

Schwenn, R., M.D. Montgomery, H. Rosenbauer, H. Miggenrieder, K.-H. Mühlhäuser, S.J. Bame, W.C. Feldman, and R.T. Hansen, Direct observations of the latitudinal extent of a high speed stream in the solar wind, J. Geophys. Res., 83, 1011, 1978.

Schwenn, R., Solar wind and its interaction with the magnetosphere: measured parameters, Adv. Space Res., 1, 3, 1981.

Schwenn, R., K.-H. Mühlhäuser, and H. Rosenbauer, Two States of the Solar wind at the Time of Solar Active Minimum, I. Boundary Layers between Fast and Slow Streams, in "Solar Wind 4", H. Rosenbauer, Ed., MPAE-W-100-81-31, Report of the Max-Planck-Institut für Aeronomie, F.R.Germany, 1981a.

Schwenn, R., K.-H. Mühlhäuser, E. Marsch, and H. Rosenbauer, Two States of the Solar Wind at the Time of Solar Activity Minimum, II. Radial Gradients of Plasma Parameters in Fast and Slow Streams, in "Solar Wind 4", H. Rosenbauer, Ed., MPAE-W-100-81-31, Report of the Max-Planck-Institut für Aeronomie, F.R.Germany, 1981b.

THE RADIAL EVOLUTION OF THE SOLAR WIND, 1-10 AU

P. R. Gazis and A. J. Lazarus
Center for Space Research and Department of Physics,
Massachusetts Institute of Technology
Cambridge, MA 02139

ABSTRACT

We review the interplanetary plasma and magnetic field observations from 1 to 10 AU. Over this distance 1) no clear reduction in average speed is seen, the range of wind speeds becomes smaller though high speed streams are still observed; 2) the density, temperature and magnetic field profiles become dominated by the large values seen in the "co-rotating interaction regions"; 3) the temperature falls more slowly than would be expected from a simple, adiabatic model; 4) co-rotating shocks appear beyond ~3 AU in Voyager data as opposed to beyond ~1.5 AU in the Pioneer data; 5) reverse shocks appear later than forward shocks: reverse shocks do not begin to appear until ~4 AU; 6) reverse shocks appear to decay more rapidly than forward shocks. No clear effect due to interaction with the interstellar medium has been seen in this radial range.

Solar Wind Bulk Parameters

In this paper we shall discuss observations of the the solar wind between 1 and 10 AU. The data were taken by the plasma science experiment aboard the Voyager 1 and 2 spacecraft between day 260 of 1977 and day 200 of 1980. Data taken by the MIT IMP plasma experiment aboard the IMP 8 spacecraft at 1 AU during the same time period were used to enable us to distinguish between radial and temporal variations in the solar wind.

Figure 1 shows solar wind bulk parameters observed by Voyager 1 at 1.3 and at 5.8 AU. One-hour averages of proton bulk velocity, number density, and temperature are plotted against time for two solar rotations. The density has been multiplied by heliocentric distance squared to account for an assumed radial expansion.

The velocity trace at 1.3 AU shows the characteristic pattern of high and low speed streams in the solar wind. Four high speed streams are observed in this time period, or two streams per solar rotation. The velocity varies smoothly; there are no signs of co-rotating shocks. (The apparent velocity jump on day 287 does not have a correlated density or temperature jump and is not a shock. There may be a shock on day 300, but it does not recur in the next solar rotation and thus is not a long-term stream-associated event.) At this heliocentric distance, the velocity and density are almost anticorrelated, as if the solar wind mass flux were remaining constant in time. This type of behavior has been observed from the Helios spacecraft at a smaller heliocentric distance. There is also a correlation between velocity and temperature. These correlations will be discussed at greater length later.
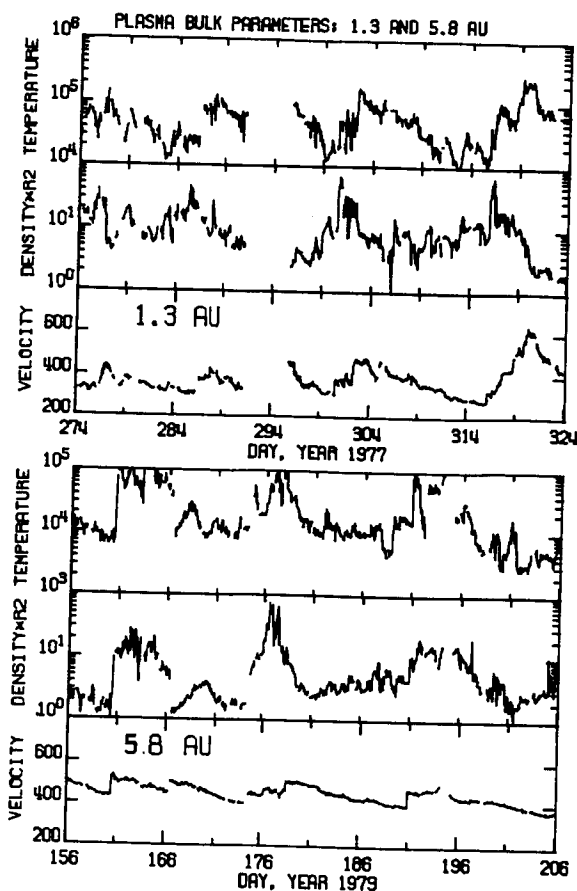
Figure 1: One-hour averages of the solar wind bulk velocity, density, and proton temperature observed from Voyager 1 are plotted against time for two solar rotations at 1.3 AU and at 5.8 AU. The density has been multiplied by heliocentric distance squared to account for an assumed radial expansion.
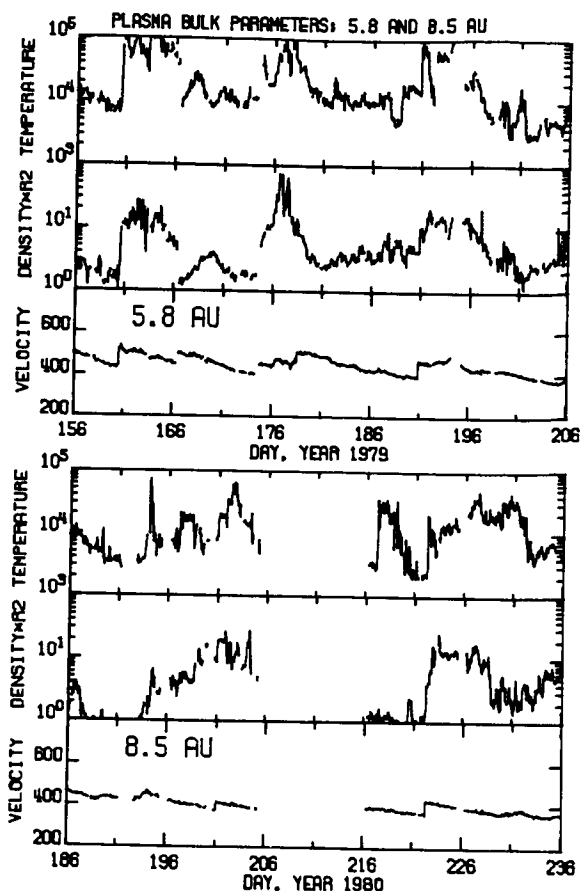
Figure 2: The solar wind bulk velocity, density, and proton temperature plotted against time for two solar rotations at 5.8 AU and at 8.5 AU. Again, the density has been multiplied by the square of heliocentric distance. The top three panels are identical with the bottom three panels of Figure 1.

At 5.8 AU, the character of the solar wind has changed markedly. As at 1.3 AU, two high speed streams are observed per solar rotation, but the smoothly varying velocity profile that was observed at 1.3 AU has been replaced by a new pattern of interaction regions bounded by shocks as was observed by the Pioneer spacecraft [Smith and Wolfe, 1976]. The shocks are observed on days 161, 167, 174, 179, and 191. The interaction regions run from day 161 to day 167, from day 174 to day 179, and from day 191 to approximately day 199. The density and temperature are high in the interaction regions and low in the surrounding streams.

Figure 2 shows a comparison of the solar wind data taken at 5.8 AU with data taken by Voyager 1 at 8.5 AU. The top three panels are identical with the bottom panels of Figure 1.

510

At 8.5 AU, from day 216 onwards, one can see the same structure of streams separated by interaction regions as was seen at 5.8 AU. A shock on day 252, preceeds an interaction region extending from day 252 to approximatly day 263. But while the density and temperature still vary over a factor of ten or more, the range of the velocity variations observed at 8.3 AU is much reduced compared with that observed at 5.8 AU, which in turn is smaller than that observed at 1.3 AU. Furthermore, the stream structure is not always well defined. In the first half of the time period shown in the figure (from day 186 to day 206) it is possible to observe a correlated density and temperature enhancement, but the velocity structure is indistinct and it is difficult to locate the shocks. The prominence of regions of enhanced temperature and density, and hence of enhanced total pressure, is characteristic of the solar wind at these large heliocentric distances.

The first two figures showed the details of the variation of solar wind bulk parameters during a solar rotation. It is interesting to look at the variation of average solar wind parameters with heliocentric radius. Many comparisons have been made of solar wind data observed at different spacecraft at different heliocentric radii during the limited time periods surrounding spacecraft lineups [Collard and Wolfe, 1974; Smith and Wolfe, 1979; Burlaga et al, 1980; Collard et al, 1982]. One can compare data taken at different spacecraft over longer time periods by taking into account the solar wind travel time and the longitudinal separation between the two spacecraft [Gazis and Lazarus, 1982; Burlaga et al, 1983]. A better way to observe large scale radial trends in solar wind parameters is to compare solar rotation averages of solar wind data taken by two spacecraft at different heliocentric radii.

Figure 3 shows a plot of the averages of the solar wind bulk velocity, density, and proton temperature versus heliocentric radius. Each average was taken over two solar rotations. The filled symbols represent data taken by Voyager 1: the open symbols represent data taken by the IMP spacecraft over a corresponding time period, allowing for the effects of solar wind travel time and the longitudinal separation between the two spacecraft. The vertical bars represent the width of the distribution of one-hour averages of each parameter during the averaging period.

Between 1 and 10 AU, the solar wind velocity is seen to remain fairly constant. While there are minor short term fluctuations, the average velocity measured at Voyager and the average velocity measured at IMP change together, indicating that the changes are temporal rather than radial variations. The discrepancy between the average velocity seen by Voyager at 6 AU and the velocity seen at IMP over the corresponding time period is due to a large flare that was seen at Voyager near day 260 of 1979 but was not seen at IMP. This event shows up elsewhere in our data. There is certainly no sign of any long term radial acceleration or deceleration of the solar wind.

The density, N, has been multiplied by the heliocentric radius squared to account for an assumed radial expansion. The resultant quantity NR^2 remains fairly constant with heliocentric radius. There are small variations in the density seen both at Voyager and at IMP which are evidentally temporal effects. The long term decrease in density seen at Voyager is also observed
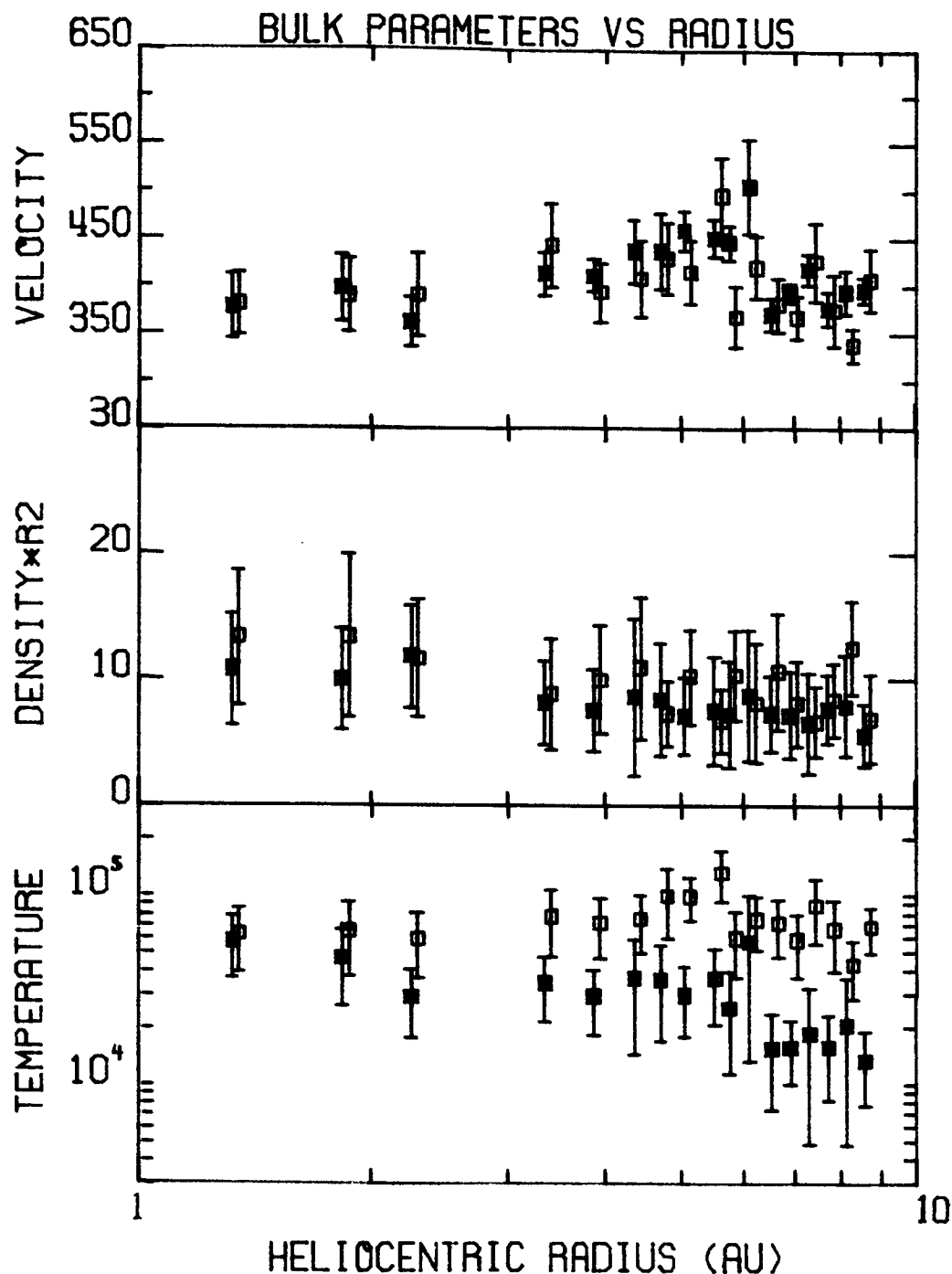
Figure 3: Two-solar-rotation averages of the solar wind bulk velocity, density, and proton temperature are plotted versus heliocentric distance. The filled symbols represent data taken by Voyager 1, the open symbols represent data taken by the IMP spacecraft over a corresponding time period, allowing for the effects of solar wind travel time and the longitudinal separation between the two spacecraft. The vertical bars represent the width of the distribution of one-hour averages of each parameter during the averaging period.

at 1 AU by the IMP spacecraft for this time period (1977 to late 1980). This decrease was also seen by the Helios spacecraft (Schwenn, 1982).

The solar wind proton temperature decreases with increasing heliocentric radius relatively slowly, approximately as $R^{-2/3}$. The temperature at 10 AU is thus a factor of ten higher than would be predicted from the temperature at 1 AU, assuming that the solar wind expanded adiabatically as a perfect gas with $\gamma=5/3$. This type of radial profile has also been observed in data taken by the Pioneer spacecraft [Smith and Wolfe, 1979; Kaiser, 1983]. The temperature decreases more or less monotonically with increasing heliocentric radius. There is no sign of any minimum, such as has been suggested might be the case due to an interaction with the interstellar medium [Holzer, 1972; Axford, 1973; Holzer, 1977]. It has been suggested by Goldstein and Jokipii [1977] that heating of the solar wind due to the interaction between high and low speed streams will produce a local minimum in solar wind temperature between 2 and 3 AU. However, the existence of such a well-defined local minimum is dependent upon the assumption that the solar wind velocity structure is very regular, which was not the case from late 1977 to late 1980.

Figure 4 is a two-dimensional contour plot showing the correlation of density versus bulk velocity. Each contour is at 50% the level of the preceeding one. The density has been multiplied by the heliocentric radius squared to account for an assumed radial expansion. Each panel is constructed from hourly averages of Voyager 1 data over two solar rotations.

The top panel of Figure 4 shows the correlation at 1.3 AU. At this heliocentric distance, the velocity appears to be anti-correlated with density. This anti-correlation is particularly evident if one examines the lower left hand boundaries of the contours.

Goldstein and Jokipii [1977] suggested that this anti-correlation between velocity and density at 1 AU would disappear at larger heliocentric radii due to the interaction between high and low speed streams in the solar wind. The second panel of Figure 4 shows the correlation at 5.8 AU. Here the range of observed velocities is much less than that observed at 1.3 AU. The anti-correlation of density and velocity observed at 1.3 AU has disappeared. Note, however, the new peak in the contours at $V\cong450$ km-sec^{-1}, and $NR^2\cong15$ cm^{-3}, which corresponds to the material at high density and intermediate velocity which has collected in the interaction regions.

The last panel of Figure 4 shows the correlation at 8.5 AU. One sees a more pronounced version of the picture seen at 5.8 AU: The velocity range is smaller still, there is no sign of an anti-correlation between density and velocity, and the peak of material at intermediate velocity and high density in the interaction regions has become clearer.

The three panels of Figure 5 show plots of the correlation between velocity and thermal speed at 1.3, 5.8 and 8.5 AU. At 1.3 AU, as shown in the top panel, the correlation between velocity and thermal speed is quite dramatic. The solar wind at 1.3 AU is seen to be maintaining a flow with an almost constant thermal Mach number, $M_t\cong8$.
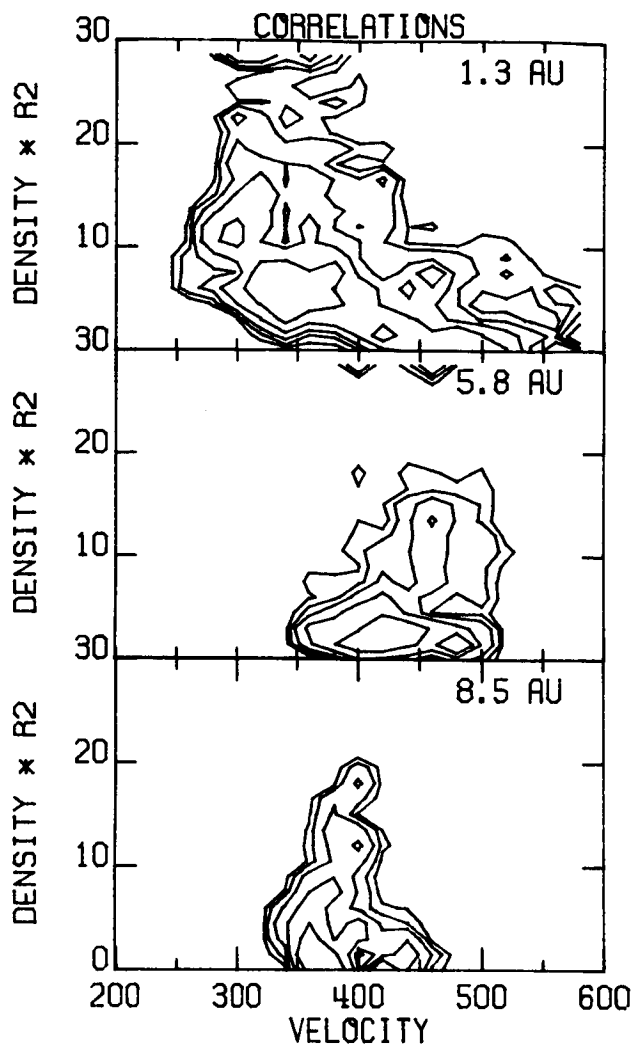
Figure 4: Two-dimensional contour plots showing the correlation of density versus bulk velocity at 1.3, 5.8 and 8.5 AU. Each panel is a plot of hourly averages of Voyager 1 data over two solar rotations. The density has been multiplied by the heliocentric radius squared to account for an assumed radial expansion.
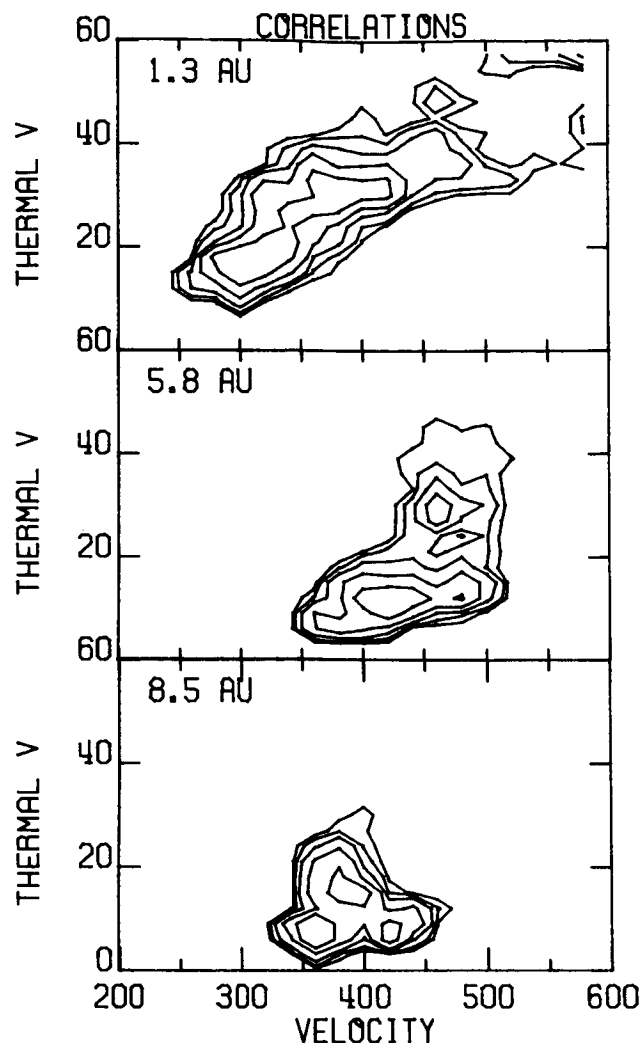
Figure 5: Two-dimensional contour plots showing the correlation of thermal speed versus bulk velocity at 1.3, 5.8 and 8.5 AU. Each panel is a plot of hourly averages of Voyager 1 data over two solar rotations.

Since the solar wind is observed to cool with increasing heliocentric radius, one might expect the thermal Mach number of the solar wind to increase with increasing heliocentric radius. As can be seen in the second panel (5.8 AU), this increase in thermal Mach number does indeed occur. In addition, a new peak has formed in the contours at an intermediate velocity $V \cong 450$ km-s^{-1}, and most probable thermal speed $W \cong 30$ km-s^{-1}. As in the last two panels of Figure 4, this new peak is due to material which has accumulated in the interaction regions.

At 8.5 AU, the thermal Mach number of the flow has increased still further, and the peak due to material in the interaction regions has become still stronger.

In summary, the average solar wind bulk velocity remains constant between 1 and 10 AU; there is no sign of any long term acceleration or deceleration of the solar wind. The average density of the solar wind varies as R^{-2}, which is consistent with uniform radial expansion; there is no sign of any lattitudinal divergence or convergence of the solar wind flow. The average proton temperature varies as $R^{-2/3}$, slower than would be expected for any adiabatic law. The radial profile of the average proton temperature shows no sign of any effect due to the interaction of the solar wind with the interstellar medium.

Co-rotating Shocks in the Solar Wind

One of the more prominent physical effects in the solar wind at large heliocentric radii is the appearance of co-rotating shocks. We made a survey of all shocks seen by the Voyager 1 spacecraft between day 260 of 1977 and day 200 of 1980. It was difficult to detect shocks with velocity jumps less than 20 km-s^{-1} reliably from our high resolution plasma data. However since the shock velocity proved to be generally of the order of twice the velocity jump, and since the observed Alfven speeds were almost always greater than 40 km-s^{-1}, we feel confident that we have observed most of the fast shocks in the solar wind. Nevertheless, this lower threshold of approximately 20 km-s^{-1} must be kept in mind when examining the data which follow.

Numerous theoretical models have been made of the solar wind stream structure and the onset and structure of co-rotating shocks in the solar wind [Hundhausen, 1973; Gosling et al, 1976; Siscoe, 1977; Pizzo, 1982]. The predicted location of shock formation generally lies between 1 and 3 AU and it is predicted that reverse shocks will form before the forward shocks.

Figure 6 shows a plot of the frequency of occurence of forward and reverse fast shocks plotted versus heliocentric radius. (At the Solar Wind V conference we showed plots of shock frequency and average parameters for all shocks. Here we show plots of data for fast shocks only) The frequency is a running average obtained from groups of twelve successive shocks. In the period during which our observations were made, the forward shocks were first observed in the region beyond 3 AU. The exact heliocentric radius at which the forward shocks began to form cannot be determined more precisely from the Voyager 1 data because the Voyager 1 plasma experiment was not operational between 2 and 3 AU. The reverse shocks form later than the forward shocks: Reverse shocks did not begin to appear in our data until the spacecraft had reached a heliocentric distance of 4 AU. The reverse shocks were only half as numerous as the forward shocks. Furthermore, the reverse shocks appear to "disappear" sooner than the forward shocks as they propagate outward from the sun, though this may be a consequence of our detection threshold of approximately 20 km-s^{-1}.

It is interesting to observe the radial variation of various parameters related to shock strength: Figure 7 shows a plot of the radial variation of the average of the density ratio for forward and reverse fast shocks. The
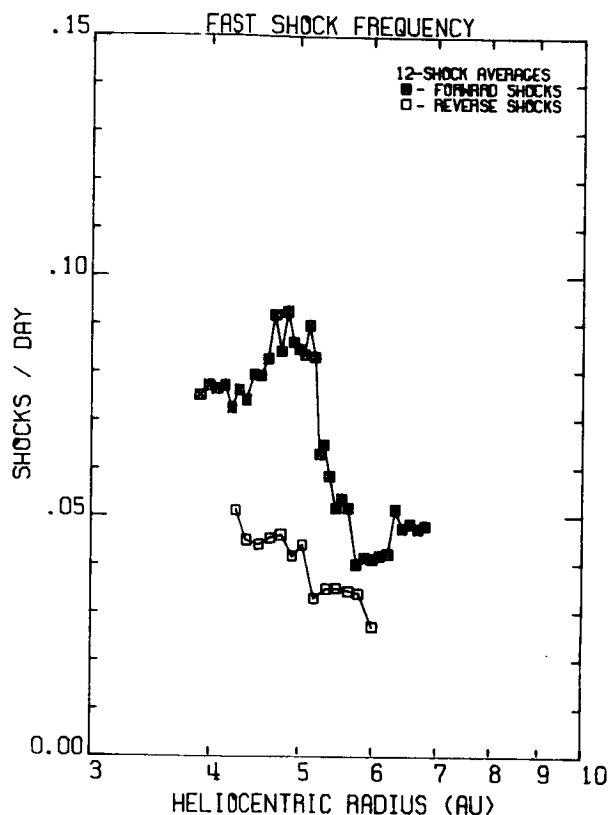
FAST SHOCK FREQUENCY

12-SHOCK AVERAGES
■ - FORWARD SHOCKS
□ - REVERSE SHOCKS

SHOCKS / DAY

HELIOCENTRIC RADIUS (AU)

FAST SHOCK DENSITY RATIO

12-SHOCK AVERAGES
■ - FORWARD SHOCKS
□ - REVERSE SHOCKS

DENSITY RATIO

HELIOCENTRIC RADIUS (AU)

Figure 6: The frequency of occurence of forward and reverse fast shocks plotted versus heliocentric radius. The frequency is a running average over groups of twelve successive shocks. The filled symbols represent averages over forward shocks, the open symbols represent averages over reverse shocks. Note the one event per solar rotation is ~0.37 events per day.
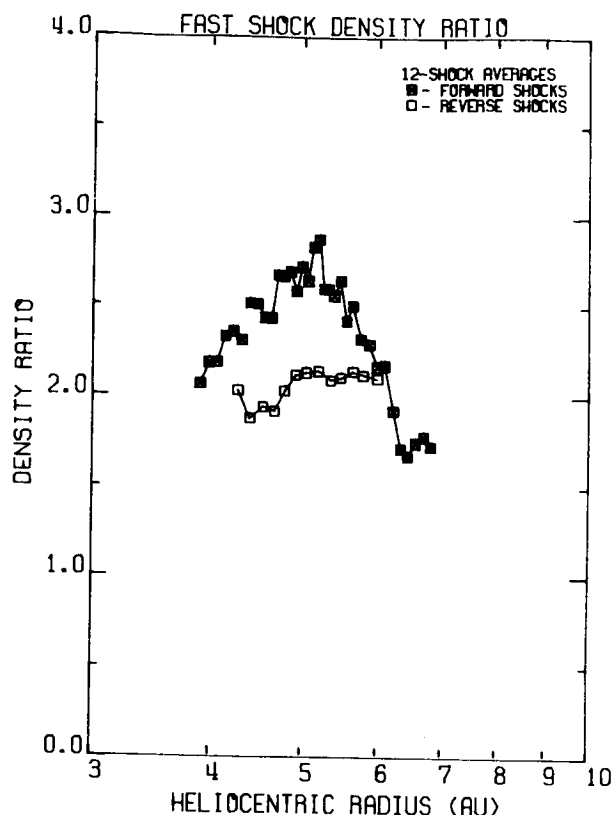
Figure 7: The radial variation of the average of the density ratio for forward and reverse fast shocks. The density has been averaged over groups of twelve successive shocks. The filled symbols represent averages over forward shocks, the open symbols represent averages over reverse shocks.

density ratio has been averaged over groups of twelve successive shocks. The average density ratio of the forward shocks does not appear to vary strongly with heliocentric distance. While the density ratio across individual shocks was observed to vary between 1 and the theoretical maximum of 4, the twelve-shock-average density ratio only varies between 1.7 and 3. The average density ratio of the reverse shocks also does not appear to depend upon heliocentric distance. The reverse shocks are weaker on the average than the forward shocks. While the density ratio across individual reverse shocks also was observed to vary between 1 and 4, the average density ratio across the reverse shocks remains in the vicinity of 2.

Figure 8 shows a plot versus heliocentric distance of twelve-shock running averages of the velocity jump across forward and reverse fast shocks. As in Figure 7, the forward shocks are once more seen to be stronger than the reverse shocks. The velocity jump across the forward shocks is larger, and
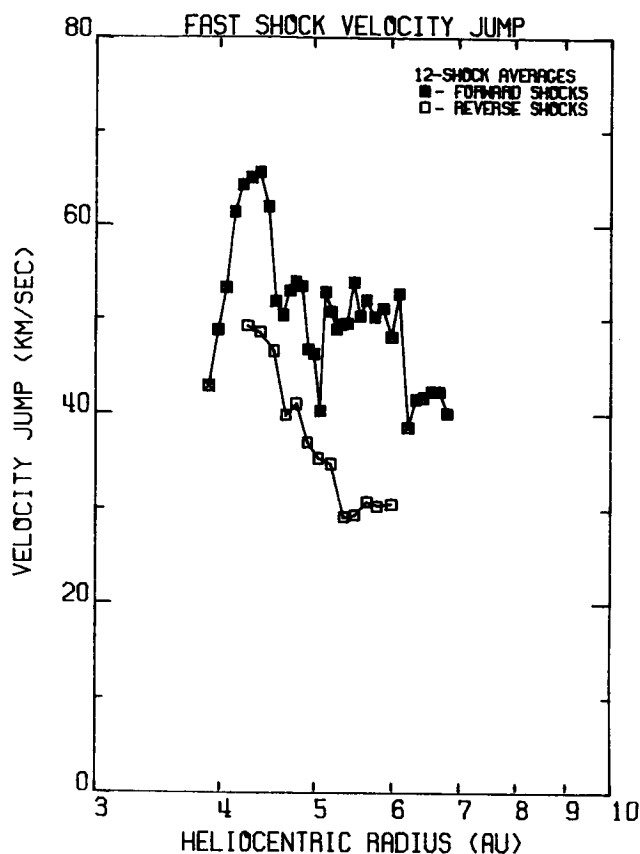
Figure 8: The radial variation of the average of the velocity jump across the shocks for forward shocks and reverse fast shocks. The shock velocity jump has been averaged over groups of twelve successive shocks. The filled symbols represent averages over forward shocks, the open symbols represent averages over reverse shocks.
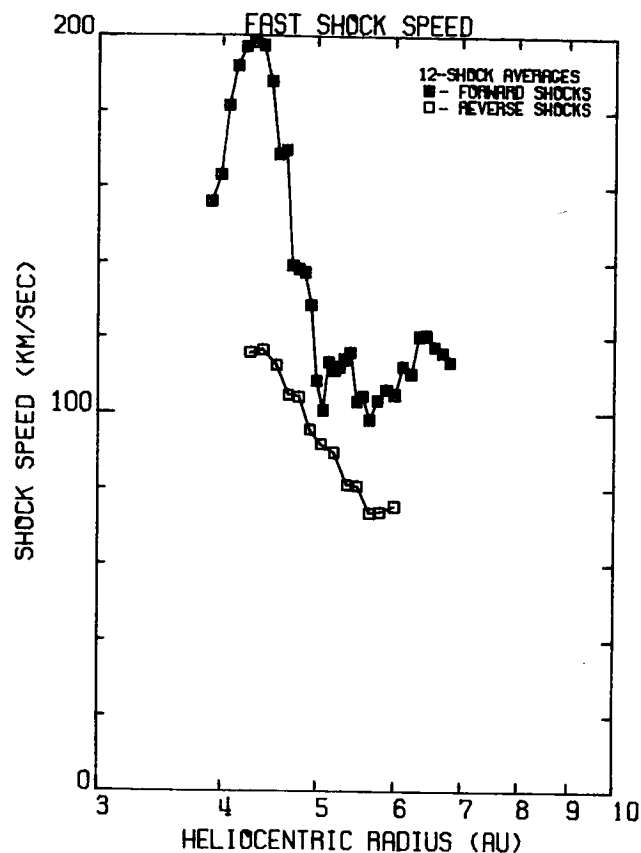
Figure 9: The radial variation of the average of the shock speed for forward shocks and reverse fast shocks. The shock speed is measured relative to the unshocked medium. The shock speed has been averaged over groups of twelve successive shocks. The filled symbols represent averages over forward shocks, the empty symbols represent averages over reverse shocks.

decreases more slowly with increasing distance than does the velocity jump across the reverse shocks.

Since we measure the vector velocities and magnetic fields before and after each shock, there are a number of means by which we can attempt to determine the shock speeds. Figure 9 shows a plot of the twelve shock running average of the shock speeds for forward and reverse fast shocks plotted versus heliocentric distance. In view of the previous results, it is not surprising to note that the forward shocks are faster and remain faster longer than the reverse shocks.

Figure 10 shows a schematic representation of the velocity profile across an interaction region. The top panel shows the velocity profile of an

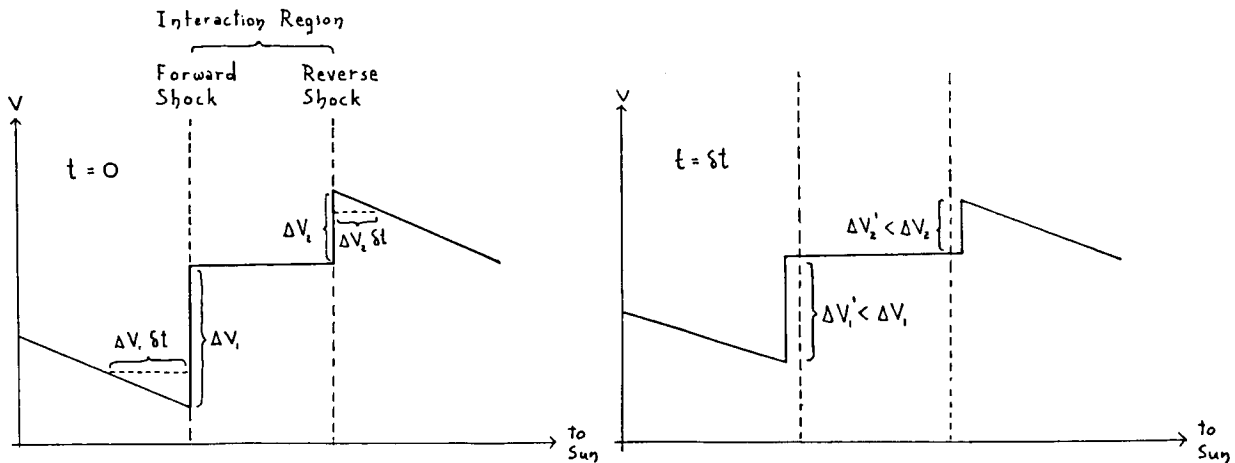## Schematic Representation of an Interaction Region

Figure 10: A schematic representation of the velocity profile across an interaction region. The top panel shows the velocity profile of an interaction region near the sun, the lower panel shows the velocity profile of the same interaction region at a larger heliocentric radius.

interaction region near to the sun, the lower panel shows the velocity profile of the same interaction region at a larger heliocentric distance. As can be seen, there are two competing processes which conspire to reduce the velocity jump across the shocks which bound the interaction regions as they are convected outward from the sun: First, the low speed material in the region which preceeds the interaction region and the high speed material in the region which follows the interaction region will be overtaken by or will overtake, respectively, the interaction region as the interaction region is convected outwards from the sun. Second, the shocks which bound the interaction region are themselves propagating into the regions outside the interaction region. But since the regions preceeding and following the interaction region contain velocity gradients, both of these effects will cause the velocity jump across the boundaries to be reduced. It is easy to see that those shocks which happen to form with a larger velocity jump will retain a larger jump than those shocks which form with a smaller velocity jump.

In summary, we observed that in our data, forward co-rotating shocks formed earlier than did the reverse co-rotating shocks: at a heliocentric distance of 2-3 AU as opposed to ≅4 AU. In many senses the forward shocks were 'stronger' than the reverse shock. The forward shocks had a larger density ratio than the reverse shocks: 3 as opposed to 2. The forward shocks were faster and had a higher velocity jump than the reverse shocks. The forward shocks were seen to occur almost twice as frequently as the reverse shocks. Finally, the forward shocks appeared to last longer than did the reverse shocks, though this observation may be due to selection effects. The reverse shocks may be becoming sufficiently weak by the end of our survey so that some of them fall below our detection threshold.

518

References

Axford, W. I., The interaction of the interstellar medium with the solar wind, Space Sci. Rev., 14, 582, 1973

Burlaga, L., Lepping, R., Armstrong, T., Goodrich, C., Sullivan, J., Gurnett, D., Kellogg, P., Mariani, F., Neubauer, F., Rosenbauer, H., and Schwenn, R., Interplanetary particles and fields November 22 to December 6, 1977, Helios, Voyager, and Imp observations between 0.6 and 1.6 AU, J. Geophys. Res., 85, 2227, 1980

Burlaga, L. J., Schwenn, R.,and Rosenbauer, H., Dynamical evolution of interplanetary fields and flows between 0.3 and 10 AU: entrainment, (submitted to J. Geophys. Res.), 1983

Collard, H. R., and Wolfe, J. H., Radial gradient of solar wind velocity from 1 to 5 AU, Solar Wind 3, ed. by C. T. Russel, p281, U. of California press, Los Angeles, 1974

Collard, H. R., Mihalov, J. D., and Wolfe, J. H., Radial variation of the solar wind speed between 1 and 15 AU, J. Geophys. Res., 87, 2203, 1982

Gazis, P. R., and Lazarus, A. J., Voyager observations of solar wind proton temperature: 1-10 AU, Geophys. Res. Lett., 9, 431, 1982

Goldstein, B. E., and Jokipii, J. R., Variation of solar wind parameters, J. Geophys. Res., 82, 1095, 1977

Gosling, J. T., Hundhausen, A. J., and Bame, S. J., Solar wind stream evolution at large heliocentric distances: experimental demonstration and test of a model, J. Geophys. Res., 81, 2111, 1976

Holzer, T. E., Interaction of the solar wind with the neutral component of the interstellar gas, J. Geophys. Res., 77, 5407, 1972

Holzer, T. E., Neutral hydrogen in interplanetary space, Rev. of Geophys. and Space Sci., 15, 467, 1977

Hundhausen, A. J., Nonlinear model of high-speed solar wind structure beyond 1 AU, J. Geophys. Res., 78, 1528, 1973

Kaiser, S., The far reaches of the solar wind: Pioneer 10 and Pioneer 11 plasma results, (submitted to Astrophs. J.), 1983

Pizzo, V., A three dimensional model of corotating streams in the solar wind. 3. Magnetohydrodynamic streams, J. Geophys. Res., 87, 4347, 1982

Schwenn, R., The "average" solar wind in the inner heliosphere: structure and slow variations, Solar Wind V conference, Woodstock, Vt., 1982

Siscoe, G. L., Three-dimensional aspects of interplanetary shock waves, J. Geophys. Res., 81, 6235, 1977

Smith, E. J., and Wolfe, J. H., Fields and plasmas in the outer solar system, Space Sci. Rev., 23, 217, 1979

SPATIAL DEPENDENCES IN THE DISTANT SOLAR WIND: PIONEERS 10 & 11

Edward J. Smith
Jet Propulsion Laboratory
Pasadena, CA   91109

and

Aaron Barnes
Ames Research Center
Moffett Field, CA   94035

ABSTRACT

Pioneer 10, 11 observations of the solar wind and magnetic field between 1 and 20 AU are reviewed. Spatial dependences, which are emphasized, must be inferred in the presence of large temporal variations including solar cycle effects. The separation of spatial and temporal dependences is achieved principally through the use of multipoint observations including baseline measurements at 1 AU. Measurements of the solar wind parameters (radial speed, flux, proton temperature) and of the magnetic field magnitude and components are compared with two theories, the Parker theory which assumes radial, azimuthally symmetric flow and the Goldstein-Jokipii theory which includes effects associated with stream-stream interactions. The observed radial gradients in the proton density and velocity and the magnetic field are consistent with the Parker model. The temperature falloff is not adiabatic which reveals the strong heating effect of stream interactions. The second order effects anticipated by the Goldstein-Jokipii model are obscured to a large extent by the much larger time variations. However, they cannot be present to the extent implied by the specific input conditions assumed in their numerical model near the sun which correspond to overly strong streams. A qualitative dependence of field magnitude on heliomagnetic latitude, i.e., referred to the observed location of the heliospheric current sheet, has been derived. The field strength has been found to decrease with distance from the current sheet. The identification of effects of the interstellar gas, e.g. mass loading, has been made difficult by the time variations and by the continuing strong influence of stream-stream interactions.

Introduction

The solar wind conferences come at convenient intervals for reviewing progress in many research areas, among them our understanding of heliospheric structure. This article is a review of Pioneer 10, 11 observations of the solar wind and magnetic field in the outer heliosphere. Pioneer 10 is now beyond 25 AU and is proceeding in the general direction of the tail of the heliosphere. Pioneer 11, after having spent several years crossing the solar system enroute to Saturn from Jupiter, is now beyond 10 AU and is travelling toward the nose of the heliosphere. This enormous extension of the limits of observation over the past decade is revealing how the heliospheric properties vary with distance from the sun.

Knowledge of spatial dependences, however, must be extracted from large temporal variations occurring over a broad range of time scales. During the time taken for the Pioneers to reach their current locations, the solar cycle has varied between the minimum in 1974 to the recent maximum of 1979. The source regions on

the sun from which the solar wind originates appear to have changed significantly, e.g., from large polar coronal holes to the lower latitude sites of flares and coronal transients. These solar cycle changes may have resulted in changes on shorter time scales that are qualitatively different during the minimum and maximum in solar activity. Various attempts are being made to cope with time variations in an effort to distinguish them from spatial dependences. When this separation is successful, useful information is obtained on both types of dependences.

Scientific interest in large scale spatial dependences derives from attempts to understand the evolution of the solar wind, its interaction with the local interstellar gas and its effect on galactic cosmic rays. As the solar wind propagates into the outer heliosphere, it not only expands radially but is strongly affected by the interaction between fast and slow streams (Hundhausen, 1973; Smith and Wolfe, 1976; Hundhausen and Gosling, 1976; Smith and Wolfe, 1977; Dryer et al., 1978). The two Pioneers are now reaching distances at which the solar wind interaction with the inflowing interstellar neutrals might become evident. An understanding of how the properties of cosmic rays are modified when they reach the inner heliosphere depends on the medium through which they have travelled (Fisk, 1979; McDonald et al., 1979; Van Allen, 1980; Webber and Lockwood, 1981; McKibben et al., 1982).

The results presented in this review complement earlier Pioneer reports on spatial dependences, some of them prepared in conjunction with past solar wind conferences (Collard and Wolfe, 1974; Smith, 1974; Parker and Jokipii, 1976; Rosenberg et al., 1978; Mihalov and Wolfe, 1978; Smith and Wolfe, 1979; Collard et al., 1982). The results are also complementary to corresponding studies based on Voyagers 1 and 2 (Gazis and Lazarus, 1982, 1983; Burlaga et al., 1982).

Theoretical Background

The simplest, physically reasonable model against which to compare the observations is based on spherically symmetric, time stationary solar wind flow (Parker 1963, Hundhausen 1972). The solar wind properties are derived from the hydrodynamic equations, which express the conservation of flux of mass, momentum and energy, combined with Maxwell's equations. These equations lead to expressions for radial gradients in the solar wind flux and in the magnetic field components. The behavior of the temperature, which is only one term among several in the energy equation, is generally more complicated. The assumption that the solar wind expands adiabatically leads to the simplest dependence of temperature on distance (Parker, 1963) although other formulations exist that include the effect of thermal conduction (see review in Hundhausen, 1972). This model involves serious limitations, specifically the complete disregard of those dependences that lead to solar wind streams and their interactions.

Some of these basic limitations are overcome in the model of Goldstein and Jokipii (1977). They write the hydrodynamic equations in a general form in which longitudinal dependences and time variations are explicitly included. Their expressions for the radial gradients of the principal conserved parameters then show their dependence on space and time. The equations of motion are solved numerically for several different cases corresponding to different solar wind properties at a base level above the corona. In one model for a high speed stream, the speed, v, and density, n, are anti-correlated since this feature of solar wind streams is commonly observed at 1 AU. Other models involve radially symmetric but time dependent streams as well as streams in which n and v are uncorrelated. Basic solar wind

parameters derived numerically from the model are then averaged over a solar rotation and their evolution with radial distances studied. In this way, the effect of stream-stream interactions on the radial gradients is exhibited.

One of the principal limitations associated with the Goldstein-Jokipii model is the extent to which the solar wind is driven by fast streams. The specific values for their input functions correspond to very strong streams with the consequence that the interaction effects are exaggerated. For example, compression ceases at ~ 5 AU and is followed at greater distances by a re-expansion of the solar wind (an effect referred to as a "rebound"). The data to be presented below do not show such behavior, certainly not at distances of 5 AU, so that the scale on which stream effects are occurring is significantly greater than implied by the model. Nevertheless, the model is useful in assessing the qualitative effects of stream-stream interactions on the radial gradients and provides a good baseline against which to compare the observations.

The predictions of these two models are summarized in Table 1. The gradients of principal interest are those involving the radial component of the solar wind velocity, v_r, the particle flux, nv_r, the isotropic temperature, T, and the radial and azimuthal field components, B_r and $B\phi$. The Goldstein-Jokipii model includes other parameters, including those representing angular momentum flux, however, they have not been compared systematically with the observations and are not included in the table.

In addition to models which deal with the evolution of the solar wind with distance, there are a number of models of the interaction of the solar wind with the inflowing interstellar gas (Axford, 1972, 1973; Holzer, 1972, 1977; Fahr et al., 1978; Wallis, 1978). The principal consequences of this interaction are charge exchange ionization of the interstellar neutrals by solar wind protons leading to so-called mass loading and a deceleration and heating of the solar wind. In face of the obvious strong effects of stream-stream interactions, the solar wind interaction with the interstellar gas has thus far received much less attention in published studies of spatial dependences.

Observations and Analysis

This section is a review of the most recent analyses of Pioneer 10, 11 observations as they pertain to spatial dependences. Most analyses have emphasized radial dependences. Suppression of longitudinal dependences, and by inference the effect of stream-stream interactions, has been attempted by averaging over an integral number of solar rotations. With few exceptions, possible latitude dependences have been ignored, presumably because the latitude differences are small compared to changes in radial distance. Care must be exercised to avoid confusing spatial with long-term temporal dependences. Multi-point observations have been used to make this distinction and to assess the extent to which time variations are present.

A study of the radial dependences of the basic solar wind parameters has recently been carried out by Kayser et al. (1983). Pioneer 10 and 11 observations of v, nv, n and T have been analyzed both separately and as a composite date set. In the following, the results obtained from the joint Pioneer 10, 11 analyses are presented. In general, these results are in good agreement with those resulting from analyzing the data from each spacecraft. Least squares fits to the observations were obtained using averages over three successive solar rotations.

TABLE 1

RADIAL GRADIENTS

| PARAMETER | RADIAL DEPENDENCE | |
	PARKER	GOLDSTEIN-JOKIPII[a]
V_r	~ constant (slight increase)	slight decrease, then increase (Figure 1)
nV_r	r^{-2}	~ r^{-2} (Eq. 6)
T	$r^{-\alpha}$ $o < \alpha < 4/3$	minimum at ~ 1 AU, then increase (Figure 4)
B_r	r^{-2}	~ r^{-2} (Eq. 7)
$B\phi$	r^{-1}	$V_r B_\phi$ ~ r^{-1}, rB_ϕ: secondary maximum (Fig. 3)

a - The figures and equations in this column are to be found in the article by Goldstein and Jokipii.

The least squares fit to the solar wind speed leads to a result:

$$v \ (km \ sec^{-1}) = (468 \pm {}^{18}_{17}) \ r** \ (-0.03 \pm .02),$$

where the double star is the usual Fortran symbol for "raised to the power as follows". There is little, if any, statistically significant dependence of the solar wind speed on radial distance. The Parker theory predicts a slight increase in speed with distance as the basic acceleration associated with the conversion of thermal into convective energy asymptomatically approaches zero. The Goldstein

and Jokipii model (for the case in which v and n are anticorrelated at the source) leads to a slight decrease in v as a result of the transfer of momentum from the faster moving, but less dense, stream to the slower moving, more dense stream. Neither effect appears to be present in the observations to a significant degree. Thus, the average solar wind speed appears to be independent of distance.

Figure 1 shows the Pioneer 10 speeds averaged over intervals of three solar rotations from launch in 1972 through 1980. The solid curve represents corresponding averages from several spacecraft making simultaneous observations near 1 AU as compiled by King (1979). A preliminary attempt was made to accommodate radial
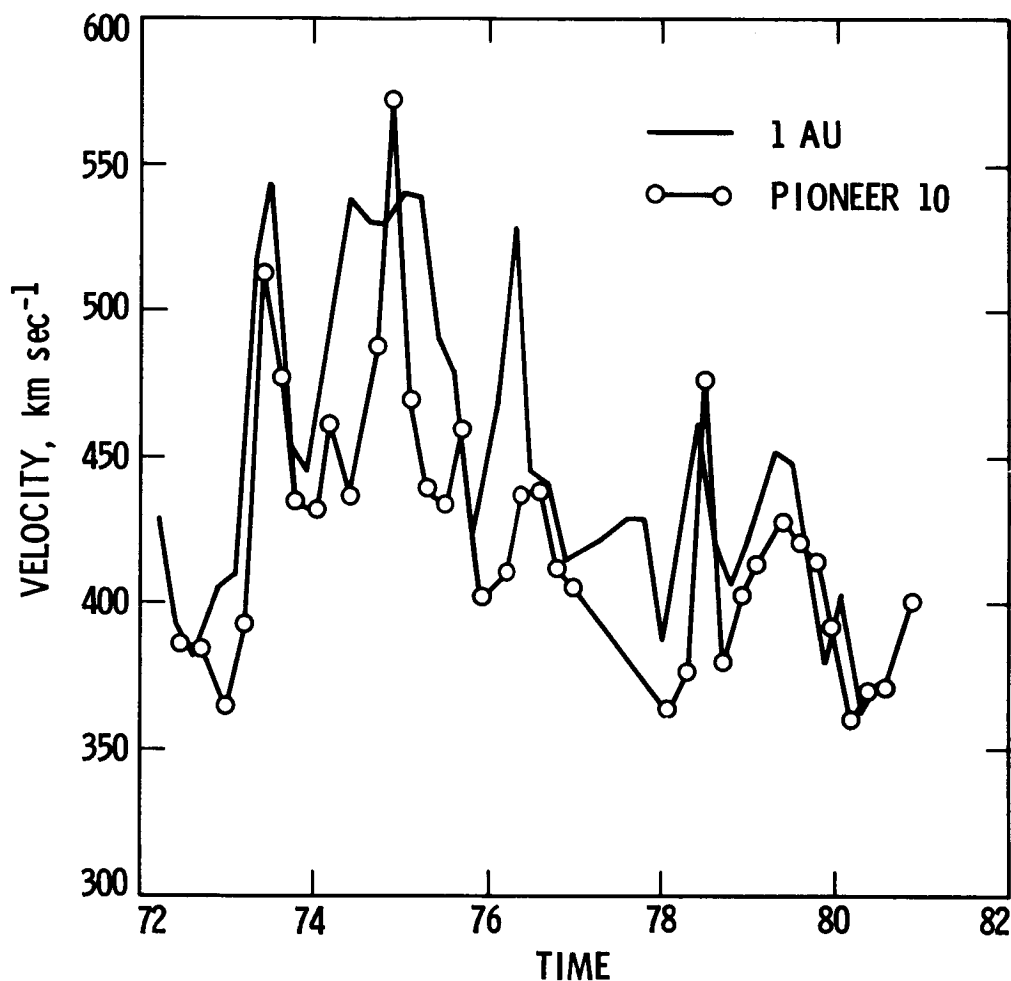

Figure 1. Solar wind speed at 1 AU and as observed by Pioneer 10. The solid line shows the variation in solar wind speed at 1 AU from 1972 (launch of Pioneer 10) to solar maximum in 1980. The well documented increase in speed during solar minimum is evident as well as the gradual decrease toward solar maximum. The open circles connected by straight lines are average Pioneer 10 speeds measured between 1 and 10 AU corotated back to 1 AU. In general, the average speed at large distances is well correlated with the solar wind speed at 1 AU. (J. A. Slavin carried out the analysis and prepared this figure.)

and azimuthal delays and to account for propagation of the solar wind from 1 AU to Pioneer. Undoubtedly, a more accurate correction for the delays is possible and desirable, but the essential features of the comparison are evident in the figure.

The figure shows the extent to which significant time variations are present. The average values vary between maximum and minimum by $\sim$ 150 km sec^{-1}. In addition to large variations from year-to-year, a secular variation is evident with high speeds prevailing near solar minimum (1974-76) and low speeds being observed near solar maximum. There is a reasonably close correspondence between the speed variations at 1 AU and at large distances, Pioneer 10 having reached 25 AU in 1982. Clearly, a small radial dependence in speed could be masked by the relatively large temporal variations.

Figure 2 is a plot of proton flux, nv, one of the parameters that is conserved in the equations of motion. A least squares logarithmic fit to these data (Kayser et al., 1983) leads to
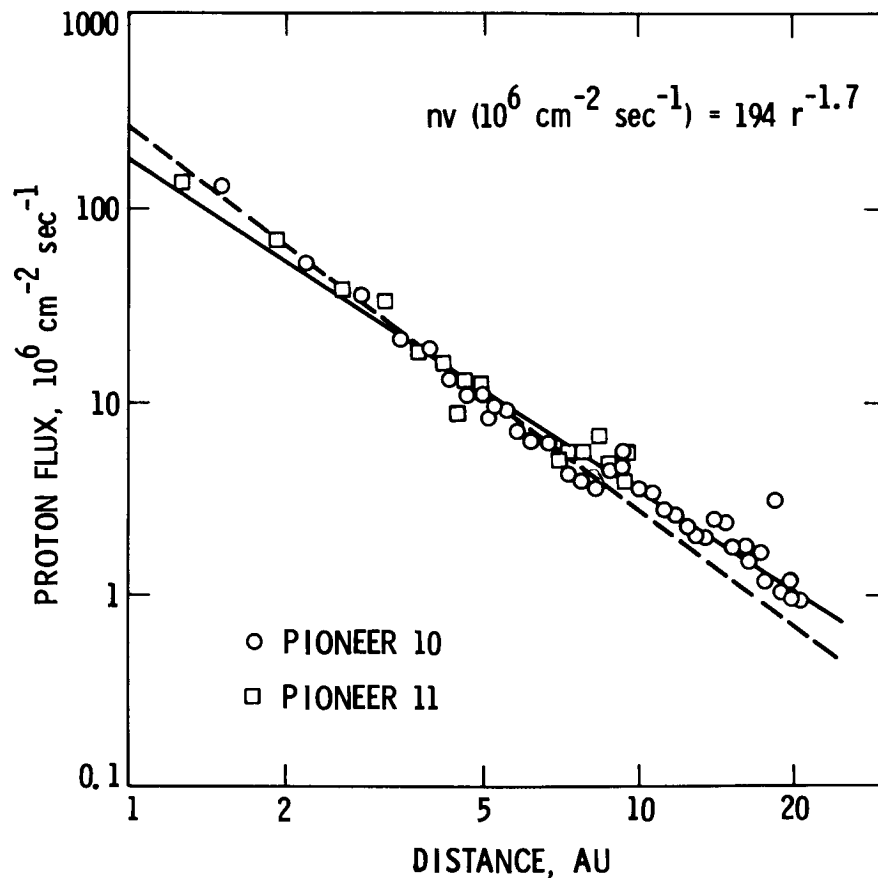
Figure 2. Solar wind proton flux as a function of radial distance from 1 to 20 AU. The flux, averaged over three successive solar rotations, is shown for both Pioneer 10 and 11. The dashed line passing through the data points corresponds to a dependence of r^{-2}. The solid line is a least squares fit to the observations. The scatter about this straight line fit appears to be substantially less than for n or v alone presumably as a consequence of the anticorrelation between n and v.

$$\text{nv } (10^8 \text{ cm}^{-2}\text{sec}^{-1}) = (1.9 \pm 0.2) \, r_{**} \, (-1.74 \pm .04).$$

Both theoretical models predict an r^{-2} dependence implying the observed decrease is less rapid than expected. This deviation is attributed to an increase in solar wind flux, specifically an increase in n since v is decreasing, during the approach to solar maximum. An analysis of n similar to that which leads to Figure 1 does reveal a significant increase in density in 1977-78 in both the 1 AU and the Pioneer data. Again, although the results appear consistent with an r^{-2} dependence if the flow had been radially symmetric, second order radial dependences could be masked by time variations. With a more careful, quantitative comparison, it might be possible to reduce this uncertainty significantly.

The radial gradient in the proton temperature is shown in Figure 3. The least squares fit to these data, obtained by Kayser et al. (1983), yields:
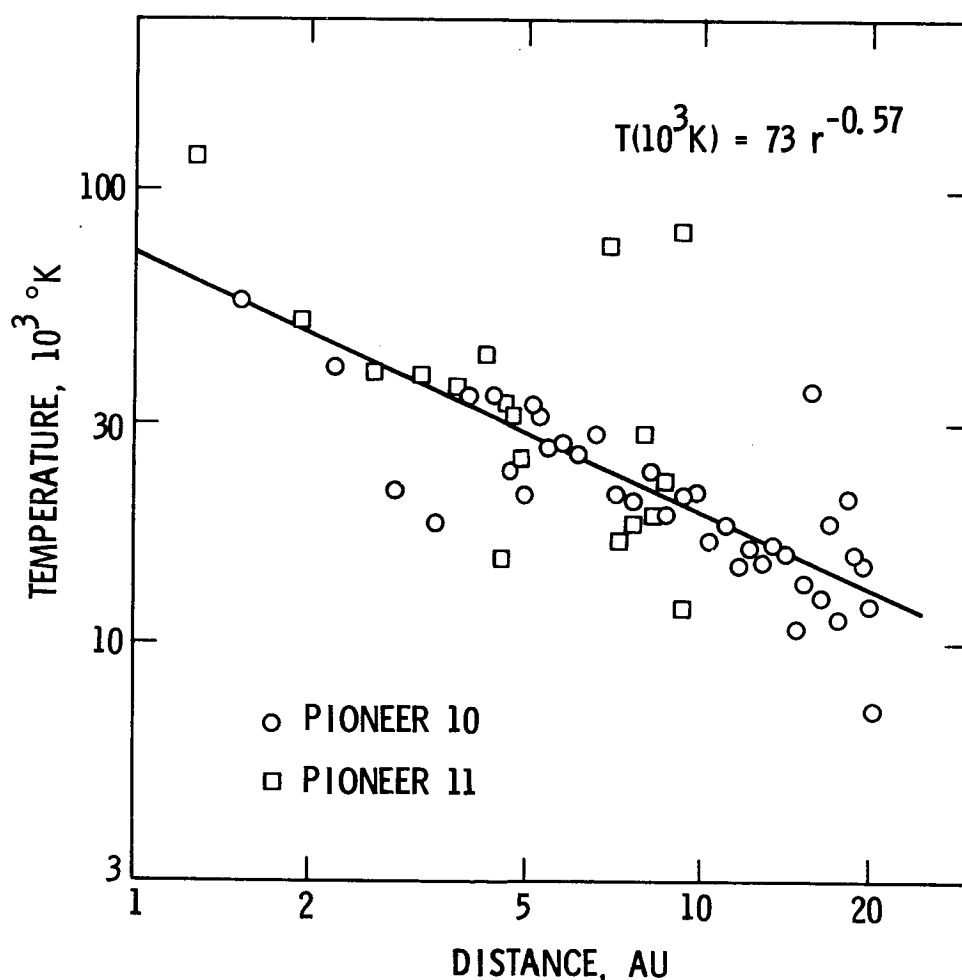

Figure 3. Proton temperature dependence on distance. The temperatures derived from both Pioneers, averaged over three solar rotations, are shown between 1 and 20 AU. The straight line is a least squares fit to the observations. A large amount of scatter is apparent in the data and seems to be correlated with simultaneous large variations in solar wind speed (shown in Fig. 1).

$$T(10^3 k) = \left(73 \pm \begin{smallmatrix} 1.1 \\ 1.0 \end{smallmatrix}\right) \ r_{**} \ (-0.57 \pm .07).$$

This result is clearly inconsistent with $r^{-4/3}$ and with a simple adiabatic expansion of the solar wind. The temperature dependence is qualitatively consistent with the Goldstein-Jokipii model in which heating is a significant accompaniment of the stream interactions. However, it does not agree quantitatively with their model which predicts an actual reversal in the gradient inside 5 AU leading to a temperature maximum near 5 AU. This feature of the model is one aspect of the solar wind being driven too hard as a result of the choice of input function.

Earlier analyses of the dependence of the magnetic field parameters on radial distance have been extended recently by Thomas et al. (1983). The field strength is a particularly appropriate parameter to study because typical interplanetary field fluctuations over intervals of minutes to hours tend to conserve B. Figure 4 shows magnetic field magnitudes from Pioneers 10 and 11 averaged over spatial intervals of 0.5 AU. The averages have been multiplied by a factor of $[(r^{-2} + r^{-4})/2]^{-1/2}$ which is appropriate to the Parker model and which adjusts the observations to the equivalent field strength to 1 AU. The least squares straight line fit implies that, on the average, the field magnitude reproduces the expected relation very closely. In addition, the average value of $\simeq$ 6 nT corresponds well with long-term averages of the field strength at 1 AU.
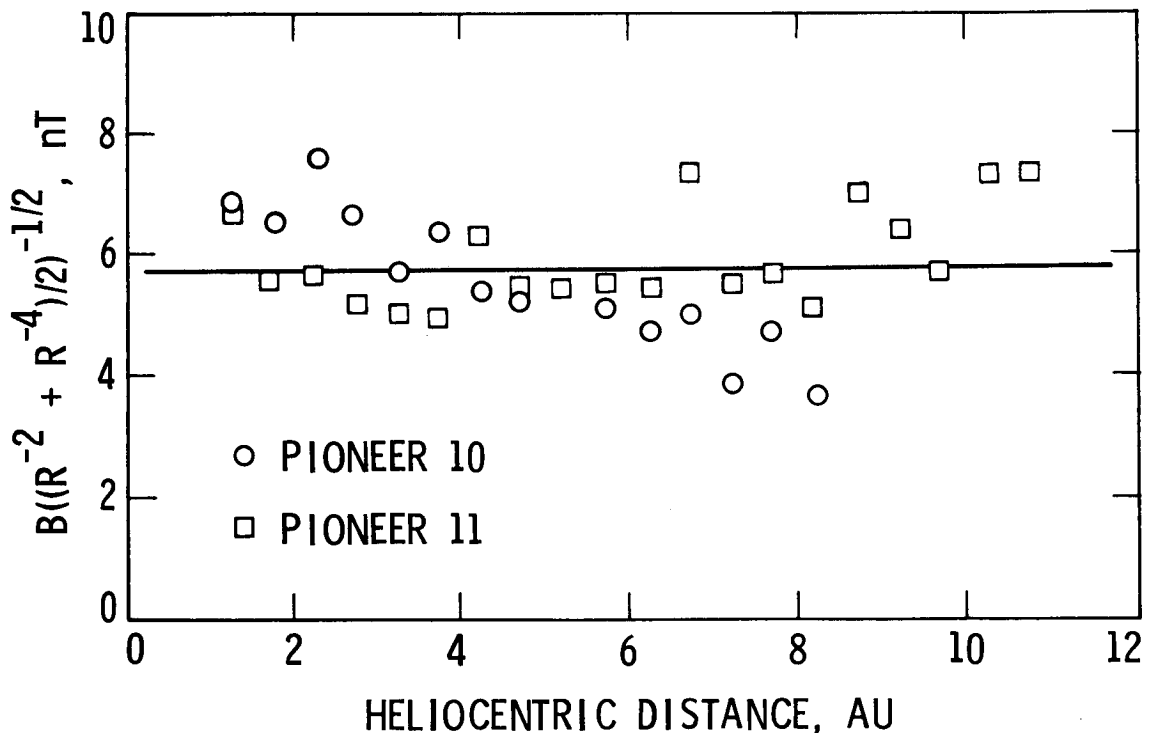
Figure 4. Interplanetary magnetic field magnitudes observed by Pioneer. The measured field strengths were averaged over successive distance intervals of 0.5 AU. They were then multiplied by a factor of $[(r^{-2} + r^{-4})/2]^{-1/2}$, derived from the Parker spiral field model, to produce the equivalent field strength at 1 AU. The values were then plotted against distance as shown. The straight line is a least squares fit to the composite data set. The absence of a significant slope shows that the decrease in B is consistent with the Parker model.

Significant departures from the average are evident in Figure 4 and these have been investigated with the results shown in Figure 5 (Slavin et al., 1983) The adjusted field magnitude from Pioneer 11 is shown as a function of time and is superposed on the annual averages as measured at 1 AU. In spite of somewhat greater variability in the Pioneer averages, the general trends and the values at 1 AU are reproduced reasonably well. The latter show the decrease in B near solar minimum, previously identified by King (1979), as well as a significant increase during the approach to solar maximum identified recently by Slavin and Smith (1983). Thus, the secular variation at 1 AU is matched by corresponding changes at large radial distances. The tendency for the field at Pioneer to be systematically less than the field at 1 AU may be attributable to a latitude dependence. This hypothesis is consistent with an analysis presented below and is presently under study.
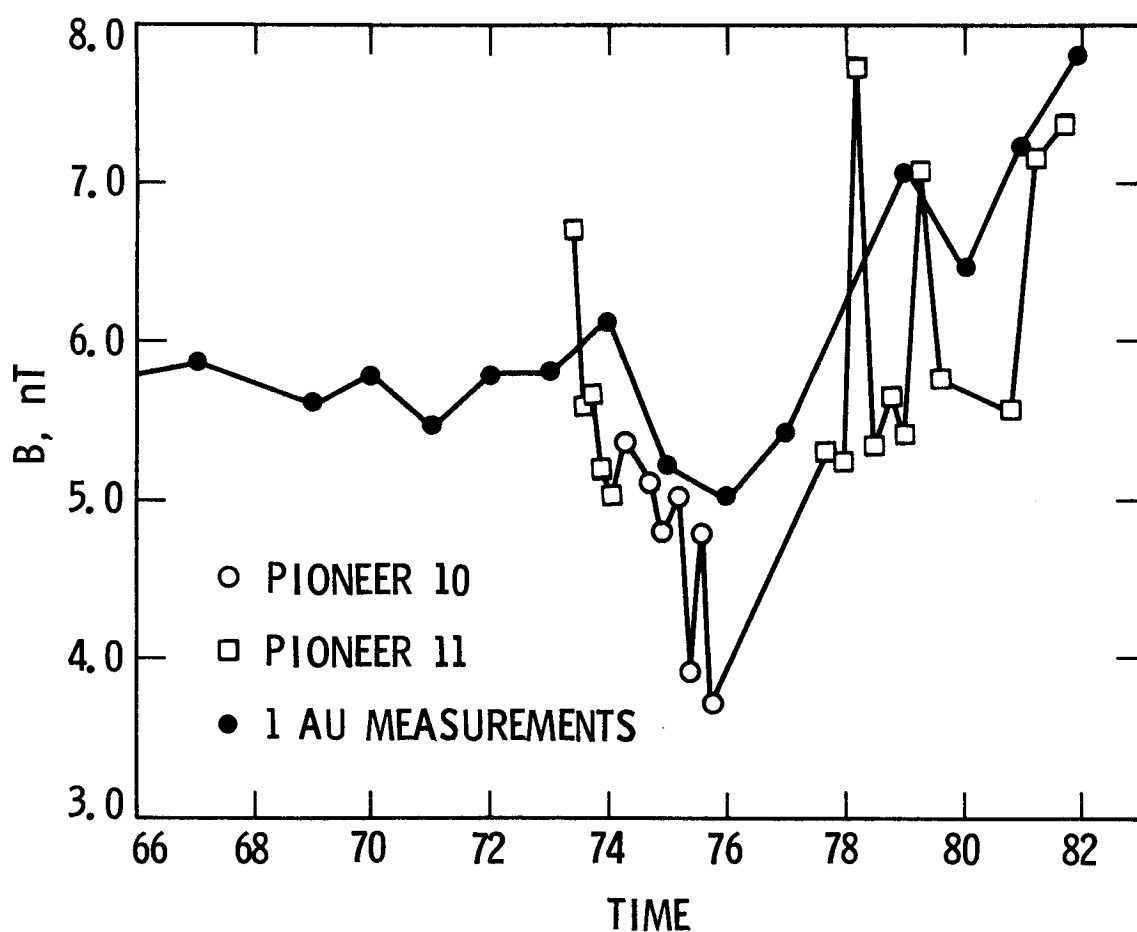

Figure 5. Variation in magnetic field magnitude at 1 AU and at Pioneer. The solid line corresponds to measured fields at 1 AU. The decrease in B near solar minimum (~ 1975) shows up at both 1 AU and at the larger distances in the Pioneer 10 and 11 data. The Pioneer field values appear to be systematically lower, a feature that is discussed in the text.

529

The azmuthal field component, B_ϕ, has also been studied in a similar analysis. Figure 6 shows values of B_ϕ, averaged over 0.5 AU intervals, after being multiplied by the corresponding radial distance. According to the Parker model, rB_ϕ should be constant, a prediction which is fulfilled very well as shown by the straight line representing a least squares fit to the observations. This result contrasts somewhat with the Goldstein-Jokipii model which for some cases implies a slightly more rapid decrease of $B\phi$ than r^{-1}. The equivalent azimuthal component at 1 AU is only about 3 nT on the average. This value is low compared to the more typical value of about $6/\sqrt{2} \simeq 4.4$ nT. This tendency is one aspect of the lower than anticipated average for B noted above and may be caused by Pioneer being persistently at a higher latitude than the spacecraft orbiting at 1 AU.
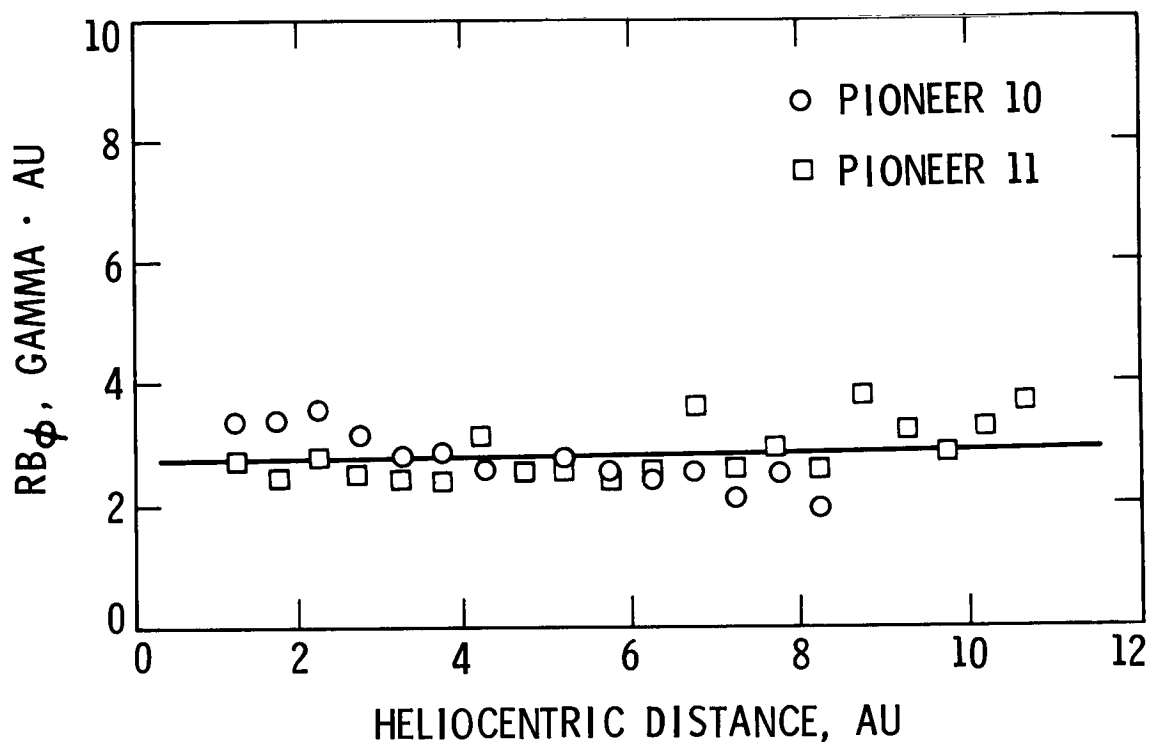

Figure 6. Azimuthal field component as a function of distance. Pioneer 10, 11 measurements of $B\phi$ were averaged over distance intervals of 0.5 AU. They were then multiplied by the average radial distance at which the data were acquired to obtain a value corresponding to the equivalent field component at 1 AU. The resulting points do not show any significant dependence on r (as attested to by the least squares straight line whose slope is approximately zero). Thus, on the average, $B\phi$ decreases as r^{-1} between 1 and 11 AU.

The radial component has been investigated and has been found to be consistent with an r^{-2} dependence as predicted by both theoretical models. The analysis of $r^2 B_r$ vs r shows much greater variability than for B or $B\phi$. Enhanced variability is attributable to B_r tending at large distance to become orthogonal to the average field direction, and, hence, susceptible to the interplanetary field fluctuations, and to the very low average values at large distances. The latitudinal or north-south field component, B_θ, has also been studied and the long-term average has been found to be zero within statistical uncertainty.

The agreement of B_r, B_ϕ, and B with the Parker model implies that, on the average, the field is along the Parker spiral. In a previous analysis, the observed field was rotated into a reference frame with one axis along the spiral direction. Histograms of the azimuth angle of the field, ϕ_B, showed a close correspondence with the two angles ($0°$ and $180°$) corresponding to the spiral from 1 to 8.5 AU and during solar minimum conditions (Thomas and Smith, 1980). The study of individual regions also showed a good correspondence with the spiral direction, especially within interaction regions.

Possible dependence of field magnitude on latitude has also been investigated by Thomas et al. (1983). Figure 7 shows the adjusted magnitude as a function of "heliomagnetic" latitude rather than heliographic latitude. Since the heliospheric current sheet (sector boundary) constitutes a basic "plane" of symmetry, the distance of the observations above or below the current sheet was considered more appropriate to a search for latitude dependences than the distance referred to the solar equator. This possibility was tested by using the sector structure, during a particularly stable interval, to obtain a qualitative measure of magnetic latitude.
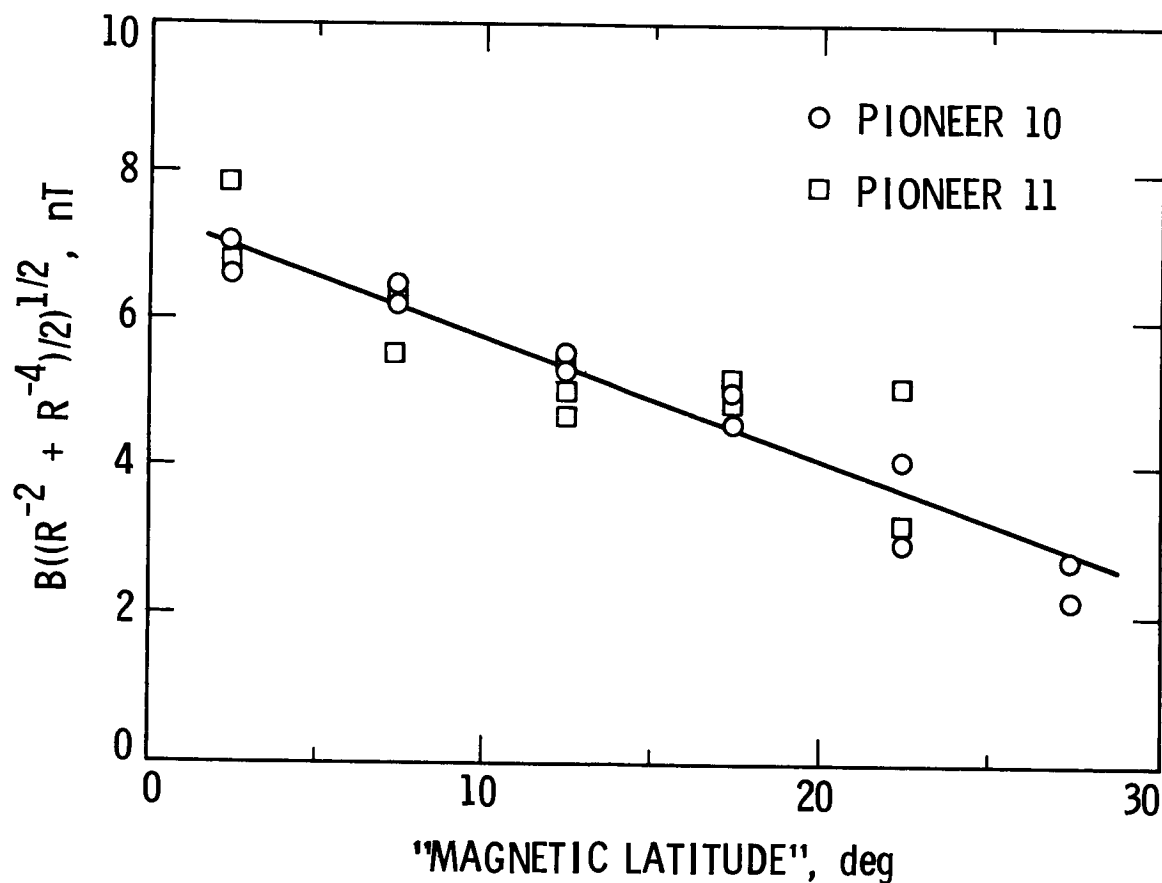
Figure 7. Interplanetary field strength as a function of heliomagnetic latitude. The adjusted magnitude of the field is plotted against a qualitative measure of the distance from the heliospheric current sheet or "magnetic latitude". The latter was basically derived from knowledge of the current sheet location (observed twice per solar rotation as a reversal in field polarity) and the assumption that the distance from the current sheet varies sinusoidally with time.

The result (Figure 7) shows a decrease in B with increasing latitude. This finding is consistent with less tightly spiraled fields at high latitude (alternatively, decreasing B_ϕ) as well as with an increase in solar wind speed with latitude (since $B_\phi = B_r \, \Omega \, r/v$). Since the current sheet (the heliomagnetic equator), is typically found inside interaction regions, which are compression regions of enhanced B, the data inside and adjacent to interaction regions were analyzed separately. The magnetic latitude effect was also found in the rarefaction regions.

Discussion

As the Pioneer observations have been extended outward, to beyond 25 AU in the case of Pioneer 10, many properties of the solar wind, averaged over one or more solar rotations, continue to agree with the simple Parker model. This result holds for the solar wind speed and proton flux and for the magnetic field magnitude and components. Although Parker pointed out the consequences of an adiabatic decrease on temperature, his analysis was based on the more general polytrope relation and he made the point that non-adiabatic behavior would not be surprising. In fact, the proton temperature is strongly affected by local heating at stream-stream interfaces.

The principal limitation on comparison between theory and observation is associated with the large time variations occurring from month-to-month, year-to-year and over the solar cycle. These variations introduce a large amount of scatter into the basic data and may be obscuring departures from the simple theory which would otherwise be apparent. The deviations from the Parker model associated with stream-stream interactions, or interactions with the interstellar gas, are clearly of low order as can be seen in the predictions of the appropriate models. Thus, although the solar wind is strongly overdriven in the Goldstein-Jokipii model, the perturbations are still relatively small. Basically, the solar wind momentum and energy fluxes are dominated by the convective terms, nmv^2 and $1/2 \, nmv^3$, on which small perturbations are superposed.

The effort to distinguish small perturbations in the presence of the large time variations has barely begun. The obvious approach is to make greater use of multipoint observations. In addition to comparisons with baseline observations near 1 AU, much more needs to be done in comparing Pioneer and Voyager observations. However, progress will inevitably depend on analyzing differences in parameters measured at two locations or differences between theory and observation. Such studies will ultimately have to face issues relating to the accuracy of the basic measurements, a problem that is undoubtedly more acute for the plasma measurements, especially n and T, than for the magnetic field measurements.

Progress in identifying the effect of the interstellar gas has been slow in the face of the continuing strong influence of stream-stream interactions. It may be that the interstellar interaction will only become evident at sufficiently large distances that the stream effects have died out. The latter is undoubtedly occurring, the most obvious evidence being the wearing away of solar wind streams as the high and low speeds are progressively eliminated. It may be that the stream effects are quenched nearer the sun during solar minimum than during solar maximum (Smith et al., 1983). Thus, the approaching minimum may provide a favorable opportunity for studying the interstellar interaction.

Another approach to discriminating against stream interactions would be to concentrate on the solar wind properties within rarefraction regions, i.e., the

trailing portions of high speed streams. It may prove simpler to identify and eliminate rarefraction effects than compression effects, especially since the former may be opposite in sense to the heating and deceleration presumably caused by the interstellar gas. Clearly, much analysis remains to be done before an assessment can be made of the extent to which the interstellar gas is affecting the solar wind properties.

An aspect of the observations that also needs more study is the nature of the correlations between the various solar wind and magnetic field parameters such as v & T, n & B, etc. (Jokipii, 1976). Such correlations, which appear to be present on different time scales, are important to studies of the internal solar wind dynamics as well as to the study of spatial dependences. Such correlations are an important aspect of the Goldstein-Jokipii model and are a potentially useful means of identifying stream interaction effects. According to the theory, they represent signatures of compression and rarefaction (including the possible rebound phenomenon).

At present we find ourselves with a network of four spacecraft proceeding into the outer heliosphere in various directions and at significantly different latitudes. A decade ago, none of us would have expected to be confronted with such a fortunate situation. However, we can expect, from this embarrassment of riches, to obtain answers in the not too distant future to many of the questions with which we are now struggling.

References

Axford, W. I., The interaction of the solar wind with the interstellar medium, Solar Wind, NASA Spec. Publ., SP-308, 609, 1972.

Axford, W. I., Interaction of the interstellar medium with the solar wind, Space Sci. Rev., 14, 532, 1973.

Burlaga, L. F., R. P. Lepping, K. W. Behannon, L. W. Klein and F.M. Neubauer, Large-scale variations of the interplanetary magnetic field: Voyager 1 and 2 observations between 1-5 AU, J. Geophys. Res., 87, 4345, 1982.

Collard, H. R., and J. H. Wolfe, Radial gradient of solar wind velocity from 1 to 5 AU, in Solar Wind Three, edited by C. T. Russell, University of California Press, Los Angeles, 1974.

Collard, H. R., J. D. Mihalov, and J. H. Wolfe, Radial variation of the solar wind speed between 1 and 15 AU, J. Geophys. Res., 87, 2203, 1982.

Dryer, M., Z. K. Smith, E. J. Smith, J. D. Mihalov, J. H. Wolfe, R. S. Steinolfson, and S. T. Wu, Dynamic MHD modeling of solar wind corotating stream interaction regions observed by Pioneer 10 and 11, J. Geophys. Res., 83, 4347, 1978.

Fahr, H. J., E. F. Petelski, H. W. Ripken, Weak shock termination of the solar wind, Solar Wind Four, edited by H. Rosenbauer, MPI fur Aeronomie, Katlenburg-Lindau, 1978.

Fisk, L. A., The interactions of energetic particles with the solar wind, in Solar System Plasma Physics, vol. 1, chap 1.2.2, edited by E. N. Parker et al., North-Holland, Amsterdam, 1979.

Gazis, P. R., and A. J. Lazarus, Voyager observations of solar wind proton temperature: 1-10 AU, Geophys. Res. Lett., 9, 431, 1982.

Gazis, P. R., and A. J. Lazarus, The radial evolution of the solar wind, 1-10 AU, proceedings of this conference, 1983.

Goldstein, B. E., and J. R. Jokipii, Effects of stream-associated fluctuations upon the radial variation of average solar wind parameters, J. Geophys. Res., 82, 1095, 1977.

Holzer, T. E., Interaction of the solar wind with the neutral component of the interstellar gas, J. Geophys. Res., 77, 5407, 1972.

Holzer, T. E., Neutral hydrogen in interplanetary space, Rev. Geophys. Space Phys., 15, 467, 1977.

Hundhausen, A. J., Solar Wind and Coronal Expansion, Springer, New York, 1972.

Hundhausen, A. J., Evolution of large-scale solar wind structures beyond 1 AU, J. Geophys. Res., 78, 2035, 1973.

Hundhausen, A. J., and J. T. Gosling, Solar wind structure at large heliocentric distances: An interpretation of Pioneer 10 observations, J. Geophys. Res., 81, 1436, 1976.

Jokipii, J. R., Radial variation of solar-wind parameters, Geophys. Res. Lett., 3, 141, 1976.

Kayser, S. E., A. Barnes and J. D. Mihalov, The far reaches of the solar wind: Pioneer 10 and Pioneer 11 plasma results, to be published, 1983.

King. J. H., Solar cycle variations in IMF intensity, J. Geophys. Res., 84, 5938, 1979.

McDonald, F. B., N. Lal, J. H. Trainor, and M. A. I. Van Hollebeke, Observations of galactic cosmic ray energy spectra between 1 and 9 AU, Astrophys. J., 216, 930, 1979.

McKibben, R. B., K. R. Pyle, and J. A. Simpson, The heliospheric intensity gradients of the anomalous He^4 and the galactic cosmic-ray components, Astrophys. J., 254, L23, 1982.

Mihalov, J. D., and J. H. Wolfe, Pioneer-10 observation of the solar wind proton temperature heliocentric gradient, Solar Phys., 60, 399, 1978.

Parker, E. N., Interplanetary Dynamical Processes, Interscience, New York, 1963.

Parker, G. D., and J. R. Jokipii, The spiral structure of the interplanetary magnetic field, Geophys. Res. Lett., 3, 561, 1976.

Rosenberg, R. L., M. G. Kivelson, P. J. Coleman, Jr., and E. J. Smith, The radial dependences of the interplanetary magnetic field between 1 and 5 AU: Pioneer 10, J. Geophys. Res., 83, 4165, 1978.

Slavin, J. A., and E. J. Smith, Solar cycle variations in the interplanetary magnetic field, proceedings of this symposium, 1983.

Slavin, J. A., E. J. Smith and B. T. Thomas, Long term variations in the IMF: HELIOS 1, 2, ISEE-3 and Pioneer 10, 11, in preparation, 1983.

Smith, E. J., Radial gradients in the interplanetary magnetic field between 1.0 and 4.3 AU: Pioneer 10, in Solar Wind Three, edited by C. T. Russell, University of California Press, Los Angeles, 1974.

Smith, E. J., and J. H. Wolfe, Observations of interaction regions and corotating shocks between one and five AU: Pioneers 10 and 11, Geophys. Res. Lett., 3, 137, 1976.

Smith, E. J., and J. H. Wolfe, Observations of evolving solar wind streams and shocks beyond 1 AU, in Study of Travelling Interplanetary Phenomena, edited by M. A. Shea, D. F. Smart, and S. T. Wu, 227, D. Reidel, Hingham, Mass, 1977.

Smith, E. J., and J. H. Wolfe, Fields and plasmas in the outer solar system, Space Sci. Rev., 23, 217, 1979.

Smith, E. J., B. T. Thomas, A. Barnes, J. Mihalov, and S. J. Bame, Observations of interaction regions at 10 AU during solar maximum and their origin, submitted to J. Geophys. Res., 1983.

Thomas, B. T., and E. J. Smith, The Parker spiral configuration of the interplanetary magnetic field between 1 and 8.5 AU, J. Geophys. Res., 85, 6861, 1980.

Thomas, B. T., E. J. Smith, and J. A. Slavin, Radial and latitudinal gradients in the interplanetary magnetic field: Pioneer 10 and 11, in prep., 1983.

Van Allen, J. A., Galactic cosmic ray intensity to a heliocentric distance of 18 AU, Astrophys. J., 238, 763, 1980.

Wallis, M. H., Interactions between the solar wind and the interstellar gas, Solar Wind Four, edited by H. Rosenbauer, MPI fur Aeronomie, Katlenburg-Lindau, 1978.

Webber, W. R., and J. A. Lockwood, A study of the long-term variation and radial gradient of Cosmic Rays out to 23 AU, J. Geophys. Res., 86, 11,458, 1981.

SOLAR WIND PROTON TEMPERATURE GRADIENT FROM PIONEER 10 AND 11 AND CLOSER DATA

J. D. Mihalov
NASA-Ames Research Center
Moffett Field, CA 94035

ABSTRACT

The heliocentric gradient of solar wind proton temperature is reported for 7 alignment periods of Pioneers 10 and/or 11 with nearer Pioneer, IMP or ISEE spacecraft, during 1973 to 1979, spanning the distance range overall of 0.7 to 18 AU. The results are consistent with other pertinent results for this gradient. In addition, it is found that the gradient is steeper when the average temperature nearer the Sun (1 AU) is higher during 1973-74.

Introduction

Results for the heliocentric gradient of scalar or isotropic proton temperature over a distance range of about 1 to 18 AU are given here. The method used is to compare data from time intervals of alignment of nearer (Pioneer Venus, IMP or ISEE) and more distant (Pioneer 10 or 11) spacecraft (±45 deg heliocentric longitude difference) similar to the procedure used for study of the heliocentric variation of speed (Collard et al., 1982). Such time intervals are 90 days long, except for a Pioneer Venus interval limited to 50 days by the longitude restriction. Seven alignment periods have been used for this study. The alignment times of the Collard et al. study were used; these were supplemented by more recent results for mean speeds and alignment times for more distant data.

Detailed Procedure

Data within the selected, aligned time intervals were organized into half-day averages of individual hourly averages for the IMP and ISEE 3 (King, 1979; 1983) and Pioneer Venus spacecraft, and into half-day averages of individual hourly samples, except for a few instances for which hourly averages were used, for the cases of Pioneers 10 and 11. Half-day temperature averages that correspond with values missing in the matching, aligned time intervals were deleted, with two exceptions. In one case a slight shift of alignment was made to a portion of a temperature record that permitted better matching of the associated stream structures. Also, the earliest Pioneer 11 time interval, which extended from 1.40 to 2.24 AU in heliocentric distance, was treated as nine separate, adjoining time intervals that correspond to separate solar wind streams.

Following these adjustments, the half-day average values remaining for each +45 deg interval of longitude were averaged together to form 90 day averages (50 days for Pioneer Venus), without further consideration of stream structure or possible three-dimensional geometry. Then a power law was assumed for the radial distance dependence of proton temperature, and the power law exponents, α , were calculated, each from one nearer and one more distant 90 day average. The results are given in the Table which presents, in addition to the power-law exponents, the time intervals of the data, the

POWER LAW HELIOCENTRIC PROTON TEMPERATURE GRADIENTS

		1 AU DATA		DISTANT DATA			
ALIGNMENT	DAY NOS.	$\overline{T}$	# SAMPS.	$\overline{T}$	# SAMPS.	α	$\overline{R}$
1973-11		*	139	*	146	-.87	1.40-2.24 AU
1973-10	164-254	121,000 K	145	36,900 K	145	-.93	4.6
1974-11		138,000	179	37,800	179	-1.00	4.65
1974-10	203-293	136,000	164	31,200	164	-.93	5.9
1975-10	247-337	81,100	122	19,000	116	-.71	8.65
1976-10	263-353	79,700	126	14,900	126	-.71	11.65
1977-10	270-360	62,100	95	11,100	95	-.64	14.8
1978-11	362-087	58,600	83	22,600	83	-.55	6.65
1978-10	276-319	61,900	69	12,100	69	-.57	17.67
1978,V-10*	286-346	68,000	56	9,860	56	-.62	17.73

*Nine separate streams used.

+Mean spacecraft distance - 0.8043 AU

numbers of half-day samples used in computation of the exponents, and the average tmperatures for the various intervals. The different spacecraft are nearly all at positive heliographic latitudes during these intervals, except for the final Pioneer 11 interval.

Discussion

The values reported here for power-law exponents represent slower decreases than that for an adiabatic expansion. This is probably a consequence of heating due to interactions associated with shocked plasma of corotating streams. Conceivably a portion of some heating above the adiabatic value, particularly at the greater distances, could be a result of interaction between the solar wind and the interstellar medium; such effects should be clearer in analyses of Pioneer 10 and 11 data from greater distances, as these two spacecraft are proceeding on escape trajectories in approximately opposite directions through the heliosphere.

The data of the Table indicate that the temperature gradient is steeper when the temperatures at 1 AU are higher. For 1973-74, average temperatures at 1 AU are hot ($1.2 - 1.4 \times 10^5$K) and power law exponents in the range from -0.87 to -1.00 are found. For 1975-78, with cooler average temperatures at 1 AU ($0.6 - 0.8 \times 10^5$ K), these exponents are in the -0.55 to -0.71 range. The later times with cooler temperatures at 1 AU tend to correspond with more distant locations for Pioneers 10 and 11.

The gradient values reported here are consistent with the results of other Pioneer and Voyager studies, e. g., those of Mihalov and Wolfe (1978) (-0.52 exponent for the 1.2 to 12.2 AU distance range), Gazis and Lazarus (1982) (-0.7+0.2 exponent for the 1 to 9 AU range), and Kayser et al. (submitted, 1982) (-0.57+0.07 exponent for the ~1 to 20.5 AU distance range).

References

Collard, H. R., J. D. Mihalov, and J. H. Wolfe, Radial variation of the solar wind speed between 1 and 15 AU, J. Geophys. Res., 87, 2203, 1982.

Gazis, P. R., and A. J. Lazarus, Voyager observations of solar wind proton temperature: 1-10 AU, Geophys. Res. Lett., 9, 431, 1982.

Kayser, S. E., A. Barnes, and J. D. Mihalov, The far reaches of the solar wind: Pioneer 10 and Pioneer 11 plasma results, Ap. J. (submitted), 1982.

King, J. H., Interplanetary Medium Data Book - Supplement 1, Report NSSDC/WDC-A-R&S 79-08, NASA Goddard Space Flight Center, Greenbelt, MD, 1979.

King, J. H., Interplanetary Medium Data Book - Supplement 2, Report NSSDC/WDC-A-R&S 83-01, NASA Goddard Space Flight Center, Greenbelt, MD, 1983.

Mihalov, J. D., and J. H. Wolfe, Pioneer-10 observation of the solar wind proton temperature heliocentric gradient, Solar Phys., 60, 399, 1978.

THEORY OF INTERSTELLAR MEDIUM DIAGNOSTICS

H.J. Fahr
Institut für Astrophysik und Extraterrestrische Forschung
Universität Bonn
Auf dem Hügel 71
5300 Bonn 1, Fed. Rep. Germany

Abstract. The theoretical interpretation of observed interplanetary resonance luminescence patterns is used as one of the most promising methods to determine the state of the local interstellar medium (LISM). However, up to now these methods have led to discrepant results that would be hard to understand in the framework of any physical LISM scenario. Assuming that the observational data are reliable, two possibilities which could help to resolve these discrepancies are discussed: a) The current modeling of resonance luminescence patterns is unsatisfactory and has to be improved, and b) the extrapolated interstellar parameters are not indicative of the unperturbed LISM state, but rather designate an intermediate state attained in the outer regions of the solar system. It is shown here that a quantitative treatment of the neutral gas - plasma interaction effects in the interface between the heliospheric and the interstellar plasmas is of major importance for the correct understanding of the whole complex.

ACCESS TO THE PARAMETERS OF THE INTERSTELLAR MEDIUM

According to a huge amount of observational material the interstellar medium is now considered to be highly structured into dense and dilute gas phases. Following theoretical models by McKee and Ostriker (1977) and McGray and Snow (1979) the bulk of the interstellar matter is concentrated in dense and cool clouds with densities $n \gtrsim 10^2$ cm^{-3} and temperatures $T \lesssim 10^2$ K, whereas the bulk of the interstellar space is filled with a very dilute and ionized interstellar medium of densities $n \simeq 10^{-2}$ cm^{-3} and temperatures $T \simeq 10^5$ K. The idea of McKee and Ostriker is that at the occurrence of supernova events, fast MHD shockfronts are emitted from the center of these events and partly evaporate the peripheral cloud material when passing over the dense clouds distributed in space. New intermediate gas phases are thus created, mainly under conditions of pressure equilibrium with the outer hot ionized medium (HIM). Two different phases are predicted to exist in the periphery of the CNM clouds (cool neutral medium): the WNM phase (warm neutral medium) which directly surrounds the CNM phase and which has densities of $n \simeq 0.3$ cm^{-3}, temperatures of $T \simeq 8 \cdot 10^3$ K, and an ionization degree of 15 percent, and a WIM phase (warm ionized medium) further away from the cloud with densities of $n \simeq 0.2$ cm^{-3}, temperatures of $T = 8 \cdot 10^3$ to 10^4 K, and an ionization degree of 70 percent.

The question then arises as to which of these phases our local interstellar medium (LISM) belongs. To answer this question specific data relevant to LISM are needed. As it turns out, most of the observational methods appropriate for the analysis of the interstellar medium average over very large astronomical distances and therefore conceal the information on the LISM properties. Essentially three methods can give more specific local information on the LISM. The analysis of Lyman-alpha absorption contours in the continuum spectra of bright O- and B-stars can yield information on the average hydrogen

density within the 10 to 70 pc environment of the sun. Average values of $n \simeq 10^{-2}$ cm^{-3} have been obtained here (Frisch, 1981 and references therein; Bohlin, 1975; Bohlin et al., 1978; Vidal-Madjar, 1978; Anderson and Weiler, 1978).

Access to even more local structures of the LISM is possible from interpretations of self-inversion structures in the contours of Lyman-alpha emission lines originating from relatively cool stars of the solar type. With this method the LISM is analyzed over distances of 1.3 to 5 pc. In these distance ranges average hydrogen density values of $n_H \simeq 10^{-1}$ cm^{-3} have been found (Moos et al., 1974, Evans et al., 1975, Dupree, 1975, McClintock et al., 1976).

This shows clearly that over distances of about 10 pc the LISM properties of our solar environment are subject to substantial changes, and thus the thermodynamic parameters of the LISM at the immediate periphery of our solar system can only be extracted from even "more local" observational methods. The most local information on the LISM available up to now is derived from theoretical modeling of interplanetary resonance luminescences originating from neutral interstellar hydrogen and helium that have propagated from the outside of the solar system into its inner regions (i.e. solar distances smaller than 5 AU). The principles of this method will be briefly reviewed here.

THEORY OF INTERPLANETARY RESONANCE RADIATION

Unlike the ionized component of the LISM, the neutral component, which consists essentially of H and He atoms, can traverse the outer regions of the plasma interface between the solar wind and the LISM plasma and thus reach the inner solar system. The motion of the atoms is characterized here by Keplerian orbits in the solar gravitational field which is partly compensated by solar radiation pressure (Fahr, 1968; Blum and Fahr, 1970; Axford, 1972; see also later reviews on this topic by Fahr, 1974; Thomas, 1978; Holzer, 1977). While moving along specific Keplerian trajectories the neutrals are subject to loss processes due to ionization by solar EUV photons, due to charge-exchange processes with solar wind ion species and due to electron impact ionization. (For specifics see reviews by Grzedzielski, 1982; Paresce, 1982.)

The change of the velocity distribution function $f(\vec{R}, \vec{v})$ of the LISM neutrals during their approach towards the inner solar system is adequately described by Boltzmann differential equations that take into account only particle loss processes. The solution of these equations can be formally written down in the following simple form (Fahr, 1978, 1979):

$$f(\vec{R}, \vec{v}) = f_0(\vec{v}_0) \, Ex(\vec{R}, \vec{v}_0) \quad , \tag{1}$$

where $\vec{v}$ designates the particle velocity vector at a position $\vec{R}$ within the solar system and $\vec{v}_0$ is the velocity vector outside the solar system that is connected with the dynamical variables $\{\vec{v}, \vec{R}\}$ by the particle trajectory. The vector $\vec{v}_0$ is distributed according to the velocity distribution function $f_0(\vec{v}_0)$ valid for the unperturbed state of the LISM and yielding, as its moments, the density n_0, the temperature T_0, the bulk velocity $\vec{V}_0$, the pressure tensor $\vec{P}_0$, and the heat conduction flow $\vec{Q}_0$.

The function $Ex(\vec{R}, \vec{v}_o)$ calculates the integral loss probability for particles moving along a specific trajectory $\{\vec{R}, \vec{v}\}$ from outside the solar system to point $\vec{R}$. This function is given by:

$$Ex(\vec{R}, \vec{v}_o) = \exp\left[-\int_\infty^{s(R)} L(s')\frac{ds'}{v(s')}\right] , \qquad (2)$$

where L is the local particle loss rate, and where the line integration has to be carried out along the dynamical trajectory from very large solar distances to point $\vec{R}$. The integration variable is the line element s' on this trajectory. Evaluations of the integral in Eq. (2) for different cases can be found in Blum and Fahr (1970), Axford (1972), Holzer (1977), and Fahr (1978).

The moments $< \phi(R) >$ of the local distribution function can be obtained with Eqs. (1) and (2) in the form

$$< \phi(R) > = \int^3 f_o(\vec{v}_o) Ex(\vec{R}, \vec{v}_o)\phi(\vec{v}) d^3\vec{v} \qquad (3)$$

which with the use of Liouville's theorem

$$\left|\frac{d^3\vec{v}}{d^3\vec{v}_o}\right|_{\vec{R}} = \left|J(\vec{v}, \vec{v}_o, \vec{R})\right| = \beta(\vec{v}, \vec{v}_o, \vec{R}) \qquad (4)$$

can be evaluated in a straightforward manner. Here J is the Jacobian of the transformation $\vec{v}_o \to \vec{v}$, and β is the focusing factor for particles with $(\vec{v} + d^3\vec{v})$ at $\vec{R}$ originating from particles with $(\vec{v}_o + d^3\vec{v}_o)$ at some distant position $\vec{R}$.

On the basis of the knowledge of f_o one is then able to calculate the resonance luminescence intensity as seen by a detector at $\vec{R}_{ob}$ in a direction $\vec{D}$ by using the expression

$$I_{res}(\vec{R}_{ob}, \vec{D}) = G\int_0^\infty dz \int_0^\gamma \sin\gamma d\gamma \int_0^{2\pi} d\psi P(\theta) \int^3 F_{sol}(\nu')\left[\frac{R_E}{R}\right]^2 s_{res}(\nu')f(\vec{v}, \vec{R}(z)) d^3\vec{v} , \qquad (5)$$

where G contains instrumental constants, F_{sol} is the solar EUV radiation intensity at $R_E = 1$ AU, s_{res} is the resonant absorption cross section and $P(\theta)$ is the phase function giving the probability for a scattering process with an angle θ between $\vec{R}$ and $(\vec{R}_{ob} - \vec{R})$. At place $\vec{R}$, the frequency ν' is a specific function of the velocity $\vec{v}$ of the absorbing atom. The integration at a position $\vec{R}$ has to be carried out over all velocities and then also over the threedimensional source field within the angle of acceptance of the instrument with polar coordinates z, γ, and ψ.

As is evident from Eqs. (1) through (5), a theoretical representation of interplanetary resonance luminescence intensities requires the knowledge of the distribution function $f_o(\vec{v}_o)$ of the unperturbed interstellar neutrals. However, since the velocity moments $< \phi_o >$ of f_o are the unknown quantities which need to be determined as accurately as possible, one has to initiate a theoretical best-fit procedure of available luminescence data in order to arrive at reasonable values for the moments $< \phi_o >$, i.e. the LISM parameters. In

this way, the function f_o is approximated as a shifted Maxwellian yielding the relevant LISM parameters.

DISCUSSION OF CURRENT MODELING TECHNIQUES

In the past, a large amount of Lyman-alpha and He-I (58.4 nm) interplanetary luminescence data was subject to the best-fit procedures mentioned above and was used to yield values for the desired LISM parameters (see for instance Morton and Purcell, 1962; Fahr, 1970; Thomas and Krassa, 1971; Bertaux and Blamont, 1971; Bertaux et al., 1972; Weller and Meier, 1974; Bertaux et al., 1977; Freeman et al., 1977; Fahr et al., 1978; Broadfoot and Kumar, 1978; Ajello, 1978; Ajello et al., 1979; Babichenko et al., 1971; Wu et al., 1981).

Looking over all these attempts to derive LISM parameters, one sees that the puzzling facts are not so much the relatively small differences in the values derived by different authors but rather the values themselves that are hard to understand in the framework of one single common physical LISM scenario.

For instance, at a recent workshop on these problems (Keller et al., 1978) the scientific community engaged in this field raised the following surprising points in the analysis of resonance luminescence data:

1) The LISM helium temperature T_o(He) is found to be definitely higher than the corresponding hydrogen temperature T_o(H). An average temperature excess of about $\Delta T_o = T_o$(He) $- T_o$(H) $\simeq 2000$ K is indicated. The problem: two different temperatures for neutral constituents belonging to the same physical environment are difficult to understand.

2) It is found that even in view of data-inherent uncertainties the helium-hydrogen density ratio seems fairly high when compared to the expected cosmic abundance ratio. The problem: the cosmic value of the helium-hydrogen abundance ratio could be conserved only if hydrogen is ionized by at least 50 percent.

3) The wind vectors $\vec{V}_o$(He) and $\vec{V}_o$(H) characterizing the directions from which the LISM helium and hydrogen are approaching the sun at least as derived from some observations are found to be inclined to each other by an angle of about 15°. The problem: truly different bulk velocities of the two LISM constituents are difficult to understand.

Therefore the question is raised whether or not these surprising results concerning the LISM state are due to unsatisfactory modeling of the interplanetary luminescence radiation field. In view of the theoretical approach that is carried out according to the conventional formalism described by Eqs. (1) through (5), the following shortcomings could be made responsible for a failure of the modeling:

a) Generally, the theories are based on the assumption of a radial symmetry of the ionizing solar radiation fields, and the solar wind affecting the neutrals by charge-exchange reactions is also represented in a radial symmetry, though both the solar radiation field and the solar wind expansion are known to have pronounced asymmetries. Only a few attempts have been made to take account of these asymmetries (Blum and Fahr, 1970; Joselyn and Holzer, 1975, Witt, 1979; Witt, Ajello and Blum, 1981).

b) The loss rates taken into account are represented by simple $1/r^2$ dependencies (r = solar distance). Though this enables one to drastically simplify

the integral in the extinction function (2), it may well give rise to incorrect modeling due to a nonspherical divergence of the solar wind flow and due to electron impact ionization rates that are connected with solar wind electron temperatures. Attempts have been made by Petelski et al. (1980) and Ripken and Fahr (1981) to incorporate these effects.

c) Up to now the radiation field has been described on the basis of single scattering processes only. However, it has been discussed (Keller and Thomas, 1979; Keller et al., 1981) that at least at large distances multiple scattering effects might have some importance for the radiation intensity distribution.

d) Furthermore, it has also been pointed out by Wu and Judge (1979) that the exciting solar line profile changes with solar distance due to absorptions in interplanetary space. This could be important, especially for the calculation of the source functions at large solar distances.

e) The effect of the secondary hydrogen component on the interplanetary Lyman-alpha isophotes has never been adquately taken into account. Though this component arises from charge-exchange reactions of primary hydrogen with protons in the heliospheric plasma interface, i.e. at relatively large distances, it could nevertheless be of importance, especially for the hydrogen distribution in the downwind wake.

f) The galactic background radiation in the EUV/UV has not been taken into account properly. This is necessary in order to be able to derive more reliable information on the LISM properties.

In view of the list above, the question to answer then is whether or not the incorporation of all improvements a) through f) into the theory of the resonance radiation field could help to substantially resolve the conflicts in the results of the data analysis.

In our opinion the inclusion of effects c) through f), rather than lessening the problems, would tend to even increase them. For instance, the hydrogen temperature $T_o(H)$ is most effectively deduced from downwind Lyman-alpha resonance intensities. However, these would clearly be increased by effects c), e), and f) and thus would lead to an even lower value for the LISM hydrogen temperature than which is derived by current modeling from the data. In addition, if c), e), and f) would turn out to contribute anything at all to the single scattering radiation field, it would mean that an even lower hydrogen density $n_o(H)$ would be derived from the data.

In our estimation, the only way out of this unsatisfactory situation if the data can be taken as reliable is to realize that the LISM parameters deduced on the basis of the above-mentioned theory represent intermediate values that are characteristic for the state of LISM neutrals in upwind regions of the solar system at distances between 50 and 100 AU. The change from the unperturbed LISM state to this intermediate one is then caused by modifications of the neutral interstellar gases during their traversal of the upwind heliospheric plasma interface. A quantitative description of this effect was recently given by Fahr and Ripken (1982) and Ripken and Fahr (1983). These papers may be consulted for details. Here we will only give a broad outline of the basic ideas.

The LISM plasma and the solar wind plasma interact in a magnetohydrodynamic way and form a contact discontinuity, the heliopause, separating the two plasma flows from one another. In the transheliopause region the state parameters of the LISM plasma and the LISM neutrals are decoupled from each other. The neutrals moving through this interface region are thus subject to non-vanishing production and loss terms due to charge-exchange reactions with the protons. A consequence of these charge-exchange reactions is a change of the velocity distribution function $f(\vec{R},\vec{v})$ of the neutrals. Due to the large H-p charge-exchange cross section, the LISM hydrogen atoms are strongly affected by these processes, whereas the LISM helium atoms, due to the relatively small He-p charge-exchange cross section, only undergo modifications of a negligible magnitude. The change of the hydrogen distribution function $f_H(\vec{R},\vec{v})$ is described adequately by the Boltzmann equation, which for the stationary case can be written in the following form:

$$\frac{d\,f_H(\vec{R},\vec{v})}{ds} = \frac{1}{v}\left[P_+(f_H,f_p) - f_H\,\bar{\nu}_-(f_p)\right]_{\vec{v}} \tag{6}$$

where ds is the differential line element on a trajectory of an atom moving with a velocity $\vec{v}$ at $\vec{R}$. The terms P_+ and $\bar{\nu}_-$ are the total production rate of atoms with velocity $\vec{v}$ at $\vec{R}$ and the average destruction frequency for such atoms. Both terms are functions of $\vec{v}$ and can be evaluated only with the knowledge of the proton velocity distribution function $f_p(\vec{R},\vec{v})$.

For the calculation of the distribution function $f_H(\vec{R},\vec{v})$ at some place $\vec{R}$ within the inner solar system all hydrogen atom trajectories reaching this point and originating in the unperturbed LISM have to be used. The integration along these trajectories starting from Eq. (6) will then yield a value for $f_H(\vec{R},\vec{v})$ at $\vec{R}$ for exactly those atoms which have a velocity $\vec{v}$. For these integrations it has to be assumed that at each place in the plasma interface the proton distribution function $f_p(\vec{R},\vec{v})$ is known. In the case of calculations carried out by Ripken and Fahr (1983) this knowledge is taken from theoretical models of the plasma interface by Parker (1963) and Baranov et al. (1976). Alternative forms of such interface models are shown in Figs. 1a and b. In Fig. 2 we show a solution for the first moment of f_H, i.e. the hydrogen density n(H), as a function of the solar distance on the upwind symmetry axis. The two solid curves show the decrease of the hydrogen density with decreasing solar distance for the interface models according to (A) Parker (1963) and (B) Baranov et al. (1979). To facilitate comparison, the unperturbed LISM proton n_o(P) have been adopted to the case of a more realistic value n_o (P) = 0.0135 cm^{-3} and a subsonic interstellar wind model. In any case, however, the solutions given in this figure demonstrate that a decrease of the hydrogen density by at least a factor of 0.5 from the unperturbed value n_o(H) to some intermediate value at about 50 AU is indicated. This means that due to the modification of the LISM hydrogen in the interface the hydrogen density value obtained from conventional Lyman-alpha resonance isophote interpretations has to be raised by a factor of about 2 in order to yield n_o(H) $\approx$ 0.1 cm^{-3}. In contrast, the helium density value that was obtained earlier can be considered as being directly indicative for the unperturbed LISM helium density n_o(He) due to the
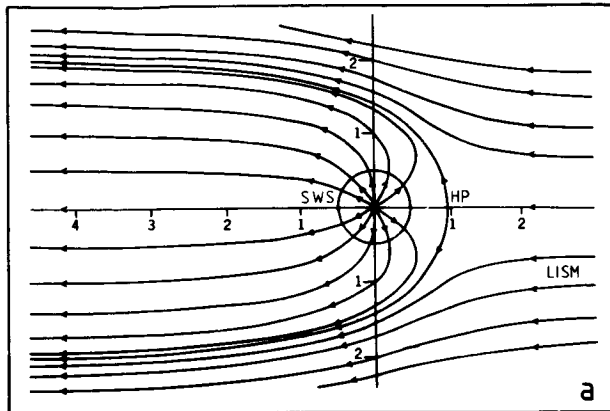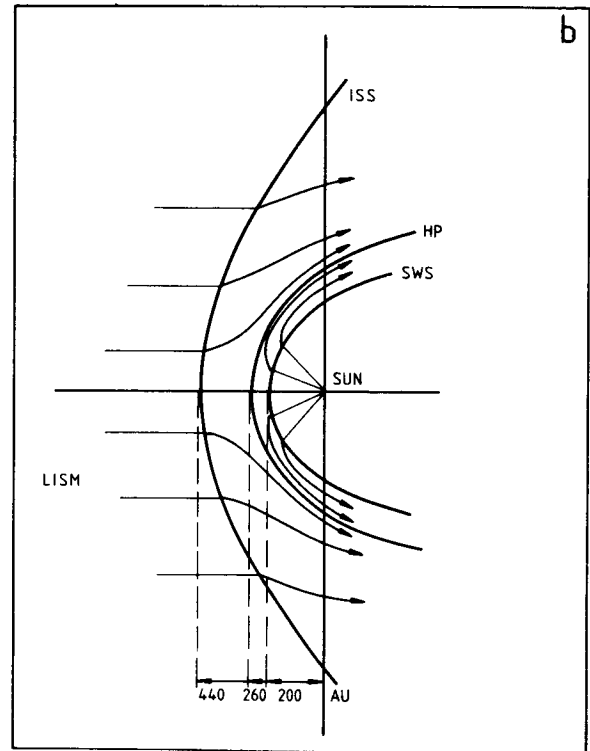
Fig. 1: Shown are theoretical models for the heliospheric plasma interface. a) Solar wind interacting with an incompressible subsonic LISM plasma flow, according to Parker (1963). b) Solar wind plasma interacting with an unmagnetized supersonic LISM plasma flow with double-shock structure according to Baranov et al. (1976).

absence of interface-induced modifications for this type of atom. These results now lead to a revised helium-to-hydrogen density ratio of $n_o(He)/n_o(H)$ = 0.1 which now is very close to the cosmic abundance value.

Other results concerning interface-induced modifications of the higher moments of f_H are presented in Ripken and Fahr (1983) and are not discussed here. As a final point we want to mention that formerly neglected reactions of the LISM neutrals onto the LISM protons have been discussed by Baranov et al. (1981) and Gruntman (1982). The former authors treat a supersonic flow of the LISM plasma towards the solar system and show that the influence of LISM neutrals on this plasma flow is reflected in a reduction of the heliocentric distance of the outer LISM shockfront. An interesting additional point is raised by Gruntman (1982) who points out the possibility that an originally supersonic LISM plasma flow might be converted into a subsonic flow. This would occur due to secondary hydrogen atoms which originate from the supersonic solar wind region and react with the counter-streaming LISM plasma in the upwind portion of the heliosphere. In conclusion we would like to state that both theoretical models and experimental results need to be improved in order to refine our understanding of the local interstellar gas.
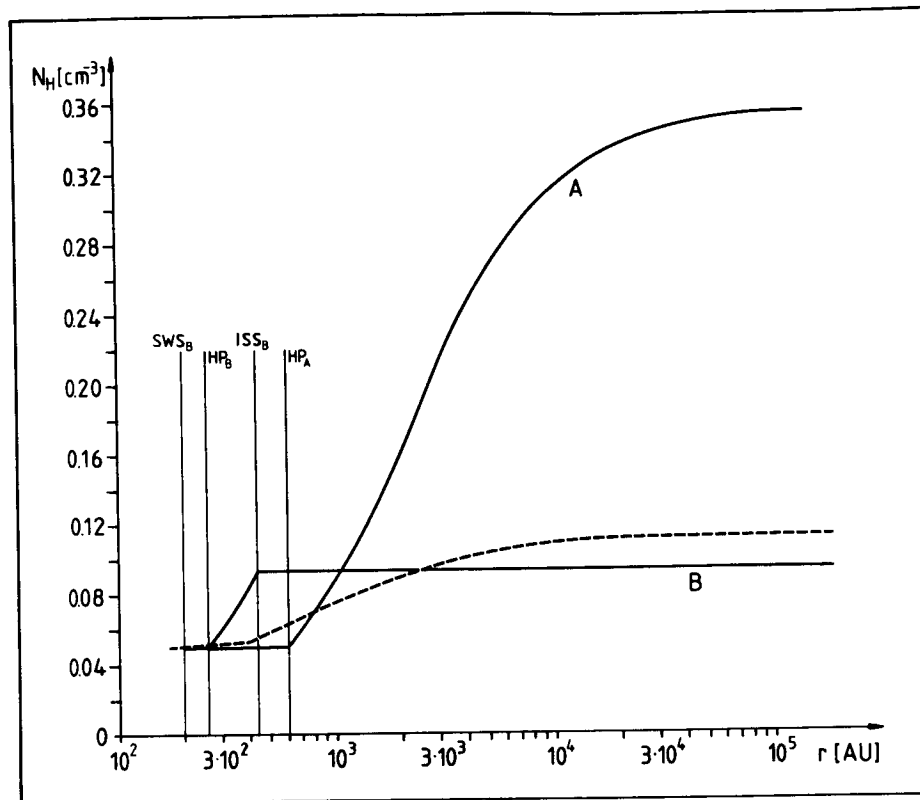
Fig. 2: Variation of the LISM hydrogen density with decreasing solar distance on the stagnation line. A: Subsonic interface model according to Parker (1963) for $n_0(P) = 0.024$ cm^{-3}. B: Supersonic interface according to Baranov et al. (1976) for identical proton density $n_0(P)$. The dashed line shows the result for a subsonic interface according to Parker, but for a more realistic proton density of $n_0(P)=0.0135$ cm^{-3}.

References

Anderson, R. C. and E. J. Weiler, Copernicus observations of interstellar matter in the direction of HR 1099, Astrophys. J., 224, 143-150, 1978.

Ajello, J. M., An interpretation of Mariner 10 He(584 Å) and H(1226 Å) interplanetary emission observation, Astrophys. J., 222, 1068, 1978.

Ajello, J. M., N. Witt and P. W. Blum, Four UV observations of the interstellar wind by Mariner 10: analysis with spherically symmetric solar radiation models, Astron. Astrophys., 73, 260, 1979.

Axford, W. I., The interaction of the solar wind with the interstellar medium, NASA SP-308, pp. 609-645, Washington, D. C., 1972.

Babichenko, S. I., E. V. Deregusov, V. G. Kurt, N. N. Romanova, V. A. Sklyankin, A. S. Smirnov, J. L. Bertaux and J. E. Blamont, Sov. Phys. Dokl., 15, 791, 1971.

Baranov, V. B., K. V. Krasnobaev and M. S. Ruderman, On the model of the solar wind - interstellar medium interaction with two shock waves, Astrophys. Space Sci., 41, 481-490, 1976.

Baranov, V. B., M. G. Lebedev and M. S. Ruderman, Structure of the region of solar wind - interstellar medium interaction and its influence on the H-atoms penetrating the solar wind, Astrophys. Space Sci., 66, 441-451, 1979.

Baranov, V. B., M. K. Ermakov, and M. G. Lebedev, A three-component model of the solar wind - interstellar medium interaction: some numerical results, Sov. Astron. Lett., 7(3), 206, 1981.

Bertaux, J. L. and J. E. Blamont, Evidence for a source of an extraterrestrial hydrogen Lyman-alpha emission: the interstellar wind, Astron. Astrophys., 11, 200, 1971.

Bertaux, J. L., A. Ammar, and J. E. Blamont, OGO-V determinations of the local interstellar wind parameters, Space Res., XII, 1559-1567, 1972.

Bertaux, J. L., J. E. Blamont, E. N. Miranova, V. G. Kurt and M. C. Bourgin, Temperature measurement of interplanetary interstellar hydrogen, Nature, 270, 156-158, 1977.

Blum, P. W. and H. J. Fahr, Interaction between interstellar hydrogen and the solar wind, Astron. Astrophys., 4, 280, 1970.

Broadfoot, A. L. and S. Kumar, The interstellar wind: Mariner 10 measurements of hydrogen (1216 Å) and helium (584 Å) interplanetary emission, Astrophys. J., 222, 1054, 1978.

Bohlin, R. C., B. D. Savage and J. F. Drake, A survey of interstellar HI from Lyman-alpha absorption measurements, II, Astrophys. J., 224, 132, 1978.

Bohlin, R. C., Copernicus observations of interstellar absorption at Lyman-alpha, Astrophys. J., 200, 402-4]4, 1975.

Dupree, A. K., Ultraviolet observations of Alpha Aurisa from Copernicus, Astrophys. J., 200, L27-31, 1975.

Evans, R. G., C. Jordan, and R. Wilson, Observations of chromospheric and coronal emission lines in F stars, M.N.R.A.S., 172, 585-602, 1975.

Fahr, H. J., On the influence of neutral interstellar matter on the upper atmosphere, Astrophys. Space Sci., 2, 474-495, 1968.

Fahr, H. J., Interstellar hydrogen densities in the surroundings of the solar system, Nature, 226, 435-546, 1970.

Fahr, H. J., The extraterrestrial UV-background and the nearby interstellar medium, Space Sci. Rev., 15, 483-540, 1974.

Fahr, H. J., Change of interstellar gas parameters in stellar-wind-dominated astrospheres: solar case, Astron. Astrophys., 66, 103-117, 1978.

Fahr, H. J., Interstellar hydrogen subject to a net repulsive solar force field, Astron. Astrophys., 77, 101-109, 1979.

Fahr, H. J., G. Lay and C. I. Wulf-Mathies, Derivation of interstellar helium gas parameters from an EUV rocket observation, Space Res., XVIII, 393-396, 1978.

Fahr, H. J. and H. W. Ripken, Modifikation der interstellaren Gasparameter im Randgebiet des Sonnensystems, Mitt. der Astron. Gesellschaft, 57, 288-291, 1982.

Freeman, J. C., F. Paresce, S. Bowyer, M. Lampton, R. Stern, and B. Margon, The local interstellar helium density, Astrophys. J., 215, L83-86, 1977.

Frisch, P. C., The nearby interstellar medium, Nature, 293, 377-379, 1981.

Grzedzielski, S., Free neutrals in interplanetary space: sources and coupling to the solar wind plasma, Proceedings of the IAU, progress report 1982 of Commission 49, III, 654, 1982.

Gruntman, M. A., The effect of the neutral solar wind component upon the interaction of the solar system with the interstellar gas stream, Sov. Astron. Lett., 8(1), 24, 1982.

Holzer, T. E., Neutral hydrogen in interplanetary space, Rev. Geophys. Space Phys., 15, 467, 1977.

Joselyn, J. A. and T. E. Holzer, The effect of asymmetric solar wind on the Lyman-alpha sky background, J. Geophys. res., 80, 903, 1975.

Keller, H. U., G. E. Thomas and R. R. Meier, Workshop on "Neutral interstellar gas diagnostics, Lindau (Harz), MPI f. Aeronomie, July 1978.

Keller, H. U. and G. E. Thomas, Multiple scattering of solar resonance radiation in the nearby interstellar medium. I, Astron. Astrophys., 80, 227, 1979.

Keller, H. U., K. Richter and G. E. Thomas, Multiple scattering of solar resonance radiation in the nearby interstellar medium, II, Astron. Astrophys., 102, 415-523, 1981.

McClintock, W., R. C. Henry, H. W. Moos, and J. L. Linsky, Ultraviolet observations of cool stars. V. The local density of interstellar matter, Astrophys. J., 204, L103-106, 1976.

McGray, R. and T. P. Snow, The violent interstellar medium, in: Ann. Rev. Astr. Ap., 17, 213-240, 1979.

McKee, C. F. and J. P. Ostriker, The theory of the interstellar medium: three components regulated by supernova explosions in an inhomogeneous substrate, Astrophys. J., 218, 148-162, 1977.

Moos, H. W., J. L. Linsky, R. C. Henry, and W. McClintock, High-spectral resolution measurements of the HIλ1226 and MgIIλ2800 emissions from Arcturus, Astrophys. J., 188, L93-95, 1974.

Morton, D. C., and J. D. Purcell, Observations of the extreme ultraviolet radiation in the night sky using an atomic hydrogen filter, Planet Space Sci., 9, 455-458, 1962.

Paresce, F., Extrapolation to the nearby interstellar matter, Proceeding of the IAU, Progress report 1982 of Commission 49, IV, 660, 1982.

Parker, E., In: Interplanetary dynamical processes, Interscience Publishers, New York, 1963.

Petelski, E. F., H. J. Fahr, H. W. Ripken, N. Brenning and I. Axnäs, Enhanced interaction of the solar wind and the interstellar neutral gas by virtue of a critical velocity effect, Astron. Astrophys. 87, 20, 1980.

Ripken, H. W. and H. J. Fahr, Solar wind interaction with neutral hydrogen inside of the orbit of the earth, Solar Wind IV, Report No. MPAE-100-81-31, Katlenburg-Lindau (FRG), pp. 528, 1981.

Ripken, H. W. and H. J. Fahr, Modification of the local interstellar gas properties in the heliospheric interface, Astron. Astrophys. (in press), 1983.

Thomas, G. E. and R. F. Krassa, OGO 5 measurements of the Lyman-alpha sky background, Astron. Astrophys., 11, 218, 1971.

Thomas, G. E., The interstellar wind and its influence on the interplanetary environment, Annual Rev. Earth Planet. Sci., 6, 173-204, 1978.

Vidal-Madjar, A. C., C. Laurent, P. Bruston, and J. Andonze, Is the solar system entering a nearby interstellar gas cloud?, Astrophys. J., 223, 589-600, 1978.

Weller, C. S. and R. R. Meier, Observations of helium in the interplanetary/interstellar wind: the solar wake effect, Astrophys. J., 193, 471-476, 1974.

Witt, N., Interstellarwindmodelle mit Sonnenwindanisotropien: Analyse der UV-Beobachtungen der Raumsonde Mariner 10, Ph. D. Thesis, Univ. Bonn, Bonn, FRG, 1979

Witt, N., J. M. Ajello, and P. W. Blum, Polar solar wind and interstellar wind properties from interplanetary Lyman-alpha radiation measurements, _Astron. Astrophys._, _95_, 80-85, 1981.

Wu, F. M. and D. L. Judge, Modification of the solar lines propagating through the interplanetary medium, _J. Geophys. Res._, _84_, 979, 1979.

Wu, F. M., K. Suzuki, R. W. Carlson and D. L. Judge, Pioneer-10 ultraviolet photometer observation of the interplanetary glow at heliocentric distances from 2 to 14 AU, _Astrophys. J._, _245_, 1145-1158, 1981.

THE LISM – SOLAR WIND INTERFACE AND ITS EFFECT ON THE NEUTRAL LISM COMPONENT

Hartmut W. Ripken
Institut für Astrophysik und Extraterrestrische Forschung
Universität Bonn
Auf dem Hügel 71
5300 Bonn 1, Fed. Rep. Germany

Based on the principles and methods described in detail by H.J. Fahr in his preceding review (Fahr, 1983), calculations of the heliospheric interface structures and of the neutral LISM modification upon traversal of these structures were performed by Ripken and Fahr (1983). Rather than concentrating on the numerical calculations, it is appropriate here to discuss the results obtained and to present a coherent picture of the neutral gas interaction with the interface plasma.

The extinction of neutral hydrogen in the heliospheric interface is calculated for the two different plasma interface models shown in Fig. 1 of Fahr (1983): a subsonic interface model according to Parker (1963) and a supersonic model by Baranov et al. (1979). Assuming the validity of current observational evidence for the solar case (Keller et al., 1980), an analysis of the two interfaces and the resulting hydrogen modifications yields the result that a subsonic motion of the heliosphere through the LISM has to be favored. Therefore the results presented in this comment pertain only to a subsonic interface model.

Using all possible hydrogen trajectories through the externally specified three-dimensional plasma interface structure (Parker, 1963), an axially symmetric, three-dimensional hydrogen velocity distribution function at the solar wind terminating shock is synthesized. Emphasis has been placed on internal model consistency, including a pressure balance at the discontinuity surface of the heliopause and a complete treatment of the relevant hydrogen production and loss terms. The geometry and sample trajectories s are shown in Fig. 1. By calculating the moments of the modified hydrogen distribution function, values for the density, the velocity-dependent extinction, the bulk velocity shift, the temperature, and the anisotropy of the temperature can be derived.
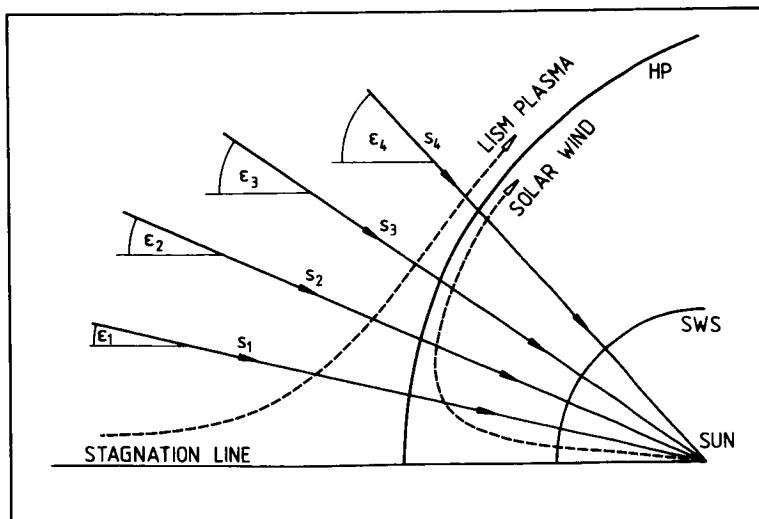

Figure 1: General interaction geometry of counter-streaming LISM and solar wind plasma in the heliospheric interface. The solar wind terminating shock is labeled "SWS", the heliopause "HP". Shown are sample hydrogen trajectories s with different inclination angles ε to the stagnation line.

The first moment of the distribution function, N_H, has already been given in the dashed curve of Fig. 2 of Fahr (1983). With this information, an unambiguous determination of the ionization degree X of the LISM hydrogen is possible. Observationally deduced values of $N_H = 0.05$ cm^{-3} at about 50 AU and a cosmic abundance ratio of $N_{He\infty}/N_{H\infty} = 0.1$ yield only one possible ratio of $N_{p\infty}/N_{H\infty}$ for any given set of boundary conditions. For the values used here one finds $N_{H\infty} = 0.1105$ cm^{-3} and $N_{p\infty} = 0.0135$ cm^{-3}, corresponding to an ionization degree of $X_{LISM} = 0.11$. This contrasts sharply with earlier derivations which pointed to values of $X_{LISM} > 0.5$.
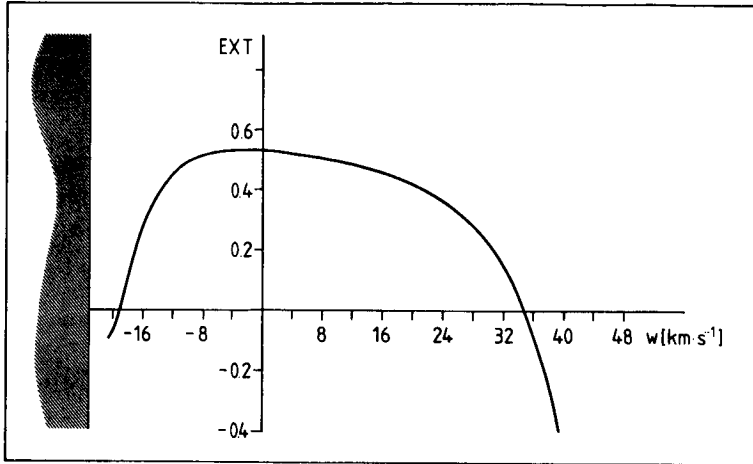

Figure 2: Hydrogen extinction EXT as a function of the thermal velocity w of hydrogen atoms. The velocity w is parallel to the stagnation line. The frame of rest is moving with the hydrogen bulk velocity $u_{H\infty}$. Atoms in the hatched area are moving away from the sun.

The average extinction, EXT = 1.0 $N_H/N_{H\infty}$, from infinity to the solar wind shock is EXT = 0.55. However, the extinction of the hydrogen atoms turns out to be strongly velocity dependent. Fig. 2 shows the hydrogen extinction EXT as a function of the thermal velocity w of the atoms and clearly indicates that the extinction is at maximum for atoms which are in or near the peak of the velocity distribution function (w = 0), while atoms in the wings are depleted much less. Atoms approaching the sun with velocities faster than about 60 km s^{-1} or slower than 4 km s^{-1} are actually enhanced. This shift of approaching hydrogen atoms away from the maximum into the wings of the distribution function implies an increase of the hydrogen gas temperature. Since the extinction is not isotropic, the second moment of the modified hydrogen distribution function yields a weak bulk velocity change ($\Delta u_H = -0.4$ km s^{-1}), and the corresponding third moments, $T_{,,}$ and $T_{\perp}$, imply a temperature anisotropy of $A_H = 1.08$. With values of $T_{,,\infty} = T_{\perp\infty} = 10^4$ K, at the solar wind shock $T_{,,} = 1.16 \cdot 10^4$ K and $T_{\perp} = 1.07 \cdot 10^4$ K are obtained.

The resulting normalized hydrogen velocity distribution function $\bar{F}_H$ is shown in Fig. 3. It is represented in three individual cuts through the three-dimensional non-Maxwellian function: parallel to the LISM bulk flow velocity vector (curve labeled 180°), antiparallel to it (0°), and at right angles to it (90°). While the curves for 180° and 90° coincide, they both clearly exhibit an enhanced temperature as compared to the normalized Maxwell distribution function M which has been supplied as a reference and which is based on a mean velocity-independent extinction of 0.5 of the original distribution function $f_{H\infty}$. The wing enhancement is strongest, however, for the 0° cut, i.e. for hydrogen atoms approaching the sun with velocities slower

than $u_{H\infty}$. A comparison with the original normalized function $\bar{f}_{H\infty}$ (not shown in Fig. 3) yields for these atoms and for the condition $w > 19$ km s^{-1} a net source of hydrogen atoms.
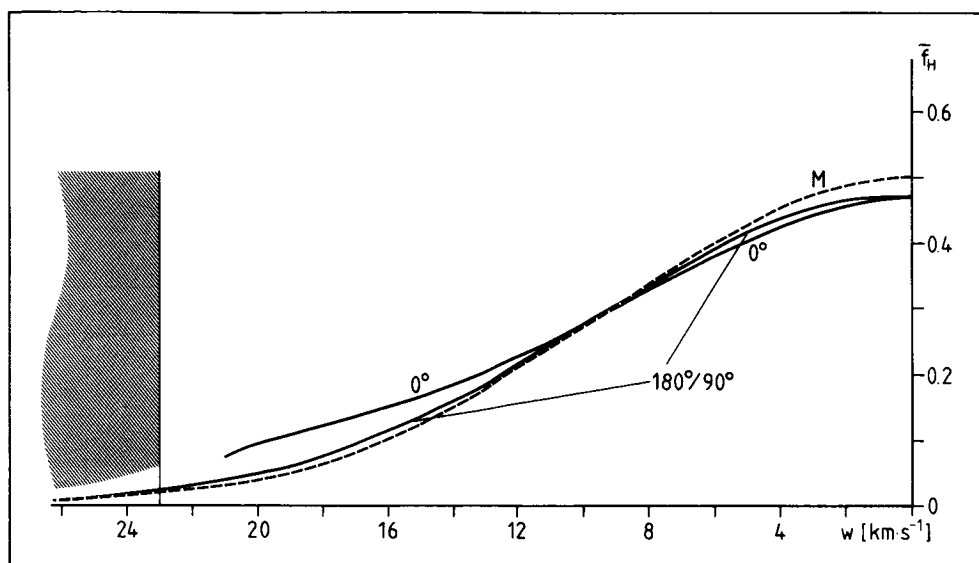

Figure 3: Normalized hydrogen velocity distribution function $\bar{f}_H$. For details see the text. Particles of the $0°$ cut with velocities corresponding to the hatched area are moving away from the sun.

One important final remark is in order here. The afore-mentioned comparison of subsonic and supersonic interface models reveals certain features of a heliospheric interface which are – rather surprisingly – independent of the type of interface (subsonic or supersonic) realized in the solar case. In both cases, the solar wind shock is located between 150 AU and 200 AU; the supersonic solar wind enclave is thus very much larger than often assumed. This needs to be remembered when analyzing and projecting results of the Voyager missions to the outer solar system. The calculated hydrogen extinction in both cases is approximately 50%, resulting in a LISM hydrogen density of about 0.1 cm^{-3} outside of the heliospheric interface. This is very consistent with astronomical observations. The abundance ratio of helium to hydrogen is about 0.1, corresponding to the observed cosmic abundance ratio. Rather low ionization degrees are computed for the nearby LISM: the subsonic model yields 11%, the supersonic model 20% ionization only. Since these results were obtained for both supersonic and subsonic interface models, they can be regarded with some confidence. They indicate that the unperturbed LISM essentially corresponds to the warm neutral medium ("WNM") defined by McKee and Ostriker (1977) (see also the introduction of Fahr, 1983).

References

Baranov, V.B., M.G. Lebedev, and M.S. Ruderman, Structure of the Region of Solar Wind – Interstellar Medium Interaction and its Influence on H Atoms Penetrating the Solar Wind, Astrophys. Space Sci. 66, 441, 1979.
Fahr,H.J., Theory of Interstellar Medium Diagnostics, in: Solar Wind 5, this volume, 1983.

Keller, H.U., R.R. Meier, and G.E. Thomas, Principal Conclusions and Results, VI. MPAE Workshop on Interstellar Gas in Interplanetary Space, Lindau/-Harz, 1980.

McKee, C.F., and J.P. Ostriker, A Theory of the Interstellar Medium: Three Components Regulated by Supernova Explosions in an Inhomogeneous Substrate, Astrophys. J. 218, 148, 1977.

Parker, E.N., Interplanetary Dynamical Processes, Interscience, New York, 1963.

Ripken, H.W., and H.J. Fahr, Modification of the Local Interstellar Gas Properties in the Heliospheric Interface, Astron. Astrophys., 1983, (in print).

THE INTERPLANETARY HYDROGEN AND HELIUM GLOW
AND THE INFERRED INTERSTELLAR GAS PROPERTIES

Darrell L. Judge
University of Southern California
Los Angeles, California 90089-1341

ABSTRACT

Observations of the interplanetary hydrogen and helium glow have been obtained by a number of spacecraft and rocket experiments during the past fifteen years. Important results have been established on the temperature, density, velocity, spacial dependence, and hydrogen to helium ratio. However, only four spacecraft launched to date are investigating the outer solar system and of these four the Pioneer 10 spacecraft is the farthest out at 28 A.U. Observations from this spacecraft at great distances have permitted an improved analysis of the effects which are only evident at large distance from the sun. Perhaps the most significant result in this regard is the clear evidence of the importance of multiple scattering of solar Ly-α; an effect which has not been observed in earlier work. Ignoring this effect can lead to a gross overestimate of the local galactic glow. In the present paper current best estimates of the galactic glow and the local interstellar wind parameters obtained by the Pioneer 10 photometer at great distances are presented, in addition to complementary experimental observations of particular interest.

INTRODUCTION

The interstellar wind consists primarily of atomic hydrogen and helium and results from the relative motion of our solar system with respect to the nearby interstellar gas. It can be studied "locally" by observing the resonantly scattered solar light at 1216Å (hydrogen) and 584Å (helium). A primary purpose of such observations is to determine the characteristics of the local pristine interstellar wind as well as to determine how it is modified as it traverses our solar system. This wind (actually a light breeze when compared to the solar wind) requires about forty years to traverse the region dominated by the solar wind i.e., the heliosphere. Thus the time scale for interaction and modification is indeed large.

As the interstellar wind passes through the solar system, it is gravitationally attracted by the sun, repelled by solar radiation, and ionized by charge exchange, photoionization, and electron ionization. The net result of these interactions is to focus helium, create a small helium cavity, and to weakly focus hydrogen and create a rather large hydrogen cavity, leaving a helium rich region within the first few A.U. of the sun.

In order to determine the spatial distribution and the physical parameters which characterize the inflowing gas a number of techniques have been employed. Isophotes and direct velocity and temperature measurements have been most useful in this regard. Velocity measurements of the interstellar wind have been obtained by Adams and Frisch (1977) by measuring the doppler shift of the Ly-α line using the high resolution spectrometer on board the Copernicus spacecraft, assuming the direction of the wind was known from the downwind

isophote observations of the gravitationally focused helium. Hydrogen and helium absorption cells have been used to infer both the temperature and velocity of these two components by measuring the width and the amplitude of the signal transmitted through them (Freeman et al. 1977; Bertaux et al. 1976). Using such direct observations of important model parameters it has been possible to greatly limit the remaining model parameters available to fit the observed isophotes. A brief review and summary of the inferred parameters is given in the next section.

SOLAR SYSTEM OBSERVATIONS

THE INNER SOLAR SYSTEM:

There has been a wealth of data obtained on the interplanetary glow from within the inner solar system and most of the earlier results are included in the reviews of Thomas (1978) and Holzer (1977). These earlier observations have provided an extensive set of data which have been fit to models of the inflowing interstellar wind. The model parameters presented at the Lindau workshop in 1981 based on several such data sets are given in Table I, in addition to the most recent density data obtained by Pioneer 10.

The earlier data will not be further discussed here other than to comment on the difficulties inherent in making observations in a region strongly affected by local solar effects. Specifically, local heating and doppler shift of the scatterers can be significant (Wu et al. 1981; Kunc 1980). For example, doppler shift of the He 584 Å emission can drastically change the emission intensity for helium atoms moving radially toward the sun even at the unaccelerated wind speed of 20 Km/sec since the solar helium linewidth is of the order of 100 mÅ. The doppler shifted wavelength in the radial direction is

$$\Delta \lambda \approx \lambda \ v/c = 40 \ mÅ \quad ,$$

which is well outside the core of the solar line. Because of such considerations as the above it is clearly desirable to limit the importance of the "local" effects (solar distances less than $\approx$ 10 A.U.) by examining data at large solar distances. Nonetheless, the considerable data available from measurements within the inner solar system are quite important for determining the interstellar wind flow direction and local anomalies in solar wind flow, as well as local temperatures, velocities, and densities.

Of these inner solar system measurements the observations of emissions near the solar poles are of particular interest with respect to the latitudinal dependence of the solar wind flow velocity. (The other inner solar system data will not be further discussed here since they have been extensively discussed in the literature and have been summarized in the reviews by Thomas (1978) and Holzer (1977)).

The specific data of interest have been obtained with the Mariner 10 spectrometer. These data show a distinct enhancement of the Ly-α glow over the solar poles which is interpreted as a latitude dependence of the solar wind proton flux or velocity, but not both (Witt et al. 1981; Ajello et al. 1979; Isenburg and Levy 1978). They conclude that the lifetime against ionization increases with increasing latitude and they obtain an asymmetry parameter which

TABLE I.   SUMMARY OF DENSITY/TEMPERATURE DETERMINATIONS FOR THE LOCAL INTERSTELLAR MEDIUM

Spacecraft and Date	Experiment	References	Derived Density (cm^{-3})	Derived Temp ($\times 10^4$ K)	Results
OGO-5 1969 - 1971	Ly-α photometer (3° FOV)	Thomas & Krassa (1971,1974); Thomas (1972)	$n_H = .12$	.35	"Hot" model
OGO-5 1969 - 1971	Ly-α photometer (40 arc min FOV)	Bertaux & Blamont (1971); Bertaux, Ammar & Blamont (1972)	$n_H = .1 - .2$	.1 - 1	"Hot" model
Rockets 1970, 1973	584 Å photometer	Paresce et al. (1974 a, b)	$n_{He} = .032$	.4 - .6	Temperatures are lower limits
STP 72-1 1972 - 1973	584 Å photometer	Weller & Meier (1974) ; Meier (1977)	$n_{He} = .009 - .024$	.25 - .1* .5 - 1**	*Uses modified cold model. ** Uses Meier's more accurate model.
Mars 7 1972 - 1973	Ly-α photometer plus H resonance cell	Bertaux et al. (1976)		1.1 - 1.3	Value of temperature assumes galactic Ly-α intensity is zero.
D2-A 1971	Ly-α photometer plus H resonance cell	Cazes & Emerich (1977)		.8 - 1.2	Observed ~10% interstellar polarization; verified that μ < 1 in 1971.
Mariner 10 Dec. 1973 & Jan. 1974	Spectrometer measured simultaneously 1216 Å and 584 Å	Broadfoot & Kumar (1977); Ajello, Kumar & Broadfoot (1977)	$n_H = .03 - .09$ $n_{He} = .006 - .012$	1 - 2	He/H = .15 ± .1
Prognoz-5 1976	4-channel photometer includes 1216 Å, 584 Å plus H resonance cell	Bertaux et al. (1977)		.78 - .98	
Apollo-Soyuz 1975	EUV telescope & broad-band photometer	Freeman et al. (1977)	$n_{He} = .002 - .006$		
Pioneer 10/11 1972 - present	2-channel photometer 1216 Å and 584 Å	Wu et al. (1981)	$n_H = .04$ $n_{He} = .01$		He/H = .23 ± .1; r = 1.5 (1972) to 14 A.U. (1981)
Black Brant IVB Rocket 1976	584 Å photometer and He resonance cell	Fahr, Lay & Wulf-Mathies (1977)	$n_{He} = .004 - .01$		

describes the solar wind latitudinal dependence. In the absence of direct measurements of particle flux at high solar latitudes, UV photometric observations are quite useful and provide information on the product of solar wind proton flux and the velocity dependent cross section. It is indeed quite likely that high latitude coronal holes are responsible for the observed increased Ly-α emission at high solar latitudes since it is known that coronal holes are sources of solar wind and that streams with velocity twice the normal wind of 400 km/sec and half the density characterize them. If the solar wind flux is constant then the cross section for ionization of hydrogen should decrease by about 30% of the increase in solar wind velocity, and thereby result in enhanced hydrogen over the poles. The increased solar wind velocity at high latitudes has in fact also been inferred from interplanetary scintillation measurements (Coles and Maagoe 1972).

THE OUTER SOLAR SYSTEM:

At large heliocentric distances the most important model parameters become the density of the interstellar gas and the galactic glow, which can be determined quite accurately, subject only to the reliability of the observing instrument calibration.

Before proceeding to the results it is informative to briefly review the glow equations to see how the measurements relate to the inferred parameters. In the equations below the measured quantity is I, the measured glow. Using the appropriate phase function, $P(\gamma)$, the volume emissivity, and I_G, the galactic glow, are adjusted until a suitable fit to the data is obtained. Since the volume emissivity depends on the solar flux, as seen below, it is clearly evident that the wind parameters determined depend upon a correct absolute measure of the observed glow and a correct value of the solar flux.
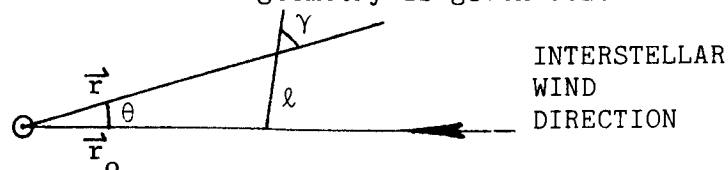
$$I = I_G + \int_{r_0}^{\infty} \epsilon(r, \theta) \, P(\gamma) \, d\ell ,$$

where $\epsilon(r, \theta)$ is the volume emissivity and $P(\gamma)$ is the light scattering phase factor.

The volume emissivity is given by

$$\epsilon(r, \theta) = \lambda^2/c \int_{-\infty}^{\infty} \pi F_\lambda \, \alpha_\nu (r, \theta) \, d\nu ,$$

where λ is the wavelength of interest, πF_λ the solar flux, and α is the absorption coefficient. The geometry is given below:

INTERSTELLAR
WIND
DIRECTION

560

From the above equations it is clear that uncertainties in the solar flux and instrument calibration can introduce significant errors. The absorption cross sections, however, are well established and are not a significant source of error. Differences in the time at which observations were obtained, as well as the observation distance from the sun, can also lead to different conclusions about the values of the interstellar wind parameters, particularly for measurements obtained within the inner solar system. Thus, the relatively good agreement among the various experimental observations shown in Table I is encouraging.

Since the Pioneer 10 measurements are currently being obtained at large heliocentric distances and, as mentioned above, the glow at large distances is largely unaffected by local heating, gas temperature, or look direction, the Pioneer 10 results at great distances are of particular interest. Model calculations showing the relative independence of near solar effects are given in Figures 1 and 2 where temperature and viewing direction are varied and plotted vs. distance from the sun. The model parameters in the figures have the conventional meanings (See Wu et al. 1981).
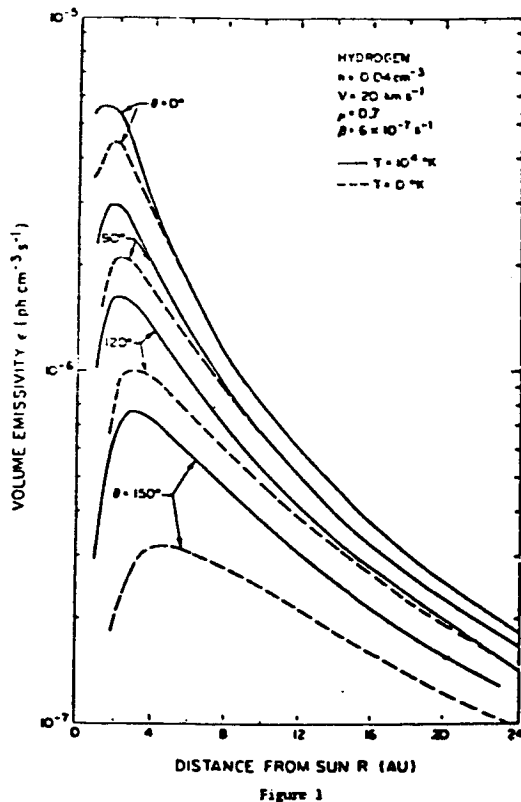

Figure 1. Calculated volume emissivity of interplanetary H Ly-α for various look angles θ. The model parameters are given in the figure.
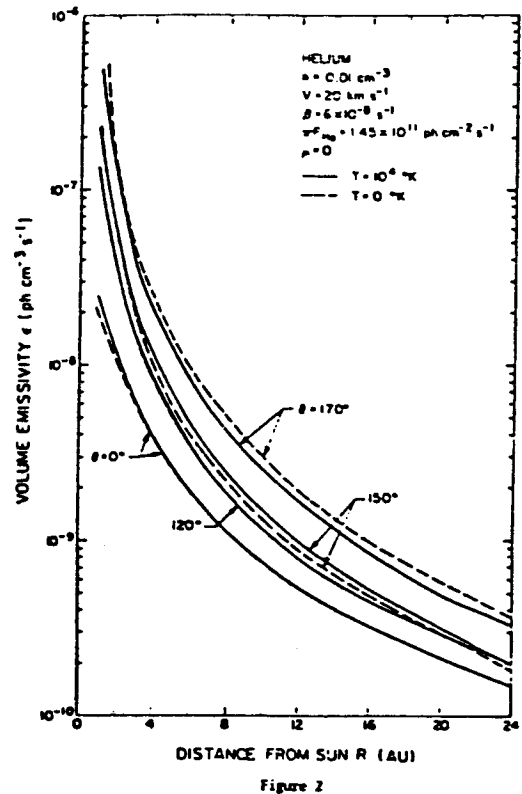
Figure 2. Calculated volume emissivity of interplanetary He 584 Å line for various look angles θ. The model parameters are given in the figure.

By fitting the Pioneer 10 data to such curves the parameters most evident

only at large solar distances can be readily determined. A parameter of particular interest which can be determined at great distances is that of the galactic glow. As observed from the inner solar system it is now clear that the apparent galactic glow is heavily contaminated by multiple scattering of solar Ly-α. The Pioneer 10 evidence for this arises from the fact that the galactic glow parameter I_g must be continually reduced as data at greater solar distances is included in the data base to be fit by the model. Thus, the "galactic glow" actually consists of the true value of the glow plus a multiply scattered component. Since the true galactic glow contribution to I_g is independent of radial distance from the sun it becomes evident only at large solar distances where single and multiple scattering of solar light within the heliosphere are greatly reduced, as observed by a photometer looking outward toward the heliosphere boundary.

As a final comment it should also be mentioned that the contribution to the glow by the multiply scattered component should vary with solar flux. In a preliminary investigation (Shemansky, Judge, in preparation) of the results obtained with the Voyager spectrometers which are observing from distances much closer to the sun (about 11 A.U.) an I_g of about 450 R for Ly-α is inferred from the model fit during the present time of high solar activity. This is an incredibly large value and one which reflects primarily the importance of multiple scattering at Ly-α. By comparison, the Pioneer 10 value is ≈ 30 R and still dropping as new data are added. As expected, there is no evidence for multiple scattering at the 584 Å helium resonance line.

Thus, it seems clear that (a) ongoing theoretical work must include hydrogen Ly-α multiple scattering and (b) that the true galactic glow in both the light of hydrogen Ly-α and helium 584 Å is quite weak. It should further be noted that the observations to date are still being obtained from well within the heliosphere. The "galactic glow" inferred here may thus include a contribution due to a splash component at the heliosphere boundary as well as other modifications to the inflowing "pristine" interstellar wind. However, such modifications will probably not change the inferred values by more than a factor of two.

ACKNOWLEDGMENT

REFERENCES

Adams, T.F., Frisch, P.C., "High Resolution Observations of the Lyman Alpha Sky Background," Astrophys. J., 212, 300, 1977.

Ajello, J.M., Witt, N., Blum, P.W., "Four UV Observations of the Interstellar Wind by Mariner 10: Analysis with Spherically Symmetric Solar Radiation Models," Astron. Astrophys., 73, 260, 1979.

Bertaux, J.L., Blamont, J.E., Tabarie, N., Kurt, V.G., Bourgin, M.C., Smirnov, A.S., Dementeva, N.N., "Interstellar Medium in the Vicinity of the Sun: A Temperature Measurement Obtained with Mars-7 Interplanetary Probe," Astron.

Astrophysics, 46, 19, 1976.

Coles, W. A., and Maagoe, S., "Solar-Wind Velocity from IPS Observations," J. Geophys. Res, 77, 5622, 1972.

Freeman, J., Paresce, F., Bowyer, S., Lampton, M., Stern, R., Margou, B., "The Local Interstellar Helium Dencity," Astrophys. J., 215, 83, 1977.

Holzer, T.E., "Neutral Hydrogen in Interplanetary Space," Rev. Geophys. Space Phys., 5, 467, 1977.

Isenberg, Philip A., Levy, E.H., "Polar Enchancements of Interplanetary Lα Through Solar Wind Asymmetries," Astrophys. J., 219, L59, 1978.

Kunc, Joseph A., "Survival Probabilities for Interstellar Hydrogen Flowing into the Interplanetary System from Far Regions of the Heliosphere," Planet. Space Sci., 28, 815, 1980.

Thomas, G.E., "The Interstellar Wind and Its Influence on the Interplanetary Environment," Ann. Rev. Earth Planet. Sci., 6, 173, 1978.

Witt, N., Ajello, J.M., Blum, P.W., "Polar Solar Wind and Interstellar Wind Properties from Interplanetary Lyman-α Radiation Measurements," Astron. Astrophys., 95, 80, 1981.

Wu, F.M., Suzuki, K., Carlson, R.W., Judge, D.L., "Pioneer 10 Ultraviolet Photometer Observations of the Interplanetary Glow at Heliocentric Distances from 2 to 14 AU," Astrophys. J., 245, 1145, 1981.

COMPARISON OF HELIOSPHERIC CURRENT SHEET STRUCTURE OBTAINED FROM
POTENTIAL MAGNETIC FIELD COMPUTATION AND FROM OBSERVED
MAXIMUM CORONAL BRIGHTNESS

John M. Wilcox
Institute for Plasma Research
Stanford University
Via Crespi, ERL 328
Stanford, CA 94305

A. J. Hundhausen
High Altitude Observatory
National Center for Atmospheric Research
Boulder, CO 80307

ABSTRACT

We compare the structure of the heliospheric current sheet early in
Sunspot Cycle 21 as computed from the observed photospheric magnetic
field with a potential field approximation, and as inferred from synop-
tic maps of the observed coronal brightness. On most of the solar rota-
tions compared the two methods give essentially the same results; the
basic shape of the warped current sheet and the amplitude (in solar
latitude) of the displacements of the sheet from the solar equator are
similar. On one rotation the current sheet computed with the potential
field approximation appears to be distorted by a large photospheric
region of unbalanced magnetic flux.

MEASUREMENTS OF THE SOLAR WIND NEAR THE SUN

G. Bourgois
Observatoire de Paris, Mendon

Observations of interplanetary scintillations of cosmic radio sources
with two 935 MHZ antennas belonging to the European Incoherent Scatter
Scientific Association allow an estimation of the solar wind properties
in the range of 10 to 60 solar radii. Because of the Earth rotation
the baseline, as seen by the source, varies both in length (from 30 to
200 KM) and in orientation with respect to the solar wind direction.
This simulates a multistation observation and provides a good sampling
of the statistical properties of the solar wind and turbulence. Ac-
curate measurements of the solar wind velocity and its random components
can be obtained as well as information about the anisotropy of the plasma
turbulence.
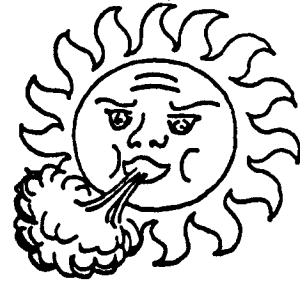
SESSION 9.

MINOR IONS

SUMMARY OF THE SESSION ON MINOR IONS

M. Neugebauer

The session began with a thorough review of observations of the properties of minor ions in the solar wind by Bame. The following papers added some new data and new theoretical considerations on the interpretation of these data. The principal areas of interest were the elemental and isotopic abundances, states of ionization, and dynamical anomalies, with the topic of ionization states receiving the most attention.

Bame summarized the He/H abundance variations, for which some systematic behavior with respect to solar wind origin is now becoming apparent. The ratio of ^{3}He/^{4}He varies widely, and the paper by Coplan et al pointed out a probable correlation of this parameter with solar activity. Mitchell discussed the systematic variations of Fe/H across coronal holes and from year to year.

Ipavich showed the charge state of Fe ions varying from +9 in coronal hole flow to +16 in post shock flows. Bame's review included discussion of observations of apparent mixtures of plasmas with different ionization states, which was extended by Bochsler's new analysis of ISEE-3 data. Owocki pointed out how several non-equilibrium effects in the corona can affect the inference of coronal temperatures from observations of ionization states at 1 AU. Ripken suggested that the solar wind may contain appreciable numbers of singly charged ions created by the interaction of the solar wind with interplanetary dust and Hovestadt presented data on the ratio of He$^+$/He^{++} at high energies and the puzzling variations of this ratio.

There is a growing data base, summarized by Bame and augmented by Schmidt, which suggests that, on the average, all minor ions flow away from the Sun with a speed which exceeds the proton speed by approximately the same amount and have roughly the same temperature per unit mass. Isenberg has studied the possible acceleration and heating of minor ions by resonant cyclotron interactions, and concludes that this interaction cannot account for the observations, which remain unexplained.

SOLAR WIND MINOR IONS – RECENT OBSERVATIONS

S. J. Bame
University of California, Los Alamos National Laboratory
Los Alamos, NM 87545

ABSTRACT

During the years following the Solar Wind Four Conference at Burghausen our knowledge of the solar wind ion composition and dynamics has grown. There have been some surprises, and our understanding of the evolution of the solar wind has been improved. Systematic studies have shown that the minor ions generally travel with a common bulk speed and have temperatures roughly proportional to their masses. It has been determined that the $^3He^{++}$ content varies greatly ; $^3He^{++}/^4He^{++}$ ranges from as high as 10^{-2} values to below 2×10^{-4}. In some solar wind flows which can be related to energetic coronal events, the minor ions are found in unusual ionization states containing Fe^{16+} as a prominent ion, showing that the states were formed at unusually high temperatures. Unexpectedly, in a few flows substantial quantities of $^4He^+$ have been detected, sometimes with ions identifiable as O^{2+} and O^{3+}. Surprisingly, in some of these examples the ionization state is mixed showing that part of the plasma escaped the corona without attaining the usual million-degree temperatures while other parts were heated more nearly in the normal manner. Additionally, detailed studies of the minor ions have increased our understanding of the coronal expansion. For example, such studies have contributed to identifying near equatorial coronal streamers as the source of solar wind flows between high speed streams.

INTRODUCTION

Since the Burghausen Solar Wind 4 Conference in 1978, a number of new observations and studies of solar wind minor ions have been reported. This survey discusses a few of these and some of their implications and mentions others more briefly. Some of the studies are treated in more detail elsewhere in this volume. The topics to be considered are listed below:

1. Abundance of $^4He^{++}$ and its variations.

2. Abundance of $^3He^{++}$ relative to $^4He^{++}$.

3. Minor ion temperatures and velocities.

4. Abundances from E/Q spectra of heavy ions.

5. Iron ions in high speed streams.

6. Ionization temperatures in high speed streams.

7. Ionizationally "hot" transient solar wind flows.

8. Ionizationally "cold" transient flows.

1. ABUNDANCE OF $^4He^{++}$ AND ITS VARIATIONS

Helium abundance variations have been studied using data obtained from Los Alamos plasma instrumentation on IMP 6, 7, and 8 in the years extending from 1971 through 1978. The study documents the association of different average abundance levels with different types of solar wind flows (Borrini et al., 1982a). As seen in Figure 1, low values of abundance are identified with those low speed, interstream flows in which polarity reversals of the interplanetary magnetic field (IMF) are embedded. Intermediate abundances are associated with high speed streams from coronal holes, as previously noted (Bame et al., 1977); abundance variations in streams are small. High abundances, of course, are associated with energetic coronal events; such an association with solar flares has been recognized and documented in many studies during the past 15 years.
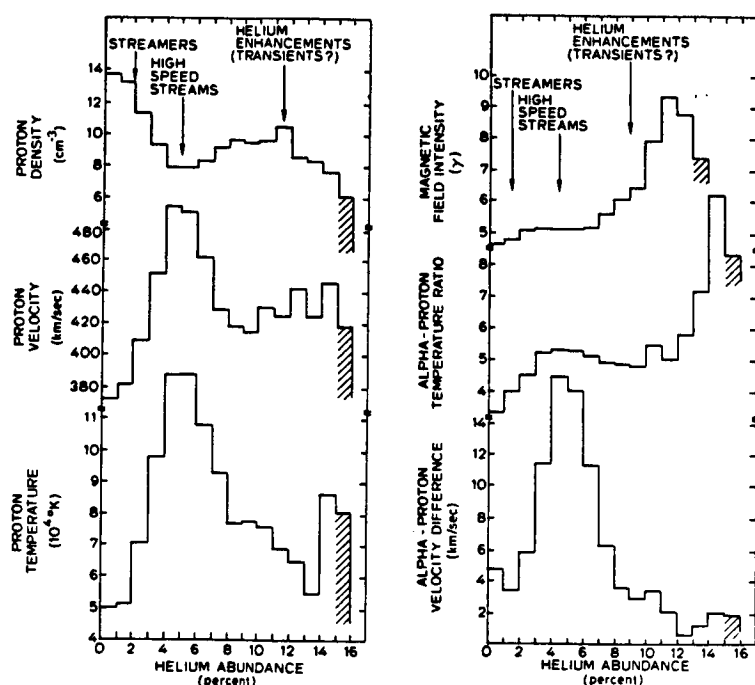
Fig. 1. Interplanetary solar wind flow characteristics associated with varying levels of the helium abundance. Low values of abundance are associated with low speed flows which can be identified with coronal streamers, median values can be identified with high speed streams arising in coronal holes, and high values can be identified with transient flows from various kinds of energetic coronal events.

Earlier studies of the solar cycle variation of the helium abundance (e.g. Bame, 1972; Ogilvie and Hirshberg, 1974; Feldman et al., 1978) have been extended using IMP 6, 7, and 8 plasma results (Borrini et al., 1982a). The IMP data, shown in Figure 2, exhibit a continuing modulation which reached a minimum in 1975-76 and was sharply rising in 1977-78, 11 years after a similar rise observed in 1966-67. An important part of this modulation is due to solar cycle changes in the mix of different types of solar wind, i.e. the low speed interstream flows with low He abundances, the high speed streams with intermediate values, and transient flows from energetic coronal events which have the highest abundances, and which, of course, occur more frequently when the sun is active.

The characteristics of solar wind flows containing helium abundance enhancements, HAEs, previously known to be associated with transient coronal disturbances, have been systematized using a superposed epoch analysis of 73 large events which occurred during 1972-78 (Borrini et al., 1982b). Nearly 50% of the HAEs were associated with interplanetary shocks and/or geomagnetic sudden commencements, but the plasma pattern associated with HAEs occurs whether or not a shock or SC is observed.
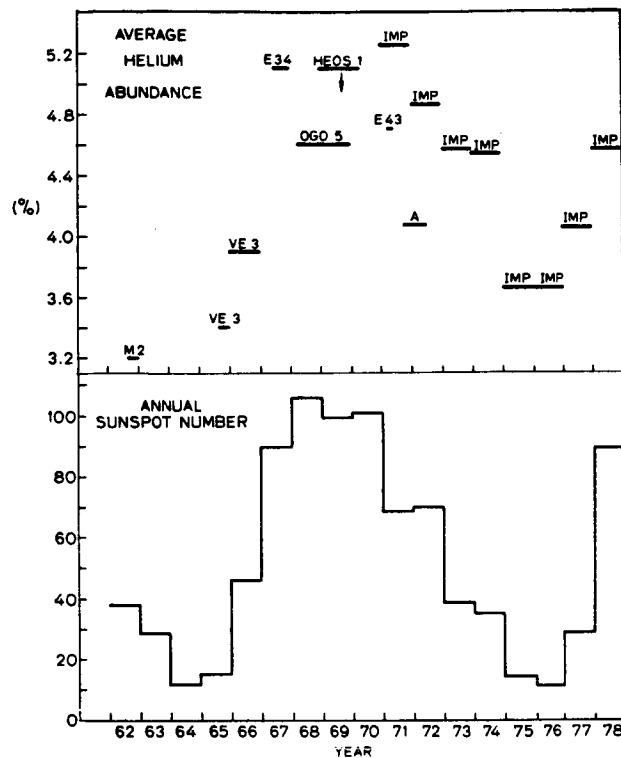

Fig. 2. Solar cycle variation of the solar wind helium abundance. Average values observed with various spacecraft are compared with the annual sunspot number.

Low levels of the He abundance are associated with the low speed solar wind, or interstream flows, which in turn are associated with IMF polarity reversals. Noting this, and tracing the low speed wind back to the corona, it is possible to identify the coronal equatorial streamer belt as the source of interstream flows (Borrini et al., 1981; Gosling et al., 1981). In these cool, low speed flows, minimums in the abundance are associated with maximums in proton density, identifying a large fraction of the flows as noncompressive density enhancements, NCDEs, in which polarity reversals often occur. The duration and multiplicity of reversal events are generally correlated, when mapped back to the sun, with the local tilt of the streamer belt to the solar equator.

Another study, making use of Vela 5 and 6 heavy ion measurements, also identifies the streamer belt as the source of interstream solar wind flows (Feldman et al., 1981). It was shown that moderate to high plasma densities and oxygen freezing-in temperatures in interstream flows match similar conditions within coronal streamers close to the sun. It was also shown that high solar wind electron temperatures at 1 AU arise from a lower coronal temperature gradient, rather than from a higher coronal temperature.

2. ABUNDANCE OF ^{3}He^{++} RELATIVE TO ^{4}He^{++}

Until recently only a few ^{3}He^{++}/^{4}He^{++} abundance ratio measurements have been available. Those from ion E/Q analyzers are rare because of the infrequent occurrence of interplanetary conditions appropriate for resolving ^{3}He^{++}, using E/Q analysis alone. Values of 1.3×10^{-3} and $\sim 3 \times 10^{-3}$ for measurement periods of ~ 1 hour have been reported (Bame et al., 1968; Bame et al., 1979); another value of 1.9×10^{-3}, measured during an interval of two days, has been reported by Grünwaldt (1976). Longer term measurements were obtained by exposing Al foils on the moon during 5 Apollo flights, and then analyzing gases released from the returned foils (Geiss et al., 1972). Remarkably similar results were obtained from the 5 flights, yielding an average value of the ^{3}He/^{4}He number ratio of 4.2×10^{-4}.
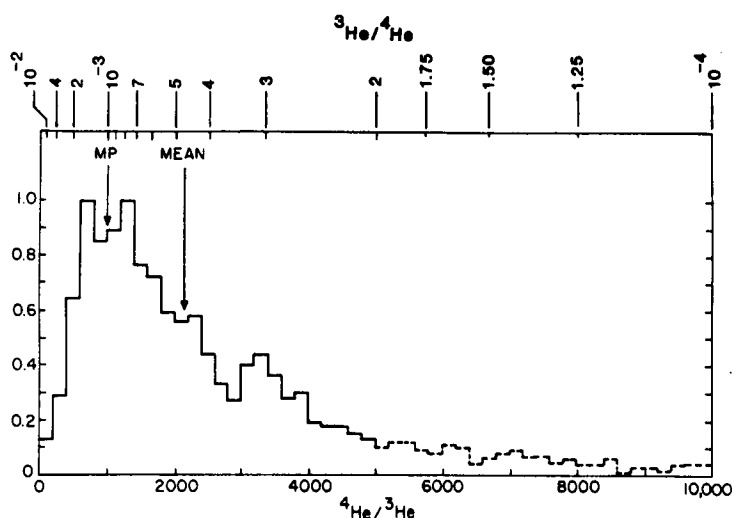

Fig. 3. Abundance level comparisons of ^{3}He and ^{4}He ions from 4334 spectra measured over two periods from August 18 to November 24, 1978 and March 24 to August 25, 1979.

Long term measurements reported by Ogilvie et al. (1980a) were made with an M/Q composition analyzer on ISEE 3 (Coplan et al., 1978). As seen in Figure 3, these results show that ^{3}He/^{4}He is extremely variable, ranging from $<10^{-4}$ to values as high as 10^{-2}. The most probable value measured is $\sim 1 \times 10^{-3}$, very near to the first reported value of 1.3×10^{-3}. Also noteworthy, the average value of these extended observations, 4.7×10^{-4}, is not far different from the average value obtained by Geiss and his coworkers from the five Apollo foil experiments. Another result of the study reported by Ogilvie et al. (1980a) shows that there is a discernible trend for ^{3}He^{++}/^{4}He^{++} to be lower when the ^{4}He^{++} flux is high.

3. MINOR ION TEMPERATURES AND VELOCITIES

Systematic studies of the local temperatures and velocities of minor ions have been reported by Schmidt et al. (1980), Ogilvie et al. (1980b), and Ogilvie et al. (1982). Briefly, these studies show that on the average the temperatures of minor ions are roughly proportional to the atomic mass of the ion species, i.e. T_i/M_i = constant. However, in individual cases there are significant deviations from this proportionality. In particular, the results obtained with the ISEE 1 M/Q analyzer described by Shelley et al. (1978) show that although the proportionality still holds for He^{++} and O^{6+} at low temperatures, it breaks down for H$^+$.

Concerning minor ion velocities, the results of the studies show that except for H^+, all ion species have very nearly the same velocities. Speed differences between a minor ion such as O^{6+} and H^+ are then like the well documented differences between He^{++} and H^+ (e.g. Asbridge et al., 1976). Using measurements from the ISEE 3 M/Q analyzer (Coplan et al., 1978), Ogilvie et al. (1982) give examples of $He^{++}-H^+$ speed differences across several high speed streams. In an unusual case, following an interplanetary shock, the post-shock H^+ ions were found travelling faster than the He^{++} ions for some hours, a reversal of the usual roles of those two ions at high speeds.

4. ABUNDANCES FROM E/Q SPECTRA OF HEAVY IONS

An observation of an enrichment of O^{6+} simultaneously with an abundance increase of He^{++} in the driver gas of an interplanetary shock has been reported by Bonifazi et al. (1980). It seems reasonable to suppose that if there is a helium enrichment, there should also be corresponding enrichments of other heavier elements, and indeed such a result has also been reported for three other transient flows (Zwickl et al., 1982). A note of caution should be given concerning the universality of this result in regard to a single ion species such as O^{6+}. If the ionization temperature of the driver plasma is high enough, the O^{6+} abundance may actually turn out to be lower because the enhanced oxygen will exist principally in the O^{8+} and O^{7+} charge levels. Examples of O^{6+} depletions, occurring on 19 November 1970 and 18 May 1971 have been given by Bame et al. (1979).

Further observations of heavy ion E/Q spectra have been reported from measurements made with the ISEE 2 solar wind experiment (Formisano and Orsini, 1981) and with the Prognoz 7 plasma spectrometer (Zastenker and Yermolaev, 1981). Unusually high abundances compared to previous measurements were cited in both reports. In the case of the ISEE 2 measurements it seems likely that the high abundance values may be, at least in part, due to counting rate losses in the proton peak. In two of the examples given, the proton peaks are double. If the double peaks were the result of a double stream, such as those observed during the declining phase of high speed streams (Feldman et al., 1973), the He^{++} peaks would probably also be double, as reported by Asbridge et al. (1974). In these examples the resolution is high enough to reveal that double He^{++} peaks are not present. Thus, it seems possible that the dips between the H^+ peaks in the ISEE 2 spectra are due to count rate saturation effects, so the high abundances cited should be viewed with caution. In the case of the Prognoz 7 measurements, which also give abundance values an order of magnitude higher than previous values, not enough information is available to determine whether a similar count rate saturation effect might be responsible for the unusually high results. It is clear that there is a great need for future solar wind composition experiments capable of operating in all types of solar wind flows for extended periods of time, in order to catalogue the extent of abundance variations.

5. IRON IONS IN HIGH SPEED STREAMS

First measurements of the abundance of iron ions in high speed solar wind streams have been reported by Mitchell and Roelof (1980). Abundance determinations from E/Q spectral measurements have not been possible due to the high kinetic ion temperatures in streams and/or insufficient energy range of the electrostatic analyzers which have been flown. Correspondingly, magnetic

577

mass analyzers have not been able to cover the appropriate range due to limitations in available magnetic field strengths.

The results of Mitchell and Roelof come from an analysis of data from the NOAA/JHU energetic particles experiment on IMP 7 and 8 (Williams, 1977) which is sensitive to iron ions at speeds above 600 km s^{-1}. Principal results from this study will be mentioned only briefly here, since the subject is covered more extensively elsewhere in this volume. Estimates of the Fe/H abundance ratio in high speed flows show it to be roughly the same as the nominal coronal abundance. There is evidence that abundance fluctuations in streams may, like those of He, be smaller than in slow and in transient flows, as determined from E/Q measurements. Further results show that the Fe ions generally are faster than H$^+$, but slower than He^{++} (Mitchell et al., 1981). In general, the Fe distribution parameters (bulk velocity, flow direction, temperature) are found to be similar to the He parameters determined with electrostatic analyzers (Mitchell et al., 1982). There are factor-of-two differences between average abundances determined in recurrent streams from different coronal holes. Similar to the He enhancements seen in flare related flows, Fe enhancements of 4-5 are also observed.

6. IONIZATION TEMPERATURE IN HIGH SPEED STREAMS

Temperatures at which the ionization states of minor ions are established or frozen in during the coronal expansion were reported in a number of early papers (e.g. Bame et al., 1968; 1970; 1974). These determinations, based on measurements of individual minor ion peak intensities in E/Q spectra, are restricted to the slow interstream solar wind in which the local kinetic temperatures are low or to the temperature-depressed drivers of transient flows coming from energetic coronal events (Bame et al., 1979; Fenimore, 1980). It is of particular interest to extend such determinations to the case of high speed solar wind streams arising out of coronal holes, since the holes have been observed to be cooler than other regions of the corona (Krieger et al., 1973). Until recently, it has not been possible to measure the ionization states of high speed flows. In those flows the kinetic temperatures are so high that individual minor ion species such as O^{6+} and O^{7+} can't be resolved in E/Q spectra. The Fe ion distribution has been inaccessible due to limited energy ranges.

This restriction has been overcome with two new experimental approaches. The first of these utilizes the ion composition experiment on ISEE 3, described by Coplan et al. (1978), with which M/Q analyses of some of the minor ions can be performed on high speed flows as well as slow flows. Ogilvie and Vogt (1980) have used ISEE 3 data to investigate the oxygen ion freezing-in temperatures by determining the ratios of ion fluxes at M/Q = 2.29 (principally O^{7+}) to that at M/Q = 2.67 (principally O^{6+}) as a function of solar wind speed, and comparing the ratios with ionization equilibrium calculations. At low speeds ionization temperatures of ~1.6 x 10^6 K are inferred, in reasonable agreement with previous determinations using E/Q analyses. However, at speeds above 450 km s^{-1}, i.e. in high speed streams, the measured ratio starts to rise rapidly, suggesting higher freezing-in temperatures in coronal holes. Values above 3 x 10^{6}K are inferred for 600 km s^{-1} speeds. The authors suggest that these results might be caused, not by a higher freezing-in temperature, but by electron distributions in coronal holes characterized by a temperature of 1.5 x 10^{6}K, but having a non-Maxwellian high energy tail similar to that of a 3 x 10^{6}K distribution.

The second experimental approach utilizes the intermediate energy ion composition experiment on ISEE 1, described by Hovestadt et al. (1978). By analyzing the shapes of charge state distributions of CNO ions in diffuse ion events upstream of the bow shock, Galvin et al. (1982) infer ionization temperatures for the types of solar wind flow incident at the bow shock. They find temperatures of ~1.5 x 10^6K for slow, interstream solar wind, ~2.5 x 10^6K for flare-related transient flows, and ~1.4 x 10^6K for coronal hole-associated flows.

Further analysis of the ISEE 3 oxygen charge state data has insured that the high speed data set is not contaminated with shock associated events. The extended study confirms that the M/Q = 2.3 to M/Q = 2.7 ratio rises at speeds above 450 km s^{-1} (Ogilvie, 1982). Some part of this rise may be due to variations in the relative abundances of elements in the CNO region of the spectrum which contribute to the O^{7+} fraction in particular. However, it is concluded that this effect is not large enough to avoid having to infer high coronal tempertures unless a non-Maxwellian shape of the electron distribution in the source region is invoked. It is clear that further work on this important subject is essential.

7. IONIZATIONALLY HOT TRANSIENT SOLAR WIND FLOWS

Following flare-related interplanetary shock waves, driver or piston flows are sometimes observed with very unusual distributions of minor ions in the E/Q spectra measured with electrostatic analyzers. These spectra show that the plasma had a "hot" origin in the solar corona (Bame et al., 1979; Bame, 1981). This is not always the case in driver flows; sometimes the spectrum cannot be distinguished from those found in the slow, interstream solar wind, and sometimes, as discussed in the next section, IP shocks are followed by driver flows which contain ions indicative of a "cold" origin.

In Figure 4 an example of a hot E/Q spectrum is contrasted with a normal spectrum obtained in a slow interstream flow. The hot case was measured with a heavy ion analyzer on Vela 6B and the normal example on Vela 5A. The two spectra have been normalized to E/Q = 2 at the $^4He^{++}$ peaks and are shown plotted on an M/Q scale which assumes equal flow speed for all ion species.

In the upper spectrum from slow interstream solar wind, a typical distribution of ion peaks is evident beyond $^4He^{++}$. Both O^{7+} and O^{6+} are prominent, with unresolved species of C, N, and Ne between them. A fit of the peaks gives a freezing-in temperature of 2.1 x 10^6K, typical of slow flows. Beyond the oxygen peaks are three peaks, C, D, and E that can be attributed to silicon with an admixture of sulfur. Beyond the Si peaks lies a group of Fe peaks ranging from 12+ to 7+, with a distribution which was formed at ~1.5 x 10^6K in the corona, again typical of a slow flow.

The lower spectrum, labelled "hot," in Figure 4 shows a distinctively different shape which has been shown to be due to a hotter than normal origin of the ionization state. This spectrum was obtained in the driver flow of an IP shock which followed a flare, variously reported as importance 1B to 3B, by 64 hours. The typical Fe species in the 12+ to 7+ charge level positions are not present at resolvable levels. Instead, a reasonable analysis shows that the Fe ionization state has shifted to a higher stage, indicative of a freezing-in temperature of ~3 x 10^6K. The prominent peak at D in the figure is due to Fe^{16+} ions; the Si ions, normally found in this range are shifted into

the Si^{12+} position, near O^{7+}. Another notable feature of hot spectra is that the normally third most prominent peak, O^{6+}, is very subdued, because most of the oxygen ions are in the O^{8+} and O^{7+} charge levels.
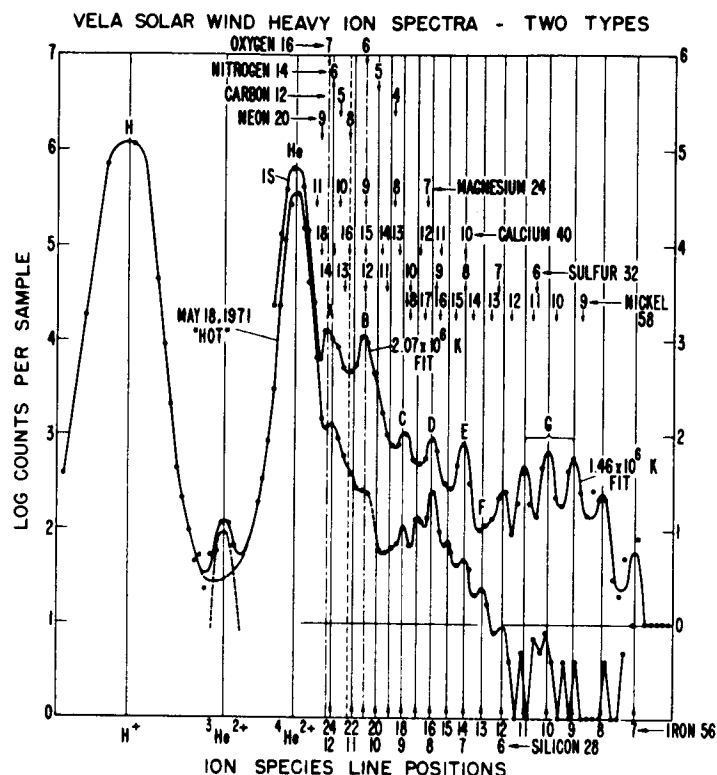

Fig. 4. A heavy ion spectrum from the slow interstream solar wind of June 23, 1969 (upper spectrum) measured with Vela 5A, contrasted with a hot spectrum measured on May 18, 1971 with Vela 6B in a flare induced, post shock, driver gas flow.

A systematic study of the types of solar wind flows associated with hot heavy ions has been reported by Fenimore (1980) using Vela 5 and 6 heavy ion data. Spectra indicating hot coronal conditions ranging from ~1.5 x 10^6K to above 9 x 10^6K are found in approximately 1/7 of the measurements. Hot spectra are found in three types of flows: 1) postshock flows, PSFs, 2) nonshock related helium abundance enhancements, HAEs, and 3) noncompressive density enhancements, NCDEs. The PSFs and HAEs are usually interplanetary manifestations of solar flares. In the case of the HAEs, the flare ejecta reach the Earth even though an IP shock is not observed. The NCDEs with hot heavy ions differ from the PSF-HAEs in several ways, suggesting that they evolve from energetic coronal events that are not flare-related but involve higher than normal coronal temeratures. Active regions, coronal mass ejections, and equatorial streamers are suggested as possible sources for the NCDEs with hot heavy ions.

8. IONIZATIONALLY COLD TRANSIENT FLOWS

The previous section discussed solar wind flows in which the minor ion relative intensity distributions show that the plasma ionization states were established in hotter than usual coronal regions. In the last few years a small number of observations have been reported which show that the opposite also occurs - minor ion distributions have been found which contain ions which could not have survived the usual million-degree temperature coronal expansion.

The first reported solar wind plasma with an anomalously "cold" origin was detected with electrostatic analyzers on HELIOS 1 and described by Schwenn et al. (1980). In the piston gas driving an IP shock on Jan. 29, 1977, very unusual spectra were found with three prominent peaks at relative E/Q positions of 1, 2, and 4 as shown in Figure 5. The peaks at 1 and 2 are readily identified as due to H^+ and He^{++} ions. The peak at 4 seemed too large to be explained by the ion species that usually occupy that position, Si^{7+} and S^{8+}. However, data are available from two different electrostatic analyzers on each of the two HELIOS spacecraft; one analyzer counts ions individually, while the other measures ion current. By normalizing spectra from the two instruments at the charge 1 H^+ peak, as shown in Figure 5, the charge of the second peak was found to be 2, as expected for He^{++}, while the charge of the third peak was approximately 1, instead of a high multiple such as 7. If the third peak had been due to the charge 7 and 8 Si and S ions, which normally occupy this position, the multiply charged ions would have created a sufficiently large current that the peak height in the electrometer spectrum would have been identifiably higher than in the counts spectrum, reaching near the arrow shown in the figure. Thus, the third peak was identified as singly charged He^+, which is at undectably low levels most of the time (Feldman et al., 1974).
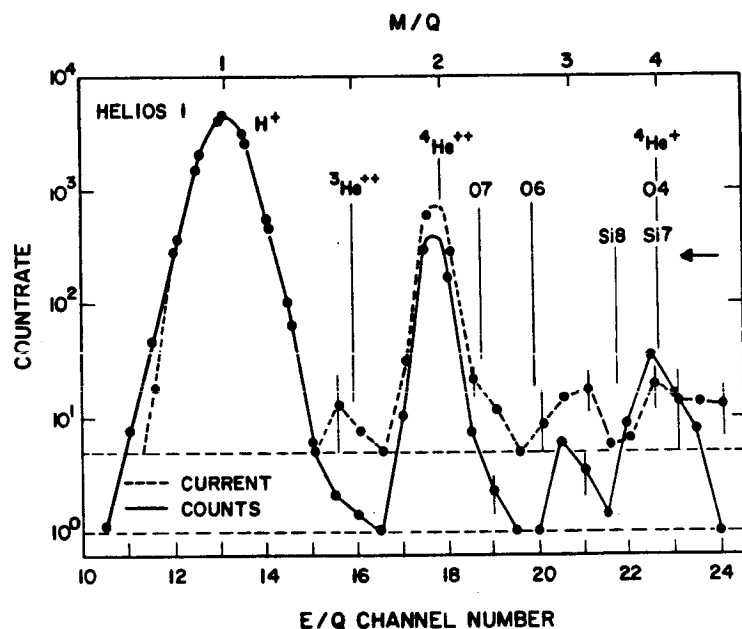

Fig. 5. Spectra measured simultaneously with two electrostatic analyzers on HELIOS 1, plotted together. Comparison of the spectrum determined by counting individual ions with the one using current detection identifies the peak at M/Q = 4 as He^+ rather than Si^{7+} which would produce a peak in the electrometer spectrum at the level shown by the arrow.

A few examples of the sporadic appearance of He^+ peaks in solar wind spectra were reported much earlier (Bame et al., 1968; Bame, 1972), but in those cases the He^+/He^{++} number ratios were much smaller than in the spectrum observed by Schwenn et al. (1980). No viable explanation for these sporadic appearances was set forth until the report of Schwenn and coworkers.

A second case of high flux levels of He^+ ions which occurred on July 29, 1977 was found in IMP 8 data and reported by Gosling et al. (1980). The interplanetary conditions associated with this event are illustrated in Figure 6 which shows a time sequence of E/Q spectra starting at 2358 UT on July 28, extending beyond 1444 UT on July 29. During this time period an IP shock passed IMP 8, leaving the spacecraft immersed in the heated ambient plasma. At

1224 UT the temperature-depressed driver gas arrived, in which the peaks of H^+ and He^{++} are sharply resolved. About 1 hour after the arrival of the driver gas, a third prominent peak appeared in the spectrum at an E/Q position four times that of H^+. The abundance of this peak is much too high to be explained plausibly by an ion species other than He^+. The He^+/He^{++} number ratio reached values as high as 0.3 during the event.
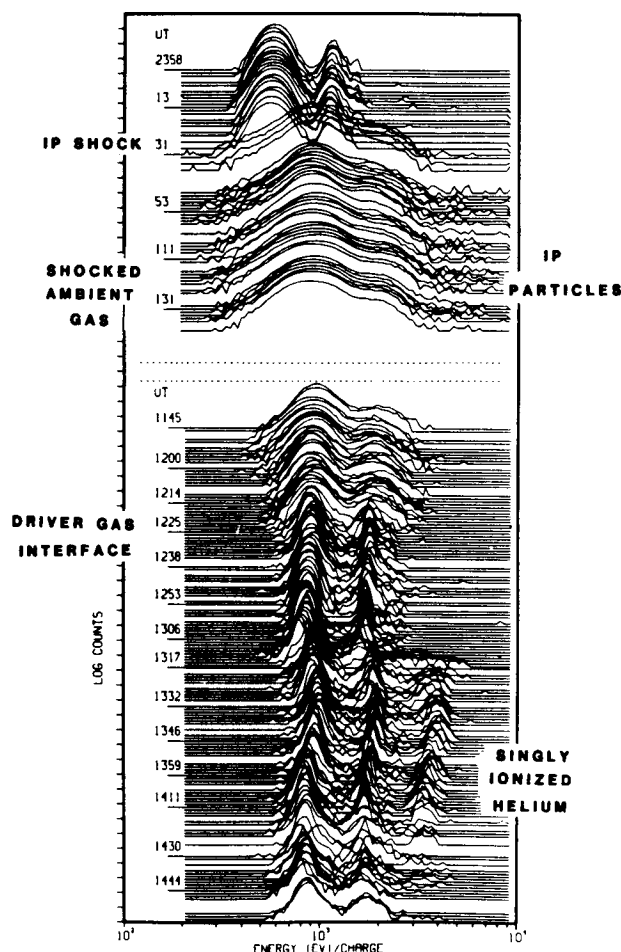

Fig. 6. Interplanetary conditions during the July 28-29, 1977 period. An IP shock heated and accelerated the ambient flow. Interplanetary ions associated with the shock passage are evident in the heated flow, creating the noise-like traces at low and high energies surrounding the H^+ and He^{++} peaks. The arrival of driver gas is marked by the sudden appearance of cold plasma with very well resolved H^+ and He^{++} peaks. About an hour later a strong third peak, due to He^+ ions, appears in the spectra.

An ion spectrum from this event, obtained by summing many of the individual spectra together is shown in Figure 7. Notable features of the spectrum in addition to the prominent third peak are the resolved peak of O^{6+} ions and the broadness of the He^+ peak compared to the He^{++} peak. No reason has been found for why the He^+ ions in this example should have a higher kinetic temperature than those of He^{++}, as they apparently do.

A study of a large number of heavy ion spectra obtained with the Vela 5A, 5B, 6A, and 6B analyzers during 1969-1975 has yielded some seven events with anomalously high numbers of counts at the M/Q = 4 position (Bame, 1980) Many more events would have been observed if fuller telemetry coverage in the solar wind had been available. The numbers of He^+ ions in these Vela events were small in comparison to the numbers in the large events mentioned above.

A systematic search of Los Alamos IMP and ISEE data received between October 1972 and February 1980 found two more events in addition to those already mentioned (Zwickl et al., 1982). The IMP and ISEE experiments were designed with sensitivities for standard solar wind ion measurements rather than for detecting low countrate exotic ions. More events would certainly have been found with more sensitive instrumentation and more complete telemetry coverage.

The most recent large He^+ event was found in HELIOS 2 data of May 29, 1979 (Schwenn, 1980; 1982). In this case, a charge 1 peak was again found at an E/Q position 4 times the position occupied by H^+.
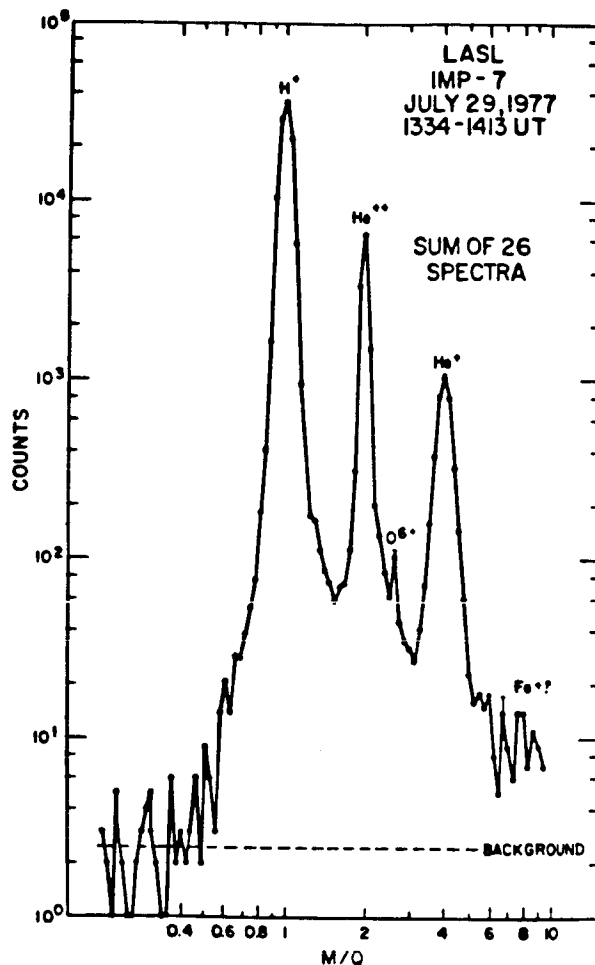

Fig. 7. Summed IMP 7 spectra showing the strong third peak of He^+ ions at M/Q = 4.

One other He^+ event, detected with the Vela 3A plasma analyzer on January 13, 1967 (Bame, 1980), is shown in Figure 8. The measured E/Q spectra are shown in time sequence vertically. The first spectrum shows a plasma flow with uncommonly well resolved H^+ and He^{++} peaks; most likely this flow is an anomalously cool driver gas from an energetic coronal event. In the second spectrum, a peak at an E/Q position 4 times that of H^+ shows the presence of He^+ ions in the flow. At 1150 UT a small amount of He^+ is still present. At 1207 UT an IP shock had passed the spacecraft leaving the ambient gas accelerated and heated. In succeeding spectra the continued presence of He^+ is evident, although the high temperature of the gas prevents complete resolution

of He$^+$ from He^{++}. In the later stages of the event, the proton bulk speed in the shocked gas was appreciably higher than that of the He ions; another case of H$^+$ ions travelling at a higher speed than He^{++}, following a shock passage, has been reported by Ogilvie et al. (1982). At 1839 UT, the He$^+$ number density is roughly 50% that of He^{++}. By 0027 UT on January 14 a new body of gas, the driver for the January 13 shock, had arrived. In this driver, which can be associated with a 3B flare, there is no longer a component of He$^+$. Instead, a well resolved peak at a relative E/Q position of 3.5 shows that this driver contained Fe^{16+} ions originating in a hot coronal region (Bame et al., 1979).
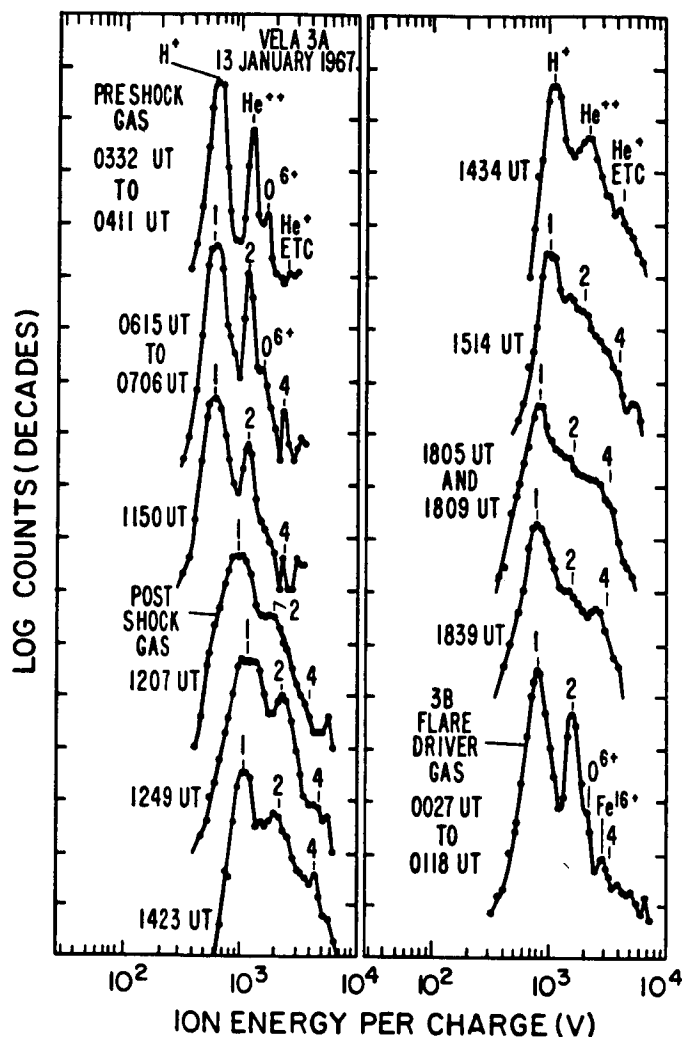

Fig. 8. Sequence of spectra from Vela 3A and 3B showing the appearance of a small narrow peak of He$^+$ ions early on January 13, 1967. Following an interplanetary shock at about noon, the He$^+$ abundance in the ambient plasma increased to levels high enough that the presence of He$^+$ ions is evident, even though the ion temperature is too high to permit full resolution. At 1839 UT the spectrum indicates that the He$^+$/He^{++} number ratio is roughly 50%.

The sources of ionizationally cold flows seem well established as energetic coronal events, generally without a flare association. Including the seven small He$^+$ events found in Vela heavy ion data and the other events mentioned above, there is strong evidence of a correlation of the events with phenomena which are associated with impulsive coronal events, i.e. mass ejections. Many, but not all events followed IP shocks and most are associated with Forbush decreases. There is a strong association with Type II and IV radio emissions, but there is no association with flares for several of the large events. Schwenn et al. (1980) suggest the possibility of direct ejection of cool chromospheric plasma into the solar wind via eruptive prominences

(disappearing filaments when observed against the solar disk). Indeed, correlations of eruptive prominences with He^{+} events are found for the events of January 29, 1977, July 29, 1977, May 29, 1979, and January 13, 1967. There are possible associations for some of the remaining 10 events; in the others there is not enough information to make a determination. There are flare associations with some of the events which is perhaps not surprising since an association between flares and disappearing filaments has been noted.

The spectra of two of the He^{+} events discussed above also show the presence of oxygen ions in low stages of ionization. Schwenn (1980; 1982) reported the observation of two E/Q spectra on May 9, 1979 which exhibited four strong peaks at E/Q values of 1, 2, 4, and 8 relative to H^+, as shown in Figure 9. Comparing the spectrum obtained by counting individual ions with one obtained by measuring the charge deposited by the analyzed ions, it was possible to show that the ion charges of the four peaks were 1, 2, 1, and 2, identifying the ions as H^+, He^{++}, He^+, and O^{2+}. This spectrum was obtained in a transient flow which was very well associated with a nonflare-related explosive prominence.
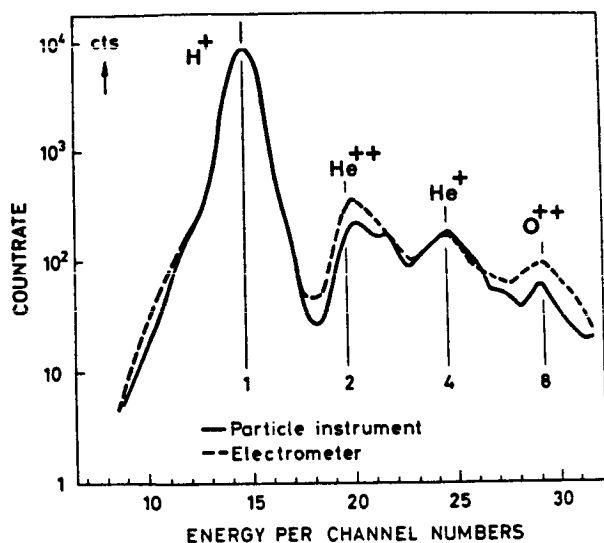

Fig. 9. Spectra measured simultaneously with two electrostatic analyzers on a HELIOS spacecraft. Comparison of the particle counting spectrum with that obtained by measuring current shows that the peaks at 4 and 8 are He^+ and O^{++}.

The second case of a spectrum with oxygen in low ionization stages was reported by Zwickl et al. (1982) and is shown in Figure 10, contrasted with a more normal high density flow. In the upper panel, envelopes which reasonably encompass the Si peaks and Fe peaks are shown. Generally, these minor ion groups in spectra measured in slow solar wind can be fitted rather well with smooth envelopes which are somewhat broader than an isothermal fit would predict. The greater broadness has been attributed to the fact that the ratios of adjacent pairs of ion species are established at different heights in the corona and hence different temperatures (Bame et al., 1970). In the lower, anomalous spectrum, reasonable envelopes for the Si and Fe species have been drawn. It is apparent that three of the peaks are far outside of the envelopes and can best be explained as being due to He^+ (with some O^{4+}), O^{3+}, and O^{2+}. Another ion indicative of a colder than normal origin is prominent, C^{4+}, and
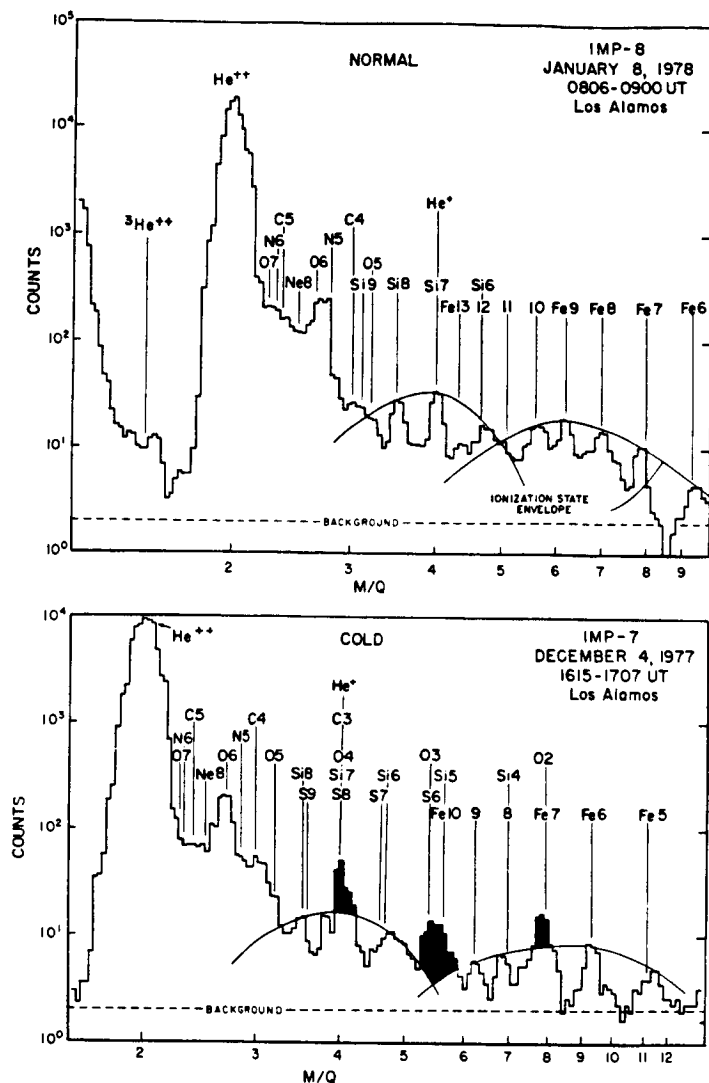
Fig. 10. Two spectra from IMP 7 and 8 obtained by adjusting for speed changes and summing E/Q spectra together. The upper normal spectrum is a somewhat cool example since C^{4+} ions are present. Well-behaved ionization state envelopes can be fit to the Si and Fe species peaks in the normal spectrum. In the lower cold spectrum C^{4+} ions are again present, but in addition reasonable ionization state envelopes do not encompass three prominent peaks. The surplus ions in these peaks can be best identified as He^{+} (with some O^{4+}), O^{3+}, and O^{2+}.

possibly N^{5+} and O^{5+}. There is evidence of some C^{4+} in the January 8, 1978 spectrum in the upper panel, as well, and indeed this spectrum, although not cold like the lower spectrum, is somewhat cooler than most of the minor ion spectra which have been obtained in low speed flows. The December 4, 1977 cold spectrum was possibly associated with a disappearing filament. It was not associated with an IP shock.

ACKNOWLEDGMENTS

References

Asbridge, J. R., S. J. Bame, and W. C. Feldman, Abundance Differences in Solar Wind Double Streams, Solar Phys., 37, 451, 1974.

Asbridge, J. R., S. J. Bame, W. C. Feldman, and M. D. Montgomery, Helium and Hydrogen Velocity Differences in the Solar Wind, J. Geophys. Res., 81, 2719, 1976.

Bame, S. J., Spacecraft Observations of the Solar Wind Composition, in Solar Wind, edited by C. P. Sonett, P. J. Coleman, and J. M. Wilcox, NASA SP-308, p. 535, 1972.

Bame, S. J., Vela Observations of He^+ Ions in the Solar Wind, Workshop on Ion Composition of Space Plasma, Deutsche Forschungsgemeinschaft and Max Planck Society, Göttingen-Lindau, West Germany, August 26-29, 1980.

Bame, S. J., Solar Wind Heavy Ions from Energetic Coronal Events, in Solar Wind Four, edited by H. Rosenbauer, Report No. MPAE-W-100-81-31, Max Planck Institut für Aeoronomie, Max Planck Institut für Extraterrestrische Physik, 1981.

Bame, S. J., A. J. Hundhausen, J. R. Asbridge, and I. B. Strong, Solar Wind Ion Composition, Phys. Rev. Lett., 20, 393, 1968.

Bame, S. J., J. R. Asbridge, A. J. Hundhausen, and M. D. Montgomery, Solar Wind Ions: Fe^{+8} to Fe^{+12}, Si^{+7}, Si^{+8}, Si^{+9}, and O^{+6}, J. Geophys. Res., 75, 6360, 1970.

Bame, S. J., J. R. Asbridge, W. C. Feldman, and P. D. Kearney, The Quiet Corona: Temperature and Temperature Gradient, Solar Phys., 35, 137, 1974.

Bame, S. J., J. R. Asbridge, W. C. Feldman, and J. T. Gosling, Evidence for a Structure-Free State at High Solar Wind Speeds, J. Geophys. Res., 82, 1487, 1977.

Bame, S. J., J. R. Asbridge, W. C. Feldman, E. E. Fenimore, and J. T. Gosling, Solar Wind Heavy Ions from Flare-Heated Coronal Plasma, Solar Phys., 62, 179, 1979.

Bochsler, P. and J. Geiss, Cross- and Autocorrelations of Speeds and Kinetic Temperatures of Minor Ions in the Solar Wind, Trans. Am. Geophys. Union, EOS, 63, 424, 1982.

Bonifazi, C., A. Egidi, and G. Moreno, Observation of Oxygen-Enriched Plasma in the Driving Piston of a Flare-Generated Shock Wave, Lett. al Nuovo Cimento, 28, 39, 1980.

Borrini, G., J. T. Gosling, S. J. Bame, W. C. Feldman, and J. M. Wilcox, Solar Wind Helium and Hydrogen Structure Near the Heliospheric Current Sheet: A Signal of Coronal Streamers at 1 AU, J. Geophys. Res., 86, 4565, 1981.

Borrini, G., J. T. Gosling, S. J. Bame, and W. C. Feldman, Helium Abundance Variations in the Solar Wind, Solar Phys., to be published, 1982a.

Borrini, G., J. T. Gosling, S. J. Bame, W. C. Feldman, Helium Abundance Enhancements in the Solar Wind, J. Geophys. Res., 87, 7370, 1982b.

Coplan, M. A., K. W. Ogilvie, P. A. Bochsler, and J. Geiss, Ion Composition Experiment, IEEE Trans. Geosci. Electron., GE-16, 185, 1978.

Feldman, W. C., J. R. Asbridge, S. J. Bame, and M. D. Montgomery, Double Ion Streams in the Solar Wind, J. Geophys. Res., 78, 2017, 1973.

Feldman, W. C., J. R. Asbridge, S. J. Bame, and P. D. Kearney, Upper Limits for the Solar Wind He^+ Content at 1 AU, J. Geophys. Res., 79, 1808, 1974.

Feldman, W. C., J. R. Asbridge, S. J. Bame, and J. T. Gosling, Long-Term Variations of Selected Solar Wind Properties: IMP 6, 7, and 8 Results, J. Geophys. Res., 83, 2177, 1978.

Feldman, W. C., J. R. Asbridge, S. J. Bame, E. E. Fenimore, and J. T. Gosling, The Solar Origins of Solar Wind Interstream Flows: Near-Equatorial Coronal Streamers, J. Geophys. Res., 86, 5408, 1981.

· Fenimore, E. E., Solar Wind Flows Associated With Hot Heavy Ions, Astrophys. J., 235, 245, 1980.

· Formisano, V. and S. Orsini, Quiet-Time Solar-Wind Ionic Composition, Nuovo Cimento, 4C, 682, 1981.

· Galvin, A. B., F. M. Ipavich, and G. Gloeckler, Solar Wind Ionization Temperatures Inferred From the Charge State Analysis of Diffuse Ion Events, Trans. Am. Geophys. Union, EOS, 63, 4242, 1982.

· Geiss, J., F. Bühler, H. Cerutti, P. Eberhardt, and C. Filleux, Apollo 16 Preliminary Science Report, NASA SP-315, Nat. Aeoronaut. and Space Admin., p. 14-1, 1972.

· Gosling, J. T., J. R. Asbridge, S. J. Bame, W. C. Feldman, and R. D. Zwickl, Observations of Large Fluxes of He^+ in the Solar Wind Following an Interplanetary Shock, J. Geophys. Res., 85, 3431, 1980.

· Gosling, J. T., G. Borrini, J. R. Asbridge, S. J. Bame, W. C. Feldman, and R. T. Hansen, Coronal Streamers in the Solar Wind at 1 AU, J. Geophys. Res., 86, 5438, 1981.

· Grünwaldt, H., Solar Wind Composition from the Helios 2 Plasma Experiment, Space Research, XVI, 681, 1976.

· Hovestadt, D., G. Gloeckler, C. Y. Fan, L. A. Fisk, F. M. Ipavich, B. Klecker, J. J. O'Gallagher, M. Scholar, H. Arbinger, J. Cain, H. Höfner, E. Künneth, P. Laeverenz, and E. Tums, The Nuclear and Ionic Charge Distribution Particle Experiments on the ISEE-1 and ISEE-C Spacecraft, IEEE Trans. on Geosci. Electron., GE-16, 166, 1978.

· Krieger, A. S., A. F. Timothy, and E. C. Roelof, Solar Phys., 29, 505, 1973.

· Mitchell, D. G., and E. C. Roelof, Thermal Iron Ions in High Speed Solar Wind Streams: Detection by the IMP 7/8 Energetic Particle Experiments, Geophys. Res. Letters, 7, 661, 1980.

· Mitchell, D. G., E. C. Roelof, W. C. Feldman, S. J. Bame, and D. J. Williams, Thermal Iron Ions in High Speed Solar Wind Streams, 2. Temperatures and Bulk Velocities, Geophys. Res. Letters, 8, 827, 1981.

· Mitchell, D. G., E. C. Roelof, and S. J. Bame, Solar Wind Iron Abundance Variations at Solar Wind Speeds >600 km s^{-1}, 1972-1976, Trans. Am. Geophys. Union, EOS, 63, 1088, 1982.

· Ogilvie, K. W., Coronal Temperatures and Oxygen Charge States, Trans. Am. Geophys. Union, EOS, 63, 1088, 1982.

· Ogilvie, K. W. and J. Hirshberg, The Solar Cycle Variation of the Solar Wind Helim Abundance, J. Geophys. Res., 75, 4595, 1974.

· Ogilvie, K. W., M. A. Coplan, P. Bochsler, and J. Geiss, Abundance Ratios of $^4He^{++}/^3He^{++}$ in the Solar Wind, J. Geophys. Res., 85, 6021, 1980a.

· Ogilvie, K. W., P. Bochsler, J. Geiss, and M. A. Coplan, Observations of the Velocity Distribution of Solar Wind Ions, J. Geophys. Res., 85, 6069, 1980b.

· Ogilvie, K. W., and C. Vogt, Variation of the Average 'Freezing-In' Temperature of Oxygen Ions with Solar Wind Speed, Geophys. Res. Letters, 7, 577, 1980c.

· Ogilvie, K. W., M. A. Coplan, and R. D. Zwickl, Helium, Hydrogen, and Oxygen Velocities Observed on ISEE-3, J. Geophys. Res., 87, 7363, 1982.

· Schmidt, W. K. H., H. Rosenbauer, E. G. Shelly, and J. Geiss, On Temperature and Speed of He^{++} and 0^{6+} Ions in the Solar Wind, Geophys. Res. Letters, 7, 697, 1980.

· Schwenn, R., Observations of Unusual Solar Wind Heavy Ions, Workshop on Ion Composition of Space Plasma, Deutsche Forschungsgemeinschaft and Max Planck Society, Göttingen-Lindau, West Germany, August 26-29, 1980.

588

- Schwenn, Rainer, Direct Correlations Between Coronal Transients and Interplanetary Disturbances, presented at the Fifth International Symposium on Solar-Terrestrial Physics, Ottawa, Canada, May 1982.

- Schwenn, Rainer, Helmut Rosenbauer, and Karl-Heinz Mühlhäuser, Singly Ionized Helium in the Driver Gas of an Interplanetary Shock Wave, Geophys. Res. Letters, 7, 201, 1980.

- Shelley, E. G., R. D. Sharp, R. G. Johnson, J. Geiss, P. Eberhardt, H. Balsiger, G. Haerendel, and H. Rosenbauer, Plasma Composition Experiment on ISEE-A, IEEE Trans. on Geosci. Electron., GE-16, 266, 1978.

- Williams, D. J., The Ion-Electron Magnetic Separation and Solid State Detector Detection System Flown on IMP-7 and 8, NOAA Tech. Report ERL 393-SEL40 (U.S. Department of Commerce), October 1977.

- Zastenker, G. N., and Yu. I. Yermolaev, Observations of Solar Wind Stream with High Abundance of Heavy Ions and Relation with Coronal Conditions, Planet. Space Sci., 29, 1335, 1981.

- Zwickl, R. D., J. R. Asbridge, S. J. Bame, W. C. Feldman, and J. T. Gosling, He^+ and Other Unusual Ions in the Solar Wind: A Systematic Search Covering 1972-1980, J. Geophys. Res., 87, 7379, 1982.

THE RELATIVE ABUNDANCE OF ^{3}He^{++} IN THE SOLAR WIND

M. A. Coplan
Institute for Physical Science
and Technology
University of Maryland

K. W. Ogilvie
Extraterrestrial Physics Branch
Goddard Space Flight Center

P. Bochsler and J. Geiss
Physikalisches Institut
University of Bern
Bern, Switzerland

ABSTRACT

Continuous measurements of solar wind ^{3}He^{++} and ^{4}He^{++} from August, 1978 to December, 1981 have been made covering a full range of solar wind conditions. The average flux ratio <R> derived from these data is 2310 ± 50, in excellent agreement with the Apollo foil measurements. A probable correlation between <R> and solar activity has been found; however, an examination of the data during periods of ^{3}He^{++}-rich solar flares shows no detectable increase in ^{3}He^{++} in the solar wind.

Introduction

Measurements of ^{4}He^{++} in the solar wind since its first discovery there (Neugebauer and Snyder, 1966) have shown its abundance to be highly variable, however the reason for this variability is not fully understood. Information about conditions in the source region can in principle be obtained by studying the abundance of ^{3}He^{++} relative to that of ^{4}He^{++}. Since the only difference between the isotopes is their mass (ionization potentials and charge being identical), changes in their relative abundances may prove to be a sensitive probe of the acceleration and mixing processes operating in the source region. Furthermore, the low abundance of ^{3}He^{++} relative to protons (approximately 1:40,000) means that it can be considered as a true test particle in the solar wind.

Up to now, studies of ^{3}He^{++} in the solar wind were limited to periods of low solar wind velocity when the kinetic energy distribution of the dominant solar wind protons was sufficiently narrow so as not to interfere with observations of ^{3}He^{++}. The ISEE-3 Ion Composition Instrument (ICI), launched in August 1978, has overcome this limitation by employing velocity as well as energy analysis (Coplan et al., 1978) with the result the ^{3}He^{++} abundances have now been measured continuously over the full range of solar wind conditions for more than four years.

In a previous publication (Ogilvie et al., 1980a) we presented a preliminary account of observations made between August and November, 1978 and March and August 1979. During this period the average ^{4}He^{++}/^{3}He^{++} abundance ratio <R> was reported to be 2.1 ± 0.2 x 10^3, in excellent agreement with measurements made by the foil method (Geiss et al., 1972). In this paper we present results derived from a data set covering the period August 1978 to December, 1981. This period includes the maximum of solar activity cycle 21 which occurred in 1980, as well

as the occurrence of a number of ^{3}He^{++}-rich solar flares. Here we will concentrate on the variation of <R> with solar activity and correlations between ^{3}He^{++} in the solar wind and flares. A more comprehensive analysis will appear elsewhere.

Experimental Method and Data Reduction

The ICI has already been described by Coplan et al. (1978). The instrument obtains mass per charge (M/Q) spectra over the range of 1.4 to 5.6 with a resolution of 30, as long as the solar wind speed is between 300 and 620 km/s. Time resolution is 15 or 30 minutes depending on the operating mode. The raw data have been corrected for background (approximately 0.3 counts/sec per observation) which is primarily due to penetrating high energy particles which excite the detectors directly. The background is determined separately for each spectrum by monitoring a part of the M/Q-V matrix in which no solar wind ions appear. During solar particle events the background increases by an order of magnitude and spectra obtained during these periods have been deleted from the data set.

The ^{4}He^{++}/^{3}He^{++} abundance ratio is obtained from the corrected data by first fitting a convected Maxwellian velocity distribution function to the ^{4}He^{++} data taking into account the instrument function. The results of the fitting procedure are values for the velocity, kinetic temperature, density, and flux of ^{4}He^{++}. Because of the small number of ^{3}He^{++} counts, a completely independent determination of the ^{3}He^{++} distribution function is not practical. The velocity of ^{3}He^{++} is taken equal to that for ^{4}He^{++} and the ^{3}He^{++} kinetic temperature is set equal to 3/4 that for ^{4}He^{++} (Ogilvie et al., 1980b). The ^{3}He^{++} density and flux are then calculated from the total corrected ^{3}He^{++} counts, using the instrument function and the values of velocity and temperature. The uncertainty in the ratio of ^{4}He^{++}/^{3}He^{++} flux, or density, R depends principally on the statistical uncertainty in the number of ^{3}He^{++} counts (typically 14 counts per observation). Errors associated with the assumed ^{3}He^{++} temperatures and velocities are expected to be small because the density is a rather weak function of these parameters. Figure 1 shows a plot of ^{4}He^{++} flux, ^{3}He^{++} flux and R for the

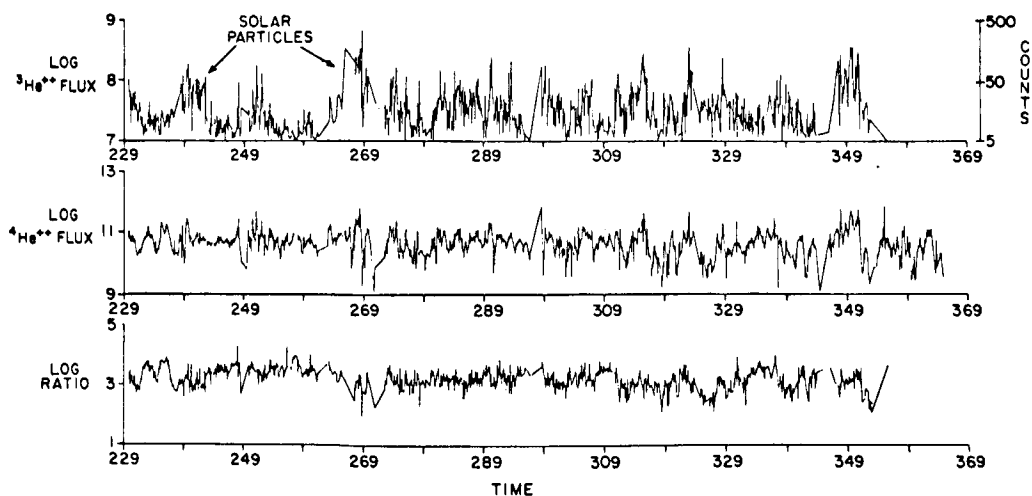Figure 1. ^{3}He^{++} flux, ^{4}He^{++} flux and ^{4}He^{++}/^{3}He^{++} flux ratio as a function of time for the period 16 August 1978 to 27 December 1978. The data are hourly averages. The units of flux are particles m^{-2}s^{-1}.

592

period 18 August to 27 December, 1978. Hourly averages are shown and data gaps are crossed by straight line segments. Superposed on the high frequency statistical fluctuations of $^3He^{++}$ flux are lower frequency fluctuations which correlate well with the fluctuations in $^4He^{++}$ flux, for which the statistical accuracy is a few percent. The calculated overall correlation coefficient for the two fluxes for the complete data set is 0.65 indicating that the fluctuations in $^3He^{++}$ flux are generally physically significant, representing real changes in the $^4He^{++}/^3He^{++}$ abundance ratio.

Results

Figure 2 is a histogram showing the distribution of values of R , based on the complete data set. The most probable value, R_{MP} , corresponding to the maximum in the histogram, is $\sim$ 1500 . The average value, <R> , is 2310 $\pm$ 50 and is obtained by summing the $^4He^{++}$ fluxes and dividing by the sum of the $^3He^{++}$ fluxes. This method for obtaining <R> gives a value which can be directly compared with the abundance ratio obtained by the foil technique in which the helium isotopes trapped by the exposed foil over a period of time are desorbed by heating and measured in a mass spectrometer. The agreement between the results of the two methods is excellent. Note that this method for calculating <R> is different from an average obtained by summing individual R values and dividing by the number of values. We estimate the signal-to-noise ratio for an individual measurement to be 2 at R = 3000. Thus, observed increases of R above $\sim$

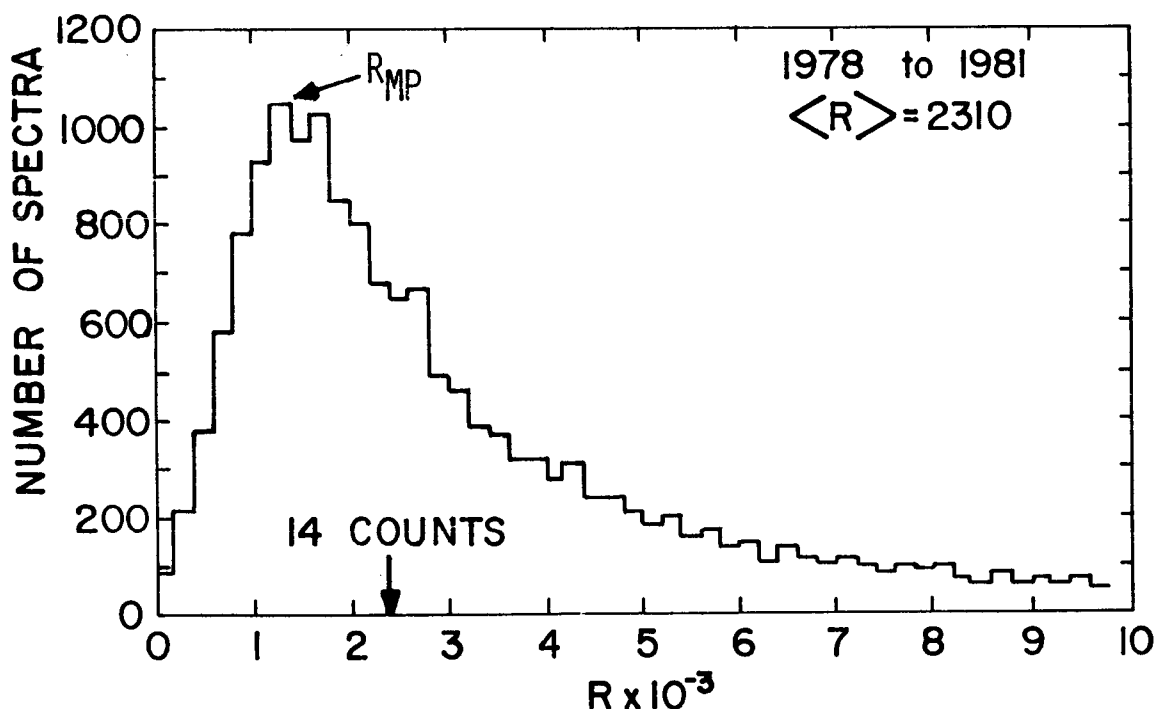Figure 2. Histogram of $^4He^{++}/^3He^{++}$ flux ratios, R . The most probable, R_{MP} , as well as the average value, <R>, of R are indicated. A value of R corresponding to <R> represents approximately 14 $^3He^{++}$ counts.

5000 which usually represent real physical changes in the abundances, are not well determined. Values of R well below <R> occur with considerable frequency, however the persistance of low R values for longer than about 6 hours is rare in our data. This is in contrast with the observations of Grünwaldt (1976) who reported R ∿ 540 for a period of 48 hours coinciding with a particularly low solar wind speed. Inspection of Figure 1 shows that such a low ratio is not particularly rare, but 48 hours is a long period for such a deviation from the most probable value to persist.

To further examine the relation between R and solar activity we have divided the data set into six-month intervals. The maximum of solar cycle 21 occurred in 1980 and from the data in Table I one can see that <R> for 1980 is 2465 ± 60 which is to be compared with 2310 ± 50 for the entire data set. Since the two averages differ by more than three standard deviations it is reasonable to conclude that events giving rise to large values of R in the solar wind are more prevalent around solar maximum than at other times. Values of R_{MP} for the six-month periods are also included in Table I.

TABLE I

$^4He/^3He$ Ratios

Period	Number of Days	< R >	R_{MP}
Aug. 18 – Dec. 31, 1978	136	2320	1600
Jan. 1 – June 30, 1979	180	2180	1600
July 1 – Dec. 31, 1979	184	2420	1600
Jan. 17 – June 30, 1980	164	2480	1200
July 1 – Nov. 27, 1980	149	2550	1600
Feb. 19 – June 30, 1981	131	2220	1600
July 1 – Oct. 18, 1981	109	2300	1700
Average 1978 – 1981		2310 ± 50	
Average 1980		2465 ± 60	

Among other sources of $^3He^{++}$ variability we have investigated a possible connection between ^3He-rich solar flares and solar wind $^3He^{++}$. The solar flares of interest are small but result in up to a thousand fold enhancement of $^3He^{++}$ at MeV/nucleon energies lasting for a few days (Reames and von Rosenvinge, 1981). Using a list of $^3He^{++}$ fluxes in the energy range from 1.3 to 1.7 MeV/nucleon kindly supplied by Reames (private communication, 1982) we selected seven ^3He events for which there was no coincident solar proton enhancement. If t_i is the time of observation of energetic particles during the ith event, plasma emitted by the sun at the same time will arrive at 1 AU at about t_i+3 days. A super-posed epoch analysis was performed to obtain <R(L)>, where <R> is computed over a period of two days, and L is a variable lag time, taking the values -4, -3,..., +4 days.

If the processes responsible for the enhancement of ^{3}He at MeV/nucleon energies also enhanced ^{3}He^{++} in the solar wind, we would expect a decrease in <R> at zero time, corresponding to a transit time of 3 days. Figure 3 shows the result; although there is a small decrease in <R> at about the expected lag, it is less than the standard deviation of the observations. The data are consistent with the emission by the sun of about 10% more ^{3}He than usual. Although estimates show this is not energetically impossible, we conclude that we did not detect increased ^{3}He in the solar wind at the time of these flares.
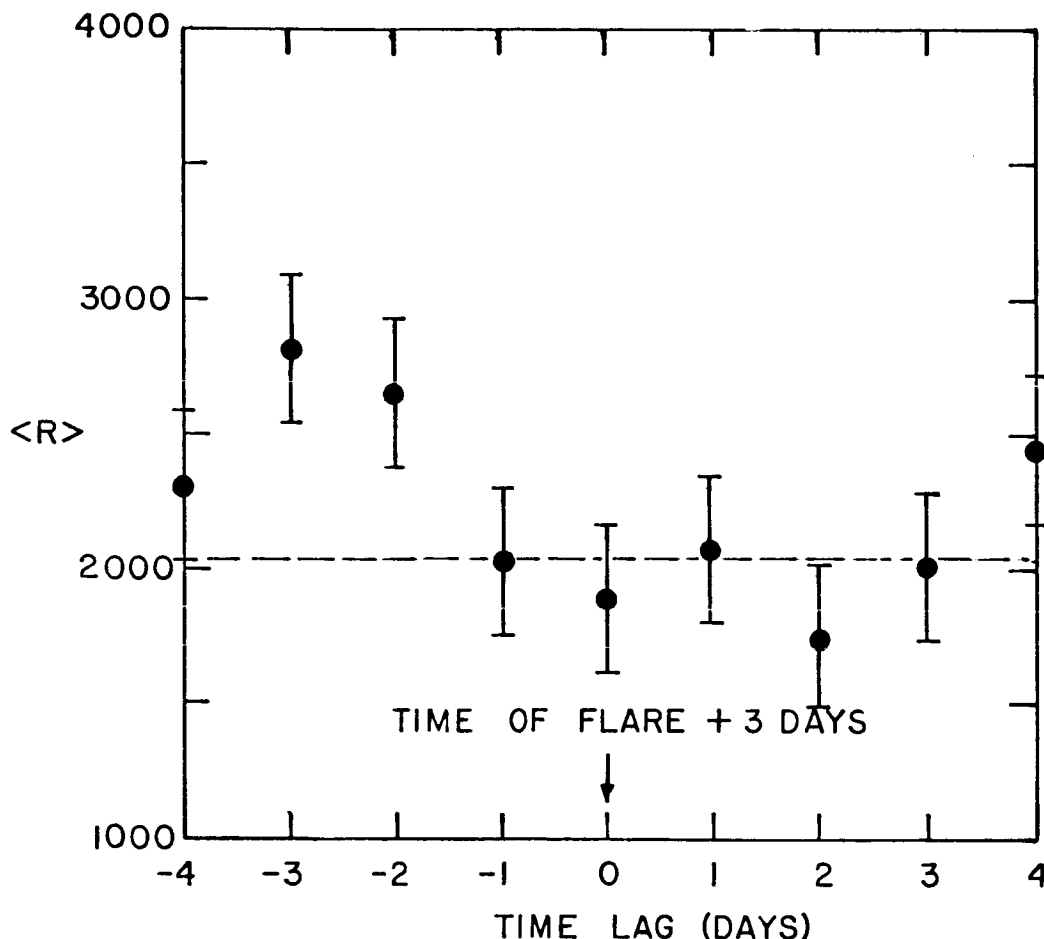
Figure 3.   The average value of the ^{4}He^{++}/^{3}He^{++} flux ratio, <R>, over the duration of 7 separate ^{3}He^{++}-enriched solar flare events as a function of the time delay between the observation of the flare and the measurement of solar wind ^{3}He^{++} and ^{4}He^{++}. The horizontal scale has been chosen so that zero time delay corresponds to the solar wind transit time of three days.   There is a horizontal dashed line at the position of the average of the nine values of <R>.

References

o Coplan, M. A., K. W. Ogilvie, P. A. Bochsler and J. Geiss, Ion composition experiment, ISEE Trans. Geosci. Electron., GE-16, 185,1978.

o Geiss, J., F. Bühler, H. Cerutti, P. Eberhardt, and C. Filleux, "Solar wind composition experiment, Apollo 16 Prel. Sci. Rep., pp 14.1-14.10 NASA SP-315 (19).

o Grünwaldt, H., Solar wind composition from the HEOS-2 plasma experiment, Space Res., 16, 681, 1976.

o Neugebauer, M., and C. W. Snyder, Mariner 2 observations of the solar wind, J. Geophys. Res., 71, 4469 1966.

o Ogilvie, K. W., M. A. Coplan, P. Bochsler and J. Geiss, Abundance ratios of $^4He^{++}/^3He^{++}$ in the solar wind, J. Geophys. Res., 85, 6021, 1980a.

o Ogilvie, K. W., P. Bochsler, J. Geiss and M. A. Coplan, Observations of the velocity distribution of solar wind ions, J. Geophys. Res., 85, 6069, 1980b.

o Reames, D. V., and T. T. von Rosenvinge, Heavy element abundances in ^3He-rich events, Proceedings 17th ICRC (Paris), 3, 162, 1981.

IRON CHARGE STATES OBSERVED IN THE SOLAR WIND

F.M. Ipavich, A.B. Galvin, G. Gloeckler
University of Maryland
Department of Physics and Astronomy
College Park, MD 20742

D. Hovestadt, B. Klecker, M. Scholer
Max-Planck-Institut fur Physik und Astrophysik
Institut fur extraterrestrische Physik
8046 Garching, W. Germany

ABSTRACT

We report solar wind measurements from the ULECA sensor of the Max-Planck-Institut/University of Maryland experiment on ISEE-3. The low energy section of the ULECA sensor selects particles by their energy per charge (over the range ~3.6 keV/Q to ~30 keV/Q) and simultaneously measures their total energy with two low-noise solid state detectors. In this paper we present solar wind Fe charge state measurements from three time periods of high speed solar wind occurring during a post-shock flow and a coronal hole-associated high speed stream. Analysis of the post-shock flow solar wind indicates the charge state distributions for Fe were peaked at ~+16, indicative of an unusually high coronal temperature ($\sim 3 \times 10^6$ K). In contrast, the Fe charge state distribution we observe in a coronal hole-associated high speed stream peaks at ~+9, indicating a much lower coronal temperature ($\sim 1.4 \times 10^6$ K). This constitutes the first reported measurements of iron charge states in a coronal hole-associated high speed stream.

Introduction

The state of ionization of the solar wind is "frozen in" at low coronal altitudes and remains essentially unchanged during the solar wind's passage through the upper solar atmosphere and interplanetary space (Hundhausen et al., 1968). Measurements of heavy ion ($Z > 2$) charge state abundances in the solar wind are used to estimate the local electron temperature at the coronal freezing-in site. In general, the more massive the element, the higher its freezing-in altitude. For example, interstream solar wind oxygen ions freeze in at ~1.5 solar radii while iron charge states are set at ~3 solar radii (Bame et al., 1974). Measurements of the charge states of different elements can therefore be used to determine temperature gradients in the corona. In addition, the ionization states are indicative of the type of solar wind flow and its origin on the coronal disc. Feldman et al. (1981) have reported moderate ionization temperatures for interstream (IS) solar wind, with average values of $\sim 2.1 \times 10^6$ K for oxygen ions and $\sim 1.6 \times 10^6$ K for iron ions. They suggest that IS solar wind may originate in near-equatorial coronal streamers, which have similar temperatures. Solar wind post-shock flows (PSFs) and helium abundance enhancements (HAEs) generally have iron and oxygen ionization states indicative of hotter than usual coronal temperatures ($>2.3 \times 10^6$ K), with origins in solar active regions (Bame et al., 1979; Fenimore, 1980).

All of the studies cited above use data obtained from solar wind electrostatic analyzer experiments which, for reasons discussed below, have been

unable to resolve heavy ion charge states in coronal hole-associated high speed streams. Using data from the solar wind ion mass-per-charge spectrometer on ISEE-3, Ogilvie and Vogt (1980) have reported oxygen ionization temperatures up to ~3 x 10^6K for high speed solar wind flows which may be coronal hole-associated. Their instrument is limited to speeds below ~600 km/s. Galvin et al. (1982) report much lower ionization temperatures (between ~1.1 x 10^6K and ~1.5 x 10^6K) for coronal hole-associated high speed streams (with speeds ranging from ~500 to ~700 km/s), based on charge state measurements of locally accelerated solar wind heavy ions in diffuse ion events observed upstream of the earth's bow shock. High speed stream Fe/H abundance ratios have been reported by Mitchell and Roelof (1980), but they make no charge state measurements.

The data presented in this paper were obtained with the Ultra Low Energy Charge Analyzer (ULECA) sensor of the Max-Planck-Institut/University of Maryland experiment on ISEE-3. The ULECA sensor is an electrostatic deflection system with an array of solid state detectors. The selection of incoming ions with a given energy per charge window and the measurement of their total energy allow the determination of the charge state distribution. The data presented are from the ULECA L1 and L2 detectors, which respectively cover the energy ranges ~4-11 keV/Q and ~10-30 keV/Q in 32 logarithmic steps with a cycle time of ~16 minutes. The L1 and L2 detectors have energy per charge bandwidths (FWHM/mean) of ~12% and ~21%, respectively, and energy thresholds ~15 keV. We report solar wind measurements from three time periods of high speed solar wind. In particular, we present charge state measurements of iron ions in both a post-shock flow and a coronal hole-associated high speed stream. This is the first reported measurement of iron charge states in a high speed stream.

Observations

The time periods we discuss occurred on Sept. 28 and 29, 1978, during which several distinct types of solar wind flows were observed. During most of Sept. 28, the solar wind may be characterized as a coronal-hole associated high speed stream (Solar-Geophysical Data, 1978). At ~2040 UT on the 28th an interplanetary shock was detected by ISEE-3. At ~0230 UT on the 29th we infer the passage of a much stronger interplanetary shock. Unfortunately, this shock passage occurred during a three hour telemetry gap. Our inference of the presence of this shock is based on a well defined SSC at earth at 0301 UT (Solar-Geophysical Data, 1978) and the detection at ISEE-3 of a classical Energetic Storm Particle event (Klecker et al., 1981; Hovestadt et al., 1982) preceding and following the inferred passage of the interplanetary shock. At ~0815 UT there was a tangential discontinuity in the interplanetary magnetic field and a dramatic decrease in the solar wind ion kinetic temperature. These signatures are often associated with the arrival of flare-generated driver plasma (e.g., Bame et al., 1979). The shock-producing flare was probably a 2B flare (N27, W19) which occurred at 1428 UT on Sept. 27 (Solar-Geophysical Data, 1979), implying an average shock propagation speed of ~1150 km/s.

The sequence of a coronal hole-associated high speed stream followed by two interplanetary shocks led to extremely large solar wind speeds on Sept. 29. Figure 1 shows our observations of proton and helium velocities from 0500 to 1800 UT on Sept. 29. The estimated error in these velocities is ~5%. We point out that solar wind protons are detected by the ULECA sensor only through multiple pulse pile-up; the energy of each of these protons is well below the threshold of the solid state detectors. As a consequence, only a small fraction

($\sim 10^{-3}$) of the incident protons is actually counted by the detectors. Although this precludes a computation of the proton density, the peak position in energy per charge (i.e., the voltage step with the highest counting rate) is a reliable measure of the proton velocity. Only protons with velocities above ~ 800 km/s can pass through the electrostatic deflection analyzer; hence in Figure 1 no proton data are shown after ~ 1000 UT. Helium ions deposit energies slightly below detector thresholds, but the finite electronic and detector noise produces an efficiency of $\sim 10\%$ (which dominates the effect of helium pile-up). Heavier ions are detected with near unity efficiency. The helium velocities shown in Figure 1 were derived by comparing the observed data with the results of a computer simulation which takes into account all known instrumental effects. The simulation assumes that helium and heavier ions have a common velocity (Schmidt et al., 1980; Ogilvie et al., 1982), and uses the relative elemental abundances presented in Table 1.

Figure 1. Helium and proton solar wind velocities during the post shock flow on 29 Sept 1978. A large magnetic field tangential discontinuity at ~ 0815 separates shock-heated solar wind ("HOT") from the flare-associated driver gas ("COLD"). We infer that the interplanetary shock passage occured at ~ 0230. The hatched bars indicate time periods selected for pulse height analysis.

Table 1

Solar Wind
Adopted Elemental Abundances

Element	Relative Abundance	Reference[*]
H	$\equiv 1 \times 10^6$	a
He	4×10^4	a,b
C	520	d
N	145	c
O	520	a,c,d
Ne	75	b
Mg	75	c
Si	75	a,c
S	26	c
Fe	53	a

[*]
a Solar wind E/Q measurement (Bame et al.,1975)
b Solar wind foil measurement (Geiss,1973)
c Coronal observation (Withbroe,1976)
d Corotating Particle Events (Gloeckler et al.,1979)

MPE/U of Md.
ULECA
ISEE 3
29 SEPT 1978

Figure 2. Energy per charge spectra for time periods before (left panel) and after (right panel) the passage of the magnetic field tangential discontinuity. Detector L1 counting rates (normalized to 1000 in each panel) are plotted vs. deflection system voltage step (v/s). The 32 logarithmically spaced voltage steps cover the range 3.6 keV/Q (step 31) to 10.6 keV/Q (step 0).

Figure 2 shows energy per charge spectra from detector L1 for time periods before and after the arrival of the driver plasma. The leftmost peak in e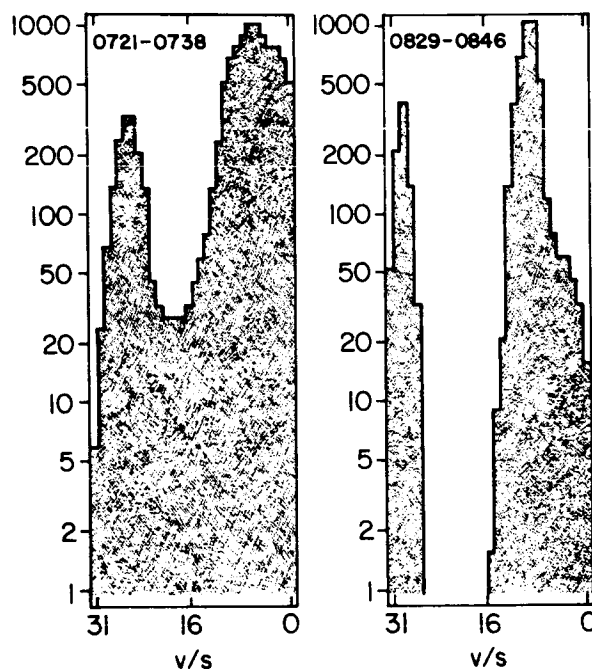ach panel is due to solar wind protons while the rightmost peak represents helium and heavier ions. The proton counting rate is severely depressed by the detector threshold, as mentioned above. The relative widths of the peaks in the left vs. right panels reflect a decrease in the solar wind kinetic temperature by a factor of ~10 near the time of arrival of the tangential discontinuity in the magnetic field; thus Figure 2 indicates the transition from shock-heated ambient plasma to the flare-associated driver plasma.

We have selected two time intervals (represented by the hatched bars in Figure 1) for detailed pulse height analysis of the driver plasma. Figure 3 shows five energy histograms (counts per keV vs. measured energy in the L2 solid state detector) summed over the time interval 1105-1430 UT. Each of the panels represents a different energy per charge range (i.e., different steps of the electrostatic deflection analyzer). Since solar wind ions moving at the same velocity have kinetic energies proportional to their mass, each energy histogram may be interpreted as a mass histogram. During this time interval we observed a helium velocity of 800 km/s. The vertical dashed lines shown in Figure 3 represent the expected FWHM measured energies for Fe ions at this velocity, based on pre-flight calibrations. There is good agreement with the observed energy histograms for the four lowest panels. The topmost panel (representing the lowest energy per charge range) indicates the presence of an additional ion, consistent with the expected position of Si. Note that by measuring the energy of heavy solar wind ions we can identify their mass directy rather than relying on indirect (albeit convincing) inference based on mass per charge values (e.g., Bame et al., 1979) or assumed (albeit reasonable) solar wind abundance ratios (Mitchell and Roelof, 1980). We point out that the assumed abundances given in Table 1 were used to derive the solar wind He velocity, but not to identify the presence of solar wind Fe.

Figure 3. Energy histograms averaged over the time period 1105-1430 UT. Counts per keV is plotted vs. measured energy in the L2 detector. Each panel covers a different energy per charge range. Also indicated are the expected measured energies of Fe and Si ions moving at 800 km/s.

After this identification of Fe based on measured energy, we can convert the fluxes in different energy per charge ranges into a distribution of charge states. We accomplish this by first selecting an energy interval which is high enough to assure no contribution from lighter ions. The number of Fe counts in this interval is then computed for each energy per charge range. This distribution of Fe counts vs. E/Q is then compared with the distribution expected from a simulated solar wind characterized by a particular charge state
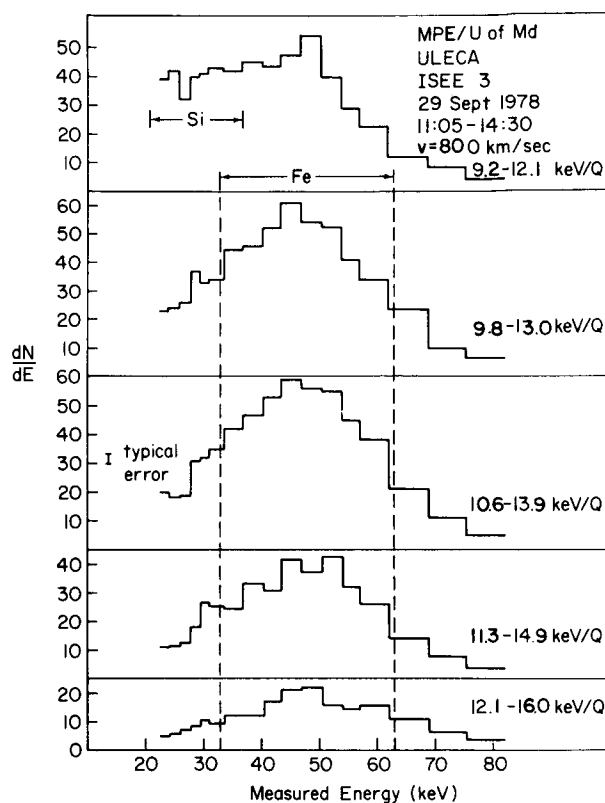
freezing-in temperature. A specific temperature corresponds to a unique Fe charge state distribution (we use the density-independent tables of Jordan, 1969). The results of such a comparison for the 1105-1430 time period are presented in Figure 4a. The observations are represented by the solid line while the simulated distributions for two different temperatures are shown as dashed lines. It is clear that the simulation characterized by 3.16×10^6K is a much better fit to the observations. Figure 4a also indicates the E/Q positions of Fe charge states 10, 13, and 16. The peak of the observed distributions is seen to be closest to the position expected for Fe^{+16}.

The above analysis was repeated for the time period 0828-0920 (leftmost hatched bar in Figure 1), which is also in the flare-driven piston plasma. The result is shown in Figure 4b. The shift of the Fe charge state positions to higher E/Q values, and the higher energy range over which the Fe pulse height is summed, is caused by the higher solar wind velocity during this time interval. The observed Fe distribution is again fit reasonaby well by a freezing-in temperature of 3.16×10^6K.

Our observations thus indicate that the driver plasma was heated to a very high temperature, $\sim 3 \times 10^6$K, by the solar flare. The simultaneously observed low kinetic temperature then suggests a magnetic topology which restricts heat transport from the corona. Such a scenario has been previously proposed by, e.g., Bame et al. (1979).

Figure 4. Fe counts vs. energy per charge in the L2 detector for the indicated time periods. The solid lines represent the observations while the dashed lines represent expected distributions for different values of the coronal electron temperature (T_c, in 10^6K) at the freezing-in altitude. The arrows show the positions of different Fe charge states based on the observed solar wind helium velocity.

The final time period we discuss is 1500-2020 UT on 28 Sept. 1978, which is before the arrival of the two interplanetary shocks. As mentioned above, the solar wind during this time period may be characterized as a coronal hole-associated high speed stream. The helium velocity was observed to be reasonably steady, with an average value of 685 km/s. Figure 4c shows the observed distribution of Fe counts vs. energy per charge. Also indicated are the expected distributions corresponding to freezing-in temperatures of 1.26×10^6K and 1.58×10^6K. We estimate that the observed distribution corresponds to a

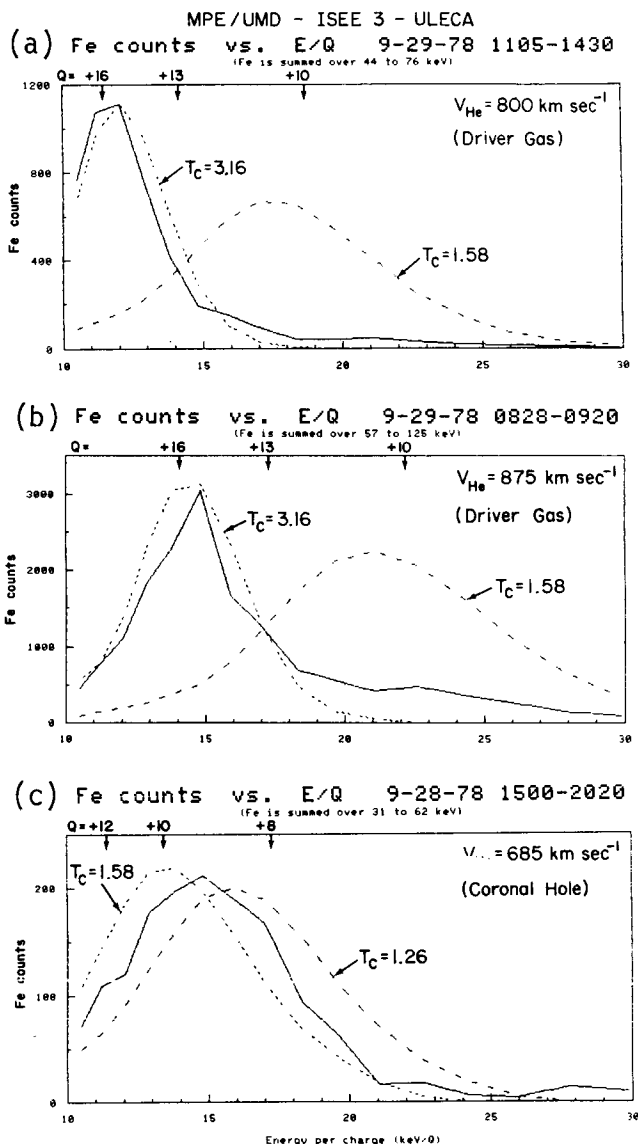temperature of 1.4×10^6K. The peak of the charge state distribution is near Fe^{+9}. We point out that Figure 4c represents the first observations of Fe charge states in a high speed stream. The reason such measurements have not been previously reported is twofold: a) the high kinetic temperatures in high speed streams make it difficult to identify ions based on energy per charge peaks, and b) the combination of high velocity with low charge states implies heavy ions have very high energy per charge values; thus Figure 4c shows the peak of the Fe charge state distribution occurs at ~14 keV/Q, which is above the range of most solar wind instruments.

Discussion

We have presented measurements of iron charge states in both post-shock flow solar wind and a coronal hole-associated high speed stream. The high ionization temperatures (~3×10^6K) we obtain for PSF iron are typical of flare-expelled solar wind. Bame et al. (1979), for example, have reported ionization temperatures between ~2.5×10^6K and ~3.0×10^6K for PSF iron. Our PSF results support those reported previously and extend them in two respects: (1) Our iron measurements were made at higher solar wind velocities. Whereas we present results at 800 km/s and 875 km/s, iron measurements by the Vela instruments are limited to speeds <650 km/s (Bame et al., 1979; Fenimore, 1980). (2) Bame et al. and Fenimore identify different ion species solely from E/Q spectra, which they convert to M/Q spectra by assuming a common bulk velocity for all heavy ions. Although we also assume all heavy ions flow at about the same speed as helium, our additional measurement of total energy allows the direct determination of the mass of the incoming particles. We can therefore unambiguously distinguish between, e.g., iron and silicon, even when these ions overlap in M/Q spectra.

We also report the first measurement of iron charge states in a coronal hole-associated high speed stream. Such measurements have previously been precluded by the high kinetic temperatures and energy per charge values of these ions in high speed streams. Model calculations based on EUV observations predict that coronal holes are cooler than the average quiet sun and have smaller temperature gradients (Munro and Withbroe, 1972). Estimates for the equilibrium temperatures in coronal holes generally range from ~1×10^6K to ~1.5×10^6K (e.g., Kopp and Orrall, 1976; Krieger et al., 1973; Mariska, 1978). These theoretical values are consistent with our measured result of $(1.4 \pm .2) \times 10^6$K derived from iron charge states.

In contrast, Ogilvie and Vogt (1980), using data from an ion mass-per-charge spectrometer, find that the ionization temperature for oxygen ions in the solar wind rises rapidy with speed, reaching more than 3×10^6K for speeds ~600 km/s. They suggest the apparent discrepancy with theoretical expectations may be the result of non-Maxwellian electron velocity distributions in the corona where freezing-in occurs. Indeed, Owocki (1982) predicts that ionization temperatures inferred from O^{+6}/O^{+7} ratios in the solar wind could overestimate the actual coronal electron temperatures if the assumption of a Maxwellian distribution was incorrect. However, he estimates the magnitude of the possible temperature overestimate is limited to ~0.8×10^6K, only partially explaining the above-mentioned discrepancy. Although our results indicate a much lower temperature than the Ogilvie and Vogt data, it should be noted that we are observing a different ion species (iron instead of oxygen) at a somewhat higher velocity (685 km/s instead of 600 km/s).

602

Galvin et al. (1982) report ionization temperatures between ~1.1 x 10^6K and ~1.5 x 10^6K for coronal hole-associated high speed streams, based on the charge state analysis of energetic upstream diffuse ions (which are presumed to be solar wind ions accelerated by the earth's bow shock) observed during high speed streams. Although their analysis technique requires certain assumptions, their derived temperatures are very different from those of Ogilvie and Vogt but are consistent with our measurements for iron. In addition, Galvin et al. find that the coronal hole-associated ionization temperatures are approximately constant over the range of solar wind speeds covered (~500-700 km/s), a result which also differs from that of Ogilvie and Vogt. The Galvin et al. results are derived from the overall charge state distribution of Z>2 ions, in contrast to the O^{+6}/O^{+7} ratio determination by Ogilvie and Vogt. However, because oxygen and carbon dominate the other heavy ions in the solar wind (see Table 1) the results should be comparable, unless carbon ions behave in some very unexpected manner. In this context we note that C^{+6}, expected to be the most abundant heavy ion in the solar wind, has never been identified because its mass per charge value is identical to that of the much more abundant He^{+2}.

Our present results for high speed stream iron indicate low ionization temperatures are present in coronal holes where freezing-in occurs. In addition, these results combined with those of Galvin et al. for carbon and oxygen would imply: (a) there are at most modest deviations from Maxwellian conditions in coronal holes, and (b) the electron temperature gradient over the range of freezing-in altitudes is quite small in coronal holes.

References

Bame, S.J., J.R. Asbridge,W.C. Feldman and P.D. Kearney, The quiet corona: temperature and temperature gradient, Solar Physics, 35, 137, 1974.

Bame, S.J., J.R. Asbridge, W.C. Feldman, M.D. Montgomery and P.D. Kearney, Solar wind heavy ion abundances, Solar Physics, 43, 463, 1975.

Bame, S.J., J.R. Asbridge, W.C. Feldman, E.E. Fenimore and J.T. Gosling, Solar wind heavy ions from flare-heated coronal plasma, Solar Physics, 62, 179, 1979.

Feldman, W.C., J.R. Asbridge, S.J. Bame, E.E. Fenimore and J.T. Gosling, The solar origins of solar wind interstream flows: near-equatorial coronal streamers, J. Geophys. Res., 86, 5408, 1981.

Fenimore, E.E., Solar wind flows associated with hot heavy ions, Astrophys. J., 235, 245, 1980.

Galvin, A.B., F.M. Ipavich and G. Gloeckler, Solar wind ionization temperatures inferred from the charge state analysis of diffuse ion events (abstract), EOS Trans. AGU , 63, 424, 1982.

Geiss, J., Solar wind composition and implications about the history of the solar system, Proc. 13th Intl. Cosmic Ray Conf., 5, 3375, 1973.

603

Gloeckler, G., D. Hovestadt and L.A. Fisk, Observed distribution functions of H, He, C, O and Fe in corotating energetic particle streams: implications for interplanetary acceleration and propagations, Astrophys. J., 230, L191, 1979.

Hovestadt, D., B. Klecker, H. Hofner, M. Scholer, G. Gloeckler and F.M. Ipavich, Ionic charge state distribution of He, C, O and Fe in an energetic storm particle enhancement, Astrophys. J. Lett., 258, L57, 1982.

Hundhausen, A.J., H.E. Gilbert and S.J. Bame, Ionization state of the interplanetary plasma, J. Geophys. Res., 73, 5485, 1968.

Jordan, C., The ionization equilibrium of elements between carbon and nickel, Mon. Not. R. Astr. Soc., 142, 501, 1969.

Klecker, B., M. Scholer, D. Hovestadt, G. Gloeckler and F.M. Ipavich, Spectral and compositional variations of low energy ions during an energetic storm particle event, Astrophys. J., 251, 393, 1981.

Kopp, R.A. and F.Q. Orrall, Temperature and density structure of the corona and inner solar wind, Astron. Astrophys., 53, 363, 1976.

Krieger, A.S., A.F. Timothy and E.C. Roelof, A coronal hole and its identification as the source of a high velocity solar wind stream, Solar Physics, 29, 505, 1973.

Mariska, J.T., Analysis of extreme-ultraviolet observations of a polar coronal hole, Astrophys. J., 225, 252, 1978.

Mitchell, D.G. and E.C. Roelof, Thermal iron ions in high speed solar wind streams: detection by the IMP 7/8 energetic particle experiments, Geophys. Res. Lett., 7, 661, 1980.

Munro, R.H. and G.L. Withbroe, Properties of a coronal "hole" derived from extreme-ultraviolet observations, Astrophys. J., 176, 511, 1972.

Ogilvie, K.W. and C. Vogt, Variation of the average 'freezing-in' temperature of oxygen ions with solar wind speed, Geophys. Res. Lett., 7, 577, 1980.

Ogilvie, K.W., M.A. Coplan and R.D. Zwickl, Helium, hydrogen, and oxygen velocities observed on ISEE-3, J. Geophys. Res., 87, 7363, 1982.

Owocki, S.P., Interpreting the solar wind ionization state, Solar Wind 5, Woodstock, Vt., (these Proceedings), 1982.

Schmidt, W.K.H., H. Rosenbauer, E.G. Shelley and J. Geiss, On temperature and speed of He^{++} and O^{6+} ions in the solar wind, Geophys. Res. Lett., 7, 697, 1980.

Solar-Geophysical Data, 411 Part I, U.S. Department of Commerce, Boulder, Colorado, 1978.

Solar-Geophysical Data, 415 Part II, U.S. Department of Commerce, Boulder, Colorado, 1979.

Withbroe, G.L., The chemical composition of the photosphere and corona, Harvard College Observatory Preprint Series No. 524, 1976.

SPATIAL VARIATION OF IRON ABUNDANCE IN THE
HIGH SPEED SOLAR WIND, 1972 - 1976

D. G. Mitchell[1], E. C. Roelof[1] and S. J. Bame[2]
[1]Applied Physics Laboratory
Johns Hopkins University
Laurel, Maryland 20707

[2]Los Alamos National Laboratory
Los Alamos, New Mexico 87545

ABSTRACT

We have analyzed the Fe/H ratios in the peaks of high speed streams (HSS) during the decline of Solar Cycle 20 and the following minimum (October 1972-December 1976). We utilized the response of the 50-200 keV ion channel of the APL/JHU energetic particle experiment (EPE) on IMP-7 and 8 to solar wind iron ions at high solar wind speeds ($V \gtrsim 600$ km sec^{-1}), and compared our Fe measurements with solar wind H and He$^{\sim}$ parameters from the Los Alamos National Laboratory (LANL) instruments on the same spacecraft In general, the Fe distribution parameters (bulk velocity, flow direction, temperature) are found to be similar to the LANL He parameters. Although the average Fe/H ratio in many steady HSS peaks agrees within observational uncertainties with the nominal coronal ratio of 4.7×10^{-5}, abundance variations of a factor of up to 6 are obtained across a given coronal-hole associated HSS. Over the period 1973-1976, a steady decrease in the average quiet-time Fe/H ratio by a factor of about 4 is measured on both IMP-7 and 8. A more detailed discussion of these findings, as well as Fe/H variations correlated with solar flare activity, can be found in Mitchell et al. (1983).

INTRODUCTION

Contemporary plasma detectors (electrostatic analyzers and mass spectrometers) are limited in measuring iron ions at high solar wind speeds (> 600 km sec^{-1}) with their attendant high kinetic temperatures. An alternate, though unexpected, technique has been shown in Mitchell and Roelof (1980) and Mitchell et al. (1981), hereafter referred to as Papers 1 and 2, to be capable of high time resolution measurements of solar wind iron under precisely these conditions. The technique uses the 50 - 200 keV ion channel of the Energetic Particle Experiments (EPE), D. J. Williams, Principal Investigator, on the IMP 7/8 spacecraft. Another measurement of iron in high speed solar wind, including charge state determination, was reported by Ipavich et al. (1983) who also employed a solid state detection system. In addition to being able to measure iron at high bulk velocities, the uniqueness of the observations presented here lies in their continuity over time scales of hours, days, or years so that we can investigate variations in abundance and other distribution function parameters in individual streams, and even the evolution of streams themselves over the decline of the last solar cycle.

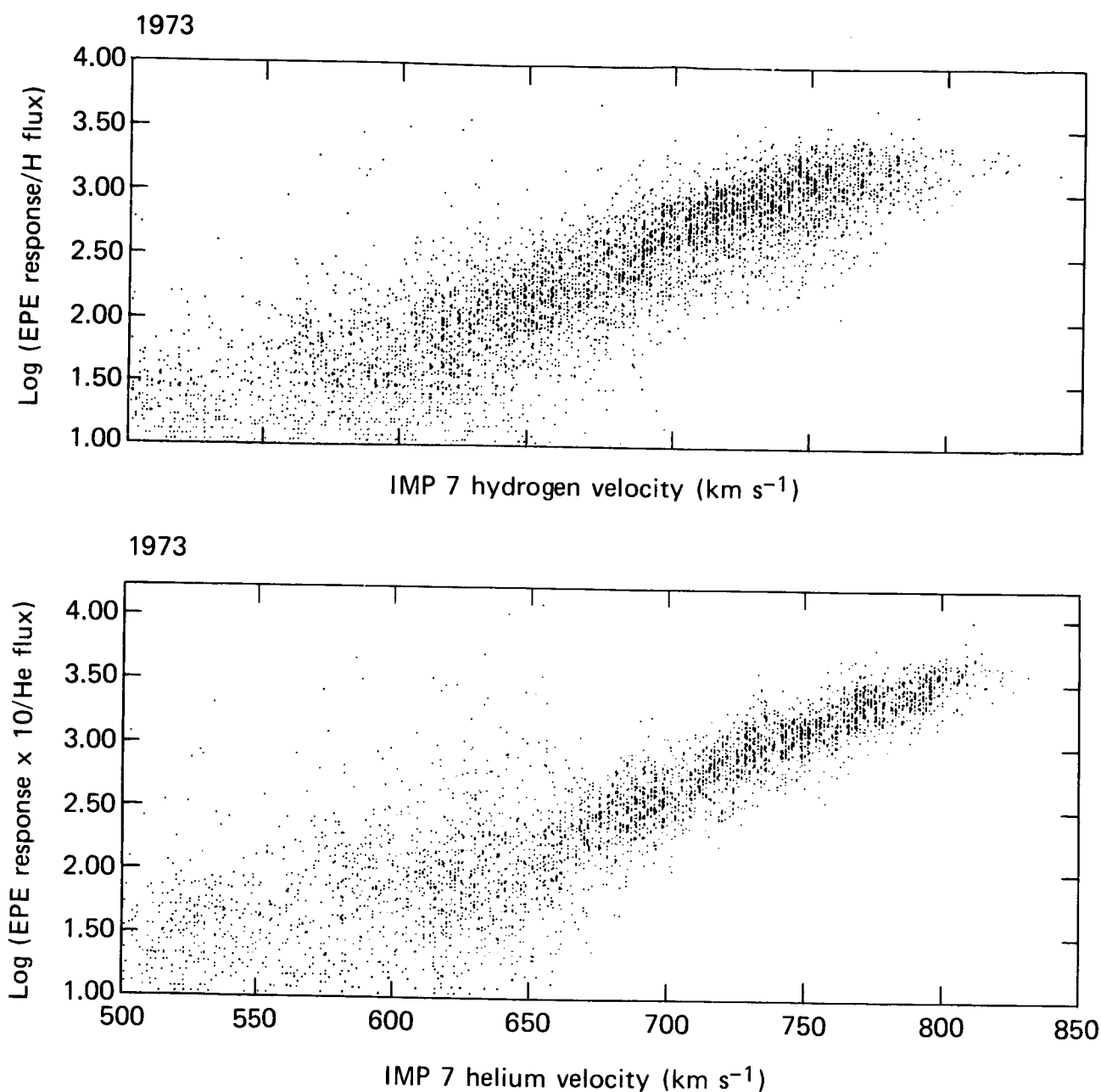FIGURE 1   (a)   Scatter plot of the logarithm of the EPE L1 detector iron response (5.5 minute averages) normalized by the LANL hydrogen flux, versus the LANL hydrogen velocity for all $V_H > 500$ km s^{-1} during 1973.   (b)   Scatter plot of the logarithm of the EPE L1 detector iron response normalized by the LANL helium flux, versus the LANL helium velocity.   Note the reduced scatter above $V_{He} \sim 660$ km s^{-1}.

As described in Papers 1 and 2, the iron is seen primarily in Sectors 9 and 10, the sunward-looking sectors of the 16 sectors in the ecliptic plane. In Paper 2, we describe in detail a method whereby for certain events we can derive both the iron bulk flow velocity (V_{Fe}) and its thermal velocity (v_{Fe}), assuming a convected Maxwellian thermal iron distribution. Using the model from Paper 2 for the instrument response based upon detector calibrations and geometry, we can use the measured V_{Fe} and v_{Fe} to obtain the iron flux, $J_{Fe} = N_{Fe} V_{Fe}$. This work will concern itself primarily with the quantity $J_{Fe}/J_H = N_{Fe} V_{Fe}/N_H V_H \approx N_{Fe}/N_H$, the iron abundance relative to hydrogen in the solar wind. We shall use the notation Fe/H for this abundance ratio through the remainder of this paper.

It has been shown (Ogilvie, 1980; Bochsler and Geiss, 1982) that minor ions up to oxygen, and perhaps iron, behave similarly to each other (same bulk velocity and thermal velocity) but dissimilarly to hydrogen (different, usually higher bulk velocity) in the non-collisional solar wind. In Figure 1a, we plot 5.5 minute averages of the sum of the count-rates in Sectors 9 and 10 on IMP-7 normalized by hydrogen flux, versus the hydrogen bulk velocity from the Los Alamos National Laboratory (LANL) solar wind detector on IMP-7. In Figure 1b we plot the sum of Sectors 9 and 10 normalized by the LANL helium flux, versus the LANL helium velocity. It can readily be seen that V_{He} orders the data much better than V_H, in agreement with $V_{He} \simeq V_{Fe} \neq V_H$. Throughout the remainder of this paper, we assume $V_{Fe} = V_{He}$ and use V_{He} to remove the detector efficiency velocity dependence.

IRON ABUNDANCE AS A FUNCTION OF HELIOGRAPHIC SOURCE LONGITUDE

Since we are interested in the coronal source regions and their influence on Fe/H, we wish to examine the variation of Fe/H as a function of the heliographic location of its source in the corona. To this end we shall map the time-ordered data into bin-averaged 2° wide bins in heliographic source longitude, using the constant radial velocity approximation from the corona to 1 AU.

In Figure 2, we show two consecutive recurrences of a particularly broad stream, with the first occurrence in light lines (V_H) and dots (V_{He}), the second in heavy lines and dots. The second panel displays Fe/H normalized by the coronal value of 4.7×10^{-5} of Withbroe (1971), which is also nearly the same as the solar wind value of 5.3×10^{-5} obtained (at lower solar wind velocity and kinetic temperature than those at which we are working) by Bame et al. (1979) for interstream solar wind. The absolute normalization of Fe/H is not well determined; flight spare detectors were used in the detector calibrations, and though there is good qualitative agreement between IMP-7, IMP-8, and the spare detectors, when simultaneously sampling data from a particular stream IMP-7 and 8 disagree with one another by a factor of ~ 3 in absolute response. On the basis of that consistent pattern, we have removed that factor of 3 difference in this paper, multiplying all IMP-7 data by 3 before plotting.

Although the stream's leading edge has moved westward approximately 40° on the second occurrence, the average value of Fe/H has not changed significantly, and, in fact, can be considered a stable signature of this source region. This stream is unusual in its breadth and the good coverage by IMP-7

1973 52 to 59
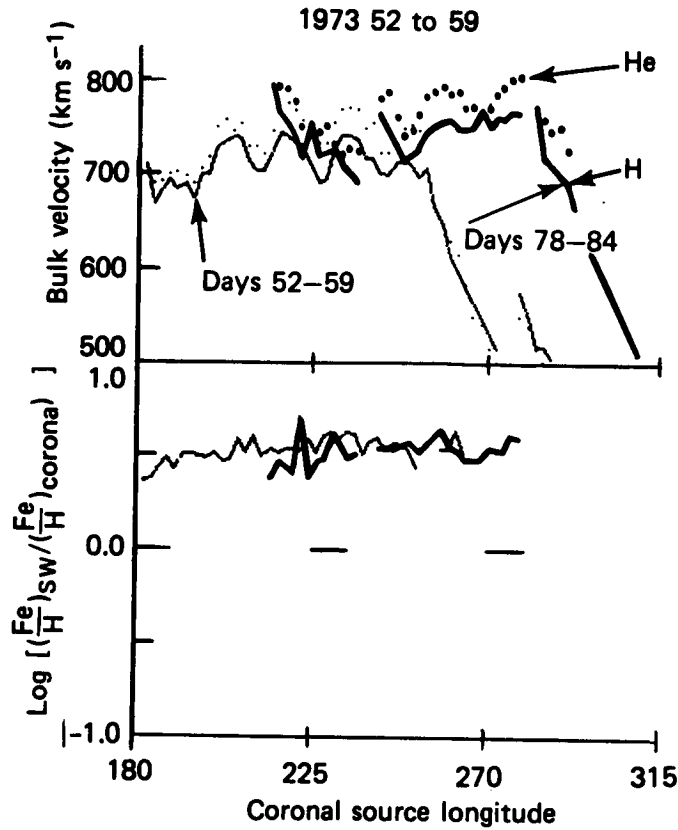
FIGURE 2   IMP-7 LANL solar wind parameters and the EPE iron abundance for a coronal hole-associated high velocity stream, days 50 - 62, 1973, (light lines and dots), plus its recurrence on the following rotation (heavy lines and dots) plotted as a function of heliographic source longitude, assuming constant radial flow from the corona to 1 AU.   The top panel shows V_H (solid line) and V_{He} (dots).   Second panel is the logarithm of the measured iron abundance (Fe/H) normalized by a coronal value of 4.7×10^{-5}.

on consecutive rotations, but the repeatability of the Fe/H profile is a common feature of other stable corotating streams associated with coronal holes.
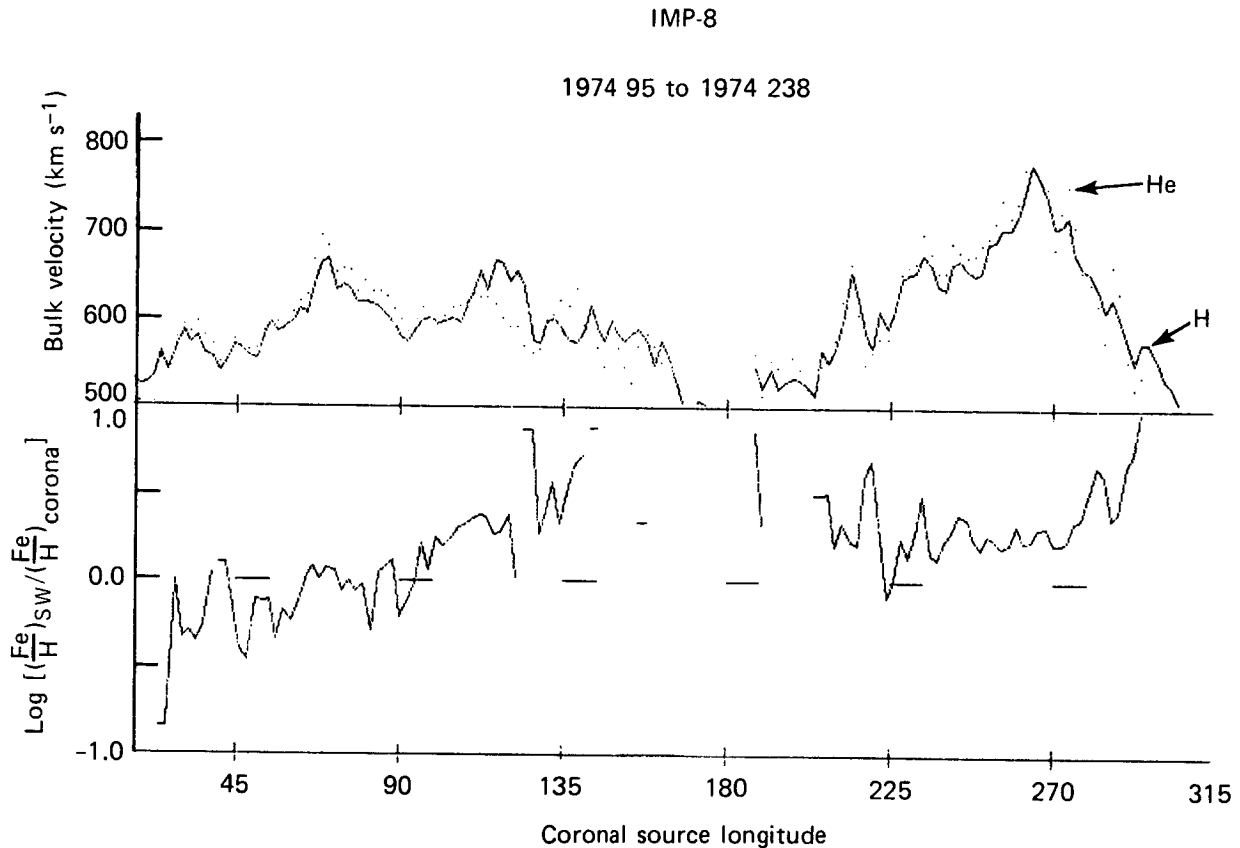
FIGURE 3   Average of velocities and Fe/H over 5 solar rotations in 1974, plotted versus source longitude.

LONG TERM TRENDS

Exploiting the repeatability of the corotating stream associated Fe/H ratios, in Figure 3 we average five consecutive solar rotations of data in mid-1974 to obtain a more continuous, representative longitude record of Fe/H than a single rotation with its attendant data gaps (due to the magnetospheric passes of the spacecraft) can provide. The stream on the right is fairly constant in Fe/H at a level lower by a factor of ~ 2 than the stream shown in Figure 2. The stream from 0° to 170° has a longitude-dependent Fe/H ratio, decreasing from a value a factor of ~ 2 above the stream centered at 260° to a value perhaps a factor of 3 below that value, for a total change of a factor

of ~ 6 from one edge of the stream to the other. The stream between 0° and 170° is associated with the equatorward extension of the south polar coronal hole. We suggest here that the topology of the coronal source region may be related to the systematic decrease in Fe/H from west to east in this stream, in which the south-easterly orientation of the eastern boundary of the coronal hole allows us to sample the composition across the edge (which is not possible for the more usual meridional orientation). If this is the case, the implication is that Fe/H is higher for solar wind originating near the inner edges of the coronal hole boundary region, decreasing as one approaches the outer edge of the boundary region.

We have taken this process of summing over multiple rotations one step further. By summing over an entire year, and then taking estimates by eye of the minimum, maximum, and mean Fe/H values for each year, we can examine (Figure 4) the yearly trend in Fe/H over the four years 1973-1976 during the decline of sunspot Cycle 20. It is clear that there is a monotonic decrease in Fe/H over the period. There is also a decline in He/H over the same period (upper curve, data from Feldman et al., 1978), but the iron abundance decrease precedes the helium abundance decrease by at least a year. The difference between the trends in Fe/H and He/H is actually greater than Figure 4 portrays, since the iron data is all from high speed streams while the downturn in He/H is dominated by the low speed solar wind; in fact, Bame et al. (1977) reported that He/H at the higher speeds remained remarkably constant (~ 5%) over this same period in the maxima of high speed streams. Thus, we find that the iron and helium abundances in high speed streams differ in their behavior on both intermediate (one stream's duration) and long term (fraction of a year to fraction of a solar cycle duration) time periods, though they are sometimes well correlated on a fraction of a day time scale.

SUMMARY AND CONCLUSIONS

Using the 50 - 200 keV ion channel of a solid state detector on the EPE experiment, we have obtained the only thermal iron measurements at solar wind speeds over 600 km s^{-1} during the decline of Solar Cycle 20, when the solar wind structure was dominated by stable corotating coronal hole associated high speed streams. We have found that:

1) The response of the EPE to Fe, when compared to the LANL He measurements, is consistent with the iron bulk velocity, thermal velocity, and bulk flow angle being the same (on average) as those for helium.

2) The profile of Fe/H as a function of time or coronal source longitude is a stable, repeatable feature of a stable corotating high speed stream.

3) Fe/H within a corotating stream can vary significantly as a function of the plasma's coronal source longitude, up to a factor of ~ 6, and we have identified the edge of a coronal hole with a gradient in Fe/H.

4) A long-term decrease of a factor of ~ 4 is measured in Fe/H from 1973 to 1976 during the decline of solar cycle 20.

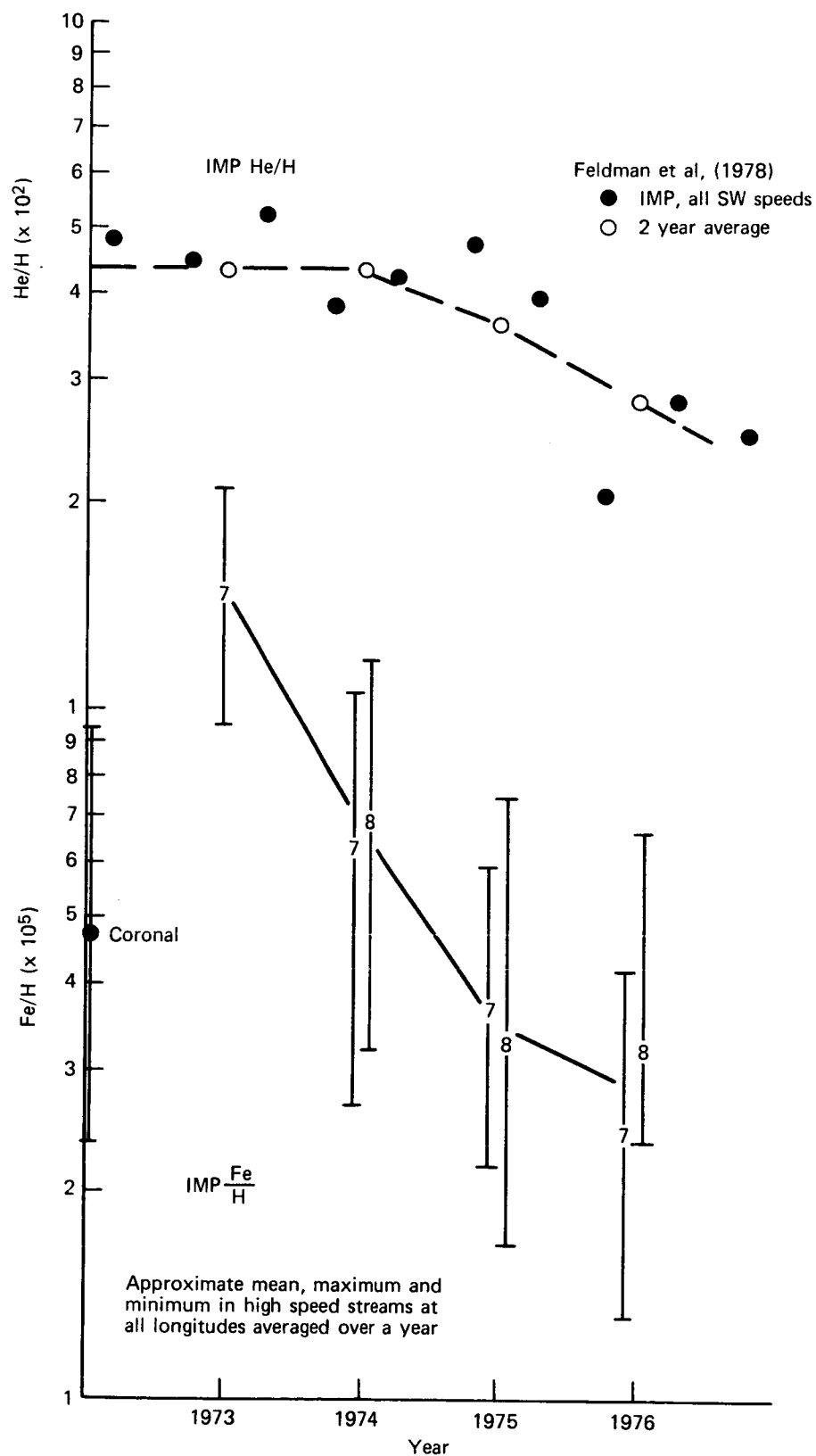FIGURE 4 Four-year decrease in Fe/H during the decline of Solar Cycle 20.

ACKNOWLEDGEMENTS

REFERENCES

Bame, S. J., J. R. Asbridge, W. C. Feldman, and J. T. Gosling, Evidence for a structure-free state at high solar wind speeds, J. Geophys. Res., 82, 1487, 1977.

Bame, S. J., J. R. Asbridge, W. C. Feldman, E. E. Fenimore, and J. T. Gosling, Solar wind heavy ions from flare-heated coronal plasma, Solar Phys., 62, 179, 1979.

Bochsler, P. and J. Geiss, Cross- and auto-correlations of speeds and kinetic temperatures of minor ions in the solar wind, EOS, Trans. AGU, 63, 424, 1982.

Feldman, W. C., J. R. Asbridge, S. J. Bame and J. T. Gosling, Long term variations of selected solar wind properties: IMP 6, 7 and 8 results, J. Geophys. Res., 83, 2177, 1978.

Ipavich, F. M., A. B. Galvin, G. Gloeckler, D. Hovestadt, B. Klecker, and M. Scholer, Heavy ion charge states observed in the solar wind, Solar Wind 5, 1983.

Mitchell, D. G. and E. C. Roelof, Thermal iron ions in high speed solar wind streams: Detection by the IMP 7/8 energetic particles experiments, Geophys. Res. Lett., 7, 661, 1980.

Mitchell, D. G., E. C. Roelof, W. C. Feldman, S. J. Bame and D. J. Williams, Thermal iron ions in high speed solar wind streams, 2. Temperatures and bulk velocities, Geophys.Res. Lett., 8, 827, 1981.

Mitchell, D. G., E. C. Roelof and S. J. Bame, Solar wind iron abundance variations at speeds > 600 km s^{-1}, 1972-1976, J. Geophys. Res., submitted 1983.

Ogilvie, K. W., Solar wind composition measurements - ISEE-3, EOS, 61, 1097, 1980.

Withbroe, G. L., The chemical composition of the photosphere and corona, The Menzel Symposium on Solar Physics, Atomic Spectra, and Gaseous Nebulae, ed. K. B. Gebbie, National Bureau of Standards Special Publication 353, 127, 1971.

MIXED SOLAR WIND ORIGINATING FROM CORONAL REGIONS OF DIFFERENT TEMPERATURES

P. Bochsler
Physikalisches Institut, University of Bern
Sidlerstrasse 5, CH-3012 Bern, Switzerland

ABSTRACT

Ionization states of elements in the solar wind have been used to determine thermal gradients in the lower corona. This method is based on the assumption, that in the beginning, solar wind material has a homogeneous temperature determining the original charge state of elements. In this paper, we investigate features in M/Q-spectra which might appear if the above assumption is violated and compare them with observational evidence.

INTRODUCTION

There is evidence for several cases of simultaneous appearance of $^4He^+$ and highly charged ions of other elements such as O^{6+} in low speed solar wind [Bame et al., 1968; Schwenn et al., 1980; Gosling et al., 1980; Zwickl et al., 1982] indicating the existence of mixtures of plasma with states of ionization frozen in at temperatures which differ by orders of magnitude. The mechanisms inherent in solar wind acceleration and heating which lead to these observations are not well understood. He^+ has a large cross section for complete ionization via electron collision at coronal temperatures. Typical rates for collisional ionization of He^+ are of the order of 10^{-8} cm^3 s^{-1} in the corona [Lotz, 1967]. This makes it obvious, that He^+ can only reach the outer part of the corona if it is somehow separated from the ambient hot plasma in the lower corona. A plausible way to achieve this separation is inclusion of the cold component into magnetic clouds [Zwickl et al., 1982]. Such clouds have been observed in connection with coronal mass ejections [Klein and Burlaga, 1982], but to our knowledge not with enrichments in $^4He^+$ in the solar wind. Hovestadt et al. [1982] find, that He^+ in an energetic solar proton event is far more abundant than expected when related to the mean charge states of C, O, and Fe.

From observations of EUV spectra in coronal loops there is evidence that these structures are cooling so rapidly that departure from thermal equilibrium occurs quite frequently [Raymond and Foukal, 1982]. Eruption of such loops into the corona will eventually provide mixtures of low and high ionization states as occasionally observed in $^4He^+$ -rich events.

Detection of $^4He^+$-rich events by means of E/Q- or M/Q-analyzers is in principle possible as long as $^4He^+$ is at least as abundant as the underlying ion Si^{7+}

which is usually the most prominent contributor at M/Q = 4.0. Only very few events of this type have been detected up to now; however this does not a priori preclude the possibility that these events are only extreme and rare cases of a more common phenomenon. In other words, it is possible that mixing of plasma from regions of different coronal temperatures occurs quite frequently in solar wind emanating from regions near sector boundaries and that generally, the degrees of ionization of the components involved in these mixtures do not differ to such a large extent as in the rare cases where $^4He^+$ is detectable.

The purpose of this study is to explore how such "moderate" mixtures without appearance of $^4He^+$ might be detected in M/Q-spectra of low speed solar wind. Specific features which can be attributed to plasma mixing will be critically discussed and investigated for uniqueness, i.e. we also look into mechanisms, other than plasma mixing, which could produce similar indicators as those found for mixing.

CHARACTERISTICS OF $^4He^+$ OBSERVED ON DECEMBER 10, 1981

In their systematic search for $^4He^+$ in the solar wind covering the period from 1972 to 1980, Zwickl et al. [1982] have found three distinct events with detectable amounts of $^4He^+$. In figure 1 we show an additional case with enhanced abundance at M/Q = 4.0 which we attribute to an excess of $^4He^+$. This event was seen with the ISEE-3 Plasma Composition Experiment during the night from December 9 to 10, 1981. A first indication of $^4He^+$ was found at 23h of December 9 when the instrument was switched into a mode which covers a M/Q-range from 1.7 to 4.1 after having been in a mode which allows better time resolution but only covers M/Q from 1.7 to 3.0. The event lasted at least until December 10, 2h30m when a data gap of 38 hours began. It cannot be excluded that $^4He^+$ was present in the solar wind for several hours before the instrument was switched to the wider M/Q-range. Indeed, indication for the fact that something unusual was going on, is given by the anomalously large O^{6+}/O^{7+}-ratio which already occurred a few hours before the first detection of $^4He^+$ and lasted throughout the period of observed enhancement of $^4He^+$. However there is no indication for $^4He^+$ before December 9, at 1.00h followed by another data gap.
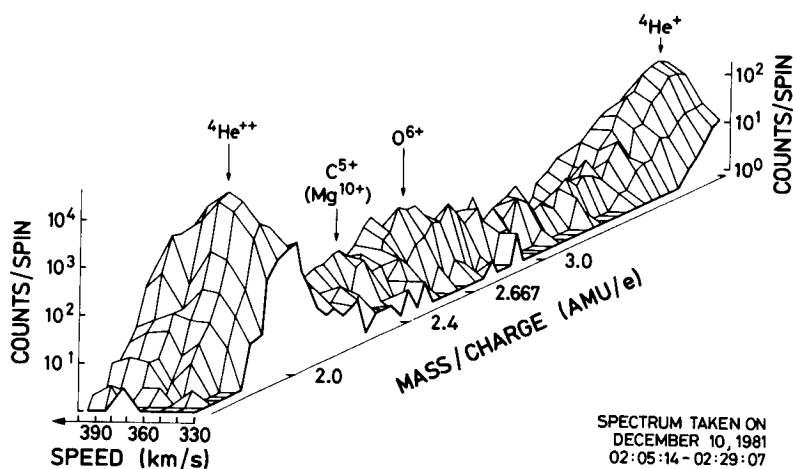

Figure 1: Three dimensional representation of a spectrum taken on December 10, 1981 from 02:05:14 to 02:29:07 UT. $^4He^{++}$, O^{6+}, and $^4He^+$ are visible. The low abundance of O^{7+} indicates that the "freezing-in temperature" of the hot component is $1.2 \cdot 10^6$K or lower.

A sudden increase in solar wind speed and kinetic temperature was observed on December 8, 14.00h. Linking this with the appearance of ^{4}He$^+$, we find that the anomalous enhancement of ^{4}He$^+$ began earlier than 33 hours after the increase in speed but not earlier than 11 hours. It lasted for at least 3 1/2 hours but no longer than 64 hours.
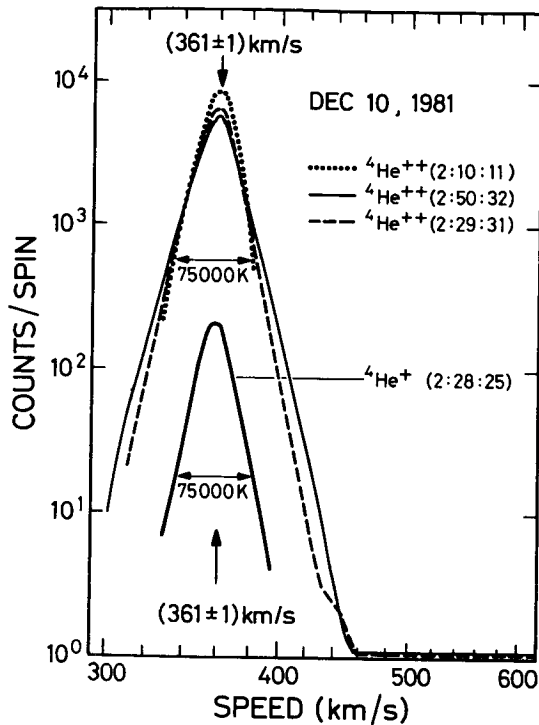

Figure 2: Cross section of the relief in figure 1 in the speed/counts plane at M/Q = 4.0 (lower parabola). For comparison, velocity distributions of ^{4}He^{++} and ^{4}He$^+$ are very similar. The flux ratio is approximately 100.

In figure 2 we show a cross section of the relief of figure 1 taken at M/Q = 4.0 in the count-rate/speed plane. The velocity distribution of ^{4}He$^+$ is compared with the distribution of ^{4}He^{++} shortly before and after the ^{4}He$^+$ profile was taken. Two things can be noted from this comparison.

- The velocity distributions of ^{4}He$^+$ and ^{4}He^{++} do not differ in any respect from each other. Speeds are equal to the narrow limits of uncertainty, the same holds for the kinetic temperature of the two ions.

- The flux ratio of ^{4}He^{++} to ^{4}He$^+$ is approximately 100.

This observation places limits on possible models for the origin of this ^{4}He$^+$-rich event. It shows that ^{4}He$^+$ is so well incorporated into the solar wind that it is indistinguishable in its kinetic behaviour from other minor ions. This can only be true if interaction of ^{4}He$^+$ with the ambient solar wind plasma is sufficiently intensive suggesting that ^{4}He$^+$ has been flowing within the solar wind from the lower parts of the corona.

SIGNATURES OF "MODERATE" MIXTURES

The most prominent signature of "extreme" mixtures in M/Q-spectra is certainly the appearance of ^{4}He$^+$. We will now look for features of plasma mixtures with less extreme temperature differences in their constituents. An example of a M/Q-spectrum produced with an artificial moderate mixture is shown in figure 3. We have mixed 50% isothermal solar wind at $3.0 \cdot 10^6$K ionization temperature with 50% at $1.0 \cdot 10^6$K using the instrument functions of the ISEE-3 Plasma Composition Instrument, chemical abundances from Ross and Aller [1976] and the rates of Shull and van Steenberg [1982] in order to compute the ionic abundances for the simulation. A good fit in the range of the O^{6+}- and O^{7+}-peaks is obtained with an isothermal solar wind at $1.6 \cdot 10^6$K. As can be seen in figure 3, an amazingly good match results. Obviously, if the simulated mixture were treated as observational
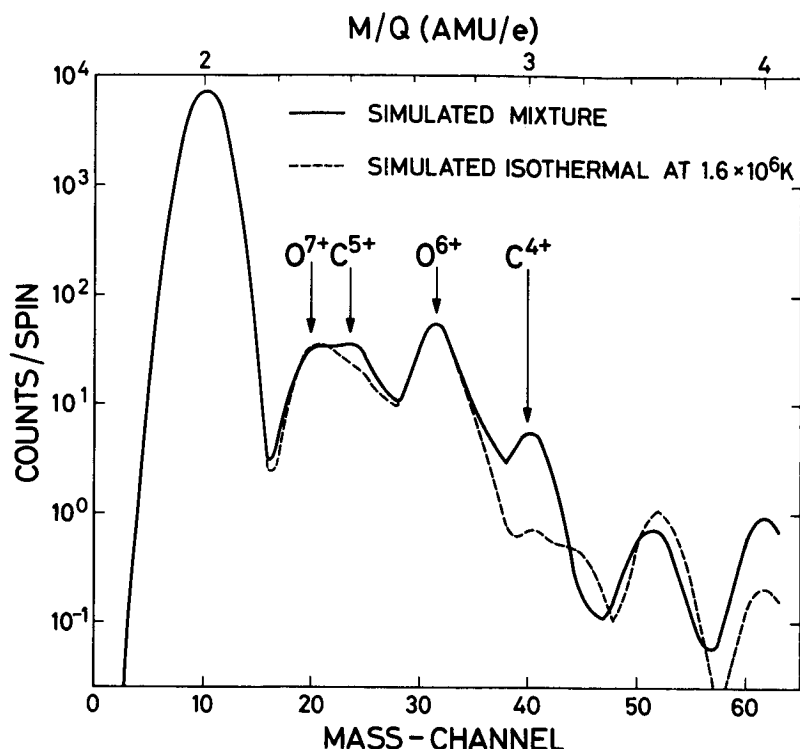
Figure 3: Artificial spectrum produced with a "moderate" plasma mixture. The hot component was $3.0 \cdot 10^6$K, the cool component at $1.0 \cdot 10^6$K. Equal fluxes for both components and the instrument functions of the ISEE-3 plasma composition experiment have been used. The dashed line represents a simulated isothermal spectrum produced with standard chemical abundances. At a temperature of $1.6 \cdot 10^6$K, an optimal fit to the mixture in the oxygen region (mass-channels 17 to 35) is obtained.

data, interpretation as an isothermal plasma would yield such a good approximation that one might be tempted to take it as reality and to proceed to a more refined interpretation basing on wrong assumptions. The most outstanding differences between mixture and isothermal spectrum at $1.6 \cdot 10^6$K is the excess of C^{5+} and C^{4+} in the mixture. This is due to the large ionic abundances of C^{4+} and C^{5+} in the low temperature component at $1.0 \cdot 10^6$K. For normal fluxes, countrates in the C^{4+}-region are only of the order 3 to 5 per spectrum with correspondingly large uncertainties; so the most significant feature remains an excess at M/Q = 2.4 due to C^{5+} for moderate mixtures. Of course, the exact shape of a spectrum composed of different isothermal components depends on the mixing ratios and the temperatures of the components. Nevertheless, in the temperature range from 1 to several million degrees, the dominant peaks next to $^4He^{++}$ will always be O^{6+} and O^{7+}; the next important ingredient will be C^{5+} with a variable size depending on the temperature of the cooler component. This is predominantly due to the relatively large abundance of C in solar material (C/O = 0.6 [Ross and Aller, 1976]).

In the following, we will have to investigate whether excessive flux at M/Q = 2.4 compared to isothermal ion distribution and standard chemical abundances necessarily requires plasma mixing in the corona or whether alternative explanations might be possible.

DEPARTURE FROM ISOTHERMAL EQUILIBRIUM IN THE CORONA

Up to now, we have implicitly assumed that in a given sample of solar wind the state of ionization of elements in the plasma depends only on a given coronal temperature which is equal for all elements. This is certainly only an approximation. As has been shown by Hundhausen et al. [1968] this assumption holds as long

as recombination times and ionization times for ions are much shorter than their characteristic travel times within the corona. Bame et al. [1974] have used the observation that several ions of iron and silicon indicate lower freezing-in temperatures than oxygen, for determining thermal gradients in the lower corona. From the fact that heavier ions in general recombine faster, one could hastily conclude that carbon would freeze-in at lower depths than oxygen, thus indicating higher freezing-in temperatures than oxygen. This however neglects that at given temperatures the most abundant ions of different elements have different electronic configurations. At $1.6 \cdot 10^6$K, oxygen is most prominent in the form of the helium-like ion O^{6+} while carbon is already fully ionized to a large extent with a significant rest of H-like C^{5+}. Thus we have to compare ions not only of elements with different masses but, more important, with different electronic configurations. Predictions of the state of ionization of an element, also qualitative ones, can therefore only be made by careful computations based on models of the solar corona. We have used a simplistic model for dependences o electron densities, electron temperatures and ion speeds upon the solar distance and performed an exploratory study for the elements carbon, oxygen, magnesium, silicon, and iron. We have assumed that the electron density decreases with r^{-3}. In order to keep the ion flux per sterad constant, we have assumed $v \sim r$. The last assumption certainly does not hold for larger solar distances, however, we depend on a good agreement of the model with reality in the inner corona, where the charge state of an element is fixed and there this assumption holds to a first approximation. The temperature has been assumed to vary with $r^{-\alpha}$, and computations have been done for a set of four values of α. Ionic abundances at 1 AU have been calculated by solving systems of equations for production and destruction of ions in the range $r = 1 R_s$ to 1 AU using the above model on depth dependences and the ionization and recombination rates compiled by Shull and van Steenberg [1982].
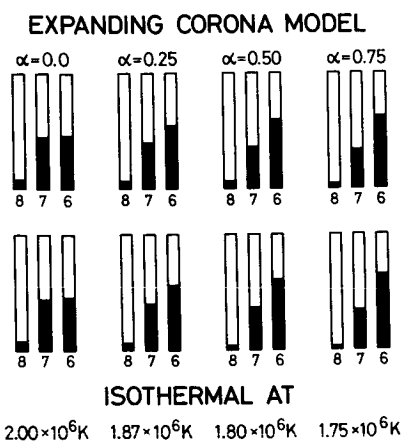
Figure 4: Using an expanding corona model we have calculated the charge state distribution of carbon and oxygen at 1 AU. An initial electron density of 10^9 per cm^3 and an initial electron temperature of $2.0 \cdot 10^6$K was assumed. The density varied with r^{-3}, the temperature with $r^{-\alpha}$, and the speed was assumed to be proportional to r. For comparison, charge state distributions for a static, isothermal corona are shown in the lower row.

Results are depicted for carbon and for oxygen in figure 4. Charge state distributions have been computed for α = 0.25, 0.5 and 0.75, assuming initial distributions as for an isothermal corona at T = 2.0 · 10^{6}K, the initial electron density was taken to be 1 · 10^{9}cm^{-3}.

For comparison we also show charge state distributions for isothermal coronae (α=0) at different temperatures. These temperatures have been chosen in order to give a good approximation of the charge state distribution of the element to the expanding corona model at the respective values for α. Evidently, there is no difference between equilibrium calculations and those for non-equilibrium for carbon and oxygen; however, in the case of carbon, temperatures derived from the isothermal fits are significantly lower than for oxygen. In figure 5 we show the result of similar computations for silicon. This figure illustrates that it is impossible to find satisfying matches to the whole range of charge states of a heavier element such as Si with isothermal models.

Since carbon in general shows lower freezing-in temperatures than oxygen, we expect to find a certain excess of C^{5+} and C^{4+} in spectra obtained from expanding corona models relative to simulations in which all elements have been assumed to have equilibrium charge state distributions at one given temperature. This is shown in figure 6 for two simulated spectra: A small excess is visible at M/Q = 2.4 and also at

CHARGE STATE DISTRIBUTION OF SILICON AT r = 1 AU
EXPANDING CORONA MODEL
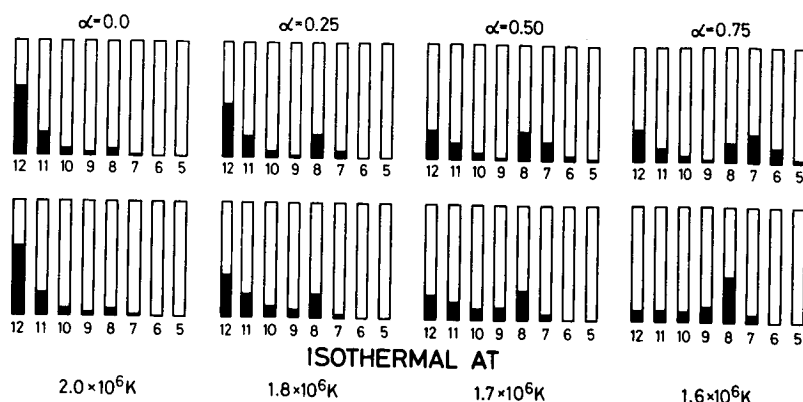
ISOTHERMAL AT

Figure 5: Same as figure 4 but for silicon. Obviously for larger values of α no good isothermal fits exist for this element.
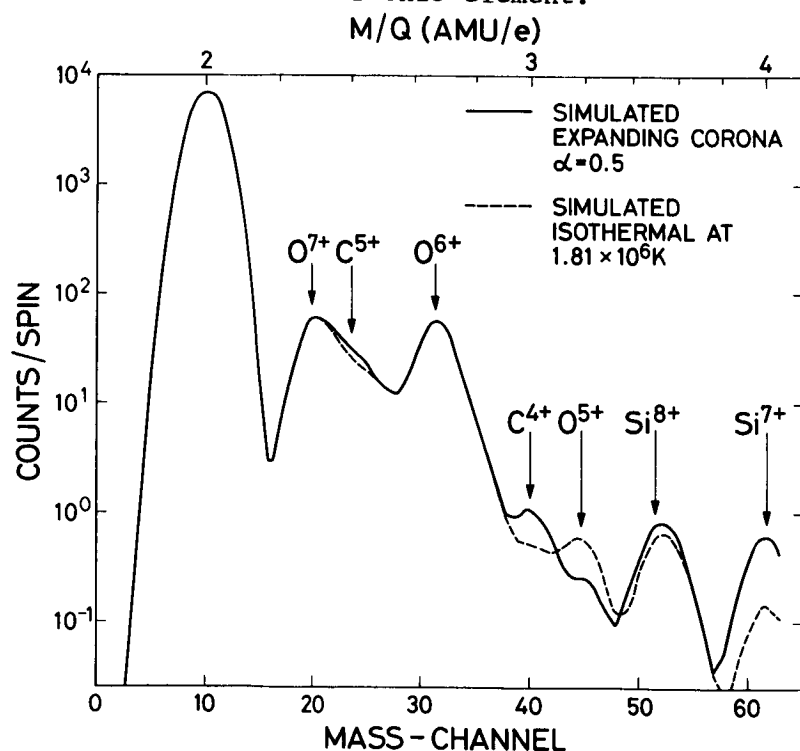
Figure 6: As in figures 4 and 5 we have used an expanding corona model with α = 0.5 and the instrument functions of the ISEE-3 plasma composition instrument in order to simulate the spectrum drawn as a solid line. For comparison, a dashed line indicates an isothermal spectrum which fits the oxygen peaks. Small excess in the C^{5+}- and C^{4+}-peaks are visible.

618

M/Q = 3.0 for the expanding corona simulation relative to the isothermal model. Although the excess is considerably smaller than in the case of plasma mixing (section 3), in view of the approximate nature of our expanding model we cannot completely exclude the possibility that an excess peak at M/Q = 2.4 might rather be due to departure from equilibrium than to "moderate" plasma mixing.

ANOMALOUS ABUNDANCE OF C AND Mg

It is possible that enhanced chemical abundances of C or Mg could produce anomalous peaks at M/Q = 2.4. A priori C seems to be the more likely candidate for such enhancements. Because of its larger solar surface abundance, an enhancement of carbon by a factor of 3 over normal solar abundance could produce a significant excess at M/Q = 2.4. Correspondingly it requires an enhancement of a factor of 10 to 30 for Mg in order to generate a significant excess. Although these enhancements are much larger than those required for carbon they cannot be excluded. In contrary, it is well known that in the case of silicon, large fluctuation in its relative abundanc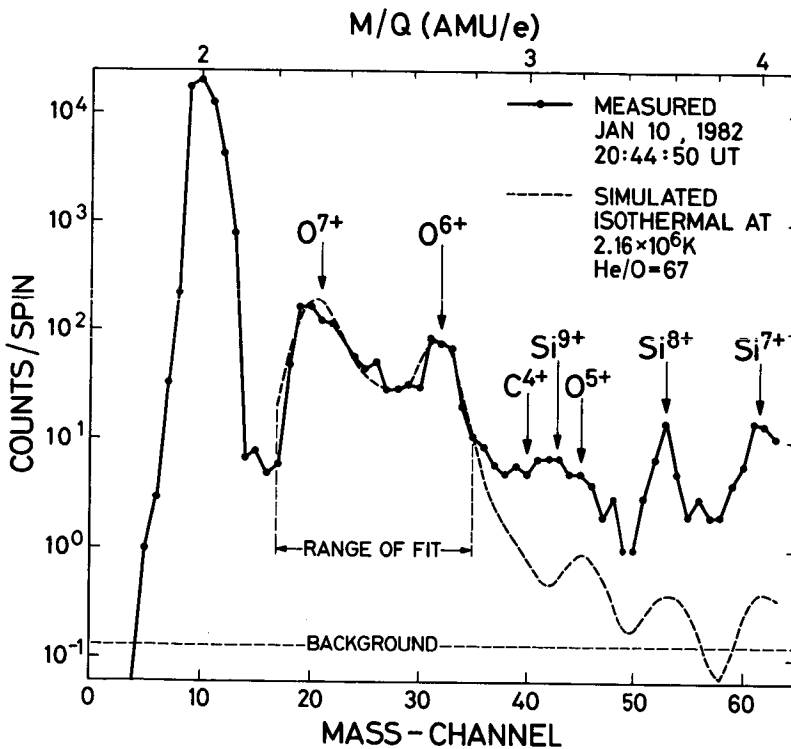e exist [Bame et al., 1975]. An example of temporary enhancement of Si is given in figure 7 which shows a spectrum obtained with ISEE-3. A fit with normal solar abundances in the oxygen region gives a good match with measured data while a large discrepancy is seen in the Si-region. Silicon seems to be enhanced relative to oxygen by a factor of 30 compared to normal solar abundances [Ross and Aller, 1976].

Figure 7: A case of enhanced silicon abundance observed with the ISEE-3 Plasma Composition Experiment on Jan. 10, 1982 (solid line). A good fit (dashed line) is obtained in the oxygen region with standard solar surface abundances, a He/O ratio of 67, and a (isothermal) freezing-in temperature of $2.2 \cdot 10^6$K. The departure in the region of the silicon peaks indicates an enhancement of silicon by a factor of 30.

Geiss [1982] has argued that such fluctuations could be caused by differences in the first ionization potential of different elements. Silicon has a first ionization potential of 8.149 V, far below Ly-α and is therefore one of the most sensitive elements among the major species. This also holds for Mg (7.644 V). Thus, if silicon shows enhanced relative abundance due to incomplete first ionization of the other elements, the same will happen to magnesium. Independent of the model for further ionization and the exact ionization - and

619

recombination rates, Mg^{10+} at $M/Q = 2.4$ will be a prominent species because of its helium-like electron shell in a wide temperature range. Therefore, we favour enhanced Mg abundances over the possibility of carbon enrichments, if anomalous chemical abundances were the reason for an excess at $M/Q = 2.4$.

DISCUSSION AND CONCLUSIONS

Kunz et al. [1983] report the observation of anomalous enhancements at $M/Q = 2.4$ based on measurements by the ISEE-3 Plasma Composition Experiment. In principle, various causes could be responsible for this observation and at present is impossible to definitely conclude in favour of the mixing hypothesis or against it. More developed instruments which allow the detection of charge and mass/charge are required to establish a final conclusion. Meanwhile, we briefly summarize our reasons for not dismissing the mixing hypothesis at once. Although, as pointed out in the introduction, the dynamics of mixture is not understood, cases of increased $^4He^+$ fluxes from the lower corona have been found and there is almost no doubt that these events are caused by incomplete ionization of solar surface material. In order to prevent $^4He^+$ from further ionization by collision with the ambient electrons in the corona, it has to be protected up to a distance of the order of 10 solar radii from the solar surface. Beyond, densities are small enough that $^4He^+$ can survive up to 1 AU. If we assume that a hypothetical magnetic structure has a typical size of 1 R_s and the time required to protect the plasma to be of the order of 10^5 s, a diffusion coefficient acting against the protective structure should be of the order of 10^{17} cm^2/s. Diffusion coefficients of charged particles across magnetic fields can be calculated using the relation

$$D_\perp = D \frac{v_c^2}{\omega_c^2} \tag{1}$$

[e.g. Krall and Trivelpiece, 1973] with v_c collision frequency, ω_c cyclotron frequency and D diffusion coefficient of neutral particles.

We find

$$D_\perp \approx 10^{14} \frac{n_9 \ln \Lambda}{B^2 [nT]} \cdot \sqrt{\frac{A}{T_6}} \tag{2}$$

T_6 : Temperature in 10^6K,

n_9 : density in 10^9 cm^{-3},

B : magnetic field in nT,

Λ : ratio of Debye length to impact parameter.

This is a very coarse estimate which will only give the order of magnitude. In any case, we can see that magnetic bottles built of fields of the order of a few nT

620

and sizes of 1 R_{solar} will prevent mixture by plasma diffusion for days. From dimensional considerations it seems probable that there is no strong change in diffusion times with distance from the solar surface r: If the size of a magnetic structure increases with r, the electron density decreases with r^{-3}, and if the magnetic fields decrease with r^{-2}, we find that the diffusion time, i.e. the characteristic time until a certain fraction of plasma has diffused into the magnetic structure, increases with r. Obviously, mixture by plasma diffusion is only a lower limit to possible transport of cool and hot plasma into each other, distortion of magnetic structures might lead to a much more efficient, turbulent mixture. In fact, since we obtain highly ionized plasma and $^4He^+$ together at 1 AU, the two components have to be mixed to a scale smaller than 1000 km. Note, that in expression (2), $D \sim T^{-1/2}$, i.e. the higher the temperature of the plasma the easier it is to separate it from other components by magnetic fields. It is certainly not more difficult to produce "moderate" mixtures than extreme ones. Raymond and Foukal [1982] have presented evidence that departure from thermal equilibrium is a common phenomenon in coronal loops, thus one would not be amazed to find plasma mixtures emanating regularly from magnetically active regions. We conclude that the appearance of some peaks in M/Q-spectra unexpected in isothermal plasma can be interpreted in terms of an expanding corona model with freezing-in occurring at different levels, hence serving as a diagnostic tool for the depth structure of the corona [Bame et al., 1974]. Alternatively in cases of more complicated magnetic field configurations, e.g. near sector boundaries, M/Q-spectra might have to be interpreted as mixtures of plasma of different freezing-in temperatures and ultimately serve as a diagnostic tool of lateral structures of the corona near the solar surface.

REFERENCES

Bame, S., J.R. Asbridge, W.C. Feldman, and P.D. Kearney, The quiet corona: Temperature and temperature gradient, Solar physics, 35, 137, 1974.

Bame, S.J., J.R. Asbridge, W.C. Feldman, M.D. Montgomery, and P.D. Kearney, Solar wind heavy ion abundances, Solar physics, 43, 463, 1975.

Bame, S.J., A.J. Hundhausen, J.R. Asbridge, and I.B. Strong, Solar wind ion composition, Phys. Rev. Lett., 20, 393-395, 1968.

Geiss, J., Processes affecting abundances in the solar wind, Space Sci. Rev., 33, 201, 1982.

Gosling, J.T., J.R. Asbridge, S.J. Bame, W.C. Feldman, R.D. Zwickl, Observations of large fluxes of He^+ in the solar wind following an interplanetary shock, J. Geophys. Res., 85, 3431, 1980.

Hovestadt, D., B. Klecker, H. Höfner, M. Scholer, G. Gloeckler, F.M. Ipavich, Ionic charge distribution of helium, carbon, oxygen, and iron in an energetic storm particle enhancement, Astrophys. J., 258, L57, 1982.

Hundhausen, A.J., H.E. Gilbert, and S.J. Bame, The state of ionization of oxygen in the solar wind, Astrophys. J., 152, L3, 1968.

Klein, L.W. and L.F. Burlaga, Interplanetary magnetic clouds at 1 AU, J. Geophys. Res., 87, 613, 1982.

Krall, N.A. and A.W. Trivelpiece, Principles of plasma physics, Mc Graw-Hill Inc., 1973.

Kunz, S., P. Bochsler, J. Geiss, K.W. Ogilvie, and M.A. Coplan, Determination of solar wind elemental abundances from M/Q observations during three periods in 1980, in preparation.

Lotz, W., Electron-impact ionization cross-sections and ionization rate coefficients for atoms and ions, Astrophys. J. Suppl., 14, 207, 1967.

Raymond, J.C. and P. Foukal, The thermal structure of solar coronal loops and implications for physical models of coronae, Astrophys. J., 253, 323, 1982.

Ross, J.E. and L.H. Aller, The chemical composition of the sun, Science, 191, 1223, 1976.

Schwenn, R., H. Rosenbauer, and K.H. Mühlhäuser, Singly-ionized helium in the driver gas of an interplanetary shock wave, Geophys. Res. Lett., 7, 201, 1980.

Shull, J.M. and M. Van Steenberg, The ionization equilibrium of astrophysically abundant elements, Astrophys. J. Suppl., 48, 95, 1982.

Zwickl, R.D., J.R. Asbridge, S.J. Bame, W.C. Feldman, and J.T. Gosling, He$^+$ and other unusual ions in the solar wind: a systematic search covering 1972 - 1980, J. Geophys. Res., 87, 7379, 1982.

INTERPRETING THE SOLAR WIND IONIZATION STATE

Stanley P. Owocki
Harvard-Smithsonian Center for Astrophysics
60 Garden St.
Cambridge, MA 02138

ABSTRACT

The ionization state of the solar coronal expansion is frozen within a few solar radii of the solar photosphere, and spacecraft measurements of the solar wind heavy ion charge state can therefore yield information about coronal conditions (e.g. electron temperature). Previous interpretations of the frozen-in ionization state have always assumed that in the coronal freezing-in region, 1. all heavy ions flow at the same bulk speed as protons, 2. the electron velocity distribution function is Maxwellian, and 3. conditions vary in space but not in time. In this paper, we examine the consequences of relaxing these assumptions for the interpretation of solar wind charge state measurements. We find that: 1. The temperature inferred by traditional interpretation of the interplanetary ionization state will overestimate (underestimate) the actual coronal electron temperature if higher ion charge stages flow systematically faster (slower) than lower stages at the coronal freezing radius. 2. Temperatures inferred from relative abundance measurements of ion-charge-stages (e.g. O^{+6}) with high ionization potentials moderately overestimate the actual coronal electron temperature if the high-energy tail of the coronal electron velocity distribution is enhanced relative to a Maxwellian distribution. 3. The propagation of a disturbance, e.g. a shock wave, through the corona can strongly affect the frozen-in charge state, but only over a time (a few times ten minutes) corresponding to the coronal transit time for the disturbance.

1. Introduction

The inferred degree of ionization of a gas is often used in astrophysics as a diagnostic of the gas temperature. For example, the solar-coronal ionization balance between collisional ionization and radiative and dielectronic recombination is very sensitive to the local electron temperature, but the balance is insensitive to electron density because each competing rate is proportional to the number density of electrons; information on the ionization state of the corona can thus be used to infer the electron temperature there (Billings 1966). On the other hand, as ions flow out of the corona and into the solar wind, the electron density sharply decreases so that solar wind ions hardly ever encounter an electron; the solar wind ionization balance is therefore not very sensitive to local conditions, but is "frozen" in the high-density corona within a few solar radii of the solar photosphere (Hundhausen et al. 1968a,b). Measurements of the solar wind ionization state can thus be used as a diagnostic

of the temperature in the regions of the solar corona from which the gas originates (Bame et al. 1974; Ogilvie and Vogt 1980).

In this paper, we shall first review the basic "freezing-in" theory for the solar wind ionization state (section 2). We shall then discuss several modifications of this theory which must be made when certain of its simplifying assumptions about conditions in the coronal expansion are relaxed (sections 3-5). Specifically, we shall examine the effect of unequal heavy-ion flow speeds in the corona (section 3), the effect of a non-Maxwellian coronal electron velocity distribution (section 4), and the effect of intrinsic time-variations in coronal conditions (section 5). Throughout this discussion we shall emphasize the relevance of such coronal effects to the interpretation of interplanetary charge-state measurements, but, in order to concentrate study on these effects, we shall not discuss the measurements themselves, their uncertainties, or uncertainties in assumed atomic rates.

2. The Ionization State from Simple Coronal Ion Outflows

Consider a (potentially) time-dependent coronal ion outflow in which the various ionization stages i of a given element s of atomic number Z are constantly undergoing ionization and recombination through interactions with electrons e. We write the conservation equation for each ionization stage ($i=1$ to Z) as,

$$\frac{\partial n_i}{\partial t} + \nabla \cdot (n_i u_i) = n_e(n_{i-1}C_{i-1} - n_i(C_i + R_i) + n_{i+1}R_{i+1}) \quad , \tag{1}$$

where n and u refer to particle number density and bulk flow velocity, and C_i and R_i refer to the ionization and recombination coefficients (cm^3/sec) for rates out of the ith ionization stage. We include here both dielectronic and radiative recombination (Burgess 1965; Tucker and Gould 1966), as well as auto- and collisional ionization (Seaton 1964; Lotz 1967), but we neglect coronal photoionization (see e.g. Billings 1966). Each rate coefficient can be written in the form $\langle\sigma v\rangle$, where σ is the cross section, v is the electron speed, and the angle brackets denote an average over the electron velocity distribution. If $n_e < 10^9 \text{cm}^{-3}$, a condition valid throughout the corona and solar wind, the cross section σ is not a strong function of density (Jordan 1969), and so, if electron-electron collisions are sufficient to establish a Maxwellian distribution, then the rates $\langle\sigma v\rangle$ vary only with electron temperature; $R_i = R_i(T_e)$, $C_i = C_i(T_e)$.

Let us first examine the case in which the coronal electron velocity distribution is locally Maxwellian and the coronal outflow is steady ($\partial n_i/\partial t = 0$). At the base of such a flow, the electron density n_e is relatively high while the ion velocities u_i are very small. This means that each individual rate term on

the right-hand-side of (1) has an absolute value that is much greater than the flow-divergence term described by the left-hand-side. Hence the two sides can only balance if competing rate terms approximately cancel. We therefore conclude that the ionization state of the lower solar corona is fixed by the <u>ionization equilibrium</u> condition,

$$\frac{n_i}{n_{i+1}} = \frac{R_{i+1}(T_e)}{C_i(T_e)} \quad , \tag{2}$$

which implies that the degree of ionization at the coronal base depends only on the local electron temperature T_e.

As ions accelerate outward from the coronal base, the local electron density rapidly decreases. In the limit of vanishing electron density at large heliocentric radii in the solar wind, each of the rate terms on the right-hand-side of (1) must individually approach zero, implying that the divergence term must also vanish, $\nabla \cdot (n_i u_i) \rightarrow 0$. We therefore find that the ionization state of the solar wind is fixed by the <u>frozen-ion-flux</u> condition,

$$\frac{n_i u_i}{n_{i+1} u_{i+1}} = \text{constant} \quad , \tag{3}$$

and thus is independent of local electron temperature in the wind. (Here we have assumed that different ionization stages have the same flow-tube areas, but not necessarily the same flow speeds.) Note that the ionization equilibrium conditions (2) for the solar corona fix the relative <u>number</u> of the ion charge stages, while the freezing conditions (3) for the solar wind fix the relative <u>fluxes</u> of these stages. For the remaining discussion in this section, we will assume that all ion-charge-stages flow at the same speed ($u_i = u$), in which case the distinction between relative number and relative flux becomes irrelevant. This distinction will be important, however, for understanding the effect of unequal ion flow speeds (see section 3).

This freezing of the relative charge-stage abundances occurs at the transition between dominance of the ionization/recombination processes in the low corona to dominance of flow-divergence effects in the solar wind. This transition takes place when the ionization/recombination exchange time, $\tau_{i<->i+1} = 1/n_e(R_{i+1}+C_i)$, becomes greater than the expansion time, $\tau_{exp} = H/u_i$, in which the ions flow through a density scale height $H = n_e/(dn_e/dr)$. Figures 1, which are adapted from Hundhausen et al. (1968a,b), illustrate this for the ionization balances among the dominant charge-stages of oxygen in a typical steady-state, spherically-symmetric coronal expansion model. In this model the electron distribution is Maxwellian, the electron temperature declines outward, and all oxygen charge-stages flow at the proton speed. Figure 1a shows how the sharp outward decline in electron density results in a rapid increase of the ion exchange time (solid curves), whereas the expansion time (dashed curves) remains
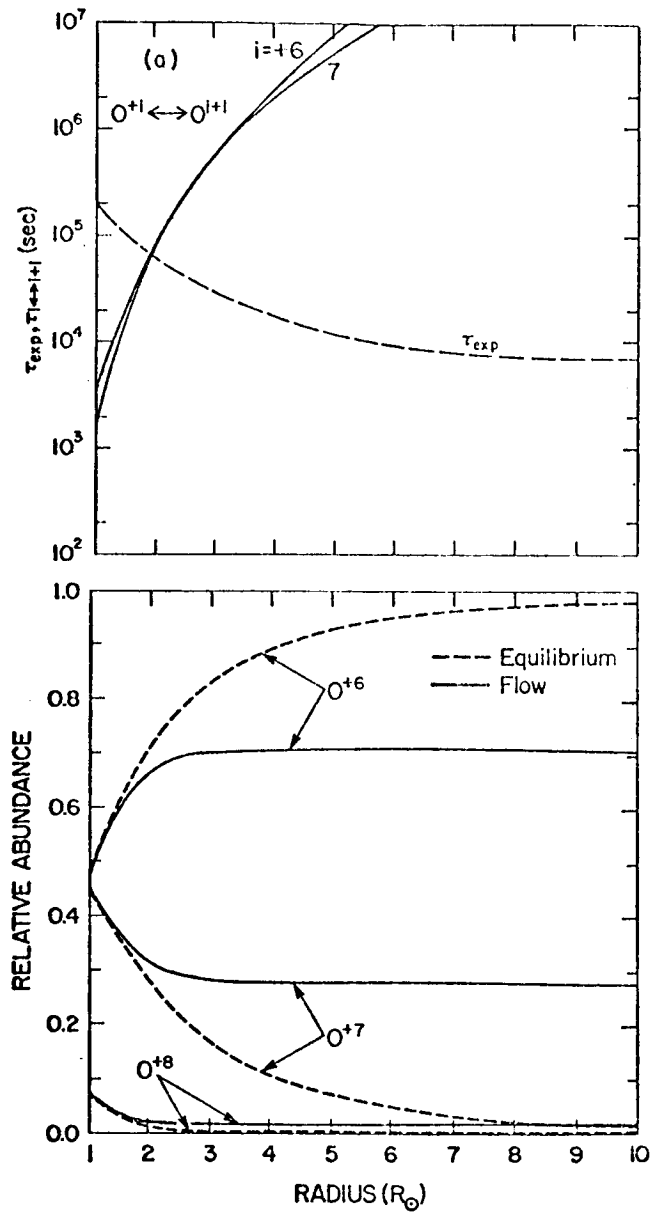
Figure 1: a. Radial variation of ion exchange time (solid curves) and ion expansion time (dashed curves) for spherically-symmetric model where all heavy ion charge-stages are assumed to flow at the proton speed. The intersection between the exchange and expansion times determine the freezing radius r_f for the given exchange.

b. Corresponding radial evolution of oxygen charge-stage abundance fractions in the flow (solid) compared with fractions that would exist in static ionization equilibrium (dashed).

relatively constant. Figure 1b compares the corresponding radial evolution of charge-stage fractions in the flow (solid) with the fractions that would exist in static ionization equilibrium (dashed). The flow-fractions initially evolve in conjunction with the equilibrium fractions (which show a shift to lower charge stages that reflects the outward decline in electron temperature); but beyond a "freezing radius" r_f (defined by $\tau_{exp}(r_f) \equiv \tau_{i \leftrightarrow i+1}(r_f)$) these flow fractions "freeze" to constant values. From numerical parameter studies (Owocki 1982; Owocki et al. 1983), it is found that the frozen-in fractions often closely approximate the equilibrium fractions at the freezing radius r_f. Since the ionization equilibrium fractions depend only on local electron temperature, we conclude that measured ion fractions at large distances from the sun (e.g. at 1 a.u.) can be used to infer the electron temperature at a specific coronal freezing radius r_f.

The exact location of this freezing radius depends on the atomic properties of the ions as well as on the details of the coronal expansion. Assuming the ions flow at the proton speed, we obtain from the equation of mass continuity and from the requirement $\tau_{i \leftrightarrow i+1}(r_f) = \tau_{exp}(r_f)$, an estimate of the freezing density $n_f \equiv n_e(r_f)$,

$$n_f = \left[\frac{n_E u_E \ (A_E/A_f)}{H \ (R_{i+1} + C_i)} \right]^{1/2} , \qquad (4)$$

where $n_E u_E$ is the particle flux at 1 a.u., and A_E/A_f is the ratio of flow tube areas between 1 a.u. and r_f. For spherically-symmetric outflow with a interplanetary mass flux, $n_E u_E = 3 \times 10^8 cm^{-2} s^{-1}$ (Feldman et al. 1977), we then find $n_f = 2 \times 10^7 cm^{-3}$ for the exchange among the dominant charge stages of oxygen $O^{+6} \leftrightarrow O^{+7}$, while for the intrinsically faster iron exchange, $Fe^{+11} \leftrightarrow Fe^{+12}$, the freezing density is much lower, $n_f = 10^6 cm^{-3}$. Using a typical "quiet" coronal density model (e.g., Newkirk 1968; Saito 1970), we obtain a freezing radius $r_f = 1.5 R_\odot$ for oxygen, and $r_f = 3.5 R_\odot$ for the iron exchange. Because of the large variation in rates for different charge-stages of iron, other iron exchanges freeze overd a range of heights from $r_f = 3$ to $5 R_\odot$ (Bame et al. 1974). Such "differential freezing" of the various ionization stages within a given species can give rise to some subtle effects that somewhat complicate the interpretation of charge state measurements for multi-stage species like iron (Owocki 1982), but, for the sake of brevity, we shall not discuss these effects here.

For other reasonable expansion models, the freezing radius of a given exchange does not vary by more than ~$0.5 R_\odot$ from that in this typical spherical expansion model. For example, for a coronal hole model with the same particle flux as above, but with a flow-tube area that increases from the sun to 1 a.u. by a factor 7 more than in spherical expansion, we find for the oxygen balance $n_f = 5 \times 10^7 cm^{-3}$, which because of the much lower coronal density (see e.g. Munro and Jackson 1977) gives $r_f = 1 R_\odot$. However, because the pressure measured (e.g. Withbroe 1977) at the coronal base is $nT > 10^{14} cm^{-3} \, {}^\circ K$, we find that the oxygen

ionization state must still freeze at coronal temperatures $T=10^6\,^{\circ}K$. This implies that all ionization exchanges as fast or faster than oxygen always freeze at or above the coronal base, and so the measured interplanetary charge state is sensitive only to coronal conditions, and not to conditions in the underlying chromosphere and transition region.

Having established this basis for understanding the ionization state freezing in simple coronal ion outflows, we shall now examine in the following sections the effect of relaxing some of the simplifying assumptions made above.

3. Effect of Unequal Ion Flow Speeds

We first examine how the above freezing-in theory is altered when the flow speeds u_i of different charge-stages of a given species are not all equal. Such unequal outflow of heavy ions from the corona cannot be precluded on either observational or theoretical grounds because only a few measurements of coronal ion flow speeds exist (Cushman and Rense 1976; Rottman et al. 1981; Withbroe et al. 1982), and because the mechanism by which the heavy ions are accelerated in the corona is not well-understood. The usual coronal pressure-gradient force is insufficient to drive these heavy ions outward against their stronger confinement by solar gravity (Geiss et al. 1970), and yet interplanetary measurements indicate substantial fluxes of all heavy ions at a common speed equal to or slightly greater than the solar wind proton speed (Ogilvie et al. 1980; Schmidt et al. 1980). This implies that unknown, additional acceleration mechanisms must exist for heavy ions in the corona. Examples of mechanisms which have been considered are coulomb friction from the protons (Geiss et al. 1970), interaction with MHD waves (Dusenbery and Hollweg 1981), and enhanced pressure-gradient forces resulting from preferential ion heating (Ryan and Axford 1975). As with most additional acceleration mechanisms that one can imagine, the forces for all of these vary with ion charge, and this suggests that the various charge-stages of a given ion species may not accelerate and flow uniformly in the corona.

The major consequence of such unequal ion flow speeds for the freezing of the solar wind ionization state can be understood from the discussion in section 2. Recall from there that, although the ionization equilibrium conditions (2) at the coronal base determine the relative number of various ion charge-stages, the freezing-in condition (3) for the solar wind fixes the relative flux of these charge stages. With unequal coronal flow speeds, an interplanetary measurement of the frozen-in values of the relative ion fluxes can therefore no longer be used to infer directly the relative ion abundances, and hence the electron temperature, in the coronal freezing-in region. If the ion flow speeds in the corona are known, this mismatch between abundances fixed by ionization equilibrium and fluxes fixed by the freezing condition can be readily resolved (see Owocki et al. 1983). One need only correct the measured frozen-in flux ratios by the ratio of the ion flow speeds at the freezing radius, r_f, to obtain the appropriate abundance ratios, from which the electron temperature at r_f can be estimated using equation (2).

628

This simple result makes it easy to estimate the error in inferred electron temperature that would result from ignoring the effects of ion flow speeds that differ in the corona by known ratios. The sense of the errors are such that the temperature inferred by traditional interpretation of the interplanetary ionization state will overestimate (underestimate) the actual coronal electron temperature if higher ion charge stages flow systematically faster (slower) than lower stages at the coronal freezing radius. For a given flow-speed-ratio, the magnitude of these errors will vary depending on how sharply the ionization/recombination rate ratio $R_{i+1}(T_e)/C_i(T_e)$ varies with electron temperature T_e. For balances among dominant coronal oxygen charge-stages, a coronal flow-speed ratio of 5 results in an error in inferred temperature of 0.5×10^6 $^{\circ}K$. Iron balances show greater sensitivity, with such a temperature error of 0.5×10^6 $^{\circ}K$ resulting from only a factor of 2 difference between neighboring iron charge-stage flow speeds.

4. Effect of a Non-Maxwellian Electron Velocity Distribution

We next examine how the relationship between coronal degree of ionization and coronal electron temperature is altered by a local electron velocity distribution that is not Maxwellian. Direct samplings of the electron velocity distributions in the solar wind have shown that, while the low-energy distribution "cores" can be well-fit by a Maxwellian, the high-energy "tails" of these distributions are best fit by a power law in energy, and so are enhanced relative to a Maxwellian of the same mean particle energy (Montgomery et al. 1968, 1972; Feldman et al 1975; Rosenbauer et al. 1976; Ogilvie and Scudder 1978). Scudder and Olbert (1979a,b) have argued that this observed enhancement in the high-energy tail of the interplanetary electron velocity distribution arises because of the decline of the coulomb collision cross-section at high electron energies. This allows higher-energy coronal electrons to travel with few collisions upward from the high-density corona into the low-density solar wind, where they enhance the tail of the local velocity distribution. According to this theory of global transport for high-energy electrons, the strong density gradient throughout the solar corona should also result in locally enhanced high-energy tails in the electron velocity distribution of the corona itself (Olbert 1983).

Recently, Owocki and Scudder (1983) have examined how the coronal ionization balances $O^{+6} \longleftrightarrow O^{+7}$ and $Fe^{+11} \longleftrightarrow Fe^{+12}$ depend on the shape of the electron distribution (i.e. on the magnitude of the high-energy tail enhancement), as well as on the electron temperature. They employ a parameterized non-Maxwellian distribution, the "kappa distribution" (Olbert 1967, 1969), for which the relative deviation of the distribution from a Maxwellian shape can be readily varied through changes in the free parameter, κ. As with the distributions observed in the solar wind and postulated for the solar corona, this kappa distribution closely approximates a Maxwellian in the low-energy "core", but varies as a power law in its enhanced high-energy tail (see figure 2). Although the lower level of each of the studied exchanges is the most abundant stage in an
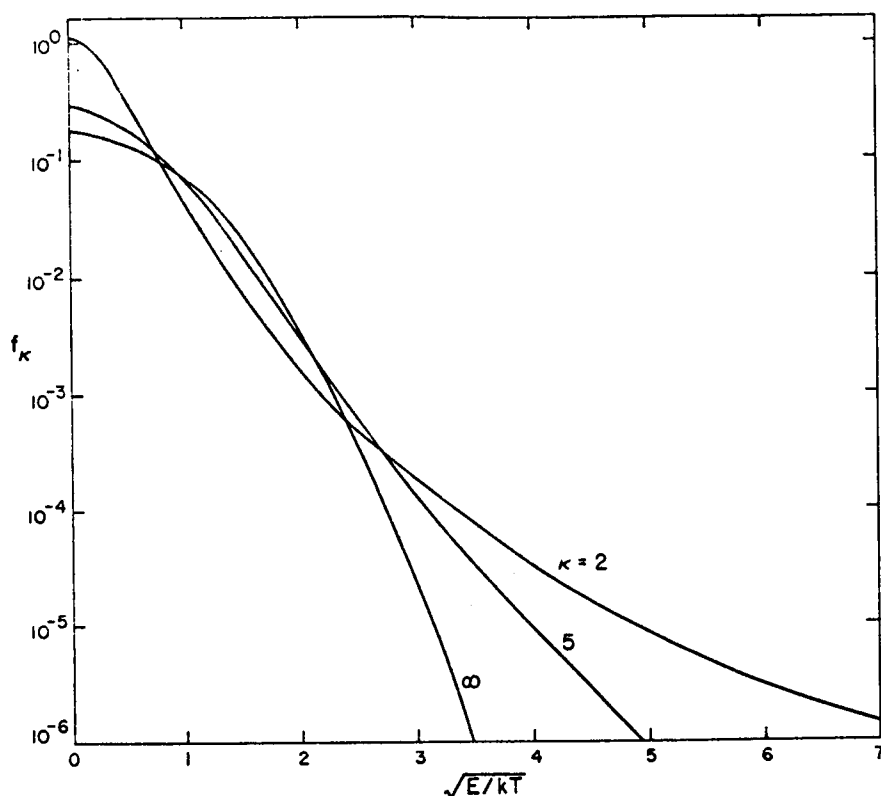
Figure 2: Kappa electron distribution function f vs. the square root of the electron kinetic energy over thermal energy, $\sqrt{E/kT}$, for kappa distributions with $\kappa = 2$ and 5 and a Maxwellian ($\kappa = \infty$). The temperature T is assumed to be equal for all three distributions.

equilibrium balance at a typical coronal temperature of 1.5×10^6 °K (Allen and Dupree 1969; Jordan 1969, 1970), the oxygen ionization threshold energy is actually more than twice that of iron (i.e. $\chi(O^{+6}) = 739$ eV vs. $\chi(Fe^{+11}) = 331$ eV). An enhanced high-energy tail in the coronal electron distribution therefore has a greater effect on the oxygen ionization balance.

Figure 3 graphically illustrates for the oxygen ionization exchange $O^{+6} \longleftrightarrow O^{+7}$ the relative sensitivity of collisional ionization rate and radiative recombination rate to the presence of an enhanced tail on the electron distribution function. In each of the upper, central, and lower two boxes of figure 3, the shaded areas are proportional respectively to the ionization rate, recombination rate, or mean electron energy (i.e. electron temperature) in either a Maxwellian distribution (i.e. with $\kappa = \infty$; left boxes) or in a kappa distribution with $\kappa = 3$ (right boxes). The two distributions have been adjusted to have equal

630
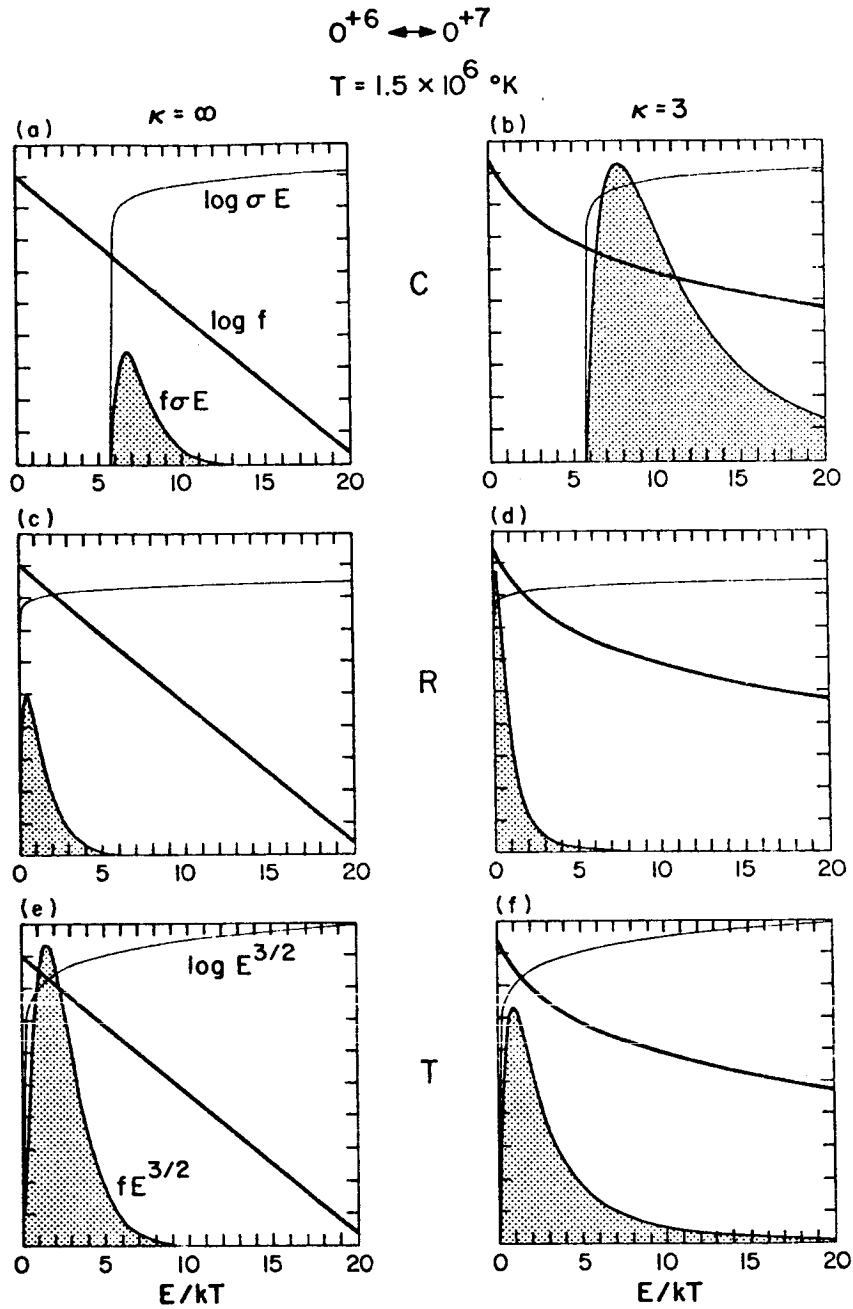
Figure 3: Comparison of collisional ionization (C) and radiative recombination (R), for the oxygen ionization balance $O^{+6} \longleftrightarrow O^{+7}$ in a Maxwellian ($\kappa=\infty$; left boxes) and in a kappa distribution ($\kappa=3$; right boxes). In the upper four boxes (a-d), the heavy and light solid lines show respectively the logarithmic variations of the distribution function f and the cross section times energy σE, while the linear variation of the relevant rate integrand $f\sigma E$ outlines the shaded areas, which are thus proportional to the relevant rates $\langle\sigma v\rangle$. In the lower two boxes (e,f) the cross section is replaced by the square root of the energy, $\sqrt{E}$, and the equality of the shaded areas, now proportional to the mean kinetic energy $\langle E\rangle=3kT/2$, shows that the two distributions have the same kinetic temperature ($T=1.5\times10^{6}$ °K).

temperatures $T=1.5 \times 10^6$ °K, as can be seen from the equality of the shaded areas in the lower two boxes (cf. figures 3e,f). Comparison of the shaded areas in the central two boxes (cf. figures 3c,d), which are proportional to the respective radiative recombination rates, shows that in the kappa distribution recombination occurs at a slightly higher rate, and with electrons of slightly lower energy, than in the Maxwellian. By contrast, the impact ionization rates are significantly increased by the enhanced high-energy tail of the kappa distribution (cf. figures 3a and 3b). The net result (see equation (2)) is that a kappa distribution can support a much higher degree of oxygen ionization than a Maxwellian with the same temperature. Qualitatively, we therefore expect that interpretations of the oxygen charge state based on the assumption of a Maxwellian will systematically overestimate the electron temperature if the electron distribution actually has an enhanced high-energy component.

Because it is the ionization ratio, n_i/n_{i+1} ($=R_{i+1}/C_i$ in ionization equilibrium; eqn. (2)), and not the individual rates R_i or C_i, that can be inferred from direct sampling of the frozen-in ratio in the solar wind, it is important to establish quantitatively the range in electron distribution function properties that are compatible with a given ratio in ionization equilibrium. In figures 4a and 4b contours of the iron (Fe^{+11}/Fe^{+12}) and oxygen (O^{+6}/O^{+7}) equilibrium ionization ratios are plotted for electron velocity distributions that range from Maxwellian ($\kappa=\infty$) to extremely non-Maxwellian ($\kappa=2$) and that range in temperature from $T=1 \times 10^6$ °K to 3×10^6 °K. The path along any contour denotes the appropriate combinations of T and κ that are consistent with an ionization ratio measurement of the value that labels the contour. For example, note from figure 4b that an oxygen ionization ratio $n_{+6}/n_{+7}=1$ is consistent with a Maxwellian distribution with $T=2 \times 10^6$ °K and $\kappa=\infty$, but it is also consistent with a kappa distribution with $T=1.3 \times 10^6$ °K and $\kappa=2.5$. If the latter parameter set better represented the electron distribution function in the solar corona, then an oxygen ionization ratio measurement, if interpreted on the basis of the traditional assumption of a Maxwellian electron distribution, would lead to an electron temperature overestimate of about 0.7×10^6 °K.

A temperature overestimate of this kind will occur whenever the contours in figure 4 slope downward as one moves away from the Maxwellian limit denoted by the left ordinate. Conversely, an upward slope implies a temperature underestimate when one incorrectly assumes a Maxwellian, while a zero (or small) slope implies that the equilibrium ionization ratio is relatively insensitive to assumptions about the form of the distribution. The oxygen contours generally slope downward; the iron contours either have zero or upward slopes (cf. figures 4a and 4b). Hence, in contrast to the temperature overestimates typical for oxygen, the iron charge state ratios are either insensitive to the form of the distribution or yield temperature underestimates when a Maxwellian is incorrectly assumed (viz. the contour labeled "1" in figure 4a). Even the oxygen contours do not, however, continue to slope downward for extreme departures from a Maxwellian; rather they reach a minimum for $\kappa=3$, so that the magnitude of temperature overestimates based on measured oxygen ionization ratios is limited to
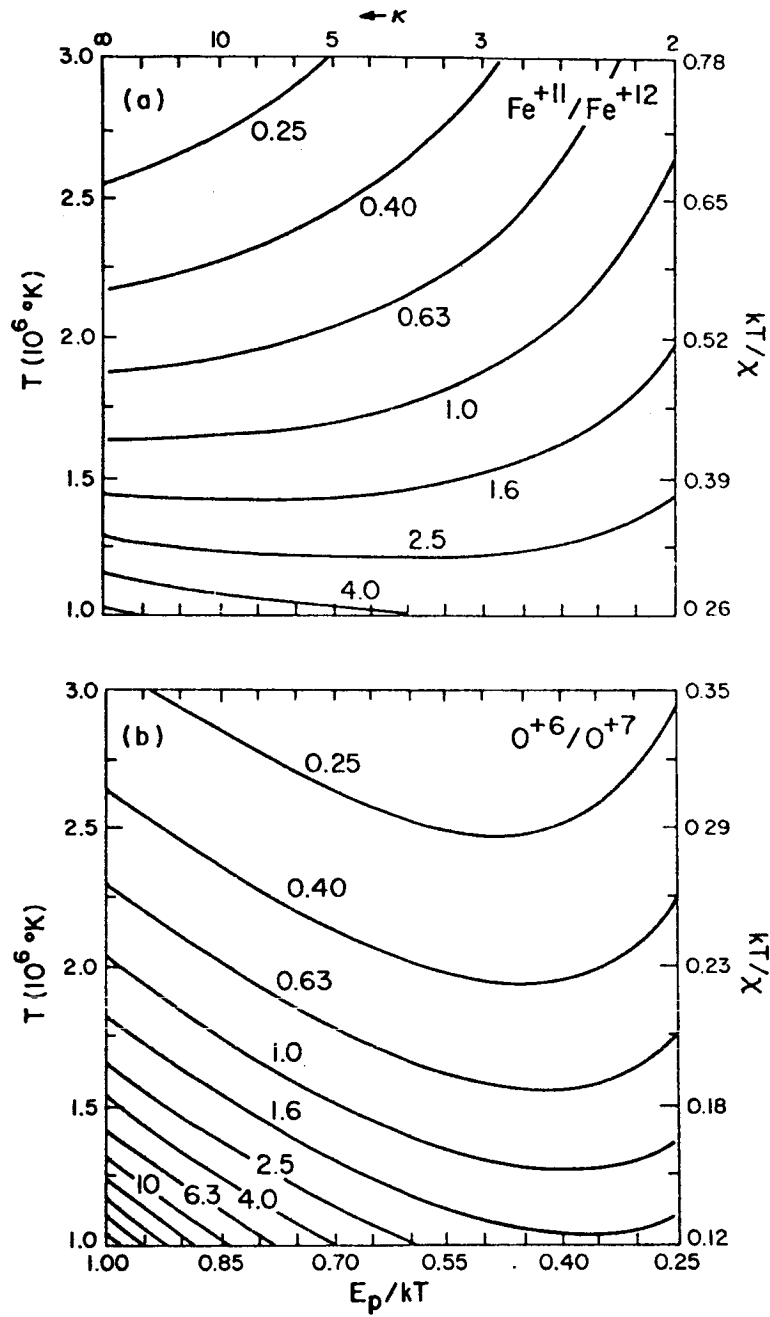
Figure 4: a. Contours of iron ionization ratio Fe^{+11}/Fe^{+12} as a function of kinetic temperature T and of core to total energy ratio $E_p/kT=(\kappa-3/2)/$. The right ordinate is labeled with the ratio, kT/χ, of thermal energy to ionization threshold energy, the upper abscissa is labeled with the value of the distribution parameter κ , and each contour is labeled with the appropriate ionization ratio.

b. Same as a, except for the oxygen ratio O^{+6}/O^{+7}.

$<0.75\times10^6$ $^\circ K$. This upturn in equilibrium ionization ratio contours for extreme non-Maxwellian distributions stems mostly from the recombination rate increase associated with the enhancement in the low-energy energy core of the distribution (see figure 2; also figures 3c,d).

We thus see that, relative to a Maxwellian of the same mean electron energy, the degree of ionization allowed by a non-Maxwellian distribution with an enhanced high-energy tail is either unchanged or slightly decreased for iron, but can be substantially increased for oxygen. As a result, the coronal electron temperature inferred from an interplanetary measurement of the frozen-in oxygen ionization ratio, O^{+6}/O^{+7}, could overestimate the actual coronal electron temperature by as much as 0.75×10^6 $^\circ K$. The unexpectedly high degree of oxygen ionization measured in the high-speed solar wind (Ogilvie and Vogt 1980) may therefore result from an enhanced tail in the electron velocity distribution in the coronal source regions of such high-speed wind, rather than from an enhanced coronal electron temperature.

5. Effect of a Time-Variations Associated with a Coronal Shock Wave

Finally, we examine how the freezing-in of the solar wind ionization state is affected by rapid time variations at the base of the coronal expansion. Observations indicate that activity in the solar photosphere and chromosphere can have an outward-propagating effect, inducing sudden changes in the solar corona and the solar wind. For example, white-light coronagraphs have detected upward-moving coronal density variations, often called "coronal transients", in association with flares and/or eruptive prominences (MacQueen 1980), and measurements with interplanetary spacecraft indicate that some 50% of the energy in large flare events is propagated through the corona and into the solar wind (Hundhausen 1972). These coronal time-variations can strongly influence the ionization state of interplanetary gas observed in association with solar activity (Bame et al. 1979; Fenimore 1980), and interpretation of interplanetary charge-state measurements should therefore take into account the effect of such intrinsic variability. We shall investigate such effects below for a relatively simple picture of the time-dependent coronal flow, based on a model of a self-similar shock wave propagating through the corona.

For simplicity we assume in this model that the electron distribution is Maxwellian, that the coronal outflow is spherically-symmetric, and that all heavy-ion charge-stages flow everywhere at the proton speed ($u_i=u$ for all i). From the last assumption, we conclude that there is no net flux of ions into or out of a fluid parcel that flows at the speed u, and so the ionization state of each parcel is independent of conditions in neighboring parcels. This means that equations (1) can be simplified so that all ionization state changes can be described in terms of a total derivative with respect to a Lagrangian coordinate r_L,

$$\frac{Dn_i}{Dr_L} \equiv \frac{1}{u}\frac{\partial n_i}{\partial t} + \frac{\partial n_i}{\partial r} = \frac{n_e}{u}\left(n_{i-1}C_{i-1} - n_i(C_i + R_i) + n_{i+1}R_{i+1}\right) \quad . \qquad (5)$$

Given the flow speed u, electron density n_e, and electron temperature T_e as functions of the Lagrangian coordinate r_L, eqn. (5) can be numerically integrated for each fluid parcel to obtain the ionization state evolution in r_L. Reconstruction of the ionization state time variation at a fixed Eulerian space coordinate r (e.g. at $r = 1$ a.u.) then follows readily from the known ionization state of many fluid parcels flowing past the fixed coordinate at the known speed u.

To investigate the ionization effects of coronal shocks, Owocki and Hundhausen (1983) (see also Owocki 1982) use a kinematic description of strong coronal shocks in which they obtain, as required for calculation of the ionization state, the Lagrangian evolution of velocity, density, and temperature. We consider here only the special case in which the shock speed V is constant and the post-shock flow is neither compressive nor expansive. In this simple shock model, each fluid parcel experiences a sudden jump in velocity, density, and
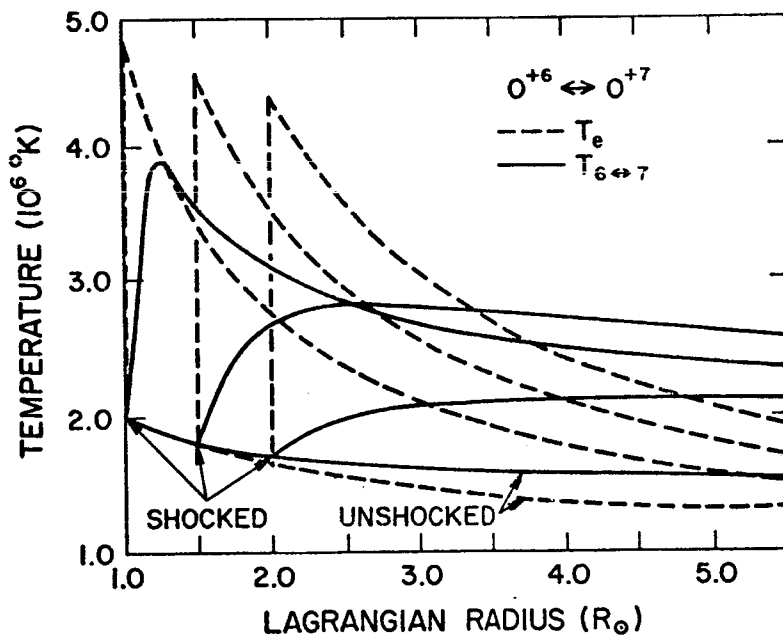

Figure 5: Lagrangian evolution of oxygen ionization ratio temperature $T_{6<->7}$ in ambient unshocked wind and in fluid parcels shocked at $R_1 = 1$, and 1.5, and $2R_\odot$ in non-compressive, constant-speed shock models with various shock speeds V. Dashed curves denote evolution of electron temperature T_e.

temperature at its shock location $r_L = R_1$, after which the velocity is constant at $u = 3V/4$, the density declines with the outward spherical expansion as $n_e = 4n_a(R_1)(r_L/R_1)^{-2}$, ($n_a$ is the density in the ambient, unshocked flow) and the temperature excess declines adiabatically as $T \sim r_L^{-4/3}$.

Figure 5 plots for this shock model the evolution of electron temperature (dashed curves) and oxygen ionization ratio temperature $T_{6 \leftrightarrow 7}$ (solid curves) vs. Lagrangian radius r_L for the ambient, unshocked flow and for three fluid parcels that are shocked respectively at $R_1 = 1$, 1.5, and $2R_\odot$. (The ionization ratio temperature is defined as the electron temperature that, in ionization equilibrium, would yield a given abundance ratio of, e.g., O^{+6} vs. O^{+7}; see Owocki 1982). Note that fluid parcels shocked at greater radii show progressively weaker ionization ratio temperature responses to the shock, but the net gain in the asymptotic, frozen-in, ratio temperature is highest for the parcel shocked at the intermediate height $R_1 = 1.5R_\odot$. The parcel shocked at $R_1 = 1R_\odot$ initially shows a stronger jump in ionization ratio temperature, but it then continues to follow the local electron temperature as the parcel adiabatically cools. It thus freezes at a ratio temperature (1.8×10^6 $^\circ$K) enhanced only slightly above the value for the ambient flow (1.6×10^6 $^\circ$K). On the other hand, the ionization state in the parcel with $R_1 = 2R_\odot$, being nearly frozen-in when shocked, does not follow this adiabatic cooling; but neither is its initial jump in ratio temperature very great, and so its frozen-in ratio temperature (1.8×10^6 $^\circ$K) is also only slightly enhanced above that of the ambient flow. The parcel shocked at $R_1 = 1.5R_\odot$ is intermediate between the frozen-in, small-jump case and the equilibrium, adiabatic-cooling case, and thus shows the greatest frozen-in ratio temperature (2.1×10^6 $^\circ$K).

Figure 6 shows the temporal variation of frozen-in oxygen ionization ratio temperature $T_{6 \leftrightarrow 7}(r = 1 \text{a.u.})$ that results at 1 a.u. from coronal shocks with various shock speeds V. The abscissa gives the time t for passage of a coronally-shocked fluid parcel relative to the time for passage of a parcel shocked at $R_1 = 10R_\odot$. All such fluid parcels trail by several hours the interplanetary passage of the shock itself. The dot that terminates each curve represents the time for passage of the parcel shocked at the coronal base; i.e. with $R_1 = 1R_\odot$. Because we have not included here any model of the driver gas, these shock calculations give no information on the ionization state after this

time. (For flare-associated disturbances, this driver gas may be flare-heated plasma that itself has a very high degree of ionization.) The calculations do suggest, however, that a few hours after the passage of a flare-associated interplanetary shock, and shortly before arrival of the flare-heated driver gas that caused the shock, a spacecraft at $r = 1$ a.u. should observe a peak in ionization temperature (e.g. for oxygen) lasting for a few time ten minutes. However, this would require time resolution that is somewhat beyond the capability of current detectors.
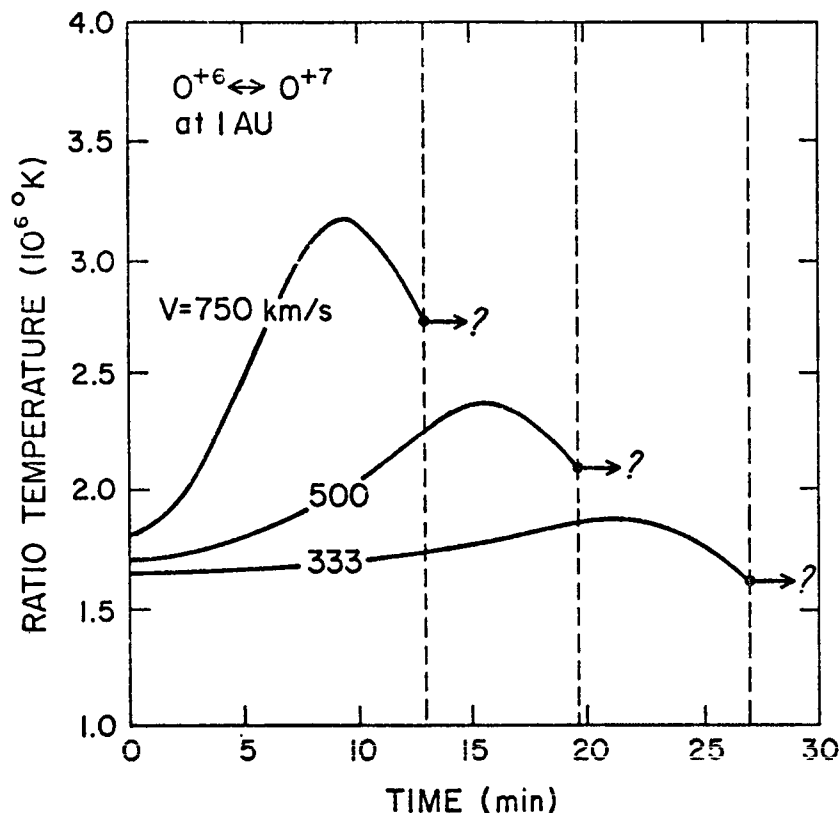
Figure 6: Interplanetary oxygen ionization ratio temperature $T_{6 \leftrightarrow 7}$ vs. time t since passage of parcel shocked at $R_1 = 10R_\odot$, for non-compressive, constant-speed shock models with various shock speeds V.

6. Summary

In this paper, we have examined the freezing of the solar wind ionization state for various conditions in the expanding solar corona. We first reviewed this freezing theory for spherically-symmetric, steady-state coronal expansion in which the coronal electron velocity distribution is Maxwellian and the coronal flow speeds of the various charge-stages of heavy ion species are all equal to the proton speed. We found in this case that the relative flux of heavy ion charge-stages could be straightforwardly interpreted to yield the electron

637

temperature at a discrete coronal freezing radius. We next examined the case in which the coronal flow speeds of the various charge-stages of a given heavy ion species were not equal. In this case frozen ion flux ratios had to be first scaled by the ratios of ion flow speeds at the freezing radius to obtain an accurate estimate of coronal charge-stage abundance ratios, from which the coronal electron temperature could then be inferred. Without this correction, the inferred temperature was found to overestimate (underestimate) the actual coronal electron temperature when higher (lower) charge-stages flowed faster at the freezing radius.

We also examined the coronal ionization balances $O^{+6} <\to> O^{+7}$ and $Fe^{+11} <\to> Fe^{+12}$ when the high-energy tail of the coronal electron velocity distribution was enhanced relative to a Maxwellian distribution. We found that the degree of oxygen ionization in such a distribution was greatly increased relative to a Maxwellian with the same mean energy (ie. same temperature), but the degree of ionization of iron was relatively unaffected. The greater sensitivity of the oxygen ionization balance to the enhancement in the high-energy tail of the electron distribution was attributed to the higher oxygen ionization potential. We find, in particular, that temperatures inferred from oxygen charge-stage ratios can overestimate the true electron temperature by as much as 0.75×10^6 $^{\circ}K$ if the electron distribution is incorrectly assumed to be strictly Maxwellian.

Finally, we examined the ionization state freezing in the time-varying conditions associated with a coronal disturbance, e.g. passage of a strong coronal shock-wave. If the various charge-stages in such a flow have equal bulk flow speeds, then the flow ionization state can be conveniently studied using a Lagrangian approach of following the evolution of individual fluid parcels. For a strong coronal shock-wave, we find that only parcels shocked near or below the ambient-flow freezing radius show a marked ionization state response to the shock. As a result, the time-variation of the charge state in the resulting interplanetary disturbance is limited to a few times ten minutes, which corresponds to the time required for the shock to transit the low corona.

In summary, we find that various coronal effects, such as unequal ion flow speeds, a non-Maxwellian electron distribution, or intrinsic time-variations, can alter the usual freezing picture of the solar wind ionization state, but there remains nonetheless a close association between interplanetary charge state and coronal electron temperature. We therefore encourage the careful interpretation of interplanetary charge state measurements to infer the physical state, particularly electron temperature, in coronal outflows with a variety of conditions.

638

References

Allen, J.W. and A.K. Dupree, Calculations of ionization equilibria for oxygen, neon, silicon, and iron, Ap. J., 155, 27, 1969.

Bame, S.J., J.R. Asbridge, W.C. Feldman, and P.D. Kearney, The quiet corona: temperature and temperature gradient, Solar Phys., 35, 137, 1974.

Bame, S.J., J.R. Asbridge, W.C. Feldman, E.E. Fenimore, and J.T. Gosling, Solar wind heavy ions from flare-heated coronal plasma, Solar Phys., 62, 179, 1979.

Billings, D.E., A Guide to the Solar Corona, Academic Press, New York and London, 1966.

Burgess, A., A general formula for the estimation of dielectronic recombination coefficients in low-density plasmas, Ap. J. Lett., 141, 1588, 1965.

Cushman, G.W. and W.A. Rense, Evidence of outflow of plasma in a coronal hole, Ap. J. Lett., 207, L61, 1976.

Dusenbery, P.B. and J.V. Hollweg, Ion-cyclotron heating and acceleration of solar wind minor ions, J. Geophys. Res., 86, 153, 1981.

Feldman, W.C., J.R. Asbridge, S.J. Bame, M.D. Montgomery, and S.P. Gary, J. Geophys. Res., 80, 4181, 1975.

Feldman, W.C., Asbridge, J.R., Bame, S.J. and Gosling, J.T. 1977, in The Solar Output and Its Variation, O.R. White, ed., (Boulder: Univ. of Colorado Press).

Fenimore, E.E., Solar wind flows associated with hot heavy ions, Ap. J. 235, 245, 1980.

Geiss, J.P., P. Hirt, and H. Leutwyler, On acceleration and motion of ions in corona and solar wind, Solar Phys., 12, 458, 1970.

Hundhausen, A.J., Coronal Expansion and Solar Wind, Spring-Verlag, New York, Heidelberg, and Berlin, 1972.

Hundhausen, A.J., H.E. Gilbert, and S.J. Bame, The state of oxygen ionization in the solar wind, Ap. J. Lett., 152, L3, 1968a.

Hundhausen, A.J., H.E. Gilbert, and S.J. Bame, Ionization state of the interplanetary plasma, J. Geophys. Res., 73, 5485, 1968b.

Jordan, C., The ionization equilibrium of elements between carbon and nickel, M.N.R.A.S., 142, 501, 1969.

Jordan, C., Ionization equilibria for high ions of Fe and Ni, M.N.R.A.S. 148, 17, 1970.

Lotz, W., Electron impact ionization cross-sections and ionization rate coefficients for atoms and ions, Ap. J. Suppl., 14, 207, 1967.

MacQueen, R.M, Coronal transients: a summary, Phil. Trans. R. Soc. Lond., 297, 605, 1980.

Montgomery, M.D., Thermal energy transport in the solar wind, in Cosmic Plasma Physics, Shindler, ed., Plenum Press, New York, p. 61, 1972.

Montgomery, M.D., Bame, S.J., and Hundhausen, A.J., Solar wind electrons: Vela 4 measurements, 73, 4999, 1968.

Munro, R.H. and B.V. Jackson, Physical properties of a polar coronal hole from 2 to 5 $R_\odot$, Ap. J., 213, 874, 1977.

Newkirk, G., Structure of the solar corona, Ann. Rev. Astron. Astrophys., 5, 213, 1968.

Ogilvie, K.W. and J.D. Scudder, The radial gradients and collisionless properties of solar wind electrons, J. Geophys. Res., 83, 3776, 1978.

Ogilvie, K.W. and C. Vogt, Variations of the average 'freezing-in' temperature of oxygen ions with solar wind speed, Geophys. Res. Lett., 7, 577, 1980.

Ogilvie, K.W., P. Bochsler, J. Geiss, and M.A. Coplan, Observations of the velocity distribution of solar wind ions, J. Geophys. Res., 85, 6069, 1980.

Olbert, S., AGU Abstracts, Washington, 1967.

Olbert, S., in Physics of Magnetospheres, R.C. Carovillano, J.F. McClay, H.R. Radoski, eds., 641, D.Reidel, Dordrecht, Holland, 1969.

Olbert, S., this volume, 1983.

Owocki, S.P., The Ionization State of the Solar Wind, Ph. D. Thesis, Univ. of Colo. and National Center for Atmospheric Research, NCAR CT-66, Boulder, 1982.

Owocki, S.P., T.E. Holzer, and A.J. Hundhausen, The solar wind ionization state as a coronal temperature diagnostic, submitted to Ap. J., 1983.

Owocki, S.P. and A.J. Hundhausen, A.J., The effect of a strong coronal shock on the solar wind ionization state, submitted to Ap. J., 1983.

Owocki, S.P. and J.D. Scudder, The effect of a non-Maxwellian electron distribution on oxygen and iron ionization balances in the solar corona, Ap. J., in press, 1983.

Rosenbauer, H., H. Miggenreider, M. Montgomery, and R. Schwenn, in Physics of Solar and Planetary Environments, D. Williams, ed., 319, AGU, Washington, 1976.

Rottman, G.J., Orrall, F.Q., and Klimchuk, J.A., Measurement of systematic outflow (?) from the solar transition region underlying a coronal hole, 1981. Astrophys. J. Lett., 247, L135.

Ryan, J.M. and W.I. Axford, The behaviour of minor species in the solar wind, J. Geophys., 41, 221, 1975.

Saito, K., A non-spherical axisymmetric model of the solar K-corona of the minimum type, Ann. Tokyo Astron. Observ. - Ser. 2, 12, 53, 1970.

Schmidt, W.K.H., H. Rosenbauer, E.G. Shelly, and J. Geiss, On the temperature and speed of He^{++} and 0^{6+} ions in the solar wind, Geophys. Res. Lett., 7, 697, 1980.

Scudder, J.D. and S. Olbert, A theory of local and global processes which affect solar wind electrons: I. The origin of typical 1 AU velocity distribution functions, J. Geophys. Res., 84, 2755, 1979a.

Scudder, J.D. and S. Olbert, A theory of local and global processes which affect solar wind electrons: II. Experimental support, J. Geophys. Res., 84, 6603, 1979b.

Seaton, M.J., The spectrum of the solar corona, Planet. Sp. Sci., 12, 55, 1964.

Tucker, W.H. and Gould, R.J., Radiation from a low-density plasma at 10^{6}°K to 10^{8}°K, Ap. J., 144, 244, 1966.

Withbroe, G.L., J.L. Kohl, H. Weiser, G. Noci, and R.H. Munro, Analysis of coronal HI Lyman alpha measurements from a rocket flight on 1979 April 13, Ap. J., 254, 361, 1982.

MINOR CONSTITUENTS IN THE SOLAR WIND ORIGINATING FROM
PLASMA-DUST INTERACTIONS

Hartmut W. Ripken
Institut für Astrophysik und Extraterrestrische Forschung
Universität Bonn
Auf dem Hügel 71
5300 Bonn 1, Fed. Rep. Germany

It has long been known that high-energy keV neutral hydrogen and helium atoms are regular but very minor constituents of the solar wind (see, e.g., Gabriel, 1971; Holzer, 1977; Withbroe et al., 1982; and references therein). Ionization processes acting on these constituents in interplanetary space, mainly charge-exchange reactions, yield protons and singly ionized helium. While these "solar-wind-originating" minor constituents H, He and He^+ are generally taken into consideration in model calculations, as well as the heavy multiply-charged ions of coronal origin, a second class of minor constituents needs to be recalled and accounted for. This group of atoms, molecules, and atomic and molecular ions is generated by solar wind interactions with dust grains of the zodiacal cloud (Banks, 1971; Paresce and Bowyer, 1973; Holzer, 1977; Fahr et al., 1981). The main processes leading to the generation of these particles will briefly be described in the first part of this comment, while relevant methods of observation are discussed in the second part. A detailed analysis is given in Fahr et al. (1981).

Solar wind ions with energies in the keV range impinge on zodiacal dust grain surfaces and penetrate about 10 to 100 nm into the mineral. At the end of the particle trajectory, neutralization via electron capture will occur. The newly created neutrals are temporarily retained in the dust grain, undergoing diffusion processes and chemical reactions. Depending on the type of mineral, hydrogen atoms react to form OH, H_2O, H_2, and various carbon and silicon hydrides. Helium, of course, will stay in its atomic form. The dust grain cannot retain implanted particles indefinitely; saturation occurs on very short time scales compared to the typical residence times of the grains in a solar orbit. After saturation is reached, on the average one molecule or atom will be released from the dust grain surface for each impinging solar wind ion. For particles released from the surface by an evaporative process, the dynamics essentially are the same as those of zodiacal dust grains and can be calculated in an analogous manner. These particles are subject to strong interaction processes with the solar wind and with the solar radiation field. Most become dissociated and/or ionized and eventually form the singly-charged secondary solar wind constituents H^+, He^+, and H_2^+. In addition, singly-charged hydroxyl, carbon and silicon hydrides, and possibly other ions are formed in this process, depending on the type of parent grain. Only very few dust-generated neutrals will reach the orbit of the Earth as low-energy neutral particles.

Besides these surface-released particles, the processes of erosion, sputtering, vaporization, and sublimation of zodiacal dust grains generate atoms and molecules not containing original solar wind material, which in their singly-charged ionic forms subsequently are also incorporated into the solar wind and can be traced as very minor but heavy constituents. The most important ones should be ions of silicon and carbon compounds.

In principle, these solar wind-incorporated ions can be detected in-situ by mass spectrometers. To identify the dust-generated secondary ions in the background of the primary solar wind, the charge state of the heavy ions will be the most important factor. Ionization cross sections indicate that singly-charged ions incorporated into the solar wind flow will predominantly stay in this initial charge state. Since the zodiacal cloud source region is strongly compressed into the ecliptic plane (Figure 1), the secondary ion flow markedly decreases with heliographic latitude. If direct detection of the minor ions in the ecliptic plane can be accomplished, the spatial variation of this constituent monitored by spacecraft reaching higher helio-graphic latitudes (e.g. ISPM) would yield important information on the spatial distribution of zodiacal dust.
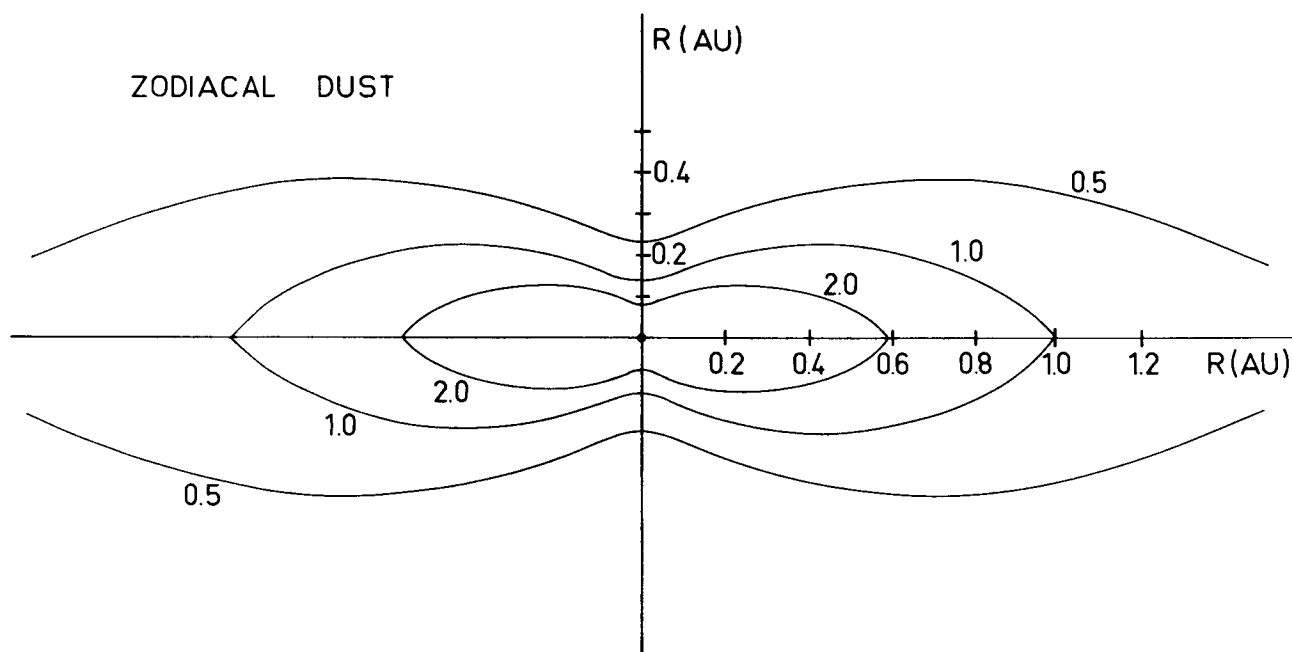
Figure 1. Isodensity lines of interplanetary zodiacal dust, according to a model derived from Helios measurements (Leinert et al., 1978).

Complementary observations of dust-deionized atomic hydrogen and helium can be accomplished by monitoring resonantly scattered solar photons at 121.6 nm (hydrogen) and 58.4 nm (helium). Due to sharp intensity increases of this resonance luminescence radiation with decreasing solar impact altitudes of the line-of-sight brought about by both density increases of the zodiacal cloud and increasing solar illumination with decreasing solar distances, observations are most promising in the immediate solar vicinity (line-of-sight solar offset angles $\approx 6°$). For details see Fahr et al. (1981). Measurements of this EUV radiation are planned (Fahr et al., 1980), and if successful, would unambiguously point towards a relatively high dust density and thus to the actual existence of singly-charged minor ions in the solar wind which have not yet been reported in the literature. Possibly, some unexplained features in recent solar wind mass spectrograms could be reinterpreted taking into account the dust-generated ions.

References

Banks, P.M., Interplanetary hydrogen and helium from cosmic dust and the solar wind, J. Geophys. Res., 76, 4341, 1971.

Fahr, H.J., H.W. Ripken, and G. Lay, Inter-Zodiak: A high-apogee rocket experiment for the observation of dust-generated neutrals in the solar vicinity, ESA SP-152, 449, 1980.

Fahr, H.J., H.W. Ripken, and G. Lay, Plasma-dust interactions in the solar vicinity and their observational consequences, Astron. Astrophys., 102, 359, 1981.

Gabriel, A.H., Measurements of the Lyman-alpha corona, Solar Phys., 21, 392, 1971.

Holzer, T.E., Neutral hydrogen in interplanetary space, Rev. Geophys. Space Phys., 4, 467, 1977.

Leinert, C., M. Hanner, and E. Pitz, On the spatial distribution of interplanetary dust near 1 AU, Astron. Astrophys., 63, 183, 1978.

Paresce, F., and S. Bowyer, Resonance scattering from interstellar and interplanetary helium, Astron. Astrophys., 27, 399, 1973.

Withbroe, G.L., J.L. Kohl, and H. Weiser, Probing the solar wind acceleration region using spectroscopic techniques, Space Sci. Rev., 33, 17, 1982.

SURVEY OF He^+/He^{2+} ABUNDANCE RATIOS IN ENERGETIC PARTICLE EVENTS

D. Hovestadt[1], B. Klecker[1], G. Gloeckler[2]

[1] Max-Planck-Institut für Physik und Astrophysik
Institut für extraterrestrische Physik
D-8046 Garching, FRG

[2] University of Maryland
Dept. of Physics and Astronomy
College Park, MD 20742, USA

A B S T R A C T

We report first results of a systematic study of the helium charge distribution in the energy range 0.4 - 0.62 MeV/nucleon in energetic particle events. The data have been obtained during the time period September 1978 to November 1979 with the Max-Planck-Institut/University of Maryland experiment on ISEE-3. We found an average He^+/He^{2+} ratio of 0.12 $\pm$ 0.04 with ratios exceeding 0.3 for 41 out of 420 days analyzed. No obvious association with optical flare events could be observed for the events richest in He^+. We did not find significant differences of the proton energy spectra, and the abundance of helium relative to protons and heavy ions for He^+-rich events ($He^+/He^{2+} > 0.3$) and for events with $He^+/He^{2+} < 0.3$, respectively. However, it has been found that He^+-rich events are predominantly low in energetic particle intensity.

Introduction

The measurement of the ionization states of solar energetic particles is of fundamental importance in two respects. Firstly, it provides information about the temperature of the source region at the sun. Secondly, it is essential for the investigation of acceleration and propagation processes at the Sun and in interplanetary space, because these processes will generally depend on the particle velocity and rigidity (i.e. mass per charge ratio). A direct determination of both the nuclear and ionic charge of heavy ions has been beyond experimental capabilities until recently. The first direct ionic charge measurements for solar flare particles in the MeV/nucleon energy range with simultaneous element identification have been reported by Hovestadt et al. (1981a, b) and Gloeckler et al. (1981). The most surprising feature of their measurements was the observation of large abundances of singly ionized helium in the energy range 0.4 - 1.5 MeV/nucleon. For 10 solar energetic particle events studied until now, the mean charge states of C, O, and Fe turned out to be consistent with "freezing-in" temperatures in the range $2 - 3 \cdot 10^6$ K, whereas for He^+/He^{2+} a ratio of $\sim$ 0.06 - 0.2 had been found, indicative of significant contributions of cold material with $T \leq 5 \cdot 10^4$ K. In this paper we report the results of a systematic study of the helium charge state distribution during the time period September 1978 to November 1979.

Instrumentation and Satellite
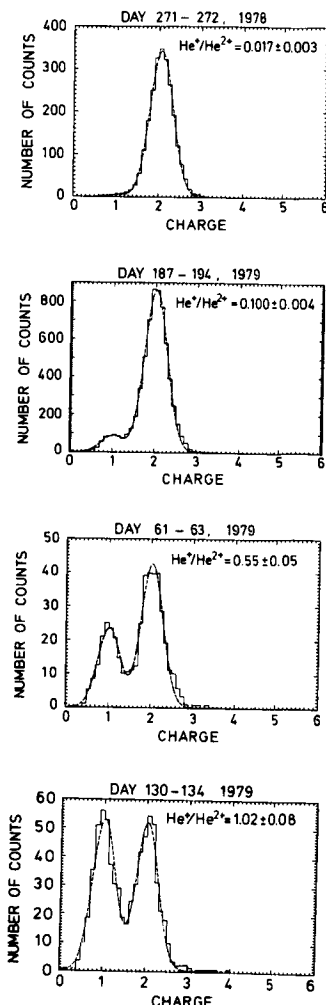
The data have been obtained with the Ultra-Low-Energy-Z-E-Q analyzer (ULEZEQ) of the Max-Planck-Institut/University of Maryland experiment on ISEE-3. During the time period investigated ISEE-3 was stationed in the interplanetary medium at the Langrangian point L_1 between the Earth and the Sun, at a distance of $\sim$ 230 R_E from the Earth. The instrument represents the combination of an electrostatic analyzer with a dE/dx versus E sensor system, thus providing the determination of the nuclear charge, the energy, and the ionic charge independently for each particle. More details of the principle of operation and of the data analysis may be found elsewhere (Hovestadt et al., 1978, 1981a).

Figure 1 shows typical helium charge histograms obtained for the energy range 0.4 - 0.62 MeV/nucleon during 4 energetic particle events in 1978 and 1979. The He^+/He^{2+} ratios are derived from gaussian fits of the histograms as indicated by dashed lines. Figure 1 demonstrates the variety of the He^+/He^{2+} ratios, it shows that variations by almost two orders of magnitude ($He^+/He^{2+} \sim 0.02 - 1.0$) can be observed.

Figure 1: Helium charge histograms for four typical energetic particle events showing the variability of the He^+/He^{2+} abundance ratios. The dashed lines are least square fits to the data.

Observations

For our survey of He^+ and He^{2+} abundances we computed daily averages of the He^+/He^{2+} ratio and of the helium flux in the energy range 0.40 - 0.62 MeV/nucleon. The survey covers the time period September 1978 to December 1979 (420 days). From this total number of 420 days we excluded days with less than 20 helium counts per day from our analysis. Figure 2 shows daily averages of the helium counting rate (upper panel) and of the He^+/He^{2+} ratio (lower panel) in the energy range 0.40 - 0.62 MeV/nucleon. It can be seen that the He^+/He^{2+} ratio is less than 0.3 for the majority of days analyzed. However, large He^+/He^{2+} abundance ratios exceeding 0.3 are observed for 41 days. Figure 2 shows also that large abundances of singly ionized helium seem to be correlated with low intensity energetic particle events.

This can be seen more clearly in Figure 3, where we correlated the daily averages of the He^+/He^{2+} ratio with the helium counting rate. The crosses in Figure 3 (and in the following Figures) indicate that for the He^+/He^{2+} ratio only upper limits could be computed. It should be noted that due to the selection criterion (≥ 20 cts/day) with the averaging period (1 day) no data are available in the shaded area of the scatter plot. It is evident from Figure 3 that large abundances of He^+

occur only at small helium fluxes; e.g. $He^+/He^{2+} > 1$ is observed only for $< 3 . 10^{-3}$ c/s. The contrary, however, is not true: small values of He^+/He^{2+} are observed for a large range of helium fluxes. It is possible that the spread in the charge abundance ratios increases with decreasing helium-fluxes similarly to observations of Mason et al. (1980), who observe an increasing spread in elemental abundance ratios of interplanetary radiation with decreasing absolute flux values.

ISEE - 3   MPE/UoMd   EXPERIMENT
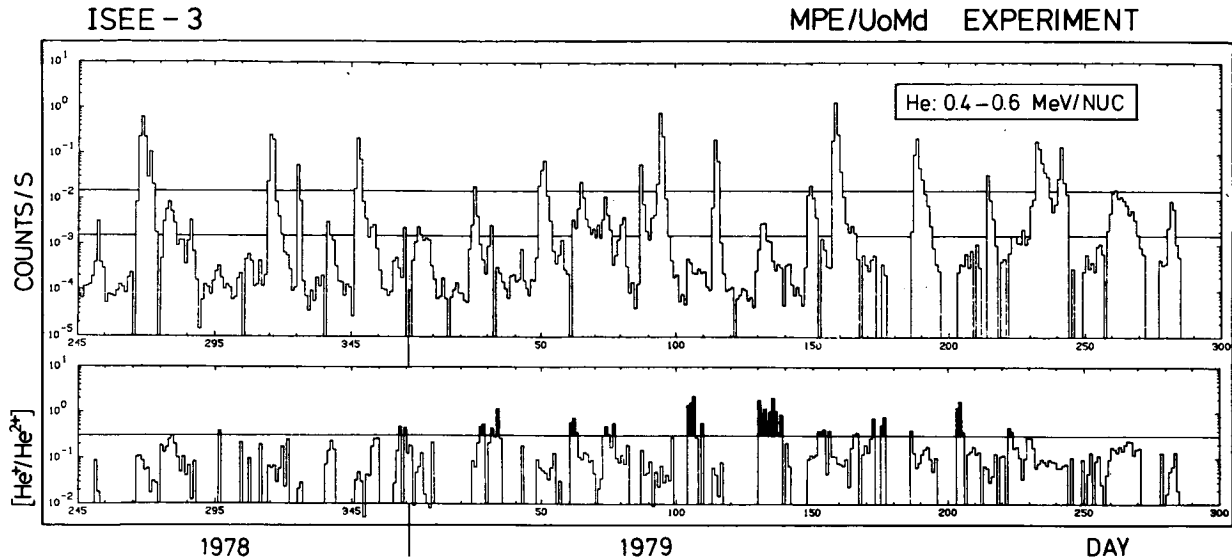
Figure 2: Helium flux (upper panel) and He^+/He^{2+} ratio for the time period September 1978 to November 1979. He^+-rich time periods ($He^+/He^{2+} > 0.3$) are marked by vertical bars.
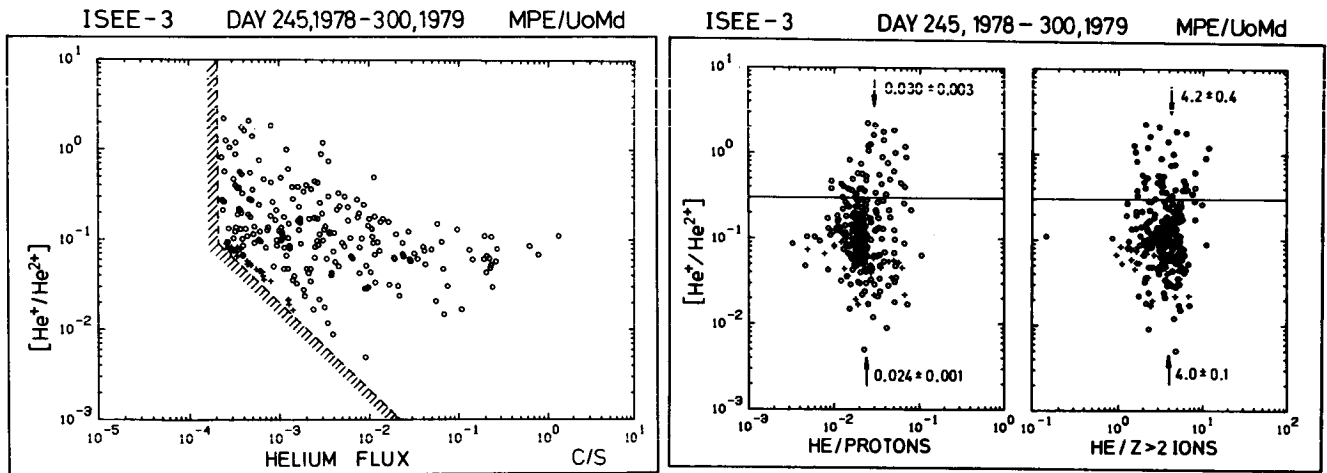
Figure 3: Correlation of the He^+/He^{2+} ratio with the helium flux in the energy range 0.4 - 0.62 MeV/nucleon.

Figure 4: Correlation of the He^+/He^{2+} ratio with helium abundances relative to protons (left panel) and $Z > 2$ ions (right panel). The abundances are given in relative units, not normalized to the same energy range.

In Figure 4 we correlated the He^+/He^{2+} ratio with the abundance of helium ($He^+ + He^{2+}$) relative to protons (left panel) and relative to $Z > 2$ ions (right panel).

The energy range is 0.45 - 1.2 MeV for protons and > 0.3 MeV/nucleon for $Z > 2$ ions (oxygen). The He/p and He/Z > 2 abundance ratios are given in relative units, not normalized to the different energy ranges of the measurement. The scatter plots show only a very weak correlation of the He^+/He^{2+} ratio with the He/p ratio and no significant correlation with the He/Z > 2 ratio. This can be seen more quantitatively from the mean values of He/p and He/Z > 2, which differ less than 2 sigma for time periods with $He^+/He^{2+} < 0.3$ and $He^+/He^{2+} > 0.3$, as shown in Figure 4.

A possible correlation of the He^+/He^{2+} ratio with the spectral index γ of the proton energy spectra at low energies has been investigated in Figure 5. The spectral index has been calculated from proton fluxes in the energy ranges 0.45 - 1.2 MeV, and 1.2- 3.0 MeV as measured with the same experiment, assuming $j_p \propto T^{\gamma}$. Figure 5 shows that the mean value of γ is not significantly different for events with $He^+/He^{2+} > 0.3$, and $He^+/He^{2+} < 0.3$ respectively. The large spread of γ for time periods with $He^+/He^{2+} < 0.3$ is partly due to time dispersion effects. These time periods include large solar energetic particle events where flat ($\gamma \sim 0$) energy spectra during the onset phase of the event are frequently observed.

ISEE-3   DAY 245,78–300,79   MPE /UoMd
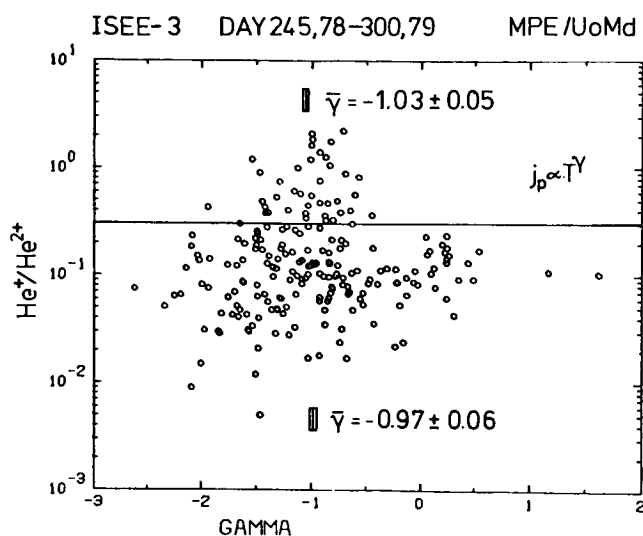
Figure 5: Correlation of the He^+/He^{2+} ratio with the spectral index of protons assuming $j_p \propto T^{\gamma}$. T is the kinetic energy.

Discussion and Summary

The results of our survey of He^+/He^{2+} abundance ratios can be summarized as follows:

(1) Small but finite abundances of singly ionized helium in energetic particle events are very common.

(2) The mean value of the He^+/He^{2+} ratio for time periods with high helium fluxes $> 1.5 \cdot 10^{-2}$ c/s corresponding to > 4 particles/cm^2 sr sec MeV/nuc has been obtained as $He^+/He^{2+} = 0.067 \pm 004$. These periods usually can be correlated with solar flares.

(3) High He^+/He^{2+} ratios are less frequently observed. However, for 41 out of 420 days $He^+/He^{2+} > 0.3$ has been measured and $He^+/He^{2+} > 1$ has been observed for 11 days.

(4) We find no correlation of the He^+/He^{2+} ratio with
   - the helium/Z > 2 ratio
   - the spectral slope of protons at low energies (0.45-3.0 MeV) and
   - only a very weak one if at all with the helium/proton ratio

(5) We do find a correlation of the He^+/He^{2+} abundance ratios with the helium flux in the sense that large He^+/He^{2+} abundance ratios are only observed for periods with small helium fluxes, but not vice versa. At small fluxes the apparent spread of the charge abundance ratio may be simply larger to include large ratios.

Our survey of the helium charge state composition in energetic particle events clearly shows that significant abundances of He^+ represent a common feature of the low energy particle population in interplanetary space. These large abundances of He^+ are certainly not compatible with the charge state of helium in a hot coronal gas, which has usually been considered as the source of energetic flare particles. At coronal temperatures above 10^6 K the fraction of singly ionized helium is expected to be much less than 10^{-4} (e.g. House, (1964)). Therefore we conclude that significant contributions of cold material are accelerated, not only in large solar particle events (discussed by Hovestadt et al., (1981a), and Gloeckler et al., (1981)), but also in small events with low particle intensities in interplanetary space.

References

Gloeckler, G., H. Weiss, D. Hovestadt, F.M. Ipavich, B. Klecker, L.A. Fisk, M. Scholer, C.Y. Fan, and J.J. O'Gallagher: Observations of the ionization states of energetic particles accelerated in solar flares. Proc. 17th Intern Cosmic Ray Conf., Paris, 3, 136, 1981

House, L.L.: Ionization equilibrium of the elements from H to Fe. Astrophys. J. Suppl., 8, 307, 1964

Hovestadt, D., G Gloeckler, C.Y. Fan, L.A. Fisk, F.M. Ipavich, B. Klecker, J.J. O'Gallagher, M. Scholer, H. Arbinger, J. Cain, H. Höfner, E. Künnneth, P. Laeverenz, E. Tums: The nuclear and ionic charge distribution particle experiments on the ISEE-1 and ISEE-C spacecraft, IEEE Transactions on Geoscience Electronics, GE-16, 166, 1978

Hovestadt, D., G. Gloeckler, H. Höfner, B. Klecker, F.M. Ipavich, C.Y. Fan, L.A. Fisk, J.J. O'Gallagher, and M. Scholer: Singly charged helium emitted in solar flares. Astrophys. J., 246, L81, 1981a

Hovestadt, D., G. Gloeckler, H. Höfner, B. Klecker, C.Y. Fan, L.A. Fisk, F.M. Ipavich, J.J. O'Gallagher, and M. Scholer: Direct observation of charge state abundances of energetic He, C, O, and Fe emitted in solar flares. Adv. Space Res., 1, 61, 1981b

Mason, G.M., L.A. Fisk, D. Hovestadt, and G. Gloeckler: A survey of $\sim$ 1 MeV Nucleon^{-1} solar flare particle abundances, 1 $\leq$ Z $\leq$ 26, during the 1973 - 1977 solar minimum period. Astrophys. J., 239, 1070, 1980

Acknowledgements

OBSERVATIONS OF MINOR IONS UP TO THE IRON GROUP

W. K. H. Schmidt
Max-Planck-Institut Fuer Aeronomie
Lindau, FRG '

In the past ISEE-1 mass spectrometer data have shown a linear correlation between temperatures and masses of solar wind ions up to six-fold ionized oxygen. The bulk velocity differences of heavy ions with respect to protons appeared to be independent of ionic species. The investigation is being extended to the group of iron ions, and the results will be presented. Also, the study of the correlation between velocity difference and superheating of minor ions is being carried out in more detail, and extended to the iron group ions.

ACCELERATION OF HEAVY IONS IN THE SOLAR WIND

Philip A. Isenberg
Space Science Center
University of New Hampshire
Durham, NH 03824

Abstract. Several recent studies of the preferential acceleration and heating of solar wind heavy ions by the resonant cyclotron interaction are reviewed. It is concluded that this interaction is incapable of producing the observed differential speeds for reasonable solar wind parameters.

Heavy ions in the solar wind are often observed to have undergone preferential heating and acceleration relative to protons. At 1 AU, the heavy ions are seen to flow faster than protons and to have comparable thermal speeds, the temperatures tending to be proportional to the ion mass. These preferential effects are positively correlated to the value of the solar wind speed. The differential speeds of the ions, $\Delta v_{ip} \equiv |\vec{v}_i - \vec{v}_p|$, are also correlated with the local Alfven speed. Helios measurements of alpha particles showed that, closer to the sun, the differential speed was often equal to the Alfven speed, even though the Alfven speed increased substantially in the inner solar system. At these times, the kinetic energy flux of the alpha particles amounted to almost one-third of the kinetic energy flux of the solar wind as a whole, and it is important to understand how so much energy is concentrated into this so-called "minor" component.

The close connection between the differential speeds and the local Alfven speed suggests that the responsible mechanism is a wave-particle interaction. One such mechanism which would favor the energization of low charge-per-mass particles is the resonant cyclotron interaction. Since the Solar Wind Four Conference in 1978, several workers have been investigating the quasilinear resonant cyclotron interaction between parallel-propagating waves and solar wind ions, and this work will be reviewed here.

A parameter study of quasilinear effects of left-polarized (Alfven and ion-cyclotron) waves on test populations of heavy ions was produced by Dusenbery and Hollweg (1981). They found that the resonant interaction is capable of accelerating heavy ions from speeds less than the proton speed to speeds greater than the proton speed. They also found indications that the resonant interaction could produce mass-proportional heating. However, they also found that the dispersion relation for ion-cyclotron waves in an electron-proton plasma resulted in a critical value of $\Delta v_{ip}/V_A$ above which the heavy ions were no longer in resonance with the waves. This implies an upper limit to the differential speed which is locally obtainable from the resonant interaction. For He^{++}, this limiting value is only $0.2\ V_A$. This point was also discussed by McKenzie and Marsch (1982).

Dusenbery and Hollweg also estimated that approximately 20% of the total wave energy near the sun would be required to accelerate the solar wind concentration of He^{++} to the Alfven speed at 0.3 AU, as observed. The problem here is that the bulk of the solar wind wave energy is seen at low frequencies and the wave power declines with increasing frequency as $P \sim \omega^{-\gamma}$ where typically $1.5 \lesssim \gamma$
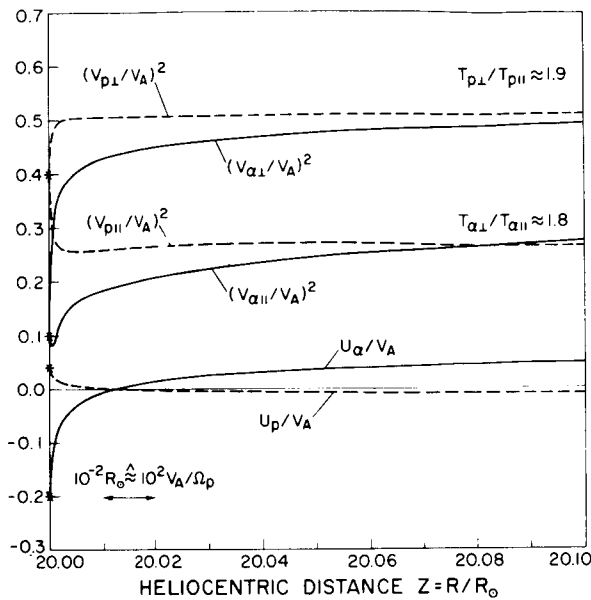
Figure 1. Calculated proton and alpha speeds relative to their center of mass frame and squared thermal speeds, all normalized to the local Alfven speed (after Marsch et al., 1982).

$\lesssim 2.0$. The energy in the high-frequency, resonant regime which is available to the cyclotron interaction is several orders of magnitude too low.

This work, however, was a calculation of the local energization of test heavy ions, and as such, it did not consider two important points. Firstly, a spectrum of waves which can cyclotron resonate with heavy ions will also interact with the solar wind protons. One must study this simultaneous interaction and determine the extent to which the heavy ions are accelerated and heated in excess of the protons. Secondly, results of this local calculation must still be incorporated into a solar wind model to determine the evolution of the heavy ion populations under the continuous action of the resonant process allowing for the ongoing adjustment of the model parameters (such as the Alfven speed and the wave power) in the expanding solar wind, as well as for the effects of other participating forces. In particular, a local upper limit of $\Delta v_{ip}/V_A$ is not necessarily significant when V_A is decreasing: a process which could produce $\Delta v_{ip} = V_A/3$ at 0.1 AU might result in $\Delta v_{ip} = V_A$ at 0.3 AU if the actual particle speeds do not change.

The first work to deal with these questions was Marsch et al. (1982). They considered a system containing bi-Maxwellian distributions of protons and alpha particles and an initial power-law spectrum of parallel-propagating waves. Starting the calculation at 20 solar radii ($\cong$ 0.1 AU), they investigated the self-consistent interaction, following the evolution of the wave spectra, as well as the velocities and temperatures of the particles. They included the effects of the shifting model parameters as a function of radius, but did not consider any non-resonant forces except those produced by a radial magnetic field on a plasma with a double-adiabatic equation of state.

Their first result was that, as expected from the work of Dusenbery and Hollweg, the observed wave power levels in the resonant frequency range were too

656

small to produce any significant effects. To continue the investigation, the wave levels were increased. Figure 1 shows an example of the normalized velocities and squared thermal speeds which result. The strong preferential heating and acceleration of alpha particles is obvious, and it is clear that the cyclotron resonant interaction can accelerate alpha particles through the proton speed. Note, however, that the total scale only extends over 0.1 R_s (R_s = solar radius). In this model, the wave effects proceed very quickly, energizing the particles within $10^{-2} R_s$. The wave energy, self-consistently calculated, is essentially depleted by this time and further energization takes place on the much slower convective scale as the expanding solar wind and decreasing field magnitude cause a rescaling of the resonant parameters. It would be interesting to follow this model system further to investigate this slower energization, but this evolution is obscured by another aspect of this model.
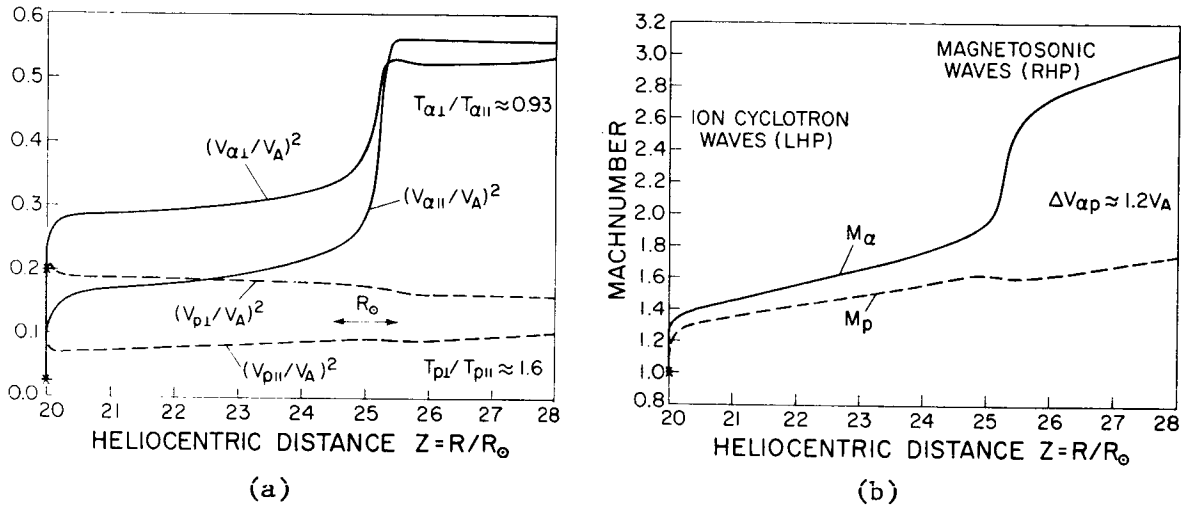
Figure 2. As in Figure 1, except that the speeds shown in (b) are shown with respect to the inertial frame, $M_i \equiv v_i/V_A$ (after Marsch et al., 1982).

The resonant interaction which produced the results in Figure 1 took place with left-polarized ion-cyclotron waves. Marsch et al. have also included the effects of a resonant cyclotron interaction with an equally intense spectrum of right-polarized magnetosonic waves. This is motivated by the observation that $T_{\alpha\parallel} > T_{\alpha\perp}$ in the fast solar wind, which could be a signature of fast-mode heating. It is also suggested that this interaction could explain why $\Delta v_{\alpha p}$ is limited to the Alfven speed. According to this model, the energization by the ion-cyclotron waves, along with the decreasing phase speed in the expanding solar wind, allows the alpha particle distribution to move into resonance with the right-polarized waves, and this interaction completes the acceleration to $\Delta v_{\alpha p} = V_A$. In the example shown in Figure 2, this has all occured within six R_s. It is certainly plausible that, once the alpha particles have attained differential speeds comparable to the Alfven speed, an interaction with magnetosonic waves could produce parallel heating and prevent $\Delta v_{\alpha p}/V_A$ from increasing further as V_A declines. However, it is hard to see how the fast mode is itself responsible for the acceleration up to $\Delta v_{\alpha p} = V_A$. In order for an alpha particle to cyclotron resonate with the right-polarized mode, it must be travelling along the

657

field at more than twice the Alfven speed with respect to the bulk plasma. Thus, only the high-velocity tail of the distribution will be able to interact with these waves. For the case shown in Figure 2, less than 5.7×10^{-4} of the alpha particles have this necessary speed at 25 R_s, where the model energization by the magnetosonic mode has already started. It is difficult to see how this enormous acceleration and heating of the entire distribution from an interaction with a tiny fraction of the particles can be other than a numerical artifact of the model.

Another model which deals with some of these questions from a different point of view has been presented by Isenberg and Hollweg (1983). This work does not include as detailed a picture of the microscopic interaction as Marsch et al., but it incorporates a reasonable simulation of the interaction into a full solar wind model which includes all other forces of interest. The central point of this model is that the energy problem is dealt with by invoking a "saturation and cascade" scenario. The authors assume that large-amplitude Alfven waves in the solar wind saturate when $\langle \delta B^2 \rangle / B_o^2 = \frac{1}{2}$, where $\langle \delta B^2 \rangle$ is the total magnetic variance (integrated over the entire spectrum). It is then hypothesized that the energy lost from the waves cascades to resonant frequencies where it is picked up by the particles through the resonant cyclotron interaction. The details of these nonlinear processes were not specified, as their physics is not well understood, but it was pointed out that this scenario is plausible and consistent with observations.

To incorporate this scenario into a solar wind model, one needs information on the propagation and dissipation properties of the waves in a multi-ion differentially flowing plasma. Unfortunately, at present, the only available theory of this type is restricted to Alfven waves in a thermally isotropic plasma (Isenberg and Hollweg, 1982). For this reason, the model particle distributions were taken to be isotropic and the waves were taken to be nondispersive, as well as parallel-propagating and left-polarized. The wave spectrum was taken to be a power law with constant spectral index γ. To simulate the interaction with ion-cyclotron waves, the spectrum was cut off at $\omega = \Omega_p$ in the proton reference frame.

The energization calculation proceeded as follows: The total plasma heating rate was obtained from the divergence of the flux of wave action of the saturated waves. This total was then distributed to the various ion species by taking the heating rate for each species proportional to the appropriate quasi-linear resonant cyclotron heating term. The wave acceleration of each species was then the sum of the non-dissipative Alfven wave pressure and a term proportional to the dissipative heating. This procedure allowed energy to be supplied to the resonant particles on a convective time scale so that high resonant power levels were no longer required. These wave effects were incorporated into the spherically-symmetric, three-fluid, corotating solar wind equations which were integrated from 10 R_s out to 1 AU.

A typical result is shown in Figure 3. For this case, the proton and wave parameters were taken from the wave-driven high speed stream model of Hollweg (1978). The alpha particles, 4% by number, had their velocity and temperature set equal to the protons', and the spectral index was $\gamma = 2$. This result shows definite preferential acceleration and heating when the waves saturate at 19 R_s, but the differential speed falls far short of the observed Alfven speed value.

658
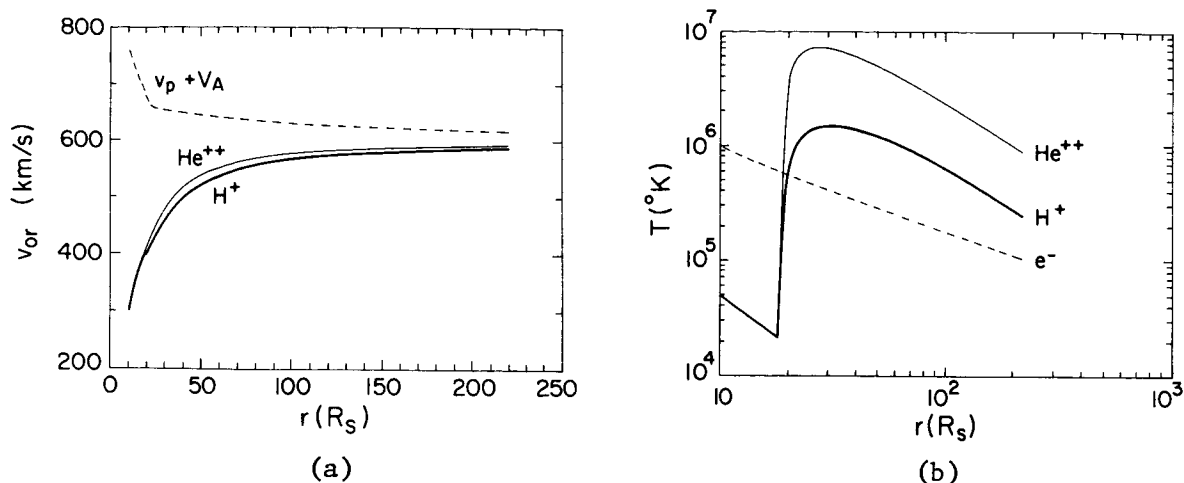
Figure 3. Ion radial speeds (a) and temperatures (b) from the model of Isenberg and Hollweg (1983) for $\gamma = 2$. Also shown in (a) is the radial component of the proton plus Alfven speed, and in (b) is the electron temperature.

Furthermore, the temperature ratio at 1 AU is only $T_\alpha/T_p = 3.6$, where we would hope to produce $T_\alpha/T_p \gtrsim 4$.

The preferential effects shown here proved essentially insensitive to changes in the initial particle velocities and temperatures. Increasing the initial wave intensity generated faster, hotter populations, but the values of $\Delta v_{\alpha p}$ and T_α/T_p changed very little. The only parameter left to vary was the spectral index and it is easy to see why γ is important. The quasilinear resonant interaction is proportional to the wave power at the resonant frequencies. When the protons and heavy ions are not moving with respect to one another, they resonate with waves near their respective gyrofrequencies. In the simplest picture, then, the power available to the ions is a factor of $(\Omega_i/\Omega_p)^\gamma$ larger than that for the protons where $\Omega_i = q_i B/(m_i c)$. Clearly, using a steeper wave spectrum will increase the preferential energization of the heavy ions.

The magnitude of the interaction is also proportional to the (charge/mass)^2 of the particle, so one might expect the total resonant acceleration to be proportional to $(A_i/Z_i)^{\gamma-2}$. This simple picture would imply that a heavy ion could not be preferentially accelerated by this process unless $\gamma > 2$. In reality, this picture is complicated by the thermal speeds, which smear out the resonance; by the differential speed, which Doppler-shifts the resonances to different relative points; and by the fall-off in wave power at Ω_p. It turns out to be the power cutoff that is most important. If the cutoff is not included and the model wave spectrum is continued with the same slope to infinite frequency, the simple picture is verified by the numerical calculations: there is no preferential acceleration of heavy ions for $\gamma \leq 2$. The cutoff in the spectrum reduces the power in the proton resonant range and allows helium to be preferentially accelerated for $\gamma > 1.5$. To produce stronger preferential effects, γ must be increased to rarely observed values > 2, and it takes a $\gamma = 4.7$ to produce alpha particles with $\Delta v_{\alpha p} = V_A$ at 60 R_s as shown in Figure 4.

659
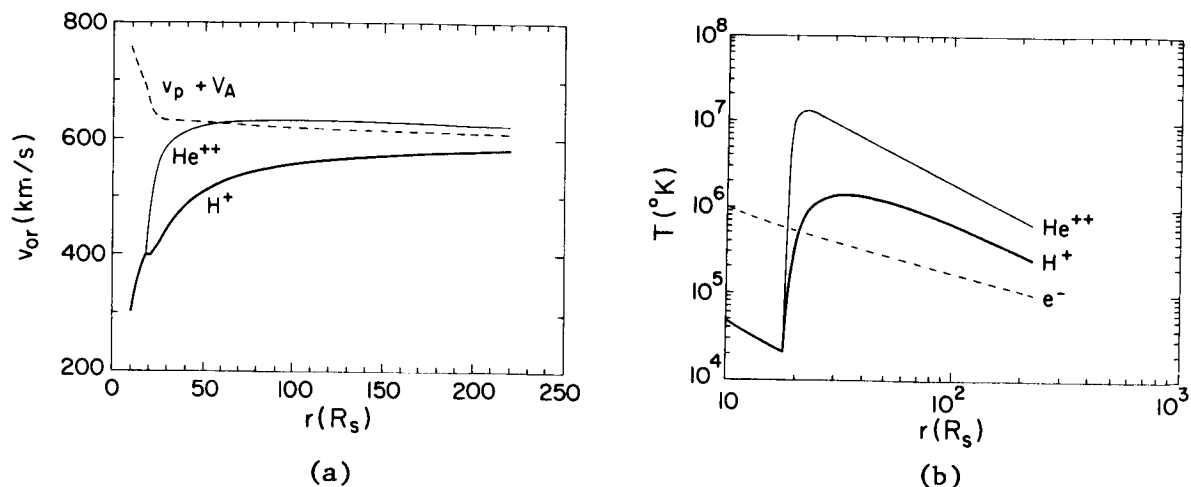
Figure 4. As in Figure 3 for $\gamma = 4.7$.

Once the alpha particles have been accelerated to $\Delta v_{\alpha p} \gtrsim V_A$ resonant interactions with right-polarized magnetosonic waves can become important. Beyond 80 R_s, in the case shown in Figure 4, almost 20% of the alpha population has sufficient parallel speed to resonate with the fast mode. However, this number is still small ($\sim$ 3% at 40 R_s) before the Alfven speed is reached and the right-hand interaction cannot play a significant role in the acceleration to V_A.

Heavier ions, with lower gyrofrequencies, are able to resonate with more intense waves and should be accelerated to higher speeds. However, this is only true if $\gamma > 2$ since the dissipative processes are proportional to $(A/Z)^{\gamma-2}$. When $\gamma = 2$, the determining factor is still the reduced proton resonant power due to the spectral cutoff, and the heavy ion velocities are the same as the alpha particle curves in Figure 3. When γ is increased it is found that oxygen ions, with A/Z near that of helium, are only slightly more accelerated. Acceleration of iron ions, on the other hand, is significantly enhanced over alpha particles, especially in the lower ionization states, such as Fe^{+8}, which reaches V_A at 50 R_s when $\gamma = 3$. Calculations by <u>Marsch</u> (1983) generate similar results for the interaction with left-polarized waves.

In summary, the Isenberg and Hollweg model of the resonant cyclotron interaction cannot explain the observed preferential acceleration and heating of heavy ions in the solar wind. To produce differential speeds on the order of those observed requires extremely steep wave spectra. Although there have been no direct observations of spectral slopes inside 60 R_s, all indications are that the spectra should be flatter there and spectral indicies of $\gamma = 4 - 5$ for $\omega < \Omega_p$ seem unlikely. The calculated temperature ratios, T_i/T_p, at 1 AU are also consistently lower than the mass-proportional values.

Several questions remain, for instance: What is the effect of allowing anisotropic particle distributions or including a spectrum of dispersive waves? These modifications should be investigated, but I suspect they will not provide

substantially more preferential acceleration of heavy ions. The resonant interaction tends to energize particles in the perpendicular direction, so the requirement of isotropy amounts to an effective transfer of perpendicular energy into parallel energy and it does not seem that relaxing this assumption will produce greater acceleration. Furthermore, dispersive ion-cyclotron waves would interact with a smaller portion of the ion distribution than the assumed non-dispersive spectrum does, and would presumably be less effective in energizing the ions. It may also be important to consider the effect of including the solar wind alpha particles in the dispersion relation of the waves. Preliminary work (Isenberg, 1982) has shown that there may actually be no waves to accelerate heavy ions to speeds faster than the proton speed by the resonant interaction.

In conclusion, it appears that the resonant cyclotron interaction cannot be responsible for the observed preferential acceleration and heating, and we must look elsewhere to find a mechanism which produces the observed effects.

References

Dusenbery, P.B. and J.V. Hollweg, Ion-cyclotron heating and acceleration of solar wind minor ions, J. Geophys. Res., 86, 153, 1981.

Hollweg, J.V., Some physical processes in the solar wind, Rev. Geophys. Space Phys., 16, 689, 1978.

Isenberg, P. A., The cyclotron resonance condition in a proton-alpha solar wind, EOS Trans. AGU, 63, 1087, 1982.

Isenberg, P. A. and J.V. Hollweg, Finite-amplitude Alfven waves in a multi-ion plasma: Propagation, acceleration, and heating, J. Geophys. Res., 87, 5023, 1982.

Isenberg, P. A. and J.V. Hollweg, On the preferential acceleration and heating of solar wind heavy ions, J. Geophys. Res., in press, 1983.

Marsch, E., Resonant wave heating and acceleration of heavy ions in the solar wind, J. Geophys. Res., submitted, 1983.

Marsch, E., C. K. Goertz, and K. Richter, Wave heating and acceleration of solar wind ions by cyclotron resonance, J. Geophys. Res., 87, 5030, 1982.

McKenzie, J.F., and E. Marsch, Resonant wave acceleration of minor ions in the solar wind, Astrophys. Space Sci., 81, 295, 1982.
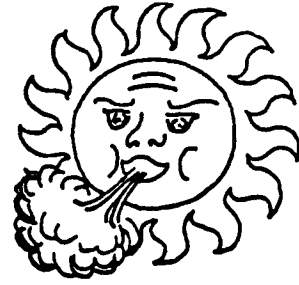
SESSION 10.

DYNAMICS

TRANSIENT CHANGES IN THE WHITE-LIGHT CORONA

R. Fisher
High Altitude Observatory
NCAR
PO Box 3000
Boulder, CO   80307

A variety of instrumentation has been used over the past few years in order to study the changes in white-light solar corona. Some of the most striking and spectacular types of solar activity, at least in terms of sheer size, have come to the attention of investigators as a result of these observational efforts. A review of the results includes the characterization of transient events in terms of the variation of brightness as a function of time, the association of these events with types of solar activity found lower in the atmosphere, and the frequency of events detected as a function of time. These properties are reviewed along with the inferred physical properties of transients, i.e., mass and energy properties and the specific event morphology.

MODELING OF TRANSIENT DISTURBANCES IN CORONAL-STREAMER CONFIGURATIONS

R. S. Steinolfson
Department of Physics
University of California
Irvine, California 92717

ABSTRACT

Numerical simulations of the formation and propagation of mass-ejection, loop transients in coronal streamers are discussed. The simulations of the streamer configuration and the subsequent transient are accomplished with numerical solutions of the single-fluid, ideal MHD equations of motion in the meridional plane. The streamer is produced by simulating the relaxation of an initially radial hydrodynamic flow coupled with a dipole magnetic field. The simulated transient then results from an energy release at the base of the streamer. The "legs" of the loop transient thus produced remain essentially stationary while the loop expands mainly in the radial direction with velocities of $400 - 750$ km s^{-1} (determined by the magnitude of the energy release). Once the leading-edge of the transient has passed out of the lower corona, the initial streamer configuration is restored after $15 - 24$ hours. A second energy release two hours later than, and with an energy release identical to, the first does not produce a significant coronal disturbance.

Introduction

The coronal response to a solar event is determined to a large extent by the magnetic-field configuration and magnitude, the thermodynamics, and the velocity of the pre-event corona. The role of the ambient magnetic field has been demonstrated (Steinolfson et al. 1978) by simulating the considerably different transients in open as opposed to closed magnetic-field configurations. However, that study, as well as the majority of other multi-dimensional numerical studies of transient formation and propagation in the lower corona, is for a hydrostatic atmosphere. A trivial extension to an ambient nonstationary corona was made by Wu et al.(1981), who considered radial flow in a radial magnetic field. In that particular study the role of the magnetic field was more passive than active.

A model for the propagation of transients through coronal-streamer configurations has been developed in a series of papers by Steinolfson et al. (1982) and Steinolfson (1982a), henceforth referred to as Papers I and II, respectively. Coronal streamers consist of open field lines, with field-aligned flow, overlying closed field lines near the solar surface in which the atmosphere is in hydrostatic equilibrium. The solar event responsible for the transient occurs at the base of the closed-field region. This model is attractive from an observational viewpoint since transients can often be associated with eruptive prominences (with or without flares, Munro et al. (1979)) which, in turn, are believed to lie over neutral lines - lines along which the vertical photospheric magnetic field reverses sign. The present paper contains a brief description of the model and the characteristic transients that it produces in streamers, as well as studies involving the coronal relaxation following the transient.

Simulation Procedure and Relevant Parameters

The ambient coronal streamer and the subsequent transient are simulated in the meridional plane with numerical solutions of the time-dependent, dissipationless (except at shock waves), magnetohydrodynamic equations of motion. The equations, the method of numerical solution, the appropriate boundary and symmetry conditions, and details of simulating the solar event are given in Papers I and II.

The entire simulation consists of two separate simulations; one for the streamer and an independent one, which uses the computed streamer as the initial state, for the transient. The streamer is obtained by allowing the corona to relax from a nonequilibrium state following the procedure in Paper I, which is reviewed in these proceedings by Suess (1983). The transient is then produced by simulating a solar event, located at the center of the base of the closed-field region, with an increase in the thermal pressure.

The most important parameters are the plasma beta β, which is referenced to the center of the base of the closed-field region in the pre-streamer corona, and the magnitude and duration of the pressure increase. For the results discussed here, the energy input was maintained for 1 hr. in all cases. The other parameters are discussed along with the separate simulations. Parametric studies involving several parameters are presented in Paper II.

Numerical Results

As mentioned previously, all of the transient simulations presented here are initiated in an ambient coronal-streamer configuration. A typical streamer is shown later [Figure 3(b)] where it is compared to the corona after it has relaxed following the passage of a transient through it.

A representative coronal response to a solar event at the base of the streamer is shown at two times (referenced to the start of the solar event) in Figure 1. The vertical axis is the equator, the horizontal axis is the pole, and the axes are labelled in units of solar radii. The mass-excess (the contour plot) is proportional to the mass in the transient ρ_t less the mass in the initial streamer ρ_s with the same definition as in Paper II; i.e.,

$$\xi = \frac{\rho_t - \rho_s}{\rho_r} \frac{r}{R_0} \sin \theta \ ,$$

where ρ_r is reference density (2.5×10^{-18} gm cm^{-3}), R_0 is the solar radius, and r and θ are locations in the meridional plane. The contours are only shown beyond the approximate location of the occulting disk on the Skylab coronagraph. The mass in the transient is less than that in the streamer below the lowest contour near the equator. As can be seen, the transient, as determined in terms of the largest values of the mass excess, has the shape of a radially expanding loop. The legs of the expanding loop remain essentially stationary (centered, at 2 solar radii, at approximately 20° from vertical) and subtend less than 60° in latitude. The latitudinal motion of the legs is restrained by magnetic pressure

(a) t = 60 min

(b) t = 90 min
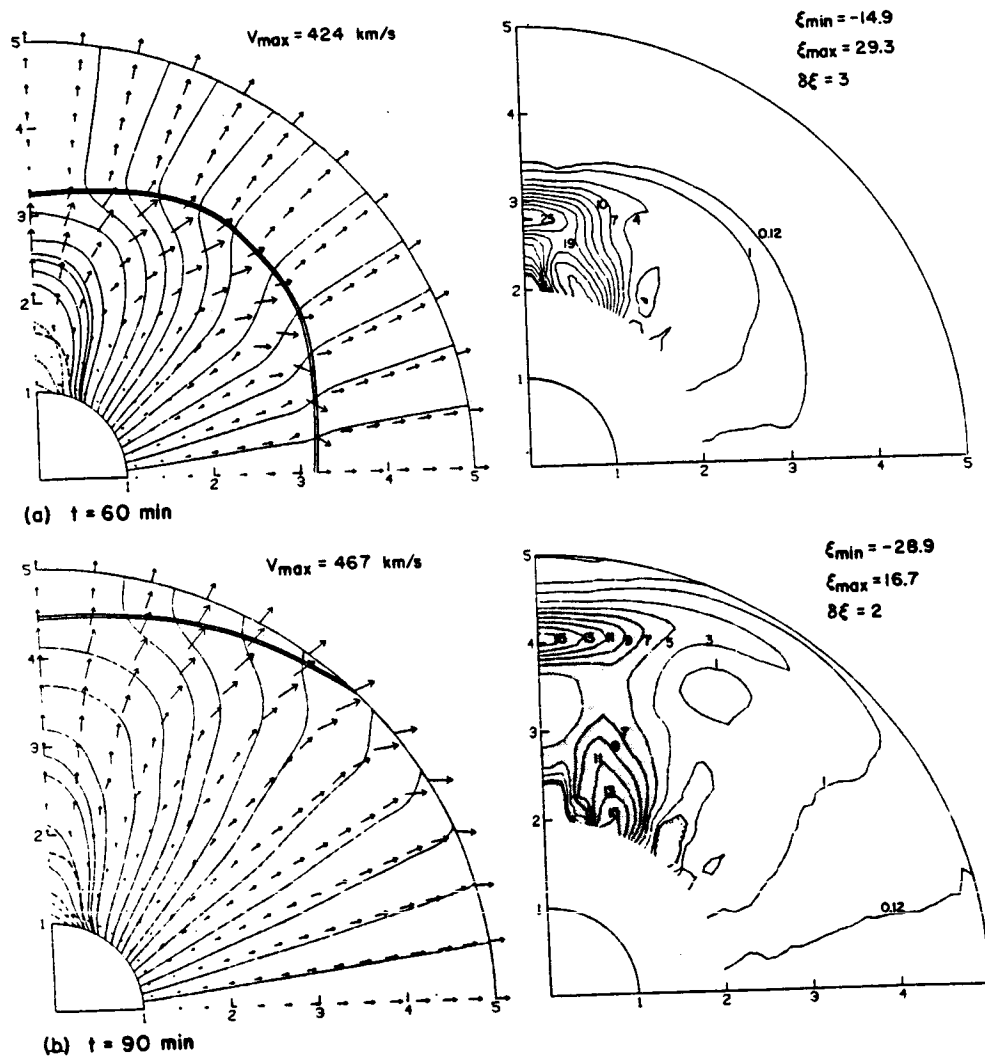
Figure 1. Coronal response for $\beta = 0.1$ and a solar event with a pressure increase of p/p_0 (where p_0 is the initial value) $= 14.3$ and a density increase of $\rho/\rho_0 = 1.3$. The left figure shows the magnetic field lines, velocity vectors, and shock trajectory (represented by the parallel lines), and the right figure shows the mass-excess contours where $\delta\xi$ is the contour increment.

forces due to the larger magnetic field in the coronal hole near the pole than near the equator in a coronal streamer. This is demonstrated in Figure 2 which shows the latitudinal variation, at 2 solar radii, of β and the magnetic-field magnitude for a streamer and for a hydrostatic atmosphere with a dipole magnetic field. The much larger magnetic-field gradient for the streamer acts to constrain the transient legs.

After the transient has passed through the lower corona and the energy input due to the solar event has ended, the corona should once again relax to an equilibrium. Approximately 15 - 24 hrs. are generally required for the streamer config-
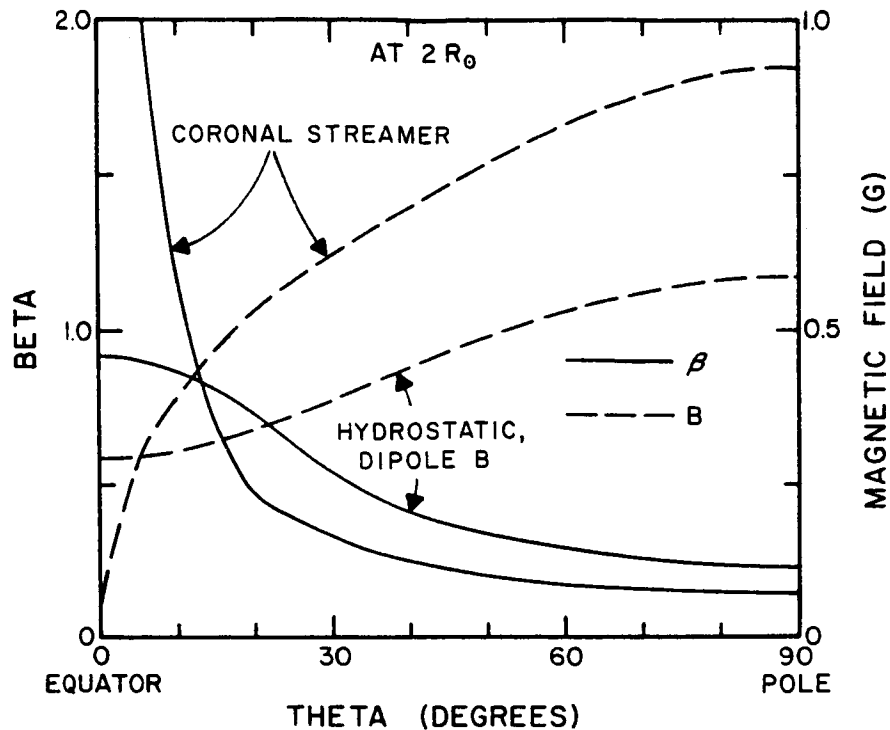
Figure 2. Latitudinal distribution of magnetic field magnitude and plasma beta at 2 solar radii for a reference value of $\beta = 0.1$, and for both a streamer configuration and a hydrostatic atmosphere.

uration to be reestablished -- depending on the parametric values and the magnitude and duration of the energy input. The corona, 16 hrs. after initiation of the energy input, is compared to the initial streamer in Figure. 3 Some slight differences still exist between the two coronae, but clearly the streamer configuration has been restored after the transient disrupted it.

Since such a relatively long period of time is required for the corona to recover following a transient, it follows that a second solar event at the same location as an earlier one may produce quite a different coronal response if sufficient time has not elapsed. Results for a simulation of such a scenario are shown in Figure 4. The simulated solar events are identical with the second initiated 2 hrs. after the start of the first. Both events last 1 hr. so the corona in Figure 4(a) is shown for the same time lapse following the first event as is the corona in Figure 4(b) following the second event. The first event produces a well-defined transient in the mass-excess contours while the second event does not produce a noticeable effect on the mass excess. In fact, the mass-excess contours in Figure 4(b) are almost identical to those that occur if the second event is not included (Steinolfson, 1982b). However, the second transient does produce a shock wave with a velocity almost identical to that produced by the first.

Comparison With Observations

One form of observational results which may be used to evaluate the physical relevance of the simulations of the previous section is the brightness images
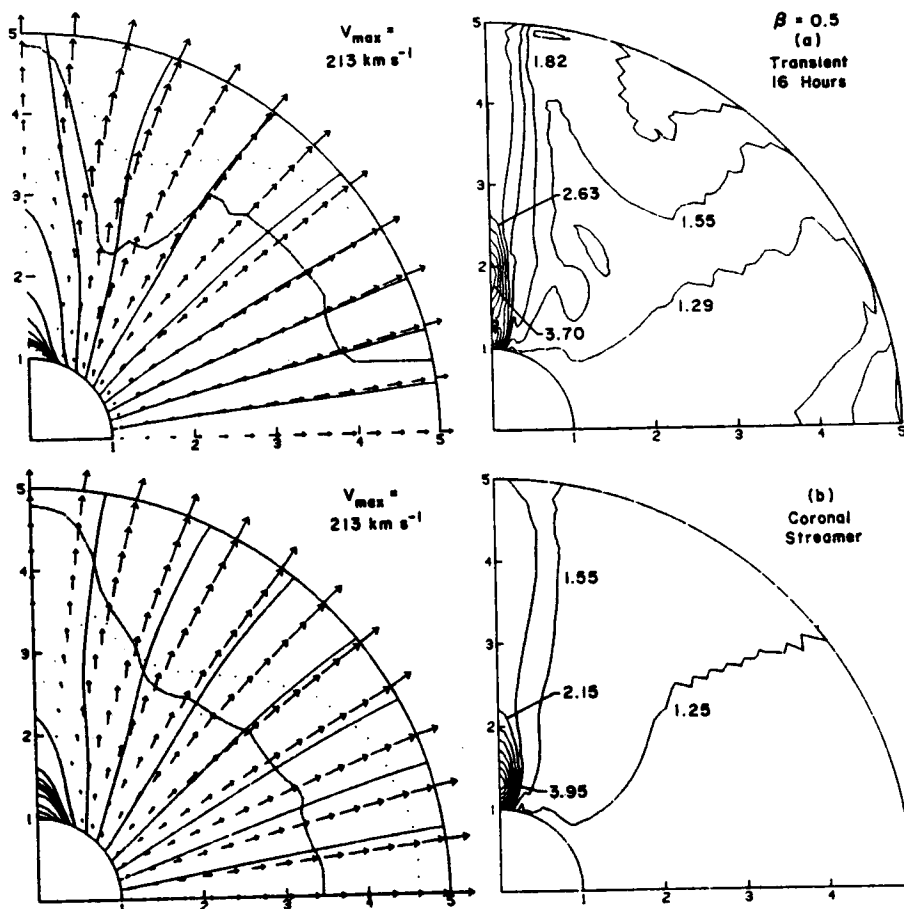
Figure 3. Coronal relaxation following a transient (a) compared with the initial streamer configuration (b). The transient was produced by a pressure increase of p/p_0 = 10. The right figures are pressure contours (p/p_0), and the left are magnetic field lines and velocity vectors. Note the high pressure (also high temperature and density) and low velocity in the closed-field region.

obtained with white-light coronographs. The technique for converting these observations into excess columnar density (a pre-event image subtracted from a transient image) has been described by Hildner et al. (1975). Aside from the absolute level (determined by unknown and, therefore, assumed geometric factors), these observations are directly comparable to the computed mass excess.

One characteristic feature of observed mass-ejection, loop transients is that the legs of the radially expanding loop remain stationary while the loop expands outward (Hildner, 1977). The success of this model in simulating this observation is shown in Figure 1.

Another observational result that the present model can simulate has been described by Wagner et al. (1981). They reported that a visible transient (by a white-light coronagraph) was not recorded for a flare at the same location as, but 2 hrs. later than, an earlier smaller flare which did produce an observed transient. Simulations, using the present model, of two successive flares and the resulting transients are consistent with this observation, as shown in

671
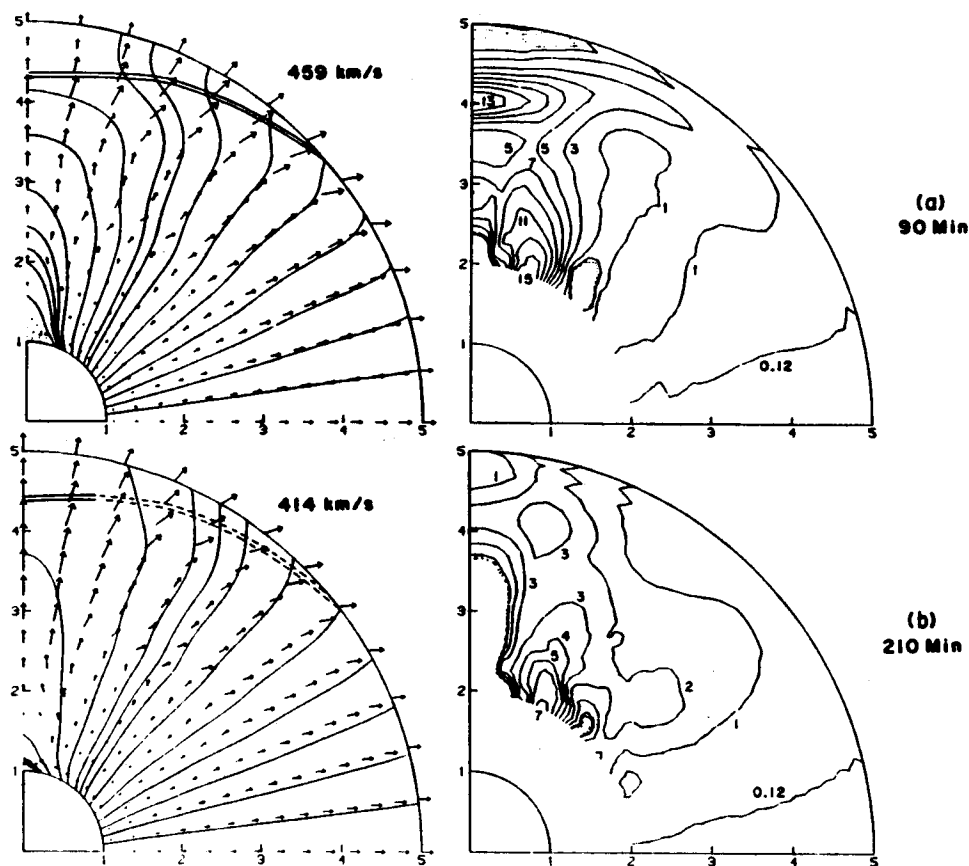
Figure 4. Coronal response to two successive solar events at the same location with the second 2 hrs. later than the first. The parameters are the same as those used for Figure 1. Mass excess contours are shown in the figures on the right.

Figure 4. The simulations also suggests that, although the second flare did not produce an effect observable in white-light coronagraphs, the fact that the second transient did contain a shock implies that it may produce observable type II or type IV radio bursts.

Conclusions

The numerical simulations discussed here demonstrate the, not unexpected, results that the state of the corona through which a transient propagates can have a large effect on the shape of the simulated transient (in terms of mass excess). The simulations also show that the larger magnetic field overlying open-field regions in streamers, as opposed to that over the closed-field region, may be responsible for constraining the latitudinal movement of the legs of the transient which gives some transients the characteristic shape of a radially-expanding loop. In addition, it is shown that approximately 15 - 24 hrs. are required for the streamer configuration to be restored after being disturbed by a transient. The above simulated results have been shown to be consistent with observations of coronal transients.

References

Hildner, E., J. T. Gosling, R. M. MacQueen, R. H. Munro, A. I. Poland, and C. L. Ross, The Large Coronal Transient of 10 June 1973, Solar Phys. 42, 163, 1975.

Hildner, E., in Study of Traveling Interplanetary Phenomena, eds.: M. A. Shea, D. F. Smart, and S. T. Wu, Reidel, Dordrecht, pp. 3 - 21, 1977.

Munro, R. H., J. T. Gosling, E. Hildner, R. M. Mac Queen, A. I. Poland, and C. L. Ross, The Association of Coronal Mass Ejection Transients with Other Forms of Solar Activity, Solar Phys. 61, 201, 1979.

Steinolfson, R. S., S. T. Wu, M. Dryer, and E. Tandberg-Hanssen, Magnetohydrodynamic Models of Coronal Transients in the Meridional Plane I. The Effect of the Magnetic Field, Astrophys. J. 225, 259, 1978.

Steinolfson, R. S., S. T. Suess, and S. T. Wu, The Steady Global Corona, Astrophys. J. 255, 730, 1982, Paper I.

Steinolfson, R. S., Coronal Loop Transients in Streamer Configurations, Astron. and Astrophys. 115, 39, 1982a, Paper II.

Steinolfson, R. S., Coronal Response to a Solar Event in a Corona Evacuated by a Prior Transient, Astron. and Astrophys. 115, 50, 1982b.

Suess, S. T., Magnetohydrodynamic Modeling of Coronal Structure and Expansion, Proceedings of Solar Wind V, Woodstock, Vermont, November 1 - 5, 1983.

Wagner, W. S., E. Hildner, L. L. House, C. Sawyer, K. V. Sheridan, G. A. Dulk, Radio and Visible Light Observations of Matter Ejected from the Sun, Astrophys. J. Lett. 244, L123, 1981.

Wu, S. T., R. S. Steinolfson, M. Dryer, and E. Tandberg-Hanssen, Magnetohydrodynamic Models of Coronal Transients in the Meridional Plane IV. Effect of the Solar Wind, Astrophys. J. 243, 641, 1981.

QUASI-STEADY SOLAR WIND DYNAMICS

V. J. Pizzo
High Altitude Observatory
National Center for Atmospheric Research[*]
P. O. Box 3000
Boulder, CO 80307 USA

ABSTRACT

This paper opens with a brief review of recent progress in understanding the large scale dynamics of quasi-steady, corotating solar wind structure. It then focuses on two new study areas that these observational and theoretical advances have made ripe for development. The first concerns the nature of the solar wind at large heliocentric distances ($r>10AU$). Preliminary calculations from a 2-D MHD model are used to demonstrate theoretical expectations of corotating structure out to 30 AU. It is found that the forward and reverse shocks from adjacent CIR's begin to interact at about 10 AU, producing new shock pairs flanking "secondary" CIR's. These sawtooth secondary CIR's interact again at about 20 AU and survive as visible entities (though not necessarily as shocks) to 30 AU. The model predicts the velocity jumps at the leading edge of the secondary CIR's at 30 AU should be very small but there should still be sizable variations (factor of 2-3 jumps at the CIR fronts) in the thermodynamic and magnetic parameters, with considerable remnant substructure to be seen. The most important points are that the driving dynamic mechanism in the distant solar wind is the relaxation of pressure gradients (not kinematic steepening, as in the near-sun solar wind) and that the models make a number of definite, quantitative predictions that can be compared with available data. The second topic is the influence of weak, non-impulsive time dependence in quasi-steady dynamics. It is suggested that modest ($\sim 75km/s$) large scale variations in the coronal flow speed on periods of several hours to a day (presumably associated with the continual coronal evolution) may be responsible for many of the remaining discrepancies between theory and observation. In particular, such temporal effects offer a ready explanation for the apparent rounding (or de-steepening) of stream fronts between 0.3 and 1.0 AU discovered by Helios.

Introduction

The last several years have witnessed a steady enrichment of our understanding of corotating stream dynamics. On the empirical front, Helios has returned marvelous data on the near-sun solar wind, while Pioneer and Voyager probe ever deeper into the far reaches of the heliosphere. Coupled with observations from numerous other spacecraft at intermediate distances, the quantity and quality of relevant data available to researchers today is truly impressive. On the theoretical front, description of interplanetary dynamics has achieved a high level of sophistication, such that most of the physical mechanisms thought to be important in the large scale evolution of corotating structures are now included in the models.

My main theme is that the conjunction of all this observational and theoretical progress finally makes it feasible to tackle certain long-standing problems with a reasonable chance of success. In this discussion, I will single out two topics I find particularly

enticing and potentially rewarding, though these by no means exhaust the possibilities. Specifically, the questions I will concentrate on are: 1) What is the nature of the distant $(r>10$ AU $)$ solar wind and does it differ very much from the familiar near-sun $(0.3<r<5AU)$ flow? 2) To what extent do slow, non-impulsive temporal variations in the coronal source regions of the solar wind affect the interplanetary evolution of steam structures, i.e.; What happens when the flows are really only quasi-steady as opposed to absolutely steady as idealized in the models?

Background for the Discussion

We begin with a brief review, largely theoretical, of the current state-of-the-art in the field of corotating stream dynamics. A schematic representation of the classic interplanetary stream interaction phenomenon is depicted in Figure 1, in which we view the flow in the solar equatorial plane from over the north pole of the sun. Alternating regions of nearly radial fast and slow flow originating in the corona are indicated by long and short dark arrows. Under the influence of solar rotation, fast flows near the sun are brought into radial alignment with more distant slow flows emitted earlier; as the former overtake the latter, the intervening material is compressed and heated (shaded area), which in turn drives small but dynamically important nonradial flows (large open arrows). If this compression is vigorous enough, a forward and reverse corotating shock pair may result further out. In regions where fast material outraces succeeding slow plasma, a relative rarefaction is formed. The magnetic field (light lines) is drawn out into a spiral configuration, whose pitch depends upon the flow speed. As the entire pattern rotates with the sun, a spacecraft situated at, say, 1 AU will see an apparent temporal variation, with most of the interesting dynamics confined to the leading edge of the high-speed stream.

STREAM INTERACTION SCHEMATIC
(INERTIAL FRAME)
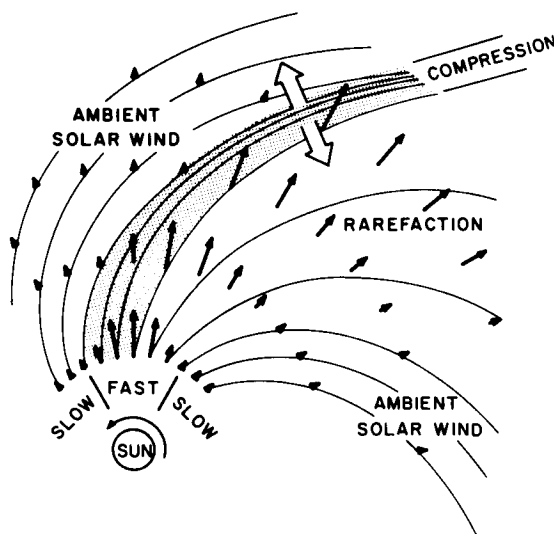
Figure 1). Stream-interaction schematic in the solar equatorial plane.

Quantitative theoretical description of these interactions has been most successfully formulated in terms of continuum MHD. For steady, superalfvenic flow in interplanetary space, the appropriate equations in a frame corotating with the sun are (in cgs units):

$$\nabla \cdot \rho \vec{v} = 0 \tag{1}$$

$$\rho[(\vec{v} \cdot \nabla)\vec{v} + 2\vec{\Omega} \times \vec{v} + \vec{\Omega} \times (\vec{\Omega} \times \vec{r})] = -\nabla P - \rho \frac{GM_s}{r^2} \hat{r} + \frac{(\nabla \times \vec{B}) \times \vec{B}}{4\pi} \tag{2}$$

$$\nabla \cdot \left[\vec{v} \left(\rho \frac{\vec{v} \cdot \vec{v} - |\vec{\Omega} \times \vec{r}|^2}{2} + \frac{\gamma}{\gamma - 1} P \right) + \frac{\vec{B} \times}{4\pi} (\vec{v} \times \vec{B}) \right] = -\rho \frac{G M_s v_r}{r^2} \hat{r} \qquad (3)$$

$$\nabla \cdot \vec{B} = 0 \qquad (4)$$

The dependent variables are: mass density, $\rho = mn$, where m is the proton mass and n the proton number density; velocity, $\vec{v}$; isotropic gas pressure, P; and magnetic field, $\vec{B}$. The other symbols are: the solar equatorial rotation rate, Ω; the spherical radius vector, $\hat{r}$; the universal gravitational constant, G; the solar mass, M_s; and the polytropic index, γ.

Among the important assumptions entering into the derivation of these equations are that the plasma behaves like an electrically neutral proton-electron fluid, that the electrical conductivity is infinite, and that the electric field in the rotating frame is zero. Heat conduction, viscosity (except at shocks), wave dissipation, and all kinetic-level effects are taken as having negligible impact upon the large scale dynamics. Hence the gas pressure is isotropic and related to the proton and electron temperatures T_p and T_e by the auxiliary relation

$$P = nk(T_p + T_e) = 2nkT \qquad (5)$$

where k is Boltzmann's constant and T is the single-fluid temperature. The internal energy is governed by a polytrope law, so that

$$(\vec{v} \cdot \nabla) P \rho^{-\gamma} = 0. \qquad (6)$$

All these approximations are reasonably justifiable in the momentum-dominated superalfvenic solar wind at, say, 0.3 AU and beyond. It should be borne in mind, however, that many of the above assumptions may prove untenable closer to the sun and almost certainly break down in the corona, which is, by clever design, outside the scope of this paper.

Even with all these restrictions, quite a variety of models can be constructed from equations 1-6. The differences among them are best discussed within the context of 2-D (planar) flows in the solar equatorial plane (three dimensional aspects of the problem will be addressed below.) By virtue of the assumptions introduced previously, all the interesting physical content of the formulation resides in the momentum equation (2). This circumstance provides a convenient means of classifying the models. The most fundamental distinction one can draw is between kinematic and dynamic formulations. The terms on the left-hand-side of (2) constitute the purely kinematic portion of the description: the velocity gradients couple with solar rotation to regulate the rate at which material is compressed or rarefied. The terms on the right-hand-side of (2) embody the truly dynamic part of the interaction: gas pressure and field gradients determine what happens once the kinematic action brings fluid elements together. (Gravitational effects are negligible in interplanetary space and are carried along for completeness only because it is a numerically trivial operation.) Purely kinematic models ($P = \vec{B} = 0$) are attractive in that they are nonlinear while retaining extreme computational simplicity (e.g. see Matsuda and Sakurai, 1972; Burlaga and Barouch, 1976.) The problem with that approach, however, is that for the kinds of structures most commonly encountered in the near-sun solar wind (i.e., sharply-bounded high-speed streams), the dynamical reaction of the gas has a profound effect upon the rate of steepening and shock formation and the resultant structure of the interaction front. Furthermore, in the distant solar wind ($>10AU$), where the initial high-speed material contained in the streams has been completely expended,

677

the subsequent interactions are driven entirely by secondary pressure waves. That is, there is hardly any kinematics left in the problem (see next section). Thus, while use of kinematic models for limited illustrative purposes, for crude tracing of the solar origin of broad interplanetary streams (e.g. Nolte et al., 1977), and for judicious mapping of select portions of streams well away from interaction regions may be warranted, on the whole they are quantitatively and sometimes even qualitatively inadequate. (For further discussion on this point, see Pizzo, "Comments on the Paper by Akasofu and Hakamada", this Conference.)

Among the dynamic models, the computationally simplest formulation is the linear model originally developed by Carovillano and Siscoe (1969). Unfortunately, this model, too, suffers a very severe flaw in that the amplitude of the variations in the solar wind are so large as to preclude a linear evolution over any but the shortest distances and the most favorable conditions (no large velocity gradients). Hence it is generally unacceptable for typical solar wind applications. The model of Hundhausen (1973a) overcomes these objections through the incorporation of both nonlinear steepening and gas pressure forces. Despite its merits, this model, too, harbors certain deficiencies that restrict its utility. Namely, it neglects the magnetic forces and the secondary nonradial flows built up in the interaction. These nonradial flows, while small, are now known to significantly relieve the compressive stresses generated at the stream front by allowing lateral slippage of the fluid, thereby retarding both the steepening and shock formation. The magnetic field has a similar, though two-fold, effect: first, the fluid has greater resistance to direct compression by virtue of the magnetic pressure gradients; and, second, the relevant characteristic speed in the fluid becomes the fast-mode speed (which is normally about twice the sound speed in interplanetary space), which means the pressure forces can more effectively distribute the compressive stresses over a larger volume of the fluid. Neglect of the nonradial flow is not too bad so long as only streams with broad boundaries are considered or attention is restricted to flows beyond 1 AU (Gosling et al., 1976; Dryer et al., 1978). However, as demonstrated by Helios (Rosenbauer, et al. 1977), streams near 0.3 AU in fact tend to have sharp boundaries. Models of the Hundhausen (1973a) type, even with some allowance for field effects (Steinolfson et al., 1975), perform poorly under such conditions, seriously overestimating the rate of steepening and shock formation.

Proper description of corotating stream dynamics is thus seen to demand at least the full formalism contained in equations (1) - (4): nonlinearity, nonradial flows, and magnetic and gas pressure effects. Models incorporating all these properties (Goldstein, 1971; Goldstein and Jokipii, 1977; Whang and Chien, 1981; Pizzo, 1982) are capable of reproducing to a reasonable approximation the sort of large scale phenomena typically observed by spacecraft over a broad range of heliocentric distances. Figures 2 and 3 illustrate an example from one such model (Pizzo, 1982). The curves in Figure 2 depict the variation of radial velocity, density, and temperature across the stream on an initial surface taken to lie at 0.3 AU, well outside the critical points. The nonradial velocity is set to zero there, while the field magnitude is held constant across the structure at a uniform value, $|\vec{B}| = 45\gamma$. This input is an idealization of the 1975 Helios perihelion observations, in which dense, slow, cold flow alternated with hot, tenuous, fast flows in a step-function-like manner. When this structure is propagated to 1 AU via a suitable numerical integration of equations (1) -(6), the longitudinal variations recorded in Figure 3 result. As fast material overtakes slow at the stream front, the compressive interaction gives rise to forward (F) and reverse (R) large-amplitude MHD waves which propagate in opposite directions away from the interaction front. (In this example they have steepened into shocks, though for other choices of intial conditions they need not. See also Whang and Chien, 1981). Sandwiched in between is a shear-flow interface (I), which arises as a natural consequence of the radial compression along the spiral front (Hundhausen and

Burlaga, 1975; Gosling *et al.*, 1978). The density, temperature, and field strength all vary in a fashion representative of 1 AU stream fronts (Siscoe, 1972; Gosling *et al.*, 1972).

WEST   EAST   2-D MHD STREAM AT 1.0 AU
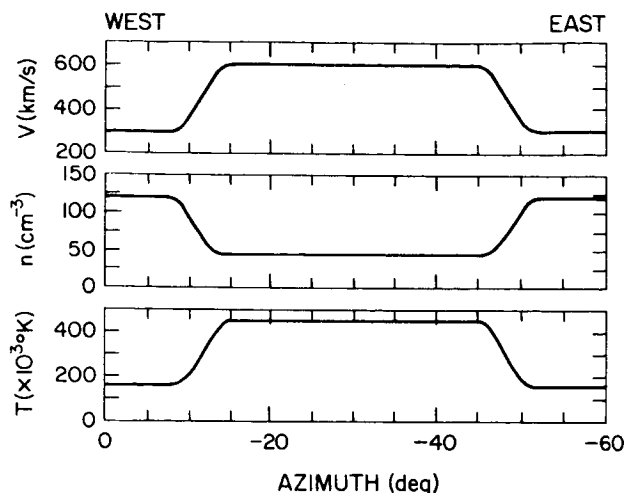
Figure 2). Input variations for hypothetical stream at 0.3 AU. Also, on this initial surface, the flow angle ϕ = 0 and $|\vec{B}|$ = 45γ. These parameters are chosen to mimic Helios perihelion data (Rosenbauer et al., 1977). Periodic boundary conditions are imposed at the two longitudinal ends.
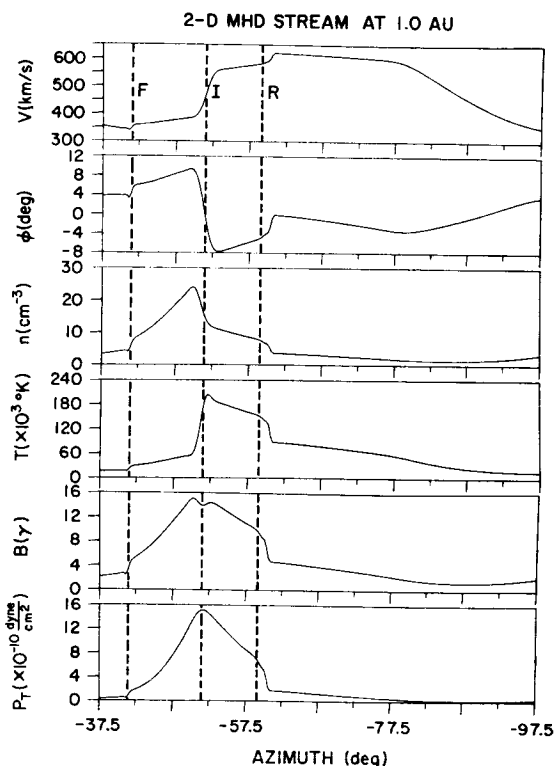
Figure 3). Appearance of the stream in Figure 2 at 1.0 AU, according to a 2-D MHD model (Pizzo, 1982). F and R refer to forward and reverse shocks, while I denotes the shear-flow interface that evolves between the high-speed and low-speed regimes. P_T is the total (gas plus magnetic) pressure.

Of course, the 3-D structure of the corona must somehow be impressed upon the solar wind, so it is natural to ask whether global effects might not seriously alter the evolution from the 2-D idealization. Owing to the limited and fragmented 3-D data currently available, the only insight to be gained comes from 3-D MHD models using hypothetical, but hopefully relevant, input structures (Pizzo, 1982; see also Riesebieter, 1977; Whang, 1980). The basic idea is to compare streams that have identical longitudinal variations at the equator but differ markedly in their geometry away from the equator. Figure 4 shows two 3-D geometries analyzed in the Pizzo (1982) study, here portrayed as contour plots of radial velocity on the r = 0.3 AU initial surface. On the left, we see a circular-shaped, sharply bounded stream centered at the equator. The radial velocity is 600 km/s throughout the middle of the stream, falling smoothly to 300 km/s all about its periphery. Temperature and density have the same correlation with velocity as in Figure 2, while both components of the nonradial flow are zero and $|\vec{B}|$ = 45γ as before. On the right, we find a geometry suggestive of a polar high-speed stream, where the velocity is 600 km/s except in a narrow 300 km/s band crossing the equator. Figure 5 compares the 1 AU solutions at the equator for 2-D (dashed), 3-D circular (solid), and 3-D polar (dotted) streams. As might be expected, the differences between the 2-D and 3-D circular projections are minimal. What is more intriguing is that the 3-D polar solution deviates so little from the other two, despite the discordant geometries. From this it can be inferred that

679

r=0.3 AU   U_r   U_r
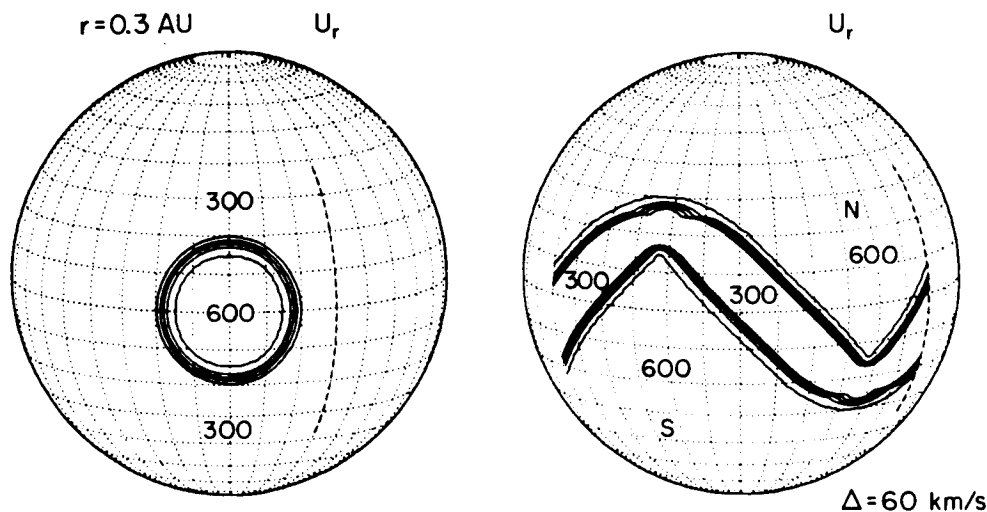
Δ=60 km/s

Figure 4). Constant velocity contours
for two different 3-D geometries at the
0.3 AU spherical initial surface. The
increment between contour levels is 60
km/s.

north-south flow effects generated by
meridional gradients in the interplane-
tary 3-D solar wind are not too severe
and that it should therefore be legiti-
mate to use 2-D models for the mapping
of flows. Nevertheless, this optimistic
assessment must be tempered with the
caution that it really applies only in the
case that the global structure at the
input be fairly regular, i.e., that the
stream fronts especially contain no
great amount of substructure (Pizzo,
1982). It is thus in the absence of any
compelling evidence that such sub-
structure is common that we tenta-
tively justify the continued use of 2-D
models.

    Much more complete and detailed
comparisons of these various models
may be found in Pizzo (1978, 1981,
1982) and Steinolfson et al. (1975).
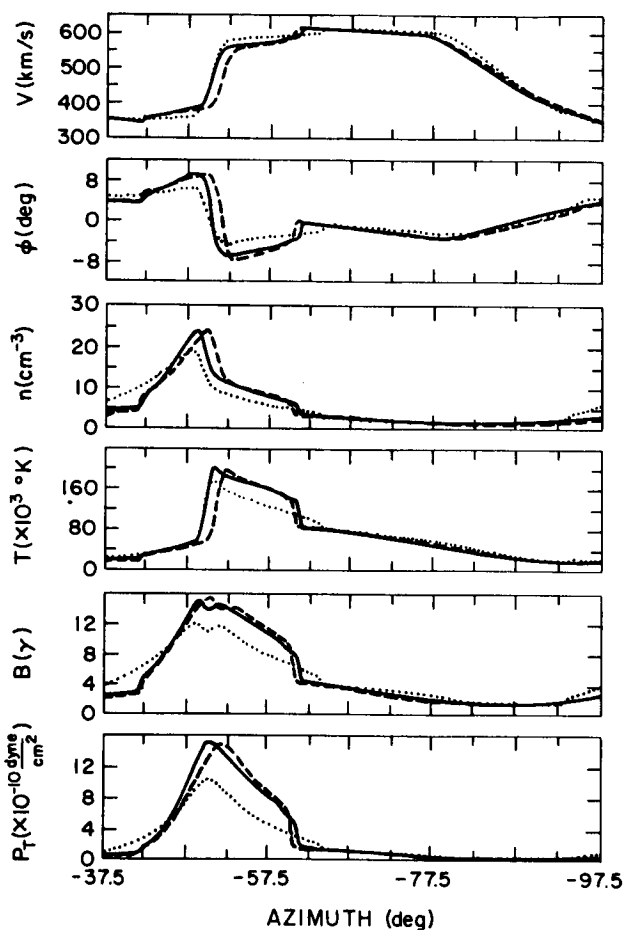
Figure 5). Comparison of 1 AU equatorial
solutions of three models, showing effects
of differing stream geometries: 2-D
(dashed); 3-D circular (solid); and 3-D
polar (dotted).

2-D Evolution of Corotating Structure
To Large Heliocentric Distances

The general picture of stream evolution outlined above can be said to be fairly well established in the inner solar system ($r < 5AU$). At least, this is the region in which numerical simulations based on MHD theory have been favorably compared with various sets of radially-aligned spacecraft data (e.g. Gosling *et al.*, 1976; Dryer *et al.*, 1978). This is not to say that important discrepancies between theory and observation do not exist or that the models are faithful in every detail (see last section, below); rather, only that the basic concept is sufficiently valid to permit us to speculate (as I will in the remainder of this talk) on new phenomena with some degree of confidence.

About a decade ago, there arose two conflicting viewpoints as to the nature of solar wind structure at large heliocentric distances. One school of thought (Jokipii and Davis, 1969) held that turbulent dissipation would efficiently smooth out both corotating and transient flows within a few AU of the sun, resulting in an essentially featureless solar wind expansion at large distances. The other view (Hundhausen, 1973b) suggested, on the basis of hydrodynamic considerations, that identifiable streams would survive far out into the solar system (tens of AU) and would be manifest there as sawtooth velocity structures, with either a shock or very steep gradients at the leading edge. Eventually, in the mid-70's Pioneer data settled the argument in favor of the latter alternative, at least out to 5 AU (Hundhausen and Gosling, 1976; Smith and Wolfe, 1976). Nevertheless, it should not be assumed that the entire story has been told, that the very distant solar wind ($\gtrsim 10$ AU) offers nothing really new. Quite the contrary, I intend to persuade you that the structure of the far solar wind should harbor exciting new phenomena and that even within the context of dynamical evolution of the sort invoked by Hundhausen (1973), the flow beyond 10 AU differs in fundamental ways from the near-sun expansion. My presentation draws heavily upon some preliminary calculations I have just completed, but the views to be expressed closely parallel those recently espoused by Burlaga (1983), which are based largely upon Voyager observations.

In my calculation, real solar wind flows in the ecliptic are projected from 1 AU to 30 AU under the assumption of ideal corotation. The input data for this study are hourly averages of IMP 7 and 8 plasma parameters from the MIT experiment and the associated magnetic field measurements from the GSFC magnetometer, all covering one solar rotation from a period late in 1977. The solar wind structure at that time was not as steady as one would like for a detailed mapping survey; but for the didactic purposes at hand they will serve quite adequately. The model used for the simulation is virtually identical to that described in Goldstein and Jokipii (1977), with only minor differences in numerical techniques. This is a slight variant of the standard 2-D MHD quasi-steady formalism laid out above, in that electron and proton pressures are accounted for separately, with the electron pressure following a polytropic expression like (6). (The electron polytropic index is $\gamma_e = 1.175$, in consideration of Sittler and Scudder, 1980.) The proton pressure and temperature at each step are derived from total energy conservation (3), thus arbitrarily channeling all the shock heating provided by the artificial viscosity into the protons. This dipolytropic treatment results in a somewhat more realistic description of the electron thermodynamics, but our findings do not depend very critically upon this detail. (A more complete explanation of the model and analysis of the flow structures of late 1977 will appear shortly in papers by Burlaga *et al.* and Pizzo *et al.*, in preparation.)

Figures 6a and 6b show a stacked sequence of speed and total pressure (gas plus magnetic) variations over the radial range 1-30 AU. The curves in each panel portray speed or total pressure as a function of an arbitrary longitude scale, which is shifted in the calculation to make the center of each panel track the average interplanetary spiral.

The increment between the panels is 2 AU (except for the top pair), so the radial evolution can be followed by reading down each plot. Any feature which moves faster or slower than the mean speed (averaged over the rotation) will appear to drift in longitude. For example, the shock fronts associated with the classic CIR's forming just beyond 2 AU expand laterally in the plots though, of course, their propagation is primarily radial. Finally, the speed scale reads 200-700 km/s (linear) for each plot, but the total pressure scale (logarithmic) changes in absolute value. However, the spread in any one pressure plot is always a factor of 1000:1, so shock strengths can always be directly gauged.
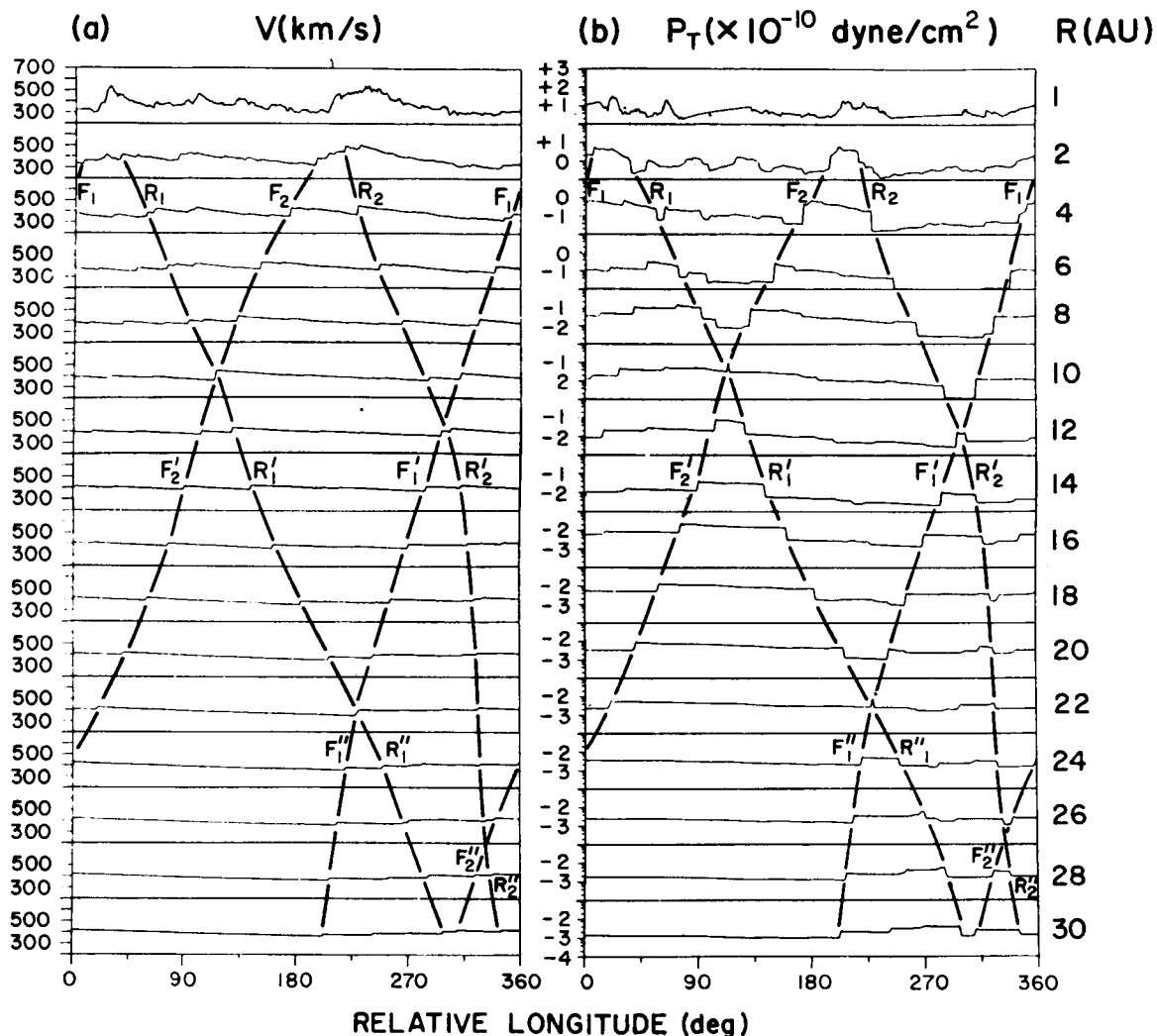
Figure 6). Bulk speed (a) and total pressure (gas + magnetic) (b) versus relative longitude for a solar rotation in late 1977. Heliocentric distance increases downwards. Data gaps in the 1 AU input have been filled in by linear interpolation and periodic boundary conditions are imposed at the longitudinal ends. The diagonal dark lines connect the main forward (F) and reverse (R) shock features, which propagate relative to the flow. Note the velocity scale is fixed; the pressure scale is variable, but always maintains a ratio of 1000:1 between maximum and minimum values. The digits just to the left of the pressure plots indicate the power of 10 by which the base value of 10^{-10} dyne/cm² must be multiplied to fix P_T, e.g. "+2" in the topmost panel denotes $P_T = 10^{-8}$ dyne/cm².

Examining the two figures, we see that out to 10 AU the evolution follows the classic steepening and CIR formation scenario well-known since Pioneer days. Forward and reverse shocks (heavy lines labelled F and R in the plots) form near 2 AU as the streams attain peak compression. The material trapped between finds itself at high pressure relative to its surroundings and begins pushing outwards from the center of the compressed region. Meanwhile, the material in the trailing portions is being steadily rarefied and cooled more rapidly than would a spherically-symmetric flow. Thus the shock strength, as measured by the pressure jumps in Figure 6b, increases rapidly between 2 and 4 AU and remains high out to 10 AU.

At 10 AU, near 120° longitude, something very interesting happens: the reverse shock (R_1) of the leftmost stream at 1 AU meets the forward shock (F_2) of the rightmost original stream. The ensuing interaction gives rise to a new, "secondary" CIR, which is characterized by elevated densities, temperatures, field strengths, and pressures and is flanked by the two modified incident shocks $(F_2'$ and $R_2')$, which have lost considerable strength (as judged by the jumps in total pressure) in the interaction. The other primary pair of shocks $(F_1$ and $R_2)$ meet with similar consequences at 12 AU, near 300° longitude. Both secondary CIR's subsequently expand, with additional interactions (accompanied by further CIR production and reduction in shock strength) at 22 AU, 26 AU, and again just beyond 30 AU. The interactions at 22 and 26 AU are of particular significance, in that shocks from successive Carrington rotations have had time to propagate all the way across the intervening structures and meet. Thus, by the latter point, the entire flow has been shocked at least once.

There are really three main points to be made here. The first is that the quasi-steady dynamics of the solar wind is driven by two distinct mechanisms. The near-sun evolution, out to 4-5 AU or so, is dominated by the familiar kinematic steepening mechanism. In this regime, the structure is characterized by the usual rotationally-coupled interaction of several discrete high-speed and low-speed flows. At about 5-10 AU, however, most of the speed differences have been eliminated and the evolution is instead regulated by the relaxation of pressure waves or pulses (i.e., the CIR's) generated by the previous kinematic interactions. By 8-10 AU, these pressure pulses are themselves beginning to interact, fostering further pressure pulse structure which survives to at least 30 AU. Hence the distant solar wind, even in the quasi-steady limit, differs qualitatively from the near-sun wind in that the primary interaction mechanism is dynamic rather than kinematic. Indeed, the very concept of streams *per se* is relevant only to the near-sun solar wind and has little bearing upon the dynamics of the distant solar wind (Burlaga, 1983).

To quantify these arguments, we turn to Figure 7, which presents a more detailed view of the 30 AU structure. From top to bottom, we have bulk speed, flow angle, density, field strength, proton temperature, and total pressure, respectively. Consider the shock jump near 200° longitude. It is most illuminating to think of the interaction between the faster flow to the right of the jump with the slower flow to the left in terms of a simple collision between two discrete blobs of gas. To an observer moving with the slower flow, the fast material (of density $n = 0.017 \text{cm}^{-3}$) is approaching with a velocity of $w \cong 15$ km/s (assuming a purely radial interaction); thus the fast material exerts a ram pressure of $\rho w^2 \cong 6.4 \times 10^{-14}$ dyne/cm^2. On the other hand, the total pressure differential across the jump is $\Delta P_T \cong 1.0 \times 10^{-13}$ dyne/cm^2. Since what matters are the relative momentum densities, it is evident that pressure forces are going to dominate in this distant solar wind interaction. This result stands in sharp contrast with the near-sun situation, which is readily illustrated by repeating the analysis on the 0.3 AU stream of Figure 2. Transforming to a frame moving with the 300 km/s slow flow, the high speed portion of the stream is found to possess a ram pressure of about 7.5×10^{-8} dyne/cm^2. For the example of Figure
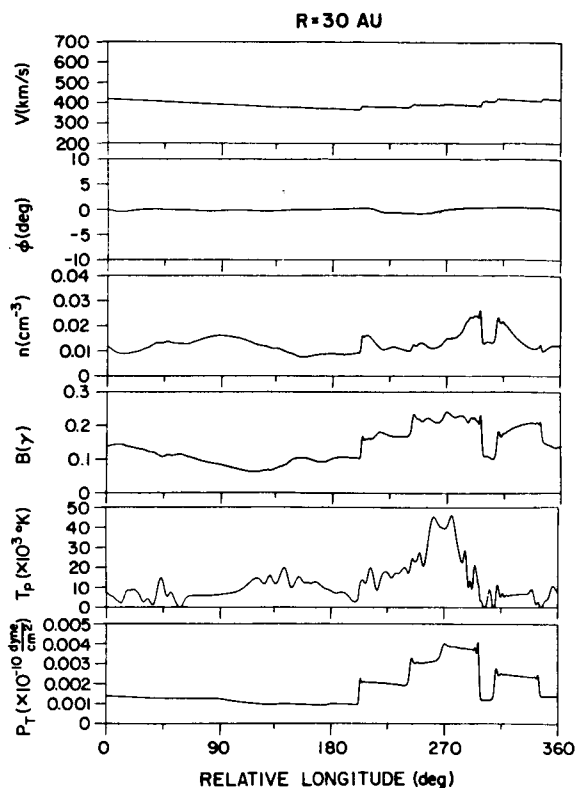
Figure 7). Flow parameters at 30 AU for the streams of Figure 6.
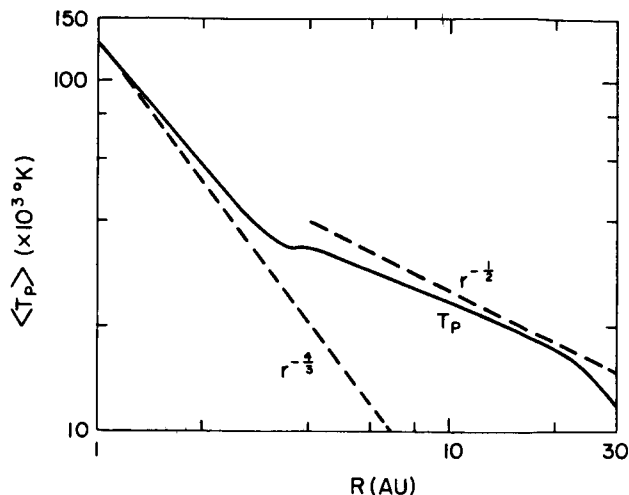
Figure 8). Longitudinally-averaged proton temperature for the streams of Figure 6. The two dashed lines provide theoretical adiabatic and tentative observed dependencies. In this model, the electrons follow a separate polytropic law ($\gamma_e = 1.175$) and the electron temperature goes approximately as $r^{-0.4}$.

2, ΔP_T was specifically chosen to be zero; but even were P_T in the stream doubled relative to that in the slow flow, ΔP_T would still amount to only 1.4×10^{-8} dyne/cm^2. Hence the mechanical advection clearly dominates near the sun.

A second major point is that the relatively dull 30 AU velocity structure portrayed in Figures 6a and 7 does not signify featureless flow, since streams can no longer be taken as the measure of inhomogeneity at these distances. While the variations in the flow speed at 30 AU are so small that the saw-tooth waveform might be very hard to discern in daily sample data of the type collected by Pioneer, the other four parameters show very sizable fluctuations, with pronounced (factor of 2-3) jumps across the CIR fronts. Note also that while the total pressure shows little variation between the big jumps, the density, field strength, and proton temperature all exhibit considerable substructure. This comes about because imbalances in total pressure directly give rise to forces that rapidly wipe out the total pressure gradient, whereas variations in the density, field strength, and temperature need not be individually obliterated to satisfy this condition. Furthermore, much of the magnetic and thermodynamic substructure evident in Fig. 7 is dynamically created in the medium. (the term "substructure" here applies only to numerically resolved features, such as the density and temperature enhancement accompanying the shock near 200° longitude. The higher-frequency oscillations right at the shocks are spurious numerical artifacts.) Refering once more to Figure 6, a number of other propagating features in addition to the two main shock pairs can be traced, smaller amplitude forward and reverse structures (not necessarily shocks) that exist only over a limited span of heliocentric distances. Some of these originate from the real input

structure, some are artifacts of the linear interpolation used to fill data gaps, and some are generated further out by the interaction of the larger CIR fronts with the ambient structure. The resultant thermodynamic structure at 30 AU thus bears virtually no resemblance to the parent 1 AU variations.

Just how realistic these calculations and, indeed, this entire picture of the distant solar wind are remains to be seen. After all, even if the model itself proves substantially accurate, we have here mapped only the flows associated with the streams of one particular rotation. The larger streams associated with the Skylab epoch, for example, might survive as separate entities to greater heliocentric distances. In that case, the interaction of shocks from adjacent streams may occur while substantial velocity gradients still exist and the details of the subsequent evolution may therefore change somewhat (e.g., see the 1-D calculation by Dryer and Steinolfson, 1976). Moreover Burlaga (1983) suggests that by 25 AU so much interaction of pressure waves will have occurred that deterministic models of the sort used to produce the above plots may not be applicable at all, that a description based upon the concepts of MHD turbulence might be more appropriate. Further justification for such an approach could be taken from considerations of the effects of swept-up transients. It is to be stressed (Burlaga, this Conference; Burlaga *et al.*, 1983) that, at least in the active phase of the solar cycle, embedded transients will severely complicate the structure of the distant solar wind, perhaps to the point of obviating direct modeling efforts.

Be that as it may, the third and final comment I will make on these matters is that it is high time to dispense with these idle speculations and to engage in some serious comparisons between observation and theory. While it is worthwhile and even imperative to attempt conventional radial-alignment mappings with the data in hand, our enthusiasm and expectations must be tempered by the cold realization that most of these observations refer to that period of the solar cycle when the corona is least steady and structured and transient effects are most pronounced. This situation should improve dramatically in the next few years as the sun settles down once again toward solar minimum. For the present, however, far brighter prospects might be in store for a more statistical approach. Obvious tests would include, for example, the radial behavior of the pressure and velocity jumps at shocks, the rate of forward and reverse shock occurrence and decay, the distance to which stream interfaces are visible, the longitudinal structure of the thermodynamic quantities, etc. It may even be possible to pick out newly-formed secondary CIR's as described above and to see if the heliocentric distance of formation agrees with the model predictions. With sufficiently high sampling rates, these structures (if they exist) should stand out by virtue of the close spacing between the forward and reverse shocks and the concomitant high values of density, temperature and field strength, all of which together would be hard to explain in terms of a discrete disturbance propagating all the way from the sun. An important quantitative distinction between the Hundhausen (1973b) hypothesis and MHD models is also amenable to observation. In the hydrodynamic description, CIR shocks in the distant solar wind can actually increase with strength owing to the monotonic decline in sound speed. With the field included, however, the characteristic speed approaches a constant and hence the shock fronts erode more rapidly, thereby providing a measurable discriminant.

Another lucrative endeavor would be to examine rotation-by-rotation averages of interesting quantities like the proton temperature. Earlier theoretical work by Goldstein and Jokipii (1977) suggested significant heating by shock dissipation beyond 2 AU, perhaps resulting in a high-temperature plateau near 5 AU. Heating of the solar wind by interaction with interstellar neutrals might have similar ramifications (Holzer, 1972). Analyses of Pioneer (Mihalov and Wolfe, 1978; Kayser *et al.*, 1983) and Voyager (Gazis and Lazarus, 1982) data, while sorely afflicted with temporal effects, seem to imply a more-

or-less monotonic fall-off in proton temperature of about $r^{-0.5}$ to $r^{-0.7}$. The corresponding predictions of the particular calculation described above (Figure 8) are consistent with these last-quoted values, but it would be desirable to run simulations on other stream data before claiming success. Accurate determination of the average temperature profile may also make it possible to distinguish shock heating from interstellar heating. For example, Figure 8 shows a distinct rapid decline in the mean temperature beyond 20 AU. What is happening in the model is that the velocity jumps are falling below the fast-mode speed (essentially the Alfven speed at these distances), i.e., most of the sawtooths have decayed from shocks into large amplitude MHD waves, which do not contribute to the overall heating. To the contrary, no drop in mean temperature beyond 20 AU would be anticipated if interstellar heating were important. Also, a general rise in the sound speed associated with interstellar heating would tend to erode the saw-tooth velocity features more rapidly than would the simple dynamical process. Hence mere observation of saw-tooths at these distances would lend credence to the dynamic view.

The Effect of Weak Time-Dependence
Upon Stream Evolution

As alluded to above, significant discrepancies between theory and observation persist even when all the dynamic factors included in equations (1) -(4) are accounted for. The worst of these, uncovered by Helios, is illustrated in Figure 9. Each of the panels displays the velocity data from one complete Carrington rotation observed during the Helios A primary mission (Rosenbauer et al., 1977). The data in the top panel were taken when the spacecraft was near 0.98 AU, the next from 0.90 AU, then 0.67 AU, and finally 0.4 - 0.3 AU. The most striking feature is the abrupt, square-wave shape of the perihelion stream (denoted by the arrowhead over the bottom panel). On the basis of early models, such structures (and more were subsequently observed) should give rise to shock pairs well inside 1 AU; but corotating shocks are a very rare phenomenon inside the orbit of earth. More disturbing was the rounding of the stream fronts with radius, which seemed to be totally at odds with established views on stream steepening. With the inclusion of the full list of dynamical mechanisms in (1) -(4), the disagreement was reduced, but not eliminated. Various mechanisms aimed at broadening the streamfronts have since been suggested (e.g. D'Angelo et al., 1979), but these can hardly be regarded as convincing.

I would therefore like to speculate on a possible mechanism that has heretofore been overlooked but is very straightforward and within the grasp of modern computational techniques. Namely, I propose that many of the residual discrepancies between observation and theory can be explained in terms of weak time dependence of the flows emanating from the corona. What I am talking about here is not the impulsive, dramatic outbursts associated with flares and coronal transients, but rather slower, modest temporal effects associated with the ongoing, continual evolution of the corona.

There is solid observational support for change in the corona on all time scales, and I need not belabor the point (e.g. see House, this Conference). Similarly, evidence for interplanetary variability on time scales of the order of a day or two is abundant (Gosling, 1971; Gold et al., this Conference). Explicit insight is to be gained from Figure 10, which shows 1 AU spacecraft observations from J. King's WDC compilation. Depicted are several rotations' worth of velocity data from the most stable period of the solar cycle. While the same pair of streams indisputably recur over and over, detailed differences from rotation to rotation are evident. Substructure with amplitudes of 100-200 km/s comes and goes, and the shape and location of the stream fronts shift back and forth. But how far from the absolutely steady idealization of the models may these temporal variations stray before noticeable effects ensue? And what is the nature of these effects?

HELIOS A PRIMARY MISSION

CARRINGTON
ROTATION
1621
1622
1623
1625

CARRINGTON LONGITUDE (deg)
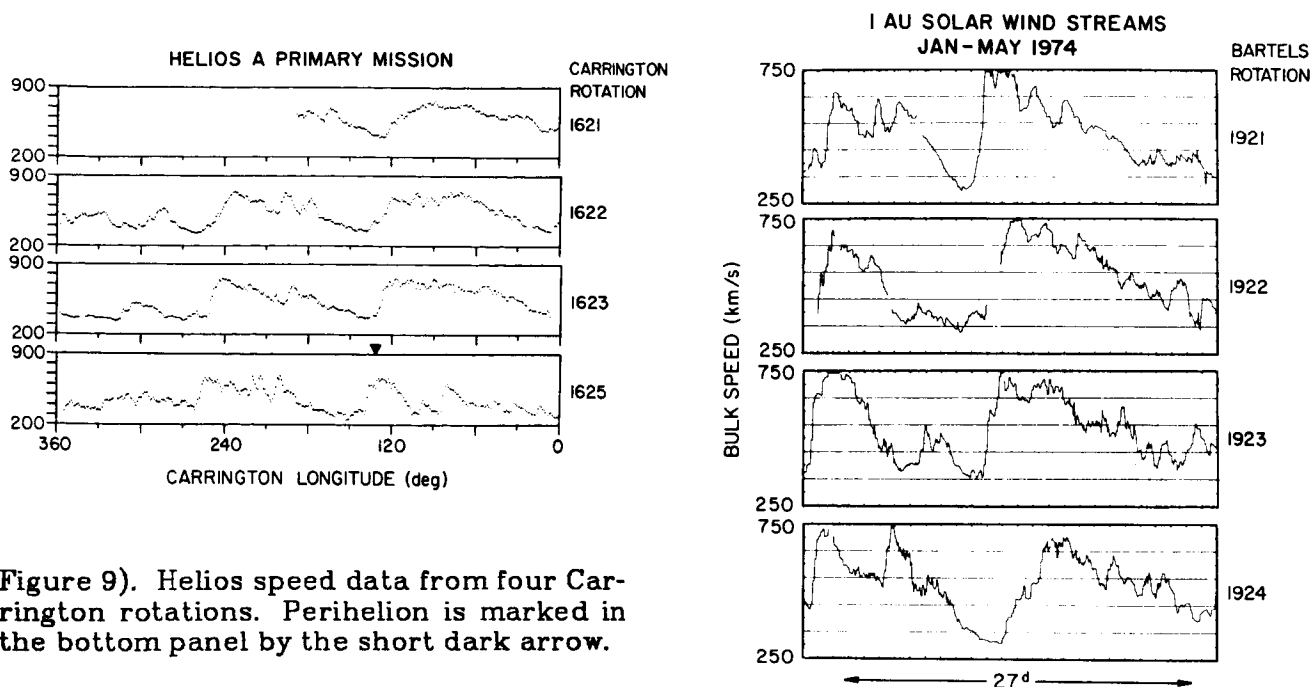
Figure 9). Helios speed data from four Carrington rotations. Perihelion is marked in the bottom panel by the short dark arrow.

I AU SOLAR WIND STREAMS
JAN – MAY 1974

BARTELS
ROTATION
1921
1922
1923
1924

BULK SPEED (km/s)

27ᵈ

Figure 10). WDC-A 1.0 AU solar wind speed data from four Bartels rotations in 1974.

My ideas on the subject are illustrated in Figure 11. (The visual interpretation of this entire Figure is not immediately obvious, and some reflection may be required to grasp its meaning.) At the top we have a schematic representation of an ideal steady flow, again looking down upon the ecliptic plane from the north. At the $r_0 = 0.2$ AU inner boundary, this simplified solar wind consists of three 90° "sectors" in each of which the flow speed is either uniformly "slow" (light shaded, v = 300 km/s) or uniformly "fast" (medium shaded, v = 500 km/s). All the fluid passing through r_0 in a twelve-hour period is delineated by an arc-shaped "segment". The segments associated with the high-speed flow therefore have 5/3 the radial extent of the slow-flow ones. All the way between r_0 and the $r = 2.0$ AU outer boundary, the evolution is taken to be purely kinematic. The dark-shaded area indicates where the high speed segments overlap the slow-speed segments, corresponding to the compression region in a dynamic model. The white area in the lower left quadrant, where the fast flow has outrun the succeeding slow flow, similarly corresponds to a rarefaction region. Thus Figure 11 is a snapshot of the location of all the fluid segments at some particular instant of time. In this absolutely steady idealization, the boundaries of the various regions are smooth and regular, the flow within each region is totally devoid of substructure, and the entire spiral pattern corotates without real temporal change.

- -

Figure 11), next page. Schematic of (a) strictly-corotating (time-independent) and (b) quasi-steady (weakly time-dependent) solar wind flow. Light shading denotes slow (300 km/s) wind, medium shading denotes high-speed flow (~500 km/s), and dark shading denotes regions where fast and slow flows interact (overlap, in this kinematic projection).

(a) COROTATING

(b) WEAKLY TIME-DEPENDENT
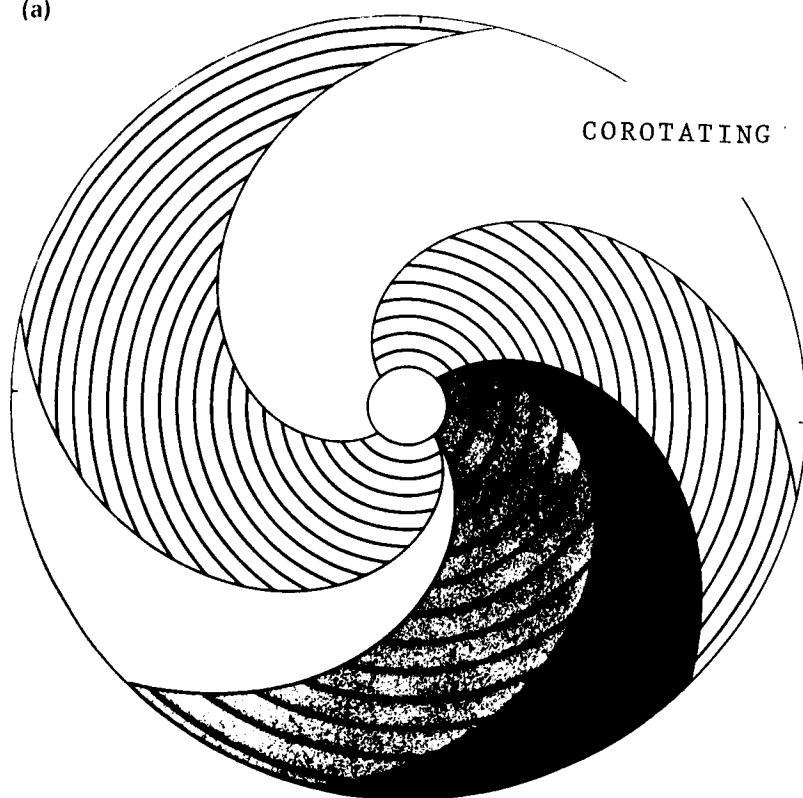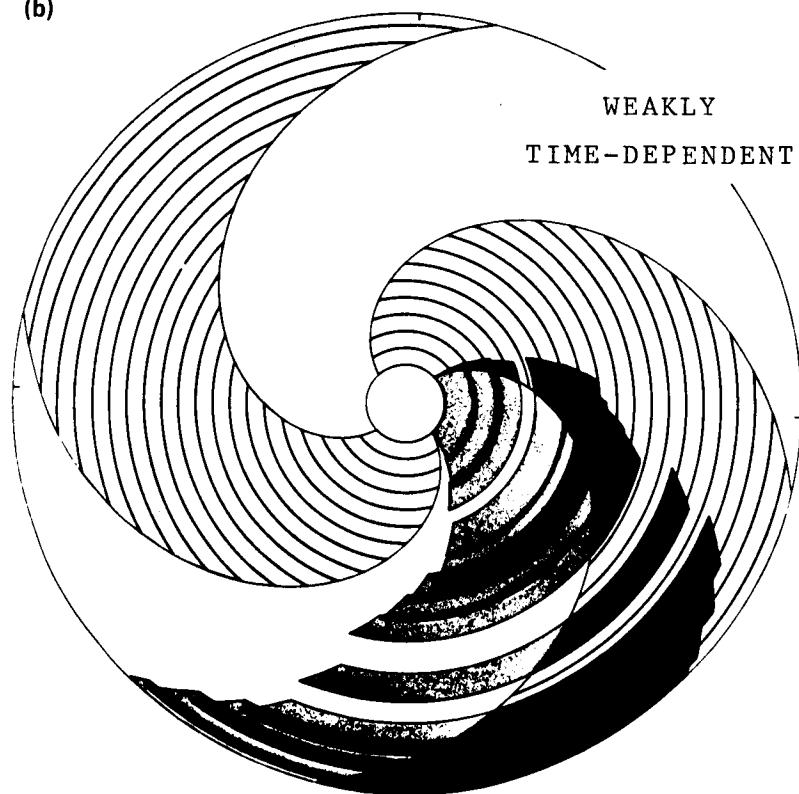
In the lower portion of Figure 11, we consider what happens when a crude time-dependence is introduced. The two slow-flow sectors are kept at 300 km/s as before, but the speed of each segment within the high-speed sector is arbitrarily allowed to change (discontinuously) at the end of every 12-hour interval by a pseudo-random amount within a ± 75 km/s range about 500 km/s. Thus the high speed segments not only overlap the ambient as in the top panel (a), but they also interact with each other. There are two main effects: (1) the boundaries of the "compression" and "rarefaction" regions are no longer smooth and regular, but fluctuate in time and space about the nominal 500 km/s boundaries; and (2), considerable substructure (miniature compressions and rarefactions) has appeared within the high-speed sector. If one now mentally generalizes the picture to allow for variations in the slow flow and furthermore permits longitudinal (and latitudinal) changes as well, it should be evident that though the basic slow-fast-slow structure remains discernible, temporal variations of even this modest amplitude envisioned above should have complicated and perceptible interplanetary consequences.

Qualitatively, we can readily deduce what the most likely observable effects will be. Beyond the trivial conclusions that at least some of the substructure within streams is of temporal origin and that multi-spacecraft and synoptic analyses are impaired by such activity, there should be some important systematic consequences that may not be so obvious. Consider the nature of the substructure engendered by weak time-dependence: it not only has a temporal scale, but a spatial one as well. And from the standpoint of dynamics, it is the spatial scale that is the more significant one. Why so? It has been known for some time that the solar wind acts like a low-pass filter in that small scale variations evolve more rapidly than large scale ones (e.g. Gosling *et al.*, 1976; Hundhausen and Pizzo, unpublished manuscript). Some of this behavior can be seen in the first several panels of Figure 6a, where numerous small scale velocity features at 1 AU have been wiped out by dynamic interaction with adjacent portions of the flow by 4 AU. What this portends for our weakly time-dependent flow is as follows: at any given point, the flow that is observed is the dynamic product of all the fluid "segments" that can reach that point at a given time. Near the sun, say at 0.3 AU, there is not much time for flow segments of differing speeds and times of origin to interact; thus the flow observed, particularly over any suitable short time span such as that required to record the passage of a stream front, is pretty much the instantaneous interplanetary image of the coronal source flow at that time. Farther out, say at 1 AU, many of the segments have had a chance to interact and the resultant flow is no longer a pure image of the coronal flow at any given time; rather it is a mishmash of various flow states, in which a succession of initially-sharp coronal flow boundaries have been transformed into a rounded interplanetary streamfront by the dynamic interaction of the temporally-driven substructure. Finally, at very great heliocentric distances, only the largest spatial scales survive and the evolution proceeds very nearly along the lines of the steady idealization. But even here, the flow seen at, say, 4 AU is not simply related to the coronal source flow at any one particular instant of time; instead, it is more faithfully the image of the composite, dynamically-mixed structure at 1 or 2 AU.

This description has necessarily been qualitative and has resorted to kinematics to press a point. Clearly, quantitative evaluation of these conjectures can only be achieved through the auspices of a full-blown 2-D MHD model, several of which have appeared in the literature (e.g. Nakagawa and Wellck, 1973; D'Uston *et al.*, 1981). Since the precise nature of weak temporal change in the corona is unknown, one of the primary objectives of such a modeling study would be to establish the minimum variation necessary to produce appreciable interplanetary effects. For example, it might be found that minor speed variations along the high-speed low-speed boundary alone could suffice to explain the apparent desteepening of streams. Though such a study would be computationally expensive, I feel confident the results would adequately compensate the efforts and constitute a meaningful contribution to our knowledge of corotating stream dynamics.

Acknowledgements

Bibliography

Burlaga, L. F., Corotating pressure waves with streams in the solar wind, submitted to J. Geophys. Res., 1983.

Burlaga, L. F., and E. Barouch, Interplanetary stream magnetism: Kinematic effects, Astrophys. J., 203, 257, 1976.

Burlaga, L. F., R. Schwenn, and H. Rosenbauer, Dynamical evolution of interplanetary magnetic fields and flows between 0.3 AU and 8.5 AU: Entrainment submitted to Geophys. Res. Lett., 1983.

Carovillano, R. L., and G. L. Siscoe, Corotating structure in the solar wind, Solar Phys., 8, 401, 1969.

D'Angelo, N. D., G. Joyce, and M. E. Pesses, Landau damping effects on solar wind fast streams, Astrophys. J., 229, 1138, 1979.

Dryer, M., Z. K. Smith, E. J. Smith, J. D. Mihalov, J. H. Wolfe, R. S. Steinolfson, and S. T. Wu, Dynamic MHD modeling of solar wind corotating stream interaction regions observed by Pioneer 10 and 11, J. Geophys. Res., 83, 4347, 1978.

Dryer, M., and R. S. Steinolfson, MHD solution of interplanetary disturbances generated by simulated velocity perturbations, J. Geophys. Res., 81, 5413, 1976.

D'Uston, C., M. Dryer, S. M. Han, and S. T. Wu, Spatial structure of flare-associated perturbations in the solar wind simulated by a two-dimensional numerical MHD model, J. Geophys. Res., 86, 525, 1981.

Gazis, P. R., and A. J. Lazarus, Voyager observations of solar wind proton temperature: 1 - 10AU, Geophys. Res. Lett., 9, 431, 1982.

Goldstein, B. E., Nonlinear corotating solar wind structure, Rep. CSR-P-71-63, Mass. Inst. of Technol., Cambridge, 1971.

Goldstein, B. E., and J. R. Jokipii, Effects of stream-associated fluctuations upon the radial evolution of average solar wind parameters, J. Geophys. Res., 82, 1095, 1977.

Gosling, J. T., Variation in the solar wind speed along the Earth's orbit, Solar Phys., 17, 499, 1971.

Gosling, J. T., A. J. Hundhausen, V. Pizzo, and J. R. Asbridge, Compressions and Rarefactions in the solar wind: Vela 3, J. Geophys. Res., 77, 5442, 1972.

Gosling, J. T., A. J. Hundhausen, and S. J. Bame, Solar wind stream evolution at large heliocentric distances: Experimental demonstration and the test of a model, J. Geophys. Res., 81, 2111, 1976.

Gosling, J. T., J. R. Asbridge, S. J. Bame, and W. C. Feldman, Solar wind stream interfaces, J. Geophys. Res., 83, 1401, 1978.

Holzer, T. E., Interaction of the solar wind with the neutral component of the interstellar gas, J. Geophys. Res., 77, 5407, 1972.

Hundhausen, A. J., Nonlinear model of high-speed solar wind streams, J. Geophys. Res., 78, 1528, 1973a.

690

Hundhausen, A. J., Evolution of large-scale solar wind structures beyond 1 AU, J. Geophys. Res., 78, 2035, 1973b.

Hundhausen, A. J., and J. T. Gosling, Solar wind structure at large solar heliocentric distances: An interpretation of Pioneer 10 observations, J. Geophys. Res., 81, 1436, 1976.

Hundhausen, A. J., and L. F. Burlaga, A model for the origin of solar wind stream interfaces, J. Geophys. Res., 80, 1845, 1975.

Jokipii, J. R., and L. Davis, Jr., Long-wavelength turbulence and the heating of the solar wind, Astrophys. J., 156, 1101, 1969.

Kayser, S. E., A. Barnes, and J. D. Mihalov, The far reaches of the solar wind: Pioneer 10 and 11 plasma results, submitted to Astrophys. J.

Matsuda, T., and T. Sakurai, Dynamics of the azimuthally-dependent solar wind, Cosmic Electrodynamics, 3, 97, 1972.

Mihalov, J. D., and J. H. Wolfe, Pioneer-10 observation of the solar wind proton temperature heliocentric gradient, Solar Phys., 60, 399, 1978.

Nolte, J. T., A. S. Krieger, E. C. Roelof, R. E. Gold, High coronal structure of high velocity solar wind stream sources, Solar Phys., 51, 459, 1977.

Nakagawa, Y., and R. E. Wellck, Numerical studies of azimuthal modulation of the solar wind with magnetid fields, Solar Phys., 32, 257, 1973.

Pizzo, V., A three-dimensional model of corotating streams in the solar wind. 1. Theoretical Foundations, J. Geophys. Res., 83, 5563, 1978.

Pizzo, V., An evaluation of corotating stream models, in Solar Wind Four, MPAE-W-100-81-31, H. Rosenbauer, ed., p. 153, 1981.

Pizzo, V., A three-dimensional model of corotating streams in the solar wind. 3. Magnetohydrodynamic streams, J. Geophys. Res., 87, 4374, 1982.

Riesebieter, W., Dreidimensionale Modelrechnungen zum solaren Wind, Ph. D. thesis, Tech. Univ. zu Braunschweig, Federal Republic of Germany, 1977.

Rosenbauer, H., R. Schwenn, E. Marsch, B Meyer, H. Miggenrieder, M. D. Montgomery, K. H. Muhlhauser, W. Pilipp, W. Voges, and S. M. Zink, A survey of initial results of the Helios plasma experiment, J. Geophys., 42, 561, 1977.

Siscoe, G. L., Structure and orientation of solar wind interaction fronts: Pioneer 6, J. Geophys. Res., 77, 27, 1972.

Sittler, E. C. Jr., and J. D. Scudder, An empirical polytrope law for solar wind thermal electrons between 0.45 and 4.67AU: Voyager 2 and Mariner 10, J. Geophys. Res., 85, 5131, 1980.

Smith, E. J., and J. H. Wolfe, Observations of interaction regions and corotating shocks between one and five AU: Pioneers 10 and 11, Geophys. Res. Lett., 3, 137, 1976.

Steinolfson, R. S., M. Dryer, and Y. Nakagawa, Numerical MHD simulation of interplanetary shock pairs, J. Geophys. Res., 80, 1223, 1975.

Whang, Y. C., Magnetohydrodynamics of corotating interplanetary structures, J. Geophys. Res., 85, 2285, 1980.

Whang, Y. C., and T. H. Chien, Magnetohydrodynamic interaction of high-speed streams, J. Geophys. Res., 86, 3263, 1981.

ASSOCIATIONS BETWEEN CORONAL MASS EJECTIONS AND INTERPLANETARY SHOCKS

N.R. Sheeley, Jr., R.A. Howard, M.J. Koomen*, D.J. Michels
E.O. Hulburt Center for Space Research
Naval Research Laboratory
Washington, DC 20375

and

R. Schwenn, K.H. Muhlhauser, H. Rosenbauer
Max-Planck-Institut fur Aeronomie
Katlenburg-Lindau 3, FRG

ABSTRACT

We are in the process of comparing nearly continuous complementary coronal observations and interplanetary plasma measurements for the years 1979-1982. Our preliminary results show that almost all low-latitude high-speed coronal mass ejections (CME's) were associated with shocks at HELIOS 1. Some suitably directed low-speed CME's were clearly associated with shocks while others may have been associated with disturbed plasma (such as NCDE's) without shocks. A few opposite-hemisphere CME's associated with great flares also seemed to have been associated with shocks at HELIOS.

Introduction

Since March 1979 the NRL white-light coronagraph (SOLWIND) has been monitoring the solar corona routinely from the Earth-orbiting satellite P78-1 while the MPAe plasma detector has been monitoring interplanetary conditions from the Sun-orbiting spacecraft HELIOS 1. During this time, the orbital phase and 0.5-year period of HELIOS 1 caused it to dwell for 6-month intervals alternately off the east and west limbs of the Sun as seen from Earth (Figure 1). In this configuration, HELIOS has been ideally situated to detect the interplanetary signatures of coronal mass ejections (CME's) in or near the plane of the sky where they are most visible from Earth. In the limited space available here, we shall summarize our progress in comparing these complementary observations during 1979-1981 and the beginning of 1982. Other discussion and illustrations are contained in the earlier paper by Schwenn (1982).
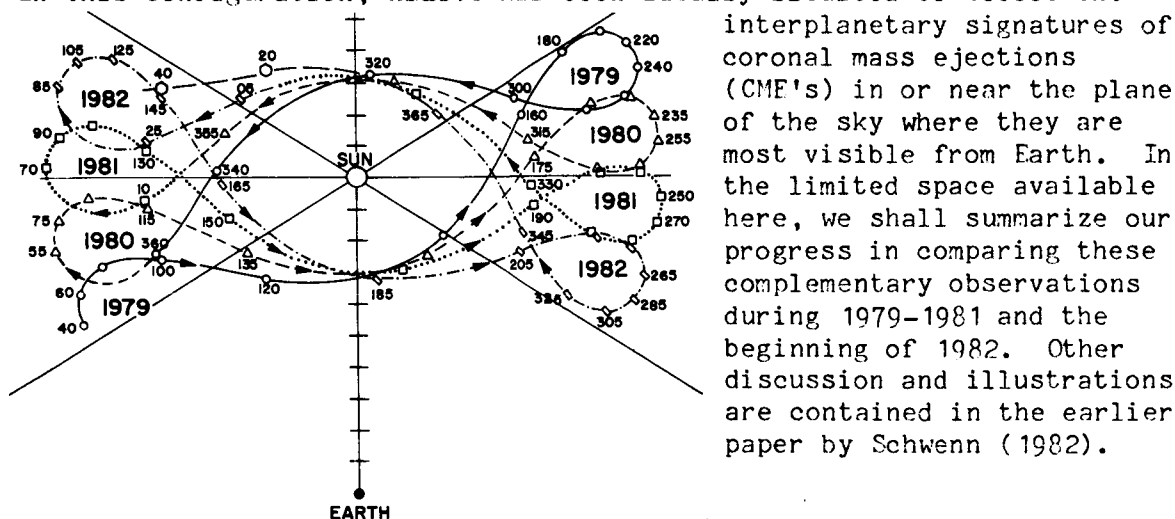

Figure 1 The HELIOS 1 orbit in a fixed Sun-Earth system during 1979-1982. Annually coded tick marks are placed at 20-day intervals, and reference lines are drawn at $\pm 32^{o}$ to the east-west direction.

* Sachs/Freeman Associates, Inc., Bowie, MD.

Although our initial objective was to identify and characterize the interplanetary signatures of coronal mass ejections, we thought that it would be more efficient to begin with the reverse association. We supposed that most outward-moving interplanetary disturbances would have detectable sources at the Sun, whereas many solar-generated disturbances would either miss HELIOS 1 or not reach it at all. In principle, after we had identified all of the HELIOS-effective CME's, we could then look to see if any of the remaining ones had interplanetary signatures that we might have overlooked initially.

Considering the vast number of irregular plasma fluctuations that might be expected at HELIOS since 1979, we began by identifying only the most prominent structures. To our surprise, nearly all of them were shocks and relatively few were non-compressive density enhancements (NCDE's) or other large density fluctuations. This meant that, at least as a starting point, we could limit our selection of prominent interplanetary disturbances to shocks without losing an appreciable number of events. This restriction had the advantage that forward shocks could be identified easily and objectively by a simultaneous sudden increase in proton speed, density, and temperature (as well as magnetic field strength for fast-mode shocks). Moreover, it would be relatively effortless to generalize our selection to include all shocks, not just the prominent ones. Although we would eventually identify and search for the origin of non-shock disturbances such as NCDE's and magnetic clouds, for the moment we should hope to obtain those relations from a consideration of the inverse (forward) associations. We have already found several examples of magnetic clouds in the driver gas following CME-associated shocks (cf. Schwenn, 1982), one of which has been described in detail by Burlaga et al. (1982).

Preliminary Results

A. From Shocks to CME's

To date (March 17, 1983), we have identified 80 shocks while HELIOS was within $\pm$ 30° of the Sun's east or west limbs and during which there were complementary SOLWIND observations. In an exploratory and partially subjective process, we have looked to see whether these shocks were associated with CME's that originated at the Sun a few days earlier, the exact time interval depending on HELIOS's distance from the Sun and an assumed average transit speed in the range 500-1500 km/sec. The breakdown of associated CME's was:

Table 1

YES	40	(50%)
POSSIBLE	19	(24%)
INDETERMINATE	20	(25%)
DOUBTFUL	1	(1%)
TOTAL	80	(100%)

In general, YES meant that we found a big, bright, suitably-timed CME whose projected direction was (with two exceptions) toward HELIOS. The fact that the two exceptional CME's were especially large (rare) and occurred in the absence of other candidates gave us some confidence that these two ill-directed associations were not coincidences. POSSIBLE meant that we found a suitably-timed CME whose association seemed possible, but less obvious, due to

a variety of factors such as the CME's faintness, small size, and unfavorable direction together with some coronal data gaps that could have hidden a more likely candidate.

INDETERMINATE meant that substantial data gaps made it impossible to determine whether or not a respectable and suitably-timed CME might have occurred. Within each search interval of 1-3 days (depending on HELIOS's distance from the Sun) such data gaps sometimes ranged from 8 hours to 24 hours of each day. For one relatively weak shock (1/23/81), the coronal observations were reasonably complete, but showed no candidate CME. There was a single 8-hour data gap, but the lack of obvious changes across the gap made the occurrence of a CME seem unlikely. We called this association DOUBTFUL. Further study of the POSSIBLE and INDETERMINATE cases may help to clarify whether or not some shocks (other than co-rotating shocks or bow-shocks) are undetectable as they transit the coronagraph's field of view.

Table 2 summarizes the 40 confident associations. The bottom line shows the average values of CME speed v(CME), shock transit speed v(AVE), and in situ shock speed v(SH) for those associations for which all three values were known. (v(SH) was computed from the mass flux conservation equation assuming the flow to be normal to the shock surface.) The three speeds v(CME), v(AVE), and v(SH) had the average values 755, 750, and 672 km/sec, respectively. The near equality of v(CME) and v(AVE) reflects the averaging effect of the high-speed but decelerating events for which v(CME) > v(AVE) and the low-speed accelerating events for which v(CME) < v(AVE). Approximately half of these CME's were associated with obvious SMS-GOES 1-8 A X-ray events, and for the associated ones the average X-ray duration was 5.5 hours. 45% of the shocks were followed by disturbed conditions that marked the presence of possible driver gas.

In those cases for which we have examined interplanetary magnetic field measurements (courtesy Dr. F. Neubauer), we have tabulated the Alfvenic Mach number, M, defined as the shock speed relative to the ambient flow divided by the Alfven speed in the ambient plasma. To the extent that the Alfven speed greatly exceeds the local sound speed, M approximates the fast-mode Mach number and should exceed 1 for fast-mode shocks. (The shocks in this list of confident associations were all fast-mode shocks in the sense that the field strength increased behind each shock. However, we did find some slow-mode shocks whose associations with CME's are classed as POSSIBLE.) Table 2 shows that, on the average, these shocks were relatively strong with M=3.4, and that virtually all of them had $M \gtrsim 1$. We have tabulated the density ratio, n_2/n_1, across the shock because it was currently available for all but the most poorly observed shocks. As one can see, this value was in the range 1-4 (as required by the Rankine-Hugoniot relations) and had a respectable average value of 2.4.

Note that the CME's in Table 2 tended to be centered at low latitudes ($23°$ on the average), and were relatively broad (averaging $\pm 43°$ on either side of center). As mentioned above, only two of these CME's (4/1/81 and 4/10b/81) originated on the west limb when HELIOS 1 was off the east limb. The fact that these two associations were so convincing suggests that on rare occasions a major CME may generate a shock wave that extends through a very wide longitude range, and that one or two similar opposite-limb associations now classed as POSSIBLE, INDETERMINATE or DOUBTFUL may be valid associations.

TABLE 2   INTERPLANETARY SHOCKS AND THEIR ASSOCIATED CME's

CME		SHOCK		V_{CME}	V_{AVE}	V_{SH}	X-RAY DURATION	DENSITY RATIO	ALFVENIC MACH NO.	
DATE	LOCATION	DATE	LOCATION		(km/sec)		(HRS)	N2/N1	M	PISTON?
5/27/79	N15($\pm$25)-W	5/28/79	0.43AU, W90	270	560	605	——	3.0	4.2	YES
6/9/79	S40($\pm$40)-W	6/11/79	0.60, W112	600 A	480	325	——	1.8	1.5	NO
7/3/79	N30($\pm$40)-W	7/5/79	0.83, W120	590	610	~655	——	~3.2	~5 ?	?
7/19/79	N45($\pm$45)-W	7/21/79	0.93, W120	$\gtrless$550	740	460	?	2.7	——	NO
10/10/79	S08($\pm$18)-W	10/13/79	0.72, W106	~170 ?	~475	440	——	2.4	1.3	YES ?
2/27/80	S40($\pm$30)-E	2/29/80	0.98, E78	$\gtrless$600	690	580	3	1.4	2.2	NO
3/2/80	S70($\pm$90)-E	3/5/80	0.98, E79	——	750 ?	525	——	2.5	3.0	YES
3/19/80	S30($\pm$30)-E	3/22/80	0.92, E84	550 A	490	435	——	1.5	4.7	NO
3/27/80	S20(?)-E B	3/29/80	0.89, E85	——	770	640	5	2.7	——	YES
6/18/80	N00($\pm$50)-W	6/19/80	0.53, W91	——	620	530	——	3.9	6.2	YES
6/20/80	N35($\pm$50)-W	6/22/80	0.57, W95	~250	430	415	——	2.8	——	?
7/9/80	N25($\pm$25)-W	7/10/80	0.76, W106	——	~680	550	——	3.7	1.7	YES ?
7/18/80	S20($\pm$70)-W	7/20+/80	0.84, W106	~400 ?	545	~465 ?	——	~1.9 ?	~4.9 ?	?
7/29/80	S20($\pm$40)-W	8/1/80	0.91, W106	~700 ?	550	495	3	2.0	1.6	NO
9/1/80	N10($\pm$50)-W	9/3/80	0.98, W99	960	770	590	——	2.2	4.8	YES
11/14/80	N25($\pm$50)-W	11/14b/80	0.51, W107	~1100 ?	~1510	1305	8	?	5.7	YES
11/17/80	N10($\pm$30)-W	11/18/80	0.46, W115	225	665	~565 ?	——	~1.6 ?	$\gtrless$1 ?	NO
1/25/81	S25($\pm$65)-E	1/27a/81	0.84, E83	——	890	705	——	2.1	2.2	YES
1/26/81	N00($\pm$30)-E	1/27b/81	0.84, E83	~1200	875	~700	——	~1.9 ?	~0.8 ?	NO
2/26/81	S05($\pm$45)-E	3/1/81	0.98, E88	660	760	655	5	3.9	——	YES
3/6/81	N00($\pm$50)-E	3/9/81	0.98, E91	——	550	445	——	3.6	——	NO
3/19/81	N40($\pm$35)-E	3/21/81	0.97, E95	——	~745	660	——	1.7	——	NO
4/1/81	S50($\pm$50)-W	4/3/81	0.94, E99	1200	740	510	5	1.8	——	NO
4/6/81	N30($\pm$35)-E	4/8/81	0.92, E100	~950	905	730	2	1.7	1.1	?
4/10a/81	N20($\pm$45)-E	4/13a/81	0.89, E100	810	520	435	2	1.7	2.2	——
4/10b/81	N25($\pm$50)-W	4/13b/81	0.89, E100	——	570	770	3	2.1	5.2	YES
4/18/81	[S45($\pm$25)-E] [& $\overline{360}°$]	4/20/81	0.85, E101	[1130] [& 750]	740	~530 ?	——	?	~2.2 ?	YES
5/8/81	N25($\pm$60)-E	5/10/81	0.67, E95	1000	970	650	12	2.7	2.7	NO
5/10/81	N05($\pm$40)-E	5/11/81	0.66, E95	1460	1440	~1330	7	2.5	4.6	YES
5/13/81	N15($\pm$50)-E	5/13/81	0.63, E94	1500	1470	1310	9	2.0	5.1	YES
5/16/81	360°	5/16/81	0.59, E93	——	1790	$\gtrless$605	13	——	$\gtrless$1	?
7/20/81	S10($\pm$55)-W	7/21/81	0.72, W90	——	870	735	4	2.9	——	YES
7/22/81	S30($\pm$40)-W	7/24/81	0.74, W91	800	710	635	10 ?	2.2	——	NO
10/18/81	N40($\pm$40)-W	10/20b/81	0.89, W76	~850 ?	620	555	——	2.9	——	NO
11/15/81	N05($\pm$55)-W	11/16/81	0.67, W79	$\gtrless$550 ?	680	545	3	2.6	——	?
11/18/81	N00($\pm$60)-W	11/20a/81	0.63, W82	900 A	910	~1170 ?	5	2.0	——	YES
11/19/81	N25($\pm$25)-W	11/20b/81	0.63, W82	800	790	985	4	1.5	——	YES
1/10/82	N25($\pm$25)-E	1/12/82	0.54, E110	570	455	405	EPL	1.7	——	?
2/10/82	N35($\pm$20)-E	2/11/82	0.84, E98	>500 ?	1020	765	1	1.9	——	NO
2/23/82	S20($\pm$40)-E	2/27/82	0.93, E100	365	500	435	——	2.4	——	YES
AVE.:	LAT 23°($\pm$43°)			755	750	672	YES 19 (48%) NO 21 (52%) AVE. 5.5 HRS	2.4	3.4	YES 18 (45%) NO 14 (35%) IND. 8 (20%)

A. These three events accelerated to the indicated speeds before leaving the field of view.

B. The 3/27/80 CME occurred in a SOLWIND data gap, but was observed by the HAO/SMM coronagraph (Illing and Sawyer, 1983).

This conclusion is consistent with past studies of interplanetary shocks associated with certain great solar flares (cf. Intrilligator 1980). However, as we shall see in section B, most major CME's do not show such a broad heliospheric influence, especially in latitude.

Finally, note that five of these confidently associated CME's had speeds less than 400 km/sec. The transit and in situ speeds were self-consistent, but were substantially higher than the observed CME speeds. We believe that this reflects the fact that some initially slow CME's produce higher-speed interplanetary shocks. It does not seem to be the result of an incorrect association or a low-speed projection of a high-speed CME well out of the sky plane. We suppose that either a much faster shock preceded the front of the coronal material or that the ejected material accelerated outside of our 10 $R_\odot$ field of view. (Accelerations of coronal material sometimes occurred in our field of view; in Table 2 we indicated such cases by the letter "A".)
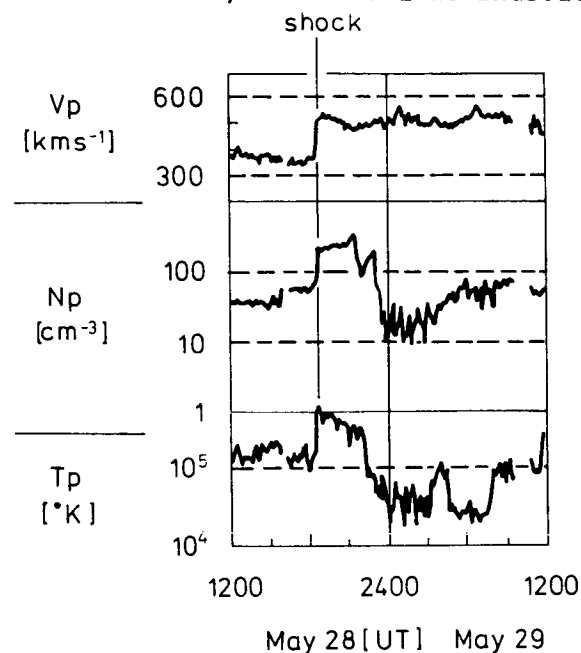

Figure 2 shows a 270 km/sec mass ejection on May 27, 1979 and its associated shock at HELIOS on May 28. SOLWIND and HELIOS data were virtually continuous and revealed no other coronal or interplanetary events. Nor were there any major X-ray events in the 1-8 Å flux. The transit speed of 560 km/sec was comparable to the in situ speeds of 605 km/sec at HELIOS (0.43 AU, W 90°) and of 570 km/sec at PIONEER-VENUS (0.73 AU, W 122°) on May 29 (Russell and Mihalov, 1982).

Figure 2 May 27, 1979 mass ejection (below) with its shock and piston signatures at HELIOS 1 (left).
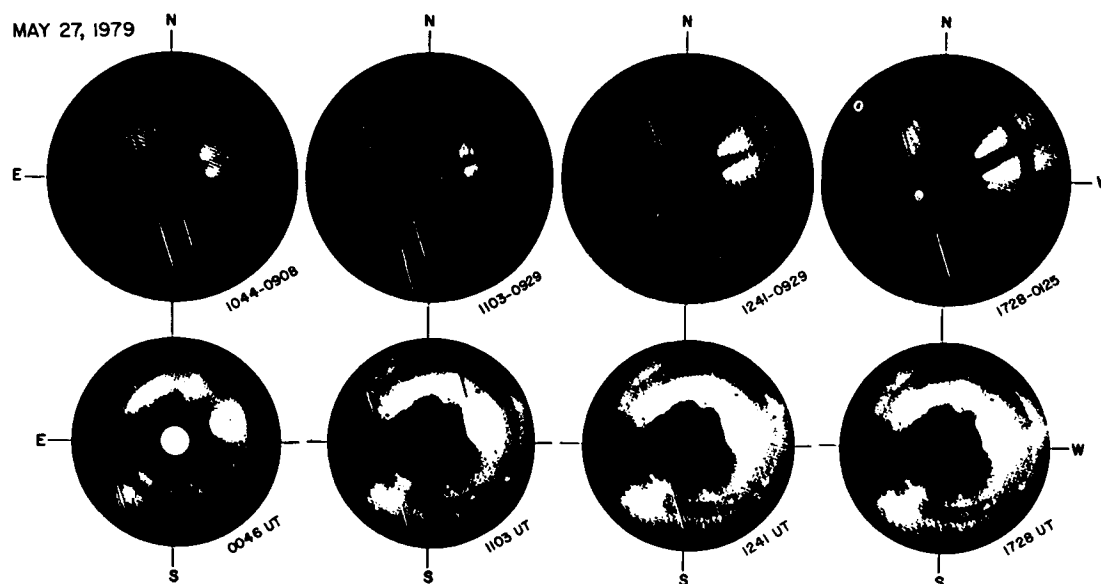
As Figure 2 shows and as we have noted elsewhere (Sheeley et al. 1982), the May 27, 1979 CME involved the eruption or splitting of a helmet streamer. Such streamer eruptions are ubiquitous and constitute a general class of CME characterized by low speed (usually 100-300 km/sec), by a narrow shape with little latitudinal expansion, and by the lack of an obvious signature in the spatially integrated X-ray flux. Several of them belong to our class of POSSIBLE shock associations.

Figure 3 shows high-speed CME's on May 10, 1981 (1460 km/sec) and May 13, 1981 (1500 km/sec), and the associated shocks at HELIOS 1 on May 11 and May 13, respectively. (The shock on May 10 was associated with a 1000 km/sec CME on May 8.) Note that the 600 km/sec speed behind the May 10 shock constituted the ambient speed for the May 11 and May 13 shocks whose post-shock flows exceeded the 1000 km/sec limit of the plotter. The two CME's in Figure 3 are not especially massive (perhaps 5×10^{15} gm) compared to other events, but are probably especially energetic due to their high speeds and correspondingly large kinetic energies. They were associated with long-duration X-ray events and H-alpha flares in the same active region. The similar whip-like structures of their northern edges suggest that this pair of CME's may be the coronal analogue of homologous flares. (It is probably impossible to tell whether or not the flares were homologous because the May 10 flare was greatly foreshortened at the east limb.)

## B. From CME's to Interplanetary Disturbances

In this phase of our study we began with the major CME's that we had not already found to be associated with shocks. A priori, we suspected that there would be many such mass ejections whose projected directions were toward HELIOS 1. This was a false impression. Of the 27 major CME's in HELIOS's hemisphere, 17 failed to come within 15° of the solar equator. On the average, they were centered at 68° and had latitudinal spans of 34° each side of center. Only one of these events had a possible association with a non-compressive density enhancement (NCDE), and we suppose that that association was a coincidence.

The remaining 10 major CME's spanned or at least grazed the solar equator (taken to coincide with the ecliptic within our measurement accuracy). On the average these CME's were centered at 24° and had spans of 32° on each side of center. Table 3 summarizes the associations of these CME's with interplanetary events:

Table 3

CME's with initially overlooked shocks	2
CME with a possible weak shock	1
CME's associated with disturbed flows, including NCDE's	5
CME with no interplanetary signature	1
CME preceding sub-Alfvenic conditions	1
Total	10

On detailed examination of the interplanetary magnetic field measurements, we found that two of these CME's were associated with weak shocks that we had overlooked initially (but which we have included now in part A of this section). Another CME may have been associated with a small shock in a plasma
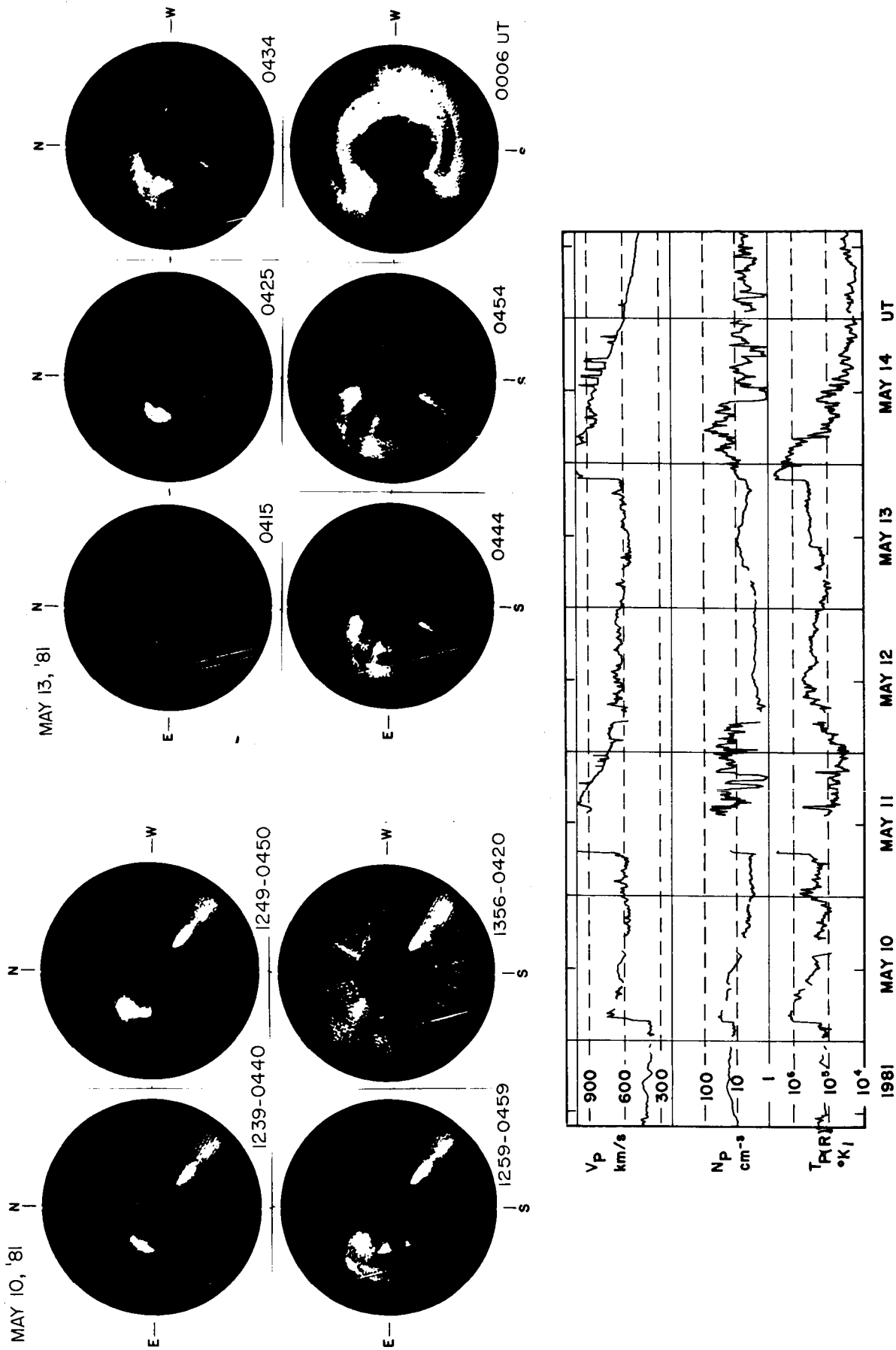
Figure 3   Homologous, 1500 km/sec mass ejections on May 10 and May 13, 1981, and their associated shocks at HELIOS 1 on May 11 and 13. (The May 10 shock was associated with an earlier CME on May 8.)

data gap. Five CME's were associated with disturbed plasma flows, three of which were NCDE's. One of these CME's had the moderately high speed of 560 km/sec, but the other four had speeds less than 450 km/sec. Two of these CME's were very slow streamer eruptions.

The CME without an obvious interplanetary signature was a wide ($\pm$ 45°), high-latitude (S45^{o}), fast (680 km/sec) event that just grazed the solar equator. This grazing condition, together with the 53° longitude difference between HELIOS's location at (.43 AU, E105^{o}) and the associated H-alpha flare's location at S22, E52 on December 3, 1979, may have been sufficient to cause the shock to have missed HELIOS.

Finally, in Table 2 a lone classic streamer eruption on June 6, 1980 preceded the anomalous sub-Alfvenic conditions that Schwenn has described elsewhere in these Solar Wind Five Proceedings. This CME occurred too late to have been the source of the anomalous interplanetary conditions. Moreover, if this CME had an interplanetary signature it was probably lost in the variety of unusual plasma fluctuations accompanying the sub-Alfvenic flow.

DISCUSSION

Our associations between high-speed CME's and interplanetary shocks are consistent with Gosling et al.'s (1976) associations between high-speed CME's and metric type II and IV radio bursts. Also, our associations are consistent with the results of Chao and Lepping (1974) who associated solar flares and shocks at Earth during the 4-year interval 1968-1971 near the peak of the previous sunspot cycle. Using metric radio burst data to make their associations "85% credible", they obtained typical transit speeds, v(AVE), of 600-700 km/sec and typical in situ shock speeds, v(SH), of 400-500 km/sec, and concluded that flare-associated shocks decelerate en route from the Sun.

In their direct comparison between the Sept. 7, 1973 flare-associated CME and its subsolar interplanetary shock, Gosling et al. (1975) obtained v(AVE) = 950 km/sec and v(SH) = 722 km/sec from which they also deduced a deceleration. Although the CME's leading edge had left the field of view prior to their first observation, their estimate, v(CME) = 960-1300 km/sec, is consistent with our results. As one can see in Table 2, for high-speed CME's, we obtained v(CME) > v(AVE) > v(SH). Not only does this general result provide strong support for the deceleration of high-speed shocks, but also it suggests that v(CME), the speed of the CME's leading edge, is closely related to the coronal shock speed. However, we do not yet know whether v(CME) represents the speed of the shock itself or whether it more properly represents the speed of the shock's driver material.

An underlying theme of post-Skylab reviews (Gosling 1975, 1976; MacQueen 1980) is that the interplanetary response to large flare events is well known. Furthermore, our future challenge is to understand the connection, if any, between typical low-speed CME's and non-shock solar wind variations such as non-compressive density enhancements (NCDE's) (Gosling et al. 1977, 1981) and, more recently, magnetic clouds (Burlaga et al. 1981; Klein and Burlaga 1982). Our preliminary results indicate that whereas some slow CME's may be associated with NCDE's, others seem to be clearly associated with interplanetary shocks. While these latter cases may not be consistent with our Skylab experience, they are consistent with a number of shock-associated

filament disappearances observed thereafter (Joselyn and Bryson 1980; Gosling et al. 1980; Schwenn et al. 1980; Sanahuja et al. 1982).

We should like to emphasize that these results are preliminary, and that our study is far from complete. We do not yet know whether some large, travelling interplanetary shocks may originate in solar events without CME's, but we have seen that a significant fraction of them do originate with CME's. (We have identified a few co-rotating shocks associated with coronal holes but not with CME's.) We have not yet studied the non-shock interplanetary disturbances in detail, but we have seen that after the shock-associated CME's were selected, there were few CME candidates left for non-shock associations. In contrast, during the Skylab mission in 1973-1974 the IMP 7 and 8 spacecraft observed approximately 2.7 NCDE's per month, but no shocks at all (Gosling et al. 1977). Finally, we should like to emphasize that this paper concerns the associations between CME's and events at HELIOS 1, but not at other spacecraft. We have also found obvious associations with shocks at HELIOS 2 (May 9, 1979), ISEE 3 (Nov. 29, 1979 and Sept. 5, 1982), and PIONEER-VENUS (May 10 and May 29, 1979). Many others will follow when we start to examine these data systematically.

References

o Burlaga, L., Sittler, E., Mariani, F., and Schwenn, R., Magnetic Loop Behind an Interplanetary Shock: Voyager, Helios, and IMP-8 Observations, J. Geophys. Res. 86, 6673, 1981.

o Burlaga, L.F., Klein, L., Sheeley, Jr., N.R., Michels, D.J., Howard, R.A., Koomen, M.J., Schwenn, R., and Rosenbauer, H., A Magnetic Cloud and a Coronal Mass Ejection, Geophys. Res. Lett. 9, 1317, 1982.

o Chao, J.K. and Lepping, R.P., A Correlative Study of SSC's, Interplanetary Shocks, and Solar Activity, J. Geophys. Res. 79. 1799, 1974.

o Gosling, J.T., Large-Scale Inhomogeneities in the Solar Wind of Solar Origin, Rev. Geophys. Spa. Sci. 13, 1053, 1975.

o Gosling, J.T., Transient Phenomena in the Solar Atmosphere and Solar Wind, in Physics of Solar-Planetary Environments, Vol I, D.J. Williams (ed.), Am. Geophys. Union, 1976.

o Gosling, J.T., Hildner, E., MacQueen, R.M., Munro, R.H., Poland, A.I., and Ross, C.L., Direct Observations of a Flare-Related Coronal and Solar Wind Disturbance, Solar Phys. 40, 439, 1975.

o Gosling, J.T., Hildner, E., MacQueen, R.M., Munro, R.H., Poland, A.I., and Ross, C.L., The Speeds of Coronal Mass Ejection Events, Solar Phys. 48, 389, 1976.

o Gosling, J.T., Hildner, E., Asbridge, J.P., Bame, S.J., and Feldman, W.C., Non-Compressive Density Enhancements in the Solar Wind, J. Geophys. Res. 82, 5005, 1977.

o Gosling, J.T., Asbridge, J.R., Bame, S.J., Feldman, W.C., and Zwickl, R.D., Observations of Large Fluxes of He$^+$ in the Solar Wind Following an Interplanetary Shock, J. Geophys. Res. 85, 3431, 1980.

o Gosling, J.T., Borrini, G., Asbridge, J.R., Bame, S.J., Feldman, W.C., and Hansen, R.T., Coronal Streamers in the Solar Wind at 1 AU, J. Geophys. Res. 86, 5438, 1981.

o Illing, R. and Sawyer, C., private communication, 1983.

o Intrilligator, D.S., Transient Phenomena Originating at the Sun - An Interplanetary View, in Solar and Interplanetary Dynamics, M. Dryer and E. Tandberg-Hanssen, eds., Reidel, Dordrecht, 357, 1980.

o Joselyn, J. and Bryson, J.F., Magalert: August 27, 1978, in Solar and Interplanetary Dynamics, M. Dryer and E. Tandberg-Hanssen, eds., Reidel, Dordrecht, 413, 1980.

o Klein, L.W. and Burlaga, L.F., Magnetic Clouds at 1 AU, J. Geophys. Res. 87, 613, 1982.

o MacQueen, R.M., Coronal Transients: A Summary, Phil. Trans. R. Soc. Lond A 297, 605, 1980.

o Russell, C. and Mihalov, J., private communication, 1982.

o Sanahuja, B., Domingo, V., Wenzel, K.-P, Joselyn, J.A., and Keppler, E., A Large Proton Event Associated with Solar Filament Activity, Solar Phys. (revised October 1982).

o Schwenn, R., Direct Correlations Between Coronal Transients and Interplanetary Disturbances, Proceedings of the Fifth International Symposium on Solar-Terrestrial Physics, Ottawa, May 17-22, 1982.

o Schwenn, R., Rosenbauer, H., and Muhlhauser, K.-H., Singly-ionized Helium in the Driver Gas of an Interplanetary Shock Wave, Geophys. Res. Lett. 7, 201, 1980.

o Sheeley, Jr., N.R., Howard, R.A., Koomen, M.J., Michels, D.J., Harvey, K.L., and Harvey, J.W., Observations of Coronal Structure During Sunspot Maximum, Spa. Sci. Rev. 33, 219, 1982.

702

VELOCITY PROFILES OF INTERPLANETARY SHOCKS

H.V.Cane
NASA/Goddard Space Flight Center,
Greenbelt, MD 20771

ABSTRACT

The type II radio burst has long been identified as being generated by a shock propagating through the solar corona. Only recently has it been possible to observe radio emission from shocks travelling through the interplanetary (IP) medium. Using the drift rates of IP type II bursts the velocity characteristics of eleven shocks have been investigated. The analysis indicates that shocks in the IP medium undergo acceleration before decelerating. The slower shocks take longer to attain their maximum velocity. Inconsistencies arise when the analysis is extended to the higher frequency (>500 kHz) data.

Introduction

At the time of the first description of the type II phenomenon (Wild and McCready, 1950) it was realized that the responsible disturbances propagated at speeds greater than 500 km/sec (Wild, 1950). Such speeds are well in excess of the speed of sound in the corona. The coincidence between the detection of a sudden commencement geomagnetic storm, initiated by a shock, and the observation of a type II burst at the sun a few days beforehand (Roberts, 1959) led to the acceptance of the theory that type II bursts are generated by shocks. The presence of two emission bands separated in frequency by about a factor of two indicated that fundamental and first harmonic electron plasma emission was being observed. Assuming a coronal density model the rate at which the burst drifted through the frequency range was then related to the shock's velocity. With the availability of 2-D spectro-heliographs it was determined that the assumed density models were consistent with the observed source positions (Wild, 1970). It should be noted though, that the deduced coronal electron densities are about a factor of 10 greater than values determined from white light measurements of the quiet corona (Stewart, 1976).

The propagation of shocks through the corona and IP medium is of considerable interest. Shocks play an important role in the energetics of the solar corona and in particle acceleration, both at the sun and in the IP medium. In situ measurements of shocks have been made for more than fifteen years and much progress has been made in understanding shock structure. However, the majority of the spacecraft used for these studies have been in earth orbit providing information at only one heliocentric distance. Thus not much is known about the evolution of shocks. One property that is known, and was first pointed out by Gosling et al.(1968), is that most shocks decelerate during their transit from the sun. Shock speeds at 1 AU are less than the transit speeds. The deceleration is presumed to be as a result of expansion of the wave and energy transfer to the ambient solar wind.

The technique of 'tracking' a shock via its radio emission provides information about the same shock over a large range of heliocentric distances. However, until the ISEE-3 radio astronomy experiment only a few events had been detected. Malitson et al.(1973, 1976) reported detecting two events with an experiment on IMP-6 and Boischot et al.(1980) reported several bursts seen with experiments on the Voyager spacecraft. These observations were obtained by much less sensitive experiments and provided no information about shock velocities. Although in the literature (e.g. Dryer, 1975) the IMP-6 data have been used to show a constant shock velocity, in fact, this was assumed in the original data analysis.

Data Analysis

In Figure 1 we sketch the ground-based dynamic spectrum for a type II event observed at the Culgoora Observatory in October 1978. This event continued to low frequencies and the 2 and 1 MHz intensity-time profiles from the ISEE-3 experiment are shown. Note that ground-based observations are not usually possible below about 20 MHz, whereas the top frequency of the ISEE-3 experiment is 2 MHz. Thus a gap of about a decade in frequency exists in the frequency regime of interest.
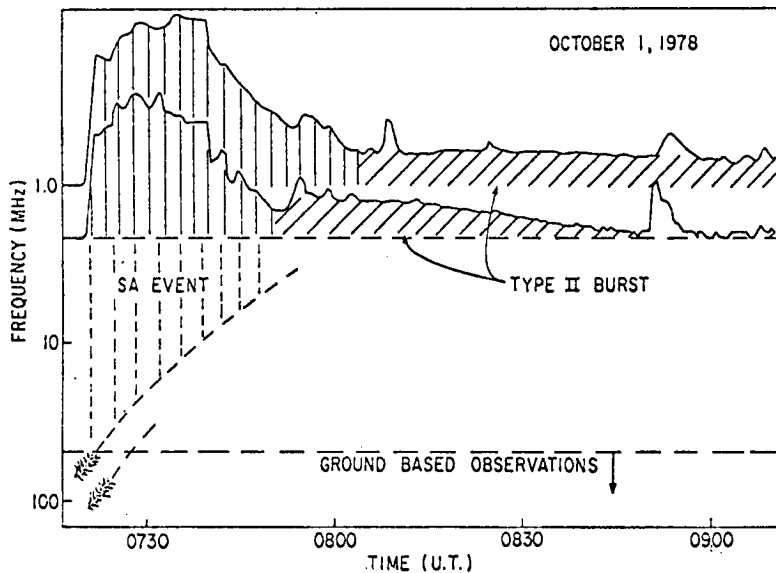

Fig. 1. This figure shows the relationship between meter wavelength phenomena and the activity detected at low frequencies. In particular the SA event is shown to precede the type II burst at 2 MHz. The dashed lines indicate what we would expect to have occurred in the unobserved region of the spectrum.

A characteristic of the October 1978 event, and other energetic events, is the occurrence of fast drift elements emerging from the 'backbone' of the type II burst observed from the ground. The 'herring-bones', as these elements are called, have been attributed to streams of relativistic electrons accelerated by the shock (Wild et al., 1963). In very energetic events these electrons propagate to 1 AU causing intense emission at low frequencies. We presume that the release and/or acceleration of these electrons ceases above approximately the 5 MHz plasma level because at 2 MHz the observed activity ceases

after about 25 minutes (see figure 1 for clarification). The intense low frequency outburst has been called a shock accelerated (SA) event (Cane et al., 1981). Type II bursts observed by ISEE-3 (which we call IP type II bursts) are preceeded by SA events. Since the SA event at 2 MHz begins within a minute or so of the type II burst observed at about 20 MHz, associations between ground and ISEE-3 type II events can be made unambiguously despite the lack of coverage in the regime between about 20 MHz and 2 MHz.

Figure 1 shows ISEE-3 intensities on a logarithmic scale and it is clear that the type II emission is much weaker than the SA event. The 2 and 1 MHz type II emission appears to be very weak but this is only because it is competing with the intense background emission from our Galaxy. We have detected type II emission at 2 and 1 MHz in only about 50% of the IP type II events. At lower frequencies the Galaxy decreases in intensity and the type II bursts are more easily discerned - provided other solar activity is at a minimum.

The characteristics of a type II burst at lower frequencies are shown in Figure 2. In the figure we show intensities as a function of time for eight frequencies for an event on May 16, 1981 and in this figure we use a linear
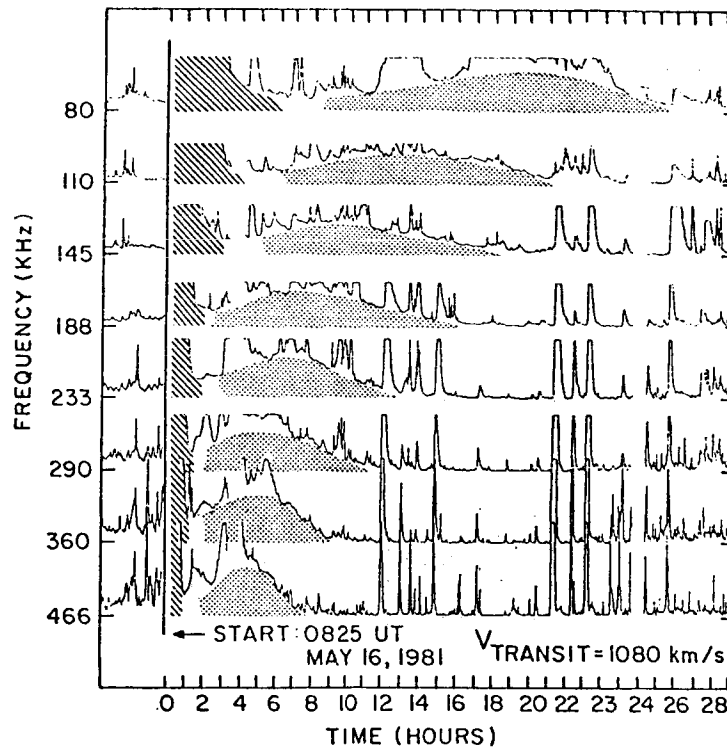

Fig. 2. Intensity versus time profiles for eight of the ISEE-3 observing frequencies. The type II emission is indicated by the stippling and the SA event by hatching.

scale. The strong type III bursts (flat-topped intensifications seen on all frequencies essentially simultaneously) have been chopped above a certain intensity to enhance the much weaker type II emission. The SA event is

indicated by diagonal hatching.   The type II event, indicated by stippling, is seen to drift through this frequency range (466 - 80 kHz) in about 25 hours. For this event the transit velocity, i.e. the velocity determined from the time interval between the start of the event at the sun and the sudden commencement, was about 1000 km/sec.

Figure 3 shows the profiles for another event whose transit velocity was about 800 km/sec and it is seen that this event drifts through the same frequency range more slowly.   The drift rates of all the bursts studied show this consistency with the derived transit velocities.   This result substantiates our identification of the flare associated with a particular sudden commencement.   Apart from a few isolated cases the transit velocities of the shock studied are basically independent of flare longitude.   This means that to a first approximation the shocks expand isotropically.
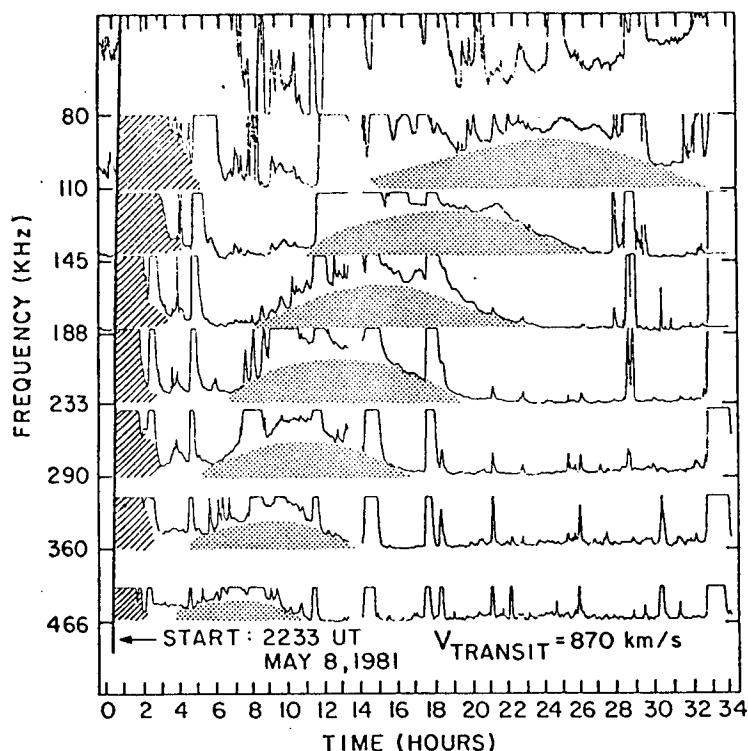

Fig. 3.   Intensity profiles for another event.   This event has been attributed to a slower shock than that associated with the event in fig.2 and has a slower drift rate.

We have determined the height of a number of shocks as a function of time by using an appropriate density model and assuming that the maximum of the burst at each frequency is the time when the shock was at the appropriate plasma level, i.e. coronal height.   The occurrence of SA events before IP type II bursts provides unambiguous identification of the start of the event at the sun.   The initial height of the shock at the commencement of the SA event is essentially the height at which shocks produce meter wavelength type II emission.   This height is in the range 1.5 - 3 solar radii heliocentric distance.   The density model comprised a constant R^{-6} term and a variable R^{-2}

term.   The R^{-6} term is negligible beyond about 10 solar radii.   The amplitude of the R^{-2} term was varied for different events so that a smooth height-time curve was obtained, with the end points anchored by the start of the event at the sun at 2 solar radii and the SC at the earth at 215 solar radii.   Small variations in the amplitude make little difference to the basic shapes of the velocity curves, and thus for most events the same density scale was used. Figure 4 shows data for the event of May 16 of 1981.   We note that a data gap at the beginning of the event covered the time interval when we expected to detect the event at 1 and 2 MHz.   The smooth curve is the spline function of least curvature fitted to the data taking into account the accuracy to which the maximum of the burst at each frequency can be estimated.
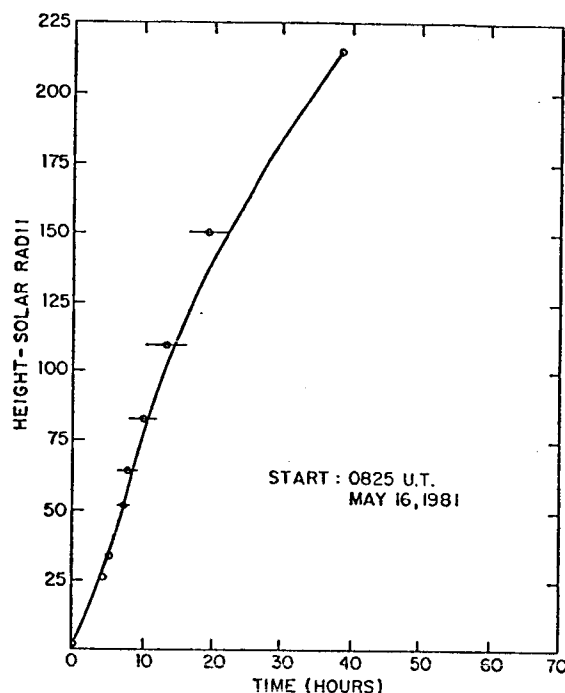

Fig. 4.   Deduced height versus time profile for an event.   The smooth curve is the spline function of least curvature fitted to the data.

This technique has been applied to a number of events.   Shock velocities as a function of heliocentric distance were obtained by taking the first derivative of the spline function fitted to the height-time data.

Results and Discussion

Figure 5 shows the velocity curves for four events.   The events have been organized as a function of transit velocity.   The fastest event is at the top left and the slowest event is bottom right.   Ignoring for the moment the profiles below about 20 solar radii one can see that for these events the shocks accelerate over a distance ranging from about 60 to 100 solar radii. The other events that have been analyzed have similar profiles.   If the shocks are being driven over the distances indicated by the acceleration region then the data suggest that the slower shocks are driven further than the fast shocks.

The upper right profile shows a large peak below 20 solar radii and this was obtained from the 1 and 2 MHz data. Note that had 2 and 1 MHz data points been available we expect, based on our results for other events, that the upper left event would also have had a sharp impulsive peak. Other events show this peak. Thus velocities obtained from the high frequency data seem to be inconsistent with the low frequency results. However, they are not inconsistent with analyses of ground-based events which give typical velocities of the order of 1000 to 1500 km/sec (Maxwell and Thompson, 1962). For some events even greater velocities have been derived (Gergely, 1982). Our
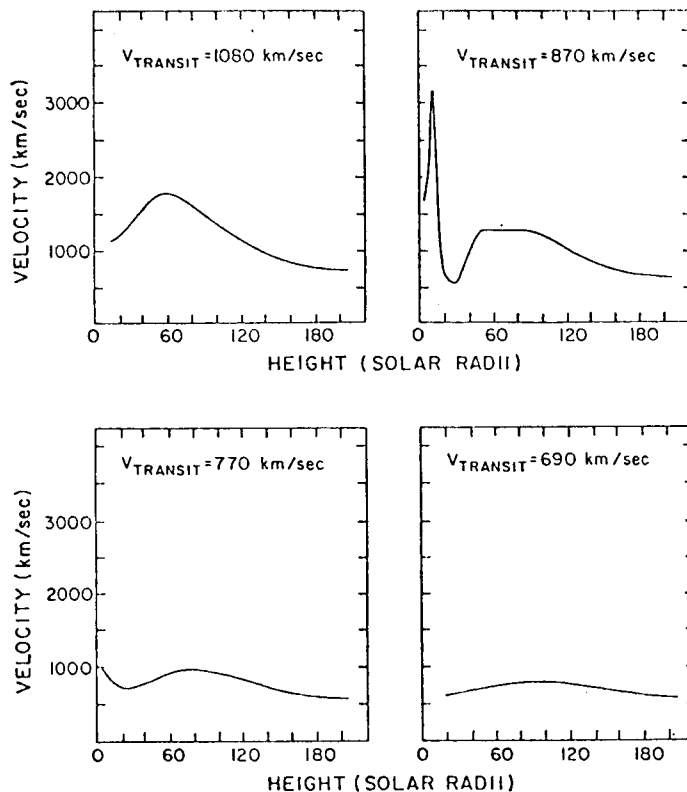

Fig. 5. Velocities as a function of heliocentric distance for four events. The top figures (L-R) are for events commencing May 16 and May 8 1981. The bottom figures (L-R) are for events commencing December 11, 1978 and August 26, 1979.

analysis assumes that the density scale derived for the low frequency (<1 MHz) data could be extended smoothly to the high frequency (1 and 2 MHz) data and that the same mode of emission was occurring. If these assumptions are incorrect certain conditions could result in the high frequency plasma levels being placed too high in the corona and this would lead to high velocities. Another explanation for our results is that the type II emission profile is being incorrectly interpreted. However, the differences in appearance of the type II emission in the two regimes suggests an interesting alternative which is that there are two shocks. The shock responsible for the high frequency emission could be a blast wave which dissipates in the low corona. The increase in velocity deduced from the low frequency data implies a driven shock. The driver would presumably be a mass ejection detectable as a white light coronal transient. From the preliminary analysis to date there is a good correlation between IP type II events and fast mass ejections as observed by the P78-1 coronagraph. Whatever the answer is it is clear that there are

708

differences between the low corona and the interplanetary medium as probed by radio emission from shocks.

In summary, interplanetary shocks produce radio bursts with frequency drift rates dependent on the shock velocities. Analyses of these drift rates indicate that the shocks accelerate out to some distance (of the order of 80 solar radii) and then decelerate. Some change in the properties of the corona or the type II emission occurs below 20 solar radii which remains to be explained.

References

Boischot, A., Riddle, A.C., Pearce, J. B. and Warwick, J. W. Shock waves and type II radiobursts in the interplanetary medium, Solar Phys., 65, 397, 1980.

Cane, H. V., Stone, R. G., Fainberg, J., Stewart, R. T., Steinberg, J. L. and Hoang, S. Radio evidence for shock acceleration of electrons in the solar corona, Geophys. Res. Lett., 8, 1285, 1981.

Dryer, M. Interplanetary shock waves: recent developments, Space Sci. Rev., 11, 277, 1975.

Gergely, T. E. On the relative velocity of coronal transients and type II bursts, Paper presented at the SCOSTEP-STIP symposium on solar interplanetary intervals, Maynooth, 1982.

Gosling, J. T., Asbridge, J. R., Bame, S. J., Hundhausen, A. J. and Strong, I. B. Satellite observations of interplanetary shock waves, J. Geophys. Res., 73, 43, 1968.

Malitson, H. H., Fainberg, J. and Stone, R. G. Observation of a type II solar radio burst to 37R$_\odot$, Astrophys. Lett., 14, 111, 1973.

Malitson, H. H., Fainberg, J. and Stone, R. G. Hectometric and kilometric solar radio emission observed from satellites in August 1972, Space Sci. Rev., 19, 511, 1976.

Maxwell, A. and Thompson, A. R. Spectral observations of radio bursts. II. Slow-draft bursts and coronal streamers, Ap.J., 135, 138, 1962.

Roberts, J. A. Solar radio bursts of spectral type II, Aust. J. Phys., 12, 327, 1959.

Stewart, R. T. Source heights of metre wavelength bursts of spectral types I and III, Solar Phys., 50, 437, 1976.

Wild, J. P. Observations of the high-intensity solar radiation at metre wavelengths. II Outbursts, Aust. J. Sci. Res., A3, 399, 1950.

Wild, J. P. Some investigations of the solar corona: The first two years of observation with the Culgoora radioheliograph, Proc. ASA., 1, 365, 1970.

Wild, J. P. and McCready, L. L. Observations of the spectrum of high-intensity solar radiation at metre wavelengths. I. The apparatus and spectral types of solar burst observed, Aust. J. Sci. Res., Ae, 387, 1950.

Wild, J. P., Smerd, S. F. and Weiss, A. A. Radio bursts from the solar corona, Ann. Rev. Astron. and Astrophys., 1, 291, 1963.

Plasma Properties of Driver Gas Following Interplanetary
Shocks Observed by ISEE-3

R. D. Zwickl, J. R. Asbridge, S. J. Bame, W. C. Feldman, J. T. Gosling
Los Alamos National Laboratory
Los Alamos, New Mexico 87544

and

E. J. Smith

California Institute of Technology
Jet Propulsion Laboratory, Pasadena, CA 91103

Abstract

Plasma fluid parameters calculated from solar wind and magnetic field data obtained on ISEE 3 were studied to determine the characteristic properties of driver gas following a select subset of interplanetary shocks. Of 54 shocks observed from August 1978 to February 1980, 9 contained a well defined driver gas that was clearly identifiable by a discontinuous decrease in the average proton temperature across a discontinuity which we assume is tangential. While helium enhancements were present somewhere downstream of the shock in all 9 of these events, only about half of them contained simultaneous changes in the two quantities. Often the He/H ratio changed over a period of minutes. Simultaneous with the drop in proton temperature the helium and electron temperature decreased abruptly. In some cases the proton temperature depression was accompanied by a moderate increase in magnetic field magnitude with an unusually low variance, by a small decrease in the variance of the bulk velocity, and by an increase in the ratio of parallel to perpendicular temperature. The cold driver gas usually displayed a bi-directional flow of suprathermal solar wind electrons at higher energies (>137 eV).

1. Introduction

Interplanetary shocks have been observed throughout that part of the heliosphere sampled by space probes during the last two decades. These shocks were generally formed either by high speed streams which steepen with increasing radial distance into forward-reverse shock pairs at their leading edges [Hundhausen and Gosling, 1976; Smith and Wolf, 1976], or by transient events at the sun which expel coronal material to drive forward shocks [see e.g. Hundhausen, 1972]. Shocks produced by transient events in the corona can also form forward-reverse shock pairs but usually outside of 1 AU. The characteristics of the plasma behind this latter type shock have been studied extensively. The "driver gas" for these shocks is usually identified by one or more of the following anomalous solar wind conditions: He abundance enhancements [Bame et al., 1968; Hirshberg et al., 1972; Borrini et al., 1982], proton temperature depressions [Gosling et al., 1973], electron temperature depressions [Montgomery et al., 1974], high magnetic field strength [Hirshberg and Colburn, 1969; Schatten and Schatten, 1972; Burlaga and King, 1979] with

low variance [Pudovkin et al., 1979], unusual heavy ion ionization states [Bame et al. 1979; Fenimore 1980; Schwenn et al., 1980; Gosling et al., 1980; Zwickl et al., 1982], and bidirectional streaming of both solar wind electrons [Montgomery et al., 1974; Temmy and Vaisberg, 1979; Bame et al., 1981] and energetic protons [Palmer et al., 1978; Kutchko et al., 1982].

The most commonly used characteristics in determining the presence of driver gas behind interplanetary shocks are He abundance enhancements and proton temperature depressions. However, these plasma signatures are observed after less than half of all shocks [Schwenn et al. 1980; Borrini et al., 1982], and when present can show a very complex pattern [Ogilvie and Burlaga, 1974; Bame et al., 1979].

Plasma fluid parameters calculated from solar wind data together with magnetic field data obtained with instrumentation on ISEE 3 have been studied to determine the characteristic properties of driver gas following a select subset of interplanetary shocks. Of 54 shocks observed from August 1978 to February 1980, 9 were followed by well defined driver gas that is clearly identifiable by a discontinuous decrease in the average proton temperature. This decrease is accompanied by an abrupt change in the magnetic field strength in 7 and possibly 8 of the 9 events and when taken together with the observed discontinuous changes in other plasma parameters implies the presence of a tangential discontinuity at the interface between the shocked ambient plasma and driver gas. In this paper the plasma properties of the driver gas from the 9 events are examined with a view toward characterizing the complexity of the most well defined events.

2. Characteristic Properties of Driver Gas

The subset of 9 events in this study were selected only on the basis of a well defined discontinuous decrease in proton temperature following a shock. Constraints were not placed on any other property of the assumed driver gas. Characteristic properties of the plasma following these 9 events are shown in Table 1. The identification of a He/H increase following a shock was not restricted just to plasma within the lowest temperature region. The first three properties are those most often used to identify the presence of driver gas in this select subset. Helium abundance increases and T_e decreases are present in all but one case, indicating both properties are commonly present in driver gas. Bi-directional streaming of plasma electrons is often but not always seen (Table 1). The thin proton density enhancement, located near the discontinuity separating the shocked plasma from the driver, is the least reliable indicator of driver gas and is probably not a general feature. The next three quantities in Table 1 have not been discussed previously and all three (a bulk speed increase, a decrease in the RMS deviation of V, σ_V, and an increase in the parallel to perpendicular proton temperature ratio) are usually present. The last two quantities in the table indicate the nature of the magnetic field magnitude (increase) at the interface between the shocked plasma and the low temperature driver gas and RMS deviation ,σ_B, decrease within the temperature depressed phase of the driver gas. The significance of a decrease in σ_B is hard to determine in cases where large macroscopic variations in B are taking place.

712

Table 1

ISEE-3
Characteristic Properties of Driver Gas

Characteristic	Nov 12 1978	Dec 14 1978	Feb 21 1979	Mar 9 1979	Mar 22 1979	Apr 1 1979	Apr 5 1979	Apr 24 1979	May 29 1979
1. T_p decrease	Y	Y	Y	Y	Y	Y	Y	Y	Y
2. He/H increase	Y	Y	Y	Y	Y	Y	Y	Y	Y
3. T_e decrease	Y	Y	Y	Y	Y	-	Y	Y	Y
4. Bi-directional streaming	Y	-	?	Y	Y	-	Y	Y	Y
5. Density spike	?	Y	Y	Y	?	-	-	-	Y
6. V increase	Y	-	-	Y	Y	-	Y	Y	Y
7. σ_v decrease	Y	Y	Y	Y	Y	-	Y	Y	Y
8. $T_\parallel / T_\perp$	Y	-	-	Y	Y	Y	Y	Y	Y
9. |B| increase	Y	?	Y	Y	Y	Y	Y	-	Y
10. σ_B decrease	Y	?	-	Y	Y	-	Y	Y	Y

Y = yes   ? = uncertain   - = not present

3. Temporal variability of driver gas

The time history of several solar wind parameters together with the strength of the interplanetary magnetic field are shown in Figure 1 for the shock occurring on 21 February 1979. The dashed line (~1515 UT) indicates the onset of the discontinuous drop in proton temperature and marks the location of the discontinuity which we assume is tangential. Simultaneous with this drop in proton temperature, the proton density increases, the He/H ratio increases, and the electron temperature decreases (not shown). While the magnetic field magnitude increases at this time, it is difficult to determine if this increase is due to the presence of the driver gas or is just another of the many variations in the field.

The plasma flow after the 21 February shock is a near classical example of what the solar wind parameters (T_p, T_e, He/H) would look like in the ideal case: all parameters change simultanously at the onset of the driver gas. However, such events are rare, only 3 of the special subset of 9 events show similar characteristics.

In general the He/H abundance ratio enhancement can occur at any time after the onset of the discontinuous drop in temperature. The most interesting example of the He/H abundance variation is found in the 22 March 1979 event shown in Figure 2. Here, the He/H abundance is enhanced before, depressed during, and enhanced after the low temperature region. Several other interesting features are also present in Figure 2. The magnitude of the magnetic field increases simultaneously with the decrease in proton temperature
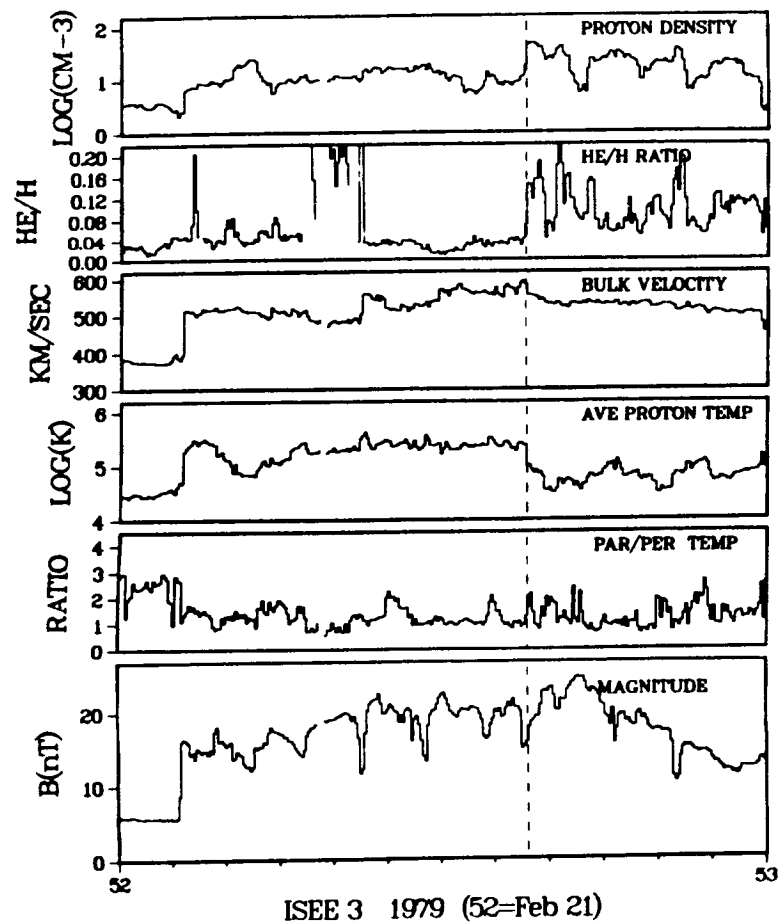
Figure 1. Time history of selected solar wind parameters for shock occurring on 21 February 1979. The dashed line at 1515 UT indicates the onset of a discontinuous drop in proton temperature.
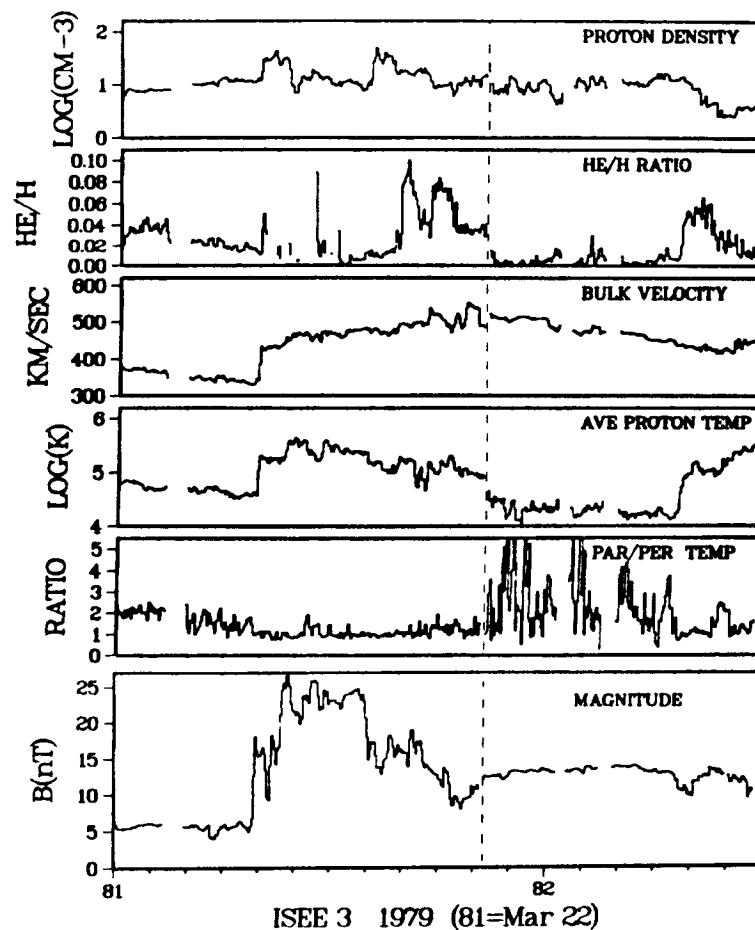
Figure 2. Time history of selected solar wind parameters for shock occurring on 22 March 1979. An unusual feature in this event is the simultaneous drop in the He/H ratio at the onset of the discontinuous drop in proton temperature.

and remains high with a reduced RMS deviation throughout the low temperature region. During the same time interval the ratio of the parallel to perpendicular proton temperature increased to relatively high levels. However, a significant part, though not all, of the increase is due to the difficulty of making accurate measurement of the two components at low temperature.

4. Discussion

Many of the parameters shown in Table 1 and Figures 1 and 2 have been examined previously. The most often studied parameter, the He/H ratio, has long been held to be the best indicator of the presence of driver gas behind a shock [Hirshberg et al., 1972]. The present study indicates that He/H increases [Bame et al., 1979] can occur anywhere with respect to the boundaries of the low temperature regions. They usually have rise and decay times on the order of minutes, a time much shorter than the overall duration of the He enhancement. Such would not be the case if the He/H increases were a necessary and sufficient identifier of cold driver gas. In the case of the He/H increase occurring prior to the T_p decrease in the 22 March 1979 event shown in Figure 2, we believe the enhanced He plasma was ejected from the corona ahead of the discontinuity, and as such is simply an extended signature of the transient disturbance which later produced the shock.

This study confirms and extends recent work concerning the nature of the magnetic field during the passage of driver gas. Borrini et al. (1982), in a statistical survey of 103 forward shocks, showed that, on the average, driver gas containing enhanced He/H ratios also exhibited increased magnetic field strength. Earlier Pudovkin et al. (1979) had indicated that the RMS deviation of the magnetic field often decreases during the passage of driver gas. These two characteristics are clearly seen in the 22 March 1979 event shown in Figure 2 and their frequency of occurrence in clearly identified cold driver gas can be determined from the data in Table 1.

The signature of the magnetic field parameters in driver gas suggests a similar examination be made of the bulk flow velocity and its RMS deviation. These parameters, shown in Table 1, indicate that while the solar wind bulk velocity often increases at the onset of the driver gas, the RMS deviation, averaged over a 10 minute interval, usually decreases slightly. Thus, the plasma data and the magnetic field data indicate that cold driver gas contains lower than normal levels of low frequency wave activity.

A schematic model illustrating a possible geometry for plasma driving an interplanetary shock is shown in Figure 3 (based on Figure 10 from Bame et al., 1979). Many of the characteristic properties of driver gas listed in Table 1 are illustrated in the figure. Of particular note in Figure 3 is the uneven distribution of helium enriched plasma and the smooth closed magnetic field lines. The geometry of our model differs considerably from that presented by Pudovkin et al. (1979). Our model suggests that it is possible to observe the shock without detecting driver gas, and when driver gas is observed the He enhancement may occur early or late or the He enhancement may occur in several distinct regions. These characteristics, which are observed in the data, are not shown in their model [Pudovkin et al., 1979].
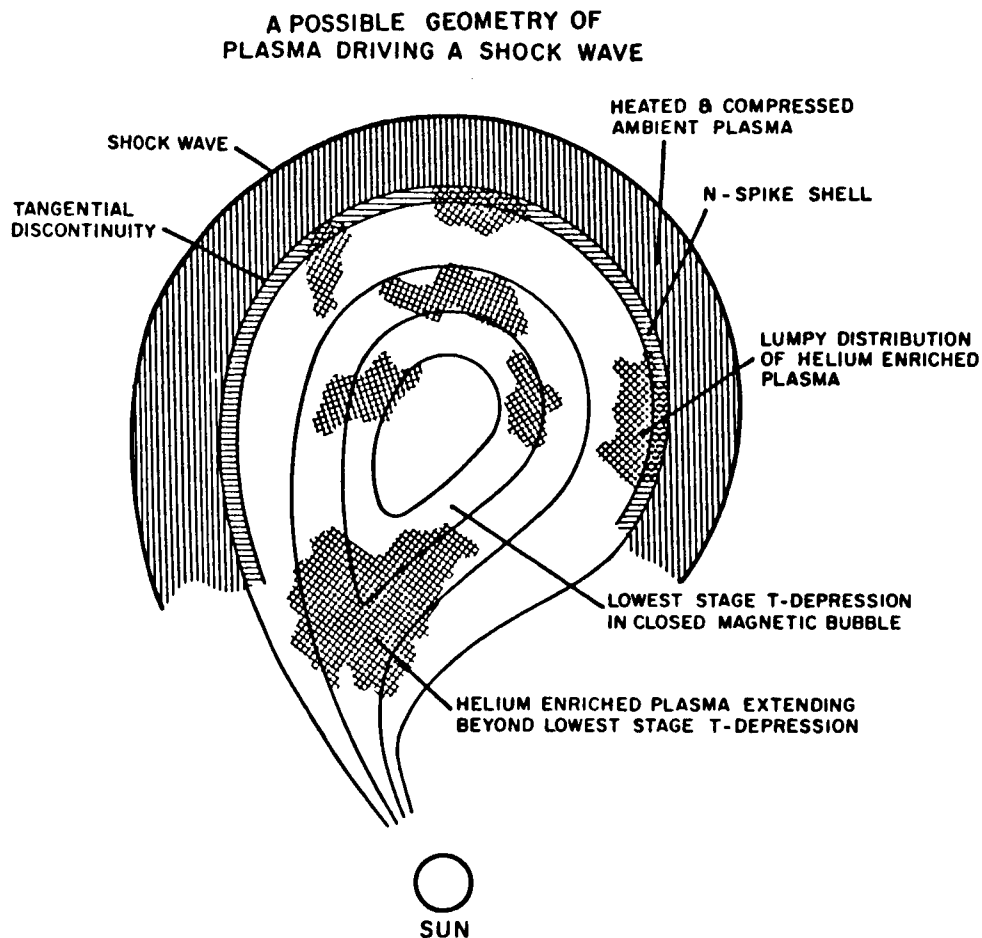
A POSSIBLE GEOMETRY OF
PLASMA DRIVING A SHOCK WAVE

Figure 3. Schematic model illustrating a possible geometry for plasma driving an interplanetary shock (based on Figure 10 from Bame et al., 1979).

References

Bame, S. J., J. R. Asbridge, A. J. Hundhausen, and I. B. Strong, Solar wind and magnetosheath observations during the January 13-14, 1967, Geomagnetic Storms, J. Geophys. Res., 73, 5761, 1968.
Bame, S. J., J. R. Asbridge, W. C. Feldman, E. E. Fenimore, and J. T. Gosling, Solar wind heavy ions from flare-heated coronal plasma, Sol. Phys., 62, 179, 1979.

Bame, S. J., J. R. Asbridge, W. C. Feldman, J. T. Gosling, and R. D. Zwickl, Bi-directional streaming of solar wind electrons >80 eV; ISEE evidence for a closed-field structure within the driver gas of an interplanetary shock, Geophys. Res. Lett., 8, 173, 1981.

Borrini, G., J. T. Gosling, S. J. Bame, and W. C. Feldman, An analysis of shock wave disturbances observed at 1 AU from 1971 through 1978, J. Geophys. Res., 87, 4365, 1982.

Burlaga, L. F., and J. H. King, Intense interplanetary magnetic fields observed by geocentric spacecraft during 1963-1975, J. Geophys. Res., 84, 6633, 1979.

Fenimore, E. E., Solar wind flows associated with hot heavy ions, Astrophys. J., 235, 245, 1980.

Gosling, J. T., V. Pizzo, and S. J. Bame, Anomalously low proton temperatures in the solar wind following interplanetary shock waves: Evidence for magnetic bottles?, J. Geophys. Res., 78, 2001, 1973.

Gosling, J. T., J. R. Asbridge, S. J. Bame, W. C. Feldman, and R. D. Zwickl, Observations of large fluxes of He$^+$ in the solar wind following an interplanetary shock, J. Geophys. Res., 85, 3431, 1980.

Hirshberg, J., and D. S. Colburn, Interplanetary field and geomagnetic variations: A unified view, Planet. Space Sci., 17, 1183, 1969.

Hirshberg, J., S. J. Bame, and D. E. Robbins, Solar flares and solar wind helium enrichments: July 1965 - July 1967, Sol. Phys., 23, 467, 1972.

Hundhausen, A. J., Coronal expansion of solar wind, Springer, New York, 1972.

Hundhausen, A. J., and J. T. Gosling, Solar wind structure at large heliocentric distances: An interpretation of Pioneer 10 observations, J. Geophys. Res., 81, 1436, 1976.

Kutchko, F. J., P. R. Briggs, and T. P. Armstrong, The Bi-directional particle event of October 12, 1977, possibly associated with a magnetic loop, J. Geophys. Res., 87, 1419, 1982.

Montgomery, M. D., J. R. Asbridge, S. J. Bame, and W. C. Feldman, Solar wind electron temperature depressions following some interplanetary shock waves: Evidence for magnetic merging?, J. Geophys. Res., 79, 3103, 1974.

Ogilvie, K. W., and L. F. Burlaga, A discussion of interplanetary postshock flows with two examples, J. Geophys. Res., 79, 2324, 1974.

Palmer, I. D., F. R. Allum, and S. Singer, Bidirectional anisotropies in solar cosmic ray events: Evidence for magnetic bottles, J. Geophys. Res., 83, 75, 1978.

Pudovkin, M. I., S. A. Zaitseva, and E. E. Benevslenska, The structure and parameters of flare streams, J. Geophys. Res., 84, 6649, 1979.

Schatten, K. H., and J. E. Schatten, Magnetic field structure in flare-associated solar wind disturbances, J. Geophys. Res., 77, 4858, 1972.

Schwenn, R., H. Rosenbauer, and K. H. Muhlhauser, Singly-ionized helium in the driver gas of an interplanetary shock wave, Geophys. Res. Lett., 7, 201, 1980.

Smith, E. J., and J. H. Wolfe, Observations of interaction regions and Corotating shocks between 1 and 5 AU: Pioneers 10 and 11, Geophys. Res. Lett., 3, 137, 1976.

Temny, V. V., and O. L. Vaisberg, Dumb-bell distributions of superthermal solar wind electrons from Prognoz-7 observations, Space Research Institute, IIp-499, preprint, 1979.

Zwickl, R. D., J. R. Asbridge, S. J. Bame, W. C. Feldman, and J. T. Gosling, He$^+$ and other unusual ions in the solar wind: A systemmatic search covering 1972-1980, J. Geophys. Res., 87, 7379, 1982.

COROTATING SHOCKS IN INNER HELIOSPHERE

Y.C. Whang
Department of Mechanical Engineering
The Catholic University of America
Washington, D.C.   20064

ABSTRACT

This paper reports two possible corotating shocks in the inner helio-sphere where the solar wind is composed of low-β plasma. In the region where the solar wind is slightly super-Alfvenic, reverse corotating fast MHD shocks can form at the leading edge of a high-speed stream. These shocks possess a switch-on mechanism for amplification of tangential small-scale fluctuations. The second one is the coronal slow shocks which may be imbedded in large coro-nal holes at low altitude in the sub-Alfvenic region.

Introduction

In a heliocentric coordinate system corotating with the sun, the large-time-scale structure of the solar wind is often quasi-steady for a few solar rotations. Many large-scale structures of the global solar wind may be treated as steady-state field-aligned flows in a frame of reference corotating with the sun at a constant angular velocity $\vec{\Omega}$. The flow velocity in the corotating frame $\vec{U}$ is either parallel or anti-parallel to the magnetic field $\vec{B}$. The solar wind process may be considered to consist of an expansion of the solar wind along each corotating stream tube and a dynamical interaction between neighboring stream tubes.

Recently, magnetohydrodynamic (MHD) treatments have been employed to study the interaction of corotating high-speed streams in the highly super-Alfvenic region of the heliosphere by several authors. For example, Pizzo (1982) has studied some 3D problems under the adiabatic assumption, and Whang and Chien (1981) have studied some MHD interaction problems near the solar equatorial plane to include the heat conduction process.

This paper reports two possible corotating MHD shocks in the low-β region of the inner heliosphere. The solar wind flow is sub-Alfvenic near the sun, and a transition from sub-Alfvenic to super-Alfvenic takes place at a heliocen-tric distance of approximately 0.1 AU. In the slightly super-Alfvenic region, we studied the interaction between two streams of solar wind at different Alfven numbers, a slow stream at a lower Alfven number precedes a fast stream. As a result of interaction, reverse corotating fast MHD shocks may form near 0.1 AU at the leading edge of the high-speed stream. These shocks possess a "switch-on" mechanism for amplification of tangential small-scale fluctuations. The second shock is the coronal slow shock, which may be imbedded in large coronal holes at altitudes of a few solar radii in the sub-Alfvenic region.

Mathematical Development

The governing equations for the expansion of the solar wind along each stream tube may be represented by a system of five equations. The equation of continuity is

$$\vec{e}_s \cdot \nabla (\rho U/B) = 0 \tag{1}$$

where ρ is the mass density, and $\vec{e}_s = \vec{U}/U$ is the unit vector along the streamline direction. The parallel component of the equation of motion is

$$\vec{e}_s \cdot (\nabla \frac{U^2}{2} + \frac{1}{\rho} \nabla p - \vec{H}) = 0 \tag{2}$$

where p is the thermal pressure, and

$$\vec{H} = -(GM/r^3) \vec{r} - 2 \vec{\Omega} \times \vec{U} - \vec{\Omega} \times (\vec{\Omega} \times \vec{r})$$

G is the gravitational constant, M is mass of the sun, and $\vec{r}$ the heliocentric position vector. The force acting on a unit mass of the solar wind plasma, $\vec{H}$, consists of the gravitational force and two fictitious body forces: the coriolis force and the centrifugal force.

The variation of p and ρ along each streamline is governed by

$$\vec{e}_s \cdot (\nabla p - c^2 \nabla \rho) = 0 \tag{3}$$

where $c = (\alpha p/\rho)^{1/2}$ is the sound speed in a heat conducting plasma, α is the polytropic index. The conduction heat flux is parallel to $\vec{e}_s$,

$$\vec{q} = -\kappa \vec{e}_s \vec{e}_s \cdot \nabla T \tag{4}$$

where T is the one-fluid temperature, and the thermal conductivity

$$\kappa = K T^{5/2}$$

with $K = 7.5 \times 10^{-7}$ erg s^{-1} cm^{-1} $deg^{-3.5}$. The polytropic index is directly related to the variation in thermal state and in heat conduction process along each streamline,

$$\vec{e}_s \cdot \left\{ (\frac{5}{3} - \alpha) \nabla \rho - \frac{mB}{3kTU} \nabla (\frac{q}{B}) \right\} = 0 \tag{5}$$

where m is the proton mass and k Boltzmann's constant, α is not a constant along each streamline. In the expansion of the solar wind, $\alpha < 5/3$ when conduction heat acts as an energy source, it continuously converts into other forms of energy. $\alpha = 5/3$ in the region where $\vec{q}$ is a divergence-free vector (including the adiabatic condition with q = 0). A special feature of the present formulation of energetics for a heat conducting plasma is the use of a varying polytropic index α in (3) and (5) instead of the equivalent equation of energy conservation

$$\vec{e}_s \cdot \nabla \left[\frac{\rho U}{B} \left\{ \frac{U^2 - (\vec{\Omega} \times \vec{r})^2}{2} + \frac{5}{2} \frac{p}{\rho} - \frac{GM}{r} \right\} + \frac{q}{B} \right] = 0$$

From equations (1) - (3), we can obtain

$$\vec{e}_s \cdot \left[(\frac{U^2}{c^2} - 1) \frac{1}{\rho} \nabla p - U^2 \nabla \ln B + \vec{H} \right] = 0 \qquad (6)$$

$$\vec{e}_s \cdot \left[(U^2 - c^2) \nabla \ln \rho - U^2 \ln B + \vec{H} \right] = 0 \qquad (7)$$

and

$$\vec{e}_s \cdot \left[(c^2 - U^2) \nabla \ln U - c^2 \ln B - \vec{H} \right] = 0 \qquad (8)$$

$-\vec{e}_s \cdot \nabla \ln B$ measures the rate of fractional change of cross-sectional area of a stream tube along the streamline direction. Once $\vec{e}_s$ and the variation of cross-sectional area are known, the expansion equations can be integrated along each streamline.

The variation in the direction and the magnitude of the cross-sectional area of each stream tube is controlled by the interaction between neighboring stream tubes (Whang, 1980). The interaction process is governed by the divergence-free condition of the magnetic field.

$$\nabla \cdot \vec{B} = 0 \qquad (9)$$

and the dynamical equilibrium of momentum transverse to the streamline direction

$$(U^2 - a^2) \vec{e}_s \cdot \nabla \vec{e}_s + (\vec{\vec{I}} - \vec{e}_s \vec{e}_s) \cdot (\frac{1}{\rho} \nabla p^* - \vec{H}) = 0 \qquad (10)$$

where $a = B/(4\pi\rho)^{\frac{1}{2}}$ is the Alfven speed, $\vec{\vec{I}}$ is a unit dyadic, and $p^* = p + B^2/8\pi$ is the sum of thermal and magnetic pressures. Making use of equation (6), we can write (9) in a new form

$$\left[U^2 (c^2 + a^2) - c^2 a^2 \right] \nabla \cdot \vec{e}_s + \vec{e}_s \cdot \left[(U^2 - c^2) \frac{1}{\rho} \nabla p^* + c^2 \vec{H} \right] = 0 \qquad (11)$$

The system of the interaction equations, (10) and (11), shows that the variation of the streamline direction is controlled by ∇p^* and $\vec{H}$. The system is elliptic or hyperbolic, depending on the sign of

$\left[U^2 (a^2 + c^2) - a^2 c^2 \right] / (U^2 - a^2)(U^2 - c^2)$. It is hyperbolic in the super-Alfvenic, supersonic regime

$$U > \max (a, c)$$

or in a sub-Alfvenic, subsonic regime with

$$\left(\frac{1}{a^2} + \frac{1}{c^2} \right)^{-\frac{1}{2}} < U < \min (a, c)$$

The system of interaction equations is elliptic in other regimes.

In the two hyperbolic flow regimes, solutions of the interaction equations respectively represent families of fast and slow MHD waves. When successive MHD waves travel faster than the preceding ones, they overtake and combine with each other. This phenomenon leads to the formation of fast or slow MHD shocks.

Corotating Shocks Near 0.1 AU

A simultaneous solution of the expansion equations and the interaction equations is carried out to demonstrate the formation of corotating shock near the equatorial plane in the hyperbolic flow region outside ~0.1 AU where the flow of a low-β plasma is supersonic and slightly super-Alfvenic. We assume that near the solar equatorial plane the flow properties are independent of the latitude. Let ϕ denote the directional angle between $-\vec{r}$ and $\vec{e}_s$, $\vec{e}_n = \vec{\Omega} \times \vec{e}_s / \Omega$ a unit vector normal to the streamline direction, $H_s = \vec{e}_s \cdot \vec{H}$ and $H_n = \vec{e}_n \cdot \vec{H}$. Then we may write the interaction equations, (10) and (11), near the equatorial plane as

$$(U^2 - a^2)(\vec{e}_s \cdot \nabla \phi - \frac{\sin \phi}{r}) + \frac{1}{\rho} \vec{e}_n \cdot \nabla p^* = H_n \qquad (12)$$

and

$$\left[U^2 (c^2 + a^2) - c^2 a^2 \right] (\vec{e}_n \cdot \nabla \phi + \frac{1 - \cos \phi}{r})$$
$$+ \frac{1}{\rho} (U^2 - c^2) \vec{e}_s \cdot \nabla p^* = -c^2 H_s \qquad (13)$$

In the super-Alfvenic hyperbolic regime, the Mach angle μ for fast MHD waves is defined by

$$\cos \mu = (1 - a^2/U^2)^{\frac{1}{2}} (1 - c^2/U^2)^{\frac{1}{2}} \qquad (14)$$

We may introduce

$$\vec{c}_{\pm} = \cos \mu \, \vec{e}_s \pm \sin \mu \, \vec{e}_n \, , \qquad (15)$$

unit vectors along the two characteristic directions. The characteristic curve defined by $\vec{c}_+$ running ahead of the streamline in the direction of solar rotation may be called the forward characteristic curve, and that defined by $\vec{c}_-$ running behind the streamline the reverse characteristic curve. We can express the interaction equations in the form of characteristic equations obtained from a linear combination of (12) and (13),

$$\vec{c}_{\pm} \cdot (\nabla \phi \pm Q \nabla p^*) = S_{\pm} \qquad (16)$$

where
$$Q = \frac{1}{\rho (U^2 - a^2) \tan \mu}$$

and
$$S_{\pm} = \frac{\cos \mu \, H_n}{U^2 - a^2} \mp \frac{c^2 \, H_s}{U^4 \sin \mu} + \frac{1}{r} \left[\sin (\phi \pm \mu) \mp \sin \mu \right]$$

Solutions for MHD interaction between solar wind streams in the low-β region of the inner heliosphere can be obtained from integrations of the expansion equations along streamlines, and integrations of the interaction equations (16) along characteristic curves. A method of solution for solar wind streams in the super-Alfvenic region has been developed previously (Whang and Chien, 1981). The present approach differs from the previous one in two aspects: (i) using a varying polytropic index in (3) and (5) instead of the equivalent equation of energy conservation, and (ii) introducing a new form (11) to represent the divergence-free condition (9). The advantages of the present approach are (i) each of the final interaction equations (16) contains only derivatives along a characteristic direction, and (ii) slow mode MHD waves are not suppressed.

The following numerical solution demonstrates the interaction between two streams of solar wind flow at different Alfven numbers, in which a slow stream precedes a sharply bounded fast stream of higher Alfven number. Assume that at the initial surface $r = 22.5\ R_\odot$, the profile for the radial speed (in km/s) be given by

$$U_r = 400 + 8\ (1 - \text{erf}\ \omega)$$

where ω is the azimuthal angle in degrees. A smooth increase of the flow speed from $U_r = 400$ km/s and $U/a = 1.087$ to $U_r = 416$ km/s and $U/a = 1.132$ takes place in a narrow region with its longitudinal width of approximately $4°$. We further assume that at the initial surface

$$U_\omega = -\Omega r$$

$$nU_r = 2.795 \times 10^5 \text{ protons cm}^{-2} \text{ s}^{-1}$$

and

$$T = 4.3 \times 10^5 \text{ K}$$

From the slow to the fast stream, B changes from 484 to 439 nT, and p* from 1.016×10^{-6} to 0.847×10^{-6} dyne/cm^2.

We have obtained the numerical solution for all flow parameters in the region $22.5 \leq r/R_\odot < 30.4$. In the top frame of Figure 1 are plotted the streamlines (in heavy curves) and the two families of characteristic curves in the physical plane. The streamline passing through $\omega = 0$ at the initial surface is identified as the central streamline. At the initial surface, the Mach angle decreases across the interface from $\mu = 83.6°$ in the slow stream to $\mu = 62.8°$ in the fast stream due to changes in Alfven numbers. Thus the slopes of those characteristic curves starting near the initial interface change rapidly. The merging of the reverse characteristic curves shown in the plot indicates the formation of a reverse corotating shock, it signifies a piling up of the fast-mode MHD waves to form a fast MHD shock. The lower frame of Figure 1 shows the profile of the total pressure p* at various heliocentric distances. Shock fronts with steep profiles of p* appear at the leading edge region. The shock fronts become broader and weaker at approximately $15°$ (or ~24 hours) behind the central streamline due to geometrical effects. Unlike the total pressure, other flow properties (U, ρ, T, etc.) change abruptly across the stream interface around the central streamline. Disturbances of flow proper-
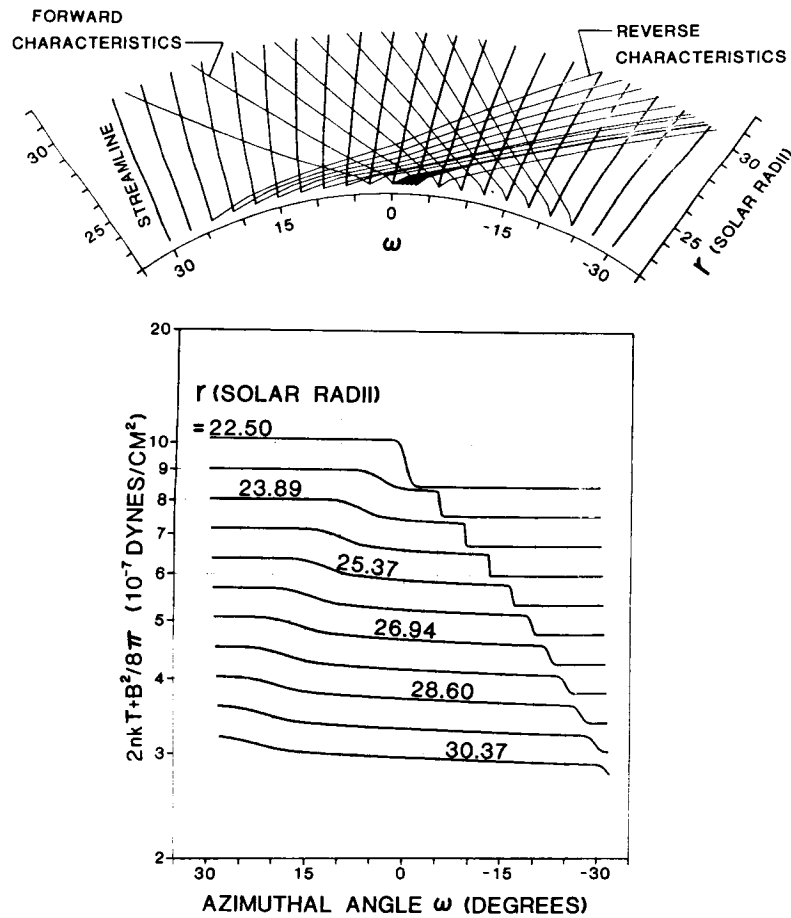
Figure 1. The top frame shows the streamlines and characteristic curves. The merging of the reverse characteristic curves signifies the formation of a reverse corotating shock at the leading edge. The lower frame shows the profile of p^* at the shock front.
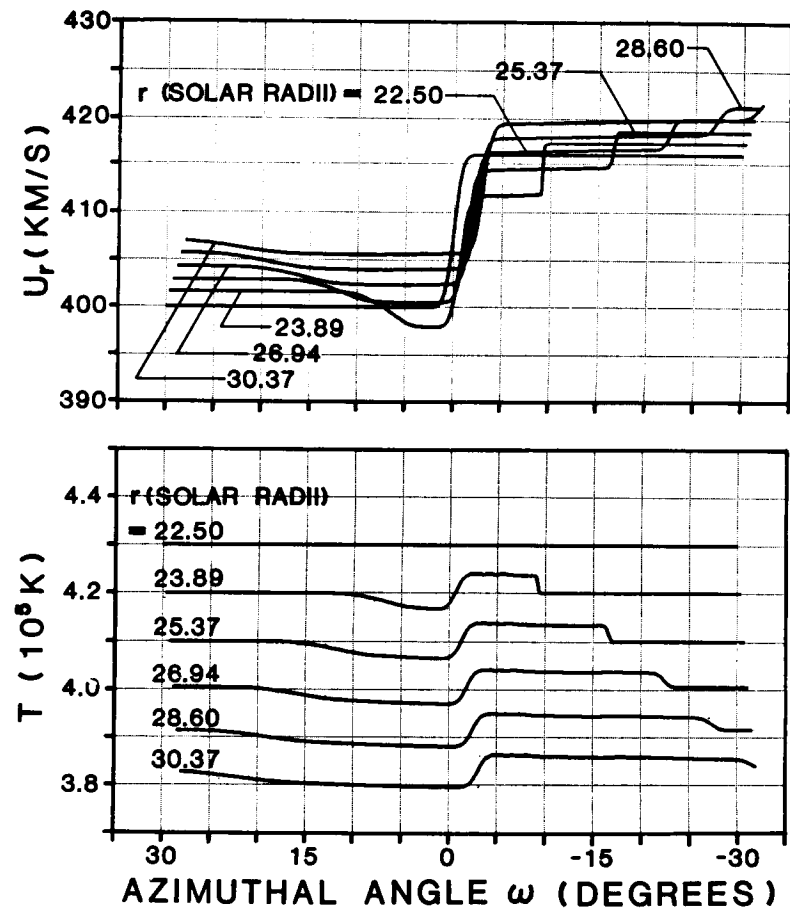

Figure 2. The radial velocity and the temperature in the interaction region. The shocked plasma between the central streamline and the reverse corotating shock has a higher temperature than its surroundings.

perties due to stream interaction are confined to an interaction region bounded by the two characteristics which intersect the initial surface near the central streamline. The solar wind streams undergo a simple expansion process without strong interaction between neighboring stream tubes outside of the interaction region. In the region where the flow is slightly super-Alfvenic, one can distinguish clearly the shock front from the interface because of large Mach angles. Between the interface and the reverse shock, the flow properties carry the signatures of a shocked plasma as shown in Figure 2, which plots the profiles of U_r and T at various heliocentric distances. Although the temperature is assumed to be uniform at the initial surface, the shocked plasma has a higher temperature in the leading edge region.

This example illustrates that in the low-β region of the inner heliosphere where the solar wind flow is slightly super-Alfvenic, if the Alfven number increases at the leading edge region of a high-speed stream even at a very slow rate, reverse corotating shocks may form in the region. These shocks are fast MHD shocks of low-β plasma, with the upstream normal Mach number slightly greater than 1. They are capable of amplifying the tangential component of the magnetic field. Thus, the presence of a small random fluctuation field upstream of these shock surfaces can be amplified to produce a large, tangential fluctuation field downstream of the shock. This effect may be called a switch-on mechanism, which will be discussed in detail in a separate paper. This amplification mechanism is probably responsible for the presence of large-amplitude anisotropic fluctuations observed at the leading edge of high-speed streams (Belcher and Davis, 1971).

Coronal Slow Shocks

At altitudes of a few solar radii, the solar wind is a sub-Alfvenic low-β plasma. It has been suggested that, in this region of the inner heliosphere, corotating slow MHD shocks might be imbedded within large polar coronal holes (Whang, 1982).

Figure 3 depicts the geometry of a coronal slow shock around a simple two-hole corona. The solar wind originating from open-field coronal holes is accelerated to high speeds at low altitudes in the corona. Streams originating from the edge of the polar open-field regions flow around the curved boundary of the helmet-shaped, closed-field region (Pneuman and Kopp, 1971). Near the inner edge of the neutral sheet, the flow direction of each stream changes suddenly, becoming parallel to the neutral sheet. An oblique slow shock can develop near or at the neutral point. The shock extends polewards to form a composite surface of discontinuity surrounding the sun. These standing shocks could occur quite close to the solar surface, at 2 to 5 solar radii above large coronal holes. Numerical solutions have been constructed for the expansion of the solar wind in open field region of the solar corona along stream tubes with prescribed geometry by Pneuman and Kopp (1971) and by Whang (1983). These solutions did not consider dynamical interaction between neighboring stream tubes, and their streamline geometry was introduced under an a *priori* assumption that no shocks exist in the corona.

For not very large coronal holes, the coronal slow shocks are weaker at lower altitudes, and could have a partially concave surface as shown in Figure 4.
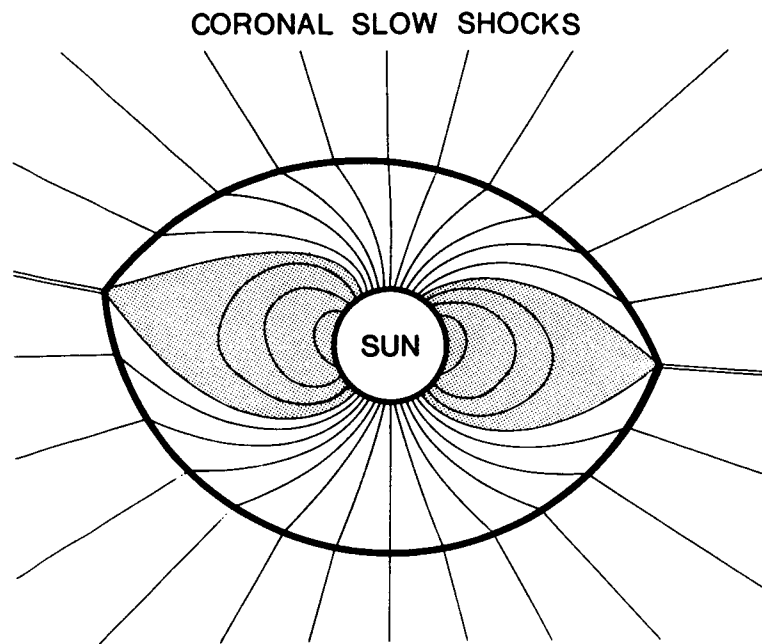
CORONAL SLOW SHOCKS

Figure 3. The geometry of a slow shock in a corona with two large polar holes.
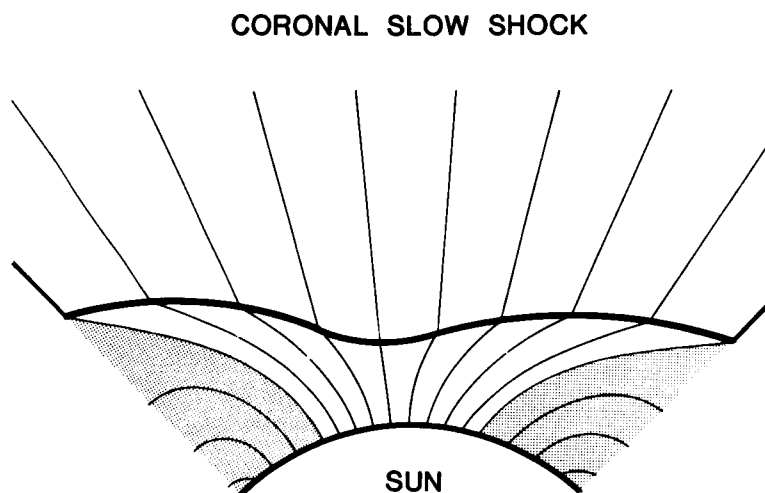
CORONAL SLOW SHOCK

Figure 4. For not very large coronal holes, the slow shocks are weaker at lower altitudes, and could have a partially concave shock surface.

Let θ denote the angle between the magnetic field and the shock normal, and C_s be the normal slow speed,

$$C_s^2 = \frac{1}{2}(a^2 + c^2) - \frac{1}{2}\left\{(a^2 + c^2)^2 - 4a^2 c^2 \cos^2\theta\right\}^{\frac{1}{2}}$$

The normal component of the flow speed U_n is greater than C_s upstream, and less than C_s downstream of a slow MHD shock. The flow downstream of a slow shock is hyperbolic, sub-Alfvenic and subsonic. In the hyperbolic flow region, solutions of the interaction equations (10) and (11) represent (obtuse) Mach angle μ with

$$\cos \mu = -\left(\frac{a^2}{U^2} - 1\right)^{\frac{1}{2}}\left(\frac{c^2}{U^2} - 1\right)^{\frac{1}{2}} \tag{17}$$

(Sears and Resler, 1961). Successive slow waves travel upstream faster than the preceding ones, so that they overtake and combine with each other to form a slow shock upstream of the sub-Alfvenic and subsonic hyperbolic flow region.

In contrast with the jump conditions for fast MHD shocks, B and θ decrease across a slow shock. β increases due to the sudden rise in the thermal pressure and the drop in the magnetic pressure. However, p*, as well as ρ and T, always increase. The possible existence of coronal slow shocks can significantly revise our understanding on the dynamical structure of the global solar wind.

References

Belcher, J.W., and L. Davis, Jr., Large-Amplitude Alfven Waves in the Interplanetary Medium, 2, J. Geophys. Res., 76, 3534, 1971.

Pizzo, V.J., A Three-Dimensional Model of Corotating Streams in the Solar Wind, 3, Magnetohydrodynamic Streams, J. Geophys. Res., 87, 4374, 1982.

Pneuman, G.W., and R.A. Kopp, Gas-Magnetic Field Interaction in the Solar Corona, Solar Phys., 18, 258, 1971.

Sears, W.R., and E.L. Resler, Jr., Sub- and Super-Alfvenic Flows Past Bodies, Adv. Aerospace Sci., 3-4, 637, 1961.

Whang, Y.C., A Magnetohydrodynamic Model for Corotating Interplanetary Structures, J. Geophys. Res., 85, 2285, 1980.

Whang, Y.C., and T.H. Chien, Magnetohydrodynamic Interaction of High-Speed Streams, J. Geophys. Res., 86, 3263, 1981.

Whang, Y.C., Slow Shocks Around the Sun, Geophys. Res. Letters, 9, 1081, 1982.

Whang, Y.C., Expansion of the Solar Wind from a Two-Hole Corona, to appear in Solar Phys., 1983.

DYNAMICAL EVOLUTION OF INTERPLANETARY MAGNETIC FIELDS AND FLOWS BETWEEN 0.3 AU AND 8.5 AU: ENTRAINMENT

L. F. Burlaga
NASA/Goddard Space Flight Center
Laboratory for Extraterrestrial Physics
Greenbelt, MD 20771

R. Schwenn and H. Rosenbauer
Max-Planck-Institut fur Aeronomie
Katlenburg-Lindau 3, Federal Republic of Germany

ABSTRACT

The radial evolution of interplanetary flows and associated magnetic fields between 0.3 AU and 8.5 AU was analyzed using data from Helios 1 and Voyager 1, respectively. During a 70-day interval in 1980 Voyager 1 observed two streams which appeared to be recurrent and which had little fine structure. The corresponding flows observed by Helios 1 were much more complex, showing numerous small streams, transient flows and shocks as well as a few large corotating streams. It is suggested that in moving to 8 AU the largest corotating streams swept up the slower flows (transient and/or corotating streams) and shocks into a relatively thin region in which they coalesced to form a single large-amplitude compression wave. We refer to this combined process of sweeping and coalescence as "entrainment". The resulting large-amplitude compression wave is different from that formed by the steepening of a corotating stream from a coronal hole, because different flows from distinct sources, with possibly different composition and magnetic polarity, are brought together to form a single new structure. As a result of entrainment, memory of the sources and flow configurations near the sun is lost. Small-scale features are erased as the flows move outward and energy is transferred from small scales to large scales by entrainment. Thus in the outer solar system the structure of the solar wind may be dominated by large scale pressure waves (compressions followed by rarefactions) separated by several AU. Beyond several AU most of the compression waves are no longer driven by streams, and the compression waves expand freely. At large distances ($\gtrsim$ 25 AU) they will have interacted extensively with one another producing yet another state of the solar wind, with fewer large-scale non-uniformities and more small-scale non-uniformities.

729

ON THE FIELD CONFIGURATION IN MAGNETIC CLOUDS

H. Goldstein
Max-Planck-Institut für Aeronomie
3411 Katlenburg-Lindau, FRG

ABSTRACT

Interplanetary magnetic clouds are represented by cylindrically symmetric equilibrium solutions of the MHD-equations. The radial magnetic pressure gradient of the force-free field is balanced by the curvature stress. The field inside is essentially parallel to the cylinder axis, far outside it is oriented in azimuthal direction. These configurations therefore differ from the non-selfconsistent model proposed by Klein and Burlaga (1982), where the field lines are tightly wound even near the axis.

1. Introduction

Interplanetary magnetic clouds are defined as extended regions ($\sim$ 0.25 AU at 1 AU) in which the magnetic field strength is higher than average, the magnetic pressure exceeds the ion pressure and the field vector rotates parallel to a plane (Klein and Burlaga, 1982). A unique model for the magnetic field does not exist, but a number of different configurations seem to be consistent with the results of a minimum variance analysis (Burlaga and Behannon, 1982). However, these models were not required to be solutions of the MHD-equations so far. In this paper we present such selfconsistent configurations, which for simplicity are cylindrically symmetric as in the model proposed by Klein and Burlaga. Two observational facts can then be understood in a different way as before. Firstly, in most cases the direction of minimum variance is essentially the radial direction. Secondly, the higher (magnetic) pressure inside the cloud does not imply a rapid expansion, but the observed flow-velocity v in the comoving frame is smaller than the Alfvén-velocity v_A.

2. The Model

We start out from the momentum equation in a frame moving with the cloud, which is assumed to be a time-independent configuration.

$$\rho \, \underline{v} \cdot \nabla \underline{v} = - \nabla p + \frac{1}{c} \, \underline{j} \times \underline{B} \tag{1}$$

Since $c |\rho \, \underline{v} \cdot \nabla \underline{v}| / |\underline{j} \times \underline{B}| \sim v^2/v_A^2 \ll 1$ and $c |\nabla p| / |\underline{j} \times \underline{B}| \sim p / (B^2/8\pi) \ll 1$. the convective term and the pressure gradient can be neglected in first approximation, such that the magnetic field is force-free, i.e. $\underline{j} \times \underline{B} = 0$ or by Ampere's law:

$$- \nabla B^2 + 2 \, (\underline{B} \cdot \nabla) \, \underline{B} = 0. \tag{2}$$

For our model we use cylindrical coordinates r, ϕ, z and assume that the magnetic field depends only on r:

$$- \frac{d}{dr} (B_\phi^2 + B_z^2) - \frac{2 B_\phi^2}{r} = 0 \qquad (3)$$

The radial component B_r is zero because of $\nabla \cdot \overline{B} = 0$. The general solution can be given in terms of a generating function $F(r) = B_\phi^2 + B_z^2$ (Schlüter, 1957):

$$B_\phi^2 = - \frac{r}{2} \frac{dF}{dr} \qquad B_z^2 = \frac{1}{2r} \frac{d(r^2 F)}{dr} \qquad (4)$$

Since B_ϕ^2 and B_z^2 are not negative, $F(r)$ has to be chosen such that $0 \geq \frac{dF}{dr} \geq - \frac{2F}{r}$. Therefore the magnetic field strength has a maximum on the axis. Equation (3) shows that the gradient of the magnetic pressure is balanced by the curvature stress. If the current density and the total current are finite, the field is oriented along the axis near the center and directed in azimuthal direction far outside. Therefore the field lines cannot be tightly wound near the axis as proposed by the model of Klein and Burlaga.

It is interesting to study the consequences for a minimum variance analysis. Figure 1 shows a configuration with its axis in the equatorial plane perpendicular to the radial direction $\underline{R}$. During the passage of this cloud a spacecraft would observe a rotation of the magnetic field vector $\overline{B}$ from a southward to a northward direction in a plane perpendicular to $\underline{R}$ so that $\underline{R}$ is the direction of minimum variance. The cylinder axis is oriented along the direction of medium variance. These results fully agree with the observations as summarized by Burlaga and Behannon, however, we give a different interpretation here.

3. Summary and Conclusion

Magnetic clouds can be represented by cylindrically symmetric equilibrium configurations, which are force-free solutions of the MHD-equations. The magnetic pressure gradient is balanced by the curvature stress of the field lines. The results of a minimum variance analysis as reported by Klein and Burlaga (1982) and by Burlaga and Behannon (1982) are consistent with configurations where the cylinder-axis is oriented parallel to the ecliptic plane and perpendicular to the radial direction. However, the search for magnetic clouds was restricted so far to cases where the field vector rotates from a northward to a southward direction or vice versa. Therefore it can be expected that different orientations of the cylinder-axis are possible. Probably, thick sector boundaries (Klein and Burlaga, 1980) may be understood as magnetic clouds with their axis normal to the ecliptic plane.
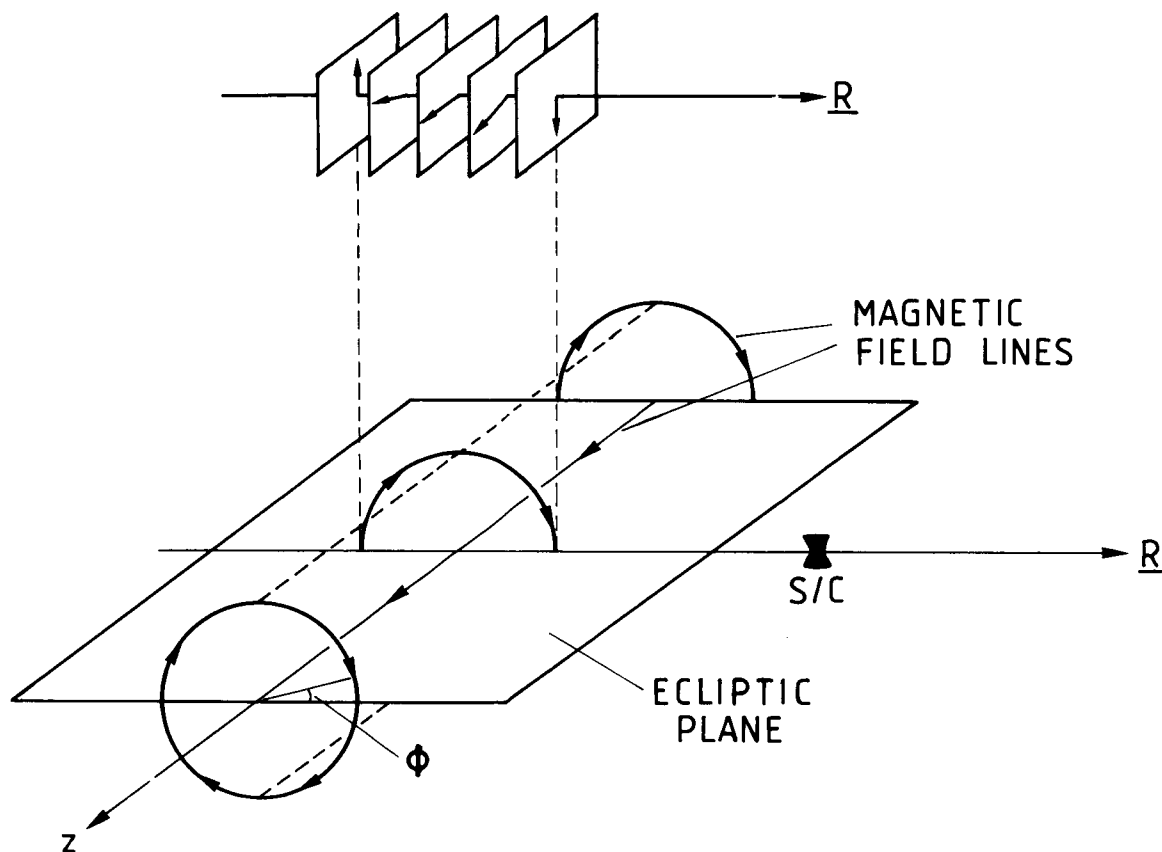
Figure 1. Cylindrical magnetic cloud with its axis in the equatorial plane perpendicular to the radial direction R. The magnetic field lines are circular far outside and straight lines parallel to the z-axis inside. When this configuration passes a spacecraft (S/C) a rotation of the field vector in a plane perpendicular to R is observed. This is illustrated in the upper part of the figure (compare with the observations sketched in figure 7 in Burlaga and Behannon (1982)). R is the direction of minimum variance and the axis is oriented parallel to the direction of medium variance.

References

Burlaga, L.F., and K.W. Behannon, Magnetic clouds: Voyager observations between 2 and 4 AU, Solar Physics 81, 181, 1982
Klein, L., and L.F. Burlaga, Interplanetary sector boundaries 1971-1973, J. Geophys. Res., 85, 2269, 1980
Klein, L., and L.F. Burlaga, Interplanetary magnetic clouds at 1 AU, J. Geophys. Res., 87, 613, 1982
Schlüter, A., Kraftfreie Magnetfelder II, Z. Naturforschung, 12a, 855, 1957

SOME SIMULATED CHARACTERISTICS OF MAGNETIC CLOUDS

M. Dryer[1], S. T. Wu[2], and G. Gislason[3]
1 - Space Environment Laboratory, NOAA, Boulder, CO 80303.
2 - University of Alabama at Huntsville, Huntsville, AL 35899.
3 - University of Alaska, Fairbanks, AK 99701.

In a number of recent MHD simulations of solar flare-generated shocks, we have examined some characteristics of the disturbed interplanetary plasma and interplanetary magnetic field in the light of recent descriptions (Klein and Burlaga, 1982) of magnetic clouds. Although our model incorporates all three components of the IMF and plasma velocity, we have confined attention primarily to shock pulses that are confined to the solar equatorial plane. The coupled motions in the north-south direction are, therefore, minor. Thus, we can consider the solar equatorial plane to be, essentially, the plane of minimum variance for the B_θ component.

We found that our results, for high velocity shocks, provide the following characteristics: the IMF magnitude is high and the direction changes appreciably by means of significant rotation of $\underline{B}$ nearly parallel to the solar equatorial plane; plasma β is low (< 1.0); and cold regions (i.e., less than ambient temperatures) are simulated within "clouds" having radial dimensions $\sim$0.25 AU (at 1.0 AU) that experienced continued expansion as they moved in the anti-sunward direction. These features have been described within a set of 45 events (out of a total of 70) described by Klein and Burlaga. In view of the fact that we considered the usual, "canonical", ambient spiral IMF without reconnection anywhere, our MHD simulations suggest that many features of shock-associated magnetic clouds can be understood in the context of a globally-restricted IMF that is temporarily twisted by the expanding shock wave. Hence, closed magnetic bubbles, caused by a reconnecting IMF, are not necessary to produce the observed symptoms of "clouds".

INTERACTION OF THE PLASMA TAIL OF COMET BRADFIELD 1979L
ON 1980 FEBRUARY 6 WITH A POSSIBLY FLARE-GENERATED
SOLAR-WIND DISTURBANCE

Malcolm B. Niedner, Jr. and John C. Brandt
Laboratory for Astronomy and Solar Physics
NASA Goddard Space Flight Center
Greenbelt, MD 20771

R. D. Zwickl and S. J. Bame
Space Physics Group
Los Alamos Scientific Laboratory
Los Alamos, NM 87545

ABSTRACT

Solar-wind plasma data from the ISEE-3 and Helios 2 spacecraft have been examined in order to explain a uniquely rapid $10°$ turning of the plasma tail of comet Bradfield 1979l on 1980 February 6. An earlier study conducted before the availability of _in situ_ solar-wind data (Brandt _et al._, 1980) suggested that the tail position angle change occurred in response to a solar-wind velocity shear across which the polar component changed by ~ 50 km s^{-1}. The present contribution confirms this result and further suggests that the comet-tail activity was caused by non-corotating, disturbed plasma flows probably associated with an Importance 1B solar flare.

Introduction

It is widely believed that most (if not fully all) rapid and large-scale changes in the plasma tails of comets are caused by structures and disturbances in the solar wind (Biermann and Lüst, 1963; Brandt and Mendis, 1979; Niedner and Brandt, 1980). This coupling is a result of the strong interaction which takes place between the magnetized solar wind and the sunward cometary ionosphere via mass loading of the solar wind by CO^+ and other cometary molecular ions. The basic picture of the plasma tail is of a magnetic flux tube consisting of swept-up interplanetary magnetic field (IMF) and guiding ions initially created in the head region in a small ($<10^3$ km) production zone (Alfvén, 1957). Thus, the tail is formed in a manner similar to that of the Venusian magnetotail (cf. Russell _et al._, 1982). The detailed physics of the comet/solar-wind interaction have recently been summarized for the head region by Schmidt and Wegmann (1982) and by Ip and Axford (1982), and for the tail region by Brandt (1982; also see Ip and Axford, 1982).

The branch of cometary study which examines associations between comet-tail transients and solar-wind structures is a dual one in the sense that _in situ_ solar-wind measurements are often necessary to establish the cause of a particular plasma-tail disturbance, whereas classes of tail transients whose solar-wind cause(s) are _generally_ well known may be used as solar-wind probes when _in situ_ coverage is lacking. This latter aspect--the use of comets as interplanetary probes--is especially important for high-latitude solar-wind studies and examples are the use of tail orientations as diagnostics of the global solar-wind velocity structure over many solar cycles (e.g., Brandt _et_

al., 1972), and plasma tail disconnection events as probable sector boundary markers (Niedner, 1982).

The 10° turning (on the plane of the sky) of the inner plasma tail axis of comet Bradfield 1979l which occurred on 1980 February 6, and which was reported by Brandt et al. (1980), is primarily an example of the first kind of cometary/solar-wind associations. The comet was a low ecliptic latitude (−5°3) object less than 0.5 AU from Earth—geometric circumstances ideal for establishing a solar-wind association—but the unavailability of interplanetary solar-wind measurements at the time of the original study (Brandt et al., 1980) restricted the analysis to a general windsock approach in which the observed tail position angle variation yielded an infinite set of vector solar-wind velocity solutions (due to the 2-D nature of the photographs). The explanation considered most likely by Brandt et al. was that the comet encountered a ~50 km s^{-1} shear in the polar component of the solar-wind speed in <30 minutes. The reader is referred to Brandt et al. (1980) for additional details.

The purpose of the present comment is to report an updated analysis based on recently available ISEE-3 and Helios 2 plasma data (Helios 2 data were kindly made available by H. Rosenbauer and R. Schwenn through the National Space Science Data Center, Greenbelt, MD). The study confirms and extends some of Le Borgne's (1982) conclusions based on the same cometary and spacecraft data.

Spacecraft Observations

The relative positions of comet Bradfield, Helios 2, and ISEE-3 at the time of the tail turning on 1980 February 6.1 UT are shown in Figure 1.
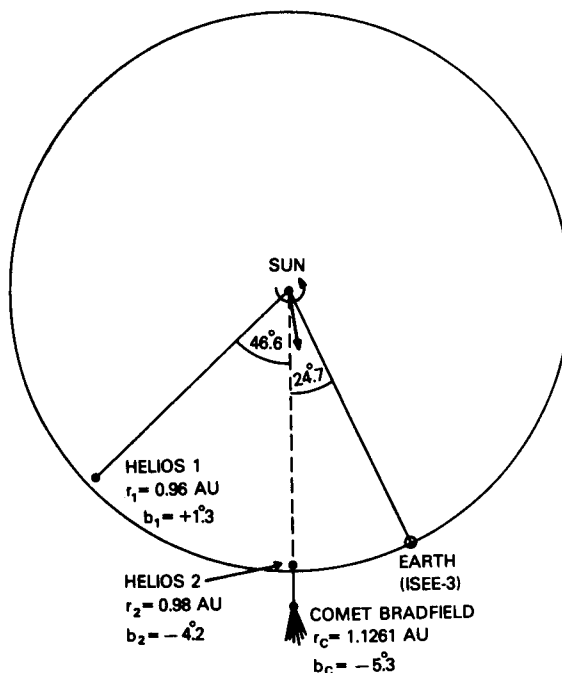

Figure 1. Ecliptic plane projection of comet Bradfield and the three spacecraft—ISEE-3, Helios 2, and Helios 1—which were making solar-wind measurements near the time of the comet-tail disturbance on 1980 February 6.1 UT. The cited latitudes are ecliptic.
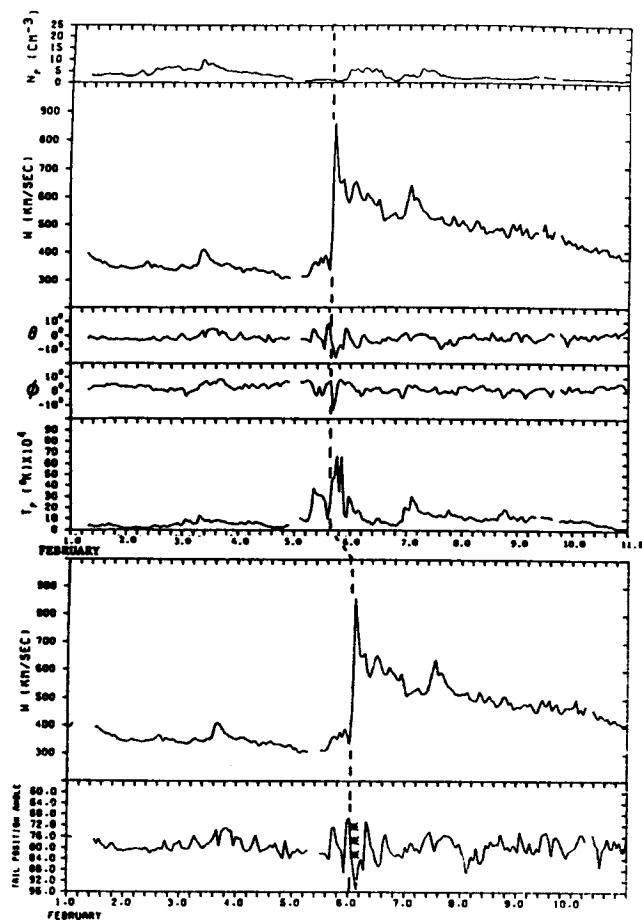
738

Figure 2. Top five panels present Helios 2 solar-wind plasma data (1-hour averages) for 1980 Febr. 1-11. From top: proton number density N_p, bulk speed W, polar flow angle θ, azimuthal flow angle ϕ, and proton temperature T_p. The lower two panels contain the bulk speed measured by Helios 2 and theoretical comet-tail position angles generated from the Helios 2 data, both shifted to the comet's position.
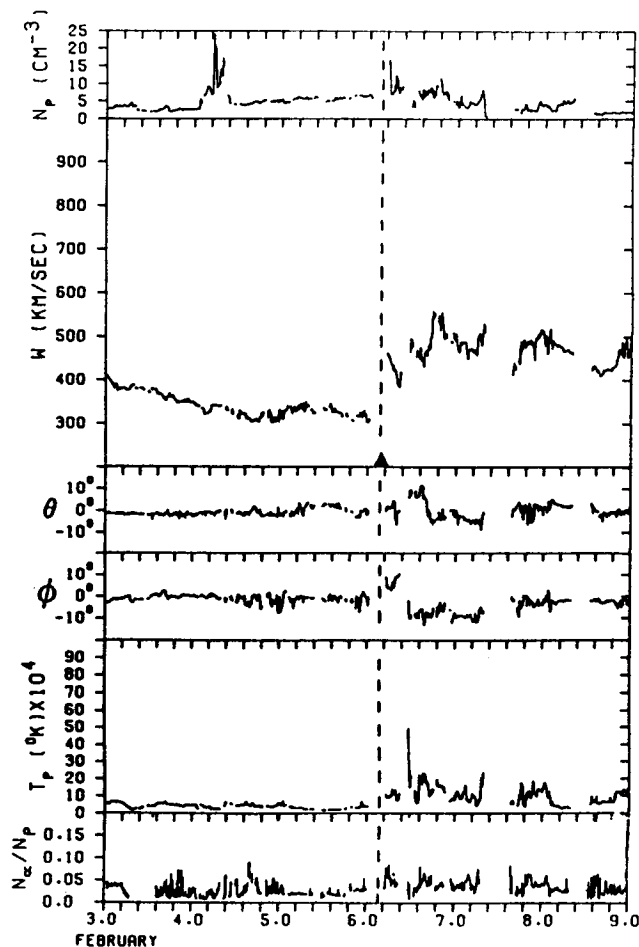
Figure 3. ISEE-3 solar-wind plasma measurements (5-minute averages) for 1980 February 3-9. The plotted quantities are identical to those in the top five panels in Figure 2 with the addition, in the last panel, of the fractional helium abundance N_α/N_p.

Although the position of Helios 1 is also shown, the present paper will address only plasma data from Helios 2 and ISEE-3. It is important to note that the comet was observed at the low ecliptic latitude of $-5°3$ and that Helios 2 was $< 1°$ off the Sun-comet line (in longitude). Specifically, Helios 2 was 0.15 AU almost directly upstream of the comet and hence should have observed, some short time (<0.5 days) earlier, whatever solar-wind feature created the comet-tail disturbance. The relatively small separation of the comet and ISEE-3 (longitudinal separation $\sim 25°$) also favored the observation of any associated solar-wind structure by ISEE-3.

Data from the Helios 2 plasma detector (H. Rosenbauer, PI) are shown in the top five panels of Figure 2. The data are one-hour averages. The feature of maximum interest is the $\Delta W = 300-500$ km s^{-1} increase in the bulk speed which took place in less than 2 hours on ~February 5.6 UT. By its steep slope, this feature looks more like an interplanetary shock (see Figure 1 of Borrini et al., 1982) than the (much more slowly changing) leading edge of a corotating high-speed stream (see Figure 1 of Gosling et al., 1978), but a feature of this structure which is distinctly unlike both shocks and streams is the lack of a density spike or compression region accompanying the velocity rise (R. Schwenn, private communication). Le Borgne (1982) has discussed this interesting aspect and further commented on the region of exceptionally low proton density ($N_p <1$ cm^{-3}) preceding the velocity rise.

The lower two panels of Figure 2 show, respectively, the Helios 2 bulk velocity data shifted to the comet on the assumption of radial propagation at approximately constant wind speeds of 600 km s^{-1}, and theoretical comet-tail position angles calculated from the windsock theory (Brandt and Rothe 1976) and the shifted Helios 2 flow angles. The asterisks are position angles measured from the three photographs presented in Brandt et al. (1980). Note the very close agreement between the predicted arrival time of the velocity feature at the comet and the time of the tail disturbance. Also significant is the very close match-up of the observed position angle variation with a steep, predicted variation caused mainly by a ~20° change in the polar flow angle immediately following the velocity increase.

Figure 3 shows 5-minute averaged data for the same time period from the Los Alamos plasma instrument on ISEE-3. The format is similar to Figure 2 except for the last panel, which gives the fractional helium abundance N_α/N_p. Despite the presence of a ~4^{h}40^m data gap, a ~150 km s^{-1} velocity rise can be seen starting early on February 6. An associated storm sudden commencement (ssc), shown on the abscissa of the velocity panel, occurred at 3^{h}20^m UT. Although of lesser amplitude and smaller maximum speed (600 vs. >800 km s^{-1}), the velocity feature seen by ISEE-3 is almost certainly the same structure as was observed by Helios 2 ~12 hours earlier.

Definitive resolution of the question of origin of the velocity feature is not possible here, but it is noteworthy that the 12 hr. time delay, when combined with the ~25° longitude separation between Helios 2 and ISEE-3, is incompatible with a corotating stream hypothesis ($\dot\Phi = 50°4$/day, $P = 7.1$ days). At the present time we favor a flare origin for this feature although the lack of a density spike prevents its classification as an interplanetary shock. The candidate flare is the same as that mentioned by Le Borgne (1982): 1980 February 3, ~13:28 UT, S15E15, Importance 1B, with associated Type IV radio emission (Le Borgne actually quotes the Solar Geophysical Data Prompt Reports

position of N18E13, which was in error; the group line average for the same flare in the Comprehensive Reports is S15E15). It should be pointed out that probably not all five days of elevated solar-wind speed at Helios 2 (Figure 2) contain actual flare ejecta; as discussed by Borrini et al. (1982), the general persistence of high-speed wind for several days during flare-induced interplanetary disturbances may be due to a magnetic re-arrangement of the corona at and near the flare site.

The projected flare meridian is shown in Figure 1 as the Sun-centered linear arrow. Note its close proximity to the Sun-comet/Helios 2 line ($\Delta\Phi = 7°5$) and the larger distance to ISEE-3 ($\Delta\Phi = 17°5$). If it had a flare origin as tentatively suggested here, then the larger amplitude and maximum speed of the velocity structure at Helios 2 is qualitatively in agreement with many models of flare-generated interplanetary disturbances (e.g., DeYoung and Hundhausen, 1973; D'Uston et al., 1977; Borrini et al., 1982) which predict maximum plasma speeds and minimum transit times at or near the flare longitude. Assuming identification with the above-mentioned flare, the mean transit speeds between the Sun and spacecraft were 815 km s^{-1} (Helios 2) and 662 km s^{-1} (ISEE-3); the resulting longitudinal gradient of ~15 km s^{-1} deg^{-1} is approximately double the values resulting from D'Uston et al.'s (1981) models.

Summary

In summation:
1.) A solar-wind disturbance seen in both the Helios 2 and ISEE-3 plasma data was found which produced the tail turning event in comet Bradfield. Theoretical tail position angles generated from the in situ data showed that the tail event was probably caused by an observed shear in the polar speed component immediately behind a large rise in the bulk speed (ΔW = 300-500 km s^{-1}), thus confirming the earlier study by Brandt et al. (1980).

2.) Observations of the feature's arrival times at ISEE-3 and Helios 2 strongly suggest a non-corotating trajectory. Although the lack of a density enhancement prohibits classfication of this system as an interplanetary shock ensemble, a plausible solar flare origin for the feature is proposed (as first suggested by Le Borgne, 1982).

3.) The study clearly underscores the sensitivity of cometary plasma tails to sudden large-scale changes in the bulk flow of the solar wind.

References

Alfvén, H., On the Theory of Comet Tails, Tellus, 9, 92, 1957.
Biermann, L., and Rh. Lüst, Comets: Structure and Dynamics of Tails, in The Moon, Meteorites and Comets (B. M. Middlehurst and G. P. Kuiper, eds.) (Univ. of Chicago Press), p. 618, 1963.
Borrini, G., J. T. Gosling, S. J. Bame, and W. C. Feldman, An Analysis of Shock Wave Disturbances Observed at 1 AU from 1971 through 1978, J. Geophys. Res., 87, 4365, 1982.
Brandt, J. C., Observations and Dynamics of Plasma Tails, in Comets (L. L. Wilkening, Ed.) (Univ. of Arizona Press), p. 519, 1982.

Brandt, J. C., J. D. Hawley, and M. B. Niedner, A Very Rapid Turning of the Plasma-Tail Axis of Comet Bradfield 19791 on 1980 February 6, Astrophys. J. (Lett.), 241, L51, 1980.

Brandt, J. C., and D. A. Mendis, The Interaction of the Solar Wind with Comets, in Solar System Plasma Physics. Volume II (C. F. Kennel et al., eds.) (North-Holland Publishing Co.), p. 255, 1979.

Brandt, J. C., R. G. Roosen, and R. S. Harrington, Interplanetary Gas XVII. An Astrometric Determination of Solar-Wind Velocities from Orientations of Ionic Comet Tails, Astrophys. J., 177, 277, 1972.

Brandt, J. C., and E. D. Rothe, The Wind-Sock Theory of Comet Tails, in The Study of Comets (B. Donn et al., eds.) (NASA SP-393), p. 878, 1976.

DeYoung, D. S., and A. J. Hundhausen, Simulation of Driven Flare-Associated Disturbances in the Solar Wind, J. Geophys. Res., 78, 3633, 1973.

D'Uston, C., J. M. Bosqued, F. Cambou, V. V. Temny, G. N. Zastenker, O. L. Vaisberg, and E. G. Eroshenko, Energetic Properties of Interplanetary Plasma at the Earth's Orbit following the August 4, 1972 Flare, Solar Phys., 51, 217, 1977.

Gosling, J. T., J. R. Asbridge, S. J. Bame, and W. C. Feldman, Solar Wind Stream Interfaces, J. Geophys. Res., 79, 1349, 1978.

Ip, W.-H., and W. I. Axford, Theories and Physical Processes in the Cometary Comae and Ion Tails, in Comets (L. L. Wilkening, Ed.) (Univ. of Arizona Press), p. 588, 1982.

Le Borgne, J.-F., Comet Bradfield 1979X Event on 1980 February 6: Correlation with an Interplanetary Solar Wind Disturbance, Proceedings of ESO Workshop "The Need for Coordinated Ground-based Observations of Halley's Comet", p. 217, 1982.

Niedner, M. B., Interplanetary Gas XXVIII. A Study of the Three-Dimensional Properties of Interplanetary Sector Boundaries Using Disconnection Events in Cometary Plasma Tails, Astrophys. J. (Suppl.), 48, 1, 1982.

Niedner, M. B., and J. C. Brandt, Structures Far from the Head of Comet Kohoutek II. A Discussion of the Swan Cloud of January 11 and of the General Morphology of Cometary Plasma Tails, Icarus, 42, 257, 1980.

Russell, C. T., J. G. Luhmann, R. C. Elphic, and M. Neugebauer, Solar Wind Interaction with Comets: Lessons from Venus, in Comets (L. L. Wilkening, Ed.) (Univ. of Arizona Press), p. 561, 1982.

Schmidt, H. U., and R. Wegmann, Plasma Flow and Magnetic Fields in Comets, in Comets (L. L. Wilkening, Ed.) (Univ. of Arizona Press), p. 538, 1982.

1. Report No. NASA CP-2280	2. Government Accession No.	3. Recipient's Catalog No.
4. Title and Subtitle SOLAR WIND FIVE		5. Report Date November 1983
		6. Performing Organization Code
7. Author(s) Marcia Neugebauer, Editor		8. Performing Organization Report No.
		10. Work Unit No.
9. Performing Organization Name and Address Jet Propulsion Laboratory 4800 Oak Grove Drive Pasadena, CA 91109		11. Contract or Grant No.
		13. Type of Report and Period Covered Conference Publication
12. Sponsoring Agency Name and Address Office of Space Science and Applications Astrophysics Division National Aeronautics and Space Administration, Washington, DC 20546		14. Sponsoring Agency Code

15. Supplementary Notes

16. Abstract

This volume contains the proceedings of a conference held in Woodstock, Vermont, November 1-5, 1982. Topics include the solar corona, MHD waves and turbulence, solar wind acceleration, stellar coronae and winds, long-term variations in the solar wind, plasma distribution functions and waves, energetic particles, spatial dependences, minor ions, and dynamics or transient events. The proceedings include 6 session summaries, 65 papers, and 20 abstracts of papers presented at the conference but published elsewhere.

17. Key Words (Suggested by Author(s)) Solar wind Interplantary medium Sun, Solar corona, Stellar winds	18. Distribution Statement Unclassified - Unlimited Subject Category 92	
19. Security Classif. (of this report) Unclassified	20. Security Classif. (of this page) Unclassified	21. No. of Pages 751	22. Price A99

N-305